# Proceedings of the ICFA mini-Workshop on Mitigation of Coherent Beam Instabilities in Particle Accelerators

Zermatt, Switzerland, 23–27 September 2019

Editors:
E. Métral, CERN
G. Rumolo, CERN
T. Pieloni, EPFL

ISBN 978-92-9083-588-2 (paperback)
ISBN 978-92-9083-589-9 (PDF)
ISSN 2519-8084 (Print)
ISSN 2519-8092 (Online)
DOI http://dx.doi.org/10.23732/CYRCP-2020-009

Copyright © CERN, 2020

Creative Commons Attribution 4.0

This report should be cited as:

Proceedings of the ICFA mini-Workshop on Mitigation of Coherent Beam Instabilities in Particle Accelerators, Zermatt, Switzerland, 23–27 September 2019, E. Métral, G. Rumolo, T. Pieloni (eds.), CERN-2020-009 (CERN, Geneva, 2020), http://doi.org/10.23732/CYRCP-2020-009

A contribution in this report should be cited as:

[Author name(s)], in Proceedings of the ICFA mini-Workshop on Mitigation of Coherent Beam Instabilities in Particle Accelerators, Zermatt, Switzerland, 23–27 September 2019, E. Métral, G. Rumolo, T. Pieloni (eds.), CERN-2020-009 (CERN, Geneva, 2020), pp. [first page]–[last page], http://doi.org/10.23732/CYRCP-2020-009.[first page]

Corresponding editor: Elias.Metral@cern.ch

Accepted in December 2020 by the CERN Reports Editorial Board (contact Carlos.Lourenco@cern.ch).

Published by the CERN Scientific Information Service (contact Jens.Vigen@cern.ch).

Indexed in the CERN Document Server and INSPIRE.

Published Open Access to permit its wide dissemination, as knowledge transfer is an integral part of the mission of CERN.

## Abstract

This ICFA Mini-Workshop on "Mitigation of Coherent Beam Instabilities in Particle Accelerators" (MCBI2019) focused on all the mitigation methods for all the coherent beam instabilities, reviewing in detail the theories (and underlying assumptions), simulations and measurements on one hand, but on the other hand trying to compare the different mitigation methods (e.g. with respect to other effects such as beam lifetime) to provide the simplest and more robust solutions for the day-to-day operation of the machines.


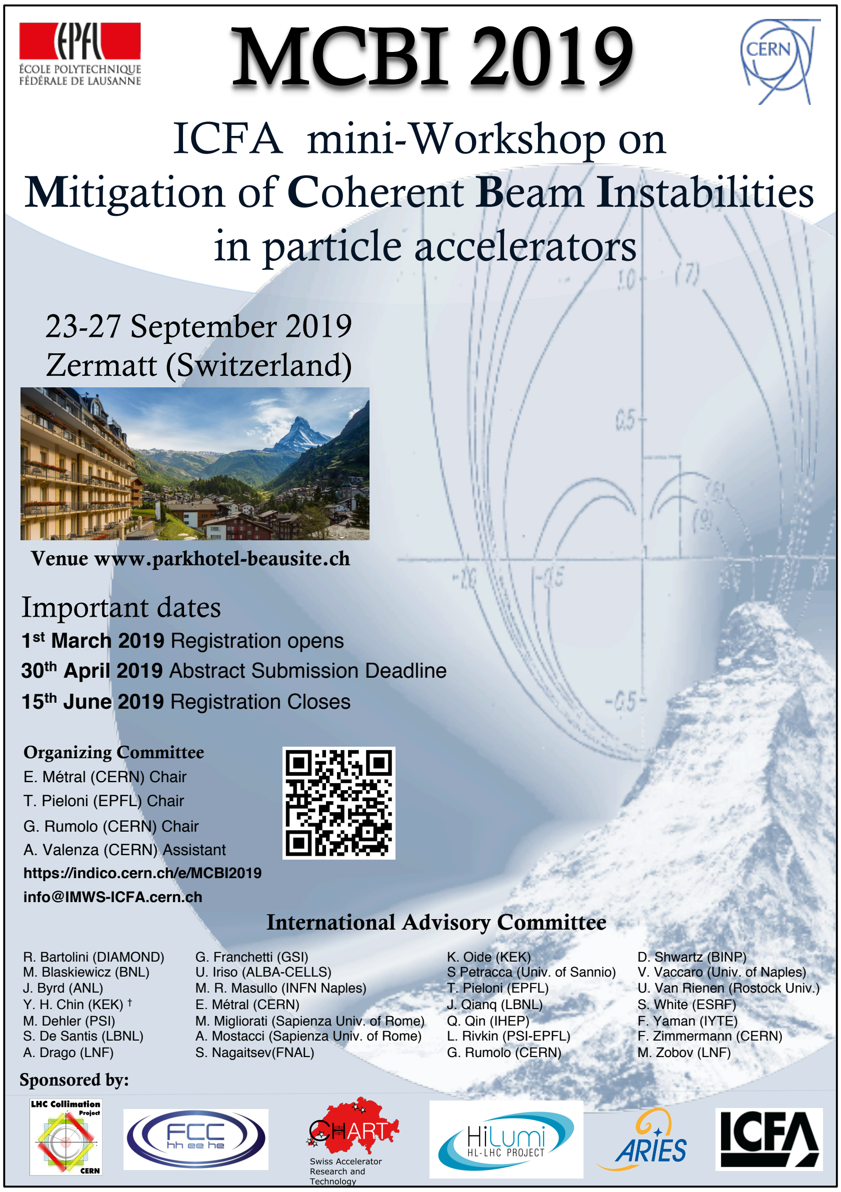

**Preface**

From 23 to 27 September, 2019, more than 90 world experts gathered in the small village of Zermatt in Switzerland for the ICFA mini-Workshop on "Mitigation of Coherent Beam Instabilities in Particle Accelerators" (MCBI 2019). The group photo was taken with the iconic Matterhorn mountain as background (Fig. 1). Three quarters of the participants came from Europe while the last quarter was split between North America and Asia.

Figure 1: Group photo showing many of the 92 participants.

The detailed program and talks are available via the workshop website: https://indico.cern.ch/event/775147/. We would like to thank all the sponsors (https://indico.cern.ch/event/775147/attachments/1797894/3222764/Sponsors.pdf), who with their contributions made it possible to organize the workshop in this beautiful location: ARIES[1], CHART (Swiss Accelerator Research and Technology), the FCC study, the HL-LHC project, ICFA, the LHC Collimation project and the University of Sannio (where the previous workshop of the series took place). CHART together with EPFL supported and sponsored the students' participation to the workshop by offering a reduced registration fee and the best student poster prize.

[1] Funded under H2020-EU.1.4.1.2., grant agreement ID: 730871 (https://cordis.europa.eu/project/id/730871)

# A GENERAL OVERVIEW OF THE MCBI 2019 ICFA MINI-WORKSHOP

E. Métral† and G. Rumolo, CERN, Geneva, Switzerland
T. Pieloni, EPFL, Lausanne, Switzerland

*Abstract*

After the ICFA Mini-Workshop on "Electromagnetic Wake Fields and Impedances in Particle Accelerators" (organised by Vittorio Vaccaro, Maria Rosaria Masullo and Elias Métral) held in Erice (Sicily) from 24 to 28 April, 2014, and the ICFA Mini-Workshop on "Impedances and Beam Instabilities in Particle Accelerators" (organised by Giovanni Rumolo, Maria Rosaria Masullo and Stefania Petracca), held in Benevento (Italy) from 18 to 22 September, 2017, this third workshop of the series was organised jointly between CERN and EPFL and it took place in Zermatt (Switzerland) from 23 to 27 September, 2019.

This ICFA Mini-Workshop on "Mitigation of Coherent Beam Instabilities in Particle Accelerators" (MCBI2019) focused on all the mitigation methods for all the coherent beam instabilities, reviewing in detail the theories (and underlying assumptions), simulations and measurements on one hand, but on the other hand trying to compare the different mitigation methods (e.g. with respect to other effects such as beam lifetime) to provide the simplest and more robust solutions for the day-to-day operation of the machines.

## INTRODUCTION

The programme of the MCBI 2019 workshop was made with the active participation of the 27 members of the International Advisory Committee. It was sponsored and supported by ICFA, the LHC Collimation project, the FCC study, CHART (Swiss Accelerator Research and Technology), the HL-LHC project, ARIES and the University of Sannio (where the previous workshop of the series took place).

The workshop was attended by 92 participants, with 12% of students, who came from all over the world and who shared their experience to address the various subjects of the workshop. Beam stabilization is an increasingly interesting subject across the accelerator community, with new challenging beam parameters targeted for future or upgraded accelerators (high beam current, low emittance, ultra-short bunches, tight bunch spacing) and the following questions were therefore raised:

- Which tools do we have to ensure that new and upgraded machines are able to operate within their desired beam parameter range?
- Is the current modeling of all these items satisfactory or should it be improved in any of the cases?
- Are we covering all types of instabilities?
- What are the limits of current active feedback systems?
- Can we rank the methods to introduce stabilizing Landau damping?
- How far can we take impedance identification and reduction?
- Can we always disentangle the stabilizing effect of Landau damping from that of head-tail dephasing?
- Are there alternative and efficient ways to introduce Landau damping (e.g. beam-beam collisions, electron lens, RFQ)?
- Can we fold in new techniques of machine learning?
- Etc.

## MCBI 2019 WORKSHOP DEDICATED TO Y.H. CHIN AND A. HOFMANN

The MCBI 2019 workshop was dedicated to two outstanding accelerator physicists, who recently passed away (https://cds.cern.ch/record/2668914/files/vol59-issue2-p059-e.pdf): Yong Ho Chin (Fig. 1) and Albert Hofmann (Fig. 2)

Yong Ho Chin obtained his PhD in accelerator physics from University of Tokyo (Japan). He was a leading theoretical accelerator physicist from KEK and he made numerous essential contributions in the fields of beam-coupling impedances, coherent beam instabilities, RF klystron development, space-charge and beam-beam collective effects. His name is linked, in particular, to 2 computer codes he wrote and which have been widely used over the past decades: MOSES (MOde-coupling Single bunch instabilities in an Electron Storage ring) and ABCI (Azimuthal Beam Cavity Interaction). Since November 2016, he has been the chair of the ICFA beam dynamics panel.

Albert Hofmann performed his studies at ETH Zurich (Switzerland) and first worked on the Cambridge Electron Accelerator (CEA) at Harvard. He had a lifelong interest in the new discipline of Synchrotron Radiation, which he explained in detailed in his book "The Physics of Synchrotron Radiation". He moved to CERN to work on the ISR collider and when the ISR was closed, he returned to the USA, accepting a professorship at Stanford, where he could work on SLC. He came back to CERN to work on LEP and served as advisor for a number of synchrotron-radiation facilities. Albert gave many inspiring lectures at the CERN Accelerator School, simplifying, as only he could, some of the most difficult concepts in accelerator physics.

† Elias.Metral@cern.ch


Figure 1: Picture of Yong Ho Chin who passed away in 2019.

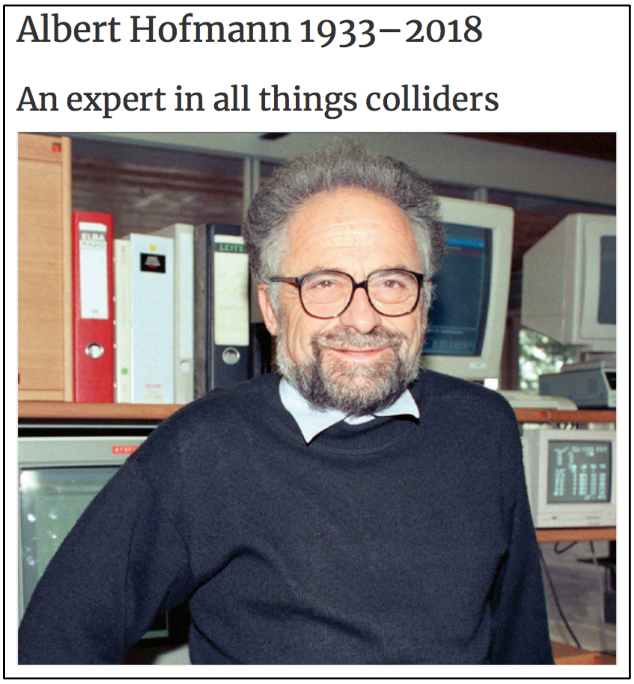


Figure 2: Picture of Albert Hofmann who passed away in 2018.

## WORKSHOP STRUCTURE AND TOPICS

During the four-day workshop, 56 talks were given distributed in 8 sessions set up by the 27 members of the International Advisory Committee: (1) Review of beam instability mechanisms and mitigations, convened by G. Rumolo (CERN); (2) Landau and BNS damping, convened by E. Métral (CERN); (3) Optics and RF knobs, convened by E. Shaposhnikova (CERN); (4) Feedbacks, convened by G. Stupakov (SLAC); (5) Identification and reduction of instability sources, convened by M. Zobov (INFN LNF); (6) Diagnostics for instability observations, convened by T. Pieloni (EPFL); (7) Interplay between coherent and incoherent effects, convened by G. Franchetti (GSI); (8) Future challenges for MCBI, convened by F. Zimmermann (CERN).

In addition to the talks, 24 posters were presented. Student posters, 14 in total, have participated to the "Best Student Poster Award", which was awarded to M. Schenk (Fig. 3). The Poster Award Committee was composed of all the session conveners and was chaired by Q. Qin (IHEP).


Figure 3: "Best Student Poster Award" awarded to M. Schenk for his work on "Longitudinal- to-transverse Landau damping: RFQ (or Q")". Next to him: Q. Qin (IHEP), chair of the Poster Award Committee.

## DISCUSSIONS AND OUTCOME

Beam instabilities, and their mitigation, cover a wide range of effects in particle accelerators and they have been the subjects of intense research for several decades. As the machines performance was pushed new mechanisms were revealed and nowadays the challenge consists in studying the interplays between all these intricate phenomena, as it is very often not possible to treat the different effects separately.

The beam coupling impedance is the first cause of coherent beam instabilities but many other mechanisms are important to take into account to quantitatively describe the observed instability mechanisms and thresholds of our particle accelerators. And not only all these mechanisms have to be understood separately, but all the possible interplays between the different phenomena need to be analyzed in detail, including the beam coupling impedance (both driving and detuning ones in the transverse planes), the linear and nonlinear chromaticity, the transverse damper (including a detailed description versus frequency of the gain, the bandwidth and the noise), the Landau octupoles (and other intrinsic nonlinearities), space charge, beam-beam (with both long-range and head-on effects for colliders), electron cloud or/and ions, linear coupling strength, tune separation between the transverse planes (bunch by bunch), tune split between the two beams (bunch by bunch, for colliders), transverse beam separation between the two beams (for colliders), noise, etc.

For existing machines, trying to push the machine performance usually requires a detailed impedance model and a systematic analysis to identify the main contributors and reduce their impedance, which requires a lot of time and resources. In case of instabilities due to additional electrons or ions, all the methods to try and reduce/suppress the later should be put in place (it is worth noting for instance that nanostructuring of material surfaces by laser ablation is a well-established science and manufacturing with more than 25 years of experience). In many machines, longitudinal and transverse feedbacks exist and realistic modellings of them need to be included in the beam stability analyses, as they considerably modify both coupled-bunch and single-bunch motions (it is worth noting that in some machines, many feedbacks are used: 35 feedback loops are used for instance in the CERN PS machine for the LHC-type beams!). Feedbacks are working very well but they cannot, at the moment (this might change in the future if we succeed to reach the necessary bandwidth), damp all types of instabilities. And in some cases, destabilising effects from feedbacks can also be observed. Therefore, the next step is to optimise the machine linear and nonlinear optics (tunes, linear and nonlinear chromaticity, amplitude detuning, linear coupling, transition energy, etc.) and the RF knobs (such as RF voltage or controlled longitudinal emittance) and rely on Landau damping. However, a trade-off between coherent beam stability and single-particle stability (i.e. dynamic aperture) needs to be found and all the sources of Landau damping should be considered and studied carefully together: some interplays can be beneficial and some others can be detrimental. Furthermore, it was recently found that the stability diagram (deduced from the analysis of Landau damping for independent coherent beam modes) can significantly evolve with time in the presence of noise, which could then be detrimental to the "long-term" beam stability. Landau octupoles are usually used to provide Landau damping in the transverse plane but some other proposals have been made, such as using beam-beam (long-range and/or head-on) in colliders, or an electron lens (which is doing something similar in non-collider rings), or an RFQ (which has a similar effect as the second-order chromaticity Q", providing longitudinal-to-transverse Landau damping). I. Hofmann, the chair of the ICFA Beam Dynamics panel, motivated the whole community to work more on the effect of Landau damping, as there is still a lot to be done on Landau damping and its possible loss, looking in more detail to theories, simulations and measurements (e.g. with BTF, Beam Transfer Function, or, as recently proposed, using an anti-damper as a controlled source of impedance).

For future machines, it is recommended to try and integrate all the above aspects already in the design stage, i.e. reduce as much as possible the impedance and electron cloud (surface) effects (in close collaboration with all the equipment groups) and optimise the optics design by including already from the beginning all the collective effects (such as IBS, etc.).

Finally, knowledge transfer and collaboration between experts and operations are key to ensure that all the teams are moving in the same direction to produce stable beams.

## CONCLUSIONS AND FUTURE

After a first workshop in 2014 on impedances and a second workshop in 2017 on impedances and instabilities, this third workshop of the series on instability mitigations closed the loop and provided a great platform to expose and debate all the scientific questions raised above.

Beam instabilities and their mitigation have been studied for several decades and many intricate phenomena have been revealed. They were very often treated separately in the past but since some time the need to study several mechanisms together appeared, to try and better explain the reality of our accelerators. With the increasing power of our computers this becomes easier but the need to continue and develop theories remains, to have a better understanding of the interplays between all these effects, which is the current challenge in the study of beam instabilities.

The subject of beam instabilities in particle accelerators is far from being exhausted and the community is motivated to exchange experience and join efforts to advance further. The amount of open questions, the continuing progress recorded on different fronts and the promising outlook of many studies in terms of development and search for solutions fully legitimate the quest to pursue this series of workshops and to envisage a continuation in two or three years' time. More information on this workshop, including program and slides of the single talks, can be found on the web site of the workshop (https://indico.cern.ch/event/775147/).

## ACKNOWLEDGEMENTS

We would like to thank all the workshop participants, in particular all the speakers, the poster presenters and the session chairs, who gave their active contributions to the success of this event. Concerning these proceedings, we also would like to warmly thank the many people who took the time to contribute, both as authors and as internal referees, to reach a total of 68 well-written papers. Finally, we would like to express our sincere gratefulness to Alessia Valenza and Hervé Martinet for all the workshop logistics.

# Contents

# REVIEW OF IMPEDANCE-INDUCED INSTABILITIES AND THEIR POSSIBLE MITIGATION TECHNIQUES*

M. Migliorati†, University of Rome La Sapienza and INFN-Roma1, Rome, Italy
E. Métral, CERN, Geneva, Switzerland
M. Zobov, INFN-LNF, Frascati, Italy

*Abstract*

In this paper, some important impedance-induced instabilities are briefly described for both the longitudinal and transverse planes. The main tools used nowadays to predict these instabilities and some considerations about possible mitigation techniques are also presented.

## INTRODUCTION

The first studies of impedance-induced instabilities were developed in mid-end 60s, with the initial concepts regarding dispersion relations and coupling impedance described in the first works of V. Vaccaro and A. M. Sessler [1,2]. In the following years, many influential researchers made the history of this important, intriguing, and always in fashion topic of particle accelerators. Over these 50 years a considerable amount of papers has been, and continues to be, published. Among them, without the intention of being exhaustive, we suggest to the reader the following references: [3–14].

In this paper we try to summarise the work done so far and the tools which are used nowadays to predict these impedance-induced instabilities. Of course, due to the vastness of the subject, we have to cut some of the many interesting effects that have been studied and, for others, we will just mention some aspects. Moreover, we focus only on instabilities in circular machines.

## SOME USEFUL DEFINITIONS

When a beam of charged particles traverses a device which is not a perfect conductor or is not smooth, it produces electromagnetic fields that perturb the following particles. Differently from the fields generated by magnets and RF cavities, these ones depend on beam intensity and their amplitude cannot be easily changed.

These fields are generally described in time domain through the concept of wake field, or, in frequency domain, by its Fourier transform, called coupling impedance. Their importance is due to the fact that, under some conditions, they can induce instabilities. Referring to Fig. 1, let us consider two charges, a leading one (the source) $q_1$, in the position $(z_1, \vec{r}_1)$, which, interacting with an accelerator device (the red shape that we suppose of cylindrical symmetry), produces an electromagnetic field and therefore a Lorentz force on a test charge $q$ following at a distance $\Delta z = (z_1 - z)$ and with a transverse displacement from the ideal orbit $\vec{r}$.

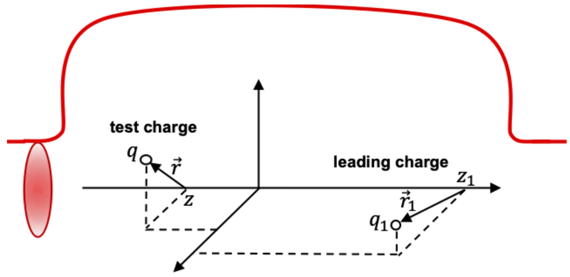


Figure 1: Sketch used for the definition of wake fields.

With this geometry, by using the rigid beam approximation (the distance between the two charges remains constant inside a device) and the impulse approximation (what it cares is the impulse) [15, 16], the effects of the longitudinal and transverse components of the Lorentz force can be separated. In the longitudinal plane the effect is summarised in an energy change:

$$U(\Delta z) = \int_{\text{device}} F_{\parallel} ds \longrightarrow w_{\parallel}(\Delta z) = -\frac{U(\Delta z)}{qq_1} \qquad (1)$$

while in the transverse plane we have a momentum kick:

$$\vec{M}(\vec{r}, \Delta z) = \int_{\text{device}} \vec{F}_{\perp} ds \longrightarrow \vec{w}_{\perp}(\Delta z) = \frac{1}{r}\frac{\vec{M}(\vec{r}, \Delta z)}{qq_1} \qquad (2)$$

Here $w_{\parallel}$ and $\vec{w}_{\perp}$ are defined as the longitudinal and the transverse dipole wake functions. For Eq. (2) we have supposed a cylindrically symmetric structure and the speed of light, otherwise also another term, called quadrupolar wake field, would have been necessary [17–20].

## VLASOV SOLVERS AND SIMULATION CODES

The tools used to simulate the effects of wake fields on beam dynamics have been improved over the years, also thanks to the increased computing power. The fundamental idea to deal with these effects is quite simple: we start from the motion of a single particle inside an accelerator and include the Lorentz force due to all the others. This basic and simple idea has, however, its limits. Generally a bunch contains $10^{10}$ – $10^{12}$ charges, requiring the same number of equations of motion to be integrated in time. Of course, even with the computing resources available nowadays, this is still not possible. Therefore two approaches are generally used:

* This project has received funding from the European Union's Horizon 2020 Research and Innovation programme under Grant Agreement No 730871.
† mauro.migliorati@uniroma1.it

1. at one extreme we consider a continuous distribution function describing the motion of a beam as a superposition of coherent modes of oscillation. This leads to the Vlasov (or Fokker Plank) equation (and corresponding solvers [21, 22]);

2. on the opposite side, we simplify the problem and reduce the number of equations by using simulation codes, which track, in time domain, about $10^6 - 10^7$ macro-particles, taking into account their electromagnetic interactions by using the concept of wake field.

These two methods have pros and cons. For example, while Vlasov solvers in some cases may present issues related to the number of coherent modes to take into account (a convergence study is necessary), simulation codes could give non-physical results due to noise produced by the discretization with macro-particles. Moreover, with tracking codes we can simulate any complex case while with Vlasov solvers we are limited to simpler cases. However, with tracking simulations we might miss some instabilities which would develop after the total simulated time, while with Vlasov solvers we know if the beam (some modes) will become unstable or not. It is important to remind, however, that, in parallel, simple models, as the two-particle one, have been developed to describe in a simple way some instabilities. These models allow to understand many physical aspects with quite manageable expressions.

Concerning the Vlasov equation, it describes the collective behaviour of a system of multiple particles under the influence of electromagnetic forces. Strictly speaking, the Vlasov equation is valid only for proton beams when we can ignore diffusion or damping effects. For electron, for example, synchrotron radiation cannot be neglected and, in this case, we have to use the Fokker-Plank equation that, for the longitudinal plane, can be written as [23]

$$\frac{\partial\psi}{\partial t} + \frac{\partial\psi}{\partial q}\frac{\partial H}{\partial p} - \frac{\partial\psi}{\partial p}\frac{\partial H}{\partial q} = A\frac{\partial}{\partial p}(\psi p) + \frac{D}{2}\frac{\partial^2\psi}{\partial p^2} \quad (3)$$

where $\psi$ is the longitudinal phase space distribution function, $H$ is the Hamiltonian of the system, $t$ is the time, $(q, p)$ is a set of canonical longitudinal coordinates (as, for example, time and energy offset), $A$ and $D$ depend on the synchrotron radiation and are related, respectively, to the damping and diffusion coefficients. When the left-hand side of the equation is equal to zero, i. e. the local particle density in phase space is constant, Eq. (3) becomes the Vlasov equation. If we want to treat the transverse plane, we need to consider a 4D phase space and Eq. (3) will contain other terms.

This equation can be solved in the stationary condition: $\partial\psi/\partial t = 0$. This leads to the so called Haissinski equation [24], valid for electrons, which is an integral equation that, in presence of the wake fields, gives the potential well distortion: the zero current distribution changes according to the bunch intensity and to the kind of wake field. As an example, in the left-hand side of Fig. 2 we have reported the solution of the equation for a broad band resonator coupling impedance at different intensities starting from an unperturbed Gaussian distribution. On the right-hand side of the same figure, the results from the simulation code SBSC [25] are shown. Further examples of the bunch shape distortion due to some other impedances (resistive, capacitive and inductive) can be found in [26].

For proton beams, instead of the Haissinski equation, the solution of the Vlasov stationary equation $\psi_0(q, p)$ is any function of the Hamiltonian $H_0(q, p)$. On its turn, $H_0(q, p)$ depends on the wake fields and, in the end, we have, similarly to electrons, a potential well distortion.

Instead of a continuous function, simulation codes track, in time domain, some macro-particles representing the whole bunch. Let us consider, for simplicity, only the longitudinal plane, with an energy exchange due to a single RF system, the wake field and the synchrotron radiation. Similar equations can also be written in the transverse plane. Under these conditions, for each macro-particle $i$, we have two equations, which can be written as

$$\Delta\varepsilon_i = \frac{qV_{RF}(\sin\varphi_i - \sin\varphi_s)}{E_s} + \frac{-qV_{wf}(\varphi_i) + R(T_0)}{E_s} - 2\frac{T_0}{\tau_s}\varepsilon_i \quad (4)$$

$$\Delta(\varphi_i - \varphi_s) = -\frac{2\pi h\eta}{\beta^2}\varepsilon_i \quad (5)$$

where $\Delta$ means the variation of a given quantity in one integration step $T_0$ (that can be one revolution turn for example), $\varepsilon_i$ is the normalised energy difference with respect to the synchronous particle, $q$ is the particle charge, $V_{RF}$ is the RF peak voltage, $\varphi_i$ is the particle phase with respect to the RF, $\varphi_s$ is the synchronous phase, $R$ is a stochastic variable changing at each integration step and taking into account the fact that the electromagnetic radiation occurs in quanta of discrete energy, $E_s$ is the synchronous particle energy, $\tau_s$ is the longitudinal damping time, $h$ is the harmonic number, $\eta$ is the slippage factor, $\beta$ is the relativistic velocity factor, and the effect of the wake field, which couples the equations to those of all the other macro-particles, is given by the beam induced voltage

$$V_{wf}(\varphi_i) = \frac{Q_{tot}}{N_m}\sum_{j=1}^{N_m} w_{\parallel}(\varphi_i - \varphi_j) \quad (6)$$

with $Q_{tot}$ the total bunch charge and $N_m$ the number of macro-particles. We have also considered that $\varphi_i - \varphi_s > 0$ for a particle behind the synchronous one, that is with positive time delay.

Since Eq. (6) has to be evaluated for each of the $N_m$ macro-particles, then $(N_m - 1)N_m/2$ operations are needed for each time step. In order to reduce the computing time and only for the evaluation of the wake field effects, the bunch is generally divided into $N_s$ slices ($N_s < N_m$), and the beam induced voltage is calculated at the centre of each slice $i'$ such that

$$V_{wf}(\varphi_{i'}) = \frac{Q_{tot}}{N_m}\sum_{j'=1}^{N_s} n_{j'} w_{\parallel}(\varphi_{i'} - \varphi_{j'}) \quad (7)$$

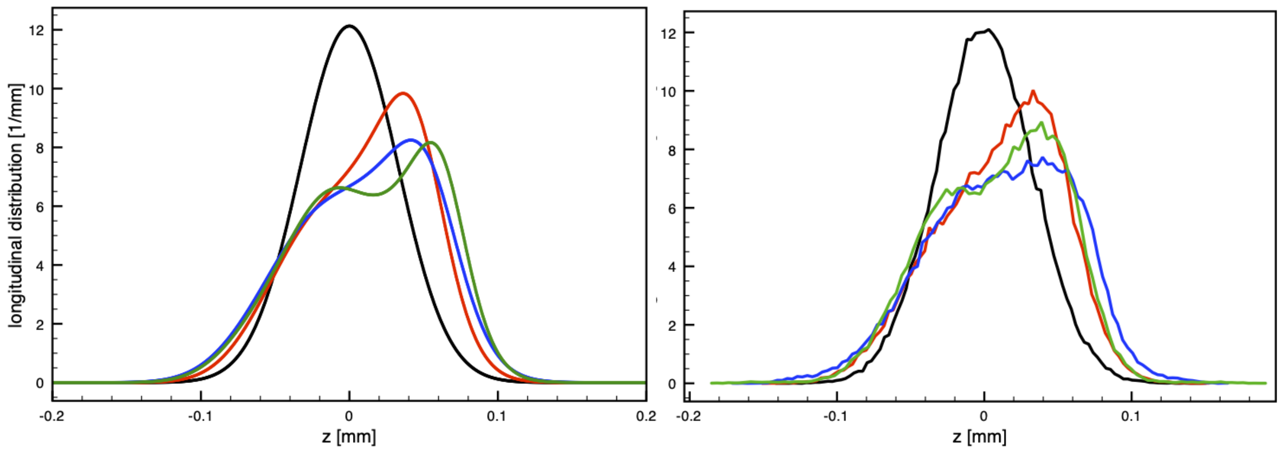


Figure 2: Longitudinal electron distribution distorted by a broad band resonator for four different intensities. Left: analytical results, right: SBSC simulation code. With increasing intensity the shape is more distorted from the unperturbed Gaussian distribution. The plot has to be considered in a qualitative way since the distortion depends not only on the intensity, but also on the impedance and other machine parameters.

with $n_{j'}$ the number of macro-particles in the slice $j'$. To obtain the induced voltage for each macro-particle, an interpolation on the Eq. 7 is used. As shown in the right-hand side of Fig. 2, simulation codes, for the stationary case, give the same results as the analytical approach.

## INSTABILITIES IN CIRCULAR ACCELERATORS

For the study of instabilities in circular accelerators, it is convenient to separate the longitudinal and transverse planes as we did for the wake field described by Eqs. (1) and (2). Moreover, for each plane, we generally distinguish between the single-bunch effects, generated by the short-range wake field, which has, in the corresponding frequency domain, coupling impedances with a poor frequency resolution (broad-band impedance), and the multi-bunch (or multi-turn) effects produced by long-range wake fields or, in frequency domain, by high quality (often unwanted) resonant modes.

Let us first consider single-bunch effects at low intensity in the longitudinal plane. As already discussed in the previous section, the effect in this case is a distortion of the distribution function that depends on the bunch current. There exists a bunch distribution which corresponds to the stationary solution of the Vlasov, or the Fokker-Plank, equation. There is a different behaviour between protons and electrons since, in the first case, we can neglect the effects of synchrotron radiation, and the bunch length and energy spread change with intensity in such a way to preserve the longitudinal emittance, as shown in Fig. 3, left-hand side. For electrons, instead, shown in the right-hand side of the same figure for two different initial bunch lengths, the energy spread remains constant, due to an equilibrium between radiation damping and quantum fluctuations noise, while the potential well distortion changes the bunch length (and shape).

In both cases we can observe an intensity threshold above which the longitudinal emittance (for protons) or the energy spread (for electrons) start to increase. Above this threshold we are in the so-called microwave instability regime, characterised by an anomalous increase of bunch length and energy spread. In some cases, longitudinal oscillations of the bunch are observed (no stationary solution exists). However, for this kind of longitudinal instability, typically there are no beam losses.

To study analytically the single-bunch instabilities in the longitudinal plane (but the same method is also valid in the transverse plane), the steps to do can be summarised as follows:

1. use a perturbation method and write the phase space distribution as $\psi(q,p;t) = \psi_0(q,p) + \Delta\psi(q,p;t)$;

2. use, as canonical longitudinal coordinates, the action-angle coordinates $(I,\phi)$ and consider the perturbation as sum of azimuthal coherent modes $R_m(I)$ oscillating with an unknown coherent frequency $\Omega$:

$$\Delta\psi(q,p;t) = \sum_{m=-\infty}^{\infty} R_m(I) e^{im\phi} e^{-i\Omega t}; \qquad (8)$$

3. consider the instability produced by the wake fields excited only by the perturbation (not by the stationary distribution);

4. from the Valsov equation, the so-called Sacherer integral equation is then obtained (the multi-bunch case can be treated in a similar way);

5. solve the integral equation: there are several methods to obtain the solution [5]. For example it is possible to expand each azimuthal mode $R_m(I)$ in terms of a set

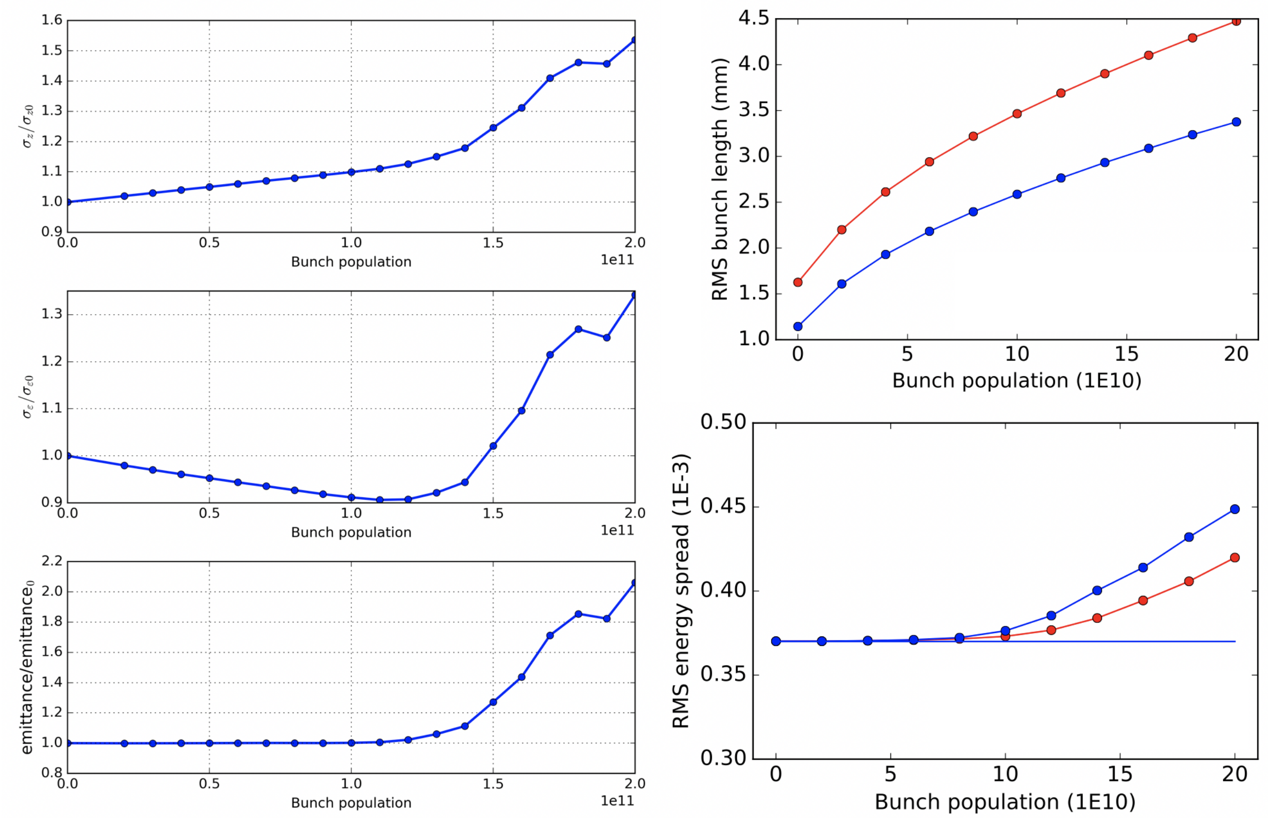


Figure 3: Bunch length, energy spread and longitudinal emittance vs bunch intensity for a case with protons (left). Bunch length and energy spread vs bunch intensity for electrons (right) for two different initial bunch lengths.

of orthonormal functions $g_{mk}(I)$ with unknown amplitude $\alpha_{mk}$ and a proper weight function $W(I)$ which depends on (the derivative of) the stationary distribution:

$$R_m(I) = W(I) \sum_{k=0}^{\infty} \alpha_{mk} g_{mk}(I); \tag{9}$$

6. from Eq. (9) an infinite set of linear equations is obtained. The eigenvalues represent the coherent frequencies and the eigenvectors the corresponding modes:

$$(\Omega - m\omega_s)\alpha_{mk} = \sum_{m'=-\infty}^{\infty} \sum_{k'=0}^{\infty} M_{kk'}^{mm'} \alpha_{m'k'}. \tag{10}$$

For low intensity, we ignore the coupling of radial modes that belong to different azimuthal families ($m = m'$), the matrix of the eigenvalue system is Hermitian, the eigenvalues are always real and no instability occurs (this is true only in longitudinal plane). Only coupled-bunch instabilities (interaction with high Q resonators) can occur if we consider single azimuthal modes. At high intensity, however, mode coupling can occur by taking into account different azimuthal modes. An example of this behaviour is shown in Fig. 4, where we have reported, in black, the coherent frequencies of the first azimuthal modes as a function of bunch intensity, as given by GALACLIC Vlasov solver [27] for a broad-band resonator impedance. From the figure, with the parameters used for this case, we observe a mode coupling of modes 6 and 7 around 1.3×10$^{11}$ particles per bunch.

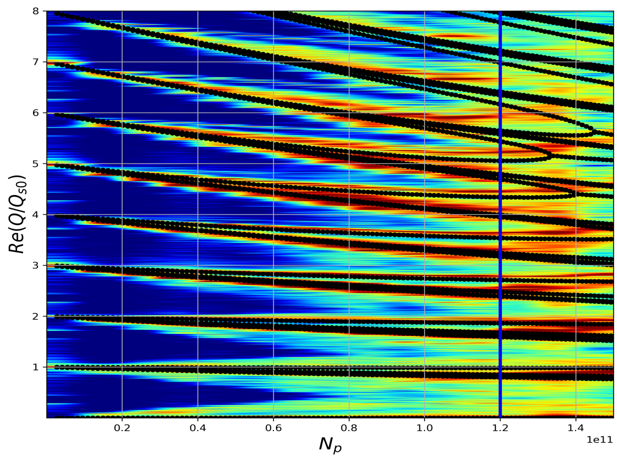


Figure 4: Real part of longitudinal coherent frequency normalised to the synchrotron frequency vs bunch intensity for a broad-band resonator impedance.

In the same figure we have also shown the results from a simulation code [28] which predicts a similar behaviour even with some small differences. It is important to stress, however, that, for the Vlasov solver, we considered here the simplest model of potential well distortion where the synchronous phase shift vs bunch intensity is neglected, i.e. the shape of the longitudinal distribution is conserved. The effect of the full potential well distortion should be studied in the future.

For proton machines, the synchrotron tunes are in general much smaller than those in electron machines. As a consequence, when considering collective instabilities, in some cases the synchrotron period of protons can be neglected because it is much longer than the instability growth times. Moreover, the wavelength of the perturbation producing the instability is often of the size of the radius of the vacuum chamber, which is usually much shorter than the length of the proton bunch. Therefore, proton bunches, in some cases, can be viewed locally as coasting beams in many instabilities considerations. Boussard [29] suggested to apply the same criterion of coasting beams (Keil-Schnell) [30] to bunched beams, obtaining a threshold current of

$$I_{th} = \frac{\sqrt{2\pi}|\eta|(E_s/e)\sigma_\varepsilon^2\sigma_z}{R|Z_\parallel/n|} \tag{11}$$

where $\sigma_\varepsilon$ is the RMS energy spread, $\sigma_z$ the RMS bunch length, and $|Z_\parallel/n|$ the coupling impedance evaluated at the $n^{th}$ harmonic of the revolution frequency. In this case the microwave instability is not due to a mode coupling but each single revolution harmonic can be considered as an independent mode. The Boussard criterion can be a good indicator on how to cope with the microwave instability and where to act to mitigate such effect.

For the transverse plane the procedure is similar to the longitudinal one with few differences:

- the bunch is supposed to have only a dipole moment in the transverse plane;
- this dipole moment is not constant longitudinally, but it has a structure which depends on the longitudinal mode number $m$;
- the modes are called transverse modes, but the transverse structure is a pure dipole and the main task is to find their longitudinal structure;
- the Vlasov equation needs to take into account both the transverse and the longitudinal phase spaces. Fortunately, however, in several cases, the transverse structure of the beam is simple.

The eigenvalue system that is obtained from the Vlasov equation in the transverse plane is

$$(\Omega - \omega_\beta - m\omega_s)\alpha_{mk} = \sum_{m'=-\infty}^{\infty}\sum_{k'=0}^{\infty} M_{kk'}^{mm'}\alpha_{m'k'}, \tag{12}$$

with $\omega_\beta$ the angular betatron frequency. The matrix elements, in this case, depend also on chromaticity. When chromaticity is zero, similarly to the longitudinal plane, the only instability for low intensity beams is due to high Q resonators. However, if the chromaticity is different from zero, differently from the longitudinal plane, single azimuthal modes can be unstable producing the so called head-tail instability. This is not an intensity threshold mechanism, and it is due to the coupling of the real part of the transverse impedance at negative frequency with the coherent modes shifted from the origin due to the chromaticity, as shown, for example, in Fig. 5 for the resistive wall impedance. In the figure, indeed, a positive chromaticity above transition shifts the coherent modes toward the positive frequency side. In this situation, the mode $m = 0$ becomes stable but mode $|m| = 1$ is unstable because it samples a real part of the impedance in the negative frequency range higher than that at positive frequencies.

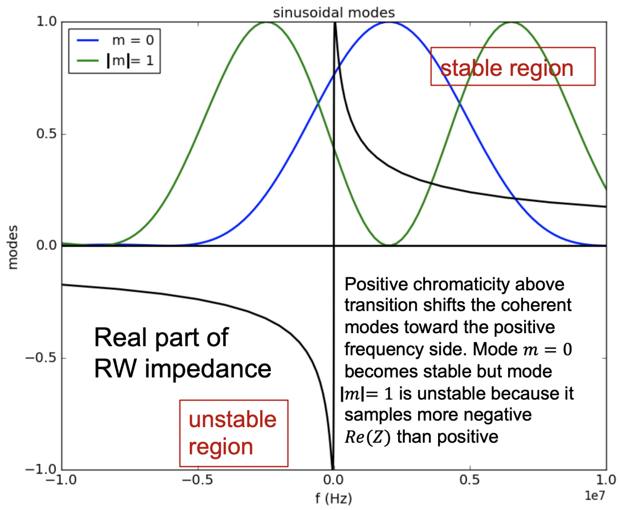


Figure 5: Sketch of the real part of a resistive wall impedance vs frequency together with the first two coherent modes of oscillation.

In addition to the head tail instability, at high intensity, mode coupling can occur for zero chromaticity, as shown in Fig. 6 where we have reported, as for the longitudinal case, a comparison between the GALACTIC Vlasov solver [27] and the PyHEADTAIL simulation code [31]. In this case an excellent agreement has been reached (for both the real and imaginary parts of the coherent frequency shifts).

## SOME CONSIDERATIONS ABOUT MITIGATION TECHNIQUES

A very effective way to mitigate any kind of impedance-induced instability is, of course, that of reducing the machine coupling impedance. This can be achieved, for example, by tapering abrupt transitions, by avoiding electrical discontinuities, by shielding unwanted parasitic cavities, and so on. However, there could be cases in which these measures are not possible (or are insufficient). As further comments about mitigation, in the longitudinal plane we observe that no feedback systems can be used to suppress the microwave instability. However, the Boussard criterion can give important indications on how to cope with this instability. For example the increase of momentum compaction (which can

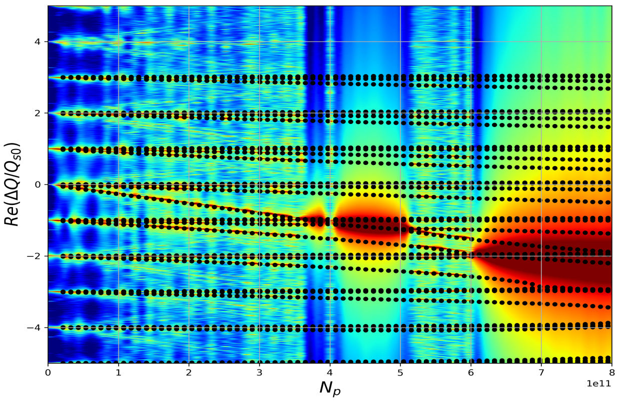


Figure 6: Real part of transverse coherent frequency normalised to the synchrotron frequency vs bunch intensity.

be considered a strong factor), of energy spread (heating the bunch, e.g. with wigglers in electron machines) are effective means to increase the instability threshold. It is also important to note that some machines work in the microwave instability regime. For the transverse plane, in general the lattice choice is quite a strong factor to mitigate the instabilities by acting on: tunes, linear and nonlinear chromaticity, coupling, tune dependence on the oscillation amplitude etc. Feedback systems can be used for both proton and electron beams, and they are working very well for coupled-bunch instabilities, as discussed below.

A particular mention needs the coupled-bunch instability due to high quality resonant modes. The analytical treatment is similar to the single-bunch case, with an additional index in the coherent modes taking into account the coupled-bunch oscillations. This kind of instability leads to a loss of the beam in both planes if mitigation techniques are not used. For example in Fig. 7 we show the growth rates of the coherent coupled-bunch modes for a case with 7 bunches (modes from 0 to 6) by considering a bunch as a point charge (left-hand side).

We can see that some coherent modes are unstable, others are not excited, and others are stable. If we use a bunch with a given length (right-hand side), due to a spread in the synchrotron tunes within a bunch caused by the non linearities of RF system, there is a Landau damping stabilizing the modes [28]. The effect, of course, depends on bunch length. Other mitigation techniques for this instability consist in damping unwanted resonant high quality modes, in using a feedback system, in recurring to a higher harmonic cavity (Landau cavity), both active or passive, in recurring to a RF voltage modulation which creates non-linear resonances which redistribute the longitudinal distribution in phase space reducing the density in the bunch core and thus decoupling the multi-bunch motion, or, finally, in recurring to uneven fill of the beam [32] which changes the bunch spectrum.

Finally, we observe that sometimes interplay with other effects can have a beneficial role in suppressing the impedance related instabilities. For example, the Landau damping due to beam-beam interaction helps in the damping of both transverse [33, 34] and longitudinal [35] instabilities, and in the future supercolliders, FCC-ee [36] and CEPC [37], the energy spread due to beamstrahlung in beam-beam collision helps increasing the microwave instability threshold [38].

More details about mitigation techniques can be found in the talks of this Workshop.

## CONCLUSIONS

In this paper some impedance-induced instabilities have been shortly reviewed. We focused principally on the longitudinal and transverse single-bunch instabilities. However the subject is very broad and this short discussion cannot do justice of the high quality and large amount of work that has been done since the first pioneering works of mid-end 60s. A short, non exhaustive list of arguments that have not been touched is the following: coasting beam instabilities (as negative mass instability), not relativistic beams, space charge effects (which are not strictly impedance-induced instabilities), Landau damping and dispersion integrals, saw-tooth instabilities for electrons, Robinson's instability, transition crossing, impedance effects in LINACS, such as the beam break-up instability, the microbunching instability in RF and magnetic compressors, other impedance-induced effects which are not real instabilities but can influence the machine performances (as the effect of detuning impedance, beam energy spread in LINACS and so on).

The subject of impedance-induced instability is one of the main topics for modern high performance accelerators. Even if the roots of this subject are more than 50 years old, it is still a cutting-edge in the beam physics. Many researchers have been working over the years on this subject and very elegant and well-established theories have been proposed explaining many experimental observations. In some cases we still need to study in more detail the interplay among different mechanisms (e.g. with optics) and in particular we need to better understand some mitigation techniques.

The best proof about our comprehension of these instabilities is that particle accelerators work and are successful. After 50 years, this couldn't be only a coincidence. However, there are still "dark sides" that have to be illuminated by the young generation, which, we hope, will continue the work with the passion that has marked so far the protagonists of this fascinating subject.

## ACKNOWLEDGEMENTS

This work was partially supported by the European Commission under the HORIZON 2020 Integrating Activity project ARIES, Grant agreement No. 730871, and by INFN National committee V through the ARYA project.

## REFERENCES

[1] V. G. Vaccaro, CERN Technical Report No. ISR-RF/66-35, 1966.

[2] A. M. Sessler and V. G. Vaccaro, CERN Technical Report No. CERN 67-2, 1967.

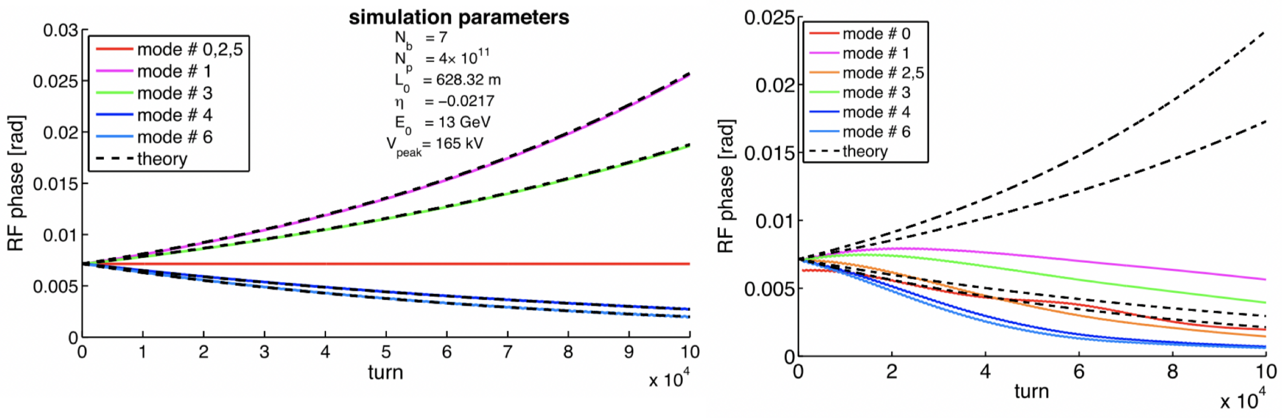


Figure 7: Growth rates of coupled-bunch modes as a function of time (number of turns) for a multi-bunch instability. In the left figure the bunch is supposed a point charge, on the right-hand side a finite length is given.


[3] F. Sacherer, IEEE Trans. Nucl. Sci. 20, 825, 1973; 24, 1393, 1977.

[4] A. W. Chao, Physics of Collective Beam Instabilities in High Energy Accelerators, John Wiley & Sons, New York, 1993.

[5] J.L. Laclare, CERN Report No. 87-03, Vol. I, p. 264, Geneva, Switzerland, 1987.

[6] B. Zotter, CERN Reports No. CERN-SPS/81-18 (DI), No. CERN-SPS/81-19 (DI), and No. CERN-SPS/81-20 (DI), Geneva, Switzerland, 1981.

[7] C. Pellegrini, AIP Conf. Proc. 87, 77 (1982).

[8] M. Sands, Reports No. SLAC-TN-69-8 and No. SLAC-TN-69-10, 1969.

[9] L. J. Laslett, V. K. Neil, and A. M. Sessler, Rev. Sci. Instrum., vol. 36, no. 4, pp. 436–448, 1965.

[10] E. D. Courant and A. M. Sessler, Rev. Sci. Instrum., vol. 37, no. 11, pp. 1579–1588, 1966.

[11] Y. H. Chin and K. Satoh, Nucl. Instrum. Methods Phys. Res. A, no. 207, pp. 309–320, 1983.

[12] See, e.g., T. Suzuki and K. Yokoya, Nucl. Instrum. Methods Phys. Res. 203, 45, 1982.

[13] E. Métral et al., IEEE Transactions on Nuclear Science, Vol. 63, No. 2, 50 p, April 2016.

[14] E. Métral (Issue Editor), ICFA Beam Dynamics Newsletter No. 69 devoted to the Collective Effects in Particle Accelerators, 310 p, December 2016.

[15] K. Y. Ng, Physics of Intensity Dependent Beam Instabilities, World Scientific, Singapore, 2006.

[16] L. Palumbo, V. G. Vaccaro, and M. Zobov, CERN Technical Report No. CERN 95-06, 1995 [arXiv:physics/0309023].

[17] S. Heifets, A. Wagner, B. Zotter, SLAC/APll0, January 1998.

[18] S. Persichelli, N. Biancacci, M. Migliorati, L. Palumbo, and V.G. Vaccaro, Phys. Rev. Accel. Beams 20, 101004, 2017.

[19] M. Migliorati, N. Biancacci, M. R. Masullo, L. Palumbo, and V. G. Vaccaro, Phys. Rev. Accel. Beams 21, 124201, 2018.

[20] M. Migliorati, L. Palumbo, C. Zannini, N. Biancacci, and V. G. Vaccaro, Phys. Rev. Accel. Beams 22, 121001, 2019.

[21] E. Métral, Proc. 10th Int. Particle Accelerator Conf. IPAC2019, Melbourne, Australia, 19-24 May 2019, pp. 312-315. doi:10.18429/JACoW-IPAC2019-MOPGW087

[22] N. Mounet, DELPHI: an analytic Vlasov solver for impedance-driven modes (2014), CERN-ACC-SLIDES-2014-0066 `http://cds.cern.ch/record/1954277/files/CERN-ACC-SLIDES-2014-0066.pdf`

[23] C. Bernardini, and B. Touschek: On the quantum losses in an electron synchrotron, Laboratori Nazionali di Frascati del CNEN, Nota interna No. 34 (April 1960).

[24] J. Haïssinski, Il Nuovo Cimento B 18, 72, 1973.

[25] M. Migliorati et al., Phys. Rev. ST Accel. Beams, vol. 16, p. 031001, March 2013.

[26] K. L. F. Bane, SLAC-PUB-5177 February 1990 (A).

[27] E. Métral, M. Migliorati, "Vlasov solvers and simulation code analysis for mode-coupling instabilitites in both longitudinal and transverse planes", these proceedings.

[28] M. Migliorati, L. Palumbo, Phys. Rev. ST Accel. Beams, vol. 18, p. 031001, March 2015. doi:10.1103/PhysRevSTAB.18.031001

[29] D. Boussard, CERN LabII/RF/75-2, 1975.

[30] E. Keil, W. Schnell, CERN Report ISR-TH-RF/69-48, 1969.

[31] K. Li, "Headtail code," 2015. `https://indico.cern.ch/event/378615/`, [Online; accessed 16.05.2019].

[32] S. Prabhakar, J. D. Fox, and D. Teytelmann, Phys. Rev. Lett., vol. 86, pp. 2022-2025, Mar. 2001.

[33] M.G. Minty et al., Rep. SLAC-PIB-8363, Feb. 2000. https://www.slac.stanford.edu/cgi-bin/getdoc/slac-pub-8363.pdf

[34] X. Buffat et al., Stability diagrams of colliding beams in the Large Hadron Collider, PRSTAB 17 111002 2014.

[35] A. Drago, P. Raimondi, M. Zobov, D. Shatilov, Phys. Rev. ST Accel. Beams vol. 14, p. 092803, 2011. doi:10.1103/PhysRevSTAB.14.092803

[36] The FCC Collaboration, FCC-ee: The Lepton Collider: Future Circular Collider Conceptual Design Report Volume 2, European Physical Journal Special Topics, 228, 261-623, 2019, doi: 10.1140/epjst/e2019-900045-4.

[37] CEPC Study Group, CEPC Conceptual Design Report: Volume 1 - Accelerator, 2018. arXiv:1809.00285

[38] M. Migliorati, E. Belli, M. Zobov, Phys. Rev. Acc. and Beams, vol. 21, p. 041001, 2018. doi: 10.1103/PhysRevAccelBeams.21.041001.

# Space Charge Effects for Transverse Collective Instabilities in Circular Machines

A. Burov*
*Fermilab, PO Box 500, Batavia, IL 60510-5011*
(Dated: May 18, 2020)

A brief historical review is presented of progressing understanding of transverse coherent instabilities of charged particles beams in circular machines when both Coulomb and wake fields are important.

## I. INTRODUCTION

Fifty years ago, the first significant publication was presented on transverse collective instabilities of space-charge-dominated beams in circular machines; it was a CERN preprint of G. Merle and D. Möhl "The stabilizing influence of nonlinear space charge on transverse coherent oscillations" [1]. A relatively simple equation of motion was suggested there as something obvious. Although it was, strictly speaking, neither obvious nor even quite correct, as further studies have shown, it played and continues to play an extraordinarily important role. Thus, this anniversary adds a special flavor to the request of the workshop organizers to review the main results in this area of beam dynamics.

Purporting to fulfill that, this paper is divided in two sections, on coasting and bunched beams respectfully. We rather rarely deal with coasting beams in circular machines, but still they deserve a special attention not only for themselves [2, 3] but also as relatively simple configurations to start from and get some key ideas. This set of ideas includes a concept of rigid slices and strong space charge as its justification. Also, it includes interplay of Landau damping (LD), space charge (SC) and octupoles, showing the importance of their polarity, in particular. These ideas, common for coasting and bunched beams, are presented in Sec. II and used in Sec. III. In the latter section, SC-modification of the transverse mode coupling instability (TMCI) is discussed, including paradoxes which were resolved in a discovery of convective instabilities.

The goal of this paper is to present, in a compact way, the main results in the area of beam dynamics, specified by the subject, where both SC and wake field are important. To a certain degree, such a task cannot be free from some subjectivity and arbitrariness, and I beg pardon of those colleagues who will find some valuable results underrepresented or not presented at all.

## II. COASTING BEAMS

To analyze the beam stability with SC, a linear equation of motion was suggested by G. Merle and D. Möhl in 1969 [1]:

$$\frac{d^2 x_i}{dt^2} + \omega_{xi}^2 x_i + 2\omega_x \omega_i^{\mathrm{sc}} (x_i - \bar{x}) + 2\omega_x \omega^{\mathrm{c}} \bar{x} = 0\,. \tag{1}$$

Here $x_i = x_i(t)$ is a transverse offset of a particle $i$, $\omega_{xi}$ is the betatron frequency of the particle $i$, $\omega_x$ is the average betatron frequency, $\bar{x} = \bar{x}(t)$ is an average offset of that beam *slice* where the particle $i$ is located at the given moment of time $t$, $\omega_i^{\mathrm{sc}} < 0$ is the SC frequency shift of the particle, and $\omega^{\mathrm{c}}$ is the coherent frequency shift parameter, proportional to the ring impedance. The full time derivative $d/dt$ is expressed through the partial ones, $d/dt = \partial/\partial t + \omega_i \partial/\partial\theta$, where $\omega_i$ is the revolution frequency of the particle, and $\theta = s/R$ is the azimuthal angle, with $s$ as the conventional longitudinal coordinate and $R$ as the average ring radius. The term 'slice' refers to the group of beam particles which Coulomb fields affect the given particle number $i$, i.e. the particles with positions somewhere between $s_i - a/\gamma$ and $s_i + a/\gamma$, where $a$ is the beam transverse size and $\gamma$ is the Lorentz factor.

Equation (1) implies two important things.

First, it implies that $x_i$ relates to the driven part of the single-particle oscillations, excited by the collective motion of the centroids $\bar{x}$, while constant amplitudes of free oscillations determine the space charge frequency shifts. That is why the offset $x_i$ is of the order of centroid offsets, $x_i \sim \bar{x}$, so it can be considered infinitesimally small, while the incoherent amplitudes are of the order of the beam transverse size.

Second, this equation assumes that each beam slice oscillates as a rigid body, allowing for a representation of the SC force in the simple way it is done there. Because of this assumption, Merle-Möhl approach is sometimes addressed as the *rigid-slice* or *frozen-field* model. Possible incorrectness of this assumption, as well as its very existence, was realized much later, when some strange features of Eq. (1) were discovered.

For a coasting beam, eigenfunctions of Eq. (1) have the form

$$x_i\,, \bar{x} \propto \exp\left[-i\left(\omega_x + n\omega_0 + \omega\right)t + in\theta\right] \tag{2}$$

where $n$ is an arbitrary integer, $\omega_0$ is the average revolution frequency, and $\omega$ is a frequency shift of the mode $n$. Substitution of this form into Eq. (1) yields for the complex amplitudes

$$x_i = \bar{x}\frac{\omega^{\mathrm{c}} - \omega_i^{\mathrm{sc}}}{\omega - \omega_i^{\mathrm{sc}} - \delta\omega_{xi} - n\delta\omega_i}\,, \tag{3}$$

* burov@fnal.gov

with the lattice frequency shifts $\delta\omega_{xi} = \omega_{xi} - \omega_x$ and $\delta\omega_i = \omega_i - \omega_0$. Note that without lattice frequency spread, $\delta\omega_{xi} = \delta\omega_i = 0$, there is always the rigid-bunch solution, $x_i = \bar{x}$, with $\omega = \omega^{\mathrm{c}}$, independently of the SC tune shifts $\omega_i^{\mathrm{sc}}$. This important physical property of Eq. (1) is a consequence of its SC representation by means of the term $\propto x_i - \bar{x}$. In fact, the Merle-Möhl equation is the only possible linear dynamic equation consistent with the given incoherent spectrum, its lattice and SC parts, which represents the coherent SC term by means of $\propto \bar{x}$ term only, preserving the rigid-bunch mode for zero lattice tune spread, as it must be from the first principles.

By averaging over the particles, writing the sums as the phase space integrals with the distribution function, one gets the dispersion relation, i.e. the equation for the sought-after eigenfrequency $\omega$,

$$1 = -\int d\Gamma\, J_x \frac{\partial f}{\partial J_x} \frac{\omega^{\mathrm{c}} - \omega_i^{\mathrm{sc}}}{\omega - \omega_i^{\mathrm{sc}} - \delta\omega_{xi} - n\delta\omega_i + io} \tag{4}$$

Here $f = f(J_x, J_y, \delta p/p)$ is the unperturbed distribution density as a function of transverse actions $J_{x,y}$ and the relative momentum offset $\delta p/p$, normalized to unity, $\int d\Gamma f = 1$, where $d\Gamma = dJ_x\, dJ_y\, d\delta p/p$; the single-particle subscript $i$ has to be understood as indication to related functional dependences, i.e. $\delta\omega_{xi} \to \delta\omega_x(J_x, J_y, \delta p/p)$, etc. To get Eq. (4) from Eq. (3), the Hereward rule [4] was used,

$$\sum_i (\ldots) \to -\int d\Gamma\, J_x\, \partial f/\partial J_x\, (\ldots)\,,$$

and the Landau rule of going around the pole is explicitly marked, $\omega \to \omega + io$, where $o$ is an infinitesimally small positive number.

It is straightforward to see from the dispersion relation (4) that without lattice frequency spreads, at $\delta\omega_{xi} = \delta\omega_i = 0$, the eigenfrequency $\omega = \omega^{\mathrm{c}}$, independently of the SC tune shift. Thus, even if the phase space density of the resonant particles were not zero, i.e. there were particles with the same tune as the coherent mode, still there would be no Landau damping (LD), irrespectively to nonlinearity of SC distribution.

The dispersion relation in the form (4) was first derived by D. Möhl and H. Schönauer in 1974 [5], not in the original preprint of Merle and Möhl. In the latter, some mathematical mistakes were adopted, so the dispersion relation was derived incorrectly. Due to this, it was mistakenly concluded there that SC nonlinearities may contribute to Landau damping of coasting beams even without the lattice frequency spread. This mistake was later repeated in Ref. [6] and corrected by Möhl and Schönauer [5]. That is why it seems fair to call Eq. (1) Merle-Möhl equation of motion and Eq. (4) Möhl-Schönauer dispersion relation.

After the simplest case of no lattice frequency spreads, the next by simplicity is a two-stream beam, $\delta\omega_i = \pm\delta\omega_0$. For KV transverse distribution with a constant SC frequency shift, $\omega_i^{\mathrm{sc}} = \omega^{\mathrm{sc}}$, Eq. (4) yields the following spectrum:

$$\omega = \frac{\omega^{\mathrm{c}} + \omega^{\mathrm{sc}}}{2} \pm \sqrt{\frac{(\omega^{\mathrm{c}} - \omega^{\mathrm{sc}})^2}{4} + n^2\delta\omega_0^2} \tag{5}$$

The instability is driven by the coherent tune shift $\omega^{\mathrm{c}}$, so the most unstable modes are positive ones, i.e. those associated with the sign + in Eq. (5). A more detailed analysis shows that for them the two streams of the beam oscillate approximately in phase, so their wakes add to each other. For strong SC, $|\omega^{\mathrm{sc}}| \gg \max(|n|\delta\omega_0, |\omega^{\mathrm{c}}|)$, the spectrum of positive modes reduces to

$$\omega = \omega^{\mathrm{c}} + n^2\delta\omega_0^2/\omega^{\mathrm{sc}}\,, \tag{6}$$

being far away from the incoherent spectrum localized around $\omega^{\mathrm{sc}}$. Thus, the negative modes not only are barely excited by the wake, but also stay close to the incoherent spectrum, so their stability would be provided automatically when the positive modes are stable.

A very general method of analysis of integral dispersion relations like Eq. (4) was presented in Ref. [7]. The idea was to reverse the problem: instead of finding the eigenfrequency $\omega$ when the coherent tune shift $\omega^{\mathrm{c}}$ is given, let us do the opposite, find the coherent tune shift $\omega^{\mathrm{c}}$ for a given eigenfrequency $\omega$ for the same dispersion relation. If to run the eigenfrequency along the real axis, the corresponding coherent tune shift will follow a certain line in its complex plane, the conformal map of the real axis in the complex plane of $\omega$ to the complex plane of $\omega^{\mathrm{c}}$. This line, $\omega^{\mathrm{c}}(\omega)$, is conventionally called the stability diagram; the beam is stable if and only if its actual coherent tune shift is below the diagram.

Certain historical investigations [8] convinced the author of this paper that it would be fair to call the stability diagram the Vaccaro diagram (VD), by name of Vittorio Vaccaro, who found how Nyquist's stability plots can be modified to become an effective tool for the collective beam dynamics. With Möhl-Schönauer dispersion relation (4), VD is determined by the beam distribution function $f$, the lattice frequency shifts and SC tune shifts, being independent of wakes.

In 2001, M. Blaskiewicz suggested an original method of solving the Vlasov equation with SC and lattice tune spread [9]. The method was free from hidden assumptions of Merle-Möhl approach, being, arguably, more complicated and less transparent in the computations. The method allowed to make conclusions regarding SC effects for VD. In case of the chromatic lattice tune spread, the diagram of a Gaussian beam essentially shifted to the left by one half of the maximal SC tune shift. In case of the octupole nonlinearity M. Blaskiewicz found that focusing octupoles are much more beneficial for LD than defocusing ones, confirming the same conclusion by D. Möhl [10].

The first analytical attempt to build VD for Eq. (4) was presented in 2004 by E. Metral and F. Ruggiero [11].

Namely, they suggested a solution of the dispersion relation with SC and octupolar nonlinearity, where, instead of the coasting beam term $n\delta\omega_i$, the bunched beam term $k\omega_\mathrm{s}$ was put, with $\omega_\mathrm{s}$ as the synchrotron frequency and $k$ as the head-tail mode number. Such extension of the coasting beam theory to the bunched case was, however, left unexplained both in the paper itself and the references it suggested for that matter, including Ref. [10]. As it became more clear later, this extension works reasonably well only when the SC term could be safely omitted. However, the actual merit of the paper was not in its applicability to bunched beams with SC, but in its analytical building of VD for coasting beams with octupoles, nonlinear SC, and insignificant revolution frequency spread, $n\delta\omega_i = 0$. It was confirmed, in particular, that the octupole sign becomes crucial for strong SC; namely, the focusing octupoles are much preferable. The reason is that the octupoles affect mostly the tail particles, so the collective frequency is barely touched by them. Landau damping requires resonant particles, i.e. those which individual tunes are the same as the collective one. Space charge moves the incoherent tunes down, and does almost nothing for the collective tunes, thus killing LD. Thus, to restore the latter, the incoherent tunes have to be moved up to provide higher population of the resonant particles, so the octupoles have to be focusing. It was also shown in this reference that SC can be beneficial if it shifts VD on top of the coherent tune, which would be outside (on the left) of VD without space charge. For very strong SC, it meant that it is detrimental since it shifts the stability diagram far on the left.

Among multiple reasonable features, Vaccaro diagrams of Ref. [11] showed a strange one: for defocusing octupoles, there was a kink point of the curve at the real axis, which prevented the line from going to the lower half-plane, $\Im\omega^\mathrm{c} < 0$. The kink point looked strange, since VD should be analytical by the definition.

In 2006, D. Pestrikov published an article [12] where a similar problem was solved, but instead of the kink point, the diagram smoothly continued to the lower half-plain, thus demonstrating Landau antidamping. Later that year Landau antidamping was confirmed by K.Y. Ng for the same model as Metral and Ruggiero proposed [13]. On the ground of these findings, the kink point of Ref. [11] was dismissed as a mistake of the sign. Due to this, however, another problem appeared: at certain conditions, a Gaussian-like beam with time-independent Hamiltonian started looking unstable even when the coherent tune shift $\omega^\mathrm{c}$ suggested a decay of the mode. Next year Pestrikov published another paper [14], presenting "a self-consistent model" which showed no antidamping, contrary to the Merle-Möhl model; he expressed doubt in the validity of the latter.

This doubt was enhanced to a stronger claim by V. Kornilov, O. Boine-Frankenheim, and I. Hofmann in their publication of 2008 [15]. First, they confirmed that VD of Eq. (4) indeed yields Landau antidamping for defocusing octupoles. Second, they supported this confirmation by macroparticle simulations within the *frozen field* model, equivalent to Merle-Möhl approach. Third, they ran self-consistent macroparticle simulations for the same conditions, and saw no antidamping. From this, they concluded "that antidamping can be related to the non-self-consistent treatment of nonlinear space charge in the simulations and also in the dispersion relation."

At that stage, several issues remained unresolved for coasting beams. First, it was not clear if Landau antidamping is ever possible for Gaussian-like beams with SC, octupoles and chromaticity. Second, with evidence of incorrectness of Merle-Möhl analytical approach at certain cases, it was not clear if their equation could be ever used at all, and under what conditions. Third, no analytical formulas for the instability thresholds were yet obtained. These issues were addressed in Ref. [16].

A possibility of Landau antidamping was denied there as contradicting to the Second Law of Thermodynamics. Indeed, a beam with real coherent tune shift $\omega^\mathrm{c}$, corresponding to imaginary transverse impedance, i.e. to zero energy losses, can be described by energy-preserving time-independent Hamiltonian, so the growing coherent oscillations might take energy from the incoherent degrees of freedom only. For a Gaussian beam it would mean a perpetuum mobile of the second kind, forbidden by the Second Law. Landau antidamping, demonstrated for some parameters by Merle-Möhl dynamic system (1), is caused by the non-Hamiltonian character of its SC term. Specifically, the term $\propto \omega_i^\mathrm{sc}\bar{x}$ is non-Hamiltonian unless all the SC frequency shifts are identical within the beam slice. Having said that, it is important to stress that the Merle-Möhl equation of motion with real coherent tune shift, $\Im\omega^\mathrm{c} = 0$, may lead to Landau antidamping only if the incoherent spectrum $\omega_i^\mathrm{sc} + \delta\omega_{xi}$ reaches a local maximum in the action space, which may happen for a defocusing octupole. Although the equation is not Hamiltonian, for monotonic spectra $\omega_i^\mathrm{sc} + \delta\omega_{xi}$ all its van Kampen eigenfrequencies with real coherent tune shift are real as well, no unphysical dissipation is introduced.

How reliable is Eq. (1) for LD computation for the monotonic spectra? When the SC tune shifts depend on the transverse actions, as they normally are, the defect of the model still should not play a role, if the slices were sufficiently rigid in their transverse oscillations. In this case only the tail particles would be responsible for LD, so the energy transfer to them could be reasonably approximated with the rigid core model. To see when the core is really rigid, note that if the lattice tune shifts are small with respect to the tune separation,

$$|\delta\omega_{xi} + n\delta\omega_i| \ll |\omega^\mathrm{c} - \omega_i^\mathrm{sc}|\,, \tag{7}$$

the particles move together with the related centroids, $x_i \approx \bar{x}$, as it follows from Eq. (3). Thus, if the SC is so strong that this condition is satisfied for the majority of particles, the slices oscillate almost without distortions, since almost all the particles oscillate almost identically to their centroids; so the rigid-slice approximation is justified. Luckily, for many low- and medium-energy machines, typical SC tune shifts are much larger than the imaginary part of the coherent tune shifts, $|\omega_i^{\rm sc}| \gg \Im\omega^{\rm c}$, so stabilization is achieved at such a small lattice nonlinearity that Eq. (7) is satisfied, justifying Merle-Möhl equation. In this case of strong SC, instability thresholds were explicitly found in Ref. [16] for Gaussian beam, both for octupolar and chromatic frequency spreads. Recently, this method was extended to electron lenses; Landau damping rate introduced by a Gaussian e-lens for a coasting beam with SC was analytically estimated and presented in Ref. [3].

## III. BUNCHED BEAMS

The coherent spectrum of bunched beam with SC was presented for the first time by M. Blaskiewicz in 1998 [17] within a simple model of an air-bag bunch in a square potential well. For a delta-wake, the eigenfrequencies were found to be same, as Eq. (5) for the two-stream coasting beam, with the substitution $n\delta\omega_0 \to k\omega_{\rm s}$, where $k = 0, 1, 2, ...$ is the mode counter and $\omega_{\rm s}$ is the synchrotron frequency. A new and rather surprising mathematical result of M. Blaskiewicz [17] showed suppression of the transverse mode coupling instability (TMCI) by SC; the wake threshold was demonstrated to grow with SC tune shift, linearly at the strong SC limit, $|\omega^{\rm sc}| \gg \omega_{\rm s}$. This result was obtained for exponential wakes and the ABS model (Air-Bag, Square-well), so a question was raised about the sensitivity of this unexpected result to the details of the wake, potential well and bunch distribution. Also, it was not clear if there was any limit to this growth of the instability threshold. An explanation of this growth at moderate SC was suggested to the author by V. Danilov [18] and reproduced in Ref. [19]. Without SC, TMCI typically results from crossing of the head-tail mode 0, shifted down by the wake, and the mode $-1$, not shifted as much. Space charge, on the contrary, does not influence the mode 0 and shifts down the mode $-1$, thus moving their coupling point to higher intensity.

In the year of 2009, when it was understood that Merle-Möhl approach of rigid slices is justified for sufficiently strong space charge, it was applied to bunched beams by the author [20]. Under the condition of SC tune shift being much stronger than all other tune shifts and spreads, as well as the synchrotron tune (strong space charge, SSC), an ordinary linear integro-differential equation was derived for the bunch modes for an arbitrary potential well, driving and detuning wakes, longitudinal and transverse bunch distribution functions. Later that same year V. Balbekov published a paper [21] with an alternative derivation of the SSC equation, which result differed from mine. After checking his derivation and rechecking mine, I found an algebraic error in my calculations, and derived my ultimate form of the SSC mode equation, which agreed with Balbekov's result, suggesting a slightly more compact form in the erratum [22],

$$i\frac{\partial \bar{x}}{\partial t} + \frac{1}{\omega^{\rm sc}}\frac{\partial}{\partial s}\left(u^2\frac{\partial \bar{x}}{\partial s}\right) = \mathbb{W}\bar{x} + \mathbb{D}\bar{x}\,. \tag{8}$$

Here $\omega^{\rm sc} = \omega^{\rm sc}(s)$ is the SC frequency shift averaged over the transverse actions at every position $s$, $u^2 = u^2(s)$ is the local rms spread of the longitudinal velocities, $u^2 \equiv \langle R^2\delta\omega_i^2\rangle$, while $\mathbb{W}$ and $\mathbb{D}$ are conventional driving and detuning wake linear integral operators [23]; in more details see [22]. The equation is complemented by zero-derivative boundary conditions, $\partial\bar{x}/\partial s = 0$ at the bunch edges or at $s = \pm\infty$. For the eigenfunctions, the time derivative has to be substituted by the sought-for eigenfrequency $\nu$, i.e. $i\partial/\partial t \to \nu$. Without wakes, this equation leads to the Blaskiewicz-type collective spectrum, $\nu_k \simeq k^2\omega_{\rm s}^2/\omega^{\rm sc}$. The mathematical elegance of Eq. (8) has its price: missing is the Landau damping, which required additional ideas and computations.

Analytical estimations for LD at SSC were also suggested in Ref. [20, 22] for weak head-tail cases, when the wake does not influence the eigenfunction much. Contrary to coasting beams, it was found that there is an intrinsic LD, caused by the longitudinal variation of the SC tune shift only, even without any lattice tune spreads. The physical mechanism of the dissipation was associated with a break of the slice rigidity at the bunch edges, where the SC is not strong any more. The slice softening at the bunch edges opens a way for the energy transfer to the incoherent degrees of freedom. According to the related estimation, the intrinsic LD rate $\Lambda_k$ at SSC was found to be a steep function of the SC parameter $q \equiv \omega^{\rm sc}/\omega_{\rm s}$ and the positive mode number $k$, $\Lambda_k \simeq k^4\omega_{\rm s}/q^3$; the SSC assumes $q \gg 2k$. Six years later these analytical results for SSC eigenfunctions and LD rates were fully confirmed in Synergia macroparticle simulations by A. Macridin et al. [24], where the intrinsic LD rates were shown to have their maxima at $q \simeq 2k$. A more subtle case of *parametric Landau damping* was treated by A. Macridin et al. in Ref. [25] by means of analytical modeling and macroparticle simulations. Analytical estimations of octupoles-related LD suggested in Ref. [20, 22] are still waiting for at least numerical verifications; nothing yet has been published in that matter. Octupoles, however, are rather inefficient for LD, which requires significant nonlinearity inside the beam, not far outside, as octupoles provide. That is why a better instrument for LD is an electron lens, at least as thin as the beam. Such e-lenses are able to provide LD without deterioration of the dynamic aperture, as it was pointed out by V. Shiltsev et al. [26]. Estimations of e-lens-caused LD rates for bunches with SC were suggested by Yu. Alexahin, A. Burov and V. Shiltsev in 2017 [27].

With the wake taken into account, the Blaskiewicz' result of linear growth of the TMCI wake threshold was confirmed in a series of publications, see Refs. [28, 29] and references therein. A hidden obstacle with this problem, sometimes caused misleading results, was realized by V. Balbekov [30], who showed that convergence of the expansion of the sought-for eigenfunction over the zero-wake basis degrades with SC, requiring more and more terms for higher SC parameter $q$. The physical reason of the convergence worsening was recently found by the author of this paper; it is associated with the head-to-tail amplification, or the *convective instabilities* driven by wakes at SSC. When eigenfunctions are significantly amplified, their expansion over any even basis cannot be of a good convergence. Clearly manifest subsiding of the instability with SC was presented in the two-particle model of Ref. [31].

With the theoretical proof of TMCI vanishing with SC, two problems became rather obvious, one experimental and the other theoretical. The former consisted in a reasonable agreement of the transverse instability at CERN SPS with no-SC theory, while SC tune shift was very strong there, especially with the old lattice [32, 33]. The latter problem was related to the linear growth of the wake threshold with SC. Due to this feature, the bunch should be stable up to infinite intensity, as soon as its emittance is low enough, which did not sound as a reasonable statement. The resolution of both problems was presented by the author two years ago [34]. The main idea, already mentioned above, was that, while moving out TMCI, SC moves another instability in its place, a convective one. Contrary to TMCI, which is an absolute instability, i.e. has nonzero growth rate, the convective instabilities grow not in time, but in space, from head to tail [35]. This head-to-tail amplification increases exponentially with bunch intensity, resulting in one or another physical limit, set by lattice nonlinearity, beam loss or feedback. When the amplification is large, even a tiny feedback from tail to head may be sufficient to close the loop and turn the convective instability into an *absolute-convective* one, like those with a microphone close to its loudspeaker. Such a feedback may be presented with a bunch-by-bunch damper, coupled-bunch wakes, or a halo of the same bunch. Here a question may be asked, why is the halo needed for the feedback? Why can core particles not play this role, when they move to the bunch head with their high transverse amplitudes acquired at the tail? The answer is that due to strong SC, the bunch slices are rigid, as it was discussed in the previous section. Strong SC means that all tune shifts are small compared with the SC tune shift, so intra-slice degrees of freedom cannot be excited, and thus the tail particles do not preserve their large amplitudes while moving to the bunch head; instead, they just follow the existing spacial pattern of the rigid-slice oscillations.

However, what is impossible for the bunch's core, might work for its halo, which SC tune shift is smaller, so the halo slices can be soft, providing a tail-to-head feedback. At strong SC, this feedback would be small due to the low population of the halo, but, if the convective amplification is large enough, even a small feedback could be sufficient to ignite the absolute-convective instability, as it was suggested and modeled in Ref. [36]. Apparently, the same effect is responsible for the non-monotonic behavior of the wake threshold on the SC parameter reported by Yu. Alexahin at this workshop [37]. A good agreement of his analytically calculated highly convective mode with the pattern of oscillations seen by A. Oeftiger in macroparticle simulations for the same conditions also deserves to be mentioned.

It is already clear, that convective instabilities constitute a common obstacle for high intensity circular machines of low and medium energy, where SC is significant; they definitely take place at CERN Booster, PS and SPS rings, as well as at the Fermilab Booster. That is why it is important to understand how they behave together with other factors of beam dynamics. Transverse instabilities of a bunch with SC, wake and damper were considered in Ref. [38]. In Ref. [39], measurements of a microwave instability at transition crossing in PS were reported; the instability was characterized as *convective.* Recently an analytical model for it was proposed [40] by means of Eq. (8). A simple threshold formula derived there was found to be in good agreement with the data of Refs. [39, 41]. A statement made in Ref. [39] that "The bunch parameter measurements demonstrate... that the space-charge effect does not affect the instability thresholds" does not actually contradict to rather weak dependence of the threshold bunch intensity $N_{\rm th}$ on the transverse emittance, $N_{\rm th} \propto \epsilon_\perp^{1/4}$ of Ref. [40], since the limited range of the emittances examined in Ref. [39] and the measurement errors do not allow to resolve rather weak dependence on the emittance on the ground of this set of measurements alone [42].

## ACKNOWLEDGMENTS

I am indebted to Elias Metral for detailed discussions in May 2018 which clearly showed me the contradiction between the SPS observations and theory of the vanishing TMCI, as the latter was understood at that time. I am also grateful to Elias for his support in researching the historical issues that I tried to reflect here. I appreciate the clarifications of Vladimir Kornilov concerning his PS measurements and remarks of Valeri Lebedev which helped me prepare this paper.

Fermilab is operated by Fermi Research Alliance, LLC under Contract No. DE-AC02-07CH11359 with the United States Department of Energy.

[1] G. Merle and D. Möhl, *The stabilizing influence of nonlinear space charge on transverse coherent oscillations*, Tech. Rep. CERN-ISR-300-GS-69-66 (1969).
[2] L. Prost, C. Bhat, A. Burov, J. Crisp, N. Eddy, M. Hu,

and A. Shemyakin, Conf. Proc. C **110328**, 1698 (2011), arXiv:1208.2019 [physics.acc-ph].
[3] V. Lebedev and et al., "Conceptual design report: A ring-based electron cooling system for the electron-ion collider," to be published in JINST (2020).
[4] H. Hereward, *Landau damping by non-linearity*, Tech. Rep. CERN-MPS-DL-69-11 (1969).
[5] D. Möhl and H. Schönauer, in *Proceedings, 9th International Conference on the High-Energy Accelerators (HEACC 1974): Stanford, California, May 2-7, 1974*, CERN-MPS-DL-74-6, CERN-MPS-INTBR-74-11 (1975) pp. 380–384.
[6] K. Reich and H. Schönauer, *Transverse stability of a coasting PSB beam*, Tech. Rep. CERN/SI/Int. BR/72-2 (1972).
[7] A. Ruggiero and V. Vaccaro, *Solution of the dispersion relation for longitudinal stability of an intense coasting beam in a circular accelerator (application to the ISR)*, Tech. Rep. CERN-ISR-TH/68-33 (1968).
[8] I appreciate historical investigations made by Elias Metral in this respect. (2018).
[9] M. Blaskiewicz, Phys. Rev. Accel. Beams **4**, 044202 (2001).
[10] D. Möhl, Part. Accel. **50**, 177 (1995).
[11] E. Metral and F. Ruggiero, in *9th European Particle Accelerator Conference (EPAC 2004)*, EPAC-2004-WEPLT030, CERN-AB-2004-067 (2004).
[12] D. Pestrikov, Nucl. Instrum. Meth. A **562**, 65 (2006).
[13] E. Metral, RLC meeting communication, 19/09/06 (2006).
[14] D. Pestrikov, Nucl. Instrum. Meth. A **578**, 65 (2007).
[15] V. Kornilov, O. Boine-Frankenheim, and I. Hofmann, Phys. Rev. Accel. Beams **11**, 014201 (2008).
[16] A. Burov and V. Lebedev, Phys. Rev. Accel. Beams **12**, 034201 (2009).
[17] M. Blaskiewicz, Physical Review Special Topics-Accelerators and Beams **1**, 044201 (1998).
[18] V. Danilov, private communication (1998).
[19] K. Y. Ng and A. V. Burov, *Instabilities of high intensity hadron beams in rings. Proceedings, Workshop, Brookhaven, Upton, USA, June 28-July 1, 1999*, AIP Conf. Proc. **496**, 49 (1999).
[20] A. Burov, Phys. Rev. Accel. Beams **12**, 044202 (2009).
[21] V. Balbekov, Phys. Rev. Accel. Beams **12**, 124402 (2009).
[22] A. Burov, Phys. Rev. Accel. Beams **12**, 109901 (2009).
[23] A. Burov and V. Danilov, Phys. Rev. Lett. **82**, 2286 (1999).
[24] A. Macridin, A. Burov, E. Stern, J. Amundson, and P. Spentzouris, Phys. Rev. Accel. Beams **18**, 074401 (2015).
[25] A. Macridin, A. Burov, E. Stern, J. Amundson, and P. Spentzouris, Phys. Rev. Accel. Beams **21**, 011004 (2018).
[26] V. Shiltsev, Y. Alexahin, A. Burov, and A. Valishev, Phys. Rev. Lett. **119**, 134802 (2017).
[27] Y. Alexahin, A. Burov, and V. Shiltsev, (2017), arXiv:1709.10020 [physics.acc-ph].
[28] T. Zolkin, A. Burov, and B. Pandey, Phys. Rev. Accel. Beams **21**, 104201 (2018).
[29] V. Balbekov, Phys. Rev. Accel. Beams **22**, 044401 (2019).
[30] V. Balbekov, Phys. Rev. Accel. Beams **20**, 034401 (2017).
[31] Y. H. Chin, A. W. Chao, and M. M. Blaskiewicz, Phys. Rev. Accel. Beams **19**, 014201 (2016).
[32] H. Bartosik, *Beam dynamics and optics studies for the LHC injectors upgrade*, Ph.D. thesis, TU Vienna (2013-10-23).
[33] E. Metral, "Instabilities in CERN machines," talk at the Workshop on Megawatt Rings, Fermilab, USA, 08/05/2018.
[34] A. Burov, Phys. Rev. Accel. Beams **22**, 034202 (2019), arXiv:1807.04887 [physics.acc-ph].
[35] E. Lifshitz and L. Pitaevskii, *Physical Kinetics* (Elsevier, 1981) p. 268.
[36] A. Burov, *Core-Halo Collective Instabilities*, Tech. Rep. FERMILAB-PUB-18-420-AD-APC (2018) arXiv:1808.08498 [physics.acc-ph].
[37] Y. Alexahin, "Identification and reduction of space-charge and beam-beam effects," talk at ICFA Workshop on Mitigation of Coherent Beam Instabilities in particle accelerators, 23-27 September 2019, Zermatt, Switzerland.
[38] A. Burov, *Transverse Instabilities of a Bunch with Space Charge, Wake and Feedback*, Tech. Rep. FERMILAB-PUB-18-493-AD-APC (2018) arXiv:1809.06927 [physics.acc-ph].
[39] V. Kornilov, S. Aumon, S. Gilardoni, and P. Freyermuth, *MD at the PS: Beam Break-Up Instability Near Transition*, Tech. Rep. CERN-ATS-Note-2013-038 MD (2013).
[40] A. Burov, *Transverse Microwave Convective Instability at Transition Crossing*, Tech. Rep. FERMILAB-PUB-19-394-AD-APC (2019) arXiv:1908.02916 [physics.acc-ph].
[41] M. Migliorati, S. Aumon, E. Koukovini-Platia, A. Huschauer, E. Métral, G. Sterbini, and N. Wang, Phys. Rev. Accel. Beams **21**, 120101 (2018).
[42] V. Kornilov, private communication (2020).

# REVIEW OF INSTABILITIES WITH IONS OR/AND ELECTRONS AND POSSIBLE MITIGATIONS

L. Mether*, CERN, Geneva, Switzerland

*Abstract*

The presence of ions and electrons from gas ionization, photoemission or secondary emission is unavoidable in the vacuum chambers of high intensity accelerators and storage rings. Under suitable conditions, these ions and electrons can accumulate and drive the beams unstable. In this contribution, the mechanisms behind and the main conditions for ion and electron accumulation in the bunched beams are summarized. The characteristics of the induced instabilities, as well as common modelling techniques and mitigation strategies are reviewed. The possible interplays between ions and electrons are also discussed.

## INTRODUCTION

Electromagnetic fields in the beam environment, in addition to the externally applied RF and magnetic fields, may perturb the motion of the beam particles and give rise to instabilities. Whereas impedance and space charge are caused by electromagnetic fields induced by the beam itself, electron and ion instabilities are two-stream instabilities that are caused by the presence of another set of charged particles. Typically, this other set of particles is generated by the beam itself directly or indirectly. Electrons and ions are produced through, for example, the beam-induced ionization of residual gas in the beam chamber, photoemission from synchrotron radiation and outgassing due to particles impacting the beam chamber. Particles with the same sign of electrical charge as the beam particles are repelled by the beam and therefore rarely accumulate, whereas particles with the opposite sign of electrical charge, which are attracted by the beam field, are prone to accumulation. Consequently ion accumulation is typically observed in electron machines and electron cloud build-up in positron and proton machines.

## ION INSTABILITIES

Beam-induced gas ionization gives rise to electrons and ions along the beam path. In electron machines, positive ions are attracted by the negative beam field and may become trapped in the beam potential and oscillate around the bunch train, as illustrated in Fig. 1a. Classical ion instabilities, where ions are trapped and accumulate over several turns in a synchrotron, can be avoided with a sufficiently long clearing gap in the bunch train pattern. In the presence of a clearing gap, ions can only accumulate over a single turn, but can still give rise to a fast beam-ion instability [1,2]. Fast beam-ion instabilities can occur also in linear accelerators.

Due to their relatively large mass, ions typically do not move sufficiently during the passage of individual bunches to cause head-tail instabilities. Instead, the ions transfer information on the offset of their generating bunch to the following bunches and thus may lead to coupled-bunch instabilities. The instabilities are typically accompanied by transverse emittance growth and a coherent tune shift. In particular for the fast beam-ion instability, the effects are usually stronger at the tail of the bunch trains, since the density of trapped ions increases along the trains.

Classical ion instabilities have been observed in several machines since the 60's [3]. Fast beam-ion instabilities have also been observed in many machines since they were first predicted in the 90's [4]. In most cases, fast beam-ion instabilities have been observed in the presence of vacuum degradation e.g. during commissioning, due to a local pressure rise such as from impedance heating, or during dedicated experiments with additional injected gas.

The fast beam-ion instability can be analytically modelled using the linear approximation of a two-dimensional Gaussian beam field [1]. In this approximation, an ion with mass number $A$ at the transverse position $(x, y)$ receives the following velocity kick by the beam

$$\frac{2N_b r_p c}{A}\frac{x, y}{(\sigma_x+\sigma_y)\,\sigma_{x,y}} \equiv k_{x,y} * x, y\ , \tag{1}$$

where $N_b$ is the bunch intensity, $r_p$ the classical proton radius, $c$ the speed of light and $\sigma_{x,y}$ are the transverse beam sizes. During the bunch spacing $T_b$ the ions drift. By analogy with the stability condition of a linear beam trajectory, $|\mathrm{Tr}(M)| < 2$, the motion is stable if $k_{x,y}T_b < 4$. This leads to a lower limit on the ion mass number for trapping to occur

$$A > A_{\mathrm{trap}} = \frac{N_b r_p T_b c}{2\,(\sigma_x+\sigma_y)\,\sigma_{x,y}}\ . \tag{2}$$

Neglecting the presence of a spread in the oscillation frequency of the trapped ions, the instability rise time can be estimated as

$$\tau_{\mathrm{inst}}^2 \propto \frac{\gamma^2 A\omega_\beta}{n_b^4 N_b^3 P^2 T_b c}\,(\sigma_x+\sigma_y)^3\,\sigma_{x,y}^3\ . \tag{3}$$

Here $\gamma$ is the Lorentz factor of the beam, $n_b$ is the number of bunches in the train, $\omega_\beta$ is the (angular) betatron frequency and $P$ is the partial vacuum pressure for the species considered.

However, the linear approximation is accurate only for ions oscillating within a small region around the centre of the beam, with $x, y \lesssim \sigma_{x,y}$. This condition is more easily satisfied for heavier ions with mass numbers that are well above the trapping mass number $A_{\mathrm{trap}}$. In the non-linear regime, ion trajectories are significantly altered with respect

* lotta.mether@cern.ch

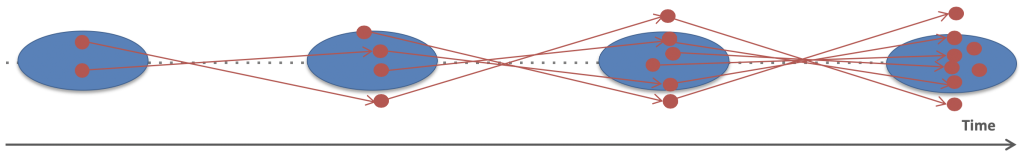


(a) Ion accumulation along an electron bunch train.

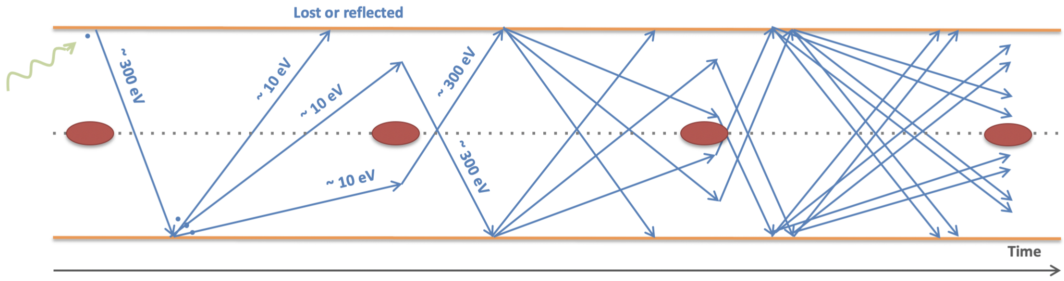


(b) Electron cloud build-up along a proton/positron bunch train.

Figure 1: Schematic diagrams of ion accumulation in electron machines (a) and electron cloud build-up in positron or proton machines (b).

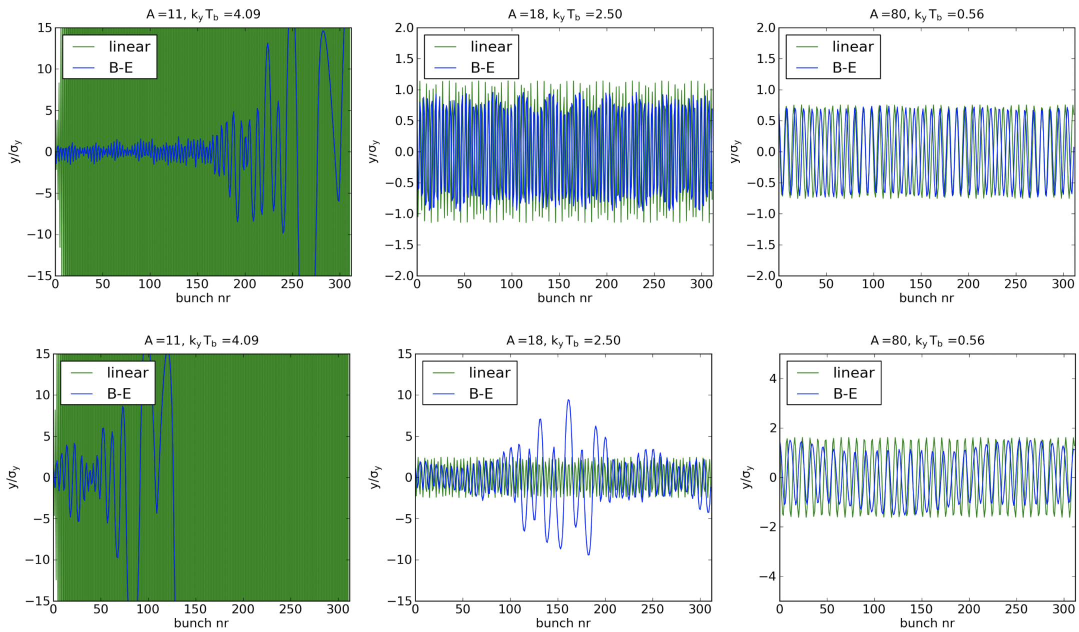


Figure 2: Comparison of ion trajectories along a bunch train using the linear approximation and the Bassetti-Erskine formula [5] for the beam field for different ion mass numbers (left to right). The top and bottom rows show trajectories with initial amplitudes of 0.7 $\sigma$ and 1.5 $\sigma$ respectively.

to the linear approximation and the trapping condition Eq. (2) is not strictly valid, as shown in Fig. 2. As illustrated in the left column of the figure, the non-linearity of the beam field alters the ion trapping such that ions that would be over-focused and lost in the linear regime are in fact trapped in an oscillation around the beam for a significant amount of time. The non-linear beam field also introduces a spread in the ion oscillation frequency. Extensions of the theory to the non-linear regime suggest that the non-linearity damps the instability, such that the growth rate becomes linear rather than exponential [6].

The full beam-ion interaction, including non-linearities, can be accurately modelled using macro-particle simulations. The simulations can be done in the strong-strong regime, where both the beam and ions are represented by macro-particles, or the weak-strong regime, where only the ions are modelled with macro-particles. The strong-strong simulations, in particular, are typically computationally very heavy, but they have the benefit of being able to model also the evolution of the beam emittance. Instabilities caused by ion trapping in the non-linear regime were observed in a recent simulation study [7]. Compared to the standard fast beam-ion instability, these instabilities showed atypical characteristics, e.g. the instability developed simultaneously over most of the train rather than developing from the tail of the train towards the head and the instability was stronger for larger ion mass numbers contrary to the prediction of Eq. (3).

Apart from the non-linearity of the beam field, the variation of the beta functions along the machine and the presence of multiple gas species can also have a damping effect on the instability. In addition, the instability also strongly depends on the filling pattern. All of these effects can readily be taken into account in macro-particle simulations. Fast beam-ion instabilities have also successfully been modelled using a wake field formalism [8, 9], which allows taking into account several of these effects.

## ELECTRON INSTABILITIES

Electrons are produced in the beam chamber e.g. through beam-induced gas ionization and photoemission from synchrotron radiation. Such seed electrons are accelerated by the beam and can induce secondary electron emission from the chamber wall on their impact. With a positively charged beam, a subsequent bunch will accelerate these secondary electrons across the chamber and, as they hit the wall, further secondary emission can be induced. In this way, as illustrated in Fig. 1b, secondary electron emission can lead to avalanche electron multiplication through beam-induced multipacting over several bunch passages, until a dynamical equilibrium is reached.

The conditions for electron cloud build-up depend on several parameters including the bunch spacing, the chamber geometry, external magnetic fields, the bunch charge and length, as well as the secondary emission yield (SEY) of the chamber surface. The SEY is defined as the ratio between the emitted and impacting electron currents and is a function of the energy and angle of incidence of the impacting electrons. The SEY of a given surface depends on its chemical and physical properties, which may change over time.

Whereas ions barely move during the passage of individual bunches, the much lighter electrons move significantly during a single bunch passage. Electrons attracted by the beam field are pulled into the bunch (the so-called pinch) and oscillate in the beam field during the bunch passage. This gives rise to a $z$-dependent electron density along the bunch, which can induce coupling between the head and the tail of the bunch and eventually drive the bunch unstable. As a consequence of the electron motion within the bunch, fast intra-bunch motion is characteristic for single bunch electron cloud instabilities. The instabilities are often accompanied by beam losses and transverse emittance growth.

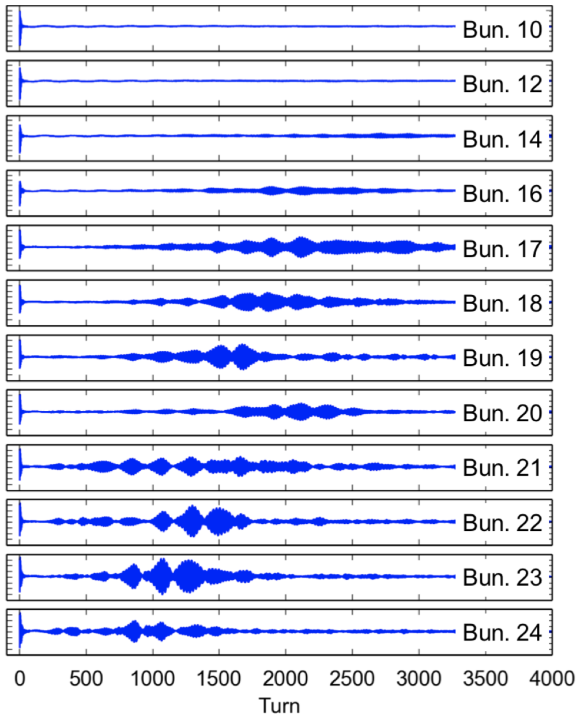


(a) Single-bunch (vertical) instabilities in the LHC [10].

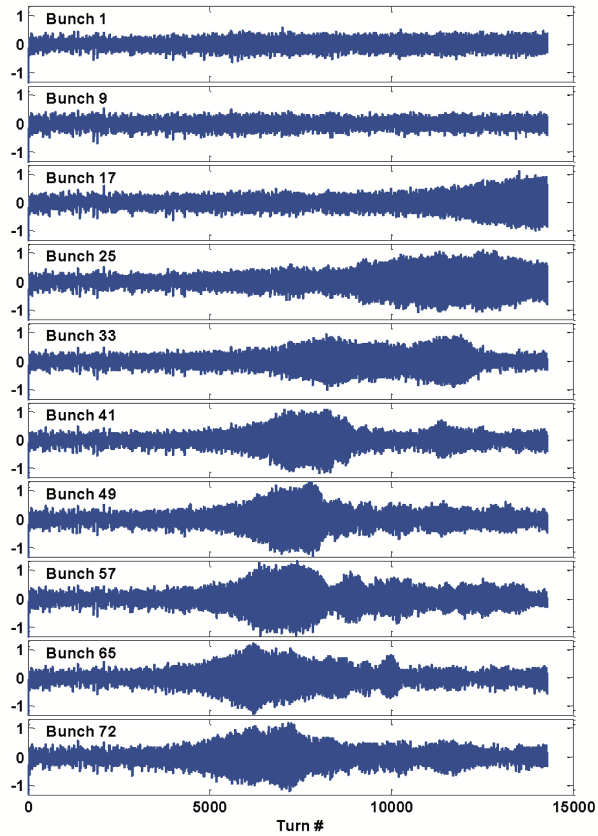


(b) Coupled-bunch (horizontal) instability in the PS [11].

Figure 3: Measured centroid positions for selected bunches along bunch trains suffering from single- and coupled-bunch electron cloud instabilities in CERN accelerators.

Since the electron cloud survives on the time scale of several bunch passages, it can also be responsible for bunch-to-bunch coupling and coupled-bunch instabilities. These instabilities are likely to occur in situations where the electron motion is constrained, such that a memory of the electron distribution is maintained from one bunch to the following. This can be the case e.g. in the presence of externally applied magnetic fields such as dipole fields. Since electron clouds build up along the bunch trains, bunches at the tail of trains encounter a larger electron density than bunches at the head of trains and are therefore most affected by both single- and coupled-bunch instabilities. This is illustrated by the transverse position measurements shown in Fig. 3.

Electron cloud instabilities were first observed in the 60's. Since then, electron cloud has been observed in several different machines, through many related effects [10,12]. Apart from instabilities, electron cloud effects on the beam dynamics include tune shifts along the bunch train and incoherent effects such as tune spread and emittance growth, which may lead to slow beam losses. An RF stable phase shift is induced as a consequence of the beam energy lost to the electrons [13]. Electron clouds can also affect the vacuum quality, through outgassing leading to a pressure rise. Finally, the impinging electrons deposit a heat load on the chamber walls, which can be problematic in particular in superconducting machines. Currently electron cloud effects are present during operation e.g. in the LHC [14] and at SuperKEKB [15].

Analytical models have been developed to study the behaviour of electrons in the beam potential and the induced instabilities. The electron oscillations in the beam field during the pinch can be modelled similarly to the ion motion in the electron beam in Eq. (1). As shown in Fig. 4, within the validity regime of the linear approximation, i.e. for an electron with an oscillation amplitude that is smaller than the rms beam size, there is good agreement between the linear analytical theory and simulations [16]. Models using a wake field formalism have been developed for studying the resulting head-tail instability, although the electron cloud cannot be considered a time-invariant system due to the electron motion during the bunch passage [17–19].

Due to the complexity of the electron cloud build-up and instability processes, a comprehensive understanding of electron cloud effects currently relies on macro-particle simulations. For single-bunch electron cloud instabilities the problem can be divided into two parts: electron cloud build-up simulations with a rigid beam and subsequent beam dynamics simulations of the instability, where electron distributions saved in build-up simulations can be used to initialize the electrons [20]. For coupled-bunch instabilities, on the other hand, the build-up must be performed dynamically over the full bunch train to capture the instability mechanism [21]. However, several aspects of coupled-bunch instabilities have successfully been modelled analytically with wake field models [22–24], similarly to the fast beam ion instability.

Full scale electron cloud instability simulations are demanding both in terms of computing resources and time.

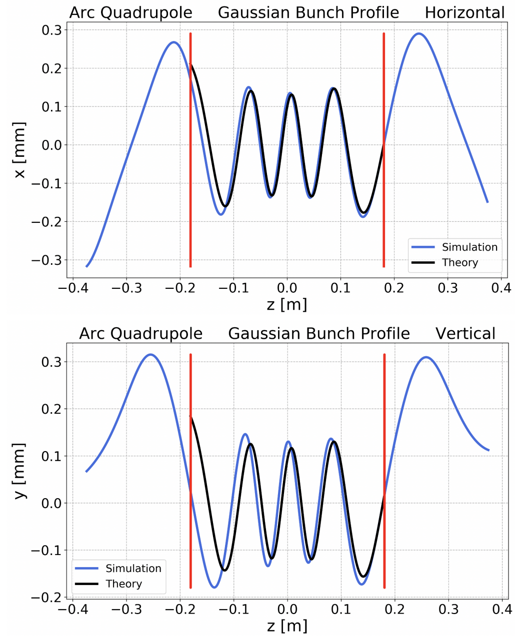


Figure 4: Comparison between macro-particle simulations and the linear theory of the electron trajectories within a Gaussian bunch in an LHC arc quadrupole [16].

This is due to the large range of the time and distance scales involved in the process. The entire chamber must be simulated and, at the same time, the small beam must be resolved very well, requiring a fine grid mesh over a large area. The fast electron motion requires small time steps, of the order of 10 ps, but the instability evolution can take several seconds amounting to a very large number of time steps. Consequently, electron cloud simulations can benefit from advanced computational methods such as multi-grid Poisson solvers and parallel computing [25,26]. However, due to the sequential nature of the electron cloud build-up, parallelization strategies are more limited than e.g. for simulations with only a lumped impedance. Even with advanced techniques, a single simulation can require several weeks of computing time on tens or hundreds of CPU cores.

## MITIGATION STRATEGIES

Electron and ion instabilities can naturally be mitigated by preventing the accumulation of the corresponding particles. One approach to achieving this is to directly suppress the production of electrons and ions. A first step towards suppressing primary electrons and ions is to ensure a good vacuum or low residual gas pressure, to which end chamber surfaces with low outgassing or active pumping such as Non Evaporable Getter (NEG) coatings can be helpful [27]. For ion instabilities, this can be a sufficient measure to prevent significant accumulation. For electron cloud prevention, it may be necessary to suppress also the amount of photoelectrons emitted by the synchrotron radiation e.g. with the help of saw-tooth surfaces [28]. Furthermore, it is not sufficient to suppress primary electron production if secondary emission is large, as this can lead to exponential growth of the electron density.

Secondary electron emission can be suppressed through several different methods. For many materials, conditioning the surface with electrons lowers the secondary emission yield as a function of the accumulated electron dose [29]. This allows for beam-induced conditioning (or scrubbing), occurring gradually during accelerator operation [30]. Another commonly used technique is to coat exposed surfaces with materials that naturally have a low SEY, such as amorphous carbon or NEG [31, 32]. In addition, a low SEY can also be achieved by modifying the surface topology, e.g. through laser ablation [33, 34].

An alternative, or complementary, approach to direct suppression is to actively perturb the electron and ion motion, so as to prevent their accumulation. This can be achieved e.g. by using clearing electrodes, which generate electric fields that attract the charged particles towards the walls [35–38]. For electrons, a similar effect can be achieved with weak magnetic fields that bend the trajectories of emitted particles back onto the chamber wall, such as solenoids [39, 40].

If accumulation cannot be prevented, there are some means of addressing the resulting instabilities. Coupled-bunch instabilities, whether due to electrons or ions, can typically be suppressed with conventional bunch-by-bunch transverse feedback systems, see Fig. 5. Landau damping can also help mitigate coupled-bunch instabilities from electrons and ions. For ion instabilities, a spread in the ion oscillation frequencies e.g. due to the non-linearity of the beam field and the presence of different ion species can give rise to Landau damping that has a mitigating effect on the instability [2, 42]. Amplitude detuning from octupole magnets can mitigate the coupled-bunch electron instability [43].

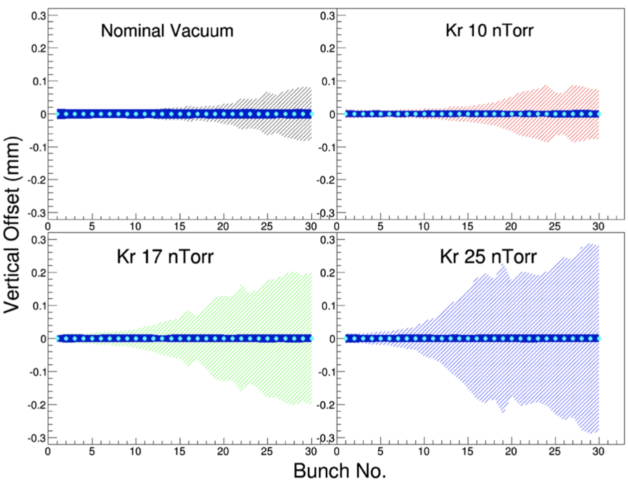


Figure 5: Vertical bunch offsets as a function of bunch number measured at CESR-TA with different Kr gas pressures [41]. With the transverse feedback switched on (filled area in blue) the fast beam-ion instability is fully suppressed.

Single-bunch electron instabilities, on the other hand, typically cannot be efficiently suppressed with conventional feedback systems, due to their characteristic fast intra-bunch motion. Wideband feedback systems, currently under development, have the potential to efficiently suppress also the fast intra-bunch motion [44]. Meanwhile, chromaticity and amplitude detuning from octupole magnets can suppress the instabilities to some extent [45].

Since both the electron and ion densities needed to cause instabilities accumulate over several bunch passages, the instabilities can also be mitigated by tailoring the filling pattern to minimize their accumulation. This can be achieved e.g. by increasing the bunch spacing or reducing the length of bunch trains [8, 41, 46], although it often comes at the cost of a reduced total beam current.

## ELECTRON-ION INSTABILITIES

Above, it has been assumed that any seed particles with the same sign of electrical charge as the beam are negligible as they don't accumulate in the chamber volume, since they are repelled by the beam and eventually will reach the chamber walls and be absorbed. In this section, we discuss conditions under which this may not be a reasonable assumption.

Certainly, in most situations some effects that impact the dynamics indirectly can occur at the wall, such as outgassing when repelled ions or electrons impact on the wall. Apart from such potential secondary effects, it is reasonable to ignore the second species when the amount of seed particles produced at each bunch passage is small compared to the accumulated charge in the electron or ion cloud. On the other hand, if large amounts of electrons and ions are generated at each bunch passage, e.g. if very high gas densities occur in the beam pipe, one can expect the two species to have a significant impact on each other's dynamics. This could result in a collective behaviour involving the two species that is qualitatively different from the behaviour of either species on its own.

Events falling under this category occurred in the LHC during operation in 2017 and 2018 [47]. The recurring events, which were characterized by very fast beam instabilities accompanied by unusual beam losses in a certain machine location, would inevitably lead to beam dumps. The instabilities are thought to have been caused by a very high local gas density, predicted by beam loss rates to $10^{18}$–$10^{22}$ $m^{-3}$, depending on the longitudinal extent of the gas [48]. These transient pressure bumps were generated by the beam-induced phase transition of macro-particles of frozen air, present due to an accidental inlet of air during the preceding machine cool-down.

Observations of large positive tune shifts and fast intra-bunch motion suggest that large electron densities were present during the events [49]. However, electron cloud simulations with high gas densities could not reproduce the observations [50]. To model the instability, electron cloud simulation tools were extended with multi-cloud capabilities to model both the build-up and beam stability in the presence of electrons and ions simultaneously [51]. For high gas densities, the simulations show a significant impact of the

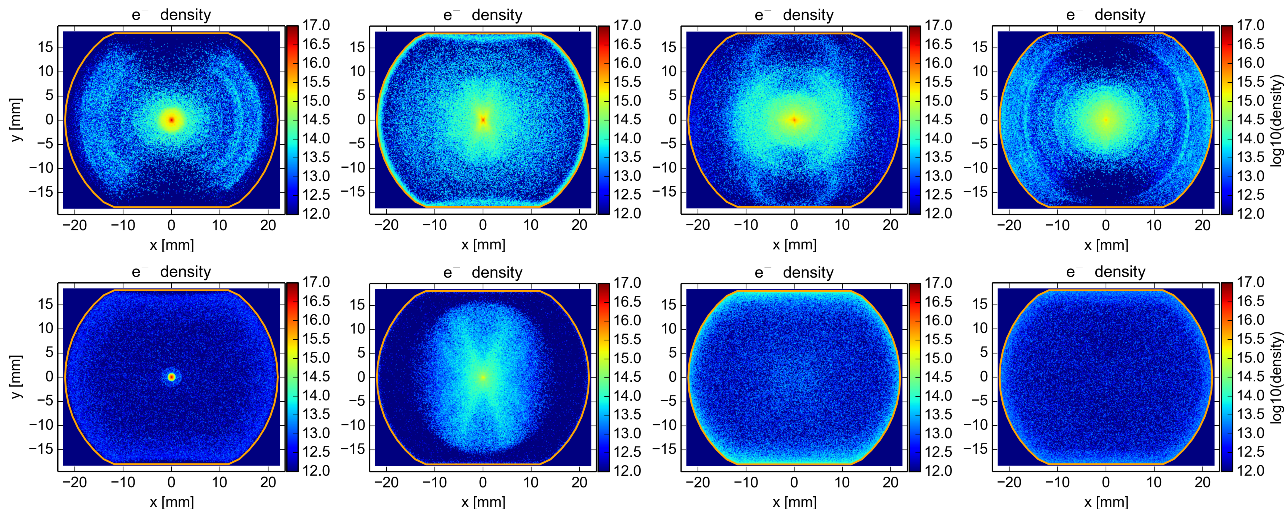


(a) t = 0 (b) t = 1 ns (c) t = 5 ns (d) t = 15 ns

Figure 6: Simulation snapshots of the electron density in the LHC beam chamber during a bunch passage [51]. Images from a multi-species simulation (top), are compared to the equivalent images in a simulation tracking only electrons (bottom). The first image on each row (t = 0) is taken during the passage of the centre of the bunch.

field from the ion population on the electron dynamics, as illustrated in Fig. 6, confirming that, at high concentrations, the two species must be modelled together.

## OUTLOOK

Electron and ion instabilities have been observed in several machines. Electron cloud is present in several operating machines. Ion instabilities are currently observed mainly under vacuum degradation, but may become more prevalent in future machines with higher beam brightness. In addition, an instability mechanism relying on the interplay between electrons and ions may occur under exceptional conditions.

In order to avoid problems from electron and ion instabilities, predictions and development of mitigation strategies are important. Macro-particle simulations can model the phenomena comprehensively using modern computational tools, but large amounts of computing time and resources are still needed for realistic simulations. For electron cloud, the development and implementation of mitigation strategies are needed for several on-going as well as future projects, such as the HL-LHC and the FCC. For ion instabilities more comprehensive studies are needed to assess their impact in future machines.

## ACKNOWLEDGEMENTS

The author would like to thank G. Arduini, G. Iadarola, E. Métral, A. Oeftiger, A. Romano, G. Rumolo, and L. Sabato for their input to the present contribution.

## REFERENCES

[1] T. O. Raubenheimer and F. Zimmermann, "Fast beam-ion instability. I. Linear theory and simulations", *Phys. Rev. E* 52, pp. 5487–5498, 1995.

[2] G. V. Stupakov, T. O. Raubenheimer, and F. Zimmermann, "Fast beam ion instability. 2. Effect of ion decoherence", *Phys. Rev. E* 52, pp. 5499–5504, 1996.

[3] F. Zimmermann and G. Rumolo, "Two stream problems in accelerators", proceedings of APAC'01, Beijing, China, 2001.

[4] F. Zimmermann, "Two-stream effects in present and future accelerators", proceedings of EPAC2002, Paris, France, 2002.

[5] M. Bassetti and G. Erskine, "Closed expression for the electrical field of a two-dimensional Gaussian charge", Technical Report, CERN-ISR-TH/80-06, 1980.

[6] S. Heifets, "Saturation of the ion transverse instability", proceedings of PAC'97, Vancouver, Canada, 1997.

[7] L. Mether, A. Oeftiger, and G. Rumolo, "Modeling of fast beam-ion instabilities", *CERN Yellow Rep. Conf. Proc.* 1, pp. 63–68, 2018.

[8] L. Wang, Y. Cai, T. O. Raubenheimer, and H. Fukuma, "Suppression of beam-ion instability in electron rings with multi-bunch train beam fillings", *Phys. Rev. ST Accel. Beams* 14, p. 084401, 2011.

[9] L. Wang *et al*, "Beam ion instability: Measurement, analysis, and simulation", *Phys. Rev. ST Accel. Beams* 16, p. 104402, 2013.

[10] G. Iadarola and G. Rumolo, "Electron cloud effects", *CERN Yellow Rep. Conf. Proc.* 1, pp. 49–56, 2018.

[11] G. Iadarola *et al.* "Electron cloud studies for the upgrade of the CERN PS", proceedings of IPAC'13, Shanghai, China, 2013, paper WEPEA013.

[12] F. Zimmermann, "Electron-cloud effects in past and future machines – walk through 50 years of electron-cloud studies", proceedings of ECLOUD'12, Isola d'Elba, Italy, 2012.

[13] J. F. Esteban Müller, P. Baudrenghien, T. Mastoridis, E. Shaposhnikova, and D. Valuch, "High-accuracy diagnostic tool for electron cloud observation in the LHC based on synchronous phase measurements", *Phys. Rev. ST Accel. Beams* 18, p. 112801, 2015.

[14] G. Rumolo *et al*, "Electron cloud effects at the LHC and LHC injectors", proceedings of IPAC'17, Copenhagen, Denmark, 2017, paper MOZA1.

[15] K. Ohmi, "Coherent and incoherent effects of e-cloud", presented at MCBI 2019, this conference.

[16] L. Sabato, "Analysis of electron motion within the beam", presentation at the 65th Electron Cloud Meeting, CERN, Feb. 2019. `https://indico.cern.ch/event/790352/`

[17] K. Ohmi and F. Zimmermann "Head-tail instability caused by electron clouds in positron storage rings", *Phys. Rev. Lett.* 85, pp. 3821–3824, 2000.

[18] K. Ohmi, F. Zimmermann, and E. Perevedentsev, "Wake-field and fast head-tail instability caused by an electron cloud", *Phys. Rev. E* 65, p. 016502, 2002.

[19] E. Perevedentsev, "Head-tail instability caused by electron cloud", proceedings of ECLOUD'02, Geneva, Switzerland, 2002.

[20] G. Rumolo and F. Zimmermann, "Electron cloud simulations: beam instabilities and wakefields", *Phys. Rev. ST Accel. Beams* 5, p. 121002, 2002.

[21] G. Iadarola, "New tools for the simulation of coupled bunch instabilities driven by electron cloud", presentation at the 64th Electron Cloud Meeting, CERN, Dec. 2018. `https://indico.cern.ch/event/776089/`

[22] G. Arduini *et al.*, "Beam observations with electron cloud in the CERN PS and SPS complex", proceedings of ECLOUD'04, Napa, USA, Apr. 2004.

[23] S. S. Win *et al.*, "Numerical study of coupled-bunch instability caused by an electron cloud", *Phys. Rev. ST Accel. Beams* 8, p. 094401, 2005.

[24] S. A. Antipov, P. Adamson, A. Burov, S. Nagaitsev, and M.-J. Yang, "Fast instability caused by electron cloud in combined function magnets", *Phys. Rev. Accel. Beams* 20, p. 044401, 2017.

[25] J.-L. Vay, M. A. Furman, and M. Venturini, "Direct numerical modeling of e-cloud driven instability of three consecutive batches in the CERN SPS", proceedings of IPAC'12, New Orleans, Louisiana, USA, 2012, paper TUEPPB006.

[26] G. Iadarola *et al.*, "Evolution of Python tools for the simulation of electron cloud effects", proceedings of IPAC'17, Copenhagen, Denmark, 2017, paper THPAB043.

[27] C. Benvenuti *et al.*, "A novel route to extreme vacua: the non-evaporable getter thin film coatings", *Vacuum* 53, pp. 219–225, 1999.

[28] N. Mahne *et al.*, "Photon reflectivity distributions from the LHC beam screen and their implications on the arc beam vacuum system", *Appl. Surf. Sci.* 235, pp. 221–226, 2004.

[29] R. Cimino *et al.*, "Nature of the decrease of the secondary-electron yield by electron bombardment and its energy dependence", *Phys. Rev. Lett.* 109, p. 064801, 2012.

[30] G. Iadarola, B. Bradu, P. Dijkstal, L. Mether, and G. Rumolo, "Impact and Mitigation of Electron Cloud Effects in the Operation of the Large Hadron Collider", proceedings of IPAC'17, Copenhagen, Denmark, 2017, paper TUPVA019.

[31] C. Yin Vallgren *et al.*, "Amorphous carbon coatings for the mitigation of electron cloud in the cern super proton synchrotron", *Phys. Rev. ST Accel. Beams*, vol. 14, p. 071001, 2011.

[32] B. Henrist, N. Hilleret, C. Scheuerlein, and M. Taborelli, "The secondary electron yield of TiZr and TiZrV non-evaporable getter thin film coatings", *Appl. Surf. Sci.* 172, pp. 95–102, 2001.

[33] G. Tang, A. C. Hourd, and A. Abdolvand, "Nanosecond pulsed laser blackening of copper", *Appl. Phys. Lett.* 101, p. 231902, 2012.

[34] O. B. Malyshev *et al.* "Electron cloud effect mitigation with the laser ablation technique", presented at MCBI 2019, this conference.

[35] F. Caspers, JP. Delahaye, JC. Godot, K. Hubner, and A. Poncet, "EPA beam-vacuum interaction and ion clearing system", proceedings of EPAC'88, Rome, Italy, 1988.

[36] M. Zobov *et al.*, "Impact of Ion Clearing Electrodes on beam dynamics in DAΦNE", *J. Instrum.* 2, p. 08002, 2007.

[37] L. F. Wang, D. Raparia, J. Wei, and S.Y. Zhang, "Mechanism of electron cloud clearing in the accumulator ring of the Spallation Neutron Source", *Phys. Rev. ST Accel. Beams* 7, p. 034401, 2004.

[38] Y. Suetsugu *et al.*, "Demonstration of electron clearing effect by means of a clearing electrode in high-intensity positron ring", *Nucl. Instrum. Meth. A* 598, pp. 372–378, 2009.

[39] H. Fukuma *et al.*, "Status of solenoid system to suppress the electron cloud effects at the KEKB", *AIP Conf. Proc.* 642, pp. 357–359, 2002.

[40] A. Kulikov, A. Novokhatski, and J. Seeman, "Suppression of the beam instability related to electron cloud at PEP-II B-factory", proceedings of ECLOUD'04, Napa, CA, USA, 2004, pp. 21-24.

[41] A. Chatterjee, K. Blaser, W. Hartung, D. Rubin, and S. T. Wang, "Fast ion instability at the Cornell Electron Storage Ring Test Accelerator", *Phys. Rev. ST Accel. Beams* 18, 064402, 2015.

[42] G. Stupakov, "Suppression of the fast beam-ion instability by tune spread in the electron beam due to beam-beam effects", presented at MCBI 2019, this conference.

[43] L. Mether, "Electron cloud stability at injection: coupled bunch effects", presented at the 165th HL-LHC WP2 meeting, CERN, Dec. 2019. `https://indico.cern.ch/event/863723/`

[44] K. Li *et al.*, "Modelling and studies for a wideband feedback system for mitigation of transverse single bunch instabilities", proceedings of IPAC'13, Shanghai, China, 2013, p. 3019.

[45] K. Li and G. Rumolo, "Mitigation of electron cloud instabilities in the LHC using sextupoles and octupoles", proceedings of IPAC'12, New Orleans, LA, USA, 2012, p. 3084.

[46] G. Skripka *et al.* "Comparison of electron cloud build-up simulations against heat load measurements for the LHC arcs with different beam configurations", proceedings of IPAC'19, Melbourne, Australia, 2019, paper WEPTS051.

[47] J. M. Jiménez *et al.*, "Observations, analysis and mitigation of recurrent LHC beam dumps caused by fast losses in arc half-cell 16L2", proceedings of IPAC'18, Vancouver, Canada, 2018, paper MOPMF053.

[48] A. Lechner *et al.*, "Beam loss measurements for recurring fast loss events during 2017 LHC operation possibly caused by macroparticles", proceedings of IPAC'18, Vancouver, Canada, 2018, paper TUPAF040.

[49] B. Salvant *et al.*, "Experimental characterisation of a fast instability linked to losses in the 16L2 cryogenic half-cell in the CERN LHC", proceedings of IPAC'18, Vancouver, Canada, 2018, paper THPAF058.

[50] L. Mether *et al.*, "16L2: operation, observations and physics aspects", proceedings of 7th Evian Workshop on LHC Beam Operation, Evian Les Bains, France, 2017, pp. 99–105.

[51] L. Mether, G. Iadarola, K. Poland, G. Rumolo, and G. Skripka, "Multi-species electron-ion simulations and their application to the LHC", proceedings of IPAC'19, Melbourne, Australia, 2019, paper WEPTS050.

# REVIEW OF INSTABILITIES WITH BEAM-BEAM EFFECTS AND POSSIBLE MITIGATIONS

T. Pieloni *, EPFL, Lausanne, Switzerland

*Abstract*

In circular colliders the two counter rotating beams interact electromagnetically at various locations along the ring, where sharing a common beam pipe, and at the interaction regions via the so called beam-beam force. These interactions are of different nature, long-range or head-on and they represent a very important non-linear force acting on the particle beams. When mitigating impedance driven instabilities the impact of beam-beam effects has to be accounted for, since these effects change many of the optical properties and particle dynamics with very important impacts to the stability conditions. Since the beam-beam force can change single particle properties as well as coherent beam oscillations they need to be added in all their aspects to the study of mitigation methods for coherent impedance driven instabilities. The beam-beam effects can help mitigating but can be detrimental in enhancing the coherent motion. Several observations from past colliders have shown the impact of beam-beam effects on beam stability but more recently the Large Hadron Collider (LHC) has given the possibility to experimentally probe the impact of these interactions on the beam stability due to the constant appearance of instabilities. A very dense experimental and theoretical campaign has been motivated to better understand their role in the instability picture. In this paper the main contributions to beam stability and mitigations coming from beam-beam effects are explained with direct observations and experimental evidences from the LHC. The challenges arising from the higher energy reach of future colliders has also boosted at a study level the development of alternative mitigating methods and a new strategy for the design of future accelerators with conventional mitigation techniques.

## INTRODUCTION

The accelerator impedance [1, 2] can be a source of coherent instabilities. The general strategy for mitigating such effects is that the coupled-bunch instability modes will be cured by a transverse feed-back [3], while single-bunch instabilities will be suppressed by Landau damping [4]. As for the LHC, Landau octupoles provide the necessary Landau damping [5–7] while a transverse feedback is constantly used to suppress any coupled bunch mode [8,9]. Over many years of operation several instabilities have appeared requiring a much larger octupole strength providing Landau damping. Therefore several studies have been conducted to understand the effectiveness of Landau damping and the role of beam-beam interactions in the stability of the beams. In Fig. 1 a factor 2 difference between expected and required octupole strength to mitigate coherent instabilities via Landau damping is shown together with an historical sketch of the different types of instabilities observed over RUN I and II [10]. In colliders anything relevant in conventional single beam instabilities [3] (i.e. chromaticity, tune spread, tune shifts, linear coupling) will be modified by the beam-beam interactions. Depending on the operational configuration the beam-beam effects can enhance stability or might deteriorate it [11]. For these reasons these effects need to be understood, evaluated and kept under control to ensure long term stability. An extensive campaign devoted to understand the impact of beam-beam effects as a possible source of this discrepancy between expected and measured instability thresholds has been conducted and a summary is given in this paper.

## BEAM-BEAM INTERACTIONS AND BEAM STABILITY

In synchrotrons, the beam is kept stable partially by Landau damping due to the tune spread within each bunch. The stability diagram in plane j = (x, y) is calculated from [12]:

$$SD^{-1} = -\int_0^\infty dJ_x \int_0^\infty \frac{J_{x,y}\frac{d\Phi(J_x,J_y)}{dJ_{x,y}}}{Q_0 - Q_{x,y}(J_x,J_y)} dJ_y \qquad (1)$$

where $J_{x,y}$ and $Q_{x,y}$ are the action variable and particle detuning, respectively The horizontal and vertical planes are indicated as $x$ or $y$. $Q_0$ is the unperturbed betatron tune, and $\Phi$ is the particle distribution. Due to the dependency on the particle distribution derivative, it is clear that the stability can be changed significantly by a small change in the distribution and or by a change in the detuning with amplitude. In addition a transverse feedback is constantly used to damp the coupled bunch instabilities. The fastest growing instability modes can be damped with very low damper bandwidth, while the damping of the high frequency modes is very sensitive to the exact frequency response of the feedback system above the cutoff frequency [8, 9]. Impedance driven instabilities have still be present during the LHC operations. The beam-beam interactions are strongly non-linear electromagnetic interactions that modify in a substantial way the beam properties and optical characteristics in addition to the accelerator lattice [13]. For the case of Gaussian particle distributions the angular deflection a particle will fill going through the opposite beam has only a radial component and can be expressed by the known relation:

$$\Delta r' = \frac{2Nr_0}{\gamma} \cdot \frac{1}{r} \cdot (1 - e^{-\frac{r^2}{2\sigma^2}}) \qquad (2)$$

where N is the number of charges, $r_0$ is the classical proton radius, $\gamma$ is the relativistic factor and $\sigma$ is the transverse RMS beam size.

* tatiana.pieloni@epfl.ch

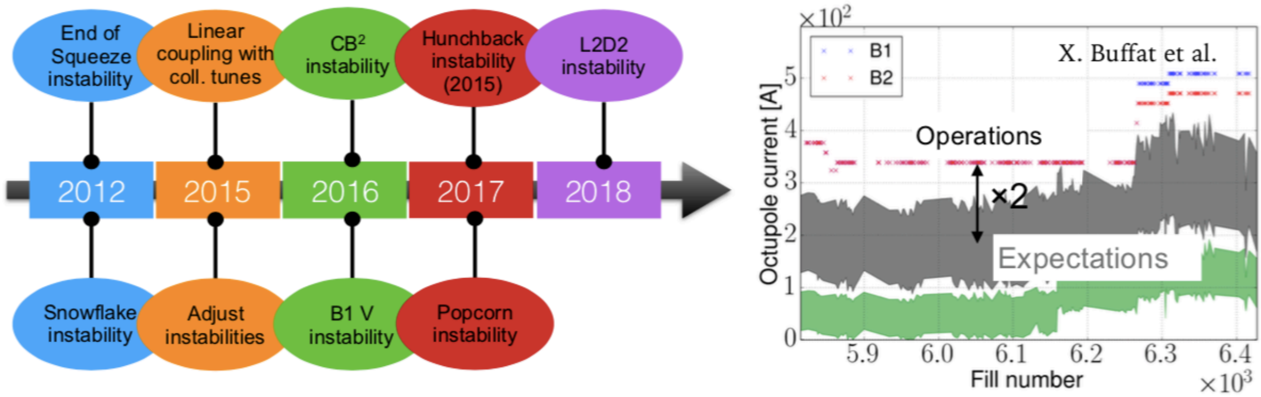


Figure 1: Chronological summary of the different instabilities detected in the LHC (left plot). Plot of the expected ( green and grey lines ) versus operationally used (red and blue crosses) octupole strengths to mitigate coherent instabilities (right plot) for different physics fills. A factor two is evident between the models and the reality. Courtesy of X. Buffat.

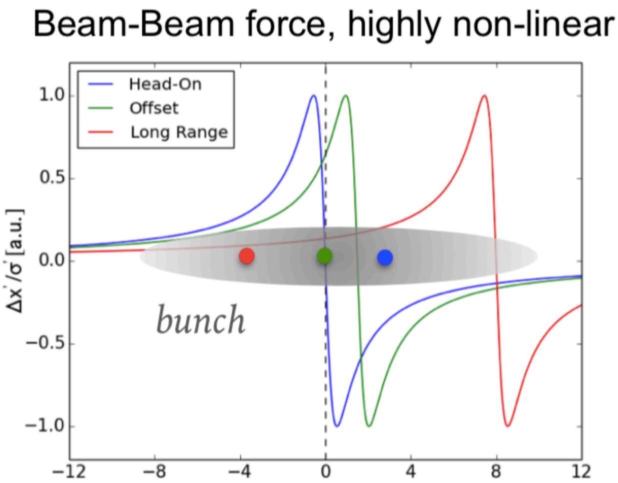


Figure 2: Beam-beam force as a function of the test particle position in units of $\sigma$ for different beam to beam separations: the blue line for zero offset, the green line for offset of 1 $\sigma$ and the red line for 8 $\sigma$ separation.

In Fig. 2 the beam-beam force, as expressed in Eq. (2), is shown for different separations $r$ in units of $\sigma$ between the force produced by a bunch and the probing one (the grey area). The blue line shows the force when a head-on collision occurs $r \approx 0$, the green line shows the case of a small offset $r \approx 1\sigma$ (as for example when levelling luminosity with a transverse offset or when collapsing the separation bumps) and the red line shows the case of a 8 $\sigma$ long-range interaction. The interactions can occur at different beam to beam distances and the effects on the counter rotating beam can be very different because different particles are involved in the interactions. In head-on collisions the core of the beams are the most affected while for long-range interactions tail particles are the one most affected. In a collider with many bunches and multiple Interaction Points (IPs) all these effects occur at different stages of the operational cycle and at different locations along the ring. While head-on or small offsets collisions can occur only at the IPs the long range interactions can occur either around the interaction regions where the beams are bought into collision (i.e. a la LHC [5]) or regularly spaced around the machine when they share a common beam pipe (i.e. at the Tevatron [14]).

In the LHC the interactions are of all types: head-on, long-range or with small offsets. The beams interact at more than 124 locations along the circumference at each turn.

These effects can enhance stability or reduce it depending on the effects involved, for this reason they must be taken into account when understanding the coherent stability of beams in hadron colliders. Several lessons come from past experience (i.e. Tevatron, RHIC) but more have been experimentally explored in the LHC during the past years of operation due to the continuous presence of instabilities during the operation of the collider.

## INCOHERENT EFFECTS

Since 2012 the LHC has experienced strong impedance driven instabilities during the whole physics runs. To mitigate such effects the Landau octupoles have been powered at maximum strength and high chromaticity operation has been put in place (from 2 to 15-17 units increase) as summarised in [10, 15]. These strong non-linearities have negative effects on the beams dynamics of colliding beams but were necessary to mitigate the instabilities. In addition they interplay with beam-beam incoherent effects change the beam stability thresholds. This occurs via several effects: the detuning with amplitude [16], via a change of chromaticity from long-range as well as head-on collisions, the impact of noise and diffusive mechanisms at reduced dynamical aperture.

The beam-beam LR separation at the first encounter can, for the high luminosity experiments, be defined as:

$$r = \alpha \cdot \sqrt{\frac{\beta^* \cdot \gamma}{\epsilon_{norm}}} \tag{3}$$

where $\alpha$ is the crossing angle, $\beta^*$ the beta function at the IP and $\epsilon_{norm}$ is the normalized emittance at the IP. This approximation is valid only for the case where the $\beta^*$ is much smaller than the $s$ location of the first long-range encounter (for a 25 ns beam spacing, this corresponds to 3.75 m from the IP). Reducing the long-range separation will make the force stronger and reduce as a consequence the dynamical aperture.

### *Detuning with amplitude and Stability*

In the presence of the beam-beam interactions, the transverse beam stability provided by the Landau octupoles is modified [15, 17, 18]. In fact, the detuning with amplitude (tune spread) given by the octupole magnets is modified by the beam-beam detuning with amplitude coming from the different types of interactions. When the beams collide head-on, the transverse beam stability is maximised due to the large tune spread provided by the beam-beam head-on interaction [7]. For this reason, a detailed analysis of the transverse beam stability is required taking into account the presence of the opposite beam.

The transverse stability of the beams can be evaluated by solving the dispersion integral [12] in the presence of all non-linearities in the machine. The detuning with amplitude is obtained from multi particle tracking simulations through a realistic model of the machine lattice and through the different beam-beam interactions [18] while the particle distribution is assumed Gaussian.

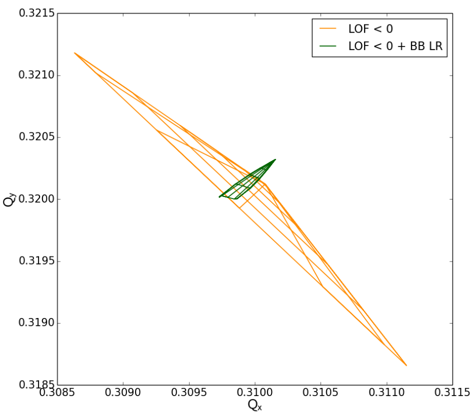


Figure 3: Two dimensional detuning with amplitude from Landau octupoles (yellow lines) and Landau octupoles plus long-range beam-beam interactions (green lines). Courtesy of C. Tambasco.

Figure 3 shows the detuning with amplitude from the Landau octupoles alone (yellow lines) and when beam-beam long-range interactions are added (green lines). A reduction of the detuning is visible for the configuration studied in these cases: the beam-beam long-range interactions compensate, due to their octupolar component [16], the effect of the octupole magnets. One can have also the case where the beam-beam detuning enhances the octupoles effects increasing the tune spread. As a consequence the Stability Diagrams (SD) are strongly modified as shown in Fig. 4. Coherent modes otherwise damped when beam-beam effects reduces the detuning with amplitude can become unstable because the stability area is reduced. This is clearly visible in Fig. 4 where in yellow line the SD due to only octupoles is compared to the one obtained when also beam-beam long-range interactions are included. The black dot is illustrative of an impedance induced coherent mode that can become unstable when the SD is reduced. In addition to the beam-beam effects any other non-linearity can give similar results. When the beams collide, the head-on interaction affects mostly core particles creating a much larger stable area [7]. In Fig. 5 the SDs for the Landau octupoles (green-line), in the presence of long-range beam-beam (blue line) and for a head-on collision (red line) are shown. In collision, thanks to the very effective and large stability area, beams have shown a very stable behaviour in physics. This has also inspired the possibility to use collisions to stabilize the beams and has pushed for the implementation of the collide and squeeze [19].

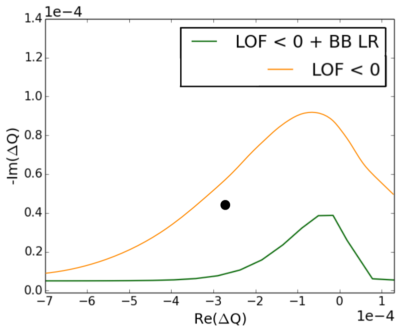


Figure 4: Stability diagram for the case with Landau octupoles and long-range beam-beam interactions (green lines). Courtesy of C. Tambasco.

The idea beyond the collide and squeeze mitigation is to reduce the effects of long-range beam-beam interactions by keeping the beam to beam distance $r$ of Eq. (3) as large as possible. This is obtained by keeping a large $\beta^*$. Instead of reducing the beta function to its minimum value (squeezing the beams) with a consequent increase of the beam-beam effects and then collide. One should collide before the detuning from long-range beam-beam becomes relevant and after reduce the $\beta^*$. By colliding the stability is then ensured by the head-on interaction as illustrated in Fig. 5 where a comparison of the SDs from the different effects is shown. More details can be found in [15, 18].

### *Dynamic Aperture and resonance excitation*

Increasing the particle spread to have a larger stability diagram is not the whole story. By increasing the tune spread, either pushing non linear elements (i.e. Landau Octupoles) or enhancing the beam-beam interactions, the particles long

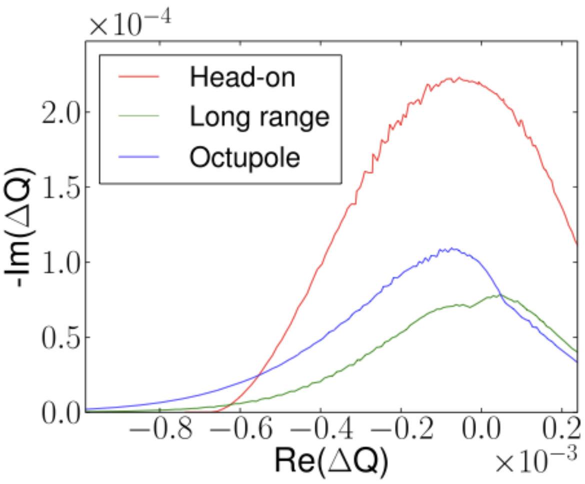


Figure 5: Stability diagram for the case with Landau octupoles (blue line), octupole magnets and long-range beam-beam interactions (green lines) and for a head-on collision (red line).

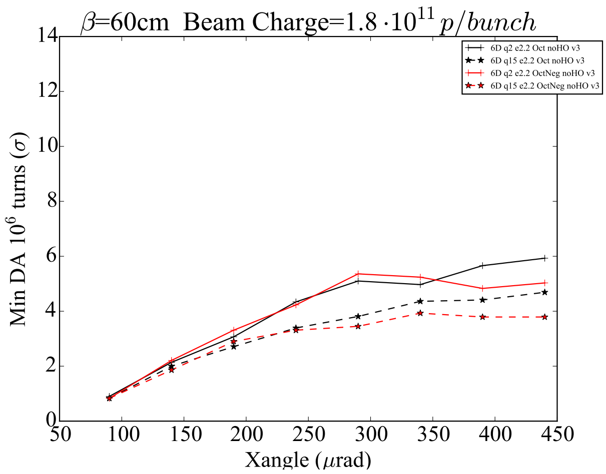


Figure 6: Dynamic aperture as a function of crossing angle for different configurations of the LHC 2012 beams with high octupole strength, high chromaticity operation and long-range beam-beam effects.

term stability will be affected and particles might be pushed to larger amplitudes and they could eventually be lost if they reach the dynamic aperture amplitude [20, 21]. If too many particles are lost then the damping efficiency of the Landau octupoles is reduced because of the modifying particle distribution. Another mechanism that can reduce the Landau damping stability areas is due to the very strong non-linear elements resonant behaviour that can change the particles distributions in frequency space via the excitation of resonances in tune space [22–24]. The indicator of the non-linear and chaotic behaviour of particles is the so called dynamical aperture defined as the amplitude in units of the transverse beam RMS size beyond which particles are eventually lost over long tracking, typically $10^6$ turns. If particles drift at larger apertures due to the non-linearities and or are trapped into resonant behaviours they will create a change in particle density and finally they might eventually be lost. These two effects have a clear impact to the Landau damping with octupole magnets since this depends on the derivative of the particle distribution, that in case of particle losses due to a reduced dynamical aperture or by the mutation of the particle distributions due to strong resonances can change the Landau damping properties in a fundamental manner. The fact that particles re-distribute has a clear impact to the distributions in action space and consequently to the stability diagram via the dependency on the derivative of the distributions ($\frac{d\Phi(J_x,J_y)}{dJ_{x,y}}$ in Eq. (1)). Reducing the long-range separation of Eq. (3) will make the force stronger (Eq. (2)) and reduce as a consequence the dynamical aperture. This is visible in Fig. 6 where the dynamic aperture as a function of the crossing angle is shown for four different configurations of the LHC 2012 operation [11, 25, 26].

The impact of a reduced dynamic aperture can be evaluated by cutting particles at the DA aperture in units of the beam RMS size. This is done in Fig. 7 where the SDs are computed for different values of dynamic aperture. A collider with operational settings too close to the dynamical aperture can result in a drastic cut of large amplitude particles that provide Landau damping. As a result a relevant reduction of SD is expected [27]. Such a scenario is not far from the LHC 2012 physics configurations [28].

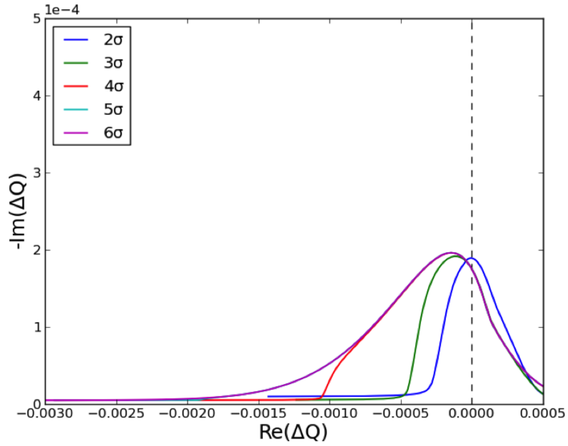


Figure 7: SD diagram for different dynamic aperture values from 6 to 2 $\sigma$ for the LHC case.

In addition to the dynamical aperture the presence of strong resonances excited by the non-linearities in the machine and among them beam-beam effects can also have detrimental effects to the Landau damping. Among many the linear coupling as studied in [29] can be a very important source of distortion in the detuning with amplitude. This is shown in Fig. 8 where the two dimensional tune spread (left plot) is shown when linear coupling is applied (blue lines) and when it is (red lines). On the right the particle distributions in action space are also plotted with the particle density as color code. This plot shows the change in particle distribution as a consequence of the resonance excited. In Fig. 9 the stability diagrams are plotted for two different unperturbed tunes using the tracked particle distributions from Sixtrack of Fig. 8. The horizontal plane SD (cyan and dark blue lines) are large and not changed by the resonance. On the contrary the vertical plane shows a very strong reduction of the SD (the pink line) and a sensitivity to a tune change that enhances the resonance effect (the green line). This effect has been described in [30] and experimentally measured via Beam Transfer function measurements in [31].

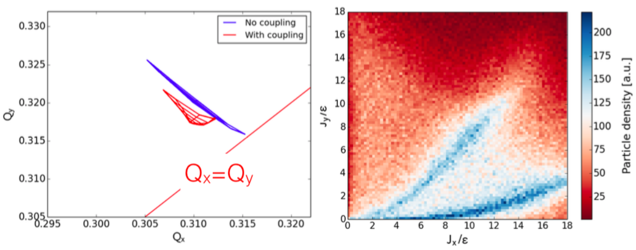


Figure 8: Two dimensional footprint (left plot) for different tune values and particle distribution in action space for the case with shifted tune closer to the linear resonance (right plot).

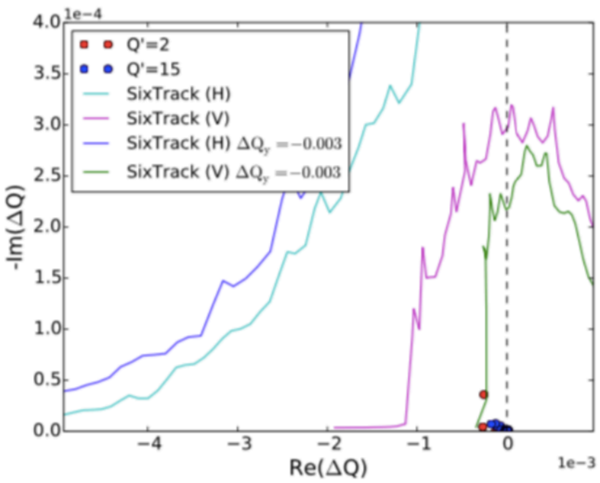


Figure 9: SD diagram in the presence of linear coupling resonance and for different tunes moving the footprints far away from the resonance.

The dynamic aperture and resonances effects on the beam stability has been proved to play a very important role. For these reasons it is fundamental to include in the overall stability strategy a global optimisation of the non-linearities to avoid a deterioration of the Landau damping properties.

### *Noise*

As initially explored in [15] the long lasting delay of instabilities in the LHC already back in 2012 raised the question if this very slow process could have been linked to a modification of the particle distributions due to resonance excitation, diffusion and/or noise.

Two approaches have been followed to try to bring light to these effects: an experimental effort to characterise the Landau damping properties of the beams via beam transverse transfer function measurements [31] and the theoretical and numerical studies of the impact of noise and diffusive mechanisms to the beam stability [15].

The experimental evolution of Landau damping with and without beam-beam effects has been probed in the LHC via beam-transfer function measurements. The goal was to try to experimentally observe the evolution of the Landau damping during an operational cycle in the presence of all non linearities, beam-beam interactions included. This was achieved with the development of the beam transfer function measurements because of the relation $BTF \propto SD^{-1}$. These measurements are meant to understand the effective Landau damping for different machine configurations and to possibly collect evidences of possible particle distribution deformations due to diffusive processes and or resonances effects as in [22].

The second path was to theoretically and numerically explore the impact of noise sources to the beam stability [15]. The aim was to understand the mechanisms that can lead to a loss of Landau damping linked to diffusive mechanisms as a possible explanation of the observed beam behaviours. Instabilities of high latencies have been observed in LHC before collision. The impact of coloured noise to the beam stability has been observed with direct measurements during BTF experiments [32] while indirect measurements have reproduced fully the instability characteristics in [33]. The instabilities observed are driven by noise and not caused by machine variations. Instabilities of high latencies can develop in high-energy hadron machines with noise and impedance, by changing the distribution of particles. Several studies have shown such behaviours theoretically and experimentally [34–37]. A possible mitigation technique considered is to reduce the modification speed of particles but studies are still on-going. More recently also [38] proves the possibility of such mechanism for instabilities in hadron synchrotrons. Studies of the impact of noise to the beam dynamics will have to change to take into account the possible loss of Landau damping associated to. This is a new feature never evaluated before for any collider.

## COHERENT EFFECTS

Due to the beam-beam interaction particles of the beams organise their motion and coherent oscillations take place during collision [39–43]. This coherent behaviour of the bunches in a beam can lead to limitations to the machine performances since the system of bunches colliding is a coupled system and actions of one bunch are transmitted to all the rest. These coherent modes have been routinely observed in various colliders and are generally not self-excited. The coherent motion moreover is not always damped by Landau damping mechanisms mainly when the frequencies of the collective oscillations are outside the continuum incoherent spectrum. Under external excitation, such as machine impedance, these modes could therefore become unstable. Therefore, one should always try to avoid or suppress collective motion by breaking the organised dynamics of particles.

In addition a transverse feedback is constantly used to damp the coupled bunch instabilities.The fastest growing instability modes can be damped with very low damper bandwidth, while the damping of the high frequency modes is very sensitive to the exact frequency response of the feedback system above the cutoff frequency.

## *Mode Coupling*

The existence of a strong mode coupling instability when one of the beam-beam coherent modes crossed a higher order head-tail mode has been studied theoretically and experimentally in [44]. The instability has very similar characteristics as the classical impedance driven TMCI [8] and could occur even at low bunch intensities providing the beam-beam parameter is sufficiently large to overlap the $\pi - mode$ frequency with the higher order head-tail modes. In [44] it has been shown that the chromaticity appears to be rather inefficient by itself to cure this instability while a bunch-by-bunch transverse damper would easily suppress it. From these studies it is clear that an optimum combination of damper gain and chromaticity should be found to minimise unwanted side effects as for example reduction of beam lifetime or emittance degradation. In Fig. 10 the amplitude of the spectral line (color code) is shown as a function of the coherent beam-beam and synchro-betatron modes frequencies Q per different beam-beam strengths ( $\xi$). It is evident that when the coherent beam-beam pi-mode approaches the head-tail mode -1 ($\xi \approx 0.003$) the modes couple leading to a strong instability.

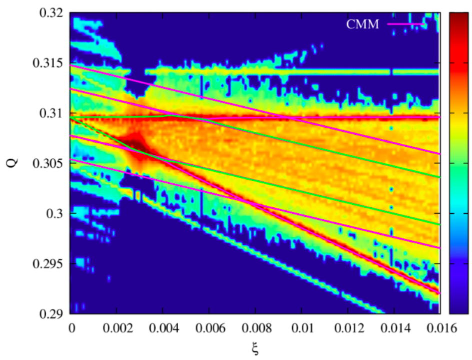


Figure 10: Synchro-betatron modes as a function of the beam-beam parameter $\xi$. The color code represents the amplitude of the spectral line.

While in Fig. 11 the amplitude of oscillation and rise time of a single and two-beam instability is shown. The magnitude of the instability and rise time is increased by an order of magnitude with respect to the single beam one when it occurs at the overlap of a beam-beam coherent mode. In addition the beneficial effect of a transverse damper in suppressing such instability is also marked with a black line.

Details of such study can be found in [44]. The coupled-bunch beam stability in the presence of the transverse

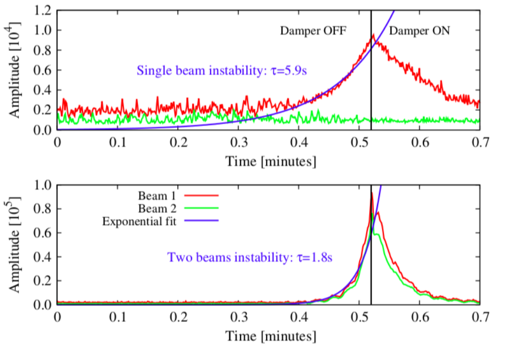


Figure 11: Measured oscillation amplitude in the vertical plane of both beams and exponential fit. An example of the single beam instabilities and two beams instabilities are shown on the top and bottom plots, respectively. The time at which the damper was turned ON is marked by the vertical black line.

feedback, chromaticity, and Landau octupoles using the NHT [45], DELPHI [46] and BIM-BIM [47] has been described in [10].

## *Suppressing coherent beam-beam modes*

Due to the beam-beam interaction, particles of the beams organise their motion and coherent oscillations take place during collision [40–43]. This coherent behaviour of the bunches in a beam can lead to limitations to the machine performances since the system of bunches colliding is a coupled system and actions of one bunch are transmitted to all the rest. Since coherent beam-beam modes are not always damped by Landau damping mechanisms one should always try to avoid or suppress collective motion by breaking the organised dynamics of particles. Since coherent behaviours develop mainly when a high degree of symmetry is present between the two beams (same betatron frequencies, same intensities, same sizes) one can reduce these effects by breaking this symmetry. There are different ways to suppress coherent beam-beam modes. Here a list of the mitigation methods:

**Different bunch intensities**: if the two bunches will have intensities that differ of around 60% then the coherent motion between the colliding bunches will be suppressed [40,48]. This technique is not used operationally because of its very bad impact to the colliders luminosity that will be reduced by the reduction factor on the bunch intensity.

**Different tunes in the two beams**: in the case the two beams will have different tunes the system will be decoupled if the difference in tune will be larger than the beam-beam parameter $\xi$ [22, 49, 50]. This technique has been also proved experimentally at the Relativistic Heavy Ion Collider RHIC for example.

**Unequal distribution of interaction points**: multiple interactions will create a mixing of coherent modes as for example for the case of the LHC with multiple long-range interactions. The coherent modes will be so many to create a continuum of frequency [41,51,52].

**Phase differences between interaction points**: similarly to the impact of the tunes, if the phase advances between interaction points are not symmetric the phase difference will make coherent motion more difficult to organize [43, 53].
**Synchrotron motion**: if transverse coherent modes overlap with the incoherent spread coming from the longitudinal motion then transverse modes can be damped thanks to the synchrotron betatron coupling one has in the beam-beam interactions when a crossing angle is applied at the interaction points [54, 55].

## FUTURE STUDIES AND CHALLENGES

Future colliders aim at beams of much higher energies to explore new physics process beyond the known playground. In particular presently CERN has undertaken a preliminary conceptual design for a 100 TeV center of mass energy hadron collider and a conceptual design report has been recently issued [56]. For such machines stability of beams is an issue since the classical approach of using octupole magnets to provide the needed Landau damping can be quite inefficient. Octupole magnets provide the frequency spread needed for Landau damping, the effectiveness of such devices decreases with energy because the detuning is affected by both adiabatic damping and increased beam rigidity. The tune spread follows the scaling law $\Delta Q_{octupoles} \propto 1/\gamma^2$. For this reason new devices and or techniques should be studied and explored to mitigate coherent instabilities. The main mitigation methods explored for the design of future colliders are:

- **Optics and beam-beam global design**: at the design stage fully integrate beam-beam effects into the Landau damping evaluations and in the lattice design to maximise the Landau damping and the dynamical aperture. This is obtained by fully integrating the beam-beam effects at the lattice and interaction region design level (i.e. phase advance studies, larger beta functions at the location of the Landau octupoles, global compensations schemes) [57–59]. Maximise the tune spread $\Delta Q$.

- **Collide and squeeze**: as soon as the beam stability approaches its limits ,i.e. at top energy, go into collision to have maximum Landau damping from the head-on beam-beam interaction. Then squeeze the beams to introduce gradually the long-range effects and allow a luminosity levelling knob on demand. With very little impact to the collider performances it allows to have the largest stability diagram and the best use of the lattice and of the two beams for mitigating coherent impedance driven instabilities [59, 60]. Use the $\Delta Q_{bb\ head-on}$ which is independent of the beam energy.

- **Electron lenses**: since the beam-beam head-on collision is independent of the beam energy the tune spread (Landau damping) produced can be much larger and if margins are needed then the use of a well controlled electron beam can be a powerful source of Landau damping. Detailed studies of electron lenses and their proved impact on the beam tune spread can be found in [61–63]. The impact on the beam stability and Landau damping is studied in [64].

- **Radio frequency quadrupoles**: these devices are studied because the detuning with amplitude comes from the longitudinal action variable and not from the transverse plane. The tune spread for Landau damping is given by $\Delta Q_{x,y} = \Delta Q_{x,y}(J_z)$ and therefore it is not affected by the adiabatic damping due to the higher energy. The RF quadrupole is only affected by the increased beam rigidity, so the tune spread is $\Delta Q_{RFQ} \propto 1/\gamma$.

These devices have been studied and a first experimental test to prove the Landau damping has been attempted in the LHC with very promising results. Detailed studies are reported in [65–69].

From the experience of the LHC it is clear that the effort at the design stage to fully integrate Landau damping devices and the impact of all beam-beam interactions to Landau damping, mode coupling and the modification of the optical properties of the lattice has to be studied and optimised in order to maximize the stabilising effects of such strong non-linearity.

Designing a future collider will then require a challenging set of studies to foresee:

- Full study of the impact of beam-beam effects to the Landau damping and use them to enhance it where possible with operational choices as learned from [15]

- Analysis of the dynamic aperture and resonance excitation in terms of impact to the Landau damping to foresee possible losses of stability as done in [20].

- Study the effect of particles diffusion and or emittance growth from noise sources as a possible source it self of loss of Landau damping as learned from [34].

- Explore the interplay of a transverse feedback and mode coupling instabilities from beam-beam coherent modes as described and proved experimentally in [71, 72]

- Explore alternative methods to provide efficient Landau damping at very high energies.

Any future design study has to take all these lessons into account at the design stage in order to fully implement all the effects in the design of the optics to optimise the stability and have a better control of the different aspects. This has been the strategy for the FCC-hh design as presented in [**?**] and summarised in the conceptual design report [56]. Stability studies cover fully the impact of two beams and the lattice design is also conceived to optimise at the maximum the beam-beam effects interplaying with octupoles and sextupole magnets. Operational scenarios have been defined to profit of head-on collisions using collide and squeeze [59] to further increase the Landau damping when at top energy. And in parallel effort has been made to advance the concepts and studies of new devices to possibly support and increase the Landau damping [64, 65].

## SUMMARY

Beam-beam effects typical of colliders have shown over the last 10 years at the LHC to be a fundamental ingredient for beam stability. This has manifested in many ways as explained and highlighted in this paper. Several experimental tests and evidences have been carried out to demonstrate the mechanism beyond the effects linked to beam-beam interactions and their role in loss of Landau damping and the mode coupling instability. The understanding of the impedance driven instabilities at the LHC over this last decade has paved the path for an improved design of a future hadron collider. Pushing the single particle studies to merge into collective beam stability as shown to be fundamental because the resulting stability of the beams is the result of the interplay of all these effects. The treatment of the effects independently is not anymore sufficient to describe the behaviour of operational beams and to reproduce the observations. Pushed by the need to mitigate the still present LHC instabilities, new devices to experimentally verify the Landau damping and or to possibly explain the discrepancies with respect to the known models have been developed. The use of this techniques have brought a much better understanding of the underlying physics and they have highlighted the need for new tools to model and explain the beam stability issues observed. Interesting developments on active devices to provide Landau damping as electron lenses and RFQs have been studied in the recent years showing very powerful tools for future machines. At the present the study of noise and its impact to stability is very demanding but can represent the missing ingredient to the understanding of the coherent instabilities observed.

## REFERENCES


[1] V. Vaccaro, Longitudinal instability of a coasting beam above transition, due to the action of lumped discontinuities, ISR-RF/66-35 CERN, Geneva, Switzerland, 1966.

[2] A. G. Ruggiero and G. V. Vaccaro, "Solution of the dispersion relation for longitudinal stability of an intense coasting beam in a circular accelerator (Application to the ISR)", CERN-ISR-TH-68-33, 1968.

[3] A.W.Chao, "Physics of collective beam instabilities in high-energy accelerators", Wiley (1993) 371 p, New York, USA, 1993.

[4] L. Landau, J. Phys. USSR 10, 25 (1946).

[5] O. Brüning, P. Collier, P. Lebrun, S. Myers, R. Ostojic, J. Poole, and P. Proudlock, eds., "LHC Design report, Vol. 1 : The LHC Main ring" CERN, Geneva, Switzerland, 2004.

[6] F. Sacherer, "Methods for computing bunched-beam instabilities", CERN/SI-BR/72-5, CERN, Geneva, Switzerland, 1972.

[7] W. Herr, "Introduction to Landau Damping", in the Proceedings of the CAS-CERN Accelerator School: Advanced Accelerator Physics, Trondheim, Norway, 19–29 August 2013, CERN Yellow Report CERN-2014-009, pp.377-403.

[8] N. Mounet, EPFL PhD Thesis 5305, EPFL, 2012.

[9] A. Burov *et al.*, "Efficiency of feedbacks for suppression of transverse instabilities of bunched beams", Phys. Rev. ST Accel. Beams 19 084402, (2016).

[10] E. Métral *et al.*, "Beam Instabilities in Hadron Synchrotrons", IEEE Trans. Nucl. Sci. **63** (2016) no.2, 1001-1050, doi:10.1109/TNS.2015.2513752.

[11] T. Pieloni et al.,"Two Beam Effects", in Proceedings of the 2014 Evian workshop on LHC beam operation, CERN-ATS-2013-045, Evian, 2014.

[12] J. S. Berg and F. Ruggiero, "Landau damping with two- dimensional betatron tune spread", CERN-SL-AP-96-071-AP, 1996.

[13] W. Herr and T. Pieloni, "Beam-Beam Effects", doi:10.5170/CERN-2014-009.431, [arXiv:1601.05235 [physics.acc-ph].

[14] V. Shiltsev for the Tevatron Beam-Beam Team, Overview of beam-beam effects in the Tevatron, doi:10.5170/CERN-2014-004.11 [arXiv:1410.3326 [physics.acc-ph]].

[15] X. Buffat, EPFL PhD Thesis 6321, 2015.

[16] D. Neuffer and S. G. Peggs, "Beam-Beam Tune Shifts and Spreads in the SSC – Head On, Long Range, and PACMAN Conditions", SSC-063, 1986.

[17] W. Herr and L. Vos, "Tune distributions and effective tune spread from beam-beam interactions and the consequences for Landau damping in the LHC", LHC-PROJECT-NOTE-316, Apr. 2003.

[18] X. Buffat *et al.*, "Stability diagrams of colliding beams in the Large Hadron Collider", Phys. Rev. ST Accel. Beams 17, 111002 (2014).

[19] X. Buffat *et al.*, "Colliding during the Squeeze and $\beta^*$ Levelling in the LHC", Proceedings of IPAC2013, Shanghai, China TUPFI033, (2013).

[20] H. Grote, F. Schmidt and L. Leunissen, "LHC dynamic aperture at collision", LHC Project Note 197, CERN, Geneva, Switzerland, 1999.

[21] J. Gareyte, *et al.*, "Landau damping, dynamic aperture and octupoles in the LHC", CERN LHC Project report 91, 1997.

[22] A. Hoffman and B. Zotter, "Measurements of beam stability and coupling impedance by RF excitation", CERN ISR-TH/77-12, Geneva, Switzerland, 1977.

[23] E. Keil and K. Hirata, Linear beam-beam resonances due to coherent dipole motion, Part. Acc. 56, 13 (1996).

[24] A. Chao, P. Bambade and W. Weng, "Non-linear beam-beam resonances", Lecture Notes in Physics, Vol. 247, Springer, (1986).

[25] N. Mounet *et al.*, "Impedance and Instabilities, in Proceedings of the 2014 Evian workshop on LHC beam operation", CERN-ATS-2013-045, 2014.

[26] T. Pieloni *et al.*, "Beam-beam Effects Long-range and Head-on", 6th Evian Workshop on LHC beam operation, Evian Les Bains, France, 15 - 17 Dec 2015, pp.111-122.

[27] C. Tambasco *et al.*, "Impact of Incoherent Effects on the Landau Stability Diagrams at the LHC", Proceedings of IPAC2017, Copenhagen, Denmark, TUPVA031, (2017).

[28] M. Crouch *et al.*, "Dynamic aperture studies of long-range beam-beam interactions at the LHC", in Proceedings of IPAC2017, Copenhagen, Denmark, THPAB056, (2017).

[29] E. Métral, "Coupled Landau damping of transverse coherent instabilities in particle accelerators", Ph.D. thesis, Université Joseph Fourrier (1999).

[30] L. R. Carver *et al.*, "Transverse beam instabilities in the presence of linear coupling in the Large Hadron Collider", Phys. Rev. Accel. Beams 21 044401, 2018.

[31] C. Tambasco, EPFL PhD Thesis 7867, (2017).

[32] C. Tambasco *et al.*, "MD 3292: measurements of Landau damping by means of BTF measurements", CERN-ACC-NOTE-2019- 0045, 2019.

[33] S. V. Furuseth *et al.*, "Instability latency in the LHC", 10th Int. Partile Accelerator Conf. IPAC2019, Melbourne, Australia, doi:10.18429/JACoW-IPAC2019-WEPTS044.

[34] S. V. Furuseth and X. Buffat, "Change of beam distribution due to decoherence in the presence of transverse feedback", J. Phys. Conf. Ser. 1350, 012118 (2019).

[35] V.A. Lebedev, "Emittance growth due to noise and its suppression with the feedback system in Large Hadron Colliders", in AIP Conference Proceedings Accelerator physics at the Superconducting Super Collider, Dallas, Texas, USA (AIP Publishing, Dallas, Texas, 1995), pp. 396-423, https://doi.org/10.1063/1.47298.

[36] S. V. Furuseth and X. Buffat, "Noise and possible loss of Landau damping noise excited wakefields", these proceedings.

[37] S. V. Furuseth and Xavier Buffat, "Long-term evolution of Landau damping in the presence of transverse noise", feedback, and detuning, Phys. Rev. Accel. Beams 23, 034401, 2020.

[38] V. Lebedev, "Transverse dampers with ultimate gain for suppression of instabilities in Large Hadron Colliders", these proceedings.

[39] K. Hirata, "Coherent betatron oscillation modes due to beam-beam interactions", Nucl. Inst. and Meth. in Phys. Res. A 269 (1988) 7.

[40] Y. Alexahin, "A study of the coherent beam-beam effect in the framework of the Vlasov perturbation theory", Nucl. Inst. and Meth. in Phys. Res. A 380 (2002) 253.

[41] T. Pieloni, EPFL PhD Thesis 4211, 2008.

[42] M.P. Zorzano and F. Zimmermann, "Simulations of coherent beam-beam modes at the Large Hadron Collider", Phys. Rev. ST Accel. Beams 3, 044401 (2000).

[43] K. Hirata and E. Keil, "Barycentre motion of beams due to beam-beam interactions in asymmetric ring colliders", Nucl. Inst. and Meth. in Phys. Res. A 292 (1990) 156.

[44] S. White *et al.*, Phys. Rev. ST Accel. Beams 17, 041002 (2014).

[45] A. Burov, Nested Head-Tail Vlasov Solver, Phys.Rev.ST Accel. Beams 17 (2014) 021007.

[46] N. Mounet, "DELPHI: an analytic Vlasov solver for impedance-driven modes", Hadron Synchrotron Collective Effects Meeting, CERN, Apr. 2014.

[47] S. White *et al.*, "Transverse mode coupling instability of colliding beams", Phys. Rev. ST Accel. Beams 17, 041002 (2014).

[48] Y. Alexahin, "On the Landau damping and decoherence of transverse dipole oscillations in colliding beams", Part. Acc. 59, 43 (1996).

[49] A. Hofmann, "Beam-beam modes for two beams with unequal tunes", Proceedings of the workshop on beam-beam effects in large hadron colliders, LHC99, Geneva, 12-17 April, 1999, CERN-SL-99-039 (AP) (1999) p. 56.

[50] Y. Alexahin and M.P. Zorzano, "Excitation of coherent beam-beam resonances for beams with unequal tunes in the LHC", CERN LHC Project Note 226 (2000).

[51] M.P. Zorzano, "Coherent dipole modes for multiple interaction regions", CERN LHC Project Report 462 (2001).

[52] W. Herr and T. Pieloni, "Coherent beam-beam modes in the CERN Large Hadron Collider for multiple bunches, different collision schemes and machine symmetries", Proc. First CARE-HHH-APD Workshop on Beam Dynamics in Future Hadron Colliders and Rapidly Cycling High-Intensity Synchrotrons, CERN, Geneva 8-10 November 2004, also CERN 2005-006 Yellow Book.

[53] E. Keil, "Coherent beam-beam effect in machines with unequal betatron phase advances between crossing points", LEP Note 226, unpublished, (1980).

[54] W. Herr, "Landau damping of coherent modes by overlap with synchrotron sidebands", CERN LHC Project Note 304 (2002).

[55] W. Herr and R. Paparella, "Landau damping of coherent modes by overlap with synchrotron sidebands", CERN LHC Project Note 304 (2002).

[56] "FCC-hh: The Hadron Collider", Eur. Phys. J. Special Topics 228, 755–1107 (2019), https://doi.org/10.1140/epjst/e2019-900087-0.

[57] C. Tambasco *et al.*, "Landau damping studies for the FCC: octupole magnets, electron lens and beam-beam effects", 9th International Particle Accelerator Conference IPAC2018, THPAF074, Vancouver, BC, Canada, 2018, doi:10.18429/JACoW-IPAC2018-THPAF074.

[58] J. Barranco and T. Pieloni, "Global compensation of long-range beam-beam effects with octupole magnets: dynamic aperture simulations for the HL-LHC case and possible usage in LHC and FCC", CERN-ACC-NOTE-2017-036, 2017.

[59] X.Buffat *et al.*, "Colliding during the squeeze and $\beta^*$ levelling in the LHC", in Proceedings of IPAC 2013, TUPFI033, 2013.

[60] X. Buffat, W. Herr, M. Lamont, T. Pieloni, S. Redaelli and J. Wenninger, "Colliding during the squeeze and $\beta^*$ levelling in the LHC", CERN-ACC-2013-0140 `https://cds.cern.ch/record/1581727/files/CERN-ACC-2013-0140.pdf`.

[61] V.D. Shiltsev, "Electron Lenses for Super-Colliders", Springer 2015.

[62] V.D. Shiltsev *et al.*, "Considerations on compensation of beam-beam effects in the Tevatron with electron beams", Phys. Rev. ST Accel. Beams 2, 071001 (1999).

[63] X.Gu *et al.*, "Electron lenses for head-on beam-beam compensation in RHIC", Phys. Rev. ST Accel. Beams 20, 023501 (2017).

[64] V. Shiltsev, Y. Alexahin, A. Burov, and A. Valishev, "Landau Damping of Beam Instabilities by Electron Lenses", Phys. Rev. Lett. 119, 134802, September 2017.

[65] A. Grudiev, "Radio frequency quadrupole for Landau damping in accelerators", Phys. Rev. ST Accel. Beams **17** (2014) no.1, 011001, doi:10.1103/PhysRevSTAB.17.011001

[66] A. Grudiev, K. Li and M. Schenk, "Radio Frequency Quadrupole for Landau Damping in Accelerators: Analytical and numerical studies", Proceedings of HB2014, East-Lansing, MI, USA.

[67] M. Schenk, X. Buffat, L. Carver, A. Grudiev, K. Li, A. Maillard, E. Metral and K. Papke, "RF Quadrupole Structures for Transverse Landau Damping in Circular Accelerators", doi:10.18429/JACoW-IPAC2017-WEOAB3.

[68] M. Schenk, D. Amorim, N. Biancacci, X. Buffat, L. Carver, R. De Maria, K. Li, E. Métral and B. Salvant, "Practical Stabilisation of Transverse Collective Instabilities with Second Order Chromaticity in the LHC", doi:10.18429/JACoW-IPAC2017-THPVA026.

[69] M. Schenk, PhD Thesis 9298 EPFL, 2019.

[70] M. Schenk, X. Buffat, L. R. Carver, R. De Maria, K. Li, and E. Métral, "Experimental stabilization of transverse collective instabilities in the LHC with second order chromaticity", Phys. Rev. Accel. Beams 21, 084401 ? Published 17 August 2018.

[71] E. A. Perevedentsev and A. A. Valishev, Phys. Rev. ST Accel. Beams 4, 024403 (2001).

[72] E. G. Stern, J. F. Amundson, P. G. Spentzouris, and A. A. Valishev, Phys. Rev. ST Accel. Beams 13, 024401 (2010).

# OPERATIONAL EXPERIENCE OF BEAM STABILITY CONTROL

R. Steerenberg†, CERN, Geneva

*Abstract*

The CERN accelerator complex, as well as other accelerator facilities world-wide, produce a large variety of particle beams for use in experiments. The beam quality is of prime importance and can be characterised by many parameters, such as beam or bunch intensity, longitudinal and transverse beam size, time structure, etc. Certain combinations of these beam parameters, along with the machine characteristics such as impedance, can lead to challenging configurations that can drive the particle beams unstable, potentially leading to degradation of the beam quality and particle losses around the circumference of the accelerator. These losses result in activation of the accelerator components and therefore prolong the cooldown time to allow for hands-on preventive and corrective maintenance, hence reducing the beam time available for physics.

Beam stability control is therefore of major importance for the operation of accelerators and can be obtained through distinct means for different accelerators and beam characteristics. This paper outlines the principal operational instability observations and mitigations applied for the CERN accelerator complex, complemented with approaches used in some other accelerator laboratories around the world. An attempt is made to illustrate the interplay between the beam dynamics experts and the operations teams.

## CERN ACCELERATOR COMPLEX AND PARTICLE BEAMS

The CERN accelerator complex (Fig. 1), as it is in used today, has evolved over more than 60 year. The CERN Proton Synchrotron (PS), initially foreseen for internal target experiment, was designed for beam intensities of a few $10^{10}$, while upgrades and addition of the PS Booster (PSB) allowed to increase the beam intensity up to more than $3\times10^{13}$ protons per pulse. Similarly, the Super Proton Synchrotron (SPS) has gone through many transformations and performance increase steps. Initially it was used as high energy protons synchrotron, then transformed into a proton – antiproton collider, before being used as injector to the Large Electron Positron (LEP) collider. Today besides producing the beams for the Large Hadron Collider (LHC), the PSB, PS and SPS provide various types and configurations of particle beams to a rich variety of fixed target experiments. The performance increase and the large spectrum of beam characteristics gave rise to rich panel of beam instability observations and mitigation techniques, most of which are used operationally.

Another interesting period is upcoming, with the commissioning of the LHC injector upgrade project that has as principal aim to more than double the LHC beam brightness. Although potential beam instabilities have been studied and mitigation measures have been foreseen, new challenges will arise and will have to be dealt with efficiently, by beam dynamics experts and the operations teams.

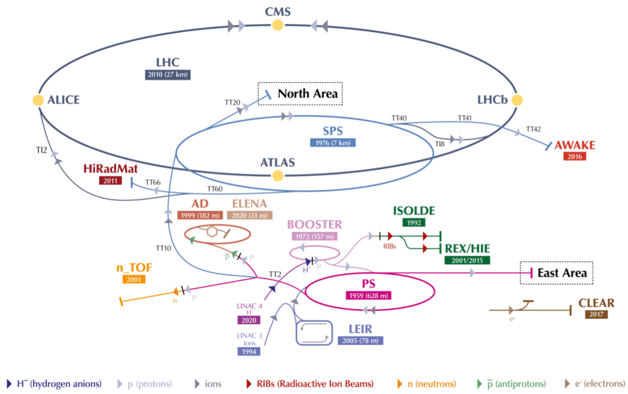


Figure 1: Schematic overview of the CERN accelerator complex today.

## *Operational Instability Observation*

Beam instabilities that developed over the years as a result of the performance increases have been studied in detail analytically, through simulations, but also during numerous machine development sessions. The latter led to the implementation and/or extension of a large spectrum of observation and diagnostics tools. Many of these were initiated as proof of principle or prototypes to cover the need of the study, but many were later converted into operational tools.

Wideband longitudinal and transverse pick-ups, power converter signals and feedback loop signals are connected to a distributed analogue/digital signal observation system, called OASIS [1]. This allows remotely connecting signals or data streams around the accelerator complex to the local OASIS sub-systems and to visualise them, using a common trigger, on displays in the control room. A few examples of the signals and their observation modes are given in Fig. 2.

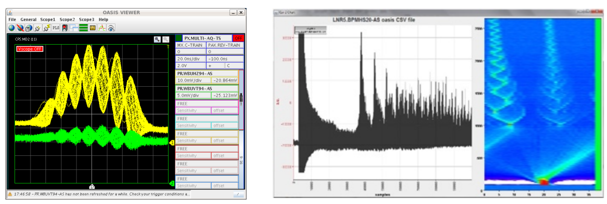

Figure 2: Examples of visualisation of signals on the OASIS system, normal analogue mode (left) and analogue mode with waterfall image (right).

† rende.steerenberg@cern.ch

More dedicated systems, such as Bunch Shape Monitors (BSM) combined with tomographic algorithms, allow for tools such as Tomoscope [2] and Beam Quality Monitors (BQM). The BQM makes a real-time analysis of the beam quality and can be parametrised to dump the beam prior to transferring it to the LHC if the quality does not meet the pre-defined requirements [3].

More recently, the LHC transverse damper system was equipped with enhanced diagnostic tools, called ADT-Obsbox [4]. This system forms a rich source of digitised beam signals for instability studies. It triggers on instabilities and stores the signals for many thousands of turns bunch-by-bunch for off-line analysis (see fig. 3). In some places spectrum analysers are still available and used for on-line observations, but the abovementioned systems allow more sophisticated analysis, hence the decrease in number of spectrum analysers over the years.

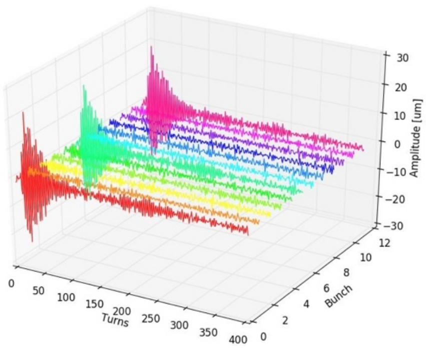


Figure 3: Example of ADT-ObsBox signals for four bunches over 400 turns.

The extensive logging of machine parameters, as is done for the LHC, but also more and more, for the LHC injector chain, froms a rich source of data for the analysis of beam instabilities and allows correlating them with machine parameters.

## *Operational Instability Mitigation*

Once beam instabilities are observed and analysed mitigation measures will have to be applied. The most common operational knobs in the control rooms for the transverse plane are tune, chromaticity, linear coupling and Landau octupoles, complemented by the various parameters of the transverse feedback system. For the longitudinal plane these are RF cavity voltage, higher order cavity voltage and the various parameters of the longitudinal feedback system. If the beam specifications allow, controlled transverse and/or longitudinal blow up are also powerful tools to palliate operationally beam instabilities.

Synchrotron radiation damping is an effective means to moderate beam instabilities, but apart from the CLEAR facility, only protons, antiprotons and different ion species are accelerated and decelerated at CERN, which do not provide useable synchrotron radiation damping in any of the accelerators.

Stochastics and electron beam cooling are used in the low energy machines at CERN, such as the Antiproton Decelerator (AD), the Extra Low ENergy Antiprotons machine (ELENA) and the Low Energy Ion Ring (LEIR), but not for any of the high energy, high intensity and/or high brightness proton beams.

# OPERATIONAL EXPERIENCE WITH BEAM INSTABILITY AT CERN

## *PS Booster (PSB)*

The PSB is the first link in the LHC injector chain and is at the source of all beams for the downstream experimental areas and machines. It has its own experimental facility, the Isotope mass Separator On-Line DEvice (ISOLDE) for which it produces a 4-bunch high intensity beam of ~$3.4\times10^{13}$ protons per pulse at 1.4 GeV kinetic energy and 2 GeV in 2021.

The PSB beams can potentially be impaired by a horizontal beam instability in the presence of high space charge, resulting in a tune spread of up to $dq \sim 0.5$. This instability is efficiently suppressed owing the good working transverse damper. The cause for this instability, which was recently identified, are the cables of the extraction kicker system [5]. The PSB relies on the transverse feedback in coming years for the mitigation of this instability. However, studies for a definitive solution at the source has been launched.

Apart from the transverse damper and the capability of applying a controlled longitudinal blow-up, the PSB is not equipped with chromaticity sextupoles nor Landau octupoles.

## *CERN Proton Synchrotron (PS)*

All operational beams, apart from the ISOLDE beam, are accelerated and manipulated in the PS. The main instability related phenomena observed on some of these beams are:

- Head-tail instability in the presence of space charge, resulting in a tune spread of up to $dq \sim 0.5$;
- Beam break-up at transition crossing in the presence of space charge [6], or Transverse Microwave Convective Instability [7];
- Longitudinal coupled bunch instabilities;
- Transverse coupled bunch instabilities.

The principal means in the PS to correct for beam instabilities are:

- Transverse damper, not much used until recently;
- Tune and coupling, for coherent instabilities;
- Chromaticity, sign flip at γ-jump;
- Landau octupoles, rarely used and only available below transition crossing (~6 GeV/c);
- RF cavity voltage, reduced after γ-jump to maximise Landau damping;
- Controlled longitudinal blow-up though dedicated 200 MHz cavities;
- Longitudinal damper, recently installed.

The following paragraphs illustrate examples of operational beams on which the abovementioned phenomena have been observed and to which corrections are applied, together with some operational experience where relevant.

The n-TOF beam, which is a single bunch high intensity beam (~$8\times10^{13}$ protons), suffered from the beam break up instability at transition crossing. Initially the controlled longitudinal blow up was increased with a positive effect on the instability, but a detrimental effect on the beam quality occurred, as ghost bunches were created by particles leaking out of the bucket into the neighbouring empty buckets. Careful studies on the controlled blow-up parameters have identified a set of parameters that blow up most efficiently the core of the bunch and less the particle trajectories on the outskirts of the bunch. These blow-up parameters are now routinely used and if necessary adapted by the operations teams.

The LHC beam uses a double batch injection, hence a waiting time of 1.2 s for the first injected batch on the injection plateau. The beam is intrinsically unstable in the horizontal plane with nominal chromaticity, $\xi_{h,v}$ = -1 below transition. Until recently, approaching the horizontal and vertical tunes close to the coupling resonance and adding linear coupling through skew quadrupoles were used to damp the instability, hence improved the beam quality and reduced the beam losses [8]. More recently, the low energy working point was modified. Small but negative values for the chromaticity in both planes were, combined with the use of the transverse damper to damp the head-tail modes. The working point adjustments together with the transverse damper settings are performed by the operations teams.

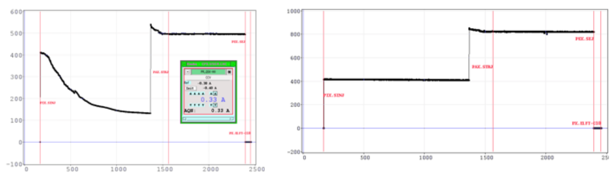

Figure 4: (left) the instability causing losses on the flat bottom, (right) Stable beam without losses.

The LHC beam, during the energy ramp, exhibits dipolar and quadrupolar coupled bunch instabilities, limiting the bunch intensity [9]. The RF system was modified such that two out of the ten 10 MHz cavities could be used to damp the instability. In addition, partial mitigation was found applying controlled longitudinal blow up in the PSB prior to extraction, and in the PS at low energy. However, for beam specification reasons the maximum longitudinal emittance at extraction cannot exceed 0.35 eVs. For the future a dedicated longitudinal damper has been installed and the 10 MHz cavity impedance will be reduced through an upgrade of the amplifiers. The operational experience with this is that the two 10 MHz cavities used to damp the instabilities in addition to their main role, accelerating the beam, tripped more regularly, causing beam downtime. The bunch splitting processes, used to produce the 25 ns bunch spacing, required regular manual adjustments by the operations team for the optimisation of the beam quality. Good measurement and correction tools are available in the control room to diagnose and mitigate the instability.

### *Super Proton Synchrotron (SPS)*

The SPS receives its beam from the PS and produces various types of beams for the LHC, the Fixed target experiments in the North Area of the Prevessin site, the AWAKE experiment and the HiRadMat facility. The main instability related phenomena observed on some of these beams are:

- Fast vertical single bunch instability;
- Horizontal coupled bunch instability during the injection plateau for $1.8\times10^{11}$ protons per bunch on the LHC beam;
- Electron cloud induced instability
- Longitudinal coupled bunch instability, due to RF cavity beam loading.

The principal means in the SPS to correct for beam instabilities are:

- Chromaticity;
- Landau octupoles;
- Transverse damper;
- Lowering of the γ-transition, through a well-studied optics modification;
- Prototype intra-bunch damper in the vertical plane only. Presently only used for studies and limited in power;
- 800 MHz RF cavity used as Landau cavity, in the past also for controlled longitudinal blow-up;
- RF cavity voltage, but no or little margins available.

The following paragraphs illustrate examples of operational beams on which the abovementioned phenomena have been observed and to which corrections are applied, together with some operational experience, where relevant.

The TMCI-like fast vertical single bunch instability or Transverse Microwave Convective Instability forms a performance limiting factor in the SPS. Running the machine at higher chromaticity values contributes to stabilising the instability but is not satisfactory. Studies and tests with beam have confirmed that lowering the γ-transition by switching from the so-called Q26 optics to the Q20 low gamma transition optics, provides an efficient cure for this TMCI-like instability [10]. For the Q20 optics, the frequency slip factor increases by a factor 2.8 at injection and 1.6 at high energy compared to the Q26 case. The drawback of the Q20 solution is that it imposes a higher RF voltage, which is already limited with the present RF system. As a result, the SPS RF system is being upgraded and more voltage will become available. In addition, an alternative scheme with Q22, a compromise between stabilisation and available RF voltage, is being studied. The Q20 optics has been deployed operationally on the LHC beams and is used for routine operation and filling of the LHC. The SPS is now awaiting the upgrade of the RF system to take full benefit of the scheme. This is a clear example of an expert driven change with a good and close collaboration with the

Operations group for operational deployment of the new scheme.

A horizontal coupled bunch instability is present at flat bottom in the SPS on the LHC beam for bunch intensities approaching $1.8\times10^{11}$ protons. The transverse damper in combination with the Landau octupoles are used rather efficiently to mitigate this instability. With the Q20 optics the Landau octupoles generated a large second order chromaticity as a result of the high dispersion at their location and enhanced the beam losses due to the large incoherent tune spread. As a result, in 2018, following careful machine studies the Landau octupoles were partially re-configured with the aim to reduce the second order chromaticity *Q"* for which the before and after situation is given in Fig. 5 [11].

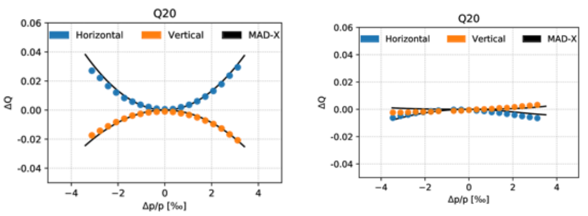


Figure 5: The non-linear chromaticity before (left) and after (right) deploying the Landau octupole reconfiguration.

The LHC beam in the SPS is also undergoing electron cloud induced instabilities, which can severely impact the beam quality. Two main operational mitigation measures are used to combat the build-up of electron cloud:
1) running the machine with higher values for the chromaticity and 2) perform scrubbing runs following vacuum interventions or prolonged stops. The latter is very effective but can be rather time consuming depending on the extend and duration of the vacuum interventions. The operations team, in close collaboration with the electron cloud experts, perform the yearly scrubbing runs. Until recently the scrubbing run required frequent interruptions to avoid overheating of the kickers due to impedance. The serigraphy on the ceramic chambers will be adapted to reduce the kicker heating in the future. A solution at the source, amorphous Carbon coating of the vacuum chambers, is also being deployed gradually, reducing or even eliminating the need for the scrubbing runs in the future.

### *Large Hadron Collider (LHC)*

The LHC receives the beam from the SPS in multiple batches of bunch trains, ranging in length from 12 to 288 bunches. In order to increase the physics production, the luminosity in the LHC is continuously optimised by reducing as much as possible the physical beam size in the interaction points, but also by injecting beams of increased brightness from the injectors. The main instability related phenomena observed on the beam in the LHC are:

- Electron cloud driven instability at injection;
- Beam instability driven by the impedance from the closing collimators;
- Very fast instability as a result of a vacuum related non-conformity (16L2);
- Longitudinal beam instability after injection.

The principal means in the LHC to correct for beam instabilities are:

- Transverse feedback (ADT) in both planes;
- Tune and linear coupling control;
- Chromaticity, a large chromaticity is imposed during the whole cycle due to instabilities;
- Landau octupoles;
- RF Cavity voltage;
- Controlled longitudinal blow up, to maintain constant longitudinal emittance and bunch length that decreases over log fills, as a result of synchrotron radiation damping.

The following paragraphs illustrate examples of operational beams for which the abovementioned phenomena have been observed and to which corrections are applied, together with some operational experience, where relevant.

The electron cloud driven instability at injection is cured in a similar manner as for the SPS. Prior to a physics run and during the gradual intensity ramp-up, a scrubbing run is performed to reduce the secondary electron emission yield. This drastically reduces the electron cloud formation but does unfortunately not suppress it. Therefore, the LHC runs with a chromaticity of ~ 15 units in both planes, which, combined with an increased strength of the Landau octupoles and the correction of the linear coupling at low energy, allows for sufficient mitigation for operation with the required bunch intensities and bunch patterns. The operations teams regularly measure and correct the chromaticity. Following the findings on the linear coupling by beam dynamics experts, the operations team has developed a tool to measure and correct the linear coupling which is also used by the operations teams on a regular basis.

The closure of the collimators at high energy gives rise to an impedance induced beam instability that is cured by applying a high value for the chromaticity in both planes of ~ 15 units, in combination with the Landau octupoles that run close the maximum available current of 550 A. The latter have been used both in negative and positive polarity. This topic is generally seen as very complex by the majority of the operations team members, but they closely collaborate with the beam dynamics experts for the measurement campaigns. The accelerator physicists in the operations team are highly involved in the setting-up of the cures and development of the monitoring tools.

Following a beam vacuum non-conformity, fast beam instabilities, caused by a local high gas density, have led to beam dumps in 2017 and 2018 [12][13]. Since this phenomenon arose unexpectedly during the intensity ramp-up in 2017, no predefined cure was readily available, and the logging of the beam and machine signals prior to and during each instability-induced beam dump contributed significantly to the understanding of the instability mechanism.

Through trial and error several mitigation measures have been attempted. An extra solenoid to evacuate electrons and/or ions in the suspected area of the machine was installed and contributed to the reduction of instability induced beam dumps. Also conditioning with a lower beam intensity, following a beam dump, turned out to be a working recovery strategy. Taking a step back on the beam performance contributed significantly to the reduction of the number of instability-induced beam dumps and increased again the beam availability for the experiments. Combing in the operational experience with the enhanced understanding of the instability mechanism by the beam dynamics experts resulted in exploiting the enormous flexibility of the injector chain. The so-called 8b4e LHC beam, where the short 8-bunch trains were separated by four empty buckets, was setup in a short period of time and suppressed the electron cloud production in the LHC at the expense of a slightly reduced, but still respectable peak luminosity of close to the $2{\times}10^{34}$ cm$^{-2}$s$^{-1}$, twice the LHC design value. This beam configuration therefore contributed greatly to the reduction of the beam-induced heat load, hence the number of instability-induced beam dumps. The definitive cure of the problem is the removal of the non-conformity, foreseen for LHC Run 3.

Persistent injection phase oscillations caused a longitudinal beam instability after injection prior to 2018 (Fig. 6) [14]. This was identified to be due to the mismatch between the LHC bucket height and the momentum spread of the arriving bunch. The theoretically optimum voltage with respect to the momentum spread of the injected SPS bunch is 2 MV. However, this voltage resulted in too high injection losses in the past. As result, the RF beam dynamic expert performed studies and found that 4 MV would be the optimum voltage for the beam coming from the SPS as opposed to the 6 MV that was applied operationally. During the 2018 physics run, under a close collaboration between the RF beam dynamics expert and the operations team, the voltage was reduced in steps over many LHC fills. This was done by carefully observing the effects and evaluating if a next step could be made safely without compromising beam quality or perturbing the collisions for the experiments. Since then the 4 MV has been successfully used beam injection without observing the longitudinal instability after injection.

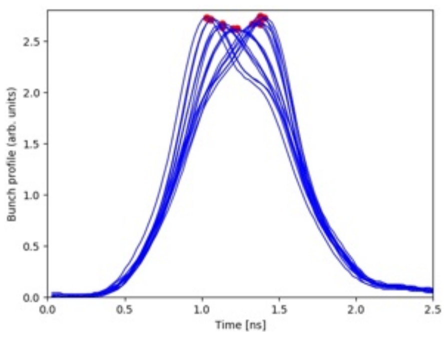


Figure 6: Dipole oscillations observed on the bunch profile approximately one minute after injection.

## BEAM INSTABILITY OBSERVATION AND MITIGATION IN OTHER ACCELERATOR LABORATORIES

### *J-PARC*

The J-PARC complex is a multipurpose high-power proton accelerator facility comprising a 400 MeV H$^-$ Linac, a 3 GeV Rapid Cycling Synchrotron (RSC) and a 30 GeV Main Ring (MR). The design power of the MR is 750 MW, but a performance improvement scheme aims at increasing the beam power to 1.3 MW with a beam intensity of $3.3{\times}10^{13}$ protons per pulse [15].

A transverse instability causing beam losses in the RCS is suppressed effectively by programming a negative chromaticity of seven units. Reducing to smaller absolute values of the chromaticity the beam is unstable and larger negative values provoke beam losses, likely due to the large chromatic tune spread.

In the longitudinal plane of the MR, dipolar coupled bunch instabilities have been observed for beam powers approaching 500 kW, as a result of RF cavity beam loading. A feedback system has been developed and is being tested on low power beams before being deployed operationally on the high-power beams.

A resistive wall impedance and kicker impedance cause transverse beam instabilities in the MR. Also here, a large value for the chromaticity, together with Landau octupoles provides a cure [16].

The performance increase and optimisation are iterative processes that are mainly driven by the beam dynamics experts. The operations team is not really involved in this process, until new settings and procedures have become fully operational.

### *FermiLab*

The FNAL Booster experiences a transverse instability under high space charge regime [17]. These instabilities are until now suppressed by applying a large value for the horizontal and vertical chromaticity of ~12 units. The plans to build and install a transverse damper will allow lowering the values for the horizontal and vertical chromaticity again.

Longitudinal coupled bunch modes are also observed, probably as a result of RF cavity beam loading. The longitudinal emittance is blown-up after transition by voluntary mismatch of the bucket. Longitudinal dampers are available, but the longitudinal coupled bunch mode 2 is not yet well-controlled.

The booster is tuned on a daily basis by experts with all the knobs available.

### *Brookhaven National Laboratory*

The BNL Booster accelerates protons and ions and is running near its natural chromaticity without losses. The octupole winding were retired, as they had little or no use anymore. Space charge issues are prominent at injection and a dual harmonic RF system is used to control the bunching factor.

The AGS accelerates polarised protons and ions, but at low or moderate intensities. In the past the AGS accelerated proton beam intensities of more than $8\times10^{13}$ protons per pulse for slow extraction to fixed target experiments. At that epoch many beam instabilities have been observed and cures have been put in place. The main systems used were transverse damper, higher frequency dilution cavities at injection and transition, skew quadrupoles for empirical linear coupling correction by the operations teams and higher order multipoles used by the operations teams to empirically improve beam transmission.

Today the AGS no longer accelerates these high intensities and activity on the beam instability front has decreased drastically.

At RHIC [18] that collides polarised protons and ions the injection is dominated by intra-beam scattering and capture losses. The transition crossing with high intensities was often accompanied with beam instabilities, most likely due to electron clouds. NEG coating has been applied and scrubbing runs to reduce the secondary electron emission yield are performed. The transverse damper combats the injection oscillations and is, if necessary, adjusted by experts and monitored by the operations teams. A transverse bunch-by-bunch system was deployed in 2014 but is not yet fully operational for technical reasons. The chromaticity, which is slightly increased with respect to the design value (5 units instead of 2 units) for higher intensities, to avoid beam losses, is measured and controlled by the operations teams with support from the beam dynamics experts. Linear coupling and tune are controlled by feedback systems. The setting up of these systems is done by experts and the monitoring by the operations teams.

Landau damping cavities are necessary for beam stability at high ion intensities during injection and acceleration past transition. A longitudinal bunch-by-bunch damper is in use since 2013 for protons, which allows for relaxing the voltage on the Landau cavities. For low energy physics the Low Energy RHIC electron Cooling (LEReC) has been commissioned and the operations teams start now participating in the electron beam tuning too.

## CONCLUSION

Beam instabilities and their mitigation are sometimes seen as black magic from an operations point of view, but this perception changes when basic understanding of the phenomena and their mitigation have been achieved. The good communication and collaboration between the beam dynamics experts and the operations teams are of key importance to achieve this basic understanding,

In different accelerator laboratories various approaches towards the operational mitigation of beam instabilities are applied, ranging from full expert control to a large involvement and autonomy by the operations teams. At CERN the much appreciated inter-group collaborative approach is favoured, leaving a large autonomy to the operations teams and freeing up time for the experts to study and/or simulate in more depth the theoretical background for the phenomena and to provide reliable models that help to predict and correct beam instabilities. At a later stage, these models are often integrated by the operations teams in operational software applications, increasing the ability to act upon arising instability issues more autonomously by the operations teams that is present 24/7.

There is also a general tendency to push the performance wherever it is possible. However, making a small step back, to the benefit of the stable and routine operation, often results in an overall gain of the performance for the experiments.

The presently available diagnostics systems and tools for the mitigation of beam instabilities in the control room seems adequate, and wherever shortcomings were identified upgrades are foreseen in the near future.

With the commissioning and subsequent performance ramp-up following the deployment of the LHC Injector upgrade programme, there will be challenges and interesting times ahead.

Knowledge transfer and close collaboration between beam dynamics experts and the operations teams in the control room are key to ensure proper diagnosis and understanding of the beam instabilities and to deploy operational mitigations and tools to ensure stable beam operation efficiently.

## ACKNOWLEDGEMENTS

I thank all the beam dynamics experts and the Operations group members that contributed to the good collaboration with the aim to continuously improve the accelerator performance, by understanding the underlying instability mechanisms. I want to particularly thank, M. E. Convery, T. Koseki and G. Marr for the time and informative discussions on instabilities and their operational mitigation at Fermilab, J-Parc and BNL.

## REFERENCES

[1] S. Deghaye, D. Jacquet, D. Kozar, J. Serrano, “Oasis: A New System to Acquire and Display the Analog Signals for LHC”, CERN, Geneva, Switzerland, Rep. CERN-AB-2003-110-CO, 2003.

[2] S. Hancock, M. Lindroos, E. McIntosh, M. Metcalf, “Tomographic Measurements of Longitudinal Phase Space Density”, in *Comput. Phys. Commun.118 (1999) 61-70.*

[3] G. Papotti, “A Beam Quality Monitor for LHC Beams in the SPS”, in *Proc. 11th biennial European Accelerator Conference. (EPAC'08)*, Genoa, Italy, June 2008.

[4] M. Söderén, “ADTObsBox to Catch Instabilities”, *these proceedings*.

[5] E. Koukovini Platia, “Identification of the Horizontal Instability Mechanism at the CERN Proton Synchrotron Booster”, *these proceedings*.

[6] R. Cappi, E. Métral, G. Metral “Beam Break-up Instability in the CERN PS near Transition”, in *Proc. 7th Int. Particle Accelerator Conf.*, Vienna, Austria, June 2000.

[7] A. Burov, “Transverse Microwave Convective Instabilities at Transition Crossing”, arXiv:1908.02916 [physics.acc-ph], August 2019.

[8] R. Cappi, E. Métral, D. Möhl “Control of Coherent Instabilities by Linear Coupling”, in *Proc. 18th Int Conf. on High-energy Acc. (HEACC 2001)*, Tsukuba, Japan, March 2001.

[9] H. Damerau, A. Lascheen, M. Migliorati, "Observation and Damping of Longitudinal Coupled-bunch Oscillations in the CERN PS", in *Proc. ICFA Mini-Workshop on Imp. and Beam Instab. In Part. Acc.*, Benevento, Italy, September 2017, pp 33-37.

[10] Y. Papaphilippou, *et al.*, "Operational Performance of the LHC Proton Beams with the SPS Low Transition energy Optics", in *Proc. 4th Int. Particle Accelerator Conf. (IPAC'13)*, Shanghai, China, May 2013.

[11] H. Bartosik, M. Carlà, K. Cornelis, "Reconfiguration of SPS Landau Octupoles Circuits to Minimise Second Order Chromaticity", in *Proc. 10th Int. Particle Accelerator Conf. (IPAC'19)*, Melbourne, Australia, May 2019.

[12] J.M. Jimenez, *et al.*, "Observations, Analysis and Mitigation of Recurrent LHC Beam Dumps Caused by Fast Losses in Arc Half-Cell 16L2", in *Proc. 9th Int. Particle Accelerator Conf. (IPAC'18)*, Vancouver, Canada May 2018.

[13] L. Mether, "Review of Instabilities with Ions or/and Electrons and Possible Mitigations", *these proceedings*.

[14] H. Timko, T. Argyropoulos, I. Karpov, E. Shaposhnikova "Beam Instabilities After Injection to the LHC", in *Proc. 61st ICFA ABDW on High-Intensity and High-Brightness Hadron Beams (HB2018),* Daejon, Korea, June 2018.

[15] S. Igarashi, "High-Power Beam Operation at J-PARC", in *Proc. 61st ICFA ABDW on High-Intensity and High-Brightness Hadron Beams (HB2018),* Daejon, Korea, June 2018.

[16] T. Koseki, J-PARC, Japan, *private communications*

[17] M.E. Convery, FNAL, USA, *private communications*

[18] G. Marr, BNL, USA, *private communications*

# STABILITY DIAGRAMS FOR LANDAU DAMPING*

J. S. Berg†, Brookhaven National Laboratory, Upton, NY, USA

*Abstract*

Stability diagrams allow one to determine whether a system is stable due to the presence of incoherent tune spread in a beam, a phenomenon known as Landau damping. This paper presents an overview of the mathematical foundations that underpin stability diagrams. I first describe stability diagrams as a mapping between two complex planes: the space of eigenvalues of the underlying Vlasov equation, and a space which can most easily be described as the product of beam current and an effective impedance. I go on to describe the circumstances when the Vlasov description of impedance-driven instabilities can or can not be formulated to construct a stability diagram. Finally I outline how this is applied to impedance-driven collective effects in particle accelerators.

## INTRODUCTION

Stability diagrams allow one to determine whether a beam is stabilized by Landau damping by plotting the result of a relatively simple calculation involving the accelerator impedance and beam current on the same plane as a curve; the stability of the beam depends upon which side of the curve the point lies. The earliest use of stability diagrams was by Pease [1] for the case of longitudinal stability of unbunched beams. Several papers [2–4] expanded up on this with more examples and including the case of transverse stability of unbunched beams. Zotter [5] appears to be the first showing longitudinal bunched beam stability diagrams, and Chin [6] introduces transverse bunched beam stability diagrams.

The intention of this paper is to describe some mathematical foundations for the use of stability diagrams to calculate the point at which Landau damping is lost. I will describe the mathematics of the problem in terms of eigenmodes: complex (in the mathematical sense of "complex numbers") distributions of particles that are invariant in all phase space variables except for the independent variable (for particle accelerations, often the length along a reference curve, but time for some applications). The dependence on the independent variable is exponential in the independent variable, with $i$ times the coefficient being the eigenfrequency.

These eigenmodes can be divided into what are known as incoherent and coherent modes. Incoherent modes have a continuous spectrum for the eigenfrequency: the number of modes is uncountable (in the mathematical sense); the spectrum is generally a union of intervals on the real line. Incoherent modes appear even in the absence of collective interactions. Their frequencies are the single particle frequencies we refer to as tunes, or multiples thereof. They have a spread in frequencies due to tune shift with amplitude, or chromaticity in the absence of longitudinal focusing. Their modes are distributions along a single line of constant action, and constant energy in the absence of longitudinal focusing.

The coherent modes have a discrete spectrum: there is a region in the complex plane around any mode in which there are only a finite number of modes. There are a countable (in the mathematical sense: the number could be infinite) number of such modes. These coherent modes are what one computes when the equations for collective effects are solved in the absence of tune shift with amplitude or chromaticity caused by the magnetic lattice or potential-well distortion.

In single particle dynamics, there is a phenomenon known as filamentation which is directly related to Landau damping. Imagine one starts with a distribution whose shape is not "matched" with the lines of constant amplitude. When there is a tune spread in amplitude, particles with different amplitudes rotate in phase at different rates, leading to a distribution which is effectively uniform in phase, without any particle actually changing its own amplitude. Simplistically, Landau damping occurs when the rate at which this filamentation occurs for the incoherent modes, which have real eigenvalues and therefore no change in their amplitude, is greater than the growth rate of the coherent modes.

For collective effects in particle accelerators, generally there is an intensity threshold below which the eigenvalue equation has no discrete modes: this is the mathematical manifestation of Landau damping. A stability diagram is a diagrammatic technique that can, for some restricted cases, allow one to quickly compute where this threshold lies. For cases where a stability diagram can be applied to a problem, one can plot the complex coherent mode frequencies in the absence of tune spread, or equivalently impedances, in the complex plane, and in the same plane draw a curve (the stability diagram); if the frequency lies on the inside the curve, the mode is said to be stabilized by Landau damping. In reality it is a statement that there is no such discrete mode.

## GENERIC FORMULATION OF EIGENVALUE EQUATION

The equations describing the evolution of a distribution including collective effects can be Fourier transformed in the independent variable, and become an eigenvalue equation where the eigenvalue is the frequency corresponding to that independent variable. A generic form of the resulting

* This manuscript has been authored by employees of Brookhaven Science Associates, LLC under Contract No. DE-SC0012704 with the U.S. Department of Energy. The United States Government retains a non-exclusive, paid-up, irrevocable, world-wide license to publish or reproduce the published form of this manuscript, or allow others to do so, for United States Government purposes.

† jsberg@bnl.gov

eigenvalue equation is

$$[\Omega - \omega(x)]f(x) = \lambda \int K(x, \bar{x}) f(\bar{x})\, d\bar{x} \tag{1}$$

For particle accelerators: $\omega$ can be the tune (in which case $x$ is an action variable) or an orbit frequency ($x$ will be the energy); $\lambda$ will be proportional to the beam current; $K$ will be proportional to the impedance; and the phase space distribution will be contained in $K$. This description is very simplistic (in particular $x$ can be a vector of variables, and these can be matrix equations), but sufficient for this initial discussion.

If $\omega(x)$ does not depend on $x$ and $K$ is sufficiently well-behaved, $f(x)$, the beam distribution in the frequency domain, can be written as a sum of coefficients times basis functions. The eigenvalue problem then becomes a linear algebra problem for the coefficients, with the matrix elements being integrals of products of $K$ and the basis functions:

$$(\Omega - \omega)c_m = \lambda \sum_n Z_{mn} c_n \tag{2}$$

$$f(x) = \sum_k c_k B_k(x) \qquad c_k = \int C_k^*(x) f(x)\, dx \tag{3}$$

$$Z_{mn} = \int C_m^*(x) K(x, \bar{x}) B_n(x)\, dx\, d\bar{x} \tag{4}$$

A complete basis can be chosen so that the basis functions required to represent an arbitrary function is countably infinite. The resulting eigenvalue spectrum is also countably infinite but discrete. On formulating the linear algebra problem, one necessarily would take a finite number of basis functions, but as one increases the number of basis functions, the coefficients of the basis functions already included and their corresponding eigenvalues are expected to converge.

When $\omega(x)$ does depend on $x$, instead one develops a continuous, and therefore uncountably infinite, set of eigenvalue and eigenvectors for the problem. The eigenvalues in the continuous spectrum for Eq. (1) are just the range of $\omega(x)$, and therefore are real, for values of $x$ where $K(x, \bar{x})$ is nonzero. The resulting eigenfunctions are not true functions but "distributions" [7]:

$$f_C(x, \Omega) = \delta\big(x - \omega^{-1}(\Omega)\big) + \mathrm{PV}\frac{g(x, \Omega)}{x - \omega^{-1}(\Omega)} \tag{5}$$

$g(x, \Omega)$ can be computed by plugging $f_C$ into Eq. (1) if so desired.

In addition, when $\omega(x)$ depends on $x$, there may still be a discrete eigenvalue spectrum with a countable number of eigenvalues as well, for which the eigenfunctions are non-singular ordinary functions. A generic distribution written in the domain of the independent variable ($t$ here) will be a combination of the discrete and continuous modes:

$$f(x, t) = \int c(\Omega) f_C(x, \Omega) e^{-i\Omega t} d\Omega + \sum_n c_n f_{Dn}(x) e^{-i\Omega_n t} \tag{6}$$

For a sufficiently smooth $c(\Omega)$, the moments of $f(x, t)$, which lead to nonzero values on the right hand side of Eq. (1), that arise from the continuous part of Eq. (6) will decrease with time. Note that the coefficients in Eq. (6) are not changing in amplitude: particle amplitudes are not decreasing, only the moments that drive collective effects are. Any discrete modes (the second term in Eq. (6)) can still be exponentially increasing. However, for sufficiently small $\lambda$, there may not be any discrete modes: this disappearance of discrete modes is Landau damping.

## GENERIC FORMULATION OF STABILITY DIAGRAMS

To determine when a system is "Landau damped," one needs to find $\lambda$ for which Eq. (1) has no discrete modes. The equation itself is not amenable to direct numerical solution due to the mixture of singular and non-singular modes and the uncountable eigenvalue spectrum. A stability diagram is an attempt to avoid this direct numerical simulation while still finding the $\lambda$ for which the system has no discrete modes.

$f(x)$ can be expanded as a series of basis functions and Eq. (1) can be written similarly to Eqs. (2–4), but with $\Omega - \omega(x)$ moved to the side of the equation with $K(x, \bar{x})$:

$$c_m = \lambda \sum_n K_{mn}(\Omega) c_n \tag{7}$$

$$K_{mn}(\Omega) = \int \frac{C_m^*(x) K(x, \bar{x}) B_n(\bar{x})}{\Omega - \omega(x)} dx\, d\bar{x} \tag{8}$$

Consider the properties of the functions $K_{mn}(\Omega)$. $|K_{mn}(\Omega)| \sim O(|\Omega|^{-1})$ as $|\Omega| \to \infty$. $K_{mn}(\Omega)$ is defined everywhere except for the line where $\Omega$ is in the range of $\omega(x)$ for $x$ real and $K(x, \bar{x})$ is nonzero. Thus $K_{mn}(\Omega)$ defines a mapping of the entire complex plane, except for that line, to a bounded region of the complex plane:

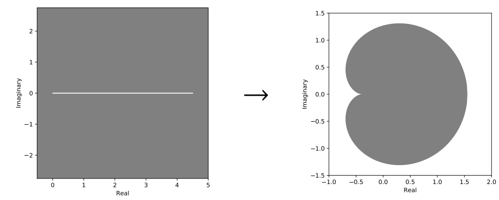


The boundary of the region can be found by evaluating $K_{mn}(\omega(x) \pm i\epsilon)$ for real $x$ and infinitesimal $\epsilon$.

Now consider a simplification of Eq. (7) where the matrix $K_{mn}(\Omega)$ is diagonal. Then the equation becomes

$$\lambda = 1/K_{mm}(\Omega) \tag{9}$$

The right hand side of Eq. (9) is a mapping of the complex $\Omega$ plane, except for the line mentioned above, to the complex plane with a hole in it:

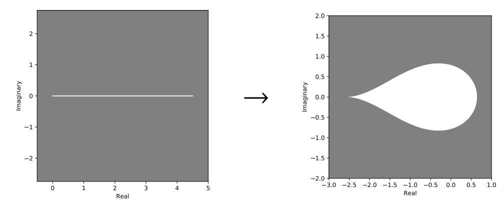

Now consider the definition of $K_{mn}(\Omega)$ from Eq. (8), and assume that $\omega(x)$ did not depend on $x$; then

$$K_{mn}(\Omega) = \frac{Z_{mn}}{\Omega - \omega} \tag{10}$$

where $Z_{mn}$ is defined in Eq. (4). If $K_{mn}(\Omega)$ were diagonal, then $Z_{mn}$ would be as well, in which case (if $\omega$ were constant), the equation for the eigenvalue $\Omega_0$ would be

$$\Omega_0 - \omega = \lambda Z_{mm} \tag{11}$$

Combining Eq. (11) with Eq. (9), we have

$$\Omega_0 - \omega = \frac{Z_{mm}}{K_{mm}(\Omega)} \tag{12}$$

Equation 12 is the general form for any stability diagram, and indicates how a stability diagram is used. The eigenvalue equation is first solved without frequency spread (Eq. (11)), then the difference of the eigenvalue from $\omega$ is plotted in the same plane as the range of $Z_{mn}/K_{mn}(\Omega)$. In practice one plots the boundary $Z_{mn}/K_{mn}(\Omega \pm i\epsilon)$ for $\Omega$ real. If $\Omega_0 - \omega$ is outside the range of $Z_{mn}/K_{mn}(\Omega \pm i\epsilon)$ (i.e., on the origin side of the boundary), then such a solution cannot exist as a discrete mode: it is Landau damped. If $\Omega_0 - \omega$ is within the range of $Z_{mn}/K_{mn}(\Omega)$, then its frequency and growth rate can be determined by solving Eq. (12) for $\Omega$. Note that $Z_{mn}/K_{mn}(\Omega) = \Omega + O(1)$ for large $\Omega$.

If diagonalizing the problem is not acceptable, then one could start with the eigenvalue problem in Eq. (7), and treat it as an eigenvalue problem for $\lambda^{-1}$ for fixed $\Omega$. One can plot each eigenvalue as a function of $\Omega_0 \pm i\epsilon$ for $\Omega_0$ real. That will give a closed curve for each eigenvalue; the region outside the closed curves for all of the eigenvalues is the region corresponding to values of $\lambda$ that will result in no discrete eigenvalues for the original problem with $\Omega$ as the eigenvalue. $\lambda$ will be a (possibly complex) constant times the beam current; taking a line along the appropriate direction in that region will allow one to determine the maximum current that is stable from Landau damping.

## FORMULATION FOR PARTICLE ACCELERATORS

Now consider the accelerator problem. Equation (9) will usually (but not always) take the form

$$1 = -iC\frac{IZ_{\mathrm{eff},\boldsymbol{m}}}{E}\int \frac{\boldsymbol{m}\cdot\dfrac{\partial\psi_0}{\partial\boldsymbol{J}}}{\Omega - \boldsymbol{m}\cdot\omega(\boldsymbol{J})}d\boldsymbol{J} \tag{13}$$

where $I$ is the beam current, $E$ is the beam energy, $Z_{\mathrm{eff},\boldsymbol{m}}$ an effective impedance (the impedance weighted by a function of frequency), and $\psi_0$ is a phase space distribution. $\omega(\boldsymbol{J})$ can be a tune that varies with amplitude or an orbit period that varies with energy, or both. The phase space distribution is often Gaussian or a distribution that goes to zero reasonably smoothly at some number of $\sigma$ [8, 9]. Using distributions with step truncations ("truncated Gaussian" distributions, for instance) should be avoided for these computations, since one effectively picks up a discrete mode at the truncation (though collimation might make something similar occur).

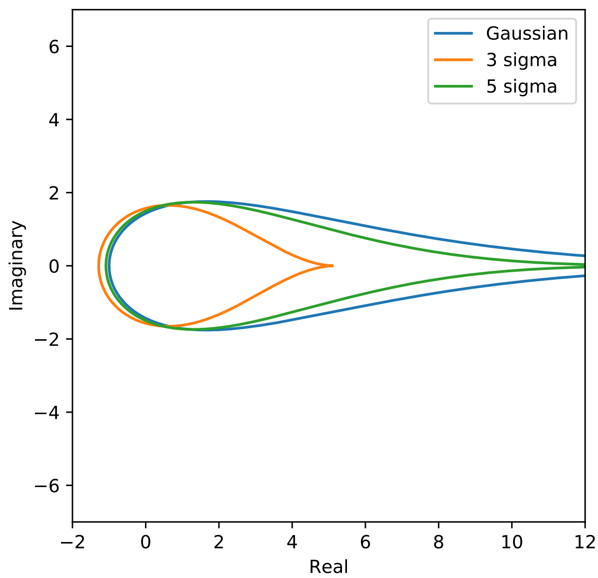


Figure 1: Stability diagrams for longitudinal motion and an unbunched beam. Different curves are for distributions smoothly truncated at a certan number of standard deviations, and a Gaussian distribution.

Using Eq. (13) in Eq. (12), the impedance, current, and energy all disappear from the right hand side. Thus the stability diagram only depends on the phase space distribution $\psi_0$ and the mode $\boldsymbol{m}$ under consideration.

In the following subsections I outline the common cases for particle accelerators. These are meant only to summarize the characteristics of the behavior of these systems. I will leave out constants that do not serve to illustrate the points I am making. More detailed discussions are left to other references. I adopt the conventions of [9] for dimensionless functions used in constructing stability diagrams (Eqs. 14–17 are derived in detail there).

### *Longitudinal Impedance, Unbunched Beam*

For a longitudinal impedance with no RF, the eigenvalue equation becomes

$$\frac{1}{\bar{B}_\parallel\left(\dfrac{k\omega_0 - \omega}{k\omega_0\eta_c\sigma_\delta}\right)} = iC\frac{I}{E\eta_c\sigma_\delta^2}\frac{Z_\parallel(k\omega_0)}{k\omega_0} \tag{14}$$

$B_\parallel$ is dimensionless, only depending on the shape (and not the scale) of the energy distribution in the beam. It's behavior differs from what was described previously in that $1/B_\parallel(x)$ is proportional to $x^2$, not $x$, for large $x$. Curves of $1/B_\parallel(x \pm i\epsilon)$ are plotted in Fig. 1 for both a Gaussian distribution and a distribution that goes smoothly to zero at 3 and 5 standard deviations [8, 9]. Note that the curve for $1/B_\parallel(x - i\epsilon)$ lies on top of the curve for $1/B_\parallel(x + i\epsilon)$; this behavior is unique

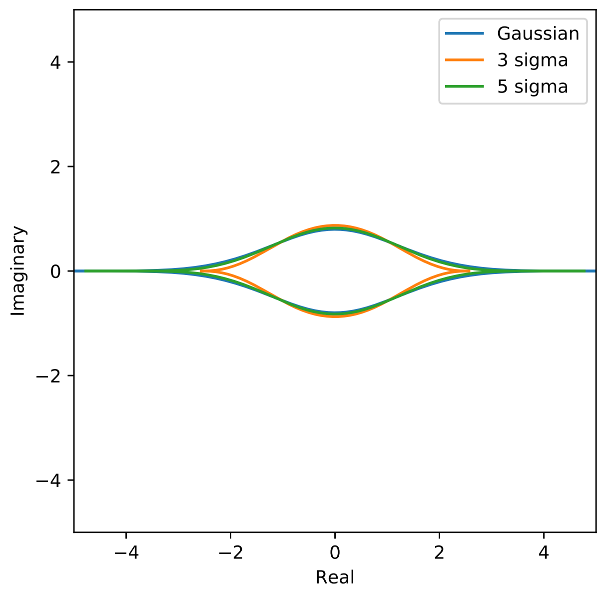


Figure 2: Stability diagrams for transverse motion and an unbunched beam where frequency spread arises from energy spread.

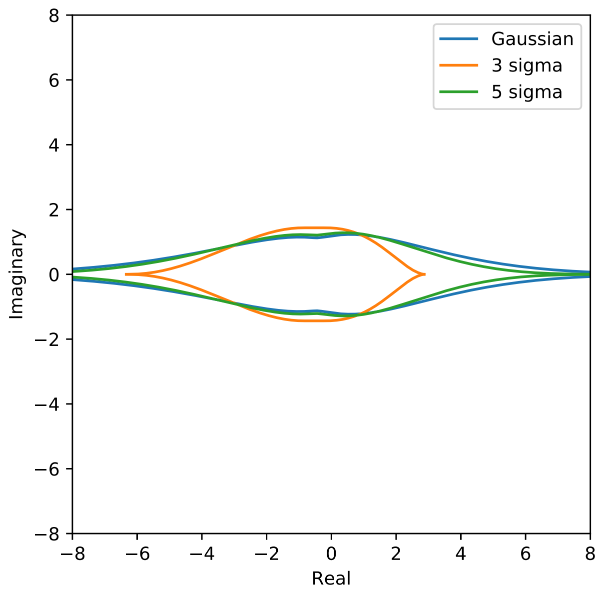


Figure 3: Stability diagrams for transverse motion and an unbunched beam where frequency spread arises from transverse tune spread. Tune shifts with amplitude are in opposite directions for the two planes.

to the longitudinal unbunched case. To use this stability diagram, one plots the right hand side of Eq. (14) in the plane with the stability diagram; if the right hand side is inside the curve, then the mode is stable.

The longitudinal diagram gives the known behavior: the beam is stable for highly inductive impedances for $\eta_c > 0$ and for highly capacitive impedance for $\eta_c < 0$ due to the long tail in that direction; the tail is reduced for a more truncated distribution; and stability is lost when $\eta_c = 0$.

### *Transverse Unbunched, Energy Spread*

For a transverse impedance with no RF and a frequency spread arising from energy spread, the eigenvalue equation becomes

$$\frac{\sigma_\delta[(k\omega_0 \pm \omega_\perp)\eta_c \mp \omega_\perp\xi]}{\bar{B}_\perp\left(\dfrac{k\omega_0 \pm \omega_\perp - \omega}{\sigma_\delta[(k\omega_0 \pm \omega_\perp)\eta_c \mp \omega_\perp\xi]}\right)} = -iC\frac{IZ_\perp(k\omega_0 \pm \omega_\perp)}{E} \quad (15)$$

$\bar{B}_\perp(x)$ is dimensionless and for large $x$ is approximately $x^{-1}$. Figure 2 shows plots of $1/B_\perp(x \pm i\epsilon)$ for the same distributions as in Fig. 1. The upper curve and lower curves are for the two signs in $x \pm i\epsilon$. Due to the symmetry of the impedance (assuming feedback is not included), the right hand side of Eq. (15) must be between both of the curves for stability, since even if it on the stable side of both of the curves for one of the $\pm$ signs in Eq. (15), it will be on the unstable side of both curves for the other sign of $\pm$ (and the negative $k$) in that equation.

### *Transverse Tune Spread*

When variation in transverse amplitude is the dominant source of frequency spread, the formulations for bunched and unbunched beams are very similar. This is because it is the longitudinal motion that creates the distinction between bunched and unbunched beams, and that longitudinal motion is effectively integrated out.

When there is no RF and the energy spread gives a small contribution to the frequency spread (for instance when $(k\omega_0 \pm \omega_\perp)\eta_c \mp \omega_\perp\xi$ reaches its smallest value), the tune shift with transverse amplitude may become the dominant contribution to the frequency spread. In this case the eigenvalue equation takes the form

$$\frac{\omega - k\omega_0 - \omega_y}{\bar{T}_y\left(\dfrac{\omega - k\omega_0 - \omega_y}{\alpha_{xy} - \omega\omega_x\xi_x\epsilon_x/c}, \dfrac{\omega - k\omega_0 - \omega_y}{\alpha_{xy} - \omega\omega_x\xi_x\epsilon_x/c}\right)} = -iC\frac{IZ_\perp(\omega_y + k\omega_0)}{E} \quad (16)$$

There should be a $\pm$ in various places in this equation, but that can be generally ignored, at least if there is feedback. The two arguments to $\bar{T}_y$ take into account tune shift with amplitude in the two horizontal planes. If the tune shift with amplitude is negative, the tail of the stability diagram will correspond to an inductive impedance. If the tune shifts with amplitudes have opposite signs, the stability diagram will have tails in both directions (Fig. 3). The top and bottom curves are drawn for the two signs in $y/\bar{T}_y(x \pm i\epsilon, y \pm i\epsilon)$, and for stability the right hand side needs to be between the two curves due to the symmetry in the impedance.

The case of bunched beam with transverse tune spread is nearly the same as the transverse unbunched case. The first important difference is that an “effective impedance” is used, which is an integral or sum over the impedance times a weighting function. The weighting function is shifted by a frequency $\xi\omega_0/\eta_c$, breaking the symmetries mentioned earlier, meaning that we could have damped discrete modes that do not have corresponding growing discrete modes. The second important difference is that multiples of the synchrotron frequency enter in, as well as the amplitude dependence of those tune shifts, while the chromaticity terms are no longer present in the arguments to $\bar{T}_y$. The chromaticity terms seen when there is no RF in Eqs. (15) and (16) are still present in the bunched case, they manifest themselves in the shift in frequency in the weight function when computing the effective impedance (and that frequency shift can be seen in Eq. (15)). The stability diagram is valid for individual modes for either the single or multi-bunch case. Thus, one solves the corresponding uncoupled problem for the eigenvalue $\Omega$, and plots $\Omega - \omega_y - m\omega_z$ on the same diagram as

$$\frac{\Omega - \omega_y - m\omega_z}{\bar{T}_y\left(\dfrac{\Omega - \omega_y - m\omega_z}{\alpha_{yx} + m\alpha_{zx}}, \dfrac{\Omega - \omega_y - m\omega_z}{\alpha_{yx} + m\alpha_{zx}}\right)} \tag{17}$$

evaluated at $\Omega = \omega + i\epsilon$ for $\omega$ real.

With coupling between modes with different $m$, this formulation can still be used because the integrals only depend on the distribution and the form of the tune shift with amplitude. One does not use a stability diagram: the coupled nonlinear equations are solved, and Eq. (17) is evaluated at an arbitrary complex $\Omega$; since $m$ is different for each mode, the function must be evaluated at a number of different points. Chin *et al.* [6, 10] appear do this.

### *Longitudinal Tune Spread*

Incorporating longitudinal tune spread in a bunched beam for a calculation for Landau damping presents the largest challenge for accelerator applications. But doing so is desirable since the longitudinal tune shift with amplitude can be the largest source of tune spread in the system. The challenge can be seen in the computation of $K(\Omega)$. This computation requires integrals of the form

$$\int \frac{[C_m^*(\boldsymbol{J})J_y\boldsymbol{m}\cdot(\partial\psi_0/\partial\boldsymbol{J})B_m(\boldsymbol{J}')Z(\omega) \; J_m(\sqrt{2J_z\beta_z}\omega)J_m(\sqrt{2J_z'\beta_z}\omega)]}{\Omega - \omega_y(\boldsymbol{J}) - m\omega_z(\boldsymbol{J})} \, d\boldsymbol{J}\, d\boldsymbol{J}'\, d\omega \tag{18}$$

This is the form for transverse modes, but the form for longitudinal modes is similar. The problem is the appearance of $\omega$ in the argument of the Bessel functions. The integrals of $\boldsymbol{J}$ and $\boldsymbol{J}'$ create a frequency-dependent weight function that multiplies the impedance. If the tunes in the denominator depend on $J_z$, then that weighting function depends on $\Omega$, and their is not a single stability diagram that can be drawn. One approach that can be taken is to expand the first Bessel function form small arguments [5]; unfortunately, this can get the high-frequency contribution for the effective impedance wrong. Initial experiments indicated that this approximation is optimistic [8]. Chin *et al.* [10] approach the difficulty with an additional summation.

For transverse instabilities, the tails in the stability diagrams are lost because modes with opposite signs of $m$ generally have similar effective impedances (at least if the chromaticity is zero), but the tail of the stability diagram along the real frequency shift axis is in opposite directions for the two signs of $m$, so the resulting stability diagram has a very reduced area [8]. This problem is not present for longitudinal impedances.

## REFERENCES


[1] R. L. Pease, “Analysis of longitudinal accelerator instabilities,” *IEEE Trans. Nucl. Sci.*, vol. NS-12, no. 3, pp. 561–565, 1965, *Proc. 1st Particle Accelerator Conf. (PAC’65), Washington D.C., USA, Mar. 1965*. DOI: 10.1109/TNS.1965.4323695. https://www.jacow.org/

[2] A. G. Ruggiero and V. G. Vaccaro, “Solution of the dispersion relation for longitudinal stability of an intense coasting beam in a circular accelerator (application to the ISR),” CERN, Geneva, Switzerland, report CERN-ISR-TH/68-33, Jul. 1, 1968.

[3] K. Hübner and V. G. Vaccaro, “Dispersion relations and stability of coasting particle beams,” CERN, Geneva, Switzerland, report CERN-ISR-TH/70-44, Aug. 25, 1970.

[4] K. Hubner, A. G. Ruggiero, and V. G. Vaccaro, “Stability of the coherent transverse motion of a coasting beam for realistic distribution functions and any given coupling with its environment,” in *Proceedings, 7th International Conference on High-Energy Accelerators, HEACC 1969: Yerevan, USSR, August 27–September 2, 1969*, A. I. Alikhanian, Ed., also CERN-ISR-TH-RF/69-23, Akad. Nauk Armyanskoj. Inst. Fiz., 1970, pp. 343–325.

[5] B. Zotter, “Longitudinal stability of bunched beams part ii: Synchrotron frequency spread,” CERN, Geneva, Switzerland, report CERN-SPS/81-19 (DI), Nov. 1981.

[6] Y. H. Chin, “Hamiltonian formulation for bunched beam instabilities in the presence of betatron tune spread,” CERN, Geneva, Switzerland, report CERN-SPS-85-9 (DI-MST), May 28, 1985.

[7] N. G. van Kampen, “On the theory of stationary waves in plasmas,” *Physica*, vol. 21, pp. 949–963, 1955, ISSN: 0031-8914. DOI: 10.1016/S0031-8914(55)90413-4.

[8] J. S. Berg and F. Ruggiero, “Stability diagrams for landau damping,” in *Proc. 17th Particle Accelerator Conf. (PAC’97)*, (Vancouver, Canada, May 1997), paper 7V030, IEEE, Piscataway, NJ, 1998, pp. 1712–1714. https://www.jacow.org/

[9] J. S. Berg, “Beam transfer functions, stability diagrams, and schottky spectra for unbunched beams,” CERN, Geneva, Switzerland, report CERN-SL-97-049-AP, Dec. 7, 1999.

[10] Y. Chin, K. Satoh, and K. Yokoya, “Instability of a bunch beam with synchrotron-frequency spread,” *Part. Accel.*, vol. 13, pp. 45–66, 1983.

# LANDAU DAMPING IN THE TRANSVERSE PLANE

N. Mounet*, CERN, Geneva, Switzerland

*Abstract*

In these proceedings we sketch a general theory for Landau damping in the transverse plane, in the particular case of beam-coupling impedance with linear (octupolar) detuning as the source of tune spread. Using a Hamiltonian formalism and perturbation theory, we will go beyond the traditional stability diagram approach to obtain the general non-linear determinant equation that leads to modes determination. Limiting cases are studied, and preliminary results of the full formalism are obtained in an attempt to generalize the concept of stability diagram.

## INTRODUCTION

In particle accelerators and storage rings, the beam can in principle be affected by various mechanisms that can lead to collective instabilities. Nevertheless, it typically remains stable thanks to a natural stabilization mechanism originating from the spread of the particles tune [1]. This phenomenon, first observed in plasmas, is called Landau damping [2].

When a beam is under the effect of a coherent, possibly unstable, mode, Landau damping can be understood intuitively as the de-synchronization of the beam individual particles from the collective motion, due to the fact that their oscillation frequency (or tune) gets modified, via the spread, as the amplitude of the unstable mode grows. There are simple ways to mathematically theorize Landau damping (see e.g. in Ref. [1]). For instance, in the transverse plane and with a dipolar beam-coupling impedance as the source of the coherent instability, one can simply use Hill equation, with a collective force depending on the beam average position on the right hand side of the equation, and integrate the solution over a continuous distribution of betatron frequencies. Such a formalism can be very handy to understand quickly the physics of the phenomenon, but lacks generality, as it is in particular not able to handle the case when the spread in frequency is in the same plane as the collective excitation, unless rather complicated developments are made on top of the theory [3].

Here we will use phase space distribution functions, Vlasov equation [4] and linear perturbation theory, to compute coherent modes originating from a beam-coupling dipolar impedance, similarly to what is done in Chao's book [1], but adding as additional ingredient a tune spread in the form of a linear, octupolar detuning. We will derive the complete formalism and get an extension of Sacherer equation, obtained first by Chin in 1985 [5]. The equation will be then transformed into a determinant equation, that can be reduced to the usual stability diagram theory as a limiting case. Finally, an indirect analysis of the general equation is performed as an application of the formalism, showing that the stability diagram theory can be potentially recovered also in the general case.

The conventions and notations are identical to those in Ref. [6], which were inspired from Chao's book [1].

## SACHERER EQUATION WITH LINEAR AMPLITUDE DETUNING

The system of beam particles is governed by an Hamiltonian $H$ split in two parts: the unperturbed Hamiltonian $H_0$ and a first order perturbation $\Delta H$

$$H = H_0 + \Delta H. \tag{1}$$

The phase space density is represented by a distribution function $\psi$, also separated into an stationary part $\psi_0$ (governed by $H_0$) and a perturbation $\Delta\psi$:

$$\psi = \psi_0 + \Delta\psi. \tag{2}$$

For a beam of particles, using the coordinates $(x, x' = \frac{dx}{ds}, y, y' = \frac{dy}{ds}, z, \delta)$ – with $s$ the longitudinal coordinate along the orbit and $\delta$ the relative deviation of the longitudinal momentum from that of the synchronous particle, we consider a lattice without coupling and use the smooth approximation, including the effect of chromaticities $(Q'_x, Q'_y)$ and of linear (octupolar) amplitude detuning:

$$\begin{aligned} H_0 = {} & \omega_0 \left( Q_{x0} + Q'_x\delta + \frac{a_{xx}}{2}J_x + \frac{a_{xy}}{2}J_y \right) J_x \\ & + \omega_0 \left( Q_{y0} + Q'_y\delta + \frac{a_{xy}}{2}J_x + \frac{a_{yy}}{2}J_y \right) J_y - \omega_s J_z, \end{aligned} \tag{3}$$

with $Q_{x0}$ and $Q_{y0}$ the unperturbed transverse tunes, $\omega_0$ the angular revolution frequency, $\omega_s = Q_s\omega_0$ the angular synchrotron frequency, and the actions $(J_x, J_y, J_z)$ defined by

$$J_x = \frac{1}{2}\left( \frac{Q_{x0}}{R}x^2 + \frac{R}{Q_{x0}}x'^2 \right), \tag{4}$$

$$J_y = \frac{1}{2}\left( \frac{Q_{y0}}{R}y^2 + \frac{R}{Q_{y0}}y'^2 \right), \tag{5}$$

$$J_z = \frac{1}{2}\left( \frac{\omega_s}{v\eta}z^2 + \frac{v\eta}{\omega_s}\delta^2 \right), \tag{6}$$

with $R$ the machine physical radius, $v$ the beam velocity and $\eta = \alpha_p - \frac{1}{\gamma^2}$ the slippage factor. The corresponding angle variables are given by

$$\theta_x = \operatorname{atan}\left( \frac{Rx'}{Q_{x0}x} \right), \tag{7}$$

$$\theta_y = \operatorname{atan}\left( \frac{Ry'}{Q_{y0}y} \right), \tag{8}$$

$$\phi = \operatorname{atan}\left( \frac{v\eta\delta}{\omega_s z} \right). \tag{9}$$

* nicolas.mounet@cern.ch

In the case of octupoles distributed all around the ring, the amplitude detuning coefficients are given by [7]

$$
\begin{aligned}
a_{xx} &= \frac{3}{8\pi}\int_0^{2\pi R} \mathrm{d}s\beta_x^2(s)\frac{O_3(s)}{\frac{p_0}{e}},\\
a_{yy} &= \frac{3}{8\pi}\int_0^{2\pi R} \mathrm{d}s\beta_y^2(s)\frac{O_3(s)}{\frac{p_0}{e}},\\
a_{xy} &= -\frac{3}{4\pi}\int_0^{2\pi R} \mathrm{d}s\beta_x(s)\beta_y(s)\frac{O_3(s)}{\frac{p_0}{e}},
\end{aligned}
\tag{10}
$$

with $(\beta_x, \beta_y)$ the beta functions, $e$ the elementary charge, $O_3 \equiv \frac{1}{6}\frac{\partial^3 B_y}{\partial x^3}$ the octupolar strength in T.m$^{-3}$ and $p_0$ the longitudinal momentum of the synchronous particle.

The stationary distribution, solution of Vlasov equation [4] for the unperturbed Hamiltonian, is in general a function of the invariants of motion. Since the Hamiltonian does not depend on the angles $\theta_x$ and $\theta_y$, $J_x$ and $J_y$ are invariants of motion. On the other hand, $H_0$ depends on $\phi$ through the chromatic term, but this dependency being much weaker than the main longitudinal motion (given by the term $-\omega_s J_z$), the standard approximation is to neglect it [1, chap. 6], which is equivalent to the assumption

$$
\frac{\partial H_0}{\partial \phi} \approx 0,
\tag{11}
$$

(see Ref. [6] for more details). Moreover, one can neglect the weak coupling induced by both the indirect amplitude detuning and the chromaticities, such that it is reasonable to assume that the stationary distribution can be written by separating all three degrees of freedom:

$$
\psi_0(x, x', y, y', z, \delta) = N f_{x0}(J_x) f_{y0}(J_y) g_0(J_z),
\tag{12}
$$

with $N$ the total number of particles in the full phase space. The normalization conditions are chosen as:

$$
\begin{aligned}
\int_0^{+\infty} \mathrm{d}J_x\, f_{x0}\left(J_x\right) &= \frac{1}{2\pi},\\
\int_0^{+\infty} \mathrm{d}J_y\, f_{y0}\left(J_y\right) &= \frac{1}{2\pi},\\
\int_0^{+\infty} \mathrm{d}J_z\, g_0\left(J_z\right) &= \frac{1}{2\pi}.
\end{aligned}
\tag{13}
$$

The perturbative part of the Hamiltonian $\Delta H$ is assumed to be responsible for a collective, $z$-dependent, vertical dipolar force $F_y^{coh}$, e.g. to be of the form [6]

$$
\Delta H = -\frac{y F_y^{coh}\left(z;t\right)}{p_0} = -\sqrt{\frac{2J_y R}{Q_{y0}}}\cos\theta_y \frac{F_y^{coh}\left(z;t\right)}{p_0},
\tag{14}
$$

using

$$
y = \sqrt{\frac{2J_y R}{Q_{y0}}}\cos\theta_y.
\tag{15}
$$

Having defined $H_0$, $\Delta H$ and $\psi_0$, we want to obtain now at first order the perturbation of the distribution $\Delta\psi$. Our starting point will be the linearized Vlasov equation expressed with Poisson brackets [8]:

$$
\frac{\partial \Delta\psi}{\partial t} + [\Delta\psi, H_0] + [\psi_0, \Delta H] = 0,
\tag{16}
$$

with the definition (using action-angle variables as expressed above):

$$
\begin{aligned}
[\mathcal{F}, \mathcal{G}] = &\frac{\partial \mathcal{F}}{\partial J_x}\frac{\partial \mathcal{G}}{\partial \theta_x} - \frac{\partial \mathcal{F}}{\partial \theta_x}\frac{\partial \mathcal{G}}{\partial J_x}\\
&+ \frac{\partial \mathcal{F}}{\partial J_y}\frac{\partial \mathcal{G}}{\partial \theta_y} - \frac{\partial \mathcal{F}}{\partial \theta_y}\frac{\partial \mathcal{G}}{\partial J_y} + \frac{\partial \mathcal{F}}{\partial J_z}\frac{\partial \mathcal{G}}{\partial \phi} - \frac{\partial \mathcal{F}}{\partial \phi}\frac{\partial \mathcal{G}}{\partial J_z},
\end{aligned}
\tag{17}
$$

for two differentiable functions $\mathcal{F}$ and $\mathcal{G}$. We refer the reader to Ref. [9] for more details on classical Hamiltonian mechanics, and to Refs. [10–12] for a detailed description of Hamiltonian dynamics in the case of single particle beam physics. Vlasov equation applied to a distribution of beam particles, in the context of linear perturbation theory, is thoroughly explained in Ref. [1, chap. 6]. A short primer on both Hamiltonian and Vlasov aspects can be found in Ref. [6].

Neglecting as above $\frac{\partial H_0}{\partial \phi}$, we can write

$$
\begin{aligned}
[\Delta\psi, H_0] &\approx -\frac{\partial \Delta\psi}{\partial \theta_x}\frac{\partial H_0}{\partial J_x} - \frac{\partial \Delta\psi}{\partial \theta_y}\frac{\partial H_0}{\partial J_y} - \frac{\partial \Delta\psi}{\partial \phi}\frac{\partial H_0}{\partial J_z}\\
&\approx -\omega_0 Q_x \frac{\partial \Delta\psi}{\partial \theta_x} - \omega_0 Q_y \frac{\partial \Delta\psi}{\partial \theta_y} + \omega_s \frac{\partial \Delta\psi}{\partial \phi},
\end{aligned}
\tag{18}
$$

with

$$
Q_x = Q_{x0} + Q_x'\delta + a_{xx}J_x + a_{xy}J_y,
\tag{19}
$$

$$
Q_y = Q_{y0} + Q_y'\delta + a_{xy}J_x + a_{yy}J_y.
\tag{20}
$$

The other Poisson brackets is given by (using the fact that $\Delta H$ does not depend on $\theta_x$ and that $\psi_0$ does not depend on any of the angles)

$$
\begin{aligned}
[\psi_0, \Delta H] &= N f_{x0}(J_x)\left(\frac{df_{y0}}{dJ_y} g_0(J_z)\frac{\partial \Delta H}{\partial \theta_y} + f_{y0}(J_y)\frac{dg_0}{dJ_z}\frac{\partial \Delta H}{\partial \phi}\right)\\
&= N f_{x0}(J_x)\frac{df_{y0}}{dJ_y} g_0(J_z)\sqrt{\frac{2J_y R}{Q_{y0}}}\sin\theta_y \frac{F_y^{coh}\left(z;t\right)}{p_0}\\
&\quad + N f_{x0}(J_x) f_{y0}(J_y)\frac{dg_0}{dJ_z}\frac{\partial \Delta H}{\partial z}\frac{\partial z}{\partial \phi}\\
&\approx N f_{x0}(J_x)\frac{df_{y0}}{dJ_y} g_0(J_z)\sqrt{\frac{2J_y R}{Q_{y0}}}\sin\theta_y \frac{F_y^{coh}\left(z;t\right)}{p_0}.
\end{aligned}
\tag{21}
$$

In the above we have neglected $\frac{\partial \Delta H}{\partial z}$. This is a standard approximation, made in Ref. [1, chap. 6], which has its grounds in the general idea that we neglect any effect of the transverse coherent force on the longitudinal motion. This should be valid as long as one remains far from low-order synchro-betatron resonances $Q_{y0} + lQ_s = n$ (and provided the transverse beam size is small enough).

The linearized Vlasov equation (16) then takes the form

$$\frac{\partial \Delta\psi}{\partial t} - \frac{\partial \Delta\psi}{\partial \theta_x}\omega_0 Q_x - \frac{\partial \Delta\psi}{\partial \theta_y}\omega_0 Q_y + \frac{\partial \Delta\psi}{\partial \phi}\omega_s + N f_{x0}(J_x)\frac{df_{y0}}{dJ_y} g_0(J_z)\sqrt{\frac{2J_y R}{Q_{y0}}}\sin\theta_y \frac{F_y^{coh}(z;t)}{p_0} = 0. \tag{22}$$

For convenience we switch to the $r$ coordinate instead of $J_z$, as in Ref. [1, chap. 6]:

$$r = \sqrt{\frac{2J_z v\eta}{\omega_s}}, \quad z = r\cos\phi, \quad \delta = \frac{\omega_s}{v\eta} r\sin\phi. \tag{23}$$

Then we express the perturbation assuming a single coherent mode of complex angular frequency $\Omega = Q_c\omega_0$, and decompose it using Fourier series for all three angles, in a completely general way:

$$\Delta\psi\left(J_x,\theta_x,J_y,\theta_y,r,\phi;t\right) = e^{j\Omega t}\sum_{m=-\infty}^{+\infty} e^{jm\theta_x}\sum_{p=-\infty}^{+\infty} e^{jp\theta_y} \times e^{-\frac{j\left(mQ'_x+pQ'_y\right)r\cos\phi}{\eta R}}\sum_{l=-\infty}^{+\infty} e^{-jl\phi} h^{m,p,l}\left(J_x,J_y,r\right), \tag{24}$$

where we have introduced, without loss of generality, the head-tail phase factor

$$e^{-\frac{j\left(mQ'_x+pQ'_y\right)r\cos\phi}{\eta R}},$$

similarly to what is done in Ref [1, chap. 6]. This phase factor is a convenience introduced to simplify the equation, as we will see below. To proceed further, we again assume that the dependency between the longitudinal and transverse actions is separable, in other words that

$$h^{m,p,l}\left(J_x,J_y,r\right) = f^{m,p,l}\left(J_x,J_y\right) R_l(r). \tag{25}$$

Now we expand the linearized Vlasov equation from Eq. (22) as

$$e^{j\Omega t}\sum_{m=-\infty}^{+\infty}\sum_{p=-\infty}^{+\infty}\sum_{l=-\infty}^{+\infty} e^{jm\theta_x} e^{jp\theta_y} e^{-jl\phi} e^{-\frac{j\left(mQ'_x+pQ'_y\right)r\cos\phi}{\eta R}} \times \left[jQ_c - jmQ_x - jpQ_y - jlQ_s + \frac{j\omega_s\left(mQ'_x+pQ'_y\right)r\sin\phi}{\eta v}\right] \times \omega_0 f^{m,p,l}\left(J_x,J_y\right)R_l(r) = -Nf_{x0}(J_x)\frac{df_{y0}}{dJ_y}g_0(J_z) \times \sqrt{\frac{2J_yR}{Q_{y0}}}\frac{e^{j\theta_y}-e^{-j\theta_y}}{2j}\frac{F_y^{coh}(z;t)}{p_0}, \tag{26}$$

where we have used the identity $\omega_0 = \frac{v}{R}$. In the above, the expression within square brackets can be simplified further since the chromatic terms in Eqs. (19) and (20) cancel out with the term

$$\frac{j\omega_s\left(mQ'_x+pQ'_y\right)r\sin\phi}{\eta v} = j\left(mQ'_x+pQ'_y\right)\delta,$$

using Eq. (23) – this is the reason why we introduced the head-tail phase factor in the first place. Then, comparing the expressions in $\theta_x$ and $\theta_y$ on both sides of the equation, term by term identification in the Fourier series gives:

$$f^{m,p,l}\left(J_x,J_y\right) = 0 \quad \text{for any } m \neq 0 \text{ and any } p \neq \pm 1. \tag{27}$$

Equation (26) thus becomes

$$e^{j\Omega t}\sum_{p=\pm1}\sum_{l=-\infty}^{+\infty} e^{jp\theta_y} e^{-jl\phi} e^{-\frac{jpQ'_y r\cos\phi}{\eta R}} \times j\left[Q_c - p\left(Q_{y0}+a_{xy}J_x+a_{yy}J_y\right) - lQ_s\right] \times \omega_0 f^{0,p,l}\left(J_x,J_y\right)R_l(r) = -Nf_{x0}(J_x)\frac{df_{y0}}{dJ_y}g_0(J_z) \times \sqrt{\frac{2J_yR}{Q_{y0}}}\frac{e^{j\theta_y}-e^{-j\theta_y}}{2j}\frac{F_y^{coh}(z;t)}{p_0}. \tag{28}$$

Now we make the standard assumption that $Q_c \approx Q_{y0}$ such that

$$\left|Q_c + \left(Q_{y0}+a_{xy}J_x+a_{yy}J_y\right) - lQ_s\right| >> \left|Q_c - \left(Q_{y0}+a_{xy}J_x+a_{yy}J_y\right) - lQ_s\right|.$$

This means that the term for $p = -1$ can be neglected as well as $e^{-j\theta_y}$ on the right-hand side [1, chap. 6], and we end up with (after simplification by $e^{j\theta_y}$)

$$e^{j\Omega t} e^{-\frac{jQ'_y r\cos\phi}{\eta R}}\sum_{l=-\infty}^{+\infty} e^{-jl\phi} f^{0,1,l}\left(J_x,J_y\right)R_l(r) \times \omega_0\left[Q_c - \left(Q_{y0}+a_{xy}J_x+a_{yy}J_y\right) - lQ_s\right] = Nf_{x0}(J_x)\frac{df_{y0}}{dJ_y}g_0(J_z)\sqrt{\frac{2J_yR}{Q_{y0}}}\frac{F_y^{coh}(z;t)}{2p_0}. \tag{29}$$

Renaming $f^{0,1,l} \equiv f^l$, and re-arranging to put all terms in $J_x$ and $J_y$ on the left-hand side, we get

$$\frac{\omega_0}{N}\sum_{l=-\infty}^{+\infty} e^{-jl\phi}R_l(r) \times \left\{\frac{f^l\left(J_x,J_y\right)\left[Q_c - \left(Q_{y0}+a_{xy}J_x+a_{yy}J_y\right) - lQ_s\right]}{f_{x0}(J_x)\frac{df_{y0}}{dJ_y}\sqrt{\frac{2J_yR}{Q_{y0}}}}\right\} = e^{-j\Omega t} e^{\frac{jQ'_y r\cos\phi}{\eta R}} g_0(J_z)\frac{F_y^{coh}(z;t)}{2p_0}. \tag{30}$$

If we take the derivative with respect to $J_x$, the right-hand side goes to zero, which means that for any $l$ the term between curly brackets in the left-hand side must be a constant with respect to $J_x$. The same goes if we take instead the derivative with respect to $J_y$. Hence

$$f^l\left(J_x, J_y\right) \propto \frac{f_{x0}(J_x)\frac{df_{y0}}{dJ_y}\sqrt{\frac{2J_yR}{Q_{y0}}}}{Q_c - \left(Q_{y0} + a_{xy}J_x + a_{yy}J_y\right) - lQ_s}. \quad (31)$$

The proportionality constant may be included in $R_l(r)$ – thus we can write the above as an equality rather than a proportionality relation. We can finally write the full perturbation to the distribution as

$$\Delta\psi\left(J_x, \theta_x, J_y, \theta_y, r, \phi; t\right) = e^{j\Omega t}e^{j\theta_y}e^{-\frac{jQ'_y r\cos\phi}{\eta R}}$$
$$\times \sum_{l=-\infty}^{+\infty} R_l(r)e^{-jl\phi}\frac{f_{x0}(J_x)\frac{df_{y0}}{dJ_y}\sqrt{\frac{2J_yR}{Q_{y0}}}}{Q_c - \left(Q_{y0} + a_{xy}J_x + a_{yy}J_y\right) - lQ_s}. \quad (32)$$

Up to now, the only assumptions on the coherent force considered were that it is vertical, dipolar and $z$-dependent. To proceed further, we will take the specific case of an impedance distributed along the ring, i.e. given by [6]

$$F_y^{coh}(z;t) = \frac{q^2}{2\pi R}\sum_{k=-\infty}^{+\infty}\iint \mathrm{d}\tilde{z}\mathrm{d}\tilde{\delta}\, W_y(\tilde{z} + 2\pi kR - z)$$
$$\cdot \iiiint \mathrm{d}\tilde{J}_x\mathrm{d}\tilde{\theta}_x\mathrm{d}\tilde{J}_y\mathrm{d}\tilde{\theta}_y\Delta\psi\left(\tilde{J}_x, \tilde{\theta}_x, \tilde{J}_y, \tilde{\theta}_y, \tilde{r}, \tilde{\phi}; t - k\frac{2\pi R}{v}\right)\tilde{y},$$

with $q = Ze$ the charge of each particle, $W_y(z)$ the wake function, and where the infinite sum stands for the multiturn effect (i.e. the fact that the wake does not decay completely after one or several turns). Only the perturbed distribution $\Delta\psi$ enters the expression above as the stationary distribution is assumed to be perfectly centred and hence not giving rise to any dipolar force. Plugging Eqs. (15) and (32) into the above we get

$$F_y^{coh}(z;t) = \frac{q^2}{\pi Q_{y0}}\sum_{k=-\infty}^{+\infty} e^{j\Omega\left(t - k\frac{2\pi R}{v}\right)}\iint \mathrm{d}\tilde{z}\mathrm{d}\tilde{\delta}$$
$$\cdot W_y(\tilde{z} + 2\pi kR - z)\iint \mathrm{d}\tilde{\theta}_x\mathrm{d}\tilde{\theta}_y e^{j\tilde{\theta}_y}\cos\tilde{\theta}_y e^{-\frac{jQ'_y\tilde{r}\cos\tilde{\phi}}{\eta R}}$$
$$\sum_{l'=-\infty}^{+\infty} R_{l'}(\tilde{r})e^{-jl'\tilde{\phi}}\iint \frac{\mathrm{d}\tilde{J}_x\mathrm{d}\tilde{J}_y \cdot \tilde{J}_y \cdot f_{x0}\left(\tilde{J}_x\right)\cdot\frac{df_{y0}}{dJ_y}\left(\tilde{J}_y\right)}{Q_c - \left(Q_{y0} + a_{xy}\tilde{J}_x + a_{yy}\tilde{J}_y\right) - l'Q_s}.$$

This can be further simplified thanks to

$$\iint \mathrm{d}\tilde{z}\mathrm{d}\tilde{\delta} = \frac{\omega_s}{v\eta}\iint \tilde{r}\mathrm{d}\tilde{r}\mathrm{d}\tilde{\phi} = \frac{Q_s}{\eta R}\iint \tilde{r}\mathrm{d}\tilde{r}\mathrm{d}\tilde{\phi},$$
$$\int_0^{2\pi}\mathrm{d}\tilde{\theta}_x = 2\pi, \qquad \int_0^{2\pi}\mathrm{d}\tilde{\theta}_y e^{j\tilde{\theta}_y}\cos\tilde{\theta}_y = \pi,$$

and defining the dispersion integral $\mathcal{I}(Q_c - lQ_s)$ using[1]

$$\mathcal{I}(Q) = \iint \frac{\mathrm{d}J_x\mathrm{d}J_y \cdot J_y \cdot f_{x0}\left(J_x\right)\cdot\frac{df_{y0}}{dJ_y}}{Q - \left(Q_{y0} + a_{xy}J_x + a_{yy}J_y\right)}, \quad (33)$$

such that we get

$$F_y^{coh}(z;t) = \frac{2\pi q^2 Q_s}{\eta R Q_{y0}}\sum_{k=-\infty}^{+\infty} e^{j\Omega\left(t - k\frac{2\pi R}{v}\right)}$$
$$\cdot \iint \tilde{r}\,\mathrm{d}\tilde{r}\,\mathrm{d}\tilde{\phi} W_y(\tilde{r}\cos\tilde{\phi} + 2\pi kR - r\cos\phi)\cdot e^{-\frac{jQ'_y\tilde{r}\cos\tilde{\phi}}{\eta R}}$$
$$\cdot \sum_{l'=-\infty}^{+\infty} R_{l'}(\tilde{r})e^{-jl'\tilde{\phi}}\mathcal{I}(Q_c - l'Q_s). \quad (34)$$

Note that analytical expressions exist for the dispersion integral expressed in Eq. (33), for various kinds of unperturbed distributions, e.g. Gaussian or parabolic [14, 15].

We can now plug Eq. (34) into Eq. (30), using also Eq. (31) (taken as an equality) and recalling that $\omega_0 = \frac{v}{R}$, to get

$$\sum_{l'=-\infty}^{+\infty} e^{-jl'\phi}R_{l'}(r) = \frac{N\pi q^2 Q_s}{\eta v Q_{y0}p_0}e^{\frac{jQ'_y r\cos\phi}{\eta R}}g_0\left(J_z\right)$$
$$\times \sum_{k=-\infty}^{+\infty} e^{-j2\pi kQ_c}\iint \tilde{r}\,\mathrm{d}\tilde{r}\,\mathrm{d}\tilde{\phi}W_y(\tilde{r}\cos\tilde{\phi} + 2\pi kR - r\cos\phi)$$
$$\times e^{-\frac{jQ'_y\tilde{r}\cos\tilde{\phi}}{\eta R}}\sum_{l'=-\infty}^{+\infty} R_{l'}(\tilde{r})e^{-jl'\tilde{\phi}}\mathcal{I}(Q_c - l'Q_s). \quad (35)$$

Multiplying each side of the equation by $\frac{e^{jl\phi}}{2\pi}$, integrating over $\phi$, and considering $g_0$ as a function of $r$, we can write:

$$R_l(r) = \frac{Nq^2 Q_s g_0(r)}{2\eta v Q_{y0}p_0}\int_0^{2\pi}\mathrm{d}\phi e^{jl\phi}e^{\frac{jQ'_y r\cos\phi}{\eta R}}\sum_{k=-\infty}^{+\infty} e^{-j2\pi kQ_c}$$
$$\times \iint \tilde{r}\,\mathrm{d}\tilde{r}\,\mathrm{d}\tilde{\phi}W_y(\tilde{r}\cos\tilde{\phi} + 2\pi kR - r\cos\phi)\cdot e^{-\frac{jQ'_y\tilde{r}\cos\tilde{\phi}}{\eta R}}$$
$$\times \sum_{l'=-\infty}^{+\infty} R_{l'}(\tilde{r})e^{-jl'\tilde{\phi}}\mathcal{I}(Q_c - l'Q_s). \quad (36)$$

This is an extension of Sacherer integral equation, expressed with the wake function and including tune spread. Formally, this is an equation in $Q_c$ – the coherent complex tune shift looked for – and in the unknown functions $R_l(r)$.

The equation can also be expressed with the impedance $Z_y(\omega)$ instead of the wake function [1, chap. 6], using the

[1] Compared to the definition used in the code DELPHI [13], there is an additional factor $\frac{1}{4\pi^2}$ due to the normalization chosen in Eqs. (13), i.e.

$$\mathcal{I}^{\mathrm{DELPHI}}(Q) = 4\pi^2\mathcal{I}^{\mathrm{here}}(Q).$$

relation (see Ref [6] for a mathematical derivation):

$$\sum_{k=-\infty}^{+\infty} e^{-j2\pi k Q_c} W_y(\tilde{r}\cos\tilde{\phi} + 2\pi k R - r\cos\phi) \approx \frac{-j\omega_0}{2\pi} \sum_{k=-\infty}^{+\infty} Z_y\left[(Q_{y0}+k)\,\omega_0\right] e^{j(Q_{y0}+k)\frac{\tilde{r}\cos\tilde{\phi} - r\cos\phi}{R}}, \quad (37)$$

where we have used again $Q_c \approx Q_{y0}$. This gives

$$\begin{aligned} R_l(r) = & \frac{-jNq^2 Q_s g_0(r)}{4\pi\eta R Q_{y0} p_0} \int_0^{2\pi} \mathrm{d}\phi e^{jl\phi} e^{\frac{jQ'_y r\cos\phi}{\eta R}} \\ & \times \sum_{k=-\infty}^{+\infty} e^{\frac{-j(Q_{y0}+k) r\cos\phi}{R}} Z_y\left[(Q_{y0}+k)\,\omega_0\right] \\ & \times \iint \tilde{r}\,\mathrm{d}\tilde{r}\,\mathrm{d}\tilde{\phi}\, e^{\frac{j(Q_{y0}+k)\tilde{r}\cos\tilde{\phi}}{R}} \cdot e^{-\frac{jQ'_y \tilde{r}\cos\tilde{\phi}}{\eta R}} \\ & \times \sum_{l'=-\infty}^{+\infty} R_{l'}(\tilde{r}) e^{-jl'\tilde{\phi}} \mathcal{I}(Q_c - l'Q_s), \quad (38) \end{aligned}$$

which we can further simplify using

$$\int_0^{2\pi} \mathrm{d}\tilde{\phi} e^{-jl\tilde{\phi}} e^{j\chi\cos\tilde{\phi}} = 2\pi j^l J_l(\chi) \quad \text{for any } \chi, \quad (39)$$

from Eq. (9.1.21) of Ref. [16], $J_l$ being the Bessel function of order $l$. This gives another version of Sacherer equation, expressed now with the impedance:

$$\begin{aligned} R_l(r) = & \frac{-jN\pi q^2 Q_s g_0(r)}{\eta R Q_{y0} p_0} \sum_{k=-\infty}^{+\infty} J_l\left[\left(Q_{y0}+k-\frac{Q'_y}{\eta}\right)\frac{r}{R}\right] \\ & \times Z_y\left[(Q_{y0}+k)\,\omega_0\right] \sum_{l'=-\infty}^{+\infty} j^{l'-l} \mathcal{I}(Q_c - l'Q_s) \\ & \times \int_0^{+\infty} \tilde{r}\mathrm{d}\tilde{r} R_{l'}(\tilde{r}) J_{l'}\left[\left(Q_{y0}+k-\frac{Q'_y}{\eta}\right)\frac{\tilde{r}}{R}\right]. \quad (40) \end{aligned}$$

A similar equation was obtained by Chin [5], with one-dimensional transverse tune spread. In the absence of tunespread, this reduces to the standard Sacherer equation [1, 6, 17, 18][2], if we put the coefficients $\mathcal{I}(Q_c - lQ_s)$ into the unknown functions $R_l(r)$ and notice that $\mathcal{I}(Q) = -1/\left(4\pi^2(Q - Q_{y0})\right)$ (see below).

## SOLVING THE EQUATION

One strategy to solve the equation is first to replace the unknown functions $R_l(r)$ thanks to

$$\rho_l(r) \equiv \mathcal{I}(Q_c - lQ_s) R_l(r).$$

This gives

$$\begin{aligned} \frac{\rho_l(r)}{\mathcal{I}(Q_c - lQ_s)} = & \frac{-jN\pi q^2 Q_s g_0(r)}{\eta R Q_{y0} p_0} \\ & \times \sum_{k=-\infty}^{+\infty} J_l\left[\left(Q_{y0}+k-\frac{Q'_y}{\eta}\right)\frac{r}{R}\right] Z_y\left[(Q_{y0}+k)\,\omega_0\right] \\ & \times \sum_{l'=-\infty}^{+\infty} j^{l'-l} \int_0^{+\infty} \tilde{r}\mathrm{d}\tilde{r}\rho_{l'}(\tilde{r}) J_{l'}\left[\left(Q_{y0}+k-\frac{Q'_y}{\eta}\right)\frac{\tilde{r}}{R}\right]. \end{aligned} \quad (41)$$

Then, one can expand $\rho_l(r)$ and $g_0(r)$ over generalized Laguerre polynomials $L_n^\alpha$, as in Refs. [5, 18], i.e.

$$\rho_l(r) = \left(\frac{r}{A}\right)^{|l|} e^{-br^2} \sum_{n=0}^{+\infty} c_{ln} L_n^{|l|}(ar^2), \quad (42)$$

$$g_0(r) = \frac{\eta R}{Q_s} e^{-br^2} \sum_{m=0}^{+\infty} g^m L_m^0(ar^2), \quad (43)$$

where $A$ , $a$ and $b$ are arbitrary constants that will be specified later. Note that the change of variable $J_z \rightarrow r$ introduces an additional factor $\frac{\eta R}{Q_s}$ in the normalization condition of $g_0$ expressed as an integral over $r$ (see Eqs. (13) and (23)), hence the proportionality constant in front of the expression for $g_0(r)$. Using the orthogonality relations of the generalized Laguerre polynomials [16, chap. 22], the $c_{ln}$ and $g^m$ coefficients can be expressed as

$$c_{ln} = \frac{2a^{1+|l|}A^{2|l|}n!}{(n+|l|)!} \int_0^{+\infty} r\mathrm{d}r \left(\frac{r}{A}\right)^{|l|} e^{(b-a)r^2} L_n^{|l|}(ar^2)\rho_l(r), \quad (44)$$

$$g^m = 2a \int_0^{+\infty} r\mathrm{d}r e^{(b-a)r^2} L_m^0(ar^2) g_0(r). \quad (45)$$

Note that any longitudinal distribution $g_0(r)$ can be dealt with in this way, generalizing the approach of Chin [5,19,20]. Multiplying both sides of Eq. (41) by

$$2a^{1+|l|}A^{2|l|}\frac{n!}{(n+|l|)!} r \left(\frac{r}{A}\right)^{|l|} e^{(b-a)r^2} L_n^{|l|}(ar^2),$$

and integrating from $r = 0$ to $r = +\infty$ we get

$$\begin{aligned} \frac{c_{ln}}{\mathcal{I}(Q_c - lQ_s)} = & \frac{-j2\pi N q^2 Q_s}{\eta R Q_{y0} p_0} \frac{a^{1+|l|}A^{2|l|}n!}{(n+|l|)!} \\ & \times \sum_{k=-\infty}^{+\infty} Z_y\left[(Q_{y0}+k)\,\omega_0\right] \int_0^{+\infty} r\mathrm{d}r g_0(r) \\ & \times \left(\frac{r}{A}\right)^{|l|} e^{(b-a)r^2} L_n^{|l|}(ar^2) J_l\left[\left(Q_{y0}+k-\frac{Q'_y}{\eta}\right)\frac{r}{R}\right] \\ & \times \sum_{l'=-\infty}^{+\infty} j^{l'-l} \int_0^{+\infty} r\mathrm{d}r \rho_{l'}(r) J_{l'}\left[\left(Q_{y0}+k-\frac{Q'_y}{\eta}\right)\frac{r}{R}\right]. \quad (46) \end{aligned}$$

[2] Note that in the impedance term of Eq. (11) in Ref. [18], the signs of the expressions between brackets in the Bessel functions have been incorrectly inverted: one should read $(\omega_p - \omega_\xi)\tau$ instead of $(\omega_\xi - \omega_p)\tau$. Moreover, the constant factor on the right-hand side of the equation depends on the normalization conditions chosen for each of the unperturbed functions $f_{x0}, f_{y0}$ and $g_0$, which is arbitrary (only the normalization of $\psi_0$ is fixed).

Now we expand $g_0(r)$ and $\rho_{l'}(r)$ using Eqs. (42) and (43), obtaining

$$\frac{c_{ln}}{\mathcal{I}\left(Q_c - lQ_s\right)} = \frac{-j2\pi N q^2}{Q_{y0}p_0}\frac{a^{1+|l|}A^{|l|}n!}{(n+|l|)!} \times \sum_{k=-\infty}^{+\infty} Z_y\left[\left(Q_{y0}+k\right)\omega_0\right]\sum_{m=0}^{+\infty} g^m$$
$$\times\int_0^{+\infty} r^{1+|l|}e^{-ar^2}L_m^0(ar^2)L_n^{|l|}(ar^2)J_l\left[\left(Q_{y0}+k-\frac{Q'_y}{\eta}\right)\frac{r}{R}\right]\mathrm{d}r$$
$$\times\sum_{l'=-\infty}^{+\infty} j^{l'-l}\sum_{n'=0}^{+\infty} c_{l'n'}$$
$$\times\int_0^{+\infty} r\left(\frac{r}{A}\right)^{|l'|}e^{-br^2}L_{n'}^{|l'|}(ar^2)J_{l'}\left[\left(Q_{y0}+k-\frac{Q'_y}{\eta}\right)\frac{r}{R}\right]\mathrm{d}r. \tag{47}$$

The two integrals above can be computed analytically using two formulas obtained from Hankel transforms [21, pp. 42-43][3](using also Eq. (9.1.5) from Ref. [16, p. 358]):

$$\int_0^{+\infty} r^{1+|l|}e^{-ar^2}L_m^0(ar^2)L_n^{|l|}(ar^2)J_l(\lambda r)\mathrm{d}r = \frac{(-1)^{m+n}}{2a}\left(\frac{\mathrm{sign}(l)\lambda}{2a}\right)^{|l|}e^{\frac{-\lambda^2}{4a}}L_n^{m-n}\left(\frac{\lambda^2}{4a}\right)L_m^{|l|+n-m}\left(\frac{\lambda^2}{4a}\right), \tag{48}$$

$$\int_0^{+\infty} r^{1+|l|}e^{-br^2}L_n^{|l|}(ar^2)J_l(\lambda r)\mathrm{d}r = \frac{\mathrm{sign}(l)^{|l|}}{2b}\left(\frac{\lambda}{2b}\right)^{|l|}\left(\frac{b-a}{b}\right)^n e^{\frac{-\lambda^2}{4b}}L_n^{|l|}\left(\frac{a\lambda^2}{4b(a-b)}\right), \tag{49}$$

valid for any $a>0$, $b>0$ and $\lambda$. Defining then

$$G_{ln}(\lambda) \equiv (2a)^{1+|l|}A^{|l|}\sum_{m=0}^{+\infty} g^m\int_0^{+\infty} r^{1+|l|}e^{-ar^2} \times L_m^0(ar^2)L_n^{|l|}(ar^2)J_l(\lambda r)\mathrm{d}r$$
$$= (\mathrm{sign}(l)\lambda A)^{|l|}e^{\frac{-\lambda^2}{4a}}\sum_{m=0}^{+\infty}(-1)^{m+n}g^m \times L_n^{m-n}\left(\frac{\lambda^2}{4a}\right)L_m^{|l|+n-m}\left(\frac{\lambda^2}{4a}\right), \tag{50}$$

and

$$I_{ln}(\lambda) \equiv A^{-|l|}\int_0^{+\infty} e^{-br^2}r^{1+|l|}L_n^{|l|}(ar^2)J_l(\lambda r)\mathrm{d}r$$
$$= \begin{cases} \frac{1}{2b}\left(\frac{\mathrm{sign}(l)\lambda}{2bA}\right)^{|l|}\left(1-\frac{a}{b}\right)^n e^{\frac{-\lambda^2}{4b}}L_n^{|l|}\left(\frac{a\lambda^2}{4b(a-b)}\right) & \text{if } a \neq b, \\ \left(\frac{\lambda}{2}\right)^{2n+|l|}\frac{\mathrm{sign}(l)^{|l|}}{2n!a^{n+|l|+1}A^{|l|}}e^{-\frac{\lambda^2}{4a}} & \text{if } a = b, \end{cases}$$

(taking the expression to its limit when $a=b$), Sacherer equation finally becomes

$$0 = \sum_{l'=-\infty}^{+\infty}\sum_{n'=0}^{+\infty}\left(\frac{\delta_{ll'}\delta_{nn'}}{\mathcal{I}\left(Q_c-l'Q_s\right)} + \mathcal{M}_{ln,l'n'}\right)c_{l'n'}, \tag{51}$$

with the matrix $\mathcal{M}$ defined by

$$\mathcal{M}_{ln,l'n'} = \frac{j^{1+l'-l}\pi N q^2\, n!}{Q_{y0}p_0\, 2^{|l|}\,(n+|l|)!}\sum_{k=-\infty}^{+\infty}\left\{Z_y\left[\left(Q_{y0}+k\right)\omega_0\right] \times G_{ln}\left(\frac{Q_{y0}+k}{R}-\frac{Q'_y}{\eta R}\right)I_{l'n'}\left(\frac{Q_{y0}+k}{R}-\frac{Q'_y}{\eta R}\right)\right\}. \tag{52}$$

In the DELPHI code [13, 18], for an initially Gaussian longitudinal distribution, $b=\frac{1}{2\sigma_z^2}$ (with $\sigma_z$ the RMS bunch length) and all $g^m$ are zero except $g^0=\frac{b}{\pi}$ to respect the normalization condition in Eqs. (13). Then the choices $a=b$ and $A=4\sigma_z$ were found to optimize convergence with respect to the matrix size in the case without tunespread (see next section)[4].

Non-trivial solutions of Eq. (51) are found if and only if

$$\det\left(\left[\frac{\delta_{ll'}\delta_{nn'}}{\mathcal{I}\left(Q_c-l'Q_s\right)} + \mathcal{M}_{ln,l'n'}\right]\right) = 0. \tag{53}$$

This equation in $Q_c$ generalizes the similar determinant equation obtained in Ref. [5] to the case of a two-dimensional tune spread and any longitudinal distribution. Mathematically, it is a transcendental equation, because the dispersion integral is non-polynomial in general, hence there is a priori no general strategy to find all possible roots.

As a final remark, one can easily add two extensions to this formalism, both implemented in the DELPHI code:

- if the beam is made of $M>1$ equidistant bunches, and assuming the intrabunch motion in all the bunches is identical (only the phase of the oscillation may differ from one bunch to another), the equation obtained is

[3] To obtain Eq. (48), we have corrected a typo in Ref [21, p. 43], Eq. (8): the two lower indices of the Laguerre polynomials on the right-hand side were inverted.

[4] In Ref. [18], the functions $G_{ln}$ and $I_{ln}$ were chosen slightly differently: $G_{ln}^{\text{Ref. [18]}}(\omega) = v^2\tau_b^{-|l|}G_{ln}^{\text{here}}\left(\frac{\omega}{v}\right)$ and $I_{ln}^{\text{Ref. [18]}}(\omega) = v^{-2}\tau_b^{|l|}I_{ln}^{\text{here}}\left(\frac{\omega}{v}\right)$, with $\tau_b=\frac{4\sigma_z}{v}$. The matrix $\mathcal{M}$ of Ref. [18] is also multiplied by $\frac{\omega_0}{4\pi^2}$ with respect to the one written in Eq. (52): the $\omega_0$ factor is because in Ref. [18] the problem is expressed in terms of angular frequency shifts rather than tune shifts, while the $\frac{1}{4\pi^2}$ factor gets compensated by the same factor in $\mathcal{I}(Q)$ here.

still of the form (51) but with a slightly modified matrix $\mathcal{M}$: one has to multiply the matrix given in Eq. (52) by $M$ and replace [22]

$$Q_{y0} + k,$$

by

$$[Q_{y0}] + kM + p,$$

in all the terms of the infinite sum over $k$, where $[\cdot]$ indicates the fractional part and $0 \leq p \leq M - 1$ is the coupled-bunch mode considered (one has to solve the problem for each coupled-bunch mode, in principle),

- an ideal, bunch-by-bunch transverse damper can be added by considering it as an impedance proportional to a delta function and replacing the infinite sum over $k$ in Eq. (52) by an integral. This gives a matrix $\mathcal{D}$ that can be added to $\mathcal{M}$ above, of the form

$$\mathcal{D}_{ln,l'n'} = \frac{j^{1+l'-l} N\pi q^2\, n!}{Q_{y0} p_0\, 2^{|l|}\, (n+|l|)!} \times \mu G_{ln}\left(-\frac{Q'_y}{\eta R}\right) I_{l'n'}\left(-\frac{Q'_y}{\eta R}\right), \quad (54)$$

with $\mu$ a constant adjusted, in the case without tune-spread (see next section), in such a way as to damp the rigid-bunch mode in $n_d$ turns, with a damping phase $\varphi$ (the origin $\varphi = 0$ being chosen as the perfectly resistive damper). This means that one chooses $\mu$ such that (see also the first limiting case below) [18]

$$\frac{1}{4\pi^2}\mathcal{D}_{00,00} = \frac{j e^{j\varphi}}{2\pi n_d}.$$

## LIMITING CASES

One can find two well-known limiting cases to the determinant equation (53). First, in the absence of tune spread, $a_{xy} = a_{yy} = 0$ and

$$\mathcal{I}(Q) = -\frac{1}{4\pi^2(Q - Q_{y0})}, \quad (55)$$

from the normalization conditions in Eqs. (13). This means that Eq. (51) becomes

$$\left(Q_c - Q_{y0}\right) c_l^n = \sum_{l'=-\infty}^{+\infty} \sum_{n'=0}^{+\infty} \left( l' Q_s \delta_{ll'} \delta_{nn'} + \frac{1}{4\pi^2} \mathcal{M}_{ln,l'n'} \right) c_{l'}^{n'}, \quad (56)$$

which is the usual eigenvalue problem in the absence of tune spread [1, 18]. The coherent tune shifts looked for can then be obtained through a diagonalization.

Another limiting case appears in the absence of coupling between different modes, i.e. when all non-diagonal terms are zero in the matrix $\mathcal{M}$. Then the determinant equation becomes

$$\det\left(\left[\delta_{ll'}\delta_{nn'}\left(\frac{1}{\mathcal{I}(Q_c - l'Q_s)} + \mathcal{M}_{ln,l'n'}\right)\right]\right) = \prod_{l=-\infty}^{+\infty}\prod_{n=0}^{+\infty}\left(\frac{1}{\mathcal{I}(Q_c - lQ_s)} + \mathcal{M}_{ln,ln}\right) = 0, \quad (57)$$

(as the matrix is now diagonal), which means that we get a set of equations of the form (for each $l$ and $n$):

$$-1 = \mathcal{M}_{ln,ln} \times \mathcal{I}(Q_c - lQ_s), \quad (58)$$

which gives one possible coherent tune $Q_c$ for each $(l, n)$. We hence can consider separately the coherent tune shift and the dispersion integral, in other words we recover the stability diagram theory [23, 24].

## RESULTS

Notwithstanding the difficulty to find all the roots of the general determinant equation (53), we can try to get a generalization of the concept of stability diagram. To do so, we simply compute the determinant along lines of constant real tune shift $\Re(Q_c) - Q_{y0}$ in the absence of imaginary tune shift ($\Im(Q_c) = 0$), and get the one-dimensional minimum along such curves. At the exact location of the stability diagram (if it exists), this minimum should get to zero. This is illustrated in Fig. 1, in a case with only a transverse damper that is set in antidamper mode [25] i.e. with a phase above $\pi/2$ in order to create instabilities.

Doing this exercise for a set of configurations that span a large portion of the complex plane of possible unperturbed coherent tune shifts (i.e. tune shifts in the absence of tune spread) thus allows us to find a (potential) stability diagram by plotting as a color the minimum of such 1D curves. The way to find a set of configurations that span a large part of the complex plane is to use an ideal (bunch-by-bunch) damper with arbitrary phase and gain [25]. The unperturbed tune shifts that serve as abscissa and ordinate of the plot, are obtained by diagonalization of the eigenvalue problem in Eq. (56), using routines from the DELPHI [18] code with LHC-like parameters, in the absence of impedance (see Table 1 for details).

In Fig. 2 we show the result of this exercise, in a case where the chromaticity is zero. Looking at the brightest region (which represents the closest to zero minima of the aforementioned 1D curves), we clearly recover the standard stability diagram as obtained in e.g. [14]. On the other hand, for $Q' = 5$ we see in Fig. 3 that one deviates from the usual stability diagram for an unperturbed tune shift close to $Q_s$. Note, still, that one cannot really tell at this stage if the brightest region really represents a stability diagram, i.e. that it delimits the boundary between the unstable and the stable region of unperturbed tune shifts – this is under investigation.

## CONCLUSION

We have derived an extension of Sacherer integral equation in the case of two-dimensional transverse tune spread, generalizing several approaches in the literature. This allowed us to obtain both the usual eigenvalue problem and the stability diagram theory as limiting cases. The final determinant equation turns out to be very challenging to solve in general; still, preliminary results were obtained, in an attempt to generalize the concept of stability diagram.

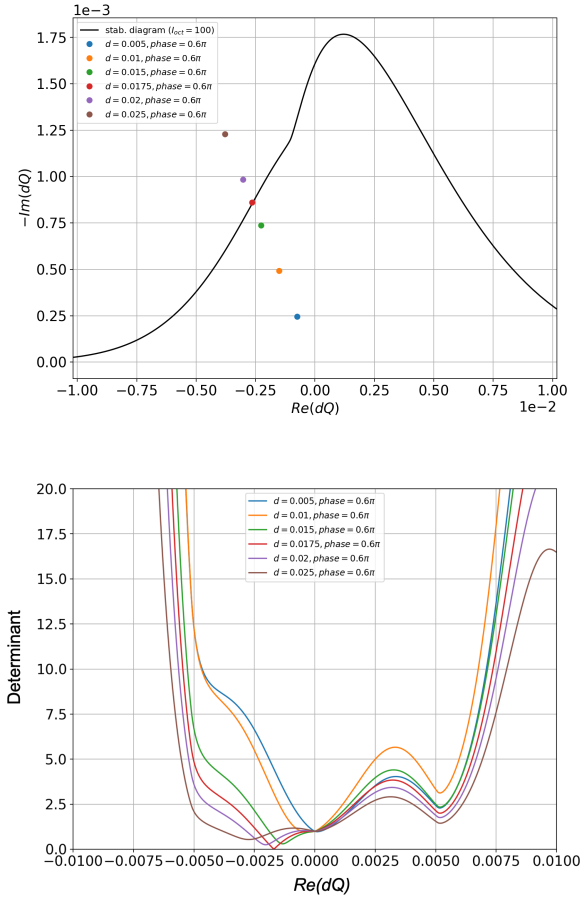


Figure 1: (Top) Unperturbed modes (color dots) for an ideal bunch-by-bunch damper at different transverse damper gains, at a given phase (here a phase of zero means a perfectly resistive damper, and phase of $\pi$ is a perfectly resistive anti-damper), at $Q' = 0$. The standard stability diagram for a Gaussian transverse distribution is also shown (black curve). (Bottom) Determinant of Eq. (53) plotted vs. real tune shift (for an imaginary tune shift of zero).

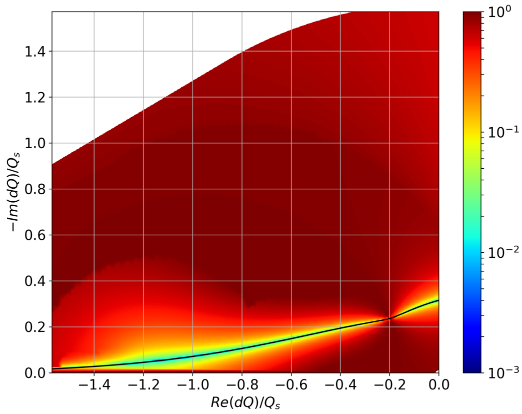


Figure 2: Minimum (color) of the 1D curve obtained when the determinant of Eq. (53) is plotted vs. real tune shift as in Fig. 1 (bottom). The x and y axes represent the coherent tune shift in the absence of tune spread, for an ideal bunch-by-bunch damper, with $Q' = 0$. The black curve represents the standard stability diagram theory (for a Gaussian distribution).

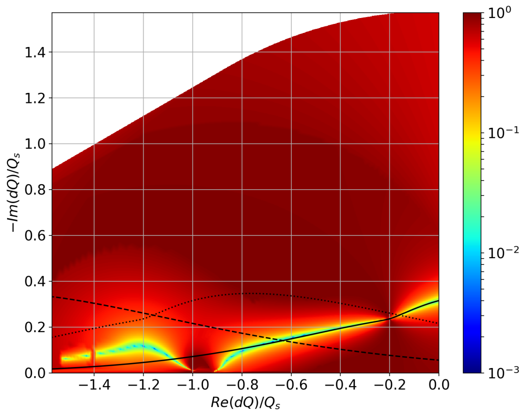


Figure 3: Minimum (color) of the 1D curve obtained when the determinant of Eq. (53) is plotted vs. real tune shift as in Fig. 1 (bottom). The x and y axes represent the coherent tune shift in the absence of tune spread, for an ideal bunch-by-bunch damper, with $Q' = 5$. The black curves represent the standard stability diagram theory (for a Gaussian distribution), replicated periodically every $Q_s$.

## ACKNOWLEDGEMENTS

I am very grateful to Kevin Li for enlightening discussions on Hamiltonians and Poisson brackets. I would like to thank as well Sergey Arsenyev, Xavier Buffat, Sondre Vik Furuseth, Elias Métral and Giovanni Rumolo for various and numerous discussions on the subject, and Sergey Antipov for providing the idea of the generalized damper to explore the complex plane. My special thanks go to Giovanni Iadarola for great and insightful discussions around Vlasov solvers, which provided an additional and welcomed motivation for the writing of these proceedings.

## REFERENCES

[1] A. W. Chao, *Physics of Collective Beams Instabilities in High Energy Accelerators* (John Wiley & Sons, 1993), http://www.slac.stanford.edu/~achao/wileybook.html.

[2] L. D. Landau, *Russ. Phys. J.* **10**, 1 (1946) 25.

[3] H. G. Hereward, Landau damping by non-linearity, CERN-MPS-DL-69-11 (1969), https://cds.cern.ch/record/1114390/files/cer-002766878.pdf.

[4] A. A. Vlasov, *Russ. Phys. J.* **9**, 1 (1945) 25.

[5] Y.-H. Chin, Hamiltonian formulation for transverse bunched beam instabilities in the presence of betatron tunespread, CERN-SPS-85-9-DI-MST (1985), https://cds.cern.ch/record/160217/files/198507010.pdf.

Table 1: Parameters used.

| | |
|---|---|
| Number of bunches $M$ | 1 |
| Charge of each particle $q$ | $e$ |
| RMS bunch length $\sigma_z$ | 7.49 cm |
| Synchrotron tune $Q_s$ | $5.09096 \cdot 10^{-3}$ |
| Machine physical radius | 4242.89 m |
| Revolution frequency $\frac{\omega_0}{2\pi}$ | 11.2455kHz |
| Unperturbed tune $Q_{y0}$ | 62.31 |
| Direct detuning $a_{yy}$ | $7.67 \cdot 10^5$ |
| Indirect detuning $a_{xy}$ | $-5.54 \cdot 10^5$ |
| Normalized emittances $\varepsilon_x = \varepsilon_y$ | $1\mu$m |
| Relativistic $\gamma$ | 479.6 |
| Slippage factor $\eta$ | $3.43 \cdot 10^{-4}$ |

[6] N. Mounet, Direct Vlasov solvers, in Proc. of the CAS-CERN Accelerator School on Numerical Methods for Analysis, Design and Modelling of Particle Accelerators, Thessaloniki, Greece, 11–23 November 2018, Ed. H. Schmickler, CERN-ACC-2020-0012 (CERN, Geneva, 2020), https://arxiv.org/abs/2006.09080.

[7] J. Gareyte, J. P. Koutchouk, and F. Ruggiero, Landau damping, dynamic aperture and octupoles in LHC, CERN LHC Project Report 91 (revised) (1997), https://cds.cern.ch/record/321824/files/lhc-project-report-91.pdf.

[8] K. Li, Perturbation formalism, Lecture at the US Particle Accelerator School, Hampton, Virginia, USA, 19–23 January 2015, http://kli.web.cern.ch/kli/USPAS_Lectures_Collective_Effects/Lectures/USPAS_05a_Vlasov_equation.pdf.

[9] H. Goldstein, C. P. Poole Jr., and J. L. Safko, *Classical Mechanics*, 3rd ed. (Addison Wesley, San Francisco, California, 2002).

[10] J. S. Bell, Hamiltonian mechanics, in Proc. of the CAS-CERN Accelerator School: Accelerator Physics, Oxford, UK, 16–27 September 1985, Ed. S. Turner, CERN-1987-003-V-1 (CERN, Geneva, 1987), p. 5, https://doi.org/10.5170/CERN-1987-003-V-1.5.

[11] R. D. Ruth, Single-particle dynamics in circular accelerators, in Proc. of the SLAC Summer School on the Physics of High-energy Particle Accelerators, Standford, California, USA, 15–26 July 1985, Eds. M. Month and M. Dienes, [*AIP Conf. Proc.* **153** (1987) 150], https://doi.org/10.1063/1.36365.

[12] W. Herr, Mathematical and numerical methods for non-linear beam dynamics, in Proc. of the CAS-CERN Accelerator School: Advanced Accelerator Physics, Trondheim, Norway, 18–29 August 2013, Ed. W. Herr, CERN-2014-009 (CERN, Geneva, 2014), p. 157, https://doi.org/10.5170/CERN-2014-009.157.

[13] N. Mounet, D. Amorim, and N. Biancacci, 2020, DELPHI repository, https://gitlab.com/IRIS_mirror/DELPHI_mirror.

[14] J. Scott Berg and F. Ruggiero, Landau damping with two-dimensional betatron tune spread, CERN SL-AP-96-71 (1996), https://cds.cern.ch/record/318826.

[15] E. Métral and A. Verdier, Stability diagram for Landau damping with a beam collimated at an arbitrary number of sigmas, CERN-AB-2004-019-ABP (2004), https://cds.cern.ch/record/733611/files/ab-2004-019.pdf.

[16] M. Abramowitz and I. A. Stegun, editors, *Handbook of Mathematical Functions With Formulas, Graphs, and Mathematical Tables* (US Dep. of Commerce, National Bureau of Standards, 1972), Tenth Printing, with corrections, http://www.iopb.res.in/~somen/abramowitz_and_stegun/toc.htm.

[17] F. J. Sacherer, Methods for computing bunched-beam instabilities, CERN/SI-BR/72-5 (1972), https://cds.cern.ch/record/322545/files/CM-P00063598.pdf.

[18] N. Mounet, Vlasov solvers and macroparticle simulations, in Proc. ICFA Mini-Workshop on Impedances and Beam Instabilities in Particle Accelerators, Benevento, Italy, 18–22 September 2017, Eds. V. Brancolini, G. Rumolo, M. R. Masullo, and S. Petracca, CERN-2018-003-CP (CERN, Geneva, 2018), Vol. 1, p. 77, https://doi.org/10.23732/CYRCP-2018-001.77.

[19] Y.-H. Chin, Transverse mode coupling instabilities in the SPS, CERN-SPS-85-2-DI-MST (1985), https://cds.cern.ch/record/157995/files/198503163.pdf.

[20] Y.-H. Chin, User's guide for new MOSES version 2.0: Mode-coupling single bunch instability in an electron storage ring, CERN-LEP-TH-88-05 (1988), https://cds.cern.ch/record/187253/files/198805308.pdf.

[21] A. Erdélyi, W. Magnus, F. Oberhettinger, and F. G. Tricomi, *Tables of Integral Transforms* Vol. 2 (McGraw-Hill, 1954).

[22] F. J. Sacherer, Transverse instabilities of relativistic particle beams in accelerators and storage rings – Part II: Bunched beams, in Proc. of the 1st International School of Particle Accelerators "Ettore Majorana", Erice, Italy, 10–22 November 1976, Ed. M. H. Blewett, CERN-77-13 (CERN, Geneva, 1977), p. 198, https://doi.org/10.5170/CERN-1977-013.198.

[23] A. G. Ruggiero and V. G. Vaccaro, Solution of the dispersion relation for longitudinal stability of an intense coasting beam in a circular accelerator (application to the ISR), CERN-ISR-TH-68-33 (1968), https://cds.cern.ch/record/296973/files/198111105.pdf.

[24] J. M. Wang, Longitudinal symmetric coupled bunch modes, BNL 51302 (1980), https://inis.iaea.org/collection/NCLCollectionStore/_Public/12/608/12608140.pdf?r=1&r=1.

[25] S. Antipov *et al.*, MD 4145: Study of Landau damping with an antidamper, CERN-ACC-NOTE-2019-0034 (2019), https://cds.cern.ch/record/2685297/files/CERN-ACC-NOTE-2019-0034.pdf.

# LANDAU DAMPING IN THE LONGITUDINAL PLANE

E. Shaposhnikova, T. Argyropoulos, I. Karpov
CERN, Geneva, Switzerland

*Abstract*

Loss of Landau damping in the longitudinal plane can limit the performance of an accelerator and lead to particle losses via undamped bunch oscillations or to single- and multi- bunch instabilities. The threshold for loss of Landau damping for a single bunch is usually defined by comparing the position of the coherent bunch oscillation frequency with respect to the incoherent synchrotron frequency spread. Different ways of calculating this threshold are presented and compared, using the LHC as an example. Loss of Landau damping in longitudinal plane can be cured by increasing the synchrotron frequency spread, either through controlled emittance blow-up or the installation of an additional, higher-harmonic RF system.

## INTRODUCTION

Landau damping is lost when the coherent bunch frequency moves outside the incoherent frequency band modified by beam-induced voltage. In longitudinal plane, Landau damping of coherent modes is achieved by synchrotron frequency spread, which can be increased by increasing bucket filling factor (minimum RF voltage for a given longitudinal emittance; limited by particle losses), increasing bunch emittance (applying controlled longitudinal emittance blow-up; limited by available RF voltage) or using a higher-harmonic RF system (in active or passive mode).

All these methods are used in CERN synchrotrons for beam stabilisation. Voltage programs through acceleration ramp are usually designed to keep buckets as full as possible while avoiding particle losses. The 4th harmonic RF system provides beam stability in the SPS together with controlled emittance blow-up, which is also necessary in LHC (see illustration in Fig. 1).

## LANDAU DAMPING IN LHC

In absence of a longitudinal wide-band feedback and a higher harmonic RF system, single bunch stability in LHC should be provided by natural Landau damping thanks to the sufficient synchrotron frequency spread $\Delta\omega_s$ in the main 400 MHz RF system. The initial analysis [1] was based on Sacherer stability criterion [2], [3], which in simplified form [4] can be written as

$$\delta\omega_c < \Delta\omega_s/4, \tag{1}$$

where $\delta\omega_c$ is the coherent dipole oscillation frequency shift and $\Delta\omega_s$ is the synchrotron frequency spread inside the bunch. It suggested that a nominal, 1 ns long, bunch will be stable at top energy of 7 TeV up to intensity of $2.4 \times 10^{11}$ protons per bunch (p/b) in an RF voltage $V$ of 16 MV, assuming an inductive impedance $\mathrm{Im}Z/n = 0.28$ Ohm. With

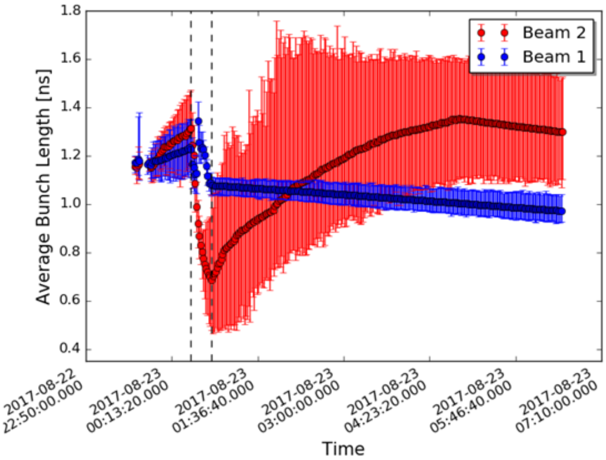


Figure 1: Measured average bunch length evolution during LHC acceleration ramp for Beam 1 with controlled emittance blow-up applied (blue line) and Beam 2 without it (red line). Continuous reduction of the bunch length in Beam 2 during the ramp (marked by the two vertical dotted lines). The stability threshold was reached and many bunches became unstable, indicated by the large bunch length spread.

a nominal bunch intensity of $1.0 \times 10^{11}$ p/b, the stability margin seemed to be sufficient and wide-band feedback was not planned for LHC [5].

To avoid loss of Landau damping (LLD) during acceleration ramp, the longitudinal emittance should be increased with beam energy as $\propto E_s^{1/2}$ [6], which in operation means keeping bunch length $\tau$ constant during controlled emittance blow-up (as for Beam 1 in Fig. 1). This requirement also follows from the scaling of the LLD threshold for bunch intensity $N_b$, which can be derived from the criterion (1)

$$\mathrm{Im}Z/n \propto \xi = \frac{\tau^5 V}{N_b}. \tag{2}$$

It was noticed from the start of the LHC operation that nominal bunch parameters are at the limit of longitudinal stability due to LLD. Indeed, undamped injection phase oscillations continued not only during the long flat bottom, but even survived the acceleration ramp with controlled emittance blow-up. At the top energy, a lower single-bunch stability threshold of $2 \times 10^{11}$ p/b was found in measurements for a bunch length of 1 ns and low-frequency LHC impedance $\mathrm{Im}Z/n$ of 0.09 Ohm, three times smaller than the previously assumed (with safety margins) 0.28 Ohm.

Macro-particle simulations [7], performed using the code BLonD [8] and the existing LHC impedance model [9], shown in Fig. 2, agree well with measurements. Note that the simulations using constant impedance $\mathrm{Im}Z/n$ =

0.09 Ohm gave similar results to those performed with the full impedance model.

In longitudinal phase-space, bunches can be presented by a binomial particle distribution

$$\mathcal{F}(\mathcal{E}) = \mathcal{F}_0 \left(1 - \frac{\mathcal{E}}{\mathcal{E}_{\max}}\right)^{\mu}. \qquad (3)$$

Here $\mathcal{E}$ is the energy of synchrotron oscillations $\mathcal{E} = \dot{\phi}^2/(2\omega_{s0}^2) + U(\phi)/(V\cos\phi_s)$ and $\mathcal{E}_{max}$ its maximum value inside the bunch; $\omega_{s0}$ is the frequency of linear synchrotron oscillations in a single RF system, $U(\phi)$ is the RF potential and $\phi_s$ is the synchronous phase.

In the LHC, $\mu = 2.0$ is giving a good fit to the measured bunch line density, which for short bunches in a single RF system can be presented in a simple form

$$\lambda(\phi) = \lambda_0\,(1 - \phi^2/\phi_{\max}^2)^{\mu+1/2}, \qquad (4)$$

with normalisation $\int \lambda(\phi)d\phi = 1$. Here $\phi_{max} = h\omega_0\tau/2$, $h$ is the harmonic number, $\tau$ the bunch length and $\omega_0 = 2\pi f_0$ is the revolution frequency.

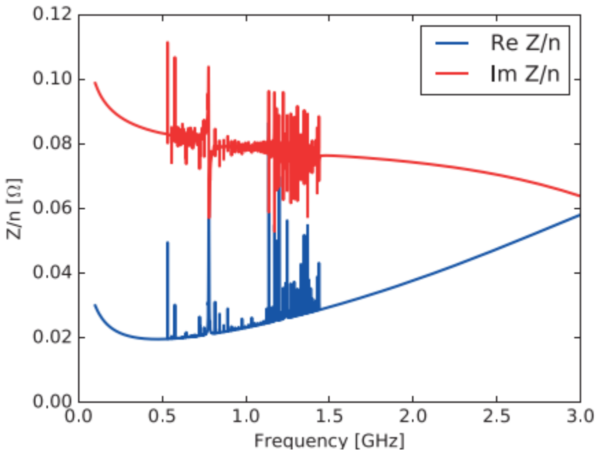


Figure 2: Longitudinal impedance model of LHC [9].

Beam measurements during acceleration ramp, at injection and top energies, as well as with various RF voltages have confirmed the expected scaling of the LLD threshold with beam energy, voltage and bunch length (in relatively small available range) giving for $\xi$ from Eq. (2) a value of $(5.0 \pm 0.5)\cdot 10^{-5}$ [ns$^5$V], see Ref. [7] for more details.

However, the comparison of absolute threshold values indicates that the criterion (1) used for the prediction of the LLD threshold underestimates it by more than a factor 3. Since this simplified criterion is often used for design of future accelerators assuming constant $\mathrm{Im}Z/n$ in absence of the detailed impedance model, it is worthwhile to try and understand the reasons for the observed discrepancy.

## SACHERER STABILITY DIAGRAMS

The large difference between measurements in LHC and predictions based on Sacherer criterion cannot be attributed to any “missing“ contribution in the LHC impedance model due to a good agreement between measurements and simulations. Another possible explanation could be that Eq. (1) is a simplified version of more accurate criterion which can be obtained from the Sacherer dispersion relation for a specific stationary particle distribution $F(\mathcal{E})$ [3]

$$1 = \frac{\delta\omega_{c,m}}{W_m}\int_0^{\infty} \frac{\mathcal{E}^m \mathcal{F}'(\mathcal{E})}{\omega - m\omega_s(\mathcal{E})}\,d\mathcal{E}, \qquad (5)$$

where

$$W_m = \int_0^{\infty} \mathcal{E}^m \mathcal{F}'(\mathcal{E})\,d\mathcal{E},$$

and $\delta\omega_{c,m}$ is the coherent synchrotron frequency shift relative to the incoherent synchrotron frequency affected by the potential well distortion. In this approach, suggested by F. Sacherer [2], the coherent frequencies $\omega_{c,m}$ are obtained as solutions of a general matrix equation for zero synchrotron frequency spread, using the notation of the effective impedance $(\mathrm{Im}Z/n)_{\mathrm{eff}}$. Stability diagrams are then obtained as some approximation for the so-called “synthetic kernel”. This corresponds to an assumption that the wake force is proportional to the longitudinal displacement of the bunch center, valid only for a rigid bunch motion.

The dispersion relation (5) leads to stability diagrams, widely used for analysis of single bunch stability and, in particular, for the loss of Landau damping (see, for example Refs. [10] - [12]). Note that this method predicts zero LLD threshold for distribution functions (3) with $\mu \le 1$ for $\eta\mathrm{Im}Z/n < 0$ (space charge above transition), where slip factor $\eta = 1/\gamma_t^2 - 1/\gamma^2$ and $\gamma_t$ is the relativistic gamma at transition energy.

The widely-used expression for the LLD threshold current

$$I_{\mathrm{th}} = \frac{m+1}{m}\frac{3\pi^2}{16}\frac{Vh^3\,(f_0\tau)^5}{(\mathrm{Im}Z/n)_{\mathrm{eff}}}\left[\frac{\delta\omega_{c,m}}{\Delta\omega_s}\right]_{\mathrm{stab}} \qquad (6)$$

was found for parabolic bunches with $\mu = 0.5$. From the corresponding stability diagram, for dipole mode ($m = 1$) one gets $\left[\delta\omega_{c,m}/\Delta\omega_s\right]_{\mathrm{stab}} = 2/3$ (e.g. Ref. [12]). To obtain the criterion (1), the stability limit for $\mu = 2$ ("smooth distribution") is replaced by a semi-circle with radius $\delta\omega_c/\Delta\omega_s = 0.25$. Analytical solutions for $\omega_{c,m}$ have been found for other particle distributions (Gaussian and binomial (3) with $\mu = 0, 1$) [2]. However, analytical calculations become more involved due to the necessity to include the incoherent frequency shift.

## HOFMANN-PEDERSEN APPROACH

Another possible method to evaluate the LLD threshold is based on direct comparison of the coherent oscillation frequency $\omega_c$ with the incoherent frequency band $\Delta\omega_s$ for a constant inductive impedance $\mathrm{Im}Z/n$. Self-consistent analytical solutions for $\delta\omega_c$ and $\Delta\omega_s$ have been found for the specific particle distribution with a local elliptic energy distribution in longitudinal phase space [13], which corresponds to so called “parabolic” line density with $\mu = 0.5$ in Eq. (3). Only the case of $\eta\mathrm{Im}Z/n > 0$ was considered, assuming a rigid bunch motion.

The coherent frequency of rigid dipole motion does not depend on bunch intensity (see also Fig. 3) and in a single RF system can be found for any bunch profile from the relation [14]

$$\omega_c^2 = \omega_{s0}^2 \int \lambda(\phi) \cos\phi \, d\phi. \tag{7}$$

Contrary to the Sacherer stability diagrams, the spread $\Delta\omega_s$ is taken into account in calculation of $\omega_c$, giving non-zero threshold also for the case $\eta \mathrm{Im}Z/n < 0$, which can be evaluated in similar way. The results for LHC are shown in Fig. 3.

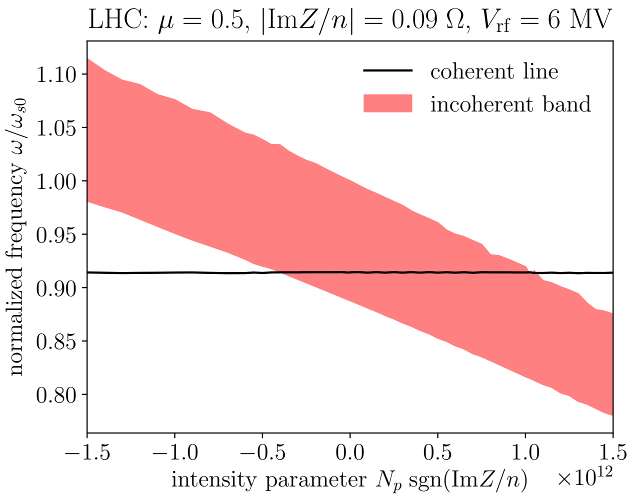


Figure 3: Coherent frequency (solid black line) and incoherent frequencies (red region) in the bunch as a function of intensity parameter, calculated using the Hofmann-Pedersen approach for $\eta > 0$ (LHC), $\mu = 0.5$ and $\tau = 1.05$ ns.

For short bunches in a stationary bucket, the LLD threshold can be presented in a simple form [13]

$$I_{\rm th} = F \frac{V h^3 (f_0 \tau)^5}{\mathrm{Im}Z/n} \tag{8}$$

with the form-factor $F = \pi^4/30$. It agrees quite well (~ 30% higher) with Sacherer criterion for dipole motion and $\mu = 0.5$, where $[\delta\omega_c/\Delta\omega_s]_{\rm stab} = 2/3$, giving $F = \pi^2/4$ in Eq. (8). As can be seen from Fig. 3, the threshold is much lower for $\eta \mathrm{Im}Z < 0$. This is the case for $\mu = 0.5$ only, for higher $\mu$ values, the situation can be opposite. The solutions for other particle distributions can be found in semi-analytical way using formula (7) and taking into account the potential well distortion for the calculation of both coherent (small effect) and incoherent synchrotron frequencies inside the bunch. The results of these calculations for bunch lengths, scaled from FWHM (full-width half-maximum) value found for each distribution for a Gaussian bunch, are shown in Fig. 4, with $\mu = 2$ suitable for the LHC bunch profiles [7].

As can be seen in Fig. 4, a large difference (almost factor 4) between measurements and predictions for a rigid-bunch dipole motion cannot be explained by a difference in particle

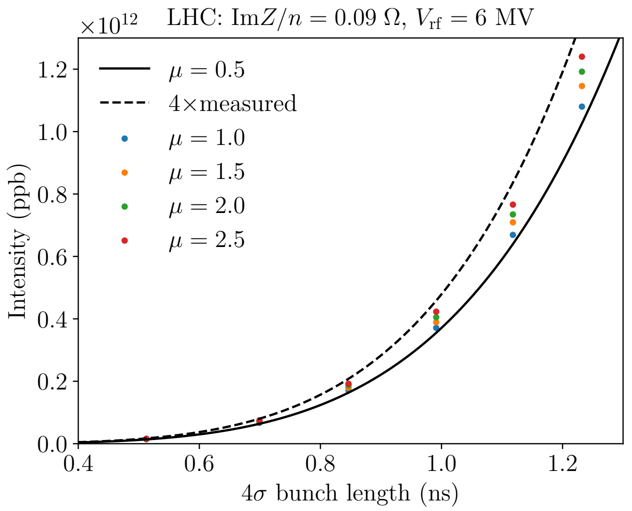


Figure 4: Intensity thresholds for the loss of Landau damping (LHC flat bottom energy of 0.45 TeV) as a function of bunch length (scaled from FWHM), calculated using the Hofmann-Pedersen approach for different particle distributions from binomial family (solid line for $\mu = 0.5$ and colored circles for $\mu - 1.0, 1.5, 2.0, 2.5$) together with the measured threshold (dashed black line) increased for comparison by a factor of 4.

distribution: the thresholds for various distributions are similar for the same FWHM bunch length (this was also seen in simulations [7]).

The Hofmann-Pedersen approach allows to find solutions for a rigid bunch motion in self-consistent way and it was also used for calculations of the LLD thresholds in single and double RF systems [14], [15].

## VAN-KAMPEN MODES

There are several ways to find general solutions of the linearised Vlasov equation in the longitudinal plane for high azimuthal and radial modes without neglecting the synchrotron frequency spread [16] - [18], which allow then to obtain the LLD thresholds in a self-consistent way.

The method applied in Ref. [19] is based on appearance of so-called Van-Kampen modes [20] in solutions of the Vlasov equation for a perturbation $\tilde{\mathcal{F}}(\mathcal{E}, \psi, t)$ to a stationary distribution function $\mathcal{F}(\mathcal{E})$, expanded in harmonics $m$ of synchrotron motion with eigen-functions $C_m(\mathcal{E})$ and $S_m(\mathcal{E})$ [18]:

$$\tilde{\mathcal{F}}(\mathcal{E}, \psi, t) = e^{-i\Omega t} \sum_{m=1}^{\infty} \left[ C_m(\mathcal{E}) \cos m\psi + S_m(\mathcal{E}) \sin m\psi \right].$$

Substitution into the linearised Vlasov equation gives

$$\left[\Omega^2 - m^2 \omega_s^2(\mathcal{E})\right] C_m(\mathcal{E}) = -\frac{2i\, I_0 h\, m^2}{V \cos\phi_s} \omega_s^2(\mathcal{E}) \mathcal{F}'(\mathcal{E})$$

$$\times \sum_{m'=1}^{+\infty} \int_0^{\mathcal{E}_{\max}} \frac{d\mathcal{E}'}{\omega_s(\mathcal{E}')} \sum_{k=-\infty}^{+\infty} \frac{Z_k(\Omega)}{k} I_{mk}(\mathcal{E}) I^*_{m'k}(\mathcal{E}') C_{m'}(\mathcal{E}'),$$

where function

$$I_{mk}(\mathcal{E}) = \frac{1}{2\pi}\int_{-\pi}^{\pi} d\psi\, e^{i\frac{k}{h}\phi(\mathcal{E},\psi)-im\psi}, \tag{9}$$

and $I_0$ is the average beam current. When the integration over energy is replaced here by a sum, one has to solve an eigenvalue problem for the corresponding matrix equation. This technique was used to analyse numerically in Refs. [18], [21] - [23] bunch instability due to radial mode coupling and in Ref. [19] - the thresholds for the loss of Landau damping. Below the LLD threshold, there is a continuous spectrum consisting of singular modes from incoherent synchrotron frequency band. Existence of discrete modes, coherent solutions described by regular eigen-functions, outside incoherent band serves as a criterion for the LLD [17], [19]. This method was fruitfully applied to understand and cure dancing bunches at Tevatron [24]. The results of calculations for LHC are shown in Fig. 5. They agree with available experimetal data and simulations. However, as it was noticed already before [19], the LLD threshold from Van Kampen modes differs significantly from the Sacherer criterion.

The Van Kampen modes were used to compare the LLD thresholds in single and double RF systems [19], [25], [26].

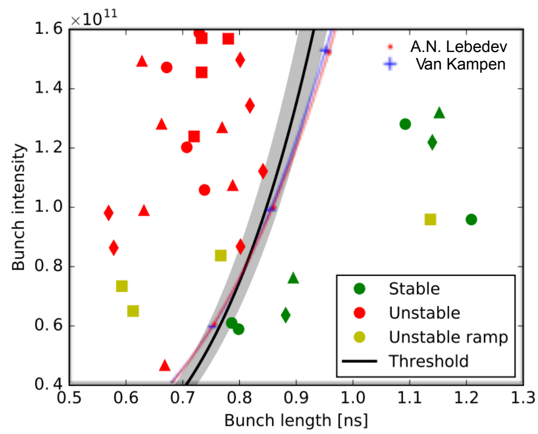


Figure 5: Measured (symbols) and calculated (red and blue lines) intensity thresholds versus bunch length in LHC (flat top energy 6.5 TeV, $V$ = 12 MV) for the particle distribution (3) with $\mu = 2$.

## LEBEDEV EQUATION

The first self-consistent system of equations suitable for analysis of beam stability thresholds was proposed by A. N. Lebedev in 1968 [16] and it can be written in the form (see also [27], [28])

$$\tilde{\lambda}_p(\Omega) = \frac{I_0 h}{V\cos\phi_s}\sum_{k=-\infty}^{\infty} G_{pk}(\Omega)\frac{Z_k(\Omega)}{k}\tilde{\lambda}_k(\Omega), \tag{10}$$

where the matrix elements are

$$G_{pk}(\Omega) = -2\pi i\,\omega_{s0}^2 \sum_{m=-\infty}^{\infty} m \times \int_0^{\mathcal{E}_{\max}} \frac{I_{mk}(\mathcal{E})I_{mp}^*(\mathcal{E})}{\Omega - m\omega_s(\mathcal{E})}\mathcal{F}'(\mathcal{E})\,d\mathcal{E},$$

and $\lambda_k$ is Fourier harmonic of the line density perturbation. For short bunches in a single RF system $\phi(\mathcal{E},\psi) \simeq \sqrt{2\mathcal{E}}\cos\psi$, and function (9) can be presented as

$$I_{mk}(\mathcal{E}) \approx i^m J_m\left(\frac{k}{h}\sqrt{2\mathcal{E}}\right), \tag{11}$$

where $J_m(x)$ is the Bessel function of the first kind and the order $m$.

Matrix equation (10), converted into integral equation by performing inverse Fourier transform over azimuthal harmonics, was used for analysis of single-bunch stability threshold in presence of an inductive impedance with constant Im$Z/n$ [16] and later in Ref. [29], where the threshold, very similar to the Sacherer criterion (6), was obtained.

For small arguments $k\sqrt{2\mathcal{E}}/h < 1$ in Eq.(11), or for the frequency range well inside stable bunch spectrum $f = kf_0 < 1/(\pi\tau)$, the Bessel function can be approximated as

$$J_m(k\sqrt{2\mathcal{E}}) \simeq \left(\frac{k}{h}\sqrt{2\mathcal{E}}\right)^m \frac{1}{2^m\, m!}. \tag{12}$$

In this case, for uncoupled mode $m$, the eigen-functions of Eq.(10) have a form

$$\lambda_k(\Omega) = \left(\frac{k}{h}\right)^m B_m(\Omega),$$

Using this solution in Eq.(10) and keeping only resonant term with positive $m$ allows the dispersion relation (5) to be reproduced up to the coefficient in front of the integral, obtained here in the low-frequency approximation

$$1 = -\frac{i2\pi\omega_{s0}^2 I_0 h}{V\cos\phi_s}\,\frac{m}{2^m\,(m!)^2}\,Z_{\text{eff}}^* \times \int_0^{\infty}\frac{\mathcal{E}^m\mathcal{F}'(\mathcal{E})}{\Omega - m\omega_s(\mathcal{E})}d\mathcal{E}. \tag{13}$$

Here the effective impedance is defined as

$$Z_{\text{eff}}^* = \sum_{k=-\infty}^{\infty}\frac{Z_k}{k}\left(\frac{k}{h}\right)^{2m},$$

and it obviously doesn't converge for constant Im$Z/k$ and, as Eq. (13) itself, is valid only for $k < 1/(\pi f_0\tau)$. So the Sacherer dispersion relation is applicable only in this, low-frequency approximation.

The matrix equation (10) has been solved numerically using the code MELODY [30] and the results for the LLD agree very well with those obtained from Van Kampen modes (see Fig. 5) for the same impedance model. However there is no threshold for a constant Im$Z/n$ (the solution does not converge with higher and higher frequencies included), and the physical impedance model should be used. For LHC, the results strongly depend on the cut-off frequency $f_{\rm cut}$ for constant Im$Z/n$ or the resonant frequency of the broad-band impedance model. Good agreement with measurements in LHC was obtained for $\mu = 2$ and broad-band impedance with $f_r = 5$ GHz, $Q = 1$, Im$Z/n = 0.076$ Ohm and $f_{\rm cut} = 20$ GHz. It is also observed that the potential well distortion does not affect the thresholds significantly.

## DOUBLE RF SYSTEM

The most efficient way to increase synchrotron frequency spread inside the bunch is to use a higher harmonic RF system. The total RF voltage will be

$$V_t = V_1 \sin\phi + V_2 \sin(n\phi + \phi_2),$$

where the phase $\phi_2$ defines the mode of operation: bunch-lengthening (BL) if total voltage gradient at bunch center is reduced and bunch-shortening (BS), if increased. At CERN, a higher harmonic RF system is applied for beam stabilisation in the SPS (with $n = 4$) [31]; it was considered for LHC (with $n = 2$) [7] and for the PS (with $n = 3 - 4$) [32].

Only the BS-mode is used at CERN for beam stabilisation, since the application of the BL-mode for multi-bunch beams is less obvious [31]. One of the main reasons is an existence of the flat region in the synchrotron frequency distribution ($\omega_s'(\mathcal{E}) \sim 0$) inside the bunch, where $\mathcal{F}'(\mathcal{E}) \neq 0$ [33]. This problem can be seen from Eq.(10), where, at the threshold of stability, the element $G_{pk}$ can be written in the form

$$G_{pk}(\Omega) = -2\pi^2 \,\mathrm{sgn}(\Omega) \sum_{m=1}^{\infty} \frac{\omega_{s0}^2 \mathcal{F}'(\mathcal{E}_m)}{\omega_s'(\mathcal{E}_m)} I_{mk}(\mathcal{E}_m) I_{mp}^*(\mathcal{E}_m)$$

$$-i\,4\pi\omega_{s0}^2 \sum_{m=1}^{\infty} \mathcal{P} \int_0^{\mathcal{E}_{\max}} d\mathcal{E}\, \mathcal{F}'(\mathcal{E}) \frac{I_{mk}(\mathcal{E}) I_{mp}^*(\mathcal{E})\, \omega_s(\mathcal{E})}{\Omega^2/m^2 - \omega_s^2(\mathcal{E})}.$$

Here $\mathcal{E}_m$ is defined by $|\Omega| = m\omega_s(\mathcal{E}_m)$ if the coherent mode frequency belongs to the incoherent frequency band, and $\mathcal{P}$ denotes the principle value.

Equation (10) becomes very simple when used for a narrow-band impedance with resonant frequency $f_r$, so that only azimuthal harmonics with $k \sim f_r/f_0$ can be kept. The stability threshold of a multi-bunch beam in a double RF system is not defined if the region with $\omega_s'(\mathcal{E}) \sim 0$ is inside bunch emittance [33].

A similar region, with $\omega_s'(\mathcal{E}) \sim 0$, may also exist in the BS-mode for $n > 2$ above certain voltage ratio $V_2/V_1$, see Fig. 6. However, for the same voltage $V_2$, the relative synchrotron frequency spread increases with $n$, and therefore large $n$ is still attractive as a design choice if used for relatively short bunches.

Possible reduction of stability threshold for large bunch emittances in both BS-mode and BL-mode was confirmed in simulations [19], [25], [26], see also example in Fig. 7. In simulations, in order to excite the coherent motion of the particles, a small phase kick is initially given to the matched bunch. The LLD threshold is then determined from the residual bunch oscillations and in particular, by the ratio of the residual maximum amplitude oscillations to the initial kick. However, special care should be taken when defining this threshold, since it may strongly depend on the criterion chosen. This is illustrated in Fig. 7, where the residual oscillation amplitude found from simulations for a double RF system (BL-mode) is shown [26]. As can be seen in the plot, a selection of a certain criterion (horizontal line in the plot) affects the absolute LLD threshold, although it gives similar relative results (for the different emittances).

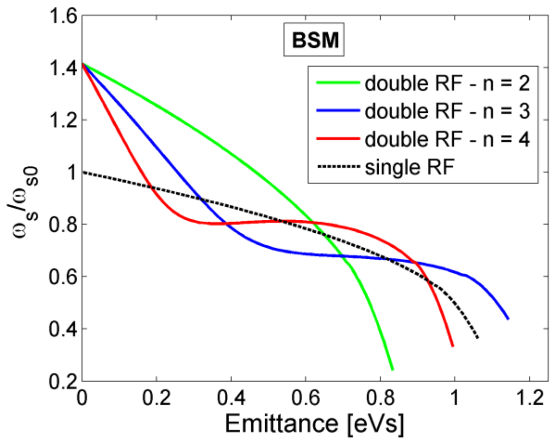


Figure 6: Relative synchrotron frequency as a function of longitudinal emittance in double RF system in BS-mode with different $n$ and $V_1/V_2 = n$ (example for the SPS bottom energy).

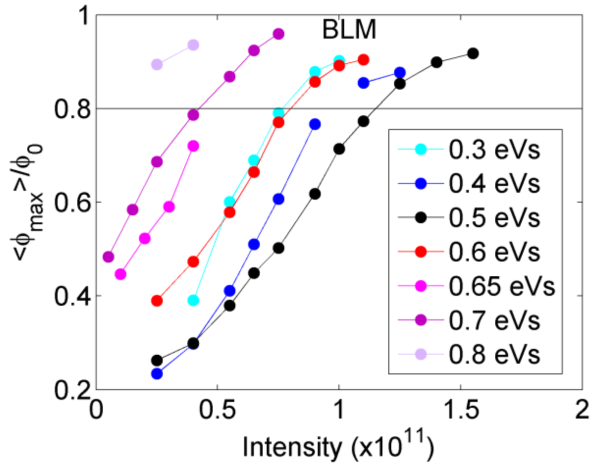


Figure 7: Ratio of the residual dipole oscillation amplitude to the amplitude of the initial phase kick (color circles) as a function of the bunch intensity found in simulations performed for various bunch emittances in a double RF system with $n = 2$ (BL-mode). The horizontal line indicates a possible criterion for the LLD threshold.

## SUMMARY

In longitudinal plane, simplified analytical criteria are often used for the scaling of the loss of Landau damping threshold with beam and machine parameters. The Sacherer stability diagram in longitudinal plane is justified only for low-frequency impedance and in other cases should be used with caution. More advanced methods (Van-Kampen modes and Lebedev equation) together with particle simulations are available for accurate threshold estimations, also based on a realistic impedance model, since a constant $\mathrm{Im}Z/n$ may not give converging LLD thresholds. In case of $\eta\mathrm{Im}Z/n > 0$, the dependence of thresholds on particle distribution can be reduced by using the FWHM bunch lengths.

Landau damping can be significantly increased by additional, higher harmonic RF system, but its limitations in BL-mode and, for $n > 2$, in BS-mode should be taken into account for the choice of the beam and RF parameters.

## ACKNOWLEDGMENTS

We acknowledge important input from J. E. Muller and useful discussion with A. Burov.

## REFERENCES


[1] The LHC Study Group, "The Large Hadron Collider - Conceptual Design", CERN/AC/95-05 (LHC) (1995).

[2] F. Sacherer, Methods for computing bunched beam instabilities, CERN/SI-BR/72-5 (1972).

[3] F. Sacherer, A longitudinal stability criterion for bunched beams, IEEE Transactions on Nuclear Science, 825-829, (1973).

[4] K. Hubner and V.G. Vaccaro, Dispersion relations and stability of coasting beams, CERN-ISR-TH/70-44 (1970).

[5] D. Boussard, D. Brandt and L. Vos, Is a longitudinal feedback required for LHC? CERN LHC-Project-Note-205 (1999).

[6] E. Shaposhnikova, Longitudinal beam parameters during acceleration in the LHC, CERN LHC-Project-Note-242 (2000).

[7] J. Esteban Muller, Longitudinal intensity effects in the CERN Large Hadron Collider, PhD thesis, Apr 2016, `https://cds.cern.ch/record/2196930`.

[8] BLonD: Beam Longitudinal Dynamics code, CERN website `http://blond.web.cern.ch`.

[9] N. Mounet, The LHC transverse coupled-bunch instability. PhD thesis, EPFL (2012).

[10] E. Metral, Longitudinal bunched-beam coherent modes: from stability to instability and inversely, CERN-AB-2004-002 ABP (2004).

[11] K.Y. Ng, Physics of Intensity Dependent Beam Instabilities, World Scientific Publishing (2006).

[12] I.S. Gonzalez, Loss of longitudinal Landau damping in the LHC injectors, CERN AB-Note-2008-001 ABP (2008).

[13] A. Hofmann and F. Pedersen. Bunches with local elliptic energy distributions. IEEE Transactions on Nuclear Science, 26(3):3526–3528 (1979).

[14] O. Boine-Frankenheim and T. Shukla, Space charge effects in bunches for different rf wave forms, PRST-AB **8**, 034201 (2005).

[15] O. Boine-Frankenheim and O. Chorniy, Stability of coherent synchrotron oscillations with space charge, PRST-AB **10**, 104202 (2007).

[16] A.N. Lebedev, Coherent synchrotron oscillations in the presence of a space charge, Sov. Atom. Energy. vol. 25, n0. 2, pp.851-856 (1968).

[17] Y.H. Chin, K. Satoh and K. Yokoya, Instability of a bunched beam with synchrotron frequency spread, PA 13 (1983) 45.

[18] Oide and Yokoya, Longitudinal single bunch instability in electron storage rings, KEK Preprint 90-10 (1990).

[19] A. Burov, Van Kampen modes for bunch longitudinal motion, 46th ICFA Advanced Beam Dynamics Workshop HB2010, Morschach, Switzerland (2010).

[20] N. G. van Kampen. The dispersion equation for plasma waves. Physica, 23:641–650, (1957).

[21] M. D'yachkov and R. Baartman, Longitudinal single bunch stability, Part. Acc. 50, 105 (1995).

[22] K. Oide, A mechanism of longitudinal single-bunch instability in storage rings, Part. Acc, 51, 43 (1995).

[23] A. Mosnier, Microwave instability in electron storage rings, Nucl. Instrum. Methods Phys. Res., Sect. A 438, 225 (1999).

[24] A. Burov, Dancing bunches as Van Kampen modes, FERMILAB-CONF-1-121-AD (2011).

[25] T. Argyropoulos, A. Burov, E. Shaposhnikova, Loss of Landau damping for inductive impedance in a double RF system, IPAC'13 (2013).

[26] T. Argyropoulos, Longitudinal beam instabilities in a double RF system, PhD thesis CERN-THESIS-2015-421 (2015).

[27] V.I. Balbekov, S.V. Ivanov, Longitudinal instability threshold of bunched beams in proton synchrotrons, Sov. Atom. Energy, vol.60, no. 1, pp.58-66 (1986).

[28] E. Shaposhnikova, Bunched beam transfer matrices in single and double RF systems. Tech. Rep. CERN-SL-94-19-RF (1994).

[29] V.I. Balbekov and S.V. Ivanov, Thresholds of longitudinal instability of bunched beam in the presence of dominant inductive impedance. IHEP Preprint 91-14, Protvino (1991).

[30] I. Karpov, Matrix Equations for LOngitudinal beam DYnamics (MELODY) code, `https://gitlab.cern.ch/ikarpov/melody`.

[31] E. Shaposhnikova, T. Bohl, and T.P.R. Linnecar, Beam transfer functions and beam stabilisation in a double RF system, CERN-AB-2005-026 (2005).

[32] H. Damerau, A. Lasheen, E. Shaposhnikova, Higher-harmonic RF system for Landau damping in the CERN PS, IPAC'18 (2018).

[33] S.V. Ivanov and V.I. Balbekov, Methods for suppressing the longitudinal instability of a bunched beam with the help of Landau damping. Atom. Energ., 62 (2) pp.117–125 (1987).

# ADVANCED LANDAU DAMPING WITH RADIO-FREQUENCY QUADRUPOLES OR NONLINEAR CHROMATICITY

M. Schenk[1*], X. Buffat, A. Grudiev, K. Li, E. Métral
European Organization for Nuclear Research, 1211 Geneva, Switzerland
[1]also at École Polytechnique Fédérale de Lausanne, 1015 Lausanne, Switzerland

A. Maillard
École Normale Supérieure, 75230 Paris, France

*Abstract*

Landau damping is a powerful mechanism to suppress impedance-driven coherent instabilities in circular accelerators. In the transverse planes it is usually introduced by means of magnetic octupoles. We will discuss a method to generate the required incoherent betatron frequency spread through detuning with the longitudinal rather than the transverse amplitudes. The approach is motivated mainly by the high-brightness, low transverse emittance beams in future colliders where detuning with the transverse amplitudes from magnetic octupoles becomes significantly less effective. Two equivalent methods are under study: a radio-frequency quadrupole cavity and the nonlinear chromaticity. The underlying beam dynamics mechanisms are explained based on a recently extended Vlasov theory and relevant results are discussed for different longitudinal beam distributions under specific approximations. Finally, the analytical studies are benchmarked against numerical simulations employing a circulant matrix and a macroparticle tracking model.

## INTRODUCTION

The use of radio frequency (rf) quadrupole cavities against coherent beam instabilities has first been discussed in [1, 2] to suppress coupled-bunch modes, and later in [3, 4] to raise the intensity threshold of the transverse mode-coupling instability (TMCI). Here, rf quadrupoles are considered to provide Landau damping of weak single-bunch head-tail modes [5–7]. Detailed theoretical, experimental, and simulation studies of the latter have been reported in [8–12] and a summary of relevant extracts thereof is given here.

The purpose of the rf quadrupole for Landau damping is to generate transverse quadrupolar kicks on the beam particles with a strength that depends on their longitudinal coordinate. Every particle feels a different focusing (defocussing) force as it passes through the device and hence experiences a change in its betatron frequencies depending on its longitudinal position within the bunch. The result is an incoherent betatron frequency spread which leads to Landau damping in the transverse planes. Other than for magnetic octupoles, the frequency spread from an rf quadrupole is dependent on the longitudinal amplitude spread within the bunch [7, 8]. It can be shown that nonlinear chromaticity can introduce an equivalent longitudinal amplitude dependent frequency spread (see e.g. [10]). This result will be used here to discuss the analytical studies.

Thanks to the orders of magnitude larger spread in the longitudinal compared to the transverse amplitudes of the beams in future hadron colliders, a longitudinal amplitude-dependent frequency spread can be produced very efficiently compared to magnetic octupoles. The differences are particularly important at increased beam energies and for reduced transverse emittances. In addition, the amount of frequency spread remains unaffected by beam manipulations in the transverse planes, such as beam halo cleaning through collimation, for example. Recently, it has also been demonstrated that transverse linear coupling can strongly reduce the incoherent betatron frequency distributions generated through detuning with the transverse amplitudes [13]. This can lead to a loss of Landau damping and requires an accurate correction of the linear coupling in future machines [14]. The shape and amount of frequency spread introduced through detuning with the longitudinal amplitude, on the other hand, is not affected by linear coupling [15]. It is hence expected that there is no loss of Landau damping in that case. Another effect that is currently under detailed investigation is transverse noise that can locally significantly reduce the stability diagrams generated by magnetic octupoles and hence lead to a loss of Landau damping [16]. It is believed that this effect will not be present for rf quadrupoles or nonlinear chromaticity thanks to the separation of the longitudinal amplitude space and the transverse planes where the frequency spread is created.

## THEORY

Berg and Ruggiero developed the basic formalism for longitudinal amplitude dependent Landau damping in [17]. They also demonstrated that it differs to some extent from Landau damping introduced by octupole magnets. The theory has been further developed and thoroughly analyzed in [9]. Only the key equations and a summary of their interpretations are presented here.

The goal is to extend the existing Vlasov formalism by introducing a general variation $\Delta\omega_\beta(\delta)$ of the betatron frequency with arbitrary orders of chromaticity $\xi^{(n)}$

$$\Delta\omega_\beta(\delta) = \omega_{\beta,0} \sum_{n=1}^{m} \frac{\xi^{(n)}}{n!}\delta^n, \tag{1}$$

* michael.schenk@epfl.ch

with

$$\xi^{(n)} = \frac{1}{\omega_{\beta,0}} \frac{\partial^n \omega_\beta}{\partial \delta^n}\bigg|_{\delta=0}, \tag{2}$$

$\omega_{\beta,0}$ the zero-amplitude betatron frequency, and $\delta$ the relative momentum deviation. One may, analogously, introduce a general variation of the betatron frequency with the longitudinal position $\Delta\omega_\beta(z)$ to describe the frequency spread from an rf quadrupole. The two approaches eventually lead to the same results. Here, we assume that the frequency spread is produced by nonlinear chromaticity.

Following the path laid out by Chao in [6], but using the general dependence of $\Delta\omega_\beta$ on $\xi^{(n)}$, one can derive an eigenvalue equation (details in [9])

$$\sigma_{lk} = -iK \sum_{l',\,k'=-\infty}^{\infty} \sigma_{l'k'}\, Z_\perp\left(k'\omega_0 + \Omega^{(l)}\right) \times \int_0^\infty \frac{r g_0(r)\, \overline{H_l^{k'}}(r)\, H_l^k(r)}{\Omega^{(l)} - \omega_{\beta,0} - l\omega_s - \langle\Delta\omega_\beta\rangle_\phi(r)}\, dr, \tag{3}$$

where

$$\sigma_{lk} = \int_0^\infty r R_l(r)\, H_l^k(r)\, dr. \tag{4}$$

$K$ is a constant, $Z_\perp$ the dipolar impedance function, $g_0$ the longitudinal particle distribution, $\omega_0$ the revolution frequency, $\omega_s$ the synchrotron frequency, $\Omega^{(l)}$ the complex coherent frequency of the $l^{\text{th}}$ azimuthal mode, $(r,\phi)$ are polar coordinates in longitudinal phase space, and $R_l$ the radial beam modes. The $H_l^k$ functions can be perceived as generalized Bessel functions. They reduce to Bessel functions of the first kind for a purely linear chromaticity. The term $\langle\Delta\omega_\beta\rangle_\phi$ describes the betatron frequency spread introduced through detuning with the longitudinal amplitude $r$

$$\langle\Delta\omega_\beta\rangle_\phi(r) = \frac{1}{2\pi}\int_0^{2\pi} \Delta\omega_\beta\left[\delta(r,\phi)\right]\, d\phi. \tag{5}$$

This term appears in the denominator of the dispersion integral on the right hand side of Eq. (3) which demonstrates that it indeed provides Landau damping. One realizes that for odd orders of chromaticity the average frequency spread vanishes $\langle\Delta\omega_\beta\rangle_\phi(r) \equiv 0$. This result is independent of the longitudinal particle distribution. Hence, odd orders of chromaticity do not introduce Landau damping, at least for instabilities with rise times in the order of several synchrotron periods where the frequency spread averages to zero[1]. On the other hand, even orders of chromaticity introduce a frequency spread with longitudinal amplitude that does not average out over time which leads to Landau damping, similarly to an rf quadrupole operated (anti-) on-crest of the rf wave. There is yet another mechanism, however. Both odd and even orders of chromaticity introduce a change of the effective impedance and modify the complex frequencies of the coherent modes in that manner. This effect is described by the generalized Bessel functions introduced above. The $H_l^k$ functions contain complex, chromaticity-dependent, phase terms which describe the alteration of the interaction of the beam with the impedance. The result is that the overlap sum over index $k'$ in Eq. (3) between the $H_l^{k'}$ functions and the impedance changes. In time domain these chromatic phase terms can be interpreted as a change of the synchronicity between wake kicks, betatron, and synchrotron motion of the particles. They lead to a change of the coherent frequencies of all the modes. Note that such modification of the effective impedance is independent of frequency spread and there is no increase of the area of stability in the complex frequency space. Thus, this effect is not related to Landau damping.

[1] This is analogous to an rf quadrupole operated at the zero crossing of the rf wave studied in [3,4] to increase the TMCI threshold.

## SOLUTIONS

Solutions to the Vlasov Eq. (3) are determined for two different types of longitudinal particle distributions. The analytical results presented here are benchmarked against the PyHeadtail macroparticle tracking model and the BimBim circulant matrix solver [18–20].

### *Airbag beam*

For the airbag model the beam particles are assumed to populate an infinitesimally thin elliptical shell in the longitudinal phase space, i.e. they all oscillate with the same longitudinal amplitude. As a result, the betatron frequency spread from nonlinear chromaticity or rf quadrupoles vanishes and hence there can be no Landau damping. In the weak-wake approximation considered here, azimuthal mode coupling can be neglected and one can solve the equations for all the azimuthal modes $l \in \mathbb{Z}$ independently of each other. For an airbag distribution the dispersion integral can be easily evaluated and one obtains the solutions

$$\Omega^{(l)} - \omega_{\beta,0} - l\omega_s - \langle\Delta\omega_\beta\rangle_\phi(\hat{z}) = -i\,\frac{Ne^2c}{2\omega_{\beta,0}T_0^2E_0}\sum_{k=-\infty}^{\infty} Z_\perp(\omega')\left|H_l^k(\hat{z})\right|^2, \tag{6}$$

where $\omega' = k\omega_0 + \omega_{\beta,0} + l\omega_s$. $N$ denotes the bunch population, $T_0$ the revolution period, $E_0$ the beam energy, $\hat{z}$ the longitudinal amplitude of the airbag beam, $e$ the elementary charge, and $c$ the speed of light. We have obtained an explicit expression for the coherent frequency shift of every azimuthal mode. The detuning term $\langle\Delta\omega_\beta\rangle_\phi(\hat{z}) = \text{const.}$ is now independent of the longitudinal amplitude $r$ and is identical for all the particles. As expected, the dispersion integral has disappeared from the equation which can be interpreted as the absence of Landau damping. Equation (6) is a generalization of Eq. (6.188) in [6] and is valid for arbitrary orders of chromaticity. It reduces to Chao's equation for a purely linear chromaticity as shown in [9].

The new formalism is first benchmarked against the well-known case of a purely linear chromaticity and a broad-band resonator impedance. The results are summarized in Fig. 1. The analytical calculations are given by the colored lines and represent the real (upper plot) and imaginary (lower plot)

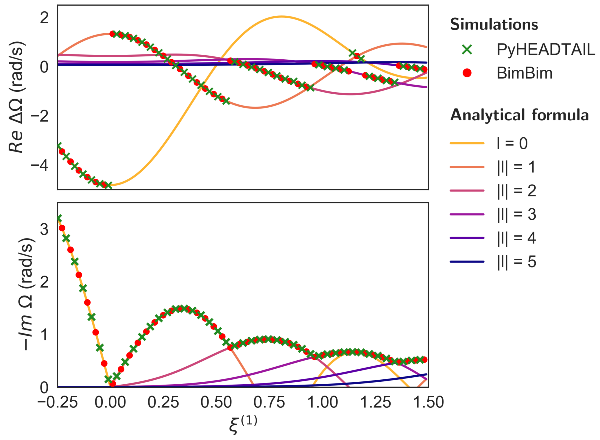


Figure 1: Real (top) and imaginary (bottom) coherent frequency shifts as a function of $\xi^{(1)}$ for an airbag model.

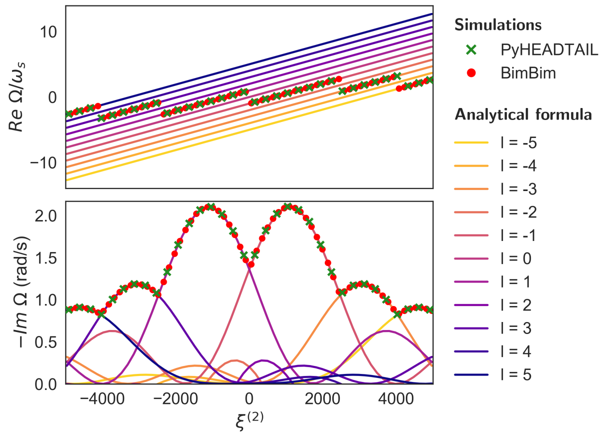


Figure 2: Real (top) and imaginary (bottom) coherent frequency shifts as a function of $\xi^{(2)}$ at fixed $\xi^{(1)}$ for an airbag model.

coherent frequency shifts of the six lowest-order azimuthal modes vs. $\xi^{(1)}$. The real part is measured with respect to the respective unstable synchrotron side band. It can be seen that the azimuthal modes for a specific positive and negative azimuthal number are identical. This will no longer be the case when introducing second-order chromaticity as described below. For $\xi^{(1)} < 0$ the most unstable mode is a head-tail mode zero (above transition). For increasing $\xi^{(1)} > 0$, the most unstable mode changes from azimuthal mode one through five. The outputs from BimBim (red) and PyHeadtail (green) after post-processing are shown on top of the analytical results. The three approaches are in excellent agreement which confirms that they all work well for the basic linear chromaticity case.

Figure 2 summarizes the more interesting case in presence of nonlinear chromaticity. The coherent frequency shifts obtained from analytical formula [Eq. (6)], PyHeadtail, and BimBim are shown as functions of $\xi^{(2)}$ for constant $\xi^{(1)}$. Similar to the case with linear chromaticity, $\xi^{(2)}$ changes the effective impedance and eventually, transitions to other, more unstable azimuthal modes occur. A major difference with respect to Fig. 1, however, is that the degeneracy in the azimuthal mode number is lifted. For a certain absolute value of the mode number, the modes with the two opposite signs are no longer identical. Additionally, the real part of the coherent frequency shift is dominated by the constant and real-valued $\langle \Delta\omega_\beta \rangle_\phi(\hat{z})$ which is the same for all the azimuthal modes. This is specific to the airbag beam and is again a result of the absence of a spread in longitudinal amplitude. As for the linear case, the theoretical predictions are in perfect agreement with both the tracking and circulant matrix models which confirms that the formalism developed above is indeed valid for the airbag beam.

### *Arbitrary distributions*

The new theory describes the change of the effective impedance from nonlinear chromaticity very accurately and produces satisfying results for the airbag model. The next step is to introduce beam distributions where the particles exhibit a spread in their longitudinal amplitudes, for example Gaussian, to validate the theory also in presence of Landau damping. Unfortunately, Eq. (3) could not be solved exactly for the general case. To make the dispersion relation and the presence of Landau damping more apparent and to bring the equation into a form that can be solved and benchmarked against numerical models, strict assumptions are made on the shape of the transverse dipolar impedance instead

$$Z_\perp(\omega') = \begin{cases} Z_{k_0} \neq 0, & k = k_0, \\ 0, & \text{otherwise.} \end{cases} \tag{7}$$

Equation (3) then simplifies to

$$1 = -iKZ_{k_0} \int_0^\infty \frac{r g_0(r) \left| H_l^{k_0}(r) \right|^2}{\Omega^{(l)} - \omega_\beta(r) - l\omega_s}\, dr, \tag{8}$$

where $\omega_\beta(r) = \omega_{\beta,0} + \langle \Delta\omega_\beta \rangle_\phi$. Equation (8) is a dispersion relation. The formula for stability boundary diagrams can now be easily determined

$$\begin{aligned} \frac{1}{\Delta\Omega_{\text{lin}}^{(l)}} &= \frac{1}{\mathcal{N}} \int_0^\infty \frac{r g_0(r) \left| H_l^{k_0}(r) \right|^2}{\Omega^{(l)} - \omega_\beta(r) - l\omega_s}\, dr, \\ \mathcal{N} &= \int_0^\infty r g_0(r) \left| H_l^{k_0}(r) \right|^2 dr, \end{aligned} \tag{9}$$

where $\Delta\Omega_{\text{lin}}^{(l)} = \Omega_{\text{lin}}^{(l)} - \omega_{\beta,0} - l\omega_s$ and $\Omega_{\text{lin}}^{(l)}$ denotes the complex coherent frequency of the azimuthal mode $l$ in absence of Landau damping. It can be demonstrated that the dispersion relation derived here is equivalent to the results found by Berg and Ruggiero in [17] (proof in [9]).

To benchmark the analytical model against PyHeadtail tracking simulations we assume a Gaussian beam distribution and define a scenario which fulfills best the approximations and assumptions made when deriving Eq. (9). The main assumption is to use a highly narrow-band resonator impedance to mimic the single-peak impedance approximation. This can be achieved by tuning the quality factor and the frequency of the resonator accordingly. The parameters were set to match the spectral maximum of the azimuthal mode zero while remaining small for all the other modes. It was verified that the error in both the real and imaginary coherent frequencies between the single-peak approximation and the simulation was less than ten percent.

Next, the dispersion relation in Eq. (9) is solved numerically to obtain the stability boundary diagrams in complex frequency space. The solutions are displayed in Fig. 3 for four different values of $\xi^{(2)}$, increasing in absolute value from top left to bottom right. The plots illustrate the increase of the stability boundary (black line, $-\text{Im}\ \Omega = 0$) and hence of the stable area (blue hatched region, $-\text{Im}\ \Omega \leq 0$) in complex frequency space. The coherent frequency shift of the unstable mode under consideration (red cross) is obtained from PyHeadtail simulations. It is demonstrated in [9] that the change of the effective impedance (chromatic effect) introduced by $\xi^{(2)}$ is negligible for this particular instability and that Landau damping is the dominant mechanism here. The unperturbed coherent frequency can hence be assumed to be independent of $\xi^{(2)}$. The colored lines in the figure refer to constant values of imaginary frequency shift ($-\text{Im}\ \Omega = \text{const.}$) and follow the distortion of the frequency space caused by the spread introduced by $\xi^{(2)}$. By means of these isolines one can read off the effective change of the imaginary frequency shift of the unstable mode as a function of frequency spread, or $\xi^{(2)}$. This illustrates the damping process: with increasing spread the imaginary part of the unstable mode is effectively reduced, meaning that the growth rate of the instability decreases. For $\xi^{(2)} \leq -9.6$, the area of stability has become large enough to include the unstable mode. At this point the instability is Landau damped. The final comparison of the imaginary frequency shifts, or instability growth rates, between stability diagram theory (red), obtained from the isolines in Fig. 3, and from PyHeadtail simulations (green) is shown in Fig. 4. They are both in excellent agreement with each other. Not only the stabilizing threshold for the amount of $\xi^{(2)}$ matches, but also the intermediate stages of $\xi^{(2)}$ show a remarkable agreement on the imaginary frequency shifts. This proves that the theory works successfully and that nonlinear chromaticity or rf quadrupoles indeed provide Landau damping. It should be pointed out, however, that the one-sidedness of the stability diagrams is a limitation of this method. A frequency spread from $\xi^{(2)} < 0$, for example, would only be able to Landau-damp the modes with $\text{Re}\ \Omega < 0$. The modes with $\text{Re}\ \Omega > 0$ could potentially be suppressed by means of a second, complementary method such as frequency spread from octupole magnets.

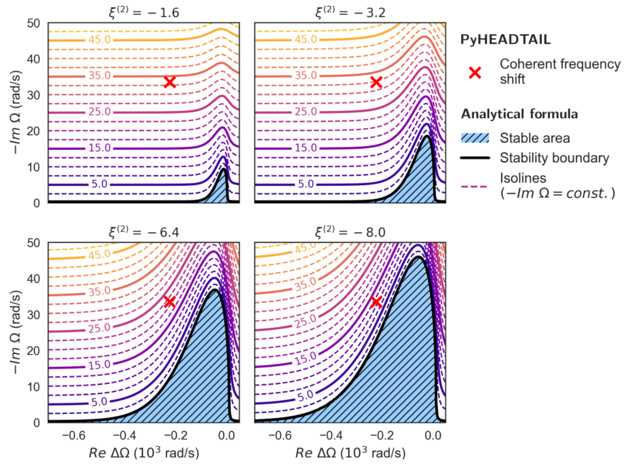


Figure 3: Stability boundary diagrams for four different values of $\xi^{(2)}$ increasing in absolute value from top left to bottom right.

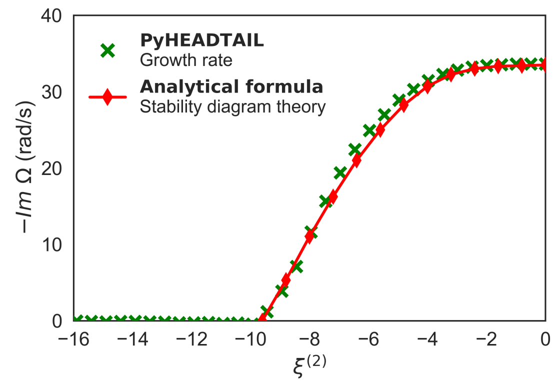


Figure 4: Stabilization of the head-tail mode zero vs. $\xi^{(2)}$ for a Gaussian beam. PyHeadtail simulations (green crosses) are shown together with analytical predictions calculated by means of stability diagram theory (red diamonds).

## CONCLUSIONS

The existing Vlasov theory on transverse dipole modes has been extended to include the effects of nonlinear chromaticity up to arbitrary orders. This new formalism made it possible to confirm the hypothesis that nonlinear chromaticity and rf quadrupoles have two effects on the beam dynamics of transverse coherent modes: (1) they lead to a change of effective impedance; and (2) they introduce Landau damping thanks to the incoherent betatron frequency spread with longitudinal amplitude. The two mechanisms have been identified and studied separately using analytical formulae. In addition, the theory has been successfully benchmarked up to second-order chromaticity for an airbag model and a Gaussian beam. In the first case, there is no Landau damping due to the missing frequency spread from detuning with longitudinal amplitude. Analytical results have been validated both with a tracking model and a circulant matrix solver which revealed an outstanding agreement. For the Gaussian beam it has been demonstrated that, given the assumption of a strongly peaked impedance, analytical predictions from stability diagram theory are in excellent agreement with tracking simulations. This proves that detuning with longitudinal amplitude indeed provides Landau damping. The results are also in accordance with experiments and simulations that were carried out on the rf quadrupole and on nonlinear chromaticity in the Large Hadron Collider and provide the foundation for the interpretation of these results. The study also demonstrates, however, that beam stabilization with rf quadrupoles or nonlinear chromaticity is not easily evaluated analytically for arbitrary impedances. Macroparticle tracking simulations are instead the most accurate way to study these effects.

## ACKNOWLEDGMENT

M. Schenk would like to thank the institute for Swiss Accelerator Research & Technology (CHART) for supporting his participation in this workshop.

## REFERENCES

[1] Y. H. Chin, "Landau damping of a multi-bunch instability due to bunch-to-bunch tune spread", in Proc. of the Particle Accelerator Conference 1987 (1987), p. 1213.

[2] S. Sakanaka and T. Mitsuhashi, "Construction of an RF Quadrupole Magnet for Suppressing Transverse Coupled-Bunch Instabilities", in Proc. of the Particle Accelerator Conference 1991 (1991), p. 1836.

[3] V. V. Danilov, "Increasing the transverse mode coupling instability threshold by RF quadrupole", Phys. Rev. ST Accel. Beams **1**, 041301 (1998).

[4] E. A. Perevedentsev and A. A. Valishev, "Synchrobetatron dynamics with a radio-frequency quadrupole", in Proc. of the 8th European Particle Accelerator Conference, Paris, 2002 (EPS-IGA and CERN, Geneva, 2002), p. 1574.

[5] L. Landau, "On the vibrations of the electronic plasma", Zh. Eksp. Teor. Fiz. **16**, 574 (1946) [J. Phys. USSR **10**, 25 (1946)].

[6] A. Chao, *Physics of Collective Beam Instabilities in High Energy Accelerators*, Wiley Series in Beam Physics and Accelerator Technology (Wiley, New York, 1993).

[7] A. Grudiev, "Radio frequency quadrupole for Landau damping in accelerators", Phys. Rev. ST Accel. Beams **17**, 011001 (2014).

[8] M. Schenk et al., "Analysis of transverse beam stabilization with radio frequency quadrupoles", Phys. Rev. Accel. Beams **20**, 104402 (2017).

[9] M. Schenk et al., "Vlasov description of the effects of nonlinear chromaticity on transverse coherent beam instabilities", Phys. Rev. Accel. Beams **21**, 084402 (2018).

[10] M. Schenk et al., "Experimental stabilization of transverse collective instabilities in the LHC with second order chromaticity", Phys. Rev. Accel. Beams **21**, 084401 (2018).

[11] M. Schenk, "A novel approach to Landau damping of transverse collective instabilities in future hadron colliders", EPFL Thesis 9298, PhD thesis (Ecole Polytechnique Fédérale de Lausanne, Lausanne, Switzerland, 2019).

[12] K. Papke and A. Grudiev, "Design of an rf quadrupole for Landau damping", Phys. Rev. Accel. Beams **20**, 082001 (2017).

[13] L. R. Carver, X. Buffat, K. Li, E. Métral, and M. Schenk, "Transverse beam instabilities in the presence of linear coupling in the Large Hadron Collider", Phys. Rev. Accel. Beams **21**, 044401 (2018).

[14] E. Métral, S. Antipov, F. Antoniou, R. B. Appleby, G. Arduini, J. Baranco García, P. Baudrenghien, N. Biancacci, C. Bracco, R. Bruce, et al., *Update of the HL-LHC operational scenarios for proton operation*, tech. rep. CERN-ACC-NOTE-2018-0002 (CERN, Geneva, Switzerland, 2018).

[15] M. Schenk, L. R. Carver, A. Grudiev, K. Li, and E. Métral, *Tune footprints in presence of linear coupling*, *presented at* "74$^{\text{th}}$ HSC Meeting" (CERN, Geneva, Switzerland, Apr. 2016).

[16] S. Vik Furuseth et al., *MD3288: Instability latency with controlled noise*, tech. rep. CERN-ACC-NOTE-2019-0011 (CERN, Geneva, Switzerland, 2019).

[17] J. S. Berg and F. Ruggiero, "Stability Diagrams for Landau Damping", in Proc. of the Particle Accelerator Conference, Vancouver, Canada (1997).

[18] K. Li et al., "Code Development for Collective Effects", in Proc. of HB2016, Malmö, Sweden (July 2016), pp. 362 – 357.

[19] K. Li, "Code presentation: PyHEADTAIL", *presented at* 5th ABP-CWG Meeting, (CERN, Geneva, Switzerland, Nov. 2016).

[20] X. Buffat, "Transverse beams stability studies at the Large Hadron Collider", EPFL Thesis 6321, PhD thesis (Ecole Polytechnique Fédérale de Lausanne, Lausanne, Switzerland, 2015).

# ON LANDAU DAMPING RESTORATION WITH ELECTRON LENSES IN SPACE-CHARGE DOMINATED BEAMS*

Y. Alexahin#, A. Burov, V. Shiltsev, A. Valishev, Fermilab, Batavia, IL 60510, USA

*Abstract*

It is shown that the Lorentz forces of a low-energy, magnetically stabilized electron beam, or "electron lens", can introduce transverse nonlinear focusing sufficient for Landau damping of transverse beam instabilities in accelerators. Unlike other nonlinear elements, the electron lens can provide the frequency spread mainly at the desirable range of particle amplitudes, thus permitting to avoid the beam lifetime degradation.

## INTRODUCTION

There are many impedance-driven collective instability phenomena in high intensity charged particle beams [1, 2] limiting the single-bunch and total beam intensities. Suppression of the collective instabilities can be obtained via the stabilizing effect of Landau damping [3] when the spectrum of incoherent frequencies $\omega_{x,y}$ overlap the frequencies of the unstable collective modes, thus allowing absorption of the collective energy by the resonant particles.

But the direct space charge forces in high intensity beam shift the incoherent frequencies away from the frequency of the zero head-tail mode leaving it exposed to instability. Similar effect happens with the Σ-mode in colliding beams.

To restore Landau damping the octupole magnets are commonly used with the transverse magnetic field $B_x + iB_y = O_3(x+iy)^3$ which generates the amplitude-dependent betatron frequency spread [4]. Damping by octupoles has several drawbacks: first of all, the corresponding frequency spread $\delta\omega_{x,y}$ scales with beam energy increase as $1/E^2$ due to increasing rigidity and smaller beam size, hence, one needs to increase strength of these magnets accordingly. Secondly, strong octupoles significantly reduce machine's dynamic aperture.

Another method involves beam-based feedback system which suppresses coherent motion of the beam or bunch centroid. Though generally effective, such feedback systems which act only on the modes with non-zero dipole moment, leaving the multitude of other "head-tail" modes unsuppressed [5]. Electron lenses [6] were shown to provide effective Landau damping [7] mechanism free of all the above listed drawbacks of other methods.

## ELECTRON LENS

Over the years the electron lenses served for a number of purposes [8]. Here we discuss their use for restoration of Landau damping switched off by the beam space-charge (or by the beam-beam effect). In these cases the electron lens should provide a comparable tuneshift/tunespread raising the possibility of an adverse effect on the incoherent particle motion in the beam. There are a number of ideas how to avoid this, e.g. by making the optics with electron lens integrable.

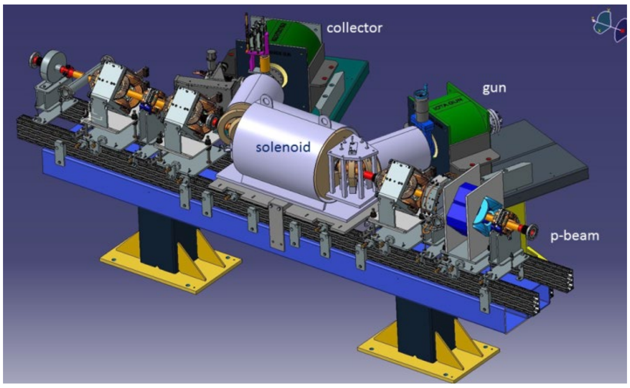


Figure 1: IOTA electron lens (courtesy of G. Stancari)

Such experiment is planned at the Integrable Optics Test Accelerator (IOTA) at Fermilab [9]. Figure 1 shows the lens being built for this purpose. By changing the gun cathode shape and voltage it is possible to form electron beam of different transverse profile and current and – by changing the solenoid magnetic field – to adjust the e-beam size.

### *Danilov-Nagaitsev Paradigm*

In Ref. [10] V. Danilov and S. Nagaitsev proposed a recipe for building nonlinear integrable optics which in the simplest case can be described as follows:

- The lattice outside a special nonlinear insertion should be (almost) linear with phase advances being multiples of $\pi$.
- Beta-functions in the nonlinear insertion should be equal ($\beta_x = \beta_y = \beta_\perp$). In the particular case of an octupole-like nonlinearity its gradient $O_3(s)$ in order to preserve the Hamiltonian should be distributed along the path $s$ as

$$O_3(s) \sim 1/\beta_\perp^3(s). \tag{1}$$

It can be expected that weak nonlinearities outside the special insertion will not break the KAM tori leaving the motion stable in a wide range of amplitudes.

In the case of a hollow electron beam which does not affect the beta-functions the longitudinal profiling can be achieved simply by variation of the solenoid magnetic field, while in the case of solid electron beam the situation is complicated by the effect of the lens itself on the beta-functions.

* Work supported by Fermi Research Alliance LLC. Under DE-AC02-07CH11359 with the U.S. DOE
# alexahin@fnal.gov

## HOLLOW E-LENS

A hollow electron lens was considered as the nonlinear element for creating a tunespread for Landau damping in the Recycler [11]. The lattice of the RR30 strait section (which housed the antiproton electron cooler in the past) was redesigned to have a 22.5 m drift with $\beta_x = \beta_y = \beta^*$ and $\alpha_x = \alpha_y = 0$ at its center. $\beta^*$ was varied in the range 8.7÷15.5 m so that the phase advance was $(0.4÷0.6)\pi$ over the drift.

The transverse e-lens profile was chosen as

$$\rho(r) = \rho_0[\exp(-r^2/2\sigma_1^2) - \exp(-r^2/2\sigma_2^2)] \quad (2)$$

with $\sigma_{1,2} \sim \beta_\perp^{3/4}$ to produce a gradient satisfying Eq. 1.

The effect of the hollow lens with (constant) $\sigma_2/\sigma_1$=0.85 on the proton tunes is illustrated in Fig. 2.

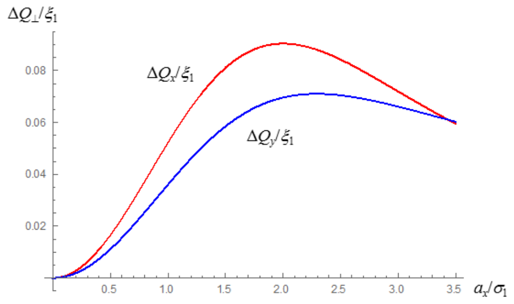


Figure 2: Tuneshifts as functions of relative horizontal amplitude $a_x/\sigma_1$ at $a_y$= 0. $\xi_1$ is the maximum tuneshift which the first term in Eq. 2 would produce alone.

Besides the electron lens, octupoles and special nonlinear magnets with strength also obeying Eq. 1 were simulated but incurred drastic reduction in dynamic aperture. On the contrary, the electron lens did not affect the dynamic aperture. The probable explanation is that the e-lens shifts both tunes in the same direction for all amplitudes thus avoiding some resonances.

### *Landau Damping by Hollow e-Lens*

Figure 3 shows histograms of the spectral density of transverse oscillations in a bunched beam after receiving a kick in the presence of a hollow electron lens. The lens transverse dimensions were chosen such that the maximum tuneshift, $\delta Q_{max}$, was reached at oscillations amplitude of $3.4\sigma_{beam}$, $\sigma_{beam}$ being the proton beam transverse r.m.s. size. With increasing $\delta Q_{max}$ the spectral peak is shifting (but not as much) and widens testifying of increased Landau damping. The synchrotron tune for this example was $Q_s = 0.02 \cdot Q_{SC}$ with $Q_{SC}$ being the maximum absolute value of the space charge tuneshift.

#### The Runaway Effect

It was naively expected that while a hollow electron lens shifts the tunes of protons with large amplitudes and compensates for the space charge tuneshift, it will not affect the coherent tune making the overlap possible. Actually there is an appreciable coherent tuneshift as well so that the gap with incoherent tunes remains (A. Burov). This can be called a run-away effect. The explanation is that the maximum contribution to the dispersion integral comes from particles with $\sim\sigma_{beam}$ transverse amplitudes which do see the e-lens field in the considered case.

A hint of this effect can be seen in Fig. 3. Still in the case of a bunched beam where the head and tail experience much weaker space charge defocusing the overlap does happen providing Landau damping.

The situation is different in the case of the ~ rectangular RF bucket as well as for the head-on colliding beam.

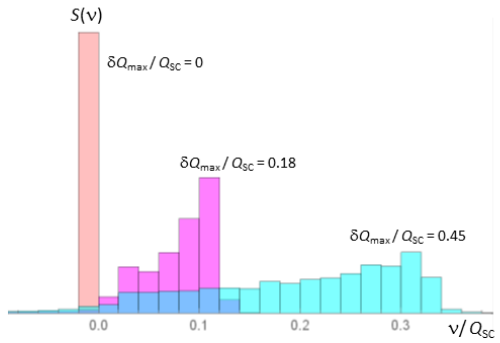


Figure 3: Spectral density of transverse oscillations in a bunch with space charge at indicated values of the maximum tuneshift due to a hollow electron lens.

## GAUSSIAN E-LENS

Limited applicability of the hollow electron lens necessitates the consideration of a solid lens, here we limit ourselves to a Gaussian transverse profile. Since the runaway effect is caused by particles with transverse amplitudes $\geq \sigma_{beam}$, we will look at a narrow "pencil" electron lens beam with the size smaller than the size of the proton beam, $\sigma_{lens} < \sigma_{beam}$.

Figure 4 shows the total tuneshift (SC + e-lens) for three values of e-lens strength.

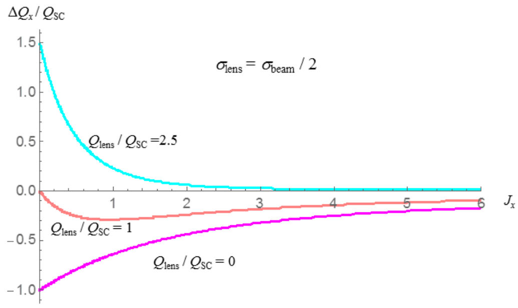


Figure 4: Tuneshift produced by space charge and a Gaussian e-lens with $\sigma_{lens} = \sigma_{beam}/2$ vs. the action variable $J_x$ normalized by the beam emittance.

### *Coasting Beam*

There is a limitation on the longitudinal bunch profile for which the eigenmode analysis of the Vlasov equation described in [12] can be applied. Besides Gaussian it can be constant which is a fair representation of a flat bunch in a multi-harmonic RF.

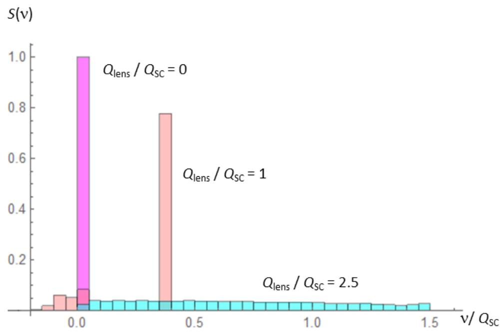


Figure 5: Spectral density of transverse oscillations in a coasting beam with space charge at indicated values of the maximum tuneshift due to a Gaussian electron lens.

The spectra for the same e-lens strength as in Fig. 4 are shown in Fig. 5. One can see that in order to intercept the runaway coherent tune the e-lens should be noticeably stronger than the space charge.

The absence of narrow peaks in the spectrum is a testimony of Landau damping but does not tell us how strong it is. For this purpose the technique of stability diagram can be employed. It shows the stability region in the plane of complex coherent tuneshift $\zeta$ produced by external impedances.

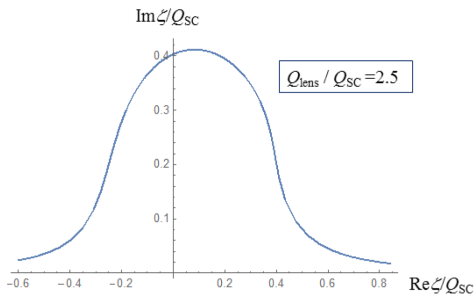


Figure 6: Stability diagram for coasting beam.

We use here the method based on the eigenmode analysis [12]. Figure 6 shows the stability diagram for the e-lens strength $Q_{\rm lens}$ / $Q_{\rm SC}$ =2.5. It proves that Gaussian lens can provide stability in the presence of large impedance no matter what the sign of its real part is (focusing or defocusing).

## *Bunched Beam*

With longitudinally bell-shaped bunch (Gaussian in our study) there is no need to make the e-beam transverse size small compared with the proton beam size. The analysis presented below was performed for $\sigma_{\rm lens} = \sigma_{\rm beam}$.

Stability diagrams were estimated analytically and calculated using the method of [12] for a range of e-lens strength parameters and synchrotron tunes $Q_s$. The results are summarized in Fig. 7. As the measure of Landau damping efficiency the boundary value $\Lambda$ = Im$\zeta_{\max}$ at Re$\zeta$ = 0 was chosen.

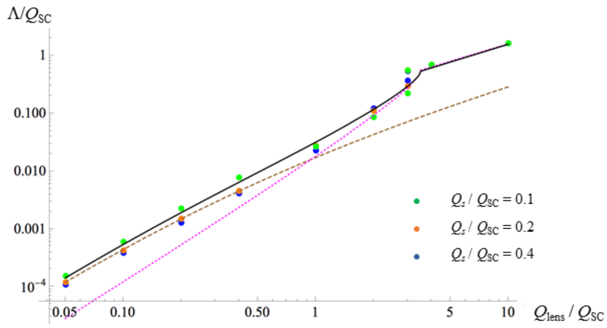


Figure 7: Landau damping rate vs e-lens strength normalized to $Q_{\rm SC}$. Dots: the Vlasov model, dashed lines: analytical approximations for weak and medium-strong e-lens, solid black line: integration of the two approximations [12].

# OUTLOOK

The presented results predict high efficiency of electron lenses in restoration of Landau damping. A few questions still remain open, such as dependence of the "runaway effect" on the thickness of the hollow e-lens, single-particle stability in the presence of a "pencil" electron beam, etc.

The analytical methods which we had used here should be complemented by numerical simulations and experimental studies planned at IOTA [9].

# REFERENCES

[1] A. W. Chao, *Physics of Collective Beam Instabilities in High Energy Accelerators* (John Wiley & Sons, New York,1993.

[2] K.Y. Ng, *Physics of Intensity Dependent Beam Instabilities* (World Scientific, 2006).

[3] L. Landau, J. Phys. USSR **10**, 25 (1946).

[4] J. S. Berg and F. Ruggiero, CERN Report No. CERN-SLAP-96-071-AP, 1996.

[5] A. Burov, "Nested Head-Tail Vlasov Solver", Phys. Rev. Accel. Beams **17**, 021007 (2014).

[6] V. Shiltsev, *Electron Lenses for Supercolliders* (Springer, 2016).

[7] V. Shiltsev et al., "Landau Damping of Beam Instabilities by Electron Lenses Phys. Rev. Lett. 119 (2017) 134802.

[8] V. Shiltsev, Phys. Rev. Accel. Beams **22**, 074801 (2019).

[9] G. Stancari, "IOTA Electron Lens: Status and Plans", FAST/IOTA Collaboration Meeting, Fermilab, 2019; https:// indico.fnal.gov/event/20279

[10] V. Danilov and S. Nagaitsev, "Nonlinear accelerator lattices with one and two analytic invariants", Phys. Rev. ST Accel. Beams 13, 084002 (2010).

[11] Y. Alexahin et al., NAPAC'16, Chicago, WEPOA17, p. 729 (2016).

[12] Y. Alexahin, A. Burov and V. Shiltsev, "Landau Damping with Electron Lenses in Space-Charge Dominated Beams", FNAL-TM-2655-APC (2017).

# BNS damping*

Alexander Novokhatski†, SLAC National Accelerator Laboratory, Menlo Park, USA

*Abstract*

Many years have passed since the invention of BNS damping, but it still attracts wide attention of accelerator physicists to implement this method in classical accelerators and future high gradient acceleration technique. In this article we recall initial background principles of the development of BNS damping.

## SOME HISTORY AS AN INTRODUCTION

In the middle of 70s of the last century the director of the Institute of Nuclear Physics at Novosibirsk (nowadays Budker Institute of Nuclear Physics), Gersh Itskovich Budker introduced a new small group of researchers under the leadership of Vladimir Balakin to study a new type of an accelerator for colliding beams. He called this future machine as "SuperLinac". Nowadays we know such type of accelerators as "Linear Colliders". The main task of the group was to investigate the possibility to achieve a high gradient acceleration of order of a 1 MV/cm and analyze possible beam dynamics problems and find solutions for them. It happened that it was not the only task. In parallel, we worked also on the proton ironless ring of 10 GeV, which Andrei Mikhailovich (as we really called Budker) extremely wanted to build. This machine could give a possibility to study very exciting physics of heavy nucleolus, predicted by Spartak Timofeyevich Belyaev, who was at that time a president of the Novosibirsk State University.

However, all studies on linear colliding beams were kept in secrete and it was forbidden to show or publish the results outside the laboratory. What happened later? In several years, our group led by the outstanding physicist Vladimir Balakin successfully solved many important problems of the linear collider project. We have developed a technology of manufacturing high-gradient accelerating structure. Using this technology, we designed, manufactured, and tested a single S-band cavity. We have achieved almost 2 MV/cm in this cavity. We have understood main beam dynamics problems of acceleration of intense bunches of electrons and positrons in a high gradient linear accelerator using analytic and numerical approach. We have developed a numerical code for calculation of the electromagnetic fields interacting with a beam in the accelerating structure. It was may be the very first code in the world for the wake field calculations. We have found solutions for almost all of them. Unfortunately, Andrei Mikhailovich died in 1977 just before he became a sixty. A new director Alexander Nikolayevich Skrinsky continued the activity on linear colliding beams at the lab. The "SuperLinac" project got an official name: VLEPP (colliding linear electron positron beams), as analog to the names of the circular colliding beam facilities developed in the lab: VEPP-1, VEPP-2, VEPP-3 and VEPP-4. And finally, the results of theoretical and experimental studies were presented outside the lab. The VLEPP project was first presented at the International Symposium devoted to 60-year anniversary of G. I. Budker and All-union particle accelerator Conference at Dubna [1-3]. The results published in the Russian language were immediately translated to English at SLAC [4-6].

The most famous result of the linear colliders study at Novosibirsk became a new method of damping the transverse instability of a single bunch in a linear accelerator. This method got the name "BNS damping" by the first letters of the inventors Balakin, Novokhatski and Smirnov. The method was first published in 1978, however references in many other publications correspond to our 5-years later publication [7] in the proceedings of the12$^{th}$ International Conference on High Energy Accelerators at Fermilab (1983). And after more than 10 years BNS damping was successfully tested at the SLAC linear accelerator and implemented for operation of the first linear collider SLC [8].

In the following chapters we give more details starting with the description of the electromagnetic forces acting on the bunch particles moving in the accelerating structure. Then we present an equation for the bunch particle motion in the present of energy spread. We discuss the physics of BNS damping using a two-particle model. Then we present analytic solutions of a simplified equation of motion and numerical solutions for the VLEPP linear collider parameters. We analyze the efficiency of the method and make comparison with the Landau damping.

## SINGLE BUNCH INSTABILITY

One of the main beam dynamics problems in a liner collider project was a transverse beam instability or beam break-up effect, discovered in operation of many linear accelerator including SLAC linac [9]. The transverse instability limits the intensity of the accelerating beams. High intensity beams are needed to achieve high luminosity of the beam collisions. Higher luminosity allows study of very rare events.

For the VLEPP project it was proposed to use a single high intensity short bunch. At that time, in comparison with a multi-bunch operation [10], it was not so much clear how a single short bunch interacts with an accelerating structure, what the beam break-up threshold can be? In the multi-bunch operation fields, exciting by passing by bunches accumulate in the structure. Accumulating fields are usually one or two eigen RF modes of the accelerating structure. A new bunch interacts with the field excited by the previously passed bunches. In a single bunch mode operation, all fields excited by the bunch particles are chasing the bunch because the field and the bunch particle moving with speed of light. There was a weak hope that a single

* Work supported by DoE contract DE-AC02-76SF005
† email address novo@slac.stanford.edu

bunch can have higher beam break-up threshold. To check it we need a reliable method for calculation of electromagnetic interaction of a charged bunch with a metal accelerating structure.

## *Electromagnetic fields and wake field code*

For calculating electromagnetic forces, we used a wake field approach. Assuming that a bunch is moving with a constant speed along the structure in a straight line. Then we can easily describe the charge and current distributions in time domain needed for Maxwell equations. The boundary conditions are determined by geometry of the accelerating structure and can be very complicated. It is not so simple to solve Maxwell equations analytically, but we can use numerical methods for this. We developed a stable numerical scheme for solving Maxwell equations in the time domain in the azimuthally symmetrical structures. An example of calculated field distribution of a bunch moving in accelerating structure is shown in Fig. 1.

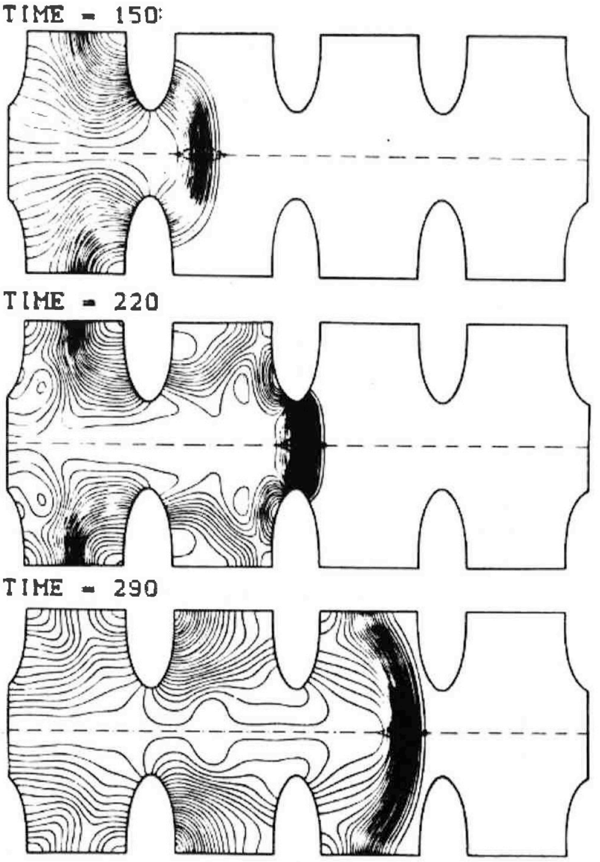


Figure 1: The dynamics of electric force lines of a charged bunch moving in “empty” periodic iris-loaded accelerating structure (1978).

This numerical scheme still in use and works very well for very short bunches [11-12]. In parallel with calculating of electromagnetic field components we calculate integrated forces (longitudinal and transverse) acting on the bunch particles. Then we average forces for a unit length of the structure.

$$F_{\parallel}(s,r_0)=\frac{1}{L}\int_{-L/2}^{L/2}E_z\left(z,r_0,t=\frac{z+s}{c}\right)dz \qquad L\to\infty$$
$$F_{\perp}(s,r_0)=\frac{1}{L}\int_{-L/2}^{L/2}\left(E_r\left(z,r_0,t=\frac{z+s}{c}\right)-H_{\varphi}\left(z,r_0,t=\frac{z+s}{c}\right)\right)dz \qquad (1)$$

## *Transverse force description*

The magnitude of the transverse force is determined by the structure geometry, by the shift of the bunch trajectory relative to the axes, by the bunch charge and the bunch length. Fig. 2 shows the distribution of the transverse force along the bunch for different bunch length.

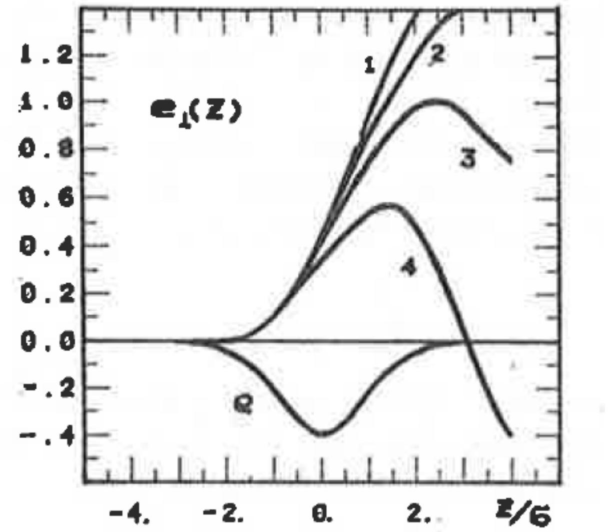


Figure 2: Transverse force acting on the bunch particles for bunches of different bunch length (1978). Line 1 is for a shorter bunch and line 4 is for a longer bunch.

Electromagnetic fields generated by a bunch in an accelerating structure have a defocusing action on the bunch particles if they travel off axes. The more leading particles are far away of axes the more effect on the following particles. Naturally, the force grows along the bunch. We may assume that a particle trajectory is not very far from the axes, so the dipole component of the excited field, which is proportional to the transverse coordinate, plays the main role. With our code we can calculate electromagnetic fields of a very short bunch. This gave us a possibility to derive an approximation for the Green’s function. With a Green’s function $g_{\perp}(s)$ we can present the dipole transverse force in the following way

$$F_{\perp}(s)=\frac{eQ}{4\pi\varepsilon_0 a_w^3}\int_{-\infty}^{s}\rho(\xi)X(\xi)g_{\perp}(\xi-s)d\xi \qquad (2)$$

$X(\xi)$ is a bunch particle transverse coordinate and $a_w$ is an effective parameter, characterizing the geometry of the accelerating structure. The Green’s function is a dimensionless function in this presentation. The bunch charge longitudinal distribution is normalized:

$$\int_{-\infty}^{\infty}\rho(\xi)d\xi=1 \qquad (3)$$

### *Equation for the transverse motion*

Now using the transvers force description, we can write an equation for a bunch particle transverse motion in a linear accelerator with a FODO focusing system

$$\frac{\partial}{\partial\tau}\left(\frac{\gamma(\tau,s)}{\gamma_0}\frac{\partial}{\partial\tau}X(\tau,s)\right)+\frac{\gamma(\tau,s)}{\gamma_0}\mu(\tau)^2X(\tau,s)= \\ =\int_{-\infty}^{s}\rho(\xi)X(\tau,\xi)g_{\perp}(s-\xi)d\xi \tag{4}$$

In this equation $\gamma(s)$ is a relativistic factor of a particle with a longitudinal position in the bunch $s$, $\gamma_0$ is the initial relativistic factor, which may depend upon the particle longitudinal position in the bunch. For simplicity of the equation we introduced a special parameter, a characteristic length of the accelerator where the transverse force produces a noticeable effect

$$L^* = a_w\sqrt{\frac{\gamma_0 mc^2}{\frac{eQ}{4\pi\varepsilon_0 a_w}}} \tag{5}$$

The characteristic length becomes smaller when the bunch charge increases. Also, in this equation we measure time and betatron wave vector (frequency) in characteristic length

$$t=\frac{\tau}{c}L^* \qquad \nu=\frac{\mu}{L^*} \tag{6}$$

It is interesting that solving the equation (4) for the case of a zero energy spread and strong focusing $\mu=\nu*L^*\geq 1$ we can find that characteristic length can be consider to be an instability growth rate parameter. The bunch emittance will grow exponentially as

$$\varepsilon\sim\exp\left(\sqrt{\frac{\tau}{\mu}}\right)=\exp\left(\frac{1}{L^*}\sqrt{\frac{ct}{\nu}}\right) \tag{7}$$

## PHYSICS OF BNS DAMPING

With a very precise description of the forces acting on the bunch particles we have found immediately in the beam dynamics study a very strong transverse instability of a single bunch. We can describe it in the following way. The particles of the head of a bunch do not experienced action of the wake field and freely oscillate in the focusing lattice at the betatron frequencies. However, this oscillation produce a periodical force for the particles of the tail of the bunch because they experience the action of the wake field. As the frequency of the force and the frequency of free oscillations are the same, then the amplitude of oscillations of the tail particles will grow up in time because of the resonance. Considering that this action goes through the entire bunch we got an exponential growth of the amplitude of the particle oscillations.

An immediate solution for cancelling the oscillation growth is to destroy the resonance, that means to give different betatron frequencies to the particle of the bunch head and particles of the bunch tail. It can be done in many different ways, but a simple solution is to utilize the fact that the betatron oscillation frequency depends by virtue of the chromaticity on the energy of the beam particles. So, if we give different energy to the particles then we will have different betatron frequencies. The difference in energy along the bunch must have a definite sigh. Since the transverse wake field introduces defocusing force, then we need the additional chromatic focusing to compensate defocusing. That means that particles of the bunch tail must have smaller energy. By accelerating the bunch behind the crest of the accelerating field, the tail particles gain less energy than the head. Therefore, the tail particles are focused more by the quadrupoles than the head. The longitudinal wake field actually helps to increase the energy spread. The tail particles loss more energy due to the action of this field. With increasing of the particle energy during the acceleration, the energy difference can be reduced. The beam break up effect becomes smaller $\sim \gamma_0/\gamma$ and the bunch is now moved ahead of the crest to reduce the energy spread in the beam. We can see that that BNS damping does not require any additional accelerator elements like special focusing elements. It can be easily applied to any linear accelerator, just change the phases of the klystrons along the linac.

### *Two-particle model*

We can get a reliable solution in a two-particle model. Assuming that we have particles with different betatron frequencies. The head particle has only oscillations due to the focusing system, but the tail particle has an additional force proportional to the transverse coordinate of the head particle

$$\frac{\partial^2}{\partial\tau^2}X_H(\tau)+\mu_H{}^2X_H(\tau)=0. \\ \frac{\partial^2}{\partial\tau^2}X_T(\tau)+\mu_T{}^2X(\tau)=X_H(\tau) \tag{8}$$

The solutions of these equations with an initial nonzero coordinate are

$$X_H(\tau)=\cos(\mu_H\tau) \\ X_T(\tau)=1+\frac{\cos(\mu_H\tau)-\cos(\mu_T\tau)}{\mu_H^2-\mu_T^2} \tag{9}$$

To keep the oscillation amplitude of tail particle we need the following condition for the difference of betatron frequencies

$$\frac{\Delta\mu}{\mu}\geq\frac{1}{2\mu^2} \tag{10}$$

Or

$$\frac{\Delta\nu}{\nu}=\frac{\Delta\mu}{\mu}\geq\frac{1}{2\mu^2}=\frac{1}{2\nu^2\left(L^*\right)^2}=\frac{1}{2\left(\nu a_W\right)^2}\frac{eQ/4\pi\varepsilon_0 a_W}{\gamma mc^2}$$

We can consider the minimum frequency spread needed to damp oscillation growth of the tail particle, to be the BNS damping condition.

$$\frac{\Delta\mu_{\min}}{\mu}=\frac{1}{2\mu^2} \tag{11}$$

## *Analytical solutions for many particles*

The equation for the particle motion (4) is rather complicated for analytical solution but can be easily solved by using the numerical methods. However, some properties of BNS damping can be found based on the analytical solutions of a simplified equation with the following assumption:

No acceleration $\frac{d\gamma}{d\tau}=0$

Bunch longitudinal distribution is constant

$$\rho(s)=const[0,1]$$

Green's function is constant

$$g(s)=const$$

Linear distribution of energy along the bunch

$$\gamma(s)=\gamma_0\left(1-\frac{\Delta\gamma}{\gamma_0}s\right)$$

Correspondent linear distribution of the betatron frequency

$$\mu(s)=\mu_0\left(1+\frac{\Delta\mu}{\mu_0}s\right)\quad \frac{\Delta\mu}{\mu_0}=\frac{\Delta\gamma}{\gamma_0}$$

Simplified equation takes the following form

$$\frac{\partial^2}{\partial\tau^2}X(\tau,s)+\mu(s)^2X(\tau,s)=\frac{\gamma_0}{\gamma(s)}\int_{-\infty}^{s}X(\tau,\xi)d\xi \tag{12}$$

We found a way to solve this equation analytically using the Laplace transformation because this problem is a problem with initial conditions. Laplace transform

$$V(p,s)=\int_0^{\infty}X(\tau,s)e^{-p\tau}d\tau \tag{13}$$

Using it we can get an analytical solution in the Laplace presentation

$$V(p,s)=\frac{\gamma_0}{\gamma(s)}\frac{pX_0}{\mu^2(s)+p^2}\left(\frac{\mu^2(s)+p^2}{\mu_0^2+p^2}\right)^{\eta}\times \\ \times\left(1-\mu_0\int_{\mu_0}^{\mu(s)}\left(\frac{\mu^2(s)+p^2}{\mu_0^2+p^2}\right)^{-\eta}d\tau\right) \tag{14}$$

Immediately we found a parameter $\eta$, which gives the ratio between the BNS condition (12) and total frequency spread

$$\eta=\frac{1}{2\mu_0\Delta\mu}=\frac{\frac{1}{2\mu_0^2}}{\frac{\Delta\mu}{\mu_0}} \tag{15}$$

The inverse Laplace transform is easy to derive for integer values of $\eta$

- $\boldsymbol{\eta}$ **=0** There are no transverse forces. Just to check the model. Free oscillations with natural frequencies

$$X(s,\tau)=X_0\frac{\gamma_0}{\gamma(s)}\cos(\mu(s)\tau)$$

- $\boldsymbol{\eta}$ **=2** Instability. Resonant build-up of oscillations at a frequency of the "head" particle

$$X(s,\tau)=X_0\frac{\gamma_0}{\gamma(s)}\cos(\mu_0\tau)+ \\ +X_0\frac{\gamma_0}{\gamma(s)}\frac{\mu^2(s)-\mu_0^2}{2\mu_0^2}(\mu_0\tau)\sin(\mu_0\tau)$$

- $\boldsymbol{\eta}$ **=-1** Instability. Resonant build-up of oscillations at the natural frequencies

$$X(s,\tau)=X_0\frac{\gamma_0}{\gamma(s)}\cos(\mu(s)\tau)+ \\ +X_0\frac{\gamma_0}{\gamma(s)}\frac{\mu^2(s)-\mu_0^2}{2\mu_0^2}(\mu(s)\tau)\sin(\mu(s)\tau)$$

- $\boldsymbol{\eta}$ **=1** BNS damping. All particles oscillate at the frequency of the "head" particle without any growth

$$X(s,\tau)=X_0\frac{\gamma_0}{\gamma(s)}\cos(\mu_0\tau)$$

This nice behavior of the bunch is possible for other combinations of the Green's function and bunch distribution.

- $\boldsymbol{\eta}$ **=1/2** One more exciting solution. The amplitude of oscillation of the "tail" particles is going down in time

$$X(s,\tau)=X_0\frac{\gamma_0}{\gamma(s)}J_0\left(\frac{\mu(s)-\mu_0}{2}\tau\right)\cos(\mu(s)\tau)$$

$J_0$ is the Bessel function of zero order. The amplitude of oscillations goes down as a square root of time. Unfortunately, analysis shows that this interesting result holds only for the constant Green's function.

## APPLICATION TO THE VLEPP PROJECT

Computer simulations with realistic Green's function and bunch distribution showed the same particle dynamics. Analysis of the longitudinal beam dynamics including longitudinal wake fields showed that it is possible to make a linear energy variation along the bunch. The results of the numerical integration of equation (4) exhibit the similar regularities of the transverse motion of the bunch particle. Fig. 3 gives the phase images (X X' plane) of particles along the bunch at different energy spread. The dependence of the bunch effective emittance upon the sign and the value of energy variation along the bunch is shown in Figure 4. One can see here the results of numerical simulation for the 100 GeV section of the accelerator VLEPP. As is seen, to suppress the transvers instability, an initial energy spread of 10% needs to be introduced. During the acceleration this linear spread can be decreased down to 3% and can reach a minimally achievable one on the final section. Without BNS damping the beam emittance could be many orders higher. The effect of application of BNS damping is is very strong.

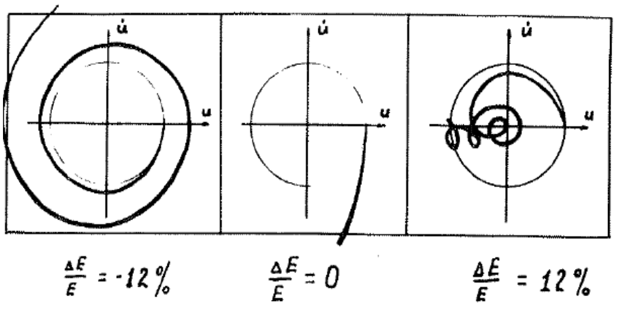


Figure 3: X' X phase plot for different energy spreads (1978)

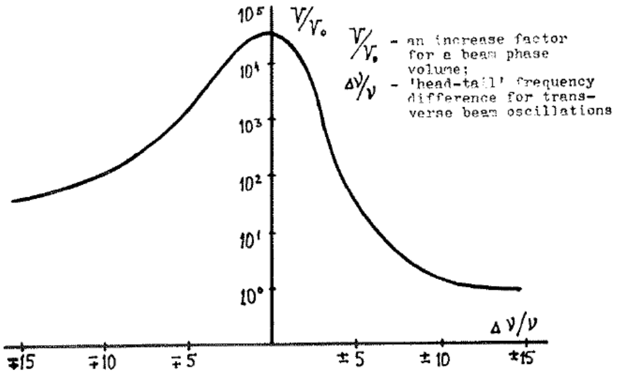


Figure 4: Relative emittance at the exit of the 100 GeV accelerator section versus the initial energy spread. With the initial energy spread of 12% the beam can reach at the section exit with a minimally achievable spread of 3% (1978)

## EFFICIENCY AND COMPARISON WITH LANDAU DAMPING

We would like to mention that the efficiency of the BNS damping strongly depends upon the focusing system. For higher betatron frequencies less frequency spread is needed, and much higher intensity bunch can be accelerated without emittance growth. This is in general good for any linear accelerator to have more periods of transverse oscillations, made by the bunch particles on the accelerator length. Very important the sign of the linear energy spread along the bunch to completely damp the instability. For the opposite sign of the energy spread, the instability growth rate decreases, but instability cannot be fully damped. Such feature is very close to Landau damping, where betatron oscillation frequencies are not corelated with the longitudinal positions of particles in the bunch. Usually is it a random distribution of betatron frequencies. This is the main difference between the damping methods. Maybe it is possible to use Landau damping to decrease the instability growth, however a comparison with BNS damping showed that Landau damping is not so effective as BNS damping. Fig. 5 shows comparison of BNS damping and Landau damping. The function of Landau damping is mirrored for negative values of energy spread.

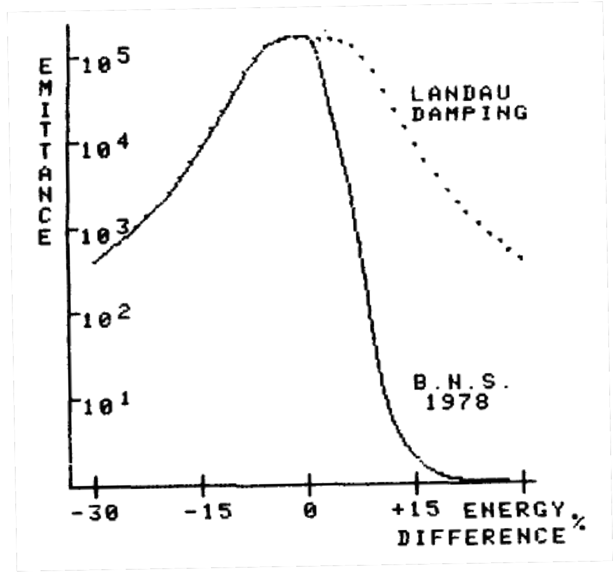


Figure5: Beam emittance upon the linear energy spread for BNS damping (a solid line) and for the case of Landau damping (a dotted line). For the negative values of energy spread the result form Landau damping is mirrored from positive values. One can see that Landau damping works something like BNS damping but for an opposite sign of the energy spread and cannot damp instability completely.

## CONCLUSION

- BNS damping is a very efficient method for damping the transverse instability in a linear accelerator
- Naturally, it works in the multi-bunch regime as well.
- SLC, the first linear collider using this method increased luminosity several times.
- BNS damping was effectively used in the injector of intense beams for the SLAC PEP-II B-factory.
- In the linear accelerators BNS damping works much better than Landau damping.

## ACKNOWLEDGEMENTS

It was a great time of the high energy accelerator physics activity in the world and I am very grateful to all people with whom I was lucky to work.

## REFERENCES

[1] V. E. Balakin, G. I. Budker, A. N. Skrinsky, "Feasibility of Creating of a Superhigh Colliding Electron-Positron Beam Facility", *in Proc. of Int. Symposium on Problems of high energy physics and controlled fusion*, Novosibirsk, 1978, Nauka, Moscow, 1981, p.11. Also, in *the Proc. of the 6th All-Union Conf. on Accelerators of charge particles*, Dubna, 1978. p.27 (in Russian).

[2] V. E. Balakin, O. N. Brezhnev, A. V. Novokhatsky, Yu. I. Semenov, "Accelerating Structure of a Colliding Linear Electron-Positron Beam (VLEPP). Investigation of the Maximum

Attainable Accelerating rate", *in Proc. of the 6th All-Union Conf. on Accelerators of charge particles*, Dubna, 1978, p. 147.

[3] V. E. Balakin, I. A. Koop, A. V. Novokhatski, A. N. Skrinsky, V. P. Smirnov, "Beam Dynamics of a Colliding Linear Electron-Positron Beam (VLEPP)", *in Proc. of the 6th All-Union Conf. on Accelerators of charge particles*, Dubna, 1978, p.143

[4] V. E. Balakin, G. I. Budker, A. N. Skrinsky, "Feasibility of Creating of a Superhigh Colliding Electron-Positron Beam Facility", *Report Number:* SLAC-TRANS-0186, November 1978.

[5] V. E. Balakin, O. N. Brezhnev, A. V. Novokhatsky, Yu. I. Semenov, "Accelerating Structure of a Colliding Linear Electron-Positron Beam (VLEPP). Investigation of the Maximum Attainable Accelerating Rate", *Report Number:* SLAC-TRANS-0187, November 1978.

[6] V. E. Balakin, I. A. Koop, A. V. Novokhatski, A. N. Skrinsky, V. P. Smirnov, "Beam Dynamics of a Colliding Linear Electron-Positron Beam (VLEPP)", *Report Number:* SLAC-TRANS-0188, November 1978.

[7] V. E. Balakin, A. V. Novokhatsky, V. P. Smirnov, "VLEPP: Transverse beam dynamics", *in Proc. of the 12th Int. Conf. on High Energy Accelerators,* Fermilab, (1983), p.119.

[8] J. T. Seeman, F.-J. Decker, R. L. Holtzapple, W. L. Spence, "Measured Optimum BNS Damping Configuration of the SLC Linac", *in Proc. of the 1993 IEEE Particle Accelerator Conf.*, Washington, D.C., (1993), p. 3234.

[9] O. H. Altenmueller, E. V. Farinholt , Z. D. Farkas, W. B. Herrmannsfeldt, H. A. Hogg, R. F. Koontz, C. J. Kruse, G. A. Loew, and R. H. Miller, "Beam Break-Up Experiments at SLAC", *in Proc. of the 1966 Linear Accelerator Conf.*, Los Alamos, New Mexico (1966), p. 267

[10] W. K. H. Panofsky and M. Bander, "Asymptotic Theory of Beam Break-Up in Linear Accelerators", *The Rev. of Scientific Instruments,* V. 39, Num. 2, p. 206, Feb.1968.

[10] A. Novokhatski, "A new Green's function for the wake potential calculation of the SLAC S-band constant gradient accelerating section", *Nucl. Instr. and Meth. In Phys. Research* A 684(2012), pp. 46–51.

[12] A. Novokhatski and A. Mosnier, "Short bunch wake potentials for a chain of TESLA cavities", *Nucl. Instr. and Meth. In Phys. Research* A 763(2014), pp. 202–209

# MITIGATION OF COLLECTIVE EFFECTS BY OPTICS OPTIMISATION

Y. Papaphilippou, F. Antoniou and H. Bartosik, CERN, Geneva, Switzerland

*Abstract*

This paper covers recent progress in the design of optics solutions to minimize collective effects such as beam instabilities, intra-beam scattering or space charge in hadron and lepton rings. The necessary steps are reviewed for designing the optics of high-intensity and high-brightness synchrotrons but also ultra-low emittance lepton storage rings, whose performance is strongly dominated by collective effects. Particular emphasis is given to proposed and existing designs illustrated by simulations and beam measurements.

## INTRODUCTION

The physics quantities parametrising the performance of a large variety of hadron and lepton rings, as, for example, the average beam power of synchrotron based proton drivers, the luminosity of colliders, the brightness of their associated injectors or the brilliance of X-ray storage rings, are proportional to the beam intensity or to its ratio with the beam dimensions. The modern tendency is to push the performance frontiers towards extreme conditions, i.e. the highest beam intensity contained within ultra-low beam volumes, under which the collective behaviour of the beam becomes predominant. It is thus of paramount importance to take measures in order to alleviate collective effects in the early phase of the design, which usually begins with the optimisation of the linear optics.

This is by far not an easy task, as already there is a large amount of optics conditions based on single-particle constraints to be satisfied, including non-linear dynamics. Thereby, the parameter space becomes entangled and difficult to control and optimise. One should rely on analytical and numerical methods for obtaining a global parameterisation, including collective effects.

In the case of rings in operation, dealing with collective effects usually implicates mitigation techniques based on the use of multi-pole magnets [1] or higher harmonic RF cavities [2] for providing Landau damping, dedicated feedback systems [3] or the reduction of the beam interaction with its environment through careful vacuum and low-impedance component design [4]. Changing the linear optics, without major upgrade involving radical modifications of the machine configuration, is an unconventional approach, since it is subject to the constraints of the existing magnet and powering systems. It can be even more challenging because of its interplay with the already optimised operation of critical systems, such as beam transfer elements or RF. On the other hand, if a viable solution is found, it can be a very cost effective way to overcome existing intensity or brightness limits. In addition, it may be used to relax tolerances associated with the above-mentioned mitigation measures for reducing collective effects.

This paper is organised as follows: after describing the basic linear optics parameters which affect collective effects, optics design strategies are reviewed, underlining specific examples of high-power or high-brightness synchrotrons and low emittance damping rings, studied in recent years, mainly at CERN. Of particular interest is the application of these approaches to operating rings with illustrations from the direct impact of the optics modifications to machine performance.

## IMPACT OF OPTICS PARAMETERS ON COLLECTIVE EFFECTS

In this section, three fundamental quantities that affect collective effects are described, following the logical route of an optics study: starting from the most basic one, the beam energy, passing to the most fundamental, the transverse beam sizes and ending with the phase slip factor, which will be shown to be most intimately connected to the collective beam behaviour.

### *Beam energy*

The beam energy is one among the basic parameters that have to be specified even before starting the optics design of a ring. Although, strictly speaking, it cannot be considered as an optics constraint, it is indirectly related through the integrated magnet strengths and the size of the lattice cells, i.e. the ring circumference. At the same time, in the absence of strong synchrotron radiation damping, the transverse emittance is inversely proportional to the energy, thus reducing the physical beam size. Almost all collective effects become less pronounced with increasing beam energy, with the notable exception of the electron cloud instability thresholds [5]. Hence, for hadron rings, it is natural to target always the highest possible energy although this heavily depends on the users' physics needs, the reach of the pre-injectors and finally on cost. In the case of beams dominated by synchrotron radiation damping, e.g. for ultra-low emittance $e^+/e^-$ rings, the quadratic dependence of the horizontal equilibrium emittance to the energy puts an additional restriction to this increase, and a careful optimisation has to be performed, in order to meet the specific design targets and reaching high brightness.

### *Betatron functions*

Transverse beam sizes are also playing an important role to the collective beam behaviour, especially in the case of self-induced fields. For example, the space-charge tune-shift [6] and IBS growth rates [7] are inversely proportional to their product raised to a certain power. For high-intensity/power rings, there is usually no specific preference on the size of transverse emittances and the trend is to produce them large enough, for limiting the aforementioned effects. When the performance target is high brightness, which corresponds to small (transverse) emittances, the optics is the only "knob" for increasing beam sizes. For hadron rings, the FODO cells are well suited for this, due to the alternating behaviour of the optics functions. In particular, weaker focusing can maximise not only betatron beam sizes but also their dispersive part (through the contribution of momentum spread and dispersion), within the limits set by the machine aperture. In the case of $e^+/e^-$ rings targeting low emittances, doublet-like cells are usually employed for minimising horizontal beam sizes. On the other hand, the vertical beta functions can be increased, especially along the bending magnets, where the horizontal ones are small. Although this strategy is valid for space-charge or IBS, beam current thresholds of instabilities such as transverse mode coupling or coupled bunch, present an opposite dependence and call for a reduction of the average (vertical) beta functions. Finally, the enhancement of betatron functions at the location of non-linear magnetic elements can provide additional tune-shift with amplitude for Landau damping in case of need [8].

### *Slippage factor*

The slippage (or phase slip) factor $\eta$ is defined as the rate of change of the revolution frequency with the momentum deviation. At leading order, it is a function of the relativistic $\gamma$ factor (i.e. the energy) and the momentum compaction factor $\alpha_p$:

$$\eta = \alpha_p - \frac{1}{\gamma^2} \ . \tag{1}$$

The momentum compaction factor is the rate of change of the circumference $C$ with the momentum spread and, again at leading order, it is given by

$$\alpha_p = \frac{1}{C}\oint \frac{D_x(s)}{\rho(s)} ds \ , \tag{2}$$

which depends clearly on the variation of the horizontal dispersion function along the bending magnets. The phase slip factor unites transverse and longitudinal particle motion. In fact, the synchrotron frequency or the bunch length are proportional to $\eta^{1/2}$, which means that increasing the slippage factor makes synchrotron motion faster, with an equivalent increase of the bunch length.

The phase slip factor vanishes when $\gamma = \alpha_p^{-1/2} \equiv \gamma_t$ and the corresponding energy is named transition energy. It is widely known, since the commissioning of the first synchrotrons, that crossing transition can cause various harmful effects with respect to the collective behaviour of the beam [9], as the longitudinal motion basically freezes, at this point. Although several transition crossing schemes have been proposed and operated reliably in synchrotrons like the CERN PS for more than 40 years (see [10] and references therein), the call for beams with higher intensity (or power) resulted in the consideration of ring designs which avoid transition, either by injecting above ($\eta > 0$), or always remaining below ($\eta < 0$) transition energy. The former case is almost always true for electron/positron rings above a few hundred MeV (unless $\alpha_p < 0$). For hadron rings, it requires the combination of high energy (i.e. large circumference) and a large momentum compaction, which is translated to larger dispersion excursions and, generally speaking, weaker focusing, thereby resulting in larger beam sizes [11]. For remaining below transition, the operating energy range has to be kept narrow and a positive momentum compaction factor should be low, which points towards stronger focusing and smaller beam sizes. The case of negative momentum compaction (NMC) [12] is indeed very interesting because the beam remains always below transition independent of energy. Again, as in the case of the rings remaining above transition, the need to excite dispersion oscillations for getting an overall negative dispersion integral on the bends, results in larger beam sizes.

The above discussion is even more interesting when combined with the dependence of intensity thresholds for most transverse and longitudinal instabilities to the absolute value of the slippage factor [1]. A large slip factor provides additional spread in the synchrotron tunes, thereby increasing Landau damping. Although the particular characteristics of each machine may direct to different optics optimisation routes, the above mentioned simple considerations trace some generic guidelines for reducing collective effects, i.e. increase of the slippage factor (in absolute) combined with increased beam sizes can be achieved simultaneously above transition, or below transition and negative momentum compaction. Remaining below transition has the additional benefit of enabling the damping of the lowest head-tail instability modes with negative chromaticity [1], as the natural one, hence avoiding the use of strong sextupoles which excite resonances and induce beam losses.

## HIGH-POWER SYNCHROTRONS

Recent optics design of high-intensity and/or high-power rings such as the J-Parc main ring [13], the PS2 [14], or the High-Power PS [15] are based on NMC arc cells, for avoiding transition and reducing losses. These are sequences of modified FODO cells with an increased number of quadrupole families (up to four) for inducing negative dispersion, leading to an overall "imaginary" $\gamma_t$ [12]. In that case, the absolute value of the slippage factor could be increased for raising instability thresholds but also because a fast synchrotron frequency would be beneficial for longitudinal beam manipulation [16]. A complete picture of the achievable tuning range of a ring such as the PS2 can be obtained by the Global Analysis of all Stable Solutions

(GLASS), a numerical method pioneered in low emittance rings [18], where all possible quadrupole configurations (within some gradient limits) providing stable solutions are obtained, together with the optics parameters associated to them. In the top part of Fig. 1, the imaginary transition $\gamma_t$ is presented for all stable solutions in the tune diagram, along with resonance lines up to 3rd order. Low imaginary values of $\gamma_t$ (i.e. large absolute values of the momentum compaction), indicated in blue are obtained for higher horizontal tunes, where there is large flexibility for the vertical tunes. In the bottom part of the figure, the geometrical acceptance is computed for the most demanding beam parameters with respect to emittance. The red colour corresponds to small acceptance (above a limit of 3.5 $\sigma$), which means larger beam sizes. The trend shows that the larger sizes (red colour) are obtained for lower vertical tunes. This type of global analysis including linear and non-linear dynamics constraints was used for choosing the working point during the conceptual design of the PS2 ring, and locate it at ($Q_x$,$Q_y$)=(11.81,6.71), with $\gamma_t = 25.3i$ [17].

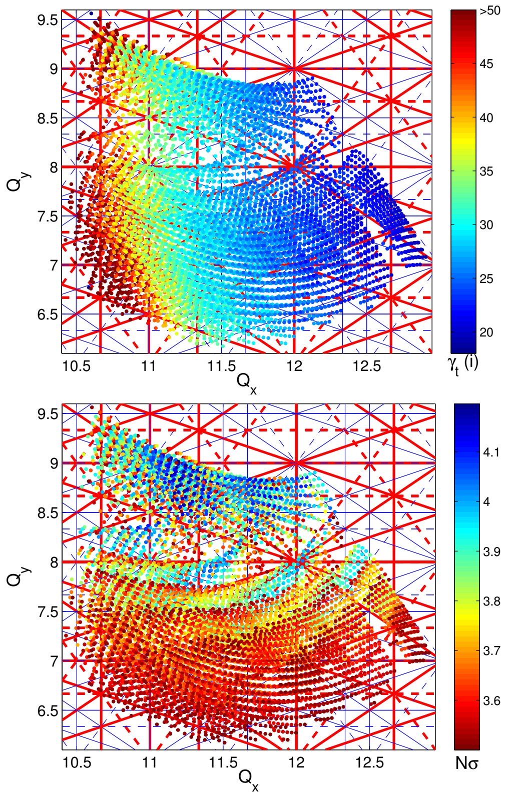


Figure 1: Transition energy $\gamma_t$ (top) and geometrical acceptance in units of beam sizes N$_\sigma$ (bottom), for a global scan of optics solutions in the tune diagram (showing resonances up to $3^{rd}$ order), with blue corresponding to lower $\gamma_t$ or larger acceptance [17].

## LOW EMITTANCE RINGS

The present trend of ultra-low emittance rings is to target the highest beam intensities within the smallest dimensions, at least in the transverse plane. The additional complication in the case of damping rings (DRs) for linear colliders is that they aim to produce low longitudinal emittances, as well. The output beam dimensions are largely dominated by IBS and even space-charge effects become important, especially in the vertical plane. A careful optimisation of the optics parameters is crucial for reducing these effects and obtaining a solid conceptual design [20].

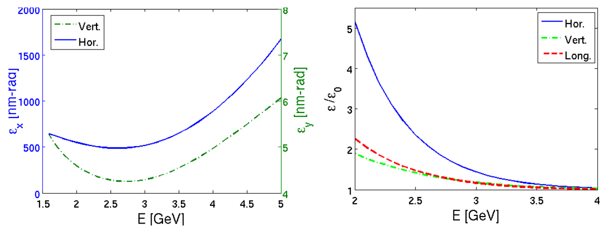


Figure 2: Steady-state emittances (left) and their blow-up (right) due to IBS, as a function of the energy [20].

### *Mitigating collective effects in the CLIC DRs*

Due to the fact that not only the IBS growth rates but also the equilibrium emittances vary with energy, it is important to find their interdependence, when the IBS effect is included [21]. Evaluated through a modified version of the Piwinski method [22], and for constant longitudinal emittance, the dependence of the steady state transverse emittances of the CLIC DRs on the energy is plotted in Fig. 2 (left). A broad minimum is observed around 2.6 GeV for both horizontal (blue) and vertical planes (green). The IBS effect becomes weaker with the increase of energy, as shown in Fig. 2 (right), where the emittance blow-up for all beam dimensions is presented. Although higher energies may be desirable for reducing further collective effects, the output emittance is increased above the target value, due to the domination of quantum excitation. In this respect, it was decided to increase the CLIC DR energy to 2.86 GeV, already reducing the IBS impact by a factor of two, as compared to earlier designs at 2.42 GeV [21].

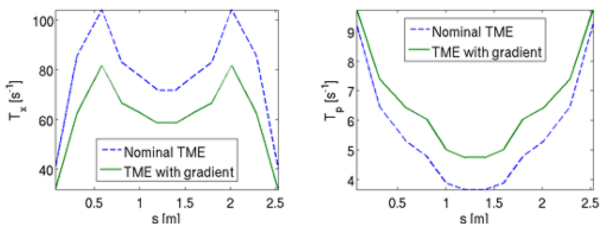


Figure 3: The horizontal (left) and longitudinal (right) IBS growth rate evolution for a standard TME cell (blue dashed) and a TME cell with a dipole with gradient (green).

In modern low emittance rings, theoretical minimum emittance (TME) arc cells or multi bend achromats are employed. In order to reach minimum emittance, the horizontal beam optics is quite constrained, whereas the verti-

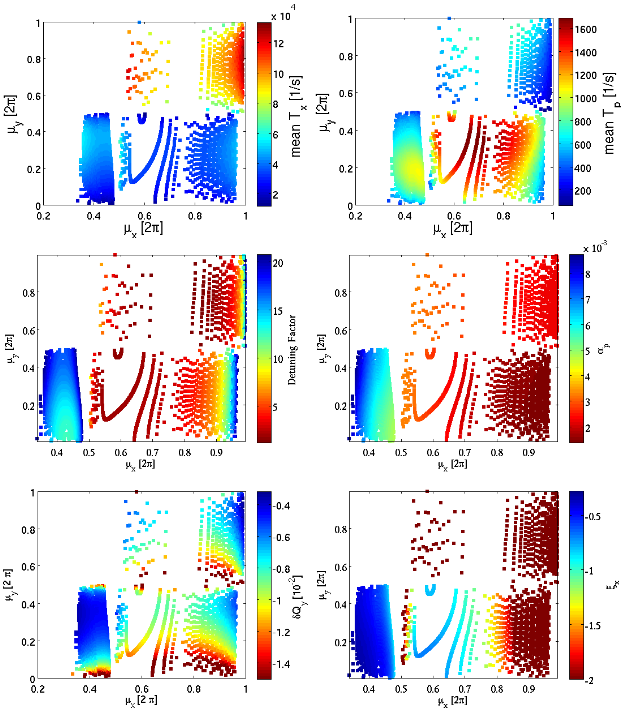


Figure 4: Analytical parameterization of the TME cell phase advances with the IBS horizontal (top, left) and longitudinal (top, right) growth rates, the detuning factor (middle, left), the momentum compaction factor (middle, right), the horizontal chromaticity (bottom, left) and the Laslett tune shift (bottom, right) [20].

cal one is free, but also completely determined by the two quadrupole families of the cell. It turns out that the vertical beta function reaches a minimum at the same location as the horizontal, which is the worst case for IBS. A way to reverse this tendency, is to use a combined function dipole with a low defocusing gradient. Although this gradient does not provide a significant effect to the emittance reduction, it reverses the behaviour of the vertical beta function at the middle of the dipole, maximizing the vertical beam size at that location, and thus reducing IBS growth rates [23]. This is shown in Fig. 3, where the horizontal (left) and longitudinal (right) IBS growth rate evolution are presented for a standard TME cell (blue dashed lines) and compared to the corresponding ones when the dipole includes a vertical focusing gradient (green curves). A reduction of the horizontal growth rate of almost a factor of two can be achieved in the shown example corresponding to the CLIC damping rings arc cell, by allowing a smaller increase to the longitudinal IBS growth rate.

A crucial step in the optimisation of the TME cell with respect to its impact on collective effects is the analytical derivation of the two quadrupole focal lengths, in thin lens approximation, depending only on the horizontal optics functions at the centre of the dipole and the drift space lengths [20, 24]. Using this representation, the dependence of various parameters on the cell phase advances in the case of the CLIC DRs are presented in Fig. 4, including the aver-

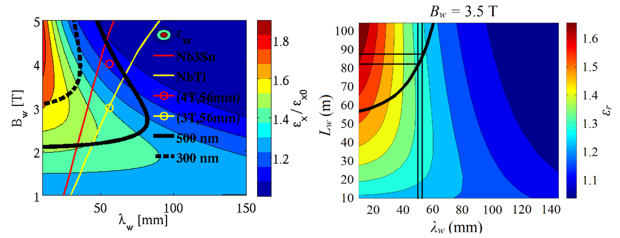


Figure 5: Dependence of the steady state emittance ratio with the equilibrium emittance as a function of the wiggler peak field and period (left) [20, 26] and as a function of the total wiggler length and period for a 3.5 T peak field (right) [27].

age IBS growth rates (top), the detuning from the minimum emittance (middle, left) the momentum compaction factor (middle, right), the vertical space-charge tune-shift (bottom, left) and the horizontal chromaticity (bottom, right). This parameterisation permitted to find the best compromise for the phase advances (between 0.4 and 0.5) where the IBS growth rates, the horizontal and vertical chromaticities and the Laslett tune shift are minimized, while the momentum compaction factor is maximized. These low phase advances correspond to emittances that deviate from the absolute minimum by a factor of around 15, as shown in Fig. 4 (middle left). Even at this large detuning factor, the TMEs are preferable for their compactness, in particular for a ring in which radiation damping is dominated by wigglers. The use of variable bends with gradient in the TME cell was also studied using a similar approach, further reducing the IBS growth rates [25].

A similar study was performed in order to find the optimal wiggler field and wavelength, while minimising the IBS effect [20, 25–27]. In Fig. 5 (left), the steady state emittance ratio with the equilibrium emittance as a function of the wiggler peak field and period is presented [20, 26]. The limits for the two superconducting technologies are shown in yellow (NbTi) and red (Nb3Sn) and the 300 nm and 500 nm target steady state emittance contours in black. Based on these studies, the highest field within the limit of technology would be desirable, but a moderate wavelength is necessary for reducing IBS. At the same time, as shown in Fig. 5 (right), by raising the field and using Nb3Sn wire technology, the reduction of the ring circumference can be also achieved, with beneficial impact to all type of collective effects, including to a potential impedance reduction [25, 27]. These specifications were used for the superconducting wiggler prototype and short model developed for the CLIC DRs [26, 27].

## HIGH-BRIGHTNESS SYNCHROTRONS

Hadron collider injectors need to achieve the highest brightness with the smallest possible losses. A typical example is the CERN SPS whose performance limitations and their mitigations for LHC beams are the subject of a study group [28], in view of reaching the required beam parameters for the high luminosity LHC (HL-LHC). The upgrade of the main 200 MHz RF system will solve beam loading issues for reaching higher intensities, but a variety of single and multi-bunch instabilities remain to be confronted. The transverse mode coupling instability (TMCI) in the vertical plane and e-cloud instability (ECI) for 25 ns beams are the most prominent transverse problems, especially for HL-LHC intensities. Longitudinal instabilities necessitate the use of a higher harmonic 800 MHz RF system as Landau cavity and the application of controlled longitudinal emittance blow-up throughout the ramp. For constant longitudinal bunch parameters and matched RF-voltage, higher intensity thresholds for the above instabilities are expected when increasing the phase slip factor.

### *Lowering transition energy in the SPS*

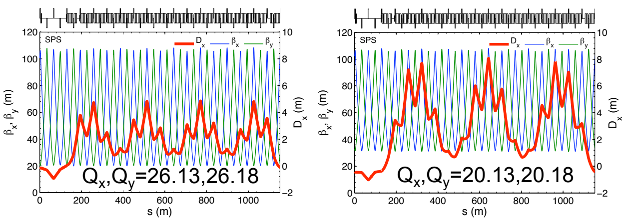


Figure 6: Nominal optics (Q26) and modified (Q20) optics of the SPS (1/6 of the circumference) [29].

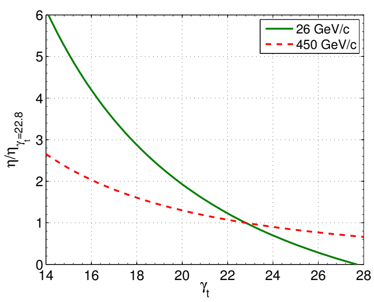


Figure 7: Slippage factor $\eta$ relative to the value of the nominal optics (nominal $\gamma_t = 22.8$) as a function of $\gamma_t$ [29].

The SPS has a super-symmetry of 6 with a regular FODO lattice built of 108 cells, 16 per arc and 2 per long straight section. In the nominal SPS optics (called Q26), the phase advance per FODO cell is close to $\pi/2$, resulting in betatron tunes between 26 and 27. Low dispersion in the long straight sections is achieved setting the arc phase advance to $4 \cdot 2\pi$. Figure 6 (left) shows the optics functions in the SPS lattice for the nominal optics. The LHC-type proton beams are injected at 26 GeV/c ($\gamma = 27.7$), i.e. above transition ($\gamma_t = 22.8$). By reducing $\gamma_t$, the slippage factor is increased throughout the acceleration cycle with the largest relative gain at injection energy, as shown in Fig. 7, where $\eta$ normalized to the value in the nominal SPS optics ($\eta_{\mathrm{nom}}$) is plotted as a function of $\gamma_t$, for injection and extraction energy. Significant gain of beam stability can be expected for a relatively small reduction of $\gamma_t$, especially in the low energy part of the acceleration cycle.

In 2010, alternative optics solutions for modifying $\gamma_t$ of the SPS were investigated [29]. Based on the fact that in a regular FODO lattice, the transition energy is approximately equal to the horizontal tune, $\gamma_t$ can be lowered by reducing the horizontal phase advance around the ring. One of the possible solutions, with low dispersion in the long straight sections, is obtained by reducing the arc phase advance by $2\pi$, i.e. $\mu_x, \mu_y \approx 3 \cdot 2\pi$ and the machine tunes are close to 20 (“Q20 optics”). Figure 6 (right) shows the corresponding optics functions for one super-period of the SPS. Note that in comparison to the nominal optics (“Q26”), the dispersion function follows 3 instead of 4 big oscillations along the arc with peak values increased from 4.5 m to 8 m. In this case, the transition energy is lowered from $\gamma_t = 22.8$ in the nominal optics to $\gamma_t = 18$ and $\eta$ is increased by a factor 2.85 at injection and 1.6 at extraction energy (Fig. 7). The maximum $\beta$-function values are the same in both optics, whereas the minima are increased by about 50%. The optics modification is mostly affecting peak dispersion which is almost doubled. The fractional tunes have been chosen identical to the nominal optics in order to allow for direct comparison in experimental studies.

### *Transverse mode coupling instability*

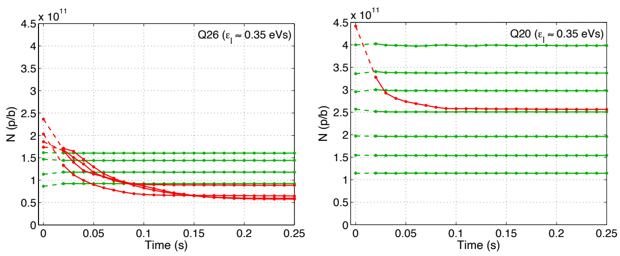


Figure 8: Examples of the intensity evolution as a function of time after injection in the Q26 optics (left) and the Q20 optics (right). Green curves correspond to stable beam conditions, red traces indicate cases above the TMCI threshold [33].

A series of measurements with high-intensity single bunches were conducted [30–33] in order to quantify the benefit of the Q20 optics with respect to TMCI. In the nominal optics, the threshold is found at $1.6\times10^{11}$ p/b, for zero chromaticity, as shown in Fig. 8 (left) [33]. In order to pass this threshold with Q26, the vertical chromaticity has to be increased so much that the losses are excessive due to single-particle effects. In the Q20 optics, it was demonstrated that up to $4\times10^{11}$ could be injected with no sign of the TMCI and low chromaticity, as shown in Fig. 8 (right) [33]. Such high intensity single bunches were already sent to the LHC for beam studies [34].

### *Electron cloud*

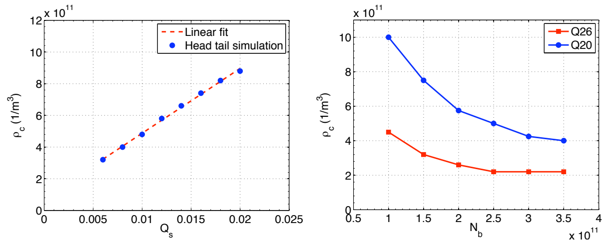


Figure 9: Instability threshold density $\rho_c$ as function of the synchrotron tune for constant bunch parameters (left) and the predicted linear dependence. ECI thresholds for various intensities comparing the nominal (red) with the low $\gamma_t$ SPS optics (blue) [36].

Since the ECI threshold scales with the synchrotron tune, as shown in Fig. 9 (left) [35], a clear benefit from the larger $\eta$ in the Q20 optics is expected. Numerical simulations were performed, assuming that the electrons are confined in bending magnets [36]. The expected threshold electron density $\rho_c$ for the ECI instability in the nominal (red) and the Q20 optics (blue), as a function of the bunch intensity $N_b$ at injection energy, for matched RF voltages, is presented in Fig. 9 (right). Clearly, higher thresholds are predicted for Q20.

### *Longitudinal multi-bunch instabilities*

In the Q26 nominal SPS optics the longitudinal multi-bunch instability has a very low intensity threshold, which is decreasing with the beam energy. It is expected that for RF voltage programs providing similar beam parameters (emittances, bunch lengths) the corresponding instability threshold is higher in the Q20 optics. Figure 10 presents the calculated narrow band impedance thresholds along the cycle for both optics in the 200 MHz single RF system for a longitudinal emittance of $\epsilon_l = 0.5$ eV.s and the corresponding voltage programs. For better comparison a constant filling factor $q_p = 0.9$ (in momentum) is chosen. Note that the impedance threshold reaches its minimal value at flat top for both optics.

To stabilize the LHC beam at flat top in the Q26 optics, controlled longitudinal emittance blow-up is performed during the ramp, in combination with the use of a double harmonic RF system (800 MHz) in bunch shortening mode. The maximum voltage of the 200 MHz RF system is needed in order to shorten the bunches for beam transfer to the LHC 400 MHz bucket. Due to the limited RF voltage, bunches with the same longitudinal emittance at extraction will be longer in the Q20 optics. In fact, for the same longitudinal bunch parameters of a stationary bucket, the required voltage would need to be scaled with $\eta$. However, the longitudinal instability threshold at 450 GeV/c is about 50% higher in the Q20 optics and therefore less or no controlled longitudinal emittance blow-up is required compared to the nominal optics, for achieving the same beam stability.

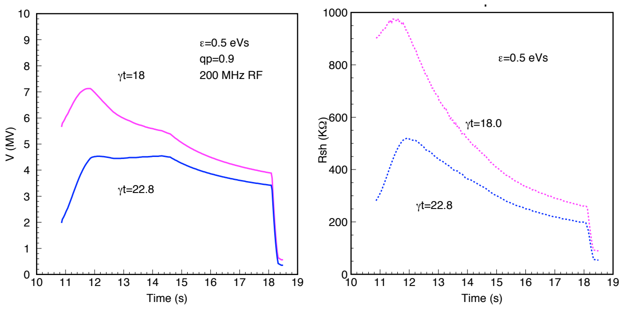


Figure 10: Voltage programs (left) and narrow-band impedance thresholds (right) through the cycle for Q26 (blue curve) and Q20 (magenta curve) optics in a single RF system for longitudinal emittance $\epsilon_l = 0.5$ eV.s. Acceleration starts at 10.86 s.

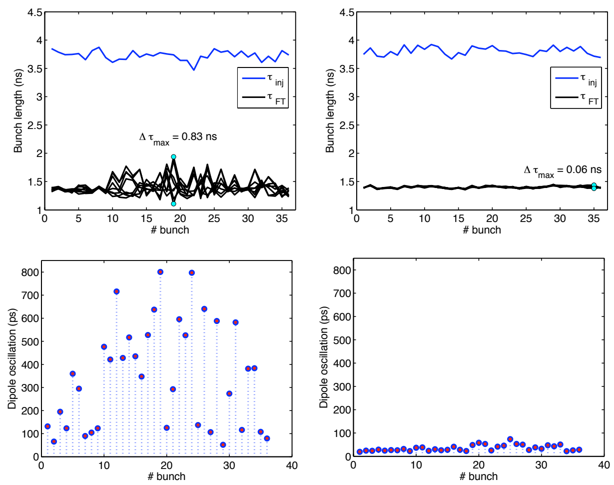


Figure 11: Bunch length (top) and bunch position oscillations (bottom), at flat top, for the bunches of a single batch 50 ns LHC beam, for Q26 (left) and for Q20 (right) [30–32].

Figure 11 shows a comparison of the beam stability (bunch length and bunch position) between the two optics, for one 50 ns LHC batch with $1.6 \times 10^{11}$ p/b. The Q20 optics is stable even in the absence of emittance blow-up, with mean bunch length of around $\tau = 1.45$ ns at flat top, which is compatible with injection into the LHC.

The low transition energy optics in the SPS became operational in September 2012. The switch to this new optics was very smooth, allowing very high brightness beams to be delivered to the LHC providing record luminosities [34]. An indication of the increased brightness delivered to the LHC is presented in Fig. 12, where the mean bunch intensity divided by the average of the horizontal and vertical emittance is plotted along the different LHC fills, for the second part of 2012. The green triangles represent the brightness delivered in the LHC flat bottom using the nominal Q26 optics, whereas the blue diamonds show the one

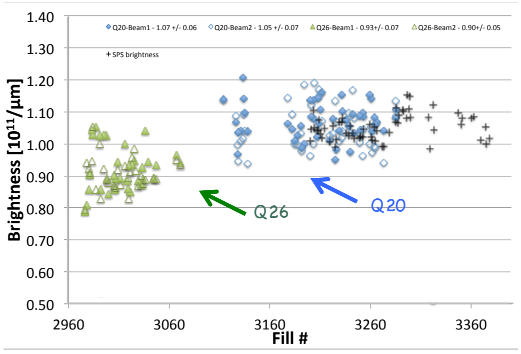


Figure 12: Average intensity over mean emittance (brightness) along the run, during the SPS operation with the nominal (green triangles) and the Q20 (blue diamonds) optics, in the LHC flat bottom for both beams. The SPS brightness since the Q20 deployment is represented by the black crosses.

corresponding to the Q20 optics, for both beams. There was a clear brightness increase at the LHC flat bottom of the order of 15 % on average, due to the Q20 optics. It is also worth noting, that the SPS brightness (black crosses) is similar, demonstrating an excellent brightness preservation between the two rings. This optics have been routinely used in operation during LHC run II (2015-2018) and opened the way for ultra-high brightness beams to be delivered in the HL-LHC era for protons and eventually for ions [37].

## SUMMARY

Using analytical and numerical methods, linear optics parameters, which have a direct impact on collective effects, were optimised for specific examples of high-intensity, high brightness, hadron and lepton rings. These approaches allowed a solid conceptual design of ultra-low emittance damping rings and permitted to break intensity limitations in an existing LHC injector, without any cost impact or hardware change. It is certain that there is a growing need for the optics designer to transcend the single-particle dynamics mentality and apply such optimisation procedures for reaching the optimal performance of rings, in design or operation.

## ACKNOWLEDGEMENTS

It is a pleasure to thank G. Arduini, T. Argyropoulos, T. Bohl, H. Braun, E. Shaposhnikova, the LIU-SPS working group and the SPS operation team for invaluable contributions in several parts of this work.

## REFERENCES


[1] A. W. Chao, Physics of Collective Beam Instabilities in High Energy Accelerators, New York, Wiley, 1993.

[2] T. Argyropoulos et al., “Loss of Landau Damping for Inductive Impedance and a Double RF System”, TUPWA040, IPAC13, 2013.

[3] W. Höfle, “Progress in Transverse Feedbacks and Related Diagnostics for Hadron Machines ”, FRXCA01, IPAC13, 2013.

[4] P. Collier et al., “Reducing the SPS Machine Impedance”, EPAC02, WEPRI082, p.1458, 2002.

[5] G. Rumolo, et al., “Dependence of the Electron-Cloud Instability on the Beam Energy”, PRL 100, 144801, 2008.

[6] L. J. Laslett, “On Intensity Limitations Imposed by the Transverse Space- Charge Effects in Circular Accelerators”, BNL-7534, 1963.

[7] A. Piwinski, in Handbook of Accelerator Physics and Engineering, ed. A. W. Chao, M. Tigner, World Scientific, p. 127, 2002; J. Bjorken, S. K. Mtingwa, Part. Accel. 13, 115, 1983.

[8] S. Fartoukh, “Achromatic telescopic squeezing scheme and application to the LHC and its luminosity upgrade”, PRST-AB 16, 111002, 2013

[9] J. Wei, in Handbook of Accelerator Physics, and Engineering, op. cit., p. 285. ed. A. W. Chao and M. Tigner, World Scientific, Singapore, p. 285, 2002.

[10] T. Risselada, “Gamma transition jump schemes, 4th CAS, CERN-91-04, p. 161, 1991.

[11] K.Y. Ng, in Handbook of Accelerator Physics, and Engineering, op. cit., p. 94. ed. A. W. Chao and M. Tigner, World Scientific, Singapore, p. 94, 2002.

[12] S. Y. Lee, K. Y. Ng, D. Trbojevic, “Minimizing dispersion in flexible-momentum-compaction lattices”, PRE, 48(4), p. 3040, 1993.

[13] Y. Yamazaki ed., “Technical design report of J-PARC”, KEK-2002-13, 2002.

[14] Y. Papaphilippou et al., “Linear optics design of negative momentum compaction lattices for PS2”, TH6PFP044, PAC09, p. 3805, 2009.

[15] Y. Papaphilippou et al., “Design Options of a High-Power Proton Synchrotron for LAGUNA-LBNO”, THPWO081, IPAC13, 2013.

[16] S. Hancock, “Gamma at Transition of the proposed PS2 Machine”, CERN-AB-Note-2006-39, 2006.

[17] H. Bartosik et al., “Linear Optimization and Tunability of the PS2 Lattice”, THPE022, IPAC10, 2010.

[18] D. S. Robin, W. Wan, F. Sannibale, and V. P. Suller, “Global analysis of all linear stable settings of a storage ring lattice”, PRST-AB 11, 024002, 2008.

[19] Y. Papaphilippou et al., “Conceptual design of the CLIC Damping Rings”, TUPPC086, IPAC12, p. 1368, 2012.

[20] F. Antoniou, “Optics design of Intrabeam Scattering dominated damping rings”, PhD Thesis, NTUA, 2013.

[21] F. Antoniou et al., “Parameter scan for the CLIC Damping Rings under the influence of intrabeam scattering”, WEPE085, IPAC10, p. 3542, 2010.

[22] K. Kubo et al., “Intrabeam scattering formulas for high energy beams”, PRST-AB 8, 081001, 2005.

[23] H.H. Braun et al., “Alternative Design of the CLIC Damping Ring Lattice”, CLIC Note 849, 2010.

[24] F. Antoniou and Y. Papaphilippou, “Analytical considerations for linear and nonlinear optimization of TME cells. Application to the CLIC pre-damping rings”, PRST-AB 17, 064002, 2014.

[25] S. Papadopoulou, F. Antoniou, and Y. Papaphilippou, “Emittance reduction with variable bending magnet strengths: Analytical optics considerations and application to the Compact Linear Collider damping ring design”, PRAB 22, 091601, 2019.

[26] D. Schoerling et al., “Design and system integration of the superconducting wiggler magnets for the Compact Linear Collider damping rings”, PRST-AB 15, 042401, 2012.

[27] L. G. Fajardo, F. Antoniou, A. Bernhard, P. Ferracin, J. Mazet, S. Papadopoulou, Y. Papaphilippou, J. Pérez and D. Schoerling, “Design of Nb3Sn Wiggler Magnets for the Compact Linear Collider and Manufacturing of a Five-Coil Prototype,” IEEE Trans. Appl. Supercond.,26 no.4, 4100506, 2016.

[28] LIU-SPS Beam Dynamics Working Group, chaired by E. Shaposhnikova, http://paf-spsu.web.cern.ch/paf-spsu/

[29] H. Bartosik G. Arduini, Y. Papaphilippou, “Optics considerations for lowering transition energy in the SPS”, MOPS012, IPAC11, p. 619, 2011.

[30] H. Bartosik et al., “Experimental studies with low transition energy optics in the SPS” MOPS010, IPAC11, p. 613, 2011.

[31] H. Bartosik et al., “Increasing Instability Thresholds in the SPS by Lowering Transition Energy”, WEPPR072, IPAC12, p. 3096, 2012;

[32] H. Bartosik et al., “Low-gamma transition optics for the SPS: simulation and experimental results for high brightness beams”, WEO1B01, Proceedings of HB2012, Beijing, China, 2012.

[33] H. Bartosik et al., “Experimental studies for future LHC beams in the SPS”, TUPME034, IPAC13, 2013.

[34] Y. Papaphilippou et al., “Operational Performance of the LHC Proton Beams with the SPS Low Transition Energy Optics” THPWO080, IPAC13, 2013.

[35] K. Ohmi and F. Zimmermann, “Head-Tail Instability Caused by Electron Clouds in Positron Storage Rings”, PRL 85, 3831, 2000.

[36] H. Bartosik et al., “Impact of low transition energy optics to the electron cloud instability of LHC beams in the SPS”, MOPS011, IPAC11, p. 616, 2011.

[37] F. Antoniou et al., “Considerations on SPS low-transition energy optics for LHC ion beams”, TUPME046, IPAC13, 2013.

# Transverse Beam Instabilities and Linear Coupling in the LHC

L.R. Carver, X. Buffat, E. Métral, K. Li, M. Schenk
*CERN, Geneva, Switzerland*

Transverse beam instabilities were observed in the Large Hadron Collider (LHC) when the effect of linear coupling was known to be large. This motivated a campaign of simulations on the effect of linear coupling on the transverse stability. Measurements and simulations found that the linear coupling was greatly diminishing the effectiveness of the Landau octupoles, leading to a loss of Landau damping. All of the information shown here is summarised from Refs. [1, 2].

## I. INTRODUCTION

Transverse beam instabilities had been observed in the LHC when the tunes were moving closer together (Laslett tune shift at injection) or when the coupling was known to be large (the beam measurement of the closest tune approach, $|C^-|$ showed an increase to approximately the tune separation). This knowledge, in addition to the examples of transverse beam instabilities see during the energy ramp at the HERA proton ring, hinted at a link between linear coupling and transverse stability [3, 4].

Linear coupling had been used in the Proton Synchrotron (PS) at CERN to stabilise a strong horizontal instability by coupling into the vertical plane [5, 6]. This was possible due to a sharing of the instability rise times between the two planes. These two sets of observations are seemingly in contradiction to each other. This provided the motivation for a study into how linear coupling plays a role in transverse beam stability in the LHC.

## II. MAIN RESULTS

It had been known from LHC optics simulations that the presence of linear coupling can change the detuning coefficients from the Landau octupoles [7, 8]. However a link had never been drawn to how this impacts the effectiveness of the Landau damping.

The reduction in the size of the tune footprints due to modification of the detuning coefficients causes a reduction of the stable area of the stability diagram, shown in Fig.1. It can be seen from the figure that instabilities can develop (due to a loss of Landau damping) when the $|C^-|$ becomes about 60% of the tune separation, $Q_{sep}$ .

A simple model of the LHC was developed where the strength of the coupling is designated by the value of the $|C^-|$. The transverse stability of this model was simulated in the collective effects tracking code PyHEADTAIL [9] and showed similar results to frequency domain computations which were performed using a combination of DELPHI [10] and stability diagram analysis.

Dedicated beam measurements were made in the LHC at 6.5 TeV, where the coupling was accurately measured and the tune separation was slowly reduced until an instability developed. The simple LHC model, as well as frequency domain simulations was seen to agree with these measurements in the machine.

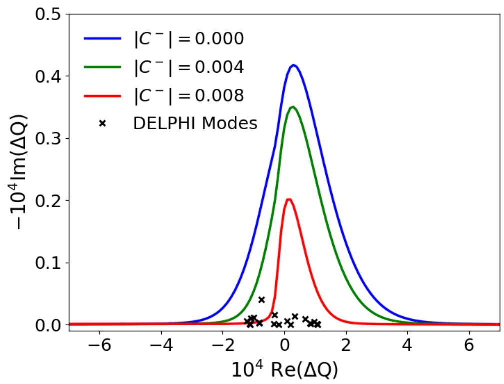


FIG. 1. Comparison of the stability diagrams for fixed tunes ($Q_x = 0.31, Q_y = 0.32$) for different levels of coupling. Shown for comparison are unstable modes computed with DELPHI.

## III. FUTURE WORK

Linear coupling is now an integral part of the LHC stability model and must be well controlled in all stages of the machine cycle. New measurement techniques have been employed to ensure that the linear coupling can be measured regularly and accurately to prevent any loss of performance due to transverse instabilities [11, 12].

The studies performed for the LHC only took into account the effect of linear coupling on the tune spread generated by the Landau octupoles. In fact in the LHC there are several other contributors to the tune spread, beam-beam interactions, electron cloud effects and to a lesser extent, space charge (at injection energy). Linear coupling can have an effect on the tune spread generated by each of these effects, it could be either stablizing or destablizing depending on the specific configuration. The full picture of linear coupling and collective effects in the LHC is yet to be studied in detail. With one of the primary sources of unwanted linear coupling coming from the triplets, when the $\beta^*$ is reduced (as is anticipated for the HL-LHC) the beta-function is increased in the triplets which means that increased linear coupling is expected.

[1] L.R. Carver, X. Buffat, K. Li, E. Métral, M. Schenk, 'Transverse beam instabilities in the presence of linear coupling in the Large Hadron Collider', Phys. Rev. Accel. Beams, 21, 044401, 2018

[2] L.R. Carver, D. Amorim, N. Biancacci, X. Buffat, K.S.B. Li, E. Métral, B. Salvant, M. Schenk, 'Destabilising Effect of Linear Coupling in the LHC', Proc. 8th Int. Particle Accelerator Conf. (IPAC'17), Copenhagen, Denmark, May 2017, paper THPAB040, pp. 3791–3794,

[3] E. Métral, G. Hoffstaetter, F. Willeke, 'Destabilising Effect of Linear Coupling in the HERA Proton Ring' Presented at the 8th European Conference of EPAC02, Paris, Paris, France, June 2002, pp. 1535-1537

[4] E. Métral, 'Theory of coupled Landau damping', Part. Accel., CERN-PS-99-011-CA, Vol. 62, pp. 259-273, Feb, 1999

[5] R. Cappi, E. Métral, D. Möhl, 'Control of Coherent Instabilities by Linear Coupling', 18th International Conference on High-energy Accelerators, Tsukuba, Japan, 26-30 Mar 2001, pp.P2new01

[6] E. Métral, G. Rumolo, B. Salvant, R. Steerenberg, 'Simulation study of the horizontal head-tail instability observed at injection of the CERN Proton Synchrotron' 22nd Particle Accelerator Conference, Albuquerque, NM, USA, 25-29 Jun 2007, pp.4210

[7] E. H. Maclean, R. Tomás, F. Schmidt, T. Persson, 'Measurement of nonlinear observables in the Large Hadron Collider using kicked beams', 17, 081002 (2014)

[8] E. Maclean, F. Carlier, M. Giovannozzi, T. Persson, R. Tomás, "Effect of Linear Coupling on Nonlinear Observables at the LHC", presented at the 8th Int. Particle Accelerator Conf. (IPAC'17), Copenhagen, Copenhagen, Denmark, May 2017, paper WEPIK092, pp 3151-3154

[9] K. Li et al, 'Code Development for Collective Effects', Presented at the 57th ICFA Advanced Beam Dynamics Workshop on High-Intensity, High Brightness and High Power Hadron Beams (HB2016), Malmö, Malmö, Sweden, July 2016, paper WEAM3X01, pp. 362-367

[10] N.Mounet, 'DELPHI: an Analytic Vlasov Solver for Impedance-Driven Modes', Presented at the CERN BE-ABP-HSC Section Meeting, CERN, Geneva, Switzerland, 5th July 2014, https://espace.cern.ch/be-dep-workspace/abp/HSC/Meetings/DELPHI-expanded.pdf

[11] J. Olexa, O. Ondracek, Z. Brezovic, M. Gasior, 'Prototype system for phase advance measurements of LHC small beam oscillations', CERN-ATS-2013-038, CERN, Geneva, Switzerland (2013)

[12] A. Calia, K. Fuchsberger, M. Gabriel, G.-H. Hemelsoet, M. Hostettler, M. Hruska, D. Jacquet, M. Soderen, T. Persson, D. Valuch, "Online Coupling Measurement and Correction Throughout the LHC Cycle", presented at the 16th Int. Conf. on Accelerator and Large Experimental Control Systems, ICALEPCS2017, pp. 686-691, Barcelona, Spain (2017)

# COPING WITH LONGITUDINAL INSTABILITIES USING CONTROLLED EMITTANCE BLOW-UP

H. Timko*, S. Albright, T. Argyropoulos, P. Baudrenghien, H. Damerau, J. Esteban Müller,
A. Haas, G. Papotti, D. Quartullo, J. Repond, E. Shaposhnikova, CERN, Geneva, Switzerland

*Abstract*

Controlled emittance blow-up is a widely-spread method to mitigate beam instabilities in accelerators. This paper summarises the different methods used to generate and apply RF phase noise or RF phase modulation in the RF systems of the CERN synchrotrons. It also details machine by machine when and how different methods are used.

## INTRODUCTION

Many synchrotrons are operated at the limit of longitudinal beam stability, with pushed performance, whether they are already existing machines [1, 2] to be upgraded, or future projects [3] that have to cope with design constraints. To mitigate these instabilities, often a mixture of passive methods, such as impedance reduction and increased synchrotron tune spread due to a double-RF system, and active methods, such as beam and cavity feedbacks, is applied [4]. Controlled emittance blow-up in the longitudinal plane is another mitigation tool complementary to these.

In the synchrotrons at CERN, uncontrolled emittance blow-up can occur for many operational beams, despite using other instability-mitigation methods. An uncontrolled blow-up can lead to violent bunch length increase with a perturbed longitudinal distribution and excessive beam losses. In order to avoid these effects, controlled emittance blow-up can be applied when sufficient bucket area is available, preventively before the typical onset of instability in the cycle, see Fig. 1.

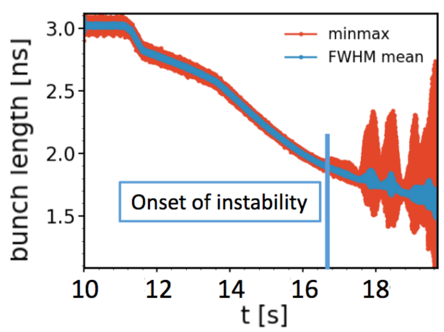


Figure 1: Uncontrolled emittance blow-up of the LHC-type beam occurring during the SPS energy ramp, seen as a violent increase in bunch length of some bunches; simulation with 12 bunches. Red: minimum and maximum bunch length deviations over the beam, blue: mean, four-sigma equivalent FWHM bunch length.

* helga.timko@cern.ch

Controlled emittance blow-up is operationally used in the CERN machines for the LHC-type proton beam, and also some other beams, ranging from the PSB, over the PS and SPS, to the LHC, where it was even anticipated by design. For the FCC-hh [3], it is foreseen during the ramp, and even during physics, to counteract synchrotron radiation damping [5].

It is not only used to mitigate beam instabilities, but there is a wide range of other applications, too. In accelerators at CERN, it is operationally used to stabilise transition crossing and to obtain a large enough emittance for bunch splitting or other RF manipulations. It can be applied to reduce intra-beam scattering, transverse space-charge effects, or synchrotron radiation shrinkage. In addition, controlled emittance blow-up can also be interesting for bunch length control or longitudinal beam profile shaping.

## METHODS USED IN CERN MACHINES

This section presents the different methods that can be applied to achieve particle diffusion in the longitudinal phase space of the bunches. At CERN, the methods used are phase modulation applied to a high-harmonic RF voltage[1] and phase noise injection into the principal RF system around the central synchrotron frequency. For the latter, the noise can be generated in frequency or time domain, as shown below. Bunch profile shaping, in particular, can also be achieved through RF phase modulation with a frequency close to the central synchrotron frequency.

### *RF Phase Noise Generated in Frequency Domain*

In order to diffuse particles within a given phase-space area of the bunch, a noise with a band-limited spectrum or with a coloured spectrum can be applied to target exactly this region of the bunch distribution, see Fig. 2. For a diffusion in this phase-space region, noise with a flat spectrum could be generated and injected into the phase of the RF voltage. In practice, however, the beam phase loop is usually required to be closed during the noise injection, and will counteract the noise applied around the central synchrotron frequency [6], see Fig. 3. To better target the bunch core, in some cases it might be required to inject a noise with a coloured spectrum that takes into account the response of the beam phase loop and results in a flat effective spectrum, as is done in the LHC.

One way of generating a band-limited phase noise spectrum is via the algorithm described in [7]. With this algorithm, a white-noise sequence is generated in time domain,

$$w_k = e^{2\pi r_k}\sqrt{-2\ln q_k}\,, \tag{1}$$

[1] In this paper, RF voltage refers to the voltage vector of amplitude and phase.

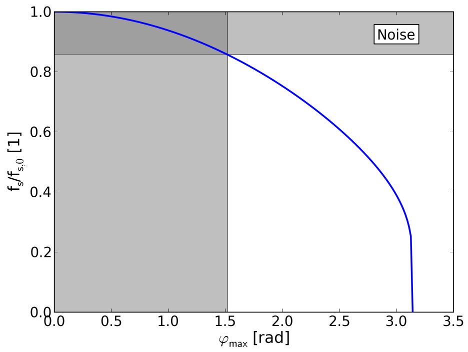


Figure 2: Synchrotron frequency distribution in the single-harmonic RF system of the LHC as a function of synchrotron-oscillation phase amplitude. The shaded regions indicate how the frequency limits of the LHC noise spectrum target the length of the bunch.

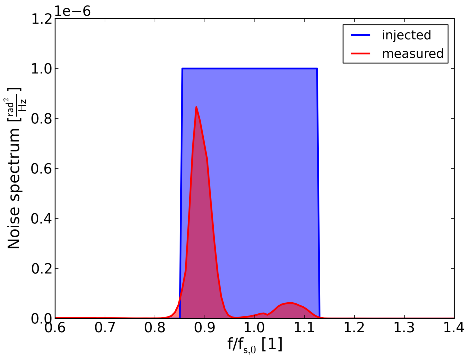


Figure 3: Intended (blue) and effective, measured (red) noise spectrum when injected through the beam phase loop.

where $r, q \in [0, 1]$ are uniformly distributed random numbers and $k \in \mathbb{N}$ is the turn number in the sequence of $N$ turns. In the frequency-domain, the discrete Fourier image of this sequence,

$$W_n = \sum_{k=0}^{N-1} e^{-2i\pi\frac{kn}{N}} w_k \, , \tag{2}$$

is then multiplied with the desired band-limited noise probability density $S_n$,

$$\Phi_n = S_n W_n \, . \tag{3}$$

The turn-by-turn phase noise sequence applied to the bunch is finally obtained as a backward discrete Fourier transform,

$$\phi_k = \frac{1}{N} \sum_{n=0}^{N-1} e^{2i\pi\frac{kn}{N}} \Phi_n \, . \tag{4}$$

This method has been used operationally in the SPS [8] and the LHC [9], and it has been tested for the LIU upgrade of the PSB [10].

### *RF Phase Noise Generated in Time Domain*

Alternatively, a phase-noise equivalent sequence in turn $k$ can directly be generated in time domain, by summing $N$ single-tone modulations with a given weight (amplitude) $A$ [11],

$$\phi_k = \sum_{i=1}^{N} A_i \sin\left(\int_0^{T_k} 2\pi f_i(t) dt + \varphi_i\right) , \tag{5}$$

where $T_k = \sum_{n=1}^{k} T_{\mathrm{rev},n}$ is the sum of revolution periods elapsed, $f_i(t)$ is a time-dependent frequency component and $\varphi_i$ a phase offset. During an acceleration ramp, for instance, each $f_i(t)$ can be calculated to track the evolution of the synchrotron frequency distribution by maintaining a fixed ratio relative to the difference between the small-amplitude synchrotron frequency $f_{s,0}(t)$ and the synchrotron frequency at the target longitudinal emittance $f_{s,1}(t)$, or $f_i(t) = f_{s,1}(t) + x_i \left[f_{s,0}(t) - f_{s,1}(t)\right]$, where $x_i \in [0, 1]$. This is illustrated also in Fig. 4.

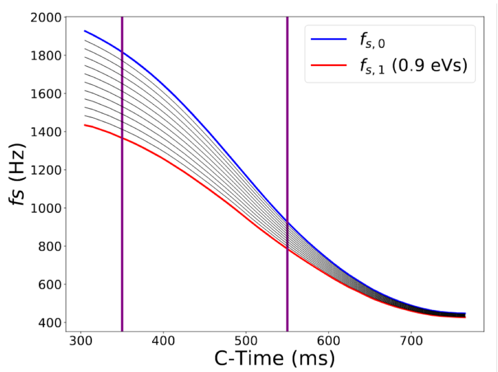


Figure 4: Noise spectrum as a sum of single-tone modulations along the ramp, tracking the time evolution of the central synchrotron frequency in the CERN PSB.

### *RF Phase Modulation in the Main RF System*

Contrary to the previously mentioned methods, RF phase modulation in the main RF system does not result in a diffusion process, but in a resonant excitation of a single frequency within the synchrotron frequency distribution [12]. Shaping the longitudinal distribution by these means can help to improve beam stability, reduce heat load or pile-up density [13, 14]. It is done by modulating the phase of the main RF voltage $V(t)$ with a modulation amplitude $\phi_m$ and frequency $f_m$ as follows:

$$V(t) = V_1 \sin\left(2\pi h_1 f_{\mathrm{rev}} t + \psi_1(t)\right) = \tag{6}$$

$$V_1 \sin\left(2\pi h_1 f_{\mathrm{rev}} t + \phi_m \sin\left[2\pi f_m t\right] + \phi_1\right) , \tag{7}$$

where $V_1$, $h_1$, and $\phi_1$ are the voltage amplitude, harmonic, and phase of the main RF system and $f_{\mathrm{rev}}$ is the revolution frequency.

An example of measured bunch profile modification due to phase modulation is shown in Fig. 5. The resulting bunch length and bunch profile is determined by the modulation frequency applied [13], and thus allows only for a discrete regulation of the bunch length. In addition, the amplitude of the excitation has to be above a critical value for resonant excitation to occur.

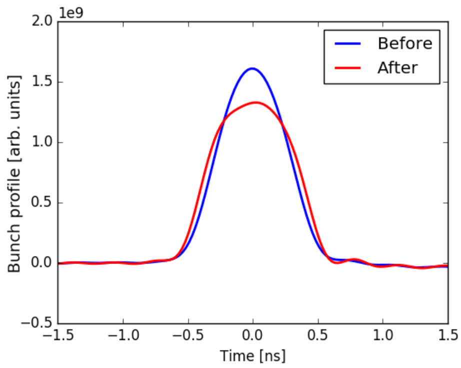


Figure 5: Bunch profile before (blue) and after (red) RF phase modulation applied in the LHC during collisions.

### *RF Phase Modulation in a High-Harmonic RF System*

RF phase modulation can also be performed in a high-harmonic RF system,

$$V(t) = V_1 \sin(2\pi h_1 f_{\mathrm{rev}} t + \phi_1) + \tag{8}$$

$$V_2 \sin(2\pi h_2 f_{\mathrm{rev}} t + \phi_m \sin[2\pi f_m t] + \phi_2)\,, \tag{9}$$

where $V_2$, $h_2$, and $\phi_2$ are the voltage amplitude, harmonic, and phase of the high-harmonic system, respectively. The effect on the beam can be two-fold. As long as the modulation frequency remains a few times the synchrotron frequency, and the harmonic ratio $h_2/h_1$ remains small, the effect of the modulation on the bunch remains in the resonant-excitation regime [15, 16]. For larger modulation frequencies, and with growing harmonic ratio, a noise-equivalent regime is entered [17].

## APPLICATIONS IN CERN MACHINES

In this Section, we summarise the main operational applications of controlled emittance blow-up throughout the CERN synchrotrons.

### *Proton Synchrotron Booster*

In the PSB, controlled emittance blow-up is used for the emittance regulation of all beams produced. The amount of blow-up used, and the duration of the process, depend on the beam type.

In the course of the LIU upgrade of the PSB, its injection energy will be increased from 50 MeV to 160 MeV, and its maximum extraction energy will be raised from 1.4 GeV to 2 GeV. Proton beams for the LHC required already before the Long Shutdown 2 (LS2) a controlled emittance blow-up to provide uniform and reproducible longitudinal distributions, and to minimise space-charge effects at PS injection; this blow-up, however, was ‘only’ from 1 eVs to 1.4 eVs. For the future HL-LHC production beams with twice the intensity, a blow-up to 3 eVs is required [10]. This is more challenging not only due to enhanced intensity effects, but also because the cycle time available for the blow-up remains the same.

Prior to LS2, a sinusoidal phase modulation of a high-harmonic (C16) cavity [18] was used for emittance blow-up of all operational beams. This method has the advantage of being relatively fast, however it is also relatively sensitive to uncertainties in machine parameters, such as the relative phase offset between the RF systems. After LS2, the use of blow-up through a high-harmonic is kept solely for longitudinal shaving in the ramp.

For operational beams that do not require shaving, instead, phase noise will be injected directly at the main RF frequency, in single- or double-harmonic RF buckets. As a baseline, the generation of the noise is going to be a sum of distinct frequency components [11], which was used already for the PSB reliability run in 2018 with success, see Fig. 6. This ensures better frequency tracking in the quickly-changing acceleration ramp of the PSB than noise generation in frequency domain, which requires fixing the frequency band of the noise spectrum during a certain amount of time.

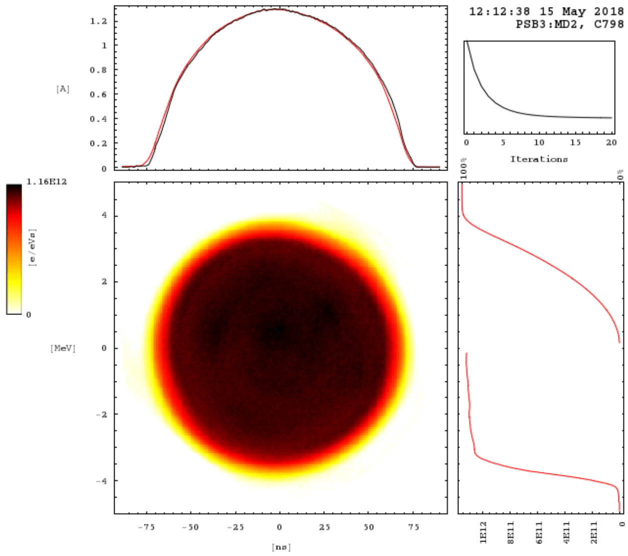


Figure 6: Tomographic reconstruction of a PSB bunch blown up with a sum of single-frequency phase noise components; BCMS-type proton beam from the start of the reliability run in 2018.

### *Proton Synchrotron*

Also in the PS, a single-tone phase modulation of a higher-harmonic cavity at 200 MHz is used for controlled emittance blow-up [17, 19]. For comparison, the main RF system is operated in the range of 2.8 MHz to 10 MHz. The blow-up through the higher-harmonic cavity results in a smooth bunch-length increase over time, see Fig. 7, and it is also approximately proportional to the RF voltage of the 200 MHz system. This allows to easily adjust the final emittance. The longitudinal distribution after the blow-up can moreover be influenced by the choice of the modulation frequency, which is typically in the range of a few kHz, corresponding to several times the synchrotron frequency.

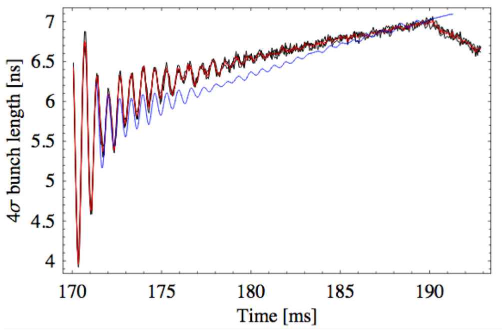


Figure 7: Bunch length growth during controlled emittance blow-up in the PS is approximately linear with time. The strong bunch length oscillations during the first 10 ms are triggered by an intentional longitudinal mismatch at injection and not related to the blow-up with the 200 MHz RF system. Comparison of measurements (black: single measurement, red: average of multiple measurements) and simulations (blue); a plot from [19].

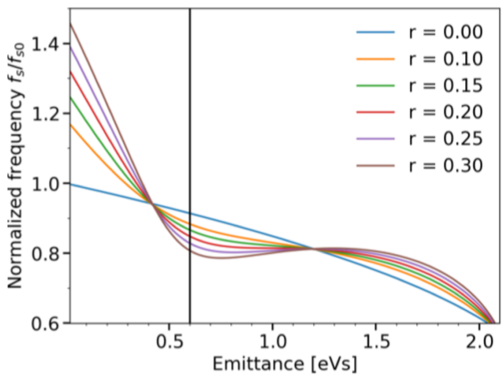


Figure 8: Synchrotron frequency distribution at SPS flat top, without intensity effects, in bunch-shortening mode, relative to the central synchrotron frequency in the single-harmonic RF system. Different voltage ratios of the 800 MHz to 200 MHz voltages $r$ are shown in different colours; a plot from [25].

The blow-up is applied for various reasons at different times and energies of the PS acceleration ramp. As the resonant frequency of 200 MHz cavities cannot sweep with the increasing revolution frequency, the harmonic number is adapted during the cycle. At energies below transition crossing, the blow-up can moreover only be performed at constant-energy plateaus to gain sufficient time within the frequency range of cavities without a harmonic number change.

The proton beam for the LHC is blown up at four distinct times in the cycle. The blow-up is essential for the production and stability of all high-intensity beams. In particular, it is used to (i) obtain a large enough emittance prior to bunch splittings, (ii) stabilise the beam during RF manipulations, (iii) stabilise the transition crossing, and to (iv) regulate the final emittance desired for extraction to the SPS. Also for ions, blow-up is used to stabilize the beam during transition crossing.

### *Super Proton Synchrotron*

In the SPS, the operational method of controlled emittance blow-up is RF phase noise injection through the beam phase loop in the main RF system [8, 20], although in the past also phase modulation in the fourth-harmonic RF system was tried [21, 22]. It is primarily applied for LHC-type protons, and was not needed for ions in the past. First studies suggest that the LHC ion beam produced after LS2 will have additional emittance blow-up during slip-stacking [23, 24].

LHC-type proton beams, in particular, are produced in a double-harmonic RF system of 200 MHz and 800 MHz operated in bunch-shortening mode. The synchrotron frequency distribution for different voltage ratios is shown in Fig. 8. For high-intensity proton beams, adapting the blow-up spectrum to target the desired region of the bunch is challenging. Firstly, because high-intensity protons require a higher 800 MHz to 200 MHz voltage ratio for beam stability. At high ratios the desired ~0.6 eVs region of the bunch cannot be targeted without touching also the halo population, which in return can lead to beam losses. Secondly, intensity effects shift the relative RF phase and distort the synchrotron frequency distribution. For post-LS2 operation, studies are on-going on how to best adapt the frequency limits of the blow-up spectrum for varying, high beam intensity in the future [26].

### *Large Hadron Collider*

By design, nominal-intensity proton beams require a controlled emittance blow-up in the LHC [27] to prevent single- and coupled bunch instabilities [28] during the acceleration ramp. Machine studies showed that for the nominal-intensity beam, the coupled-bunch stability threshold is not lower than the single-bunch threshold for the loss of Landau damping [29]. Thus, the primary reason to use controlled blow-up for the nominal proton beam is the mitigation of single-bunch loss of Landau damping.

For proton beams with low, 'pilot' intensity, the blow-up is not required from beam stability point of view; it is, however, often applied to regulate the bunch length. For the ion beams in the LHC, blow-up is primarily used to minimize intra-beam scattering in physics by using suitably large emittances at arrival to flat top.

Compared to other accelerators at CERN, the blow-up in the LHC has several particularities. Firstly, it happens over almost 13 million turns (1210 s) for a ramp from 450 GeV to 6.5 TeV, much slower than in the injector synchrotrons, and increases the emittance by at least a factor 4, which is much larger than in other machines. In addition, it is used in a single-RF system, without a Landau-cavity being present and stabilising the beam. In exchange, a feedback on the FWHM bunch length regulates the amplitude of the phase noise injected and makes sure that the target bunch length is not exceeded. Indeed, machine studies showed that without the bunch-length feedback, a regulation of the blow-up simply via the noise spectrum and application time span, as is done in other machines, is practically impossible [30]; an example is shown in Fig. 9. Even with the bunch-length feedback present, regulation for the fast, 'parabolic-parabolic-linear-parabolic' ramp is more demanding than for the operational, 'parabolic-exponential-linear-parabolic' ramp.

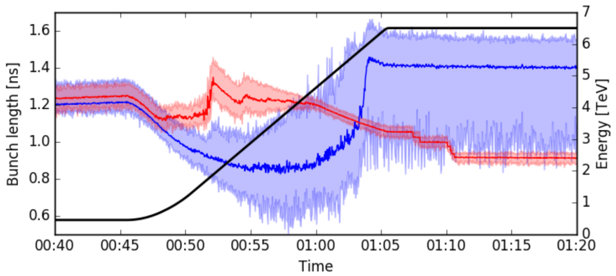


Figure 9: Bunch length evolution of the LHC Beams 1 (blue) and 2 (red) with the bunch length feedback off; the blow-up is started close to the stability threshold of the beam and cannot regulate the bunch length. A plot from [30].

In collisions at 6.5 TeV, both the bunch length and the bunch intensity are decreasing, and in long physics fills, loss of Landau damping is approached slowly, on the timescale of hours, see Fig. 10. As a mitigation measure against loss

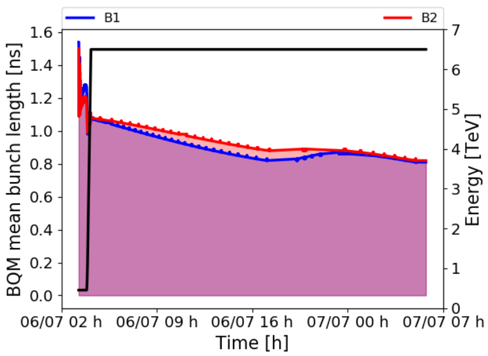


Figure 10: Bunch length evolution in long physics fills in the LHC Beams 1 (blue) and 2 (red). A slow blow-up occurs due to loss of Landau damping.

of Landau damping, and as a bunch length regulation, sinusoidal phase modulation is applied in operation, whenever the bunch length drops below 0.95 ns for nominal-intensity protons. A good bunch length control in physics is also important for the collision-vertex resolution of the LHC detectors.

### *Future Circular Collider*

Also in the FCC-hh, controlled blow-up is foreseen during acceleration to counteract loss of Landau damping [3]. In addition, a constant blow-up via phase noise injection in physics is considered to counteract the fast bunch length shrinkage due to synchrotron radiation; the required double-sided noise spectral density $P$ would be, in small-bunch approximation [5],

$$P = \frac{1}{4}\frac{\Delta E_{\mathrm{SR}}}{E_s} f_{\mathrm{rev}} \left(\frac{h}{Q_{s0}}\tau_0\right)^2 , \qquad (10)$$

where $\Delta E_{\mathrm{SR}}$ is the energy loss per turn due to synchrotron radiation, $E_s$ the synchronous energy, $Q_{s0}$ the central synchrotron tune and $\tau_0$ the initial bunch length.

## CONCLUSIONS

Controlled longitudinal emittance blow-up is used in all synchrotrons at CERN to mitigate, among others, single-bunch loss of Landau damping or multi-bunch instabilities. It is also used to stabilise transition crossing, reduce intra-beam scattering and transverse space-charge effects, and to prevent from bunch length shrinkage due to synchrotron radiation. The two main blow-up methods are band-limited RF phase noise injection and RF phase modulation of a high-harmonic RF system. The latter has been used in the PSB ramp and in the PS on intermediate flat tops or towards the end of the ramp. In the SPS and LHC, as well as in the post-LS2 PSB, phase noise injection is used. In the fast-cycling injectors, the blow-up is done over a relatively short period, and the blow-up parameters, such as amplitude and frequency of modulation or noise spectrum, result in reproducible beam quality. In the LHC, a bunch length feedback is required to regulate the resulting bunch length. After LS2, increased intensities will challenge the reproducibility of the bunch length regulation and studies are on-going to improve the noise spectrum and its generation for high-intensity beams.

## REFERENCES

[1] H. Damerau *et al.*, 'LHC Injectors Upgrade, Technical Design Report, Vol. I: Protons', CERN-ACC-2014-0337, CERN, Geneva, Switzerland, 2014.

[2] G. Apollinari *et al.*, 'High-Luminosity Large Hadron Collider (HL-LHC): Technical Design Report V. 0.1', CERN Yellow Reports: Monographs, CERN-2017-007-M, CERN, Geneva, Switzerland, 2017.

[3] M. Benedikt *et al.*, 'Future Circular Collider Study. Volume 3: The Hadron Collider (FCC-hh) Conceptual Design Report', CERN-ACC-2018-0058, CERN, Geneva, Switzerland, 2018.

[4] E. Shaposhnikova, 'Instability observations and cures', talk at the International Workshop on Impedances and Beam Instabilities in Particle Accelerators, Benevento, Italy, 2017.

[5] A. Haas and H. Timko, 'Compensation of Synchrotron Radiation at Top Energy in the FCC-hh', Rep. CERN-ACC-NOTE-2020-0017, CERN, Geneva, Switzerland, 2020.

[6] P. Baudrenghien and T. Mastoridis, 'Longitudinal emittance blowup in the large hadron collider', Nucl. Instrum. Meth. A, 726, 181–190, 2013.

[7] J. Tückmantel, 'Digital generation of noise-signals with arbitrary constant or time-varying spectra (A noise generation software package and its application)', LHC-PROJECT-Report-1055, CERN, Geneva, Switzerland, 2008.

[8] G. Papotti *et al.*, 'Study of Controlled Longitudinal Emittance Blow-Up for High Intensity LHC Beams in the CERN SPS', Rep. LHC-PROJECT-Report-1117, Geneva, Switzerland, 2008.

[9] P. Baudrenghien *et al.*, 'Longitudinal emittance blow-up in the LHC', Proc. IPAC'11, San Sebastian, Spain, 2011.

[10] D. Quartullo, E. Shaposhnikova, and H. Timko, 'Controlled longitudinal emittance blow-up using band-limited phase noise in CERN PSB', Proc. IPAC'17, Copenhagen, Denmark, 2017.

[11] S. Albright and D. Quartullo, 'Time varying RF phase noise for longitudinal emittance blow-up', Proc. IPAC'19, Melbourne, Australia, 2019.

[12] S. Y. Lee, 'Accelerator Physics', Third Edition, World Scientific, 2012.

[13] C. Y. Tan and A. Burov, 'Phase modulation of the bucket stops bunch oscillations at the Fermilab Tevatron', Phys. Rev. ST Acc. Beams 15, 044401, 2012.

[14] E. Shaposhnikova *et al.*, 'Flat Bunches in the LHC', Proc. IPAC'14, Dresden, Germany, 2014.

[15] V. Balandin, M. Dyachkov, and E. Shaposhnikova, 'The Resonant Theory Of Longitudinal Emittance Blowup By Phase modulated high Harmonic Cavities', Part. Accel., 35, 1-14, 1991.

[16] R. Cappi, R. Garoby, and E. Shaposhnikova, 'Experimental study of controlled longitudinal blow-up', Rep. CERN-PS-92-40-RF, CERN, Geneva, Switzerland, 1992.

[17] D. Boussard, 'The RF noise theory applied to the PS longitudinal controlled blow-up', Rep. CERN-SPS-Tech-Note-85-007-ARF, CERN, Geneva, Switzerland, 1985.

[18] M. E. Angoletta *et al.*, 'PSB beam longitudinal blow-up by phase modulation with the digital LLRF prototype system', Rep. CERN-ACC-NOTE-2014-0007, CERN, Geneva, Switzerland, 2014.

[19] H. Damerau, 'Controlled Longitudinal Emittance Blow-Up in the CERN PS', Proc. PAC'07, Albuquerque, U.S.A., 2007.

[20] T. Bohl *et al.*, 'Controlled Longitudinal Emittance Blow-up in the SPS as Injector and LHC Test-Bed', Rep. AB-Note-2003-084-MD, CERN, Geneva, Switzerland, 2004.

[21] T. Bohl *et al.*, 'Study of controlled longitudinal blow-up in the SPS using the 800 MHz RF system', Rep. SL-MD-Note-221, CERN, Geneva, Switzerland, 1996.

[22] E. Shaposhnikova, 'Controlled Longitudinal Emittance Blow-up in the SPS Using A 4th Harmonic rf System', Proc. International LHC Workshop, Montreux, Switzerland, 1997.

[23] D. Quartullo, 'Simulations of RF beam manipulations including intensity effects for CERN PSB and SPS upgrades', PhD Thesis, Sapienza University of Rome, Rome, Italy, 2019.

[24] T. Argyropoulos, private communication, 2020.

[25] J. Repond, 'Simulations of longitudinal beam stabilisation in the CERN SPS with BLonD', Proc. ICAP'18, Key West, USA, 2019.

[26] G. Papotti, private communication, 2020.

[27] O. Brüning *et al.*, 'LHC Design Report', CERN, Geneva, Switzerland, 2004.

[28] E. Shaposhnikova, 'Longitudinal beam parameters during acceleration in the LHC', LHC-Project-Note-242, Geneva, Switzerland, 2000.

[29] J. F. Esteban Müller *et al.*, 'LHC MD 652: coupled-bunch instability with smaller emittance (all HOMs)', Rep. CERN-ACC-NOTE-2017-0017, CERN, Geneva, Switzerland, 2017.

[30] 'H. Timko *et al.*, 'LHC MD 1087: Controlled Longitudinal Emittance Blow-up with Short Bunches', Rep. CERN-ACC-NOTE-2017-0018, CERN, Geneva, Switzerland, 2017.

# SUPPRESSION OF THE FAST BEAM-ION INSTABILITY BY TUNE SPREAD IN THE ELECTRON BEAM DUE TO BEAM-BEAM EFFECTS

Gennady Stupakov*, SLAC National Accelerator Laboratory, Menlo Park, CA, USA

*Abstract*

The fast beam-ion instability (FII) is caused by the interaction of an electron bunch train with the residual gas ions. The ion oscillations in the potential well of the electron beam have an inherent frequency spread due to the nonlinear profile of the potential. However, this frequency spread and associated with it Landau damping typically is not strong enough to suppress the instability. In this work, we develop a model of FII which takes into account the frequency spread in the electron beam due to the beam-beam interaction in an electron-ion collider. We show that with a large enough beam-beam parameter the fast ion instability can be suppressed. We estimate the strength of this effect for the parameters of the eRHIC electron-ion collider.

## INTRODUCTION

A fast beam-ion instability (FII) which is caused by the interaction of a single electron bunch train with the residual gas ions, has been proposed and studied theoretically in Refs. [1, 2]. The instability mechanism is the same in linacs and storage rings assuming that the ions are cleared in one turn. The ions generated by the head of the bunch train oscillate in the transverse direction and resonantly interact with the betatron oscillations of the subsequent bunches, causing the growth of an initial perturbation of the beam.

An important element that has to be included into the treatment of the instability is the frequency spread in the ion population due to the nonlinearity of the potential well for the trapped ions [2], as well as the spatial variation of the ion frequency along the beam path [3]. This frequency spread introduces the mechanism of Landau damping, or decoherence, but does not completely suppress the instability — it only makes it somewhat slower. In this work, we study another source of the decoherence in the fast ion instability originating from the tune spread in the electron beam. Such a tune spread may be due to the beam-beam collisions in a lepton or electron-ion collider.

For an analytical study we adopt a model that treats the bunch train as a continuous beam. This model is applicable if the distance between the bunches $l_b$ is smaller than the betatron wavelength, $l_b \ll c/\omega_\beta$, and is also smaller than the ion oscillation wavelength, $l_b \ll c/\omega_i$. We assume a one-dimensional model that treats only vertical linear oscillation of the centroids of the beam and the ions. We treat the electron tune spread using the method developed in Ref. [4].

## EQUATIONS OF MOTION

We use the notation $\tilde{y}_e\left(s, t|\omega_\beta\right)$ for the vertical offset of an electron in the beam that is characterized by the betatron frequency $\omega_\beta$, at time $t$ and longitudinal position $s$. The distance $s$ is measured from the injection point at $t = 0$. The equation for $\tilde{y}_e$, including the interaction with the ion background, is derived in Refs. [1, 2],

$$\begin{aligned}&\left(\frac{1}{c}\frac{\partial}{\partial t}+\frac{\partial}{\partial s}\right)^2 \tilde{y}_e\left(s,t|\omega_\beta\right)+\frac{\omega_\beta^2}{c^2}\tilde{y}_e\left(s,t|\omega_\beta\right)\\&=(ct-s)\kappa\left[\bar{y}_i(s,t)-\bar{y}_b(s,t)\right].\end{aligned} \tag{1}$$

The left-hand side of this equation accounts for the free betatron oscillations of a moving beam (we assume $v_{\text{beam}} \approx c$). On the right hand side, we included the force acting on the beam from the ions whose centroid is offset by $\bar{y}_i(s,t)$. The centroid of the electron beam is denoted by $\bar{y}_b(s,t)$. In the linear theory, which is the subject of this work, the interaction force between the electron beam and ions is proportional to the relative displacement between the beam and ions centroids; it is also proportional to the ion density. Assuming a continuous electron beam with a uniform density per unit length, the ion density increases due to collisional ionization as $ct - s$ behind the head of the beam (it is equal to zero before the beam head arrives at the point $s$ at time $t = s/c$). After separating the factor $ct - s$ on the right hand side of Eq. (1), the coefficient $\kappa$ is

$$\kappa \equiv \frac{4\dot{\lambda}_{ion} r_e}{3\gamma c\sigma_y(\sigma_x+\sigma_y)}, \tag{2}$$

where $\gamma$ is the relativistic factor of the beam, $r_e$ is the classical electron radius, $\sigma_{x,y}$ denote the horizontal and vertical rms-beam size respectively, and $\dot{\lambda}_{ion}$ is the number of ions per meter generated by the beam per unit time. Assuming a cross section for collisional ionization of about 2 Mbarns (corresponding to carbon monoxide and the electron energy $\sim$ 10 GeV), we have

$$\dot{\lambda}_{ion}[\mathrm{m^{-1}s^{-1}}] \approx 1.8\cdot 10^9 n_e[\mathrm{m^{-1}}]p_{gas}[\mathrm{torr}]\,, \tag{3}$$

where $n_e$ is the number of electrons in the beam per meter, and $p_{gas}$ the residual gas pressure in torr.

We assume that there is a betatron frequency spread in the electron beam due to the beam-beam interaction which is described by the distribution function $f_e(\omega_\beta)$ normalized by unity, $\int f_e(\omega_\beta)d\omega_\beta = 1$. The betatron frequency spread is assumed small, so that the function $f_e(\omega_\beta)$ is localized around the central frequency $\omega_{\beta 0}$. The centroid offset is obtained through averaging $\tilde{y}_e(s,t|\omega_\beta)$ with the help of the distribution function,

$$\bar{y}_b(s,t)=\int f_e(\omega_\beta)\tilde{y}_e(s,t|\omega_\beta)d\omega_\beta. \tag{4}$$

To find the equation for ions, we will assume that they perform linear oscillations inside the beam with a frequency

* stupakov@slac.stanford.edu

$\omega_i$. Furthermore, we will allow a continuous spectrum of $\omega_i$ given by a distribution function $f_i\,(\omega_i)$ normalized so that $\int f_i\,(\omega_i)\,d\omega_i = 1$. The distribution $f_i\,(\omega_i)$ is peaked around the frequency $\omega_i = \omega_{i0}$ corresponding to small vertical oscillations on the axis,

$$\omega_{i0} \equiv \left[\frac{4n_e r_p c^2}{3A\sigma_y(\sigma_x+\sigma_y)}\right]^{1/2}, \tag{5}$$

where $A$ designates the atomic mass number of the ions, $n_e$ the number of electrons in the beam per unit length, and $r_p$ the classical proton radius ($r_p \approx 1.5\cdot 10^{-16}$ cm). Typically, the frequency spread $\Delta\omega_i$ is not large; we assume $\Delta\omega_i \ll \omega_{i0}$.

We have to distinguish between the ions generated at different times $t'$ because they will have an initial offset equal to the beam coordinate $\bar{y}_b\,(s,t')$. Let us denote by $\tilde{y}_i\,(s,t|t',\omega_i)$ the displacement, at time $t$ and position $s$, of the ions generated at $t'$ ($t' \le t$) and oscillating with the frequency $\omega_i$. We have an oscillator equation for $\tilde{y}_i$

$$\frac{\partial^2}{\partial t^2}\tilde{y}_i(s,t|t',\omega_i) + \omega_i^2\left[\tilde{y}_i(s,t|t',\omega_i) - \bar{y}_b(s,t)\right] = 0, \tag{6}$$

with the initial condition

$$\tilde{y}_i(s,t'|t',\omega_i) = \bar{y}_b(s,t'), \qquad \left.\frac{\partial\tilde{y}_i}{\partial t}\right|_{t=t'} = 0. \tag{7}$$

Finally, averaging the displacement of the ions produced at different times $t'$ and having different frequencies $\omega_i$ gives the ion centroid $\bar{y}_i\,(s,t)$,

$$\bar{y}_i(s,t) = \frac{1}{t-s/c}\int_{s/c}^{t} dt' \int d\omega_i f_i(\omega_i)\tilde{y}_i(s,t|t',\omega_i). \tag{8}$$

Equations (1), (6)-(8) constitute a full set of equations governing the development of the instability.

## AVERAGING EQUATIONS

Equation (6) can be easily integrated with the initial conditions (7) yielding

$$\tilde{y}_i\,(s,t|t',\omega_i) = \bar{y}_b\,(s,t) - \int_{t'}^{t} \frac{\partial\bar{y}_b(s,t'')}{\partial t''}\cos\omega_i(t-t'')dt''. \tag{9}$$

Now using Eq. (8) and (9) in Eq. (1) we find an integro-differential equation for $\tilde{y}_e$,

$$\begin{aligned}&\left(\frac{1}{c}\frac{\partial}{\partial t}+\frac{\partial}{\partial s}\right)^2 \tilde{y}_e\,(s,t|\omega_\beta) + \frac{\omega_\beta^2}{c^2}\tilde{y}_e\,(s,t|\omega_\beta)\\ &= -\kappa\int_{s/c}^{t}(ct'-s)\frac{\partial\bar{y}_b(s,t')}{\partial t'}D_i(t-t')dt',\end{aligned} \tag{10}$$

where $D_i(t-t')$ denotes the ion decoherence function defined as

$$D_i(t-t') = \int d\omega_i \cos\omega_i(t-t')f_i(\omega_i). \tag{11}$$

This function represents the oscillation of the centroid of an ensemble of ions with a given frequency distribution $f_i(\omega_i)$ having an initial unit offset. If there is no frequency spread in the beam ($f_i = \delta(\omega_i - \omega_{i0})$) we have $D_i(t) = \cos(\omega_{i0}t)$.

Instead of $t$ and $s$, it is convenient to transform to new independent variables $z$ and $s$, where $z = ct - s$. The variable $z$ measures the distance from the head of the beam train and for a fixed $z$ the variable $s$ plays a role of time. Denoting

$$\begin{aligned} y\,(s,z) &\equiv \bar{y}_b\left(s, \frac{1}{c}(s+z)\right),\\ y_e\left(s,z|\omega_\beta\right) &\equiv \tilde{y}_e\left(s, \frac{1}{c}(s+z)|\omega_\beta\right),\end{aligned} \tag{12}$$

Eq. (10) takes the form

$$\begin{aligned}&\frac{\partial^2}{\partial s^2}y_e\left(s,z|\omega_\beta\right) + \frac{\omega_\beta^2}{c^2}y_e\left(s,z|\omega_\beta\right)\\ &= -\kappa\int_0^z z'\frac{\partial y\,(s,z')}{\partial z'}D_i[(z-z')/c]dz'.\end{aligned} \tag{13}$$

We will assume that the parameter $\kappa$ that defines the interaction between the beam and the ions is small,

$$c^2\kappa l \ll \omega_{i0}^2,\ \omega_\beta^2, \tag{14}$$

where $l$ denotes the length of the bunch train. This inequality means that the instability develops on a time scale that is much larger than both the betatron period and the period of ion oscillations. Typically this inequality is easily satisfied. In such a situation, the most unstable solution of Eq. (13) can be represented as a wave propagating in the beam with a slowly varying amplitude and phase,

$$y_e(s,z|\omega_\beta) = \mathrm{Re}A_e(s,z|\omega_\beta)e^{-i\omega_{\beta0}s/c+i\omega_{i0}z/c}, \tag{15}$$

where the complex amplitude $A_e(s,z|\omega_\beta)$ is a 'slow' function of its variables,

$$\left|\frac{\partial\ln A_e}{\partial s}\right| \ll \frac{\omega_{\beta0}}{c},\quad \left|\frac{\partial\ln A_e}{\partial z}\right| \ll \frac{\omega_{i0}}{c}. \tag{16}$$

For a fixed $z$, the $s$-dependence of Eq. (15) describes a pure betatron oscillation, while, for a fixed $s$ (that is in the frame co-moving with the ions) the $z$-dependent part implies oscillations (in time $t$) with the frequency $\omega_{i0}$. Hence the wave resonantly couples the oscillations of ions and electrons. Note that from Eq. (4) it follows that for the average offset of the electron beam we have

$$y(s,z) = \mathrm{Re}A(s,z)e^{-i\omega_{\beta0}s/c+i\omega_{i0}z/c}, \tag{17}$$

with

$$A(s,z) = \int f_e(\omega_\beta)A_e(s,z|\omega_\beta)d\omega_\beta. \tag{18}$$

Substituting Eq. (15) into Eq. (13) and averaging it over the rapid oscillations with the frequencies $\omega_{i0}$ and $\omega_{\beta0}$, we can re-formulate Eq. (13) so that it describes a slow evolution of the complex function $A_e$,

$$\frac{\partial A_e(s,z|\omega_\beta)}{\partial s}+\frac{i}{c}(\omega_\beta-\omega_{\beta 0})A_e(s,z|\omega_\beta) = \frac{\kappa\omega_{i0}}{4\omega_{\beta 0}}\int_0^z z'A(s,z')\hat{D}_i(z-z')dz', \quad (19)$$

where the function $\hat{D}_i(z)$ is

$$\hat{D}_i(z)=\int d\omega_i f_i(\omega_i)e^{i(\omega_i-\omega_{i0})z/c}. \quad (20)$$

Eqs. (18) and (19) constitute a full set of equations that we need to solve.

We can make one more step and formulate an equation for the amplitude of the averaged offset $A$. For this, we integrate Eq. (19) over $s$,

$$A_e(s,z|\omega_\beta)=A_e(0,z|\omega_\beta)e^{-i(\omega_\beta-\omega_{\beta 0})s/c} + \frac{\kappa\omega_{i0}}{4\omega_{\beta 0}}\int_0^s ds' e^{-i(\omega_\beta-\omega_{\beta 0})(s-s')/c} \times\int_0^z z'A(s',z')\hat{D}_i(z-z')dz'. \quad (21)$$

We now average this equation with the distribution function $f_e(\omega_\beta)$. It is reasonable to assume that the initial offset $A_e(0,z|\omega_\beta)$ does not depend on $\omega_\beta$, and write it as $A_0(z)$. We then obtain

$$A(s,z)=A_0(z)\hat{D}_e(s)+\frac{\kappa\omega_{i0}}{4\omega_{\beta 0}}\int_0^s ds'\hat{D}_e(s-s') \times\int_0^z z'A(s',z')\hat{D}_i(z-z')dz', \quad (22)$$

where

$$\hat{D}_e(s)=\int d\omega_\beta f_e(\omega_\beta)e^{-i(\omega_\beta-\omega_{\beta 0})s/c}. \quad (23)$$

Note that from Eq. (22) follows the initial condition for function $A$,

$$A(s,0)=A_0(0)\hat{D}_e(s). \quad (24)$$

We can also re-write Eq. (22) as an integro-differential equation

$$\frac{\partial}{\partial s}A(s,z)=A_0(z)\hat{D}'_e(s)+\frac{\kappa\omega_{i0}}{4\omega_{\beta 0}}\int_0^z z'A(s,z')\hat{D}_i(z-z')dz' + \frac{\kappa\omega_{i0}}{4\omega_{\beta 0}}\int_0^s ds'\hat{D}'_e(s-s')\int_0^z z'A(s',z')\hat{D}_i(z-z')dz', \quad (25)$$

where the prime denotes the derivative with respect to $s$, and we have used $\hat{D}_e(0)=1$. The first and the third terms on the right-hand side vanish for a constant $\hat{D}_e$ that corresponds to the case of the zero electron tune spread, and in this limit we recover the result of Ref. [2].

## SOLUTION OF FII EQUATIONS FOR SPECIAL CASES

In this section will show how to solve Eq. (22) for the case when one can neglect the ion decoherence, $\hat{D}_i(z)=1$. In this case Eq. (22) reduces to

$$A(s,z)=A_0(z)\hat{D}_e(s)+\frac{\kappa\omega_{i0}}{4\omega_{\beta 0}} \times\int_0^s ds'\hat{D}_e(s-s')\int_0^z z'A(s',z')dz'. \quad (26)$$

We first make the Laplace transform with respect to the variable $s$, introducing the Laplace image $a(\varkappa,z)$,

$$a(\varkappa,z)=\int_0^\infty A(s,z)e^{-\varkappa s}ds. \quad (27)$$

Making the Laplace transform of Eq. (26) we find

$$a(\varkappa,z)=A_0(z)d(\varkappa)+\frac{\kappa\omega_{i0}}{4\omega_{\beta 0}}d(\varkappa)\int_0^z z'a(\varkappa,z')dz', \quad (28)$$

where

$$d(\varkappa)=\int_0^\infty \hat{D}_e(s)e^{-\varkappa s}ds. \quad (29)$$

We can solve Eq. (28) analytically for the special case when the initial amplitude of the beam offset, $A_0$, does not depend on $z$, $A_0=$ const. Differentiating Eq. (28) with respect to $z$ and solving the resulting differential equation with the initial condition $a(\varkappa,0)=A_0 d(\varkappa)$ gives the following result

$$a(\varkappa,z)=A_0 d(\varkappa)e^{qd(\varkappa)z^2}, \quad (30)$$

with $q=\kappa\omega_{i0}/8\omega_{\beta 0}$. Making the inverse Laplace transform, we can find $A$,

$$A(s,z)=A_0\frac{1}{2\pi i}\int_{\sigma-i\infty}^{\sigma+i\infty} d\varkappa e^{\varkappa s}d(\varkappa)e^{qd(\varkappa)z^2}. \quad (31)$$

In the case when the tune spread in the electron beam is so small that it can be neglected, we have $\hat{D}_e(s)=1$ and $d(\varkappa)=1/\varkappa$. We arrive at the integral

$$\frac{1}{2\pi i}\int_{\sigma-i\infty}^{\sigma+i\infty}\frac{d\varkappa}{\varkappa}e^{\varkappa s+qz^2/\varkappa}=I_0\left(2z\sqrt{qs}\right), \quad (32)$$

and $A=A_0 I_0\left(2z\sqrt{qs}\right)$. This is the result of Refs. [1, 2] when the ion frequency spread is neglected.

Consider now a model electron decoherence function $\hat{D}_e(s)=e^{-ps}$ with $p>0$, for which we have $d(\varkappa)=1/(\varkappa+p)$. For the integral we have

$$A(s,z)=\frac{A_0}{2\pi i}\int_{\sigma-i\infty}^{\sigma+i\infty}\frac{d\varkappa}{\varkappa+p}e^{\varkappa s+qz^2/(\varkappa+p)} = A_0 e^{-ps}I_0\left(2z\sqrt{qs}\right). \quad (33)$$

Asymptotically, in the limit $s\to\infty$, we have $I_0(2z\sqrt{qs})\propto \exp(2z\sqrt{qs})/\sqrt{2z\sqrt{qs}}$, and the exponential factor $e^{-ps}$ overcomes the growing Bessel function, and hence, suppresses the instability.

## DECOHERENCE DUE TO BEAM-BEAM COLLISIONS

The decoherence function $\hat{D}_e(s)$ for the case when the betatron tune spread is due to the beam-beam collisions at the interaction point in a collider was derived in Ref. [5]. Assuming round beams at the interaction point, the following expression for $\hat{D}_e(s)$ was obtained:

$$\hat{D}_e(s) = 4\int_0^\infty \int_0^\infty da_1\, da_2 \times \exp\left[-2(a_1+a_2) + i(s/cT)\Delta\nu_y(a_1,a_2)\right], \quad (34)$$

where $T$ is the revolution period in the ring and the tune shift $\Delta\nu(a_1,a_2)$ is given by the following formula [6],

$$\Delta\nu = \xi \int_0^1 du\, e^{-u(a_1+a_2)} I_0(a_2 u)\,[I_0(a_1 u) - I_1(a_1 u)]\,.$$

Here $a_1$ and $a_2$ are the dimensionless amplitudes of the betatron oscillations, $I_n(z)$ is the modified Bessel function of the $n$-th order and $\xi$ is the tune shift parameter, $\xi = N_p r_e/4\pi\epsilon$ with $N_p$ the number of particles in the bunch, $r_e$ the classical electron radius and $\epsilon$ the normalized beam emittance. The tune shift $\Delta\nu$ is positive due to the opposite signs of the charges of the colliding beams in an electron-ion collider. The plot of function $\hat{D}_e(s)$ is shown in Fig. 1.

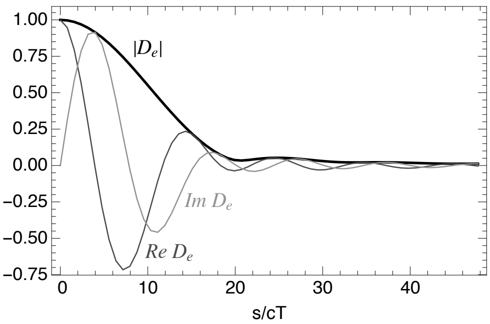


Figure 1: Plot of the real (black) and imaginary (magenta) parts of the function $\hat{D}_e(s)$. The black line is the absolute value $|\hat{D}_e(s)|$.

## NUMERICAL SOLUTION OF EQ. (25)

Here we outline the numerical solution of (25) following the method proposed in Ref. [7]. We first normalize the variable $z$ by the length of the bunch train $l$, $\zeta = z/l$, and then replace $s$ in this equation by $\xi = s(\kappa\omega_{i0}l^2/4\omega_{\beta 0})$. Note that positions within the bunch train correspond to the interval $0 < \zeta < 1$. We then have

$$\frac{\partial}{\partial\xi}A(\xi,\zeta) = A_0(\zeta)\hat{D}_e'(\xi) + \int_0^\zeta \zeta' A(\xi,\zeta')\hat{D}_i(\zeta-\zeta')d\zeta' + \int_0^\xi d\xi' \hat{D}_e'(\xi-\xi') \int_0^\zeta \zeta' A(\xi',\zeta')\hat{D}_i(\zeta-\zeta')d\zeta', \quad (35)$$

where $\hat{D}_e'$ now denotes the derivative of $\hat{D}_e$ with respect to $\xi$.

We first introduce a mesh in the unit interval $0 < \zeta < 1$, $\zeta_k = k\Delta$, $k = 1,\dots,n$, with $\Delta = 1/(n-1)$. The function $A(\xi,\zeta)$ is now represented on this mesh, $A(\xi,\zeta_k)$, and we use the trapezoidal integration rule to carry out the integration over $\zeta$ in Eq. (25),

$$\int_0^\zeta \zeta' A(\xi',\zeta')\hat{D}_i(\zeta-\zeta')d\zeta' = \frac{\Delta}{2}\left[\zeta_1 A(\xi',\zeta_1) + 2\zeta_2 A(\xi',\zeta_2) + \dots + 2\zeta_{n-1}A(\xi',\zeta_{n-1}) + \zeta_n A(\xi',\zeta_n)\right]. \quad (36)$$

We will use the notation $\mathcal{A}(\xi)$ for the vector $A(\xi,\zeta_k)$ and denote the discretized integration (36) by the operator $T$,

$$\int_0^\zeta \zeta' A(\xi',\zeta')\hat{D}_i(\zeta-\zeta')d\zeta' \to T\cdot\mathcal{A}. \quad (37)$$

Then Eq. (35) can be written as

$$\mathcal{A}'(\xi) = \mathcal{A}_0\hat{D}_e'(\xi) + T\cdot\mathcal{A}(\xi) + \int_0^\xi d\mu \mathcal{D}(\xi,\mu)T\cdot\mathcal{A}(\mu), \quad (38)$$

where to simplify the notation we introduced $\mathcal{D}(\xi,\mu) \equiv \hat{D}_e'(\xi-\mu)$.

Introducing the step $h$ in variable $\xi$ we denote by $\mathcal{A}_k$ the value of $\mathcal{A}$ at $\xi_k = h(k-1)$. Likewise $\mathcal{A}_k'$ denotes the value of $\partial\mathcal{A}/\partial\xi|_{\xi=\xi_k}$. Again, using the trapezoidal method of integration, we find

$$\mathcal{A}_k' = \mathcal{A}_0\hat{D}_e'(\xi_k) + T\cdot\mathcal{A}_k + \frac{h}{2}\left[\mathcal{D}(\xi_k,\xi_1)T\cdot\mathcal{A}_1 + 2\mathcal{D}(\xi_k,\xi_2)T\cdot\mathcal{A}_2 + \dots + 2\mathcal{D}(\xi_k,\xi_{k-1})T\cdot\mathcal{A}_{k-1} + 2\mathcal{D}(\xi_k,\xi_k)T\cdot\mathcal{A}_k\right]. \quad (39)$$

To advance the step from $\xi = \xi_k$ to $\xi = \xi_k + h$ we first integrate (38) to obtain

$$\mathcal{A}_{k+1} = \mathcal{A}_k + \mathcal{A}_0[\hat{D}_e(\xi_{k+1}) - \hat{D}_e(\xi_k)] + \int_{\xi_k}^{\xi_{k+1}} d\xi T\cdot\mathcal{A}(\xi) + \int_{\xi_k}^{\xi_{k+1}} d\xi \int_0^\xi d\mu\mathcal{D}(\xi,\mu)T\cdot\mathcal{A}(\mu) = \mathcal{A}_k + \mathcal{A}_0[\hat{D}_e(\xi_{k+1}) - \hat{D}_e(\xi_k)] + I_1 + I_2. \quad (40)$$

For $I_1$ we use the trapezoidal rule together with the approximation $\mathcal{A}_{k+1} = \mathcal{A}_k + h\mathcal{A}_k'$ to yield

$$I_1 = \frac{h}{2}\left[T\cdot\mathcal{A}_k + T\cdot(\mathcal{A}_k + h\mathcal{A}_k')\right]. \quad (41)$$

For $I_2$ we use the trapezoidal rule for the outer integral to obtain

$$I_2 = \frac{h}{2}\left[\int_0^{\xi_k} d\mu\mathcal{D}(\xi_k,\mu)T\cdot\mathcal{A}(\mu) + \int_0^{\xi_{k+1}} d\mu\mathcal{D}(\xi_{k+1},\mu)T\cdot\mathcal{A}(\mu)\right]. \quad (42)$$

We then use the trapezoidal rule for the inner integral and again use the approximation $\mathcal{A}_{k+1} = \mathcal{A}_k + h\mathcal{A}'_k$ to obtain

$$\begin{aligned}I_2 = \frac{h^2}{4}\,[&\mathcal{D}(\xi_k,\xi_1)T\cdot\mathcal{A}_1 + 2\mathcal{D}(\xi_k,\xi_2)T\cdot\mathcal{A}_2\ldots\\ &+2\mathcal{D}(\xi_k,\xi_{k-1})T\cdot\mathcal{A}_{k-1} + \mathcal{D}(\xi_k,\xi_k)T\cdot\mathcal{A}_k]\\ &+\frac{h^2}{4}\,[\mathcal{D}(\xi_{k+1},\xi_1)T\cdot\mathcal{A}_1 + 2\mathcal{D}(\xi_{k+1},\xi_2)T\cdot\mathcal{A}_2\ldots\\ &+2\mathcal{D}(\xi_{k+1},\xi_k)T\cdot\mathcal{A}_k + \mathcal{D}(\xi_{k+1},\xi_{k+1})T\cdot(\mathcal{A}_k + h\mathcal{A}'_k)\big].\end{aligned} \tag{43}$$

Eqs. (40), (41) and (43) finalize the one step advance in the numerical solution of Eq. (25).

## FII AT ERHIC

In this section we will analyze the fast ion instability for the electron storage ring of the proposed Electron Ion Collider at BNL, eRHIC [8]. The parameters of eRHIC electron beam relevant for the fast ion instability are summarized in Table 1. The nominal tune shift for the electron beam is $\xi = 0.1$.

| | |
|---|---|
| Electron beam energy | 10 GeV |
| Vertical beam emittance, $\epsilon_y$ | 4.9 nm |
| Horizontal beam emittance, $\epsilon_x$ | 20 nm |
| Residual gas pressure, $p$ | 0.75 nTorr |
| Averaged beta function, $\beta_x$, $\beta_y$ | 18 m |
| Vertical betatron tune, $\nu_y$ | 31.06 |
| Number of electron bunches, $N_b$ | 567 |
| Length of the bunch train, $l_b$ | 3451 m |
| Atomic mass number for ions, $A$ | 28 |
| Number of electrons per unit length, $n_e$ | $5.6\times10^{10}$ m$^{-1}$ |

Table 1: Parameters of the eRHIC collider relevant for FII.

Using the beam emittance and the value for the averaged beta functions we find the characteristic beam sizes in the vertical and horizontal directions, $\sigma_y = 0.3$ mm and $\sigma_x = 0.6$ mm. From Eq. (5) we obtain the ion frequency $\omega_{i0} = 4.5\times10^7$ s$^{-1}$ and for the vertical betatron frequency we calculate $\omega_\beta = 1.5\times10^7$ s$^{-1}$. From Eq. (3) it follows that $\dot\lambda = 7.5\times10^{10}$ m$^{-1}$s$^{-1}$ and the characteristic time of FII [2] is

$$\tau = \frac{4\omega_{\beta0}}{\kappa\omega_{i0}cl^2} = 2.1\ \mu\text{s}. \tag{44}$$

In our calculations we assume the worst case scenario when all residual gas pressure is due to the carbon monoxide (lighter ions are usually less trapped inside the beam).

Note that the parameter $c/\omega_\beta \approx 20$ m is several times larger than the distance between the electron bunches, $l_b = 6.1$ m, but $c/\omega_{i0} = 6.5$ m is comparable with $l_b$, which means that, for the parameters of eRHIC, the model of continuous electron beam that we use in this paper is actually at the edge of its applicability range.

We first simulated the fast ion instability for eRHIC parameters neglecting the electron decoherence by taking into account only ion decoherence effects. This case is described by Eq. (25) with $\hat{D}_e(s) = 1$. For the ion decoherence function $\hat{D}_i(z)$, following Ref. [2], we took

$$\hat{D}_i(z) = \left(1 + \frac{i}{4c}\omega_{i0}z\right)^{-1/2}. \tag{45}$$

Fig. 2 shows the plot of the FII amplitude obtained by numerical solution of Eq. (25) for this case at different locations along the bunch train. This plot shows that the amplitude $A$

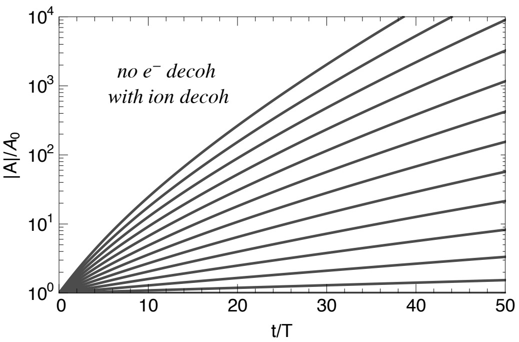


Figure 2: Amplitude $A$ normalized by its initial value $A_0$ at 13 equidistant positions in the bunch train as a function of time measured in the revolution periods $T$ in the ring. Electron decoherence effects are neglected. The amplitude grows faster with increase of the distance from the head of the train.

at the end of the electron bunch train grows more then four order of magnitude after 50 revolution periods in the ring.

Using Fig. 2 as a reference case, we then simulated FII with account of the electron beam decoherence. This case is described by Eq. (25) with the electron decoherence function (34). For the ion decoherence function we again used Eq. (45). The result is shown in Fig. 3. One can see that

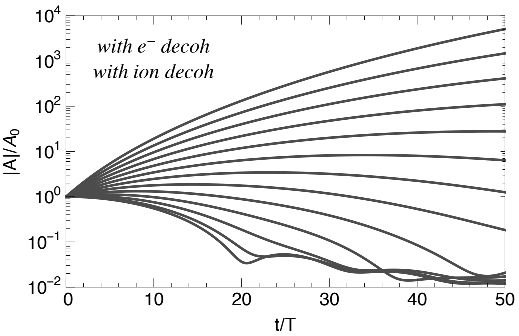


Figure 3: Amplitude $A$ normalized by its initial value $A_0$ at 13 equidistant positions in the bunch train as a function of time measured in the revolution periods $T$ in the ring. Electron decoherence effects are taken into account.

the electron decoherence suppresses the instability in the region close to the head of the bunch train (the lowest 4-5 lines in the plot corresponding to positions near the head). However, the amplitude $A$ still grows to unacceptably large values at the tail of the train. Simulations show that if the numerical solution is continued to even larger values of $t$, the amplitude $A$ starts to decrease, but at its maximum at intermediate times, it is amplified by many orders of magnitude relative to the initial value. We conclude that while electron decoherence effects do provide some stabilization effect, it is not sufficient, for the nominal parameters of Table 1 (and 100% carbon monoxide residual gas), to fully suppress FII.

Finally, we repeated the previous simulation, but with 3 times smaller residual gas pressure, $p = 0.25$ nTorr. The result is shown in Fig. 4. This case can be characterized as a

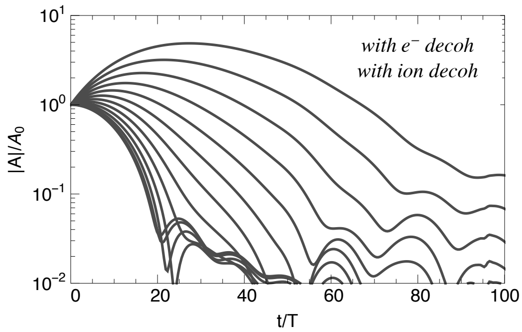


Figure 4: Amplitude $A$ normalized by its initial value $A_0$ at 13 equidistant positions in the bunch train as a function of time measured in the revolution periods $T$ in the ring. Electron decoherence effects are taken into account. The residual gas pressure is $p = 0.25$ nTorr.

stable one: after some increase in the tail of the bunch train the amplitude is suppressed through the electron decoherence effects to the values below the initial value $A_0$.

## SUMMARY

In this paper, we extended the theoretical analysis of Ref. [2] of the fast ion instability to include decoherence effects due to the tune spread in the electron beam. Specifically, we calculated the electron decoherence function for the case when the tune spread is caused by the beam-beam collisions in an electron-ion collider. We derived an equation that governs the evolution of the amplitude of the transverse oscillations in the beam, and numerically solved it for the nominal parameters of the eRHIC collider. We found that while the electron decoherence weakens the instability, it does not fully suppress it for the nominal parameters of eRHIC. The instability however is suppressed for three times smaller residual gas pressure.

We note that our model of continuous electron beam is not fully applicable for eRHIC parameter because the distance between the electron bunches is of the same order as the parameter $c/\omega_{i0}$.

Qualitatively similar results have been recently obtained by M. Blaskiewicz [9] who used computer simulations of FII for eRHIC.

## ACKNOWLEDGMENTS

The author thanks M. Blaskiewicz who initiated this work and provided relevant information for the eRHIC project, and B. Podobedov for useful discussions.

This work was supported by Department of Energy contract DE-AC03-76SF00515.

## REFERENCES

[1] T. O. Raubenheimer and F. Zimmermann. A fast beam-ion instability in linear accelerators and storage rings. *Phys. Rev.*, E52:5487–5497, 1995.

[2] G. V. Stupakov, T. O. Raubenheimer, and F. Zimmermann. Fast beam ion instability. 2. Effect of ion decoherence. *Phys. Rev.*, E52(5):5499–5504, 1995.

[3] G.V. Stupakov. Fast ion instability in real lattice. In *Proceedings of the 1997 Particle Accelerator Conference*, volume 2, pages 1632–4, Piscataway, NJ, 1998.

[4] G. V. Stupakov and A. W. Chao. Collective effects and beam decoherence. Preprint SSCL-621, Superconducting Supercollider Laboratory, May 1993.

[5] G. Stupakov, V. Parkhomchuk, and V. Shiltsev. Decoherence of a gaussian beam due to beam-beam interation. Preprint SSCL-Preprint-495, Superconducting Supercollider Laboratory, August 1993.

[6] Alexander W. Chao. Beam-beam instability. *AIP Conference Proceedings*, 127(1):201–242, 1985.

[7] James Thomas Day. Note on the Numerical Solution of Integro-Differential Equations. *The Computer Journal*, 9(4):394–395, 02 1967.

[8] C. Montag, G. Bassi, J. Beebe-Wang, J.S. Berg, M. Blaskiewicz, J.M. Brennan, A.V. Fedotov, W. Fischer, W. Guo, Y. Hao, A. Hershcovitch, Y. Luo, F. Méot, R.B. Palmer, B. Parker, S. Peggs, V. Ptitsyn, V.H. Ranjbar, S. Seletskiy, T.V. Shaftan, V.V. Smaluk, S. Tepikian, D. Trbojevic, E. Wang, F.J. Willeke, H. Witte, and Q. Wu. Overview of the eRHIC Ring-Ring Design. In *Proc. of International Particle Accelerator Conference (IPAC'17)*, International Particle Accelerator Conference, pages 3035–3037, Geneva, Switzerland, May 2017. JACoW. https://doi.org/10.18429/JACoW-IPAC2017-WEPIK049.

[9] M. Blaskiewicz. Beam-beam damping of the ion instability. In *Proc. of North American Particle Accelerator Conference (NAPAC2019)*, 2019.

# BEAM LOADING COMPENSATION FOR OPTIMAL BUNCH LENGTHENING WITH HARMONIC CAVITIES

Naoto Yamamoto*, Takeshi Takahashi, Shogo Sakanaka KEK, Tsukuba, Japan

*Abstract*

Emittance growth and short beam lifetime due to intrabeam scattering in extremely low emittance storage rings can be mitigated if harmonic rf cavities are used for the purpose of lengthening the longitudinal bunch size. The "flat potential condition" can be achieved with harmonic cavities, lengthening the bunch by a factor of ~ 5. However, the performance is limited by the transient beam-loading effect in the rf cavities, which is induced by gaps in the ring fill pattern. As a counter-measure of this effect, we have proposed the active compensation techniques by using a single kicker cavity having a bandwidth of several times the revolution frequency. The transient effect can be compensated when the kicker cavity voltage is determined to suppress bunch phase shifts along the train.

## INTRODUCTION

Extremely low emittance storage rings, which aim at achieving the beam emittances of < 100 pm-rad, are being actively designed as future ring-based synchrotron light sources. In such rings, emittance growth and short beam lifetime due to intrabeam scattering are of serious concern. To mitigate such adverse effects, a harmonic radio-frequency (rf) system [1] is used to lengthen the beam bunches, so that the particle density at the core of the bunch can be reduced.

Harmonic rf systems have been successfully operated to lengthen beam bunches in several light sources [2–9]. However, in some of them, the bunch-lengthening performance was limited due to the transient beam-loading (TBL) effect when the large bunch gaps are introduced [3–5]. It was reported [10] that the reduction of a total $R/Q$ of rf cavities is essential to alleviate such transient effects.

The voltage fluctuations due to the TBL effect can be reduced when rf cavities having a small total $R/Q$ are employed as shown in Fig. 7 in reference [11]. When the remaining variation of cavity voltages is kept smaller than several tens kV, we can further improve the bunch lengthening performance using a single kicker cavity within technical feasibility. In reference [11], we proposed two measures for active compensation techniques: compensation on the fundamental and harmonic cavities, and compensation using a separate kicker cavity.

As a next step of this work, feasiblity studies of the active compensation techniques using a separate kicker cavity were made. In this paper, we present numerical calculation results after the details of the compensation techniques are described.

* naoto.yamamoto@kek.jp

Table 1: Main parameters of the KEK-LS without harmonic rf systems, including insertion device losses.

| Parameter | Value |
|---|---|
| Nominal beam energy | 3.0 GeV |
| Stored beam current | 500 mA |
| RF frequency (fundamental) | 500.07 MHz |
| Harmonic number | 952 |
| Revolution frequency | 525 kHz |
| Unperturbed synchrotron frequency | 2.65 kHz |
| Synchrotron radiation loss per turn | 851 keV |
| Main rf voltage | 2.5 MV |
| Natural relative energy spread (rms) | $7.3 \times 10^{-4}$ |
| Momentum compaction factor | $2.2 \times 10^{-4}$ |
| Longitudinal radiation damping time | 7.0 ms |
| Natural bunch length (rms) | 9.5 ps |

Table 2: Parameters of the KEK-LS rf systems used in calculations at the beam current of 500 mA. For the fundamental and third harmonic cavities, the PF-type cavity and the TM020 cavity were assumed, respectively. The synchronous phases are shown in the cosine definition.

| Parameter | Fund. rf | Harmonic rf (3rd) |
|---|---|---|
| Rf voltage | 2.5 MV | 777 kV |
| Synchronous phase | 1.178 rad | -1.708 rad |
| Tuning angle | -0.962 rad | 1.433 rad |
| Total $R/Q$ ($R = V_c^2/P_c$) | 875 Ω | 386 Ω |
| Total shunt impedance | 35 MΩ | 14.48 MΩ |
| Cavity coupling | 3.5 | 0.27 |
| Cavity detuning amount | -40.3 kHz | 185 kHz |

## KEK-LS STORAGE RING

As an example of the extremely low emittance storage rings for feasibility study of the TBL compensation, we assumed the KEK light source (KEK-LS) [12]. Table 1 shows the main parameters of the KEK-LS. The KEK-LS has a design based on the hybrid multi-bend achromatic lattice. Although the natural emittance of 0.13 nm-rad is expected with zero beam current, the emittance affected by the intra-beam scattering is estimated to be 0.31 nm-rad at the nominal beam current of 500 mA. Then we have planned to introduce the harmonic cavities to mitigate the impact of the intra-beam scattering.

The assumed parameters for the fundamental and harmonic rf system are summarized in Table 2. The existing Photon Factory (PF) type cavities [13] are assumed for the fundamental cavity. A typical total RF voltage of 2.5 MV is

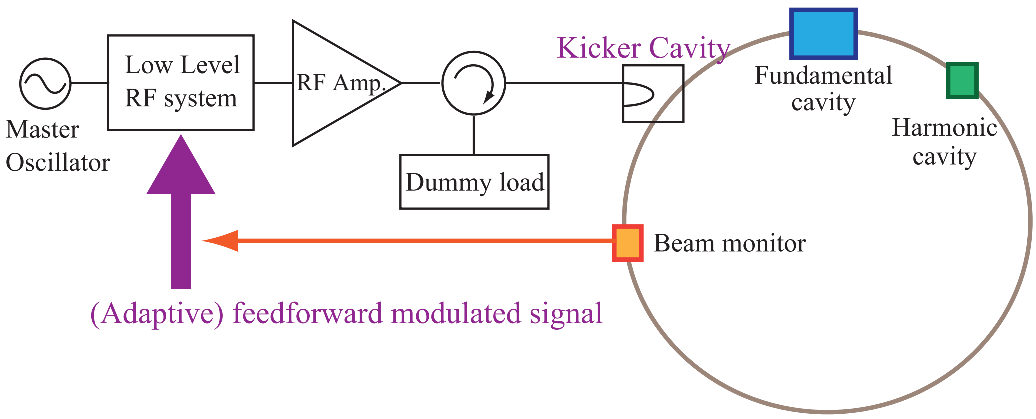


Figure 1: A Schematic of active compensation for transient beam loading effect.

produced by five cavities, where each cavity has an unloaded Q of 40,000 and $R/Q$ of 175 Ω.

Concerning harmonic rf cavities for the KEK-LS, the candidate is a normal conducting TM020 cavity having the resonant frequency of 1.5 GHz, which is the third harmonic of the fundamental frequency, since lower $R/Q$ and higher unloaded Q, as compared to the conventional TM010 cavity are expected [14, 15]. In this investigation, $R/Q$ of 77.2 Ω and unloaded Q of 37,500 are expected for one 1.5 GHz-TM020 cavity. At nominal stored current of 500 mA, the "flat potential condition", which means that the voltage slope and the first derivative of the slope become zero, is satisfied with the cavity coupling of 0.27 and detuning amount of 185 kHz. At these conditions, the input power of the harmonic cavities ideally becomes zero, that is to say, passive cavity operation.

## ACTIVE COMPENSATION SYSTEM

The schematic of an active compensation system using a separate kicker cavity is shown in Fig. 1. We have considered to use a kicker cavity having the wide bandwidth, a solid state amplifier and a feedforward low level rf (LLRF) control.

For the bandwidth of the feedforward signal, we consider the frequency range of about several megahertz, covering multiples of the repetition frequency of the fill pattern for typical synchrotron sources.

### *Kicker cavity*

A single kicker cavity is the key equipment of this system. The cavity parameters shown in Table 3 are assumed for the feasibility studies. The summarized parameters are based on that of the PF-type 500-MHz cavity [13]. The cavity coupling is changed to realize the adequate cavity bandwidth. The 3dB full bandwidth of 5.0 MHz, which is given by $(1+\beta)/Q_0 \times f_r$, is expected if the cavity coupling ($\beta$) is set to 199 for a cavity having the resonant frequency ($f_r$) of 500 MHz and unloaded Q ($Q_0$) of 40,000, respectively.

### *Solid state amplifier*

In order to compensate the transient voltages, the bandwidths of rf generators should be wider than the bandwidths of feedforward signal. Then as a high power rf amplifier for the active compensation system, a solid state amplifier is preferred option due to the intrinsic advantage of the wider bandwidth as compared to a klystron-based amplifier. As a result of feasibility test, we obtained a 1-dB full bandwidth of about 10 MHz with our prototype 1-kW, 500-MHz solid-state amplifier.

Table 3: Assumed parameters for a single cavity of the compensation system.

| Parameter | Value |
|---|---|
| Resonant frequency | 500.07 MHz |
| $R/Q$ | 175 Ω |
| Unloaded Q | 40,000 |
| Cavity number | 1 |
| Cavity coupling coefficient | 199 |
| -3dB full bandwidth | 5.0 MHz |

### *Adaptive feedforward LLRF system*

The LLRF system should provide an rf signal including a fast feedforward pattern to compensate the transients while stabilizing both amplitude and phase of rf voltage on average using some feedback loops. We believe that both the feedforward and the feedback should be realized compatibly if they have much different response time.

At this moment, we have not determined the practical design of the feedforward LLRF system. A possible solution is reading both fill pattern and beam current in the system, calculating necessary feedforward pattern, and outputting the desired rf signal from the LLRF system.

## COMPENSATION USING SINGLE KICKER CAVITY

In this section, we explain how to obtain the feedforward signal of a single kicker cavity in case that the voltage fluctuations along the bunch train for the fundamental and harmonic cavities are given. Then, the calculation results obtained in the KEK-LS case are shown as an example of the transient compensation.

The voltage fluctuations are anticipated numerically by using analytical [11] or tracking [16] tools if the operation parameters of the ring, including the bunch fill pattern , are known. For practical cases, it is considered that we can measure the fluctuations through rf cavity pickups experimentally.

### *Feedforward signal*

Once cavity voltage fluctuations are caused by TBL effect, synchronous phases of bunches are varied according to the location in the bunch train. The amount of the phase shift is larger in the bunch lengthening operation mode compared to the other operation modes because of the nonlinearity of the harmonic rf voltage. The feedforward signal for a kicker cavity should be determined to minimizing these phase shifts.

When in the complex plane, voltages of both the fundamental and $n$-th harmonic cavity are represented by $\tilde{V}_{\mathrm{c},1}(m)$ and $\tilde{V}_{\mathrm{c},n}(m)$ as functions of the bucket number $m$, the kicker cavity voltage $\tilde{V}_{\mathrm{c,k}}(m)$ should satisfied the following requirement for canceling the bunch phase shift,

$$\mathrm{Re}[\tilde{V}_{\mathrm{c,k}}(m)] = -(\mathrm{Re}[\tilde{V}_{\mathrm{c},1}(m) + \tilde{V}_{\mathrm{c},n}(m)] - U_0/e), \quad (1)$$

where $U_0$ is the radiation loss per turn, e is the electron charge and $\mathrm{Re}[\tilde{V}_\mathrm{c}]$ is the accelerating voltage seen by the beam. If the resonant frequency of the kicker cavity is exactly the same or integer multiple of the ring rf frequency, the amplitude of the kicker cavity voltage is represented by

$$|\tilde{V}_{\mathrm{c,k}}(m)| = \mathrm{Re}[\tilde{V}_{\mathrm{c,k}}(m)]/\cos\phi_{s,\mathrm{k}}, \quad (2)$$

where $\phi_{s,\mathrm{k}}$ is the cavity synchronous phase of the kicker cavity in the cosine definition.

Then using the beam induced voltage in the kicker cavity $\tilde{V}_{\mathrm{b,k}}(m)$, we obtain the required generator voltage

$$\tilde{V}_{\mathrm{g,k}}(m) = \tilde{V}_{\mathrm{c,k}}(m) - \tilde{V}_{\mathrm{b,k}}(m). \quad (3)$$

The generator current can be calculated using the kicker cavity response given in Eq. (25) of Ref [11]. Consequently, we deduce the input signal for the LLRF system after some band-limiting treatments to keep the peak generator power technically feasible.

### *Analytical simulation for KEK-LS case*

In a standard operation of the KEK-LS ring, all rf buckets will be equally filled with electrons, except for the bunch gaps. To avoid ion trapping, we introduce several bunch gaps symmetrically in the ring. The number and duration of the gaps are tentatively 2 and 60 ns, respectively.

With the bunch gaps assumed, the amplitude of cavity voltages for both the fundamental and 3rd harmonic cavities are evaluated as shown in Fig. 2. For the harmonic cavity driven mainly by the beam induced power, the amplitude decreases at the head part of the bunch train, then

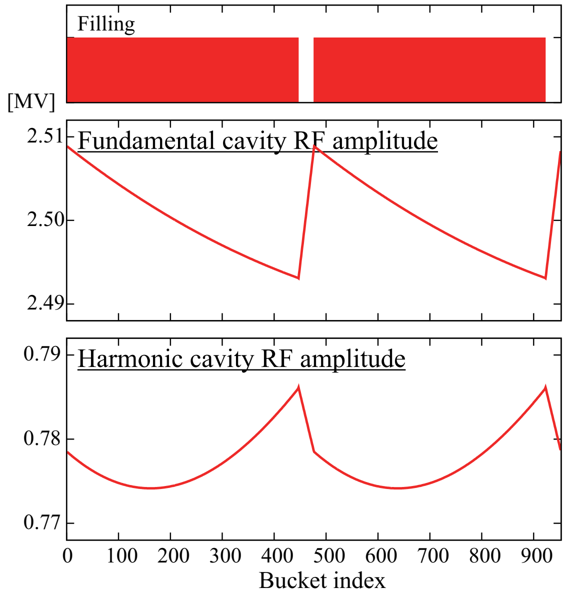


Figure 2: Amplitude variations in the fundamental and harmonic voltage due to bunch gap. A beam current of 500 mA with the standard fill pattern of the KEK-LS, where the number and duration of the gaps are 2 and 60ns respectively, is assumed.

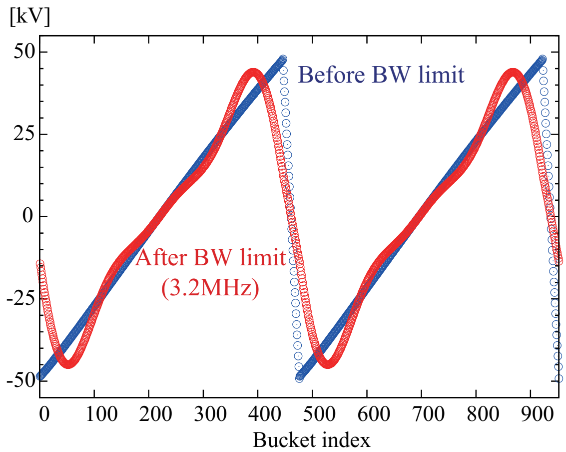


Figure 3: Required amplitude signal of the kicker cavity with assumption of the standard fill pattern of the KEK-LS. The red circles represent the band-limited signal with the bandwidth of 3.2 MHz for the primary signal shown in blue circles.

increases as the number of the bunch passing through the cavity increases.

The amplitude of the kicker cavity voltage calculated by Eq. (1) is plotted by blue circles in Fig. 3, where $\phi_{s,\mathrm{k}}$ is assumed to be zero. It is preferred that the bandwidth of the feedforward signal for the kicker cavity is limited to keep the generator power technically feasible. By omitting the frequency components above 3.2 MHz (frequency which is slightly higher than three times the repetition frequency of bunch train) in the Fourier series of the generator cur-

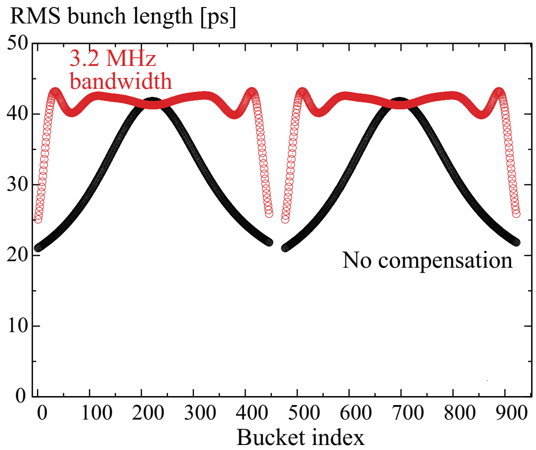


Figure 4: Rms bunch length versus the bucket index with (red) and without (black) the kicker cavity. The feedforward modulated signal with the frequency components below 3.2 MHz is assumed.

rent and re-calculating the generator voltage in the cavity, the feedforward signal indicated by red circles in Fig. 3 is obtained.

The rms bunch length with the kicker cavity is also calculated by using the semianalytical measure detailed in Ref. [11], where each longitudinal bunch distribution along the train is numerically calculated by considering the rf-potential shape at each bunch location, and is compared to the length obtained without the kicker cavity. In the Fig. 4, the red and black circles indicate the rms bunch lengths with and without the kicker cavity, respectively. The average bunch length with the active compensation over the bunch trains is 40.9 ps, which is close to that (42.5 ps) obtained under ideal conditions without any bunch gaps. Note, that the average bunch length without the kicker cavity is estimated to be 31.1 ps.

To confirm its technical feasibility, the voltage required for the kicker cavity is plotted together with the dissipated, generator and reflected powers as a function of bunch index in Fig. 5. These values are calculated using the cavity parameters listed in Table 3. The cavity voltage required for this compensation scheme is ~ 45 kV, while the peak generator power is ~ 50 kW. Both of them are technically feasible.

## CONCLUSION

To mitigate the impact of the TBL to the bunch lengthening operation in extremely low emittance storage ring, we have proposed the feedforward compensation technique using a single kicker cavity. The kicker cavity having the band width around several megahertz allows us to minimize the phase shifts of the stored beam, and as a consequence, to recover the bunch lengthening performance degraded by the TBL effect.

In the case of the KEK-LS standard operation, the bunch lengthening factor can be improved from 3.3 to 4.3 by using the 500-MHz kicker cavity and the feedforward modulated signal having 3.3-MHz frequency components. In that case, the average and peak generator powers are estimated to be 14.7 and 46.7 kW, respectively.

In addition, it is considered that this technique can be applied even to a passive harmonic system consisted of superconducting (SC) harmonic cavities. By using SC cavities, the total $R/Q$ can be reduced. However, the large bunch phase shifts and degradation of the rms bunch length due to the TBL effect were reported when the large bunch gap is introduced for hybrid operation mode [5]. Even in such case, the compensation technique described in this paper can be applied, and expected to mitigate them.

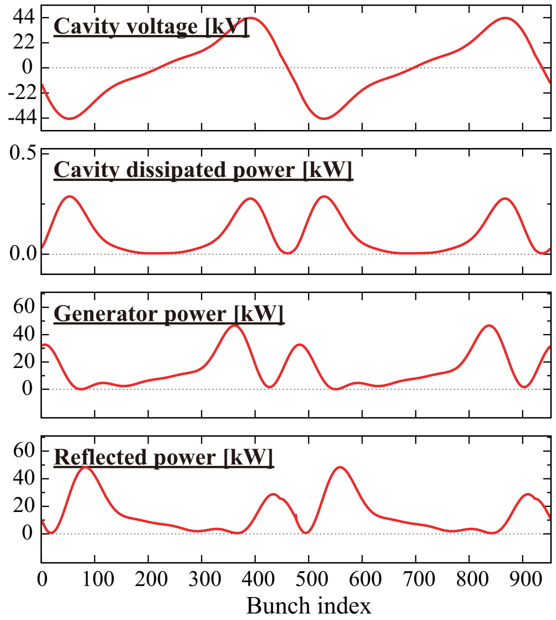


Figure 5: Cavity voltage required for the kicker cavity and comparison of the dissipation, generator and reflected powers as a function of bunch index when the cavity voltage indicated by red circles in Fig. 3 is produced in the assumed kicker cavity.

## ACKNOWLEDGEMENTS

This work was supported by JSPS KAKENHI Grant Number JP17K05131.

## REFERENCES

[1] A. Hofmann and S. Myers, “Beam dynamics in a double rf system,” in *11th Int. Conf. on High-Energy Accelerators*, CERN-ISR-TH-RF-80-26, Springer, 1980, pp. 610–614.

[2] M. Georgsson, W. Anders, D. Krämer, and J. Byrd, “Design and commissioning of third harmonic cavities at BESSY II,” *Nucl. Instr. Meth. A*, vol. 469, no. 3, pp. 373–381, 2001, ISSN: 0168-9002. DOI: 10.1016/S0168-9002(01)00783-5. http://www.sciencedirect.com/science/article/pii/S0168900201007835

[3] J. Byrd, S. Santis, M. Georgsson, G. Stover, J. Fox, and D. Teytelman, "Commissioning of a higher harmonic RF system for the advanced light source," *Nucl. Instr. Meth. A*, vol. 455, no. 2, pp. 271–282, 2000, ISSN: 0168-9002. DOI: `10.1016/S0168-9002(00)00504-0`. `http://www.sciencedirect.com/science/article/pii/S0168900200005040`

[4] W. Anders and P. Kuske, "HOM damped NC passive harmonic cavities at BESSY," in *Proc. of the 2003 Particle Accelerator Conf.*, paper TPAB004, vol. 2, 2003, pp. 1186–1188.

[5] M. Pedrozzi *et al.*, "SLS operational performance with third harmonic superconducting system," in *Proc. of 11th SRF workshop*, paper MOP25, 2003, pp. 91–94.

[6] N. Milas, L. Stingelin, *et al.*, "Impact of filling patterns on bunch length and lifetime at the sls," *IPAC10, Kyoto, Japan*, 2010.

[7] P. Bosland *et al.*, "Third harmonic superconducting passive cavities in ELETTRA and SLS," in *Proc. of 11th SRF workshop*, paper TUO06, 2003, pp. 239–243.

[8] G. Penco and M. Svandrlik, "Experimental studies on transient beam loading effects in the presence of a superconducting third harmonic cavity," *Phys. Rev. ST Accel. Beams*, vol. 9, p. 044401, 4 Apr. 2006. DOI: `10.1103/PhysRevSTAB.9.044401`. `http://link.aps.org/doi/10.1103/PhysRevSTAB.9.044401`

[9] P. F. Tavares *et al.*, "Commissioning and first-year operational results of the MAX IV 3 GeV ring," *Journal of Synchrotron Radiation*, vol. 25, no. 5, pp. 1291–1316, Aug. 2018. DOI: `10.1107/s1600577518008111`.

[10] J. M. Byrd, S. De Santis, J. Jacob, and V. Serriere, "Transient beam loading effects in harmonic rf systems for light sources," *Phys. Rev. ST Accel. Beams*, vol. 5, p. 092001, 9 Sep. 2002. DOI: `10.1103/PhysRevSTAB.5.092001`. `http://link.aps.org/doi/10.1103/PhysRevSTAB.5.092001`

[11] N. Yamamoto, T. Takahashi, and S. Sakanaka, "Reduction and compensation of the transient beam loading effect in a double rf system of synchrotron light sources," *Phys. Rev. Accel. Beams*, vol. 21, 1 Jan. 2018, 012001. DOI: `10.1103/PhysRevAccelBeams.21.012001`. `https://link.aps.org/doi/10.1103/PhysRevAccelBeams.21.012001`

[12] Y. Honda *et al.*, "Resonant coherent diffraction radiation system at ERL test accelerator in KEK," in *Proceedings of the 8th Internatinal Particle Accelerator Conf., IPAC'17, Copenhagen, Denmark*, MOPVA018, JACOW, Geneva, Switzerland, 2017, pp. 887–889.

[13] M. Izawa *et al.*, "Installation of new damped cavities at the photon factory storage ring," *JSR*, vol. 5, no. 3, pp. 369–371, May 1998. DOI: `10.1107/S0909049597015070`. `http://dx.doi.org/10.1107/S0909049597015070`

[14] H. Ego, J. Watanabe, S. Kimura, and K. Sato, "Design of a HOM-damped rf cavity for the SPring-8-II storage ring," in *Proc. 11th Annual Meeting of Particle Accelerator Society of Japan*, paper MOOL14 in Japanese, PASJ, Tokyo, 2014, 2014, pp. 237–241. `http://www.pasj.jp/web_publish/pasj2014/proceedings/PDF/MOOL/MOOL14.pdf`

[15] N. Yamamoto, S. Sakanaka, and T. Takahashi, "Simulation study of parasitic-mode damping methods for a 1.5-ghz tm020-mode harmonic cavity," en-us, in *Proceedings of the 9th Internatinal Particle Accelerator Conf., IPAC'18, Vancouver, BC, Canada*, vol. IPAC2018, JACoW Publishing, Geneva, Switzerland, 2018, p. 2822. DOI: `10.18429/jacow-ipac2018-wepml055`.

[16] N. Yamamoto, A. Gamelin, and R. Nagaoka, "Investigation of Longitudinal Beam Dynamics With Harmonic Cavities by Using the Code Mbtrack," in *Proc. 10th International Partile Accelerator Conference (IPAC'19), Melbourne, Australia, 19-24 May 2019*, (Melbourne, Australia), ser. International Partile Accelerator Conference, Geneva, Switzerland: JACoW Publishing, Jun. 2019, pp. 178–180, ISBN: 978-3-95450-208-0. DOI: `doi:10.18429/JACoW-IPAC2019-MOPGW039`. `http://jacow.org/ipac2019/papers/mopgw039.pdf`

# SUPPRESSION OF THE LONGITUDINAL COUPLED BUNCH INSTABILITY IN DAΦNE IN COLLISIONS WITH A CROSSING ANGLE

Alessandro Drago, Mikhail Zobov, Istituto Nazionale di Fisica Nucleare, Laboratori Nazionali di Frascati, Via Enrico Fermi 40, Frascati, Italy

Dmitry Shatilov, BINP, Novosibirsk, Russia

Pantaleo Raimondi, ESRF, Grenoble, France

*Abstract*

In DAΦNE, the Frascati e+/e- collider operating since 1998, an innovative collision scheme, the crab waist, has been successfully implemented during the years 2008-09. During operations for the Siddharta experiment an unusual synchrotron oscillation damping effect induced by beam-beam collisions has been observed. Indeed, when the longitudinal feedback is off, the positron beam becomes unstable with currents above 200–300 mA due to coupled bunch instability. The longitudinal instability is damped by colliding the positron beam with a high current electron beam (of the order of 2 A). A shift of about -600 Hz in the residual synchrotron sidebands is observed. Precise measurements have been performed by using both a commercial spectrum analyzer and the diagnostic capabilities of the longitudinal bunch-by-bunch feedback. The damping effect has been observed in DAΦNE for the first time during collisions with the crab waist scheme. Our explanation, based both on theoretical consideration and modelling simulation, is that beam collisions with a large crossing angle produce longitudinal tune shift and spread, providing Landau damping of synchrotron oscillations.

## INTRODUCTION

DAΦNE is a Φ-factory, a e+/e- collider built at Frascati in the years 1991-1996 [1], [2] and operating since 1998. DAΦNE accelerator complex is composed by one linac that can accelerate electron beams with energy up to 800 MeV (510 MeV in operation) or positron beams with energy up to 510 MeV, an accumulator-damping ring, a transfer line and two main rings (MR) with one or two interaction points for collisions at 1.02 GeV in the centre of mass. The linear accelerator, the accumulator ring and the transfer line can be set to inject in the MR a single positron or electron bunch every ½ second. In the typical injection scheme of DAΦNE, the electron bunches are stored in the MR before the positron ones because the electron injection efficiency is higher than for the other beam. It must be underlined that the different behaviour is related mainly to the parasitic e-cloud effect limiting the top beam current storable in the e+ ring.

Electrons are therefore stored in MR with a rather high current (≈2A), then the injection system is switched to the positron production mode, operation which takes >1 minute. At the end of the switch, the positrons are injected. The electron beam current decays rather rapidly, due to the low beam energy (510 MeV) and to the small transverse emittance, and eventually the two beams collide at approximately the same currents, starting usually in the range between 1.5 and 1.0 A.

After electron injection and during the transfer line switching time, there are beam collisions with very high electron currents (between 2A and 1.5A) and relatively low positron ones (between 500 and 200 mA). In this particular situation, a longitudinal damping of the positron beam has been observed even with the longitudinal bunch-by-bunch e+ feedback turned off. This damping effect has been observed in DAΦNE for the first time during collisions with the crab waist scheme [3], [4], implemented in 2008 and 2009 years.

After first observations of this behaviour, three dedicated machine study runs have been carried out with the goal of precisely measuring characteristics of the effect [5]. In this paper we describe first of all the measurements results. Then, we propose an analytical formula to explain the longitudinal beam-beam tune shift. Finally, we compare the measured tune shift with its analytical estimates and numerical calculations.

## INSTRUMENTATION AND MEASUREMENTS

In order to perform the measurements in the positron main ring, we have used two different diagnostic tools comparing the results. Precise measurements on this effect have been performed by using the following systems:

a) a commercial Real-time Spectrum Analyzer RSA 3303 by Tektronix, working from DC to 3 GHz. The spectrum analyzer is connected to a high bandwidth beam pickup, made by four buttons. The bunch signals, after going to the H9, hybrids parts by MA-COM, produce horizontal and vertical differences from the zero orbit and also the sum of the signals.

The sum makes possible the detection of longitudinal oscillations. To have a better signal-to-noise ratio the acquisition system is completed by a bandpass passive filter working at 360MHz and by a small signal amplifier;

b) a longitudinal bunch-by-bunch feedback developed in collaboration with SLAC and LBNL in the years 1993-96 with its powerful beam diagnostic capability both in real time and off line [6], [7], [8]. The feedback has been used in closed loop and open loop.

Fig. 1 shows an image of the spectrum analyzer screen. The highest observed peak at 362.484 MHz corresponds to the 118-th revolution harmonic while the synchrotron sidebands are separated by 35.25 kHz. The e+ feedback is off (i.e. in open loop) and the total positron beam current is 130 mA in 103 bunches.

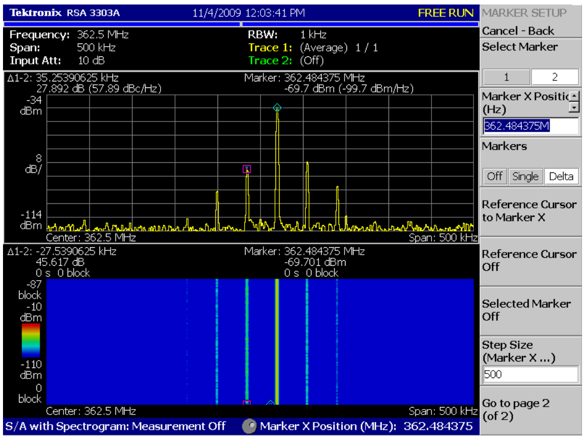


Fig. 1 – Positron beam 118-th revolution harmonic with synchrotron sidebands (feedback off, out of collision)

In the following plot (Fig. 2) showing the positron beam behaviour, the electron beam with ~1700 mA current and the feedbacks on (i.e. in closed loop) is colliding with e+ beam having the longitudinal feedback turned off.

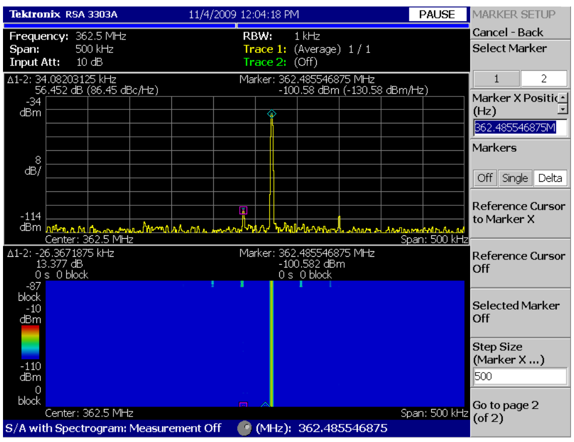


Fig. 2 – Positron synchrotron sidebands damped by beam-beam collisions (feedback off).

The result is clearly visible in the Fig. 2: the e+ beam synchrotron sidebands are almost completely damped when placing the beams in collision, even though the e+ longitudinal feedback is turned off.

Fig. 3 compares the cases “in collision – out of collision” with the same setup as the previous ones, that is with the e+ longitudinal feedback turned off and all the other systems turned on. The sidebands frequency shift of the order of 1kHz is clearly visible but the resolution of the instrument setup is not accurate enough to be exactly measured. Nevertheless it is evident from the historical plot that the damping effect induced by the beam-beam collisions makes lower the synchrotron frequency on both sidebands. In the case of Fig. 3, the beam currents are 1550 mA for the electrons and 390 mA for the positrons.

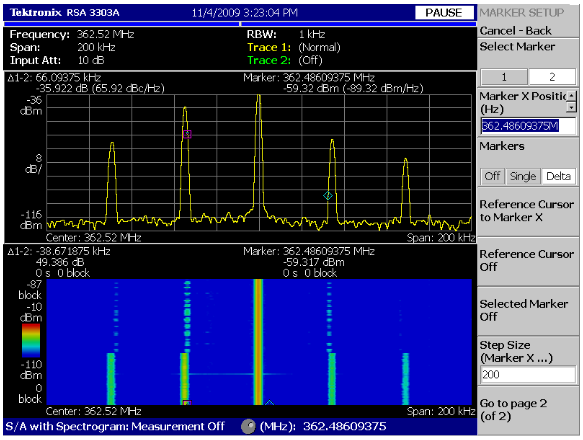


Fig. 3 - Positron beam longitudinal behaviour showing the “in collision – out of collision” cases.

It is also possible to download the traces from RSA 3303A as numerical values. Transferring the data to a PC/MATLAB environment a new plot has been created as shown in the following Fig. 4.

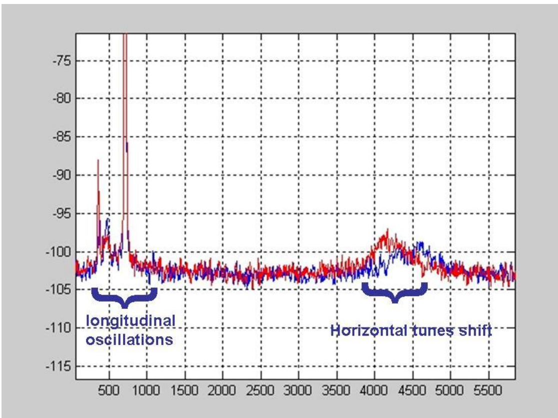


Fig. 4 - Data plot elaborated from the RSA acquisition showing the longitudinal and horizontal tunes in collision (blue) and out of collision (red trace). Vertical scale is in dBm, horizontal axis shows the number of bins (proportional to the frequency)

In Fig. 4 the highest peak corresponds to the e+ 118-th harmonic of the revolution frequency; the red trace shows the positron spectrum out of collision, while the blue one corresponds to the case of colliding beams. The vertical scale is in dBm, the horizontal axis is in number of bins (proportional to the frequency). This case is interesting because it shows a situation where the electron beam damps longitudinally and shifts in frequency the positron synchrotron oscillations. Besides, it is possible to see that the beam collisions produce also a horizontal tune shift (in this case increasing the frequency).

With the goal to confirm the measurements done with the spectrum analyzer and to evaluate more precisely the beam-beam effect, the beam diagnostic tools of the DAΦNE longitudinal feedback have been used. With this system it is possible to record longitudinal data for each bunch. Data can be recorded both in closed loop and in open loop.

Fig. 5 shows the positron beam modal growth rate analysis for the cases respectively in and out of collisions.

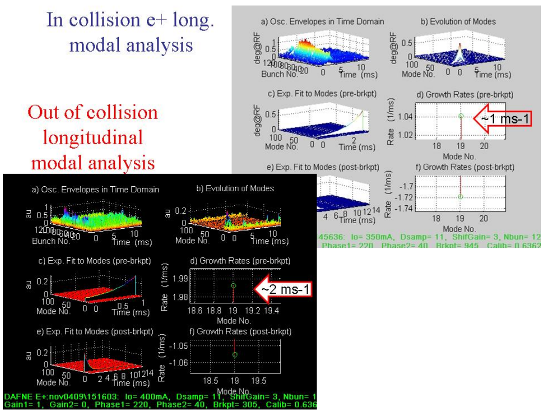


Fig. 5 - Mode 19 growth rate out of collision is 1.99 ms-1. Mode 19 growth rate in collision is 1.04 ms-1

In both cases the mode 19 is the strongest unstable longitudinal mode; out of collisions it has a growth rate, in inverse units, of 1.99 ms-1, (corresponding to 502 microseconds), in collision the growth rate is halved, 1.04 ms-1, corresponding to 961 microseconds. This, once again, confirms the damping effect of beam-beam interaction.

Analyzing with great detail these data, it is possible to measure the synchrotron frequency shift induced on the positron beam by the beam-beam collisions with the e+ longitudinal feedback turned off. As shown in Fig. 6 and 7, the synchrotron frequency (out of collisions) is 34.86 kHz, while the synchrotron frequency (in collisions) is 34.23 kHz. The longitudinal frequency shift induced by the beam-beam collisions is therefore -630 Hz at e+ beam current of 320 mA (out) and 250 mA (in) for the positrons. The e- beam currents were 520 mA (out) and 476 mA (in) respectively.

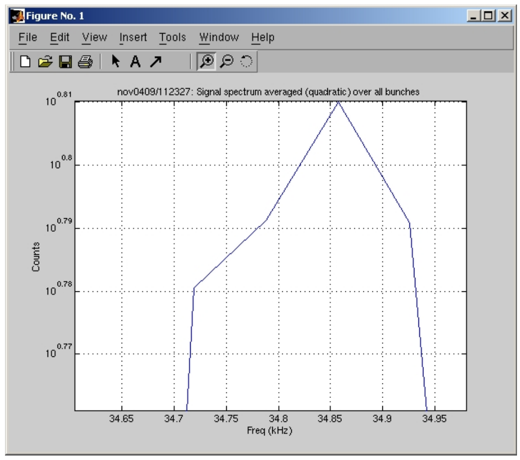


Fig.6 - The e+ synchrotron frequency out of collision is 34.86 kHz.

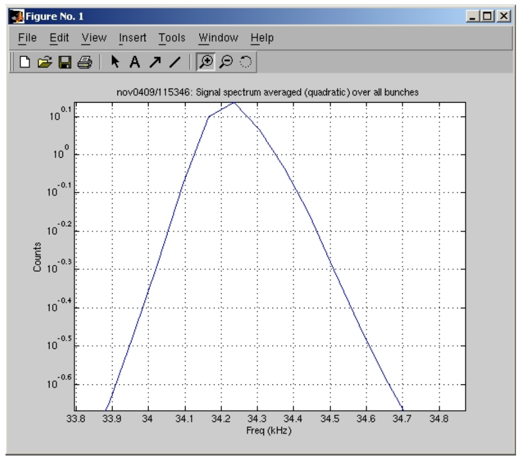


Fig.7 - The e+ synchrotron frequency in collision is 34.23kHz

In the following section, we want to show an analytical expression for the synchrotron tune shift, that is also a measure of the synchrotron tune spread, and eventually to compare the formula with numerical simulations.

## ANALYTICAL FORMULA AND COMPARISON WITH NUMERICAL SIMULATIONS

Summarizing, the experimental observations and measurements at DAΦNE have shown that beam-beam collisions can damp the longitudinal coupled bunch instability. Bringing into collisions a high current electron beam with an unstable positron one was stabilizing the synchrotron oscillations of the e+ beam, even with the longitudinal feedback system switched off. Besides, a negative frequency shift of positron beam synchrotron sidebands has been observed during beam collisions.

The authors attribute these two effects to a nonlinear longitudinal kick arising by beam-beam interaction under a finite crossing angle. It is worthwhile to note here that we have observed this effect clearly only after implementation of the crab waist scheme of beam-beam collisions at DAΦNE having twice larger horizontal crossing angle with respect to the previous operations with the standard collision scheme [9].

In the following an analytical expression for the synchrotron tune shift is outlined [10], and this expression gives also a measure of the synchrotron tune spread. The formula is compared with numerical simulations too.

## Tune shift analytical formula

In collisions with a crossing angle the longitudinal kick of a test particle is created due to a projection of the transverse electromagnetic fields of the opposite beam onto the longitudinal axis of the particle. The kicks that the test particle receives while passing the strong beam with rms sizes $\sigma_x$, $\sigma_y$, $\sigma_z$ under a horizontal crossing angle $\theta$ [11] are shown in the following eq. (1):

$$x' = \frac{2 r_e N}{\gamma}\left(x - z\,tg(\theta/2)\right)\int_0^{\infty} dw \frac{\exp\left\{-\frac{\left(x - z\,tg(\theta/2)\right)^2}{\left(2\left(\sigma_x^2+\sigma_z^2 tg^2(\theta/2)\right)+w\right)} - \frac{y^2}{\left(2\sigma_y^2+w\right)}\right\}}{\left(2\left(\sigma_x^2+\sigma_z^2 tg^2(\theta/2)\right)+w\right)^{3/2}\left(2\sigma_y^2+w\right)^{1/2}}$$

$$y' = \frac{2 r_e N}{\gamma}\, y \int_0^{\infty} dw \frac{\exp\left\{-\frac{\left(x - z\,tg(\theta/2)\right)^2}{\left(2\left(\sigma_x^2+\sigma_z^2 tg^2(\theta/2)\right)+w\right)} - \frac{y^2}{\left(2\sigma_y^2+w\right)}\right\}}{\left(2\left(\sigma_x^2+\sigma_z^2 tg^2(\theta/2)\right)+w\right)^{1/2}\left(2\sigma_y^2+w\right)^{3/2}}$$

$$z' = x'\,tg(\theta/2)$$

where x, y, z are the horizontal, vertical and longitudinal deviations from the synchronous particle travelling on-axis, respectively. N is the number of particles in the strong bunch, $\gamma$ is the relativistic factor of the weak beam. Then, for the on-axis test particle (x = y = 0) the longitudinal kick is given by:

$$z' = -\frac{2 r_e N}{\gamma} z\,tg^2(\theta/2)\int_0^{\infty} dw \frac{\exp\left\{-\frac{\left(z\,tg(\theta/2)\right)^2}{\left(2\left(\sigma_x^2+\sigma_z^2 tg^2(\theta/2)\right)+w\right)}\right\}}{\left(2\left(\sigma_x^2+\sigma_z^2 tg^2(\theta/2)\right)+w\right)^{3/2}\left(2\sigma_y^2+w\right)^{1/2}} \quad (2)$$

For small synchrotron oscillations $z << \sigma_z$ the exponential factor in the integral can be approximated by 1 and we obtain an expression for the linearized longitudinal kick:

$$z' = -\frac{2 r_e N}{\gamma} z\,tg^2(\theta/2)\frac{1}{\left(\sigma_x^2+\sigma_z^2 tg^2(\theta/2)\right)+\sqrt{\left(\sigma_x^2+\sigma_z^2 tg^2(\theta/2)\right)\sigma_y^2}} \quad (3)$$

For the case of flat beams with $\left(\sigma_y << \sqrt{\sigma_x^2+\sigma_z^2 tg^2(\theta/2)}\right)$ the tune shift expression can be simplified to [10]

$$\xi_z = -\frac{r_e N^{strong}}{2\pi\gamma^{weak}}\frac{\left(\frac{\sigma_{z0}}{(\sigma_E/E)}\right)^{weak}}{\left(\left(\frac{\sigma_x}{tg(\theta/2)}\right)^2+\sigma_z^2\right)^{strong}} \quad (4)$$

As we see from (4), for the flat bunches the synchrotron tune shift practically does not depend on the vertical beam parameters. So, one should not expect any big variations due to crabbing and/or hour-glass effect. Since particles with very large synchrotron amplitudes practically do not “see” the opposite beam (except for a small fraction of synchrotron period) their synchrotron frequencies remain very close to the unperturbed value $\nu_{z0}$. For this reason, like in the transverse cases, the linear tune shift can be used as a measure of the nonlinear tune spread.

## Numerical Simulations

In order to check validity of the formulae we performed numerical simulations with the beam-beam code LIFETRAC [12] comparing the tune shift calculated numerically with the one obtained by using the analytical formula (4). As it has been shown [10] by using the typical parameters of SuperB [13] and DAΦNE, the formula agrees well with the simulations when the horizontal tune is far from the linear synchrobetatron coupling resonance, see Fig. 8. The agreement improves for larger Piwinski angles.

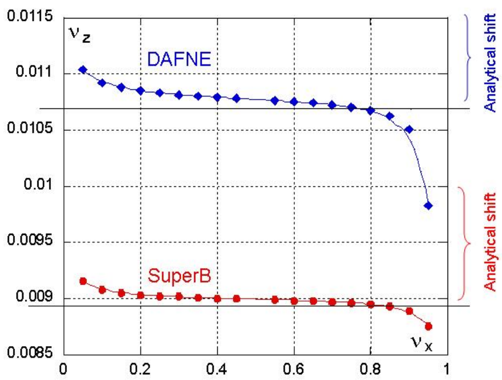


Fig. 8 - Synchrotron tune dependence on the horizontal tune. The solid straight lines correspond to the analytically predicted synchrotron tunes

In Fig. 9 the blue curve shows the calculated synchrotron tune dependence on the normalized synchrotron amplitude for the DAΦNE “weak” positron beam interacting with the “strong” electron beam having a current of 1.7 A. For comparison, the green curve shows the tune dependence on amplitude arising due to nonlinearity of the RF voltage. As we can see, the synchrotron tune spread due to the beam-beam interaction is notably larger than that due to the RF voltage alone, at least within 5 $\sigma_z$. In the past it was shown that the RF voltage nonlinearity is strong enough to damp quadrupole longitudinal couple bunch mode instability [14]. So, we can expect a strong Landau damping of longitudinal coupled bunch oscillations by the beam-beam collision. This conclusion is in accordance with performed measurements.

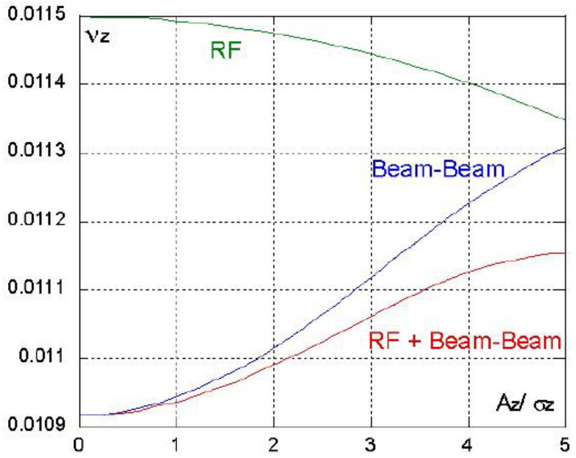


Fig. 9 - Synchrotron tune dependence on normalized amplitude of synchrotron oscillations (blue curve – tune dependence created by beam-beam collisions alone, green – RF nonlinearity alone, red – both contributions).

Summarizing the results of the computation, first of all our numerical simulations have confirmed that the synchrotron tune shift does not depend on parameters of the vertical motion. As a second point, the agreement between the analytical and numerical estimates for the synchrotron tune shift is quite reasonable for the horizontal tunes far from integers. Quite naturally, in a scheme with a horizontal crossing angle, synchrotron oscillations are coupled with the horizontal betatron oscillations. One of the coupling's side effects is the $\nu_z$ dependence on $\nu_x$, which becomes stronger in vicinity of the main coupling resonances. In order to make comparisons with the analytical formula we need to choose the horizontal betatron tune $\nu_x$ closer to half-integer, where its influence on $\nu_z$ is weaker. The coupling vanishes for very large Piwinski angles. Since $\nu_x$ for DAΦNE is rather close to the coupling resonance, we use numerical simulations in order to compare the calculated synchrotron tune shift with the measured one. In particular, when colliding the weak positron beam with 500mA electron beam, the measured synchrotron frequency shift was about -630 Hz (peak-to-peak). In our simulations we use the DAΦNE beam parameters with respectively bunch current $N=0.9\times10^{10}$ and bunch length $\sigma_z = 1.6$ cm. These values give a result in the synchrotron tune shift of -0.000232 corresponding to the frequency shift of -720 Hz. In our opinion the agreement is good considering experimental measurement errors and the finite width of the synchrotron sidebands.

## CONCLUSION

The synchrotron oscillations damping in beam-beam collisions with a crossing angle has been observed in DAΦNE [15], [16]. The respective experimental data have been collected by the commercial spectrum analyzer and by the bunch-by-bunch longitudinal feedback system. The measurement results obtained by the two diagnostics tools are in a good agreement. A simple analytical formula to explain synchrotron tune shift and tune spread due to beam-beam collisions with a crossing angle has been presented. The formula agrees well with the simulations when the horizontal tune is far from the synchro-betatron resonances. The agreement is better for larger Piwinski angles. Calculations have shown that at high beam currents the synchrotron tune spread induced by the beam-beam interaction at DAΦNE can be larger than the tune spread due to the nonlinearity of the RF voltage. This may result in additional Landau damping of the longitudinal coupled bunch oscillations. The effect of the longitudinal kick arising in collisions with a crossing angle has been taken into account in design of the low energy electron-positron collider for production and study of ($\mu$+$\mu$-) bound state in Novosibirsk [17] as well as for the evaluation of the energy change at the IP in the FCC-ee [18].

## REFERENCES

[1] The DAΦNE Project Team presented by G.Vignola, " DAΦNE, The Frascati PHI-factory". PAC '93, Washington, May 1993, p.1993.

[2] The DAΦNE Project Team presented by G.Vignola, "DAΦNE Status and Plans", 16th IEEE Particle Accelerator Conference (PAC 95), Dallas, Texas, May 1-5, 1995. Published in IEEE PAC 1995: 495-499.

[3] P. Raimondi et al., “Beam-Beam Issues for Colliding Schemes with Large Piwinski Angle and Crabbed Waist”, e-Print:physics/0702033, 2007.

[4] M. Zobov et al., “Test of crab-waist collisions at DAΦNE Phi factory”, Phys.Rev.Lett. 104 (2010) 174801.

[5] A. Drago, P. Raimondi and M. Zobov, “Beam-Beam Longitudinal Damping”, DAΦNE Technical Note G-71, 08 February 2010.

[6] J. Fox *et al.*, “Observation, Control and Modal Analysis of Coupled-Bunch Longitudinal Instabilities”, EPAC’96 Proceedings, 1996.

[7] D. Teytelman, “Architectures and Algorithms for Control and Diagnostics of Coupled-Bunch Instabilities in Circular Accelerators”. Stanford Univ. PhD thesis, SLAC-R-633, June 2003.

[8] S. Prabhakar, “New Diagnostics and Cures for Coupled-Bunch Instabilities”, Stanford Univ. PhD thesis, SLAC-R-554, August 2001.

[9] C. Milardi *et al.*, “Crab Waist Collision at DAΦNE”, published in ICFA Beam Dyn. Newslett. 48, pp. 23-33, 2009.

[10] M. Zobov and D. Shatilov, "Synchrotron Tune Shift and Tune Spread Due to Beam-Beam Collisions with a Crossing Angle", DAΦNE Technical Note G-72, 04 March 2010.

[11] P. Raimondi and M. Zobov, "Tune Shift in Beam-Beam Collisions with a Crossing Angle", DAΦNE Technical Note G-58, 26 April 2003.

[12] D. Shatilov, "Beam-beam simulations at large amplitudes and lifetime determination", Part. Accel., vol.52 , pp. 65-93, Jul. 1996.

[13] "SuperB: A High-Luminosity Asymmetric e+ e- Super Flavor Factory. Conceptual Design Report", e-Print: arXiv:0709.0451 [hep-ex].

[14] M. Migliorati *et al.*, "Landau Damping of Longitudinal Multi-Bunch Instabilities in DAΦNE", DAΦNE Technical Note G-21, 13 September 1993.

[15] A. Drago *et al.*, "Synchrotron Oscillation Damping Due to Beam-Beam Collisions", THOBRA01, oral talk presented at the first International Particle Accelerator Conference held in Kyoto, Japan, May, 23-28, 2010.

[16] A. Drago, P. Raimondi, D. Shatilov, and M. Zobov, "Synchrotron oscillation damping by beam-beam collisions in DAΦNE", Phys. Rev. ST Accel. Beams, Vol. 14, p.092803, Sep. 2011. doi: 10.1103/PhysRevSTAB.14.092803

[17] A.Bogomyagkov *et al.*, "Low-energy electron-positron collider to search and study (μ+μ-) bound state", EPJ Web of Conferences 181, 01032 (2018). doi.org/10.1051/epjconf/201818101032

[18] D. Shatilov, "Impact of beam-beam effects on beam energy and crossing angle at IP", talk at FCC Week 2019, 24-28 June 2019, Brussels, Belgium.

# RF scheme to mitigate longitudinal instabilities in the SPPC

Linhao Zhang†, Jingyu Tang*

Institute of High Energy Physics, CAS, Beijing 100049, China
University of Chinese Acadamy of Sciences, Beijing 100049, China
Spallation Neutron Source Science Center, Dongguan 523803, China

*Abstract*

A large collider project CEPC-SPPC is under study with a global effort and a leading role from IHEP, with CEPC (Circular Electron-Positron Collider, Phase I) to probe Higgs physics and SPPC (Super Proton-Proton Collider, Phase II) to explore new physics beyond the Standard Model. The key design goal for SPPC is to reach 75 TeV in center-of-mass energy with a circumference of 100 km. As an important part of the SPPC conceptual study, the study on the longitudinal dynamics at SPPC has been conducted, with a focus on the RF scheme to meet the requirements for luminosity and mitigate the relevant instabilities. The longitudinal instability bottleneck associated with the longitudinal dynamics is the loss of Landau damping. To mitigate the beam instabilities, a higher harmonic RF system (800 MHz) together with the basic RF system (400 MHz) to form a dual-harmonic RF system is found helpful, which also increases the luminosity by producing shorter bunches. The preliminary results indicate that longitudinal impedance threshold can be increased.

## INTRODUCTION

Following the discovery of Higgs boson at the Large Hadron Collider (LHC) in 2012, which opens a brand new door to the unknown physics, new large colliders are being proposed and studied by the international high-energy community to explore the Higgs boson in depth and probe new physics beyond the Standard Model. In China, a two-stage project including two colliders of unprecedented scale – CEPC and SPPC (Circular Electron-Positron Collider & Super Proton-Proton Collider) was initiated, with CEPC (Phase I) focusing on the Higgs physics and SPPC (Phase II) being an energy frontier collider and a discovery machine which is far beyond the performance of the LHC [1]. The two colliders share the same tunnel of 100 km in circumference.

The key design goal for SPPC is to reach 75 TeV in center-of-mass energy [2]. In such a high-energy proton-proton collider, synchrotron radiation becomes non-negligible during the acceleration cycle, especially in the collision phase. In addition, as the bunch population of $1.5\times10^{11}$ protons will be utilized to reach the nominal luminosity of $1\times10^{35}$ cm$^{-2}$s$^{-1}$, beam instabilities become a major concern. Therefore, the longitudinal beam dynamics including the emittance radiation damping and controlled blow-up, instabilities and mitigations has been studied. In this paper, the longitudinal dynamics design and RF schemes to mitigate the longitudinal instabilities at SPPC are presented.

† zhanglinhao@ihep.ac.cn
* tangjy@ihep.ac.cn

## MAIN LONGITUDINAL INSTABILITIES IN SPPC

According to the phenomena observed and the experience accumulated during SPS and LHC design and operation [3-4], the main single bunch longitudinal collective effects requiring to be carefully considered for the next-generation proton collider like SPPC are intra-beam scattering, longitudinal microwave instability and loss of Landau damping, among which the latter plays a critical role. Concerning the mitigation of the longitudinal instabilities, more attention should be paid to the increase of Landau damping.

### *Intra-beam Scattering*

Intra-beam Scattering (IBS) is a multiple small-angle Coulomb scattering of charged particles within a bunch. It normally leads to two effects in proton or ion accelerators: redistribution of beam momenta and impact on beam quality due to transverse and longitudinal emittance blow-up. In SPPC, it is found that IBS is well under control during the whole acceleration cycle, provided that the longitudinal emittance at the collision is maintained at a high value in the presence of strong synchrotron radiation damping. The emittance blow-up is also needed for compressing the other instabilities.

### *Longitudinal Microwave Instability*

The longitudinal microwave instability is normally caused by the higher frequency part of impedance. When this instability occurs, it will normally first cause a high-frequency structure on the bunch profile. In proton synchrotrons the microwave instability is observed as a fast increase of the bunch length and thus of the longitudinal emittance [5]. The threshold of this instability can be estimated by the well-known Keil-Schnell-Boussard criterion [6],

$$\left|\frac{Z_{//}}{n}\right| \leq \frac{2\pi\beta^2 E\sigma_\delta^2 |\eta| F}{e\hat{I}} . \quad (1)$$

Here, $\hat{I}$ is peak beam current, $\beta$ is Lorentz factor, $E$ is the total energy, $\sigma_\delta$ is the momentum spread, $\eta$ is the slip factor and $F$ is a form factor depending on the particle distribution. Usually, longitudinal microwave instability will not be worsened for larger hadron machines with the assumption of keeping the same bunch length and momentum spread [7]. In SPPC, the overall longitudinal impedance should be well controlled to avoid the instability. A reasonable assumption of 0.2 Ω is adopted in the studies, following 0.1 Ω at LHC which has a smaller circumference.

### *Loss of Landau damping*

The Landau damping in the longitudinal phase plane comes from the spread in the synchrotron frequency due to the nonlinearity of the RF voltage. This is a natural stabilizing mechanism for different longitudinal instabilities. Here a particular instability concerning the single bunch instability, that was observed in SPS, is described, which is often called the loss of Landau damping and caused by the excitation due to reactive impedance overshadowing the Landau damping. Based on the well-known Sacherer dispersion relation, an approximate stable boundary can be given by $S > 4/\sqrt{m}|\Delta\omega_m|$ for Sacherer's smooth distribution, where $m$ is the azimuthal mode which specifies the oscillation type of single bunch, like $m = 1$ for dipole mode, $m = 2$ for quadrupole mode, $S$ is the synchrotron frequency spread and $\Delta\omega_m$ is the total coherent frequency shift from the contribution of various impedance [8]. It is notable that the dispersion relation as well as the size of the stable region is related to the bunch distribution [9]. Using the stability criteria with $m = 1$ mode, the broad band impedance threshold, above which the single bunch instability will be generated, corresponding to the loss of Landau damping can be derived [10]:

$$\frac{|\mathrm{Im}\,Z|}{n} \le F\frac{|\eta|E}{eI_b\beta^2}\left(\frac{\Delta E}{E}\right)^2\frac{\Delta\omega_s}{\omega_s}f_0\tau\,. \tag{2}$$

where $f_0$ is the revolution frequency, $I_b = eN_bf_0$ is the single bunch current with bunch intensity $N_b$, $\tau$ is the full bunch length, $\Delta\omega_s/\omega_s$ is the synchrotron frequency spread within the bunch and $\Delta E/E$ is the relative energy spread.

Given that the stable region will be bigger for the flat bunch distribution, it seems favourable to induce a dual-harmonic RF system to lengthen the bunch and to increase the frequency spread which is an effective cure for loss of Landau damping. However, it has been demonstrated that Landau damping is lost when the derivative of synchrotron frequency is zero outside the bunch center [11], which makes the dual harmonic RF system working in bunch-lengthening mode (BLM) not preferable at SPS [12]. In SPPC, this instability is also of major concern, and the corresponding measures are studied in detail as shown below.

## LONGITUDINAL DYNAMICS DESIGN FOR SPPC

The main parameters related to the SPPC longitudinal dynamics are listed in Table 1. One of the main goals of the collider design is to achieve a high luminosity which is relevant to the beam current, kinetic energy, beam-parameter and the reduction factor due to the hourglass effect and the Piwinski angle [13]. The influence of hourglass effect can be neglected if $\beta^*/\sigma_z \gg 1$, with $\beta^*$ being the beta function at the collision point and $\sigma_z$ the RMS bunch length. This is the case for the SPPC. However, the reduction factor $F_{ca}$ with respect to different $\beta^*/\sigma_z$ and bunch spacings that is caused by the Piwinski angle is shown in Fig. 1. While $\beta^*$is constrained by the overall design of the interaction point, it is the goal of the longitudinal dynamics design to provide a bunch as short as possible. There are two main constraints in limiting very short bunches, one from the intra-beam scattering (IBS) and the other from the longitudinal instabilities. In the SPPC baseline design, an RF system at 400 MHz is used. We are trying to improve the design by optimizing the RF system in order to have a better control over the above constraints or an even higher luminosity.

Table 1: Main RF and beam parameters

| Parameter | Value | Unit |
|---|---|---|
| Circumference, C | 100 | km |
| Injection/collision energy, $E$ | 2.1/37.5 | TeV |
| Transition gamma, $\gamma_{tr}$ | 99.21 | |
| Bunch intensity, $N_b$ | $1.5\times10^{11}$ | |
| Number of bunches, $n_b$ | 10080 | |
| Bunch spacing, $\Delta t$ | 25 | ns |
| RF frequency, $f_{rf}$ | 400 | MHz |
| RMS bunch length in collision, $\sigma_z$ | 7.55 | cm |
| Harmonic number, $h$ | 133333 | |
| Energy loss in collision, $U_0$ | 1.48 | MeV/turn |
| Longitudinal emittance damping time in collision, $\tau_\varepsilon$ | 1.17 | h |

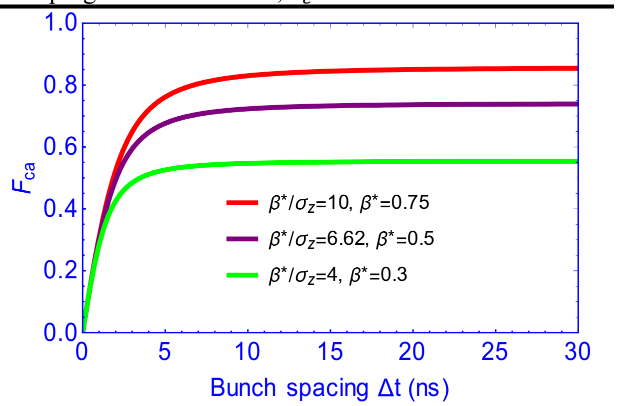


Figure 1: Luminosity reduction factor due to the Piwinski angle for different $\beta^*/\sigma_z$ and bunch spacing.

The growth time of the IBS effect is quite different in the different phases of the SPPC cycle and those at the injection and collision are shown in Fig. 2. At the injection, the longitudinal emittance between 1.5 eVs and 2.5 eVs seems to be a good choice because the IBS growth time, at least 20 h, is much greater than the injection duration of 840 s. However, in collision, the longitudinal emittance has to be increased to at least 6 eVs due to the long physics collision time as long as 14 h, and the short longitudinal emittance damping time of 1.07 h. Therefore, a controlled emittance blow-up scheme during the acceleration cycle is crucial.

The longitudinal instability constraint mainly results from the loss of Landau damping. With Eq. (2), a simplified formula corresponding to loss of Landau damping can be derived:

$$\frac{|\mathrm{Im}\, Z|}{n} \leq \frac{3\pi^2}{32} \frac{h^3 V_{rf}}{I_b} \left(\frac{L}{C}\right)^5. \tag{3}$$

where $h$ is the harmonic number, $C$ is the ring circumference, $L = 4\sigma_z$ is the full bunch length. Thus, the threshold on the longitudinal reactive impedance varies with the bunch length at injection and in collision, as is shown in Fig. 3. At injection, the RMS bunch length is at least 8 cm in order to have the longitudinal impedance threshold greater than 0.2 Ω and match with the upstream accelerator in the injector chain in the longitudinal phase plane. Thus, a lower RF voltage should be used. However, in collision, to reach the RMS bunch length of 7.55 cm that is required by the luminosity in the baseline design, an RF voltage of at least 32 MV is needed, and a similar limitation on the impedance threshold above 0.2 Ω is maintained. Based on the above considerations, in the SPPC baseline design, the RF voltage is chosen to be 20 MV and the RMS bunch length is 9 cm at injection, whereas in collision, the RF voltage increases to 40 MV. The corresponding longitudinal reactive impedance threshold during the cycle is above 0.2 Ω. To obtain a shorter bunch length during collision than 7.55 cm, it will need a higher RF voltage but at the cost of a slight reduction in the longitudinal impedance threshold. Besides, we can also use a higher harmonic RF system of 800 MHz, or a dual harmonic RF system of 400 MHz and 800 MHz working in the bunch shortening mode, which will be illustrated below.

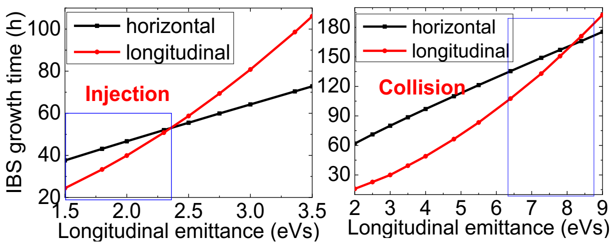


Figure 2: IBS growth time at SPPC injection/collision.

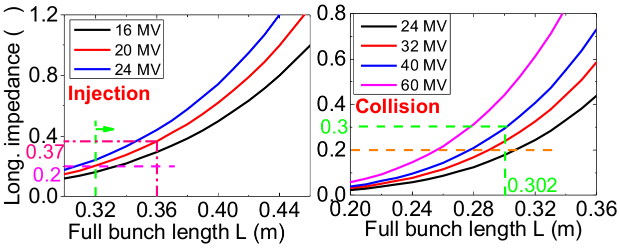


Figure 3: Longitudinal reactive impedance threshold at SPPC injection/collision.

## RF SCHEMES TO MITIGATE INSTABILITIES

In order to enhance the Landau damping in the SPPC, a large synchrotron frequency spread inside the bunch is required, which can be achieved by using either a higher harmonic RF system of 800 MHz, or a dual harmonic RF system of 400 MHz and 800 MHz. A controlled emittance blow-up is also needed to avoid too small emittance that naturally shrinks due to synchrotron radiation.

For the option of a single harmonic RF system at 800 MHz, due to the limit of the momentum filling factor below 0.8 during physics running to avoid beam loss, the RMS bunch length will be reduced to 5.56 cm or less from 7.55 cm in the case of 400 MHz, as illustrated in Fig. 4. In this study, the RMS bunch length was taken as 5.2 cm which is beneficial to the luminosity, and the relevant parameters are: the longitudinal emittance 6.4 eVs, RF voltage 52 MV and RMS momentum spread $0.79\times 10^{-4}$. The corresponding longitudinal impedance threshold is about 1.6 times as high as that in the case of 400 MHz. However, the RF bucket is occupied too much which will have an adverse effect on the bunch storage and collision during physics running of up to 14 h.

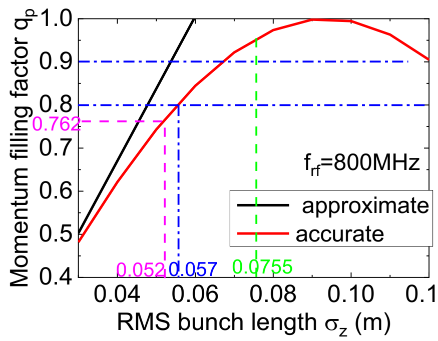


Figure 4: Momentum filling factor and bunch length for 800 MHz

A dual harmonic RF system can work in two different modes: the bunch lengthening mode (BLM) and bunch shortening mode (BSM) which are determined by the relative phase difference between the two harmonic systems. Fig. 5 shows the composed RF voltage curve, potential well and bucket for the SRF (Single 400 MHz), BSM and BLM. One can see that BLM has a larger bucket area and a smaller peak line density which is beneficial to reduce space charge effects. These are extremely beneficial in lower-energy high-intensity proton synchrotrons such as the p-RCS of the SPPC injector chain, while is negligible in the SPPC. However, as shown in Fig. 6, the BLM has relatively larger synchrotron frequency spread in the mode of $k$=0.4 and $k$=0.5 for the RMS bunch length 7.55 cm or less, which corresponds to the maximum phase extension is about 1.3 rad, but it will significantly decrease with small phase errors and introduce regions with zero derivative, which are disadvantageous for Landau damping. Furthermore, the average synchrotron tune is smaller, which is unfavorable for controlling the Transverse Mode Coupling Instability (TMCI) [14]. However, both the synchrotron frequency spread and the average synchrotron tune at BSM are improved as compared with SRF. In addition, the bunch length is slightly shorter which is helpful to enhance the luminosity. Although the bucket area is relatively smaller, it can be cured by giving a larger voltage on the fundamental harmonic RF.

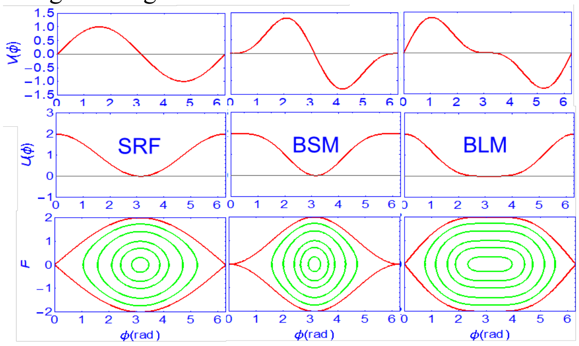


Figure 5: RF voltage, potential well and bucket for SRF, BSM and BLM.

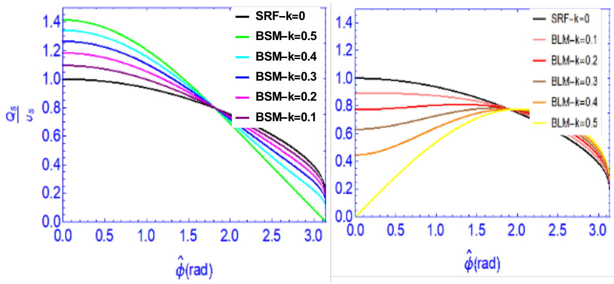


Figure 6: Synchrotron tune distribution for different RF voltage ratios ($k$ value) between 800 MHz and 400 MHz.

Another vital measure in the longitudinal beam dynamics is to blow up the longitudinal emittance in a controlled way. There are two main ways: (1) one injects a bandwidth limited RF phase noise from $\omega_{down}$ to $\omega_{up}$ into the fundamental RF system during the ramp-up through a phase loop, where $\omega_{up}$ is a little beyond the bunch central synchrotron frequency $\omega_s$ to fully influence the bunch core, but $\omega_{down}$ is the frequency of the bunch edge associated with the desired bunch emittance. The particles with synchrotron frequencies falling in this frequency range are excited. Outside the frequency range, there is no resonant excitation, thus the longitudinal motion remains unchanged. Then a controlled larger longitudinal emittance is obtained [15]. This method has been adopted by LHC, SPS and PSB [16-18] at CERN. (2) One adds a phase-modulated higher frequency RF to the fundamental RF, which will drive bunches towards resonant islands and cause the bunch density redistribution [19]. This method is used in PS [20]. The controlled longitudinal emittance plays a critical role in the reduction of the intra-beam scattering, counteracting of the synchrotron radiation damping, suppression of the collective instabilities and mitigation of the space charge effects.

## SUMMARY

The potential key longitudinal instabilities in the SPPC are reviewed. In order to enhance the Landau damping for longitudinal microwave instability, loss of Landau damping, a dual harmonic RF system composed of 400 MHz and 800 MHz is proposed. In the bunch shortening mode, it can provide larger tune spread which is good for suppressing the instabilities and shorter bunch length which can enhance the luminosity.

## ACKNOWLEDGEMENTS

We would like to thank the organizers of the 2019 MCBI workshop for providing us a good opportunity to learn the progress in the field and discuss with the other participants. Special thanks to Dr. Elena Shaposhnikova of CERN for beneficial discussions and comments on the longitudinal instabilities and mitigation schemes at LHC/SPS.

## REFERENCES

[1] The CEPC-SPPC study group, “CEPC-SPPC Preliminary Conceptual Design Report, Volume II-Accelerator”, IHEP-CEPC-DR-2015-01, IHEP-AC-2015-01, Mar. 2015.

[2] The CEPC-SPPC study group, “CEPC Conceptual Design Report, Volume I-Accelerator”, Chapter 8, IHEP-CEPC-DR-2018-01, IHEP-AC-2018-01, Aug. 2018.

[3] T. Argyropoulos, “Longitudinal beam instabilities in a double RF system”, CERN-Thesis-2015-421, Jan. 2015.

[4] J. Esteban Müller, “Longitudinal intensity effects in the CERN Large Hadron Collider”, CERN-THESIS-2016-066, Jun. 2016.

[5] T. Argyropoulos, “Longitudinal Microwave Instability in a Multi-RF System”, in *Proceedings of HB2014*, East-Lansing, MI, USA, Nov. 2014.

[6] S. Y. Lee, “Accelerator Physics”, 2nd Edition, World Scientific Publishing, Singapore, Dec. 2004, p376.

[7] K.Y. Ng, “Coupling Impedances and Beam Instabilities in Accelerator Rings”, US Accelerator School, Hampton, Virginia, Jan. 2015.

[8] F. J. Sacherer, “A longitudinal stability criterion for bunched beams”, IEEE Transactions on Nuclear Science, vol. 20, no. 3, pp. 825–829, Jun. 1973. doi:10.1109/TNS.1973.4327254.

[9] I. S. González, “Loss of Longitudinal Landau Damping in the LHC Injectors, AB-Note-2008-001 ABP, CARE-Note-2007-012-HHH, Jan. 2008.

[10] E. Shaposhnikova, “Longitudinal beam parameters during acceleration in LHC”, LHC Project Note 242, Dec. 2000.

[11] E. Shaposhnikova, “Bunched beam transfer matrices in single and double RF systems”, CERN-SL/94-19 (RF), Aug. 1994.

[12] E. Shaposhnikova et al., “Longitudinal instabilities in the SPS and beam dynamics issues with high harmonic RF system”, in 52nd ICFA Advanced Beam Dynamics Workshop HB2012, Beijing, China, Sep. 2012.

[13] F. Su et al., "Method study of parameter choice for a circular proton-proton collider." Chinese physics C, vol.40, no.1, pp.17001-017001, 2015.

[14] E. Métral et al., “Beam Instabilities in Hadron Synchrotrons”, IEEE Trans.Nucl.Sci. 63 (2016) 2, 1001-1050, FERMILAB-PUB-15-646-APC, Apr. 2016.

[15] T. Toyama, “Uniform bunch formation by RF voltage modulation with a band-limited white signal.” Nuclear Instruments & Methods in Physics Research, 2000, 447(3):317-327.

[16] P. Baudrenghien et al., “Longitudinal emittance blowup in the large hadron collider.” Nuclear Instruments & Methods in Physics Research 726.oct.21:181-190, 2013.

[17] T. Argyropoulos et al., “Controlled Longitudinal Emittance Blow-up in Double Harmonic RF System at CERN SPS”, in Proceedings of HB2010, Morschach, Switzerland, Sep. 2010.

[18] D. Quartullo et al., “Controlled longitudinal emittance blow-up using band-limited phase noise in CERN PSB”, in Proc. 8th Int. Particle Accelerator Conf. (IPAC’17), Copenhagen, Denmark, May 2017, doi :10.1088/1742-6596/874/1/012066.

[19] V. V. Balandin et al., “The resonant theory of longitudinal emittance blow-up by phase-modulated high harmonic cavities”, in Particle Accelerators, 1991, Vol. 35, pp. 1-14, Aug. 1989.

[20] H. Damerau et al., "Controlled longitudinal emittance blow-up in the CERN PS." CERN-AB-2007-052, Aug, 2007.

# MITIGATION OF SPACE CHARGE EFFECTS USING ELECTRON COLUMN AT IOTA RING

C.S. Park*, Korea University Sejong Campus, Sejong, South Korea
B. Freemire, Euclid Techlabs LLC, Bolingbrook, IL USA
E. Stern, Fermi National Accelerator Laboratory, Batavia, USA
C.E. Mitchell, Lawrence Berkeley National Laboratory, Berkeley, USA

*Abstract*

We investigate a novel method to mitigate space charge effects of high intensity proton beams propagating in circular accelerators by means of trapping and controlling electrons generated from beam- induced residual gas ionization. This compensation method uses Coulomb repulsion force between a proton beam and electrons to mitigate self-space charge effects of the beam if it passes through a plasma column. The transverse electron-proton (e-p) instability in the plasma column is well controlled by the longitudinal magnetic field of a solenoid magnet and the bias voltages on electrodes. In this report, we will show simulation results how to control distributions of electrons and ions as well as that of the proton beam inside the column.

## INTRODUCTION

Mitigation of space charge effects is a crucial challenge in high intensity hadron accelerators. In order to mitigate these effects, various techniques have been implemented such as by adding opposite charges (e.g., electron lens and electron column), by accelerating beam rapidly, by scraping beam halos, and by using solenoidal fields [1–3]

At Fermilab, the Integrable Optics Test Accelerator (IOTA) ring is built to enable accelerator researchers to study the frontiers of accelerator science, and is designed to explore and improve the particle beams and machines for the future high intensity accelerators [4]. IOTA is being commissioned to investigate a novel technique called nonlinear integrable optics. The IOTA ring will be also used to study the space charge compensation (SCC) using both electron lens and electron column.

The SCC method with an electron lens uses co-propagating beams of opposite charge (electron beam) to collide with proton beams inside the strong magnetic field by a solenoid. This results in the compensation of proton beams' space charge tune shift. This method requires a precise control of transverse profile of e-beam. It is experimentally mature "Swiss Knife," and has been employed in Tevatron, RHIC, and now LHC [5]. However, the space charge compensation with an electron column utilizes proton beam itself to ionize residual gas and to generate electrons. Electrons are approximately at rest longitudinally compared to co-moving electrons in the electron lens scheme. Electrons are trapped, matched, and controlled using external solenoid and electrodes. In this report we present recent simulation results to mitigate space charge effects using electron column method at Fermilab's IOTA ring.

* kuphy@korea.ac.kr

## EXPERIMENTAL SETUP

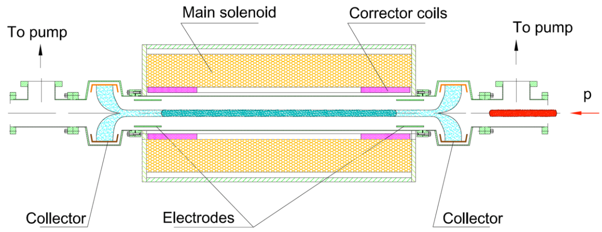


Figure 1: Schematic Layout of an Electron Column Experimental Setup

Space charge effects can be compensated by making proton beam pass through plasma column of opposite charge with matched distribution. In linear machines, this concept was successfully applied to transport high-current low energy proton and $H^{-}$ beam (gas focusing), Gabor lens, etc [6]. In circular machines, e-p instabilities can be suppressed using an external magnetic field of sufficient strength.

Electrons are generated from the beam-induced ionization of residual gas without an external electron source. Then their density profile is matched to that of proton beam by using external magnetic field and precisely controlled by using electrostatic electrodes. The schematic drawing of the experimental setup is in Figure 1. The magnetic field should be strong enough to stabilize electrons' motion inside the column, so that coherent e-p instabilities should be mitigated. However, it also needs to be weak enough to allow ions escape the column easily.

In IOTA, we will use e-lens' central solenoid for e-column operation. Ionization rate of residual gas by proton beam can be controlled with the vacuum pressure, therefore it also plays an important role to control the electron distribution.

## SIMULATION SETUP

We investigate the dynamics of proton beam, electrons, and ions with external E and B fields using Warp3D code [8]. The goal of the simulation is first to find matching conditions of the transverse electron profile with B-field, voltages on electrodes, and vacuum pressure. With these conditions, a pulsed proton bunch is injected and passed through the column. Density distributions of electrons and ions right after the proton beam passed the column are recorded during

Table 1: Beam and IOTA ring simulation parameters

| Parameter | Value | Units |
|---|---|---|
| Beam Species | proton | |
| Beam Energy | 2.5 | MeV |
| Beam Current | 8 | mA |
| Beam Pulse Length | 1.77 | $\mu s$ |
| Column Length | 1 | m |
| Revolution Period | 1.83 | $\mu s$ |
| Gas Species | Hydrogen | |
| Macroparticle/step | 500 | |
| Grid Spacing (x,y,z) | 5, 5, 10 | mm |
| Timestep | 70 | ps |

one revolution period. Then, the second proton beam is injected into the column with these preserved distributions. Table 1 shows IOTA and SCC simulation parameters.

## MATCHING CONDITION

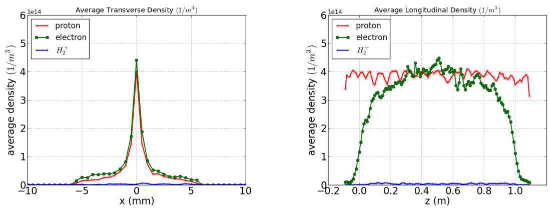


(a) Transverse density profile (b) Longitudinal density profile

Figure 2: Transverse and longitudinal density profiles when $B = 0.1\ T$, $V = -5\ V$, and $P = 5 \times 10^{-4}\ Torr$.

To find matching conditions, initial optimization of the column parameters (gas density, electrode potential, and magnetic field) are performed using a coasting proton beam. For given beam parameters, one can find the proton beam potential at the center, which is given by $\phi = 30I/\beta \approx 3.5\ V$, where $I$ is the beam current and $\beta$ is the relativistic velocity of the beam. With this estimation, we could estimate the optimal voltage on the electrodes. In addition, the vacuum pressure also plays an important role to control the electron density level. As a result, for $B = 0.1\ T$, $V = -5\ V$, and $P = 5 \times 10^{-4}\ Torr$, matched transverse and longitudinal distributions of electrons are achieved as shown in Figure 2.

## SCC AFTER FIRST PASS

For the proton bunched beam, the KV distribution is used in the transverse direction, while the uniform, step function is used in the longitudinal direction. In order to quantify SCC effects, simulations with ionization (SCC) and without ionization (no SCC) are compared. Figure 3 shows the radial electric field along the x direction at the center of the column for both cases (left) and their ratio (SCC to no SCC, right). There are significant reduction in the radial electric field by a factor of 2 inside the beam with the space charge compensation.

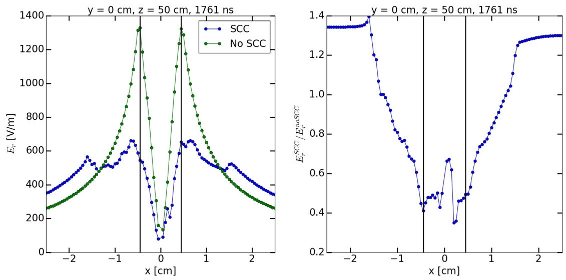


Figure 3: Radial electric fields along x at the center of the column for no SCC (green) and SCC (blue) at the end of the first pass of the beam through the Electron Column (left) and ratio of radial electric fields (SCC to no SCC, right). Vertical black lines indicates the boundary of the proton beam.

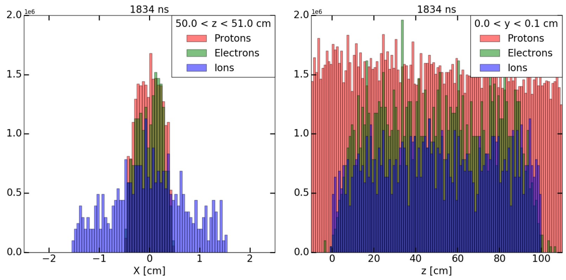


Figure 4: Distribution along x for the beam (red), electrons (green), and ions (blue) at the center of the Electron Column in z just before the beam would reenter the Column for a second pass - top. Note the beam distribution plotted is for the last time step that the beam is in the Column, for reference. Bottom - same as the top, but plotted along z at the center of the Column in y. The bin widths correspond to the simulation grid spacing.

Figure 4 shows the density profiles (left: transverse and right: longitudinal) of the proton beam, electrons, and ions after the beam passes the column. The density distributions of electrons are not perfectly matched to those of proton beam for both directions. These under-compensation can be precisely controlled by increasing the electrode voltage or by increasing the vacuum pressure. The ions are are not strongly confined by the magnetic field, so that they are more homogeneously distributed.

## SCC AFTER SECOND PASS

Figure 5 shows the radial electric field along the x direction at the center of the column for both cases (left) and their ratio (SCC to no SCC, right) after the second pass of the proton beam. After the second pass, the transverse distribution of electrons are still closely matched to that of the proton beam. Therefore, there is still significant reduction of the radial electric field within the beam. However, as shown in Figure 6, there is a huge build up of ions near the beam, and ion density surpasses the proton beam density. This will lead to significant reduction in space charge compensation.

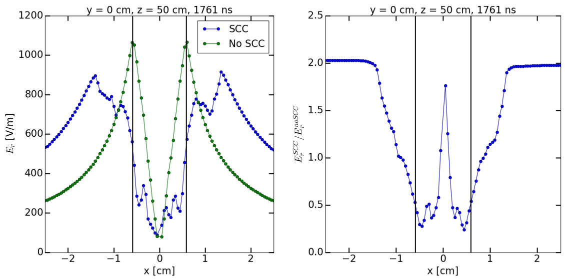


Figure 5: Same at Fig. 3, but at the end of the second pass of the beam through the Column.

This could be mitigated by reducing the gas density and/or magnetic field strength.

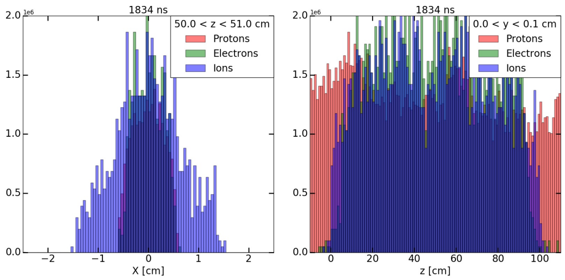


Figure 6: Same as Fig. 4, but just before the beam would reenter the Column for a third pass.

## CONCLUSION

Simulations results show that the density profile of e-column can be tuned with axial B-field, electrode voltages, and vacuum pressure for (partial/full/over) SCC in the IOTA ring. Simulations of the Space Charge Compensation using an Electron Column shows positive effects to reduce radial electric fields inside the pulsed beam. However, these reduction is about 50 % after the first and second pass. Additional optimization is required to find suitable settings for E and B fields as well as gas pressure for each turn. Electron and ion distributions for each turn need to be monitored precisely. Longer period (multiple passes throughout the ring) of simulations are to be investigated. Evolution of tune foot print and phase space are also to be studied.

## REFERENCES

[1] V. D. Shiltsev, *et al.*, in *Proc. PAC'13*, Pasadena, CA, USA, Sep. 2013, pp. 99-101.

[2] A. W. Chao and M. Tigner, (Eds), Handbook of Accelerator Physics and Engineering, 2013, p. 395.

[3] O. Meusel *et al*, "Beam transport and space charge compensation strategies," *Rev. Sci. Instr.*, vol. 87, 02B937 (2016).

[4] K. Schulte *et al*, in *in Proc. HB'14*, East Lansing, MI, USA, Nov. 2014, pp 67-69.

[5] S. Antipov *et al.*, "IOTA (Integrable Optics Test Accelerator): facility and experimental beam physics program", *J. Inst.*, vol. 12, T03002, Mar. 2017.

[6] G. D. Stancari *et al.*, in *in Proc. IPAC'15*, Richmond, VA, USA, May 2015, pp. 46-48.

[7] G.I. Dimov and V.E. Chupriyanov, "Compensated Proton-Beam Production in an Accelerating Ring at a Current Above the Space-Charge Limit", *Part. Accel.*, vol. 14, pp. 155-184, 1984.

[8] A. Friedman *et al.*, "Computational Methods in the Warp Code Framework for Kinetic Simulations of Particle Beams and Plasmas", *IEEE Trans. Plasma Sci.*, vol. 42, no. 5, p. 1321, May 2014.

# BEAM TRANSFER FUNCTION AND STABILITY DIAGRAM IN THE LARGE HADRON COLLIDER*

C. Tambasco †, T. Pieloni, EPFL, Lausanne, Switzerland
X. Buffat, E. Métral, CERN, Geneva, Switzerland

*Abstract*

Predictions of transverse instability thresholds in the LHC are based on the computation of Landau damping by calculating the Stability Diagram (SD). However any modification of the tune spread and/or particle distribution modifies the expected Landau damping in the beams. The Beam Transfer Function (BTF) provides direct measurements of the Landau damping and can be used to understand the limitations of the models.

## INTRODUCTION

The instabilities driven by the beam coupling impedance can be mitigated by chromaticity, transverse feedback and/or Landau damping mechanisms. As long as the different modes of oscillations can be treated independently, the Landau damping is quantified by the dispersion integral for a given detuning with amplitude $q_{x,y}$ and particle distribution $\psi(J_x, J_y)$ as a function of the transverse actions $J_x$ and $J_y$ in each plane [1, 2]

$$SD^{-1}_{(x,y)} = \frac{-1}{\Delta Q_{x,y}} = \int_0^\infty \frac{J_{x,y}}{Q_{x,y} - q_{x,y}(J_x, J_y)} \frac{d\psi}{dJ_{x,y}} dJ_x dJ_y, \quad (1)$$

where $\Delta Q_{x,y}$ are the complex tune shifts at the stability limit for each coherent tune $Q_{x,y}$. The transverse amplitude detuning (or tune spread) is generated in the beams by any non-linearities (including beam-beam interactions when beams are in collisions [3]).The dispersion integral is the inverse of the SD that defines the stability limit in the complex plane of the coherent tune shifts. In order to be stabilized, the coherent impedance modes must lie inside the SD. The BTF is proportional to the dispersion integral

$$BTF_{(x,y)} = A_{x,y} \int_0^\infty \frac{J_{x,y}}{Q_{x,y} - q_{x,y}(J_x, J_y)} \frac{d\psi}{dJ_{x,y}} dJ_x dJ_y \quad (2)$$

and therefore the BTF is proportional to the inverse of the SD

$$SD^{-1}_{(x,y)} = \frac{-1}{\Delta Q_{x,y}} = \frac{BTF_{(x,y)}}{A_{x,y}}. \quad (3)$$

The proportionality constant $A_{x,y}$ depends on the excitation amplitude of the BTF and on the beam conditions themselves. The BTFs are sensitive to the tune spread in the beams, as well as to particle distribution changes. In the LHC, the tune spread is mainly provided by the so-called Landau octupoles [2] and beam-beam interactions [3, 4] (long range and head-on) when present. In case of diffusive mechanisms and/or reduced dynamic aperture with particle losses or redistributions, the expected Landau damping for a Gaussian distribution of the beams is modified. The BTF provides measurements of Landau damping when in the presence of such effects. Therefore, in 2015 a transverse BTF system was installed in the LHC in order to measure the Landau damping of the beams and compare the measurements with the models that did not fully reproduce the instability observed [4]. For this purpose, a new method for the data analysis has been developed and applied to the measurements acquired in different configurations allowing quantitative comparisons with models.

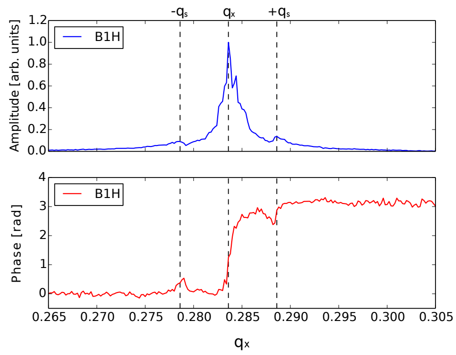


Figure 1: Example of a BTF measurement: amplitude and phase response for B1 in the horizontal plane at the LHC injection energy. Synchrotron sidebands are visible in the amplitude, with the corresponding phase jumps at $q_x \pm Q_s$ (where $Q_s = 5 \times 10^{-3}$).

## THE LHC BTF SYSTEM

During a BTF acquisition the beam is excited (without causing beam losses or emittance blow-up) at a frequency close to the tune. The response of the beams itself is of course real, but the BTF is complex as we combine the amplitude and the phase separately [5]. An example of BTF measurement is shown in Fig. 1 for Beam 1 (B1) in the horizontal plane at injection energy. The blue line is the amplitude response while the red line is the phase response. The maximum amplitude corresponds to the fractional part of the horizontal betatron coherent tune ($q_x \approx 0.284$). At this frequency the phase assumes a value of $\pi/2$. The first synchrotron sidebands are also visible in the amplitude response, with the corresponding phase jumps, occurring at $q_x \pm q_s$, where $q_s = 5 \times 10^{-3}$ is the fractional longitudinal tune at injection energy. The synchrotron sidebands are

* Work supported by the Swiss Institute for Accelerator Research and Technology (CHART).
† claudia.tambasco@epfl.ch

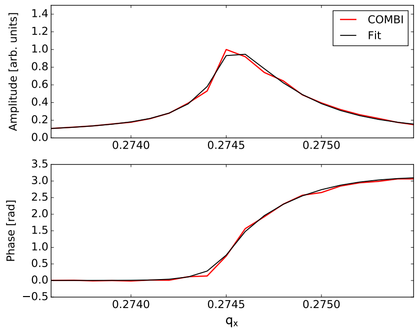


Figure 2: Amplitude and phase BTF responses simulated by using the COMBI code (red line) in the presence of linear detuning with amplitude. The black line represents the results of the parametric fit. The same tune spread has been applied for both cases and, as expected, the fit gives a tune spread factor close to 1 ($p_1 = 1.02$).

visible due to non-zero chromaticity $Q' \approx 5.0$ during the acquisition of the BTF measurements.

### *The fitting method*

In order to quantitatively compare the BTF measurements with the expected Landau damping from the models, a fitting method has been developed. The amplitude of the beam oscillation driven by the BTF excitations is not calibrated, therefore, the amplitude response of the beam can be expressed in arbitrary units only. In addition, a full calibration of the system cannot be accomplished since the proportionality constant $A_{x,y}$ in Eq.(2) cannot be known a priori. Indeed, it depends not only on the calibration factor of the BTF excitation amplitude, but also on the tune spread introduced by the machine non-linearities. To overcome this problem, the following fitting method is applied to the BTF measurements. The fitting function takes as input the amplitude $A_{model}$ and the phase $\varphi_{model}$ of the computed dispersion integral with the PySSD code [3], by using the following parameterization

$$\begin{cases} \varphi(Q_{meas}) = \varphi_{model}\left[p_0 + p_1 \cdot (Q_{model} - Q_0)\right] \\ A(Q_{meas}) = p_2/p_1 \cdot A_{model}(Q_{model}) \end{cases} \tag{4}$$

where both $A_{model}$ and $\varphi_{model}$ depend on the $Q_{model}$. The parameter $p_0$ gives the tune shifts with respect to the frequency of the analytical detuning ($Q_{model} - Q_0$) with $Q_0$ the transverse coherent tune, $p_1$ is the factor related to the tune spread with respect to the expected one and it is called *tune spread factor*. For example, if the tune spread factor $p_1 > 1$ it means that the measured tune spread is bigger than the expected one. An example of the application of the fitting method to simulations for a well known case of linear detuning with amplitude the tune spread parameter $p_1 \approx 1$. This is shown in Fig.2 where the simulated BTF response (the red line) is compared to the fitting function (the black line).

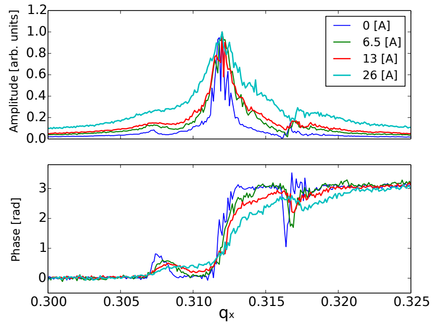


(a) Horizontal beam response.

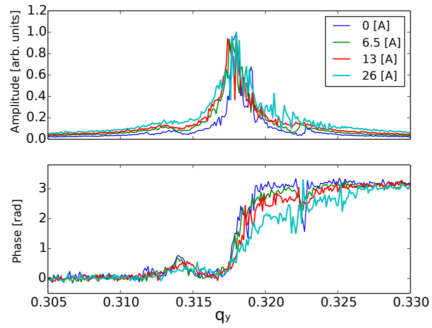


(b) Vertical beam response.

Figure 3: Measured BTF amplitude and phase responses for Beam 1 for different octupole currents at injection energy.

## MEASUREMENTS ON SINGLE BEAM

### *Measurements of Landau damping with octupole magnets at injection energy*

An octupole current scan has been performed at injection energy with collisions tunes (64.31, 59.32). The acquired BTF responses are presented in Fig. 3 for various Landau octupole currents (0 A, 6.5 A, 13 A, 26 A). The measured tune spread is therefore provided by the Landau octupole magnets and lattice non-linearities. As visible the tune spread increases as a function of the octupole current. However for the largest octupole strength (26 A) a larger tune spread is measured in the horizontal plane than in the vertical plane. The fitting method has been applied to compare the measurements with the expectations from the model. Figure 4 shows the results of the application of the fitting method. The measured tune spread factor is plotted as a function of the octupole current in the horizontal (blue dots) and in the vertical (green dots) planes. The solid black line represents the factors expected from the model with respect to a current $I_{oct} = 6.5$ A for which no asymmetry in the two transverse planes has been observed. As expected for such a current the tune spread factor of the model it is equal one. The red shadow is given by the model expectations including the initial non-zero tune spread corresponding to $\approx 5.5$ A and considering an uncertainty of $\pm 10\%$ on the measured emittance. As expected the tune spread factor linearly increases as a function of the octupole current [2]. However in the ver-

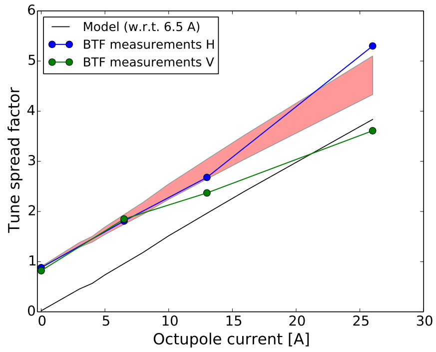


Figure 4: Measured tune spread factors as a function of the octupole current at injection energy in the horizontal (the blue dots) and in the vertical (the green dots) planes. The solid black line represents the factors expected from the model for a current $I_{oct} = 6.5$ A. The red shadow represent the model expectations including the initial non-zero tune spread corresponding to $\approx 5.5$ A with an uncertainty of $\pm 10\%$ on the measured emittance.

tical plane a deviation from the linear trend is observed for an octupole current of 26 A. Beam losses were observed for high octupole current at the moment of the data acquisition, due to a reduction of the Dynamic Aperture at injection with collisions tunes. The results of particle tracking simulations by using the SixTrack [6] code are presented in Fig. 5 where the surviving particle ratio is plotted as a function of the integral lower bound ($l$) used for the evaluation of the particle integral. The ratio is defined as the integral of the final distribution ($H_{Fin}$) over the integral of the initial distribution ($H_{Ini}$)

$$R_{surv} = \frac{\int_l^{6\sigma} H_{Fin}(x,y)dxdy}{\int_l^{6\sigma} H_{Ini}(x,y)dxdy} \tag{5}$$

where $l$, expressed in units of transverse rms beam size $\sigma$, is the integral lower bound and varies from 0 to 5.5 $\sigma$. The upper bound of the particle distribution integral is fixed to 6 $\sigma$. As visible, particles are lost more and more from the

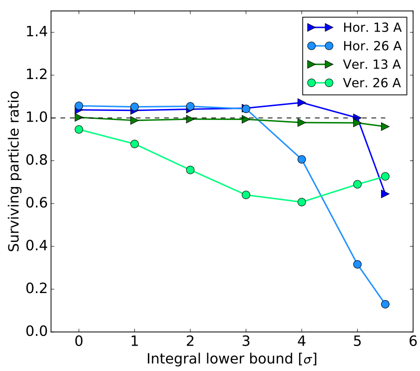


Figure 5: Surviving particle ratio as a function of the integral lower bound. The dark blue line with dark blue triangles and the light blue dotted line represent the horizontal plane for an octupole current of 13 A and 26 A respectively. The dark green line with dark green triangles and the light green dotted line represent the vertical plane for an octupole current of 13 A and 26 A respectively.

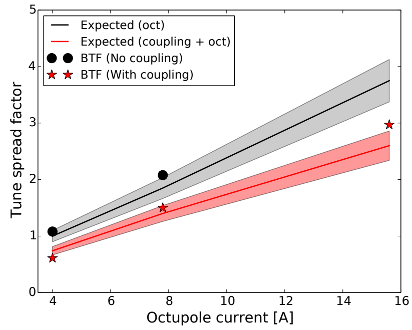


(a) Tune spread factors measured in the horizontal plane.

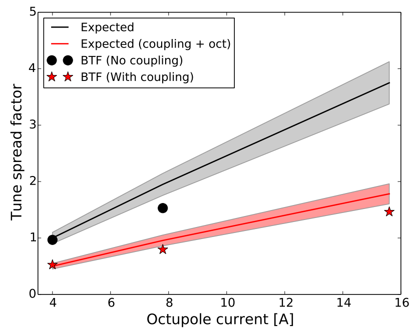


(b) Tune spread factors measured in the vertical plane.

Figure 6: Measured tune spread factors with respect to the analytical reference case of 4 A without linear coupling. The black dots are the measurements without linear coupling while the red stars are the measurements. The red and the black shadows represent the analytical expectations with an uncertainty of $\pm 10\%$ on the measured emittance for the case with and without linear coupling respectively.

tails to the core while increasing the octupole current. For the case with an octupole current of 26 A, a reduction up to the 40 % is observed in the core of the beam for the vertical plane (light green dotted line). This is in agreement with the reduction of the tune spread observed in the BTF measurements in the vertical plane. Indeed, the particles that mostly contribute to the BTF response are those in the beam core and not the ones in the tails [7]. If the particle lost are the ones in the core of the beam, a reduction of Landau damping is expected with respect to the unperturbed Gaussian distribution.

## *Measurements of Landau damping in the presence of linear coupling*

In the presence of transverse linear coupling a reduction of the Landau damping is expected [8–10]. This has been measured by means of BTFs in the LHC. Measurements have been acquired at injection energy for global linear coupling coefficient (defined as the closest-tune approach) $|C^-| = 0.006$. The measurements were acquired for an octupole current of 4 A, 8 A and 15.6 A. The measured tune spread factors are shown in Fig. 6 as a function of the octupole current. The red line represents the model expectations including both octupoles and linear coupling in the MAD-X lattice [11], while the black line only includes octupoles. The red and the black shadows represent the model uncertainty of $\pm 10\%$ on the measured emittance value. The black dots are the measurements without coupling while the red stars are the measurements in the presence of linear coupling. As expected, an overall reduction of the tune spread is measured in both planes. However, the reduction is more important in the vertical plane for which the tune spread is reduced by a factor 2 with respect to the horizontal plane for the largest octupole current of 15.6 A value. The experimental data reproduce well the expectations for both cases.

### *Measurements of impedance tune shifts with BTFs*

During a dedicated BTF MD in the 2018, measurements were acquired at flat top energy (6.5 TeV). The measurements were acquired after the correction of the linear coupling in the LHC for an octupole current of 546 A and a chromaticity of 2.5 units in order to minimize the synchrotron sidebands in the BTF response. An example of the acquired BTF response at flat top energy is shown in Fig. 7 where various horizontal BTF measurements (different colors) for Beam 1 were acquired. The solid black dashed lines corresponds to synchrotron sidebands at $q_{x0} \pm q_s$ due to the non zero chromaticity during the measurements, with $q_{x0}$ the incoherent bare tune in the horizontal plane. As visible, the measured coherent tune is shifted with respect to the incoherent bare tune with a coherent tune shift $\Delta Q_{coh} \approx -3.4 \times 10^{-4}$. This observation suggested that the impedance was not negligible and it was modifying the BTF response [5, 12, 13]. This was also confirmed by the application of the fitting method. By including only the octupole magnets in the model the fitting function was not reproducing the measurements meaning that other effects need to be considered. In order to study the impact of the impedance in the BTF response, simulations using the COMBI code [14] have been carried out. Figure 8 shows the coherent tune shifts, as a function of the bunch intensity, evaluated from the simulated BTF response including the 2018 wake field model [15] (the light blue line) and the wake field evaluated from the collimator settings as during the MD (the orange line). As visible, in order to reproduce the observed tune shift in the measured BTF ($\Delta Q_{coh} \approx -3.4 \times 10^{-4}$) at flat top energy, one has to rescale the bunch intensity to $1.2 \times 10^{11}$ p/bunch (the bunch intensity during the experiment was $\approx 0.8 \times 10^{11}$ p/bunch). This translates into a factor 1.5 on the impedance with respect to measurements. This value is in agreement with independent impedance measurements in the LHC for the horizontal plane of Beam 1 [16]. A first attempt to directly compare the measured BTF response to simulations is shown in Fig. 9 where the measured BTF response at flat top energy (red line) is compared to the simulated BTF response (the light blue line) including in the model the impedance and the Landau octupoles powered with a current of 546 A (as during the measurements). For completeness the analytical case without impedance is also plotted (black line) in the same picture. A factor 1.5 stronger impedance has been used as measured in the LHC.

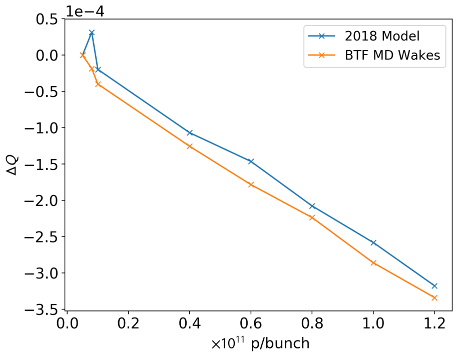


Figure 8: Coherent tune shifts as a function of bunch intensity. The tune shifts have been evaluated from the simulated BTF response including the 2018 wake field model (light blue line) and the wake field evaluated from the collimator settings as during the MD (orange line).

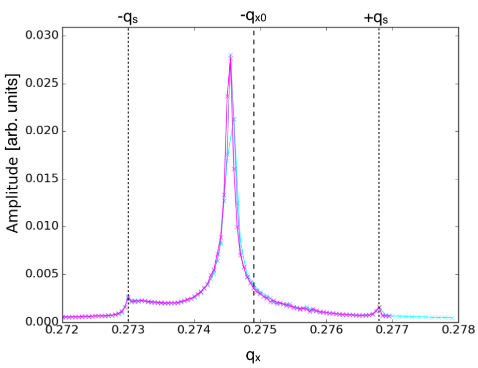


Figure 7: Various horizontal BTF acquisitions for Beam 1 at flat top energy. The chromaticity was reduced to 2.5 units during the measurements. The black dashed lines corresponds to synchrotron sidebands at $q_{x0} \pm q_s$ with $q_{x0}$ the incoherent bare tune in the horizontal plane.

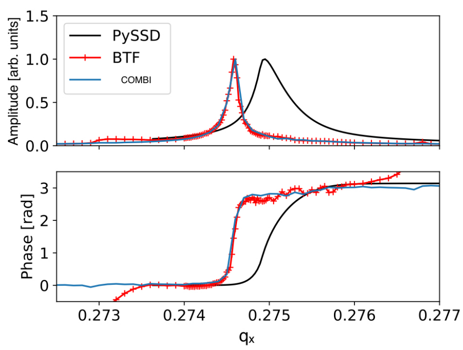


Figure 9: Measured BTF response at flat top energy (red line) compared to simulated BTF response (the blue line) including in the model the impedance and an octupole current of 546 A (as during the measurements). The analytical case without impedance is the black line.

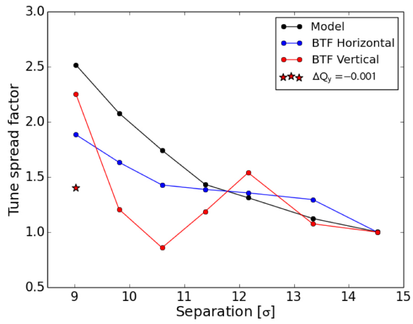


Figure 10: Measured tune spread factor as a function of the long range encounter separation at the interaction points in units of the rms beam size. Measurements were acquired at the end of the betatron squeeze. The red star represents the measured tune spread in the vertical plane with a reduced tune of $\Delta Q_y = -0.001$.

As visible the coherent tune shift is also fully reproduced. The shape of the measured BTF is fully recovered for a chromaticity of 1.0 units (the light blue line).

## MEASUREMENTS IN THE PRESENCE OF BEAM-BEAM INTERACTION

The LHC beams collide in the interaction points (IPs) with a certain crossing angle to avoid multiple head-on collisions causing the so-called beam-beam long range interactions. A crossing angle scan was performed at the end of the betatron squeeze (with positive octupole polarity) in order to measure the modifications of Landau damping due to the beam-beam long range interactions. The fitting method has been applied to the BTF measurements with respect to the case with nominal crossing angle and the measured tune spread factor is plotted as a function of the long range separation at the first encounter (in units of the transverse rms beam size) in Fig.10. An unexpected behavior was found with respect to models (the black line): a larger tune spread was measured in the horizontal plane (the blue line), but still smaller than prediction below 11.5 $\sigma$, while a smaller one in the vertical plane (the red line) except for the measurement at 12 $\sigma$ and for the last measurement at 9 $\sigma$ separation for which a strong dependency on the working point was observed. The red star represents the measured tune spread in the vertical plane with a reduced tune of $\Delta Q_y = -0.001$. The tune spread reduction was not expected from the models unless the transverse linear coupling is considered. A parallel separation scan (from 0 to 6 $\sigma$ in units of transverse beam size) was performed with beams in head-on collisions. The BTF measurements were acquired as a function of the parallel separation at the IPs. Figure 11 shows the measured BTF amplitude responses in the presence of head-on collisions in IP1 and IP5 for various beam offsets at the IPs. As visibile in fully head-on collisions the amplitude response is wider, meaning that the tune spread is the largest one, while at 1.45 $\sigma$ the amplitude response is qualitatively the narrowest. Therefore, the tune spread results to be reduced, confirming the presence of a minimum of Landau damping

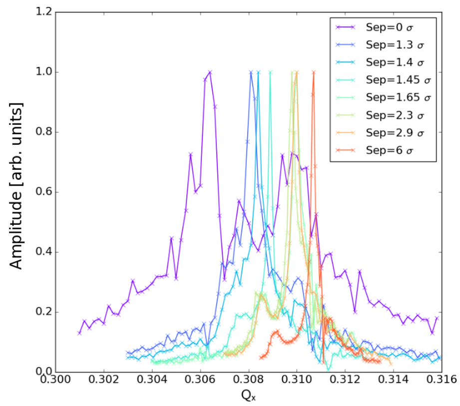


Figure 11: Measured BTF amplitude responses with head-on collisions in IP1 and IP5 for different offsets at the IPs.

at this separation as expected [3, 4]. Tune shifts due to the head-on interaction were also observed while separating the beams. The measured tune shifts were compared to MAD-X expectations [17] with a good agreement for separations below 2 $\sigma$.

## CONCLUSIONS

The transverse BTF system was installed in the LHC in order to measure the Landau damping of the beams. A fitting method was successfully applied to the data for quantitative comparison with expectations. The effects of the linear coupling resonance on the Landau damping of the beams was measured at injection energy with a good agreement with models. It was observed that beam losses, due to a reduced dynamic aperture at injection energy for high octupole current, reduce the expected Landau damping of the beams. In the presence of long range beam-beam interaction unexpected behaviors were observed showing that other mechanisms should play a role such as linear coupling and/or particle redistributions in the beams [7]. The minimum of Landau damping expected at 1.5 $\sigma$ beam to beam separation at the IP was observed in the width of the BTF amplitude response, confirming the presence of a minimum of Landau damping during the collapse of the separation bumps at such separation. The tune shifts due to the coupling impedance were quantified confirming a factor 1.5 on the effective imaginary part of the impedance expectations. The BTF measurements provided a good reconstruction of Landau damping especially at injection energy and for low chromaticity values helping to understand mechanisms responsible for reduction of the expected Landau damping for instance due to beam particle losses or linear coupling. However the BTF system and the fitting method present some limitations: when the chromaticity is not negligible it causes distortion in the reconstruction of the SD. It is not possible to apply the fitting method either when the impedance is too strong or when the beam is too close to the stability limit, the BTF excitation may cause coherent instability as observed in the 2017 due to an increase of the impedance [18].

## ACKNOWLEDGMENTS

We would like to thank T. Levens, N. Mounet and D. Amorim for fruitful discussions and advices in particular for the data analysis.

## REFERENCES

[1] J. Berg, F. Ruggero, "Landau Damping with two-dimensional betatron tune spread", CERN, Geneva, Switzerland, CERN-SL-96-071-AP, Dec. 1996.

[2] J. Gareyte *et al.*, "Landau Damping, Dynamic Aperture and Octupoles in LHC", CERN, Geneva, Switzerland, LHC Project Report 91, Apr. 1997.

[3] X. Buffat *et al.*, "Stability Diagrams of colliding beams", Phys. Rev. ST Accel. Beams 17 111002, 2014.

[4] X. Buffat, Transverse beams stability studies at the Large Hadron collider, École Polytechnique Fédérale de Lausanne, CERN-THESIS-2014-246, September 2014.

[5] D. Mohl and A. M. Sessler, The use of the RF-knockout for determination of the characteristics of the transverse coherent instability of an intense beam, in Proceedings of The 8th International Conference on High-Energy Accelerators, p.334, Lawrence Berkeley Laboratory, University of California, Berkeley, USA, 1971 Accelerators, HEACC 1971: CERN, Geneva, Switzerland, September 20–24, 1971.

[6] SixTrack, `http://sixtrack.web.cern.ch/SixTrack/`.

[7] C. Tambasco, Beam Transfer Function measurements and transverse beam stability studies for the Large Hadron Collider and its High Luminosity upgrade, École Polytechnique Fédérale de Lausanne, EPFL-THESIS-7867, August 2017.

[8] L. R. Carver *et al.*, "Transverse beam instabilities in the presence of linear coupling in the Large Hadron Collider", Phys. Rev. Accel. Beams 21 044401, 2018.

[9] E. Métral, "Coupled Landau damping of transverse coherent instabilities in particle accelerators", Université Joseph Fourrier, CERN-THESIS-1999-074, 1999.

[10] E. Métral *et al.*, "Destabilising Effect of Linear Coupling in the HERA Proton Ring", CERN/PS 2002-021 (AE), CERN, Geneva, Switzerland.

[11] MAD-X, `http://mad.web.cern.ch/mad/`

[12] A. Hoffman and B. Zotter, Measurements of beam stability and coupling impedance by RF excitation,CERN ISR-TH/77-12, Geneva, Switzerland, 1977

[13] A. W. Chao, Physics of collective beam instabilities in high-energy accelerators, Wiley (1993) 371 p, New York, USA, 1993.

[14] T. Pieloni and W. Herr, "Coherent beam-beam modes in the Cern Large Hadron Collider (LHC) for multiple bunches, different collision schemes and machine symmetries", in *Proc. PAC'2005*, Knoxville, Tennessee, Oct. 2011, paper TUP014, pp. 89–91.

[15] `http://impedance.web.cern.ch/LHC_impedance/LHC_summary_2018.htm`

[16] D. Amorim *et al.*, Comparison of LHC impedance model predictions to beam based measurements, 29th Impedance Working Group, February 29th 2019, `https://indico.cern.ch/event/797962`, CERN, Geneva, Switzerland.

[17] C. Tambasco *et al.*, "MD 3292: Measurements of Landau damping by means of BTF measurements", CERN-ACC-NOTE-2019-0045, 22-10-2019.

[18] C. Tambasco *et al.*, Triggering of instability by BTF measurements, LBOC Meeting 27/03/2018, Geneva, Switzerland, `https://indico.cern.ch/event/715467/`.

# TRANSVERSE DAMPER AND STABILITY DIAGRAM

S. A. Antipov[1*], D. Amorim[2], N. Biancacci, X. Buffat, E. Métral, N. Mounet, A. Oeftiger[3], D. Valuch
CERN, Geneva, Switzerland, [1] also at DESY, Hamburg, Germany,
[2] also at Synchrotron SOLEIL, Gif-sur-Yvette, France, [3] also at GSI, Darmstadt, Germany

*Abstract*

We describe a proof-of-principle test to measure Landau damping in a hadron ring using a destabilizing transverse feedback acting as a controllable source of beam coupling impedance. The test was performed at the Large Hadron Collider and stability diagrams for a range of its Landau octupole strengths have been measured for its injection energy of 450 GeV. In the future, the procedure could become an accurate way of measuring stability diagrams throughout the machine cycle.

## LANDAU DAMPING

A common technique of measuring Landau Damping is by means of Beam Transfer Function (BTF) measurements [1], where the frequency dependence of the response to forced beam oscillations is used to quantify the Stability Diagram (SD) [2]. BTF has been successfully used to measure SDs at GSI [3], RHIC [4] and at injection energy in LHC [6, 7]. The method has some limitations though: first, it might be challenging to maintain both good beam stability and high signal to noise ratio when driving the oscillation as seen at top energy in LHC [7]. Second and most importantly, the measurement does not test the strength of the Landau damping itself, but the transfer function. Numerous approximations are usually made to obtain the SD from the BTF: the synchrotron frequency spread is neglected, the betatron frequency spread is assumed to be small, the beam response to an external excitation is assumed to be linear.

A new alternative approach for measuring the strength of Landau damping involves using the transverse feedback with a reverted polarity (anti-damper) to excite a collective mode in the beam. The anti-damper such acts as a controllable source of beam coupling impedance. By knowing the strength of the feedback excitation, and observing at which feedback gain the beam becomes unstable, one obtains a direct measurement of the strength of Landau damping in the synchrotron. Further, with an accurate control over the feedback phase one can explore the full complex plane of tune shift and growth rate. One can such derive the SD and compare with theoretical predictions. In this paper we describe the first proof of principle test to measure the strength of Landau damping created by the LHC octupole system at 450 GeV injection energy.

* Sergey.Antipov@desy.de

## MEASUREMENT OF LANDAU DAMPING AT LHC

### *Feedback as Controlled Impedance*

If the variation of the feedback's dynamic response over the bunch length can be neglected, i.e. it is 'flat', it can be described as a constant wake force acting on the beam $W(z) = W_0 = const$. This is true e.g. for the LHC transverse feedback whose bandwidth goes up to 40 MHz or 1/10 of the radio frequency (RF) period or RF bucket width. This wake function corresponds to a $\delta$-function-like coupling impedance (see [8] or [9] for reference):

$$Z_d(\omega) \sim ig \times e^{i\phi} \times \delta(\omega), \tag{1}$$

where $g$ stands for feedback gain in inverse turns and $\phi$ for its phase: 0 indicates a resistive feedback (picking up on beam position) and 90 deg a reactive one (picking up on transverse beam momentum). A resistive feedback thus drives a coherent beam mode upwards in the diagram, driving it unstable, with an instability growth rate of $-g$ (Fig. 1). Such a system has been proposed for the IOTA ring [10, 11], where the researchers considered an anti-damper with $\phi = 0$.

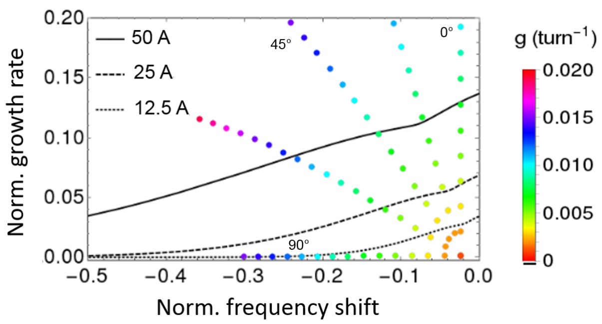


Figure 1: Controlling the gain and the phase of the feedback one explores the full relevant area of SD in LHC. Real and imaginary mode frequency shifts are normalized by the synchrotron frequency $\omega_s$. SDs for a nominal 1.0 $\mu$m emittance Gaussian beam distribution are shown in black for various Landau octupole currents.

A realistic impedance of various accelerator components ranges from inductive impedance of high-Q RF modes, to broadband imaginary impedance of bellows and tapers. These impedances can be modelled by different phases of the feedback: from 0 for a purely imaginary tune shift to 90 deg for a purely real one. In practice, a variation of the phase is convenient to achieve with two feedback pick-ups: one picking up on the beam momentum and the other on its position. The LHC transverse feedback system features two pick-ups (Fig. 2). This allows producing an arbitrary complex gain $g \times e^{i\phi}$ by adjusting phase delay between them and their gain [12].

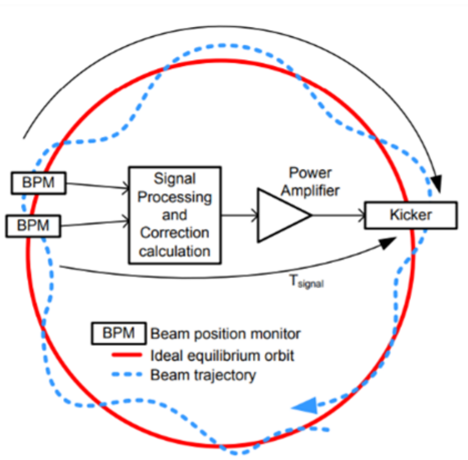


Figure 2: LHC feedback system uses two pickups per plane allowing acting independently on both beam transverse position and its transverse momentum.

It has to be noted that in normal operation the LHC transverse feedback phase setting is optimized for a particular tune value. When operating away from the optimal tune, the phase of the pickup signal receives an error with respect to an ideal value. The error is deterministic and occurs merely from the specifics of signal processing. The error vanishes for phase shifts of 0 and $\pi/2$, and is largest for $\pi/4$. For the MD parameters with the tune close to 0.27 the error should have never exceeded 4 deg (Fig. 3). Furthermore, the impact of the pickup phase error on the transverse damper phase seen by the beam is actually smaller, since the damper sums signals from two pickups, each with a different relative phase to the kicker. Our estimates suggest that the phase error seen by the beam is sufficiently small and should not exceed 1 deg at the nominal LHC tune settings.

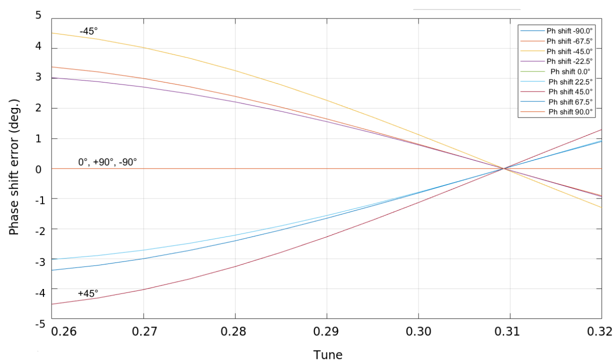


Figure 3: Signal processing phase error as a function of tune (horizontal axis) and the requested phase shift (colored traces) in a range from -90 to +90 degrees.

## *Choice of parameters*

In order to have a good comparison with theory it is beneficial to perform a measurement at the nominal settings at the top energy of 6.5 TeV, where the optics is well under control, space charge is negligible, and there are plenty of experimental data for instability thresholds and the impedance to compare with. Such a measurement however requires a lot of machine time to perform, which is detrimental for obtaining reproducible results. On the other hand, performing a measurement at the injection energy of 450 GeV allows for a rapid machine setup and re-injection to perform multiple repetitive measurements; also working at injection energy allows applying a large octupolar detuning in order to stabilize the beam without the need of resorting to the feedback, which simplifies the measurement procedure. The space charge tune shift remains small when using the low intensity pilot beams, while the low beam intensity also minimizes mode tune shift from beam coupling impedance.

Having a single dominating coherent mode is useful for being able to draw accurate predictions on the instability growth rate at various settings of feedback gain and phase. For example, at a nominal beam intensity and relatively high chromaticity there may be several azimuthal modes with similar growth rates. Which of them becomes unstable first in the measurement is then determined by the shape of the SD and the mode frequency shift from impedance (Fig. 4). While, in principle, these effects can be simulated (e.g. by using a Vlasov solver) they also add unnecessary parameters to the measurement procedure, which might be not very well known or poorly controlled. Therefore such interference of different modes should be avoided when designing the experiment to measure Landau damping.

Based on the above considerations and limited by the time constraint of a realistic LHC machine study we have chosen to work at nominal LHC injection settings with an injection pilot beam, i.e. a single bunch of $0.5 \times 10^{10}$ p with 1 $\mu$m normalized rms emittance. At these parameters the azimuthal dipolar head-tail mode typically dominates the landscape with higher order modes featuring much weaker growth rates. Beam and machine parameters are summarized in Table 1.

In LHC the betatron frequency spread required to produce the Landau damping is largely generated by a dedicated system of 84 focusing and 84 defocusing 30 cm long superconducting octupoles [14]. The initial calibration measurement was performed with the betatron tune spread provided only by the machine nonlinearities. This measurement is needed to confirm the experimental procedure and quantify the action of the feedback as the source of controlled impedance. Then another set of measurements was performed with Landau damping produced by several configurations of relatively high Landau octupole currents: ±11 and +17 A, which correspond to roughly 4 and $7 \times 10^{-5}$ rms tune spread. This measurement was repeated at about nominal ring chromaticity of $Q' = +14$ and at low chromaticity of $Q' = +3$.

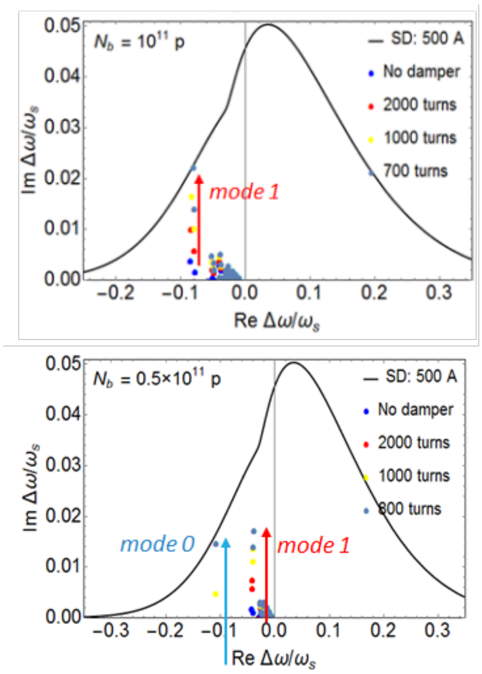


Figure 4: At Top energy and Nominal machine settings there could be several interfering modes with similar growth rates, depending on beam intensity. Top – nominal intensity of $10^{11}$ ppb, bottom – half the beam intensity. $E = 6.5$ TeV, $Q' = 15$, $I_{oct} = +500$ A, $\epsilon_n = 2.5$ $\mu$m, nominal collimator settings.

### *Feedback calibration*

In order to ensure an independent control over both the feedback gain and phase, the system was calibrated with no octupole current at three anti-damper phases: 0, 45 and 67.5 deg. At each phase the feedback excited a beam instability and the growth rate of the center-of-mass oscillations was measured as a function of the feedback gain. An example of raw data is shown in Fig. 5 and a larger data set is provided in the Appendix.

Table 1: Key parameters used for the study

| Parameter | Value |
|---|---|
| Beam energy | 450 GeV |
| Beam intensity | $0.5 \times 10^{10}$ ppb |
| Number of bunches | 1 |
| Norm. tr. emittance, rms | 1.0 – 1.1 $\mu$m |
| Bunch length, $4\sigma_{rms}$ | 1 ns |
| Coupling, $\lvert C^{-}\rvert$ | 0.001 |
| RF voltage | 6 MV |
| Tunes: x, y, z | 0.275, 0.295, 0.005 |
| Chromaticity, $Q'$ | 14 |
| Synch. freq., $\omega_s$ | 0.03 rad$^{-1}$ |
| SC tune shift | $O(10^{-4})$ |

An instability has been declared if the beam centroid excursion from the reference orbit exceeded 200 $\mu$m, which corresponds to the order of an rms beam size at the pickup locations. After triggering the instability, the last 64'000 turns of beam position data were saved for future processing. In order to assess the instability growth rate from the data $x_i$, it has been first passed through a low-pass digital filter to subtract any constant offset $y_i = x_{i+1} - x_i$. Then the oscillation envelope was obtained with a 50-turn moving Gaussian filter applied to $y^2$. Finally, a linear interpolation with a 5000-turn moving window was applied to $\log y^2$ and the growth rate was determined as $1/2$ the maximum slope.

Examining the data we realised that the measurements done at the smallest gains probably had the beam emittance spoiled due to the approach we took – slowly steadily increasing the gain until the first instability is observed. As a results in those cases the beam was oscillating at large amplitudes before from the beginning, a pattern not observed at higher feedback gains with fresh beams (Fig. 6). The spoiled emittance might have severely affected the growth rate and thus these data points could not be trusted. For several data points second measurements with fresh beam were performed – in that case those measurements were taken. All the unreliable data for which no measurement with fresh beam was available was discarded. In order to avoid this if the measurements are repeated in the future we propose performing the calibration starting with a large feedback gain and gradually lowering it, reinjecting fresh beams after each observed instability.

After filtering the data the resulting dependence of the instability growth rate on the feedback gain was found to be linear, as expected (see Fig. 7). Also, the growth rate slope reduces gradually with the phase, as expected. The magnitude of the slope yields the calibration factor for the feedback gain (i.e. a setting of $g$ units drives an instability with an exponential rise time of $t$ turns) for any following measurements.

At the time of experiment no on-the-fly analysis of the tune shift was done, as it was complicated by the presence of tune significant tune jitter of the order of $1 \times 10^{-4}$. Nevertheless, the tune shift sign was verified using a bunch-by-bunch tune monitor (the base-band Q-meter, BBQ). Post-factum, an accurate reconstruction of the tune turned out to be possible only for the measurements at 45 deg phase, where the tune shift are large enough to overcome the noise while the instability growth rate is still slow enough to obtain sufficient data points during the developing instability. The tune was computed using a moving window of 1024 turns with a Fast Fourier Transform (FFT) with zero-padding and a Hanning filter – a standard technique for identifying the major tune lines in spectra of realistic accelerator data [15]. An example of the observed tune shift can be seen in the center panel of Fig. 5. As the anti-damper is turned on and the instability starts developing, the tune changes from its average unperturbed value (blue line) to the shifted one (red line). Periodic 'bumps' can also be seen in the data which are attributable to the tune feedback system.

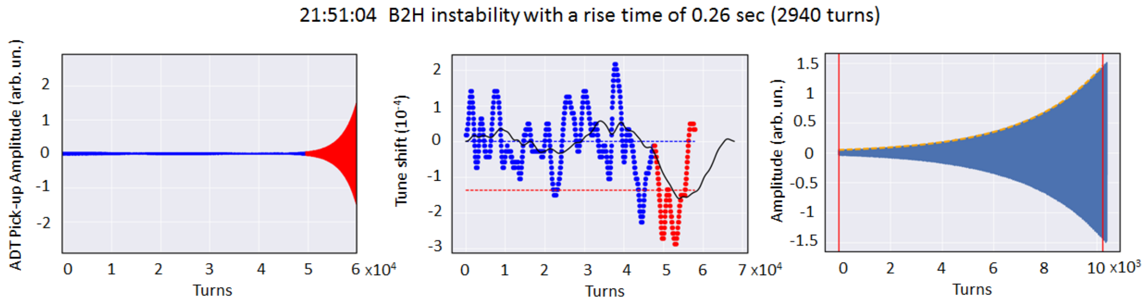


Figure 5: An example of an instability observed during the feedback calibration process. Left – the full 64'000 turn acquisition of the center of mass position, the unstable area is highlighted in red. Right – zoom-in of the instability. The dashed yellow line represents an exponential fit of the data. Center – the frequency domain: the black line shows the moving average of the tune. The blue and red lines indicate mean values for the stable and unstable regions.

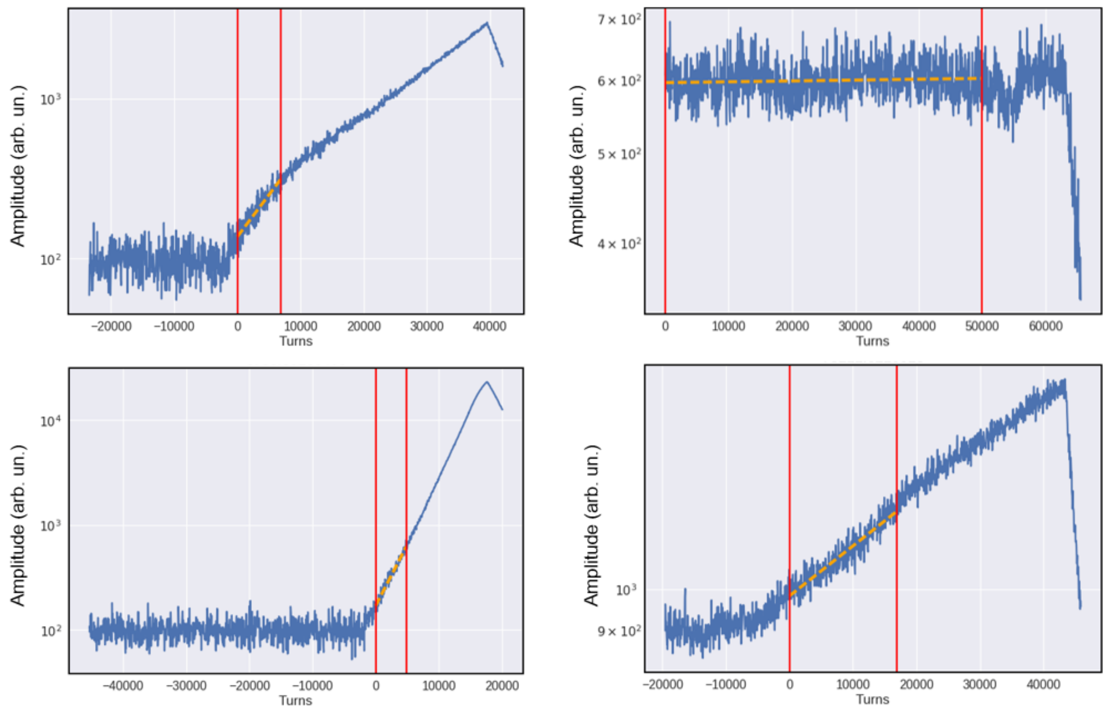


Figure 6: Left – examples of 'good' data: center of mass position oscillations start at around 100 units and increase exponentially as the destabilising feedback is turned on. The growth rate is determined as the maximum slope (dashed orange line) observed at the onset of the instability (highlighted with two vertical red lines). Turn 0 corresponds to the start of the process. Right – examples of 'bad' data, with the beams likely having suffered an instability before, which had affected the bunch distribution: the initial center of mass position oscillates around larger values, as the feedback gains is increased no growth is observed in some cases. Even though in some cases an exponential growth is observed, the slope might be affected by the blown up emittance.

The tune is observed to vary linearly with the feedback gain, and its slope matches what the growth rate measurement implies: $1.3 \times 10^{-2}$ vs. $\frac{1}{2\pi}6.39 \times 10^{-2} = 1.1 \times 10^{-2}$ (Fig. 7). A small discrepancy of about 15% can be explained by the uncertainty of the tune shift determination procedure. An uncertainty in damper phase can also contribute to the discrepancy, while it is expected to remain rather small at the above-mentioned less than 1 deg level.

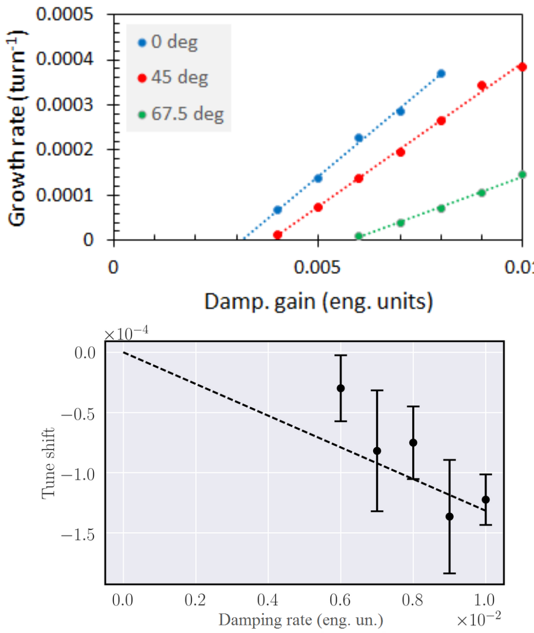


Figure 7: The transverse feedback drives an instability (top) and induces a tune shift proportional to its gain (bottom).

### *Stability Diagram scans*

After calibrating the feedback we performed a series of measurements at different octupole settings. At each setting the feedback gain was gradually increased in small steps until reaching the limit of stability. At this point the feedback phase was increased – as the SD contour should have an increasing distance to the origin at increasing phase, the beam should return to stable conditions at higher phases. This procedure has been repeated for a few different phases between 0 and 90 deg. At each step the feedback gain was kept constant for about 30 sec, which should have excluded potential impact of latency effects. This time window has been chosen following a recent study, where latency effects could be excluded in single bunch octupole threshold measurements with sufficiently short 1 min steps [16]. In our experiment, an instability was declared as soon as the beam centroid excursion from the reference orbit exceeded 200 $\mu$m – a value comparable to the rms transverse size of the beam. In this case the feedback was automatically switched back to a resistive stabilizing mode with a strong damping time of 200 turns (Fig. 8). We used an automated script to perform these stability diagram scan. The procedure of locating the the boundary of stability typically took 5 min or less per data point (octupole current, feedback phase setting). The

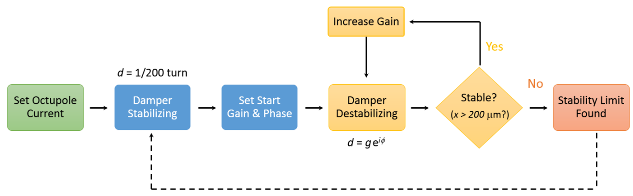


Figure 8: Procedure for measuring SDs: feedback gain is increased at a fixed phase until a threshold amplitude is exceeded, then the feedback is reverted back to the stabilizing mode.

measurement was only performed in one of the LHC beams – Beam 2 and only in the horizontal plane due to resource and machine constraints at the time of the study.

The beam emittance should remain unaffected throughout the measurement – a condition which was closely monitored during the experiment by means of the beam synchrotron radiation monitor. Therefore, in order to save time, the beam was only re-injected when an emittance growth by more than 10% had been observed. A disadvantage of this approach is that the distribution tails might have been affected by previous measurements, as they correspond to a large tune shift and thus play a crucial role in Landau damping. While no systematic study of the effect was attempted during this proof-of-principle test, several data points were measured twice to check reproducibility of the results. The results with an ‘old’ and with a ‘fresh’ beam turned out to be in good agreement within 10% and less fluctuation.

## RESULTS AND DISCUSSION

### *Landau damping by LHC octupoles*

The shape of the measured SDs at 11, 17, and -11 A qualitatively matches the expectations from simple linear SD theory. Both the height and the width scale with the octupole current: e.g. the SD for 17 A turns out to be around 50% taller than the SD for 11 A, which matches the 1.5 times higher current (Fig. 9). The second measurement for 11 A current made at a lower chromaticity of 3 units matches within 10 – 20 percent the first one performed at 14 units. The negative octupole polarity offers around 30% greater coverage of the negative tune shifts. This illustrates the reason why negative octupole polarity is preferred, namely to suppress impedance-driven instabilities in LHC that feature negative mode frequency shifts. The exact figure of the required threshold gain will eventually depend on the details of the beam distribution.

Injection-to-injection spread of the strength of Landau damping, measured over 5 consecutive injections at 11 A and 0 deg phase (i.e. resistive anti-damper) turned out to be rather small at around 7% indicating sufficient reproducibility of the beam distribution. The 7% value gives a lower limit on the systematic uncertainty for all subsequent measurements.

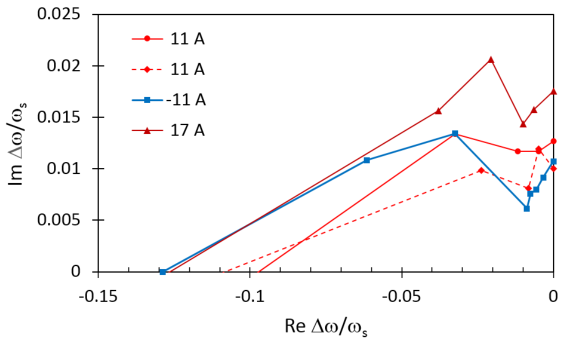


Figure 9: The measured height of the diagrams scales linearly with the octupole current with the negative octupole polarity providing around 30% larger coverage of negative mode frequency shifts, which are relevant for coherent beam stability. LHC SDs were measured at 450 GeV in the horizontal plane, solid lines – $Q' = 14$, dashed line – $Q' = 3$. Real and imaginary tune shifts are normalized by the synchrotron frequency.

Depending on the damper phase and thus the direction of the tune shift, the modes would probe different parts of the octupole SD: for the imaginary shift it would be the center that is nearly independent of the beam distribution or the octupole polarity, whereas for the real shift it would be the tail of the diagram that strongly depends on the beam parameters (i.e. emittance, intensity, bunch profile, etc.), which all vary slightly from fill to fill. Hence, measurements probing the central SD peak around 0 deg damper phase are less affected by these beam parameter variations, while the SD tails (probed around ±90 deg damper phase) underlie a significant uncertainty.

Quantitatively, from simple detuning considerations one would expect to measure about a factor two larger SDs than what was observed in the experiment. There are several factors that could contribute to this discrepancy. First of all, it has to be mentioned that the mode complex frequency shift is affected by the machine's impedance and neglecting the latter might lead to a considerable miscomputation of the octupole threshold as demonstrated in Fig. 10. If one excites with a resistive feedback, the border of the SD is crossed at a different location, closer to the tail of the diagram, at a factor two lower feedback gain. If one then uses this lower gain to infer the octupole threshold without considering the mode shift produced by the impedance, one might underestimate the threshold by about a factor two.

Other effects include natural machine nonlinearities that might generate a linear detuning with amplitude equivalent to about −2.5 A of octupole current [17–19] and linear coupling that can distort the amplitude detuning from the Landau octupoles, reducing the footprint locally, but leading as well to a large second order amplitude detuning [18, 20]. While the coupling had been corrected to a sufficiently low value in the beginning of the test at $|C^-| = 0.001$, it may have drifted away from this initial value over time, which would shrink the octupole tune footprint and result in a slightly smaller the SD for larger $|C^-|$ values [21].

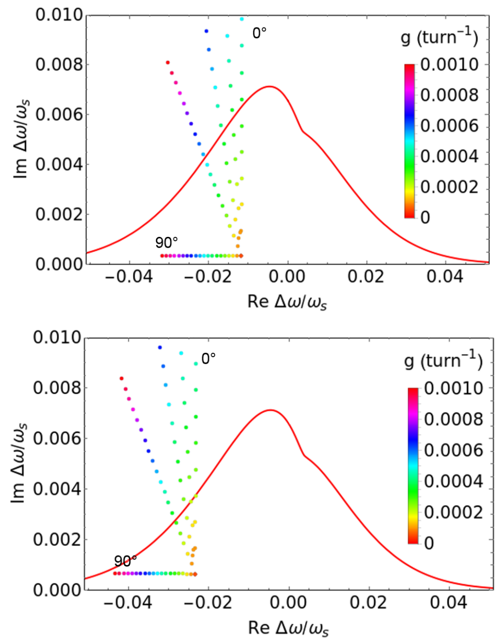


Figure 10: Machine impedance creates a negative tune shift, affecting the position of SD crossing when a destabilizing feedback is applied. Top – nominal machine impedance; bottom – double machine impedance. The SD depicted by a red line corresponds to a Gaussian beam with 1 $\mu$m rms normalized emittance and 2.5 A positive octupole current. Various feedback gains for 5 equidistant phases between 0 and 90 deg are shown as coloured dots.

Finally, although space charge on its own does not provide Landau damping for the rigid dipole mode, as pointed out by Möhl [22], it does modify the SD produced by lattice nonlinearities. In general, an interplay of octupole detuning and nonlinear space charge may be important as observed in particle tracking simulations [23]. When the strength of space charge detuning is small relative to other sources its impact can be estimated analytically in a simple model [24], assuming a quasi-parabolic transverse distribution [25], coasting beam conditions, and a linear space charge detuning (the model can be extended to bunched beams [26], although the impact of the bunching is minor). Depending on the strength of space charge, it leads to a negative real tune shift of the SD maximum, a widening of the diagram, and a slight reduction of its height. For the studied parameters, the impact of space charge should be relatively weak providing a shift of the SD of around $\Delta_0 = 10^{-4}$. Nevertheless, the space charge interaction could significantly affect the spread of betatron frequencies and thus the Landau damping when the machine nonlinearities were small enough, i.e. during the feedback calibration, as discussed below.

*Comparison with macro-particle simulations*

To investigate the space charge issue further we performed macro-particle simulations in the PyHEADTAIL macroparticle tracking code, which performs 6-dimensional tracking [27–29]. The tracking utilizes smooth optics approximation and a drift/kick model for non-linear synchrotron motion, treating the accelerator ring as a collection of interaction points connected by ring segments where the beam is transversely transported via transfer matrices. Nonlinear optics effects such as chromatic detuning and octupolar amplitude detuning are applied as effective tune shifts for each individual macro-particle. Collective effects, arising from impedance, space charge, or external feedback are applied at the interaction points where the beam is longitudinally divided into a set of slices via a 1D particle-in-cell (PIC) algorithm.

The natural machine nonlinearities were modelled by a −2.5 A equivalent octupole linear amplitude detuning ($\sim 10^{-5}$ rms tune spread). The numerical model also included nonlinear longitudinal motion inside the RF bucket while linear coupling effects were neglected, since they are expected to have little effect on beam stability if the coupling is sufficiently well corrected as discussed before. Without space charge, $1 \times 10^6$ macro-particles have been tracked for $1 \times 10^6$ turns. Simulations including self-consistent space charge (via a 2.5D slice-by-slice PIC algorithm) are based on $3 \times 10^6$ macro-particles being tracked during $60 \times 10^3$ turns corresponding to a machine time of more than 5 s.

Tracking results shown in Fig. 11 demonstrate that SC significantly affects the instability growth rate for a given gain of the destabilizing feedback increasing the stable area. With SC included the simulation results remain in good agreement with the experimental observations. This highlights the importance of including the space charge interaction into the picture when comparing experimental data to models or tracking results. Further comprehensive numerical studies including all potential effects are required to understand the magnitude and shape of the measured SDs and compare with the available analytical models.

Table 2: Key simulation parameters in addition to Table 1

| Parameter | Value |
|---|---|
| Chromaticity | $Q'_{x,y} = 15$ |
| Transverse tunes | $(Q_x, Q_y) = (64.28, 59.31)$ |
| Synchrotron tune | $Q_s = 4.9 \times 10^{-3}$ |

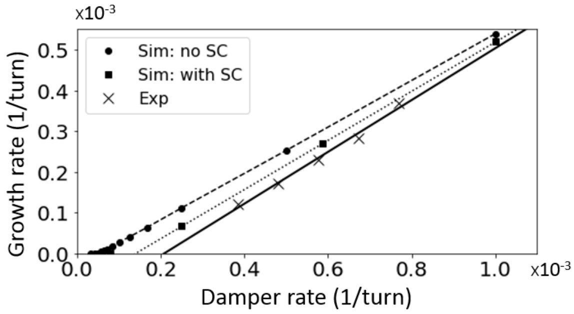


Figure 11: Instability growth rate scales linearly with the damper gain, allowing to calibrate the feedback strength. The non-zero gain required to start an instability is caused by natural nonlinearities of the machine. Overall, experimental data (crosses and the solid line) are in good agreement with numerical simulations (squares and the dotted line). Numerical simulations performed with space charge show a greater amount of feedback gain required to destabilize the beam than in the no-space-charge case (circles and the dashed line), emphasizing the importance of accounting for the space charge interaction at the LHC injection energy, $E = 450$ GeV.

## CONCLUSION

In this proof-of-principle test we have demonstrated that the active feedback system can be used as a source of controlled impedance to probe the strength of Landau damping. The experiment has been carried out in the LHC at the injection energy of 450 GeV using single bunches at low intensity. First, the active feedback system has been calibrated in order to produce arbitrary complex tune shifts. Both tune shift and instability growth rate have been demonstrated to increase linearly with the feedback gain, as expected. Then, the feedback has been utilized to directly measure the strength of Landau damping by gradually increasing its gain until a transverse activity is observed. The possibility of exploring the SD by changing the damper phase has also been demonstrated. The results are in qualitative agreement with the details of theoretical SD predictions. A more extensive quantitative analysis (in particular comparing to tracking simulations with space charge) is required to include effects of lattice nonlinearities and coherent effects in the picture.

The technique has a potential to become a fast non-destructive tool for measuring the strength of Landau damping throughout the accelerator cycle. In LHC it would be well suited for studies at the top energy, where the constraints arising from Landau damping are the tightest and the effect of space charge is negligible. In order to explore this potential, further studies including the top energy (6.5 TeV at the moment, with plans to reach the nominal 7 TeV in the future) should be carried out after the current Long Shutdown. This approach also has a potential of shedding light on the interplay between Landau damping and space charge – an area where currently one has to rely on computationally demanding macroparticle simulations. For example, at LHC after demonstrating sufficient safety for the machine, the bunch intensity could be increased up to $\sim 10^{11}$ p or $\Delta Q_{SC} \sim Q_s$ at 450 GeV. This would allow investigating how an increasing space charge force affects Landau damping by the octupoles.

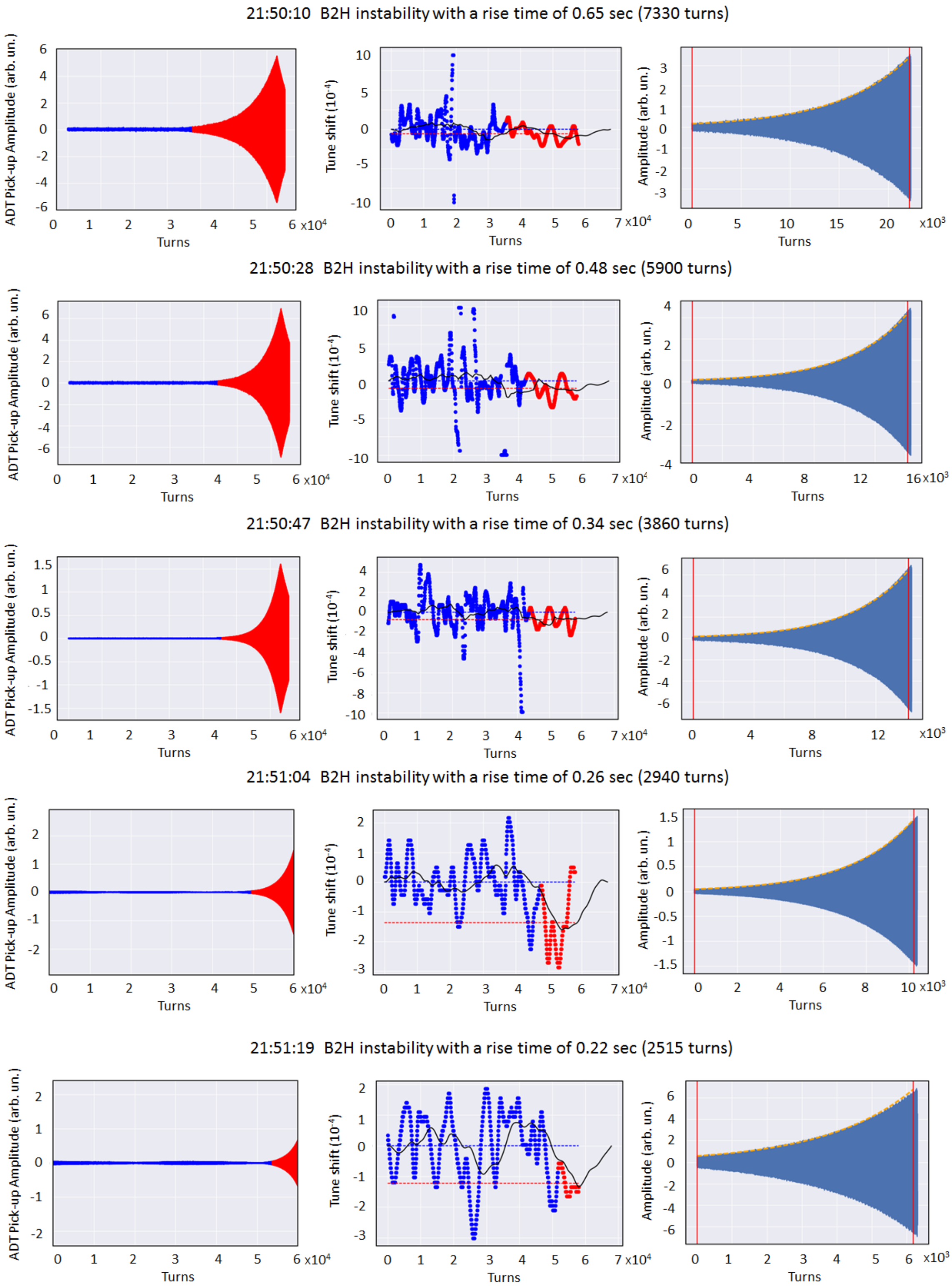


Figure 12: Beam position data for a 45 degree phase. Left – oscillation envelope over 64000 acquisition turns, the unstable area, defined by a crossing of the threshold, is shown in red. Center – tune variation over time, obtained with a moving FFT window of 2000 turns; solid black line shows the moving average, dashed blue – average stable tune, dashed red - average unstable tune. Right – exponential amplitude blow-up observed in the unstable region; exponential fits are shown in orange.

## ACKNOWLEDGEMENTS

The authors would like to thank Alexey Burov (FNAL) for sharing his ideas on the use of a transverse feedback as a source of controlled impedance which triggered this research. We express our gratitude to the LHC Operations Team and especially Francesco Velotti for a fruitful and productive collaboration that helped sketching a realistic plan and ultimately successfully carry out tests. We shall also thank Lukas Malina for his insightful tips on the analysis of turn-by-turn data, Gianluigi Arduini for his comments on the paper, and Ewen Maclean and Tobias Persson for discussion on the sources of lattice nonlinearities in LHC.

## REFERENCES

[1] A. W. Chao and M. Tigner, "Handbook of accelerator physics and engineering," Singapore: World Scientific (2006)

[2] K. Hübner, A. G. Ruggiero, and V. G. Vaccaro, "Stability of the coherent transverse motion of a coasting beam for realistic distribution functions and any given coupling with its environment," CERN-ISR-TH-RF-69-23

[3] V. Kornilov, O. Boine-Frankenheim, W. Kaufmann, and P. Moritz, "Measurements and Analysis of the Transverse Beam Transfer Function (BTF) at the SIS 18 Synchrotron," GSI-Acc-Note-2006-12-001, GSI, Darmstadt (2006)

[4] Y. Luo, W. Fischer, A. Marusic and M. Minty, "Measurement and Simulation of Betatron Coupling Beam Transfer Function in RHIC," doi:10.18429/JACoW-IPAC2018-MOPMF010

[5] C. Tambasco *et al.*, "First BTF Measurements at the Large Hadron Collider," doi:10.18429/JACoW-IPAC2016-WEPOY030

[6] C. Tambasco *et al.*, "Beam Transfer Function and Stability Diagram," these proceedings

[7] T. Pieloni *et al.*, "MD 3292: Summary of BTF studies MD Block 3&4," CERN, 4 Dec 2018 `https://indico.cern.ch/event/776844`

[8] A. W. Chao, "Physics of collective beam instabilities in high-energy accelerators," New York, USA: Wiley (1993) 371 p

[9] A. Burov, "Nested Head-Tail Vlasov Solver," Phys. Rev. ST Accel. Beams **17**, 021007 (2014) doi:10.1103/PhysRevSTAB.17.021007

[10] S. Antipov *et al.*, "IOTA (Integrable Optics Test Accelerator): Facility and Experimental Beam Physics Program," JINST **12**, no. 03, T03002 (2017) doi:10.1088/1748-0221/12/03/T03002

[11] E. Stern, J. Amundson, and A. Macridin, "Suppression of Instabilities Generated by an Anti-Damper with a Nonlinear Magnetic Element in IOTA," doi:10.18429/JACoW-IPAC2018-THPAF068

[12] A. Butterworth *et al.*, "LHC transverse feedback," in Proc. 6th Evian Workshop on LHC beam operation, Evian Les Bains, France, Dec 2015

[13] W. Höfle *et al.*, "Transverse feedback in the HL-LHC era," 5th Joint HighLumi LHC - LARP Meeting Fermilab, USA, Oct 2015

[14] O. S. Brüning, P. Collier, P. Lebrun, S. Myers, R. Ostojic, J. Poole and P. Proudlock, (Eds.), "LHC Design Report Vol.1: The LHC Main Ring," doi:10.5170/CERN-2004-003-V-1

[15] R. Bartolini, A. Bazzani, M. Giovannozzi, W. Scandale, and E. Todesco, "Tune evaluation in simulations and experiments," Part. Accel. **52**, 147-177 (1996) CERN-SL-95-84-AP.

[16] X. Buffat *et al.*, "Summary of instability observations at LHC and implications for HL-LHC," CERN, 9 Jul 2019, `https://indico.cern.ch/event/831847/`

[17] M. McAteer *et al.*, "Magnet polarity checks in the LHC," CERN-ACC-NOTE-2014-0012

[18] E. H. Maclean, R. Tomás, F. Schmidt, and T. H. B. Persson, "Measurement of nonlinear observables in the Large Hadron Collider using kicked beams," Phys. Rev. ST Accel. Beams **17**, no. 8, 081002 (2014). doi:10.1103/PhysRevSTAB.17.081002

[19] E. H. Maclean, "Observations relating to MCDO alignment," CERN, Geneva, Switzerland, Feb 2019 `https://indico.cern.ch/event/812944/`

[20] E. H. Maclean, F. Carlier, M. Giovannozzi, T. Persson, and R. Tomás, "Effect of Linear Coupling on Nonlinear Observables at the LHC," doi:10.18429/JACoW-IPAC2017-WEPIK092

[21] L. R. Carver, X. Buffat, K. Li, E. Métral, and M. Schenk, "Transverse beam instabilities in the presence of linear coupling in the Large Hadron Collider," Phys. Rev. Accel. Beams **21**, no. 4, 044401 (2018). doi:10.1103/PhysRevAccelBeams.21.044401

[22] D. Möhl, "On Landau damping of dipole modes by nonlinear space charge and octupoles," Part. Accel. **50**, 177 (1995).

[23] V. Kornilov, O. Boine-Frankenheim, and I. Hofmann, "Stability of transverse dipole modes in coasting ion beams with nonlinear space charge, octupoles, and chromaticity," Phys. Rev. ST Accel. Beams **11**, 014201 (2008). doi:10.1103/PhysRevSTAB.11.014201

[24] E. Métral and F. Ruggiero, "Stability diagrams for Landau damping with two-dimensional betatron tune spread from both octupoles and non-linear space charge," CERN-AB-2004-025-ABP.

[25] E. Métral and A. Verdier, "Stability diagram for Landau damping with a beam collimated at an arbitrary number of sigmas," CERN-AB-2004-019-ABP.

[26] K. Y. Ng, "Landau damping of space-charge dominated Fermilab Booster beam," FERMILAB-CONF-08-410-AD.

[27] K. Li *et al.*, "Code development for collective effects," doi:10.18429/JACoW-HB2016-WEAM3X01

[28] E. Métral *et al.*, "Beam Instabilities in Hadron Synchrotrons," IEEE Trans. Nucl. Sci. **63**, no. 2, 1001 (2016). doi:10.1109/TNS.2015.2513752

[29] A. Oeftiger, "An Overview of PyHEADTAIL," CERN-ACC-NOTE-2019-0013

[30] E. H. Maclean *et al.*, "Tune-footprint through the LHC cycle," CERN, 17 Oct 2017, `https://indico.cern.ch/event/672805/`

## APPENDIX

An example of gathered data for the 45 deg phase, obtained during feedback calibration when increasing the gain from 0.006 to 0.010 units (Fig. 12). Turn-by-turn data was gathered for 64000 turns for each event.

# DIAGNOSTICS WITH QUADRUPOLAR PICK-UPS

A. Oeftiger*, GSI Helmholtzzentrum für Schwerionenforschung, Darmstadt, Germany

*Abstract*

The spectrum of a quadrupolar pick-up gives access to coherent second-order modes of a beam in a non-invasive way. The signature of bunched beams not only features the first-order and second-order dipolar modes, but also most notably (1.) bands of even envelope modes, (2.) odd (skew) envelope modes and (3.) coherent dispersion modes. The odd (skew) envelope modes can provide information on linear coupling and mismatch thereof. The tunes of even envelope modes and the coherent dispersion modes shift significantly with space charge and can thus provide a measurement thereof.

The paper presents measurements of the various modes at the CERN Proton Synchrotron, demonstrates how the spectral amplitudes depend on the mismatch conditions, and suggests a new, alternative way to quantify space charge at high brightness conditions via the coherent dispersion mode.

## INTRODUCTION

Quadrupolar pick-ups (QPU) in a beam line provide information about the coherent transverse second-order moments of a passing bunch of particles. These devices have often been used in studies measuring the beam emittance or injection mismatch of the optics functions [1–3], or the strength of space charge in synchrotrons [4–8]. The advantage is the non-invasive and thus non-destructive nature of measuring the quadrupolar moment $S_{QPU}$ via induced currents in the four symmetrically arranged electrodes, in particular for inferring the transverse RMS emittances in comparison to destructive profile measurement methods like flying wire scans or secondary electron emission (SEM) grids. Typically, *time domain* oriented methods to determine the emittance from a measured quadrupolar moment demand well controlled experimental setups, where differential offsets in the quadrupolar moments need to be understood and controlled precisely while the strong dipolar component in the signal needs to be suppressed. These challenges could possibly be the main reason why QPUs are typically not yet used as beam diagnostics in regular operation. A technically less demanding and thus potentially more rewarding approach in a synchrotron is to profit from the *frequency domain* and measure the bunch eigenmodes, where only the frequency content and not the absolute values of $S_{QPU}$ matter.

The quadrupolar spectrum of a circulating beam has a rich structure. Most often the two even transverse envelope modes of the oscillating $\sigma_{x,y}(s)$ are studied, most prominently for measuring the strength of space charge by determining the coherent tune shift of the envelope due to space charge defocusing. Past experiments mainly studied coasting beam conditions [4–7]. A relatively recent study extends this space charge measurement to bunched beams [8]: since the envelope oscillations due to injection mismatch typically decohere very rapidly in bunches, they are much more challenging to measure than in coasting beams. As an alternative, the study establishes the quadrupolar beam transfer function (Q-BTF) technique based on a transverse feedback system, which quadrupolarly excites the bunch in a frequency sweep while measuring the beam response in the QPU. The such measured "bands" of coherent envelope modes (due to varying defocusing by space charge depending on the longitudinal line charge density) reveal the maximum coherent envelope tune shift at the longitudinal peak line charge density.

While a quadrupolar kick exciting the beam sizes would intrinsically lead to RMS emittance growth $\Delta\epsilon/\epsilon_0$, the discussed Q-BTF approach lead to well constrained values $\Delta\epsilon/\epsilon_0 \leq 5\%$ (comparable to the impact of the flying wire scan technique). Nonetheless, this method remains principally destructive. It may be a good moment to reflect on simpler non-destructive measurements of space charge than via the envelopes $\sigma_{x,y}$, since they decohere so rapidly after injection for bunched beams (i.e. usual operation mode in most synchrotrons).

In this contribution, we turn our attention to other second-order beam moments in the QPU frequency spectrum, which may last much longer and would thus be more accessible for precision measurements of space charge detuning. The odd (skew or tilting) envelope modes are identified in measurements for the first time. In the perturbative space charge conditions of synchrotrons, these linear coupling modes do not exhibit significant scaling with space charge though, nonetheless they can provide a measure of linear coupling. Furthermore, we discuss the coherent dispersion mode, which represents the correlation between transverse and longitudinal degrees of freedom.The dispersion mode tune does shift with space charge, which could make it an interesting alternative candidate to the envelope modes in order to measure space charge. Also, the dispersion mode could provide new insights on beam dynamics regarding the topic of head-tail instabilities vs. space charge: head-tail instabilities correlate the transverse planes with the longitudinal plane, i.e. they naturally provide amplitude to the coherent dispersion mode.

The CERN Proton Synchrotron (PS) is equipped with a sensitive strip-line pick-up featuring a diode set-up for precise tune measurements ("Base-Band Q-meter"). Using the quadrupolar combination of its four electrode signals gives access to the quadrupolar spectrum. Based on this set-up, we can identify the various modes in the spectrum by varying the underlying beam dynamics such as dipolar mismatch etc. We structure this paper as follows: first we outline the relevant beam modes in the quadrupolar spectrum, before we turn to the PS measurements – starting from the dominant

* also at CERN, Geneva, Switzerland

dipolar modes, then investigating the odd envelope modes and finally discussing the coherent dispersion mode.

## OVERVIEW QUADRUPOLAR SPECTRUM

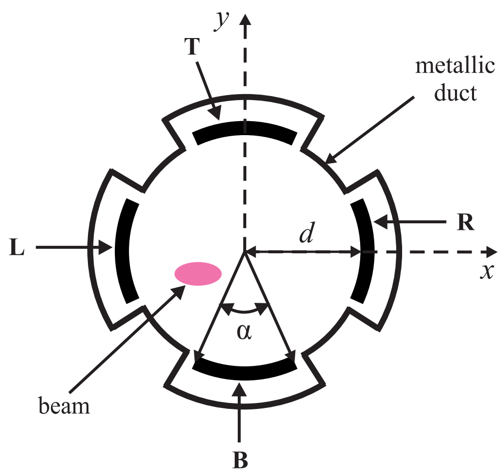


Figure 1: Schematics of four electrodes in quadrupolar pick-up, taken from Ref. [9]

Four electrodes, symmetrically arranged in 90° steps in the transverse plane around the passing beam as indicated in Fig. 1, pick up on the quadrupolar moment of the passing beam by combining their induced voltages as $S_{QPU} = (U_T + U_B) - (U_L + U_R)$ [9]. This quadratic signal

$$S_{QPU} \propto \langle y^2 \rangle - \langle x^2 \rangle \tag{1}$$

contains contributions from all collective second-order modes coupling into the transverse plane, where $x$ denotes the horizontal particle offset and $y$ the vertical offset. $\langle \cdot \rangle$ denotes the expectation value summing over all particles in the beam.

Let us consider betatron motion $x_\beta$ around a constant equilibrium orbit $\overline{x}$ with overlaid dispersive motion $D_x\delta$ for dimensionless momentum offset $\delta \doteq \frac{\Delta p}{p_0}$. $D_x$ denotes the horizontal dispersion for this particle, $D_x = \partial x / \partial \delta$. The horizontal particle coordinate at the QPU location thus amounts to

$$x = \overline{x} + x_\beta + D_x \delta \quad , \tag{2}$$

and likewise for the vertical plane. The collective quadratic signal thus splits up into

$$S_{QPU} \propto \underbrace{\left(\langle y_\beta^2 \rangle - \langle x_\beta^2 \rangle\right)}_{\left(\sigma_y^2 - \sigma_x^2 + \langle y_\beta \rangle^2 - \langle x_\beta \rangle^2\right)} + 2 \cdot \overline{y} \, \langle y_\beta \rangle - 2 \cdot \overline{x} \, \langle x_\beta \rangle \tag{3}$$
$$+ \left\langle y_\beta \, \delta \right\rangle - \left\langle x_\beta \, \delta \right\rangle + \text{longitudinal } \delta \text{ terms} \quad .$$

On top, for skew components in the focusing channel, additional coupling terms appear involving $\sigma_x \sigma_y$ and a skew envelope term $\sigma_{xy}^2$ (first discussed by Chernin [10]).

The spectral content of $S_{QPU}$ comprises all the corresponding eigenmodes for these coherent first- and second-order moments. Given the bare betatron tunes $Q_{x,y}$, we thus conceptually expect to see

- $Q_{x,y}$: dipolar transverse motion from $\overline{x} \cdot \langle x \rangle$, $\overline{y} \cdot \langle y \rangle$,
- $2Q_{x,y}$: dipolar transverse motion from $\langle x_\beta \rangle^2$, $\langle y_\beta \rangle^2$,
- $2Q_{x,y} - \Delta Q_{x,y}^{\mathrm{env,SC}}$: horizontal and vertical even envelope modes from $\sigma_{x,y}^2$,
- $Q_{x,y} - \Delta Q_{x,y}^{\mathrm{disp,SC}}$: horizontal and vertical coherent dispersion mode from $\left\langle x_\beta \, \delta \right\rangle$, $\left\langle y_\beta \, \delta \right\rangle$, and
- $|Q_x - Q_y|, Q_x + Q_y$: odd envelope or Chernin modes from $\sigma_{xy}^2$, $\sigma_x \sigma_y$.

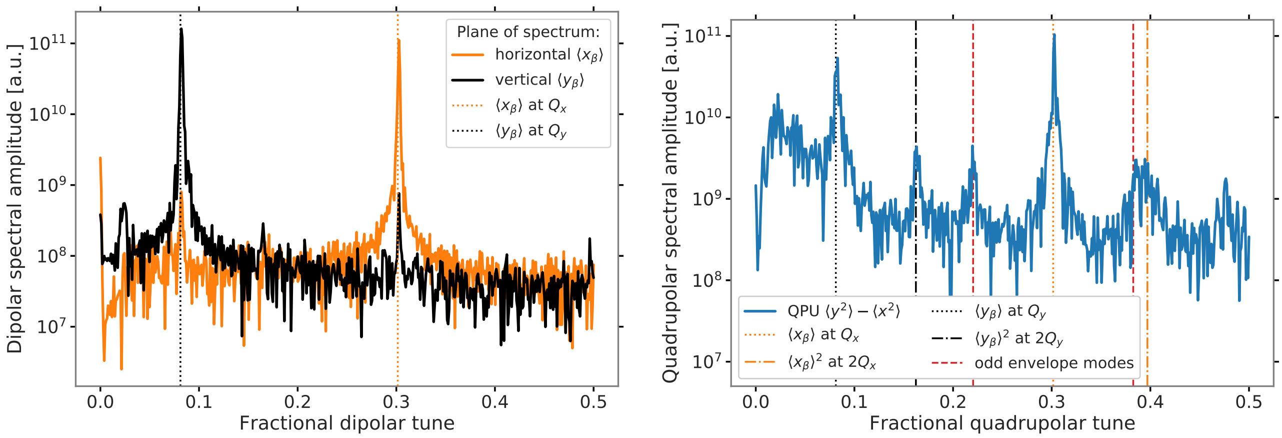


(a) Spectra of dipolar channels: horizontal and vertical dipole moment tunes $Q_x, Q_y$ appear as peaks in the signal of the respective plane.

(b) Spectrum of quadrupolar channel: dipolar tunes appear in first $(Q_x, Q_y)$ and second harmonic $(2Q_x, 2Q_y)$ besides the two odd envelope modes $Q_x - Q_y$ and $Q_x + Q_y$.

Figure 2: Spectra of the dipole and quadrupole moments, recorded for a single shot at injection with amplitudes to scale.

Note that this association of the two even envelope modes with a respective transverse degree of freedom is only valid for vanishing coupling. For full coupling, i.e. isotropic focusing $Q_x = Q_y$, the two modes become simultaneous anti-phase and in-phase oscillations of both planes, often called "anti-symmetric" and "breathing" quadrupole modes.

In general, the second-order modes are affected by coherent tune shifts due to direct space charge defocusing (unlike the first-order modes). This is indicated by $\Delta Q_{x,y}^{\mathrm{env,SC}}$ for the even envelope modes and by $\Delta Q_{x,y}^{\mathrm{disp,SC}}$ for the coherent dispersion mode.

The coherent tune shift of the odd envelope modes does not significantly depend on space charge under typical conditions of synchrotrons, as discussed by Aslaninejad and Hofmann [11], which is why we do not consider a corresponding $\Delta Q^{SC}$ term above. The odd envelope tunes coherently shift mainly due to the emittance ratio, which is rather small for the typically round PS beams.

## EXPERIMENTAL SETUP IN PS

The CERN PS is equipped with two skew quadrupole families. One can hence adjust the strength of linear coupling in the machine. Until this year, the PS has typically been operated with maximised linear coupling to mitigate the appearing horizontal head-tail instability, as the coupling shares Landau damping between the two planes – this effect significantly weakens the otherwise strong horizontal instability [12].

In order to freely scrutinise the modes in the quadrupolar spectrum in the CERN PS, we prepare a short bunch of relatively low intensity ($N = 5 \times 10^{11}$ ppb) and very low space charge ($\Delta Q_{x,y}^{KV} \approx 0.01$ due to blown up transverse emittances) in the upstream PS Booster machine. The low intensity weakens the horizontal head-tail instability and we can thus freely choose the coupling strength without the necessity of using the (new) transverse feedback system for stabilisation during the first part of the cycle. To start with, the skew quadrupoles are adjusted for maximised linear coupling. The two transverse betatron tunes have been adjusted to a larger distance than the usual PS setting (at around $Q_x \approx 6.24$ and $Q_y = 6.21$) to enable us to clearly distinguish between horizontal and vertical first-order $Q_{x,y}$ and second-order $2Q_{x,y}$ dipolar modes.

Figure 2 compares the spectra for the horizontal, vertical and quadrupolar channel of the strip-line pick-up for a single shot. Each spectrum is recorded over 1024 turns, starting right after the injection bump closure in the PS to avoid any related tune shifts thereof [13, Fig. 20]. While the two transverse dipolar spectra mainly only contain the respective betatron tune peaks at $Q_x$ and $Q_y$, the quadrupolar spectrum exhibits several distinct modes. Besides the first-order dipolar modes $Q_{x,y}$ one observes the second-order dipolar modes $2Q_{x,y}$ and the two odd envelope modes at $|Q_x \pm Q_y|$.

The low space charge conditions entail vanishing coherent dispersion mode tune shifts $\Delta Q_{x,y}^{disp,SC} \to 0$. The dispersion mode tunes are thus inseparable from the dominating first-order dipolar mode tunes at $Q_{x,y}$ under the present conditions.

The "longitudinal $\delta$ terms" in Eq. (3) contribute to the very low frequency part of the quadrupolar spectrum. Indeed, Fig. 2b shows significant amplitude in a broad area to the left of the vertical dipolar tune peak, which is absent in the dipolar spectra in Fig. 2a.

In the following we confirm the nature of the beam modes in the quadrupolar spectrum as seen in Fig. 2b. To this end, we discuss the panels of Fig. 3 showing spectograms of the quadrupolar pick-up signal over about 1000 turns starting at injection.

## DIPOLAR MODES

For this first part we aim to carve out only the dipolar modes in the spectrum while suppressing all other modes. To this end, we operate at minimised linear coupling to suppress the odd coupling modes.

Figure 3a illustrates a typical optimised injection into the decoupled PS where dipolar injection mismatch has been minimised. One observes mainly the two transverse first-order dipolar modes at $Q_x$ and $Q_y$ (due to remaining small but finite dipole motion of the beam around the orbit). The first-order horizontal dipolar mode $\langle x_\beta \rangle$ oscillates at fractional horizontal tune $q_x = 0.3$ and the vertical dipolar mode $\langle y_\beta \rangle$ at fractional vertical tune $q_y = 0.06$. The second-order dipolar modes $\langle x_\beta \rangle^2$ and $\langle y_\beta \rangle^2$ at respective fractional tunes $1 - 2q_x = 0.4$ (mirrored at 0.5) and $2q_y = 0.12$ turn out to be very faint for the matched set-up, they almost vanish in the noise background.

By using a horizontal steering dipole magnet in the upstream transfer line for a horizontal dipolar injection mismatch, the beam performs significant dipole oscillations after injection for more than 1000 turns. Correspondingly, we can clearly observe both first-order $q_x = 0.3$ and second-order $1 - 2q_x = 0.4$ signals in Fig. 3b. At a closer look one can observe the PS injection bump closure leading to a shifting tune during the first 400 turns. The bump closure implied tune shift manifests as a downwards bent horizontal tune shift for the dipole mode, which correspondingly appears as an upwards bent shift in the mirrored second-order case. Applying the same mismatch only in the vertical plane yields the dominating first-order $q_y = 0.06$ and second-order $2q_y = 0.12$ signals in Fig. 3c – both bending upwards from the injection bump. In both transverse cases, the dipolar mismatch is also confirmed through large oscillation amplitudes in the usual beam position monitor (BPM) system of the PS.

These dipolar signals are always present in the QPU spectrum with the first-order components $\langle x_\beta \rangle$ and $\langle y_\beta \rangle$ being the most dominant in the spectrum.

## ODD ENVELOPE MODES

We return to the usual set-up of the PS with maximised linear coupling via the skew quadrupoles. Figure 3d shows a quadrupolar spectrogram with four distinct modes visible. They persist at least for several hundreds of turns. The two

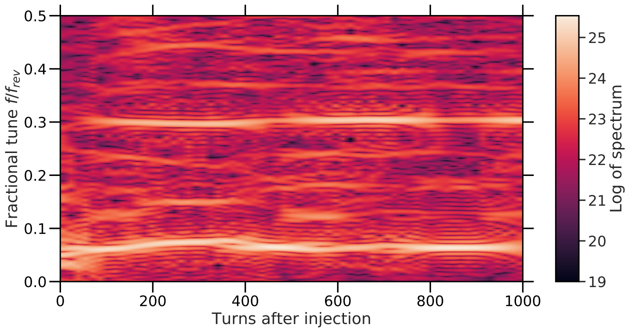


(a) Typical optimised injection with minimal mismatch, mainly the two dipolar fractional tunes $q_x, q_y$ are visible.

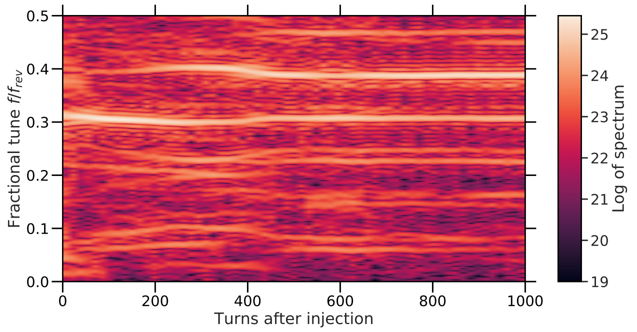


(b) Intentional horizontal dipolar offset, the horizontal dipolar tune appears in first order $q_x$ and mirrored second order $1 - 2q_x$.

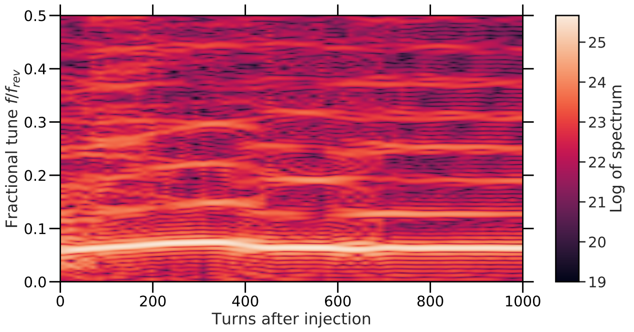


(c) Intentional vertical dipolar offset, the vertical dipolar tune $q_y$ dominates over the horizontal plane.

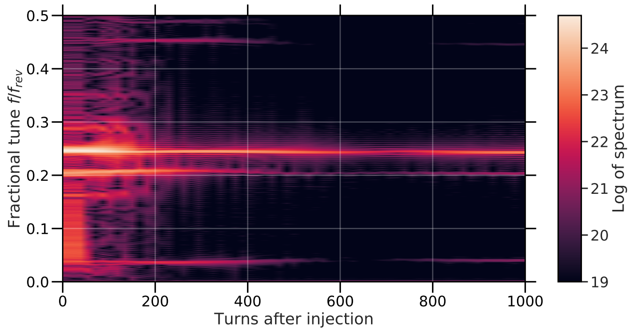


(d) Linear coupling mismatch via maximised skew component, the horizontal and vertical dipolar fractional tunes $q_x, q_y$ appear together with the fainter odd envelope mode tunes at $q_x \pm q_y$.

Figure 3: Quadrupolar spectograms for various injection and lattice settings.

first-order dipolar modes $\langle x_\beta \rangle$ and $\langle y_\beta \rangle$ are again clearly visible at fractional tunes $q_x = 0.24$ and $q_y = 0.20$. Below we find the low-frequency odd envelope mode $\sigma_{xy}^2$ (corresponding to the difference resonance $|Q_x - Q_y|$) which oscillates at $q_x - q_y = 0.04$. On the other side we find the high-frequency odd envelope mode $\sigma_x \sigma_y$ to oscillate at $q_x + q_y = 0.44$, as expected for the sum resonance term. Since the transverse emittances are approximately equal, the coherent tune shift of the odd envelope modes vanishes [11].

Although the odd envelope mode tunes do not shift with space charge and can thus not provide a measurement thereof, they can still serve a useful purpose as they give access to measuring linear coupling: any injection mismatch with respect to linear coupling leads to amplitude in these modes. At the same time, the beams arrive mainly without transverse correlation from the upstream transfer line. Their oscillating tune can then readily be identified in the spectrum of a QPU along with the corresponding amplitude.

By adjusting the skew quadrupole families one can thus minimise the linear coupling experienced by the beam in a beam-based approach by simply minimising the amplitude of the two odd envelope modes. This suggested new approach turns out to be rather flexible and is not restricted to equal tunes – as opposed to the often employed "closest tune approach" [14], where one measures the tune distance $|C^-|$ between the two dipolar modes when setting equal tunes.

On the other hand, one can precisely measure coherent frequency shifts in the case of unequal transverse emittances since the odd modes persist for a sufficiently long time. For a horizontally 1.5 times larger emittance, the chart in Aslaninejad and Hofmann [11, Fig. 4] predicts a coherent tune shift on the order of $0.1\Delta Q_x^{KV}$. For a typical strong space charge beam at PS injection the incoherent KV tune shift amounts to $\Delta Q_x^{KV} \approx 0.1$. Thus the coherent tunes of the odd modes shift by $\Delta Q^{odd} \approx 0.01$, which should be well identifiable in future experiments and thus providate a means to measure the transverse emittance ratio.

## COHERENT DISPERSION MODE

The impact of space charge on dispersion has first been discussed in the context of extended RMS envelope equations by Venturini and Reiser [15] and Lee and Okamoto [16]. To the author's knowledge, the first experimental evidence of the corresponding dispersion mode comes from the Q-BTF measurements at the CERN PS in Ref. [8]: the comparison between measurement and simulation identifies the peak shifted below $Q_x = 6.18$ as the coherent dispersion mode, as has been presented in Fig. 4 [8, Fig. 3].

The RF excitation with a quadrupolar kick in frequency sweep exhibits a dipolar feed-down component, coming from any finite residual offset of the beam centroid when passing through the kicker module (which has been minimised due to

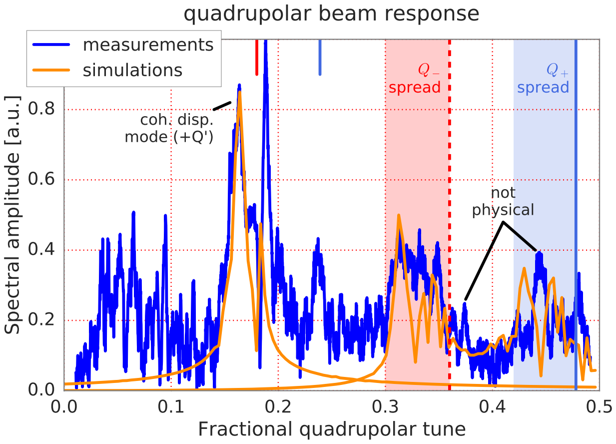


Figure 4: Comparison between measured beam frequency response and simulated eigenmodes, taken from [8, Fig. 3].

careful orbit adjustment to the centre of the kicker before the experiment). In the presence of finite chromaticity, dipolar excitation of the beam at the eigenfrequency of a head-tail mode of radial order $k$, i.e. at the $k$th synchrotron sideband of the dipolar tune $Q_{x,y} \pm k \cdot Q_s$, builds up amplitude in this head-tail mode. This approach has been successfully applied e.g. in Singh [17, Fig. 5.16], where dipolar RF excitation in frequency sweep mode individually excites the lowest order head-tail modes.

Non-rigid head-tail modes (for $k \neq 0$) correlate the longitudinal phase space with the transverse plane. In particular, the transverse amplitude exhibits nodes and maximum displacement depending on the longitudinal location $z$ or, equivalently, the longitudinal momentum offset $\delta$. This means nothing else than providing energy to the coherent dispersion mode $\langle x_\beta\, \delta \rangle$.

The dipolar feed-down of the quadrupolar excitation is thus the reason why (1.) the excited dipolar tunes become visible in the dipolar beam response which had been recorded along with the quadrupolar one [8, Fig. 1] and (2.) why also the dispersion modes become excited along with the even envelope bands.

As the PS injection plateau intrinsically exhibits the horizontal head-tail instability (for sufficient beam intensity) at natural chromaticity, the coherent horizontal dispersion mode can persist for a long time. This feature makes it a candidate for precise tune measurement. The space charge conditions for the above Q-BTF experiment were relatively low at $\Delta Q^{KV}_{x,y} \approx 0.02$ [8, Table 1] (about a factor 5 below the then operational LHC beams). While the even envelope mode bands displayed maximum tune shifts of around 0.06, the dispersion mode peak shifted only by about 0.01. In this weak space charge regime and at vanishing chromaticity (suppressing its corresponding widening effects on the even envelope mode band as described in Ref. [8]), the maximum tune shift of the even envelope mode can thus provide a good measurement of direct space charge in units of $\Delta Q^{KV}_{x,y}$.

When space charge becomes stronger (as for the LHC beams), the even envelope modes become shifted to much lower tunes: now the envelope band can easily overlap with the first-order dipolar mode peaks, which can complicate peak identification in the rather crowded fractional tune space. Under these circumstances it can become beneficial to measure space charge via its induced tune shift of the coherent dispersion mode: firstly, $\Delta Q^{disp,SC}$ shifts considerably less than the maximum even envelope mode tune $\Delta Q^{env,SC}$. Secondly, one measures a rather narrow peak as opposed to the broad band of even envelope modes implied by the longitudinally changing space charge conditions, which extend from weak shifts at the head and tail of the bunch to the maximum space charge tune shift at the peak line charge density. In the case of the Q-BTF measurement, the dispersion mode also featured a much better signal-to-noise ratio. These observations make the dispersion mode potentially much easier to identify compared to the even envelope modes, providing thus a viable alternative approach to measure direct space charge via the implied coherent tune shift $\Delta Q^{disp,SC}$.

## CONCLUSION

The spectrum of the quadrupolar signal $S_{QPU} \propto \langle y^2 \rangle - \langle x^2 \rangle$, measured non-destructively in a four electrode pick-up, provides rich information on beam dynamics. Diagnostics can be extended to coherent second-order modes involving the transverse degrees of freedom $x, y$ – beyond present tune measurement systems with BPMs measuring only the coherent first-order transverse modes at $Q_x, Q_y$. Literature on QPUs usually focusses on measurements based on the even envelope modes, also often simply called "quadrupole" modes.

The present work however scrutinises the other second-order modes typically found in the quadrupolar spectrum of a bunch, in particular due to mismatch after injection. Besides the first- and second-order dipolar modes, one encounters the odd envelope (or coherent skew) modes giving access to linear coupling and mismatch thereof. Further we have discussed the coherent dispersion modes, which measure correlation between transverse amplitude and longitudinal momentum. Energy in the coherent dispersion mode can be provided through excitation of a head-tail mode, e.g. by dipolar RF excitation at the corresponding synchrotron sideband of the coherent dipolar tune, or by a growing head-tail instability. The coherent dispersion mode can last much longer after injection than the even envelope mode (in particular for bunched beams). As the coherent dispersion mode also shifts with direct space charge, it makes for an alternative candidate to measure space charge besides the typical approach to quantify the even envelope mode shift due to space charge. This suggested new approach can be particularly beneficial under strong space charge conditions.

## ACKNOWLEDGEMENTS

The author has the great pleasure to thank his CERN colleagues – in particular Simon Albright, Vincenzo Forte, Gerd Kotzian, Tom Levens and Haroon Rafique for support in the extensive measurement campaigns.

## REFERENCES


[1] R. H. Miller, J. E. Clendenin, M. B. James and J. C. Sheppard, 'Nonintercepting emittance monitor', Stanford Linear Accelerator Center, Tech. Rep., 1983.

[2] A. Jansson, 'Noninvasive single-bunch matching and emittance monitor', *Physical Review Special Topics-Accelerators and Beams*, vol. 5, no. 7, p. 072 803, 2002.

[3] C.-Y. Tan, 'Using the quadrupole moment frequency response of bunched beam to measure its transverse emittance', Fermi National Accelerator Laboratory (FNAL), Batavia, IL, Tech. Rep., 2007.

[4] M. Chanel, 'Study of beam envelope oscillations by measuring the beam transfer function with quadrupolar pick-up and kicker', in *European Particle Accelerator Conference (EPAC 1996)*, 1996, pp. 1015–1017. http://cds.cern.ch/record/315081

[5] T. Uesugi *et al.*, 'Observation Of Quadrupole Mode Frequency And Its Connection With Beam Loss', no. KEK-99-98, 1999. http://cds.cern.ch/record/472700

[6] R. C. Bär, 'Untersuchung der quadrupolaren BTF-Methode zur Diagnose intensiver Ionenstrahlen', Universität Frankfurt, Germany, 2000.

[7] R. Singh *et al.*, 'Observations of the quadrupolar oscillations at GSI SIS-18', in *International Beam Instrumentation Conference*, 2014.

[8] A. Oeftiger, 'Requirements and Results for Quadrupole Mode Measurements', in *Proc. 61st ICFA Advanced Beam Dynamics Workshop (HB'18), Daejeon, Korea, 17-22 June 2018*, (Daejeon, Korea), ser. ICFA Advanced Beam Dynamics Workshop, https://doi.org/10.18429/JACoW-HB2018-THA1WE02, Geneva, Switzerland: JACoW Publishing, Jul. 2018, pp. 393–398, ISBN: 978-3-95450-202-8. DOI: doi:10.18429/JACoW-HB2018-THA1WE02. http://jacow.org/hb2018/papers/tha1we02.pdf

[9] J. A. Tsemo Kamga, W. F. O. Müller and T. Weiland, 'Analytical and numerical calculation of the second-order moment of the beam using a capacitive pickup', *Phys. Rev. Accel. Beams*, vol. 19, no. 4, p. 042 801, 2016. DOI: 10.1103/PhysRevAccelBeams.19.042801.

[10] D. Chernin, 'Evolution of RMS beam envelopes in transport systems with linear X-Y coupling', *Part. Accel.*, vol. 24, pp. 29–44, 1988. http://cds.cern.ch/record/1053510

[11] M. Aslaninejad and I. Hofmann, 'Effect of space charge on linear coupling and gradient errors in high-intensity rings', *Phys. Rev. ST Accel. Beams*, vol. 6, p. 124 202, 2003. DOI: 10.1103/PhysRevSTAB.6.124202.

[12] E. Métral, 'Theory of coupled Landau damping', *Part. Accel.*, vol. 62, no. CERN-PS-99-011-CA, 259. 14 p, Feb. 1999. http://cds.cern.ch/record/380927

[13] P. Zisopoulos, Y. Papaphilippou and J. Laskar, 'Refined betatron tune measurements by mixing beam position data', *Phys. Rev. Accel. Beams*, vol. 22, p. 071 002, 7 Jul. 2019. DOI: 10.1103/PhysRevAccelBeams.22.071002. https://link.aps.org/doi/10.1103/PhysRevAccelBeams.22.071002

[14] P. P. Bagley and D. L. Rubin, 'Correction of transverse coupling in a storage ring', in *Particle Accelerator Conference, 1989. Accelerator Science and Technology., Proceedings of the 1989 IEEE*, Mar. 1989, 874–876 vol.2. DOI: 10.1109/PAC.1989.73286.

[15] M. Venturini and M. Reiser, 'Rms envelope equations in the presence of space charge and dispersion', *Phys. Rev. Lett.*, vol. 81, pp. 96–99, 1 Jul. 1998. DOI: 10.1103/PhysRevLett.81.96. https://link.aps.org/doi/10.1103/PhysRevLett.81.96

[16] S. Y. Lee and H. Okamoto, 'Space-charge dominated beams in synchrotrons', *Phys. Rev. Lett.*, vol. 80, pp. 5133–5136, 23 Jun. 1998. DOI: 10.1103/PhysRevLett.80.5133. https://link.aps.org/doi/10.1103/PhysRevLett.80.5133

[17] R. Singh, 'Tune measurement at GSI SIS-18: Methods and applications', PhD thesis, Technische Universität Darmstadt, 2014.

# DIAGNOSTICS OF LONGITUDINAL BUNCH INSTABILITIES AT KARA

B. Kehrer *, M. Brosi, E. Bründermann, S. Funkner, M.J. Nasse, G. Niehues
M.M. Patil, J.L. Steinmann †, A.-S. Müller, Karlsruhe Institute of Technology, Karlsruhe

*Abstract*

KARA, the Karlsruhe Research Accelerator, can be operated in different modes, including a short-bunch mode. During this mode, where the dispersion is stretched in order to reduce the momentum-compaction factor, the micro-bunching instability can occur. At KARA, several measurement setups and techniques are used to investigate this instability further with the long-term perspective to suppress and control it. In this contribution, we give an overview about the different setups and the results achieved during the past years.

## MOTIVATION

For wavelengths below the size of the emitting structure, electron bunches emit coherent synchrotron radiation (CSR), which is – if the bunches are sufficiently compressed longitudinally – not damped by the vacuum beam pipe and is thus transmitted. In bent sections of a circular accelerator the bunch interacts with its previously emitted CSR which leads to a deformation of the bunch. While this deformation is stationary for low bunch currents, it becomes dynamic for higher currents. This self-interaction can lead to a quick rise in amplitude of the resulting sub-structures which increases the intensity of the emitted CSR further. In addition, the charge distribution in the phase space is blown-up until radiation damping starts to shrink it again with the sub-structures smeared out due to diffusion. This interplay of the instability-driven blow-up and radiation damping leads to a bursting behaviour of the bunch. It shows as periodical outbursts of CSR and a sawtooth modulation of the energy spread and the bunch length.

## DIAGNOSTICS

To study the dynamics of the charge distribution in the longitudinal phase space, its two projections – the energy and the temporal profile – can be measured. The relevant time-scales are given by the bunch spacing (at KARA 2 ns), the revolution time (at KARA 368 ns) and the timescale of the bursting behaviour, which is in the order of some milliseconds. Together with the goal to record for sufficiently long time scales, this sets stringent requirements to the detector systems. At KARA, we use Schottky barrier diode detectors to sample the CSR intensity, electro-optical spectral decoding (EOSD) to measure the longitudinal bunch profile and a fast-gated intensified camera and a KALYPSO system, respectively, to measure the horizontal bunch size as a measure for the energy spread.

* benjamin.kehrer@kit.edu
† now at Argonne National Laboratory, Lemont, IL, USA

### *Coherent Synchrotron Radiation*

To sample the CSR intensity, we use Schottky barrier diode detectors with response times below 200 ps, which is sufficient for single-bunch resolution. They are commercially available and offered in various frequency ranges. To digitize the signals, either an oscilloscope in the segmented mode or the KAPTURE system is used. KAPTURE is a picosecond sampling system for individual short pulses with a high repetition rate (500 MHz) [1, 2]. It has been developed at KIT and offers up to eight channels with an analog bandwidth of 18 GHz and 12 bit ADCs.

### *Longitudinal bunch profile*

For measurements of the longitudinal bunch profile we use the technique of electro-optical spectral decoding. KARA is the worlds first storage ring where this principle is used in the near-field range [3, 4]. To do so, a gallium-phosphide (GaP) crystal is inserted into the vacuum beam pipe and brought close to the electron beam. The electric field of the passing bunch turns the crystal birefringent and the longitudinal bunch profile is imprinted into the crystal. Sending a long chirped laser pulse ($\lambda = 1050$ nm) through the crystal allows to probe the birefringence and thus the laser spectrum is modulated according to the longitudinal bunch profile.

To record and digitize the laser spectra we use the KALYPSO system [5, 6]. It is an ultra-fast line array with up to 1024 micro-strips and a maximum frame rate of 10 Mfps, which allows turn-by-turn studies at KARA as the storage ring has a revolution frequency of 2.7 MHz.

### *Energy spread*

Although being an important parameter to study the micro-bunching instability, the energy spread cannot be measured directly. Therefore, the horizontal bunch size $\sigma_x$ is studied as it is coupled to the energy spread $\sigma_\delta$:

$$\sigma_x = \sqrt{\beta_x \epsilon_x + (D_x \sigma_\delta)^2}. \tag{1}$$

In addition, it depends on the horizontal beta function $\beta_x$, the horizontal dispersion $D_x$ and the horizontal emittance $\epsilon_x$. To measure the horizontal bunch size, we use incoherent synchrotron radiation in the visible range. At KARA, we have a dedicated beam port for visible light diagnostics [7], which uses bending radiation from a dipole magnet. For time-resolved measurements of the horizontal bunch size we use a fast-gated intensified camera (FGC) [8] and a KALYPSO system [9]. The data analysis is the same for both devices and takes the particularities of the optical setup and the imaging process into account: During the acquisition, the bunch is moving horizontally and the imaging system contains two off-axis paraboloid mirrors. This leads to a distortion of the image which is expressed numerically by the filament beam-spread function (FBSF) [10]. We determined the FBSFs from simulations of the optical setup and the imaging process using OpTaliX [11].

As the final image is the convolution of the FBSF with the horizontal bunch profile, the FBSF has to be deconvolved to retrieve the horizontal bunch size. Since a numerical deconvolution is slow and numerically unstable, we use a numerical convolution of the FBSF with a Gaussian curve as a fit function [12, 13].

The FGC has intrinsic limits as the number of data points per image is limited and there are mechanical as well as electrical delays. To overcome these limits, a KALYPSO system is used here as well. Therefore it is equipped with a Silicon sensor and thus turn-by-turn images are possible with the potential for continuous streaming [9].

## SYNCHRONIZATION

In order to reconstruct the dynamics in the longitudinal phase space, the different measurement setups have to be synchronized on a single-turn basis. We use our timing system to provide a common trigger to all devices. By adjusting the trigger delays at the different setups, the setup-intrinsic delays are compensated and thus a simultaneous start of the recording is achieved [14], see Fig. 1 for a schematic principle. The measurement trigger is an *arm trigger*, which does not start the measurement directly. This is done by the next incoming pulse from the revolution clock, which is indicated by the small vertical arrow in Fig. 1.

## MEASUREMENTS

The fully synchronized detector systems allow simultaneous measurements of the different bunch parameters. In the following, two examples for these measurements are discussed. Both were taken during the occurrence of the micro-bunching instability.

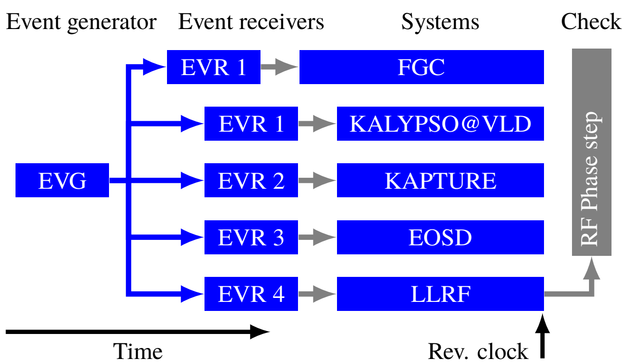


Figure 1: Schematic principle of the synchronization scheme at KARA. The timing system – which consists of one event generator (EVG) and several event receivers (EVR) – provides a common measurement trigger that arms the setups to start recording data with the next incoming trigger pulse from the revolution clock.

### *Longitudinal bunch profile at onset of burst*

In this first example we measured the longitudinal as well as the horizontal bunch profile with two KALYPSO systems and in parallel the CSR intensity with a narrow-band Schottky diode (220 GHz to 330 GHz) read-out by an oscilloscope. Figure 2 shows the corresponding signals for 120.000 turns (approx. 44 ms).

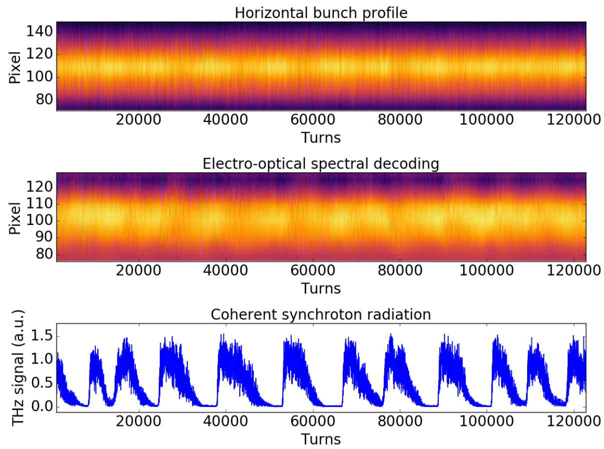


Figure 2: Top: Color-coded horizontal bunch profiles recorded using a KALYPSO system for 120.000 consecutive turns; Center: Corresponding longitudinal bunch profile from EOSD measurement using KALYPSO; Bottom: CSR intensity sampled by a narrowband Schottky diode.
Data previously published in [15, Fig. 1].

On the CSR intensity the sawtooth pattern is clearly visible which indicates the bursting behaviour of the bunch.

In Fig. 3, the longitudinal profile as well as the CSR intensity are plotted for a shorter time range which covers the onset of a CSR burst. On the longitudinal profile the occurrence of sub-structuress can be seen at the same time

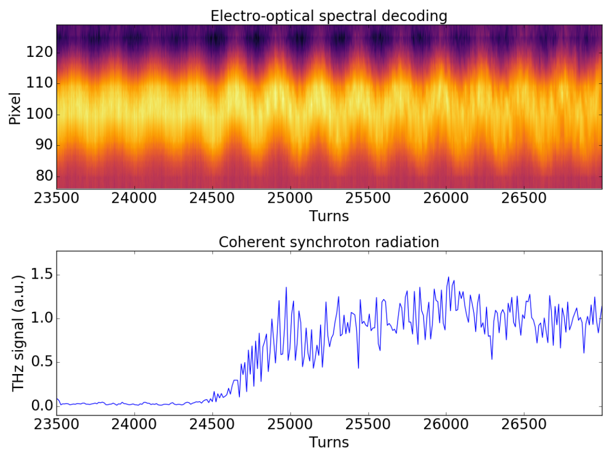


Figure 3: Detailed zoom-in into Fig. 2 around the onset of the CSR burst.
Data previously published in [15, Fig. 2].

when the CSR intensity rises, which supports the process discussed in the introduction [15].

### *Energy spread and CSR*

To study the energy spread during the micro-bunching instability, the horizontal bunch size is determined from KALYPSO measurements at the VLD port. In Fig. 4, such a measurement covering approx. 36 ms is plotted together with the corresponding CSR intensity.

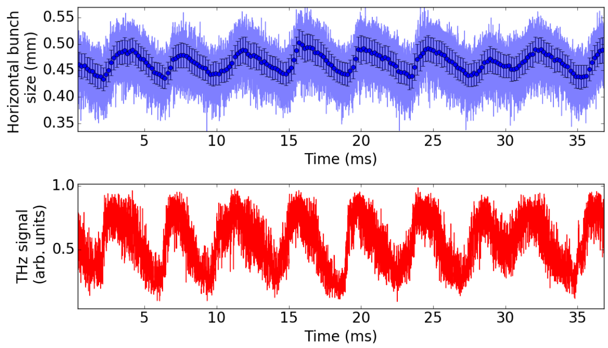


Figure 4: Top: Horizontal bunch size recorded with KALYPSO with a profile histogram applied to the data. Bottom: Corresponding CSR signal recorded by a broadband Schottky diode.
Previously published in [9, Fig. 5]

The horizontal bunch size – which is a measure for the energy spread – shows a sawtooth modulation with the same modulation period length as the bursting behaviour of the CSR in the bottom panel. At the beginning of a burst, the horizontal bunch size and thus the energy spread has a minimum and increases quickly afterwards.

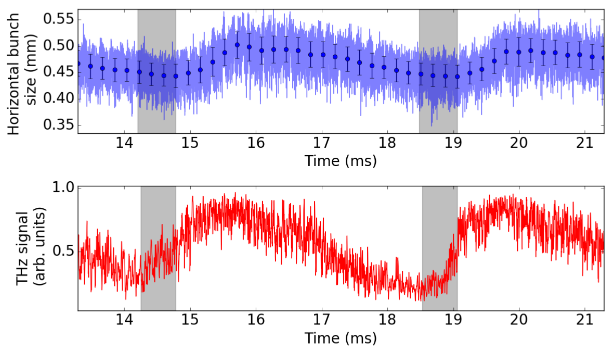


Figure 5: Detailed zoom-in into the data from Fig. 4. Top: Horizontal bunch size recorded with KALYPSO with a profile histogram applied to the data. Bottom: Corresponding CSR signal recorded by a broadband Schottky diode. The grey bars depict the time ranges, where the horizontal bunch size is still decreasing, while the CSR intensity already starts to increase.
Previously published in [9, Fig. 6]

As KALYPSO allows turn-by-turn studies, the onset of the CSR bursts can be studied in more detail. Figure 5 shows a zoom-in into the data set from Fig. 4.

The grey bars indicate the phase offset between the increase of the horizontal bunch size and the onset of the CSR burst. This offset indicates that at the beginning of a CSR burst, the sub-structures – which lead to the emission of the CSR – do not lead to an overall increase of the energy spread and thus the energy spread is still shrinking caused by synchrotron radiation damping. Here it takes for approx. 5 ms – in this case this corresponds to 4 synchrotron periods – before also the energy spread starts to increase due to the instability driven blow-up [16].

## SUMMARY AND OUTLOOK

Time-resolved measurements of the different bunch parameters allow to investigate the micro-bunching instability in more detail. At KARA, several measurement setups are used for time-resolved studies with a single turn resolution. All detector systems are synchronized on a single-turn basis. These synchronous measurements are a first step towards the reconstruction of the longitudinal phase space. In addition, this can also be used as input for a potential feedback to control the micro-bunching instability.

## REFERENCES


[1] M. Caselle *et al.*, "KAPTURE-2. A picosecond sampling system for individual THz pulses with high repetition rate", JINST 12 C01040, 2017. doi:10.1088/1748-0221/12/01/C01040

[2] M. Caselle *et al.*, "A Picosecond Sampling Electronic "KAPTURE" for Terahertz Synchrotron Radiation", in *Proc. IBIC'14*, Monterey, CA, USA, 2014, paper MOCZB1, pp. 24–28.

[3] N. Hiller *et al.*, "Single-Shot Electro-Optical Diagnostics at the ANKA Storage Ring", in *Proc. IBIC'14*, Monterey, CA, USA, 2014, paper MOPD17, pp. 182–186.

[4] S. Funkner *et al.*, "High throughput data streaming of individual longitudinal electron bunch profiles", Phys. Rev. Accel. Beams 22, 022801. doi:10.1103/PhysRevAccelBeams.22.022801

[5] M. Caselle *et al.*,"Single-Shot Longitudinal Beam Profile and Terahertz Diagnostics at MHz - Towards GHz-Rates with High-Throughput Electronics",in *Proc. IBIC'17*, Grand Rapids, MI, USA, Aug. 2017, pp. 136–140. doi:10.18429/JACoW-IBIC2017-TU2AB3

[6] L. Rota, "KALYPSO, a novel detector system for high-repetition rate and real-time beam diagnostics", Ph.D. thesis, Karlsruhe Institute of Technology, Karlsruhe, Germany, 2017. doi:10.5445/IR/1000082349

[7] B. Kehrer *et al.*, "Visible light diagnostics at the ANKA storage ring", in *Proc. IPAC'15*, Richmond, VA, USA, May 2015, paper MOPHA037, pp. 866–868. doi:10.18429/JACoW-IPAC2015-MOPHA037

[8] P. Schütze *et al.*, "A Fast Gated Intensified Camera Setup for Transversal Beam Diagnostics at the ANKA Storage Ring", in *Proc. IPAC'15*, Richmond, VA, USA,

2015, paper MOPHA039, pp. 872–875. doi:10.18429/JACoW-IPAC2015-MOPHA039

[9] B. Kehrer *et al.*, "Turn-by-Turn Horizontal Bunch Size and Energy Spread Studies at KARA", in *Proc. IPAC'19*, Melbourne, Australia, 2019, paper WEPGW016, pp. 2498–2500. doi:10.18429/JACoW-IPAC2019-WEPGW016

[10] Å. Andersson, O. V. Chubar, M. Rohrer, V. Schlott, and A. Streun, "Electron Beam Profile Measurements with Visible and X-ray Synchrotron Radiation at the Swiss Light Source", in *Proc. EPAC'06*, Edinburgh, UK, 2006, paper TUPCH090, pp. 1223–1225.

[11] Optenso, http://www.http://optenso.com/.

[12] J.L. Steinmann *et al.*, "Turn-by-Turn Measurements for Systematic Investigations of the Micro-Bunching Instability", in *Proc. FLS'18*, Shanghai, China, 2018, paper TUP2WD03, pp. 46–51. doi:10.18429/JACoW-FLS2018-TUP2WD03

[13] B. Kehrer, "Time-resolved studies of the micro-bunching instability at KARA", Ph.D. thesis, Karlsruhe Institute of Technology, Karlsruhe, Germany, 2019. doi:10.5445/IR/1000098584

[14] B. Kehrer *et al.*, "Simultaneous Detection of Longitudinal and Transverse Bunch Signals at ANKA", in *Proc. IPAC'16*, Busan, Korea, 2016, paper MOPMB014, pp. 109–111. doi:10.18429/JACoW-IPAC2016-MOPMB014

[15] M. Brosi *et al.*, "Synchronous Measurements of Electron Bunches Under the Influence of the Microbunching Instability", in *Proc. IPAC'19*, Melbourne, Australia, 2019, paper WEPTS015, pp. 3119–3122. doi:10.18429/JACoW-IPAC2019-WEPTS015

[16] B. Kehrer *et al.*, Phys. Rev. Acc. Beams, 21, 102803 (2018). doi:10.1103/PhysRevAccelBeams.21.102803

# IMPEDANCE LOCALIZATION AND IDENTIFICATION

N. Biancacci[1*], R. Alemany Fernandez[1], Y. Alexahin[2], M. Carlà[1], J. Eldred[2], W. Höfle[1], A. Huschauer[1], T. Levens[1], L. Malina[1], E. Métral[1], M. Migliorati[1], B. Popovic[1], B. Salvant[1], F. Schmidt[1], R. Tomàs[1], D. Ventura, C. Vollinger[1], N. Wang[3], C. Zannini[1],
[1]CERN, 1211 Geneva 23, Switzerland,
[2]FNAL, Batavia, IL 60510, USA,
[3]IHEP, CAS, Beijing, 100039, China.

*Abstract*

The beam coupling impedance represents one of the sources of potential beam instabilities in particle accelerators. The localization of large coupling impedance sources is therefore very important in order to focus the efforts for mitigation measures when these are needed. In this work we will focus on the common methods adopted to quantify the transverse impedance of a particle accelerator both from the global and the local point of views. This activity can be performed in both bunched and coasting beams following different strategies.

## INTRODUCTION

The beam coupling impedance represents one of the sources of potential beam instabilities in particle accelerators [1, 2]. The localization of large coupling impedance sources is therefore very important in order to focus the efforts for mitigation measures when these are needed. In this work we will describe common measurements performed in particle accelerators to quantify the transverse impedance from global and local point of views. This type of measurements can be done in both bunched and coasting beams following different strategies and methods.

For bunched beams, known techniques as the tune shift versus intensity and phase advance shift versus intensity will be reviewed. The method application to the CERN (Centre Européen pour la Recherche Nucléaire) PS (Proton Synchrotron) and the FNAL (Fermi National Accelerator Laboratory) Booster rings will be presented and advanced techniques based on the AC (Alternating Current) dipole excitation will be reviewed.

For coasting beams, it is not possible to record turn by turn data with standard BPMs (Beam Position Monitors) due to the absence of beam structure. Sources of large transverse impedance can be identified by inspection of the unstable beam spectrum. In this respect, the example of the successful identification and mitigation of the most harmful vertical impedance source of the CERN LEIR (Low Energy Ion Ring) is presented.

* nicolo.biancacci@cern.ch

## IMPEDANCE LOCALIZATION WITH BUNCHED BEAMS

### *Tune shift with intensity*

The systematic connection between transverse beam coupling impedance and main accelerator observables such as tune, phase advance between BPMs and orbit position was done starting from [3, 4].

The measurement of tune shift with intensity is a well known technique to quantify the total imaginary part of the transverse impedance of a machine.

In the following, a beam of average current $\bar{I} = qN_p/T_0$ is considered, where $q$ is the elementary charge, $N_p$ the number of particles in the beam, $T_0$ the revolution period of the machine. Given a localized impedance source at the location $s_k$ along the accelerator circumference (e.g. kickers, cavities, etc.), the induced tune shift $\Delta Q_{y_k}$ (i.e. in the vertical plane for example) will be given by

$$\Delta Q_{y_k} = -\frac{q\bar{I}T_0}{8\pi^{3/2}\beta E\sigma_\tau}\beta_{y_k}(s_k)\mathrm{Im}\left(Z_k^{eff}\right)L_k, \qquad (1)$$

and, for distributed impedance along the accelerator circumference (e.g. resistive wall, indirect space charge, etc.), by

$$\Delta Q_y = -\frac{q\bar{I}T_0}{8\pi^{3/2}\beta E\sigma_\tau}\oint_C \beta_y(s)\mathrm{Im}\left(Z^{eff}\right)\mathrm{d}s, \qquad (2)$$

where we assumed a beam with longitudinal Gaussian distribution of rms-length $\sigma_\tau$, $E$ the total energy of the beam, $\beta = v/c$ where $v$ is the beam velocity and $c$ the speed of light, $\beta_y(s)$ the beta function along the ring, $L_k$ the device length, and $Z^{eff}$ the effective beam coupling impedance per unit meter. This last parameter is defined as

$$Z^{eff} = \frac{\int_{-\infty}^{+\infty} Z(\omega)\|S(\omega)\|^2\,\mathrm{d}\omega}{\int_{-\infty}^{+\infty}\|S(\omega)\|^2\,\mathrm{d}\omega}, \qquad (3)$$

where $\|S(\omega)\|^2$ is the beam longitudinal power spectrum over the angular frequency $\omega$. For a Gaussian beam distribution this is given by

$$\|S(\omega)\|^2 = e^{-\omega^2\sigma_\tau^2}. \qquad (4)$$

From Eqs. (1) and (2) we can see how the tune linearly shifts with intensity. The tune shift constitutes the first global parameter used to estimate the total transverse reactive impedance of an accelerator and it often represents the first benchmark measurement for an accelerator transverse impedance model [5].

We present, as an example, the case of the CERN PS, in which the tune shift versus intensity has been measured at different energies in order to disentangle the energy dependent component of the impedance, i.e. the one related to the indirect space charge.

Figure 1 shows the dependence of the imaginary part of the vertical effective impedance versus kinetic energy in the PS. The agreement between the model and the measurements performed in 2015 at zero chromaticity is very good, suggesting a remaining impedance of about 2.5 $M\Omega/m$, not dependent on the energy. The measurement also validates the indirect space charge computed in the impedance model [6].

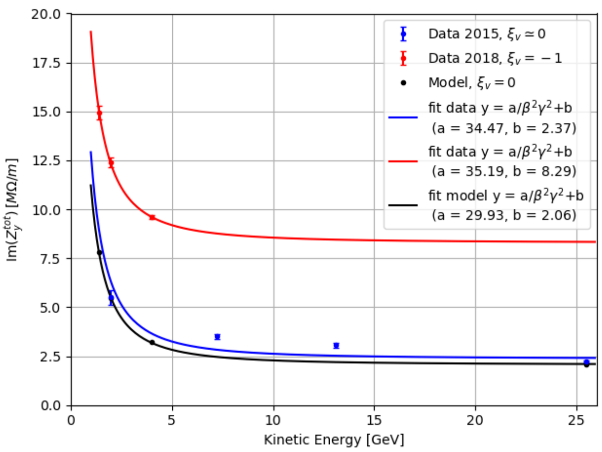


Figure 1: Effective imaginary part of the impedance dependence versus kinetic energy in the PS. Blue and red dots represent measurement data taken in 2015 and 2018 respectively at chromaticity $\xi_v = 0$ and $\xi_v = -1$, black dots are computation based on the impedance model (for zero chromaticity) [6], lines are fit following the energy scaling of the transverse indirect space charge impedance.

The comparison with respect to the 2018 measurements performed at $\xi_v = -1$, is instead in agreement only with the indirect space charge trend versus energy, but presents an offset with respect to the model prediction at zero chromaticity. This behaviour, unexpected from the impedance model, and further confirmed with systematic tune shift measurements as a function of chromaticity [6], has been investigated in 2018 by means of impedance localization measurements.

## *Phase advance shift with intensity*

In order to identify the location of the highest transverse impedance sources in a machine, an extension of the previously described method was proposed for the first time in 1995: measuring the impedance-induced betatron phase advance shift with intensity, the radio-frequency (RF) sections were found to be important impedance contributors in the CERN LEP collider [7].

A linear tune shift with intensity, can be due to the presence in the lattice of lumped or distributed intensity dependent defocusing errors [8]. For each source of impedance, the phase advance shift with intensity $\Delta\mu(s, s_k)$ in the plane of reference can be computed as

$$\Delta\mu(s, s_k) = \Delta Q_k + \frac{\Delta Q_k}{\mathcal{S}(2\pi Q_0)} C(2\psi_k - \psi)\mathcal{S}(\psi - 2\pi Q_0) \quad (5)$$

for $s \geq s_k$, and

$$\Delta\mu(s, s_k) = \frac{\Delta Q_k}{\mathcal{S}(2\pi Q_0)} \mathcal{S}(\psi) C(\psi - 2\psi_k + 2\pi Q_0) \quad (6)$$

for $s < s_k$, where $\psi$ and $\psi_k$ are the phase advance respectively at the location $s$ and the impedance location $s_k$, $Q_0$ is the bare machine tune (in the plane of reference), $\Delta Q_k$ the tune shift computed with Eq. (1) for the $k^{\text{th}}$ impedance source. We introduced the short notation $C(\psi) = \cos(\psi)$ and $\mathcal{S}(\psi) = \sin(\psi)$.

A quadrupole error, therefore, produces a phase beating wave whose amplitude is given by the corresponding tune shift, and presents a step equal to the tune shift at the impedance location. The step will be positive for focusing errors, or negative for defocusing ones. In most of the cases an impedance behaves as a defocusing quadrupole error giving rise to a descending step into the beating wave at the impedance location.

A similar method, based on the impedance-induced orbit shift with intensity, was proposed in 1999 in the Novosibirsk VEPP-4M electron-positron storage ring [9] and in 2001 in the Argonne APS synchrotron accelerator [10]. Later in 2002, the same method was tried in the Grenoble ESRF [11].

The impedance localization method using phase advance shift with intensity, was also applied to the CERN SPS machine [12,13] and in BNL RHIC [14]. In the following years, the method was applied to the PS, SPS and LHC [15] where an innovative methodology using AC dipole excitation was proposed [16]. Recently, the method was also successfully tested at the ALBA accelerator [17].

## *Application to the CERN PS ring*

The phase advance shift versus intensity method was applied during 2018 in the CERN PS in order to gather the relevant reference information before the Long Shutdown 2 (LS2). Measurements were done at the PS extraction energy of 25.4 GeV (kinetic) for minimizing the effect of indirect space charge as shown in Fig. 1. The measurement was performed with vertical chromaticity $\xi_y$ close to zero. Figure 2 shows the localized impedance sources distributed along the 100 sections of the ring together with markers at specific elements in the lattice, such as kickers, septa, wire scanner (shown as *ws*), transverse feedback (shown as *tfb*). The raw data (bottom plot in black) have been fitted by a least squares algorithm accounting for the measurement uncertainty [18]. The localized impedance locations are mostly compatible with the kickers installed in the machine (see for example sections 4, 9, 21, 45 and 71). In other locations, for example between sections 55 and 75, or in section 90, the correlation to the installed equipment is not straightforward.

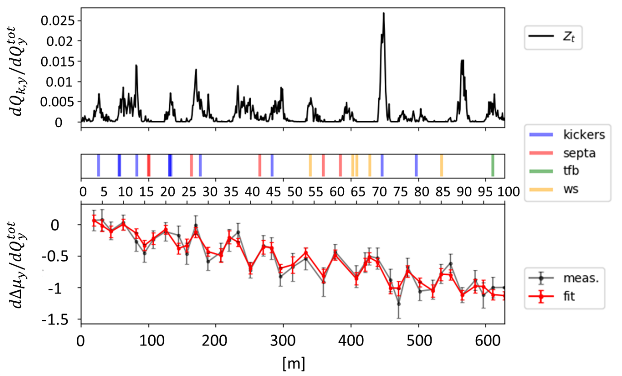


Figure 2: Impedance localization reconstruction in the vertical plane of the PS performed at 25.4 GeV kinetic energy. At the top, impedance strength in units of fraction of the total tune shift, at the middle, the 100 sections of the ring together with markers at specific elements in the lattice such as kickers, septa, wire scanner (*ws*), transverse feedback (*tfb*), at the bottom, the raw phase advance shift with intensity normalized to the total tune shift together with the curve reconstructed by the detected impedances.

The same measurement was performed at the energy of 2 GeV, i.e. below transition energy, with $\xi_y$ of $-0.15$ and $-2.5$ in order to probe the source of the impedance chromatic dependence. This measurement was not possible at extraction energy due to the fast signal decoherence.

As from Fig.1 an increment of $\sim$3 MΩ/m is expected moving from 25.4 GeV to 2 GeV kinetic energy due to indirect space charge, comparable with the total impedance measured at extraction. Figure 3, shows the reconstructed impedance and the corresponding raw data with least square fit. While, from one hand, the larger amount of impedance induces a stronger signal, on the other hand this is coming from the indirect space charge, strongly dependent on the accurate aperture model of the machine which is not yet modelled, impedance-wise, at the location by location level. This is a possible cause for the poor correspondence of the impedance sources at low energy with respect to the one at extraction energy shown in Fig. 2.

This measurement can be of interest when compared to the same one performed with larger vertical chromaticity $\xi_y = -2.5$. In this case, as shown in Figure 4, a large beating is visible on the phase advance shift with intensity and a clear lumped source appears in section 97. One of the compatible elements in proximity could be the transverse feedback kicker. Simulations and measurements did not attribute a large impedance source to this element when striplines are correctly matched to load via the RF-transformer [19] and further investigations are required.

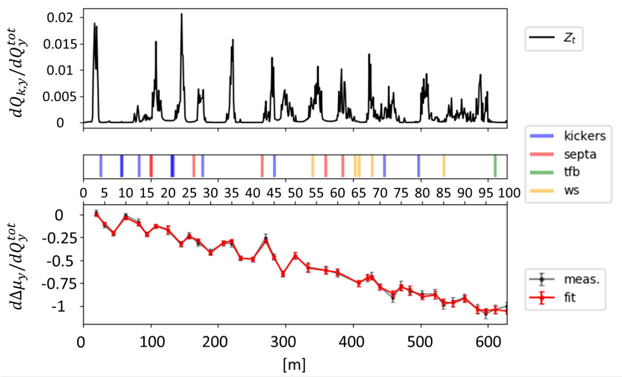


Figure 3: Impedance localization reconstruction in the vertical plane of the PS performed at 2 GeV kinetic energy with corrected chromaticity $\xi_y = -0.15$.

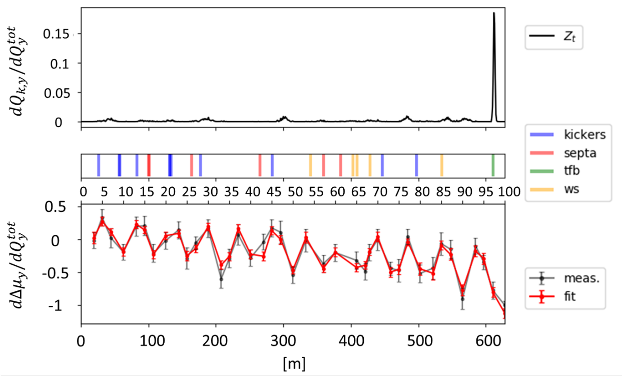


Figure 4: Impedance localization reconstruction in the vertical plane of the PS performed at 2 GeV kinetic energy with larger chromaticity $\xi_y = -2.5$.

## *Application to FNAL Booster ring*

Impedance localization measurements were performed in 2019 in the FNAL Booster ring in order to detect possible unexpected impedance sources in view of the machine upgrade [20, 21]. Measurements were performed both in so called DC (Direct Current) mode, i.e. on the injection plateau, and in *ramped* mode, i.e. throughout the ramp to flat top. The kicker was powered every 500 turns exciting coherent oscillations and the total injected intensity was varied from $\sim 1 \cdot 10^{12}$ to $5 \cdot 10^{12}$ protons. Turn by turn data were collected and their frequency spectra were calculated by Sussix [22] and Harpy [23] to extract the phase advance versus intensity. Figure 5 shows the localization sources obtained in DC mode: the accumulated phase advance steadily drifts along the machine not showing particular step-like or beating behaviour, which is translated also on the normalized impedance strength along the machine.

The result is not surprising as it is already known that the almost totality of the Booster transverse impedance is related to the main bends resistive wall impedance [24].

Measurements in DC mode for the horizontal plane were not accurate enough due to the intrinsically weaker

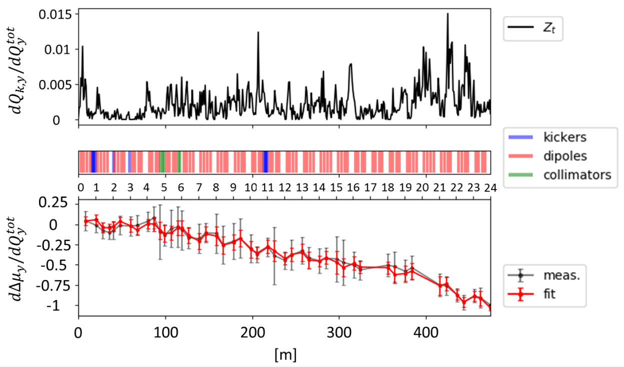


Figure 5: Localized vertical impedance sources at the kinetic energy of 400 MeV along the 25 sections of the FNAL Booster ring together with markers at specific elements in the lattice such as kickers, dipoles and collimators.

impedance [24]. Similarly, measurements in *ramped* mode suffered from reduced kicker strength which affected the quality of the turn by turn signals.

### *Advanced techniques: AC dipole*

An AC dipole is a radio frequency dipole that produces an oscillating field that excites driven oscillations in the beam. While a normal kick would naturally excite the coherent tune oscillation and sidebands, with an AC dipole it is possible to drive the beam oscillation at different frequencies and maintain coherent oscillations for many turns improving the quality and reproducibility of the optics measurement. Tracking simulations recently showed that an AC dipole can be efficiently used to localize impedance sources thanks to the improved quality of turn by turn coherent betatron oscillation data [16]. The first exploratory measurement in the LHC has been so far the only attempt to use the method and new measurement campaigns are planned in the LHC and its injectors.

## IMPEDANCE LOCALIZATION WITH COASTING BEAMS

Conventional impedance localization methods based on BPMs acquisitions cannot be easily used to get accurate turn by turn data for coasting beams, i.e. in the absence of longitudinal beam structure. On the other hand, the Schottky signals are very commonly used to inspect the longitudinal and transverse frequency content of the beam [25]. For this reason, the impedance localization methods cannot be intended in the classical way described in the previous section, but require an alternative approach. In the following we will describe the identification and suppression of a fast vertical instability in LEIR based on the inspection of the Schottky spectrum.

### *Identification and mitigation of LEIR vertical instability*

The LEIR machine is the first synchrotron accelerator of the CERN ion chain [26]. It accumulates up to 7 pulses of $Pb^{54+}_{208}$ from the Linac 3 at the kinetic energy of 4.2 MeV per nucleon and accelerates the beam up to 72.2 MeV to the PS[1]. The injection and accumulation phases occur in coasting beam and, until end of 2018, LEIR could not be operated without transverse damper due to a fast vertical instability occurring after 3-4 injections [27].

Figure 6 shows, at the top, a standard cycle of LEIR and, at the bottom, the horizontal (yellow) and vertical (green) Δ signals recorded by the damper wide band pick-ups. The reader can notice 7 spikes corresponding to the 7 injections and a signal increase during capture and acceleration, i.e. from 1840 ms when the coasting beam is captured by the RF cavities into 2 bunches.

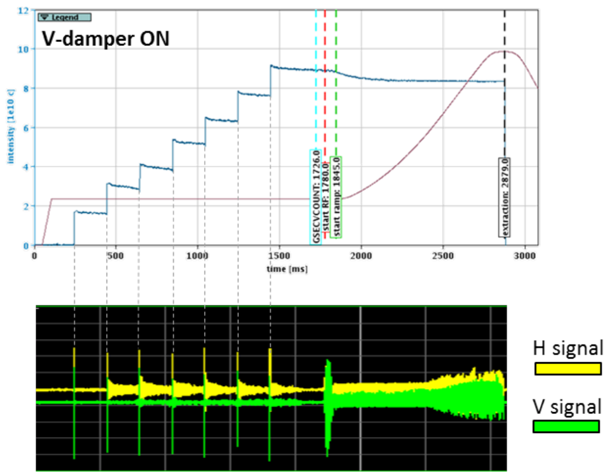


Figure 6: At the top: intensity accumulated in LEIR (blue) and magnetic program (red); in dashed lines, the end of the cooling process, start of capture and acceleration are respectively shown in cyan, red and green. At the bottom: horizontal (yellow) and vertical (green) Δ signals recorded by the damper wide band pick-ups in the ring. Spikes in the signals are correlated to the injections and capture processes. The damper is active all along the cycle.

Figure 7 shows, in a similar way, the effect of removing the vertical damper along the cycle: the vertical signal shows an exponential growth starting from the 4th injection preventing further accumulation.

At the onset of the instability, the vertical Schottky system recorded a repetitive mode pattern, occurring at multiples of 1.9 MHz as shown in Fig. 8. At the top, the Schottky frequency spectrum is showed from 0 to 10 MHz for 350 ms from the start of the instability. At the bottom, selected spectrum projections, corresponding to the dashed lines of the top plot, are taken every 50 ms and show the frequency evolution of the instability in incremental way. The rapid

[1] Other species have been accelerated as well, such as Oxygen, Argon and Xenon.

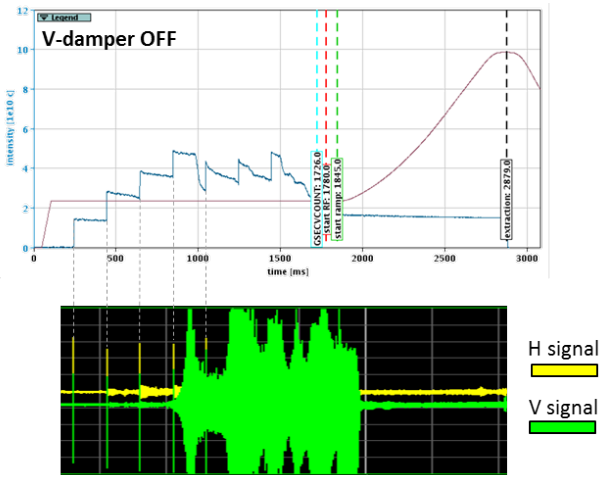


Figure 7: Intensity accumulated in LEIR when the vertical damper is switched-off along the cycle. See Fig. 6 for the details on the plotted lines.

change in the spectrum after 200 ms is associated to beam losses.

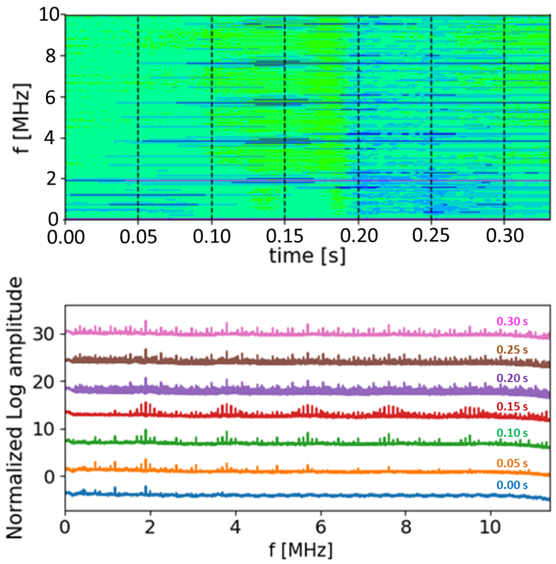


Figure 8: At the top: the Schottky frequency spectrum is showed from 0 to 10 MHz as a function of time, for 350 ms from the start of the instability. At the bottom, selected Schottky spectrum projections corresponding to the dashed lines of the top plot (an offset has been applied for clarity). A clear mode pattern resonating at multiples of 1.9 MHz is visible.

Due to the very low frequency and the resonating behavior the source of the impedance was associated to possible mismatched terminations of devices that can sustain a quasi-TEM (Transverse Electro-Magnetic) mode. These devices are usually kickers or stripline pick-ups (their transverse cross-section is not simply connected). Since the instability was observed only in the vertical plane, stripline pick-ups were considered as possible source (in LEIR kickers are only acting in the horizontal plane).

A selected list of unused devices was selectively disconnected and terminated on a matched load. After the intervention on the UQFHV41 pick-up[2], the repetitive mode pattern was not observed any longer and the instability was effectively suppressed as shown in Fig. 9. After a re-connection test, the instability reappeared confirming the source of the instability.

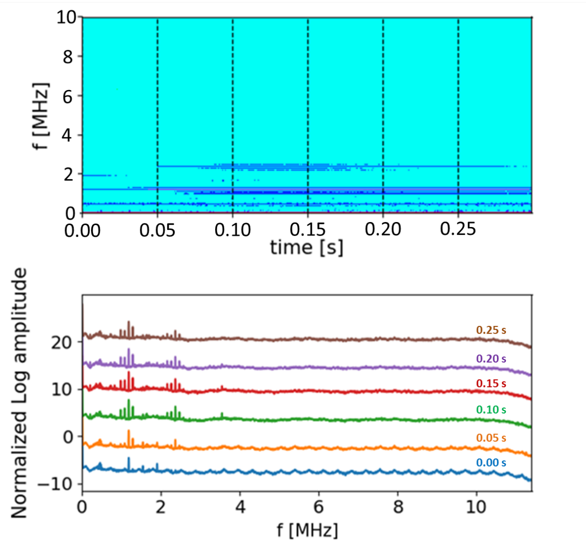


Figure 9: Schottky spectrum after termination of the UQFHV41 pick-up: resonances at multiple of 1.9 MHz have disappeared.

## CONCLUSIONS

In this paper we summarized the measurements techniques used to localize impedance sources with bunched and coasting beams.

With bunched beams, we presented the impedance localization method based on the phase advance shift with intensity and the recent application to the CERN PS and FNAL Booster rings.

In the PS, a large source of impedance was detected at injection energy and at large negative chromaticity, which is absent for corrected chromaticity. The effect has also been measured by standard tune shift versus intensity measurements. A possible source has been identified but not confirmed by bench impedance measurements. Further investigations are planned after the machine restart.

In the FNAL Booster ring, the measurement was applied both in DC (injection) and *ramped* operational modes. The achieved data quality allowed accurate measurements only in the vertical plane in DC mode, where no relevant isolated impedance sources were identified.

With coasting beams, we have presented the successful impedance identification and suppression performed in

[2] This pick-up was used for beam transfer function measurements at the time of the Low Energy Antiproton Ring (LEAR).

LEIR. The inspection of the Schottky spectrum measured during the vertical instability onset, allowed to reduce the possible sources of the instability to the machine stripline pick-ups. The instability was suppressed matching the termination of the UQFHV41 pick-up cables.

## ACKNOWLEDGEMENTS

The authors would like to acknowledge the CERN LEIR, PS, LHC, FNAL Booster operation teams for their contribution in the beam measurements setup. We would also like to acknowledge C. Bath for the help given during the data acquisition in the FNAL Booster studies.

## REFERENCES


[1] L. Palumbo, V. G. Vaccaro, and M. Zobov, "Wake fields and impedance," Sep. 1994, number: LNF-94-041-P Pages: 331 Publisher: CERN. [Online]. Available: http://cds.cern.ch/record/276437

[2] A. W. Chao, *Physics of Collective Beam Instabilities in High Energy Accelerators*. New York: John Wiley & Sons, Inc., 1993. [Online]. Available: https://www.slac.stanford.edu/~achao/wileybook.html

[3] F. J. Sacherer, "Transverse bunched beam instabilities - Theory," Apr. 1974, number: CERN-MPS-INT-BR-74-8. [Online]. Available: http://cds.cern.ch/record/322645

[4] J. L. Laclare, "Bunched beam coherent instabilities," 1987, library Catalog: cds.cern.ch Publisher: CERN. [Online]. Available: http://cds.cern.ch/record/611596

[5] B. Salvant, C. Vollinger, T. Dascalu, S. Persichelli, P. Kramer, N. Mounet, A. Farricker, A. Grudiev, E. Koukovini-Platia, E. Métral, S. Antipov *et al.*, "Building the impedance model of a real machine," in *Proceedings, 10th International Particle Accelerator Conference (IPAC2019): Melbourne, Australia, May 19-24, 2019*, 2019, p. WEYPLS1. [Online]. Available: https://doi.org/10.18429/JACoW-IPAC2019-WEYPLS1

[6] S. Persichelli, M. Migliorati, N. Biancacci, S. Gilardoni, E. Métral, and B. Salvant, "Transverse beam coupling impedance of the CERN Proton Synchrotron," *Phys. Rev. Accel. Beams*, vol. 19, p. 041001, Apr 2016. [Online]. Available: https://link.aps.org/doi/10.1103/PhysRevAccelBeams.19.041001

[7] D. Brandt, A. Hofmann, K. Cornelis, B. W. Zotter, P. Castro, G. L. Sabbi, J. Wenninger, and G. Morpurgo, "Measurements of impedance distributions and instability thresholds in LEP," Jun. 1995, library Catalog: cds.cern.ch Number: CERN-SL-95-34-AP. [Online]. Available: http://cds.cern.ch/record/283279

[8] S. Y. Lee, *Accelerator Physics*, 3rd ed. WORLD SCIENTIFIC, 2011. [Online]. Available: https://www.worldscientific.com/doi/abs/10.1142/8335

[9] V. Kiselev and V. Smaluk, "A method for measurement of transverse impedance distribution along storage ring," in *Proceedings of the 4th European Workshop on Beam Diagnostics and Instrumentation for Particle Accelerators, DIPAC Chester, UK*, 1999, pp. 202 – 204. [Online]. Available: http://accelconf.web.cern.ch/Accelconf/d99/papers/PT19.pdf

[10] L. Emery, G. Decker, and J. Galayda, "Local bump method for measurement of transverse impedance of narrow-gap ID chambers in storage rings," in *PACS2001. Proceedings of the 2001 Particle Accelerator Conference*, vol. 3, June 2001, pp. 1823–1825 vol.3. [Online]. Available: https://doi.org/10.1109/PAC.2001.987195

[11] E. Plouviez and L. Farvacque, "Probing the Transverse Impedance of the ESRF Storage Ring," in *8th European Particle Accelerator Conference*, Paris, France, 2002, pp. 1550 – 1552. [Online]. Available: http://accelconf.web.cern.ch/AccelConf/e02/PAPERS/WEPRI009.pdf

[12] G. Arduini, F. Zimmermann, and C. Carli, "Localizing Impedance Sources from Betatron-phase Beating in the CERN SPS," Aug. 2004, number: CERN-AB-2004-083. [Online]. Available: http://cds.cern.ch/record/793443

[13] R. Calaga, G. Arduini, E. Métral, G. Papotti, D. Quatraro, G. Rumolo, B. Salvant, and R. Tomás, "Transverse Impedance Localization Using Dependent Optics," in *PAC09*, Vancouver, BC, Canada, 2009, pp. 4604 – 4606. [Online]. Available: http://accelconf.web.cern.ch/AccelConf/PAC2009/papers/fr5rfp034.pdf

[14] R. Calaga, "Transverse impedance measurements in RHIC," *APEX Workshop*, 2010, Stony Brook University, NY, USA.

[15] N. Biancacci, G. Rumolo, G. Arduini, G. Sterbini, R. Tomàs, N. Mounet, R. Wasef, Y. Papaphilippou, H. Bartosik, M. Migliorati, R. Calaga, L. Palumbo, S. Persichelli, T. Argyropoulos, K. Cornelis, S. Gilardoni, B. Salvant, and E. Métral, "Beam Coupling Impedance Localization Technique Validation and Measurements in the CERN Machines," in *4th International Particle Accelerator Conference*, Shanghai, China, May 2013, pp. 3106 – 3108, number: CERN-ACC-2013-0120. [Online]. Available: https://cds.cern.ch/record/1578579

[16] N. Biancacci and R. Tomás, "Using AC dipoles to localize sources of beam coupling impedance," *Phys. Rev. Accel. Beams*, vol. 19, p. 054001, May 2016. [Online]. Available: https://link.aps.org/doi/10.1103/PhysRevAccelBeams.19.054001

[17] M. Carlà, G. Benedetti, T. Günzel, U. Iriso, and Z. Martí, "Local transverse coupling impedance measurements in a synchrotron light source from turn-by-turn acquisitions," *Phys. Rev. Accel. Beams*, vol. 19, p. 121002, Dec 2016. [Online]. Available: https://link.aps.org/doi/10.1103/PhysRevAccelBeams.19.121002

[18] N. Biancacci, "Improved techniques of impedance calculation and localization in particle accelerators," Ph.D. dissertation, La Sapienza, Rome, Italy, May 2014, library Catalog: cds.cern.ch Number: CERN-THESIS-2014-043 University: Rome La Sapienza. [Online]. Available: http://cds.cern.ch/record/1704527

[19] B. Popovic and L. Matter, "PS Transverse Feedback Kicker (SD97) Impedance Study," LIU-PS BD-WG meeting, CERN, Geneva, Switzerland, Oct. 2019. [Online]. Available: https://indico.cern.ch/event/851693/

[20] V. Lebedev, "The PIP-II Reference Design Report," 2015, FERMILAB-DESIGN-2015-01. [Online]. Available: https://doi.org/10.2172/1365571

[21] N. Biancacci, Y. Alexahin, M. Carlà, and J. Eldred, "S05. Transverse impedance localization measurements in the Booster," 2019. [Online]. Available: https://indico.fnal.gov/event/21000/

[22] R. Bartolini and F. Schmidt, "A Computer Code for Frequency Analysis of Non-Linear Betatron Motion," Feb. 1998, number: SL-Note-98-017-AP. [Online]. Available: https://cds.cern.ch/record/702438

[23] L. Malina, "Harpy: Simple, Fast and Accurate Frequency Analysis of Beam Data," ABP information meeting, CERN, Geneva, Switzerland, Sep. 2019. [Online]. Available: https://indico.cern.ch/event/846846/

[24] A. Macridin, P. Spentzouris, J. Amundson, L. Spentzouris, and D. McCarron, "Coupling impedance and wake functions for laminated structures with an application to the fermilab booster," *Phys. Rev. ST Accel. Beams*, vol. 14, p. 061003, Jun 2011. [Online]. Available: https://link.aps.org/doi/10.1103/PhysRevSTAB.14.061003

[25] F. Caspers, "Schottky signals for longitudinal and transverse bunched-beam diagnostics," 2009, in proc. of CAS - CERN Accelerator School: Beam Diagnostics: Dourdan, France 28 May - 6 Jun, p. 407, 2008. [Online]. Available: https://cds.cern.ch/record/1213284

[26] M. Benedikt, P. Collier, V. Mertens, J. Poole, and K. Schindl, Eds., *LHC Design Report, Vol.3*, ser. CERN Yellow Reports: Monographs, 2004, CERN, Geneva, Switzerland. [Online]. Available: https://cds.cern.ch/record/823808

[27] N. Biancacci, E. Koukovini-Platia, and C. Zannini, "Identification of instability sources in PSB and LEIR," *BE Newsletter Issue #24*, Dec. 2018, library Catalog: cds.cern.ch Number: CERN-BE-Note-2018-007. [Online]. Available: https://cds.cern.ch/record/2651040

# SOURCE OF HORIZONTAL INSTABILITY AT THE CERN PROTON SYNCHROTRON BOOSTER

E. Koukovini-Platia*, M. J. Barnes, H. Bartosik, G. Rumolo, L. Sermeus, C. Zannini
CERN, 1211 Geneva, Switzerland

*Abstract*

The CERN Proton Synchrotron Booster (PSB) has been known to suffer from horizontal instabilities since its early operation. These instabilities appear at specific beam energies and range of working points. The source of the instability and the reason why the instabilities appear at specific energies remained unidentified. In routine operation, the instabilities have not been limiting the performance reach thanks to the horizontal feedback system. Recently, the interest in these instabilities has been sparked by the ongoing LHC Injectors Upgrade (LIU) program, as well as, the Physics Beyond Colliders (PBC) study group. Their systematic characterization has been carried out through measurements. Macroparticle simulations and analytical modeling have been applied to explain the measurements and the dependence on the kinetic energy. Finally, the extraction kicker has been unambiguously identified as the source of the instability.

## INTRODUCTION

The PSB is the first circular accelerator of the CERN proton injector chain, in operation since 1972. Before the second long shutdown (LS2), it received beams with a kinetic energy of 50 MeV from Linac2 and accelerated them to 1.4 GeV [1]. The PSB delivers a variety of beams for the downstream Proton Synchrotron (PS), Super Proton Synchrotron (SPS), and Large Hadron Collider (LHC) machines, as well as, high intensity beams for the on-line isotope mass separator facility ISOLDE [2].

The beam requirements for the High Luminosity LHC (HL-LHC) [3] exceed the capabilities of today's CERN injector complex. In particular, the LIU project [4] aims to increase the LHC beam intensity and brightness by a factor of two for the HL-LHC era. Within the scope of the LIU project, the Linac2 has been replaced by a new machine, Linac4 [5,6], a normal conducting 160 MeV $H^-$ linear accelerator. The future kinetic injection energy to the PSB will hence be increased from 50 MeV to 160 MeV [7] to reduce space charge effects [8]. The extraction beam kinetic energy will also be increased from 1.4 GeV to 2 GeV, with the exception of the ISOLDE facility that will not be upgraded but may require higher intensity per pulse in the framework of PBC [9].

A horizontal head-tail instability has been observed in the PSB in the past (see Ref. [14] of [10]). The instability, developing when the transverse feedback (TFB) [11] is not in operation, causes severe beam losses of up to 100%. Past studies indicate that a possible source might be the resistive wall impedance [12]. Later studies [13] suggest that a large ripple in the power supply of the focusing quadrupole could be responsible for the instability. The beam coupling impedance of the extraction kickers was first suspected in [10, 14, 15] but without any measurements, simulations, or analytical studies to support the hypothesis.

Despite the numerous studies on the horizontal head-tail instability in the PSB, the true source remained unknown for many years. Moreover, the mechanism of the three instabilities [16] appearing at different energies and thus PSB cycle times, could not be identified. Although the instability is fully controlled in everyday operation by the TFB, interest on the subject has been revived in view of the LIU. In fact, 160 MeV is the energy where the instability appears for certain working points, which implies two things. First, the TFB must be active from the very beginning of the PSB cycle to be able to suppress the fast beam instability. Second, if the TFB is ineffective for even just a few ms, the choice of the working point in terms of horizontal tune can be severely restricted. Furthermore, due to the higher ejection energy of 2 GeV the question arises whether yet another critical energy for beam stability exists.

## MEASUREMENTS

Measurements using a single bunch and single harmonic radio-frequency (RF) system were performed to characterize the instability at a constant energy plateau of 160 MeV in order to mimic the future PSB injection energy from Linac4. Measurements of beam losses and rise times versus the horizontal tunes were performed with and without the TFB to disentangle the losses due to the collective instability from those due to resonance crossings. The horizontal tune is varied between 4.10 and 4.45.

The results are presented in Fig. 1 for an intensity of $2 \times 10^{12}$ p. In the upper plot, the losses are shown as a function of the horizontal tune. The losses reach up to 100% when the TFB is off (red points) and are more severe for tunes between 4.23 and 4.30. The maximum losses occur at $Q_x = 4.26$. Instead, when the TFB is on, no beam losses occur (blue crosses in the upper plot). In the bottom plot, the instability rise time versus $Q_x$ is shown. The grey points correspond to the five acquisitions per tune-setting. The red points represent the mean value at each $Q_x$, while the error bars are given by the standard deviations. The fastest rise time is observed for a horizontal tune of $Q_x = 4.26$ and is 0.6 ms.

Figure 1 shows why it is important to suppress the head-tail instability after LS2. For certain working points, the instability develops at exactly the future injection energy of

* eirini.koukovini.platia@cern.ch

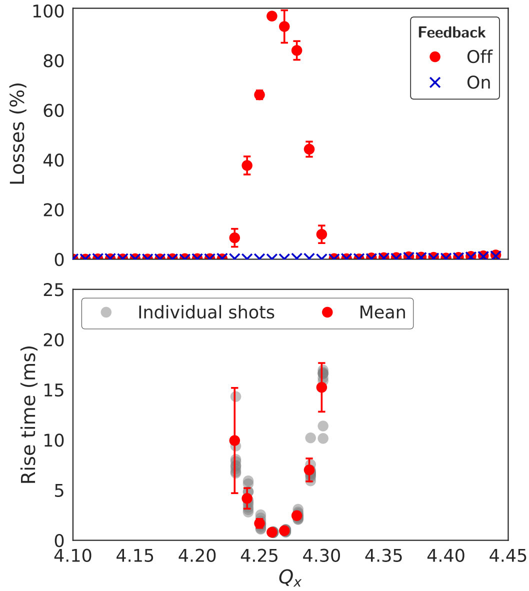


Figure 1: Measured beam losses and instability rise time versus $Q_x$ for $2 \times 10^{12}$ p. Losses reach almost 100% at $Q_x = 4.26$, and the rise time is as fast as 0.6 ms.

160 MeV. Without limiting the choice of the working point to avoid triggering the instability, the obvious requirement is that the PSB TFB should work right from injection, including during the transients of the multi-turn injection and filamentation.

An upgrade of the TFB was already envisaged for the LIU and the new hardware was installed in 2018 [17]. Thanks to the latter, it is expected that the TFB will be operational from the very beginning of the cycle and therefore be able to suppress the potential instability for tunes between 4.21 and 4.30. The new system will also be able to cope with the increased beam intensity expected in 2021 (60% increase in the PSB). Despite all the promising results on hardware testing [17], identifying the instability source remains an important task in order to improve our understanding of the underlying mechanism and to propose the implementation of permanent mitigation techniques.

## SIMULATIONS

A narrow-band resonator impedance has been suspected in the past in [10, 14, 15] as the potential source of the instability. In 2010, Chanel and Carli performed vector network analyzer (VNA) measurements of the $S_{11}$ reflection coefficient [18] on the transmission cables and kicker magnets to identify the frequencies of the resonances due to the coupling with the external circuits. This revealed three resonances at ~1.65 MHz, ~4.9 MHz, and ~8 MHz, suspected to be associated with the short-circuit terminations of the PSB extraction kicker.

In order to investigate if the 1.65 MHz line is responsible for the observed instability, 6D macroparticle tracking simulations with the PyHeadtail [19] code were performed for comparison with measurements. The main parameters are shown in Table 1.

Table 1: Main parameters used in PyHeadtail.

| **Parameter** | **Value** | |
|---|---|---|
| Circumference | C | 157 m |
| Relativistic gamma | $\gamma$ | 1.17 |
| Synchrotron tune | $Q_s$ | $1.69 \times 10^{-3}$ |
| RF voltage | $V_{\mathrm{RF}}$ | 8 kV |
| Harmonic number | $h$ | 1 |
| Bunch intensity | $N$ | $4 \times 10^{12}$ p |
| Resonator shunt impedance | $R_s$ | 4 MΩ/m |
| Resonator frequency | $f_r$ | 1.72 MHz |
| Resonator quality factor | $Q$ | 100 |
| Wake decay time | $N_{\mathrm{wake}}$ | 150 turns |
| Number of macroparticles | $N_{\mathrm{mp}}$ | $1 \times 10^6$ p |
| Number of turns | $N_{\mathrm{turns}}$ | 33000 turns |
| Chromaticity | $\xi_{x/y}$ | -0.7/-1.6 |
| Full bunch length | $l_b$ | 504 ns |

The exact frequency of the narrow-band resonator, i.e. 1.72 MHz, was found by performing a fit in simulations to best reproduce the measured behavior of the instability rise time versus horizontal tune. This value is indeed close to the lowest resonance measured by Chanel and Carli and to the expectation from the beam coupling impedance model of the kicker (see Fig. 2).

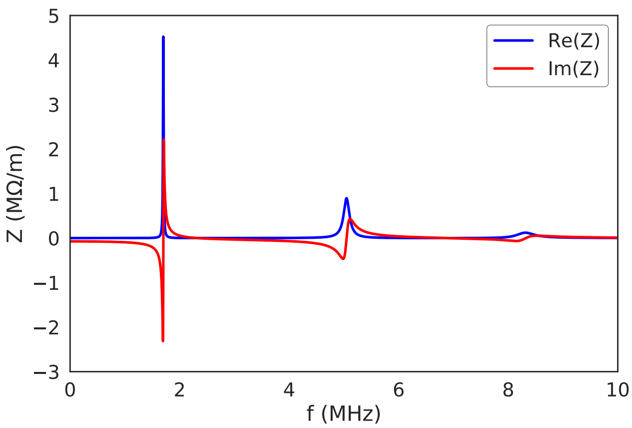


Figure 2: Horizontal impedance model of the PSB extraction kicker due to coupling with the kicker electrical circuit, including cables as coaxial transmission lines.

The impedance model of the kicker takes into account the coupling to the electrical circuit, including cables as coaxial transmission lines [20]. The frequency pattern of the resonances depends on the single-way delays and termination of the kicker circuit. The very low attenuation constant of the cables makes these resonances narrow with a Q value of about 100 and a shunt impedance in the order of MΩ/m, i.e. in very good agreement with the findings of Fig. 3.

The red points are the measured rise times with mean and standard deviation of five shots and the dashed green curve

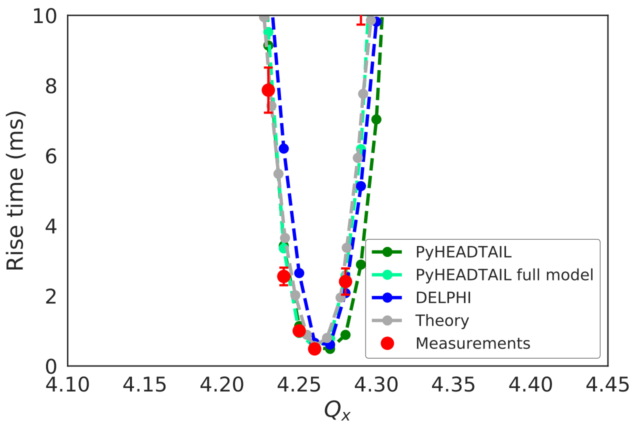


Figure 3: Rise time versus $Q_x$ from measurements (red), PyHEADTAIL (green) and DELPHI (blue) simulations with the narrow-band resonator impedance model, and PyHEADTAIL simulations (light green) and theory (grey) with the full PSB impedance model.

corresponds to the PyHEADTAIL results using the narrow-band resonator. Evidently, the measurement results are fully consistent with the first kicker resonance at ∼1.72 MHz. The frequency domain Vlasov solver DELPHI [21] (dashed blue curve in Fig. 3) is also used for comparison against measurements and PyHEADTAIL, and found to be in good agreement.

As a next step, the full PSB impedance model is used in PyHEADTAIL. The former also includes resistive wall impedance, indirect space charge, flanges, step transitions, injection kickers, extraction kicker magnet losses in the non-ultrarelativistic regime [22, 23], and cavities. A good agreement was found when compared with the measurements (dashed light green curve in Fig. 3). The rise time can also be calculated from the theoretical point of view using the Sacherer theory [24] and the full PSB impedance model. The results are plotted in Fig. 3 with the dashed grey curve.

As a next step, the azimuthal mode number of the instability is investigated. In Fig. 4, the measured horizontal centroid is shown versus turns (top left), while the simulated one using the full PSB impedance model is in the top right plot. In the bottom plots, the Fast Fourier Transform (FFT) of the measured and simulated centroid signals are shown in the left and right plots, respectively. Using a sliding-window FFT, the frequency spectra are obtained at different numbers of turns, indicated by the colored vertical lines in the top plots. The FFT from the measured data indicates that the instability is of azimuthal mode number -5 (bottom left plot), in agreement with PyHEADTAIL (bottom right plot). The slight shift of the peaks away from the integer is related to the intensity.

Last, simulations are compared with measurements in terms of the radial mode of the instability. The measured head-tail modes as recorded by the horizontal pick-up in the PSB (see Fig. 5a) agree well with DELPHI simulations [25] (Fig. 5b) for a horizontal tune of 4.26. This good agreement could not be achieved without including the indirect space charge in simulations. Over the whole range of explored tunes, however, the number of nodes in the intra-bunch patterns can differ by few units, suggesting that some additional ingredient may still need to be included in the analysis.

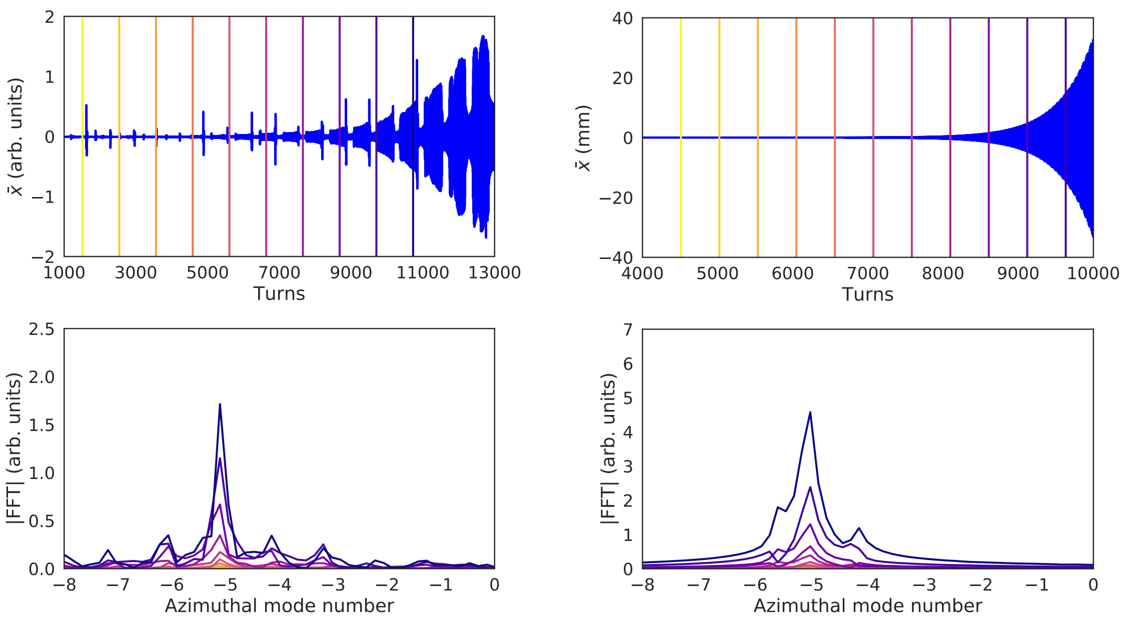


(a) Measurements (b) PyHEADTAIL

Figure 4: Horizontal centroid from measurements (top left) and PyHEADTAIL simulations using the PSB impedance model (top right). Information on the azimuthal mode number is obtained by performing a sliding-window FFT on the centroid signals. Both cases predict an azimuthal mode number -5.

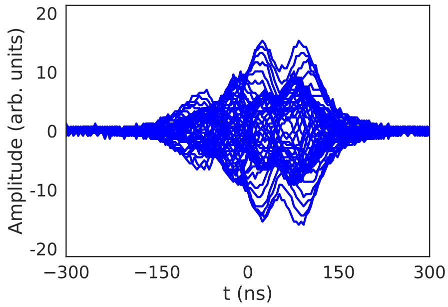


(a) Measurements

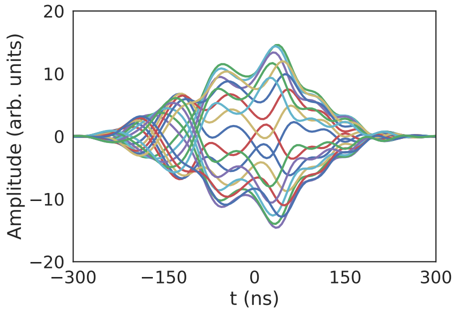


(b) DELPHI

Figure 5: Head-tail modes as recorded by the horizontal pick-up for a single bunch in the PSB with $Q_x = 4.26$, $N = 4 \times 10^{12}$ p and $\xi_x = -0.7$ (top), and as predicted by DELPHI simulations for the same parameters (bottom).

## ANALYTICAL STUDIES

The impedance model in Fig. 2 can also be used to predict the expected energies at which the instability will occur. The condition to drive an instability can be written as in [26, 27]:

$$\frac{f_i}{f_{\text{rev}}} + Q_x = n, \tag{1}$$

where $f_i$ is the resonant frequency of the impedance, $f_{\text{rev}}$ is the revolution frequency, $Q_x$ is the horizontal betatron tune, and $n \in \mathbb{Z}$. The $Q_x$ is varied as a function of the kinetic energy according to the ISOLDE beam operational tune settings. Figure 6 shows the left-hand side of Eq. (1) as a function of the kinetic energy for the first and second kicker resonance. All three experimentally observed instabilities along the PSB cycle [28] are predicted and explained either by the first or the second kicker resonance. The first kicker resonance is responsible for the instability at ~160 MeV, while the second resonance is responsible for the second and third instabilities at ~330 MeV and ~1.25 GeV, respectively. The second resonance plays a marginal role below 160 MeV because the highest significant frequency of the bunch spectrum is smaller than the resonant frequency below this energy and, hence, does not excite the resonance. For the same reason, the third kicker resonance has a minor effect all along the PSB energy range. Moreover, no further instability is predicted for energies between 1.4 GeV and 2 GeV.

Figure 6 explains for the first time why the instability in the PSB occurs only at specific energies. The revolution frequency, and thus the betatron frequency, changes with energy. As a consequence, the betatron tune at which the instability occurs due to a specific impedance also changes with energy. Interestingly, the theoretical analysis depicted in Fig. 6 predicts that a horizontal instability should also occur at ~55 MeV, which was never reported in the past. Dedicated measurements recording the horizontal pick-up signal at ~55 MeV were made to validate this prediction. The measured pick-up signal is shown in Fig. 7. It illustrates a horizontal head-tail signal with two nodes, recorded and observed for the first time at the energy of ~55 MeV.

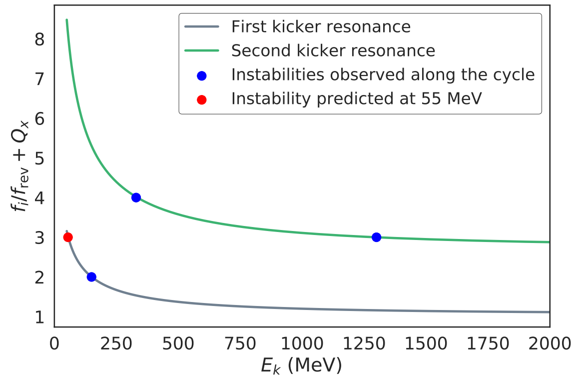


Figure 6: Left-hand side of Eq. (1) as a function of the kinetic energy up to 2 GeV for the first kicker resonance (grey line) and the second resonance (green line). The blue points mark the energies where instabilities have been observed in the PSB. The red point is a prediction that an instability should also be observed at ~55 MeV.

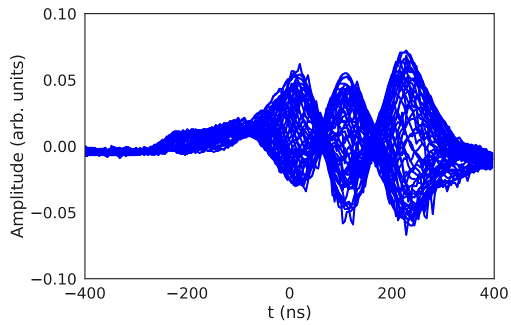


Figure 7: Head-tail mode recorded by the horizontal pick-up for a single bunch at ~55 MeV.

Theory and machine measurements are in excellent agreement and the dependence of the instability characteristics on the kinetic energy is fully understood. All observed instabilities along the PSB cycle can now be explained by a single source, namely the resonances due to the kicker magnets and low-loss transmission cables of the extraction kicker system.

## MEASUREMENTS WITH MODIFIED KICKER TERMINATION

Measurements of beam losses versus the horizontal tune were realized with a temporary modification of the kicker's electrical circuit. The 1 nF capacitor in one of the filter networks at the main switch end of the transmission cables of the kicker was replaced with a short-circuit. The high impedance of 5 Ω at the switch end of the transmission lines was also replaced by a resistance which matches the characteristic impedance of the system (6.25 Ω). The kicker system cannot be pulsed in this configuration to actually extract the beam, which was thus lost in the machine. The results from the measurements are shown in Fig. 8.

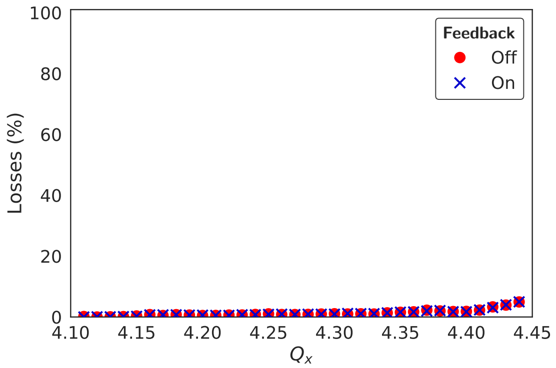


Figure 8: Beam losses at 160 MeV versus horizontal tune with intensity $N = 3 \times 10^{12}$ p with the modified kicker termination. Measurements with TFB off (red) and on (blue) are shown.

With the modified kicker termination, no sign of the instability is observed even when the TFB is kept inactive all along the cycle, as opposed to Fig. 1 with the operational kicker termination. This unambiguously confirms that the instability is caused by the high impedance at the switch end of the transmission cables to the magnets, together with the short-circuit termination of each extraction kicker magnet.

## SUMMARY

A horizontal head-tail instability has been observed for more than 40 years in the PSB. Its source remained unknown until now and the instability was suppressed during routine operation by the TFB. Thanks to recent measurements, simulations, and theoretical analysis, the source of the instability has been identified. A single source, namely the resonances introduced by the cables of the PSB extraction kicker system, is found to be responsible for all the observed instabilities along the PSB cycle. Simulations and analysis with Sacherer's formalism agree with the measurement results and clearly pinpoint the origin of the instability. It is given by the high impedance at the thyratron switch end of the transmission cables to the kicker magnets together with the short-circuit termination of each magnet. With the upgrade of the TFB hardware already envisaged for the LIU, the instability is currently expected to be suppressed from the very beginning of the PSB cycle at the future injection kinetic energy of 160 MeV. Moreover, no further instability is predicted according to the theoretical analysis for energies between 1.4 GeV and 2 GeV. Ideas how to permanently suppress the kicker resonance have been considered in [29].

## ACKNOWLEDGEMENTS

The authors would like to thank S. Albright, F. Antoniou, G. P. Di Giovanni, A. J. Findlay, G. Kotzian, A. Lasheen, T. Levens, E. Métral, B. Mikulec, and A. Santamaría García for the fruitful discussions and inputs to these studies. The authors are also grateful to K. Li, A. Oeftiger, and M. Schenk for providing expertise with the PyHeadtail code, and D. Amorim and N. Mounet for their assistance with Delphi. Furthermore, the authors thank the BE-OP-PSB teams for their support during the experiments.

## REFERENCES

[1] K. H. Reich. The CERN Proton Synchrotron Booster. In *Proc. of PAC'69: Washington DC, US, March 5-7*, 1969.

[2] R. Catherall et al. The ISOLDE facility. *J. Phys. G: Nucl. Part. Phys.*, 44:094002, August 2017.

[3] G. Apollinari, I. Béjar Alonso, O. Brüning, P. Fessia, M. Lamont, L. Rossi, and L. Tavian. High-Luminosity Large Hadron Collider (HL-LHC) Technical Design Report V. 0.1. Technical report, CERN, September 2017.

[4] J. Coupard et al. LHC Injectors Upgrade, Technical Design Report, Volume I: Protons. Technical report, CERN, December 2014.

[5] L. Arnaudon et al. The Linac4 Project at CERN. In *Proc. of IPAC'11, San Sebastián, Spain*, September 2011.

[6] A. M. Lombardi. Linac4: From Initial Design to Final Commissioning. In *Proc. of IPAC'17, Copenhagen, Denmark*, May 2017.

[7] K. Hanke et al. PS Booster Energy Upgrade Feasibility Study First Report. Technical report, CERN, September 2010.

[8] W. Weterings, G. Bellodi, J. Borburgh, T. Fowler, F. Gerigk, B. Goddard, K. Hanke, M. Martini, and L. Sermeus. 160 MeV $H^-$ Injection into the CERN PSB. In *Proc. of PAC'07, Albuquerque, USA*, June 2007.

[9] E. Koukovini Platia et al. Protons Beyond the LHC Injectors Upgrade Project. Technical report, CERN, May 2019.

[10] G. Nassibian and F. J. Sacherer. Methods for measuring transverse coupling impedances in circular accelerators. *Nucl. Instrum. Methods*, 159:21–27, February 1979.

[11] C. Carter, C. Christiansen, J. Donnat, G. Gelato, M. Le Gras, H. Schönauer, and D. J. Williams. The Transverse Feedback System for the CERN PS Booster. In *Proc. of PAC'81, Washington, DC, USA*, March 1981.

[12] D. Quatraro, A. Findlay, B. Mikulec, and G. Rumolo. Head Tail Instability Observation and Studies at the Proton Synchrotron Booster. In *Proc. of IPAC'10, Kyoto, Japan*, May 2010.

[13] M. McAteer, C. Carli, V. Forte, G. Rumolo, and R. Tomás. Observation of Coherent Instability in the CERN PS Booster. In *Proc. of IPAC'14, Dresden, Germany*, June 2014.

[14] D. Quatraro, A. Blas, M. Chanel, A. Findlay, B. Mikulec, and G. Rumolo. Coherent Tune Shift and Instabilities Measurements at the CERN Proton Synchrotron Booster. In *Proc. of PAC'09, Vancouver, BC, Canada*, May 2009.

[15] Carlo Zannini. *Electromagnetic simulation of CERN accelerator components and experimental applications*. PhD thesis, EPFL, 2013.

[16] V. Kornilov, S. Aumon, A. Findlay, B. Mikulec, and G. Rumolo. MD on Head-Tail Instability in the PS Booster. Technical report, CERN, January 2013.

[17] A. Blas and G. Kotzian. Upgraded Transverse Feedback for the CERN PS Booster. In *Proc. of HB2018, Daejeon, Korea*, June 2018.

[18] K. Kurokawa. Power Waves and the Scattering Matrix. *IEEE Transactions on Microwave Theory and Techniques*, 13:194–202, Mar 1965.

[19] E. Métral et al. Beam Instabilities in Hadron Synchrotrons. *IEEE Transactions on Nuclear Science*, 63:1001–1050, April 2016.

[20] C. Zannini, G. Rumolo, and V.G. Vaccaro. Effect of the TEM Mode on the kicker Impedance. In *Proc. of IPAC'12*, May 2012.

[21] N. Mounet. Vlasov solvers and macroparticle simulations. In *Proc. of ICFA Mini-Workshop on Impedances and Beam Instabilities in Particle Accelerators*, page 77, September 2017.

[22] N. Wang and Q. Qin. Transverse Impedance Calculation for Simplified Model of Ferrite Kicker Magnet with Beta < 1. In *Proc. of IPAC'11, San Sebastián, Spain*, September 2011.

[23] N. Biancacci et al. Impedance calculations for simple models of kickers in the non-ultrarelativistic regime. In *Proc. of IPAC'11, San Sebastián, Spain*, September 2011.

[24] F. J. Sacherer. Transverse bunched-beam instabilities. Technical report, CERN, November 1976.

[25] D. Amorim, N. Biancacci, K.S.B. Li, and E. Métral. Improvement of the analytic VLASOV solver DELPHI. In *Proc. of IPAC'17, Copenhagen, Denmark*, May 2017.

[26] B. Zotter and F. J. Sacherer. Transverse instabilities of relativistic particle beams in accelerators and storage rings. In *Proc. of the First Course of the International School of Particle Accelerators*, pages 175–218, November 1976.

[27] J. Gareyte and F. J. Sacherer. Head-Tail Type Instabilities in the CERN PS and Booster. In *Proc. of HEACC'74, Stanford, California, US*, May 1974.

[28] D. Quatraro, M. Chanel, A. Findlay, B. Mikulec, and G. Rumolo. Transverse instabilities at the PS Booster: recent observations and plans. `https://espace.cern.ch/be-dep-workspace/MSWG/Presentations2009/DQuatraro_061109.pdf`, November 2009.

[29] E. Koukovini-Platia, M. J. Barnes, H. Bartosik, G. Rumolo, L. Sermeus, and C. Zannini. Source of horizontal instability at the CERN Proton Synchrotron Booster. *Phys. Rev. Accel. Beams*, 22(124201), 2019.

# ADTOBSBOX TO CATCH INSTABILITIES

M. E. Söderén*, D. Valuch, CERN, Geneva, Switzerland

*Abstract*

During long shutdown II (2019-2020) the transverse observation system (ADTObsBox) in the LHC will undergo a substantial upgrade. The purpose of this upgrade is to allow for true low latency, online processing of the 16 data-streams of transverse bunch-by-bunch, turn-by-turn positional data provided by the beam position monitors in transverse feedback system in the LHC (ADT). This system makes both offline and online analysis of the data possible, where the emphasis will lie on online analysis, something that the older generation was not designed to provide. The new system provides a platform for real-time analysis applications to directly capture the data with minimal latency while also providing a heterogeneous computing platform where the applications can utilize CPUs, GPUs and dedicated FPGAs. The analysis applications include bunch-by-bunch transverse instability analysis which will profit from significant reduction of latency.

## ADTOBSBOX DURING RUN II

In 2015, a system called ObsBox (Observation Box) [1] was introduced by the Radio-Frequency group at CERN which allowed for buffering of multiple high-bandwidth data-streams from the Low-Level RF systems. The main purpose of the system for the transverse plane in the LHC is to make buffers with beam data (e.g. a bunch-by-bunch transverse position) of different lengths available for users. The buffers are ranging from $2^{12}$ turns to analyze injection oscillation transients, to $2^{17}$ turns to analyze transverse beam oscillations caused for example by civil engineering works close to the LHC beam tunnel [2]. Over time, the system has evolved into an important tool providing live beam parameter and transverse stability data to the accelerator operation, and it is an absolutely vital tool for the machine development sessions, where new ideas or methods are being tested in the machines. The ObsBox machines, which analyze the data in the transverse plane from the ADT are specifically called "ADTObsBox". They have been a proving-ground to test the limits of its computing system, since the transverse plane is where the analysis has gradually moved towards online analysis (<1 second, or 11k turns latency). In 2016, an online transverse instability detection system [3, 4] was introduced that analyzed the beam positional data for exponential oscillation amplitude growths to detect an onset of transverse instability (all analysis performed bunch-by-bunch). This results in a trigger sent over the LHC Instability Trigger network (LIST) so this event is captured by other observation instruments in the LHC. This also causes an observation buffer in the ADTObsBox to be triggered for later analysis. The bunch-by-bunch instantaneous amplitude is also published and made available, e.g. for the ADT beam activity monitor which is a fixed display in the control room that has been a important operational tool during run II. The ADTObsBox instability detection system made a significant contribution to the analysis and mitigation of ongoing operational issues [5].

## ADTOBSBOX AFTER LS2

During LS2, a substantial upgrade of the ADTObsBox will take place. It will be redesigned from the ground up with new I/O cards with custom firmware, driver, servers, and applications. The main reason for this upgrade is to reduce the latency between the I/O cards until the data is available for analysis. In the older generation, this latency was 364 ms and the new generation will reduce this to 120 µs. This is achieved by moving all the pre-processing from the host server to the FPGA and creating a new driver which manages a large circular buffer which allows for asynchronous transfers. This means that the data is ready to be analysed as soon as the transfer from the FPGA is completed and thus reduces the amount of computing resources needed to receive the data.

The new I/O card can receive up to ten channels so two cards can accommodate all 16 channels which the ADT provides. This allows for all channels to be available in a single host server opening up the possibility to cross-beam and cross-plane analysis, something which was not possible in the previous system.

The new servers will allow us to continuously upgrade the ADTObsBox system with new applications during run III without being limited by computing resources. The new GIGABYTE G481-HA0 servers have 384 GB of RAM and they can run 96 threads in parallel so one server has roughly the same computing capacity as four of the older generation. There will be 3 servers with different purposes, one for real-time analysis, one for buffers, and one for development. The server dedicated for buffering will have 144 TB of local storage which will be used for a circular buffer. This will be able to store turn-by-turn and bunch-by-bunch transverse positional data for a minimum of 24 hours which can be important if an interesting event occurred which did not result in a trigger of any buffer. This can also be helpful for machine development runs where the complete data-set for the session can be stored for offline analysis at a later stage.

## TRANSVERSE INSTABILITY ANALYSIS

The new system will reduce the processing latency from 364 ms to 120 µs which will make the ADTObsBox an even more powerful tool for transverse instability detection in the LHC. With the long processing delay, it can be too late for some fast rise time instabilities to be detected. If the beam is dumped due to losses on the collimators then it

* martin.soderen@cern.ch

would be captured by the post-mortem buffers but if not then the data could be lost. The current transverse instability detection implementation applies the Hilbert transform [6] to the bunch-by-bunch data. An instantaneous oscillation amplitude for each bunch is calculated. A growth can be detected by comparing the running average of the instantaneous amplitude for different time windows. A time window of $2^{10}$ turns can be seen in Fig. 1. When an instability is detected, dedicated observation buffers are triggered and saved to a storage server for further analysis. At the same time all data from the instability analysis, for example the bunch-by-bunch transverse activity is logged by the accelerator logging service (NXCALS) [7]. The implementation details of the new system have not been decided yet, but one possible solution would be to combine the data from 4 pick-ups, apply the Hilbert transform and then do an exponential curve fitting on the instantaneous amplitude. This would be performed on all bunches in the LHC and in all 4 planes so the computational resources to run this would be significant.

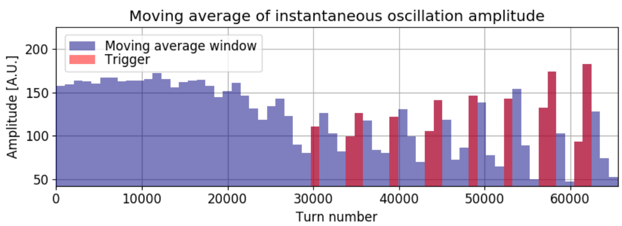


Figure 1: Moving average of instantaneous oscillation amplitudes

## CONCLUSION

The upgrade of the ADTObsBox will allow for detecting instabilities while they are occurring and trigger other observation instruments in the LHC with shorter buffers. It will also allow more powerful analysis tools to be used in the future while providing a 24h circular buffer which can be used to analyze events not triggered by other instruments. In conclusion, this is a very powerful system that has proved its value during run II and will continue to do it even better during run III.

## REFERENCES

[1] M. Ojeda Sandonís, P. Baudrenghien, A.C. Butterworth, J. Galindo, W. Hofle, T.E Levens, J.C. Molendijk, and D. Valuch, *Processing High-Bandwidth Bunch-by-Bunch Observation Data from the RF and Transverse Damper Systems of the LHC*, in *Proc. 15th Int. Conf. on Accelerator and Large Experimental Physics Control Systems (ICALEPCS'15)*, Melbourne, Australia, Oct. 2015, pp. 841–844. doi:10.18429/JACoW-ICALEPCS2015-WEPGF062

[2] M. Schaumann, D. Gamba, M. Guinchard, L. Scislo, and J. Wenninger, *Effect of Ground Motion Introduced by HL-LHC CE Work on LHC Beam Operation*, in *Proc. 10th Int. Particle Accelerator Conf. (IPAC'19)*, Melbourne, Australia, May 2019, pp. 4092–4095. doi:10.18429/JACoW-IPAC2019-THPRB116

[3] M.E. Söderén, G. Kotzian, M. Ojeda-Sandonís, and D. Valuch, *Online Bunch by Bunch Transverse Instability Detection in LHC*, in *Proc. 8th Int. Particle Accelerator Conf. (IPAC'17)*, Copenhagen, Denmark, May 2017, pp. 397–399. doi:10.18429/JACoW-IPAC2017-MOPAB117

[4] M.E. Söderén, *Online Transverse Beam Instability Detection in the LHC. High Throughput Real-Time Parallel Data Analysis*, Master's thesis, Linköpings Universitet, Linköping, 2017, CERN-THESIS-2017-401;LIU-IDA/LITH-EX-A--17/053--SE

[5] J. Jimenez, D. Amorim, S. Antipov, G. Arduini, A. Bertarelli, N. Biancacci, B. Bradu, E. Bravin, G. Bregliozzi, K. Brodzinski, R. Bruce, X. Buffat, L. Carver, P. Chiggiato, S. Claudet, P. Collier, R. Garcia Alia, M. Giovannozzi, A. Gorzawski, L. Grob, E. Holzer, W. Höfle, G. Iadarola, G. Kotzian, A. Lechner, T. Levens, B. Lindstrom, T. Medvedeva, L. Mether, A. Milanese, D. Mirarchi, E. Métral, D. Perini, S. Redaelli, G. Rumolo, B. Salvant, R. Schmidt, M. Valette, D. Valuch, J. Wenninger, D. Wollmann, C. Yin Vallgren, C. Zamantzas, and M. Zerlauth, *Observations, Analysis and Mitigation of Recurrent LHC Beam Dumps Caused by Fast Losses in Arc Half-Cell 16L2*, in *Proc. 9th Int. Particle Accelerator Conf. (IPAC'18)*, Vancouver, Canada, May 2018, pp. 228–231. doi:10.18429/JACoW-IPAC2018-MOPMF053

[6] Y. Liu, *Hilbert Transform and Applications*, in Fourier Transform Applications, S. Salih, Rijeka, Croatia: InTech, 2012, pp. 291–300.

[7] J. P. Wozniak and C. Roderick, *NXCALS - Architecture and Challenges of the Next CERN Accelerator Logging Service*, presented at the 17th Int. Conf. on Accelerator and Large Experimental Physics Control Systems (ICALEPCS'19), New York, NY, USA, Oct. 2019, paper WEPHA163

# LONGITUDINAL BEAM QUALITY MONITORING

T. Argyropoulos,
CERN, Geneva, Switzerland

*Abstract*

Reliable monitoring of the longitudinal beam quality is essential for a safe and efficient operation of any high intensity accelerator. The definition of beam quality criteria vary from one machine to the other, depending on the beam and machine parameters. In this paper, the most commonly used concepts of longitudinal beam quality monitoring are addressed with emphasis given on the applications in the circular accelerators at CERN.

## INTRODUCTION

Monitoring of the longitudinal beam quality is one of the key ingredients in the operation of high intensity particle accelerators and an essential component to increase the beam performance. Moreover, it ensures the machine safety by quickly spotting any beam degradation (instability, losses) or hardware problem (RF cavities trips, errors in the phase of successive modules in Linacs, problems during RF manipulations, etc.) and therefore allows for an efficient correction in critical situations. Reliable longitudinal beam observations are especially crucial during machine commissioning and machine studies. In addition, in certain circumstances, the longitudinal beam parameters could be used as an input to optimize other beam manipulations.

The criteria defining the longitudinal beam quality vary from one machine to the other, depending on the particle type and on the beam pattern (single- or multi-bunch beams). Specific needs and problems of each machine determine what should be monitored (instabilities, distributions or long term evolution), and therefore they define the requirements in resolution and frequency of acquisitions.

The variety of the beam parameters for the different types of accelerators define the measurement approach, which in most cases, is focused on obtaining accurate and reliable longitudinal bunch profiles. Such profiles can be further analyzed to obtain the required bunch parameters (bunch shape, length, position, and emittance). A large spectrum of diagnostic techniques has been developed over the years to cope with the increased needs in time resolution (in the order of a few fs). They can be distinguished in direct measurements of the beam: wall-current monitors (WCM) pick-ups, RF zero-phasing, transverse deflecting cavities, beam shape monitors, etc or in those using the synchrotron radiation to reconstruct the bunch distribution: streak camera, coherent radiation, etc [1].

This paper will be focused on how longitudinal beam quality is monitored in the CERN accelerator complex, and in particular in the LHC and the SPS. The bunch lengths of interest are of the order of few ns, measured by WCMs with bandwidths of around 3 GHz together with fast-sampling oscilloscopes (up to 40 GS/s).

## MONITORING OF SINGLE BUNCHES

Precise and accurate diagnostics with high resolution are needed to monitor the longitudinal quality of single bunches. The knowledge of bunch position and length are usually adequate to identify and characterize longitudinal instabilities during machine operation. However, higher resolution is often needed in order to resolve in more details the intra-bunch motion and the longitudinal distribution (higher mode of instabilities, RF manipulations, luminosity calculations, etc.). In addition, the measurements should well cover at least a few synchrotron periods, which, depending on the accelerator, could be translated to an acquisition of a few thousands of turns. Figure 1 presents an acquisition of longitudinal bunch profiles at the moment of injection into the LHC. Measurements were done using a WCM [2] pick-up

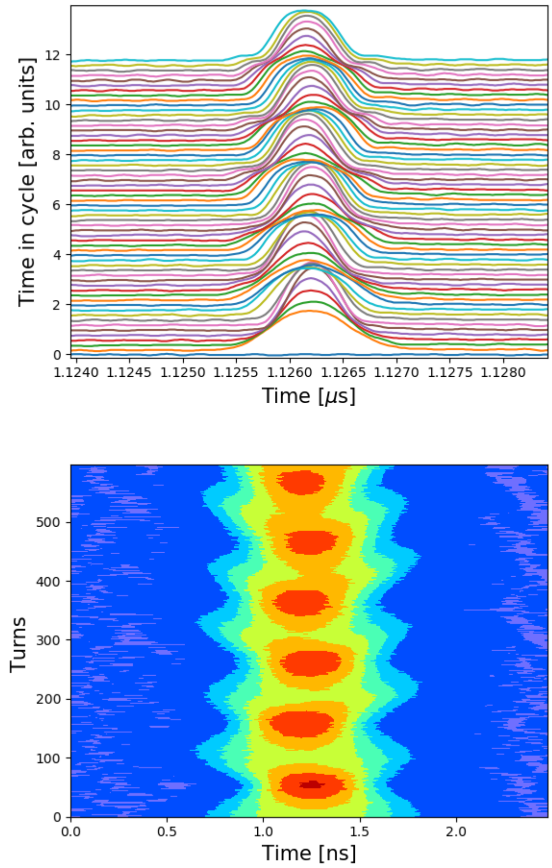


Figure 1: Two common illustrations of longitudinal bunch profile measurements at the LHC injection ($V_{RF}$ = 6 MV). Top: "mountain range" plot. Bottom: "waterfall" plot. The quadrupole oscillations of the bunch are clearly visible, initiated by an RF voltage mismatch.

with a bandwidth of around 3 GHz connected to a Tektronix, DPO7254 oscilloscope with sampling rate of 40 GS/s. Two commonly used means to illustrate the acquired data are shown, the mountain range plot (top) and the waterfall plot (bottom). In both representation, one can clearly observe the quadrupole oscillations of the bunch, triggered by the mismatch of the RF voltage at LHC injection.

In addition to a clear illustration of the intra-bunch motion, the waterfall plots can be used to identify phase and energy errors at injection. This is illustrated in Fig. 2. In the left plot, the dipole oscillations are initiated by an energy error, since the bunch is injected in the bucket center (white vertical line). In the right plot, the oscillations are caused by a phase error, as an initial phase displacement with respect to the bucket center can be observed. Note that in both cases the impact on the bunch is similar.

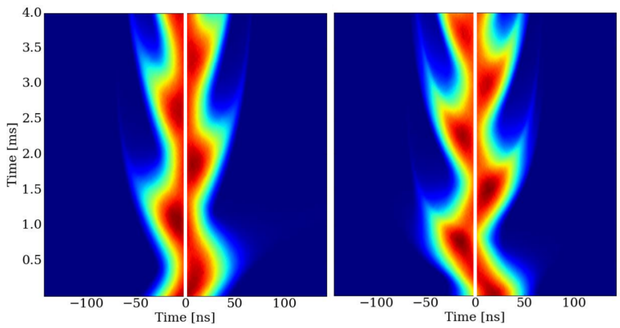


Figure 2: Waterfall plots presenting simulations of dipole oscillations of a bunch caused by energy (left) and phase (right) errors at injection. The white, vertical line indicates the bucket center [3].

The acquired bunch profiles can be fitted to obtain information on the bunch parameters (bunch position, peak, length and intensity). Different types of fits can be applied, depending on the specific bunch distribution (Gaussian, parabolic, etc). However, for an efficient monitoring of the beam quality during operation, faster algorithms (for example full-width-half-maximum of the bunch profile) are usually preferred in some cases, even at the expense of loosing accuracy.

The bunch parameters obtained after the fitting could be further analyzed to extract more information: quantify the injection errors, obtain the frequency of oscillation, the damping rate of a coherent motion or its growth rate (in case of instabilities), etc. Figure 3 depicts the bunch length oscillations due to the voltage mismatch at the LHC injection. By fitting these oscillations one can estimate the synchrotron frequency (actually $2f_s$) and the damping time of the quadrupole motion, which is used to detect possible issues with the RF voltage amplitude.

Furthermore, the 2-dimensional longitudinal phase-space distribution of the bunch can be reconstructed, based on measurements of the bunch profiles, by applying tomographic techniques. Apart from visualizing the longitudinal phase-space, longitudinal tomography provides information on the longitudinal emittance and the momentum spread of the bunch, with better precision than an analysis of bunch profile. In addition, it gives an accurate model of the particle distribution which is very important for analytical calculations and macro-particle simulations in view of beam instability studies.

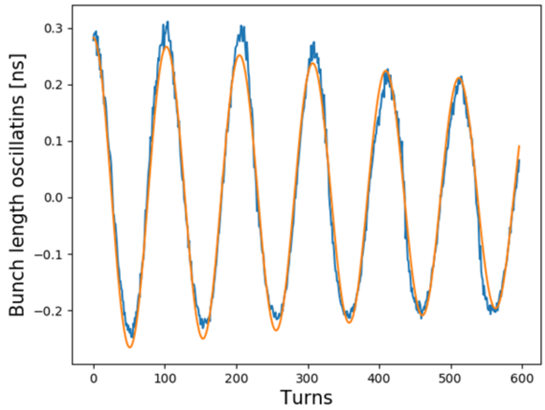


Figure 3: Bunch length oscillations at the LHC injection with $V_{RF}$ = 6 MV. The synchrotron frequency $f_s$ = 54.9 Hz and damping time of $\tau_d$ = 0.15 s were obtained after applying a sinusoidal fit (orange curve). The revolution period is $T_{rev}$ = 88.9 $\mu$s.

Longitudinal bunch tomography was originally developed at CERN [4], in order to investigate the longitudinal emittance evolution during the complex RF manipulations (bunch splitting, merging, rotation, etc.). It is now a well-established operational tool, necessary at certain times in the cycle (beam injection, extraction, RF manipulations) and has been extensively used in all machines of the CERN PS Complex. Figure 4 presents an example of the phase-space distribution of a bunch injected to the LHC with a large energy error (top figure), reconstructed by tomography. After filamentation and due to special issues with the phase-loop, a hole in the center of the longitudinal phase-space appeared (bottom figure), which was preserved until the beginning of the ramp (~30 minutes later).

## *Long term evolution*

For most of the accelerators it is essential to monitor the longitudinal beam quality during the entire cycle. Since the cycle duration varies from a few seconds to many hours (LHC case), the frequency of the acquisitions has to be adapted. In this case, the evolution of beam parameters (bunch lengths and positions) is monitored, providing an overview of the beam stability, as well as the possibility to identify instability thresholds. An example of the bunch length evolution in an SPS proton cycle is shown in Fig. 5, where depending on the bunch intensity, different types of instabilities can be observed: a slow instability which manifests with slow emittance blow-up during the ramp (green trace) and a fast instability indicated by an abrupt emittance blow-up (red trace) [5].

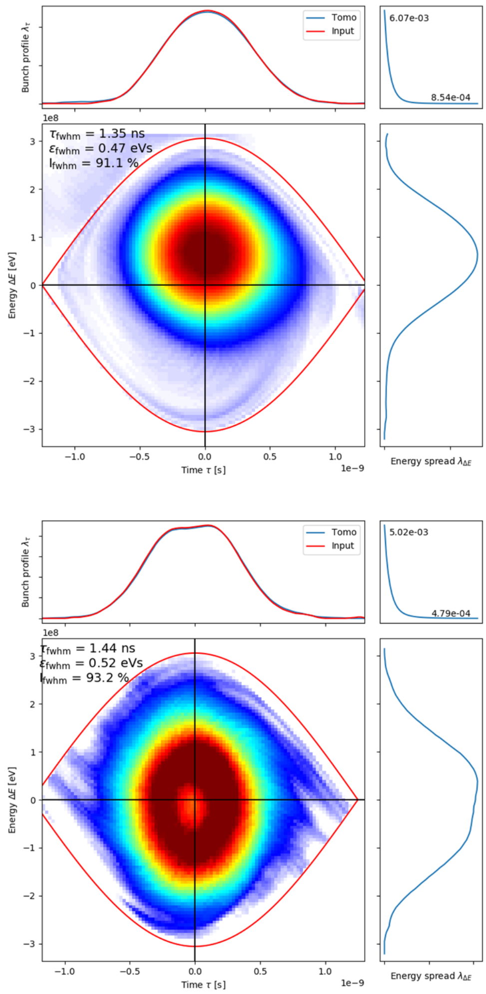


Figure 4: Tomographic reconstruction of a bunch in the LHC. Top: at the moment of injection. Bottom: 30 minutes later. A hole in the center of the longitudinal phase-space is generated due to the large energy error, and survived until the beginning of the ramp.

## MONITORING OF MULTI-BUNCH BEAMS

Similar type of plots, of the bunch parameters evolution along the cycle, can be generated to visualize the longitudinal beam quality in the case of multi-bunched beams. However, for the sake of simplicity, the average value of the bunch parameters can be plotted. The spread of the bunch parameters within the batch (rms or min-max values), which is related to the stability of the beam can be also shown in the same plot. An example of the average bunch length evolution of a nominal SPS proton cycle used for filling the LHC is shown in Fig. 6. One can see that all 4 PS batches, with 72 bunches each, become unstable at a certain moment in the cycle. The onset of instability is indicated by the black, vertical line and can be identified by the increase of the spread in the bunch lengths within the batches (shown as error bar and also with the points in the bottom of the plot).

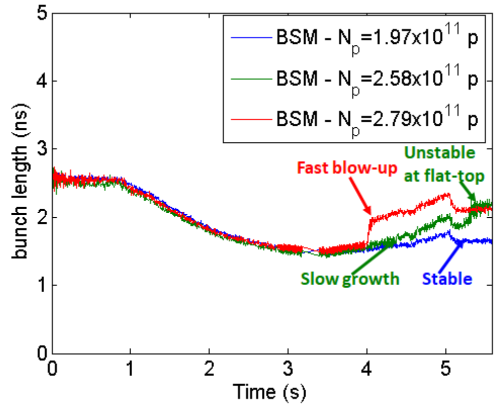


Figure 5: Bunch length evolution at the SPS in double harmonic operation (bunch shortening mode) for different intensities. Blue trace: stable bunch. Green trace: slow instability manifests with slow emittance blow-up during the ramp. Red trace: fast instability indicated by a sudden increase of the bunch length (microwave instability) [5].

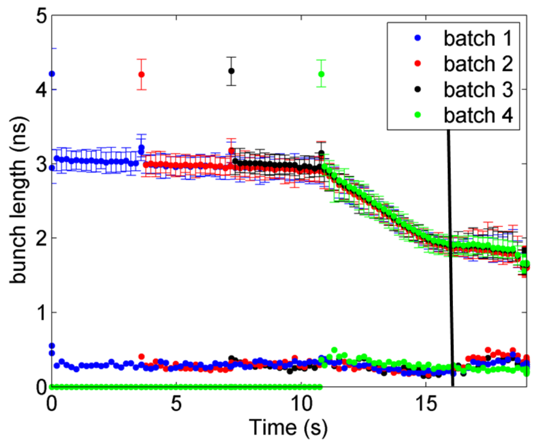


Figure 6: Average bunch length evolution along a nominal LHC proton cycle in the SPS. Different colours correspond to different batches of 72 bunches. The dots on the bottom show the bunch length spread within each batch. The black solid line corresponds to the onset of the instability.

It is clear that the increased number of bunches makes the need of faster data analysis algorithms during machine operation even more essential. Further reduction of the acquisition rate is necessary and possibly the time resolution needs to be reduced as well, in order to keep the amount of data in a reasonable range. Nevertheless, once the onset of an instability is identified the acquisition can be adjusted in order to resolve in more details the intra-bunch motion, at relevant moments during the cycle. An example of dipole and quadrupole oscillations of a 72-bunch batch, obtained from bunch profile measurements at the SPS extraction (last point in Fig. 6), is shown in Fig. 7. The large amplitudes of both dipole and quadrupole oscillations mean that the bunches are very unstable and that this beam should be prevented from transfer to the LHC.

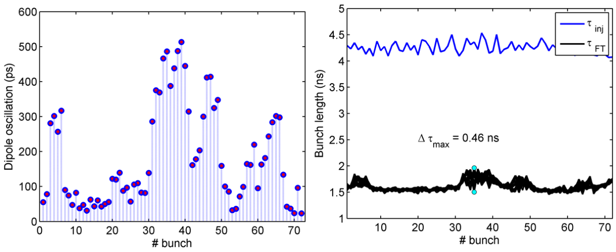


Figure 7: Example of dipole (left) and quadrupole (right) oscillations of a 72-bunch batch, obtained from bunch profile measurements at the SPS extraction. The large oscillation amplitudes (around 500 ps peak to peak) of many bunches indicate that this beam is very unstable.

## THE BEAM QUALITY MONITOR AT CERN

The importance of monitoring the longitudinal beam quality led to the implementation of the dedicated Beam Quality Monitor (BQM) [6, 7] essential for the daily operation of the SPS and LHC. The BQM measures longitudinal bunch profiles using a WCM pick-up, and monitors the longitudinal beam parameters (beam pattern, bunch lengths, bunch positions, and intensities) on a cycle-by-cycle basis. Fast algorithms for online analysis of the data have been developed and used. In particular, the bunch length is calculated using the Full-Width-Half-Maximum (FWHM) algorithm in order to save time. The FWHM of each bunch is quickly measured from the acquired beam profiles and from that the standard deviation $\sigma$ of the bunch is obtained assuming a Gaussian distribution. The bunch length is then defined as $\tau = 4\sigma$.

The role of the SPS BQM is of great importance since it ensures the beam quality at extraction in order to meet the LHC requirements (bunch lengths, intensities, etc.). The system, among other very important tasks, is specified to verify the stability of the beam (dipole and quadrupole oscillations) before extraction. In case any of its specified checks fails, the BQM removes the beam permit, preventing the beam from extracted into the LHC. A screenshot of the SPS BQM graphical user interface is shown in Fig. 8.

Similarly, the LHC BQM provides information on the longitudinal beam parameters (bunch length, position, intensity, beam pattern, etc.) along the cycle. A screenshot of the LHC BQM graphical user interface is shown in Fig. 9, where the average bunch length evolution of the two beams is shown. One can clearly observe a slow bunch lengthening during flat bottom due to RF noise and intra-beam scattering effects [10]. The irregular behaviour of the bunches during the ramp (green region in the plot of Fig. 9) is caused by the controlled longitudinal emittance blow-up, which is applied during the ramp and is essential to avoid longitudinal instabilities [8]. During that process, the average bunch length measurement from the BQM is actually used as an input to the feedback for the emittance blow-up, ensuring a specific value of the bunch length at top energy ($\tau$ ~1.2 ns).

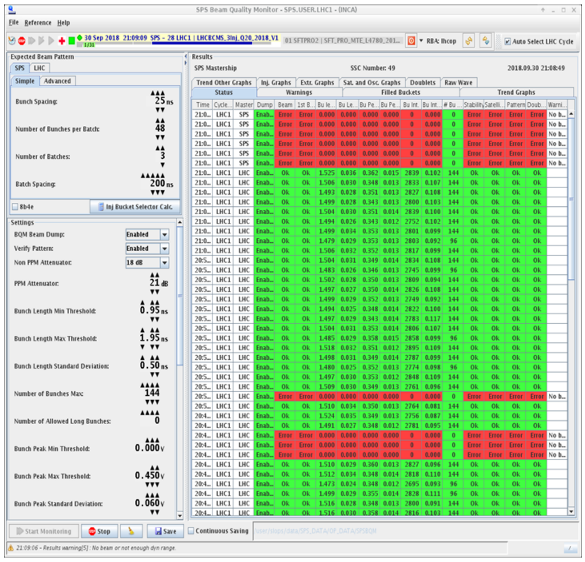


Figure 8: Screenshot of the SPS BQM graphical user interface (by F. Follin). On the left, the settings can be changed. On the right, each line shows the analysis results for a cycle: all checks green allow extraction, any check not passed (red) prevents extraction.

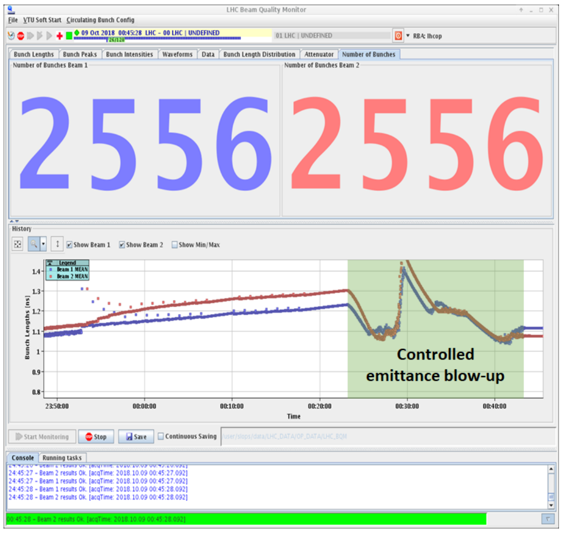


Figure 9: Screenshot of LHC BQM graphical user interface (by F. Follin), indicating the number of bunches circulating in each ring and the average bunch length evolution: bunch lengthening at injection energy and controlled longitudinal emittance blow-up during the ramp.

In the LHC, due to the long cycle, the acquisitions are done at 1 Hz, which means that it is not possible to resolve the intra-bunch motion (timescale of a few tens of synchrotron oscillations periods). However, the BQM still provides an overview of the beam stability, as well as the possibility to identify the onset of instability, since the average, minimum and maximum values of all circulating bunches are measured. An example of an instability which occurred in Beam 2 during operation is presented in Fig. 10. Due to technical problems, the controlled longitudinal emittance blow-up was not applied for this beam. This can be seen as a continuous reduction of the average bunch length during the ramp (marked by the two vertical dotted lines). As a result the instability threshold was reached and many bunches became unstable, which is indicated by the large bunch length spread.

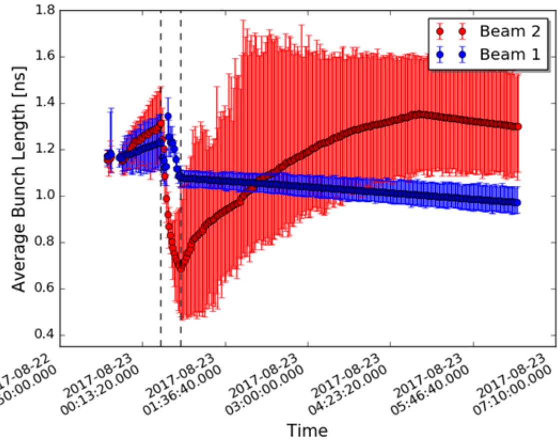


Figure 10: Example of the average bunch length evolution during a nominal LHC cycle. Continuous reduction of the average bunch length of Beam 2 during the ramp (marked by the two vertical dotted lines), since controlled longitudinal emittance blow-up was not applied. The instability threshold was reached and many bunches became unstable, indicated by the large bunch length spread.

## OBSERVATION OF BUNCH PHASES

Dipole oscillations of the bunches can be also monitored in the LHC by direct measurements of the bunch phase, using a beam phase-module, similar to the one used in the phase-loop [9]. This system determines the bunch position as the difference between the beam phase, measured from the WCM pick-up, and the RF voltage phase. Therefore, the effect of beam loading is excluded. This is not the case when bunch positions are obtained from the measured bunch profiles by the BQM, where the phase shift due to transient beam loading is also included and it is larger than the phase shift due to other effects of interest (resistive impedance and e-cloud). On the contrary, using the phase-module a relative accuracy of 0.01 degrees can be achieved in the bunch by bunch phase measurements (see Fig. 11).

Thanks to this accuracy, a diagnostic tool was implemented in the LHC (Fig. 12), in order to monitor the e-cloud activity during regular operation, as well as during the scrubbing runs that take place in the beginning of each year.

## CONCLUSION

Longitudinal beam quality monitoring is one of the main key components for a safe, reliable and efficient operation of particle accelerators. What needs to be monitored depends strongly on the requirements, issues and beam parameters of the specific machine. For the CERN accelerator complex an accurate knowledge of the bunch profile, which is generally measured with high bandwidth WCMs, is crucial both in day-by-day operation and during the various machine studies. Single- and multi-bunch analysis of the beam signal and the longitudinal parameters obtained, can be used to quickly identify instabilities or hardware problems and therefore increase the efficiency of the corrective actions. Other means to monitor the longitudinal beam quality, such as the peak-detected Schottky spectrum [11] (incoherent and coherent bunch motion) and the Beam Synchrotron Light Monitor Longitudinal [12] (satellite bunches and beam losses), also very important both in operation and machine studies were beyond the scope of this summary.

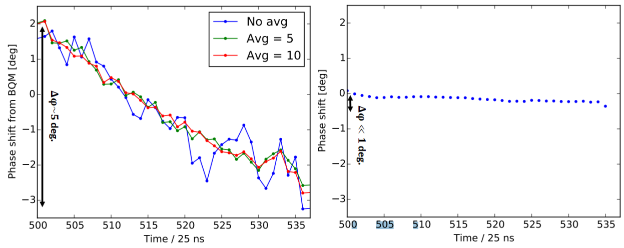


(a) From BQM (b) From phase module

Figure 11: Bunch-by-bunch phase shift computed from bunch positions measured by the BQM (left) and by the phase-module (right). The larger phase shifts in BQM (a) are due to beam loading. In both cases the one-turn feedback is off [9].

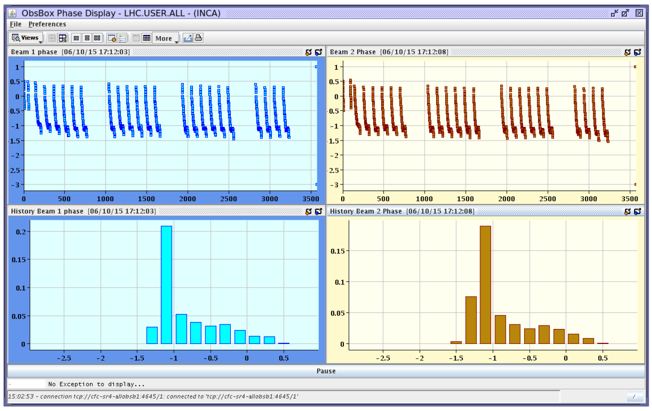


Figure 12: Screenshot of the graphical user interface (by G. H. Hemelsoet) of the bunch-by-bunch phase measurement with the phase-module. Clear e-cloud signatures along the bunch trains can be observed at the top plots, both for Beam 1 (left) and Beam 2 (right).

## ACKNOWLEDGMENTS

The author would like to thank T. Bohl, H. Damerau, J. Esteban Müller, I. Karpov, A. Lasheen, G. Papotti, E. Shaposhnikova, M. Schwarz, and H. Timko for many discussions and material provided in preparation of this talk.

## REFERENCES


[1] R. Jones, “Beam Instrumentation and Diagnostics”, CERN Accelerator School, Slangerup, Denmark, June, 2019.

[2] T. Bohl and J.F. Malo, “The APWL Wideband Wall Current Monitor”, CERN-BE-2009-006, CERN, Geneva, Switzerland, 2009.

[3] H. Damerau, “Timing, Synchronization and Longitudinal Aspects”, CERN Accelerator School, Erice, Italy, 2017.

[4] S. Hancock, S. R. Koscielniak, and M. Lindroos, “Longitudinal phase space tomography with space charge”, Phys. Rev. ST Accel. Beams 3, 124202 (2000).

[5] T. Argyropoulos, “Longitudinal microwave instability in a multi-RF system”, HB2014, East-Lansing, MI, USA, 2014.

[6] G. Papotti, T. Bohl, F. Follin, E. Shaposhnikova, “The SPS Beam Quality Monitor, from design to operation”, IPAC’11, San Sebastian, Spain, 2011.

[7] G. Papotti, T. Bohl, F. Follin, U. Wehrle, “Longitudinal beam measurements at the LHC: the LHC Beam Qualty Monitor”, IPAC’11, San Sebastian, Spain, 2011.

[8] H. Timko et al., “Coping with longitudinal instabilities using controlled longitudinal emittance blow-up ”, these proceedings.

[9] J. F. Esteban Müller, “Longitudinal intensity effects in the CERN Large Hadron Collider”, PhD thesis, EPFL, Lausanne, Switzerland, 2016.

[10] S. Papadopoulou *et al.*, ‘Update on luminosity model and emittance evolution in Run 2’, presentation at the 111th LBOC meeting, CERN, Geneva, Switzerland, 2019.

[11] E. Shaposhnikova, T. Bohl, and T. Linnecar, “Longitudinal peak detected Schottky spectrum”, HB2010, Morschach, Switzerland, 2010.

[12] A. Jeff et al. “Longitudinal density monitor for the LHC”, Phys. Rev. ST Accel. Beams 15, 032803 (2012).

# DESIGN OPTIMIZATION AND IMPEDANCE SOURCES IN LOW EMITTANCE RINGS (LER)

R. Nagaoka†, Synchrotron SOLEIL, Saint-Aubin, France

*Abstract*

There is a clear trend today that future ultra-low emittance rings adopt vacuum chambers with a significantly reduced radius of aperture. A big effort would be needed to keep the machine impedance on the same level as before.

## INTRODUCTION

A major goal of many of the next generation light source rings is to store an electron beam whose transverse emittance is diffraction limited over the main photon energy range of interest. This follows the fact that the principal figure of merit of the light source rings is the brilliance, which is inversely proportional to the product of electron beam transverse emittances and linearly proportional to the electron beam intensity. To increase the brilliance, therefore, we must lower the electron beam emittance and increase its intensity. As to the lowering of the emittance, the most effective and classically known method is to divide a bending magnet into many pieces and optically approach the condition known as the theoretical minimal emittance (TME) in each of these dipoles.

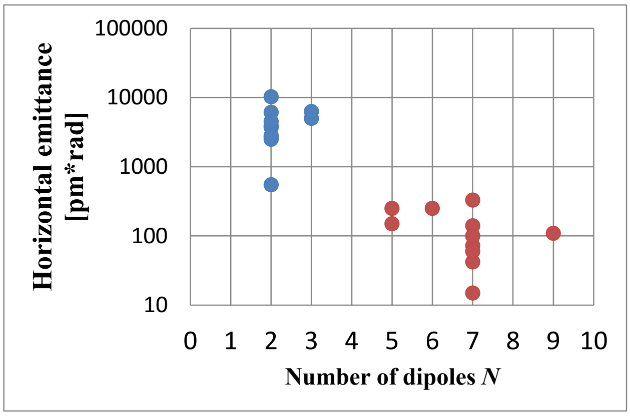


Figure 1: Horizontal emittance versus number of dipoles per achromat in light source rings (blue: existing, red: recent & future rings).

The TME scales as the inverse cube of the number of dipoles and so the effort is made to get as close as possible to this ultimate value. Over the last decades, there have been breakthroughs in beam dynamics studies, beam diagnostics and related technologies such as on magnets and vacuum, which allowed the number of dipoles per achromat to be increased from two or three of the 3rd generation light sources, to typically 7, thus enabling to gain a reduction factor of 30-40 on the horizontal emittance, according to the above cubic law (Fig. 1). Such magnet lattices are generally called MBAs (Multi-Bend Achromat).

There is however an important chain of consequences of the employed strategy generally appearing on the design aspects of modern and future low-emittance rings (LERs): The need to approach the TME condition in every dipoles requiring strong quadrupole focusing across the entire achromat (in the range of 100 T/m as compared to 20 T/m of the 3rd generation) → Reduced magnet bore radii → Smaller beam pipe half aperture $b$ → Poorer vacuum conductance → NEG coating in a large part of the ring for vacuum pumping (Fig. 2). In addition, MBAs generally require the magnet lattice to be tightly packed with dipoles, quadrupoles, sextupoles and all other standard vacuum components such as flanges, BPMs etc. A chain of consequences emerges on the electron beam dynamics as well: Approaching TME with MBA lattice → Small horizontal dispersion all along the ring, weaker radiation damping and large natural chromaticities → Strong sextupoles → Small transverse dynamic apertures. Ultra-low emittance → Enhancement of IBS and Touschek scattering.

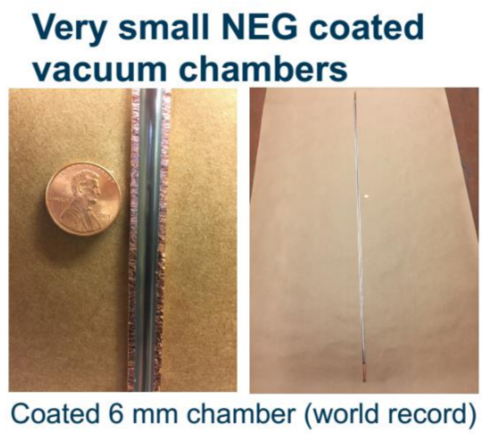


Figure 2: NEG coating on a 6-mm diameter beam tube at Advanced Light Source (D. Robin, LER2016, SOLEIL [1]).

Table 1 (found in the Appendix due to its size) presents the half aperture $b$'s adopted for some of the newly constructed and future ultra LERs. We can see that the chains described above have serious influences on the beam collective effects: First of all, the smaller vacuum chamber aperture globally around the ring shall inevitably enhance the impedance. The extensive use of NEG coating shall also have a non-negligible impact of the machine impedance (to be addressed again later). The smaller

† ryutaro.nagaoka@synchrotron-soleil.fr

horizontal dispersion shall reduce the magnitude of momentum compaction which in turn shall influence the beam collective motions. The weaker radiation damping tends to lower the instability thresholds.

## CHARACTERISTICS OF THE RESULTANT IMPEDANCES

With much smaller vacuum chamber apertures adopted all around the ring, both the geometric and resistive-wall impedances are expected to become much larger for the ultra-low emittance rings. Indeed, it is well known that the longitudinal impedance scales inversely linear or higher and the transverse impedance to $b^{-2}$ and higher. In particular, the transverse resistive-wall impedance has the well-known dependence of inversely to the cube of *b*. For this reason, it is clear that the transverse impedance of next generation LERs shall be resistive-wall dominated. Other major contributors are usually tapers, BPMs, shielded bellows, flanges, cavities, kickers, absorbers, and scrapers etc. due to their geometry. While insertion devices, particularly those which are under vacuum, would always remain as large contributors due to their particularly small gaps, the taper transitions tend to have smaller angles as the apertures in the magnet sections themselves are smaller. However, the last is not true with cavity tapers so they are expected to remain as large contributors in the impedance budget. Due to the enhanced proximity to the beam and to their high number, components such as BPMs are expected to make large contributions for the impedance and therefore, special care for the accurate evaluation of their impedances, both amplitude and frequency wise, along with effort to minimize them with optimized designs is demanded. A triangular shape BPM button electrode developed at SIRIUS is a good example, pushing the dangerous trapped mode frequencies away to high frequencies and keeping the button diameter large not to lose the BPM reading accuracy, which is vital for ultra LERs (Figs. 3). The 3D EM field solvers such as CST microwave studio [2], GdfidL [3] and ECHO3D [4] are widely used in the community to evaluate and minimize the geometric impedance of various vacuum components.

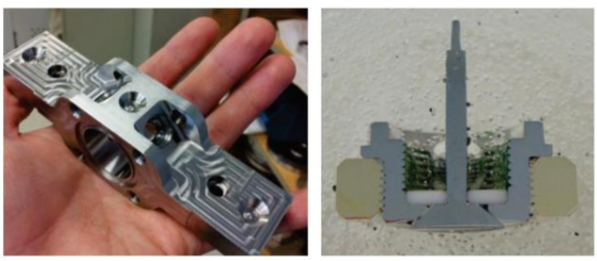

Figure 3: Bell-shaped BPM button developed at SIRIUS, optimized to increase the button cut-off frequency without losing the button sensitivity (A.R.D Rodrigues et al., IPAC2015 [5]).

The fact of chamber walls getting much closer by to the beam requires all kinds of surface impedances involved to be well understood and controlled. This is particularly true for those arising from coating on the surface, whether it is the coating of poor electric conductivity materials such as NEG on a good conductivity substrate such as copper, or the opposite such as titanium coating on a ceramic chamber to improve the image current flow on the wall. Many studies have been made analytically with methods such as field matching technique and surface impedance models [6]. Numerical codes such as ImpedanceWake2D (IW2D) developed at CERN [7] are also widely used. Since vacuum pumping using NEG coating appears to become an indispensable technique for future ultra-low emittance rings, the possible impact of NEG coating on the machine impedance must be carefully studied. An early observation was made at ELETTRA using the transverse coherent detuning of the beam [8] (Fig. 4).

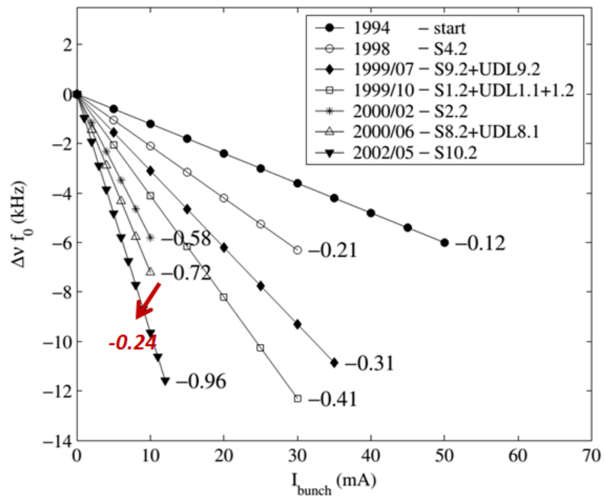


Figure 4: Increased transverse coherent detuning by nearly a factor of 2 observed at ELETTRA for a NEG-coated chamber as compared with those w/o coating [8].

A first analysis using the field matching method had shown that a micron level thin NEG coating would be transparent to beam from its real part of the impedance, but its imaginary part would be enhanced by nearly a factor of two in the frequency range seen by the beam [9]. The impedance budget evaluated at SIRIUS indeed indicates that the impedance is dominated by the resistive-wall and that there is the aforementioned enhancement by roughly a factor of two in the reactive part [10] (Figs. 5). The frequency dependence of the conductivity of NEG was studied at CERN showing factors of worsening towards hundreds of GHz [11] (Figs. 6 upper). Recent studies reveal the importance of the physical state of NEG as an outcome of deposition on the electric conductivity [12] (Figs. 6 lower).

## CONCERNED COLLECTIVE EFFECTS AND INSTABILITIES

The beam-induced heating of vacuum components would probably be the most concerned collective effect for many ultra LERs with low-gap chambers, as a trouble on a single component can seriously ruin machine operation. Not only, but the FBII (Fast Beam-Ion Instability) that causes beam losses and prevents ones from operating the ring in ¾ filling at 500 mA at SOLEIL is considered to be originated in beam-induced heating of (some unknown) vacuum components generating sudden local outgassing [13]. Loss factors and trapped modes must be carefully studied from the geometric and non-geometric (metallic coating) impedance of each vacuum component, and the results, formulated in beam-induced power, need be evaluated in terms of "heat (temperature)" in collaboration with drafting office engineers by tracing the passage of the EM fields and their possible conversion into heat.

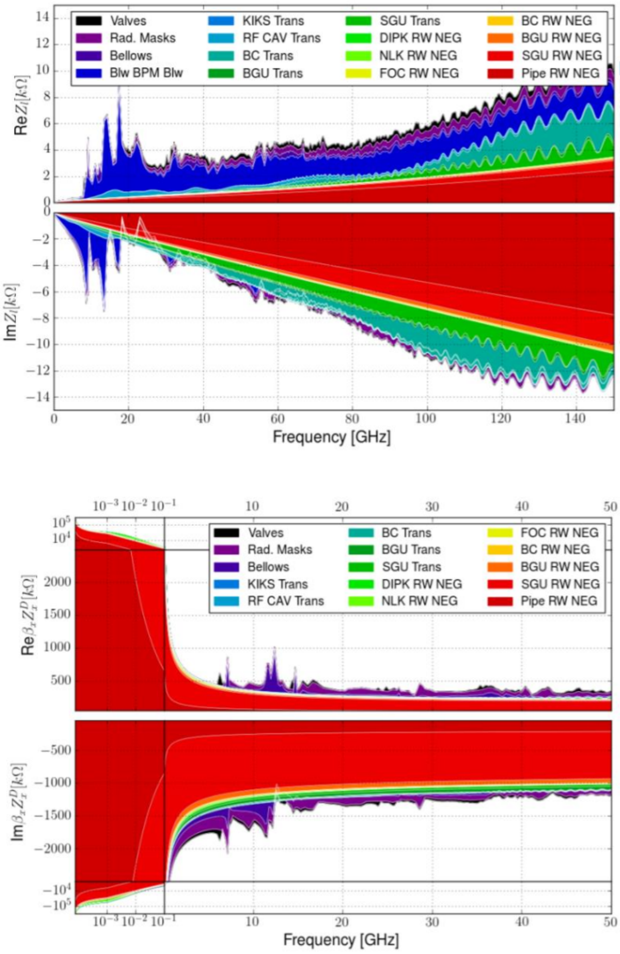


Figures 5: (Upper) longitudinal and (lower) transverse impedance budget obtained for SIRIUS. The red part represents the resistive-wall contribution [10].

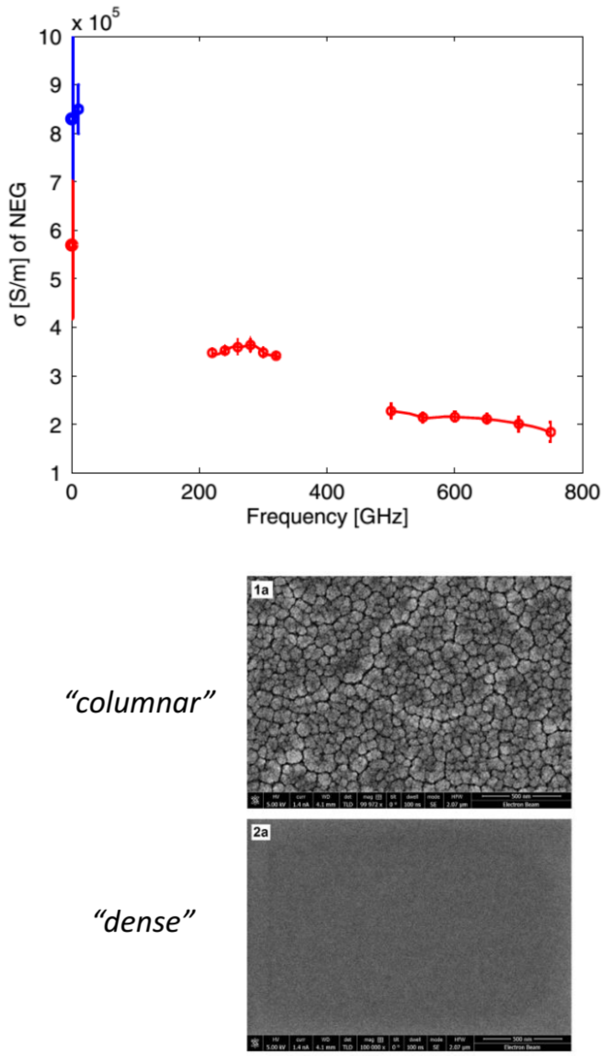


Figures 6: (Upper) experimental study of NEG electric conductivity versus frequency [11]. (Lower) experimental study of surface resistivity of two types of NEG [12].

Transverse single bunch instabilities (TMCI, head-tail and post-head-tail), which are already strongly existing in the present LERs, can only be expected to get stronger. However, some of the physical effects which are likely to get stronger in future LERs such as the transverse nonlinear optics and bunch lengthening with harmonic cavities, may give rise to significant mitigating (stabilizing) effects. Care must also be taken since it was recently found, however, that additional longitudinal tune spread arising from harmonic cavities could significantly lower the TMCI threshold [14]. The effectiveness of the conventional stabilization methods such as shifting of the chromaticity to positive and bunch by bunch feedback must be well studied. Longitudinally, bunch lengthening is expected to be always present and may even be enhanced due to the reactive effect of NEG coating. The microwave instability, for which the standard longitudinal feedback provides no cure, must be avoided above all in LERs that make use of higher harmonics of the undulator spectra as the associated beam energy spread widening seriously spoils them. Since the instability is excited due to high frequency resistive components of the longitudinal impedance, bunch lengthening with harmonic cavities could help mitigate the instability. Since MBA lattices tend to have longer radius of curvature for bending magnets, along with reduced chamber apertures, the so-called the shielding parameter of the instability [15] should tend to increase. One would therefore expect the CSR instability to be less influential. Detailed studies are required to verify such zeroth order reflection.

The resistive-wall (RW) instability may be said to be the most concerned beam instability for many present and future light source rings as the resistive-wall impedance is large for these machines as already explained and as most machine operate in high multibunch current where the instability becomes important. For example at SOLEIL whose nominal current is 500 mA in the multibunch filling, the threshold of instability is merely around 30 mA vertically at zero chromaticity. However, the threshold generally rises quickly as we shift the chromaticity to positive due to head-tail damping (Figs. 7 left). Many light sources actually operate in such a manner. However, the chromaticity shift may induce beam lifetime drop through reduced off-momentum dynamic aperture. Bunch by bunch feedback may be used instead to avoid such issues. Both the time domain multibunch tracking and frequency domain Vlasov solvers can well follow these instabilities in general. An example of the results obtained with a Vlasov solver is shown in Figs. 7 (right) for the parameters considered for the SOLEIL upgrade, where the vacuum chamber half aperture of $b$ = 5 mm is assumed. The low thresholds found with the resistive-wall impedance alone are alarming, but several elements that are not yet included in this computation, such as the broadband impedance, the low beta nature of the upgraded lattice, as well as bunch lengthening cavities, found to bring about significant stabilization in a recent study for this instability as well [16], are expected to much improve the situation. Caution must be taken if there is a non-negligible portion of non-circular cross section vacuum chambers in a ring, as quadrupolar wakes arising from them may be strong enough, due to their small aperture, to distort the ultra-low emittance tuning and spoil the target emittance. The effect is expected to be particularly strong for electrons in a high intensity bunch. Studies made at SOLEIL indicated that the betatron tune shifts in an intense bunch of 20 mA get nearly 20 times larger than in multibunch at 500 mA (Fig. 8) [17]. Since the quadrupole wakes come from the imaginary part of the impedance, NEG coating is expected to enhance the effect.

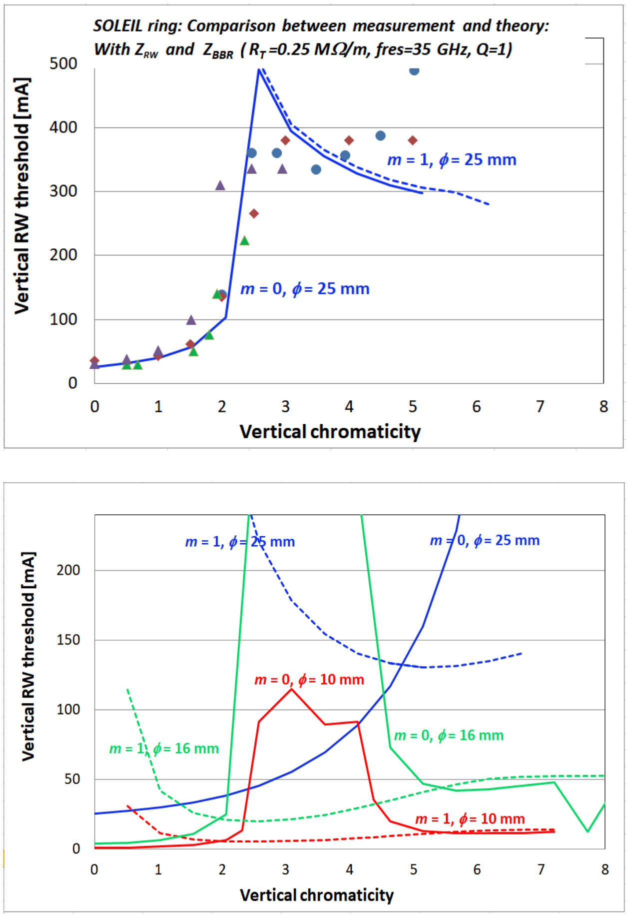


Figures 7: (Upper) vertical resistive-wall (RW) instability threshold versus chromaticity, computed with the expected RW and broadband resonator impedance, in comparison with measured thresholds for the present SOLEIL ring. (Lower) expected RW instability threshold for the SOLEIL upgrade for different $\phi = 2{\times}b$ values, by taking into account the RW impedance alone (i.e. no headtail damping). Index $m$ stands for azimuthal (headtail) modes.

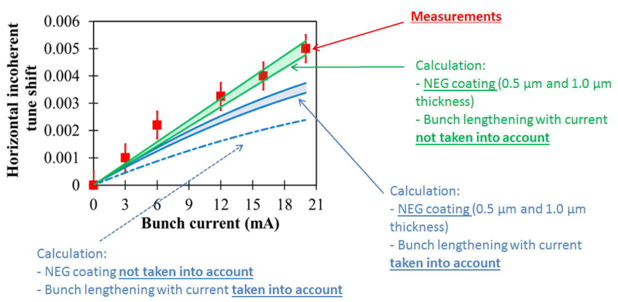


Figure 8: Measured (red square) horizontal incoherent tune shift as a function of bunch current. Values expected from theory: w/o NEG coating and with bunch lengthening (blue dashed line); with NEG coating (0.5 and 1.0 µm thickness) and with bunch lengthening (blue area); with NEG coating (0.5 and 1.0 µm thickness) and w/o bunch lengthening (green area) [17].

## SUMMARY

There is a clear trend today that future ultra-low emittance rings adopt vacuum chambers with a significantly reduced radius of aperture $b$. As the wakefields scale basically as $b^{-n}$ ($n \geq 1$), their sensitivity to the sources of impedance could only be larger. A big effort would be needed to keep the machine impedance on the same level as before. Innovative vacuum components designs, including coating technology, should be made in collaboration with machine physicists to keep machine heating and beam instability under control. Special efforts would be required to avoid heating due to ceramic chambers and trapped modes, as well as to develop means to cleverly evacuate generated heat without damaging vacuum components. Due to its $b^{-3}$ dependence, the contribution of the transverse resistive-wall impedance to the total impedance budget would tend to dominate the rest. For the SOLEIL case as an example, the value of $b$ for the standard chamber of 12.5 mm is to be reduced to 5 mm for the upgraded ring, meaning that the transverse resistive-wall impedance shall increase by a factor $(12.5/5)^3 = 15.6$. The NEG coating would non-negligibly enhance the impedance, but its impact should appear in the reactive part amplifying bunch lengthening and coherent tune shifts as long as the beam is only sensitive to the low frequency part of the impedance. The cross section of low-gap chambers may better be kept circular to avoid quadrupolar wakes that could spoil the ultra-low-emittance tuning especially for high intensity bunches. Due to lower vacuum chamber gaps and the proximity of vacuum components in future rings, the risk of wakes interference should be carefully monitored.

## ACKNOWLEDGEMENT

The author thanks M. Aiba (SLS), R. Bartolini (DIAMOND), M. Borland (APS), F. Cullinan (MAXIV), E. Karantzoulis (ELETTRA), V. Smaluk (NSLS-II), M. Venturini (ALS), S. White (ESRF), H. Xu (IHEP) for providing him with information on their (future) machines. He thanks A. Gamelin and other colleagues at SOLEIL for helpful discussions.

## REFERENCES

[1] D. Robin, "Overview of ALS Project", LER2016, Synchrotron SOLEIL, October 2016

[2] CST Microwave Studio, https://www.cst.com/Products/CSTMWS

[3] W. Bruns, "The GdfidL Electromagnetic Field Simulator", http://www.gdfidl.de

[4] I. Zagorodnov, T. Weiland, Phys. Rev. ST Accel. Beams **8**, 042001 (2005)

[5] A.R.D Rodrigues et al., "SIRIUS Accelerators Status Report", IPAC2015, Richmond, VA, USA

[6] S. Arsenyev, "Analytical Impedance Estimates for Coated Surfaces", ALERT2019, Ioannina, Greece, July 2019

[7] N. Mounet et al., "CERN IW2D code", https://twiki.cern.ch/twiki/bin/view/ABPComputing/ImpedanceWake2D

[8] E. Karantzoulis et al., Phys. Rev. ST Accel. Beams, **6**, 030703 (2003)

[9] R. Nagaoka et al., "Study of Resistive-Wall Effects on SOLEIL", EPAC2004, Lucerne, Switzerland, July 2004

[10] F.-E. De Sá, "Study of Collective Effects in SIRIUS", LER2016, Synchrotron SOLEIL, October 2016

[11] E. Koukovini-Platia et al., Phys. Rev. Accel. Beams **20**, 011002, 2017

[12] O. B. Malyshev et al., NIM **A844** (2017) 99–107

[13] R. Nagaoka et al., "Fast Beam-Ion Instability Arising from Local Outgassing", LER workshop TWIICE, EuCARD-2, Synchrotron SOLEIL, 2014

[14] M. Venturini, Phys. Rev. Accel. Beams **21**, 024402

[15] R. Nagaoka and K. Bane, "Collective effects in a diffraction limited storage ring", J. Synchrotron Rad. **21**, 937 (2014)

[16] F. J. Cullinan et al., Phys. Rev. Accel. Beams **19**, 124401 (2016)

[17] P. Brunelle et al., Phys. Rev. Accel. Beams **19**, 044401 (2016)

## APPENDIX

| | E [GeV] | b [mm] | crossection | remarks | b [mm] | crossection | remarks | b [mm] | crossection | remarks |
|---|---|---|---|---|---|---|---|---|---|---|
| **ALS-U** | 2 | **6.5** | circular | Strongly focusing sections | **10** | circular | Outer arc sections | | | |
| **APS-U** | 6 | **11** | circular | Hybrid of NEG coated Cu, Cu plated SS with NEG strips, bare Al | **3 × 8** | non-circular | Al chambers, 125 m in total | **3** | circular | Al chambers, 50 m in total |
| **DIAMOND-II** | 3.5 | **10** | circular | Thickness 1 mm, Chamber design at early stage | | | | | | |
| **ELETTRA-II** | 2 - 2.4 | **11** | circular | Cu and SS in some parts | **4.5 × 20** | non-circular | Al NEG coated (4 and 5 m long) | **3** | | IVU × 3 (4 m); Wiggler×2 with b = 5 mm (1.5 m) Al + NEG |
| **ESRF-EBS** | 6 | **10** | | In moderate focusing sections | **6.5** | | In strongly focusing sections | **4** | | Straight sections |
| **HEPS** | 6 | **11** | circular | Standard chambers | **2.5** | non-circular | CPMU chamber | **~4** | non-circular | IAU chamber |
| **MAXIV 3 GeV** | 3 | **11** | circular | copper, NEG coated | **4 × 18** | non-circular | Aluminium, EPU chambers, NEG coated, 4 m long | **2** | non-circular | IVUs and wiggler 2.1 m long |
| **MAXIV 1.5 GeV** | 1.5 | **11 × 20** | elliptical | SS | **11 × 29** | non-circular | SS, Arc sections | **4 × 18 (or 4 × 28.5)** | non-circular | EPU chambers, NEG coated, 3.2 m long |
| **NSLS-II** | 3 | **12.5 × 38** | non-circular | | **2.5 - 3.5** | non-circular | IVU × 10 | **6.0 - 8.0** | non-circular | EPU × 7; DW × 3 have b = 7.5 mm |
| **SLS-II** | 2.4 | **9** | circular | Design at early stage (cf. A. Zandonella's talk) | | | | | | |
| **SOLEIL-U** | 2.75 | **5 to 8?** | circular? | Likely be NEG coated | | | | | | |

Table 1: Half aperture $b$ values for some of the recently constructed and proposed LERs.

# LOW IMPEDANCE DESIGN WITH EXAMPLE OF KICKERS (INCLUDING CABLES) AND POTENTIAL OF METAMATERIALS

C. Zannini*, M. Barnes, N. Biancacci, A. Danisi, E.Koukovini-Platia, E. Métral, G. Rumolo, B. Salvant,
CERN, 1211 Geneva, Switzerland

*Abstract*

Unmatched terminations of single elements were recently identified to be responsible for beam instabilities in the CERN PSB and LEIR machines. Impedance models are needed to estimate the impedance of similar devices and to assess potential intensity limitations. A circuital model that includes the effect of coupling to cables on the beam coupling impedance will be discussed. Moreover, examples of low impedance design with special emphasis on the mitigation of the impedance of ferrite kickers (e.g. longitudinal serigraphy) will be presented and guidelines for optimized impedance design will be provided. Finally, the potential of metamaterials for impedance mitigation will be discussed.

## INTRODUCTION

A correct modeling of the beam coupling impedance of accelerator elements is essential to identify potential issues and to build an accurate impedance model of the complete accelerator for beam dynamics studies. The beam coupling impedance can cause issues on single accelerator elements (equipment degradation and damage due to induced heating or sparking) as well as instability of the particle beam. Both the undesired effects translate into intensity limitations. Therefore, the optimization of the beam coupling impedance is crucial to push the performance of the accelerators and to achieve the desired beam. In order to optimize the design of accelerator elements, firstly the consistency of the impedance computation tools should be verified. Secondly, the completeness of the impedance models should be ensured through different (and complementary) sets of bench and, if possible, beam-based measurements. Thirdly, impedance checks of any layout modification or new device installations should be performed. Finally, the impedance sources causing performance limitations should be identified and impedance optimization strategies implemented. The choice of the most appropriate strategy requires the knowledge of the knobs to manipulate the impedance. Simplified formulae where all the main dependencies are explicit or step by step simulations, which allow a deep understanding of the impedance mechanism, are very useful to define the optimization strategy.

## SPS FERRITE LOADED KICKERS

In this section the example of the SPS ferrite loaded kickers will be discussed to give an example of how a deep understanding of the impedance mechanism can be reached. A kicker is a special type of magnet designed to abruptly deflect the beam off its previous trajectory, to inject the beam into a ring or extract it to a transfer line or to a beam dump. H. Tsutsui derived a field matching theory to obtain the longitudinal [1, 2] and transverse dipolar [3] impedance of a geometrical model made of two ferrite blocks inserted inside a metallic chamber (see Fig. 1), for an ultra-relativistic beam. The model for the ferrite permeability $\mu$ as a function of frequency $f$ can be obtained from a first order dispersion fit on measured data:

$$\mu = \mu_0 \cdot \mu_\mathrm{r} = \mu_0 \left(1 + \frac{\mu_\mathrm{i}}{1 + \mathrm{j}\mathrm{f}2\pi\tau_\mathrm{u}}\right) \tag{1}$$

where $\mu_i$ and $\tau_u$ are the parameters of the fit and $\mu_0$ is the vacuum permeability. The ferrite dielectric properties are characterized by a complex permittivity $\varepsilon$:

$$\varepsilon = \varepsilon_0 \cdot \varepsilon_r = \varepsilon_0 \left(\varepsilon_r' - \frac{j\,\sigma_{el}}{2\pi f \varepsilon_0}\right) \tag{2}$$

where $\sigma_{el}$ is the DC electrical conductivity of the ferrite, $\varepsilon_0$ the vacuum permittivity and $\varepsilon_r'$ the dielectric constant. Tsutsui's theoretical impedance calculations were compared to HFSS [4] simulations and subsequently to measurements of PS and SPS kickers in references [5–7]. In his paper [3], H. Tsutsui only derived the transverse dipolar impedances, while the quadrupolar part was first derived in [8]. The analytical calculations of the beam impedance using, for instance, the models of Tsutsui are unfortunately restricted to simplified geometrical models so that the equations can be solved analytically. We will gradually move from the simplified models to more realistic, and hence complicated, structures.

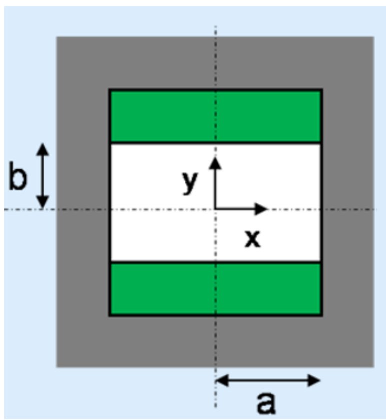


Figure 1: Geometrical kicker model described by Tsutsui: vacuum (white); 2 ferrite blocks (green) transversely surrounded by perfect electric conductor (gray).

* carlo.zannini@cern.ch

### *EM simulations of SPS kickers*

First of all, CST Particle Studio Wakefield simulations [9] of the model of Fig. 1 have been performed [10, 11]. These simulations have been compared to the theoretical impedance obtained with the H. Tsutsui formalism for the longitudinal and the transverse impedances [12]. The very good agreement between the analytical model and the simulations makes the Wakefield solver of CST Particle Studio a reliable tool to simulate the impedance of dispersive materials such as ferrite. The Tsutsui model of Fig. 1, despite its simplicity, could explain both the "negative" total horizontal impedance observed in bench measurements [12] and the positive horizontal tune shift measured with beam in the SPS [6]. However, in this simple model several features of the kicker magnets have been neglected.

As a first step, the impedance of a C-Magnet kicker without the High Voltage (HV) conductor has been calculated analytically [13]. However, a device of finite length inserted in the vacuum tank and equipped with an inner conductor can support propagation of a Quasi-TEM mode when interacting with the beam. The device behaves as a transmission line formed by the vacuum tank and the inner conductor which are continued on the external cables and closed on the appropriate circuit terminations. This behaviour disappears as soon as we allow for 2-D geometries (infinite in the longitudinal direction) because the Quasi-TEM mode arises at the discontinuities. For this reason, if we want to consider the interaction of the beam with the Quasi-TEM mode, we must resort to a 3D C-Magnet model (see Fig. 2).

In the frame of an improvement of the kicker impedance model we performed a step by step simulation study starting from the simplest model and introducing one by one the new features that bring the model gradually closer to reality. This approach allows for a good understanding of the different contributions brought to the kicker impedance by the different aspects. First, the ferrite is assumed to be C-shaped and the whole finite length device is inserted in the vacuum tank and equipped with an inner conductor [14].

In order to further approach a more realistic model other aspects must be included: the cell longitudinal structure (also called segmentation), transitions between the ferrite blocks and the beam pipe, external coupling circuits, geometry outside of the ferrite yoke and shieldings.

**Effect of the longitudinal segmentation** C-cores ferrites are sandwiched between HV capacitance plates. Plates connected to ground are interleaved between the HV plates: the HV and ground plates form a capacitor to ground. One C-core, together with its HV and ground capacitance plates, is named a cell [15]. The impact of segmentation in cells on the beam coupling impedance has been studied in detail. In the frequency range of interest (from few tens of MHz up to few GHz) for the SPS impedance model, the segmentation is found to have a significant effect only on the injection kickers (MKPs). For the other kickers the effect of the segmentation is negligible since the wavelength is sufficiently small compared to the cell length.

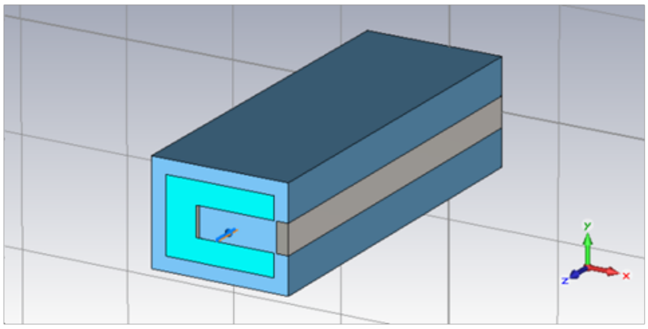

Figure 2: Geometric models for impedance calculation: ferrite in turquoise, perfect electric conductor in gray and vacuum in blue.

The 3-D simulation model of the SPS injection kicker (MKP-L) is illustrated in Fig. 3. The kicker module is divided into 22 cells, each of 26 mm length. The effect of the longitudinal segmentation on the beam coupling impedance is expected to be significant since the wavelength has been estimated to be comparable with the cell length [16]. As an example, in order to show the effect of such a dense longitudinal segmentation, we compared in Fig. 4 the longitudinal impedance with and without segmentation. The effect of segmentation is visible below 1 GHz, where a significant enhancement of the impedance is observed.

MKP-L is presently the bottleneck for the CERN-SPS beam induced heating. A design solution to optimize the impedance with serigraphy is available [17] and the prototype validation is ongoing. The impedance models of the segmented SPS injection and extraction kickers have been successfully benchmarked with bench measurements [16, 17].

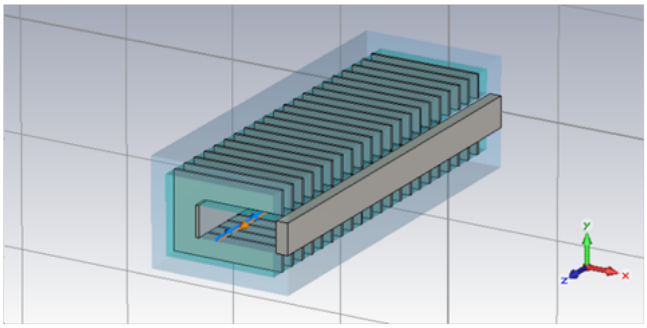

Figure 3: Advanced model of the MKP kicker module.

**SPS extraction kicker: effect of the serigraphy** Due to heating issues [18] the original design of these kickers was modified [19]. Interleaved fingers were printed by serigraphy directly on the ferrite. The beam induced heating is directly related to the beam power loss through the real part of the longitudinal impedance. The serigraphy results in a strong reduction of the real part of the longitudinal impedance over a broad frequency range [7, 19, 20]. The broad-band peak shifts from ≈ 600 MHz to ≈ 3.3 GHz

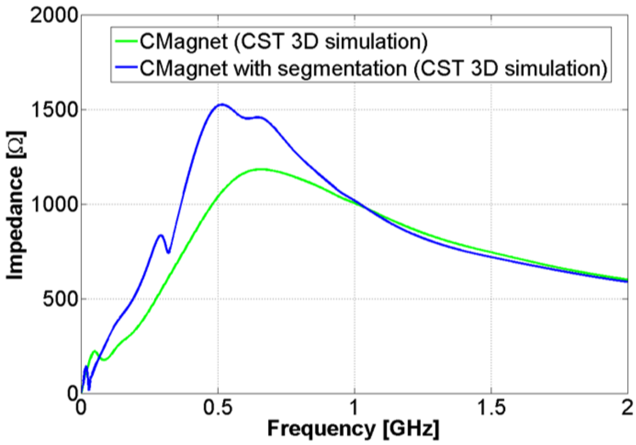


Figure 4: Comparing the longitudinal impedance for the MKP-L with and without segmentation.

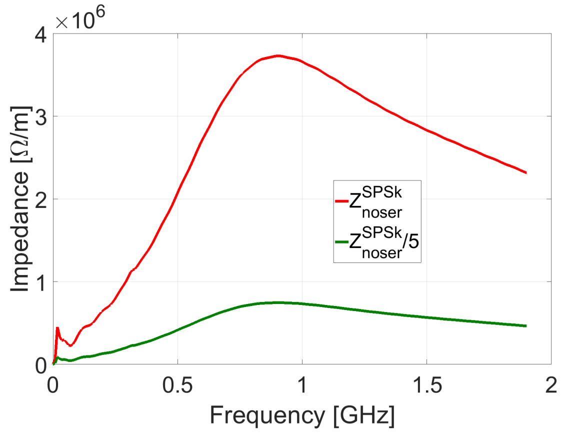


Figure 5: Impedance model of the SPS kickers without serigraphy and same impedance reduced by a factor of 5.

and at the same time the serigraphy introduces a clear resonance at 44 MHz [21]. This resonance was studied in detail and was identified to be a quarter wavelength resonance on the silver fingers [16, 21]. To minimize the impact of this resonance on the beam induced heating the finger length could be optimized to shift the resonance frequency as far as possible from the beam spectrum lines. This required shortening the serigraphy length by 20 mm [22]. The solution has been implemented and experimentally validated during SPS scrubbing runs [23]. This solution has given an additional 40% margin in the SPS bunch intensity, which is crucial for the HL-LHC beams.
The example of the SPS ferrite loaded kickers shows the importance of a step by step approach from simplified to complex models involving 3D electromagnetic simulations and analytical calculations to reach a very good understanding of the impedance mechanism and to find the best design solution for impedance optimization.

## IMPEDANCE REDUCTION IS NOT ALWAYS BENEFICIAL

Impedance optimization is an extremely complex task that requires a global view of the impedance induced effects and of the machine criticalities. The best option is not always the one with the lowest impedance. For example, while reducing the longitudinal impedance is beneficial in terms of beam induced heating, the reduction of the transverse impedance could be detrimental for beam stability. To illustrate this concept, the transverse impedance model of the SPS extraction kickers in their original design has been taken into consideration, as well as the same impedance reduced by a factor of 5 (see Fig. 5).

The effect on beam dynamics can be qualitatively assessed using the concept of effective impedance. For bunched beams the impedance is sampled at an infinite number of discrete frequencies given by the mode spectrum. An "effective coupling impedance" can then be defined as the sum over the product of the coupling impedance and the normalized spectral density. The "effective coupling impedance" is required for the calculation of both longitudinal and transverse complex tune shifts of bunched beam and can be defined in the transverse plane as [24–26]:

$$(Z_\perp)_{\text{eff}} = \frac{\sum\limits_{p=-\infty}^{p=\infty} Z_\perp\left(\omega' + \omega_\beta\right) h_l\left(\omega' + \omega_\beta - \omega_\xi\right)}{\sum\limits_{p=-\infty}^{p=\infty} h_l\left(\omega' + \omega_\beta - \omega_\xi\right)} \tag{3}$$

Here $h_l(\omega)$ is the power spectral density, $\omega_\beta$ is the betatron angular frequency, $\omega_\xi$ is the chromaticity frequency shift and $\omega' = \omega_0 p + l\omega_s$ where $\omega_0$ is the revolution angular frequency, $\omega_s$ is the synchrotron frequency and $l$ determines the type of oscillations (the case $l = 0$ describes the single-bunch head-tail instabilities). For a Gaussian bunch, $h_l(\omega)$ can be written as:

$$h_l\left(\omega\right) = \left(\frac{\omega\sigma_z}{c}\right)^{2l} e^{-\frac{\omega^2\sigma_z^2}{c^2}} \tag{4}$$

where $\sigma_z$ is the standard deviation of the Gaussian bunch profile (root mean square (RMS) bunch-length) and $c$ is the speed of light in vacuum. The real and the imaginary parts of the "effective impedance" give the growth rate and the frequency shift of the mode under consideration respectively. [26–29].

If the real part of $(Z_\perp)_{\text{eff}}$ is negative, the beam can become unstable. The real part of the transverse impedance is an odd function of frequency. Therefore, for the mode $l = 0$, simply assuming that the impedance is positive for positive frequencies leads to the conclusion that this mode would be stable for positive spectral shift and unstable for negative spectral shift (see Fig. 6). The situation is different if we consider higher mode numbers. For a given chromatic shift the sign of the effective impedance depends on the impedance type. Therefore, no general rule for stability criteria can be given for these modes. Figure 7 for example shows an illustrative view of the mode $l = 1$ together with a capacitive

impedance (decreasing with frequency) and an inductive impedance (increasing with frequency). For the resistive wall impedance (capacitive impedance) and for $\xi < |\xi_{max}|$ ($\xi_{max}$ is defined as the chromaticity value at which the first sign inversion of the growth rate occurs) the mode $l = 1$ is destabilizing for positive chromaticity and stabilizing for negative chromaticity, the situation is exactly reversed in the case of the impedance of ferrite loaded kickers (inductive impedance up to almost 1 GHz).
The overall effect of different impedance contributions depends on the weight of stabilizing and destabilizing effects. An inductive impedance has a stabilizing effect for mode $l = 1$ and $\xi > 0$. Reducing this kind of impedance makes the situation worse. Therefore, coming back to the example of Fig. 5 reducing the impedance by a factor of 5 also reduces the stabilizing effect of this impedance for positive chromaticity (see Fig. 8) making the overall situation in terms of beam stability worse (see Fig. 9). The results obtained have been also confirmed with the DELPHI Vlasov solver [30] (see Fig. 10).

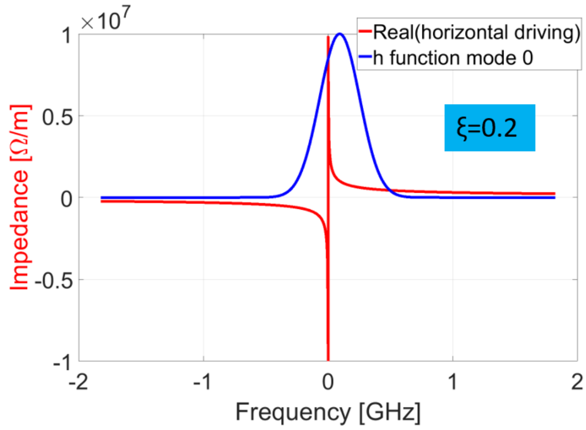


Figure 6: SPS wall impedance model (red) and power spectral density for the mode $l = 0$ in arbitrary units for a chromaticity $\xi = 0.2$ (blue) at injection energy for the Q20 optics.

## IMPEDANCE DUE TO COUPLING WITH CABLES

As previously described, as a first step a ferrite loaded kicker can be modeled as two parallel plates of ferrite surrounded by perfect electric conductor, i.e. the Tsutsui model. This model is expected to be valid only above a certain frequency (when the Quasi-TEM mode has no effect because the penetration depth in the ferrite is small compared to the magnetic circuit length [13]). In 1979 Sacherer and Nassibian [31] calculated the TEM impedance contribution for longitudinal and dipolar horizontal impedances for the C-Magnet model. These calculations have been reviewed in Ref. [14] where all the impedance terms for the C-Magnet model have been calculated and successfully benchmarked with EM simulations. The total beam coupling impedance of the C-Magnet kicker (longitudinal, constant [32], driving

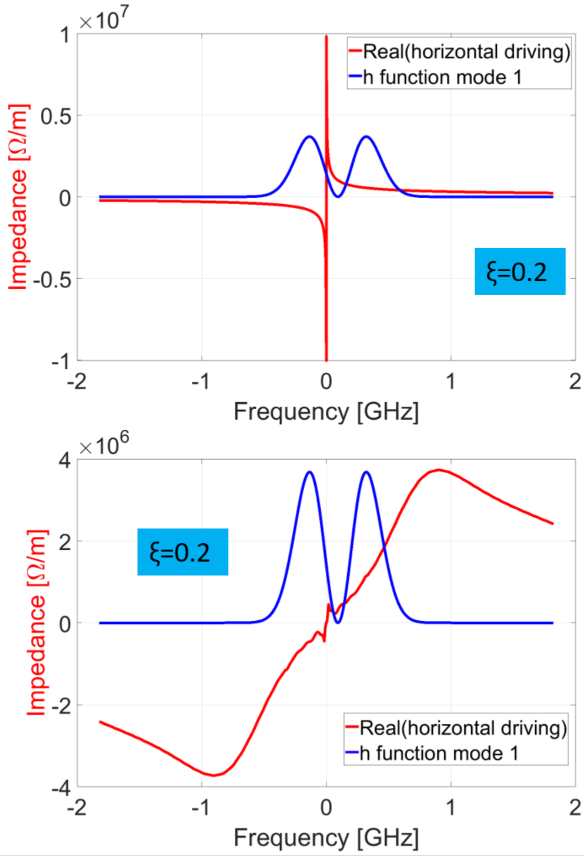


Figure 7: Power spectral density for the mode $l = 1$ in arbitrary units for a chromaticity $\xi = 0.2$ (blue) together with the SPS wall impedance model (top) and the SPS kickers without serigraphy (bottom) at injection energy for the Q20 optics.

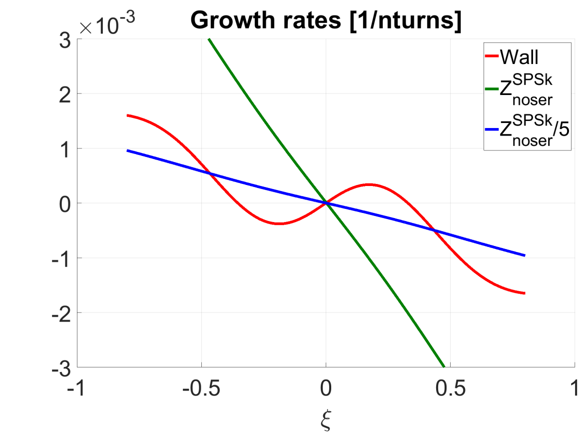


Figure 8: Horizontal growth rates versus chromaticity of the mode $l = 1$ for the SPS resistive wall impedance (red), the SPS kickers without serigraphy (green), and the SPS kickers impedance without serigraphy reduced by a factor of 5 (blue).

and detuning) of Fig. 2 is calculated using the superposition of the effects. Indeed for these devices the impedance

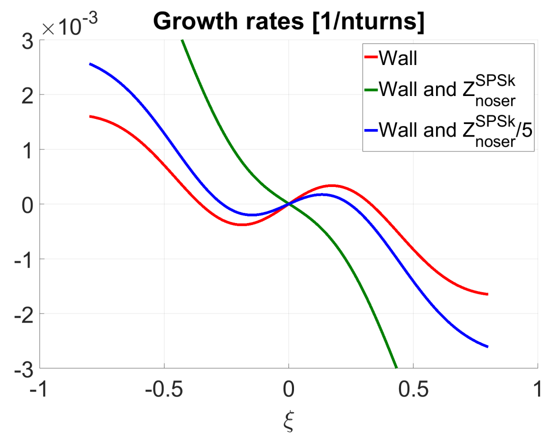


Figure 9: Horizontal growth rates versus chromaticity of the mode $l = 1$ for the SPS resistive wall impedance (red), the SPS wall impedance plus the SPS kickers without serigraphy (green), and the SPS wall impedance plus the SPS kickers impedance without serigraphy reduced by a factor of 5 (blue).

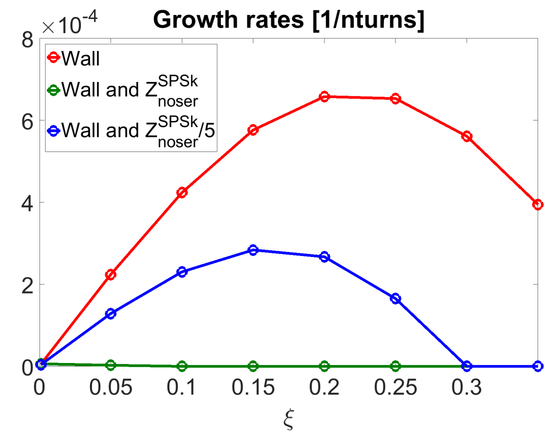


Figure 10: Horizontal growth rates versus chromaticity of the most unstable mode (DELPHI calculations) for the SPS resistive wall impedance (red), the SPS wall impedance plus the SPS kickers without serigraphy (green), and the SPS wall impedance plus the SPS kickers impedance without serigraphy reduced by a factor 5 (blue).

arises from core losses and coupling to the external circuits through the kicker supply line [14, 16]. Figure 11 shows the equivalent circuit of the model. More details about the model can be found in Ref. [14, 16]. The model allows to calculate the impedance due to coupling with the kicker circuit. The kicker circuit is represented as the equivalent impedance $Z_g$. Therefore, the model can consider whatever kind of circuit as long as this can be represented with an equivalent impedance.

The impedance due to coupling with the external circuits can also be directly simulated with the Wakefield solver of CST Particle Studio using the simulation method described in Ref. [16].

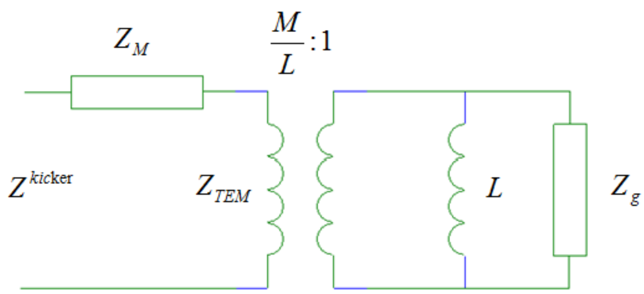


Figure 11: Circuit model of the kicker including cables. $Z_{\mathrm{TEM}}$ is the impedance contribution due to the coupling with the external circuits, $Z_{\mathrm{M}}$ the impedance contribution due to core losses, $L$ is the inductance of the magnet circuit, $Z_g$ the external impedance including cables and $M$ the mutual inductance of the magnet.

### *Example of the PSB extraction kicker*

The ejection kicker of the PSB is analyzed as an example of interest for the model. A schematic of the kicker circuit is shown in Fig. 12. The external impedance including cables $Z_g$ is calculated solving the circuit and transporting the loaded impedance at the termination over the cable length using the transmission line theory. Figure 13 shows the dipolar horizontal impedance of the ejection kicker (EK) of the PSB calculated using Eq. 2.58 of Ref. [16] with $Z_g$ obtained solving the circuit of Fig. 12. The frequency pattern of the resonances depends on the single-way delays and termination of the kicker circuit. The very low attenuation constant of the cables makes these resonances narrow with a Q value of about 100 and a shunt impedance in the order of MΩ/m. The first resonance appears at 1.72 MHz. The frequency values found in the model mainly depend on cable length and properties. The height and width of the peaks depend on the cable attenuation that is in the order of few mdB/m for the PSB cables. Concerning this point it is worth noting that the impedance of the resonances is inversely proportional to the attenuation. Figure 14 shows the impedance of the PSB extraction kicker assuming different cables attenuation. Therefore, decreasing cable attenuation the growth rate of the instability driven by the mode will also increase while the tune band at which the instability is driven will be narrowed due to the higher quality factor of the resonance.

The impedance of Figure 13, previously suspected in [16], was proven to be responsible for the head-tail horizontal instability observed in the PSB when the feedback system is off [33]. Once the source of the PSB horizontal instability was confirmed to be the impedance of the extraction kicker due to coupling with the external circuits, different design solutions have been investigated for impedance optimization [33]. The more promising impedance mitigation solution for the PSB extraction kicker which is presently under study is to insert a saturating inductor between the kicker module and the coaxial cables. This is expected to shift the first resonance to significantly lower frequency (see

Fig. 15). With this circuit modification a stable scenario is expected below half integer tune (see Fig. 16 and [33]). The example of the PSB extraction kicker highlights that the impedance from unmatched terminations of one single device can lead to violent beam instability. Therefore, a reliable model for the estimation of the impedance due to cable termination effects is crucial.

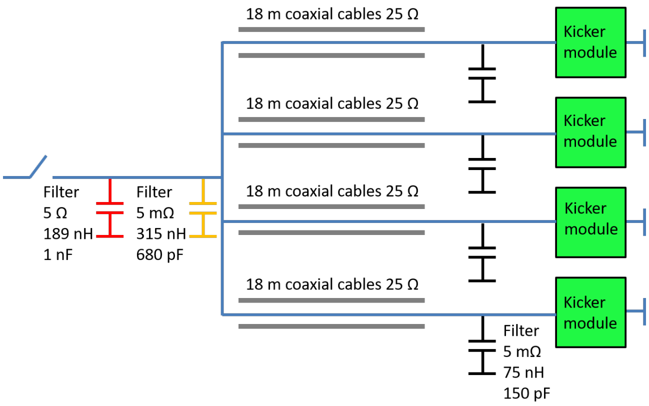


Figure 12: Schematic of the PSB extraction kicker circuit.

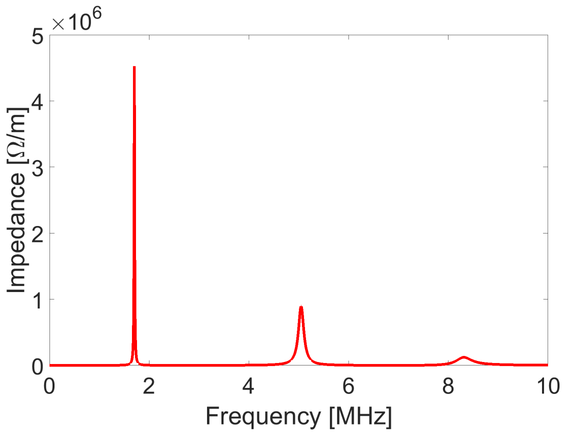


Figure 13: Real part of the driving horizontal impedance of the PSB extraction kicker due to the coupling with the circuit of Fig. 12.

## POTENTIAL OF METAMATERIALS FOR IMPEDANCE MITIGATION

Metamaterials or, more in detail, composite materials with negative values of either relative permittivity or relative permeability have been intensively studied in the last decades [34]. Concerning metamaterials insertions for beam-coupling impedance mitigation, their effect has been first addressed in [35] for resistive-wall beam-coupling impedance reduction. The effect of metamaterial insertions on beam-coupling impedance has been studied theoretically by means of a transmission-line model [16, 36]. Overall, the observed results demonstrate a remarkable influence on the resistive-wall beam-coupling impedance, which can lead to the identification of theoretical design rules for impedance mitigation, exploiting the different degrees of freedom: the type of material (epsilon negative (ENG) or mu negative (MNG)), its values of constitutive parameters, its thickness and its length. Therefore, a proper engineering of such insertions can be performed, with the aim of substantially reducing the resistive-wall impedance of a beam line.

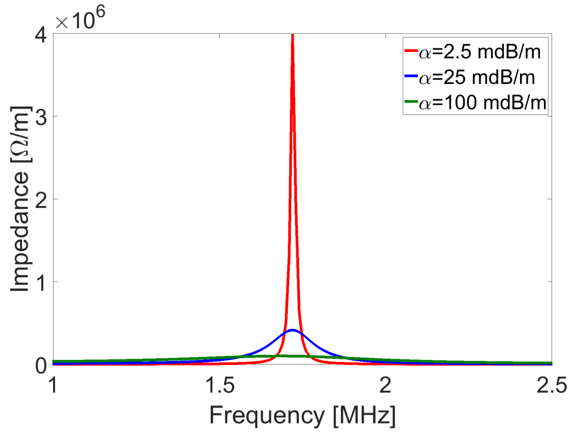


Figure 14: First resonance of the real part of the driving horizontal impedance of the PSB extraction kicker due to the coupling with the circuit of Fig. 12 for different cables attenuation.

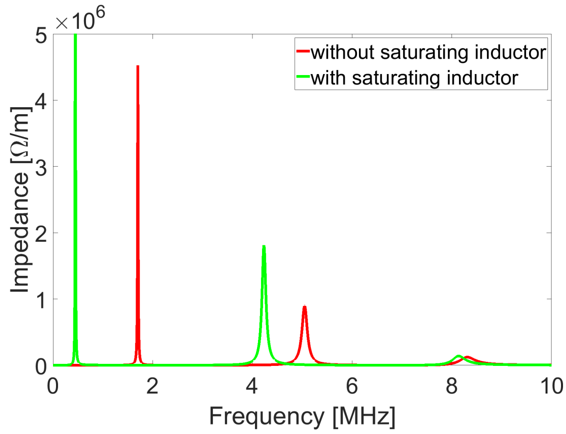


Figure 15: Real part of the driving horizontal impedance of the PSB extraction kicker due to the coupling with the circuit of Fig. 12 with and without saturating inductor between kicker module and coaxial cables.

As a proof of principle, experimental measurements were performed with splitting ring resonators (SRR) metamaterials. The measurements discussed and presented in [37] have been performed by evaluating the quality factor Q of several resonances in a cavity. The cavity has been obtained using a straight section of a rectangular waveguide WR284, enclosing it between two metallic plates and inserting a tiny antenna on one side, in order to excite the modes. Measurements have been performed with and without metamaterial insertions (two SRR stripes on the cavity walls, as depicted in Fig. 5 of Ref. [37]). The resonance frequencies on the $S_{11}$

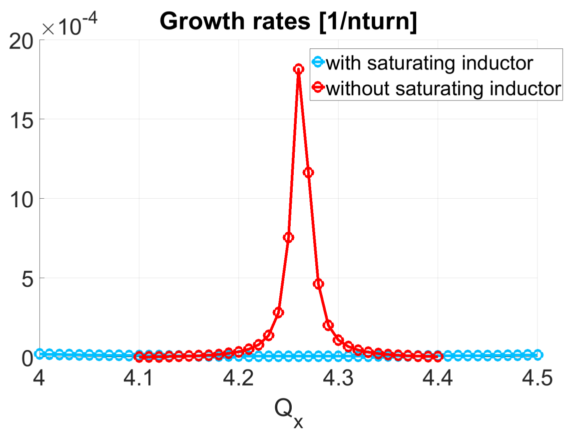


Figure 16: Horizontal growth rates versus betatron tune of the PSB due to the coupling with the circuit of Fig. 12 with and without saturating inductor between kicker module and coaxial cables.

spectra have been identified and the corresponding unloaded Q factors have been measured using a Vector Network Analyzer (VNA) and post-processing techniques.

The unloaded quality factor of a resonance associated to an empty waveguide section is related solely to the losses on the conductive walls. Such losses are due to the surface impedance of the walls, which depends on the material conductivity and frequency. The quality factor is inversely proportional to the surface resistance. Therefore, to interpret the results coming from the measurements, one should note that an increase of the unloaded quality factor testifies a proportional decrease of the resistive-wall impedance (caused by a decrease of the surface impedance). The measurement results of Fig.6 of Ref. [37] show that at about 2.9 GHz the measured unloaded Q is significantly higher in the case of metamaterial presence, meaning a decrease of an order of magnitude of the surface impedance. This demonstrates the potential of metamaterials to approach the equivalent behaviour of a perfect electrical conductive wall. The other peaks instead show little or no variation when the SRRs are put in the waveguide. This is expected since both material properties and the condition to get the equivalent behaviour of a perfect electric conductor are frequency dependent [37]. The possibility of using metamaterials to approach the behaviour of a perfect electric conductor could lead to the fascinating scenario of developing superconductive like cavities at ambient temperature and lossless guiding structures.

## CONCLUSION

A deep understanding of all the impedance induced effects is needed to make the best choice in terms of impedance optimization considering both local effects (direct effect on the device) and global effects (interplay between the different impedances). Impedance optimization is a very challenging task due to the several concurrent induced effects. As an example, it has been shown that impedance reduction, though desirable for equipment heating mitigation, can also be detrimental in terms of beam stability. This also means that it could be considered to introduce ad hoc impedances to have beneficial effects on beam stability.

## REFERENCES

[1] H. Tsutsui, “Some Simplified Models of Ferrite Kicker Magnet for Calculation of Longitudinal Coupling Impedance,” *CERN-SL-2000-004-AP*, January 2000.

[2] H. Tsutsui, “Longitudinal impedances of some simplified ferrite kicker magnet models,” *CERN-SL-2000-050-AP*, June 2000.

[3] H. Tsutsui and L. Vos, “Transverse Coupling Impedance of a Simplified Ferrite Kicker Magnet Model,” *LHC-PROJECT-NOTE-234*, September 2000.

[4] https://www.ansys.com/products/electronics/ansys-hfss.

[5] F. Caspers, A. Mostacci, and H. Tsutsui, “Impedance Evaluation of the SPS MKE Kicker with Transition Pieces between Tank and Kicker Module,” *CERN-SL-2000-071-AP*, October 2000.

[6] E. Métral, F. Caspers, M. Giovannozzi, A. Grudiev, T. Kroyer, and L. Sermeus, “Kicker impedance measurements for the future multiturn extraction of the CERN Proton Synchrotron,” *CERN-AB-2006-051*, July 2006.

[7] M. J. Barnes, F. Caspers, T. Kroyer, E. Métral, F. Roncarolo, and B. Salvant, “Measurement of the longitudinal and transverse impedance of kicker magnets using the coaxial wire method,” *CERN-ATS-2009-018*, July 2009.

[8] B. Salvant, N. Mounet, C. Zannini, E. Métral, and G. Rumolo, “Quadrupolar Transverse Impedance of Simple Models of Kickers,” *CERN-ATS-2010-076*, June 2010.

[9] “`http://www.cst.com/`,”

[10] C. Zannini and B. Salvant, “Update on the impedance of the SPS kicker,” Presented at the SPS impedance meeting (`https://impedance.web.cern.ch`), October 2009.

[11] C. Zannini, “Simulations of the SPS kickers with CST Particle Studio,” Presented at the SPS impedance meeting (`https://impedance.web.cern.ch`), August 2009.

[12] C. Zannini, N. Mounet, B. Salvant, E. Métral, and G. Rumolo, “Electromagnetic simulations of simple models of ferrite loaded kickers,” *CERN-ATS-2010-098*, June 2010.

[13] C. Zannini, V. G. Vaccaro, E. Métral, G. Rumolo, and B. Salvant, “Electromagnetic modeling of C-shaped ferrite loaded kickers,” *CERN-ATS-2011-103*, September 2011.

[14] C. Zannini, G. Rumolo, and V. G. Vaccaro, “Effect of the TEM Mode on the Kicker Impedance,” *CERN-ATS-2012-134*, May 2012.

[15] M. Barnes, “Kicker systems,” *CERN Yellow Rep. School Proc.*, vol. 5, p. 229. 55 p, 2018.

[16] C. Zannini, *Electromagnetic Simulation of CERN accelerator components and experimental applications*. PhD thesis, Lausanne, EPFL, Switzerland, 2013. CERN-THESIS-2013-076.

[17] M. S. Beck, “Simulation, measurement and mitigation of the beam induced power loss in the SPS injection kickers,” Master’s thesis, KIT, Germany, 2015. CERN-THESIS-2015-374.

[18] M. Timmins, "SPS extraction kicker magnet: thermal analysis," *TS-Note-2004-016*, July 2004.

[19] T. Kroyer, F. Caspers, and E. Gaxiola, "Longitudinal and Transverse Wire Measurements for the Evaluation of Impedance Reduction Measures on the MKE Extraction Kickers," *CERN-AB-Note-2007-028*, July 2007.

[20] E. Gaxiola, J. Bertin, F. Caspers, L. Ducimetière, and T. Kroyer, "Experience with Kicker Beam Coupling Reduction Techniques," *CERN-AB-2005-024*, June 2005.

[21] C. Zannini and G. Rumolo, "EM Simulations in Beam Coupling Impedance Studies: Some Examples of Application," EuCARD-CON-2012-016 (`http://cds.cern.ch/record/1498077`), ICAP12, 2012.

[22] C. Zannini, "Multiphysics Simulations of Impedance Effects in Accelerators," *CERN Yellow Rep. Conf. Proc.*, vol. 1, pp. 141–144, 2018.

[23] M. Barnes, M. Beck, H. Day, L. Ducimetière, E. Garcia-Tabares Valdivieso, B. Goddard, H. Neupert, A. Romano, L. Vega Cid, W. Weterings, and C. Zannini, "Upgrading the SPS Fast Extraction Kicker Systems for HL-LHC," *CERN-ACC-2017-217*, 2017.

[24] B. W. Zotter, "The effective coupling impedance for instabilities of Gaussian bunches," *CERN-ISR-TH-80-03*, 1980.

[25] B. W. Zotter, "The effective coupling impedance for bunched beam instabilities," *CERN-ISR-TH-78-16*, 1978.

[26] A. W. Chao, Physics of collective beam instabilities in high energy accelerators. New York: Wiley, 1993.

[27] B. W. Zotter, "Collective effects: General description," *CERN-85-19-V-2*, pp. 415–431, 1984.

[28] J. L. Laclare, "Introduction to coherent instabilities: Coasting beam case," *CERN-85-19-V-2*, pp. 377–414, 1985.

[29] J. L. Laclare, "Bunched beam coherent instabilities," *CERN-87-03-V-1*, pp. 264–326, 1987.

[30] N. Mounet, "Vlasov Solvers and Macroparticle Simulations," *CERN Yellow Rep. Conf. Proc.*, vol. 1, pp. 77–85, 2018.

[31] G. Nassibian and F. J. Sacherer, "Methods for measuring transverse coupling impedances in circular accelerators," *Nucl. Instrum. Methods*, vol. 159, no. 1, pp. 21–27, 1979.

[32] C. Zannini, K. Li, and G. Rumolo, "Effects of an Asymmetric Chamber on the Beam Coupling Impedance," *CERN-ATS-2012-081*, May 2012.

[33] E. Koukovini-Platia, M. J. Barnes, H. Bartosik, G. Rumolo, L. Sermeus, and C. Zannini, "Source of horizontal instability at the CERN Proton Synchrotron Booster," *Phys. Rev. Accel. Beams*, vol. 22, no. 12, 2020.

[34] N. Engheta and R. Ziolkowski, *Metamaterials: Physics and Engineering Explorations*. John Wiley & Sons, Inc., 9 2006.

[35] A. Danisi, C. Zannini, A. Masi, R. Losito, and B. Salvant, "Theoretical Analysis of Metamaterial Insertions for Resistive-Wall Beam-Coupling Impedance Reduction," *CERN-ACC-2014-0191*, 2014.

[36] C. Zannini, "TLwall: transmission line model for wall impedance calculation," Presented at the CERN HSC section meeting (`https://indico.cern.ch/event/795854/`), February 2019.

[37] A. Danisi, C. Zannini, R. Losito, and A. Masi, "Metamaterial insertions for resistive-wall beam-coupling impedance reduction," *arXiv:1910.02246*, 2019.

# LOW-IMPEDANCE BEAM SCREEN DESIGN FOR FUTURE HADRON COLLIDERS*

S. Arsenyev†, CEA Saclay, Gif sur Yvette, France
D. Schulte, CERN, Geneva, Switzerland

*Abstract*

In future hadron colliders with collision energies greater than the energy of the Large Hadron Collider (LHC), the beamscreen becomes an increasingly important source of beam coupling impedance. This may lead to coherent beam instabilities, especially in the transverse plane, and potentially a failure to reach the desired beam intensity. Here we discuss design choices affecting the beamscreen impedance in the proposed Future Circular Collider (FCC-hh). We consider the resistive impedance of the copper walls and their high-temperature superconductor alternative, the impedance due to the surface treatment for electron cloud suppression, and the geometric impedance of the pumping holes and the interconnects.

## INTRODUCTION

The Future Circular Collider (FCC) study includes three different collider options: the hadron-hadron collider FCC-hh, the electron-positron collider FCC-ee, and the hadron-electron collider FCC-eh. Details on the design of all the proposed FCC options can be found in the conceptual design report [1]. Furthermore, the machine design of the FCC-hh is thoroughly described in the extended version of the CDR [2]. As far as the FCC-ee is concerned, the impedance issues of the vacuum chamber are discussed in [3] (in particular, impedance due to the synchrotron radiation absorbers and the NEG coating). The FCC-hh and the FCC-eh both rely on the same 100 km long hadron ring and the same beamscreen impedance design. In this paper, we focus exclusively on the FCC-hh beamscreen, with the described impedance study potentially applicable to other future hadron colliders (e.g. the proposed High Energy Large Hadron Collider - HE-LHC [4]).

In the FCC-hh, the beamscreen is the part that separates the particle beam from the magnet cold bore in the long and the short arc sections, occupying 86% of the collider circumference. The cross-section of the beamscreen is shown in Figure 1. In comparison to the LHC, in the FCC-hh the beamscreen becomes a much more significant source of impedance, overshadowing the collimators for some instabilities [2, 5]. This is due to the following necessary design choices driving the beamscreen impedance up:

- Low aperture to reduce the magnet cost
- High surface temperature (50K) to extract the heat from synchrotron radiation 200 times higher than in the LHC
- Large pumping holes for high vacuum quality
- Surface coating (or treatment) for e-cloud suppression

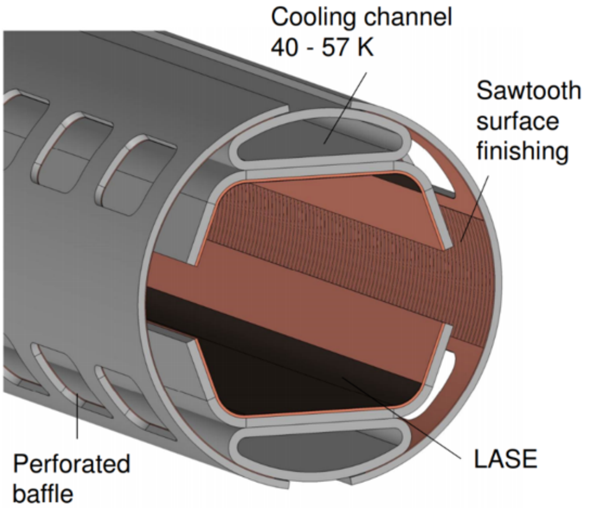


Figure 1: FCC-hh beamscreen cross-section. The copper coating is shown in brown, with the Laser Ablation Surface Engineered (LASE) part shown in black. The pumping holes are marked as the perforated baffle.

Below we summarize the studies on different sources of the impedance of the beamscreen, starting with the resistive impedance of the copper-coated walls and mentioning the alternative of the high-temperature superconductor, then the impedance e-cloud surface treatment which is studied separately, and finally the geometric impedance due to the pumping holes and the interconnects. The data presented in this paper correspond to the FCC-hh impedance database [6] which also contains the impedance information on the other elements of the collider.

## RESISTIVE WALL IMPEDANCE

The walls of the beamscreen are made of stainless steel (grade P506, resistivity $6 \times 10^{-7}$ Ωm), with the sides facing the beam co-laminated with a 300 $\mu$m thick layer of copper. To slow down the coupled-bunch instability, this copper layer has to be much thicker than that of the LHC beamscreen (due to the longer skin depth at the lower collider revolution frequency). The copper layer is assumed to have the Residual Resistance Ratio (RRR) of 70, similar to the LHC beamscreen (see [7], p.185). The temperature of the beamscreen walls is set to 50 K, resulting in the copper resistivity of $7.5 \times 10^{-10}$ Ωm in the absence of an external magnetic field.

* This work was supported by the European Union's Horizon 2020 research and innovation programme under grant No 654305.
† sergey.arsenyev@cea.fr

The resistivity increases with the dipole magnetic field according to Kohler's rule [8], becoming $7.9 \times 10^{-10}$ Ωm at injection and $1.4 \times 10^{-9}$ Ωm at the top energy. The impedance of the two-layer walls is calculated with the Impedance-Wake2D code [9] for a circular pipe with a radius of 12.22 mm - the vertical aperture of the beamscreen. Then, form factors are applied to account for the non-circular cross-section: $F_x = 0.45$, $F_y = 0.83$, $F_z = 0.82$, as estimated with the wakefield solver of CST [10]. Finally, the dipolar impedances are weighted with the average $\beta$-functions in the arc FODO cell. The resulting transverse impedance in the vertical plane is shown in Figure 2 as the most critical one, with impedance in the other planes available in [6].

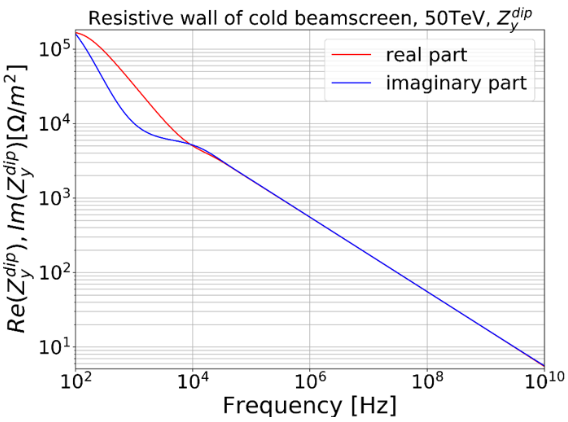


Figure 2: The *per unit length* resistive wall impedance of the beamscreen. The data shows the transverse dipolar impedance in the vertical plane at the collision energy (50 TeV).

It is also important to mention a potential problem of the current design. The copper coating is absent on some walls that do not face the beam but nevertheless affect the impedance due to the non-zero surface electromagnetic fields. In particular, at the edges of the slit a small area of uncoated stainless steel is exposed, which affects the dipolar impedance in the horizontal plane. A number of solutions to this issue exist, including re-shaping the edge or applying a thin copper coating. See [11] for more details.

While the copper coating of the walls is the baseline solution, an exciting new alternative is being investigated. The interior of the beam screen can instead be coated with a High-Temperature Superconductor (HTS) such as REBCO or Tl-1223 [12, 13]. The first measurements of the surface resistance in a dielectric resonator are very promising (Fig. 3). The measured surface resistance for the REBCO tapes with artificial pinning centers is lower than the predicted value and might be even lower for further custom-tailored tapes.

## SURFACE TREATMENT FOR E-CLOUD SUPPRESSION

There are two proposed solutions for the e-cloud surface treatment. The solution currently assumed in the impedance

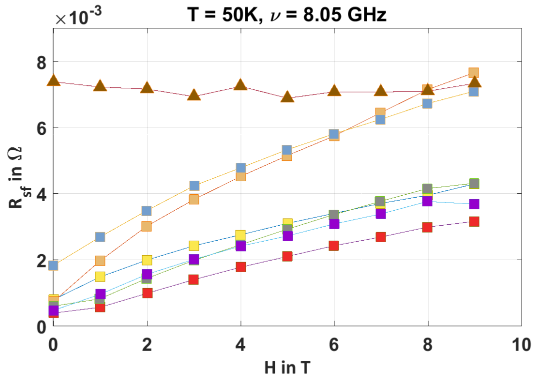


Figure 3: Measured surface resistance of REBCO Coated Conductors (squares) compared to copper (triangles) as a function of applied magnetic field. The lower four curves (red, purple, yellow, green) are measured for materials having artificial pinning centers.

model is to coat the inner surface of the beamscreen with a layer of amorphous carbon. The coating prevents an electron cloud build-up by reducing the secondary emission yield (SEY) of the surface. The thickness and the resistivity of the coating are assumed to be 200 nm, and $10^{-4}$ Ωm, respectively. The increase of the longitudinal impedance is proportional to the frequency, and the increase of the transverse impedance is a constant of frequency. In the frequency range of interest, the coating impedance is purely imaginary and gives a moderate (around 30%) increase in the dipolar broadband impedance of the beamscreen [2].

Alternatively, laser treatment of the beamscreen surface can be used. A laser beam causes $\mu$m-level roughning of the surface which reduces the SEY [14, 15]. A potential problem with this method is that a rough surface could lead to a significant increase in the beamscreen impedance at the frequencies of single bunch instabilities (on the order of 1 GHz) [16]. The technique is continuously evolving in order to achieve the best SEY reduction and at the same time avoid the impedance increase. Some latest results show no impedance increase at room temperature and at a frequency of 3.9 GHz [17]. Nevertheless, more measurements are needed to estimate the impedance increase in realistic conditions (the temperature of 50 K and a strong external magnetic field) [18].

## PUMPING HOLES AND INTERCONNECTS

Pumping holes connect the space inside the beamscreen to the outer region from where the air is pumped out (labeled as "perforated baffle" in Figure 1). The novel design of the FCC-hh beamscreen significantly reduces the impedance of the pumping holes by shielding them away from the beam, so that the holes are only connected to the beam region through a narrow slit.

The complexity of the beamscreen geometry does not allow to apply analytical methods to estimate the impedance of the holes. In order to estimate the broadband dipolar impedance of the holes, numerical simulations were carried out accounting for traveling waves synchronous with the beam [19], and the results are shown in Figure 4. They agree with Wakefield solver of CST when the impedance is high enough to be measured with the wakefiled solver (artificially increased slit to worsen the shielding). Both the value obtained for the actual shielding and the extrapolation of the curve for the increased slit size show that all 10.5 million holes amount to less than 0.1 MΩ/m of broadband dipolar impedance in the horizontal plane. Estimation of the real part of the longitudinal impedance is on-going to prevent excessive heat loss in the cold bore.

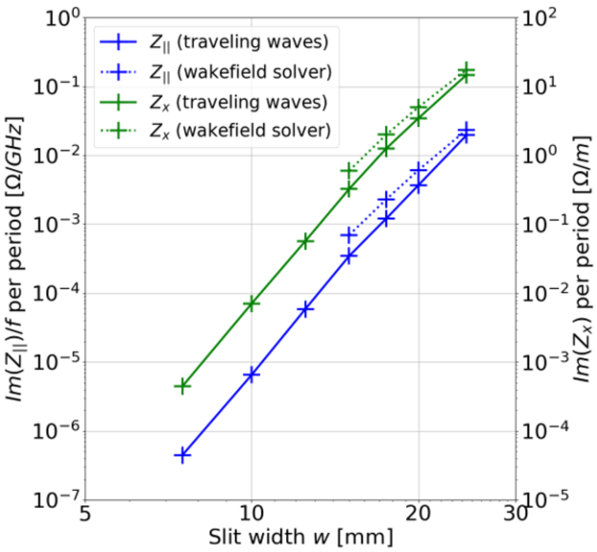


Figure 4: Imaginary part of the longitudinal (blue) and horizontal dipolar (green) impedance per one period of pumping holes as a function of the slit width. Comparison between the traveling wave method (solid lines) and the CST-wakefied solver (dashed lines).

Another source of the geometric impedance of the beamscreen is the interconnects placed between the cryo-modules. Each interconnect has tapers that transform the complex beamscreen shape to a circle on both sides such that the two sides can be connected with RF fingers. Unlike in the LHC, such transformation involves an abrupt change in the cross-section, although only behind the shielding. Additionally, the upstream taper is made of the taper-down and the taper-up parts to form a barrier that prevents the intense synchrotron radiation from hitting the RF fingers. The low-frequency broadband impedances of the tapers are simulated with the CST Wakefield solver [10]. The resulting total broadband imaginary impedances are $\mathrm{Im}\,(Z_x)^{\mathrm{inter}}_{\mathrm{total}} = 1.5\times10^6\ \Omega/m$ and $\mathrm{Im}\,(Z_y)^{\mathrm{inter}}_{\mathrm{total}} = 1.9\times10^6\ \Omega/m$ which constitutes a significant part of the allowed broadband impedance at injection [20].

## CONCLUSIONS

We have summarized the most important impedance aspects in the FCC-hh beamscreen, and the design choices related to these aspects. Despite the beamscreen impedance being much more critical than in the case of the LHC, the beamscreen fits in the allowed impedance budget of the machine. With the current baseline solutions, no insurmountable problems have been identified. Nevertheless, an investigation of the non-traditional design solutions (HTS coating, LASE surface treatment) is on-going and can pave the way to an even better design in the future.

## ACKNOWLEDGEMENTS

This work was supported by the European Union's Horizon 2020 research and innovation programme under grant No 654305.

## REFERENCES

[1] "Conceptual Design Report of the Future Circular Collider", https://fcc-cdr.web.cern.ch

[2] "Extended Conceptual Design Report of the FCC-hh", to be published as a CERN yellow report.

[3] E. Belli, et al., "Coupling Impedances and Collective Effects for FCC-ee", https://cds.cern.ch/record/2314447?ln=en

[4] "Conceptual Design Report of the High-Energy LHC", https://fcc-cdr.web.cern.ch/#HELHC

[5] S. Arsenyev, D. Schulte, O. Boine-Frankenheim, "FCC-hh transverse impedance budget", in Proc. of IPAC 2018, April 29 - May 4, Vancouver, Canada, MOPMF029.

[6] FCC-hh impedance database, https://impedance.web.cern.ch/impedance/fcchh/index.html

[7] N. Mounet, "The LHC Transverse Coupled-Bunch Instability", Ph.D. thesis (2012).

[8] E. Métral, "Beam screen issues", https://arxiv.org/abs/1108.1643 (2011).

[9] https://twiki.cern.ch/twiki/bin/view/ABPComputing/ImpedanceWake2D.

[10] CST PARTICLE STUDIO - Wakefield Solver, https://www.cst.com/products/cstps/solvers/wakefieldsolver.

[11] Daria Astapovych, "Collective Effects in the Hadron Future Circular Collider", Darmstadt, Technische Universität, [Ph.D. Thesis], 2020

[12] S. Calatroni and R. Vaglio, "Surface resistance of superconductors in the presence of a dc magnetic field: frequency and field intensity limits," IEEE Trans. Appl. Supercond., vol. 27, p. 3500506, 2017.

[13] S. Calatroni, et al., "Thallium-based high-temperature superconductors for beam impedance mitigation in the future circular collider," Supercond. Sci. Technol., vol. 30, p. 075002, 2017.

[14] R. Valizadeh, O.B. Malyshev, S. Wang, T. Sian, L. Gurran, P. Goudket, M.D. Cropper, N. Sykes, "Low secondary electron yield of laser treated surfaces of copper, aluminium and stainless steel", in proc. of IPAC'16, 8-13 May 2016, Busan, Korea (2016), p. 1089.

[15] R. Valizadeh, O.B. Malyshev, S. Wang, T. Sian, M. D. Cropper and N. Sykes, "Reduction of Secondary Electron Yield for E-cloud Mitigation by Laser Ablation Surface Engineering", Appl. Surf. Sci. 404 (2017) 370–379.

[16] S. Arsenyev, D. Schulte, “Modeling coupling impedance of a rough surface", in Proc. of IPAC 2018, April 29 - May 4, Vancouver, Canada, MOPMF031.

[17] Reza Valizadeh, “Evaluation of LASER ablated surface engineering of copper and stainless steel for particle accelerators", presentationn at the FCC week 2019, Brussels, Belgium.

[18] S. Calatroni, presentation “Proposals for impedance measurements at CERN”, 2017, https://indico.cern.ch/event/619380/contributions/2527440/attachments/1437324/2210723/Impedance_proposal.pdf

[19] S. Arsenyev, et al., “Traveling wave method for simulating geometric beam coupling impedance of a beamscreen with pumping holes", Phys. Rev. Accel. Beams 22, 051002, https://journals.aps.org/prab/abstract/10.1103/PhysRevAccelBeams.22.051002

[20] S. Arsenyev, D. Schulte, “Broadband Impedance of Pumping Holes and Interconnects in the FCC-hh Beamscreen", in proc. of IPAC 2018, April 29 - May 4, Vancouver, Canada, MOPMF030.

# IMPEDANCE REDUCTION FOR LHC COLLIMATORS

A. Mereghetti*, D. Amorim, S. A. Antipov, N. Biancacci, R. Bruce, F. Carra, E. Métral, N. Mounet, S. Redaelli, B. Salvant, CERN, 1211 Geneva 23, Switzerland

*Abstract*

The LHC at CERN is equipped with a sophisticated collimation system, aimed at protecting superconducting magnets against quenches in case of losses from the circulating beams. The collimation system is one of the major contributors to the machine impedance at top energy. A relevant hardware upgrade of the system will take place in the context of the High Luminosity LHC (HL–LHC) project; one of the main objectives is to make stabilisation of the brighter HL–LHC beams reachable within the capabilities of the Landau octupoles. In fact, a relevant fraction of the carbon–based collimators will be exchanged with new ones, the jaws of which are made of materials more optimised in terms of impedance; hence, the footprint of the collimation system will be significantly reduced. The present contribution gives an overview of the baseline low–impedance upgrade of the LHC collimation system as foreseen by the HL–LHC project and the expected impact on impedance. Additional options that could further improve the footprint of the collimation system on the machine impedance are briefly summarised.

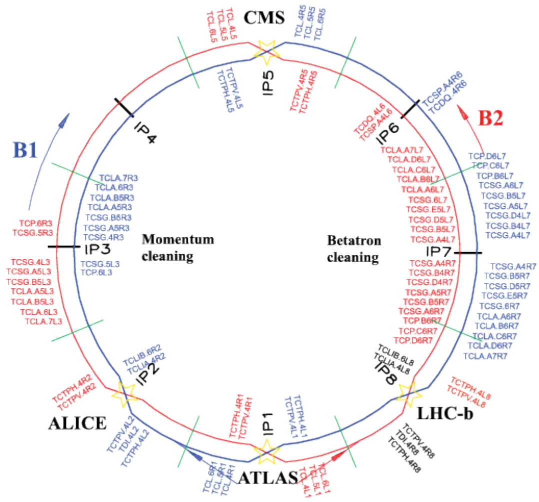


Figure 1: Layout of the LHC collimation system as of Run 2 [17].

## INTRODUCTION

The Large Hadron Collider (LHC) [1] at CERN is equipped with a sophisticated collimation system [2], fundamental to protect the machine against regular and abnormal beam losses. Since the LHC is a superconducting machine, its magnets can quench[1] if local losses are not kept within acceptable levels, leading to considerable machine downtime [3]. To ensure high–efficiency operation, the system meets very challenging design criteria, ranging from handling unprecedented power losses of up to 500 kW while granting a global cleaning efficiency as high as 99.99 % to precise jaw positioning, down to 5 μm, and reproducibility of the mechanical movements [4].

The operation of the LHC requires a distance between the beam and the material of the collimator jaws as small as 1 mm for the collimators closest to the beams [5, 6]. Carbon–based materials are extensively deployed in the LHC collimation system, due to the very good thermo–mechanical properties, which make them suitable for standing high loads caused by losses [4]. Therefore, the LHC collimators have a substantial impact on the total machine impedance budget, making them one of the main contributors [7]. While impedance–driven instabilities have never been a show–stopper during LHC operation so far [8], collimator settings have been set increasingly tighter during the first two periods of exploitation of the LHC (i.e. Run 1, 2010–2013, and Run 2, 2015–2018) [5, 6], still always ensuring stable operation with Landau octupoles within limits on currents [9–12].

The High-Luminosity LHC (HL–LHC) project [13, 14] aims at boosting the integrated luminosity collected by the LHC high luminosity experiments by a factor of 10. To do so, it envisages a thorough hardware upgrade, aimed at achieving more focussed beams at the interaction points and with a better geometrical overlap between colliding bunches. At the same time, thanks to the hardware upgrade implemented by the LHC Injectors Upgrade (LIU) project [15] in the LHC injection chain, HL–LHC beams will be brighter than those typically injected in the LHC, thanks mainly to the doubled bunch population. Such an increase in the beam brightness poses new challenges in terms of robustness of the collimation system and beam stability. In particular, if no collimation upgrade takes place, the octupole currents required to stabilise the HL–LHC beams would be too high, leaving no margin to compensate for sources of beam instability other than impedance [16].

After a brief presentation of the present LHC collimation system, this contribution summarises the foreseen baseline collimation upgrade that will be carried out in the context of the HL–LHC project and the expected performance; the focus is only on impedance aspects. Afterwards, dedicated measurements with beams to benchmark predictions are briefly presented, showing the solidity of the planned upgrade. The contribution is closed by an overview of other options of modifications to the LHC collimation system presently under study and their impact on impedance.

* alessio.mereghetti@cern.ch

[1] A quench is the sudden transition of the magnet from the superconducting state to the normal conducting one.

## THE LHC COLLIMATION SYSTEM

The LHC collimation system is mainly located in two Insertion Regions (IRs) of the LHC, namely IR3 and IR7 for momentum and betatron cleaning, respectively (see Fig. 1). While the former is responsible for cleaning away off–momentum beam particles, like uncaptured beam at the beginning of the energy ramp, the latter ensures that the machine aperture is well protected against transverse beam losses, e.g. in case of transverse instabilities. Single–turn losses when injecting or extracting beams are dealt with by protection devices specifically installed in IR2 and IR8, where beams are injected, and in IR6, where the beams are extracted. Finally, a few collimators are installed in the IRs where the experimental detectors are located, in order to lower the experimental background induced by the machine [18, 19], and provide local protection to superconducting magnets against fast failures [20, 21] and leakage from IR7 or collision debris.

The LHC collimators are made of two parallel jaws centered around the circulating beam [22, 23]. Collimators are organised in families, where every family absorbs the unavoidable leakage out of the upstream one. Primary collimators (TCPs) are the devices impacted first by the beams; they are located in IR3 and IR7. Their jaws are 60 cm in length, made of carbon–fiber composite (CFC), a special carbon–based material specifically chosen for its enhanced thermo–mechanical properties. IR3 and IR7 are equipped with secondary collimators (TCSGs), 1 m long and made of CFC, located downstream of the TCPs, and with showers absorbers (TCLAs), 1 m long and made of a tungsten–based alloy called Inermet 180, installed towards the end of IR3 and IR7. The IR7 collimation system is further complemented by tertiary collimators (TCTs), located in the experimental IRs; the hardware is similar to that of TCLAs. This hierarchy is fundamental for the optimal performance of the system, and it is assured by setting collimator families at increasing jaw opening with sufficient operational margins between adjacent families.

### *Contribution to Impedance*

At top energy, the LHC collimators are the main contributors to the impedance budget (see Fig. 2) [24]; IR7 TCPs and TCSGs give the largest footprint, because they are numerous (3 and 11 units per beam, respectively), their jaws are made of CFC, which has a non optimal resistivity, and their openings are the smallest in the ring.

Throughout Run 2, beam sizes at the collision points were made progressively smaller [25, 26], implying a smaller machine aperture available at every step. Therefore, IR7 collimator settings were made progressively tighter [6], implying an increasing contribution to machine impedance; this was carefully verified with measurements in the LHC and with simulations at every change of settings. In this detailed benchmark, it was found that the predicted effective imaginary impedance of the present system is similar to that reconstructed with beam measurements, even though in many occasions a discrepancy by ~50 % is found [16, 27]. Such a discrepancy is still under investigation while a continuous effort in improving the LHC impedance model is on–going.

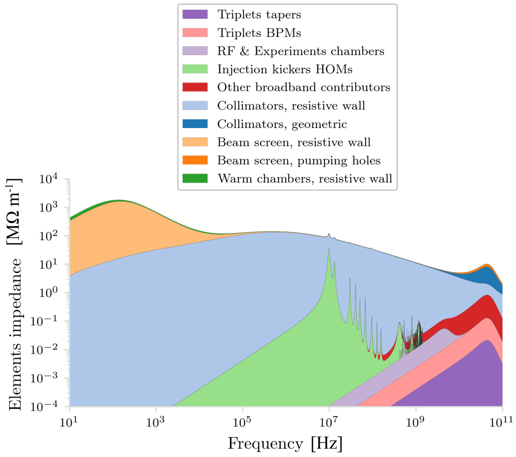


Figure 2: Expected real part of the dipolar horizontal impedance of the LHC at 6.5 TeV with 2018 operational parameters [24]. The breakdown of contributions from various systems is shown as a function of frequency.

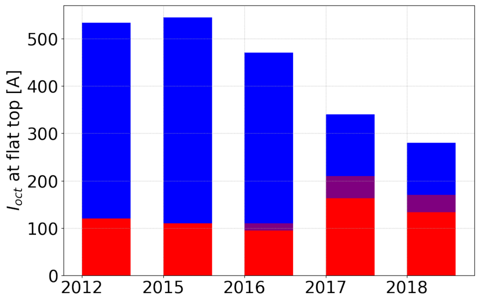


Figure 3: Current of Landau octupoles as expected by simulations (red bars) and required by operation (blue bars) [8]. The shaded bars show the stabilising contribution from long range beam–beam encounters. Values are for a chromaticity of ~15 and a damper gain set for damping oscillations within 50 – 100 turns.

LHC operation in Run 1 and Run 2 was characterised by a high current of the Landau octupoles, significantly above predictions by numerical simulations (see Fig. 3) [8]; the discrepancy with respect to predictions was made progressively smaller, thanks to the increasing knowledge and control of the machine, attaining a factor 2 in 2017 and 2018. While only a fraction of such a discrepancy can be explained by limits of the impedance model, the interplay between the different phenomena leading to instability needs to be analysed in detail [16, 28–31]. Therefore, with such an analysis still on–going [8, 16], the factor 2 of uncertainty in the stability model must be taken into account for estimating octupole currents necessary to stabilise LHC beams in future configurations; this is the most accurate assumption based on the

Table 1: LHC operational (as of the 2018 run) [25] and HL–LHC [32] (both nominal and ultimate values are reported for standard beams) parameters: $\beta$ function at the high-luminosity collision points ($\beta^*$), peak luminosity ($L_{\text{peak}}$), integrated luminosity ($L_{\text{int}}$), beam energy ($E_b$), number of bunches ($n_b$), bunch population ($N_p$), and normalised emittance ($\epsilon_N$).

| Parameter | LHC 2018 | HL–LHC Nominal | HL–LHC Ultimate |
|---|---|---|---|
| $\beta^*$ [cm] | 25 | 15 | |
| $L_{\text{peak}}$ [$10^{34}$ cm$^{-2}$ s$^{-1}$] | 2 | 5 | 7.5 |
| $L_{\text{int}}$ [fb$^{-1}$ year$^{-1}$] | 66 | 262 | 325 |
| $E_b$ [TeV] | 6.5 | 7 | |
| $n_b$ | 2544 | 2760 | |
| $N_p$ [$10^{11}$ per bunch] | 1.2 | 2.2 | |
| $\epsilon_N$ [μm] (flat top) | 1.9 | 2.5 | |

present knowledge. In any case, predicted octupole currents should not exceed the maximum available, i.e. 570 A.

## THE HL–LHC CHALLENGE

The HL–LHC [13, 14] is an upgrade of the LHC aimed at increasing the integrated luminosity collected by the LHC high luminosity experiments by one order of magnitude compared to the LHC baseline program. Table 1 compares key machine parameters expected for the HL–LHC era [32] to those achieved so far in the LHC as of 2018 [25]. In the context of the HL–LHC project, the IR7 collimation system will be substantially upgraded, to lower its impedance and to stand the losses of the HL–LHC beams, expected to double the LHC ones following the increased bunch population (see Table 1).

### *Present Baseline and Expected Performance*

The backbone of the HL–LHC collimation impedance upgrade of IR7 [33] is the change of jaw material of those collimator families impacting impedance the most, i.e. TCPs and TCSGs. The existing collimators will be exchanged with new ones, where materials of lower resistivity [16, 34–36] will be deployed in the jaws instead of CFC:

**TCPs** the horizontal and vertical TCPs will be replaced by new collimators (TCPPMs), the jaws of which are made of MoGr, a composite material made of Molybdenum and graphite, thanks to the consolidation project but for the jaw material, paid by the HL–LHC project;

**TCSGs** 9 out of 11 TCSGs per beam will be replaced by new collimators (TCSPMs), the jaws of which are made of Mo–coated MoGr jaws (TCSPMs).

The upgrade will proceed in stages [37], with the TCPPMs and 4 TCSPMs per beam installed in LS2 (2019–2020); the remaining TCSPMs will be installed in LS3 (2023–2024).

The new hardware will come with a new design (see Fig. 4 for the design of the TCSPM) [38], characterised by:

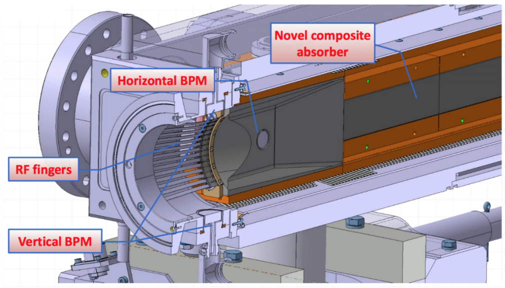


Figure 4: Zoom on the jaw of the TCSPM collimator design [38].

- in–jaw button beam position monitors (BPMs), for precise jaw alignment and monitoring of the beam closed orbit. There will be also the possibility to interlock the BPM readouts;
- a tank BPM, monitoring the beam orbit on the plane orthogonal to that of cleaning;
- the possibility to move the entire collimator assembly along the direction orthogonal to that of cleaning, in order to expose to the beam a fresh new surface following scratching or accidental beam impacts (so called 5$^{\text{th}}$ axis functionality);
- a universal housing of the absorbing material and improved thermal conductivity between the absorbing material and the jaw structure;
- smoother tapering, i.e. transition to the region exposing the absorbing material to the beam.

The key characteristics of the design have been thoroughly tested with beam in the HiRadMat test facility [39]; the collected measurements [40–43] allowed to conclude that the design of the new hardware is adequate for the planned upgrade.

Figure 5 shows the Landau octupole current necessary to attain single–beam stability in the HL–LHC era for different IR7 layouts, as predicted by numerical simulations [16]. As it can be seen, the present LHC collimation system would not allow to keep the required octupole current below the maximum with the HL–LHC brighter beams. On the contrary, the full HL–LHC impedance upgrade of IR7 (labelled as “LS3 upgrade” in the figure) is fundamental to substantially meet the requirements on the Landau octupole current. The partial upgrade foreseen for LS2 will provide more than half of the impedance reduction already in Run 3 (2020–2023); at the same time, it will allow to swallow the progressively brighter beams available in the LHC injectors, and get acquainted with the new hardware.

Even with the low–impedance upgrade of IR7, the LHC collimators will remain one of the major contributors to machine impedance at flat top (see Fig. 6) [16].

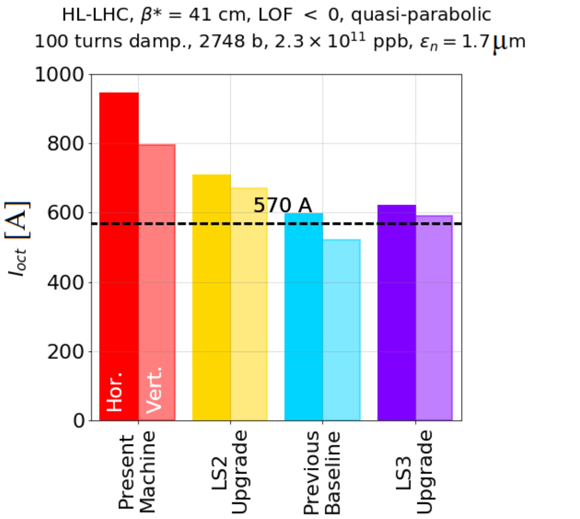


Figure 5: Landau octupole current predicted by numerical simulations in the HL–LHC era for different IR7 layouts [16]. Predictions refer to the single beam stability. Key parameters used in the estimations are reported in the figure. "Previous baseline" refers to the exchange of all TCPs and TCSGs with the upgraded ones. Predictions take into account the factor 2 of uncertainty in the stability model.

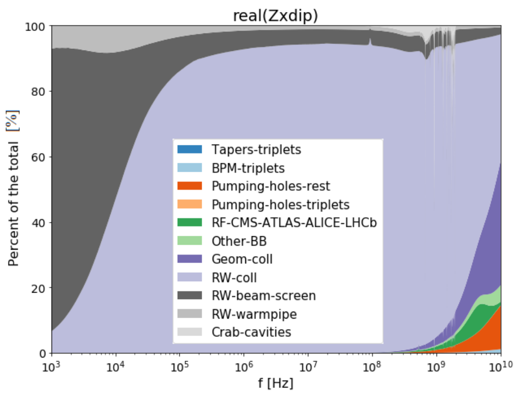


Figure 6: Expected real part of the dipole horizontal impedance of the HL–LHC at 7 TeV [16]. The breakdown of contributions from various systems is shown as a function of frequency.

*Benchmark Measurements*

The beneficial effects of the TCSPM design on impedance were verified with an extended campaign of measurements with beam. In early 2017, a prototype of TCSPM was installed in the LHC for this purpose [45]. The prototype was characterised by jaws with three stripes of materials to be tested (see Fig. 7); two of them were the materials chosen for the design (i.e. MoGr and pure Mo); the third one was TiN, considered as possible alternative to Mo with a higher robustness. The chosen installation slot was adjacent to a regular TCSG, for direct comparisons to CFC; the slot is also characterised by the smallest beam size on the cleaning

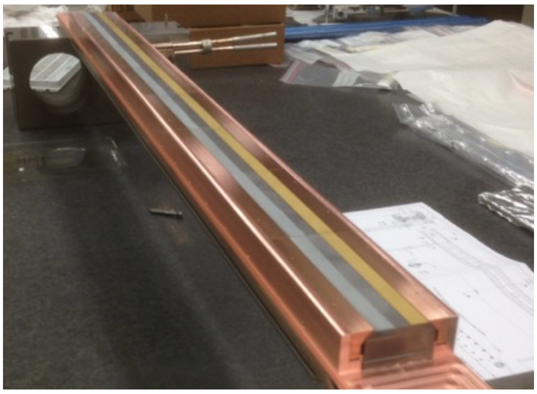

Figure 7: Jaw of the TCSPM prototype jaw installed for impedance measurements. The yellow stripe is made of TiN, whereas the light grey one is made of pure Mo; the central stripe is the bulk MoGr.

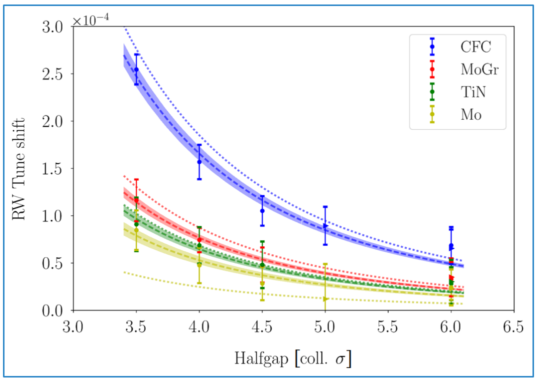


Figure 8: Comparison between tune–shift measurements obtained with the TCSPM prototype and the adjacent TCSG collimator (points with error bars) and the simulation predictions (densely dashed lines); fits through data (dashed lines) are also given (shaded areas represent 1 $\sigma$ uncertainty of fit error). Results from all materials are shown. Measurements were carried out with typical LHC single bunches and with HL–LHC–like single bunches; in the latter case, results have been scaled to match the LHC bunch population to fit into the plot.

plane among all the IR7 TCSGs, such that signatures from impedance were as clear as possible.

The measurements were carried out cycling the collimator gap and monitoring the tune signal reconstructed from the damped oscillations after kicking the whole bunch. The measurements were challenging, especially because of the sensitivity in the tune shift that had to be achieved, i.e. in the order of $10^{-5}$, in order to correctly resolve tune variations from the resistive wall impedance of the materials under test. As it can be seen (see Fig. 8), measurements are in good agreement with predictions, apart from the case of Mo, where measurements are constantly twice the expectations. Further investigations have shown the importance of the micro–structure of the substrate below the coating layer as well as the quality of the coating process, which would explain the higher measured values [46]. After these measurements took place, the supplier of Mo–coated MoGr jaws managed to build jaws for which the Mo conductivity is now very close to the theoretical value of the pure metal [46].

### *Other Options*

The presented estimates of the Landau octupole current necessary to stabilise the HL–LHC beams take into account the factor 2 uncertainty in the stability model. Even though the origin of the discrepancy is presently not fully understood [16], there is no better extrapolation to the HL–LHC era as of writing. At the moment, it is believed that part of the discrepancy could come from a larger than expected impedance (maybe due to a higher resistivity than anticipated) and part of it from the destabilising effect of noise on beam stability [47].

Other options for IR7 update or modification are presently under study. Even though they are not all in the HL–LHC baseline, their deployment can have a positive impact on the impedance footprint of the LHC (and hence HL–LHC) collimation system. The various options are summarised in the following.

**New IR7 Optics** A new IR7 optics has been proposed [48], targeting larger values of $\beta$–functions at collimators (in the collimation plane). For the same normalised settings, collimator gaps would be larger in mm, implying a lower impact on beam impedance. In addition, larger $\beta$–functions at TCPs would imply larger changes in normalized amplitude of scattered out protons. Simulation results show that this option is a promising one, reducing the integrated losses of several tens of percent and the peak ones by up to a factor of 3 with respect to the nominal LHC values. The gain in octupole current is estimated to be $\sim$25 %.

**IR7 Asymmetric Collimator Settings** LHC collimators are two–jaws devices with the beam passing in–between. Since halo cleaning of the circulating beam is a process taking place over multiple LHC revolutions, the same cleaning effect from a two–sided device can be achieved with a single–sided device. Fully retracting a jaw per collimator would have a beneficial effect on the resistive–wall impedance footprint of the collimation system, but may increase the leakage to the arc immediately downstream of IR7, which is essentially a single pass process. Even if the studies have not been finalised, first results show some potential in terms of impedance reduction with a limited loss in cleaning performance, even though the impedance reduction is not as sizeable as that obtained with the new IR7 optics [49, 50].

**Electron Lens –Assisted Collimation** In the context of the HL–LHC project, hollow electron lenses (HELs) [51] are studied [52] to deplete on purpose beam tails at specific moments during the LHC cycle, providing a method for active halo control. HELs are devices where a hollow electron beam is made travelling co–axial to the main proton beam; the electron beam is hollow, such that it transversely overlaps only with the tails of the main beam and hence the Lorentz force exerted by the electrons onto the main beam affects only the tails. When the HEL is switched on, the diffusion speed of particles in the tails is enhanced, driving them on the collimation system. Such a device is presently part of the HL–LHC upgrade as means to mitigate fast failures of crab cavities [53] or to scrape away overpopulated tails that in case of jitters of the beam orbit would trigger unnecessary beam dumps.

Even though the primary goal of the HELs in the HL–LHC baseline is not to mitigate impedance aspects, their use at flat top could open to the possibility of progressively tightening the IR7 collimator settings while beams are in collision and hence deploying more relaxed settings at the beginning of data taking, when the beam is still highly populated and the octupole current necessary to Landau–damp it is high. Such an operational mode of IR7 collimators has never been explored so far and it is not planned for the future, since the reduction of collimator gaps would imply producing uncontrolled losses during data taking, with risks of spurious dumps. In this perspective, HELs could be deployed prior to tightening the collimator gaps, generating losses in a controlled way and hence avoiding dumps.

This operational mode, not studied yet, would a priori be beneficial for the footprint of the collimation system on impedance. In fact, it would allow to deploy larger collimator gaps at the beginning of the fill, when the beam intensity is higher, and tighten collimator settings while the beam intensity is reduced because of collision burn–off.

## CONCLUSIONS

The present LHC collimation system substantially contributes to the total LHC impedance budget, especially at flat top energy; without upgrading the system, the brighter HL–LHC beams would need a too high octupole current to be Landau–damped. The expectations for the HL–LHC era are based on the present knowledge of sources of beam instability in the LHC, which account for only half of the octupole current required to operationally stabilise the LHC beams as of Run 2. The origin of the uncertainty is still being investigated, while improving numerical models and understanding the interplay between destabilising processes.

The current baseline of the impedance upgrade of the LHC collimation system in IR7 has been presented. It is based on the replacement of most of the present primary and secondary collimators with new ones. The new hardware is characterised by jaws made of a low–impedance material; in particular, MoGr has been chosen as baseline material, following a rich R&D program, as best compromise between impedance improvement and adequate robustness. In addition, secondary collimators will be coated with pure Mo, to further reduce their footprint on the total machine impedance. The impedance upgrade will bring the expected octupole current required to stabilise the beam within acceptable values.

Other options, currently under study, have been summarised, possibly improving not only the footprint of the system on impedance, but also the cleaning performance. They consider a wide range of changes in IR7, including a new optics, alternative collimator settings, and innovative technologies for achieving beam cleaning.

## REFERENCES


[1] O. Brüning *et al.* (eds), "LHC Design Report", vol. I, CERN, Geneva, Switzerland, Rep. CERN–2004–003–V–1, Jun. 2004.

[2] R. W. Assmann *et al.*, "The Final Collimation System for the LHC", in *Proc. 10th European Particle Accelerator Conf. (EPAC'06)*, Edinburgh, UK, Jun. 2006, paper TUODFI01, pp. 986–988.

[3] R. Bruce *et al.*, "Simulations and measurements of beam loss patterns at the CERN Large Hadron Collider", *Phys. Rev. ST Accel. Beams*, vol. 17, p. 081004, 2014. doi: `10.1103/PhysRevSTAB.17.081004`

[4] A. Bertarelli *et al.*, "The Mechanical Design for the LHC Collimators", in *Proc. European Particle Accelerator Conf. (EPAC'04)*, Lucerne, Switzerland, July 2004.

[5] B. Salvachua Ferrando *et al.*, "Cleaning Performance of the LHC Collimation System up to 4 TeV", in *Proc. 4th Int. Particle Accelerator Conf. (IPAC'13)*, Shanghai, China, May 2013, paper MOPWO048, pp. 1002-1004.

[6] N. Fuster Martínez *et al.*, "Run 2 collimation overview", in *Proc. of the 9th Evian Workshop*, Evian, France, 30th – Jan. 1st Feb. 2019. `https://indico.cern.ch/event/751857/`

[7] N. Mounet *et al.*, "Collimator Impedance", presentation at the LHC Collimation Review 2013, 30th–31st May 2013, CERN, Geneva, Switzerland. `https://indico.cern.ch/event/251588/`

[8] X. Buffat *et al.*, "Transverse Instabilities", in *Proc. of the 9th Evian Workshop*, Evian, France, 30th Jan. 1st – Feb. 2019. `https://indico.cern.ch/event/751857/`

[9] A. Mereghetti *et al.*, "$\beta^*$-Reach – IR7 Collimation Hierarchy Limit and Impedance", CERN, Geneva, Switzerland, Rep. CERN–ACC–NOTE–2016–0007, Jan. 2016. `https://cds.cern.ch/record/2120132`

[10] A. Mereghetti *et al.*, "MD1447 – $\beta^*$-Reach: 2016 IR7 Collimation Hierarchy Limit and Impedance", report in preparation.

[11] D. Mirarchi *et al.*, "MD1878: Operation with primary collimators at tighter settings", CERN, Geneva, Switzerland, Rep. CERN–ACC–NOTE–2017–0014, Jan. 2017. `https://cds.cern.ch/record/2254674`

[12] A. Mereghetti *et al.*, "MD2191 – $\beta^*$-Reach: 2017 IR7 Collimation Hierarchy Limit and Impedance", report in preparation.

[13] G. Apollinari *et al.* (eds.), "High Luminosity Large Hadron Collider (HL–LHC) Technical Design Report V.01", CERN, Geneva, Switzerland, Rep. CERN–2017–007–M, Sep. 2017. `https://cds.cern.ch/record/2284929`

[14] L. Rossi and O. S. Brüning, "Progress with the High Luminosity LHC Programme at CERN", in *Proc. 10th Int. Particle Accelerator Conf. (IPAC'19)*, Melbourne, Australia, May 2019, paper MOYPLM3.

[15] H. Damerau *et al.*, "LHC Injectors Upgrade, Technical Design Report, Vol. I: Protons", CERN, Geneva, Switzerland, Rep. CERN–ACC–2014–0337, Dec. 2014. `https://cds.cern.ch/record/1976692`

[16] D. Amorim *et al.*, "HL–LHC impedance and related effects", CERN, Geneva, Switzerland, Rep. CERN–ACC–NOTE–2018–0087, Dec. 2018. `https://cds.cern.ch/record/2652401`

[17] S. Redaelli, "Beam Cleaning and Collimation Systems", CERN, Geneva, Switzerland, Rep. CERN–2016–002.403, Aug. 2016. `https://cds.cern.ch/record/2207182`

[18] R. Bruce *et al.*, "Sources of machine-induced background in the ATLAS and CMS detectors at the CERN Large Hadron Collider", *Nucl. Instrum. Meth. A*, vol. 729, p. 825–840, Nov. 2013. doi: `10.1016/j.nima.2013.08.058`

[19] R. Bruce *et al.*, "Collimation-induced experimental background studies at the CERN Large Hadron Collider", *Phys. Rev. Accel. Beams*, vol. 22, p. 021004, 2019. doi: `10.1103/PhysRevAccelBeams.22.021004`

[20] R. Bruce *et al.*, "Calculations of safe collimator settings and $\beta^*$ at the CERN Large Hadron Collider", *Phys. Rev. Accel. Beams*, vol. 18, p. 061001, 2015. doi: `10.1103/PhysRevSTAB.18.061001`.

[21] R. Bruce *et al.*, "Reaching record-low $\beta^*$ at the CERN Large Hadron Collider using a novel scheme of collimator settings and optics", *Nucl. Instrum. Meth. A*, vol. 848, p. 19–30, 2017. doi: `10.1016/j.nima.2016.12.039`.

[22] G. Valentino *et al.*, "Semiautomatic beam-based LHC collimator alignment", *Phys. Rev. ST Accel. Beams*, vol. 15, p. 051002, May 2012. doi: `10.1103/PhysRevSTAB.15.051002`

[23] G. Valentino *et al.*, "Final implementation, commissioning, and performance of embedded collimator beam position monitors in the Large Hadron Collider", *Phys. Rev. Accel. Beams*, vol. 20, p. 081002, 2017. doi: `10.1103/PhysRevAccelBeams.20.081002`

[24] D. Amorim, "Update on the LHC impedance model", presentation at the 35th Impedance Working Group meeting, 19th Sep. 2019, CERN, Geneva, Switzerland. `https://indico.cern.ch/event/844161`

[25] J. Wenninger, "Operation and Configuration of the LHC in Run 2", CERN, Geneva, Switzerland, Rep. CERN–ACC–NOTE–2019–0007, Mar. 2019. `https://cds.cern.ch/record/2668326`

[26] R. Bruce *et al.*, "Machine configuration", in *Proc. of the 9th Evian Workshop*, Evian, France, 30th Jan. 1st–Feb. 2019. `https://indico.cern.ch/event/751857/`

[27] D. Amorim *et al.*, "Comparison of LHC impedance model predictions to beam based measurements", presentation at the 30th Impedance Working Group meeting, 5th Mar. 2019, CERN, Geneva, Switzerland. `https://indico.cern.ch/event/802620`

[28] E. H. McLean *et al.*, "Implications of IR-corrector loss to LHC operation", presentation at the LMC meeting, CERN, Geneva, Switzerland, 4th Apr. 2018. `https://indico.cern.ch/event/719201/`

[29] L. R. Carver *et al.*, "Transverse beam instabilities in the presence of linear coupling in the Large Hadron Collider", *Phys. Rev. Accel. Beams*, vol. 21, p. 044401, 2018. doi: 10.1103/PhysRevAccelBeams.21.044401

[30] X. Buffat *et al.*, "Beam stability and quality in the presence of beam-beam and transverse damper", presentation at the 7th HL–LHC Collaboration Meeting, Madrid, Spain, Nov. 2017. https://indico.cern.ch/event/647714

[31] C. Tambasco *et al.*, "Triggering of instability by BTF measurements", presentation at the 96th LBOC meeting, CERN, Geneva, Switzerland, 27th Mar. 2018. https://indico.cern.ch/event/715467

[32] S. Antipov *et al.*, "Update of the HL–LHC operational scenarios for proton operation", CERN, Geneva, Switzerland, Rep. CERN–ACC–NOTE–2018–0002, Jan. 2018. https://cds.cern.ch/record/2301292

[33] S. Redaelli *et al.*, "Collimation upgrade plans", presentation at the International Review of the HL–LHC Collimation System, CERN, Geneva, Switzerland, 11th–12th Feb. 2019. https://indico.cern.ch/event/780182

[34] A. Bertarelli *et al.*, "2014 Development and testing of novel advanced materials with very high thermal shock resistance", in *Proc. Tungsten, Refractory and Hardmetals Conference*, Orlando, Florida, USA, May 2014.

[35] N. Mariani, "Development of Novel, Advanced Molybdenum–based Composites for High Energy Physics Applications", PhD. thesis, Politecnico di Milano, 2014.

[36] J. Guardia-Valenzuela *et al.*, "Development and properties of high thermal conductivity molybdenum carbide - graphite composites", in *Carbon*, vol. 135, 2018. doi: 10.1016/j.carbon.2018.04.010

[37] S. Antipov *et al.*, "Staged implementation of low–impedance collimation in IR7: plans for LS2", CERN, Geneva, Switzerland, Rep. CERN–ACC–NOTE–2019–0001, Jan. 2019. http://cds.cern.ch/record/2654779

[38] F. Carra *et al.*, "Mechanical Engineering and Design of Novel Collimators for HL–LHC", in *Proc. 5th Int. Particle Accelerator Conf. (IPAC'14)*, Dresden, Germany, 15th–20th Jun. 2014, paper MOPRO116, pp. 369–372.

[39] I. Efthymiopoulos *et al.*, "HiRadMat: A New Irradiation Facility for Material Testing at CERN", in *Proc. 2nd Int. Particle Accelerator Conf. (IPAC'11)*, San Sebastian, Spain, 4th–9th Sep. 2011, paper TUPS058, pp. 1665–1667.

[40] A. Bertarelli *et al.*, "Dynamic Testing and Characterization of Advanced Materials in a New Experiment at CERN HiRadMat Facility", in *Proc. 9th Int. Particle Accelerator Conf. (IPAC'18)*, Vancouver, BC, Canada, 29th April – 4th May. 2018, paper WEPMF071, pp. 2534–2537.

[41] M. Pasquali *et al.*, "Dynamic response of advanced materials impacted by particle beams: The multimat experiments", *Journal of Dynamic Behavior of Materials*, vol. 5, p. 266–295, 2019. doi: 10.1007/s40870-019-00210-1

[42] F. Carra *et al.*, "Mechanical robustness of HL–LHC collimator designs", *Journal of Physics: Conference Series*, vol. 1350, p. 012083, 2019. doi: 10.1088/1742-6596/1350/1/012083

[43] G. Gobbi *et al.*, "Novel LHC collimator materials: High-energy Hadron beam impact tests and non–destructive post–irradiation examination", *Mechanics of Advanced Materials and Structures*, 2019. doi: 10.1080/15376494.2018.1518501

[44] X. Buffat *et al.*, "Strategy for Landau damping of head-tail instabilities at top energy in the HL–LHC", report in preparation.

[45] "Installation of a low–impedance secondary collimator (TCSPM) in IR7", EDMS doc. 1705738 (v.1.0), LHC–TC–EC–0006 (v.1.0) (2017).

[46] C. Accettura *et al.*, "Resistivity measurements on coated collimator materials", presentation at the ColUSM meeting, CERN, Geneva, Switzerland, 28th February 2020. https://indico.cern.ch/event/883715

[47] S.V. Furuseth and X. Buffat, "Noise and possible loss of Landay damping", presentation at the ICFA mini–workshop on "Mitigation of Coherent Beam Instabilities in particle accelerators", Zermatt, Switzerland, 23rd–27th Sep. 2019, these proceedings.

[48] R. Bruce *et al.*, "New IR7 optics with removed MQW magnets", presentation at the HSS section meeting, CERN, Geneva, Switzerland, 6th December 2017. https://indico.cern.ch/event/681507

[49] D. Kodjaandreev, "Single-sided collimation and the effects on beam cleaning and impedance in the LHC", MSc. thesis, University of Malta, Malta, 30th May 2019. https://cds.cern.ch/record/2690267

[50] A. Mereghetti *et al.*, "Review of the system with asymmetric settings", presentation at the 112th ColUSM meeting, CERN, Geneva, Switzerland, 29th Jan. 2019. https://indico.cern.ch/event/789529

[51] V. Shiltsev, "Electron Lenses for Super-Colliders", Springer (2016), ISBN: 9781493933150.

[52] D. Mirarchi *et al.*, "Beam dynamics simulations with a Hollow Electron Lens", presentation at the 9rh HL–LHC Collaboration meeting, Fermilab, Batavia, Illinois, USA, 14th–16th Oct. 2019. https://indico.cern.ch/event/806637

[53] A. Santamaria Garcia, "Experiment and Machine Protection from Fast Losses caused by Crab Cavities in the High Luminosity LHC", PhD. thesis, Ecole Polytechnique Federale de Lausanne, Lausanne, Switzerland, 2019. https://cds.cern.ch/record/2636957

# SURFACE EFFECTS FOR ELECTRON CLOUD*

A. Novelli[1], University of Rome “La Sapienza", 00185 Rome, Italy
M. Angelucci, A. Liedl, L. Spallino, and R. Cimino†, LNF-INFN, 00044 Frascati, Italy
Rosanna Larciprete[1], ISC-CNR, 00185 Rome, Italy
[1]also at LNF-INFN, 00044 Frascati, Italy

*Abstract*

The ability of a low Secondary Electron Yield coating to mitigate detrimental electron cloud effects potentially affecting accelerators' performances has been convincingly validated. The interference of such coatings with other properties required to accelerator constructive materials (i.e. vacuum compatibility, magnetic permeability, high surface conductivity, etc.) is of great concern and has recently attracted a lot of interest and studies. For instance, the severe impedance budget constraint requires the highest conductivity in the surface layers within the skin depth (typically some $\mu$m) characteristic of the e.m. interaction. It is therefore of uttermost importance to define the minimum thickness one overlayer should have in order to be an effective electron cloud mitigator and minimize its impact to surface conductivity.
To this purpose, XPS and Secondary electron spectroscopy have been simultaneously applied to the prototypical system formed by increasing coverages of amorphous Carbon (a-C) deposited on atomically clean Cu. XPS has been successfully used to qualify and quantify the a-C thickness, rendering possible a detailed coverage dependent study. A significantly thin a-C layer, of about 5 to 7 nm, is surprisingly enough to lower the secondary emission properties of the whole system below 1. This observation opens up the possibility to develop, on industrial scale, thin enough electron cloud mitigators that will not affect impedance issues.

## INTRODUCTION

Electron clouds - generated in accelerator vacuum chambers by photoemission, residual-gas ionization, and secondary emission - can affect the operation and performance of hadron and lepton accelerators in a variety of ways. They can induce increases in vacuum pressure, emittance growth, beam instabilities, beam losses, beam lifetime reductions, or additional heat loads on a (cold) chamber wall [1, 2]. When electrons are accelerated by the positive passing beam in the direction perpendicular to it, they gain energy and, when finally hit the vacuum chamber, they create other secondary electrons at the accelerator walls. The number of electrons created during such occurrence is governed by a material surface property called Secondary Electron Yield (SEY). SEY is defined as the ratio between the number of emitted electrons (also called secondary electrons) to the number of incident electrons (also called primary electrons) and is commonly denoted by $\delta$. When the effective SEY at the chamber is larger than unity, the electron population rapidly grows with successive bunch passages. This can lead to a high electron density and hence, to Electron cloud effects (ECE). One powerful method to control and overcome such effects is to ensure a low SEY, ideally always less or just around one. Different solutions have been proposed to this end, one being to treat the surface by Laser Ablation Surface Engineering (LASE) [3, 4] or by TiZrV [5, 6] or amorphous Carbon (a-C) coating [7]. LASE surfaces have a low SEY due to their particular micro and nano-metrical grooves morphology. TiZrV is a Non-evaporable Getter (NEG) that, once activated at ~ 180 °C, not only is an extremely powerful vacuum pump, but shows a SEY typically less than 1. Also a-C has a quite low SEY thanks to its intrinsic properties connected to the sp$^2$ Carbon bonds typical of graphite-like materials [8–10].

All those coatings, used as ECE mitigation remedies, must necessarily be compliant to a number of stringent specifications [11]. Material conductivity, magnetic properties, vacuum, constructive compatibility, impedance issues are among the most stringent ones, suggesting a more general approach when qualifying a material to be used in accelerators. In terms of vacuum constructive compatibility, for example, NEG, LASE and a-C do behave quite differently. Activated NEG is an active pump that can ensure superb vacuum performances if sufficiently thick (more than a $\mu$m to grant some reservoir for pumped gasses). However, for space reasons, it is not always easy or possible to implement its activation and it is not yet known its ability to pump at cryogenic temperatures. LASE is certainly vacuum compatible and does not require activation. Recently, it was shown [12] that ices cryo-sorbed on its surface, desorb in a temperature interval much larger than the very sharp one observed from a flat surface. The cryogenic vacuum properties of LASE augmented effective surface are still under study.
One more intriguing example, where material constraints are challenging, relates to the surface conductivity required to build an accelerator within a given impedance budget. LASE, TiZrV and a-C have a significantly reduced surface conductivity in respect to Cu and their use may indeed have a significant impact on this issue [13, 14, 16, 17]. Impedance issues require to minimize surface resistance in the first few microns, the typical skin depth of the e.m. interaction between beam and materials. One line of research is then to try thinning the ECE mitigator coating well below the size of this skin-depth. A very thin coating, even if badly conduc-

* Work supported by INFN National committee V trough the “MICA" project.
† roberto.cimino@lnf.infn.it

tive, will not add any significant contribution to the machine impedance. This coating thickness reduction is indeed possible even if it may significantly affect other properties: a thinner LASE will have smaller grooves and porosity and will possibly be less effective as ECE mitigator, a very thin NEG will have a significantly reduced pumping capacity. Synergic to this research line, at the Frascati National Laboratory, we launched a detailed study to define more precisely how thin a coating should be to act as an effective ECE mitigator. We report here some preliminary data that refer to the case of a-C grown on polycrystalline atomically clean copper. The data are relative to a laboratory designed surface science experiment and, therefore, consequences on real coatings, to be performed on industrial scale, must be extrapolated with caution.

## EXPERIMENTAL

The experiment was performed in the Material Science Laboratory of the INFN-LNF at Frascati (Rome, Italy), in an ultra-high vacuum system routinely used for XPS/SEY experiments. It consists of a preparation chamber and an analysis chamber, both having a base pressure of $1 \times 10^{-10}$ mbar and is described in some more details in the literature [1, 8–10, 18]. Polycrystalline Cu substrate was cleaned by cycles of $Ar^+$ sputtering at 1.5 kV and prolonged thermal annealing at temperatures of 800-1000 K. Atomically clean Cu substrate, even if not representative of realistic carbon coatings for accelerators, was chosen to minimize spurious effects (like contaminations or electron beam induced SEY modification [10]) and be able to single out only the desired phenomenon.

Carbon was deposited by an electron beam evaporator (Tectra GmbH.) from a 99.999 purity C rod with a stable rate of ≈ 0.03 nm/min. This method, though unpractical for industrial productions, allows a very careful monitoring of thickness, especially at very low coverages, and produces well controlled and clean a-C films. During C evaporation, the background pressure was $\leq 5 \times 10^{-10}$mbar. C layers were deposited in steps and after each evaporation XPS and SEY analysis were performed. XPS measurements were carried out by using an Omicron EA125 analyzer to reveal the photoelectrons excited by the non monochromatic radiation of an Mg K ($h\nu$ = 1256 eV). SEY is measured as described in detail in Refs [1, 8–10]. SEY is, by definition, equal to $I_{out}/I_p = (I_p - I_s)/I_p$, where $I_p$ is the current of the primary electron beam hitting the sample, $I_{out}$ is the current of the electrons emerging from the sample and $I_s$ is the sample current to ground, as measured by a precision amperometer. In brief $I_p$ (some tens of nA) was measured by means of a Faraday cup positively biased, whereas $I_s$ was determined by biasing the sample at -75 V. SEY curves as a function of the primary energy $E_p$ are characterized by a maximum value ($\delta_{max}$) reached at a certain energy ($E_{max}$). As already discussed [18], we can correctly measure SEY starting from few hundreds of meV above the sample work function. SEY measured curve drops from 1 to 0 within an $E_p$ region whose width ( 0.85 eV) is determined by the thermally broadened electron beam emitted by the thermoionic cathode. SEY measurements are only valid after this drop, which occurs at an energy related to the surface vacuum level. XPS was used to quantitatively define a-C coverage by looking at the increase of the C 1s signal and the concomitant Cu 2p decrease during deposition, which is assumed to be homogeneous. Standard practice XPS analysis procedures [20] was used to estimate, after each deposition, the carbon layer quality and thickness. This standard practice in XPS analysis is based on reasonable assumptions on the electron mean free path in a-C and in Cu [19], on a close to layer by layer growth and by assuming that the Cu core level intensities follows a Beer-Lambert low in a layer on a substrate model [20, 21].

## RESULTS

The prototypical system we decided to investigate - namely a-C on atomically clean polycrystalline Cu - offered the possibility to follow XPS and SEY data as a function of deposition time. XPS analysis [21], not shown here, allows us to determine with an experimental uncertainty of approximately 30 %, the thickness, in nm, of the a-C film. XPS also confirms that the a-C film is mainly $sp^2$ in character and can be indeed assumed to be closer to a distorted graphite than to diamond. Once XPS allows us to define the thickness of the various a-C films deposited, we can plot the evolution of SEY versus a-C coverage.

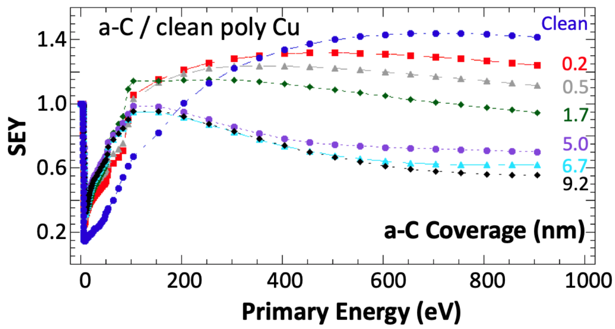


Figure 1: SEY evolution at different a-C thicknesses.

This is shown in Fig. 1, where we can observe:

- The SEY of the atomically clean polycristalline Cu shows a $\delta_{max}$ of ∼ 1.4 at around $E_{max}$ ∼ 640 eV consistent with literature results [1, 18, 22];
- For the initial low coverages of a-C, we notice some significant effect, specially in the very low energy part of the SEY spectrum. This confirms how this low energy range of SEY is sensitive to very small quantities of adsorbates, and even of contaminants [22] in the sub-monolayer regime;
- Increasing carbon coverages, the low energy part of the SEY spectrum does not change significantly any more, while the overall curve is severely modified in shape, $\delta_{max}$ and $E_{max}$;
- $\delta_{max}$ is steadily reduced from ∼1.4 (clean copper) to less than 1 (after ∼ 6 nm of a-C );

- Also $E_{max}$ is significantly and steadily reduced with increasing a-C thickness going from ~650 eV (clean copper) to ~100 eV after already 6 nm.
- For intermediate coverages, the $\delta$ curve can be considered as a superposition of the modified yield of the substrate and the SEY of the overlayer.

We report, in Fig. 2, $\delta_{max}$ and $E_{max}$ versus the estimated a-C coverage. On increasing the thickness, $\delta_{max}$ goes from the value of clean Cu, to the one typically measured for graphite and a-C [8, 9]. On the other hand, $E_{max}$ starts from the clean Cu value but ends up significantly lower than what is observed in graphite. Something similar, if not so effective, was observed for $E_{max}$ after repeated $Ar^+$ sputtering cycles on otherwise crystalline Graphite, implying that $E_{max}$ could get reduced by increasing disorder (and/or amorphization) [9].

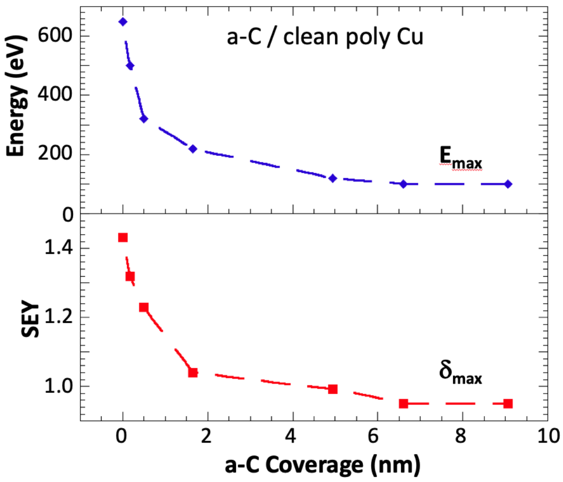


Figure 2: $\delta_{max}$ (bottom panel) and $E_{max}$ at different a-C thicknesses. $\Delta\delta_{max}/\delta_{max}$= 5% and $\Delta E_{max}/E_{max}$ = 10%

For the test case studied here, SEY curve does not seem to vary after that 5 to 6.5 nm of a-C were deposited on the atomically clean Cu surface. After this coverage, SEY is dominated by the overlayer signal.

## DISCUSSION

Here, we are reporting results from a prototypical system which can not be used for production both due to the use of an atomically clean Cu substrate and to the EB-PVD used to evaporate Carbon. Clearly, our results should be confirmed and extended to other systems and materials. They are still extremely challenging and call for a reexamination of the coating thickness normally used to mitigate e-cloud. Even with safety margins ( up to 5 to 10 times in thickness) typical of an industrial production, it is indeed possible to have an ECE mitigator coating which only marginally affects the surface resistance within the skin depth and therefore is fully compliant with the impedance budget. Maybe, magneto-sputtering deposition technique, which is routinely used for coating accelerator pipes, is not easily controlled in the very low coverage regimes and could either been implemented / modified or even substituted with coating techniques more apt to control the quality in the very low coverage regime. What is here clear, for the first time in this context, is that 5 to 6.5 nm of a-C coating are enough to finally reduce SEY below one. This observation would call for a technological effort to be able to reproduce and safely control such low thickness coatings on industrial scale with the aim to finally produce ECE mitigators that do not affect impedance.

## CONCLUSIONS

We have studied a prototypical system formed by a thin C layer incrementally evaporated, at low rate, on a polycrystalline Cu substrate. We address the question on what is the minimal layer thickness that defines the SEY of the system as the one of the overlayer and not of the substrate. We demonstrate that, in this case, 5 to 6.5 nm are sufficient to reduce the SEY from 1.4 (copper) to ~1 (a-C). More data are needed to confirm this to be a general trend, valid also for different substrates, eventually with significantly higher SEY and overlayer materials. The results open up the possibility to design ECE mitigators fully compliant with impedance issues.

## ACKNOWLEDGMENT

We thank for technical assistance V. Tullio, M. Pietropaoli, V. Sciarra and G. Viviani from the DAΦNE-L support group.

## REFERENCES

[1] R. Cimino and T. Demma, Int. J. Mod. Phys. A. 29, (2014), 1430023.

[2] O. Malyshev, "Vacuum in Particle Accelerators: Modelling, Design and Operation of Beam Vacuum Systems" (Wiley, 2019).

[3] R. Valizadeh, O. B. Malyshev, S. Wang, S. A. Zolotovskaya, W. Allan Gillespie, and A. Abdolvand, Appl. Phys. Lett. 105, (2014) 231605.

[4] R. Valizadeh, O. Malyshev, S. Wang, T. Sian, M. Cropper, and N. Sykes, Appl. Surf. Sci. 404, (2017), 370.

[5] P. Chiggiato, P. Costa Pinto, Thin Solid Films 515, (2006), 382.

[6] P. C. Pinto, S. Calatroni, P. Chiggiato, H. Neupert, W. Vollenberg, E. Shaposhnikova, M. Taborelli, and C. Y. Vallgren, in: Proceedings of the 24th Particle Accelerator Conference, PAC-2011, 2096.

[7] C.Y. Vallgren, G. Arduini, J. Bauche, S. Calatroni, P. Chiggiato, K. Cornelis, P.C. Pinto, B. Henrist, E. Metral, H. Neupert, G. Rumolo, E. Shaposhnikova, M. Taborelli, Phys. Rev. ST Accel. Beams 14 (2011) 071001.

[8] R. Larciprete, D. Grosso, A. Di Trolio and R. Cimino, Appl. Surf. Sci. 328 (2015) 356.

[9] L. A. Gonzalez, R. Larciprete and R. Cimino AIP Advances Vol.6, Number 9, (2016), 095117.

[10] R. Cimino, M. Commisso, D. R. Grosso, T. Demma, V. Baglin, R. Flammini, and R. Larciprete, Phys. Rev. Lett. 109, (2012), 064801.

[11] V. Baglin, P. Lebrun, L. Tavian, and R. van Weelderen, Tech. Rep. CERN-ATS-2013-006, CERN, Geneva (2013).

[12] L. Spallino, M. Angelucci, R. Larciprete, and R. Cimino, Appl. Phys. Lett. 114, (2019), 153103.

[13] E. Koukovini-Platia, G. Rumolo and C. Zannini Phys. Rev. ST Accel. Beams 20, (2017), 011002.

[14] S. Calatroni, E. Garcia-Tabares Valdivieso, H. Neupert, et al., Phys. Rev. Accel. Beams 20, (2017), 113201.

[15] O.B. Malyshev, L. Gurran, P. Goudket, K. Marinov, S. Wilde, R. Valizadeh and G. Burt, Nucl. Instrum. Methods Phys. Res. A 844, (2017), 99-107.

[16] M. Migliorati, E. Belli, M. Zobov, Phys. Rev. Accel. Beams 21, (2018), 041001.

[17] E. Belli, P. Costa Pinto, G. Rumolo, A. Sapountzis, T. Sinkovits, M. Taborelli, B. Spataro, M. Zobov, G. Castorina, and M. Migliorati Phys. Rev. Accel. Beams 21, (2018), 111002.

[18] R. Cimino, L. Gonzalez, R. Larciprete, A. Di Gaspare, G. Iadarola, and G. Rumolo, Phys. Rev. ST Accel. Beams 18, (2015), 051002.

[19] S.Tanuma, C.J. Powell and D.R. Penn, Surf. Interface Anal., 43: (2011), 689-713.

[20] “An Introduction to Surface Analysis by XPS and AES", by John F. Watts and John Wolstenholme, WILEY, 2003.

[21] A. Novelli, M. Angelucci, A. Liedl, L. Spallino and R. Cimino in preparation.

[22] L. A. Gonzalez, M. Angelucci, R. Larciprete, and R. Cimino, AIP Advances 7, (2017), 115203.

# ELECTRON CLOUD MITIGATION WITH LASER ABLATED SURFACE ENGINEERING TECHNOLOGY*

O.B. Malyshev† and R. Valizadeh, STFC Daresbury Laboratory, Warrington, WA4 4AD UK

*Abstract*

Parameters of the high intensity accelerators with positively charged beams could be compromised by electron cloud (e-cloud) effect. One of the most efficient mitigation method is providing the beam vacuum chamber walls with low secondary electron yield (SEY). A discovery of low SEY surfaces produced with Laser Ablated Surface Engineering (LASE) brought a new technological solution for e-cloud mitigation. This paper highlights the main results obtained since its discovery in 2014.

## INTRODUCTION

Electron cloud (e-cloud) and beam induced electron multipacting (BIEM) are two coupled effects that can badly affect the performance of high intensity particle accelerators with positively charged beams [1,2]. Among many developed methods for the e-cloud and BIEM mitigation, one of preferred solutions is an inner surface with a low secondary electron emission (SEY) yield. The advantage of this method that after implementing it requires no controllers, no power sources, no cables, no feedthroughs, etc. Low SEY surface is a result of using low SEY materials for vacuum chamber, a thin film of low SEY materials on inner walls of vacuum chamber or surface geometry engineering (grooves or special surface structures). Many research teams are involved in these activities around the world, different techniques (machining, etching, thin film coating, etc.) allow to reach SEY ≤ 1. In this paper a short overview of Laser Ablated Surface Engineering (LASE) is given.

## LASE AS A LOW SEY SOLUTION FOR E-CLOUD MITIGATION

### *What is LASE?*

Nanostructuring of material surfaces by Laser Ablated Surface Engineering (LASE) is well established science and manufacturing with more than 25 years of experience, see review papers in Ref. [3-6]. However, it was not looked at as a surface treatment for accelerator vacuum chambers.

### *Discovery of LASE for SEY mitigation*

In 2014 it was discovered that LASE on copper, aluminium and stainless steel surfaces may lead to dramatic reduction of SEY, with its maximum value $\delta_{max} < 0.8$ [7,8]. Figure 1 shows an untreated and LASE copper samples and Fig. 2 shows SEY for untreated and LASE copper samples as a function of incident electron energy for two conditions: as-received (i.e. measured shortly after installing on SEY measurement facility and after conditioning (electron bombardment with a dose of $1.0 \times 10^{-2}$ C/mm$^2$ for Cu and $3.5 \times 10^{-3}$ C/mm$^2$ for black Cu). One can see that even as-received LASE sample demonstrate $\delta_{max} < 1.1$ in comparison to $\delta_{max} = 1.9$ for the untreated sample, and the electron conditioning lead to further reduction of SEY: $\delta_{max} < 0.8$ for LASE sample in comparison to $\delta_{max} < 1.25$ for the untreated sample. The main result reported in Ref. [7,8] that SEY < 1 can be achieved on Cu, Al and stainless steel with LASE, and this technology could be applied for suppression of PEY/SEY and solving the e-cloud problem.

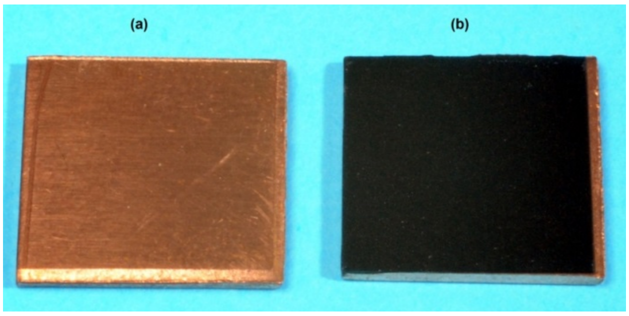


Figure 1: (a) Untreated and (b) LASE copper samples.

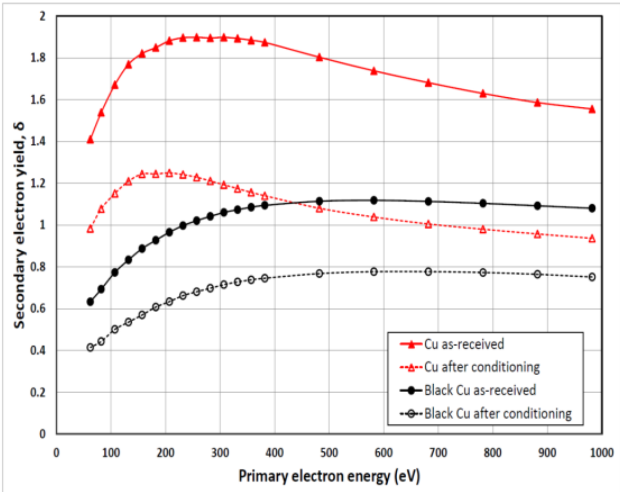


Figure 2: SEY for Cu as a function of incident electron energy: Cu – untreated surface, black Cu – laser treated surface, and conditioning – electron bombardment with a dose of $1.0 \times 10^{-2}$ C/mm$^2$ for Cu and $3.5 \times 10^{-3}$ C/mm$^2$ for black Cu. Reproduced from Ref. [8].

### *Further LASE development*

In the following years, the emphasis was focused on better understanding of the following:

- How and why SEY is reduced on LASE surfaces
- Further reduction of SEY
- Study how LASE surface may affect other characteristics which are important for an accelerator:
  - RF surface resistance
  - Particulate generation

† oleg.malyshev@stfc.ac.uk

- Vacuum properties

It was demonstrated [9-10] that a treatment of copper using a λ = 355 nm laser resulted in creation of three different scales structures show in Fig. 3:

- microstructure grooves ranging from 8 to 100 µm deep,
- coral-like submicron particles superimposed on the grooves which is made of agglomeration of
- nano-spheres.

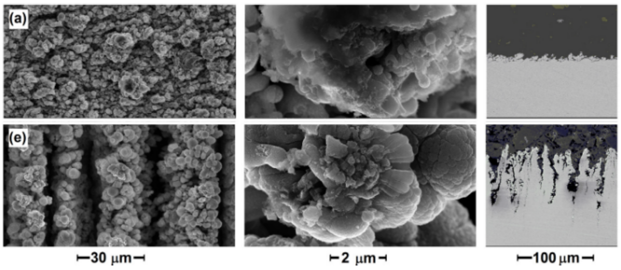


Figure 3: Low (on the left) and high (in the middle) resolution planar and X-Section (on the right) SEM micrographs of 1 mm thick copper samples treated with a laser using different scan speeds: (a) 180 mm/s and (e) 30 mm/s. Reproduced from Ref. [10].

It was demonstrated, as reported in Ref [10]:

– The SEY reduction is happening due to a superposition of these structures.
– Low SEY surfaces can be produced using various lasers with different wavelength, such as λ=355 nm and λ=1064 nm, different power, with a variety of other parameters.

### First accelerator test

Two of the LASE surfaces reported in Ref. [10] has been selected for the first accelerator test of vacuum components with LASE surfaces for electron-cloud mitigation [11]. A specially designed SPS liner was treated on two areas of 40 mm × 490 mm with different LASE parameters, see Fig. 4.

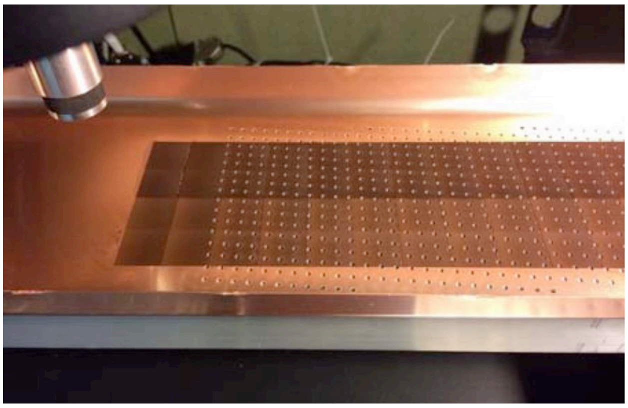

Figure 4: Perforated side of the SPS liners treated by ASTeC. The two regions treated with a different set of laser parameters are clearly visible. Reproduced from Ref. [11].

The following test at SPS accelerator has demonstrated a complete eradication of e-cloud achieved with both set of LASE parameters [11]. That was the first demonstration of efficiency of e-cloud mitigation with LASE technology.

### RF surface resistance

Vacuum chamber RF surface resistance should be below a certain threshold to avoid two possible problems:

– An increase of beam energy spread due to beam impedance induced by the RF surface resistance;
– Significant resistive heal loss of beam image current on vacuum chamber walls.

The depth of microstructure grooves produced by LASE ranging from 8 to 100 µm. the RF surface resistance has been measured at 7.8 GHz with a 3-choke cavity as shown in Fig. 5. It was shown that the RF surface resistance $R_s$ can be reduced with reducing the groove depth (main source of surface resistance) and the depth of other LASE structures, see Fig. 6 [9,10].

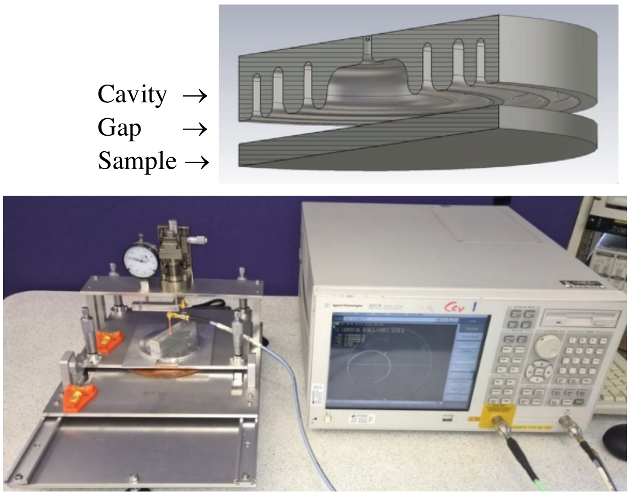


Figure 5: The 3-choke cavity (top) and a facility (bottom) for contactless surface resistance measurements.

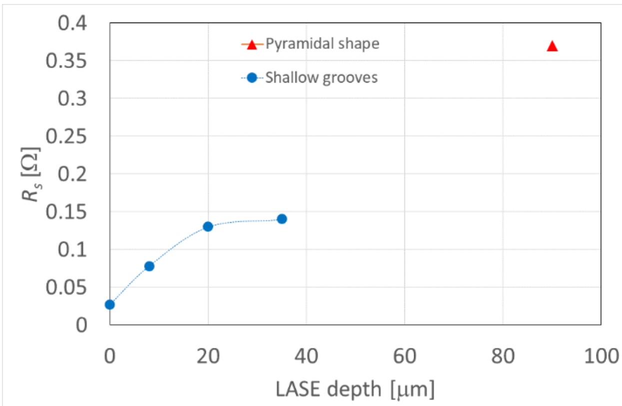


Figure 6: The RF surface resistance as a depth of LASE structures.

## EUROCIRCOL STUDIES FOR FCC

The successful results on SEY mitigation with LASE lead to consider LASE as baseline solution for FCC-hh beam chamber in the H2020 EuroCirCol programme. More than 120 different LASE samples were produced and tested in STFC. The sample were produced with different lasers (nanosecond lasers with λ = 355 nm and 1064 nm, picosecond lasers with λ = 355 nm and 1064 nm), in different atmospheres (air, vacuum, Ar, $CH_4$). More than 60 samples demonstrated $\delta_{max} < 1$ [12-13].

A number of samples has been investigated by the EuroCirCol WP4 partners:

- A compatibility of LASE surfaces with cryogenic vacuum in future high-energy particle accelerators has been studied in INFN [14-16];
- Reflectivity and photoelectron yield has been studied under synchrotron radiation at INFN [17];
- Thermal outgassing and electron stimulated desorption measurements has been performed at STFC [18];
- A 2-m long porotype of the FCC-hh vacuum chamber for photodesorption measurements at KARA:
  - a tube in two halves,
  - it has been LASE treated with a laser (λ = 1064 nm), treated area of each half is 2 m × 20 mm.

## ADVANTAGES OF LASE OVER OTHER PASSIVE MITIGATION METHODS

- LASE can be done in air or selected gas atmosphere, i.e. there is no need for vacuum or clean room facilities:
  - reduced cost
- The laser is capable of fabricating the desired micro/nanostructure in a single step process:
  - reduced processing time
- Surface engineering is performed by photons and, thus, contactless:
  - no contamination from the tools or the process materials
- The process is applicable to the surfaces of any 3D object:
  - i.e. inner walls of beam vacuum chambers
- It is possible to lase in many different environments, such as gases, liquids, or in a vacuum
  - i.e. controlling surface composition (oxides, nitrides, carbonises…) and surface formation.

## CONCLUSIONS

LASE is an e-cloud mitigation technology for future high intensity accelerators. It has been demonstrated that low SEY surfaces can be produced with different lasers (different wavelength, power, frequency and other parameters). The technology is ready for scaling up to be applied on large vacuum chambers.

## REFERENCES


[1] F. Zimmermann. Electron-cloud effects in past & future machines – walk through 50 years of electron-cloud studies. Conf. Proc. C 1206051, 9-17 (2013).

[2] V. Baglin and O.B. Malyshev. Beam-Induced Electron Multipacting, Electron Cloud and Vacuum Design. Chapter 8 in book "Vacuum in Particle Accelerators: Modelling, Design and Operation of Beam Vacuum Systems", ed. O.B. Malyshev, Willey-VCH, 2019.

[3] K.-H. Leitz, B. Redlingshöfer, Y. Reg, A. Otto, M. Schmidt. Metal ablation withshort and ultrashort laser pulses, Physics Procedia 12B (2011) 230–238.

[4] A. Shih, J. Yater, C. Hor, R. Abrous. Secondary electron emission studies, Appl. Surf. Sci. 111, 251 (1997).

[5] K.M. Tanvir Ahmmed, C. Grambow, A.-M. Kietzig. Fabrication of Micro/Nanostructures on metals by femtosecond laser micromachining, Micromachines 5, 1219 (2014).

[6] J. Byskov-Nielsen, J.-M. Savolainen, M.S. Christensen, P. Balling. Ultra-short pulse laser ablation of metals: threshold fluence, incubation coefficient and ablation rates, Appl. Phys. A 101, 97 (2010).

[7] R. Valizadeh, O. Malyshev. Apparatus and methods relating to reduced photoelectron yield and/or secondary electron yield. Patent publication number WO2015189645 A1. 17th Dec 2015.

[8] R. Valizadeh, O.B. Malyshev, *et al*. Appl. Phys. Lett. 105, 231605 (2014); doi: 10.1063/1.4902993

[9] R. Valizadeh, O.B. Malyshev, S. Wang, *et al*. Low secondary electron yield of laser treated surfaces of copper, aluminium and stainless steel. In Proc. of IPAC'16, p. 1089 (2016).

[10] R.Valizadeh, O.B.Malyshev, S.Wang, *et al*. Reduction of Secondary Electron Yield for E-cloud Mitigation by Laser Ablation Surface Engineering, Applied Surface Science 404, 370 (2017).

[11] S. Calatroni, E. Garcia-Tabares Valdivieso, H. Neupert, V. Nistor A. Perez Fontenla, *et al*. First accelerator test of vacuum components with laser-engineered surfaces for electron-cloud mitigation. Phys. Rev. Accel. Beams 20, 113201 (2017).

[12] T. Sian, R. Valizadeh, O. Malyshev. LASE surfaces for mitigation of electron cloud in accelerators. In Proc. of IPAC'18, p. 3958 (2018).

[13] T. Sian. PhD thesis, Manchester University (2019).

[14] L. Spallino, M. Angelucci, R. Larciprete, R. Cimino. On the compatibility of porous surfaces with cryogenic vacuum in future high-energy particle accelerators. Appl. Phys. Lett. 114, 153103 (2019).

[15] L Spallino. Material properties compliance with cryogenic vacuum for particle accelerators. J. Vac. Sci. Technol. B 38, 032803 (2020);

[16] L. Spallino, M. Angelucci and R. Cimino. On the cryogenic vacuum behaviour of laser treated copper. Submitted to Phys. Rev. Special Topics on 8/4/2020.

[16] E. La Francesca, M. Angelucci, A. Liedl, *et al*. Reflectivity and Photoelectron Yield from Copper in Accelerators. Submitted to Phys. Rev. Special Topics on 2/4/2020.

[17] O.B. Malyshev and R. Valizadeh. Electron stimulated desorption from laser ablated surface engineered surfaces of copper and stainless steel. Submitted to J. Vac. Sci. Technol. A in June 2020.

# VLASOV EIGENFUNCTION ANALYSIS OF SPACE-CHARGE AND BEAM-BEAM EFFECTS*

Y. Alexahin#, Batavia, IL 60510, USA


*Abstract*

Space-charge and beam-beam interaction affect both incoherent and coherent motion of particles potentially leading to instabilities and deterioration of the beam parameters. An overview of these phenomena will be given with an emphasis on the observable spectral characteristics and the mitigation methods of their harmful effects.


## INTRODUCTION

With the advent of supercomputers with thousands of cores massive tracking simulations became the main method for studying intensity-related effects such as beam-beam and space-charge effects. Still, other methods can be useful to get insight in the observed phenomena and for preliminary study of mitigation strategies.

This report is devoted to the eigenvalue analysis of the Vlasov equation which fills an important niche between analytical calculations and tracking simulations providing the insight of the former and accuracy of the latter.

In the context of the beam-beam interaction this approach was successfully used in Ref. [1] and further developed by the author of this report [2, 3].

An extension of the method on the coherent modes in space-charge dominated beam will be discussed here for the case of a Gaussian beam in a parabolic RF well.

## COHERENT BEAM-BEAM MODES

Traditionally the nonlinearity of the unperturbed motion is taken into account as the amplitude dependence of incoherent tunes entering the dispersion relation. However, in the case of strong-strong beam-beam interaction the deformation of the charge distribution of the beams also should be taken into account [1].

Let us emphasize that perturbation is considered infinitesimal, it is the unperturbed single particle oscillations that are nonlinear. Linearizing w.r.t. the perturbation the Liouville equation with self-consistent electromagnetic forces we come to the Vlasov equation.

For a Gaussian unperturbed distribution $F_0$ the Vlasov equation for perturbation $F_1$ in the action-angle variables $\underline{I} = (I_x, I_y, I_s)$, $\underline{\psi} = (\psi_x, \psi_y, \psi_s)$ has the form

$$i\frac{\partial}{\partial\theta}F_1^{(k)} = \hat{A}F_1^{(k)} = -i\underline{Q}^{(k)}\frac{\partial}{\partial\underline{\psi}}F_1^{(k)} - i\frac{r_p N_{3-k}}{2\pi\gamma}F_0\underline{\varepsilon}^{-1}\cdot\frac{\partial}{\partial\underline{\psi}}\int G^{(k)}F_1^{(3-k)}d^3I'\,d^3\psi' \quad (1)$$

where $\theta$ is the generalized azimuth, $k$=1,2 is the beam number, $N_k$ is the number of particles per bunch, $\underline{Q}^{(k)} = (Q_x^{(k)}, Q_y^{(k)}, -Q_s^{(k)})$, $\underline{\varepsilon}^{-1} = (\varepsilon_x^{-1}, \varepsilon_y^{-1}, \varepsilon_s^{-1})$ being the incoherent tunes and emittances in all three planes.

By performing Fourier expansion in the angle variables we obtain from Eq. (1) a system of equations (generally coupled) for the Fourier components of $F_1$. Outside of the resonances the coupling of the modes can be neglected so that they can be treated independently.

### *Van Kampen modes*

Yokoya et al. [1] showed that the spectrum of operator $\hat{A}$ – let us call it the Vlasov operator – includes continuum covering the range of single particle tunes and possibly some discrete values lying outside the continuum. In particular, they found that out of phase dipole oscillations (π-mode) of two round beams with equal sizes, intensities and bare lattice tunes have the tuneshift 1.214 times the maximum (by absolute value) incoherent tuneshift, $\xi$, raising question of stability of this mode.

In-phase dipole oscillations (Σ-mode) also have mixed spectrum: a discrete value corresponding to a rigid bunch oscillations unaffected by the beam-beam interaction and a continuum covering the same range of incoherent tunes.

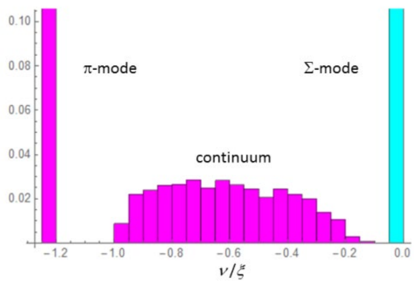


Figure 1: Spectrum of dipole beam-beam oscillations of particles with the same charge sign.

A crude picture of the spectrum of oscillations excited by a dipole kick is presented in Fig. 1 with the discrete mode peaks cut for better continuum visibility. Out of the Σ-modes only the discrete one can be seen, the continuum Σ-modes – being orthogonal to it – cannot be excited by a dipole kick.

The continuum modes – despite the coincidence of their spectrum with single particle tunes range – are truly coherent modes involving all particles in the bunch. However, they have a $\delta$-function like singularity which does not permit to use smooth basis functions in the action variable space [2].

The physical significance of the continuum modes is

* Work supported by Fermi Research Alliance LLC. Under DE-AC02-07CH11359 with the U.S. DOE
# alexahin@fnal.gov

that they describe Landau damping as it was shown by Van Kampen in the case of plasma oscillations [4].

The Vlasov eigenfunction method not only correctly predicts the spectrum, but allowed to understand why the coherent beam-beam modes were not always seen in practice. First of all, for the strong-strong regime to occur the parameters of the colliding beams should be close, in particular the weak/strong intensity ratio should exceed 0.65 for round beams [2]. Another natural mechanism that may be also at play is Landau damping by the synchrotron sidebands of incoherent tunes [3].

### LHC example

A number of cures were proposed to suppress the discrete modes or move them inside the continuum, among them a split in bare lattice tunes between the two rings and a difference in phase advances separating two main IPs in each ring. Also, the effect of the long-range collisions can be minimized with alternating crossing: horizontally at one IP and vertically at the other.

In LHC the difference between IP1 $\rightarrow$ IP5 phase advances that particles see in ring 1 and ring 2 are 0.54 $\pi$ horizontally and -0.18 $\pi$ vertically. The alternating crossing is also implemented with 28 long-range collisions around each IP at $\approx 9.5\sigma$ average separation.

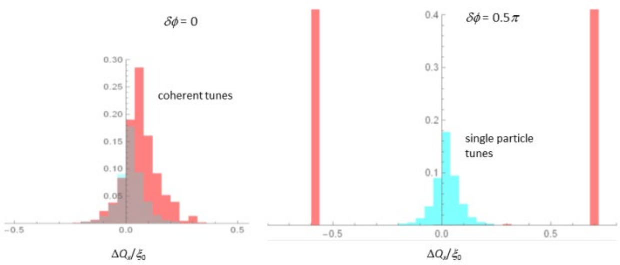


Figure 2: End-of-squeeze coherent beam-beam spectra (burgundy) and single particle tune distribution (cyan) at indicated values of the phase advance difference. The discrete mode peaks are cut.

Analysis showed that these two measures fight each other as far as it concerns the coherent modes. Figure 2 shows the end-of-squeeze single particle tune distribution and spectra of coherent oscillations with and without phase advance difference in units of the head-on beam-beam parameter $\xi_0$. The neighbouring long-range interactions were lumped at each IP.

Without phase advance difference there is no discrete modes, while with the difference as large as in the horizontal case there are two peaks of coherent oscillations well separated from incoherent tunes.

This result suggests that the horizontal oscillations are more prone to the end-of-squeeze instability. It can be damped by the transverse feedback.

## SPACE-CHARGE MODES

The main distinction of the Vlasov eigenfunction method is treating the beams as transversely soft. It can be dubbed – making provision for the head-tail modes not discussed yet – as the soft-slice approach while the traditional approach is to consider the longitudinal slices transversely rigid.

In the case of a coasting beam with space-charge the coherent transverse oscillations are similar to the beam-beam Σ-mode. The only observable mode is "rigid-slice" mode with tune not shifted by the direct space-charge. In absence of other tuneshifts it is not Landau damped.

For treatment of bunched beam modes it is important that the transverse space-charge force is longitudinally local. In a sufficiently long bunch the locality can be described by $\delta$-function. Mathematically this makes the use of action-angle variables in the longitudinal plane cumbersome. Instead we have to stay with coordinate and momentum.

Introducing normalized variables $\tau = z/\sigma_z$, $\upsilon = (p - p_0)/\sigma_p$, $J_x = I_x / \varepsilon_x$ we will search for the perturbed distribution function in form

$$F_1 = e^{i\psi_x - J_x/2-(\tau^2+\upsilon^2)/2} f(J_x,\tau,\upsilon;\theta)/(2\pi)^2\varepsilon_x\varepsilon_z + c.c. \quad (2)$$

and introduce the Vlasov operator

$$\begin{aligned}&\hat{A}_0 f = -iQ_s\left(\upsilon\frac{\partial}{\partial\tau} - \tau\frac{\partial}{\partial\upsilon}\right)f + Q_x^{(\mathrm{ext})} f + \\ &e^{-\tau^2/2}\left[Q_x^{(SC)}(J_x)f + \frac{1}{\sqrt{2\pi}}\hat{G}\int_{-\infty}^{\infty} e^{-\upsilon'^2/2} f(J_x,\tau,\upsilon';)d\upsilon'\right]\end{aligned} \quad (3)$$

where in the case of horizontal oscillations in flat beam (see Ref.[1] for details)

$$\begin{aligned}&Q_x^{(SC)} = -Q_{\mathrm{SC}}\cdot(1-e^{-J_x})/J_x, \\ &\hat{G}f = Q_{\mathrm{SC}}\int_0^{\infty} e^{-(J_x+J'_x)/2}\sqrt{J_x^{<}/J_x^{>}}\, f(J'_x)dJ'_x\end{aligned} \quad (4)$$

Longitudinally – in absence of external impedances at least – operator (3) is well behaved and allows expansion in smooth basis functions. For a Gaussian bunch we can use the set

$$\Phi_k(\tau) = \sqrt{\frac{2k+1}{\sqrt{2\pi}}}P_k[\mathrm{erf}(\frac{\tau}{\sqrt{2}})], \quad k = 0,1,\ldots,\infty \quad (5)$$

where $P_k(u)$ are the Legendre polynomials, which is orthonormal with weight $w$=exp(-$\tau^2$/2). Figure 3 shows a few basis functions which look like the head-tail waveforms found in Ref. [5] for the rigid slice model.

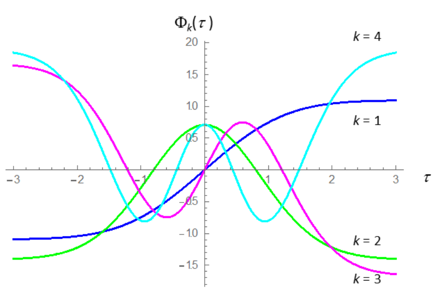


Figure 3: Longitudinal basis functions.

Using this basis the Vlasov operator eigenfunctions can be sought as

$$\underline{\upsilon}_m(J_x,\tau,\upsilon)=\sum_{k,l} a_{m;\,k,l}(J_x)\Phi_k(\upsilon)\Phi_l(\tau) \qquad (6)$$

The corresponding eigenvalues will be denoted as $\lambda_m$.

## *Landau Damping of the Head-Tail Modes*

Just like it the case of the coherent beam-beam oscillations [1] the spectrum may contain a discrete set as well as continuum, the latter covering the range of incoherent tunes. A qualitative necessary condition of stability is absence of discrete spectrum.

This condition can be visualized with the help of spectral coefficients describing the projection of eigenmodes on a pickup and their excitation by a dipole kick varying longitudinally as $\Phi_l(\tau)$

$$c_{m;\,l}=\int_0^\infty \mathcal{R}(J_x)a_{m;\,0,l}(J_x)dJ_x \qquad (7)$$

where $\mathcal{R}(J_x)=\sqrt{J_x}e^{-J_x/2}$ is function describing horizontal "rigid-slice" motion.

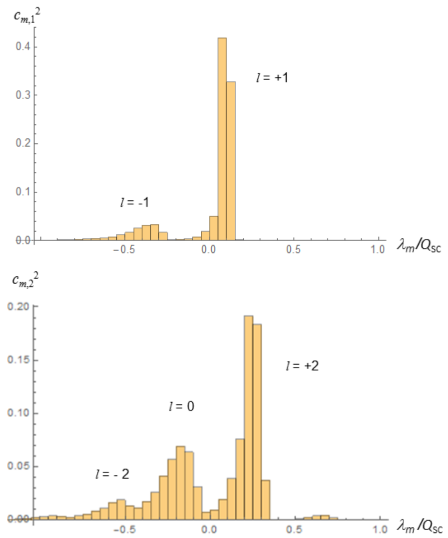


Figure 4: Spectral density of head-tail modes projection on $l_0$=1 and $l_0$=2 basis functions for $Q_s$ = 0.2·$Q_{SC}$, $Q_{SC}$ being the maximum absolute value of the SC tuneshift.

As Figure 4 shows other head-tail modes of the same parity have projection on the given basis function*, not only $l = l_0$.

The peak positions and the Landau damping rate estimated from the width of the peaks coincide almost exactly with Ref. [6] results obtained by tracking.

Since the $l \neq 0$ modes are intrinsically damped the main concern is Landau damping of the $l = 0$ mode. The possibility of employing an electron lens for this purpose was discussed at this Workshop [7].

## *TMCI with Strong Space Charge*

The main mechanism of the single bunch transverse instability is TMCI. There was a long-standing question whether a strong space charge can suppress the TMCI (see e.g. Refs. [5, 8] and references therein).

To address the issue the following term originating from an external impedance is added to the Vlasov operator:

$$\hat{A}f=\hat{A}_0 f+i\sqrt{\frac{1}{2}\beta_x J_x}\,e^{-J_x/2}\frac{\delta p_x}{2\pi} \qquad (8)$$

with $\beta_x$ being taken at the impedance location. The kick is produced by the wake function $W_\perp$

$$\frac{\delta p_x}{2\pi}=-\frac{e^2N}{mc^2\beta_0^2\gamma_0}\int_{-\infty}^{\infty}W_\perp(\tau-\tau')\langle x(\tau')\rangle\frac{1}{\sqrt{2\pi}}e^{-\tau'^2/2}d\tau' \quad (9)$$

where $N$ is the full number of particles in the bunch, $\beta_0$ is the average velocity in units of the speed of light $c$ and $\gamma_0$ is the relativistic mass factor.

The causality requires $W_\perp(\tau)=0$ for $\tau>0$ breaking reciprocity and leading to the emergence of complex eigenvalues.

### Vanishing TMCI threshold

Analysis in the simplest case of a step-like wake [9] showed that the growth rates go down with increase in the ratio $Q_{SC}/Q_s$ but the threshold in $|N\cdot W_\perp|$ does not go to infinity as was suggested on the basis of the rigid-slice model (see e.g. [8]) but on the contrary goes to zero†.

Qualitatively the same behaviour was observed with a resonator wake. Figure 5 shows obtained by the described method growth rates for the SPS Q26 lattice and beam parameters and Rs=10MΩ/m (CERN units).

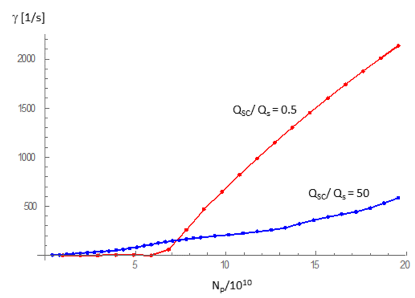


Figure 5: TMCI growth rate at the indicated values of the space charge strength.

At large ratio $Q_{SC}/Q_s$ there is no well-defined threshold so that instead of "vanishing TMCI" we have a vanishing TMCI threshold. Similar results were independently obtained by tracking simulations [10, 11].

### Tail-to-head feedback

We come to a conclusion that additional (w.r.t. the rigid-slice model) degree of freedom introduces

* It is interesting that in projection on the $l_0$=2 basis function we see the $l$=0 continuum modes, while in projection on the $l_0$=0 function only the discrete peak at zero tuneshift can be seen, just like in the case of the beam-beam Σ-mode.

† The main result of Ref. [8] is that a large number of longitudinal eigenfunctions should be taken into account. In the soft-slice approach developed here the convergence is better, especially with smooth wakes.

qualitatively new effects. To understand them let us look at the obtained solutions in more detail.

Figure 6 shows the dipole moment $d_x = <x>\cdot\exp(-\tau^2/2)$ along the bunch at a number of close moments in time in the strong space charge case of Fig. 5. The oscillation amplitude grows significantly from head to tail as in the case of the convective instability [12]. However, there is an appreciable growth rate: Im $\nu/Q_s = 0.21$. This means that there is a feedback from tail to head which is absent in the rigid-slice model.

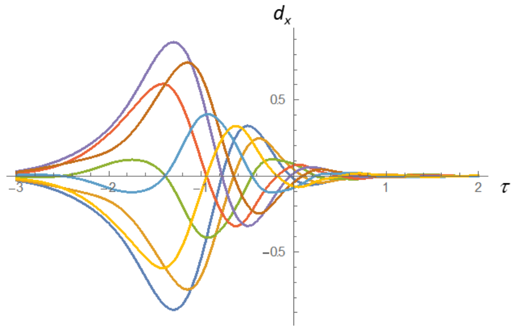


Figure 6: Dipole moment of the most unstable mode at $Q_{SC}/Q_s = 50$. The head of the bunch is at $\tau > 0$.

Figure 7 shows the eigenfunction of the mode presented in Fig. 6 as a function of the normalized action $J_x$ at positions in the head (blue), center (green) and the tail (red) of the bunch. For comparison the dashed line shows function $\mathcal{R}(J_x)$ which describes the rigid-slice mode and was rescaled for convenience.

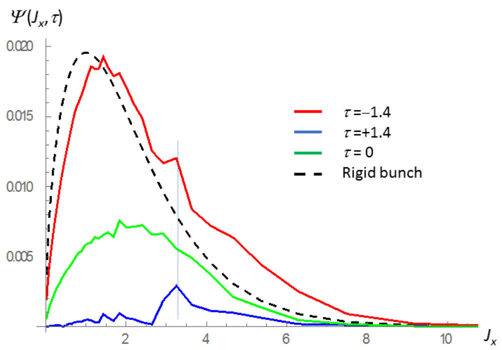


Figure 7: Eigenfunction of the most unstable mode at $Q_{SC}/Q_s = 50$ at the indicated positions inside the bunch.

The point to note here is that particles with larger unperturbed amplitudes participate stronger in coherent oscillations. This is especially noticeable at the head of the bunch. Of course it is not the unperturbed amplitude *per se* that matters but the reduced space-charge tuneshift.

It appears that particles with $J_x$ marked in Fig. 7 by vertical line transfer perturbation from tail to head making the instability absolute. This mechanism was revealed by A. Burov and called by him the core-halo instability [13].

### Practical conclusion

The fact that TMCI with strong space-charge requires for development the participation of large-amplitude particles with significantly reduced space-charge tuneshift suggests a cure: transverse KV distribution which equalizes the tuneshifts within a slice. Still – due to the longitudinal modulation – there will remain a tunespread to suppress other types of transverse instabilities.

## ACKNOWLEDGEMENTS

The author is grateful to many people with whom he had the privilege to discuss the subject of this report, in particular to T. Pieloni (CERN/EPFL), A. Burov (FNAL), X. Buffat and E. Métral (CERN).

## REFERENCES


[1] K. Yokoya et al., “Tune Shift of Coherent Beam-Beam Oscillations”, KEK Preprint 89-14 (1989); *Particle Accelerators*, v.27, p.181 (1990).

[2] Y. Alexahin, “On the Landau Damping and Decoherence of Transverse Dipole Oscillations in Colliding Beams”. CERN SL-96-064 AP, Geneva, 1996; 'Particle Accelerators', v.59, pp.43-74 (1998).

[3] Y. Alexahin, “A Study of Coherent Beam-Beam Effect in the Framework of the Vlasov Perturbation Theory”. LHC Project Report 461 (2001); NIMA 480 pp.253-288 (2002).

[4] N.G. Van Kampen, "On the Theory of Stationary Waves in Plasmas", Physica, v.21, No.12, pp.949-963 (1955).

[5] A. Burov, “Head-tail modes for strong space charge”, Phys. Rev. ST Accel. Beams **12**, 044202 (2009). *Erratum:* Phys. Rev. ST Accel. Beams **12**, 109901 (2009).

[6] A. Macridin et al., “Simulation of transverse modes with their intrinsic Landau damping for bunched beams in the presence of space charge”, Phys. Rev. ST Accel. Beams 18, 074401 (2015).

[7] Y. Alexahin et al., “On Landau Damping Restoration with Electron Lenses in Space-Charge Dominated Beams”, this Workshop; FERMILAB-CONF-19-690-APC (2019)

[8] V. Balbekov, “Transverse mode coupling instability threshold with space charge and different wakefields”, Phys. Rev. Accel. Beams 20, 034401 (2017).

[9] Y. Alexahin, “Vlasov Theory of Head-Tail Modes in Bunched Beams with Strong Space Charge”, https://indico.cern.ch/event/676489/contributions/2768943/attachments/1549082/2432938/VlasovTheory_YA_30-10-17.pdf (2017).

[10] E. Métral et al., “Space charge and transverse instabilities at the CERN SPS and LHC”, ICAP’18, Key West, Florida, USA, October 2018, pp. 43-49.

[11] A. Oeftiger, “SPS Impedance-driven Instability with Space Charge at Q26”, (2019, unpublished)

[12] A. Burov, “Space Charge Effects for Transverse Collective Instabilities in Circular Machines”, this Workshop.

[13] A. Burov, “Core-Halo Collective Instabilities”, https://arxiv.org/abs/1808.08498

# ACTIVE METHODS OF SUPPRESSING LONGITUDINAL MULTI-BUNCH INSTABILITIES

F. Bertin, H. Damerau, G. Favia, A. Lasheen, CERN, Geneva, Switzerland

*Abstract*

Longitudinal multi-bunch instabilities limit the beam intensity and quality reach of hadron synchrotrons. In case the impedance source driving the instability is well known, for example an RF cavity, active feedback can be set up locally to reduce its effect on the beam. For multi-bunch instabilities excited by other impedances, global feedback systems are needed. A combination of both types is required to produce the high intensity beam for the future High-Luminosity LHC (HL-LHC) in the CERN Proton Synchrotron (PS). All RF cavities at 10 MHz, 20 MHz, 40 MHz and 80 MHz involved in the generation of LHC-type beams are equipped with direct, wideband feedback. To achieve an impedance reduction beyond their electrical stability limit, they are complemented by local 1-turn delay and multi-harmonic feedback systems. Additionally, a global coupled-bunch feedback loop operating in the frequency domain with a Finemet cavity as longitudinal wideband kicker damps all possible dipole oscillation modes. Beam measurements in the PS are presented, highlighting the key contributors needed to stabilize the highest intensity beams for the LHC.

## INTRODUCTION

Longitudinal multi-bunch instabilities in high-intensity hadron synchrotrons are driven by the beam current inducing voltage in components of the accelerator. This voltage acts back on successive bunches, or even the same bunch after one revolution. Effort is therefore made to reduce the beam-coupling impedance as far as possible in high-intensity synchrotrons by, e.g. avoiding unnecessary cross-section changes of the beam pipe and by installing shielding or damping material in resonant structures like tanks for beam instrumentation devices. However, to improve stability beyond the feasibility of these passive impedance reduction techniques, active feedback systems are required. Additionally, some impedance sources must be kept intentionally large like accelerating cavities, to efficiently transfer energy to the beam.

Two main strategies can be applied to mitigate instabilities using feedback. In case an RF system has been identified as driving impedance source [1], a local feedback system per RF station can be deployed, which reduces the cavity impedance at the relevant frequencies. This includes the revolution harmonics at $n f_{\mathrm{rev}}$, as well as the synchrotron frequency, $f_{\mathrm{S}}$, side-bands next to them at $n f_{\mathrm{rev}} \pm m f_{\mathrm{S}}$. Such feedback effectively reduces the impedance at the source, preventing instabilities from developing. However, the driving impedance source of an instability may not be known or difficult to reduce by passive and active techniques. The signature of the instability itself is then the only observable, as for example the presence of a specific component in the beam spectrum. In this case global feedback can be set up to detect that signature and to reduce it. Such feedback systems are mostly dedicated to a specific category of instabilities and can hence only cure the consequences of that particular type.

The PS at CERN is an example of an accelerator using a combination of both types of feedback to mitigate longitudinal instabilities. Within the framework of the LHC Injector Upgrade (LIU) programme the PS is prepared for its role as a pre-injector of the High-Luminosity LHC (HL-LHC), and the intensity of LHC-type multi-bunch beams will be doubled from $N_{\mathrm{b}} = 1.3 \cdot 10^{11}$ p/b to $2.6 \cdot 10^{11}$ p/b in trains of 72 bunches spaced by 25 ns [2]. Two major contributors to achieve this intensity with excellent longitudinal beam quality are presented in this contribution as examples for the two complementary approaches for mitigating longitudinal instabilities: the global coupled-bunch feedback system to suppress dipole oscillations and the local multi-harmonic feedback loops to reduce the impedance of the high-frequency cavities.

## GLOBAL COUPLED-BUNCH FEEDBACK

For the production of LHC-type beams, a bunch train of 18 bunches is accelerated on harmonic $h = 21$ in the PS from a kinetic energy of $E_{\mathrm{kin}} = 1.4$ GeV to a momentum of 26 GeV/$c$. Three buckets remain empty as a gap for the extraction kicker. Longitudinal coupled-bunch oscillations are observed in the PS during acceleration after transition crossing and at the flat-top. An example of these oscilla-

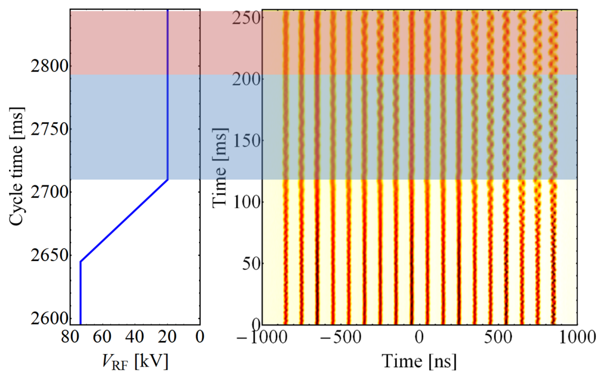


Figure 1: Dipole coupled-bunch oscillations developing at the flat-top at an intensity of about $7.2 \cdot 10^{11}$ p/b, which corresponds to $1.8 \cdot 10^{11}$ p/b at extraction after the splittings at the flat-top. The RF voltage (left) at $h = 21$ is lowered. The voltage programs for the RF systems at $h = 42$ and $h = 84$ are disabled for the measurement. The blue and red areas indicate the time periods when the two double-splittings usually take place.

tions at the flat-top is shown in Fig. 1. The dipole instability develops along the batch within 150 ms and affects particularly the bunches at the batch tail, while the first bunches are almost stable. The global coupled-bunch feedback system is an example of a damping loop suppressing the signature of the instability, independent of its driving source.

### *Damping of Dipole Oscillations*

Damping of dipole oscillations can be achieved by detecting the phase of each bunch individually and applying a longitudinal kick to move the bunch back to its reference position in phase. While this time domain approach is common in electron accelerators operated at fixed frequency, it is less obvious to realize for hadron synchrotrons where the revolution frequency sweeps during acceleration. As an alternative approach in the frequency domain one can profit from the properties of the beam spectrum. Coupled-bunch oscillations with a phase advance of $\Delta\phi = 2\pi n/h$ from one bunch to the next, show up in the beam spectrum as an upper side-band of $n f_{\mathrm{rev}}$ and a lower side-band of $(h-n) f_{\mathrm{rev}}$, with $n$ indicating the mode number [3]. This spectrum from 0 to $f_{\mathrm{RF}} = h f_{\mathrm{rev}}$ repeats periodically from $f_{\mathrm{RF}}$ to $2 f_{\mathrm{RF}}$ and above. The frequency offset with respect to the revolution frequency harmonic is an integer multiple of the synchrotron frequency, $f_{\mathrm{S}}$ and depends on the type of oscillation. For dipole ($m = 1$), quadrupole ($m = 2$) and higher order oscillations it appears at $n f_{\mathrm{rev}} \pm m f_{\mathrm{S}}$.

Detecting and actively removing a synchrotron frequency side-band from the beam spectrum by applying longitudinal kicks effectively results in damping the corresponding coupled-bunch oscillations [4]. This is the principle of feedback in the frequency domain. Compared to the approach in time domain, it has the advantage that a specific mode can be suppressed independently of the bunch spacing. Additionally, the feedback system is independent of the bunch arrival time and bunch pattern, as long as the phase advance from the pick-up to the longitudinal kicker is correct. This approach is therefore well suited for proton accelerators with sweeping revolution frequency.

Narrow filters are required to remove the revolution frequency harmonic from the beam spectrum, keeping only the weak synchrotron frequency side-bands nearby. The measured transfer function of one signal processing chain of the PS coupled-bunch feedback system is plotted in Fig. 2. Thanks to the symmetry of the beam spectrum, a single filter can treat two dipole coupled-bunch modes, with mode number $n$ at $n f_{\mathrm{rev}} + f_{\mathrm{S}}$ and mode number $h - n$ at $n f_{\mathrm{rev}} - f_{\mathrm{S}}$, simultaneously.

For LHC-type beams accelerated on $h = 21$, the zero dipole oscillation mode is removed by the beam phase loop which locks the phase of the accelerating voltage to the average phase of the bunches. The remaining 20 modes with non-zero phase advance from bunch to bunch are treated by a bank of 10 parallel filters, each processing two modes as illustrated above. A wideband cavity based on Finemet material serves as a longitudinal kicker [5]. The feedback system profits from the symmetry of the beam spectrum and detects side-bands at harmonics from $f_{\mathrm{RF}}/2$ to $f_{\mathrm{RF}}$, where the signals at revolution frequency harmonics are weaker and therefore easier to filter. Following a band change, the correction kicks are then applied in the base band from $f_{\mathrm{rev}}$ to $f_{\mathrm{RF}}/2$, where the Finemet cavity has its largest impedance.

The coupled-bunch feedback system in the PS is very efficient against dipole coupled-bunch oscillations and removes them almost entirely during acceleration and at the flat-top (Fig. 1). However, when increasing the bunch intensity beyond $7.2 \cdot 10^{11}$ p/b, corresponding to $1.8 \cdot 10^{11}$ p/b at extraction, quadrupole oscillations develop at the flat-top as illustrated in Fig. 3. The coupled-bunch mode spectrum is very similar for dipole and quadrupole oscillations, pointing to the same driving impedance source. Again, bunches at the tail of the batch are oscillating much stronger than the first few bunches after the kicker gap.

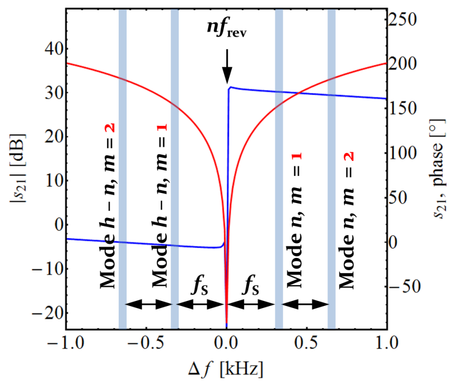


Figure 2: Transfer function in amplitude (red) and phase (blue) of one synchrotron frequency side-band filter of the PS coupled-bunch feedback system. A steep notch removes the spectral component at $n f_{\mathrm{rev}}$. The gain difference between the revolution frequency harmonic and the synchrotron frequency side-band is more than 40 dB within a frequency difference of only 300 Hz.

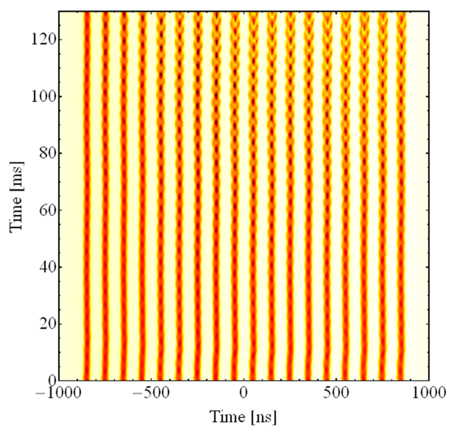


Figure 3: Measured evolution of the bunch profiles with an intensity of $7.2 \cdot 10^{11}$ p/b ($1.8 \cdot 10^{11}$ p/b at extraction after the splittings on the flat-top). Coupled-bunch feedback removes any dipole oscillations.

The coupled-bunch feedback system has no effect on these oscillations. Although the gain at the $\pm 2 f_S$ side-bands is even larger that at $\pm f_S$ (Fig. 2), the phase advance, adjusted to damp dipole oscillations, is not adapted. Beam tests showed that a compromise to treat dipole and quadrupole modes with the same feedback system cannot be found.

### *Excitation of Quadrupole Oscillations*

To check the feasibility of damping the observed quadrupole coupled-bunch instabilities with the existing longitudinal kicker cavity in the PS, the excitation efficiency has been measured. Signals at the synchrotron frequency side-bands around $19 f_{\mathrm{rev}}$ and $20 f_{\mathrm{rev}}$ were injected to excite either dipole or quadrupole coupled-bunch oscillations. The measured relative amplitudes of the oscillations allow to estimate the maximum efficiency of an additional quadrupole damping system.

The measured mode spectrum following the excitation of a dipole oscillation is shown in Fig. 4. When moving the driving side-band from $\Delta f = f_S$ to $\Delta f = 2 f_S$, the bunch position oscillations are transformed into coupled-bunch oscillations of the bunch length. The mode spectrum (Fig. 5) is very similar to the one for the dipole oscillations. However, for the same excitation amplitude, the absolute amplitude is $2 - 3$ times smaller in the case of bunch length oscillations. This suggests that damping of quadrupole coupled-bunch instabilities is possible with the existing longitudinal damper cavity. However, with a damping efficiency approximately proportional to the amplitude of the excited oscillations, a reduced gain is expected for the damping of quadrupole modes compared to the one achieved with the feedback system for dipole modes.

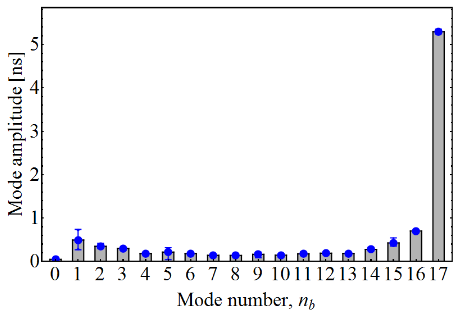


Figure 4: Measured mode spectrum at the flat-top, following an excitation at $20 f_{\mathrm{rev}} + f_S$. The amplitude of the oscillations is measured as the maximum excursion of the bunch position with respect to the position of the stable bunches.

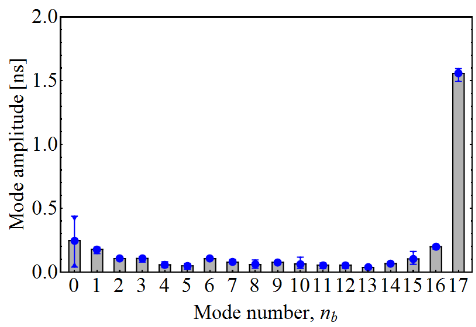


Figure 5: Measured quadrupole mode spectrum at the flat-top, following an excitation at $20 f_{\mathrm{rev}} + 2 f_S$. The mode amplitude is defined as the maximum excursion of the bunch length oscillations.

## LOCAL IMPEDANCE REDUCTION FEEDBACK

The RF cavities with their intentionally large shunt impedance require particular measures to reduce beam induced voltages.

### *Direct RF Feedback*

Direct RF feedback is applied to most RF systems in the PS, 2.8 . . . 10 MHz [6], 20 MHz [7], 40 MHz [8] and 80 MHz [9], reducing the impedance by one to more than two orders of magnitude depending on the system. The gap voltage, containing contributions from the driving amplifier and beam induced voltage, is picked up by a probe and compared to the drive signal for the amplifier (Fig. 6, blue box). The latter does, of course, not contain any beam induced

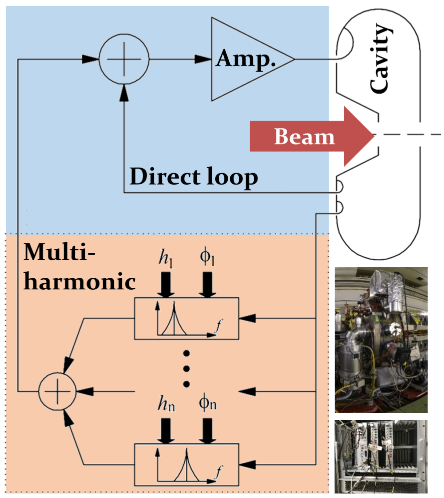


Figure 6: Simplified diagram of the local feedback systems of the 40 MHz and 80 MHz consisting of direct feedback (blue box) combined with multi-harmonic feedback (orange).

contribution. The difference, mainly corresponding to the voltage induced by the beam, is amplified and applied back to the cavity with a phase shift, effectively reducing any beam induced voltage. This technique is very efficient since it reduces the cavity impedance in the entire bandwidth of the cavity. However, due to the purely proportional gain of such systems, any phase error introduced by a loop delay limits the maximum achievable gain and bandwidth. Every effort is therefore made for direct feedback loops to reduce any delays as far as technically achievable.

The maximum gain, $G_{\max}$, of the direct feedback system, with no other bandwidth limitations than the cavity itself, can be written as [10]

$$\begin{aligned} G_{\max} &= \frac{\pi}{2}\frac{1}{R/Q}\frac{1}{\omega_{\mathrm{RF}}\tau} \\ &= \frac{\pi}{2}\cdot\frac{1}{R}\cdot\frac{1}{\Delta\omega_{-3\mathrm{dB}}}\cdot\frac{1}{\tau}\,, \end{aligned} \tag{1}$$

where $R$ is the cavity impedance at resonance, $Q = \omega_{\mathrm{RF}}/\Delta\omega_{-3\mathrm{dB}}$ its quality factor and $\tau$ the overall loop delay. Although the amplifier chain is installed close to the cavity, the minimum loop delay limits the maximum gain of the direct feedback system.

### *Narrow-band RF Feedback*

Significantly higher feedback gain can be obtained by artificially reducing the bandwidth $\Delta\omega_{-3\mathrm{dB}}$ of the feedback loop with filters. Keeping in mind that the longitudinal beam spectrum is concentrated around the revolution frequency harmonics, it is actually sufficient to reduce the cavity impedance only in these frequency ranges. A 1-turn delay feedback loop [11] uses a comb filter, a periodic system of narrow band-pass filters, centered around the revolution frequency harmonics. The width of the pass-bands then defines the maximum gain in Eq. (1) instead of the cavity bandwidth.

Even more flexibility is achieved by treating each revolution frequency harmonic within the frequency range of the RF system by an independent signal processing chain. Such a multi-harmonic feedback system has been recently implemented for the 40 MHz and 80 MHz RF systems in the PS [12]. Since these cavities are operated at fixed frequency, while the revolution frequency of the beam sweeps during acceleration, a 1-turn delay feedback loop would be difficult to realize. This is different for multi-harmonic feedback, where the gain and phase of each signal processing chain can be dynamically adjusted to perfectly match the phase of the cavity transfer function at any time during acceleration.

The measured transfer function of the prototype multi-harmonic feedback system is shown in Fig. 7. In between the revolution frequency harmonics the feedback system has little effect on the cavity impedance or may even increase it. However, at frequencies close to $n f_{\mathrm{rev}}$, where the beam current can induce voltage, deep notches in the transfer function reduce the impedance. The bandwidth of these notches must nonetheless be sufficient to cover also the first few synchrotron frequency side-bands (Fig. 8).

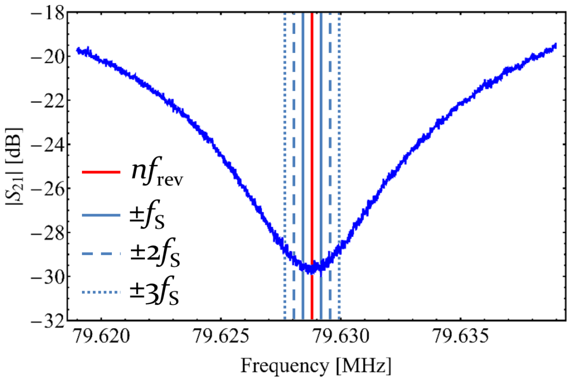


Figure 8: Transfer function measurement zoomed around one notch. The bandwidth is sufficiently large to cover the central notch and several synchrotron frequency side-bands.

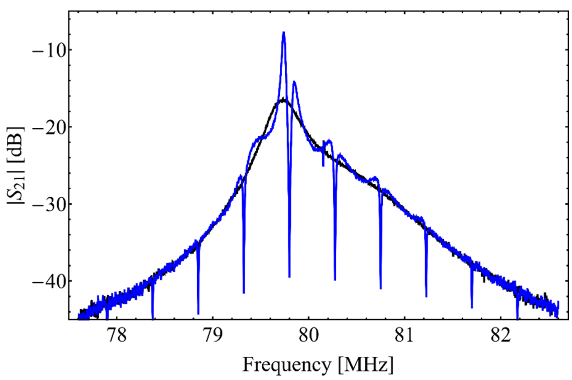


Figure 7: Measured transfer function of direct and multi-harmonic feedback loops in parallel (blue), as well as with direct feedback alone (black).

To qualify the efficiency of feedback with beam, one can compare the beam induced voltage with and without the multi-harmonic feedback systems. Figure 9 illustrates the induced power in a 40 MHz cavity during the cycle for an LHC-type beam accelerated at $h = 21$ without (top) and with multi-harmonic feedback systems (bottom). The cavity is tuned to a fixed frequency corresponding to $84 f_{\mathrm{rev}}$ at the flat-top energy, where maximum voltage is required during the bunch rotation for the transfer to the SPS. The fourth harmonic of the RF frequency at $21 f_{\mathrm{rev}}$ hence sweeps into the pass-band of the 40 MHz cavity during acceleration. Before transition crossing, this spectral component is still well below the resonance frequency of the cavity, and

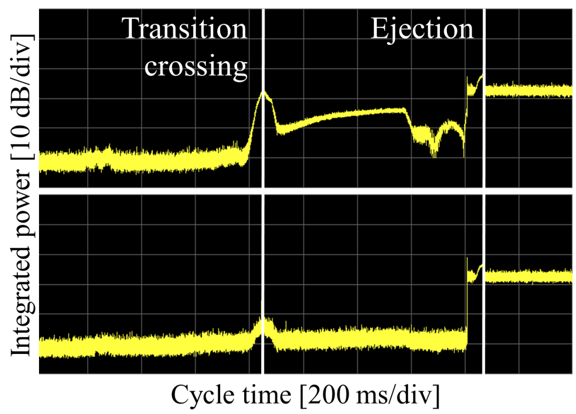


Figure 9: Beam induced power in a 40 MHz cavity without (top) and with the multi-harmonic feedback system active (bottom). With a bandwidth of ±3 MHz all revolution frequency harmonics within the bandwidth of the RF system are covered.

the bunches are yet too long to induce detectable voltage at 40 MHz. The induced voltage increases around transition crossing, as well as during the final part of acceleration to the flat-top when bunches become shorter. In this regime the feedback system efficiently counteracts the induced voltage. The observed reduction of beam induced power by up to 20 dB, corresponding to an impedance reduction by up to one order of magnitude, validates the impedance reduction expected from the transfer function measurement.

The beneficial effect of the impedance reduction on the longitudinal beam quality thanks to the multi-harmonic feedback systems can be directly observed by measuring the longitudinal emittance along the batch of 18 bunches at the arrival on the flat-top. At the HL-LHC intensity of $1.04 \cdot 10^{12}$ p/b, an uncontrolled longitudinal emittance blow-up is measured for the bunches at the tail of the batch (Fig. 10, blue) without the multi-harmonic feedback systems active

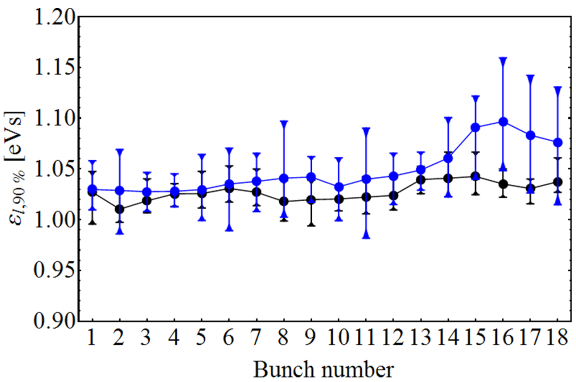


Figure 10: Longitudinal emittance along the batch without (blue) and with multi-harmonic feedback active (black) around both 80 MHz cavities at an intensity of $1.04 \cdot 10^{12}$ p/b, corresponding to $2.6 \cdot 10^{11}$ p/b at extraction. The emittance is evaluated based on bunch-by-bunch tomographic reconstruction [13] of the longitudinal distributions.

around the 80 MHz cavities. These cavities, only needed during the final bunch rotation before extraction, are equipped with a mechanical short-circuit to shield them entirely from the beam. Although it has been shown that their impedance is indeed responsible for the emittance blow-up, the mechanical short-circuit can only be used for dedicated machine development studies as the cavity cannot be pulsed for the bunch rotation under these conditions.

Activating the multi-harmonic feedback loops removes the uncontrolled emittance blow-up along the batch almost entirely (Fig. 10, black), equally well as shielding the cavity impedance with the mechanical short circuit. In the case of the 80 MHz cavities in the PS, the combination of direct and multi-harmonic feedback hence proved to reduce the impedance at the revolution frequency harmonics sufficiently well to make them transparent to the beam.

## CONCLUSIONS

Active feedback systems to suppress longitudinal multi-bunch instabilities make an important contribution to preserve good longitudinal beam quality at highest intensities. In case of known impedance sources, like RF cavities, local feedback can deliver an impedance reduction well beyond the capabilities of passive techniques, in particular without requiring excessive additional RF power. Wherever possible direct feedback should be applied first. It is very robust and provides the first layer of impedance reduction. To push the feedback gain at the revolution frequency harmonics well beyond the stability limit of direct feedback, narrow-band filter feedback is applied. They may be based on comb filters, periodic with the revolution frequency, in sequence with a delay line to apply the correction on the next turn, as for the 2.8 . . . 10 MHz cavities in the PS. Multi-harmonic feedback systems like the ones implemented for the high frequency cavities in the PS provide more flexibility and gain margin. They treat the revolution frequency harmonics individually in terms of gain and phase, matching them perfectly to the impedance source they are reducing. Thanks to this flexibility, multi-harmonic feedback systems can achieve significantly higher gain than 1-turn delay feedback systems based on periodic filters.

When the source of a longitudinal instability cannot be attributed to a single driving impedance, the signature of the instability must be detected globally and compensated for by dedicated feedback to stabilize the beam instead. This path has been chosen with the frequency-domain coupled-bunch feedback system in the PS. Independent of their origin, it detects synchrotron frequency side-bands of revolution frequency harmonics as a signature of longitudinal coupled-bunch instability and actively removes them from the beam spectrum, rendering the beam stable again.

A combination of local and global feedback is used in most high-intensity accelerators to mitigate longitudinal instabilities. In the PS more than 30 feedback systems acting together (Tab. 1) allowed in 2018 to deliver LHC-type beams with an intensity of $N_\mathrm{b} = 2.6 \cdot 10^{11}$ p/b required for HL-LHC at the PS extraction. Figure 11 shows the bunch profiles during the last turn, together with practically constant bunch length along the batch of 72 bunches spaced by 25 ns.

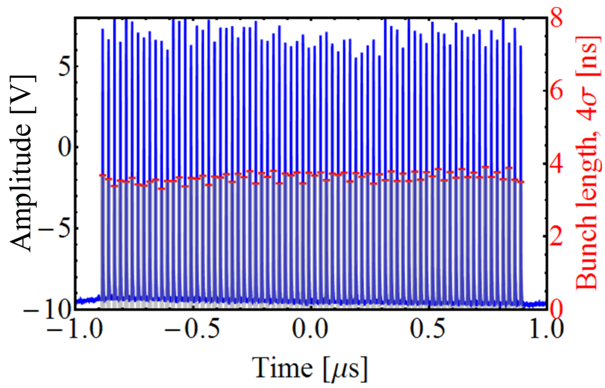


Figure 11: Beam profile (blue) and bunch length (red, $4\sigma$ Gaussian fit) during the last turn of an LHC-type beam with a bunch intensity of $2.6 \cdot 10^{11}$ p/b.

Table 1: Summary of RF feedback systems in the CERN PS

| **Feedback type** | **Remarks** | **RF system, $f_{\mathrm{res}}$** 2.8 . . . 10 MHz | 20 MHz | 40 MHz | 80 MHz |
|---|---|---|---|---|---|
| Direct (18×) | • Delivers base impedance reduction<br>• Reduction of transient beam loading<br>• Impossible to operate without | ✓ [6] | ✓ [7] | ✓ [8] | ✓ [9] |
| 1-turn delay (11×) | • Reduction of transient beam loading<br>• Little effect on coupled-bunch instabilities | ✓ [11] | | | |
| Multi-harmonic (7×) | • Flexible to dynamically adapt to cavity impedance<br>• Larger gain than 1-turn delay feedback | | (✓) [12] | (✓) [12] | (✓) [12] |
| Coupled-bunch (1×) | • Controls dipole coupled-bunch oscillations<br>• Studying extension to quadrupole mode damping | Dedicated Finemet cavity as longitudinal wideband kicker [4, 5, 14] | | | |


## ACKNOWLEDGEMENTS

The authors are grateful to Philippe Baudrenghien, Javier Galindo, Matthias Haase, Gregoire Hagmann, Mauro Paoluzzi, Damien Perrelet, Elena Shaposhnikova (CERN) and Fumihiko Tamura (J-PARC) for sharing their experience.


## REFERENCES


[1] A. Lasheen *et al.*, "Identification of Impedance Sources Responsible of Longitudinal Beam Instabilities in the CERN PS", *these proceedings*.

[2] M. Meddahi, *et al.*,"LHC Injectors Upgrade Project: Towards New Territory Beam Parameters", IPAC19, Melbourne, Australia, 2019, p. 3385.

[3] F. Pedersen, F. Sacherer, "Theory and Performance of the Longitudinal Active Damping System for the CERN PS Booster", PAC77, Chicago, Illinois, USA, 1977, p. 1396.

[4] H. Damerau, A. Lasheen, M. Migliorati, "Observation and Damping of Longitudinal Coupled-bunch Oscillations in the CERN PS", CERN-2018-003-CP, ICFA Mini-Workshop on Impedances and Beam Instabilities in Particle Accelerators, Benevento, Italy, 2017, p. 33.

[5] H. Damerau, M. Paoluzzi, "Design of the PS Longitudinal Damper", CERN-ACC-NOTE-2013-0019, CERN, Geneva, Switzerland, 2013.

[6] R. Garoby *et al.*, "RF System for High-intensity Acceleration in the CERN PS", PAC89, Chicago, Illinois, USA, 1989, p. 135.

[7] M. Morvillo *et al.*, "The PS 13.3-20 MHz RF Systems for LHC", PAC03, Portland, Oregon, USA, 2003, p. 1724.

[8] R. Garoby *et al.*, "The PS 40 MHz Bunching Cavity", PAC97, Vancouver, Canada, 1997, p. 2953.

[9] E. Jensen *et al.*, "The PS 80 MHz Cavities", EPAC98, Stockholm, Sweden, 1998, p. 1773.

[10] P. Baudrenghien, "Low-level RF - Part I: Longitudinal Dynamics and Beam-based Loops in Synchrotrons", CAS - CERN Accelerator School: RF for Accelerators, Ebeltoft, Denmark, 2010, p. 341.

[11] A. Blas, R. Garoby, "Design and Operational Results of a "One-turn-delay Feedback" for Beam Loading Compensation of the CERN PS Ferrite Cavities", PAC91, San Francisco, California, USA, 1991, p. 1398.

[12] F. Bertin *et al.*, "Impedance Reduction of the High-frequency Cavities in the CERN PS by Multi-harmonic Feedback", LLRF19, Chicago, Illinois, USA, 2019, arXiv:1910.06874.

[13] S. Hancock, P. Knaus, M. Lindroos, "Tomographic Measurements of Longitudinal Phase Space Density", EPAC98, Stockholm, Sweden, 1998, p. 1520.

[14] L. Ventura *et al.*, "Excitation of Longitudinal Coupled-bunch Oscillations with the Wide-band Cavity in the CERN PS", IPAC16, Busan, Korea, 2016, p. 1724.

# DAMPING RATE LIMITATIONS FOR TRANSVERSE DAMPERS IN LARGE HADRON COLLIDERS *

V. A. Lebedev †, Fermilab, Batavia, USA

*Abstract*

The paper focuses on two issues important for the design and operation of bunch-by-bunch transverse damper in a very large hadron collider, where fast damping is required to suppress beam instabilities and noise induced emittance growth. The first issue is associated with kick variation along a bunch which affects the damping of head-tail modes. The second issue is associated with effect of damper noise on the instability threshold. The paper accounts for developments motivated by the discussions at this conference and carried out after it.

## INTRODUCTION

An achievement of maximum luminosity in a collider requires large beam current and small emittance. In hadron colliders of very large energy the collider size becomes so large that the frequency of lowest betatron sideband approaches kHz range where spectral density of acoustic and magnetic field noise is unacceptably large. This noise drives the emittance growth resulting in fast luminosity decay. Effective suppression of this emittance growth may be achieved by fast transverse damping [1,2]. Fast emittance growth and its suppression by the damper was demonstrated at the LHC commissioning [3,4]. The required damper gain grows with the size of the collider and approaches few turns for a collider which will follow the LHC (like FCC). The instability suppression is typically less demanding to damping rate but still it is another important reason for fast damping.

There are many phenomena which limit the maximum damper gain [5]. Here we discuss two of them in details.

(1) A damper gain increase results in a better suppression of zeroth order head-tail mode. However, such increase may excite higher order head-tail modes, and thus make the bunch unstable. This effect is exacerbated by presence of non-zero chromaticity and wake-fields which destroy symmetry of head-tail motion. As will be seen below an introduction of kick non-uniformity along the bunch may allow significant reduction of excitation of head-tail modes and, consequently, increases the beam stability margin.

(2) Any practical damper has internal noise. Depending on damper design it is related to the thermal noise of its preamps and/or noise of digitization. This noise drives small amplitude beam motion which due to betatron frequency spread results in an emittance growth. The betatron motion non-linearity introduced for suppression of head-tail modes makes this noise-induced diffusion depending on a particle betatron amplitude. With time that changes the particle transverse distribution and, consequently, may result in a loss of Landau damping. This phenomenon was observed in the LHC where the beam could lose transverse stability minutes after bringing the beams to the collision energy without any visible changes in the machine. The effect was pronounced stronger in the case of external excitation of transverse motion [6,7]. The beam stability study based on the multiparticle tracking is reported in Ref. [7]. It showed that the latency of stability loss is related to changes in the distribution function induced by the damper noise. In this paper we consider a semi-analytical theory which attempts to show details of the process in a one-dimensional model.

Below we assume that the damper is bunch-by-bunch type so that each bunch is damped separately.

## DAMPING OF INTRABUNCH MOTION

For analysis of intrabunch motion we use the air-bag square-well (ABS) model initially suggested in Ref. [8] and actively used by A. Burov for analysis of bunch damping (see for example [9]).

In this model the bunch is presented by two fluxes moving in opposite directions with particle reflection at the bucket boundaries. In difference to the linear longitudinal motion in the air-bag model [10] where the bunch density is picked at the bunch ends this model has a uniform density distribution along bunch. Therefore, ABS model better suits for description of damper effect on damping of head-tail modes.

In dimensionless variables the equations of motion for two fluxes are:

$$\begin{aligned}\frac{\partial x_1}{\partial \tau}+\frac{\partial x_1}{\partial s}+\frac{\chi}{i}x_1&=\frac{f}{2i}+\frac{q}{2i}\left(x_1-x_2\right),\\ \frac{\partial x_2}{\partial \tau}-\frac{\partial x_2}{\partial s}-\frac{\chi}{i}x_2&=\frac{f}{2i}+\frac{q}{2i}\left(x_2-x_1\right).\end{aligned}\tag{1}$$

where $x_1$ and $x_2$ are the transverse coordinates for the respective fluxes, $\chi=\left(\xi/\nu_s\right)\left(\Delta p/p\right)$ is the head-tail phase, $\xi$ is the tune chromaticity, $\nu_s$ is the synchrotron tune, $\pm\Delta p/p$ represent the momentum deviations for particles in the positive and negative fluxes, $\tau=\omega_s t$ is the dimensionless time, $s\in[0,\pi]$ is the dimensionless longitudinal particle coordinate, $q=\Delta\nu_{sc}/\nu_s$ is the space charge parameter, $\Delta\nu_{sc}$ is the space charge tune shift, and $f$ characterizes the forces coming from the damper and wake-fields. Following Ref. [9] we introduce the new transverse coordinate:

$$x=\begin{cases}e^{i\chi s}x_1\ , & s=\psi\ , \quad 0\le\psi\le\pi\ ,\\ e^{-i\chi s}x_2\ , & s=-\psi\ , \quad -\pi\le\psi\le 0\ .\end{cases}\tag{2}$$

Here we also introduced the phase $\psi$ describing the syn-

* Work supported by Fermi Research Alliance, LLC under Contract No. De-AC02-07CH11359 with the United States Department of Energy

† val@fnal.gov

chrotron motion so that $s=|\psi|, \psi\in[-\pi,\pi]$. Performing substitutions we can reduce two equations in Eq. (1) to one:

$$\frac{\partial x}{\partial \tau}+\frac{\partial x}{\partial \psi}=\frac{1}{2i}\left(fe^{-i\chi s}+q\left(x(\psi)-x(-\psi)\right)\right). \tag{3}$$

The force coming from the wake is determined by the following equation:

$$f(s)=\int_0^{\pi} W(s'-s)\left(x_1(s')+x_2(s')\right)ds'. \tag{4}$$

In this paper we consider two wake-functions: the constant wake –

$$W(s)=W_0\theta(s) \ , \tag{5}$$

and the resistive wall wake –

$$W(s)=\sqrt{\pi/4}\,W_0\,\theta(s)/\sqrt{s} \ . \tag{6}$$

The coefficient in the resistive wake definition was chosen so that for the uniform bunch displacement the force at the bunch tail would be equal for both wakes.

We assume that the force coming from the damper is determined by the following equation:

$$f(s)=-i\frac{G}{2\pi}\cos\left(k_k(s-\pi/2+\phi_k)\right)\times \\ \int_0^{\pi}\left(x_1(s')+x_2(s')\right)\cos\left(k_p(s'-\pi/2+\phi_p)\right)ds'. \tag{7}$$

Here $k_p$ and $\phi_p$ determine the sensitivity of damper pickup to a particle position along the bunch, and $k_k$ and $\phi_k$ determine dependence of the kick on the longitudinal coordinate along the bunch.

In the absence of space charge, damping and wakes the solutions of Eq. (3) are:

$$x_n\equiv x_n(\tau,\psi)=a_n e^{in(\tau-\psi)} . \tag{8}$$

In the first order of perturbation theory when only a damper is present (no wakes and space charge) we obtain the growth rate:

$$\lambda_n\equiv\frac{1}{2|a_n{}^2|}\frac{d}{d\tau}|a_n{}^2|=-\frac{G}{2}\mathrm{Re}\left(R_n(k_p,\phi_p)\overline{R(k_k,\phi_k)}\right), \tag{9}$$

where

$$R_n(k_x,\phi_x)=\int_0^{\pi}e^{i\chi\psi}\cos\left(k_x\left(\psi-\frac{\pi}{2}+\phi_x\right)\right)\cos(n\psi)\frac{d\psi}{\pi}, \tag{10}$$
$$x=k,p.$$

As one can see from Eq. (9) all modes are damped (have negative growth rates) if $k_p=k_k$ and $\phi_p=\phi_k$.

In the general case we look for a solution in the form:

$$x_n=e^{\lambda_n\tau}\sum_{m=-N_m}^{N_m}A_{nm}e^{im\psi} . \tag{11}$$

where $N_m$ determines how many harmonics approximate the exact solution. Substituting this equation into Eq. (3), using definitions of Eqs. (4) and (7), multiplying obtained equation by $e^{-in\psi}$ and integrating we obtain a system of $2N_m+1$ linear equations. The eigen-values and eigen-vectors of this matrix equation yield complex frequencies for each mode and its structure ($x_n(\psi)$). To warrant a solution accuracy, 161 modes (±80) were used. After finding the eigen-vectors the modes were renumbered in ascending order of imaginary part of $\lambda_n$ (tune shift).

First, we consider the instability in the absence of damper and the space charge. Calculations show that for $\chi=0$ the transverse mode coupling instability threshold is: $W_0 = W_{th} \approx 0.363$ for the step-like wake and for $W_0 = W_{thr} \approx 0.383$ for the resistive wall wake. In the following discussion we will characterize the wake strength relative to these thresholds.

Figure 1 shows dependencies of growth rates on mode frequencies for few lowest modes for the wake strengths twice above threshold, and for $\chi = 0$ and $\chi = -2$. For $\chi = 0$ (strong head-tail case) and the wake twice above threshold only 0-th and 1-st modes are coupled making only one mode unstable. As one can see from the bottom plot many modes became unstable for $\chi = -2$. Although growth rates for both wakes (step-like and resistive wall) are close the tune shifts of the modes are significantly larger for the resistive wall wake.

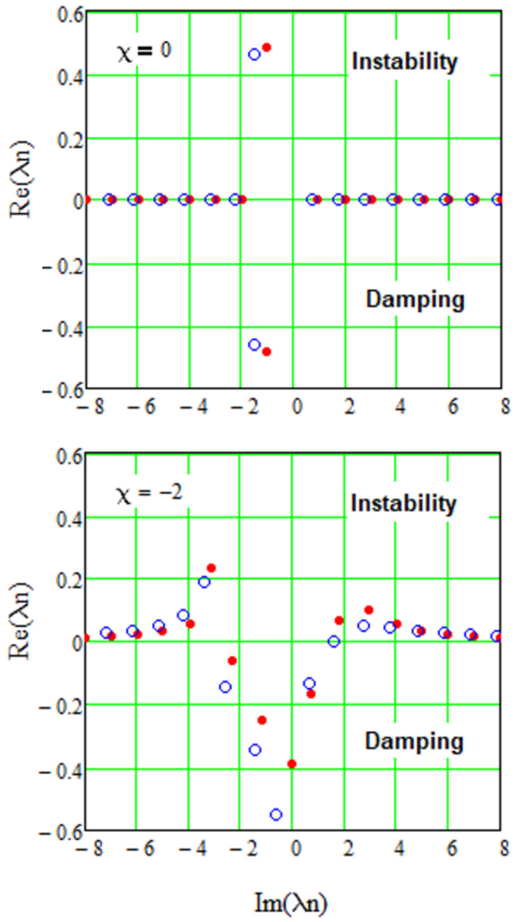


Figure 1: Dependence of growth rate, Re($\lambda_n$), on the mode coherent frequency, Im($\lambda_n$), for different modes and the wake amplitude twice above threshold; top – $\chi = 0$, bottom – $\chi = -2$; red dots – step-like wake, blue circles – resistive wall wake.

Further we characterize damping by the growth rate of the most unstable mode. Typically, it is the mode for which $n \approx \chi$. Figure 2 shows the dependence of the growth rate of the most unstable mode on the head-tail phase, $\chi$, for different damper gains when both pickup and kicker have flat responses ($k_p$=$k_k$=0). One can see in the top plot that there is no instability for $G = 0$ and $\chi = 0$ as should be expected below the instability threshold. However, for $G = 0$ the beam is unstable for any other (non-zero) head-tail phase. An increase of the damper gain reduces the growth rate for the most unstable mode everywhere except close vicinity of $\chi = 0$. Optimal damping is achieved at $G \approx 4$ where for the case twice below threshold the beam is stable for $\chi \in [0.5, 1.4]$ for both wakes. Further increase of the gain does not improve beam stability. For the wake twice above the threshold the beam is unstable for all $\chi$. Note that the considered model does not have Landau damping (discussed below) which stabilizes the beam if the growth rate is sufficiently small and these calculations do not show actual stability thresholds. Note also that the oscillations in the growth rates with $\chi$ are related to switching from one to another most unstable mode, so that one period represents the growth rate for one mode.

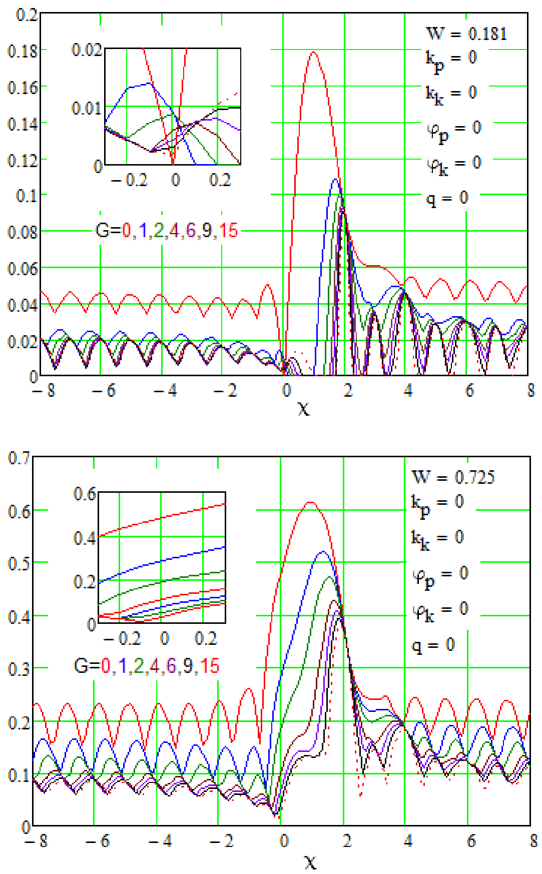


Figure 2: Dependence of the growth rate of the most unstable mode on $\chi$ for different damper gains ($G$ = 0, 1, 2, 4, 6, 9, 15) for wake amplitudes twice below (top) and twice above the threshold; the step-like wake. Insets show dependences near $\chi = 0$.

Now we consider how changes in the response functions of pickup and kicker affect the beam stability. Figure 3 presents dependences of the growth rate of the most unstable mode on $\chi$ for different damper responses. As one can see for negative $\chi$ an increase of $k_p = k_k$ from 0 to 1 reduces the growth rate of most unstable mode by about 2 times. One can also see from the top plot that there is an area near $\chi = 0$ where all modes are stable. Variations of $\phi_p$ and $\phi_k$ and making $k_p$ and $k_k$ different did not exhibit stability improvement.

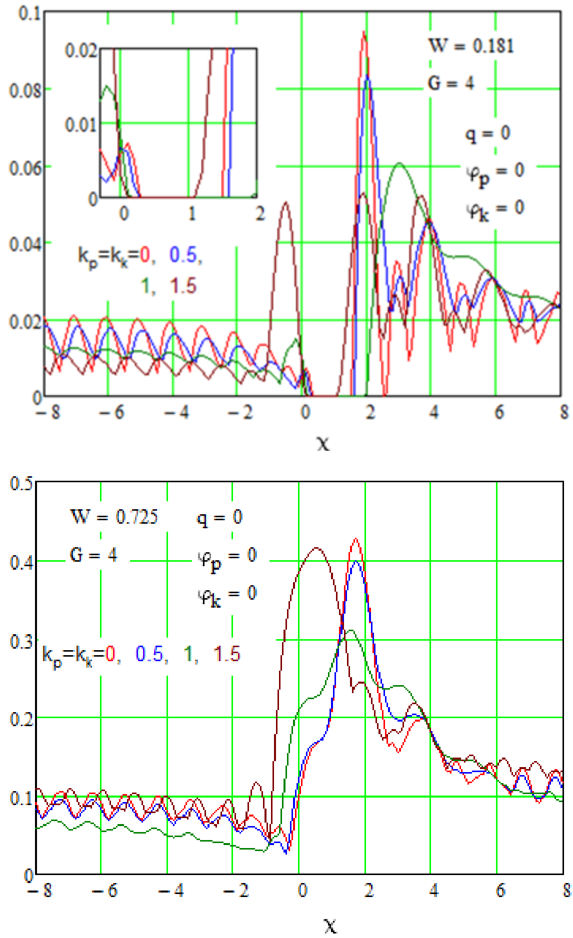


Figure 3: Dependence of the growth rate of the most unstable mode on $\chi$ for different damper responses for the cases of the beam intensity twice less (top) or twice more (bottom) than the strong head-tail threshold; the step-like wake.

All calculations were also repeated for the resistive wall wake and for different space charge parameter $q$. The results show that there is a reduction of the growth rate of most unstable mode by about two times for $k_p = k_k \approx 1$ in comparison with $k_p = k_k = 0$. Similar improvement happens in transition from $k_p \approx 1$, $k_k = 0$ to $k_p = k_k \approx 1$.

In the present LHC damper the pickup response to particle position is harmonic at 400 MHz frequency. The bunch length of 18 cm (~2σ) corresponds $k_p \approx 1.5$. That is already close to the optimum. However, the present kicker response is flat ($k_k = 0$) and as can be seen in Figure 4 that negatively affects the beam stability. Thus, making the kicker waveform as a few-periods 400 MHz sinusoid (short enough to avoid overlapping of signals of different bunches) would reduce the excitation of head-tail modes by factor of ~2.

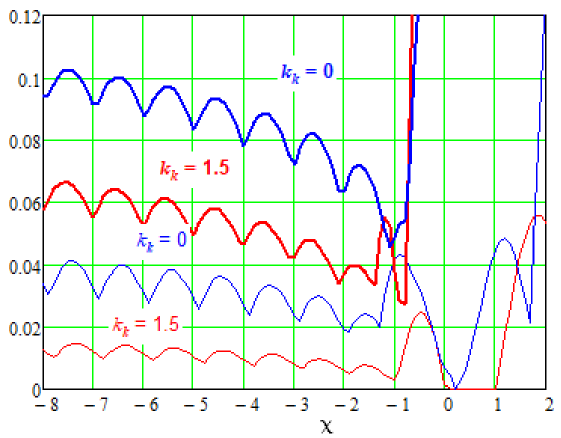


Figure 4: Dependence of the growth rate of the most unstable mode on $\chi$ for different kicker responses: red lines - $k_k$ = 1.5, blue lines - $k_k$ = 0; top two lines - $W$ is twice above threshold, bottom two lines - $W$ is twice below threshold; for all curves: $k_p$ = 1.5, $\phi_p$ = $\phi_k$ = $q$ =0; the resistive wall wake.

## EFFECT OF DAMPER NOISE ON THE INSTABILITY THRESHOLD

For a continuous beam and the smooth lattice approximation the equation of a particle motion under external force $F(t)=F_\omega e^{-i\omega t}$ is [10]:

$$-\omega^2 x_i+\omega_0^2\left(Q_0+\Delta Q_{lat_i}\right)^2 x_i=-2\omega_0^2 Q_0\left(\Delta Q_c\bar{x}-F_\omega\right). \quad (12)$$

Here $i$ enumerates particles, $\omega_0$ is the circular frequency of particle revolution, $Q_0$ is the small amplitude betatron tune, $\Delta Q_{lat_i}\equiv\Delta Q_{lat}(J_{x_i},J_{y_i})$ is the tune shift of particle betatron motion due to lattice non-linearity for a particle with betatron actions $J_{x_i}$ and $J_{y_i}$, $\Delta Q_c=\Delta Q_{cw}-ig/(4\pi)$ is the coherent tune shift which includes the tune shifts due to ring impedance, $\Delta Q_{cw}$, and due to transverse damper with damping rate per turn equal to $g/2$. Following the standard recipe [11, 12] we obtain the beam response to an external perturbation:

$$\frac{\bar{x}_\omega}{F_\omega}=\frac{R(\delta\omega)}{\varepsilon(\delta\omega)}. \quad (13)$$

Here $\bar{x}_\omega$ is the Fourier harmonic of beam centroid determined as $\bar{x}(t)=\sum_{i=1}^{N}x_i(t)/N$,

$$R(\delta\omega)=\int_0^\infty\frac{\partial f}{dJ_x}\frac{J_x dJ_x dJ_y}{\left(\delta\omega/\omega_0-\Delta Q_{lat}(J_x,J_y)+i0\right)} \quad (14)$$

is the response function in the absence of particle interaction, $f=f(J_x,J_y)$ is the particle distribution function normalized so that $\int f(J_x,J_y)dJ_x dJ_y=1$,

$$\varepsilon(\delta\omega)=1+\Delta Q_c R(\delta\omega) \quad (15)$$

is the beam permeability, $\delta\omega=\omega-\omega_n$ is the frequency deviation from $n$-th betatron sideband, $\omega_n=(n-Q_0)\omega_0$, $i0$ determines the rule of pole traversing, and we assume that a frequency shift with particle momentum is much smaller than the shift due to betatron motion non-linearity. That allowed us to omit an integration over momentum distribution in Eq. (14).

With minor corrections these formulas are also justified for a bunched beam in the weak head-tail approximation [13]. First, in addition to the betatron sidebands we need to account the synchro-betatron sidebands. That yields the resonant frequencies to be $\omega_{nm}=(Q_0+n+mQ_s)\omega_0$, where $Q_s$ is the synchrotron tune. Second, we need to account that a damper kick may excite multiple synchrotron-betatron modes. That is accounted by coefficients $w_m$. Below we consider how to obtain their values. Consequently, Eq. (13) is modified to the following form:

$$\bar{x}_{\omega_{nm}}=w_m\frac{R(\delta\omega_{nm})}{\varepsilon_{nm}(\delta\omega_{nm})}F_\omega\ . \quad (16)$$

Here $\delta\omega_{nm}=\omega-\omega_{nm}$ , and in Eq. (15) we need to account that the coherent tune shifts are different for each mode $\Delta Q_c\rightarrow\Delta Q_{c_{nm}}$ so that:

$$\varepsilon_{nm}(\delta\omega_{nm})=1+\Delta Q_{c_{nm}}R(\delta\omega_{nm})\ , \quad (17)$$

where $R(\delta\omega)$ is still determined by Eq. (14).

Eq. (16) determines the amplitude of particle motion for a given synchro-betatron mode. For small amplitude excitation each synchro-betatron mode is excited independently and to obtain the total motion in the bunch one needs to sum motions of all modes.

The instability boundary (*i.e.* maximum coherent tune shift $\Delta Q_{c_{nm}}$ for a given mode is determined by the condition when with growth $\Delta Q_{c_{nm}}$ the beam permeability approaches zero the first time at any possible detuning. That corresponds to the solution of equation,

$$\varepsilon_{nm}(\delta\omega)=0\ , \quad (18)$$

for real $\delta\omega$, which determines the stability boundary in the complex plane of $\Delta Q_c$. As follows from Eq. (13) the beam response of stable beam for a given mode is amplified by $1/|\varepsilon_{nm}(\delta\omega_{nm})|$ times.

Damper noise drives the transverse beam motion which due to spread in the betatron tunes results in an emittance growth. In the absence of particle interaction and active damping the emittance growth rate is [1]:

$$\left(\frac{d\varepsilon}{dt}\right)_0=\frac{\omega_0^{\,2}\beta_{kick}}{4\pi}\sum_{n=-\infty}^{\infty}P_\theta\left(\omega_n\right), \quad (19)$$

where $\beta_{kick}$ is the horizontal beta-function at the kicker location, and $P_\theta(\omega)$ is the spectral density of kicker angular noise normalized so that the rms value of the kicks is:

$$\overline{\theta^2}=\int_{-\infty}^{\infty}P_\theta(\omega)d\omega\,.$$

Taking Eq. (16) into account we can rewrite Eq. (19) in the following form:

$$\frac{d\varepsilon}{dt}=\int_0^\infty D\left(J_x,J_y\right)f(J_x,J_y)dJ_x dJ_y\ . \quad (20)$$

Here

$$D\left(J_x,J_y\right)=\frac{\omega_0^{\,2}\beta_{kick}}{4\pi}\sum_{n,m=-\infty}^{\infty}\frac{w_m^{\,2}P_\theta\left(\omega_n\right)}{\left|\varepsilon_{nm}(\omega_0\Delta Q_{lat}(J_x,J_y))\right|^2}\ , \quad (21)$$

and we accounted that the spectral density of kicker noise does not change across one synchro-betatron sideband, noises at different frequencies do not correlate, and only resonant frequencies drive the emittance growth.

It is straightforward to find the emittance growth for the case of zero chromaticity, when only zero's synchro-betatron mode is excited. Assuming strong damping, $g_n \gg 4\pi \max(|\Delta Q_{cw}|, \sqrt{\overline{\Delta\nu^2}})$, octupole non-linearity in the horizontal plane only, $\Delta Q_{lat}(J_x) = a_{xx} J_x$, and Gaussian distribution, $f(J_x) = e^{-J_x/J_a} / J_a$, we obtain:

$$D(J_x) = \frac{\omega_0^2 \beta_{kick}}{4\pi} \sum_{n=-\infty}^{\infty} \frac{16\pi^2 \overline{\Delta\nu^2} P_\theta(\omega_n)}{g_n^2 \left| \int_0^\infty \frac{x\, e^{-x}\, dx}{x - y - i0} \right|^2}, \quad y = \frac{J_x}{J_a}. \quad (22)$$

Here $\sqrt{\overline{\Delta\nu^2}} = a_{xx} J_a$ is the rms frequency tune spread, $J_a$ is the rms action, and $g_n$ is the damper gain at the $n$-th betatron sideband. Substituting diffusion of Eq. (22) into Eq. (20) and performing numerical integration one obtains a perfect coincidence with the result obtained in Ref. [1]:

$$\frac{d\varepsilon}{dt} = \frac{\omega_0^2 \beta_{kick}}{4\pi} \sum_{n=-\infty}^{\infty} \frac{16\pi^2 \overline{\Delta\nu^2}}{g_n^2} P_\theta(\omega_n), \quad g_n \gg 4\pi\sqrt{\overline{\Delta\nu^2}}. \quad (23)$$

Note that Eq. (21) is applicable in the general case while Eq. (23) in the case of zero chromaticity and far away from the instability threshold. Note also that the derivation of Eq. (23) in Ref. [1] does not actually determine the tune relative to which $\sqrt{\overline{\Delta\nu^2}}$ is computed. This question is addressed by Eq. (21).

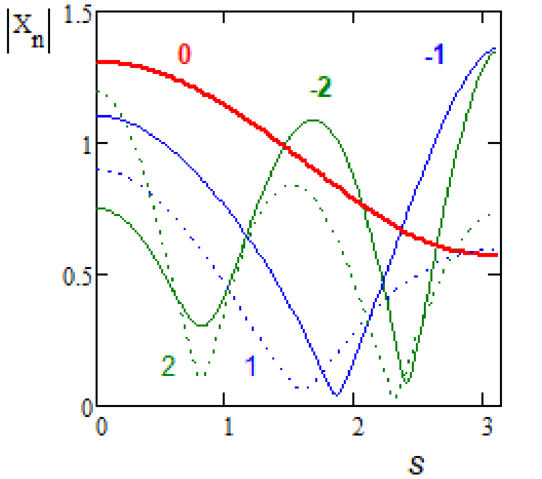


Figure 5: Dependencies of mode magnitudes, $|X_n| \equiv |x_{1n} + x_{2n}|$, along the bunch for the parameters of the LHC damper: $\chi = 1$, $k_p = 1.5$, $k_k = \phi_p = \phi_k = q = 0$, $W = 2W_{thr}$ for the resistive wall wake. Numbers show the mode numbers.

To find a change in the instability threshold related to a change in the distribution we need to investigate the distribution function evolution. Considering that the kicks are small and uncorrelated; and, consequently, the process is very slow relative to the betatron motion the evolution can be described by the diffusion equation. In the general case of uncoupled betatron motion the diffusion in the 2D-space of actions is described by the following diffusion equation [14]:

$$\frac{\partial f}{\partial t} = \frac{\partial}{\partial J_x}\left( J_x D_x(J_x, J_y) \frac{\partial f}{\partial J_x} \right) + \frac{\partial}{\partial J_y}\left( J_y D_y(J_x, J_y) \frac{\partial f}{\partial J_y} \right). \quad (24)$$

Here the diffusion in the horizontal plane is determined by Eq. (21). The vertical plane diffusion is obtained by changing corresponding indices.

In the presence of impedance and chromaticity each kicker kick excites multiple head-tail modes. Only few of them are damped by the damper. Figure 5 shows shapes of few lowest head-tail modes for the damper model described in the previous section for the LHC parameters. As one can see all of them have significant variations along the bunch while the kicker kick is the same for all particles. Therefore, each kick in addition to the zero mode excites other modes. To find corresponding contributions we equalize the kick dependence along the bunch and the weighted sum of the mode amplitudes:

$$\cos\left(k_k\left(|\psi| - \pi/2 + \phi_k\right)\right) = i\sum_m \hat{w}_m x_m(\psi). \quad (25)$$

where $x_m(\psi)$ is determined by Eq. (11) and is additionally normalized so that $x_m(\pi/2) = 1$. The solution of this equation yields coefficients $\hat{w}_m$. To obtain coefficients $w_m$ which determine relative excitation for different head-tail modes we additionally need to account how a given mode with amplitude $\hat{w}_m$ contributes to the emittance growth. That yields: $w_m^2 = \overline{|x_m(\psi)|^2}\, \hat{w}_m^2$. Figure 6 shows $\hat{w}_m$ for the modes presented in Figure 5. One can see that the mode zero has the largest contribution, $\hat{w}_0$, and the only one which has significant damping.

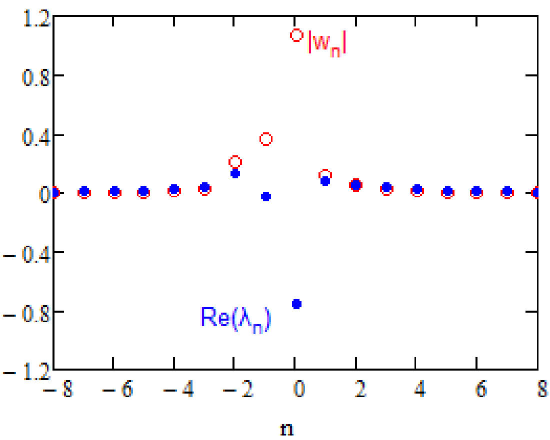


Figure 6: Dependences on the head-tail mode number for $|\hat{w}_n|$ (red circles) and the damping rate (blue dots).

To demonstrate an effect of damper noise on the beam stability boundary we initially assume that only one of the head-tail modes is near the threshold and it dominates the emittance growth. Applicability of this assumption we will discuss later. We also assume that the focusing non-linearity is in one plane only. That allows us to consider a one-dimensional problem. Then, from Eqs. (21) and (24) we obtain a simplified diffusion equation:

$$\frac{\partial f}{\partial \tau} = \frac{\partial}{\partial J_x}\left( J_x \hat{D}(J_x) \frac{\partial f}{\partial J_x} \right), \quad \hat{D}(J_x) = \frac{1}{\left|\varepsilon\left(\delta\omega(J_x)\right)\right|^2}. \quad (26)$$

Here we transited to the dimensionless variables so that the action $J_x$ is measured in units of rms action $J_a$, and time $\tau$ is chosen to make the diffusion coefficient equal to the one in the absence of beam interaction. We also took into account that the diffusion is proportional $1/|\underline{\varepsilon}|^2$ at the resonance frequency which is directly related to the action as $\Delta Q_{lat} = a_{xx} J_x$. That yields the univocal dependence of beam permeability on the action:

$$\varepsilon\left(\delta\omega(J_x)\right) = 1 + \frac{\Delta Q_c}{a_{xx}} \int_0^{J_{max}} \frac{\partial f}{dJ'_x} \frac{J'_x dJ'_x}{J_x - J'_x + i0}. \quad (27)$$

where $J_{max}$ is determined by the ring acceptance.

The solution of Eq. (26) with beam permeability of Eq. (27) was carried out numerically. The action space was binned into boxes with boundaries at $J_n = n\Delta J$, $n\in[0, N_{max}]$, so that $f_n \Delta J$ is the probability to find a particle in $n$-th box and $f_n$ is the distribution function in the center of the box bounded by $J_n$ and $J_{n+1}$. An integration of Eq. (26) over $J$ through one box yields the particle flux through the boundary between boxes $n$ and $n$+1:

$$\Phi_{n+1} = J_{n+1} D\left(J_{n+1}\right) \frac{\partial f}{\partial J}\bigg|_{J=J_{n+1}} \to J_{n+1} D_{n+1} \frac{f_{n+1} - f_n}{\Delta J}. \quad (28)$$

Consequently, the change in the distribution is:

$$f_n(t_{k+1}) = f_n(t_k) + \left(\Phi_n(t_k) - \Phi_{n+1}(t_k)\right)\Delta t, \quad \Delta t = t_{k+1} - t_k. \quad (29)$$

Time step $\Delta t$ was chosen so that to be well below the numerical instability threshold of the difference scheme, which is determined by:

$$S \equiv \max_n \left(4 D_n J_n \Delta t / \Delta J^2\right) = 1.$$

In a typical simulation $S$ did not exceed 0.1, both at the instability onset and its initial development. However, with instability development and subsequent growth of the diffusion this condition was violated and calculations were stopped well before $S$ reached 1.

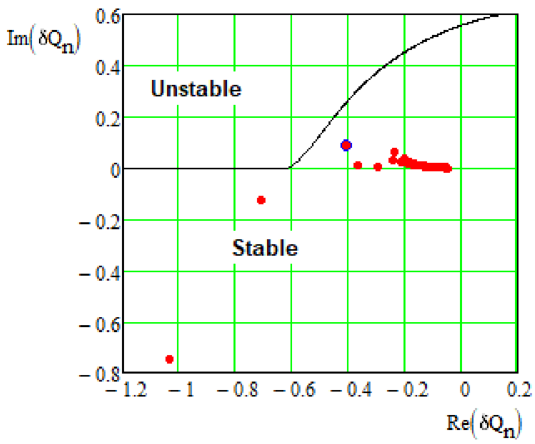


Figure 7: Ratios of coherent tune shifts to the synchrotron tune for different modes for parameters of Figure 5. Black line presents the stability boundary for Gaussian beam with non-linearity parameter $a_{xx}$ chosen so that the most unstable mode (marked by blue circle) would be 20% below stability threshold.

For a harmonic perturbation $\delta f \cos(\kappa J)$ and $S << 1$ this difference scheme yields good approximation for small $\kappa$. However, it reduces damping at the highest frequency of $\kappa_{max} = \pi/(2\Delta J)$ by $(\pi/2)^2$ times. Note that a usage of implicit methods typically applied to the diffusion equation solving is limited by two circumstances. First, a computation of diffusion at any point in the action space uses the entire particle distribution and therefore computation of distribution at the next point in time requires inversion of $N_{max}\times N_{max}$ matrix instead of three-diagonal matrix for the case of implicit scheme. Second, as will be shown below, the instability is developing at high wave-numbers in the action space. That requires small $\Delta J$. Numerical tests also showed that very small steps in time are required.

To accelerate computation of the integral in Eq. (27) it was reduced to a matrix multiplication so that the vector of beam permeability is equal to:

$$\boldsymbol{\varepsilon} = \mathbf{Rf}. \quad (30)$$

Here the vectors $\boldsymbol{\varepsilon} \equiv \varepsilon_n$ and $\mathbf{f} \equiv f_n$ determine the beam permeability and the distribution function. The elements of matrix $\mathbf{R}$ are determined by integration Eq. (27) between nearby actions $J_n$ using Tailor expansion of $f$. Numerical tests verified that Eq. (30) results in good approximation of integral (27) in the absence of discontinuities in the distribution.

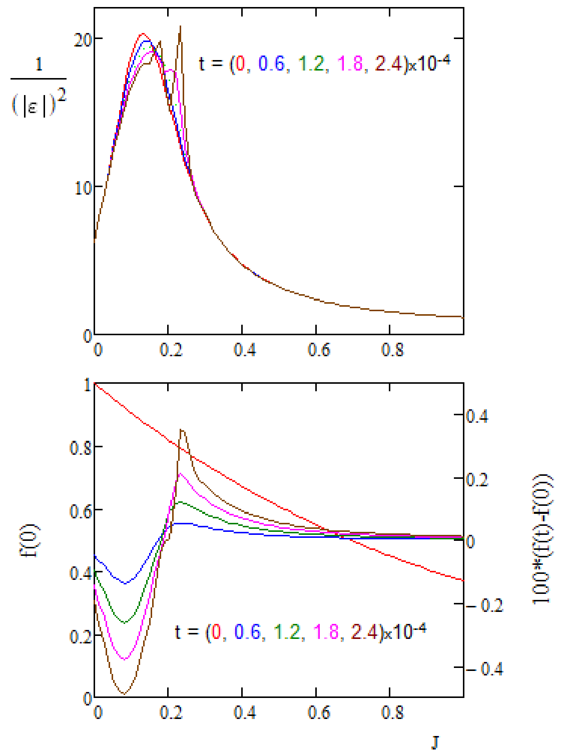


Figure 8: Dependence of dimensionless diffusion (top) and distribution function (bottom) on the action for different times, $t$; $a_{xx} = 0.02$, $\Delta Q_c = (-12.6+3.1i)10^{-3}$. Red curve in the bottom plot shows the initial distribution (left scale) and other curves changes of the distribution multiplied by 100 (right scale).

Simulations showed that loss of stability due to distribution evolution under kicker noise strongly depends on the phase of the coherent tune $r = \arg(\delta Q_n)$. Figure 7 presents the dimensionless coherent tune shifts (ratio of coherent tune shifts to the synchrotron tune) for different head tail modes for the parameters of Figure 5. The stability boundary was chosen so that the most unstable mode would be 20% below the boundary. The phase of this mode on the complex plane is equal to $r = 168^{\circ}$ ($\mathrm{Re}(\delta Q_n)/\mathrm{Im}(\delta Q_n) = -4.7$). The distance from the stability boundary to the next mode closest to the boundary is about twice larger, and consequently its effect on the diffusion is 4 times smaller. Figure 8 shows a typical example of the evolution for initially Gaussian distribution. The figure also shows the corresponding diffusion. One can see that there is a narrow peak growing fast in the diffusion plot at $J \approx 0.25$. The value of $\Delta Q_c/a_{xx}$ for Figure 8 calculations was chosen so that the beam would be 20% below instability threshold (see Figure 7). In all simulations (as well as in Figure 8) it has been clearly seen that the instability, if happens, develops at the highest possible wavenumber determined by $\Delta J$. An increase of $N_{max}$ decreases $\Delta J$ and the span in the distribution where the instability is initially developed. However, the location of the instability position in the action did not depend on $N_{max}$.

To explain the results of the simulations we consider the following model. We assume that the instability is developed in a small area near the action $J_r$. In this area we look for a solution in the following form:

$$f(J_x,t) = f_0(J_x) + \delta f(t)\cos(\kappa J + \psi) \ , \qquad (31)$$

where we assume the wavenumber, $\kappa$, being very large, and the perturbation $\delta f(t) \equiv \delta f$ to be much smaller than the initial distribution $f_0(J_x)$. A perturbation in the distribution results in a perturbation in the response function. Substituting the perturbation of Eq. (31) into Eq. (14) we obtain a perturbation of response function:

$$\delta R \equiv \delta R(J_x) = -\frac{i\kappa}{a_{xx}}\delta f \int_0^{\infty} \frac{\sin(\kappa J + \psi) J dJ}{J_x - J + i0} , \qquad (32)$$

where we accounted that the resonance frequency is $\delta\omega = a_{xx} J_x$. For large $\kappa$ the major contribution to the integral comes from the area near $J_x$. That allows us to extend the lower integration limit to $-\infty$. Then, the integration becomes straight forward. It results in:

$$\delta R = \frac{\pi \kappa J_x}{a_{xx}} e^{i(\kappa J_x + \psi)} \delta f(t) . \qquad (33)$$

Using Eqs. (15) and (26), we obtain the diffusion:

$$\hat{D} = \frac{1}{\left|1 + \Delta Q_c (R + \delta R)\right|^2} \approx D_r + \delta D ,$$
$$\delta D = -D_r \,\mathrm{Re}\left( \frac{2\pi\kappa J_r \Delta Q_c}{\varepsilon_r} e^{i(\kappa J_x + \psi)} \right) \delta f , \qquad (34)$$

where $\varepsilon_r = 1 + \Delta Q_c R_r$ is the beam permeability for unperturbed distribution computed at the resonant tune $\delta\omega/\omega_0 = J_r a_{xx}$, and $D_r = 1/\left|\varepsilon_r\right|^2$ is the corresponding diffusion. In obtaining the second equality we used the Tailor expansion and replaced $J_x$ by $J_r$ in the non-oscillating term. As one can see a harmonic perturbation of the distribution results in a harmonic perturbation of the diffusion.

Taking into account that we consider only small area in the action space in vicinity of $J_r$ and very large wavenumber $\kappa$ (see the definition below) we can replace $J_x$ inside $\partial / \partial J_x$ in Eq. (26) by $J_r$. That yields:

$$\frac{\partial}{\partial \tau}(f_0 + \delta f) = J_r \frac{\partial}{\partial J_x}\left( (D_r + \delta D) \frac{\partial}{\partial J_x}(f_0 + \delta f) \right). \qquad (35)$$

Accounting that the unperturbed function satisfies the following equation:

$$\frac{\partial f_0}{\partial \tau} = J_r \frac{\partial}{\partial J_x}\left( D_r \frac{\partial f_0}{\partial J_x} \right) \qquad (36)$$

and leaving only linear terms in Eq. (35) we obtain a linear differential equation for the perturbation

$$\frac{\partial \delta f}{\partial \tau} = J_r \frac{\partial}{\partial J_x}\left( D_r \frac{\partial \delta f}{\partial J_x} + \delta D \frac{\partial f_0}{\partial J_x} \right) . \qquad (37)$$

We look for a solution in the following form:

$$\delta f = \tilde{f} e^{-\lambda \tau} \cos(\kappa I - \nu \tau) \ . \qquad (38)$$

Substituting it into Eq. (37), assuming initial Gaussian distribution $f_0 = e^{-J_x}$, and using Eq. (34) we obtain the damping rate as a function of $J_r$:

$$\lambda = J_r D_0 \kappa^2 \left( 1 + e^{-J_r} \left( \mathrm{Im}(A) - \mathrm{Re}(A)/\kappa \right) \right) ,$$
$$A = \frac{2\pi J_r \Delta Q_c}{\varepsilon_r a_{xx}} . \qquad (39)$$

For large $\kappa$ the last term can be neglected. Thus, for the Gaussian distribution the stability area for given $\Delta Q_c$ is determined by following equation,

$$1 + \frac{2\pi J_r \Delta Q_c}{a_{xx}} e^{-J_r} \,\mathrm{Im}\left( \frac{\Delta Q_c}{\varepsilon_r} \right) \geq 0 \ , \qquad (40)$$

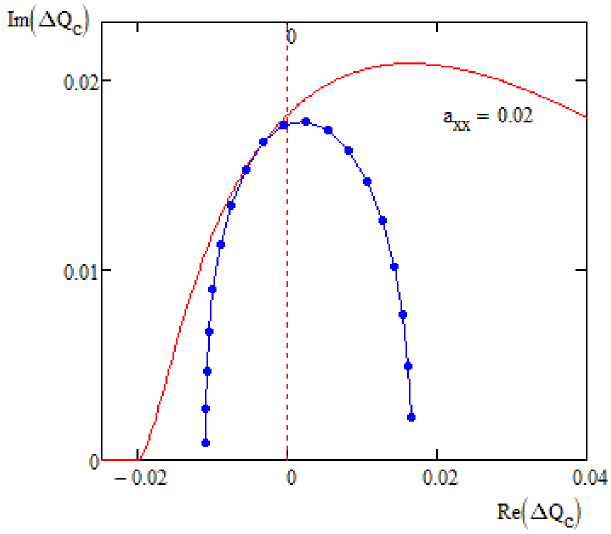


Figure 9: Stability diagram computed with accounting noise driven diffusion (blue curve) and without it (red curve.)

which must be satisfied for all $J_r$. Figure 9 presents the stability diagrams computed with the help of Eqs. (18) (red curve) and (40) (blue curve). One can see that the kicker noise results in significant reduction of the stability boundary. However, this reduction is negligible in vicinity of $\arg(\Delta Q_c) \approx 105^o$. We will call the action $J_r$, at which the left-hand side in Eq. (40) approaches zero the first time, the resonant action. It shows where instability develops when the beam is approaching to the instability boundary. Figure 10 shows how this resonant action depends on the angle of the coherent tune shift in the complex plane. The figure also shows the ratio of stability boundary sizes (ratio of $|\Delta Q_c|$ for given $r = \arg(|\Delta Q_c|)$ for curves presented in Figure 9. Numerical simulations verified the reduction of the stability boundary presented in Figure 9 and 10 and the location of the resonant action.

Taking into account that the considered above instability develops at high wavenumbers in the action and the resonant actions of different head-tail modes are different, we, in the first approximation, can neglect mutual interaction of different modes. That results in that the considered above model should be applicable to the situation when multiple modes are close to the instability boundary. If required it is straightforward to extend this model to multiple modes introducing summation of different modes in Eq. (34).

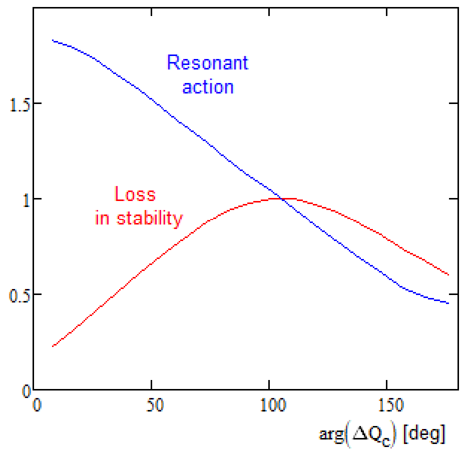


Figure 10: Dependence of the resonant action and the loss in stability on the angle of the coherent tune shift in the complex plane.

## CONCLUSIONS

An introduction of harmonic variation in the kicker waveform looks as a promising method for an increase of stability boundary for the LHC. Such a kicker does not work well for suppression of emittance growth due to injection errors. Therefore, the existing low frequency kicker should be retained and used for damping injection errors. A new kicker operating at 400 MHz base frequency could be used for the rest of the accelerating cycle and in the collisions. The power and space required for this new kicker are determined by the BPM noise and are well within the reach.

The considered above mechanism for reduction of the stability boundary points out underlying reasons behind the observations of transverse beam stability loss in the LHC. We need to note that in this model we neglected other diffusion mechanisms which affect the evolution of the distribution. In normal operating conditions the intra-beam scattering is the major diffusion mechanism. It counteracts the effects introduced by the damper noise and therefore a reduction of stability boundary due to kicker noise should be somewhat smaller. An additional noise used in the LHC experiments reduced relative effect of the IBS driven diffusion with subsequent reduction of the stability boundary observed in the experiments [6].

## ACKNOWLEDGMENTS

The author would like to thank A. Burov, E. Metral, X. Buffat and S. Furuseth for help in editing of this paper and many useful discussions on its subject.

## REFERENCES

[1] V. Lebedev, et.al., “Emittance growth due to noise and its suppression with feedback system in large hadron colliders”, Particle Accelerators, 1994, vol. **44**, pp. 147-164.

[2] V. Lebedev, “Computer simulation of the emittance growth due to noise in large hadron colliders”, Particle Accelerators, 1994, vol. **44**, pp. 165-199.

[3] G. Arduini et al., “Hump: how did it impact the luminosity performance?”, LHC Beam Operation Workshop - Evian 7-9 December 2010.

[4] W. Hofle, et.al., “Suppression of Emittance growth by excited magnet noise with the transverse damper in LHC in simulation and experiment”, Proceedings of IPAC2011, pp. 508-511, (2011).

[5] V. A. Lebedev, “Beam Physics Limitations for Damping of Instabilities in Circular Accelerators”, HB-2018, http://accelconf.web.cern.ch/AccelConf/hb2018/

[6] S. Furuseth, et.al. “Instability latency with controlled noise”, CERN-ACC-NOTE-2019-0011, https://cds.cern.ch/record/2670123; pp.3204-3207 in proceedings of IPAC-2019.

[7] X. Buffat, “Transverse beams stability studies at the Large Hadron Collider”, Ph.D. Thesis, Inst. of Physics, École polytechnique fédérale de Lausanne, Lausanne, Switzerland, 2015, CERN-THESIS-2014-246; https://infoscience.epfl.ch/record/204682/files/EPFL_TH6321.pdf.

[8] M. Blaskiewicz, “Fast head-tail instability with space charge”, Phys. Rev. ST Accel. Beams **1**, 044201 (1998).

[9] A. Burov, “Convective instabilities of bunched beams with space charge”, Phys. Rev. Acc. and Beams, **22**, 034202 (2019).

[10] H. G. Hereward, “Landau damping by non-linearity”, CERN/MPS/DL 69-11, July 1969.

[11] A. W. Chao, *Physics of Collective Beam Instabilities in High Energy Accelerators* (Wiley, New York, 1993).

[12] J. S. Berg and F. Ruggiero, CERN Report No. CERN SLAP-96-071-AP, 1996.

[13] Burov, “Nested head-tail Vlasov solver”, Phys. Rev. STAB **17**, 021007 (2014)

[14] G. Dome, “Diffusion due to RF Noise”, in Proc. of the CERN Accelerator School *Advanced Accelerator Physics Course*, Oxford, 1985, Preprint CERN 87-03 (April 1987)

# IMPLEMENTATION OF TRANSVERSE DAMPERS IN BEAM STABILITY ANALYSES

Kevin Li and Jani Komppula
CERN, Switzerland

*Abstract*

Collective effects in high intensity, high energy particle accelerators and colliders are becoming increasingly important as performance is continuously pushed to the limits. The mitigation of collective effects, in particular coherent beam instabilities, relies heavily on transverse feedback systems. The dimensioning of these feedback systems (i.e., power, bandwidth, pickup and kicker distribution) are key to the systems performance and its effectiveness in combating collective effects limitations. Consequently, their realistic modeling in computer simulation codes is also highly important. In this paper we will briefly outline recent developments in advanced modeling of transverse feedback systems in collective effects using the example of macroparticle simulation codes developed at CERN.

## INTRODUCTION & MOTIVATION

Collective effects and coherent beam instabilities are important players in today's accelerator landscape as the machine performance is continuously pushed towards the limits of the intensity and the energy frontiers. Collective effects problems are difficult to handle purely analytically (e.g., using 2-particle models or Vlasov solvers). Today's simulation tools derive from different approaches, each with their own advantages and fall-backs. Different type of simulation codes include:

**Vlasov solvers:** semi-analytic solution of the Vlasov equation in frequency domain using decompositions of the longitudinal phase space in specific basis functions (Laguerre polynomials, Airbags...);

**circulant matrix models:** matrix model representation of the particle dynamics in a specific basis (decomposition of longitudinal phase space), with linearized collective effects, including transverse feedbacks;

**macroparticle trackers:** Monte-Carlo-like approach, very close to the physical reality resembling the involved processes in a nearly one-to-one mapping.

Not all of these tools will be covered in this paper. Instead here, due to their universality and flexibility, we will focus exclusively on macroparticle simulation codes; in particular, for this paper we will base ourselves on the example of the PyHEADTAIL collective effects simulation suite [1] which is the simulation code used at CERN for collective effects beam dynamics studies.

As much as it is important to be able to simulate the driving forces of coherent beam instabilities, it is also important to have good models of the mitigation methods. One important example of mitigation devices is transverse feedback systems. These systems themselves carry a high level of complexity. In order to correctly include the effects of transverse feedback systems along with their peculiarities and limitations, it is crucial to ensure a good and complete as possible modeling of the feedback chain. In the following sections we will first stress the importance of feedback systems for collective effects mitigation. We will then show different possibilities of modeling these and then show an example of an implementation of a detailed feedback systems model. Finally, we will present some benchmarks and comparison with experimental data.

## TRANSVERSE FEEDBACK SYSTEMS - THE NEED FOR IMPROVED MODELING

Transverse feedback systems are an integral component of any modern particle accelerator. They serve a multitude of purposes ranging from injection oscillation damping, suppression of coherent beam instabilities or as multipurpose tools used for controlled emittance blow-up or tune shift measurements, for example. Essentially, they are a key component for ensuring beam quality preservation throughout the accelerator cycle. Future accelerators will rely heavily on transverse feedback systems, as they are being operated closer to the stability limits. System upgrades be it for increased resolution, more power or higher bandwidth, for example, will become crucial. To correctly characterize and dimension future transverse feedback systems, it is important to include good models in our computer simulation codes.

A simple and pretty straightforward way of modeling of the effects of a transverse feedback system in macroparticle models is by applying a correction on each individual particle proportional to the mean position of the full particle ensemble:

$$x_i = x_i - g \cdot \langle x \rangle \,, \qquad (1)$$

where $g$ is the gain defined as the damping rate in turns. In a linear machine with an initial offset $x_0$, this leads to an exponential decay of

$$x(T) = x_0 \exp\left(-g\,\frac{T}{2}\right), \qquad (2)$$

where $T$ is the number of turns. Already this simple modeling can exhibit some interesting effects which have been recently discovered and investigated more closely in different studies [2, 3]. On the other hand, many of the specific features characteristic to realistic feedback systems, such as separation of pickup and kicker, signal delays, imperfections such as noise or bandwidth limitations etc., are not at all captured. A more accurate modeling involves a detailed representation of the actual feedback chain.

Typically, two rather separate approaches are taken when studying feedback systems dimensioning and performance. From the feedback engineer's point of view, the beam dynamics are kept simple and often modeled as an harmonic oscillator. All complexity of the feedback chain, on the other hand, is well captured as highlighted in Fig 1

Contrary to this, the beam dynamics physicist has detailed models of the beam dynamics, including full impedance models and non-linear effects, but treats the feedback system either fully independently or as a simple local correction of the beam orbit (see Fig. 2 for an example of evaluating the feedback performance purely analytically). For a complete modelling of the full system, the two individual subsystems need to be combined while retaining all of their complexity.

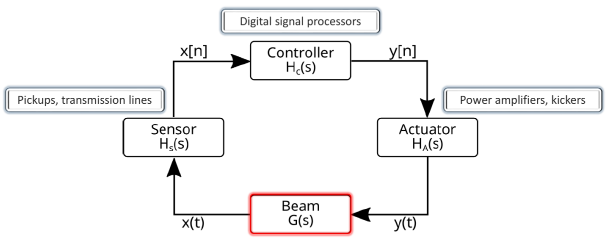


Figure 1: The engineer's view on the internal of a coupled feedback-beam dynamics system. The beam model is kept simple.

To stress the importance of a combined modeling of both feedback loop and collective effects beam dynamics, Figs. 3a and 3b show a study which highlights

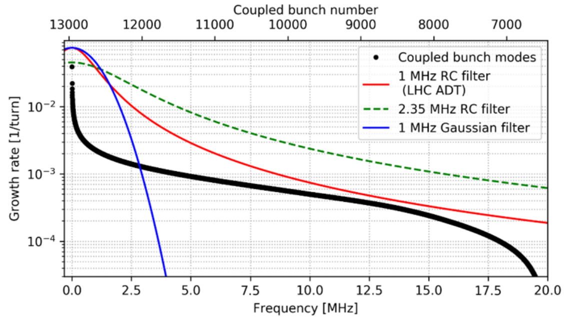


Figure 2: The beam physicist's point of view of a coupled feedback-beam dynamics system. The feedback system is modeled as a simple orbit subtraction at a given point (see Eq. 1).

the limitation of realistic feedback systems under tune shifts. For this study, a realistic model of the LHC transverse feedback system (ADT) was implemented and its performance was studied in terms of damping rate of injection oscillations of an injected beam into the machine. It becomes clear, that for instance bandwidth limitations, as highlighted in these figures, can significantly limit the dynamic range of the feedback systems and the gains that can be set. These limitations are not visible using the conventional feedback system models commonly implemented in beam dynamics simulations, as mentioned earlier on.

## IMPROVED MODELS IMPLEMENTATION

Recently, advanced simulation models have been developed to better represent numerically realistic feedback systems, with much of their specific complexity and details included [4]. The components of these advanced models have been organized in a similar fashion following a similar architecture as the PyHEADTAIL collective effects simulation suite. The latter features:

- a highly modular design;
- very simple and concise individual modules as building blocks;
- a majority of code written in Python with some few methods written in optimized Fortran or C to overcome performance bottlenecks;
- a unique interface for a generic, quick and simple assembly of a wide range of simulation studies.

Following this exact Philosophy, a dedicated feedback module has been prepared, which can be used

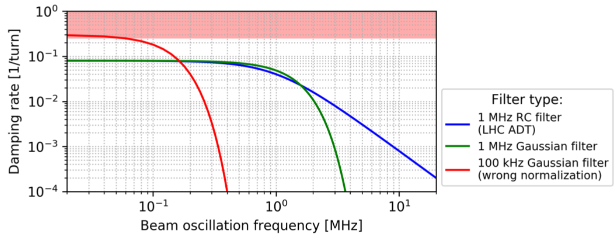


(a) Low-pass filters simulate bandwidth limitations the the feedback system and limit the available range of gains; in this case, the bandwidth limitation affects the bunch-to-bunch or intra-bunch oscillation mode that can be resolved and consequently be damped by the system.

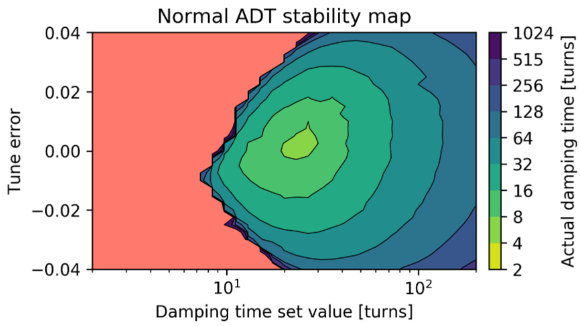


(b) The correction kick is computed internally within a digital signal processing chain. Any deviation of the beam from the design tune leads to sub-optimal damping or event to feedback system-driven instabilities.

either independently or in conjunction with PyHEADTAIL.

The applicability of this same approach becomes clear if one highlights the similarities between the two problems, namely signal propagation in a feedback loop and beam dynamics in a synchrotron.

For beams circulating in a synchrotron, one may consider particle ensembles which periodically encounter the same set of machine elements which exerts a certain given action on them. As such, one can concatenate a series of actions which are chronologically and periodically applied to the particle ensemble as the latter circulates within the ring. This very concept is represented, in PyHEADTAIL for instance, by the so-called one-turn-map which essentially is a list of different elements such as betatron maps, synchrotron maps, wake fields, space charge, electron clouds etc.; this list forms the accelerator tracking loop.

If one now thinks about a transverse feedback system, a beam signal gets registered at the pickup and is then propagated though a digital signal processing chain. There, it get transformed over several stages into a correction signal that gets played onto the kicker, which then applies a correction kick back onto the beam. This takes place turn after turn such that one again finds back a sequence of actions that is periodically applied, this time, however, onto the beam signal. In a similar manner as the one-turn-map, a list of signal processors can be constructed, consisting for instance of harmonic ADCs, Notch + Hilbert filters, N-tap FIR filters, upsamplers, DACs, low-pass filters, etc., through which the digital signal is passed turn after turn; this list now forms what can be identified as the feedback loop.

Figures 4a and 4b show an example of such a digital signal processing chain represented as a Python list. One can also see how the digital signal can be inspected at every step within the processing chain. We cannot go into the formal details on the implementation of each elements of these lists, but the idea is that any possible implementation of nearly arbitrary complexity can easily be developed and concatenated to be made available as part of the feedback processing chain.

## TESTS AND BENCHMARK RESULTS

The new feedback module was used to investigate phenomena which can not be reproduced using conventional methods to model transverse feedback systems in (macroparticle) simulation codes. On one hand, this serves as an important test and benchmark for the simulation model and, on the other hand, the same model was also used to perform an actual optimization campaign of an exiting transverse feedback system.

### *Injection oscillation damping in the LHC*

An important function of the LHC transverse damper is the quick suppression of injection oscillations to prevent emittance blow-up after injection. Beams in the LHC are injected in batches of 72 bunches separated by 25 ns. The ADT does not intrinsically have the bandwidth to act on the individual bunches of this spacing (this would require a minimum bandwidth of 20 MHz to be able to act on the highest beam mode). Instead, the damper couples neighboring bunches [1]. One characteristic feature of such a system is the roll-off of the effective gain towards the ends of the injected batches. This can be observed in measurements as an increase in the damping rate at the batch edges. Such a feature can not be reproduced in simulations using the classical approach of modeling feedback systems. A realistic

[1] there are certain high bandwidth settings of the ADT, which can be used to artificially increase the damper bandwidth; this is done by a clever signal processing [5]

```
processors_x = [
        ChargeWeighter(normalization = 'segment_average'),
#         NoiseGenerator(RMS_noise_level),
        HarmonicADC(1*f_RF/10., ADC_bits, ADC_range,
                    n_extras=extra_adc_bins),
        TurnFIRFilter(turn_FIR_filter_x, machine.Q_x, delay=1),
        FIRFilter(FIR_phase_filter, zero_tap = 40),
        Upsampler(3, [0,3,0]),
        FIRFilter(FIR_gain_filter, zero_tap = 32),
        DAC(ADC_bits, ADC_range),
        Lowpass(fc, f_cutoff_2nd=10*fc),
        BackToOriginalBins()
]
```

(a) The feedback loop represented as a digital signal processors list.

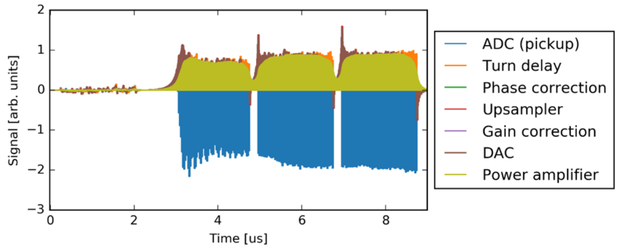


(b) The original input signal can be followed and inspected throughout the digital signal processing chain for diagnostics purposes.

implementation of the ADT should, however, clearly display this feature.

Figure 5a shows a measurement turn-by-turn and bunch-by-bunch of three injected batches into the LHC. The image clearly reveals the aforementioned effects of increased damping rates towards the batch edged. Figure 5b shows the same process modeled in simulations, where a realistic model of the ADT has been implemented using the PyHEADTAIL feedback module. It is apparent, that almost all features of the measurement are well captured by the simulation. This gives confidence that the specific features of the ADT are well modeled in these simulations.

### *FIR filter optimization for the LHC ADT*

Another peculiar feature of transverse feedback systems is the sensitivity of their performance to the design tune. This is impacted by several factors such as delays, lengths of filters, or the present oscillation modes of the beams. In fact, one important design criterion of a transverse feedback system is also its acceptance in deviation from the design tune. This can be an important aspect when taking into account bunch-by-bunch tune shifts from collective effects such as narrow-band resonator impedances or electron clouds, for example.

This time, the realistic numerical model of the ADT was used to design and evaluate in simulations an FIR filter with the target of an increased acceptance in tune deviations – we will call this the tune bandwidth, for now – compared to the FIR filter currently implemented for the ADT. After validation of the improved performance in simulations, the FIR filter was implemented in the firmware of the actual ADT and the experiment was repeated in a machine development study (MD) [6]. Figure 6 shows the results obtained in simulations and in the MD in comparison. It becomes immediately clear, that the numerical model of the ADT very well reproduces the actual feedback system behavior. It is also evident, that by means of the numerical simulation

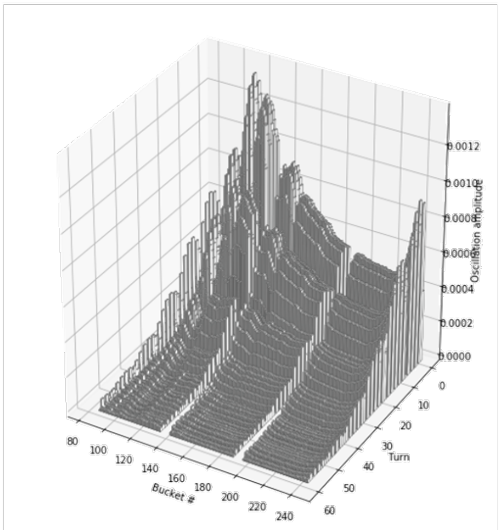


(a) Turn-by-turn and bunch-by-bunch oscillation amplitudes of the three batches after injection into the LHC as registered by the ADT pickups.

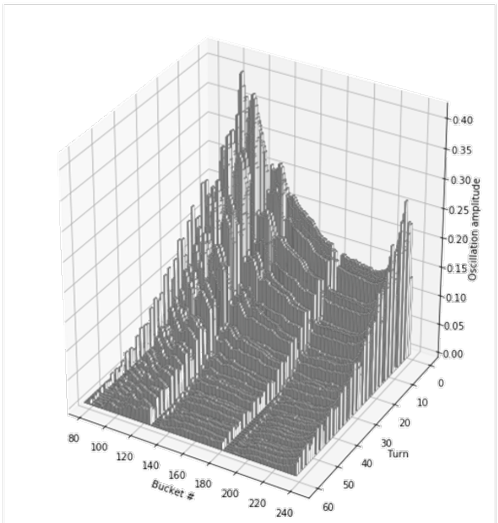


(b) Turn-by-turn and bunch-by-bunch oscillation amplitudes of the three batches after in the injection into the LHC, simulated with a realistic model implementation of the ADT.

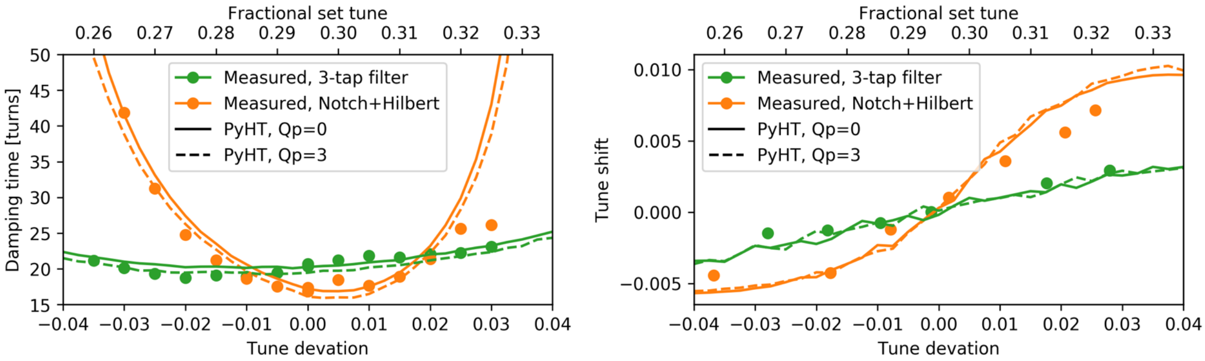


Figure 6: Comparison of simulations and measurements for the design of a high tune acceptance FIR filter in the LHC.

it was indeed possible to produce an FIR filter which features an improved performance in term of tune bandwidth. This is a very important achievement as it shows that with good and detailed numerical models of transverse feedback systems, it is actually possible to make meaningful studies the help support the design and dimensioning of both existing as well as future feedback systems. It can also save valuable machine time which would be needed to do the same types of studies in MDs.

## SUMMARY AND CONCLUSION

In this paper we highlighted the importance of accurate and realistic modeling of transverse feedback systems in simulations. Collective effects limitations are becoming increasingly important as future machines are operated closer to the performance limits. With transverse feedback systems as one of the key mitigation devices, their full accessibility through numerical simulations is of utmost importance, to catch limitations and imperfections and allow for accurate feedback dimensioning and design.

We have shown that, recently, a fully featured feedback system module has been developed for the PyHEADTAIL collective effects simulation suite in a highly generic and modular fashion.

The feedback module has been checked against real world measurements done at the LHC with the LHC transverse feedback system (ADT). These benchmarks revealed that many of the peculiarities of the real world system were well captured in the simulation model. Bandwidth limitations manifested in the simulation results as well as the improvements, which were implemented within the digital signal processing change via firmware changes. The latter study also showed how feedback simulations can be used to investigate and improve the performance with offline system optimization for existing machines (i.e. LHC ADT) or advanced system design for future machines (i.e., Future Circular Collider).

## ACKNOWLEDGEMENTS

We wish to thank W. Hofle, G. Kotzian and D. Valuch for valuable input, help and support before, during and after the MDs.

## REFERENCES

[1] K. Li *et al.* Pyheadtail on github. CERN. [Online]. Available: https://github.com/PyCOMPLETE/PyHEADTAIL/wiki/

[2] ——, "The impact of the use of alternative RF frequencies on the TMCI thresholds for HL-LHC," Jul 2018. [Online]. Available: http://cds.cern.ch/record/2633712

[3] E. Métral. Destabilising effect of the (resistive) transverse damper. CERN. [Online]. Available: https://indico.cern.ch/event/647827/

[4] J. Komppula, W. Hofle, and K. Li, "Simulation Tools for the Design and Performance Evaluation of Transverse Feedback Systems," no. CERN-ACC-2017-274, p. TUPIK091. 4 p, 2017. [Online]. Available: https://cds.cern.ch/record/2289131

[5] W. Hofle, F. Dubouchet, G. Kotzian, and D. Valuch, "Performance of the LHC Transverse Damper with Bunch Trains," no. CERN-ACC-2013-0216, p. 3 p, May 2013. [Online]. Available: https://cds.cern.ch/record/1595734

[6] J. P. O. Komppula, X. Buffat, G. Kotzian, K. S. B. Li, and D. Valuch, "MD4036: New ADT signal processing for large tune acceptance," Feb 2019. [Online]. Available: https://cds.cern.ch/record/2668389

# INTERPLAY OF TRANSVERSE DAMPER AND HEAD-TAIL INSTABILITY*

V. Smaluk†, G. Bassi, A. Blednykh, Brookhaven National Laboratory, Upton, New York, USA


### *Abstract*

Transverse head-tail instability is a major limitation for the single-bunch beam current in circular accelerators. Beam-based feedback is one of the potential tools to suppress this type of instability. The feedback systems (transverse dampers) provide active suppression of the beam oscillations by electromagnetic fields, the amplitude of which is calculated in real time from the measured beam position. The efficiency of the transverse dampers in combination with various chromaticity settings is discussed.


## HEAD-TAIL INSTABILITY

Collective instabilities of the transverse motion of particle beams in circular accelerators have been studied already since the early 1960s. Among one of the first instabilities observed and studied was likely the coherent instability caused by the beam interaction with the resistive-wall impedance of the vacuum chamber [1]. Now, this kind of instability usually affects the beams with a multi-bunch filling pattern used for the operation of most synchrotron light sources. The reason for the instability has been understood at that time, it is the bunch-to-bunch interaction via wakefields generated by the beam moving in a resistive chamber. For a coasting beam, the theoretical explanation of the instability was proposed and the stabilizing mechanisms were examined by means of the Vlasov Equation [2].

For azimuthally bunched beams, the transverse coupled-bunch instability was theoretically studied using the rigid-bunch model [3]. The modes of oscillation, stability criteria and the small-amplitude growth rates were derived by solving the eigenvalue problem. For a short single bunch, stabilization of the coherent transverse instability by Landau damping was also explored [4].

The single-bunch head-tail effect was observed in the VEPP-2 [5], ACO, and ADONE [6] electron-positron rings. The fast damping of coherent betatron oscillations, as well as the transverse head-tail instabilities, were experimentally studied with the varied beam current. As it was found, the fast damping can not be explained by resistive walls, it was caused by the beam interaction with the broad-band impedance of electrostatic $e^+/e^-$ separators.

Interaction of a bunched beam with short-range transverse wakefields characterized by the broadband impedance results in the head-tail instability. The wakefields induced by the head of a bunch act on particles of its tail; the head and tail of the bunch exchange places periodically due to synchrotron oscillations; the instability occurs if certain conditions of resonance excitation exist. The simplest two-particle model [7] assumes the bunch consisting of two macroparticles, which oscillate longitudinally with the constant amplitude.

The early studies of head-tail instability are summarized and discussed in detail in the review [8] presented at PAC-1969. The results of experimental studies of the feedback performance with varied chromaticity carried out at the ADONE ring are compared to analytical estimations. The first theoretical explanations of the head-tail effect published in [6, 7] include two-particle and multi-particle models as well as formulation and solution of an eigenvalue problem to determine the growth rates and frequency shifts of the head-tail modes.

Advanced theories were developed later using a number of approaches, such as macro-particle models, linearizing Vlasov equation, applying perturbation theory [9–14]. These comprehensive studies cover almost all aspects of the head-tail effect including mode coupling, various impedance models, chromaticity, and Landau damping. The simplified but effective mathematical model of the head-tail instability is based on the multimode analysis of the eigenvalue problem

$$\det[(\lambda - l)\,\mathbf{I} - \mathbf{M}] = 0\,, \tag{1}$$

where $\lambda = \left(\Omega - \omega_\beta\right)/\omega_s$, $\omega_\beta$ is the unperturbed betatron frequency, $\omega_s$ is the synchrotron frequency. The matrix elements are

$$M_{kk'} = I_b \frac{\beta}{2\nu_s E/e} \sum_{p=-\infty}^{\infty} Z_\perp(\omega') g_{lk}(\omega' - \omega_\xi) g_{lk'}(\omega' - \omega_\xi)\,, \tag{2}$$

where $\beta$ is the average beta function, $\omega' = p\omega_0 + \omega_\beta + l\omega_s$, $\omega_\xi = \xi\omega_0/\alpha$ is the chromatic frequency. The functions characterizing oscillation modes of the Gaussian bunch are:

$$g_{lk}(\omega) = \frac{1}{\sqrt{2\pi k!(|l|+k)!}} \left(\frac{\omega\sigma_t}{\sqrt{2}}\right)^{|l|+2k} \exp\!\left(-\frac{\omega^2\sigma_t^2}{2}\right)\,. \tag{3}$$

Solving the eigenvalue problem for specific impedance and beam parameters, one can derive the intensity-dependent shift of complex oscillation frequencies for the head-tail modes.

The simplest case is the fast head-tail instability occurring with zero chromaticity if the beam current exceeds a certain threshold determined by the coupling of two modes. In the short bunch regime ($f_r\sigma_t < 1$, where $f_r$ is the frequency of the broadband resonator representing the machine impedance and $\sigma_t$ is the bunch length), where lepton machines tend to operate, these two modes are usually the azimuthal head-tail modes 0 and 1. The exponential growth of betatron oscillation results in the loss of the beam intensity down to the threshold value. The chromatic head-tail effect

* Work supported by Department of Energy, United States of America Contract No. DE-SC0012704
† smaluk@bnl.gov

occurs if the chromaticity is not zero. In this case, there is no threshold beam intensity and some head-tail modes are unstable for any beam current. The coherent mode 0 is stable with positive chromaticity and unstable with negative chromaticity for machines operated above transition; again, this is usually the case for most lepton machines. The higher-order modes behave oppositely. The rising/damping rates decrease rapidly with the head-tail mode number, so the eigenmode analysis is quite efficient because only a few lowest modes are important.

## TRANSVERSE FEEDBACK (DAMPER)

Transverse feedback systems (dampers) were proposed to cure the beam instabilities soon after they were observed. The idea is straightforward: coherent beam oscillations are measured by a beam position monitor (capacitive pickup, stripline) and the signal with proper amplification and phase shift is used to drive a high-voltage RF amplifier connected to a stripline kicker deflecting the beam to damp the oscillations. At VEPP-2, the transverse instability has been eliminated by feedback [5], this is likely one of the first published reports on the damper suppressing the head-tail instability. A detailed description of the transverse damper developed and commissioned at SPEAR-II is published in [15] including design principles, circuit analysis, and results of beam tests. For zero chromaticity, the SPEAR-II damper helped to increase the injected beam current by a factor of 5.

The dampers to suppress coherent instabilities have been then installed at other accelerators, e.g. SPS [16] and PETRA [17], and they were efficient to suppress coherent transverse instabilities as expected. However, it was not clear if the damper able to suppress the chromatic head-tail instability, which is a combination of coherent and incoherent oscillation modes and how the chromaticity affects the damper performance. Successful application of the damper to suppress the head-tail instability was experimentally demonstrated at PETRA [18]. Now almost all electron rings are equipped by bunch-by-bunch feedbacks [19], which are available as commercial products.

The mode-coupling theory of the fast head-tail (transverse mode coupling) instability was expanded including feedback [20]. The feedback term was added to the matrix equation (1) assuming the feedback system affects the only matrix element related to the coherent mode. The resistive feedback, which damps the center-of-mass oscillation, was already successfully used at several machines to suppress multi-bunch instabilities. In the case of the intra-bunch instability, the resistive feedback was considered inadequate, because the particle motion in the bunch is complicated and damping all modes by affecting the center of mass looks unfeasible. According to [20], the reactive feedback can increase the threshold beam current up to a factor of 4 and resistive feedback is completely ineffective as a cure for this instability.

The reactive feedback systems were proposed for LEP [21, 22] and PEP [23] to cure the fast head-tail instability. However, the experimental results from PEP [24] unexpectedly demonstrated that at high gain the resistive feedback provides a larger increase of the threshold current than the reactive feedback. The reactive feedback system proposed in [22] was implemented at the LEP collider resulting in a moderate increase of the threshold current [25].

A transverse feedback system with variable phase installed at the VEPP-4M electron-positron collider allowed testing efficiency of both reactive and resistive feedback with a small positive chromaticity [26]. As it was found, the optimum feedback phase is closer to zero (resistive feedback) than to 90° (reactive feedback), however, the dependence is not very strong.

A mathematical model of the head-tail instability has been developed on the basis of the multi-mode analysis of the eigenvalue problem [27, 28], chromaticity and feedback are taken into account. Starting from the continuum model and the Vlasov equation, the analysis of beam stability with feedback is reduced to a system of algebraic equations. Analysis of symmetric modes is efficient because only the lowest modes are essential. A theory of the head-tail instability caused by electron clouds has been developed using a similar approach [29]. As concluded in [27], the resistive feedback in combination with negative chromaticity can effectively damp the instability increasing the threshold beam current by a factor of 3 to 5 with relaxed tolerances of the feedback parameters. The same conclusion is made in the recent simulation studies of the damper efficiency for the Advanced Photon Source and LHC [30]: the resistive feedback is most effective with negative chromaticity. However, as shown in [28], high positive chromaticity can suppress the head-tail instability even without feedback.

## EXPERIMENTAL RESULTS

The efficiency of the damper in combination with varied chromaticity was experimentally studied at several accelerator facilities. The results look quite contradictory. There are few experimental confirmations of the damper efficiency with negative chromaticity, theoretically predicted by the mode-coupling theory. However, other experiments show higher efficiency of the transverse feedback with positive chromaticity.

One of the first experiments was carried out at PETRA. It was noticed that for positive chromaticities close to zero the threshold currents increased by about 25% [18]. With the negative chromaticity of $-4.5$ and feedback on, the maximum bunch current was more than 6 mA, whereas it was limited to 0.3 mA without feedback [17].

The feedback performance with positive chromaticity varied up to high values was studied at ESRF [31]. The feedback gain required at low chromaticity to exceed 15 mA of the bunch current was reduced to almost zero at the increased chromaticity. For regular operations, the transverse instability limiting the single-bunch intensity is suppressed by increasing the vertical chromaticity to large positive values.

At ELETTRA [32], the dipole head-tail mode shift is quite large and increasing the chromaticity does not improve much the machine performance. A small improvement has been observed using the transverse multi-bunch feedback at positive chromaticity. With negative chromaticity and transverse feedback, the maximum stable current 50% beyond the 10 mA limit was achieved but could not be easily reproduced. Usually, the beam current saturates between 6 and 10 mA. Switching the feedback off causes the current always to drop below the threshold. Operating with negative chromaticity and transverse feedback in the single- or 4-bunch mode, the beam was very stable at all currents, unlike the operation at positive chromaticity.

On the basis of the theory [27, 28], a feedback system for suppression of transverse beam instability has been developed at the VEPP-4M electron-positron collider [33]. A special feature of this system is the simultaneous suppression of the oscillations of colliding electron and positron bunches using the same kickers and pickups. The feedback efficiency was studied experimentally with various vertical chromaticities. For the standard injection mode with the beam energy of 1845 MeV, vertical chromaticity $\xi_y = 4$, and horizontal chromaticity $\xi_x = 2$, the threshold beam current is about 5 mA. The feedback provides a reliable increase of the injected current by a factor of 3. Slowly decreasing the chromaticity leads to excitation of the instability and the beam loss down to 4.4 mA at $\xi_y = 1.4$. Increasing the chromaticity stabilizes the beam, at the vertical chromaticity $\xi_y = 6$ switching off the feedback does not cause a fast beam loss if there is no other perturbation. Further increase of positive chromaticity results in a more stable beam. With the negative vertical chromaticity $\xi_y = -8$, the injected beam current exceeding 10 mA was achieved. Switching off the feedback results in the beam loss down to 0.3-0.4 mA. So the relative increase of the beam current in comparison with the feedback off was large, however, the absolute injected beam current was lower than at the positive chromaticity.

The effect of positive chromaticity stabilizing the transverse beam instabilities was studied theoretically [34] and experimentally [35] at NSLS-II. The instability threshold was calculated and measured as a function of chromaticity. The stabilizing effect of positive chromaticity was confirmed, the single-bunch threshold current of 0.95 mA was measured at zero chromaticity, 3.2 mA at the chromaticity $\xi_x = 5, \xi_y = 5$, and 6 mA at the chromaticity $\xi_x = 7, \xi_y = 7$. No significant effect on increasing the beam current was observed varying the chromaticity below 5.

Experimental studies of the feedback efficiency with high positive chromaticity were carried out at SOLEIL [36]. Without the feedback, the single-bunch beam current is about 2 mA with the vertical chromaticity varied from 0 to 3. At the vertical chromaticity of 3, a step-like increase of the beam current up to 8 mA was observed. Further increase of the vertical chromaticity results in almost linear growth of the beam current with the chromaticity, reaching 14 mA at $\xi_y = 5$. With the feedback on, the beam current is about 8 mA at $\xi_y = 0$; 10 mA at $\xi_y = 1$; and 16 mA at $\xi_y = 3$.

Measurements of single bunch instability thresholds were done at Diamond Light Source with the chromaticity varied from -2.5 to 2.5 [37]. It was found that changing the feedback phase from resistive to reactive and intermediate was helpful to maximize the achievable beam current. There is no unique phase that works best in all chromaticity regimes. A step-like increase of the beam current with the chromaticity was also observed with and without the feedback.

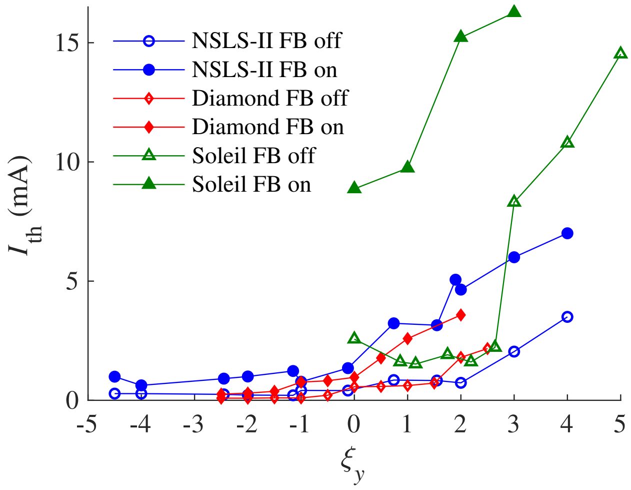


Figure 1: Measured single-bunch threshold current as a function of chromaticity, with and without feedback.

Fig. 1 shows a summary of the measured results discussed above. It looks like the threshold beam current is higher with the positive chromaticity, both with and without feedback. This is also consistent with the numerical simulation based on multi-particle tracking [33]. The bunch-by-bunch feedback systems installed at the synchrotron light sources are usually designed as narrow-band because the main purpose of these systems is to suppress the coupled-bunch instability. So the feedback acts on the center-of-mass motion only. A possible mechanism of the instability suppression discussed in [33] can result from the periodic energy exchange between the coherent and incoherent head-tail modes: the feedback is able to suppress the coherent fraction of oscillation, which always exists due to the chromatic decoherence/recoherence. Since the growth/damping rates of the head-tail modes strongly decrease with the mode number, it could be more effective to suppress the 0-th mode at positive chromaticity, when its decrement considerably exceeds the increments of higher modes. On the contrary, at negative chromaticity the higher modes are stable but the growth rate of the 0-th mode is large and much more powerful feedback is required, so the noise sensitivity is higher, which makes the beam unstable. A potential drawback of the high-chromaticity operations is a possible reduction of dynamic aperture and, therefore, the injection efficiency.

## CONCLUSION

The transverse feedback (damper) is an effective way to suppress the head-tail instability, despite it is a combination of coherent and incoherent oscillation modes. The mode-coupling theory is now the most often used tool to describe beam dynamics with impedance and feedback. The calculations can be carried out with the impedance represented by a broad-band resonator model, resistive wall, and with the results of numerical wakefield simulations. Taking bunch lengthening into account is important for electron machines with short bunches. Positive chromaticity helps to increase the instability threshold even without feedback. Feedback in combination with negative chromaticity result in a significant relative increase of the instability threshold but the absolute accumulated beam current is lower. For electron storage rings, operation with negative chromaticity does not look practical, feedback in combination with positive chromaticity is more robust. The machine nonlinearity has a significant effect too, to simulate beam dynamics with the collective effects, feedbacks, chromaticity, and nonlinearity, multi-particle tracking with momentum-dependent and amplitude-dependent effects, is necessary.

## REFERENCES

[1] C. Curtis et al., "Beam Experiments With the MURA 50 MeV FFAG Accelerator", in Proc. of HEACC-1963, Dubna, 124–156.

[2] L.J. Laslett, V.K. Neil, A.M. Sessler, "Transverse Resistive Instabilities of Intense Coasting Beams in Particle Accelerators", Review of Scientific Instruments 36, 436 (1965).

[3] E.D. Courant, A.M. Sessler, "Transverse Coherent Resistive Instabilities of Azimuthally Bunched Beams in Particle Accelerators", Review of Scientific Instruments 37, 1579 (1966).

[4] N. Dikansky, A. Skrinsky, "Transverse coherent instability of a bunch of charged particles", Atom. Energ. 21, 3 (1966) 176–179 (in Russian).

[5] V. Auslender et al., "Study of self-excitation and fast damping of coherent transverse oscillations in the VEPP-2 storage ring", Atom. Energ. 22, (1967) 198–200 (in Russian).

[6] C. Pellegrini, "On a new instability in electron-positron storage rings (The head-tail effect)", Nuovo Cimento A 64, 447–473 (1969).

[7] M. Sands, "The head-tail effect – an instability mechanism in storage rings", SLAC TN-69-008 (1969).

[8] F. Amman, "Electron positron storage rings: status and present limitations", in Proc. of PAC-1969, Washington, 1073–1081.

[9] F. Sacherer, "Methods for computing bunched-beam instabilities", CERN-SI-BR-72-5 (1972).

[10] M. Karliner, "Coherent instabilities of a beam in electron storage rings due to interaction with environment", Budker INP 74-107 (in Russian).

[11] R. Kohaupt, "Head-Tail Turbulence and the Transverse PETRA Instability", DESY-80-22 (1980).

[12] Y.H. Chin, K. Satoh, "Transverse mode coupling in a bunched beam", in Proc. of PAC-1983, Santa Fe, 2566–2568.

[13] N. Dikansky, D. Pestrikov, "The physics of intense beams and storage rings", Nauka, 1989 (in Russian); AIP Press, 1994 (in English).

[14] A. Chao, "Physics of Collective Beam Instabilities", Wiley, 1993.

[15] J.-L. Pellegrin, "Transverse oscillations damping with wideband feedback on SPEAR II", IEEE Trans. Nucl. Sci. 22, 3 (1975).

[16] R. Bossart, I. Burnod, J. Gareyte, B. de Raad, V. Rossi, "The Damper for the Transverse Instabilities of the SPS", IEEE Trans. Nucl. Sci. 26, 3 (1979) 3284–3286.

[17] K. Wille, "Damping of coherent transverse oscillations in PETRA", IEEE Trans. Nucl. Sci. 26, 3 (1979) 3281–3283.

[18] R. Kohaupt, "Single beam instabilities in PETRA", IEEE Trans. Nucl. Sci. 26, 3 (1979) 3480–3481.

[19] T. Nakamura, "Transverse and Longitudinal Bunch-By-Bunch Feedback for Storage Rings", in Proc. of IPAC-2018, Vancouver, TUZGBD2.

[20] R. Ruth, "Transverse Mode Coupling With Feedback", in Proc. of HEACC-1983, Conf. Proc. C 830811 (1984) 389–392.

[21] S. Myers, "A First Look At The Requirements For Transverse Feedback For The LEP Main Ring", CERN LEP Note 436 (1983).

[22] V.V. Danilov, E.A. Perevedentsev, "Feedback system for elimination of the transverse mode coupling instability", CERN-SL-93-38-AP (1993).

[23] S. Myers, "Effect of Reactive Feedback on the Transverse Mode Coupling Instability", SLAC:AP-30 (1984).

[24] S. Myers, "Stabilization of the Fast Head-Tail Instability by Feedback", in Proc. of PAC-1987, Washington, 503–507.

[25] S. Myers, "Conclusions of the Fifth LEP Performance Workshop", CERN SL-95-10-DI (1995).

[26] M. Karliner, V. Kiselev, A. Medvedko, V. Smaluk, A. Zelenin, N. Zinevich, "The Feedback System for Elimination the Fast Head-tail Instability at Storage Ring VEPP-4M", in Proc. of EPAC-1996, Barcelona, WEP010G.

[27] M. Karliner, "Theory of a Feedback to Cure Transverse Mode Coupling Instability", Budker INP 2001-37.

[28] M. Karliner, K. Popov, "Theory of a Feedback to Cure Transverse Mode Coupling Instability", Nucl. Instr. and Meth. A 537 (2005) 481–500.

[29] K. Ohmi, F. Zimmermann, E. Perevedentsev, "Wake-field and fast head-tail instability caused by an electron cloud", Phys. Rev. E 65, 016502 (2002).

[30] A. Burov, "Efficiency of feedbacks for suppression of transverse instabilities of bunched beams", Phys. Rev. Accel. Beams 19, 084402 (2016).

[31] J. Jacob et al., "Experimental and Theoretical Studies of Transverse Single Bunch Instabilities at the ESRF", in Proc. of EPAC-1998, Stockholm, THP05G.

[32] E. Karantzoulis, M. Lonza, "Transverse Head-tail Modes Elimination With Negative Chromaticity and the Transverse Multi-bunch Feedback System at ELETTRA", in Proc. of EPAC 2006, Edinburgh, THPCH045.

[33] V. Smaluk, D. Sukhanov, V. Oreshonok, V. Cherepanov, V. Kiselev, "Feedback for suppression of single-bunch transverse instability in electron-positron storage rings", J INSTRUM 7 (2012) P01007.

[34] S. Krinsky et al., “Collective Effects in the NSLS-II Storage Ring", in Proc. of PAC-2007, Albuquerque, TUPMS074.

[35] A. Blednykh et al., “First Collective Effects Measurements in NSLS-II With ID’s," in Proc. of IPAC-2015, Richmond, TUAB2.

[36] R. Nagaoka, “Collective Effects at SOLEIL", TWIICE-II, Abingdon, 2016.

[37] E. Koukovini-Platia, A.F.D. Morgan, G. Rehm, R. Bartolini, “Study of Single Bunch Instabilities With Transverse Feedback at Diamond", in Proc. of IPAC-2017, Copenhagen, THPVA029.

# DESTABILISING EFFECT OF RESISTIVE TRANSVERSE DAMPERS

E. Métral†, Geneva, Switzerland

*Abstract*

A resistive transverse damper is needed for multi-bunch operation in a machine like the CERN LHC and it is very efficient as it considerably reduces the necessary amount of nonlinearities (from octupoles) needed to reach beam stability through Landau damping. However, a resistive transverse damper also destabilizes the single-bunch motion below the Transverse Mode Coupling Instability (TMCI) intensity threshold (for zero chromaticity), introducing a new kind of instability, which has been called "ISR instability" (for Imaginary tune Split and Repulsion). The purpose of this contribution is to explain in detail this new instability mechanism and its mitigation.

## INTRODUCTION

A Transverse Damper (TD) generates the following complex tune shift (with $j$ the imaginary unit)

$$\Delta Q_{TD} = \frac{e^{j\phi}}{2\pi d} \ , \tag{1}$$

where $\phi$ is the betatron phase advance between the pick-up and the kicker, and $d$ is the TD damping time in machine turns (equal to $2/G$ with $G$ the gain of the TD). If $\phi = 90°$, the TD is called "resistive": it is a conventional damper/feedback system, which damps the centre-of-charge motion of the beam (see Fig. 1). If $\phi = 0°$, the TD is called "reactive": in this case, mode 0 is shifted (which can raise the intensity threshold in the presence of TMCI between modes 0 and -1).

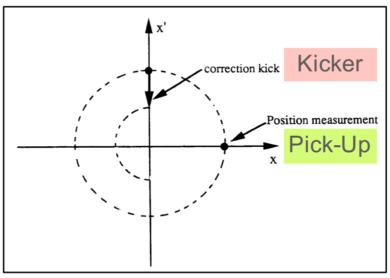


Figure 1: Schematic picture (in the horizontal phase space) of the action of a conventional TD, which damps the centre-of-charge motion of the beam.

A resistive TD is needed for multi-bunch operation in a machine like the LHC and it has been working very well over the past decade [1]. If we take the example of the LHC predictions in 2018 at 6.5 TeV, the beneficial effect of the TD on the amount of Landau octupole current needed to stabilise the beam is clearly visible (see Fig. 2).

† Elias.Metral@cern.ch

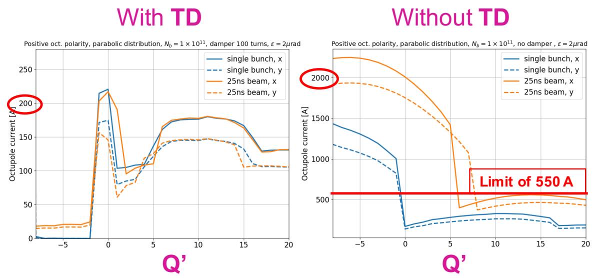


Figure 2: Required octupole current to reach beam stability, with (left) and without (right) a resistive TD, vs. chromaticity Q'. Courtesy of N. Mounet (using DELPHI Vlasov solver [2]).

A better control of the LHC has been achieved year after year, and at the end of Run 2 (2018), the following mitigation knobs were used at 6.5 TeV: Q' ~ +15; TD damping time of ~ 50-100 turns; Landau octupole current a factor ~ 2 higher than predicted (compared to the factor ~ 5 at the end of Run 1) [3]. The main lesson learned from Run 1 and Run 2 is that in a machine like the LHC, not only all the mechanisms have to be understood separately, but (all) the possible interplays between the different phenomena need to be analysed in detail [4]: the TD needs to be included in beam stability analyses (along with beam-beam); the sign of the Landau octupole has to be studied in detail together with beam-beam effects (considering both long-range and head-on effects); there is a destabilising effect of e-cloud; there is a destabilising effect of linear coupling; there is a destabilising effect of noise, which is currently under study and was demonstrated in 2018 for the first time in a machine as a possible contributor to the remaining missing factor ~ 2 in Landau octupole current; there is a destabilising effect of TD, which is the subject of this paper [5].

Several simulations performed with different (Vlasov solver and tracking) codes, considering a single bunch with zero chromaticity, revealed already in the past a more critical situation (as concerns the instability growth-rate or the required octupole current) with TD than without [2,6-10]. However, no model/explanation describing the cause/mechanism of this instability was given in any of these references (in Ref. [6] it is referred to as "a sort of TMCI"). It is worth mentioning also Ref. [11], which has been put to the attention of the author during this workshop, where a head-tail mode instability caused by a feedback is discussed. This should be reviewed in detail in the future and compared to the results presented in this manuscript.

## MOTIVATION

Three questions motivated this study for the LHC in terms of beam stability: (1) why a chromaticity close to zero seemed to require a higher octupole current than predicted during Run 1 (in 2011 and 2012) and during Run 2 (in 2015)? [12]; (2) why some past simulations with a chromaticity close to zero revealed an instability with the TD, which is absent without TD? [2,6-10]; and (3) what should be the minimum operational chromaticity in the future in the LHC and High-Luminosity LHC? To try and shed some light on these questions, a new Vlasov solver (called GALACTIC) was developed [5,13]. Thanks to it, it is possible to answer to the following two questions: (1) what is the exact predicted instability mechanism at low chromaticity in the presence of a resistive TD? (2) Is a stability diagram, which assumes independent head-tail modes, a sufficiently accurate method for computing the effect of Landau damping in this case?

## VLASOV SOLVERS GALACTIC AND GALACLIC

Starting from the Vlasov equation and using a basis of the low-intensity eigenvectors of the problem, as proposed by Laclare and Garnier [14,15], the effect of a TD was added and a new Vlasov solver code was developed, called GALACTIC (for GArnier-LAclare Coherent Transverse Instabilities Code) [5,13]. Note that a similar approach can be used in the longitudinal plane (leading to GALACLIC, for GArnier-LAclare Coherent Longitudinal Instabilities Code), which helped to understand the details of mode coupling behind some longitudinal microwave instabilities [13,16].

Predictions of transverse and longitudinal mode coupling instabilities from GALACTIC and GALACLIC can be found in Fig. 3 for the case of a single proton bunch above transition interacting with a broad-band ($Q = 1$) resonator impedance with a resonance frequency equal to 2.8 divided by the full ($4\,\sigma$) bunch length $\tau_b$ (in $s$). The predictions from Laclare (only real parts) [14] are shown in black, revealing a very good agreement for both transverse and longitudinal planes. The model of Potential-Well Distortion (PWD) used here does not take into account the real part of the longitudinal impedance and

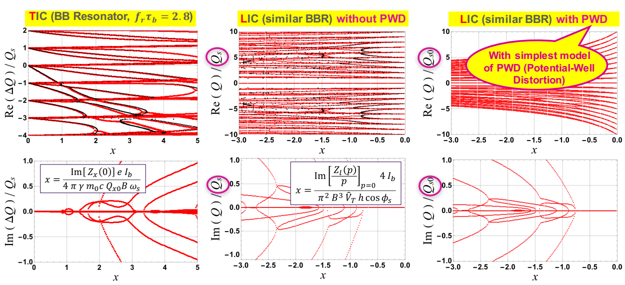


Figure 3: Usual TMCI plots vs. the normalised bunch intensity $x$ (with $Q_s$ the synchrotron tune), comparing GALACTIC and GALACLIC with Laclare's approach in black (only real parts) [14], for the case of a single proton bunch above transition interacting with a broad-band ($Q = 1$) resonator impedance with a resonance frequency equal to 2.8 divided by the full ($4\,\sigma$) bunch length.

therefore the associated asymmetry in the longitudinal bunch profile (linked to the shift of the synchronous phase) is neglected, as it is assumed to be small for the case under study.

A detailed comparison between GALACTIC and GALACLIC with simulation tracking codes has also been performed, revealing an excellent agreement as can be observed in Figs. 4 and 5. An even better agreement could be reached in longitudinal by implementing a more realistic PWD model, which will be done in the future.

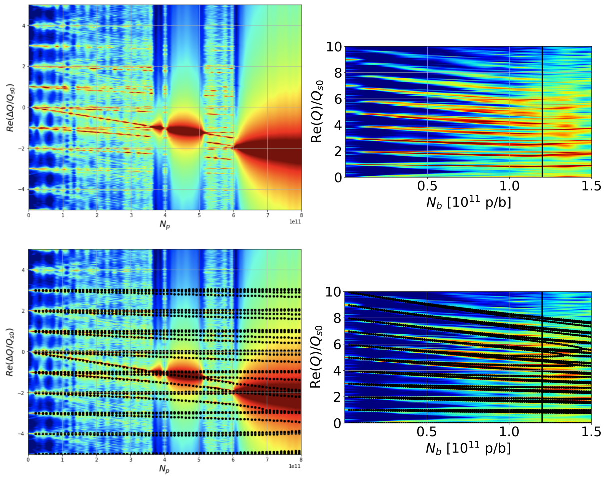

Figure 4: (Left) comparison between pyHEADTAIL [17] macroparticle tracking code (top) and GALACTIC (black dots, bottom) and (right) comparison between SBSC [18] macroparticle tracking code (top) and GALACLIC (black dots, bottom), for the case of a single proton bunch above transition interacting with a broad-band ($Q = 1$) resonator impedance with a resonance frequency equal to 2.7 divided by the full ($4\,\sigma$) bunch length. Courtesy of M. Migliorati for the PyHEADTAIL and SBSC tracking simulations (with a new mode analysis) [16].

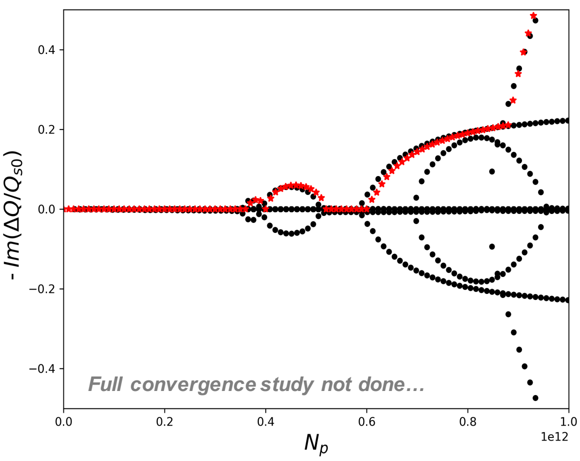


Figure 5: Comparison between pyHEADTAIL [17] macroparticle tracking code (red dots) and GALACTIC (black dots) for the case of a single proton bunch interacting with a broad-band ($Q = 1$) resonator impedance with a resonance frequency equal to 2.7 divided by the full ($4\,\sigma$) bunch length. Courtesy of M. Migliorati for the PyHEADTAIL tracking simulations.

## INSTABILITY MECHANISM WITH Q' = 0

It is important to distinguish between the long bunch and short bunch regimes as the impact of a TD is very different for the two regimes. In the long bunch regime (see Fig. 6), the main mode coupling takes place between high-order modes and the TD will not be able to modify it whatever its phase. This is not the case for the short bunch regime (see Fig. 7), for which the mode coupling takes place between the modes 0 and -1. In this case, a reactive TD is beneficial as it increases the TMCI intensity threshold, modifying the shift of mode 0 and pushing the mode-coupling towards higher bunch intensities (see Fig. 7 left). A resistive TD, on the other hand, is detrimental as it decreases the intensity threshold (see Fig. 7 right). The exact mechanism [5] will be reviewed below.

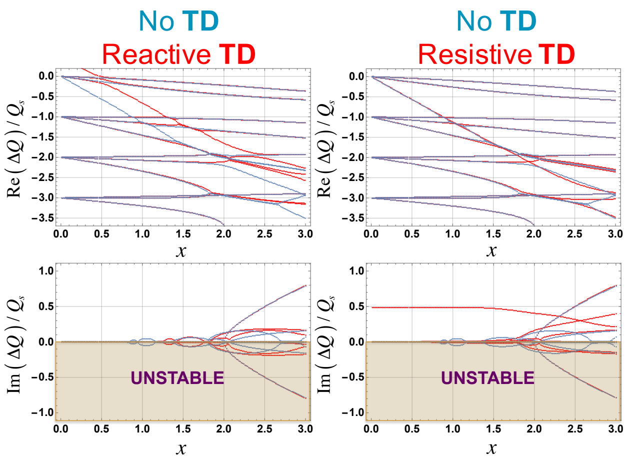


Figure 6: Usual TMCI plots from GALACTIC for the case of the long bunch regime ($f_r \, \tau_b = 2.8$), which approximately describe the CERN SPS case, assuming a TD with a damping time $d = 100$ turns.

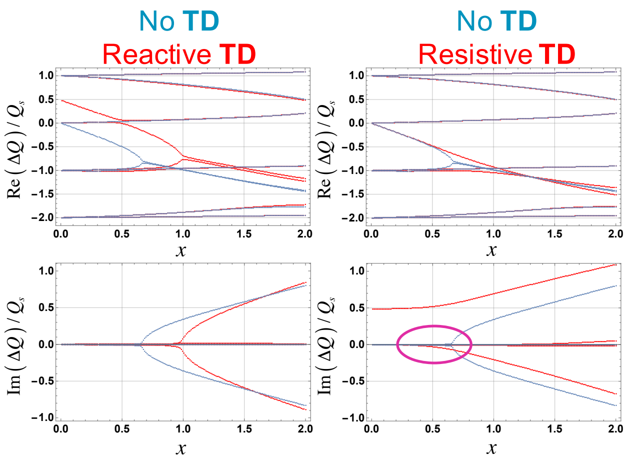


Figure 7: Usual TMCI plots from GALACTIC for the case of the short bunch regime ($f_r \, \tau_b = 0.8$), which approximately describe the CERN LHC case, assuming a TD with a damping time $d = 100$ turns.

The matrix which needs to be diagonalised in GALACTIC can be reasonably well approximated (for the purpose of the current study) by this 2×2 matrix (taking into account only the modes 0 and -1),

$$\begin{pmatrix} -1 & -0.23\, j\, x \\ -0.55\, j\, x & -0.92\, x + 0.48\, j \end{pmatrix}, \tag{2}$$

where the term "+0.48 $j$" is the contribution from the "+" resistive TD with a damping time $d = 100$ turns (it would be "+0.48" for a "+" reactive TD and its general form is given by $\Delta Q_{TD}/Q_s$). The mode -1 is described by the top-left term while the mode 0 is described by the bottom-right one (the mode coupling terms being the off-diagonal ones). Figure 8 depicts the evolution of the eigenvalues for both cases with and without the TD and it can be observed that similar results as in Fig. 7 right are obtained. It is found indeed that introducing a resistive TD lowers the intensity threshold. In fact, it completely changes the nature of the instability as no intensity threshold is observed anymore (as already spotted in Ref. [6]): the bunch is unstable whatever the intensity. Without TD, an instability appears as a consequence of the coupling between two modes (0 and -1). In the presence of the resistive TD, the mode coupling is suppressed but the interaction between the modes 0 and -1 in the presence of the TD pushes apart the imaginary parts and as the imaginary part of the mode -1 is 0, it becomes negative and leads to an instability.

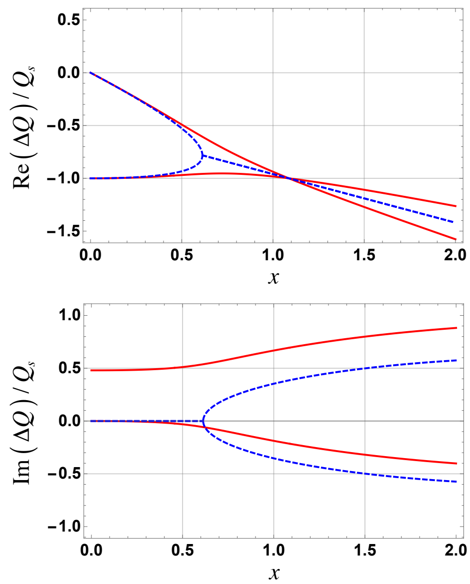


Figure 8: Solutions of the diagonalisation of the 2×2 matrix of Eq. (2): without (blue) and with (red) the resistive TD.

The fact that the TD term in Eq. (2) is given by $\Delta Q_{TD}/Q_s$ explains why a TD is not very effective for machines with a large synchrotron tune $Q_s$. Indeed, assuming for instance $Q_s = 0.1$, a resistive TD with a damping time $d = 50$ turns would almost not modify the TMCI picture, as can be seen in Fig. 9.

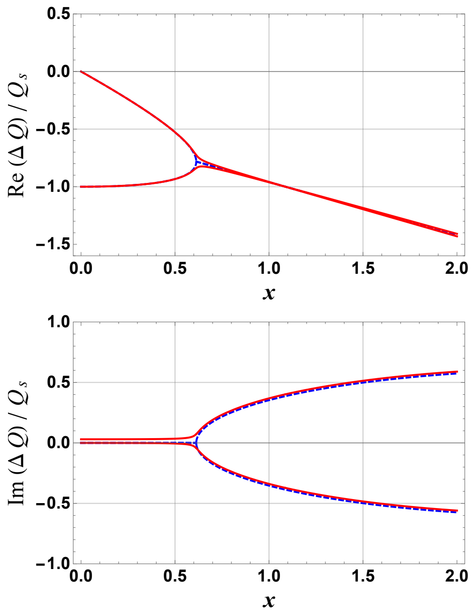


Figure 9: Solutions of the diagonalisation of the 2×2 matrix of Eq. (2): without (blue) and with (red) the resistive TD, assuming $Q_s = 0.1$ and $d = 50$ turns.

## IMPACT ON LANDAU DAMPING

As the instability mechanism involves the two modes 0 and -1, the impact on Landau damping has to be studied by considering both modes and Eq. (3) needs to be solved

$$\begin{vmatrix} I_{m=-1}^{-1} & -0.23\,j\,x \\ -0.55\,j\,x & I_{m=0}^{-1} + 0.92\,x - 0.48\,j \end{vmatrix} = 0\,, \tag{3}$$

where $I_m$ is the dispersion integral. I have solved Eq. (3) assuming an externally given elliptical tune spread, which leads to the “circle stability diagram” for the one-mode approach. In this case, the dispersion integral is given by [19] (with $y$ the unknown we are looking for)

$$I_m = \frac{2}{y - m - j\sqrt{\Delta q^2 - (y-m)^2}}\,, \tag{4}$$

where $\Delta q$ is the tune spread (half width at the bottom of the distribution) normalised by the synchrotron tune. The solution of Eq. (3), characterizing the two-mode approach, is compared to the one-mode approach in Fig. 10: it can be seen that below the TMCI intensity threshold (without TD), the one-mode approach (usual stability diagram) seems fine, whereas above the TMCI intensity threshold (without TD), the two-mode approach is needed and more tune spread is required. As the LHC has been operated until now below the TMCI intensity threshold (without TD), the one-mode approach used until now seems fully justified, which was also in agreement with some first tracking results [20]. It can also be concluded from Fig. 10 that a resistive TD has a detrimental effect below and a beneficial effect above the TMCI intensity threshold, as much less octupole current is needed for the latter case to reach beam stability through Landau damping than without a TD.

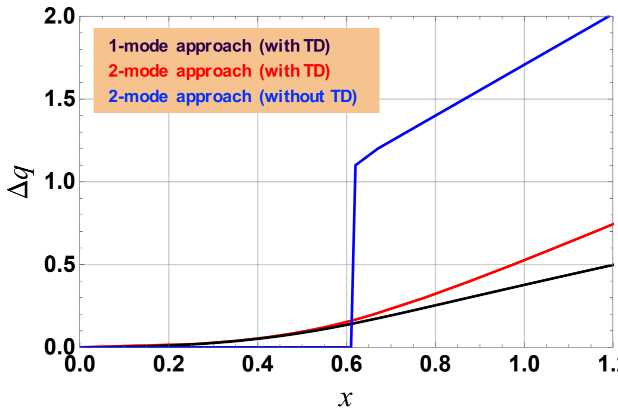


Figure 10: Required tune spread (normalised by $Q_s$) to reach bunch stability vs. the normalised bunch intensity: using the one-mode approach, leading to the usual stability diagram (black line) and the two-mode approach from Eq. (3) (red line) assuming an elliptical tune spread. The blue line corresponds to the case without TD but considering the mode coupling between modes 0 and -1.

## COMPARISON WITH PYHEADTAIL

The previous analytical description has been checked in detail through pyHEADTAIL macroparticle tracking simulations, revealing that most of the physics was captured by the simplified model (see Fig. 11).

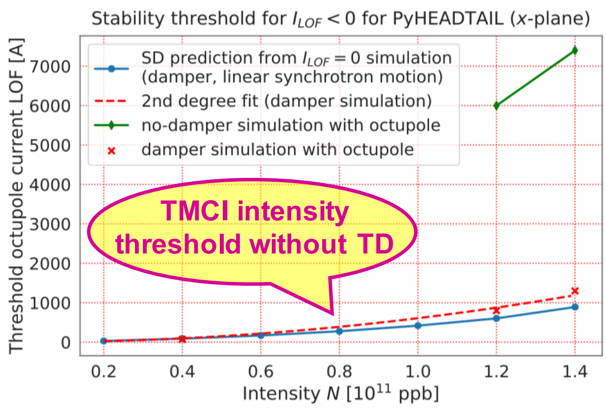


Figure 11: Case of Fig. 10 re-analysed in detail through pyHEADTAIL tracking simulations, revealing a good agreement between the two approaches. Courtesy of A. Oeftiger [21].

## DESTABILISING EFFECT OF LANDAU DAMPING FOR TMCI

In the framework of this study, it is worth mentioning that below the TMCI intensity threshold without TD, the tune spread provided by Landau octupoles (to generate some Landau damping) is also detrimental if it is not high enough (of the order of the synchrotron tune) but already quite important. This destabilising effect was already revealed a long time ago in Ref. [22]. It has been revisited with the simplified model of Eq. (3) in the absence of TD [23], confirming the results from Ref. [22] (see Fig. 12).

(a)

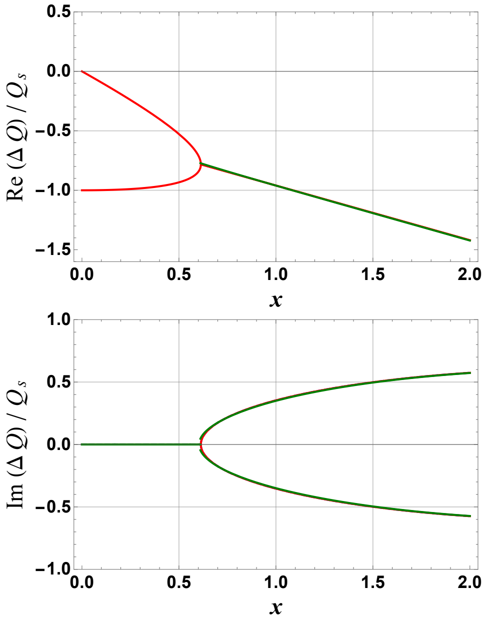


(b)

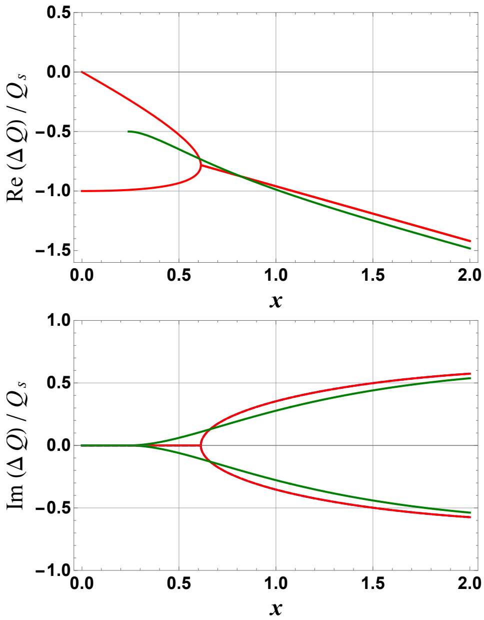


(c)

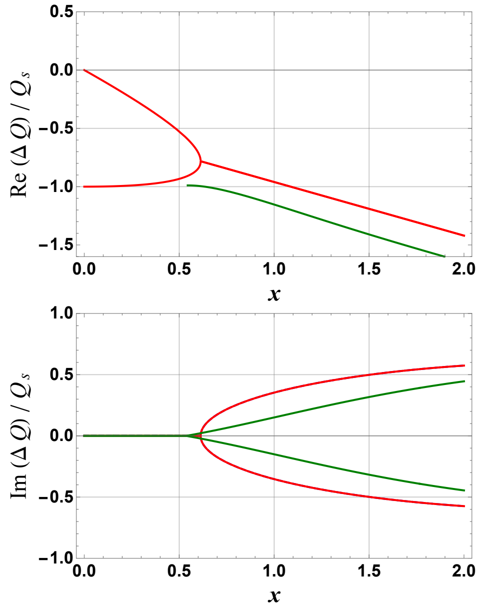


(d)

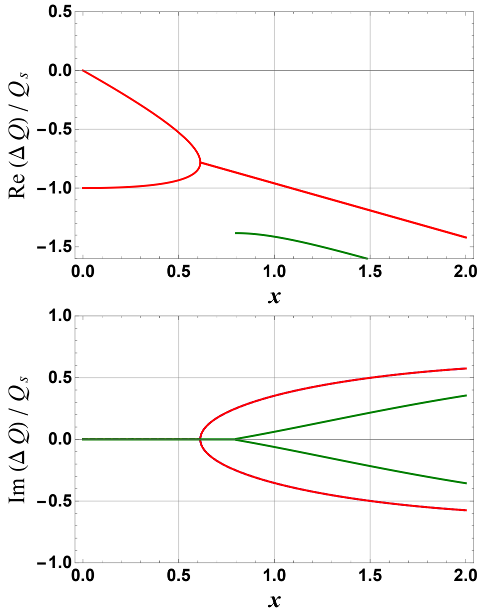


Figure 12: Solutions of the diagonalisation of the 2×2 matrix of Eq. (2) in the absence of TD: without (red) and with (green) tune spread: (a) $\Delta q = 0.1$, (b) $\Delta q = 0.5$, (c) $\Delta q = 1.0$, (d) $\Delta q = 1.4$.

## CONCLUSION

A new single-bunch instability mechanism is revealed for zero chromaticity in the presence of a resistive transverse damper. The explanation provided in this paper (and already documented in Ref. [5]) was confirmed by two other Vlasov solvers, DELPHI (using a Gaussian distribution) [24] and NHTVS (using either a Gaussian or air-bag distribution) [25], which could reproduce Figs. 7 and 8.

The detailed instability mechanism could not be identified with PyHEADTAIL macroparticle tracking simulations only. However, the impact on Landau damping could be analysed in detail with PyHEADTAIL [21], confirming the detrimental effect of resistive transverse dampers below the TMCI intensity threshold and the beneficial effect of resistive transverse dampers above the TMCI intensity threshold (see Figs. 10 and 11).

## REFERENCES


[1] D. Valuch *et al.*, "The LHC transverse damper: a multi-purpose system", these proceedings.

[2] N. Mounet, "DELPHI: an analytic Vlasov solver for impedance-driven modes", CERN HSC meeting, Geneva, Switzerland, 07/05/2014, https://espace.cern.ch/be-dep-workspace/abp/HSC/Meetings/DELPHI-expanded_Part2.pdf

[3] X. Buffat *et al.*, "Transverse instabilities", in *Proc. 9th LHC Operations Evian Workshop*, Evian, France, 30/01-01/02 2019.

[4] E. Métral, "Measurement and interpretation of transverse beam instabilities in the CERN Large Hadron Collider (LHC) and extrapolations to HL-LHC", in *Proc. HB2016*, Malmö, Sweden, July 03-08, 2016.

[5] E. Métral *et al.*, "Destabilising effect of the LHC transverse damper", in *Proc. 9th Int. Particle Accelerator Conf. (IPAC'18)*, Vancouver, BC, Canada, Apr.-May 2018, pp. 3076-3079. doi:10.18429/JACoW-IPAC2018-THPAF048

[6] M. Karliner and K. Popov, "Theory of a feedback to cure transverse mode coupling instability", *Nucl. Instr. Meth. A*, vol. 537, pp. 481-500, 2005.

[7] A. Burov, "Nested head-tail Vlasov solver", *Phys. Rev. ST Accel. Beams* 17, 021007 (2014).

[8] S. White, X. Buffat, N. Mounet, and T. Pieloni, "Transverse mode coupling instability of colliding beams", *Phys. Rev. ST Accel. Beams* 17, 041002 (2014).

[9] N. Biancacci, D. Amorim, L.R. Carver, E. Métral, and B. Salvant, "Study of TMCI in the LHC", CERN HSC meeting, Geneva, Switzerland, 30/05/2016, https://espace.cern.ch/be-dep-workspace/abp/HSC/Meetings/HSC_TMCI-LHC_30052016.pdf

[10] K. Li, "TMCI in presence of damper with PyHEADTAIL – a status report", CERN HSC meeting, Geneva, Switzerland, 27/03/2017, https://indico.cern.ch/event/625631/contributions/2526516/attachments/1434095/2204443/01_draft.pdf

[11] J. Scott Berg, "Head-tail mode instability caused by feedback", in *Proc. 6th European Particle Accelerator Conference (EPAC'98)*, Stockholm, Sweden, 22 - 26 Jun 1998.

[12] L.R. Carver *et al.*, "Current status of instability threshold measurements in the LHC at 6.5 TeV", in *Proc. IPAC2016*, Busan, Korea, May 2016, paper TUPMW011, pp. 1434-1437.

[13] E. Métral, "GALACTIC and GALACLIC: two Vlasov solvers for the transverse and longitudinal planes", in *Proc. 10th Int. Particle Accelerator Conf. IPAC2019*, Melbourne, Australia, 19-24 May 2019, pp. 312-315. doi:10.18429/JACoW-IPAC2019-MOPGW087

[14] J.L. Laclare, "Bunched beam coherent instabilities", in *Proc. CAS - CERN Accelerator School: Accelerator Physics*, Oxford, UK, 16 - 27 September 1985, pp. 264-326 (CERN-1987-003-V-1).

[15] J.P. Garnier, "Instabilités cohérentes dans les accélérateurs circulaires", Ph.D. thesis, Grenoble, France, 1987.

[16] E. Métral and M. Migliorati, "Longitudinal Mode-Coupling Instability: GALACLIC Vlasov solver vs. macroparticle tracking simulations", in *Proc. 10th Int. Particle Accelerator Conf. IPAC2019*, Melbourne, Australia, 19-24 May 2019, pp. 320-323. doi:10.18429/JACoW-IPAC2019-MOPGW089

[17] K. Li, "Headtail code," 2015. https://indico.cern.ch/event/378615/, [Online; accessed 16.05.2019].

[18] M. Migliorati *et al.*, "Beam-wall interaction in the CERN Proton Synchrotron for the LHC upgrade", *Phys. Rev. ST Accel. Beams*, vol. 16, p. 031001, March 2013. `doi: 10.1103/PhysRevSTAB.16.031001`

[19] E. Métral, "Theory of coupled Landau damping", *Particle Accelerators*, Vol. 62, pp. 259-276 (1998).

[20] X. Buffat, "Few simulations of octupole thresholds with damper and quadrupolar wakes", CERN HSC meeting, Geneva, Switzerland, 15/01/2018, https://indico.cern.ch/event/689096/contributions/2829430/attachments/1582359/2501215/2018-01-15_TMCI-expanded.pdf

[21] A. Oeftiger, "Stability around $Q' = 0$ and the LHC damper instability", 146th HiLumi WP2 Meeting, CERN, Geneva, Switzerland, 16/04/2019 (https://indico.cern.ch/event/804350/contributions/3394378/attachments/1830532/2997717/oeftiger_damper_instability.pdf).

[22] Y.H. Chin, "Hamiltonian formulation for transverse bunched beam instabilities in the presence of betatron tune spread", CERN SPS/85-9 (DI-MST), CERN, Geneva, Switzerland, 28/05/1985.

[23] E. Métral, "Landau Damping for TMCI: with vs. without Transverse Damper", CERN-ACC-NOTE-2019-0018, CERN, Geneva, Switzerland, 16/05/2019.

[24] D. Amorim, S. Antipov, N. Biancacci, E. Métral, and B. Salvant, "Study of the destabilising effet of the resistive transverse damper with DELPHI", CERN HSC meeting, Geneva, Switzerland, 27/03/2017, https://indico.cern.ch/event/625631/contributions/2526504/attachments/1434084/2204416/2017-03-27_DELPHI_results_split_modes.pdf

[25] S. Antipov, N. Biancacci, and D. Amorim, "Study of the destabilising effect of the resistive transverse damper with NHTVS", CERN HSC meeting, Geneva, Switzerland, 27/03/2017, https://indico.cern.ch/event/625631/contributions/2526515/attachments/1434080/2204404/TMCI_27.03.17.pdf

# FEEDBACK DESIGN FOR CONTROL OF THE MICRO-BUNCHING INSTABILITY BASED ON REINFORCEMENT LEARNING

T. Boltz*, M. Brosi, E. Bründermann, B. Haerer, P. Kaiser, C. Pohl, P. Schreiber, M. Yan, T. Asfour, A.-S. Müller
Karlsruhe Institute of Technology, Karlsruhe, Germany

This contribution is largely based on [1].

*Abstract*

The operation of ring-based synchrotron light sources with short electron bunches increases the emission of coherent synchrotron radiation in the THz frequency range. However, the micro-bunching instability resulting from self-interaction of the bunch with its own radiation field limits stable operation with constant intensity of CSR emission to a particular threshold current. Above this threshold, the longitudinal charge distribution and thus the emitted radiation vary rapidly and continuously. Therefore, a fast and adaptive feedback system is the appropriate approach to stabilize the dynamics and to overcome the limitations given by the instability. In this contribution, we discuss first efforts towards a longitudinal feedback design that acts on the RF system of the KIT storage ring KARA (Karlsruhe Research Accelerator) and aims for stabilization of the emitted THz radiation. Our approach is based on methods of adaptive control that were developed in the field of reinforcement learning and have seen great success in other fields of research over the past decade. We motivate this particular approach and comment on different aspects of its implementation.

## MICRO-BUNCHING INSTABILITY

Modern ring-based synchrotron light sources commonly offer a dedicated short-bunch operation mode in which the bunch length is compressed in order to support dedicated experiments. At the KIT storage ring KARA (Karlsruhe Research Accelerator), this enables the reduction of the bunch length down to several picoseconds. While the high degree of longitudinal compression leads to an increased emission of coherent synchrotron radiation (CSR) in the THz frequency range, it also causes a strong self-interaction of the electron bunches with their own emitted CSR. Above a given threshold current, that depends on several machine parameters [2], this CSR self-interaction causes the formation of dynamically changing micro-structures in the longitudinal charge distribution and hence fluctuating CSR emission. The phenomenon is thus referred to as micro-bunching or microwave instability. The effect of the CSR self-interaction on the longitudinal beam dynamics is conveniently described by the CSR wake potential

$$V_{\mathrm{CSR}}(q,t) = \int_{-\infty}^{\infty} \widetilde{\rho}(\omega,t) Z_{\mathrm{CSR}}(\omega) e^{i\omega q} \mathrm{d}\omega \,, \qquad (1)$$

* tobias.boltz@kit.edu

where $q = (z - z_s)/\sigma_{z,0}$ denotes the generalized longitudinal position, $\widetilde{\rho}(\omega)$ the Fourier-transformed longitudinal bunch profile and $Z_{\mathrm{CSR}}(\omega)$ the CSR-induced impedance of the storage ring. As an additional contribution to the effective potential the bunch is exposed to, besides the accelerating RF potential, this acts as a dynamic perturbation to the temporal evolution of the longitudinal charge distribution. The entire process can be simulated using the KIT-developed Vlasov-Fokker-Planck (VFP) solver Inovesa [3] , which has shown great qualitative agreement with measurements at KARA [4]. Figure 1 illustrates the micro-bunching dynamics in the longitudinal phase space (left) and the corresponding fluctuations of the emitted CSR power (right) simulated with Inovesa.

Depending on the application at hand, the occurrence of micro-structures can also be quite desirable as it increases the radiated power at frequencies corresponding to the size of the present structures. Thus, in order to tailor the CSR emission to each application individually, this contribution is concerned with the development of a longitudinal feedback that establishes extensive control over the micro-bunching dynamics and thereby enables, both, excitation and mitigation of the occurring micro-structures.

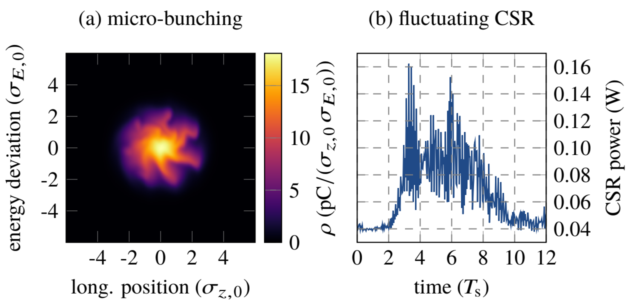


Figure 1: (a) The CSR self-interaction of the bunch causes the formation of micro-structures in the longitudinal charge distribution. (b) Their dynamic evolution leads to fluctuations in the emitted CSR power ($T_s$ denoting the synchrotron period).

## APPROACH TO CONTROL

As briefly discussed in [5], we find that the instability is largely driven by the CSR wake potential's perturbation of the restoring force provided by the RF system. Particularly, the slope of the effective potential at the synchronous position is modified considerably during the micro-bunching dynamics. To exert control, we thus aim to recover the strength of the restoring force in order to compensate a major part of the perturbation caused by the CSR wake potential. As the perturbation is, according to Eq. (1), dependent on the bunch profile and therefore on the evolution of the charge distribution, the compensation mechanism has to dynamically adjust to this as well. As an empirically effective and feasible approach we therefore aim for an RF amplitude modulation scheme

$$V_{\mathrm{RF}}(t) = \hat{V}(t)\sin(2\pi f_{\mathrm{RF}}\, t)\,, \tag{2}$$

$$\hat{V}(t) = \hat{V}_0 + A_{\mathrm{mod}}(t)\sin(2\pi f_{\mathrm{mod}}(t)\, t + \varphi_{\mathrm{mod}})\,, \tag{3}$$

in which the modulation amplitude $A_{\mathrm{mod}}(t)$ and frequency $f_{\mathrm{mod}}(t)$ are rapidly adjusted. This yields a sequential decision problem in which we would like to determine the ideal choice of $A_{\mathrm{mod}}(t_i)$ and $f_{\mathrm{mod}}(t_i)$ at every time step $t_i$. Given that the micro-bunching dynamics occur at time scales comparable to the synchrotron period, the step width $\Delta t$ of the sequence should be chosen in the same order of magnitude. As a promising approach to solve this task, the following section briefly introduces the basic concept of reinforcement learning. A more detailed introduction can be found in [6].

## REINFORCEMENT LEARNING

Reinforcement learning (RL) is an active sub-field of machine learning which led to spectacular results in recent applications, see e.g. [7, 8]. It differs from other forms of machine learning in that its learning paradigm does not require a pre-existing data set. Instead learning takes place in an iterative process based on the general concept of trial-and-error search. The learner or decision maker, usually called the *agent*, continuously interacts with an *environment* while seeking to improve its behavior. At each iteration the agent perceives the current *state* $S_t$ of the environment and is faced with the task to choose an *action* $A_t$. Based on the chosen action, the environment yields a scalar *reward* $R_t$ and transitions to the next state $S_{t+1}$. Thereby, the agent's objective is defined as maximizing the cumulative reward received over time.

Formally, the reinforcement learning problem is described as a Markov decision process (MDP). In its most rigorous form, the MDP demands a perfect fulfillment of the Markov property, which puts a specific restriction on the sequence of states: The probability of transitioning to state $S_{t+1}$ may only depend on the previous state $S_t$ and not on any other state visited in the past $(S_1, \ldots, S_{t-1})$. If this condition is satisfied, it guarantees that the agent is provided with the necessary information to choose the optimal action in every encountered state. While this rigorous formalism is very useful for modeling a wide range of problems and allows precise theoretical statements, the Markov property can sometimes be difficult to fulfill in practical applications.

## FEEDBACK DESIGN

For the sequential decision problem denoted in Eq. (3) the definition of a Markovian process is straightforward. In order to simulate the longitudinal beam dynamics VFP solvers require an initial charge distribution in the longitudinal phase space and a set of constant parameters. Subsequently, the temporal evolution of this distribution is calculated in an iterative manner. At each step, the calculation is entirely based on the preceding distribution. Hence, choosing the charge distributions $\psi_t(z, E)$ as the state signal

$$S_t \doteq \psi_t(z, E) \tag{4}$$

yields a Markov process, fully satisfying the Markov property introduced in the previous section.

As mentioned above, we are primarily interested in tailoring the emission of CSR to individual applications. We thus define the reward function based on the observed CSR signal

$$R_t \doteq R_t(P_{t,\mathrm{CSR}})\,. \tag{5}$$

In case of trying to mitigate the instability, the damping of the micro-structures in phase space corresponds to a stabilization of the emitted CSR power as it removes the fluctuation caused by the micro-bunching dynamics. One way to express this objective in a scalar reward function is

$$R_t \doteq w_1\mu_{t':t} - w_2\sigma_{t':t}\,, \tag{6}$$

where $\mu_{t':t}$ and $\sigma_{t':t}$ denote the mean and standard deviation of the time series $P_{t,\mathrm{CSR}}$ in the interval $[t', t]$, and $w_{1,2} > 0$ are simple weighting factors. As a complementary approach, trying to deliberately excite the micro-structures to increase the emission of CSR in the desired frequency range $[f_1, f_2]$, the reward function may simply be defined as the emitted power in this bandwidth

$$R'_t \doteq \mu_{t':t}(f_1, f_2)\,. \tag{7}$$

Finally, the formal definition of the action space corresponding to Eq. (3) is chosen as

$$A_t \in \{A_{\mathrm{mod}}(t) \times f_{\mathrm{mod}}(t)\}\,. \tag{8}$$

Combining the above stated definitions of $S_t$, $R_t$ and $A_t$ yields a fully functional MDP to which we can apply established RL solution methods. The VFP solver Inovesa was already adjusted to support these efforts and first tests of training an agent on simulation data are currently ongoing.

### *Feasibility of the State Signal*

While the definition of the state signal in Eq. (4) provides the theoretical comfort of perfectly fulfilling the Markov property, measuring the longitudinal charge distribution in phase space at real storage rings is a major challenge. To make this approach more applicable in practice we would thus like to use information provided by diagnostic systems that are more commonly available. For now, the simplest and most robust way to acquire information about the state of the micro-bunching at KARA is by measuring the emitted CSR power $P_{t,\mathrm{CSR}}$ in the THz frequency range, e.g. [4, 9]. As $P_{t,\mathrm{CSR}}$ is strongly correlated with the micro-bunching

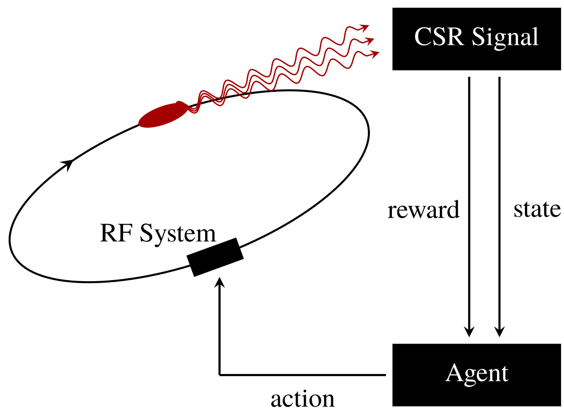


Figure 2: General feedback scheme using the CSR power signal to construct both, the state and reward signals of the Markov decision process (MDP).

dynamics, we consider the following alternative definition of the state signal

$$S_t \doteq S_t(P_{t,\mathrm{CSR}}) \, . \tag{9}$$

The resulting general feedback scheme is illustrated in Figure 2. Whether or not the CSR signal can provide enough information for the decisions the agent is confronted with has to be verified empirically. Ideally, the condensed information yields a fast learning process and convergence to a satisfying extent of control over the micro-bunching dynamics. If the CSR signal turns out to be insufficient, the state signal should be augmented with complementary information about the longitudinal phase space restoring the Markov property as closely as possible.

## SUMMARY

In order to establish extensive control over the micro-bunching dynamics in short electron bunches, a fast and adaptive longitudinal feedback is required which is capable of adjusting to the dynamic perturbation caused by the CSR self-interaction. Given that the CSR wake potential explicitly depends on the current state of the charge distribution, the action or countermeasure should, in general, be expected to be state-dependent as well.

In this contribution, we outline a general feedback scheme that is designed to make use of reinforcement learning methods in order to accomplish this challenging task.

## ACKNOWLEDGEMENT

T. Boltz and P. Schreiber acknowledge the support by the DFG-funded Doctoral School “Karlsruhe School of Elementary Particle and Astroparticle Physics: Science and Technology (KSETA)”. This research is in part supported by the Innovationspool AMALEA (Accelerating Machine Learning for Physics) in the Helmholtz Association’s Programme “Matter and Technologies”.

## REFERENCES

[1] T. Boltz *et al.*, “Feedback Design for Control of the Micro-Bunching Instability based on Reinforcement Learning”, in *Proc. 10th Int. Particle Accelerator Conf. (IPAC’19)*, Melbourne, Australia, May 2019, pp. 104–107. doi:10.18429/JACoW-IPAC2019-MOPGW017

[2] K. L. F. Bane, Y. Cai, and G. Stupakov, “Threshold studies of the microwave instability in electron storage rings”, *Phys. Rev. ST Accel. Beams*, vol. 13, p. 104402, 2010.

[3] P. Schönfeldt *et al.*, “Parallelized Vlasov-Fokker-Planck solver for desktop personal computers”, *Phys. Rev. Accel. Beams*, vol. 20, p. 030704, 2017. https://github.com/Inovesa/Inovesa

[4] J. L. Steinmann *et al.*, “Continuous bunch-by-bunch spectroscopic investigation of the microbunching instability”, *Phys. Rev. Accel. Beams*, vol. 21, p. 110705, 2018.

[5] T. Boltz *et al.*, “Perturbation of Synchrotron Motion in the Micro-Bunching Instability”, in *Proc. 10th Int. Particle Accelerator Conf. (IPAC’19)*, Melbourne, Australia, May 2019, pp. 108–111. doi:10.18429/JACoW-IPAC2019-MOPGW018

[6] R. S. Sutton and A. G. Barto, *Reinforcement Learning*. Cambridge, MA, USA: MIT Press, 2018.

[7] V. Mnih *et al.*, “Human-level control through deep reinforcement learning”, *Nature*, vol. 518, pp. 529–533, 2015.

[8] D. Silver *et al.*, “Mastering the game of Go with deep neural networks and tree search”, *Nature*, vol. 529, pp. 484–489, 2016.

[9] M. Brosi *et al.*, “Fast mapping of terahertz bursting thresholds and characteristics at synchrotron light sources”, *Phys. Rev. Accel. Beams*, vol. 19, p. 110701, 2016.

# Coherent and incoherent space charge resonance effects

Ingo Hofmann
*Technische Universität Darmstadt, Schlossgartenstr. 8, 64289 Darmstadt, Germany and*
*GSI Helmholtzzentrum für Schwerionenforschung GmbH, Planckstr. 1, 64291 Darmstadt, Germany**

The question of interplay of coherent and incoherent space charge driven resonances and of their Landau damping has found some interest in beam dynamics of modern high-intensity synchrotrons. We revisit the theoretical and simulation models describing coherent half-integer parametric resonances, analyze their Landau damping in 2D beams on the basis of simulated tune spectra and conclude that above second order (envelope modes) they play no role in realistic, Gaussian-like beam models. We also analyze incoherent resonance effects in the beam core regions and find that their role has been underestimated in part of the literature, in particular with regard to the very long-term beam evolution as in synchrotrons. We conclude that for such time scales more careful analysis of realistic simulation models is needed to support synchrotron design and evaluation of experiments.

## I. INTRODUCTION

In linear accelerators space charge resonance effects are known to occur at sufficiently high intensity and under structure resonance conditions. Their effect is often not evident due to limited length; nonetheless satisfactory comparison of experimental data with theoretical predictions was reported a few years ago by Groening [1, 2].

In circular accelerators the usually very large number of turns and the presence of external nonlinearities besides space charge lead to additional difficulties, which make progress more challenging. While coherent effects in impedance driven instabilities are a common topic, the role of coherent effects in transverse resonances is not yet adequately explored. Magnet error induced resonances with space charge effects in synchrotrons have been observed in detailed studies at the GSI and CERN synchrotrons [3–5]. Relatively satisfactory match between experiment and simulation models has been achieved in these studies, but important issues are still pending. The simplified simulation models, for example, have relied on so-called frozen space charge models (FSM), which lack selfconsistency and would suppress any kind of coherent response - if excited by whatever mechanism. The extent, to which it helps to update the rms emittance is yet unclear and requires benchmarking with selfconsistent codes.

In the following some aspects on the interplay of incoherent and coherent effects are presented. Section II reviews some historical and theoretical respectively experimental aspects of coherent frequency shifts. In Section III we discuss the so-called half-integer (parametric) coherent resonances including their Landau damping. Section IV is dedicated to incoherent versus coherent resonance effects, Section V to a comparison with experiments and Section VI attempts an outlook.

* i.hofmann@gsi.de

## II. COHERENT RESONANCE EFFECTS

The question of coherent resonant effects was first brought up by Smith [6] who pointed out - on the basis of envelope equations - that gradient error driven resonances should occur at the resonance condition for the coherent tune rather than the incoherent one. Later, his student Sacherer [7] derived conditions for higher order magnet driven resonances and their respective selfconsistently calculated coherent shifts in a 1D sheet beam model using the linearized Vlasov-Poisson equation.

The subject of coherent resonance effects found little attention in the years to follow. A pioneering selfconsistent simulation study in a synchrotron lattice with half-integer gradient error resonances using different beam distributions, and simulation limited to a few hundred turns, was carried out by Machida in 1991 [8] - with results supporting to some extent the conjecture by Smith.

It is helpful to take a quantitative look at the coherence issue on the second order level. For sufficiently split tunes a straightforward calculation of the envelope mode oscillation frequency by using the rms envelope equations yields the well-known result for the coherently shifted frequency (in "smooth approximation")

$$\omega = 2(\bar{Q}_{xy} + \frac{3}{8}\Delta\bar{Q}_{xy}), \tag{1}$$

where $\bar{Q}_{xy} \equiv Q_{0xy} - \Delta\bar{Q}_{xy}$ is the incoherent tune and $\Delta\bar{Q}_{xy}$ the space charge tune shift based on KV rms equivalence. Note that the KV-equivalent $\bar{Q}_{xy}$ is to be distinguished from the amplitude dependent $Q_{xy}$ in non-KV beams.

The resulting theoretical coherent resonance condition for the gradient error case is then

$$2(\bar{Q}_{xy} + \frac{3}{8}\Delta\bar{Q}_{xy}) = n, \tag{2}$$

where $n$ is an integer depending on the lattice. Condition Eq. 2 is in contrast with the still widely used second order incoherent resonance condition $2\bar{Q}_{xy} = n$.

The predicted intensity advantage under the assumption that only the coherent condition matters is not negligible. The situation is illustrated schematically in Fig. 1 by using the "necktie" diagrams for a 2D Gaussian distribution with a total spread $2\Delta\bar{Q}_{xy}$, and by assuming a gradient error coherent shift as in Eq. 2. The three cases

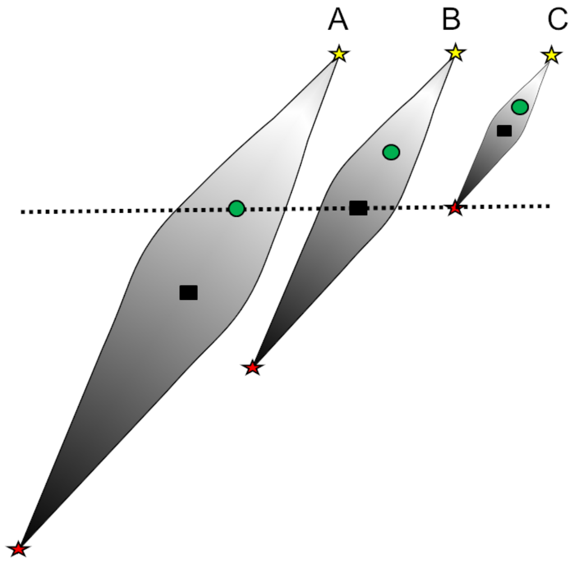


FIG. 1. Schematic comparison of different approaches to resonance diagram "neckties" referring to an assumed Gaussian distribution and a gradient error resonance line (dotted). Indicated are the coherent tune $\omega/2$ (green circle), $Q_{0xy}$ (yellow star), the lower tip of $Q_{xy}$ (red star) and $\bar{Q}_{xy}$ (black square).

depicted in Fig. 1 relate to

1. "incoherent limit" (C) assuming that the full footprint must be above the resonance
2. "coherent limit" (A): only the coherent frequency needs to be above the resonance
3. "rms limit" (B): the rms tune $\bar{Q}_{xy}$ is above the resonance.

Note that the idealized intensity advantage of A compared with C would be a factor 3.2, whereas B relates to a doubling of intensity. Smith was still pointing at the full "coherent advantage" (case A), while the simulation results of Machida have confirmed the less optimistic rms limit - still with an approximate intensity gain of a factor 2. A similar "benefit" was recently reported from simulations for the JPARC Rapid Cycling Synchrotron with the finding that no emittance growth or loss is observed as long as the rms tune stays above the driving resonance condition [9].

In fact, the coherent frequency approach entirely ignores that besides the coherent envelope frequency there is also a spectrum of incoherent single particle frequencies $Q_{xy}$ covering the whole range of frequencies. The question of their role with regard to resonances requires additional considerations not yet well understood systematically.

The idea of coherent shifts in higher than second order, driven by nonlinear magnet error or structure resonances, is summarized in the analogous smooth approximation expression

$$m(\bar{Q}_{xy} + F_m \Delta\bar{Q}_{xy}) = n. \tag{3}$$

Corresponding coherent shifts from second to fourth order in a 2D beam Vlasov-Poisson model with arbitrary (smooth) focusing and emittance ratios, and under the assumption of no frequency spread, have been derived in the late 1990's by Hofmann [10] (see also Ref. [11] for detailed examples of $F_m$). For split focusing they result as: $F_2 = 3/8$, $F_3 = 5/24$ and $F_4 = 35/256$. Note that for still higher order $m$ it can be assumed that the $F_m$ further approach zero.

For our discussion of the role of frequency spread it is helpful to generate different selfconsistent spectral tune distributions $Q_{xy}$ and allocate on them the coherent frequencies according to calculated shifts. This is shown in Fig. 2 comparing a waterbag with a Gaussian distribution for a coasting beam with a working point such that no significant resonance occurs (here $Q_{0x} = 0.158$, $Q_{0y} = 0.206$ and $\Delta\bar{Q}_{xy} = 0.0322$).

These spectra can be used also as initial spectra for any other value of $Q_{0y}$ and $\Delta\bar{Q}_{xy}$, if appropriately shifted and re-scaled in width. The spectra shown here are generated by using the TRACEWIN code [12], for this case with 32.000 particles, transported through a straight FODO latticed over 3000 cells, where the last 2000 cells are used to Fourier transform particle orbits and generate the spectral tune plot. Tunes $Q$ refer to a single FODO cell as fractions of 360°. The location of coherent frequen-

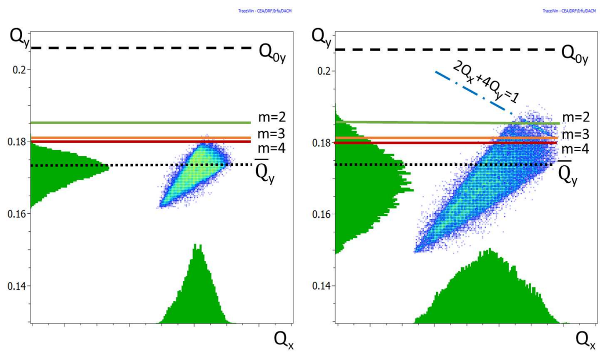


FIG. 2. Spectral distribution of $Q_{xy}$ for 2D waterbag (l.h.s.) and Gaussian (r.h.s.) distributions in a largely resonance-free region. Also shown are locations of expected $m = 2...4$ coherent mode frequencies, furthermore $Q_{0y}$ and $\bar{Q}_y$; a weak incoherent coupling resonance $2Q_x + 4Q_y = 1$ exited by the periodical space charge pseudo-dodecapole component of the matched beam is also shown.

cies has been corrected from the purely theoretical ones by using TRACEWIN simulation results for waterbag beams [13].

Comparing Fig. 2 with Fig. 1 we note that the higher order coherent $\omega/m$ would be closer to $\bar{Q}_{xy}$ than the envelope $\omega/2$ (green circle). Hence, the theoretical intensity benefit from the coherent effect shrinks for higher than second order - an argument speaking in favor of the more cautious "rms limit" (B).

A review article at the 1998 Shelter Island Workshop by Baartman [14] once more drew attention to the theoretical predictions of space charge shifted coherent resonance conditions in all orders for magnet error driven resonances (similar to Eq. 3, but using a different notation for $F_m$). The basis of Eq. 3, however, continued to be largely an analytical-theoretical one. Up to the present day clear benchmarking of the coherent resonance thesis with experimental findings for coasting or bunched beams in circular accelerators is not available.

Therefore, - apparently due to this lack of experimental evidence - the circular accelerator community widely continued to use "necktie" resonance diagrams based on the "incoherent space charge limit", with the possibly over-cautious requirement that no significant resonance line should intercept the necktie at any point.

In their recent article, Kojima et al. [15] take up a strong position by suggesting that synchrotron resonance charts should be redefined on the basis of coherent effects. However, these conditions have so far been studied in 2D and over a small (few hundred) number of lattice cells only. The real issue for synchrotrons is long-term behavior and the effect of synchrotron motion, which can be expected to enhance the emphasis on incoherent resonance effects - along with Landau damping.

## III. HALF-INTEGER (PARAMETRIC) COHERENT RESONANCES AND LANDAU DAMPING

The theoretical concept of coherent resonances discussed in Section II is not limited to the externally driven resonance cases of Eq. 3. In principle, so-called *coherent half-integer parametric resonances* driven by space charge alone and described by a half-integer r.h.s. according to

$$m(\bar{Q}_{xy} + F_m \Delta\bar{Q}_{xy}) = \frac{n}{2}, \tag{4}$$

(with $n$ an odd integer) need to be included as they potentially lead to additional lines in resonance charts. Note that the coherent half-integer modes are essentially different from half-integer or gradient error resonances described by $2\bar{Q}_{xy} = n$, or its coherent extension $2(\bar{Q}_{xy} + F_2\Delta\bar{Q}_{xy}) = n$.

Historically, these coherent half-integer parametric resonances have been introduced in a selfconsistent 2D Vlasov study in periodic focusing lattices by Hofmann et al. [16]. At that time they were called "180-degree" modes due to the fact that two lattice periods are needed to complete one mode period. The today more commonly used terminology of "parametric resonances" was later suggested in an analogous 1D sheet beam Vlasov analysis by Okamoto and Yokoya [17], which also allowed for explicit analytical expressions for coherent frequencies.

Note that these parametric cases are instabilities, which are "pumped" from noise under a half-integer resonance condition with the periodic focusing. They require no initial nonlinearity and even exist for uniform density KV-distributions. An example for a 3D Gaussian short bunch simulation by the TRACEWIN code in a periodic FODO lattice is shown in Fig. 3 (see also Ref. [18]). The primarily excited mode is the coherent parametric instability of the envelope mode $m = 2; n = 1$ in Eq. 4 - commonly called envelope instability -, which requires $Q_{xy}$ near the quarter integer. In a FODO lattice this amounts to a zero-current phase advance per cell $k_{0xy} > 90°$, and simultaneously for the space charge depressed rms phase advance $\bar{k}_{xy} < 90°$.

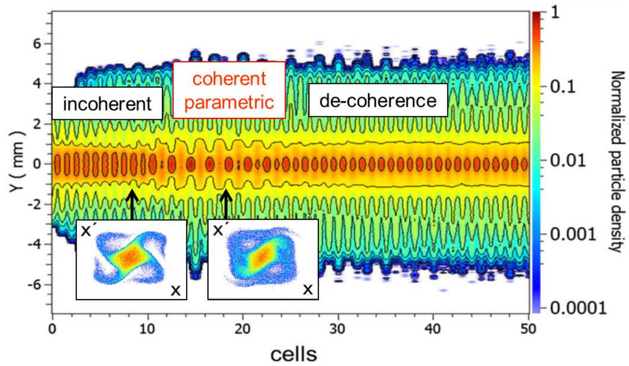


FIG. 3. Real space density evolution of a 3D high-intensity Gaussian bunch subject to parametric envelope instability in the 90° stopband of a FODO lattice ($k_{0xy} = 120°$, $\bar{k}_{xy} = 73°$) (source: Ref. [18]).

Fig. 3 shows the rapid evolution of an initial fourth order structure resonance phenomenon (note the fourfold symmetry insert of transverse phase space), which is driven by the periodic space charge pseudo octupole present in the Gaussian density profile and described by the incoherent resonance condition $4k_{xy} = 360°$ following the lattice periodicity. This is followed by the second order half-integer parametric mode described by $2(\bar{k}_{xy} + F_2\Delta\bar{k}_{xy}) = \frac{1}{2}$ (with $F_2 = \frac{1}{2}$ for the unsplit tunes in $xy$). Note that two lattice periods are needed to complete one period of the envelope instability. After more than rms emittance doubling the coherent mode de-coheres again and results in a beam distribution following again the lattice periodicity.

Theoretically, as predicted by the analytical theories of Refs. [16, 17] ignoring Landau damping, such coherent half-integer parametric modes exist in all orders. Kojima et al. [15] have suggested that for synchrotron resonance charts also these coherent half-integer modes need to be included. Such a step would double the number of lines compared with so far commonly used charts. This triggered questions as to how realistic these lines are, if Landau damping was included (see also a comment [19] and reply [20] on this article).

In fact, examples of selfconsistent simulations in FODO lattices using waterbag beams show these half-integer parametric modes up to fourth order as demonstrated in Fig. 4 (compare also similar results in Refs. [11, 13, 15]). The simulations have been carried out with the TRACEWIN code using 128.000 particles. The situation

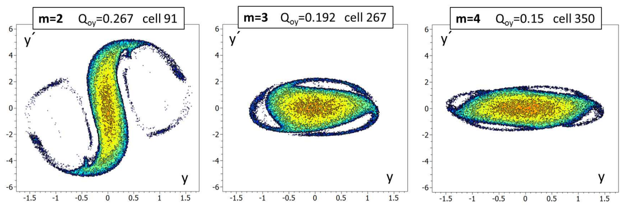


FIG. 4. Phase space projections for $m = 2, 3, 4; n = 1$ half-integer parametric modes and initial waterbag distribution ($\Delta\bar{Q}_{xy} = 0.0322$) (source: Ref. [13]).

is different for Gaussian distributions (truncated at $3\sigma$): simulations in Ref. [11] for the same parameters shown that the third and fourth order modes are not excited. For these modes Landau damping works in transverse tune space with the necessary - not always sufficient - condition of a negative slope towards higher tunes, which also means higher amplitudes as shown schematically in Fig. 5. The exponentially growing parametric modes are damped, if there is an excess of particles at smaller frequencies (amplitudes). Apparently, the sharply truncated waterbag distribution lacks Landau damping for modes with a sufficiently large coherent shift, which is the case for all modes shown in the spectra of Fig. 2. The r.h.s. of Fig. 2 also shows that in case of $m = 2$

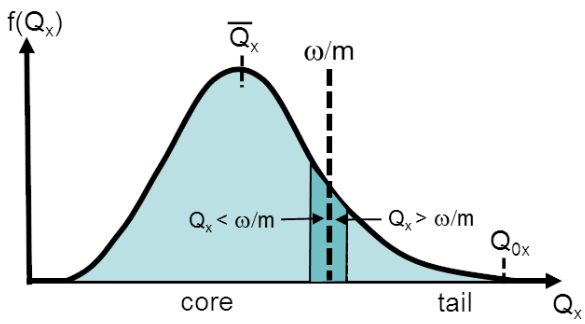


FIG. 5. Schematics of Landau damping of a coherent parametric mode with frequency $\omega$ in transverse tune space

there is only a weak overlap at the edge of the Gaussian tune spectrum, which apparently is not sufficient for Landau damping. In other words, the $m = 2$ mode is too strong to be damped by the small amount of particles near the edge.

The practical consequence following from the tune spectra is our finding that for Gaussian distributions all coherent half-integer resonances are expected to be Landau damped, with the exception of the - in practical synchrotron lattice design less relevant - second order envelope instability case. This results in the important conclusion that the suggestion in Ref. [15] to add half-integer lines in resonance charts is not supported by theory in case of Gaussian-like distributions. Our Landau damping argument so far is valid for coasting beams, but it can be assumed that Landau damping is even further enhanced by the additional effect of synchrotron oscillations.

## IV. INCOHERENT VERSUS COHERENT RESONANCES

Of practical importance is the interplay between coherent and incoherent resonance effects as described by Eq. 3. This subject has not been systematically explored in the context of high intensity synchrotrons, where long-term effects possibly raise the importance of incoherent resonance effects compared with coherent ones.

Unquestioned is the dominance of incoherent effects in the thin tail-halo region of a Gaussian-like distribution. Regarding incoherent effects in the denser beam core the discussion has been influenced by generalizing interpretations of earlier publications, which strongly emphasized the exclusive role of coherent effects in the core of a beam. The statement by Baartman [14] "In summary, we see the core is affected only by coherent core modes, and the tail affected by incoherent resonance" was originally intended for the special case of 1D sheet beams and short-term behavior of the $m = 2$ gradient error resonance.

This discussion is taken up again in the book by Ng [21] who finds "irrelevance of the incoherent tune" for resonances, except in the beam halo. It is unquestioned that these findings have some justification in the evolution of relatively short-term gradient error resonances. However, generalizing this discussion to all orders of resonances and the long-term behavior in synchrotrons - as recently postulated in Ref. [15] - needs more careful examination in a broader context.

In fact, as shown in Section III, Landau damping of the nonlinear coherent half-integer parametric resonances is a good example, where the incoherent spectrum of tunes comes into play with important consequences. For a more detailed discussion it is appropriate to include the tune space with the spectral distribution of tunes for a given phase space distribution instead of relying on short-term rms emittance evolution data. The importance of tune spectra is outlined in the following examples.

A first example of a sixth order resonance is indicated in Fig. 2 with the weak coupling resonance

$$2Q_x + 4Q_y = 1 \tag{5}$$

driven by the periodical pseudo-dodecapole space charge component of the matched beam. This resonance is a local phenomenon involving only a very small neighborhood of tune space around the exact resonance condition. For this reason it is clearly an incoherent resonance. This is also reflected by the fact that it accurately satisfies Eq. 5 with no coherent shift term. Coherent resonances, on the other hand, may affect the beam even if the coherent resonance condition has *no overlap* with the tune footprint. This is, for example, the case for the waterbag beam $m = 2, 3, 4$ modes in Fig. 2.

Further evidence of an incoherent resonance occurring deeper in the beam core is demonstrated by lowering $Q_{0y}$ such that the sixth order non-coupling resonance

$$6Q_y = 1 \tag{6}$$

is excited slightly below the edge of the Gaussian distribution (cut at $3\sigma$), with the resulting phase space projection shown in Fig. 6. The incoherent resonance is effecting the outer tail-halo region of the beam as expected. Note that the theoretically nearby coherent half-integer mode $m = 3; n = 1/2$ (following Eq. 4) is absent for a Gaussian due to Landau damping as discussed above.

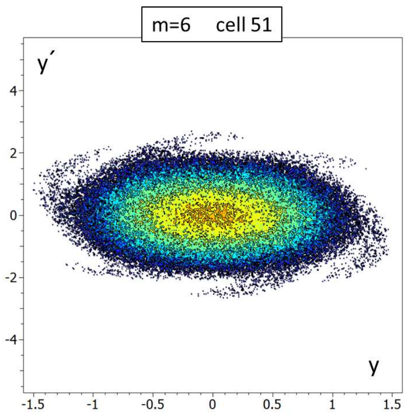


FIG. 6. Phase space projection in $y - y'$ (at cell 51) with $Q_{0y} = 0.184$ showing $m = 6$ incoherent integer resonance of Gaussian distribution.

For the slightly higher tune $Q_{0y} = 0.1875$ we show the tune spectrum on the l.h.s. graph of Fig. 7, and for $Q_{0y} = 0.1931$ in the r.h.s. graph. The incoherent resonance on the l.h.s. graph actually occurs almost at the upper edge of the tune spectrum, i.e. tail-halo region, and $\bar{Q}_y$ far below the resonance at $Q_{xy} = 1/6$. It has - as expected - a pronounced effect by pushing quite a few particles above the resonance marked at $6Q_y = 1$. A 3% emittance growth occurs over 3000 cells of simulation, which apparently is still going on.

In the r.h.s. case of Fig. 7, $\bar{Q}_y$ is still slightly below the resonance, but now deep in the beam core. Nonetheless particles are still shifted from below to above the resonance as indicated by the gap developing under it. The amount of resonant particles is much less than before, and the emittance growth only about 0.8%. We have also checked the still higher working point $Q_{0y} = 0.204$,

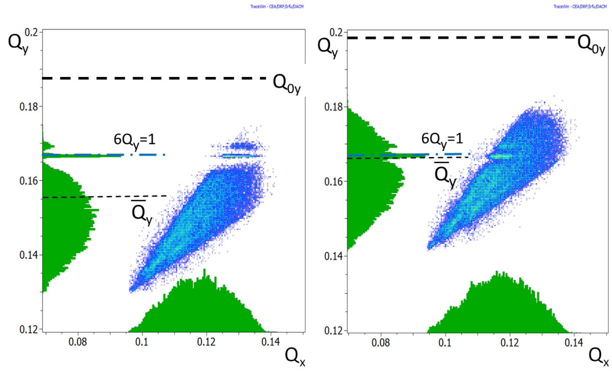


FIG. 7. Spectral distributions of $Q_{xy}$ for Gaussian distributions at $Q_{0y} = 0.1875$ (l.h.s.) and $Q_{0y} = 0.1931$ (r.h.s.) showing the incoherent $6Q_y = 1$ resonance.

such that the resonance occurs below $\bar{Q}_y$ and close to the maximum of the tune spectrum on the falling slope of it. In this case no effect of resonance could be detected. This supports the "rms tune" rule - also encountered in Section II and Refs. [8, 9] in the context of gradient error resonances - that no resonant effects should occur as long as $\bar{Q}_y$ stays above the resonance line. This finding obviously merits further detailed research.

More long-term simulations, also including synchrotron oscillations, are a subject of future studies. Our point here is that the importance of incoherent resonances is not limited to the tail-halo region - as was suggested in Ref. [15] on the basis of simulations over some hundreds of cells only -, but they may also occur deeper in the core and contribute to emittance growth up to the spectral position of $\bar{Q}_y$. Also, we have not been able to detect any evidence of a coherent shift in this particular stopband as conjectured in Ref. [15], which also needs to be explored in a broader context.

## V. COMPARISON WITH EXPERIMENTS

We suggest that these findings on incoherent resonances have a relevance for examining the validity of the FSM frozen space charge model. It has been used as relatively successful approximate simulation model to interpret experimental data on resonances with space charge in the CERN and GSI synchrotrons [3–5].

FSM simulation models only include incoherent resonance processes, while any coherent phenomena are suppressed due to the lack of selfconsistent feedback on the space charge potential. Obviously the credibility of FSM models gets weakened beyond the point, where significant changes in the distribution function or intensity occur. Nonetheless our findings on incoherent resonances lend support to the physics basis of FSM - up to some point.

In fact, the reported agreement between FSM simulations and experimental data looks better than one might have expected in view of the lack of feedback. Results from the extended SIS18 benchmarking campaign at GSI [3] are shown in Fig. 8. Shown are the results of

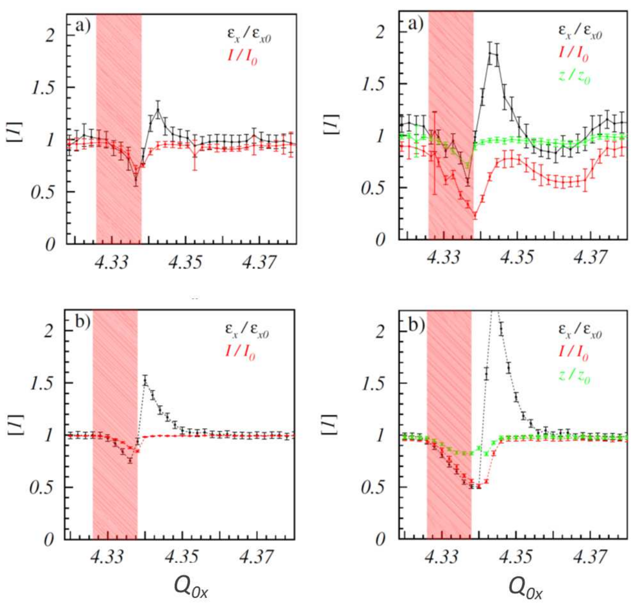


FIG. 8. Results of SIS18 measurements (a) and frozen space charge (FSM) simulations (b) near a sextupole error resonance at $Q_{0x} = 4.333$. Shown are relative changes of rms emittances and current versus the bare tune (here denoted by $Q_x$) for a coasting beam (left column) as well as for a bunched beam (right column). Also shown is the length change for the bunched beam. Source: Ref. [3].

measurements (upper row) and simulations (lower row) for a coasting (left column) and a bunched beam (right column). Rms emittance and beam loss have been obtained by scanning the working point across a horizontal third order error resonance given by $3Q_{0x} = 13$. Space charge is simulated for some $10^5$ turns by adopting the FSM method for initial Gaussian beams consistent with measured profiles, and for a maximum tune shift $2\Delta Q_x = 0.025$ for the coasting, and $2\Delta Q_x = 0.04$ for the bunched beam.

Note the surprisingly good agreement of the measured and simulated data as far as center and width of stopbands. The conjecture of Section IV and Refs. [8, 9] that no emittance growth occurs as long as $\bar{Q}_x$ is above the resonance is also surprisingly well reflected here: this amounts to $Q_{0x} > 4.35$ for the coasting, respectively $Q_{0x} > 4.36$ for the bunched beam case. Also note that the red hatched area in Fig.8 marks the stopband in the low intensity regime. The fact that the measured loss near this area is enhanced compared with simulations is attributed to the not sufficiently well-known dynamic aperture. This enhanced measured loss also limits the growth of rms emittances.

Altogether, comparison of measurements and FSM simulation justifies the preliminary interpretation that in long-term resonance response the incoherent resonance effects are the by far dominant mechanism. Coherent resonance effects, if noticeable, would have to show in Fig. 8 within the parameter regions $Q_{0x} < 4.35$ for the coasting, respectively $Q_{0x} < 4.36$ for the bunched beam case. There is, however, no evidence for this.

## VI. OUTLOOK

Our discussion of incoherent space charge effects in transverse resonances has shown their significance in Landau damping of the coherent half-integer parametric resonances. In the absence of such damping they would justify the additional doubling of lines in resonance charts as suggested in Ref. [15]. It is expected that this equally applies to the - theoretically yet unexplored - selfconsistent behavior in bunched beams.

The role of coherent constituents in externally driven (integer type) resonances with space charge needs more quantitative research and benchmarking by simulation. However, we find that the small coherent shifts for higher than second order resonances - see Fig. 2 - are unlikely to have an important effect on the overall resonance response in case of long-term behavior. The discussion following Fig. 8 suggest that in long-term resonance dynamics they are most likely overshadowed by the incoherent effects.

In summary, emphasis of future work should be on long-term bunched beam simulation studies and code comparison for different types of resonances and strengths of space charge effects, and ideally in realistic synchrotron lattices.

[1] L. Groening, W. Barth, W. Bayer, G. Clemente, L. Dahl, P. Forck, P. Gerhard, I. Hofmann, M. S. Kaiser, M. Maier, S. Mickat, and T. Milosic, D. Jeon and D. Uriot, Phys. Rev. Lett. **102**, 234801 (2009).

[2] L. Groening, I. Hofmann, W. Barth, W. Bayer, G. Clemente, L. Dahl, P. Forck, P. Gerhard, M. S. Kaiser, M. Maier, S. Mickat, T. Milosic, and S. Yaramyshev, Phys. Rev. Lett. **103**, 224801 (2009).

[3] G. Franchetti, O. Chorniy, I. Hofmann, W. Bayer, F. Becker, P. Forck, T. Giacomini, M. Kirk, T. Mohite, C. Omet, A. Parfenova, and P. Schütt, Phys. Rev. ST Accel. Beams **13**, 114203 (2010).

[4] G. Franchetti, S. Gilardoni, A. Huschauer, F. Schmidt, and R. Wasef, Phys. Rev. Accel. Beams **20**, 081006 (2017).

[5] H. Bartosik, Challenges in understanding space charge effects, *61st ICFA ABDW on High-Intensity and High-Brightness Hadron Beams (HB2018*, Daejeon, Korea

(JACOW, Geneva 2018) MOA1PL01 (2018).
[6] L. Smith, Effect of gradient errors in the presence of space charge forces, in Proc. of the 4th Intern. Conf. on High-Energy Accelerators, edited by A. A. Kolomenskij and A. B. Kuznetsov (Dubna, USSR, 1963), p. 1232.
[7] F. J. Sacherer, Ph.D thesis, Lawrence Radiation Laboratory Report No. UCRL-18454, 1968.
[8] S. Machida, Space charge effects in low-energy proton synchrotrons, Nucl. Instrum. Methods Phys. Res., Sect. A **309**, 43 (1991).
[9] H. Hotchi, H. Harada, N. Hayashi, M. Kinsho, K. Okabe, P.K. Saha, Y. Shobuda, F. Tamura, K. Yamamoto, M. Yamamotoa and M. Yoshimotoa, J-PARC 3-GeV RCS: 1-MW beam operation and beyond, JINST 15, P07022 (2020).
[10] I. Hofmann, Stability of anisotropic beams with space charge, Phys. Rev. E **57**, 4713 (1998).
[11] I. Hofmann, *Space Charge Physics for Particle Accelerators* (Springer, New York, 2017).
[12] D. Uriot and N. Pichoff, in *Proceedings of IPAC2015*, Richmond, VA, USA (JACoW, Virginia, 2015), paper MOPWA008.
[13] I. Hofmann, Revisiting coherent and incoherent resonances with space charge, JINST 15, P07022 (2020).
[14] R. Baartman, Betatron resonances with space charge, *Proceedings of Space Charge Physics in High Intensity Hadron Rings*, Shelter Island, New York, USA, 1998, AIP Conf. Proc. **448**, 56 (1998).
[15] K. Kojima, H. Okamoto, and Y. Tokashiki, Empirical condition of betatron resonances with space charge, Phys. Rev. Accel. Beams 22, 074201 (2019).
[16] I. Hofmann, L.J. Laslett, L. Smith and I. Haber, Stability of the Kapchinskij-Vladimirskij (K-V) distribution in long periodic transport systems, Part. Accel. **13** 145 (1983).
[17] H. Okamoto and K. Yokoya, Parametric resonances in intense one-dimensional beams propagating through a periodic focusing channel, Nucl. Instrum. Methods Phys. Res., Sect. A **482**, 51 (2002).
[18] I. Hofmann and O. Boine-Frankenheim, Parametric instabilities in 3D periodically focused beams with space charge, Phys. Rev. Accel. Beams **20**, 014202 (2017).
[19] I. Hofmann, Comment on "Empirical condition of betatron resonances with space charge", Phys. Rev. Accel. Beams, **23**, 028001 (2020).
[20] K. Kojima, H. Okamoto, and Y. Tokashiki, Reply to "Comment on 'Empirical condition of betatron resonances with space charge"', Phys. Rev. Accel. Beams **23**, 028002 (2020).
[21] K. Y. Ng, Physics of intensity dependent beam instabilities (World Scientific, Singapore, 2005).

# SPACE CHARGE EFFECTS ON LANDAU DAMPING FROM OCTUPOLES

V. Kornilov, GSI Helmholtzzentrum, Darmstadt, Germany
O. Boine-Frankenheim, GSI Helmholtzzentrum and TU Darmstadt, Germany

## INTRODUCTION

Octupole magnets are the cornerstone of the collective instability mitigation in many hadron synchrotrons, including the future SIS100 synchrotron [1] of the FAIR project [2]. The betatron tune shifts, and the tune spread, linearly increase with the octupole magnet current, and enhance Landau damping. On the other hand, a strong octupole field, as a nonlinearity, can reduce the dynamic aperture [3, 4]. This can put a restriction for the allowable octupole magnet power. Thus, a good understanding of the octupole magnet usage for Landau damping of the collective instabilities is important.

The direct space-charge can produce comparable or stronger tune shifts than the octupoles. Thus the effects of space-charge should be taken into account in a study for Landau damping due to octupoles. Space-charge can have manifold effects on Landau damping. Space-charge can cause loss of Landau damping, it can provide Landau damping, it changes the incoherent tune distribution and thus changes Landau damping in the beam.

The bunched beams are considered in this work, with the focus on the head-tail instability. Head-tail modes [5] are eigenmodes of the transverse collective bunch oscillations. Unstable head-tail modes are a major concern for high-intensity operation in ring accelerators. We consider unstable head-tail modes with different mode indices $k$, with the non-rigid bunch oscillations due to a finite chromaticity, even the lowest-order mode $k = 0$.

In the next section we review some properties of Landau damping in coasting beams and in bunches, the effects of octupoles and space-charge. For this discussion we consider two dispersion relations. The particle tracking simulations and the stability study method are described, followed by the results for the beam stability due to octupoles with space-charge of different strength. The results and the conclusions are discussed with the consideration of the incoherent tune distributions.

## THEORY ASPECTS

The space-charge tune shift varies along the bunch,

$$\Delta Q_{\mathrm{sc}}(z) = \frac{g_\perp \lambda(z) r_p R}{4\gamma^3\beta^2\varepsilon_x}\,, \tag{1}$$

where $\lambda(z)$ is the line density, $(2\pi R)$ is the ring circumference, $\beta$ and $\gamma$ are the relativistic parameters, $r_p = q_{\mathrm{ion}}^2/(4\pi\epsilon_0 mc^2)$ is the classical particle radius, $\varepsilon_x$ is the transverse rms emittance. The space-charge tune shift is negative (a tune depression), the modulus of the tune shift is different for every individual particle, depending on the transverse amplitudes and on the longitudinal position along the bunch. Equation 1 gives the maximal tune shift (for particles with small transverse amplitudes) for the position $z$, in a round beam. The geometric factor $g_\perp$ depends on the transverse distribution, for the Gaussian profile it is $g_\perp = 2$. The space-charge parameter is

$$q = \frac{\Delta Q_{\mathrm{sc}}(0)}{Q_s} \tag{2}$$

which is the tune shift for the rms-eqivalent K-V beam [6] ($g_\perp = 1$) in the peak of the line density, normalized by the synchrotron tune $Q_s$.

An octupole magnet of the strength $O_3$ produces the magnetic field

$$\begin{aligned} B_x &= O_3(3x^2y - y^3), \\ B_y &= O_3(x^3 - 3xy^2), \end{aligned} \tag{3}$$

which contributes to the incoherent tune shifts [3] of an octupole magnet system,

$$\begin{aligned} \Delta Q_x &= \kappa_x J_x - \kappa_{xy} J_y\,, \\ \Delta Q_y &= \kappa_y J_y - \kappa_{xy} J_x\,, \end{aligned} \tag{4}$$

where $J_x$, $J_y$ are the horizontal and vertical action variables.

For a characteristic tune shift due to octupoles, we use the parameter

$$q_4 = \frac{\Delta Q_\sigma}{Q_s}, \tag{5}$$

where $\Delta Q_\sigma$ is the tune shift $\Delta Q_x$ of a particle with the amplitudes $a_x = \sigma_x, a_y = 0$ ($\sigma_x$ is the transverse rms beam size), which corresponds to $J_x = \varepsilon_x/2, J_y = 0$.

For calculations of Landau damping due to octupole, the dispersion relation has been often used [3, 7–10],

$$\Delta Q_{\mathrm{coh}} \int \frac{1}{\Delta Q_{\mathrm{oct}} - \Omega/\omega_0} J_x \frac{\partial \psi_\perp}{\partial J_x} dJ_x dJ_y = 1. \tag{6}$$

Here, $\omega_0 = 2\pi f_0$ is the revolution frequency, the incoherent tune shift $\Delta Q_{\mathrm{oct}}(J_x, J_y)$ and the distribution function $\psi_\perp(J_x, J_y)$ are two-dimensional dependences. This represents the important role of the transverse beam profile in Landau damping. The coherent tune shift $\Delta Q_{\mathrm{coh}}$ results from the machine impedance in the case of no tune spread, i.e. no Landau damping. The collective mode frequency $\Omega$ is the solution for the given impedance, tune spread, and the beam distribution. This is the dispersion relation for the horizontal plane, the corresponding form is for the vertical oscillations. The dispersion relation Eq. (6) has been derived for a coasting beam, or for rigid dipole oscillations in bunches, but is has been commonly used also for estimations for the higher-order head-tail modes. Landau damping due to octupoles for non-rigid oscillations of different order modes has been recently studied in [11].

The effects of direct space-charge have been taken into account in another dispersion relation [12, 13],

$$\int \frac{\Delta Q_{\rm coh} - \Delta Q_{\rm sc}}{\Delta Q_{\rm oct} + \Delta Q_{\rm sc} - \Omega/\omega_0} J_x \frac{\partial \psi_\perp}{\partial J_x} dJ_x dJ_y = 1. \qquad (7)$$

This is also a 2d case, with the dependency $\Delta Q_{\rm sc}(J_x, J_y)$. This dispersion relation predicts an important role of nonlinear space-charge [14, 15] for Landau damping. The loss of Landau damping due to space-charge — the incoherent spectrum shifts away from the collective frequency due to linear space-charge [16–18] — is implicated in Eq. (7). This dispersion relation also correctly suggests that there is no Landau damping due to nonlinear space-charge only [16], even if the coherent frequency overlaps the incoherent tune spread. Particle tracking simulations with space-charge [16] confirmed these conclusions. However, for some $(\Delta Q_{\rm oct}+\Delta Q_{\rm sc})(J_x, J_y)$ dependencies Eq. (7) predicts an unphysical antidamping [16–18].

In the case of head-tail modes in bunches, there are additional aspects. Due to the chromatic phase advance along the bunch, already a $k = 0$ head-tail mode is not a rigid-bunch oscillation [11], the higher-order modes have more complicated longitudinal structures [5]. The synchrotron motion plays an important role, the longitudinal density profile $\lambda(z)$ creates space-charge tune shift variations along the bunch.

In contrast to the case of a coasting beam, the space-charge induced tune spread provides damping for the modes $k \neq 0$ [19–23]. Damping rates due to the tune spread produced by the longitudinal bunch density variations have been demonstrated and quantified in [22], effects of tune spreads in the longitudinal and transverse planes have been studied in [21,23]. This Landau damping can not be described by the dispersion relations Eqs. (6, 7) . A combination with the nonlinearities due to octupoles is even more complicated, which we study in this work using the particle tracking simulations.

## PARTICLE SIMULATIONS WITH SPACE CHARGE AND OCTUPOLES

For the particle tracking simulations we use the particle-in-cell code PATRIC [22–24, 26] in the PIC mode. The code has been validated using the exact analytical predictions [22,25,26], for the cases with and without space-charge, for bunched and for coasting beams. Chromatic effects and the octupole fields Eq. (3) are implemented as transverse momentum kicks, uniformly distributed over the ring. A linear rf bucket is used, i.e. the effects of the rf nonlinearity are not taken into account, the synchrotron tune in the simulations of this paper is $Q_s = 0.01$. The machine and beam parameters for the simulations are inspired by the heavy ion synchrotron SIS18 [27] at GSI Darmstadt, in our simulations with the uniform focusing model. The bunch distribution is 3D Gaussian, the beam is round transversally, the resistive-wall wake $W(z) = w_0/\sqrt{z}$ is applied in the horizontal plane, in the longitudinally-sliced manner [25]. For the self-field space-charge, the self-consistent solver is used in this work. This is necessary because of changes in the beam profiles during the beam oscillations with octupoles [11]. The beam profile modifications should be correctly included into the self-consistent space-charge structure. Beam losses are involved by an aperture with the radius four times larger than the initial beam radius.

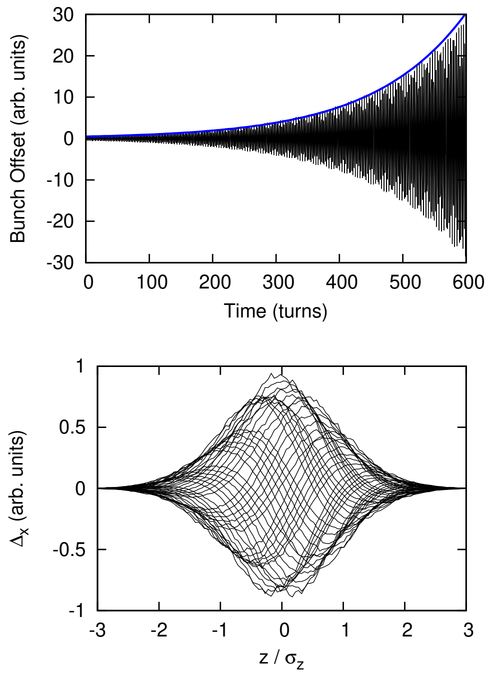


Figure 1: Example for an unstable $k = 0$ head-tail mode from a simulation without octupoles. The top plot: time evolution of the bunch offset (black line), the blue line is an exponential with the growth rate $\Gamma = 1.1 \times 10^{-3}$. The bottom plot: related offset traces along the bunch.

A simulation is started with a tiny perturbation. In the case without damping mechanism the perturbation grows into a linear instability, see Fig. 1 for an example. The amplitude increases exponentially (the blue line in Fig. 1, top) with the growth rate $\Gamma = {\rm Im}(\Delta Q_{\rm coh}) = 1.1 \times 10^{-3}$. The bottom plot in Fig. 1 shows the transverse offset overlap from this simulation, $\sigma_z$ is the rms bunch length. It has a typical pattern of a $k = 0$ head-tail mode, the wiggles demonstrate that this is a non-rigid mode.

We study the head-tail modes of different order by shifting the chromaticity $\xi$ and thus the chromaticity phase shift $\chi_b = Q_0 \xi L_b/(\eta R)$. For example, the $k = 0$ mode (Fig. 1) is the most unstable mode for $\chi_b = -1.15$ in our case. For $\chi_b = 0.55$ the most unstable mode is the $k = 1$ head-tail mode (Fig. 2, top plot), for $\chi_b = 0.88$ the most unstable mode is $k = 2$ (Fig. 2, bottom plot).

In our simulation scans we vary the octupole strength and the space-charge parameter. The wake field and the chromaticity stay fixed for every head-tail mode. As a result, the mode drive does not change within the scans. The growth

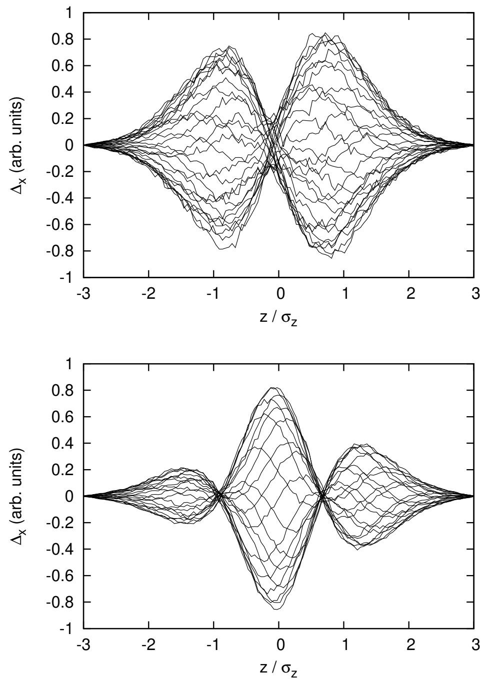


Figure 2: Examples for the unstable higher-order head-tail modes. Transverse offset traces along the bunch representing the $k = 1$ head-tail mode (top plot) and the $k = 2$ head-tail mode (bottom plot).

rate from a simulation without any damping for the $k = 0$ mode is $\Gamma = 1.1{\times}10^{-3}$, for the $k = 1$ mode it is $\Gamma = 7{\times}10^{-3}$, and for the $k = 2$ mode $\Gamma = 6 \times 10^{-3}$.

The method of our stability study implies finding the threshold octupole powers (both polarities) of the stability for a fixed space-charge condition. Figure 3 illustrates a simulation scan for $q = 2$ for the $k = 0$ mode. For the octupoles with $q_4 > 0.08$ and for the octupoles with $q_4 < -0.1$ the mode is stabilized, which are determined as the thresholds. The simulation runs are $10^4$ turns long, which should provide the resolution for the growth rate well below $\Gamma = 10^{-4}$.

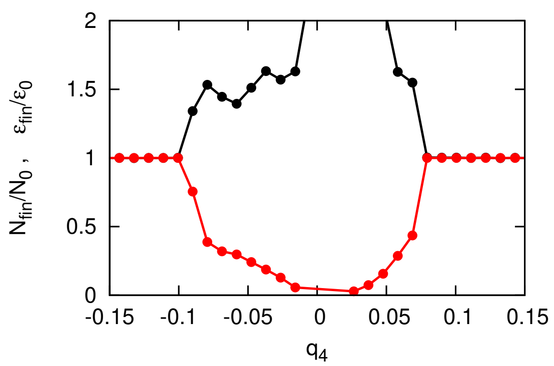


Figure 3: Output of an octupole power scan from simulations with space-charge ($q = 2$) for the unstable $k = 0$ modes. The red dots show the number of particles remained in the bunch, the black dots show the final horizontal emittance.

A stable (red lines) and an unstable (black lines) examples from simulations with octupoles and space-charge are shown in Fig. 4. The beam losses, the bunch horizontal offset and the bunch transverse emittance should be analized. Due to a strong dependency of the effective octupole from the transverse emittance, there can be a stabilizing emittance blowup [11]. In the situation with space-charge it is more complicated, because an emittance blowup also weakens space-charge.

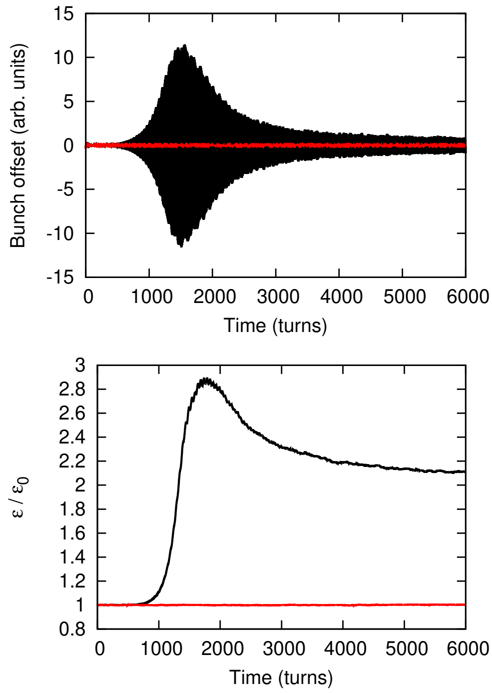


Figure 4: Time evolution of the bunch offset (top plot) and the transverse emittance (bottom plot) from simulations with octupoles and with space-charge ($q = 2$). The black lines correspond to $q_4 = 0.048$, the red lines are for $q_4 = 0.1$.

Results of the stability studies for the $k = 0$ mode are summarized in Fig. 5. The circles show the stability thresholds in the octupole power for the positive octupole polarity, the squares show the stability thresholds for the negative octupole polarity. The driving wake and the bunch parameters besides $q$ are fixed. Thus, in this scan the increasing space-charge parameter $q$ does not correspond to the increasing beam intensity, because the driving wake is not changed. We study Landau damping of a fixed instability for different space-charge conditions. Figure 6 shows the corresponding results for the $k = 1$ mode (top plot) and for the $k = 2$ mode (bottom plot).

## DISCUSSION

The simulation results in Figs. 5, 6 suggest that more octupole power is needed for stability at stronger space-charge. This is similar to the loss of Landau damping due to linear space-charge in coasting beams. The incoherent tune distributions in Figs. 7–9 illustrate how space-charge shifts

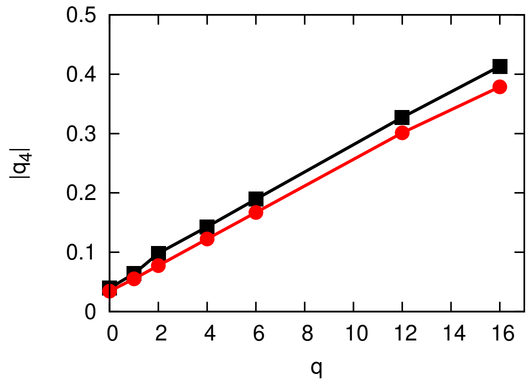


Figure 5: Results of the simulations scans for the $k = 0$ mode: stability thresholds in the octupole power in a dependency from the space-charge parameter $q$. The red circles are for the octupole polarity $q_4 > 0$, the black squares are for the octupole polarity $q_4 < 0$.

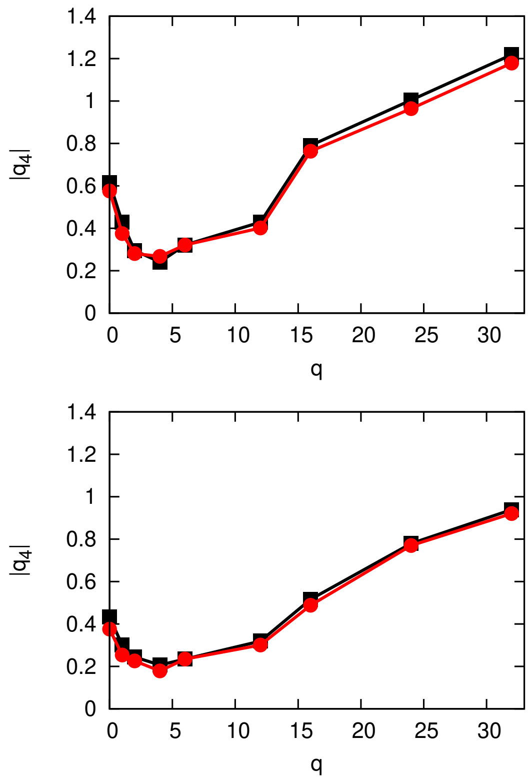


Figure 6: Results of the simulations scans for the $k = 1$ mode (top plot) and for the $k = 2$ mode (bottom plot). The plot notation corresponds to Fig. 5.

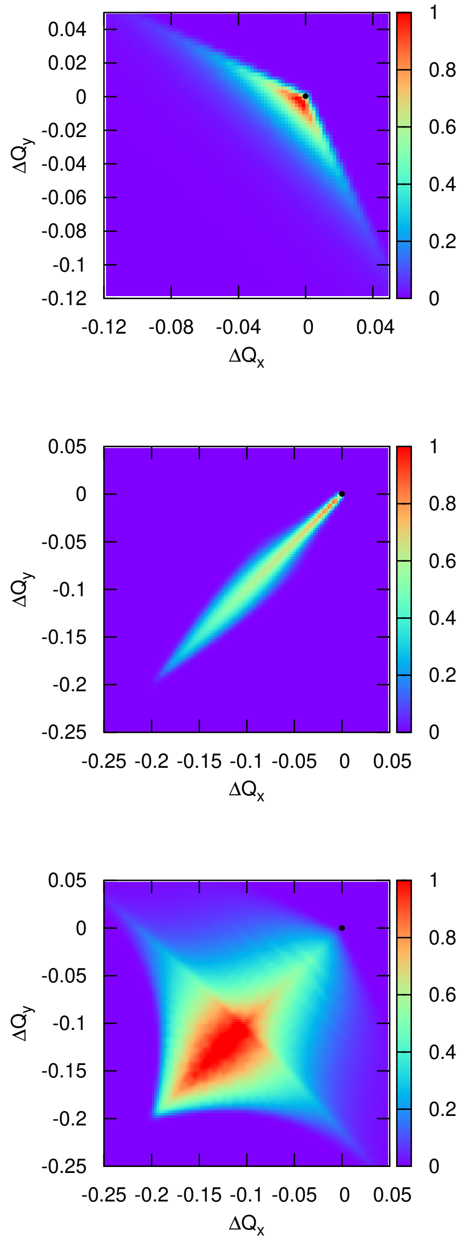


Figure 7: Tune footprints in a Gaussian bunch for the tune shifts due to octupoles $q_4 = 0.8$ (top plot), due to space-charge $q = 10$ (central plot) and for the combined effects (bottom plot). The color indicates the distribution density in arb. units, $Q_s = 0.01$.

particle tunes away from the bare tunes. Octupoles provide a tune spread, but the combined distribution is still strongly shifted. As a result, more octupole power is needed to provide enough tune spread. The coherent tune shifts of the instabilities are negative, in absolute value equal to the growth rate, which is a property of the resistive-wall wake [25]. In our case these values are below 0.01 in modulus. These tune shifts are small compared to the incoherent tune shifts, see Figs. 7–9.

Another observation from the results in Figs. 5, 6 is the "pits" in the $q_4$-growth for the $k = 1, 2$ modes at medium space-charge $q \lesssim 16$. This is in agreement with the findings about Landau damping due to space charge in bunches [19–23], for example, see Fig. 3 in [22]. In strong contrast, there is no "pit" in the results for the $k = 0$ mode (Fig. 5). This supports the conclusions [22, 23] that there is no additional

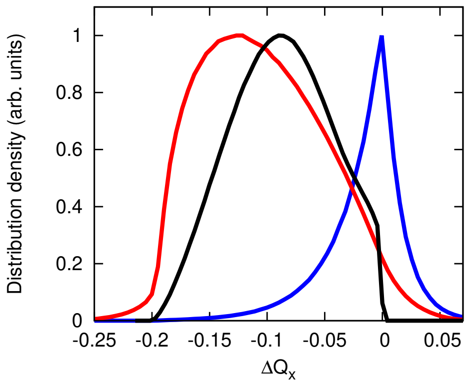


Figure 8: Incoherent tune distribution densities in a Gaussian bunch for the tune shifts due to octupoles $q_4 = 0.8$ (blue line), due to space-charge $q = 10$ (black line) and for the combined effects (red line), $Q_s = 0.01$.

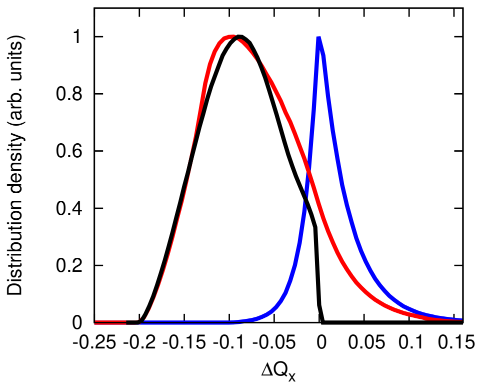


Figure 9: Incoherent tune distribution densities in a Gaussian bunch for the tune shifts due to octupoles $q_4 = -0.8$ (blue line), due to space-charge $q = 10$ (black line) and for the combined effects (red line), $Q_s = 0.01$.

Landau damping due to direct space-charge for the $k = 0$ mode.

Comparing the tune spreads due to octupoles of different polarity (blue lines in Figs. 8, 9), the related asymmetry is visible. This converts to the stability properties and can be analized using Eq. (6) or has also been observed in experiments [9]. Our results suggest that there are asymmetries for different octupole thresholds, see Fig. 3, and Figs. 5, 6. The polarity $q_4 > 0$ provides more damping and needs less octupole power for stability than that of $q_4 < 0$, especially at weak space-charge. For stronger space-charge, the differences in octupole thresholds (Figs. 5, 6) between octupole polarities are moderate. This corresponds to moderate differences for the combined space-charge and octupole effects in the tune destributions (red lines in Figs. 8, 9).

## REFERENCES


[1] P. Spiller *et al.*, Proc. of IPAC2015, Richmond, VA, USA, May 2015, paper THPF015, p. 3715

[2] P. Spiller *et al.*, Proc. of IPAC2018, Vancouver, Canada, April-May 2018, paper MOZGBF2, p. 63

[3] J. Gareyte, J.P. Koutchouk and F. Ruggiero, CERN-LHC-Project-Report-91 (1997)

[4] V. Kornilov, O. Boine-Frankenheim, V. Kapin, Proc. of IPAC2010, Kyoto, Japan, May 23-28, p. 1988 (2010)

[5] F. Sacherer, Proc. First Int. School of Particle Accelerators, Erice, p. 198, CERN-PS-BR-76-21 (1976)

[6] I.M. Kapchinsky and V.V. Vladimirsky, In Proc. of the II. Int. Conf. on High Energy Accel., 1959.

[7] J.S. Berg, F. Ruggiero, CERN SL-AP-96-71 (1996).

[8] J.S. Berg, F. Ruggiero, Proc. of PAC1997, Vancouver, Canada, May 12-16, p. 1712 (1997)

[9] X. Buffat, W. Herr, N. Monet, T. Pieloni, S. White, Phys. Rev. ST Accel. Beams **17**, 111002 (2014).

[10] Y.-H. Chin, CERN/SPS/85-09 (1985)

[11] V. Kornilov, O. Boine-Frankenheim, Nuclear Inst. and Methods in Physics Research, A 951 (2020) 163042

[12] D. Möhl, H. Schönauer, Proc. IX Int. Conf. High Energy Acc., Stanford, 1974, p. 380 (1974)

[13] D. Möhl, CERN/PS 95-08 (DI), (1995)

[14] M. Blaskiewicz, Phys. Rev. ST Accel. Beams **4**, 044202 (2001)

[15] E. Métral, F. Ruggiero, Proc. EPAC2004, Lucerne, Switzerland, 5-9 July 2004, p. 1897 (2004)

[16] V. Kornilov, O. Boine-Frankenheim, and I. Hofmann, Phys. Rev. ST Accel. Beams **11**, 014201 (2008)

[17] A. Burov and V. Lebedev, Phys. Rev. ST Accel. Beams **12**, 034201 (2009)

[18] D.V. Pestrikov, Nuclear Inst. and Methods in Physics Research, A 562 (2006) 65-75

[19] A. Burov, Phys. Rev. ST Accel. Beams **12**, 044202 (2009); A. Burov, Phys. Rev. ST Accel. Beams **12**, 109901(E) (2009)

[20] V. Balbekov, Phys. Rev. ST Accel. Beams **12**, 124402 (2009)

[21] A. Macridin, A. Burov, E. Stern, J. Amundson, P. Spentzouris, Phys. Rev. ST Accel. Beams **18**, 074401 (2015)

[22] V. Kornilov and O. Boine-Frankenheim, Phys. Rev. ST Accel. Beams **13**, 114201 (2010)

[23] V. Kornilov and O. Boine-Frankenheim, arXiv:1709.01425 [physics.acc-ph] (2017)

[24] O. Boine-Frankenheim, V. Kornilov, Proc. of 9th International Computational Accelerator Physics Conference ICAP2006, Chamonix, France, Oct. 2-6, p. 267 (2006)

[25] V. Kornilov and O. Boine-Frankenheim, Proc. of 10th International Computational Accelerator Physics Conference ICAP2009, San Francisco, USA, Aug 31 - Sep 4, p. 58 (2009)

[26] I. Karpov, V. Kornilov, O. Boine-Frankenheim, Phys. Rev. Accel. Beams **19**, 124201 (2016)

[27] K. Blasche and B. Franczak, Proc. of EPAC1992, Berlin, Germany, March 24-28, p. 9 (1992)

# ELECTRON CLOUD EFFECTS IN POSITRON STORAGE RINGS

K. Ohmi *,
KEK, Tsukuba, Japan, also at Soken-dai, Tsukuba, Japan

*Abstract*

This is a review of electron cloud effects/instabilities observed in positron storage rings. Coupled bunch and fast head-tail instabilities caused by an electron cloud have been studied for a long time, and the agreement of experiments and simulations/theory is almost perfect in positron storage rings. Mitigation of the instabilities based on the experiments and simulations have improved the accelerator performance drastically. It is essential to mitigate the instabilities in the present and future positron and proton rings.

## INTRODUCTION

Electron cloud effects have been observed clearly in positron storage ring. The primary electron source is identified without ambiguity as photo-emission. Synchrotron radiation is completely understood, and the electron production rate of the photoemission is very high: that is, the quantum efficiency is $\approx 0.1$. For the secondary emission, many measurements have been performed using samples in beam lines of synchrotron radiation sources. Electron density in accelerator chambers has been evaluated by computer simulation using the primary and secondary rates. The electron density also has been measured in the accelerator operation. The agreement of the density is reasonable.

The electron cloud causes fast coupled bunch instability [1] and fast head-tail instability [2]. These instabilities have been a serious problem for the last 30 years, and mitigation of them have improved accelerator performance, especially in $e^+e^-$ colliders. A strong coupled bunch instability had been observed in positron beam operation of KEK photon factory since 1990 [3]. Computer simulations and theory based on a photoemission model are in a good agreement with the growth rate and unstable mode of the coupled bunch instability. The instability have been observed also in $e^+e^-$ collider, KEK B factory and PEP-II. A beam size blow-up has limited the luminosity performance in KEKB. It had been identified as fast a head-tail instability caused by electron cloud. Suppression of the electron cloud contributes drastically to the luminosity increase. This effort has been continued in SuperKEKB, which is an upgrade of KEKB. In this paper, we summarize the history of the electron cloud instabilities in positron storage rings.

## COUPLED BUNCH INSTABILITY OBSERVED IN KEK-PHOTON FACTORY

KEK-PF is 2nd generation light source with the energy of 2.5 GeV and the circumference of 186 m. KEK-PF had been operated with positron storage to avoid ion instability since 1989. A coupled bunch instability was observed at a very low threshold current of 10-20 mA under multi-bunch operation with 200-300 bunches [3], where the harmonic number was $h = 312$. This instability was not observed in electron storage in the same ring, KEK-PF.

Figure 1 presents an example of unstable mode spectrum published in the paper [3]. The unstable modes are distributed broadly and relatively low frequency betatron side band, $nf_0 - f_\beta$ ($n = 20 \sim 30$), where $f_0$ and $f_\beta$ are revolution and betatron frequency, respectively. These unstable modes are explained by a short range wake up to 10 ns induced by electron cloud.

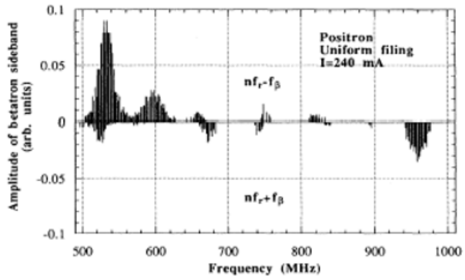


Figure 1: Unstable mode of a coupled bunch instability observed in positron beam operation in KEK-PF [3].

To understand this instability, photo-electron cloud model was proposed [1]. The scenario is summarized as follows,

1. Positron beam emits photons due to synchrotron radiation.
2. Electrons are produced at the beam pipe wall due to photo-emission, where electron production efficiency is $\sim 0.1e^-/\gamma$.
3. Electrons are attracted by positron beam and they interact with each other. Electrons travel in the beam pipe for 20-50 ns and then it is absorbed into the wall. Secondary electrons are produced from the electron absorption.
4. In multibunch operation ($\leq 10$ ns spacing), electrons are introduced continuously, leading to the formation of the electron cloud.
5. The electron cloud induces bunch-by-bunch correlation and results in an coupled bunch instability.

Figure 2 presents a simulation model and electron cloud distribution given by the model based on this scenario [1]. Top picture sketches electron production in a beam chamber cross-section. The electron density in the chamber is shown in the bottom picture. The typical electron density in KEK-PF was $\rho_e = 10^{12}$ m$^{-}$3.

* ohmi@post.kek.jp

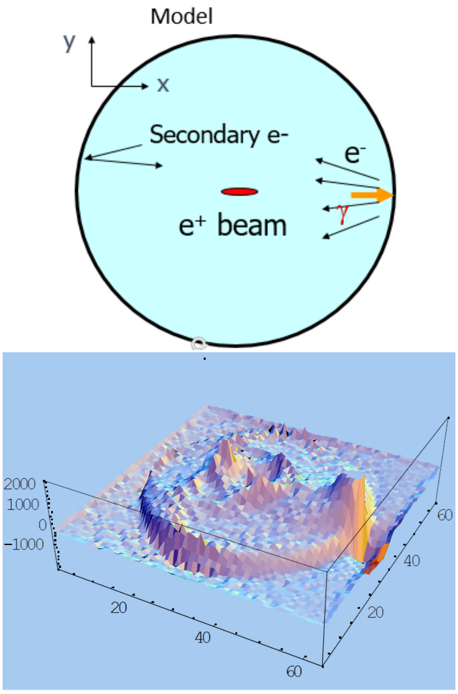


Figure 2: Simulation model of electron cloud build-up (top) and an example of electron cloud density in a beam chamber (bottom) [1].

B factories, KEKB and PEP-II planned to start the operation in 1998-1999. People were afraid of the significant impact of electron cloud instability effects on the performance of the B factories. Electron cloud study for feasibility of B factories had been performed in BEPC under a collaboration of IHEP and KEK. Similar coupled bunch instability had been observed in BEPC (Beijing electron positron collider) [4].

## ELECTRON CLOUD INSTABILITIES IN KEKB

KEKB, which is asymmetric electron-positron collider, had started operation in 1999. The energy was 3.5 and 8 GeV for positron and electron beams, respectively. 1585 bunches with the population of $6.3 \times 10^{10}(e^+)$ and $4.4 \times 10^{10}(e^-)$ were stored in the rings with the circumference 3016 m. KEKB achieved the luminosity of $2.2 \times 10^{34}$ cm$^{-2}$s$^{-1}$ in 2009. Electron cloud phenomena had been observed since the start of the operation.

### *Coupled bunch instability*

A coupled bunch instability, which was similar to the one observed at KEK-PF and BEPC, had been observed in KEKB. Though the instability had been basically suppressed by bunch-by-bunch feedback, it was an observed phenomenon, in which stored beam was sometimes dumped suddenly due to the instability. The coupled bunch instability was studied by ON-OFF of the bunch-by-bunch feedback system. Every bunch position was recorded several thousand turns after feed back OFF.

The coupled bunch instability was analyzed theoretically by evaluating the wake force of the electron cloud [1] and by simulating bunch motion under the interaction with electron cloud. The interaction between positron bunches and electron cloud is expressed by

$$\frac{d^2\boldsymbol{x}_p}{ds^2} + K(s)\boldsymbol{x}_p = \frac{r_e}{\gamma}\sum_{e=1}^{N_e}\boldsymbol{F}(\boldsymbol{x}_p - \boldsymbol{x}_e)\delta_P(s - s_e) \quad (1)$$

$$\frac{d^2\boldsymbol{x}_e}{dt^2} = 2r_e c^2\sum_{p=1}^{N_b}\boldsymbol{F}(\boldsymbol{x}_e - \boldsymbol{x}_p)\delta_P(t - t_p(s_e)) + \frac{e}{m_e}\frac{d\boldsymbol{x}_e}{dt}\times\boldsymbol{B} - \frac{e}{m_e}\frac{\partial\phi}{\partial\boldsymbol{x}}, \quad (2)$$

where indices $p$ and $e$ of $\boldsymbol{x}$ denote the positron and electron, $r_e$ the classical electron radius, $m_e$ the electron mass, $c$ the speed of light, $e$ the electron charge, $\sigma$ the transverse beam size, $\phi$ the normalized photoelectron potential, $\delta_P$, the periodic delta function for the circumference, and $F$ the Coulomb force in two-dimensional space expressed by the Bassetti-Erskine formula. The schematic view of the simulation is shown in Figure 3.

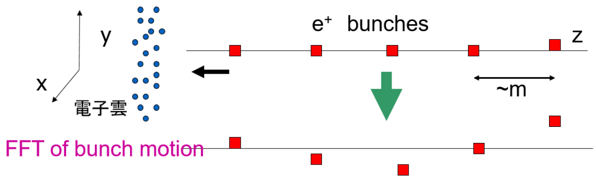


Figure 3: Simulation model of the coupled bunch instability. A bunch train interacts with electron cloud represented by macro-particles. Successive interaction induces a coupled bunch instability with certain unstable modes.

Figure 4 presents unstable modes of the coupled bunch instability given by bunch-by-bunch position measurement and the simulation. In KEKB, weak solenoid magnets are installed to suppress the electron cloud as shown later in detail. Top and bottom raws show unstable modes without and with solenoid magnets, respectively. Left and right columns present the results of the measurement and the simulation, respectively. The unstable modes of the coupled bunch instability depend on collective electron motion in the electron cloud. Electrons in the solenoid magnet slowly move along chamber surface with a frequency $\omega = \lambda_p r_e c^2/r^2\omega_c$, where $\lambda_p$ the average line density of positron beam, $r$ the radius of electron motion (smaller than chamber radius), $\omega_c = eB/m_e c$ the cyclotron frequency. Figure 5 shows the electron distribution in the drift space (top) and solenoid magnets (bottom). The radius of electron motion is around $r = 4.5$ cm, while the chamber radius is 5 cm. White dot is position of the bunch passing through. The dot oscillates each bunch passage with the mode frequency. The electron distribution also changes its shape in each bunch passage.

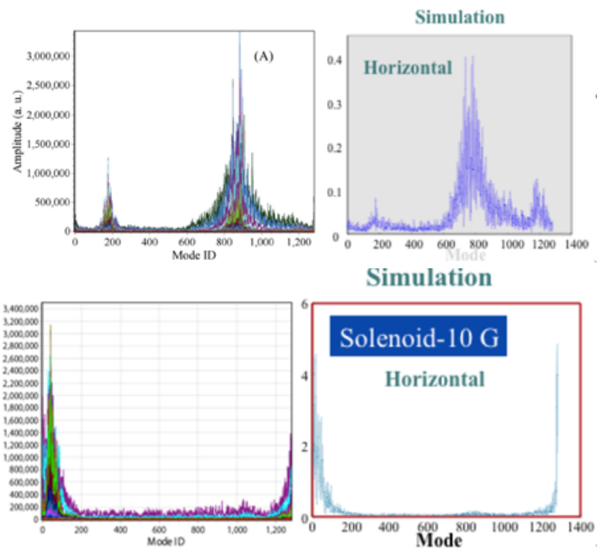


Figure 4: Unstable modes of the coupled bunch instability caused by electron cloud in KEKB positron ring. Top and bottom plots show unstable modes without and with solenoid magnets, respectively. Left and right are given by the measurement and the simulation.

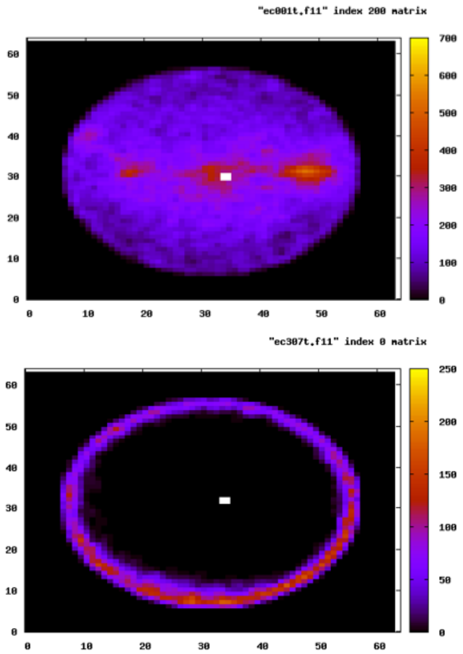


Figure 5: Simulated electron distribution in the beam chamber cross-section. White dot is bunch position passing through.

Another typical coupled bunch instability had been observed in DAFNE. Electrons in the bending magnets are dominant in DAFNE. Simulations show vertical stripe of electron density is formed in the bending magnet. Corrective motion between positron beam and the stripe induces very slow unstable mode of coupled bunch instability. Figure 6 presents simulation of beam motion, unstable modes and electron distribution interacting with the beam. Horizontal instability dominate the vertical as shown in top plot. A mode with the slowest frequency is induced as shown in the mid plot. The vertical stripe from the bottom picture of Fig.6 oscillates slowly coherently and correctively. Its collective motion is correlated with the bunch motion.

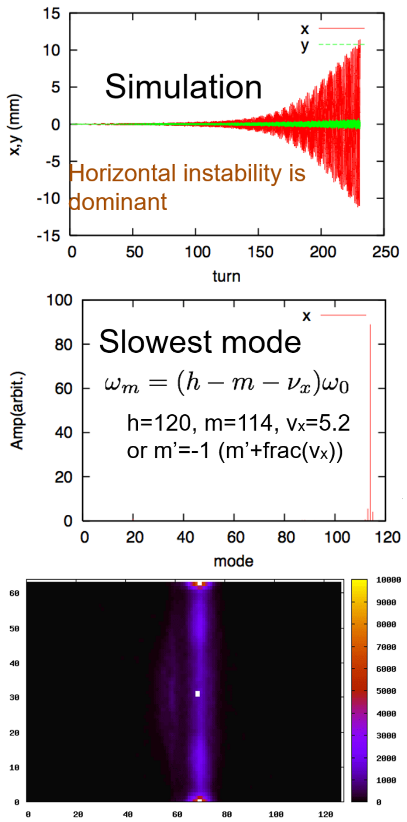


Figure 6: Simulation of a coupled bunch instability observed in DAFNE. Top and middle plots show simulated bunch motion and unstable modes. Bottom shows electron distribution interacting with bunch train (white dot).

## *Beam size blow-up and its cure*

In KEKB, a blow-up of vertical size of the positron beam had been observed above a threshold current in multibunch operation. The blow-up limited luminosity performance. Figure 7 presents the beam size blow-up. The beam size blowup started at 400 mA (green dots) for filling by 4 bucket (8ns) spacing. The beam size increased more than 5 times at 600 mA.

To cure the beam size blow-up, solenoid field is applied on the beam chamber of entire positron ring. First, permanent magnets were attached on the chamber surface. The effect was not clear because the area length attached was not sufficient (~800m) and response for magnets ON/OFF was not observable. A strong and strange beam loss caused by coupled bunch instability was observed after attachment. The growth seemed somewhat stronger than before. The permanent magnets were replaced by solenoid coil in the

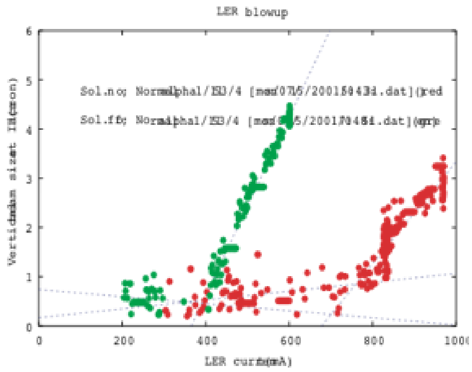


Figure 7: Beam size blow-up as function of positron beam current. Green and red dots are given for without/with solenoid magnets.

summer of 2000. Figure 8 presents pictures of the solenoid magnets wound in the ring.

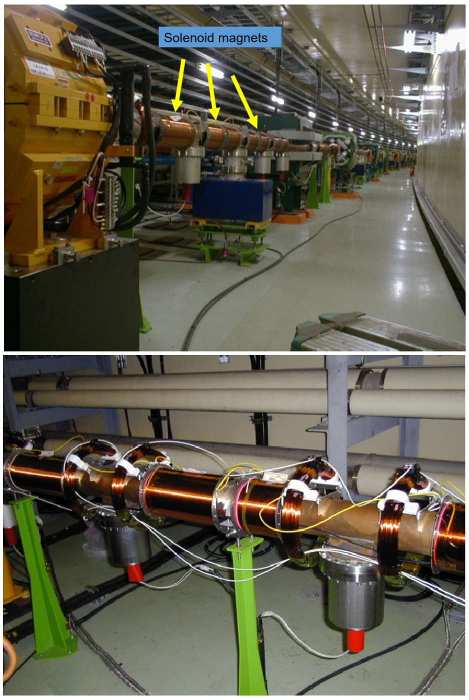


Figure 8: Weak solenoid magnets wound in the whole of KEKB-LER positron ring.

The solenoid magnets were added year-by-year. The winding history is summarized as

1. A lot of permanent magnets were put along the arc section in the ring ~800m.
2. These magnets (800m) were replaced by solenoid magnets (Summer 2000).
3. Additionally 500m magnets are wounded (Jan. 2001).
4. Magnets were added in the straight section (Apr. 2001).
5. Add solenoids even in a short free space (Summer 2001).
6. Solenoid magnets cover 95 % of the free space (~2005).
7. Inside of ¼ of Quadrupoles (2005)

The beam size blow-up was remarkably suppressed by the solenoid magnets as shown by the red dots of Figure 7.

The effect of the solenoid magnets became significant when additional winding (800+500=1300m) has been done in 2001. Luminosity performance was compared for solenoids ON/OFF. Figure 9 presents the luminosity performance for filling by 4 buckets. Top plot shows the specific luminosity for solenoids ON/OFF. The improvement of luminosity performance was more than twice in those days. Furthermore higher current operation made possible with help of the solenoid magnets. Bottom plot shows comparison of the luminosity for solenoid winding of 800 and 1300 m. The luminosity was saturated at 500 mA at 800 m winding, while the luminosity increased linearly by 750 mA at 1300m winding. Winding more solenoids, saturation of beam current and luminosity increased further. The design luminosity $1 \times 10^{34}$ cm$^{-2}$s$^{-1}$ was achieved in 2003.

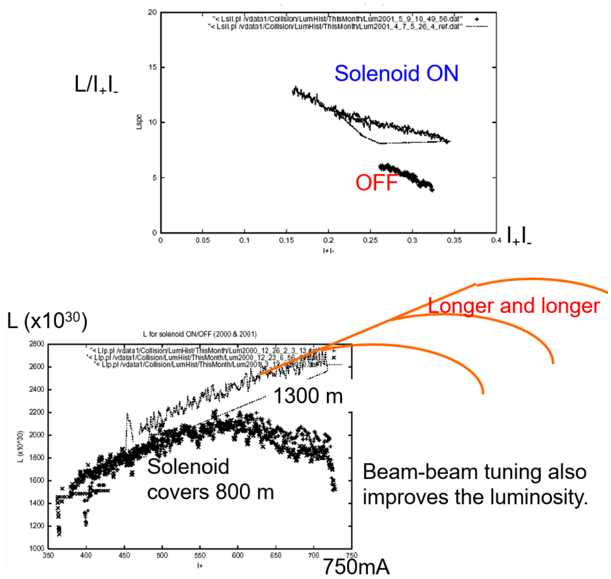


Figure 9: Luminosity performance with/without the weak solenoid magnets. Top plot shows the specific luminosity for solenoid ON/OFF. Bottom plot shows comparison of the luminosity for solenoid winding of 800 and 1300 m.

Figure 10 presents luminosity history of KEKB. We can observe luminosity increase for the solenoid winding. Finally maximum luminosity $2.2 \times 10^{34}$ cm$^{-2}$s$^{-1}$ was achived in 2009.

### *Interpretation of Fast head-tail instability*

Studies why the beam size blowup occur had continued in parallel with the solenoid winding. The blow-up was observed at multi-bunch operation with narrow bunch spacing ($\leq$ 16 ns). There were no correlation in motion between bunches. It seemed that the blow-up was due to a single

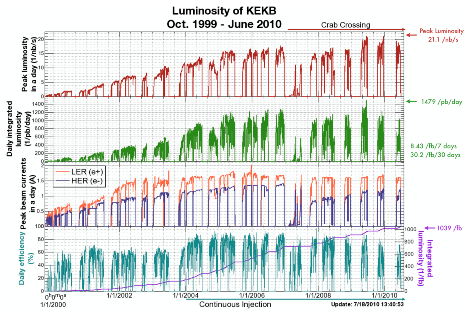


Figure 10: History of luminosity in KEKB.

bunch effect, though instability sources are accumulated in multi-bunch operation.

A synchrotron sideband correlating with the beam size blow-up had been measured in experiments [5]. Figure 11 shows the sideband along the bunch train. The sideband appears $\approx \nu_y + 1.5\nu_s$. Betatron and sideband shift is increasing along the bunch train. This tendency is explained by increasing electron cloud density along the bunch train.

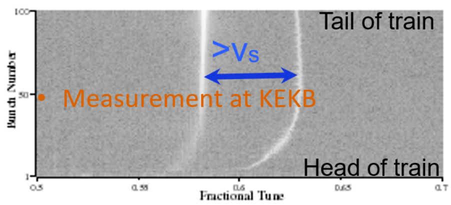


Figure 11: Measurement of synchro-betatron sideband correlated to the beam size blow-up [5].

The beam size blow-up was finally explained by fast head-tail instability caused by electron cloud. The instability was analyzed by a short range wake force induced by an electron cloud [2,6] and a simulation of bunch-electron cloud interaction. Figure 12 presents simulation results given by similar approach as the strong-strong beam-beam simulation [7]. A bunch represented by macro-particles interacts with macro electrons refreshed collision-by-collision. Top and bottom plots show variation of the vertical beam size and Fourier amplitude of vertical motion, respectively. Top plot shows the threshold of electron cloud density is $\rho_e = 0.8 \times 10^{12}$ m$^{-3}$. Synchro-betatron sideband appeared above the threshold in the Fourier analysis. Fourier amplitude for various feed back gain was given by the simulation. The betatron peak around 0.59 is suppressed by the feedback, while the sideband is not suppressed. The sideband appears somewhat higher than $\nu_y + \nu_s$. The sideband tune agrees with the measurement in Fig.11.

## ELECTRON CLOUD INSTABILITIES IN SUPERKEKB

SuperKEKB, which was an upgrade of KEKB, was designed to realize collision with a large crossing (Piwinski) angle. Piwinski angle is designed to have a very large value, $\sigma_z\theta_c/\sigma_x \approx 20 - 25$. Beam commissioning of Phase-I was

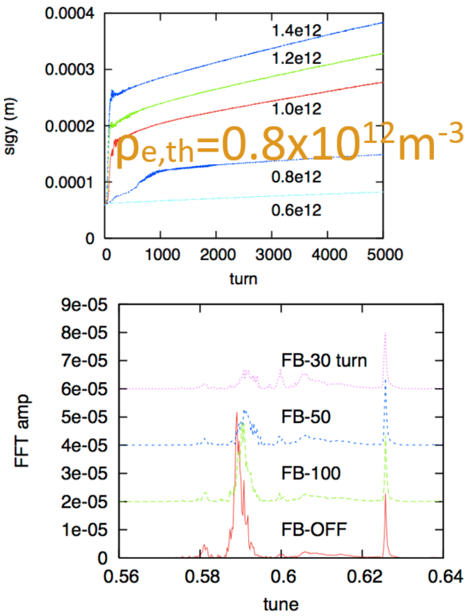


Figure 12: Simulation of bunch electron cloud interaction. Top plot depicts variation of beam size for evolution of turns, and bottom plot depicts Fourier spectrum of the vertical dipole amplitude of the bunch.

performed in 2016 from February to June without interaction region and Phase-II commissioning was performed from March to July 2018 after installation of IR magnets and the BELLE-II detector. Vertical beam size blow-up due to the electron cloud has been observed in the positron ring (LER) in the early stage of Phase-I commissioning. Occurrence of electron multi-pacting was suspected at area near bellows in the early stage of commissioning, since this area, which occupies about 5% of whole ring, was not coated by TiN. The emittance growth was suppressed by weak permanent magnets, which cover the bellow drift space. This means the electron cloud in the bellow area dominates the instability. It was good opportunity to bench mark the threshold of electron density, knowing electron density at the uncoated bellow area. Electron cloud has been monitored at an Aluminum test chamber w and w/o TiN coating.

The vertical beam size was measured for bunch train with various filling in the early stage of the commissioning as shown in Figure 13. The measurements were performed for several bunch filling, 2, 3, 4, 6 bucket spacing, where the total number of bunches is 600. Threshold current of the beam size blow-up for each bunch spacing were obtained from the figure. They are 160, 200, 260 and 500 mA for 2, 3, 4 and 6 bucket spacing, respectively. Corresponding bunch populations are 1.6, 2.0, 2.7 and 5.2×10$^{10}$, respectively.

Simulations using the beam parameters were executed to evaluate the threshold of electron density. Figure 14 presents simulation results for $N_p = 1.6, 2.0, 2.7$ and 5.2×10$^{10}$. The threshold density is weakly dependent on the bunch population, $\rho_{e,th} = 3 \sim 4 \times 10^{11}$ m$^{-3}$.

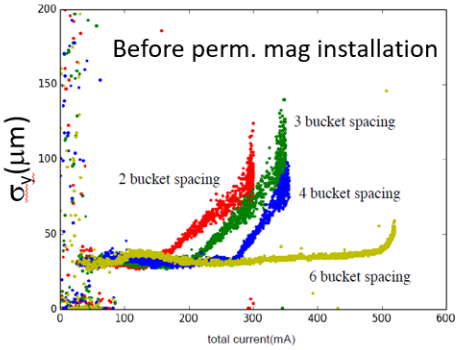


Figure 13: Beam size as a function of beam current in the early stage of SuperKEKB commissioning (June, 2018).

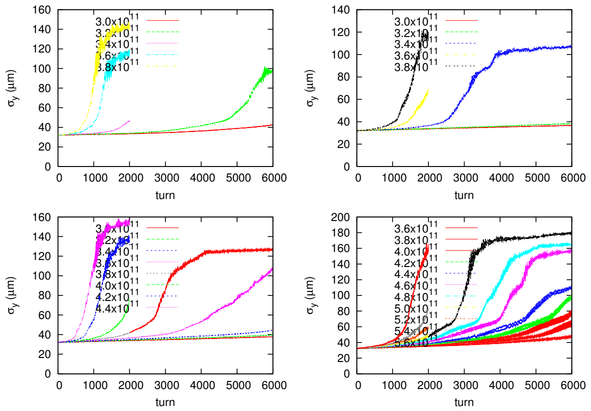


Figure 14: Vertical emittance growth in simulation PEHTS. Top left, top right, bottom left and bottom right are evolution of the vertical beam size for $N_p$ = 1.6, 2.0, 2.7 and $5.2\times10^{10}$, respectively.

Figure 15 shows measured electron density in the uncoated test chamber as a function of the beam current for the various filling. The threshold given by the blow-up measurement and simulation is plotted by circles and stars, respectively. Note that the density is the value in the uncoated chamber which occupies 5% of the ring, thus the simulated density is multiplied by 20. The brown line is given by a simple formula based on a coasting beam model [6, 8],

$$\rho_{th} = \frac{2\gamma\nu_s\omega_e\sigma_z/c}{\sqrt{3}KQr_0\beta_yL} \tag{3}$$

The electron oscillation frequency inner bunch is $\omega_e\sigma_z/c \approx 17$, where $\omega_e^2 = .2\lambda_b r_e c^2/(\sigma_y\sigma_x)$. The quality factor of electron cloud induced by the wake force is less than 10 [6]. Assuming electron accumulation factor near the beam $K = \omega_e\sigma_z/c$ and $Q = 7$, the threshold density is constant as shown in Figure 15. $Q = 7$ due to beam-electron interaction works as the quality factor in the instability, because electron oscillation frequency $\omega_e\sigma_z/c \approx 17$ is sufficiently larger than $Q$. In this condition, the threshold is independent of the bunch intensity. For short bunch, $Q$ is truncated by $\omega_e\sigma_z/c$, thus the threshold density decreases for increasing beam current. Measurement and simulation show the threshold increases for the beam current. $K$ may be somewhat smaller than $\omega_e\sigma_z/c$, or electrons other than the bellow section may contribute the instability. Nevertheless, we observe agreement between measurement and simulations of a factor of 2.

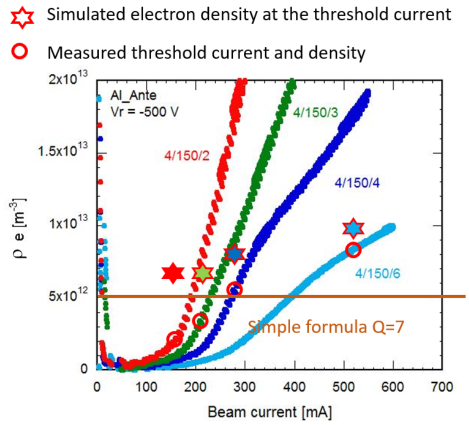


Figure 15: Measured electron density as function of the beam current for the various filling at the uncoated test chamber. The measured blow-up threshold current is plotted circle, and the simulated threshold density at the beam condition was plotted by star.

## *Tune shift and electron cloud density*

Electron cloud causes a positive tune shift due to the attractive force between beam and electron cloud. The tune shift depends on the electron density and distribution. For flat distribution along $x$, only vertcal tune shift appears as

$$\Delta\nu_y = \frac{\rho_e r_e \langle\beta_{x,y}\rangle}{\gamma}C. \tag{4}$$

Transverse tune was measured along the bunch train for 3 bucket spacing filling. Figure 16 shows horizontal (top) and vertical (bottom) tune of bunches at 0, 150,300 and 450-th bucket.

The horizontal tune shift depends on the beam current ($I$): i.e., $\nu_x = 0.003$ for $I = 450$ mA and $\nu_x = 0.001$ for $I = 300$ and 400 mA. The vertical tune shift is $\nu_y = 0.005$, while the horizontal tune shift seems to be ambiguous. The averaged electron density is estimated to be $\rho_e = 4\times10^{11}$, that is, the local density is to be $\rho_e = 8\times10^{12}$ m$^{-3}$ at the bellow area, if only the vertical tune shift is considered. Considering horizontal tune shift, the density is somewhat larger. The estimated density is in a good agreement with the one directly measured in the test chamber without TiN coating.

The coupled bunch instability caused by electron cloud has also been observed in SuperKEKB. Appearance of unstable mode was similar to that of KEKB. Attaching more solenoid magnets, unstable mode change from the drift type (top of Fig. 4) to the solenoid type (bottom of Fig. 4). Further addition of solenoid magnets suppressed the coupled bunch instability.

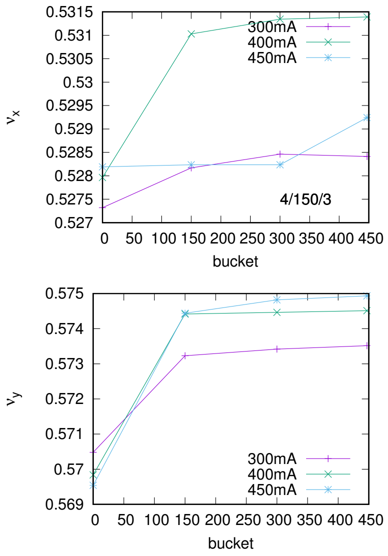


Figure 16: Tune shift along bunch train for 3 spacing filling.

## SUMMARY

Electron cloud effects have been observed at positron storage rings. Electron cloud effects presented a significant challenge to the accelerator operation for the first time in KEKB/PEP-II. The history of mitigation of the electron cloud effects can be tracked by observing the success of KEKB

Luckily, electron cloud effects have been observed at KEK-PF before KEKB started operation. Electron cloud effects have been observed since the start of KEKB operation in 1999. Vertical beam size blow-up was one of the most serious issue for the achievement of the target luminosity $L = 10^{34}$ cm$^{-2}$s$^{-1}$ in KEKB. Many collaborations have been done with SLAC, IHEP, CERN, INFN, BINP. Peak luminosity $L = 2.17 \times 10^{34}$ cm$^{-2}$s$^{-1}$ and integrated luminosity 1 ab$^{-1}$ was achieved in KEKB.

SuperKEKB was designed so as to mitigate the electron cloud effects. Beam size blow-up had been seen in the early stage of the commissioning. The electron source, which was uncoated bellow area, was cured by solenoid magnets. In 2020, the beam size blow up and coupled bunch instability have not been observed below the beam current of 1 A. The design beam current is 3.6 A. Further studies and cures may be necessary in the future.

## ACKNOWLEDGEMENT

The author thanks Drs J. Flanagan, H. Fukuma, Z. Guo, M. Izawa, Y. Suetsugu, M. Tobiyama, S. Win, F. Zimmermann, M. Zobov for many, long and continuous fruitful discussions.

## REFERENCES

[1] K. Ohmi, Phys. Rev. Lett. 75, 1526 (1995).

[2] K. Ohmi, F. Zimmermann, Phys. Rev. Lett. 85, 3821 (2000).

[3] M. Izawa, Y. Sato and T. Toyomasu, Phys. Rev. Lett. , 74, 5044 (1995).

[4] Z. Guo et al., Phys. Rev. ST-AB 5, 124403 (2002).

[5] J. Flanagan et al., Phys. Rev. Lett. 94, 054801 (2005).

[6] K. Ohmi, F. Zimmermann, E. Perevedentsev, Phys. Rev. E 65, 016502 (2001).

[7] K. Ohmi, Phys. Rev. E62, 7287 (2000).

[8] A. W. Chao, *Physics of Collective Beam Instabilities in High Energy Accelerators*, Wiley-Interscience Publication, New York, 1993), and references therein.

[9] S. Win et al., Phys. Rev. ST-AB 8, 094401 (2005).

[10] M. Tobiyama et al., Phys. Rev. ST-AB 9, 012801 (2006).

# INCOHERENT ELECTRON CLOUD EFFECTS IN THE LARGE HADRON COLLIDER

K. Paraschou*,[1], G. Iadarola,
CERN, 1211 Geneva 23, Switzerland
[1]also at Aristotle University of Thessaloniki, 54124 Thessaloniki, Greece

*Abstract*

During the operation of the Large Hadron Collider in 2018, the majority of physics data was collected with a beam energy of 6.5 TeV, a bunch spacing of 25 ns and with $\beta$-functions in the high luminosity interaction points equal to 30 cm. In this configuration, it was found through several experimental measurements that electron cloud induces a significant degradation of the beam lifetime. This contribution reviews the available experimental observations, showing in particular the role played by the e-cloud located in regions around the interaction points, where the two beams share the same vacuum chamber. Recent developments toward a reliable numerical simulation of these incoherent effects driven by electron cloud are also presented.

## INTRODUCTION

In the Large Hadron Collider (LHC), electron cloud (e-cloud) effects [1] manifest through different observables, especially when using the nominal bunch spacing of 25 ns. In particular, impacting electrons can induce increased heat loads on the beam screen of the superconducting magnets [2]; they can drive coherent instabilities [3]; they can absorb energy from the stored beam leading to longitudinal phase shifts [4]; and, due to their non-linear electromagnetic fields, they can increase particles' diffusion in the transverse phase space, causing slow emittance growth [5] as well as slow beam losses [6, 7].

This contribution is focused on the e-cloud effect on the slow continuous beam losses observed with colliding beams during the 2018 run (for a description of the LHC configuration and operation during that period see reference [8]).

In the first part we review the available experimental observations, collected during physics runs and special tests, which allow identifying e-cloud as a key source of the observed losses and to show the strong effect of the non-linearity introduced by e-cloud in the final-focusing quadrupoles (Inner Triplets - ITs). In the second part, we present ongoing development to achieve reliable simulations of these effects. A method is developed that uses a high-order local interpolation scheme to apply the e-cloud forces, computed by numerical simulations of the cloud dynamics, in a way that preserves the symplecticity of the beam particle motion.

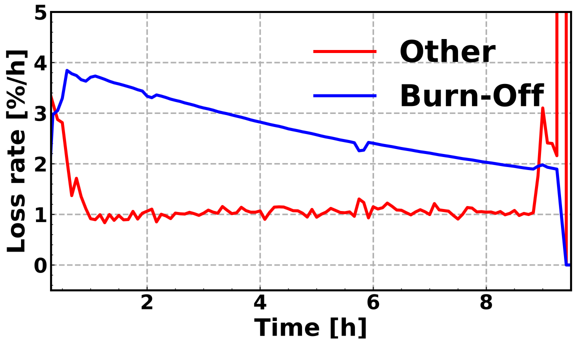


Figure 1: Beam losses from luminosity burn-off and from other sources during a typical LHC physics fill in 2018.

## EXPERIMENTAL OBSERVATIONS

In this section we present the analysis of the LHC beam losses with colliding beams, based on bunch-by-bunch intensity measurements from the LHC Fast Beam Current Transformer. We will focus on the beam circulating in the clockwise sense (so-called beam 1). The other beam presents similar features in the beam losses, although often less pronounced.

When the beams are colliding, a significant fraction of protons are lost due to luminosity burn-off. To identify the proton loss rate driven by other sources, the burn-off loss rate is estimated from luminosity measurements and subtracted from the measured loss rate [9].

### *Observations for a typical physics fill*

Figure 1 shows the burn-off loss rate (in blue) and the loss rate from other sources (in red) as they evolve during a typical physics fill, starting from the time at which the beams are brought in collision. It is possible to observe that, while burn-off losses gradually decrease during the fill following the luminosity decay, the additional losses exhibit a constant rate for most of the fill.

The LHC beam consists of several bunch trains separated by gaps of 800 ns between them. Each train is made of two or three batches of 48 bunches, with gaps of 200 ns between batches. Figure 2 shows the evolution of the loss rate for the different bunches in three consecutive trains. It is clear that bunches at the tails of the trains lose significantly more particles than those at the head of the trains, for the full duration of the fill. For all bunches the loss rate is practically constant during the fill. Stronger losses are observed at the beginning of the fill, right after collisions are established

* konstantinos.paraschou@cern.ch

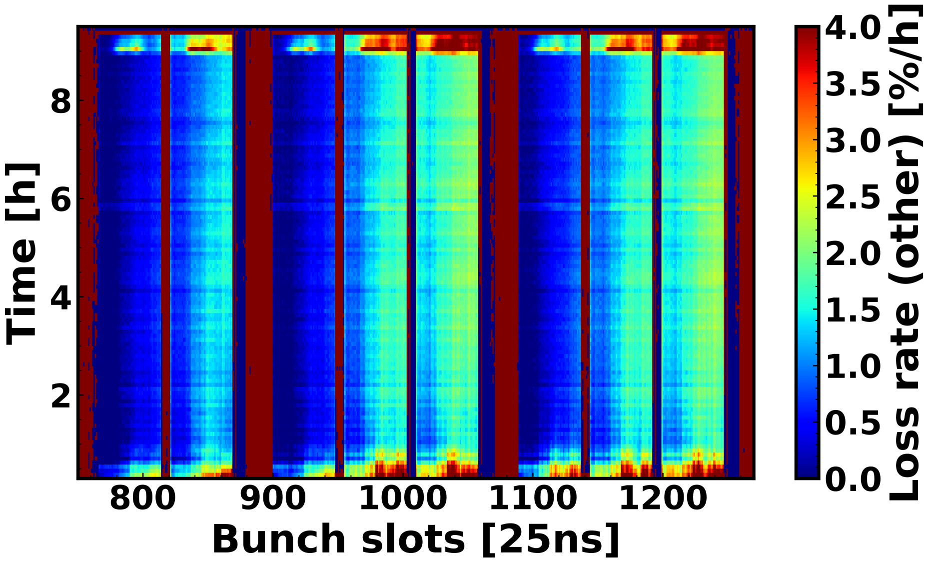


Figure 2: Bunch-by-bunch loss rate on three consecutive bunch trains during a typical LHC physics fill (loss rate from luminosity burn off is subtracted).

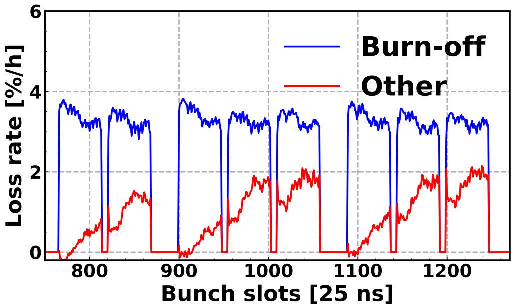


Figure 3: Comparison of the loss rates from burn-off and from other sources for the fill illustrated in Fig. 2 at the time $t = 2\,h$.

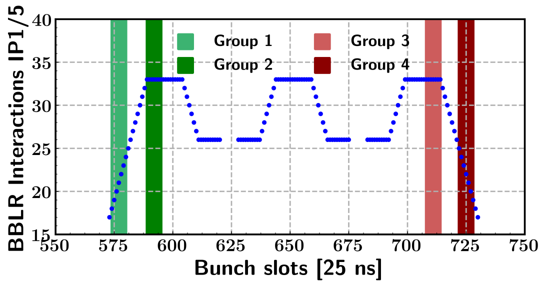


Figure 4: Number of BBLR interactions per interaction point for each bunch of a 3-batch train.

and towards the end of the fill, when the $\beta$-function at the two main experiments is reduced from 30 cm to 25 cm.

In Fig. 3, the bunch-by-bunch loss rates for burn-off and other sources are compared for a specific time ($t = 2\,h$). It is possible to notice that, while the burn-off rate is rather similar for all bunches, the additional losses strongly increase along the bunch train. Two main effects are expected to induce different loss rates for different bunches in the trains: e-cloud effects and Beam-Beam Long Range (BBLR) interactions [10].

To disentangle between these two effects, we select four groups of bunches along the trains (shown by the coloured bands in Fig. 4), having the following characteristics [6]:

**Group 1:** Bunches at the head of the leading batch of the train, experiencing the minimal amount of BBLR interactions and small e-cloud densities;

**Group 2:** Center of the leading batch of the train, experiencing the maximal amount of BBLR interactions and small e-cloud densities;

**Group 3:** Center of the trailing batch of the train, experiencing the maximal amount of BBLR interactions and large e-cloud densities;

**Group 4:** Tail of the trailing batch of the train, experiencing the minimal amount of BBLR interactions and large e-cloud densities.

Figure 5 shows the burn-off corrected losses as a function of time for these different groups of bunches. This analysis shows that the number of BBLR encounters has practically no impact on the observed losses, which instead tend to affect mostly the bunches at the tail of the trains. This observation points to e-cloud as the strongest source of the observed losses.

### *Effect of the crossing angle*

During typical physics fills, in order to increase the integrated luminosity, the crossing angle between the two beams at the interaction points is gradually decreased from 320 $\mu rad$ to 260 $\mu rad$, profiting from the fact that the BBLR interactions become weaker as the intensity of the beams decays [11].

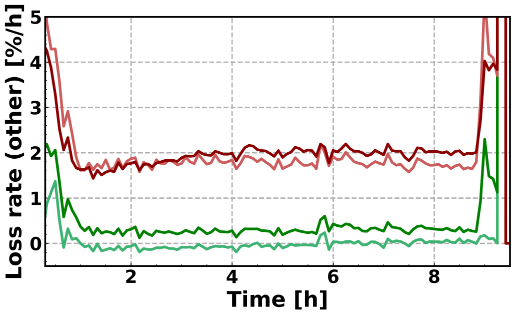


Figure 5: Loss rates measured for selected groups of bunches during a typical physics fill (color code defined in Fig. 4).

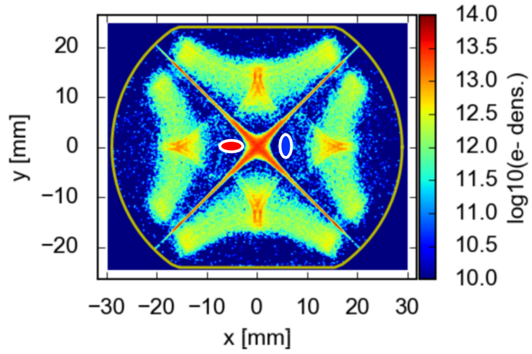


Figure 6: Electron density in one of the LHC IT quadrupoles (PyECLOUD simulation). The colored ellipses show the position and size of the two beams.

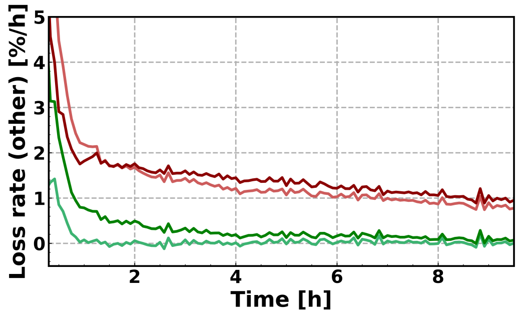


Figure 7: Loss rates measured for selected groups of bunches during a test fill performed with constant crossing angle (color code defined in Fig. 4).

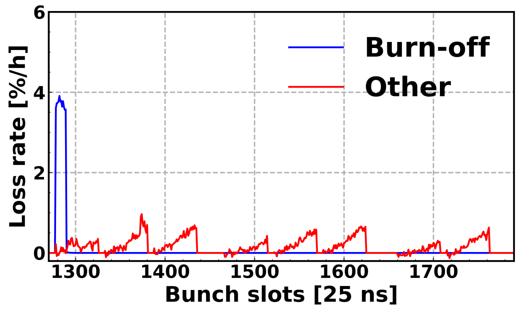


Figure 8: Loss rates measured with one circulating beam. In the other ring only 12 bunches are present, as it is visible on the burn-off trace.

In addition to changing the strength of the BBLR interactions, a reduction in the crossing angle can also change the interaction of the beams with the e-cloud in regions close to the interaction points, by shifting the orbit of the beams to a region with different electron densities (see Fig. 6).

During a test fill, the crossing angle was kept constant at 320 $\mu rad$ for the entire duration of the fill. The loss rates measured during this test are plotted in Fig. 7 with the same color code for the different bunch groups as in Fig. 5. Comparing Figs. 5 and 7, it is possible to observe a significant reduction of the loss rate when the crossing angle is kept constant, for all the bunch groups showing a visible loss rate. The fact that a dependence on the crossing angle is observed suggests that the e-cloud in the machine elements very close to the interaction point (in which a change in crossing angle results in a change in the electron density crossed by the beam) play a dominant role in generating the beam losses. The strongest e-cloud in the area develops in the LHC final-focusing quadrupoles (ITs) [12], and its effect on the beam is boosted by the extremely large $\beta$-function at their location.

### *Observations with a single circulating beam*

In another dedicated experiment, the beam losses were recorded with a single circulating beam, with the same machine and beam configuration used for physics fills. Only a small train of 12 bunches was injected in the second ring for technical reasons.

The loss rates measured during this experiment are shown in Fig. 8. These can be compared against those measured during a typical physics fill as shown in Fig. 3. With a single beam, the losses are significantly smaller. This is mainly due to the suppression of the strong non-linear forces from the beam-beam head-on interactions at the four collision points and to a reduced e-cloud density in the presence of one beam alone. Still a clear pattern along the trains is observed on the measured loss rates. In particular it is possible to observe that, with a single beam, the loss rate decreases significantly after the 200-ns gap separating the three batches of a same train, while this is not the case with two circulating beams.

This is due to a characterizing feature of the e-cloud in the ITs, revealed by e-cloud build-up simulations shown in Fig. 9, which is due to the fact that in these elements the two beams circulate in the same vacuum chamber [12]. Figure 9 a shows that, with one circulating beam, the electron density decays significantly between consecutive batches. With two beams, instead, this does not happen since, during the passage of the gap of one beam, bunches of the other beam are present in the chamber. Comparing Fig. 9 a to Fig. 8 and Fig. 9 b to Fig. 3, one can recognize the similarity between the bunch-by-bunch pattern on the loss rate and the electron density simulations.

### *Tests with a different optics configuration*

A confirmation of the fact that the losses are mainly driven by the e-cloud in the ITs is given by a test conducted to

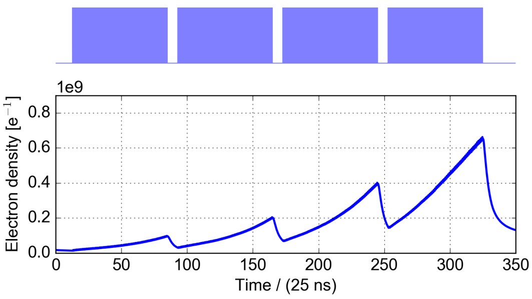


(a)

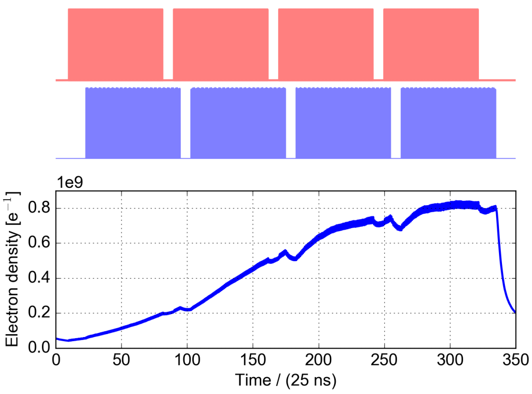


(b)

Figure 9: E-cloud build-up simulations with a) one beam and b) two beams in the common vacuum chamber of one of the IT quadrupoles.

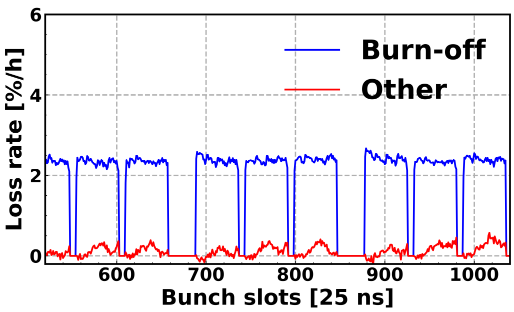


Figure 10: Bunch-by-bunch loss rates measured during a test fill with higher $\beta$-functions in the arcs and lower $\beta$-functions in the ITs.

validate a special beam optics configuration in preparation for the LHC Run 3 [13, 14].

During the test, the $\beta$-functions in half of LHC arcs were increased with respect to the configuration used for physics fills while the $\beta$-function in the ITs was significantly decreased (as the test was performed with larger $\beta$-function at the collision points). The measured bunch-by-bunch losses are shown in Fig. 10 and are much lower compared to those measured during typical physics fills as shown in Fig. 8. This can be ascribed to the fact that a reduced $\beta$-function at the ITs results in a weaker effect of the e-cloud at those locations.

## SIMULATION OF INCOHERENT EFFECTS INDUCED BY ELECTRON CLOUD

The modelling and simulation of incoherent effects driven by e-cloud, has been addressed in the past by several authors. Benedetto et al. in [15] use maps recorded from a macroparticle simulation of the cloud dynamics to apply the e-cloud forces on the beam particles at each turn. As the maps are saved on a discrete grid, an interpolation scheme needs to be used to compute the forces at each turn. In general, as we will discuss in the following, the resulting kick can become artificially non-symplectic, which is known to generate artefacts on the simulated long-term dynamics of the beam particles [16]. Symplectic kicks can be obtained by using strongly simplified cloud distributions for which the kick can be expressed analytically, as done by Ohmi et al. in [17] or by Franchetti et al. in [18]. This approach on the other hand does not allow a realistic modelling of the cloud distribution, especially in the presence of dipolar and quadrupolar magnetic fields. To obtain a realistic model of the non-linear beam dynamics in the presence of e-cloud, which would allow simulating the very long time scales involved in the slow beam degradation illustrated in the previous section, we developed a numerical scheme that allows to apply a recorded field map in a way that preserves symplecticity. This approach will be presented in the following subsections, together with some numerical examples.

### *The electron cloud kick*

It is possible to show [19] that, in the ultra-relativistic limit, the interaction of a beam particle with a short section of accelerator can be modelled with a "thin lens" map having the following form:

$$x \mapsto x \tag{1}$$

$$p_x \mapsto p_x - \frac{qL}{\beta_0 P_0 c}\frac{\partial \phi}{\partial x}(x, y, \tau) \tag{2}$$

$$y \mapsto y \tag{3}$$

$$p_y \mapsto p_y - \frac{qL}{\beta_0 P_0 c}\frac{\partial \phi}{\partial y}(x, y, \tau) \tag{4}$$

$$\tau \mapsto \tau \tag{5}$$

$$p_t \mapsto p_t - \frac{qL}{\beta_0 P_0 c}\frac{\partial \phi}{\partial \tau}(x, y, \tau) \tag{6}$$

where $\tau = \frac{s}{\beta_0} - ct$ and $p_t = \frac{E-E_0}{P_0 c}$ are canonically conjugate longitudinal variables, $E$ is the energy of the particle, $E_0, P_0$ are the energy and momentum of the reference particle respectively, $\beta_0$ is the relativistic Lorentz factors of the reference particle, $q$ is the charge of the interacting particle, $L$ is the length of the interacting e-cloud, and $\phi(x, y, \tau)$ is the scalar potential describing the e-cloud, which can be obtained by solving a 2D Poisson problem.

For the simulation of collective instabilities driven by e-clouds the kick on the longitudinal momentum is typically neglected and the kicks on the transverse momenta are computed by interpolating linearly a map defined on a discrete rectangular grid.

Although this algorithm is convenient to simulate instabilities, it is not suited to simulate slow beam losses. Its biggest drawback is the fact that the map is not symplectic for two reasons. The first reason is that since $\phi$ is dependent on all three variables $x, y, \tau$, symplecticity is lost if the change in $p_t$ is neglected. This however can easily be solved by simply applying also the longitudinal kick in Eq. 6.

The second reason is the fact that linear interpolation is used on a grid of derivatives of $\phi$, estimated with finite differences. It is easy to show that the thin-lens map of Eq. 1-6 is symplectic if [20]:

$$\frac{\partial}{\partial x}\left(\frac{\partial \phi}{\partial y}\right) = \frac{\partial}{\partial y}\left(\frac{\partial \phi}{\partial x}\right) \tag{7}$$

$$\frac{\partial}{\partial y}\left(\frac{\partial \phi}{\partial \tau}\right) = \frac{\partial}{\partial \tau}\left(\frac{\partial \phi}{\partial y}\right) \tag{8}$$

$$\frac{\partial}{\partial \tau}\left(\frac{\partial \phi}{\partial x}\right) = \frac{\partial}{\partial x}\left(\frac{\partial \phi}{\partial \tau}\right) \tag{9}$$

These conditions would be satisfied automatically if the functions $\frac{\partial \phi}{\partial x}, \frac{\partial \phi}{\partial y}, \frac{\partial \phi}{\partial \tau}$ were analytical derivatives of a well behaved function $\phi(x, y, \tau)$, while they are in general not verified when using a linear interpolation scheme [20].

The conditions given by Eqs. 7 - 8, can be verified using a "tricubic interpolation" scheme [21]. In each grid cell, the potential $\phi$ is approximated by a third order polynomial:

$$\phi(x, y, \tau) = \sum_{i=0}^{3}\sum_{j=0}^{3}\sum_{k=0}^{3} a_{ijk} x^i y^j \tau^k \tag{10}$$

where the coefficients $a_{ijk}$ change from cell to cell of the three-dimensional grid in a way that ensures continuity of the quantities:

$$\left\{\phi, \frac{\partial \phi}{\partial x}, \frac{\partial \phi}{\partial y}, \frac{\partial \phi}{\partial \tau}, \frac{\partial^2 \phi}{\partial x \partial y}, \frac{\partial^2 \phi}{\partial x \partial \tau}, \frac{\partial^2 \phi}{\partial y \partial \tau}, \frac{\partial^3 \phi}{\partial x \partial y \partial \tau}\right\} \tag{11}$$

To find the 64 coefficients $a_{ijk}$, the eight quantities of the set in Eq. 11 must be provided in all of the eight vertices of the cell. A finite difference scheme is employed to compute the required derivatives.

### *Application to a PyECLOUD simulation and mitigation of numerical artefacts*

The method described above has been tested on a map generated by simulating the e-cloud dynamics using the PyECLOUD code [22, 23] (the initial distribution of electrons is uniform and there is no externally applied magnetic field). Figure 11 shows the horizontal field $E_x = -\frac{\partial \phi}{\partial x}$ close to the center of the chamber ($x = 0.027\sigma$, $y = 0$, with $\sigma$ being the r.m.s. beam size) as a function of the longitudinal coordinate $\tau$, as derived with finite differences on the grid (black points) and the result of the interpolation (red line).

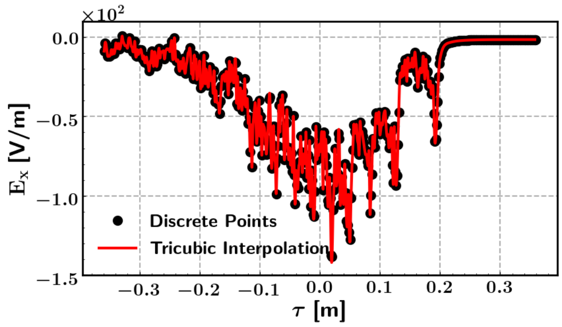


Figure 11: Horizontal field with respect to the longitudinal position for a beam particle close to the center of the beam chamber, as obtained from a single macroparticle simulation of the e-cloud dynamics.

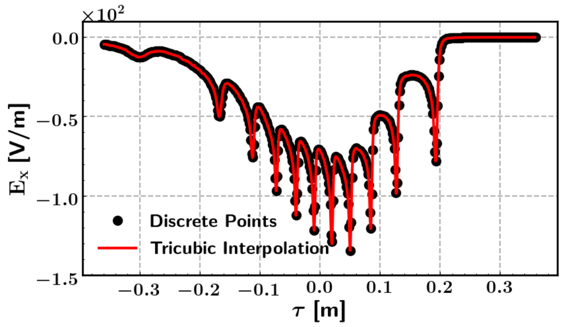


Figure 12: Horizontal field with respect to the longitudinal position for a beam particle close to the center of the beam chamber, as obtained from the average of 1000 macroparticle simulation of the e-cloud dynamics with different random seeds.

It is apparent that the simulation suffers from noise, as it can be expected from Particle-In-Cell macroparticle simulations. The noise can be effectively mitigated by averaging 1000 simulations with different random seeds. The result of the averaging shown in Fig. 12 uncovers the clear and physical structure of the modulated field produced by the e-cloud dynamics.

The interpolation technique shows some shortcomings in locations where the derivatives change rapidly. This can be seen in Fig. 13 where the horizontal field $E_x$ is drawn against the horizontal position on the axial cut of the chamber ($y = 0$) during the passage of the synchronous particle ($\tau = 0$).

The source of these artefacts was identified to be the insufficient accuracy of the derivatives evaluated with the finite difference method. To acquire more accurate estimates of $\phi$ and its derivatives, we perform a linear interpolation of the electron charge distribution on a finer grid and we obtain a refined potential by solving Poisson's equation on such a grid. By applying the finite difference scheme on this new solution we also obtain better estimates of the derivatives.

To limit the memory consumption though, the new quantities $\left\{\phi, \frac{\partial \phi}{\partial x}, \frac{\partial \phi}{\partial y}, \frac{\partial \phi}{\partial \tau}, \frac{\partial^2 \phi}{\partial x \partial y}, \frac{\partial^2 \phi}{\partial x \partial \tau}, \frac{\partial^2 \phi}{\partial y \partial \tau}, \frac{\partial^3 \phi}{\partial x \partial y \partial \tau}\right\}$ are only kept on the original coarser grid. The result of this refine-

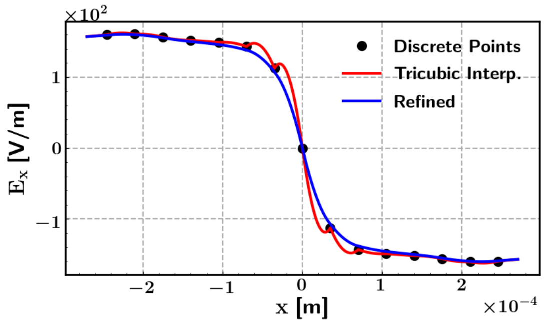


Figure 13: Horizontal field with respect to the horizontal position for a beam particle at $y = 0$, $\tau = 0$ before and after performing the refinement procedure.

ment algorithm is shown by the blue trace in Fig. 13, where it can be seen that the interpolation scheme no longer suffers from the "overshooting" artefacts [24].

To identify the effect of suppressing the artefacts, beam particles are tracked through a linear one-dimensional machine with Courant-Snyder parameters $\alpha_x = 2.3$, $\beta_x = 120\,m$, a tune of $Q_x = 0.3$ and a single e-cloud interaction. The structure of the horizontal phase space (Poincaré map) in normalized coordinates[1] is shown in Fig. 14 a when using the kick without the refinement and in Fig. 14 b when using the kick with the refinement. It is apparent that in Fig. 14 a the phase space shows considerably more (artificial) irregular motion between resonance islands compared to Fig. 14 b.

## CONCLUSIONS

The measured loss rates observed at the LHC during 2018 collision fills exceeded by a significant fraction the expectations from luminosity burn-off.

The analysis of the loss rate at a bunch-by-bunch level shows that electron clouds are the main mechanism driving the observed beam losses. Dedicated experiments showing the sensitivity to the crossing angle, the behavior with a single circulating beam and the effect of the optics configuration, highlight the important role played by the e-cloud in the ITs.

To model and simulate these effects, a direct approach has been developed that uses symplectic maps based on a tricubic interpolation scheme, which is applied to e-cloud maps from macroparticle simulations. Special care had to be taken to suppress macroparticle noise and avoid interpolation artefacts. First tracking tests showed the importance of addressing these issues to have a reliable simulation of the beam particle motion.

[1] The normalized coordinates $(\hat{x}, \hat{p}_x)$ are related to the physical coordinates $(x, p_x)$ through $\begin{pmatrix}\hat{x}\\ \hat{p}_x\end{pmatrix} = \begin{pmatrix}\frac{1}{\sqrt{\beta_x}} & 0\\ \frac{\alpha_x}{\sqrt{\beta_x}} & \sqrt{\beta_x}\end{pmatrix}\begin{pmatrix}x\\ p_x\end{pmatrix}$

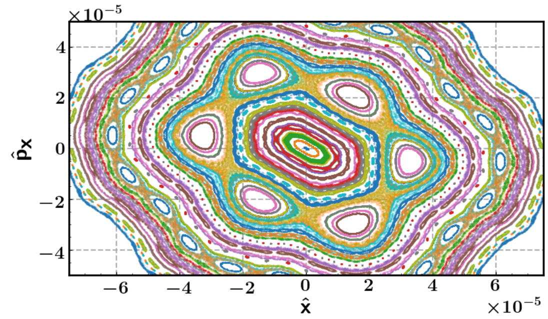


(a)

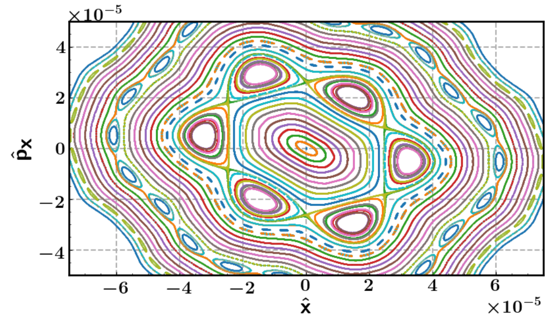


(b)

Figure 14: Normalized phase space ($\hat{x} - \hat{p_x}$) of particles tracked with the e-cloud map without (a) and with (b) the refinement procedure. Different colors correspond to particles tracked with different initial conditions.

## ACKNOWLEDGEMENTS

The authors would like to thank F. Antoniou, G. Arduini, H. Bartosik, I. Efthymiopoulos, S. Fartoukh, N. Karastathis, S. Kostoglou, E. Métral, Y. Papaphilippou, D. Pellegrini, G. Rumolo, G. Sterbini for their important input and support to the presented work.

## REFERENCES

[1] G. Iadarola and G. Rumolo, "Electron cloud effects", in *Proc. ICFA Mini-Workshop on Impedances and Beam Instabilities in Particle Accelerators*, Benevento, Italy, Sep. 2018, pp. 49–56. `doi:10.23732/CYRCP-2018-001.49`

[2] G. Skripka *et al.*, "Comparison of Electron Cloud Build-Up Simulations Against Heat Load Measurements for the LHC Arcs With Different Beam Configurations", in *Proc. 10th Int. Particle Accelerator Conf. (IPAC'19)*, Melbourne, Australia, Jun. 2019, pp. 3232–3235. `doi:10.18429/JACoW-IPAC2019-WEPTS051`

[3] A. Romano *et al.*, "Electron cloud buildup driving spontaneous vertical instabilities of stored beams in the Large Hadron Collider", *Phys. Rev. ST Accel. Beams*, vol. 21, pp. 061002, Jun. 2018. `doi:10.1103/PhysRevAccelBeams.21.061002`

[4] Esteban Müller, J. F. *et al.*, "High-accuracy diagnostic tool for electron cloud observation in the LHC based on synchronous phase measurements", *Phys. Rev. ST Accel. Beams*, vol. 18, pp. 112801, Nov. 2015. `doi:10.1103/PhysRevSTAB.18.112801`

[5] S. Papadopoulou *et al.*, "Monitoring and Modelling of the LHC Emittance and Luminosity Evolution in 2018", in *Proc. 10th Int. Particle Accelerator Conf. (IPAC'19)*, Melbourne, Australia, Jun. 2019, pp. 3212–3215. `doi:10.18429/JACoW-IPAC2019-WEPTS046`

[6] K. Paraschou *et al.*, "Analysis on Bunch-by-Bunch Beam Losses at 6.5 TeV in the Large Hadron Collider", in *Proc. 10th Int. Particle Accelerator Conf. (IPAC'19)*, Melbourne, Australia, Jun. 2019, pp. 500–503. `doi:10.18429/JACoW-IPAC2019-MOPMP029`

[7] S. Kostoglou *et al.*, "Luminosity, lifetime and modelling ", presented at the 9th LHC Operations Evian Workshop, Evian, France, Jan. 2019. `https://indico.cern.ch/event/751857/contributions/3259405/`.

[8] J. Wenninger, "Operation and configuration of the LHC in run 2", CERN, Geneva, Switzerland, Rep. CERN-ACC-NOTE-2019-0007, Mar. 2019.

[9] N. Karastathis *et al.*, "Monitoring and modeling of the LHC luminosity evolution in 2017", in *Proc. 9th Int. Particle Accelerator Conf. (IPAC'18)*, Vancouver, BC, Canada, Apr.–May 2018, pp. 224–227. `doi:10.18429/JACoW-IPAC2018-MOPMF052`

[10] W. Herr *et al.*, "Long range beam-beam effects in the LHC", in *Proc. ICFA Mini-Workshop on Beam-Beam Effects in Hadron Colliders (BB2013)*, CERN, Geneva, Switzerland, Mar. 2013, pp. 87–92. `doi:10.5170/CERN-2014-004.87`

[11] N. Karastathis *et al.*, "Crossing Angle Anti-Leveling at the LHC in 2017", in *Proc. 9th Int. Particle Accelerator Conf. (IPAC'18)*, Vancouver, BC, Canada, Apr.–May 2018, pp. 184–187. `doi:10.18429/JACoW-IPAC2018-MOPMF040`

[12] G. Skripka, G. Iadarola and A. Romano, "Electron cloud build up in two-beam regions for HL-LHC: heat load and vacuum aspects", presented at ECLOUD'18, Elba, Italy, Jun. 2018. Proceeding to be published. `https://agenda.infn.it/event/13351/contributions/18959/`.

[13] S. Fartoukh, "Achromatic telescopic squeezing scheme and application to the LHC and its luminosity upgrade", *Phys. Rev. ST Accel. Beams*, vol. 16, pp. 111002, Nov. 2013. `doi:10.1103/PhysRevSTAB.16.111002`

[14] S. Fartoukh, A. Mereghetti and M. Solfaroli, "MD3270 Round ATS + MD4023 TCDQ levelling", presented at the LHC Studies Working Group meeting, CERN, Geneva, Switzerland, Nov. 2018. `https://indico.cern.ch/event/772189/contributions/3209049/`.

[15] E. Benedetto *et al.*, "Incoherent Effects of Electron Clouds in Proton Storage Rings", *Phys. Rev. Lett.*, vol. 97, pp. 034801, Jul. 2006. `doi:10.1103/PhysRevLett.97.034801`

[16] W. Herr, "Mathematical and Numerical Methods for Nonlinear Beam Dynamics", in *CAS - CERN Accelerator School: Advanced Accelerator Physics Course*, Trondheim, Norway, Aug. 2013, pp.157–198. `doi:10.5170/CERN-2014-009.157`

[17] K. Ohmi and K. Oide, "Chaos and emittance growth due to nonlinear interactions in a circular accelerator", *Phys. Rev. ST Accel. Beams*, vol. 10, pp. 014401, Jan. 2007. `doi:10.1103/PhysRevSTAB.10.014401`

[18] G. Franchetti *et al.*, "Incoherent effect of space charge and electron cloud", *Phys. Rev. ST Accel. Beams*, vol. 12, pp. 124401, Dec. 2009. `doi:10.1103/PhysRevSTAB.12.124401`

[19] G. Iadarola, "Modelling the interaction of a relativistic beam particle with an electron cloud ", CERN, Geneva, Switzerland, Rep. CERN-ACC-NOTE-2019-0033, Aug. 2019. `https://cds.cern.ch/record/2684858/`.

[20] K. Paraschou, G. Iadarola, "Symplectic kicks from an e-cloud pinch", presented at Electron Cloud Meeting #67, CERN, Geneva, Switzerland, Nov. 2019. `https://indico.cern.ch/event/811014/contributions/3379525/`.

[21] F. Lekien and J. E. Marsden, "Tricubic Interpolation in Three Dimensions", *Int. J. Numer. Meth. Engng.*, vol. 63, pp.455—471, Mar. 2005. `doi:10.1002/nme.1296`

[22] G. Iadarola *et al.*, "Evolution of Python Tools for the Simulation of Electron Cloud Effects", in *Proc. 8th Int. Particle Accelerator Conf. (IPAC'17)*, Copenhagen, Denmark, May 2017, pp.3803–3806. `doi:10.18429/JACoW-IPAC2017-THPAB043`

[23] G. Iadarola *et al.*, "PyECLOUD". `https://github.com/PyCOMPLETE/PyECLOUD/`.

[24] K. Paraschou, G. Iadarola, "Update on development for single-particle tracking with e-cloud", presented at Electron Cloud Meeting #72, CERN, Geneva, Switzerland, Nov. 2019. `https://indico.cern.ch/event/862798/contributions/3635364/`.

# IMPACT OF COHERENT AND INCOHERENT BEAM-BEAM EFFECTS ON THE BEAMS STABILITY

X. Buffat*, CERN, Geneva, Switzerland

*Abstract*

Various coherent instability mechanisms involving colliding beams are described together with techniques for their mitigation. They are illustrated with some examples based mostly on the recent experience at the Large Hadron Collider.

## INTRODUCTION

The stability of the two beams in high energy particle colliders is heavily impacted by the electromagnetic forces that they exert on each other, the so-called beam-beam forces. The coherent oscillation of the two beams against each other may be driven unstable through a resonant mechanism or via an interaction with the machine impedance. Such instabilities are discussed in the next section. In other cases, the stabilising mechanism of single beam instabilities is jeopardised by the incoherent effects of beam-beam interactions. This occurs for example when the amplitude detuning driven by the beam-beam interaction is such that it compensates Landau damping for the head-tail instability. The description of these instability mechanisms involving coherent and incoherent beam-beam effects are briefly reviewed in the next two sections respectively. We then conclude with a summary of the corresponding mitigation techniques.

## COHERENT BEAM-BEAM MODES

### *Resonant instability*

The coupling of the two beams through the beam-beam interactions give rise to new modes of oscillation which may become unstable if their frequency matches a low order resonance driven by the lattice or by the beam-beam interactions themselves. In the simplest configuration of two symmetric beams colliding at a single interaction point, one finds two modes of oscillation corresponding to in and out of phase motion of the two beams at the Interaction Point (IP). The spectrum resulting from a self-consistent macro-particle simulation exhibiting these so-called $\sigma$- and $\pi$-modes is shown in Fig. 1. Their frequencies can be derived analytically [2], consequently it is rather straight forward to avoid resonant conditions. In more complex machines involving multiple bunches per beam, multiple IPs with asymmetric phase advances between them or even unequal revolution frequencies, the number of coherent beam-beam modes increases rapidly. Additionally, coherent synchro-betatron resonances may appear in colliders featuring collision with a significant synchro-betatron coupling due for example to a crossing angle between the beams or to the hourglass effect. Avoiding resonant conditions may become challenging and imposes

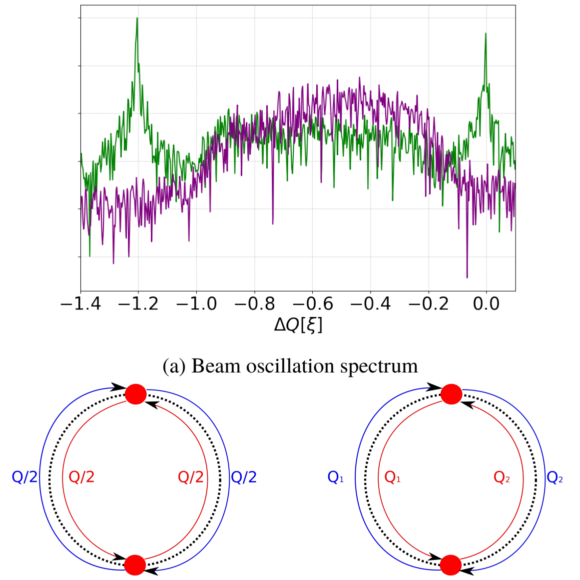


(a) Beam oscillation spectrum

(b) Symmetric phase advances

(c) Asymmetric phase advances

Figure 1: Beam oscillation spectrum of two colliding beams experiencing two head-on beam-beam interactions at opposite azimuth in symmetric rings (top plot). The beams are round at the IP and the spectrum is obtained with self-consistent macro-particle simulations (COMBI [1]). The green curve represents a configuration with equal phase advances between the IPs, as illustrated on the bottom left plot. The purple curve correspond to a configuration where the phase advances were chosen such that the coherent mode frequencies are in the incoherent spectrum, at approximatively 0.4 and 0.6 times the beam-beam tune shift. ($Q = 1.31$, $Q_1 = 0.405$ and $Q_2 = 0.905$).

constraints on the machine layout and the phase advances between IPs. The frequency of the coherent beam-beam modes and the resonant conditions can only be obtained analytically in some specific cases. Otherwise the rigid bunch model, the circulant matrix model [3, 4] or macro-particle simulations may be used to address more realistic machine configurations.

Such instabilities were a concern for asymmetric B factories which eventually were not constructed [5, 6]. Nowadays these instability mechanisms regained interest with proposals of asymmetric electron ion colliders [7–9] and high energy electron-positron colliders with crab waist [10]. In order to illustrate a mitigation technique with an example, Fig. 2 shows the instability prediction for a simplistic linearised model of the Electron-ion collider in China (EicC) [9]. The results for different ratios of the revolution

* xavier.buffat@cern.ch

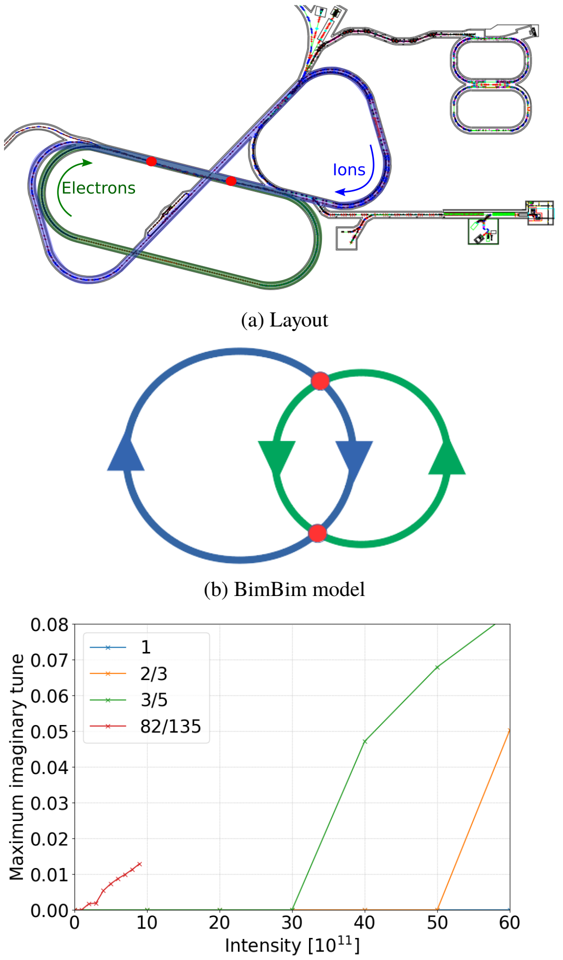


(a) Layout

(b) BimBim model

(c) Instability growth rate

Figure 2: Illustration of the EicC layout [9] featuring a 8-shape trajectory for the ions and a racetrack electron ring with two IPs in one common straight section (top plot). The topology of the rigid bunch model implemented in BimBim [11] is shown in the middle plot, the two IPs are marked with red dots and the phase advances with arrows. The lower plot shows the maximum imaginary part of the tune as a function of the bunch intensity (assumed equal in both beams) for different ratios between the electron and ion revolution frequency. Only the symmetric configuration does not feature any intensity limitation linked to coherent beam-beam resonance on the scale explored.

frequency between the two beams shows the importance of a proper choice of machine layout for the mitigation of coherent beam-beam instabilities which may limit the intensity reach of the collider. Similarly other parameters such as the machines tune and the phase advance between IPs may be adjusted to mitigate further the instabilities.

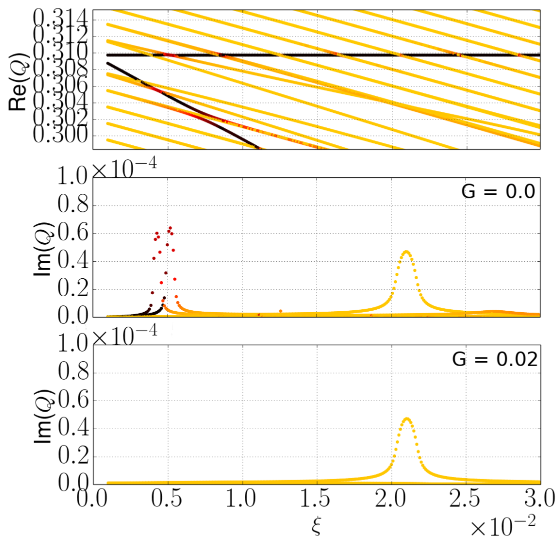


Figure 3: Mode coupling instability of two beams colliding at two IPs with alternating crossing angle. The Piwinski angle is 1.3 [12]. A resistive wall-type impedance drives the instability. The real parts (top plot) and imaginary parts of the tune (middle and lower plots) predicted with the circulant matrix model implemented in BimBim are colour coded based on their dipole moment from black (high) to yellow (low). In the lower plot, the mode coupling instability of low order head-tail modes is mitigated by an active feedback without intra-bunch capabilities.

### *Mode coupling instability*

Even if resonant conditions are avoided, the coherent beam-beam modes may be driven unstable by the machine impedance, resulting in the mode coupling instability of colliding beams [3, 4, 13]. As for the transverse mode coupling instability (TMCI), this instability may be mitigated with chromaticity and/or an active feedback, yet they are not always sufficient to fully suppress it. Figure 3 shows an example of mode coupling instability involving the $\sigma$- and $\pi$-modes, but also higher order head-tail modes in the presence of synchro-betatron resonance driven by a beam-beam interaction with a crossing angle. The active feedback based on the average position of the bunch is effective to suppress the instability of the $\sigma$- and $\pi$-modes, but not the coupling of head-tail modes +1 and +2. An active feedback with intra-bunch capabilities would be needed to stabilise such modes. Alternatively to active feedbacks, Landau damping constitutes an efficient mitigation, it is further discussed after the following discussion on longitudinal instabilities.

### *Longitudinal instabilities*

Most instabilities related to beam-beam interactions are in the transverse planes. Yet in the presence of a crossing angle, the beam-beam interaction leads to an energy change that depends on the longitudinal position of the particles [14]. We may expect that such a force generates longitudinal coherent

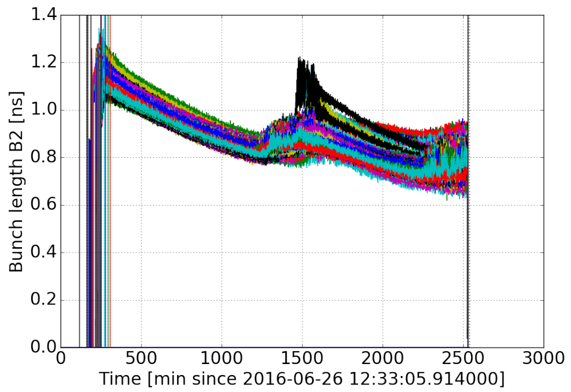


(a) Beam 2, all bunches

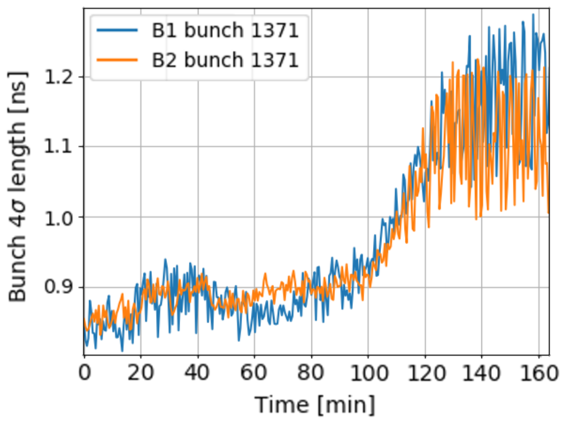


(b) Beam 1 and 2, one colliding bunch pair

Figure 4: Observation of correlated longitudinal oscillation of one colliding bunch pair at the LHC (2016). The upper plot shows the evolution of the bunch length of several bunches during a fill for physics. The impact of radiation damping is clearly visible until approximatively minute 1200, after which longitudinal Landau damping is lost [15]. At about minute 1500, the bunch length of some bunches increases significantly more than the others (e.g. black curve), indicating a different instability mechanism. For those bunches only, the longitudinal motion of bunch pairs colliding in the two main IPs shown on the lower plot seem correlated.

beam-beam modes. A correlation between the longitudinal oscillation of the two beams was observed in the LHC when the longitudinal emittance was let to shrink freely due to radiation damping, thus eventually losing longitudinal stability [15] (Fig. 4). Given the absence of limitation linked to this mechanism, the understanding of the so-called "Las Ketchup" instability remains limited.

### *Intrinsic Landau damping*

Due to its non-linear nature, the beam-beam interactions have an impact on the amplitude detuning and consequently on Landau damping. For a head-on collision, the frequency of oscillation of the individual particles in the beam extends from the beam-beam tune shift to the machine bare tune [16], forming the so-called incoherent spectrum. Since the $\sigma$- and $\pi$-mode frequencies are outside of the incoherent spectrum, Landau damping is not expected to affect their stability [16]. If a resonant condition cannot be avoided or if the mode coupling instability cannot be fully mitigated, Landau damping of the coherent beam-beam modes may be restored with a proper choice of phase advance between the IPs. An example of such a mitigation is shown in Fig. 1, where the phase advances were adjusted such that the coherent modes are all inside the incoherent spectrum, based on prediction from the rigid bunch model implemented in BimBim. In the presence of synchro-betatron coupling, Landau damping from the synchrchotron sidebands of the incoherent spectrum can be expected [16, 17]. Yet, currenty quantitative estimate of Landau damping in the presence of a given machine impedance is only obtained via macro-particle tracking simulations [18].

## LANDAU DAMPING OF THE HEAD-TAIL INSTABILITY

When instabilities of coherent beam-beam modes have been effectively mitigated, the impact of the beam-beam interactions on the amplitude detuning may still affect Landau damping of classical single beam instabilities. In high energy hadron colliders such as the LHC, the head-tail instability driven mainly by the collimators impedance remain a concern through all the cycle. Therefore, the impact of long-range, offset or head-on beam-beam interactions on the amplitude detuning during the various operational phases such as the betatron squeeze, the collapse of the separation bump or even luminosity levelling requires a dedicated control.

### *Beam-beam driven amplitude detuning*

Analytical expressions exist for the amplitude detuning generated by long-range and head-on beam-beam interactions [20, 21]. Based on those expressions, it is possible to estimate the impact of beam-beam interactions on Landau damping using the corresponding dispersion integral [22]. There exists configurations in which the beams collide with a small transverse offset between the beams (i.e. comparable to their r.m.s. transverse size) either transiently, e.g. when collapsing the separation bumps, or steadily, e.g. when levelling the luminosity or during Van der Meer scans. In such configurations, the estimation of the amplitude detuning is usually performed with single particle tracking codes. The tracking then serves as an input for the dispersion integral [23]. The amplitude detuning, and consequently the stability diagram, depends in a strongly non-linear manner on the offset between the beams in both transverse planes, the optical $\beta$ functions at the IP, the crossing and crab angles as well as on the beam intensity and emittances. It is therefore convenient to define a coherent stability factor that characterises the beam stability in order to ease the quantitative comparison between different configurations. We chose the highest ratio between the modulus of the

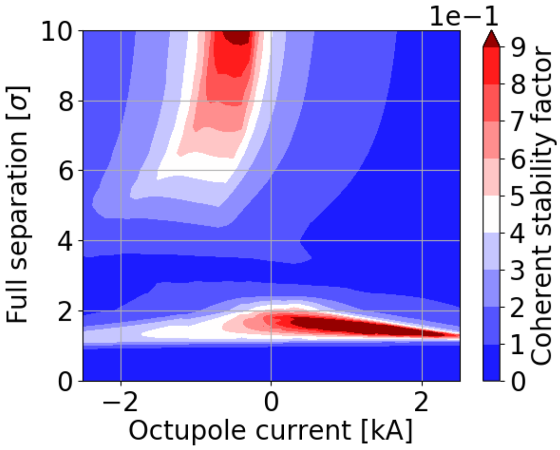


(a) $\phi$ = 250 $\mu$rad, $\phi_{CC}$ = 0

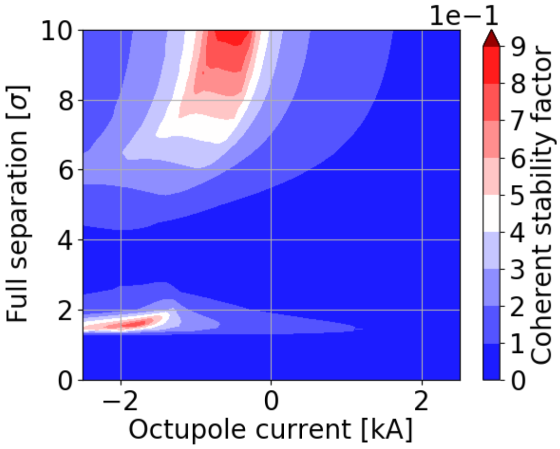


(b) $\phi$ = 250 $\mu$rad, $\phi_{CC}$ = −200 $\mu$rad

Figure 5: Coherent stability factor for different variations of the HL-LHC ultimate configuration [19] at the start of collision with offset beams in the two main IPs. The separation is in a different transverse plane in both IPs and varied simultaneously. The half-crossing angle $\phi$ is 250 $\mu$rad. The upper plot corresponds to a configuration without crab cavities and the lower plot to partial compensation of the crossing angle with crab cavities ($\phi_{CC}$=-200 $\mu$rad).

complex tune shifts to their respective projections on the stability diagram. Consequently a stability factor larger than one indicates an unstable configuration. Figure 5 illustrates the complexity of this configuration with estimates for the HL-LHC for different octupole currents and crab angles. One observes that, for large separations between the beams at the IP (larger than $10\sigma$, the r.m.s. beam size), the stability is dominated by the interplay between the arc octupole and the long-range interactions. In the convention chosen, the negative octupole current induces a negative direct detuning term which compensates the one of the long-range interactions, such that positive currents are favourable. The offset interaction at the two IPs further increases this difference for separations down to approximatively $6\sigma$. For a lower separation, the additional spread from the offset interaction at the IPs increases significantly the stability diagram, except between approximatively 1.5 and 2.0 $\sigma$. This minimum of stability corresponds to the configuration when the particles oscillating with a low amplitude, i.e. the beam core, reaches the maximum of the beam-beam force which corresponds to a zero of the first order detuning term. In this configuration the stability is entirely determined by the higher order detuning terms. In the configuration considered here, we find that the negative octupole currents are favourable in absence of crab cavities, while the positive polarity remains favourable when the crossing angle is compensated with crab cavities.
At the LHC, instabilities observed while levelling the luminosity [23] and during Van der Meer scans [24] can be attributed to the loss of Landau damping with offset beams. They were mitigated by ensuring that the bunches colliding with an offset at one IP also collide head-on in another, thus restoring Landau damping. A proper choice of external detuning using dedicated non-linear magnets (e.g. octupoles) may also mitigate this instability, requiring a detailed understanding of the non-linear dynamics in the configuration considered. Such a control was demonstrated in a dedicated experiment at the LHC [25, 26]. In the same experiment, it was also shown that transient unstable configurations such as the one described in Fig. 5 can be acceptable if short enough with respect to the instability rise time, similarly to the crossing of transition in low energy machine.

The head-on beam-beam interaction is significantly more efficient than octupole magnets at providing Landau damping with a limited impact on the beam quality thanks to the large amplitude detuning generated for particles oscillating at a low amplitude which vanishes at high amplitude [23]. In some cases, the head-on beam-beam interaction can therefore become a mitigation of coherent instabilities. Future hadron collider projects feature a cycle with collision as early as possible in the cycle thus profiting from this stabilising force [27, 28]. Electron lenses mimicking the head-on beam-beam force were also proposed as an alternative to non-linear magnets to provide Landau damping [29].

### *PACMAN linear coupling*

Most modern colliders feature several bunches which, in some cases, are non-uniformly distributed along the machine due to the need for long empty gaps for injection and extraction at the various steps of the injector chain as well as in the collider ring. As a result, different bunches may experience a different set of beam-beam interactions. Consequently, a given correction of a beam-beam driven effect with a global scheme cannot be made optimal for all bunches, it is the so-called PACMAN effect [30]. An important aspect for the beam stability is the presence of beam-beam interactions with a non-zero separation on a skew transverse plane leading to linear coupling, as the latter can significantly deteriorate Landau damping [31]. The impossibility to correct this contribution with a global scheme imposes constraints

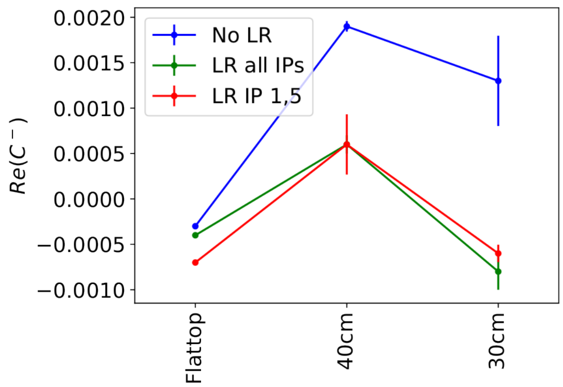


Figure 6: Linear coupling measured with the AC-dipole method [32] at different stages of a cycle of the LHC with a fully filled machine (2700 bunches). The three bunches considered experience no beam-beam collision (blue), collision in the two main IPs (red) and all beam-beam interactions (green) as indicated by the legend. The flat top phase is characterised by weak beam-beam interactions, thus linear coupling is identical for all bunches. The squeeze of the $\beta$ function at the main IPs to 40 cm increases the strength of long-range interactions there, thus generating a difference in coupling between non-colliding and colliding bunches. This difference is further increased when squeezing down to 30 cm.

on the orbit control such that skew beam-beam interactions are avoided.

In the particular case of the LHC and HL-LHC, the crossing angles in all IPs are either horizontal or vertical by design. In reality various effects may result in skew beam-beam interactions. In some parts of the cycle the combination of crossing angle and parallel separation bumps can lead to skew long-range interactions. Additionally, the measurement of orbit misalignments within the common beam chamber is rather challenging, and roll angles in the order of 10° may be expected [33]. Beam-beam induced orbit effects at other IPs may also add to the misalignment of the crossing angles with a PACMAN component [34]. The self-consistent code TRAIN [35] was recently updated to compute PACMAN linear coupling [34], showing results compatible with dedicated bunch-by-bunch measurement of linear coupling at the LHC (Fig. 6).

## CONCLUSION

Already at the level of linear stability the coupling between additional degrees of freedom generated by the beam-beam interactions with respect to a single beam model generate a large variety of coherent resonances that have to be avoided. Mitigation of these instabilities usually involve the machine layout, the tunes in all degrees of freedom and the phase advance between IPs.

Mode coupling instabilities may occur when the coherent beam-beam modes interact with head-tail modes driven unstable by the machine impedance. They may be mitigated by a combination of the transverse feedback and chromaticity. Additionally, the machine tunes or the phase advance between IPs may be used to enhance Landau damping by controlling the mode frequencies with respect to the incoherent spectrum generated by the beam-beam interactions.

For both resonant and mode coupling instabilities, the rigid-bunch model and a 6D extension of it, the circulant matrix model, are mostly used for the understanding of linear stability. Analytical derivations of the impact of the non-linearities on the frequency of the coherent modes and their damping via Landau damping exist for some specific cases, but quantitative estimates in realistic configurations are mostly obtained with self-consistent macro-particle simulation.

Single beam instability mechanisms are affected by the amplitude detuning generated by the beam-beam interactions even if the proper measures are taken to fully suppress coherent beam-beam instabilities. The additional tune spread may be beneficial. The head-on interaction is particularly well suited to generate a large stability diagram thanks to its strong action on the beam core and vanishing for the beam tail. On the other hand in some configurations the amplitude detuning generated by the beam-beam interaction may compensate other sources and result in a loss of Landau damping. A detailed understanding of the non-linear dynamics including the machine non-linearities as well as the beam-beam interactions is required to ensure that the tune spread remains sufficient through the cycle. The mitigation of this mechanism for loss of Landau damping often requires a dedicated controlled source of detuning such as octupole magnets as well as operational procedures that avoids critical configurations and/or cross through the unstable configuration faster than the instability rise time.

## REFERENCES


[1] T. Pieloni, “A study of beam-beam effects in hadron colliders with a large number of bunches,” PhD thesis, EPFL, 2008.

[2] K. Yokoya and H. Koiso, “Tune shift of coherent beam-beam oscillations,” *Part. Acc.*, vol. 27, pp. 181–186, 1990.

[3] E. A. Perevedentsev and A. A. Valishev, “Simulation of the head-tail instability of colliding bunches,” *Phys. Rev. ST Accel. Beams*, vol. 4, p. 024 403, 2 Feb. 2001.

[4] X. Buffat, “The circulant matrix model and the role of beam-beam effects in coherent instabilities,” in *Proceedings of the ICFA Mini-Workshop on Impedances and Beam Instabilities in particle accelerators*, Benevento, Italy: JACoW, 18-22 Sept. 2017.

[5] K. Hirata and E. Keil, “Coherent beam-beam interaction limit in asymmetric ring colliders,” *Phys. Lett. B*, vol. 232, pp. 413–416, 3 Dec. 1989.

[6] M. Zobov and Y. Zhang, “Coherent beam-beam resonances in SuperB with asymmetric rings,” in *Proceedings of the 2nd International Particle Accelerator Conference*, San Sebastián, Spain: JACoW, Apr. 2011, pp. 592–594.

[7] S. Abeyratne *et al.*, *Science requirements and conceptual design for a polarized medium energy electron-ion collider at jefferson lab*, arXiv:1209.0757, 2012.

[8] I. Neththikumara, B. Terzić, G. Kraft, and Y. Roblin, “Electron-ion collider performance studies with beam sychronisation via gear-change,” in *Proceedings of the 3rd North American Particle Accelerator Conference*, Lansing, Michigan, USA: JACoW, Jan. 2019.

[9] X. Chen, *A plan for electron ion collider in china*, arXiv:1809.00448, 2018.

[10] D. Shatilov, *IP Beam Parameter Optimization for FCC-ee*, Presentation at the FCC Week, Amsterdam, Netherlands, 11 Apr. 2018.

[11] X. Buffat, “Transverse beams stability studies at the large hadron collider,” PhD thesis, EPFL, 2015.

[12] A. Piwinski, “Observations of beam-beam effects in petra,” *IEEE Trans. Nucl. Sci.*, vol. NS-26, p. 4286, 3 1979.

[13] S. White, X. Buffat, N. Mounet, and T. Pieloni, “Transverse mode coupling instability of colliding beams,” *Phys. Rev. ST Accel. Beams*, vol. 17, p. 041 002, 4 Apr. 2014.

[14] K. Hirata, H. Moshammer, and F. Ruggiero, “A symplectic beam-beam interaction with energy change,” *Part. Accel.*, vol. 40, pp. 205–228, 1993.

[15] H. Timko, P. Baudrenghien, O. Brunner, A. Butterworth, J. E. Muller, and E. Shaposhnikova, “Operational and beam dynamics aspects of the RF system in 2016,” in *Proceedings of the 2016 Evian workshop on LHC beam operation*, Evian-les-Bains, France, 13 - 15 Dec. 2016.

[16] Y. Alexahin, “A study of the coherent beam-beam effect in the framework of Vlasov perturbation theory,” *Nucl. Instrum. Methods Phys. Res. A*, vol. 480, no. 2, pp. 253–288, 2002.

[17] W. Herr and R. Paparella, “Landau damping of coherent beam-beam modes by overlap with synchrotron side-bands,” CERN, Geneva, Switzerland, Tech. Rep. LHC Project Note 304, Oct. 2002.

[18] L. Barraud and X. Buffat, “Mode coupling instability of colliding beams in the HL-LHC,” CERN, Geneva, Switzerland, Tech. Rep. ACC-NOTE-2019-0032, Jul. 2019.

[19] E. Métral *et al.*, “Update of the HL-LHC operational scenarios for proton operation,” CERN, Geneva, Switzerland, Tech. Rep. ATS-Note-2018, Jan. 2018.

[20] D. Neuffer and S. Peggs, “Beam-beam tune shift and spreads in the SSC - head on, long range and PACMAN conditions,” Superconducting Super Collider Laboratory, Dallas, USA, Tech. Rep. SSC-63, Apr. 1986.

[21] A. Chao, “Lecture notes on topics in accelerator physics,” SLAC, Standford, USA, Tech. Rep. SLAC-PUB-9574, 2002.

[22] J.S.Berg and F. Ruggiero, “Landau damping with two-dimensional betatron tune spread,” CERN, Geneva, Tech. Rep. SL-96-071-AP, Dec. 1996.

[23] X. Buffat, W. Herr, N. Mounet, T. Pieloni, and S. White, “Stability diagrams of colliding beams in the large hadron collider,” *Phys. Rev. ST Accel. Beams*, vol. 17, p. 111 002, 11 Nov. 2014.

[24] X. Buffat *et al.*, “Our understanding of transverse instabilities and mitigation tools/strategy,” in *Proceedings of the 2017 Evian workshop on LHC beam operation*, Evian-les-Bains, France, Dec. 2017.

[25] S. Fartoukh, A. Mereghetti, M. Solfaroli, J. Wenninger, X. Buffat, *et al.*, “Round ATS optics with large tele-index,” CERN, Geneva, Switzerland, Tech. Rep. CERN-ACC-NOTE-2019, 2019.

[26] X. Buffat *et al.*, “Transverse instabilities,” in *Proceedings of the 2019 Evian workshop on LHC beam operation*, Evian-les-Bains, France, 30 Jan. - 1 Feb. 2019.

[27] G. Arduini, et al, “Chapter 2: Machine Layout and Performance,” in *High-Luminosity Large Hadron Collider. Preliminary Design Report*, CERN-2015-005, May 2015, pp. 21–60.

[28] A. Abada, et al., “FCC-hh: The Hadron Collider,” *The European Physical Journal Special Topics*, vol. 228, no. 4, pp. 755–1107, Jul. 2019, ISSN: 1951-6401.

[29] V. Shiltsev, Y. Alexahin, A. Burov, and A. Valishev, “Landau damping of beam instabilities by electron lenses,” *Phys. Rev. Lett.*, vol. 119, p. 134 802, 13 Sep. 2017.

[30] W. Herr, “Features and implications of different LHC crossing schemes,” CERN, Geneva, Switzerland, Tech. Rep. LHC Project Report 628, Feb. 2003.

[31] L. R. Carver, X. Buffat, K. Li, E. Métral, and M. Schenk, “Transverse beam instabilities in the presence of linear coupling in the large hadron collider,” *Phys. Rev. Accel. Beams*, vol. 21, p. 044 401, 4 Apr. 2018.

[32] T. Persson and R. Tomás, “Improved control of the betatron coupling in the large hadron collider,” *Phys. Rev. ST Accel. Beams*, vol. 17, p. 051 004, 5 May 2014.

[33] L. van Riesen-Haupt, A. Seryi, R. Tomàs, J. C. de Portugal, and E. Fol, “K-modulation developments via simultaneous beam based alignment in the LHC,” in *Proceedings of 8th International Particle Accelerator Conference*, Copenhagen, Denmark: JACoW, 14-19 May 2017.

[34] A. Ribes Metidieri and X. Buffat, “Studies of PACMAN effects in the HL-LHC,” CERN, Geneva, Switzerland, Tech. Rep. ACC-NOTE-2019-0037, Sep. 2019.

[35] E. Keil, “Truly self-consistent treatment of the side effects with bunch trains,” CERN, Geneva, Switzerland, Tech. Rep. SL/95-75 (AP), Jul. 1995.

# NOISE AND POSSIBLE LOSS OF LANDAU DAMPING THROUGH NOISE EXCITED WAKEFIELDS

S. V. Furuseth*[1], X. Buffat, CERN, 1211 Geneva 23, Switzerland
[1]also at EPFL, 1015 Lausanne, Switzerland

*Abstract*

The effect of transverse Landau damping in circular hadron colliders depends strongly on the bunch distribution. The bunches are often assumed to be Gaussian in the transverse dimensions, as it fits well to measurements and it is the expected effect of intra-beam scattering. However, a small change of the distribution can cause a loss of stability. We study the effect that external noise excites the transverse motion of the beam, which produces wakefields, which act back on the beam and cause a diffusion of incoherent particles. The diffusion is narrow in frequency space, and thus also in action space. Macroparticle simulations have shown a similar change of the distribution, which is only detectable in action space, not projected in position space. The narrow diffusion efficiently drills a hole in the stability diagram, at the location of the unstable mode, eventually leading to an instability. The advised mitigation technique is to reduce the drilling rate by operating with a stability margin.

## INTRODUCTION

Synchrotrons, such as the Large Hadron Collider (LHC), are dependent on Landau damping for the beams to avoid self-amplified coherent oscillations. Landau damping is a physical process where an ensemble of harmonic oscillators, that would otherwise be unstable, is stabilized by a spread in the natural frequencies of the incoherent oscillators [1]. Therefore, it depends on the details of the beam and bunch distribution and the source of detuning that causes the spread in frequencies. It is common to study Landau damping with a linearized Vlasov equation, considering the effect of a small perturbation on top of an equilibrium perturbation.

In the LHC, multiple instances of instability have been observed that begin at a significant delay after the last modification of the machine configuration. The delay will be referred to as the latency of the instability. Latent instabilities have now also been reproduced in experiments in the LHC with a controlled noise source [2], detailed in Fig. 1. These instabilities cannot be attributed to a change of the machine configuration, and may therefore be attributed to a change of the beam distribution from the initial equilibrium distribution. Furthermore, given the dependence on the noise amplitude, the noise must be essential to the mechanism. It has previously been hypothesized, and checked with simulations, that the external noise excites the beam, which then is amplified by wakefields [3]. This mechanism can explain parts of the discrepancy between the predicted and operationally required octupole current in the LHC [4]. The goal of the work presented here is to describe the mechanism

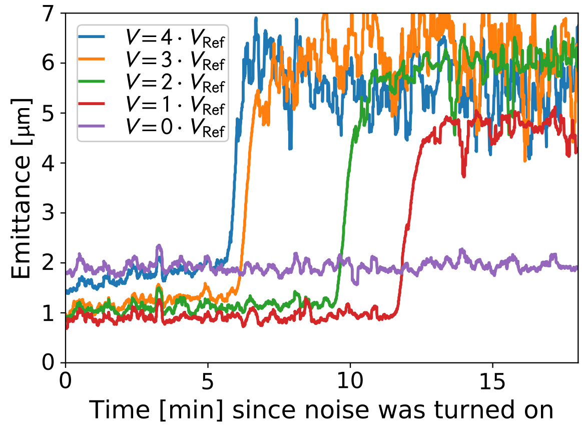


Figure 1: Emittance evolution of five bunches subject to a controlled noise source of relative magnitude given by the legend. The bunches went unstable in order of decreasing noise amplitude [2]. The six bunches not affected by noise, of which only one is displayed, did not go unstable in this configuration.

analytically as a wake-driven diffusion that causes a loss of Landau damping. The model will be used to better understand this mechanism, and to guide the search for optimal machine and beam parameters that mitigate this mechanism, relevant for the LHC and future projects.

## THEORY

In this section, the (angular) frequencies $\omega$ are referred to instead of the tunes $Q = \omega/2\pi f_{\mathrm{rev}}$. The mathematical explanation of noise excited wakefields consists of 4 steps: (i) The wakefields drive eigenmodes with complex eigenfrequencies $\omega_m$, found with the linearized Vlasov equation, assuming no tune spread and no noise; (ii) Due to the tune spread, the discrete mode mixes with the incoherent spectrum, and the complex eigenfrequencies are changed to $\Omega_m$. If $\mathrm{Im}\{\Omega_m\} > 0$, the mode is already unstable. The interesting case is when $\mathrm{Im}\{\Omega_m\} < 0$; (iii) An external noise source of amplitude $\xi(t)$ as a function of time, kicks the bunches transversely. The noise drives the eigenmodes to finite amplitudes that depend on the noise amplitude and damping rate of the modes; (iv) The non-negligible noise excited wakefields act on the incoherent particles. By considering the kicks from the wakefields as a stochastic excitation in the framework of the Liouville equation, we will derive a diffusion equation modeling the distribution evolution driven by the noise excited wakefields.

* sondre.vik.furuseth@cern.ch

### *Wakefield eigenmodes – $\omega_m$*

The standard approach used to study beam stability is with a linearized Vlasov equation [5, 6]. This method considers the beam as a continuous distribution $\Psi$ in phase space, consisting of a constant equilibrium distribution and a quickly oscillating perturbation

$$\Psi = \Psi_0 + \Psi_1. \tag{1}$$

One can similarly include the impedance as a perturbation in the Hamiltonian

$$\mathcal{H} = \mathcal{H}_0 + \mathcal{H}_{\mathrm{wake}}, \tag{2}$$

where $\mathcal{H}_0$ models the unperturbed motion. The equilibrium distribution drives no dipolar wakefields. Thus, the wakefields are proportional to the distribution perturbation, $\mathcal{H}_{\mathrm{wake}} \propto \Psi_1$.

The Liouville equation can be solved using the perturbed distribution in Eq. (1) and Hamiltonian in Eq. (2). One finds impedance normalized eigenmodes $m_m$ with eigenvalues $\omega_m = \omega_0 + \Delta\omega_m$ and amplitudes $\chi_m(t)$, dependent on impedance, chromaticity and transverse feedback. The eigenmodes are complex functions of the longitudinal phase space coordinates. The distribution perturbation can be written as a sum over these modes

$$\Psi_1 = \sum_m \chi_m(t_0)\mathrm{e}^{-\mathrm{i}\omega_m(t-t_0)} m_m, \tag{3}$$

where i is the imaginary unit, and the importance of $\mathrm{Im}\{\omega_m\}$ as a growth rate is highlighted. The amplitude of the individual modes are governed by

$$\ddot{\chi}_m m_m + \omega_m^2 \chi_m m_m = 0. \tag{4}$$

The frequency without impedance is $\omega_0 \in \mathbb{R}$. By moving the tune shift caused by the impedance over to the right hand side (RHS) one finds the impulse acted on the beam by the wakefields

$$\begin{aligned}\ddot{\chi}_m m_m + \omega_0^2 \chi_m m_m &= (\omega_0^2 - \omega_m^2)\chi_m m_m \\ &= \omega_m P_{\mathrm{wake}} m_m.\end{aligned} \tag{5}$$

### *Damped eigenmodes – $\Omega_m$*

The discrete modes discussed in the previous subsection can be stabilized by Landau damping. This can be assessed by the stability diagram theory when all the (head-tail) modes can be treated independently, as is the case for the current LHC operation. In the weak head-tail approximation, the stability diagram in plane $j \in \{x, y\}$ corresponds to the curve in the complex plane defined by $\Delta\omega_{mj} \in \mathbb{C}$ in the dispersion relation [7]

$$\frac{-1}{\Delta\omega_{mj}} = \int_0^\infty\int_0^\infty \mathrm{d}J_x\,\mathrm{d}J_y \frac{J_j \dfrac{\mathrm{d}\Psi(J_x,J_y)}{\mathrm{d}J_j}}{\Omega_{mj} - \omega_j(J_x,J_y)}, \tag{6}$$

where the real part of $\Omega_{mj} = \omega_0 + \Delta\Omega_{mj} \in \mathbb{C}$ is scanned, while it has a vanishing positive imaginary part. This is the gray curve in Fig. 2. The source of detuning considered here is Landau octupoles [8]. The tune shift driven by the wakefields without detuning, $\Delta\omega_{mj}$, can be represented by a point in the same complex plane. If the point is below the stability diagram, it is stable, if it is above, it is unstable. The subscript $j$ will be omitted from here on, when not important.

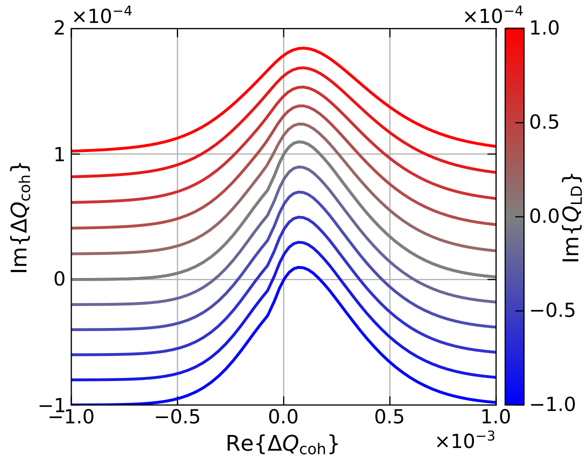


Figure 2: Curves at complex tune shift $\Delta Q_{\mathrm{coh}} = \Delta\omega_m/2\pi f_{\mathrm{rev}}$ of modes, when neglecting Landau damping, that end up with the same imaginary tune shift $\mathrm{Im}\{Q_{\mathrm{LD}}\} = \mathrm{Im}\{\Omega_m\}/2\pi f_{\mathrm{rev}}$, when including Landau damping. The grey curve is the stability diagram. The red curves with positive $\mathrm{Im}\{Q_{\mathrm{LD}}\} > 0$ are calculated directly with Eq. (6), while the blue curves are equal to the stability diagram shifted downwards by the corresponding $\mathrm{Im}\{Q_{\mathrm{LD}}\}$.

One can use Eq. (6) to find how the undamped tune shift $\Delta\omega_m$ changes due to the tune spread $\omega_j(J_x, J_y)$, by finding the corresponding $\Omega_m$ that maps to $\Delta\omega_m$. This is possible as long as the discrete mode remains unstable, $\mathrm{Im}\{\Omega_m\} > 0$ [9].

Equation (6) cannot map a mode inside the stability diagram to $\Omega_m$. When $\mathrm{Im}\{\Omega_m\} = 0^+ \to 0^-$, the sign of $\mathrm{Im}\{\Delta\omega_{mj}\}$ in Eq. (6) is flipped as well. In other words, there is a hole in the codomain of Eq. (6). The flipping has been found to be due to a mathematical choice, rather than based on physics [10].

The physics of what is happening when the most unstable modes are inside the stability diagram has previously not been given much attention [11, 12]. One reason why is that these modes are stabilized by Landau damping, and therefore are not a problem within linear Vlasov theory. However, due to noise, the dynamics of modes that are initially stable are crucial to determine whether the beams will remain stable. A similar problem has been discussed in plasma physics. Paraphrasing from [13], it was found for small distribution perturbations that "[A]n arbitrary initial distribution behaves (after a short transient time) like a superposition of [...] slightly damped plane waves, which do obey the dispersion relation". We assume for now the same to be true in a particle beam.

A new algorithm must be designed to calculate the complex frequencies of the Landau damped modes that reside inside the stability diagram. For the results that will be presented here, the hypothesis has been made that one can extend the mapping in Eq. (6) linearly from $\mathrm{Im}\{\Omega_m\} = 0^+$ into the area where the imaginary part is negative. This is illustrated by the blue lines in Fig. 2. This approach neglects the continuous spectrum of the beam that is believed to be negligible after a short transient time, when the mode is close to the stability threshold. Thus, this method is only believed to be accurate when the least stable modes are close to the stability diagram. This is the main region of interest in this paper.

### *Noise excited eigenmodes*

The unavoidable noise in the accelerator has been neglected so far for beam stability considerations. The noise can be modeled as an additional stochastic perturbation to the Hamiltonian in Eq. (2)

$$\mathcal{H} = \mathcal{H}_0 + \mathcal{H}_{\text{wake}} + \mathcal{H}_{\text{noise}}. \tag{7}$$

The external noise is expected to act at low frequencies and thus to be dipolar in nature (i.e. affecting all particles along the bunch equally). It will be included as a stochastic impulse $\xi(t)$, of zero mean, $\langle\xi(t)\rangle = 0$ and singular autocorrelation $\langle\xi(t)\xi(s)\rangle = \sigma^2\delta(t-s)$. It can be decomposed as $\xi(t) = \xi(t_c)\Xi(z)$, where $\xi(t_c)$ is the noise amplitude at the core of the bunch longitudinally, while $\Xi(z)$ is a normalized function across the length of the bunch. Under the assumption of dipolar noise, $\Xi(z)$ will be a constant. The impact of the noise on a bunch can be integrated in quadrature into a single kick per turn of variance $\sigma_{\text{ext}}^2 = \tau\sigma^2$, where $\tau = 1/f_{\text{rev}}$ is the revolution period of the machine. By the Plancherel theorem, the power spectral density of the noise is given by [14]

$$|\mathcal{F}[\xi]|^2(\omega) = \begin{cases} \dfrac{\sigma_{\text{ext}}^2}{\tau} & , \omega \in [0, \pi f_{\text{rev}}] \\ 0 & , \text{otherwise}. \end{cases} \tag{8}$$

The left hand side is the absolute value squared of the Fourier transform of the noise signal as a function of the angular frequency.

The impact of the external noise on the eigenmodes can be found by including the noise on the RHS of Eq. (4) and multiplying from the left with $\overline{m_m}$, and taking the average over the longitudinal distribution, as

$$\ddot{\chi}_m + \omega_m^2\chi_m = \omega_m\left\langle\overline{m_m}\Xi\right\rangle\xi(t_c) = \omega_m\eta_m\xi(t_c). \tag{9}$$

Thus, mode $m_m$ will on average be affected proportionally to its dipolar moment $\eta_m$. The mode is modeled as a stochastically driven damped harmonic oscillator, and one can easily find that the frequency spectrum of $\chi_m$ is

$$\mathcal{F}[\chi_m](\omega) = \frac{\Omega_m\eta_m\mathcal{F}[\xi](\omega)}{\Omega_m^2 - \omega^2}, \tag{10}$$

centred and peaked at the frequency of the mode, $\Omega_m$. In this paper, the considered noise spectrum is flat. However, in a real machine, what matters is the noise spectrum close to the mode frequency. Since the mode is damped, $\mathrm{Im}\{\Omega_m\} \neq 0$, its frequency spectrum is free of singularities.

### *Wakefield driven diffusion*

The main question that remains is how the noise excited damped modes affect the incoherent particles. The incoherent particles in a bunch, will in either transverse plane be described by their normalized canonical coordinates [15]

$$\begin{aligned} y &= \frac{Y}{\sqrt{\beta\varepsilon_0}} = \sqrt{2J}\cos(\phi), \\ p &= -\frac{1}{\sqrt{\beta\varepsilon_0}}\left(\alpha Y + \beta\frac{\mathrm{d}Y}{\mathrm{d}s}\right) = -\sqrt{2J}\sin(\phi), \end{aligned} \tag{11}$$

where $Y$ is the offset from the design orbit, $s$ is the position in the beamline, $\alpha$ and $\beta$ are the Twiss parameters, $\varepsilon_0$ is the initial beam emittance and $\phi$ is the canonical conjugate of $J$, which is the normalized absolute particle action, given in units of $\varepsilon_0$.

In the case when $\phi = \omega_0 t$, where $\omega_0$ is the constant incoherent betatron frequency, and the particle receives impulses $\Delta p(t)$, the Hamiltonian can be written as

$$\mathcal{H} = \omega_0 J - y\Delta p = \omega_0\frac{y^2+p^2}{2} - y\Delta p, \tag{12}$$

such that Hamilton's equations read

$$\dot{y} = \omega_0 p, \quad \dot{p} = -\omega_0 y + \Delta p, \tag{13}$$

which lead to the following equation of motion

$$\ddot{y} + \omega_0^2 y = \omega_0\Delta p. \tag{14}$$

In our case, the sources of the impulses $\Delta p$ are the external noise and wakefields,

$$\Delta p = \xi + P_{\text{wake}} = \xi + \sum_m \frac{1}{\omega_m}(\omega_0^2 - \omega_m^2)\chi_m. \tag{15}$$

The first term on the RHS will be referred to as the direct noise term, while the second term will be referred to as the indirect noise term. The direct impact on beam stability of the external noise was found to be negligible for the LHC in [16].

Here, we will consider the second term, the impulses from the noise excited wakefields. This will be considered by the perturbed Hamiltonian in Eq. (2), renamed as

$$\mathcal{H} = \mathcal{H}_0(J) + \mathcal{H}_1(\phi, J) = \mathcal{H}_0(J) - yP_{\text{wake}}, \tag{16}$$

consisting of $\mathcal{H}_0$ governing the unperturbed non-stochastic motion, and the perturbation $\mathcal{H}_1$ containing the stochastic forces. It is important that $\mathcal{H}_0$ only depends on the actions, not the phases $\phi$ of the particles. If the stochastic forces are sufficiently weak, and thus can be modeled as a perturbation, they drive a diffusion that can be modeled by [17, 18]

$$\frac{\partial\Psi_{\text{eq}}}{\partial t} = \frac{\partial}{\partial J}\left[JD_{\text{wake}}\frac{\partial\Psi_{\text{eq}}}{\partial J}\right]. \tag{17}$$

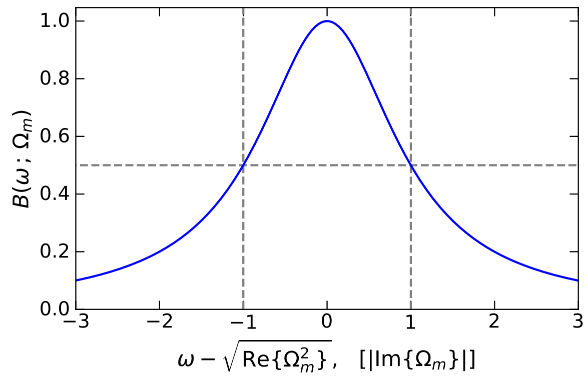


Figure 3: Shape of the diffusion coefficient due to a single stable wake driven mode, given by Eq. (19b).

The wakefield driven diffusion coefficient $D_{\mathrm{wake}}$ is given by

$$\begin{aligned} D_{\mathrm{wake}}(\omega) &= \frac{1}{2J}\left\langle \frac{\partial \mathcal{H}_1}{\partial \phi}(t)\frac{\partial \bar{\mathcal{H}}_1}{\partial \phi}(s)\right\rangle \\ &= \frac{1}{2}|\mathcal{F}[P_{\mathrm{wake}}]|^2(\omega), \end{aligned} \tag{18}$$

where the brackets signify an expectancy value, the bar signifies a complex conjugation required to get a real diffusion coefficient, and $P_{\mathrm{wake}}$ is stochastic since the beam continuously is excited by the stochastic noise. The diffusion coefficient is a function of the angular frequency of the particles.

The absolute value of the Fourier transform squared in Eq. (18) is the power spectral density of the impulse from the wakefields. In the interesting regime of this work, the modes are uncoupled, and the power of the different modes can be added in quadratures to express the diffusion coefficient as

$$D_{\mathrm{wake}}(\omega) = \sum_m \frac{\eta_m^2\sigma_{\mathrm{ext}}^2|\Delta\omega_m|^2}{2\tau\mathrm{Im}\{\Omega_m\}^2}B(\omega)C, \tag{19a}$$

$$B(\omega) = \frac{\mathrm{Im}\{\Omega_m^2\}^2}{(\mathrm{Re}\{\Omega_m^2\}-\omega^2)^2+\mathrm{Im}\{\Omega_m^2\}^2}, \tag{19b}$$

$$C = \frac{\mathrm{Re}\{\omega_m\}\omega_0 + |\Delta\omega_m|^2/4}{\mathrm{Re}\{\Omega_m\}^2}\cdot\frac{|\Omega_m|^2}{|\omega_m|^2} \approx 1. \tag{19c}$$

The $B$-function, which is illustrated in Fig. 3, defines the shape of the diffusion coefficient as a function of the incoherent angular frequency $\omega$. In the limit $|\Delta\Omega_m| \ll |\omega_0|$, $B(\omega)$ has a maximum of 1 and half width $|\mathrm{Im}\{\Omega_m\}|$ at half maximum. The $C$-function consists of additional factors that follow if one includes more than the first order terms. It is close to 1 for all realistic configurations considered here. In most cases, one mode will be dominant and be the main driver of diffusion within the bunch distribution.

The frequency dependent diffusion coefficient in Eq. (19) becomes amplitude dependent due to the amplitude dependent detuning as

$$D_{\mathrm{wake}}(J_x, J_y) = D_{\mathrm{wake}}[2\pi f_{\mathrm{rev}}Q(J_x, J_y)]. \tag{20}$$

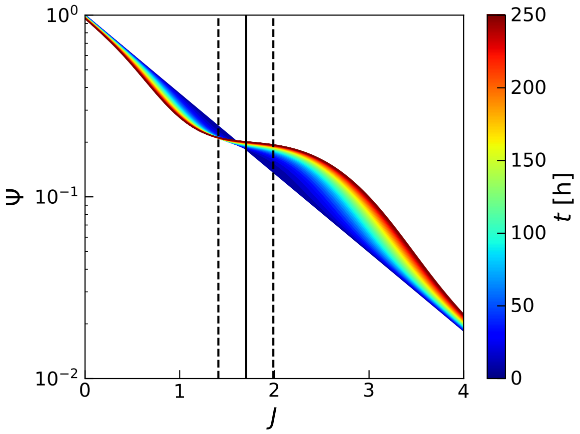


Figure 4: Evolution of transverse distribution due to wake driven diffusion with detuning only dependent on the action in the same plane. The actions at half maximum of the diffusion coefficient is marked by the vertical dashed lines. This example is intended for explaining the distribution evolution only.

In this paper, we are interested in the detuning caused by Landau octupoles, which in plane $j$ can be expressed as [8]

$$Q_j = Q_{0j} + a_jJ_x + b_jJ_y, \tag{21}$$

excluding the negligible tune shift caused by the perturbations in Eq. (7).

A qualitative understanding of what this diffusion does to the beam, can be acquired already from the expression for the diffusion coefficient in Eq. (19). Assuming noise and diffusion in the horizontal plane only, the half width of the diffusion coefficient in the horizontal action coordinate will be $W_J = \mathrm{Im}\{\Omega_m\}/2\pi f_{\mathrm{rev}}a_x$. The diffusion will lead to a local flattening of the distribution, and as it is the derivative of the distribution function that appears in the dispersion integral in Eq. (6), a local loss of Landau damping can be expected. The flattening process will be faster for a smaller $W_J$, assuming the same maximum. For sufficiently large $W_J$, the diffusion will be approximately uniform for all actions, and only lead to an emittance growth, not a qualitative change of the distribution.

## NUMERICAL METHOD

The diffusion equation in Eq. (17) must be solved numerically. The results that will be presented later have been produced with a finite volume method (FVM) solver implemented in `PyRADISE` (Python RAdial DIffusion and Stability Evolution) [16]. The two dimensional action space has been discretized into a $500 \times 500$ grid going from 0 to $J_{\mathrm{max}} = 18$. It has been assumed that a single mode is dominant. In reality, changes in the distribution will lead to a change of the frequency of the least stable mode, and consequently a change of the dependence of diffusion on the action. This evolution has not been calculated during the diffusion process in the numerical results presented in this paper. In other words, the diffusion coefficients are kept constant throughout the solving process. Given the shape of the diffusion coefficient in Eq. (19), and linear detuning driven by Landau octupoles, the diffusion will lead to a local flattening of the distribution, which is exemplified and exaggerated for $b_j = 0$ in Fig. 4.

The FVM solver gives as output the evolving distribution $\Psi_k$ at discrete times $t_k$. For each of these distributions, the stability diagram is calculated using a numerical trapezoidal integrator in `PySSD` [19], which has been imported in `PyRADISE`. If the stability diagram changes enough, so that the least stable mode is outside and above it, the bunch will be considered to have become unstable with a latency.

## RESULTS

The following results consider the change of distribution and corresponding change of the stability diagram according to `PyRADISE`. There are small variations between the configurations. The detuning coefficients in Eq. (21) are always $a_x = a_y = 5 \times 10^{-5}$ and $b_x = b_y = -3.5 \times 10^{-5}$. The product of the noise amplitude and the dipole moment of the considered least stable mode in the horizontal plane is kept at $\sigma_{\text{ext}}\eta_m = 5 \times 10^{-6}$. The noise in the vertical plane has been kept equal to zero. The revolution frequency is that of the LHC, $f_{\text{rev}} = 11.245$ kHz.

The first configuration includes a least stable mode of undamped coherent tune shift $\Delta Q_{\text{coh}} = -10^{-4} + 10^{-5}\text{i}$. Due to Landau damping, this mode has been changed to $\Delta Q_{\text{LD}} = -6.98 \times 10^{-5} - 1.17 \times 10^{-5}\text{i}$, according to the algorithm illustrated in Fig. 2. The evolution of the distribution and stability diagram is presented in Fig. 5. The change of the distribution after 10 min is a local flattening horizontally at the actions corresponding to $Q_x(J_x, J_y) = Q_{\text{LD}}$, equivalent to the flattening in Fig. 4. There is a change of the stability diagram at the real tune shift of the least stable

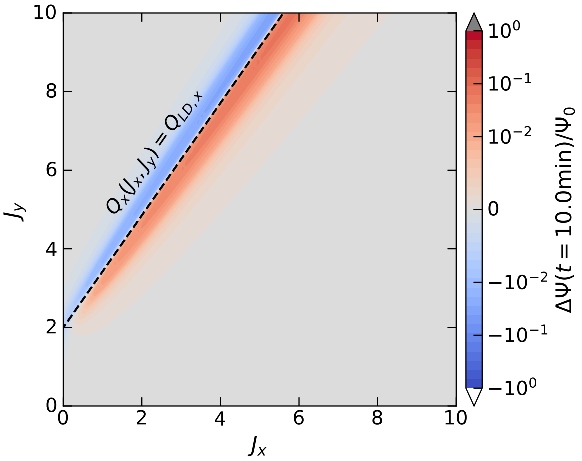


(a)

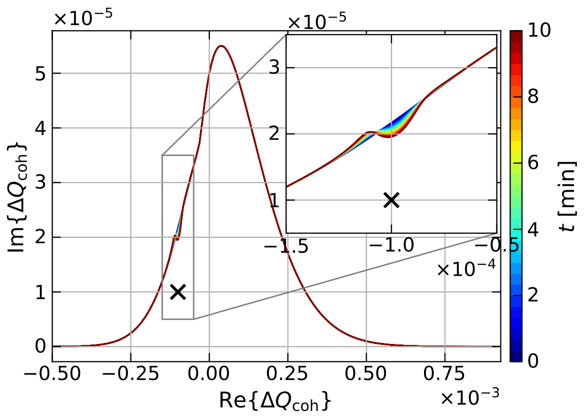


(b)

Figure 5: Evolution of distribution in 10 min in (a) and stability diagram in (b), due to diffusion driven by wakefields. The dashed line in (a) marks the actions where $Q_x(J_x, J_y) = Q_{\text{LD}}$. The cross at $\Delta Q_{\text{coh}} = -10^{-4} + 10^{-5}\text{i}$ in (b) marks the location of the least stable mode.

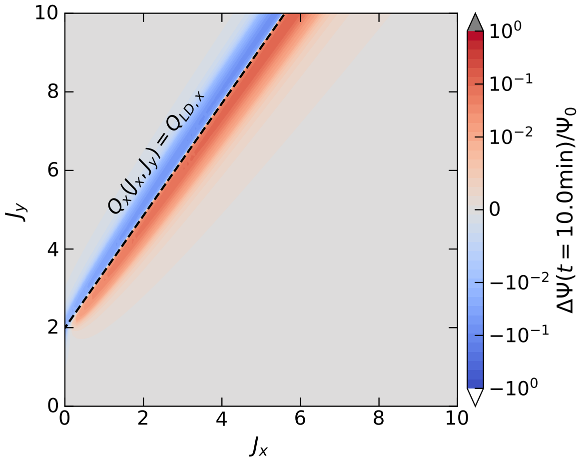


(a)

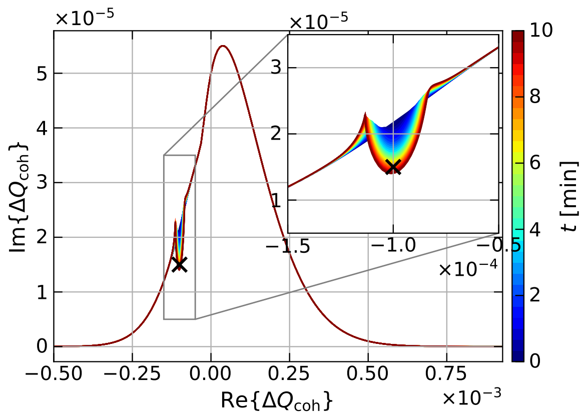


(b)

Figure 6: Evolution of distribution in 10 min in (a) and stability diagram in (b), due to diffusion driven by wakefields. The dashed line in (a) marks the actions where $Q_x(J_x, J_y) = Q_{\text{LD}}$. The cross at $\Delta Q_{\text{coh}} = -10^{-4} + 1.5 \times 10^{-5}\text{i}$ in (b) marks the location of the least stable mode.

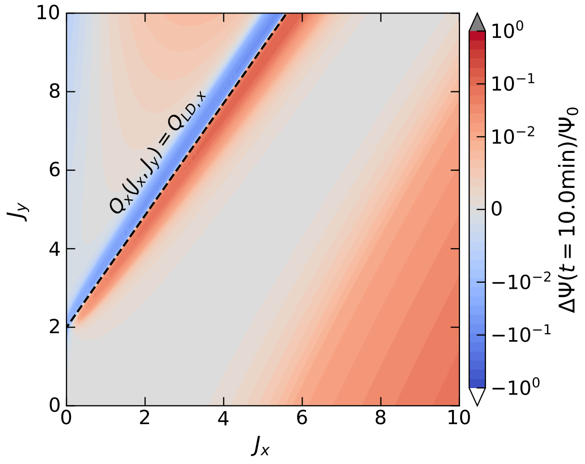


(a)

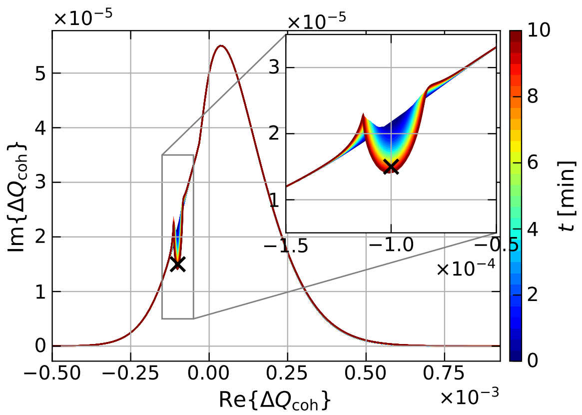


(b)

Figure 7: Evolution of distribution in 10 min in (a) and stability diagram in (b), due to diffusion driven by wakefields and the external noise directly. The dashed line in (a) marks the actions where $Q_x(J_x, J_y) = Q_{LD}$. The cross at $\Delta Q_{coh} = -10^{-4} + 1.5 \times 10^{-5}$i in (b) marks the location of the least stable mode.

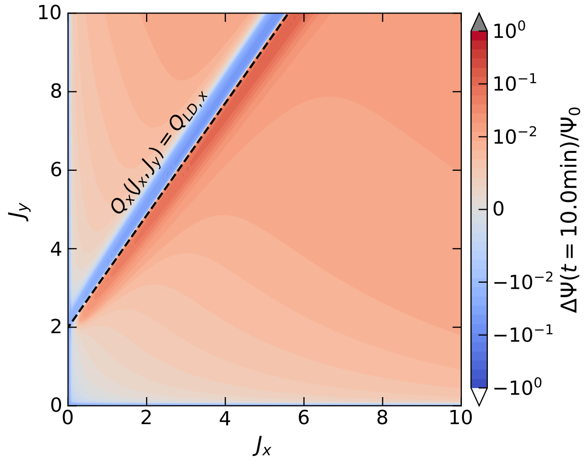


(a)

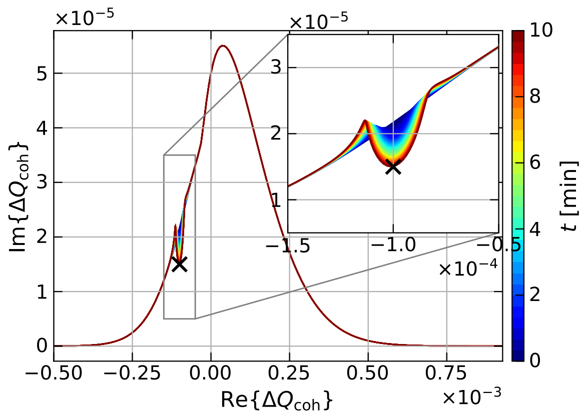


(b)

Figure 8: Evolution of distribution in 10 min in (a) and stability diagram in (b), due to diffusion driven by wakefields and intra-beam scattering. The dashed line in (a) marks the actions where $Q_x(J_x, J_y) = Q_{LD}$. The cross at $\Delta Q_{coh} = -10^{-4} + 1.5 \times 10^{-5}$i in (b) marks the location of the least stable mode.

mode, but the mode is still well within the stability diagram after 10 min.

In the second configuration, the least stable mode has been shifted to $\Delta Q_{coh} = -10^{-4} + 1.5 \times 10^{-5}$i, closer to the stability threshold. Due to Landau damping, this mode has been changed to $\Delta Q_{LD} = -6.98 \times 10^{-5} - 6.70 \times 10^{-6}$i, with a smaller absolute imaginary part than in the first configuration. The evolution of the distribution and stability diagram is presented in Fig. 6. Due to the weaker damping of the mode, the drilling of a hole in the stability diagram is more efficient, and the least stable mode would have become unstable after approximately 8 min. This mechanism is thus able to drive instabilities with latencies of the same order of magnitude as those measured in the LHC in Fig. 1.

So far, only the diffusion due to the noise excited wakefields has been studied. Other types of diffusion may be able to counteract the local flattening and thereby increase the latency or even prevent the instability. In this third configuration, the diffusion driven by the direct noise term in Eq. (15) has been included. This diffusion was studied in detail in [16] and was found to not be detrimental for stability. Including a damper gain corresponding to a damping time of $\tau_g = 20$ turns and external noise amplitude $\sigma_{ext} = 10^{-3}$, the evolution of the distribution and stability diagram is presented in Fig. 7. The additional diffusion is zero for actions such that $Q_x(J_x, J_y) = \langle Q_x(J_x, J_y)\rangle$, which is close to the tune of the least stable mode. The instability in this configuration occurs 1.3% later, compared to the case without the direct noise term that was illustrated in Fig. 6. In other words, the direct noise term has negligible stabilizing impact in this configuration.

Finally, the uniform diffusion expected due to intra-beam scattering will be considered. A diffusion corresponding to an emittance growth of 2 % h$^{-1}$ has been included in both planes, and the diffusion due to the direct noise term in Eq. (15) has been removed. The evolution of the distribution and stability diagram is presented in Fig. 8. There is now a weak nonzero diffusion at all actions, but it has not completely counteracted the local flattening close to $Q_{\mathrm{LD}}$. The least stable mode would have become unstable after approximately 10 min, 26% later than without the uniform diffusion.

## MITIGATION

Noise excited wakefields drive a narrow diffusion in frequency that leads to the drilling of a hole in the stability diagram. There are several possible approaches one can take to mitigate the total drilling. First of all, one should minimize the time spent in transient phases close to the instability threshold. In a collider, the most critical phase is between the end of the energy ramp and the start of collisions. In the LHC the bunches require stabilization by Landau octupoles alone during this phase. Second of all, one should minimize the drilling rate. The magnitude of the diffusion coefficient in Eq. (19a) is proportional to $\sigma_{\mathrm{ext}}^2 \eta_m^2 |\Delta\omega_m|^2 / |\mathrm{Im}\{\Omega_m\}|^2$. To reduce the diffusion, one can therefore act with equal success on either of these factors: (i) Minimize the noise acting on the beam in the machine; (ii) Operate in a regime where $\eta_m \ll 1$. In a machine with only dipolar noise, one should therefore operate with positive chromaticity (above transition) to stabilize the dipolar modes, as is common; (iii) Minimize the machine impedance to limit $|\Delta\omega_m|$. This is already desired to minimize the initial stability threshold, neglecting that the diffusion changes the distribution; (iv) Maximize $|\mathrm{Im}\{\Omega_m\}|$, by operating with a stability margin. This was further motivated by the numerical results.

Further mitigation techniques can be discussed based on the numerical calculations. Incoherent noise as intra-beam scattering or synchrotron radiation can to a certain extent counteract the drilling. This may explain why such latent instabilities have not been reported before, neither in lepton machines, nor in low-energy hadron machines. Since the drilling of the hole is localized at a certain frequency, it is possible to gradually change the current in the Landau octupoles, to avoid continuously flattening the distribution at the same actions. However, this must be balanced with the goal of maximizing $|\mathrm{Im}\{\Omega_m\}|$. It is also possible to consider increasing the ratio $b_j/a_j$ of the detuning coefficients, such that the width of the diffusion coefficient in action space is increased while not reducing the overall Landau damping.

If it is not possible to mitigate this mechanism with the techniques proposed so far, one must consider other sources of detuning. In addition to limiting the time before the beams are put in collision in a collider, one can try one of the following: electron-lens [20], enhanced octupole detuning due to the telescopic index [21], and wires designed to counteract beam-beam detuning [22].

## CONCLUSION

Instabilities of high latencies have been observed in the LHC, both in regular operation and in dedicated experiments. In this paper, we have shown that such instabilities can develop in high-energy hadron machines with noise and impedance, by gradually changing the distribution. The key mechanism is driven by an external source of noise that excites the beam, which in return affects incoherent particles through wakefields. These wakefields cause diffusion in a narrow frequency range centred at the eigenfrequency of the least stable wake driven coherent mode. This diffusion efficiently drills a hole in the stability diagram at the eigenfrequency of the corresponding mode. The recommended mitigation technique is to reduce the drilling rate, by minimizing the maximum of the diffusion coefficient $D \propto \sigma_{\mathrm{ext}}^2 \eta_m^2 |\Delta\omega_m|^2 / |\mathrm{Im}\{\Omega_m\}|^2$. Other sources of diffusion, as the direct external noise and intra-beam scattering, can increase the latency, but does not necessarily mitigate the drilling process completely.

It is believed that the mechanism presented here, diffusion driven by noise excited wakefields, is important in understanding the troubling observations in the LHC. Many aspects of this mechanism require and deserve further investigation. The description of the Landau damped modes deserve further studies. The chromatic tune shift of the incoherent particles remains to be included, and is believed to be important in understanding the diffusion of a mode close to a sideband of the main tune. The numerical method will be improved to self-consistently calculate the diffusion coefficient as the distribution evolves. Other types of noise, such as the crab-cavity amplitude noise, should be studied, as it is expected to drive head-tail modes as efficiently as dipolar noise drives dipolar modes. Finally, it will be of interest to compare quantitatively the latencies predicted with this theory to instability latencies measured in the LHC.

## ACKNOWLEDGEMENTS

The authors would like to thank Nicolas Mounet for discussions on the dynamics of the modes that are stabilized by Landau damping, Armando Bazzani for discussions on the diffusion, and Elias Métral and Gianluigi Arduini for feedback on this manuscript. This research was supported by the HL-LHC project.

## REFERENCES

[1] J. Rees and A. Chao, "Landau Damping Revisited", SLAC National Accelerator Laboratory, Menlo Park, California, Rep. SLAC-PUB-13469, Nov. 2008.

[2] S. V. Furuseth, D. Amorim, S. A. Antipov, X. Buffat, N. Mounet, E. Métral, T. Pieloni, B. Salvant, and C. Tambasco, "Instability Latency in the LHC", in *Proc. IPAC'19*, Melbourne, Australia, May 2019, pp. 3204–3207. doi:10.18429/JACoW-IPAC2019-WEPTS044

[3] X. Buffat, "Transverse beams stability studies at the Large Hadron Collider", Ph.D. thesis, Inst. of Physics, École poly-

technique fédérale de Lausanne, Lausanne, Switzerland, 2015, CERN-THESIS-2014-246. doi:10.5075/epfl-thesis-6321

[4] X. Buffat, G. Arduini, D. Amorim, S. Antipov, N. Biancacci, L. Carver, S. V. Furuseth, G. Iadarola, K. Li, L. Mether , E. Métral, N. Mounet, A. Oeftiger, A. Romano, G. Rumolo, B. Salvant, M. Schenk, T. Pieloni, and C. Tambasco, "Transverse instabilities", in *Proc. 9th LHC Operations Evian Workshop*, Evian, France, Jan 2019. `https://indico.cern.ch/event/751857/contributions/3259409`

[5] A. A. Vlasov, "On the kinetic theory of an assembly of particles with collective interaction", *Russ. Phys. J.* **9**, pp. 25–40, 1945.

[6] N. Mounet, "Vlasov solvers and macroparticle simulations", in *CERN Yellow Reports: Conference Proceedings* **1**, p. 77, 2018, Rep. CERN-2018-003-CP. doi:10.23732/CYRCP-2018-001.77

[7] J. S. Berg and F. Ruggiero, "Landau damping with two-dimensional betatron tune spread", CERN, Geneva, Switzerland, Rep. CERN-SL-AP-96-071-AP, Dec. 1996.

[8] J. Gareyte, J. P. Koutchouk, and F. Ruggiero, "Landau damping, dynamic aperture and octupoles in LHC", CERN, Geneva, Switzerland, Rep. CERN-LHC-PROJECT-REPORT-091, Feb. 1997.

[9] J. L. Laclare, "Introduction to coherent instabilities – Coasting beam case", CERN, Geneva, Switzerland, Rep. CERN-85-19-V-2, 1985. doi:10.5170/CERN-1985-019-V-2.377

[10] N. Mounet, "Landau-damped modes - To be or not to be, that is the question", in CERN/BE-ABP-HSC section meeting, Jan. 2020, unpublished. `https://indico.cern.ch/event/874562/contributions/3689477/` (accessed: 2020-3-6).

[11] Y. H. Chin, "Nonlinear perturbation approach to bunch lengthening and blow-up of energy spread", *Nuclear Instruments and Methods in Physics Research Section A: Accelerators, Spectrometers, Detectors and Associated Equipment* **226**, pp. 223–249, Oct. 1984. doi:10.1016/0168-9002(84)90037-8

[12] Y. H. Chin, K. Satoh, and K. Yakoya, "Instability of a bunched beam with synchrotron-frequency spread", *Particle Accelerators* **13**, pp. 45–66, 1983, Rep. KEK-82-18.

[13] N. G. Van Kampen, "On the theory of stationary waves in plasmas", *Physica* **21**, pp. 949–963, 1955. doi:10.1016/S0031-8914(55)93068-8

[14] M. Plancherel, "Contribution à l'étude de la représentation d'une fonction arbitraire par les intégrales définies", *Rendiconti del Circolo Matematico di Palermo* **30** (1), pp.289–335, 1910. doi:10.1007/BF03014877

[15] A. Wolski, *Beam dynamics in high energy particle accelerators*. London, England: Imperial College Press, 2014.

[16] S. V. Furuseth and X. Buffat, "Long-term evolution of Landau damping in the presence of transverse noise, feedback, and detuning", *Phys. Rev. Accel. Beams* **23**, 034401, 2020. doi:10.1103/PhysRevAccelBeams.23.034401

[17] A. Bazzani, S. Siboni, and G. Turchetti, "Diffusion in Hamiltonian systems with a small stochastic perturbation", *Physica D* **76**, pp. 8–21, 1994. doi:10.1016/0167-2789(94)90246-1

[18] A. Bazzani and L. Beccaceci, "Diffusion in Hamiltonian systems driven by harmonic noise", *J. Phys. A: Math. Gen.* **31**, pp. 5843–5854, 1998. doi:10.1088/0305-4470/31/28/004

[19] X. Buffat, W. Herr, N. Mounet, T. Pieloni, and S. White, "Stability diagrams of colliding beams in the Large Hadron Collider", *Phys. Rev. ST Accel. Beams* **17**, 111002, 2014. doi:10.1103/PhysRevSTAB.17.111002

[20] V. Shiltsev, Y. Alexahin, A. Burov, and A. Valishev, "Landau Damping of Beam Instabilities by Electron Lenses", *Phys. Rev. Lett.* **119**, 134802, 2017. doi:10.1103/PhysRevLett.119.134802

[21] S. Fartoukh, "Achromatic telescopic squeezing scheme and its application to the LHC and its luminosity upgrade", *Phys. Rev. ST Accel. Beams* **16**, 111002, 2013. doi:10.1103/PhysRevSTAB.16.111002

[22] S. Fartoukh, A. Valishev, Y. Papaphilippou, and D. Shatilov, "Compensation of the long-range beam-beam interactions as a path towards new configurations for the high luminosity LHC", *Phys. Rev. ST Accel. Beams* **18**, 121001, 2015. doi:10.1103/PhysRevSTAB.18.121001

# MITIGATION OF COHERENT BEAM INSTABILITIES (MCBI) FOR CERN LIU AND HL-LHC

G. Rumolo*, CERN, CH-1211 Geneva 23, Switzerland

*Abstract*

The High Luminosity upgrade of the Large Hadron Collider (HL-LHC) will meet its future yearly integrated luminosity target by means of performance improving upgrades of the LHC itself as well as by receiving significantly higher beam current and brightness from its injectors. The implications of the pushed beam parameters are twofold. On one side, all the accelerators of the LHC injection chain will have to be upgraded to produce the desired beam parameters. For this purpose, the LHC Injectors Upgrade (LIU) program has been established to implement all the needed modifications for meeting the required beam specifications. These upgrades will target the mitigation of coherent beam instabilities and space charge in the injectors, which will allow lifting their existing intensity and brightness limitations to the desired extent. On the other side, the LHC will have to be able to accept the new beam parameters and exploit them at best to produce the integrated luminosity target. This will mainly require control of impedance driven instabilities, beam-beam effects and electron cloud in the LHC itself. In this paper, we will focus on proton beams by describing the identified performance limitations of the LHC and its injectors, as well as the actions envisioned to overcome them.

## INTRODUCTION

The LHC Injectors Upgrade (LIU) project [1, 2] aims at increasing the intensity and brightness of the beams in the injectors in order to match the beam requirements set out by the High Luminosity LHC (HL-LHC) project [3], while ensuring high availability and reliable operation of the injector complex well into the HL-LHC era (up to about 2037) in synergy with the Consolidation (CONS) project [4]. For the upgrade of the LHC injector proton chain, LIU includes the following principal items:

- The replacement of Linac2, which accelerates protons to 50 MeV, with Linac4, providing 160 MeV $H^-$ ions;
- Proton Synchrotron Booster (PSB): New 160 MeV $H^-$ charge exchange injection, acceleration to 2 GeV from current 1.4 GeV with new power supply and RF system;
- Proton Synchrotron (PS): New 2 GeV injection, broadband longitudinal feedback;
- Super Proton Synchrotron (SPS): Upgrade of the 200 MHz RF system, impedance reduction and e-cloud mitigation, new beam dump and protection devices.

All these upgrades will lead to the production of beams with the challenging HL-LHC parameters and they are currently being implemented during the Long Shutdown 2 (LS2) in 2019-20.

To extend its discovery potential, the LHC will undergo a major upgrade during Long Shutdown 3 (LS3) in 2024-25 under the HL-LHC project. The goal will be to increase the rate of collisions by a factor of 5-7.5 beyond the original LHC design value, leading to a target integrated luminosity of 3000-4000 $fb^{-1}$ over the full HL-LHC run (2026-2037). The new configuration will rely on the replacement of the final focusing quadrupoles at the high luminosity Interaction Points (IPs), which host ATLAS and CMS, with new and more powerful magnets based on the $Nb_3Sn$ technology, as well as a number of key innovations that push accelerator technology beyond its present limits while enabling, or even broadening, the future desired performance reach. Among these are the cutting-edge 11 T superconducting $Nb_3Sn$-based dipoles, the new superconducting link technology with $MgB_2$, compact superconducting cavities for transverse beam tilting along the longitudinal axis to compensate for the crossing angle at collision (crab cavities), the upgrade of the cryogenic system and general infrastructure, new technology and material for collimators, hollow electron lenses for beam halo cleaning.

The beam dynamics aspects of the LIU and HL-LHC projects are challenging, because during the HL-LHC era:

- The LHC injectors will have to be able to routinely produce, stably control and safely handle beams with unprecedented intensity and brightness;
- The LHC will have to be able to run with the future beams, preserve their stability and make them available for collisions all along the calculated optimum fill length with the desired levelling scheme, ensuring as little as possible beam quality degradation.

Addressing the beam intensity limitations of the LHC and its injectors and illustrating the envisaged strategies to cope with them will be the subject of the next sections.

## BEAM PERFORMANCE LIMITATIONS IN THE LHC INJECTORS AND GOALS

In this section we will first present a general overview on the present LHC beam performance of the injectors and the beam requirements for the LIU project. We will only focus on the so called 'standard LHC beam', which is baseline for the projects and produced as follows:

- Two subsequent injections of 4+2 bunches from the four PSB rings into the PS at $E_{kin}$=1.4 GeV;
- In the PS, triple splitting of the injected bunches at 2.5 GeV, then acceleration to 25 GeV and two consecutive double splittings of all 18 bunches at 25 GeV;
- Four subsequent injections of trains of 72 bunches spaced by 25 ns into the SPS (train spacing 200 ns) at 25 GeV and acceleration to 450 GeV.

* Giovanni.Rumolo@cern.ch

Then, we will describe the actions that the LIU project has (planned to) put in place to overcome the intensity/brightness limitations in the various accelerators of the injector chain.

### *Present performance of the LHC injector chain*

An upper limit for the brightness of standard LHC beam is determined at the PSB injection, because of the efficiency of the multi-turn injection process as well as the effects of space charge during injection. The normalised transverse emittance has been measured as a function of intensity at the PSB extraction after optimization of the injection settings and for a longitudinal emittance of 1.2 eVs at extraction [5]. The relation is found to be linear and the resulting line defines the "PSB brightness" line. The longitudinal emittance at extraction can be made in principle as high as 2.8 eVs via longitudinal emittance blow up along the PSB cycle [6] compatibly with other constraints coming from the transfer to the PS and further longitudinal beam manipulation in the PS ring. This is believed to be beneficial in terms of space charge in the PS since it would allow injecting longer bunches with larger momentum spreads. The PSB does not have an intensity limitation for the LHC beams, as it already nowadays successfully accelerates to 1.4 GeV beams up to 7 times more intense than the current LHC beams, which are used for fixed target experiments at the ISOLDE facility. However, it is well-known that a horizontal instability is excited in the PSB at 160 MeV and few other defined energy values, due to the impedance associated to the external circuits of the extraction kickers [7]. In pre-LIU operation, this instability was successfully suppressed by means of a horizontal feedback system over the whole intensity range accelerated in the PSB.

Combining the experience accumulated with operational beams with the outcomes of several dedicated space charge Machine Development (MD) studies conducted throughout 2012 – 2017, it can be assumed that the maximum values of space charge vertical tune spread, $\Delta Q_y$, compatible with the beam loss and emittance blow up budgets reported below, are 0.31 and 0.21 at the PS and SPS injection, respectively. Besides, prior to the LIU upgrade program, due to longitudinal dipolar coupled bunch instabilities on the ramp and at top energy, the PS was not able to produce 25 ns beams with more than 1.8e11 p/b within the longitudinal emittance of 0.35 eVs, which is currently the optmised value to limit capture losses and keep the beam longitudinally stable in the SPS. Finally, due to RF power constraints on the main SPS RF system (200 MHz) and longitudinal coupled bunch instabilities along the cycle, beams with more than 1.3e11 p/b could not be extracted from the SPS with the desired bunch length of 1.6 ns for a basically lossless injection into LHC. E-cloud has been also affecting 25 ns beams in the SPS, but currently the SPS has undergone sufficient beam induced scrubbing to produce beams with 1.3e11 p/b transversely stable and without the characteristic pattern imprinted by e-cloud on the bunch intensities and emittances along the trains. Finally, the onset of the vertical Transverse Mode Coupling Instability (TMCI) limited in the past the bunch intensity to 1.6e11 p/b [8], but this limitation was lifted in 2012 by commissioning a new optics with $\gamma_t$ lower by 4 units, which increases the TMCI threshold by a factor 2.5 [9].

After including some predefined budgets for emittance blow up and beam loss (5% in the PSB and PS for both, and 10% in the SPS) we can represent in the plane emittance vs. intensity per bunch at the SPS extraction the curves corresponding to PSB brightness, PS and SPS space charge limits, and intensity limitations of the PS and SPS. The regions of inaccessible parameter ranges are shaded. The outcome of this exercise is displayed in Fig. 1, from which we deduce that presently the best standard LHC beam produced by the injectors has 1.3e11 p/b within about 2.7 $\mu$m transverse emittance. All the points measured at LHC injection over the years 2015 – 2018, displayed in green, fully confirm this analysis.

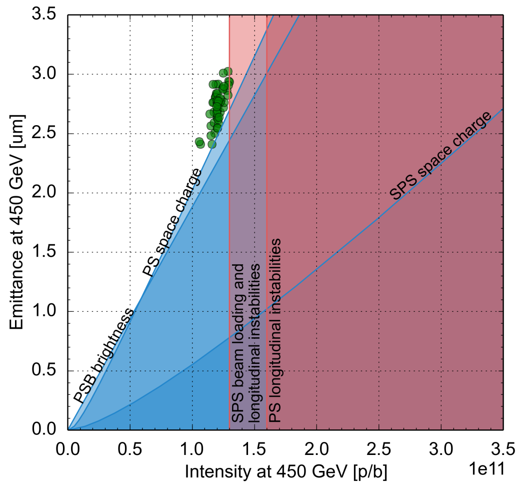


Figure 1: Limitation diagram for the standard LHC beam in the present injectors' chain.

Other methods of LHC beam production exist, which can lead to brighter bunches at the expense of the length of the trains transferred from the PS to the SPS at each cycle. For example, by transferring trains of 48 bunches instead of 72, obtained through a different sequence of batch compression and bunch merging/splitting actions at 2.5 GeV in the PS, the beam brightness can be almost doubled with respect to the scheme discussed above. The beam obtained in this way has been preferred for physics production in the LHC for most of the current run and has been routinely employed since the beginning of 2018. More details about alternative LHC beam production schemes can be found in [10–12].

### *HL-LHC beam requirements*

The HL-LHC upgrade aims at accumulating an integrated luminosity of 250 fb$^{-1}$/year at the high luminosity IPs. Assuming 50% HL-LHC performance efficiency, this goal can be achieved assuming a standard LHC beam with bunch intensity of 2.3e11 p/b and a transverse emittance of 2.1 $\mu$m injected from the SPS. In order not to exceed a pile up of 140 events/crossing, the luminosity is levelled at 5e34 cm$^{-2}$s$^{-1}$

by gradually lowering the beta functions at the IPs ($\beta^*$) down to 15 cm while partially compensating for the crossing angle with the crab cavities. An ultimate goal of 320 fb$^{-1}$/year is also set assuming levelling at 7.5e34 cm$^{-2}$s$^{-1}$, allowing for a pile up of 200 events/crossing. Table 1 shows achieved and HL-LHC specified beam parameters at the SPS exit.

Table 1: Current and HL-LHC beam parameters out of SPS

| | $\mathbf{N_b}$ ($\mathbf{10^{11}}$ **p/b)** | $\epsilon_{x,y}$ **($\mu$m)** |
|---|---|---|
| **Achieved** | 1.3 | 2.7 |
| **HL-LHC target** | 2.3 | 2.1 |

It is clear that both intensity and brightness of the LHC beams will need to be roughly doubled in the HL-LHC era. Looking back at Fig. 1, HL-LHC is basically targeting a point right in the middle of the currently inaccessible region.

## LIU CHALLENGES TO REACH THE HL-LHC BEAM PARAMETERS

Figure 1 directly suggests the path to reach the challenging beam parameters specified in the second row of Table 1. We will discuss first how to achieve the desired brightness and we will focus later on the intensity reach.

Achieving the future brightness relies on two main pillars:

- Reduction of the slope of the PSB brightness line by at least a factor two;
- Mitigation of the space charge effect in the PS.

The space charge in the SPS does not seem to limit the performance even for the future beams, as its limitation curve clearly lies below the HL-HLC target point. The two goals listed above will be realised within the LIU project by means of the following actions. Firstly, the PSB brightness line with half slope will be made possible by using Linac4 with H$^-$ charge exchange injection into the PSB at 160 MeV. It has been simulated that if Linac4 provides 40 mA within 0.4 $\mu$m, the future LHC beams can be injected in about 20 turns and the desired transverse emittance is compatible with the blow up due to space charge at the new injection energy (as was expected from a naive $\beta^2\gamma$ scaling) [13]. If the current from Linac4 is lower (compatibly with the goal set for the future fixed target beams), the number of injected turns will have to be correspondingly increased. Secondly, the injection energy into the PS will be raised to 2 GeV, which alone guarantees a 63% intensity increase for a fixed transverse emittance while keeping the space charge tune spread the same as nowadays. Besides, the longitudinal beam parameters at the PSB-PS transfer will have to be optimised to further reduce the tune spread at PS injection and ensure that the PS space charge curve in the limitation diagram ends up in the shadow of the PSB brightness line. The longitudinal emittance will be blown up along the PSB cycle to provide longer bunches at the PS injection, while the larger momentum spread will also further reduce the space charge tune spread due to the increase of the average beam horizontal size through dispersion. The longitudinal emittance blow up can be reproducibly applied in the PSB via either phase modulation of a higher harmonic or injection of band limited phase noise on the main harmonic, as has been demonstrated in MDs in 2017 [6] and 2018.

The achievement of the future intensity relies on:

- Longitudinal stabilisation of the beam along the PS accelerating ramp and at top energy;
- Increase of the available power of the 200 MHz RF system in the SPS in combination with a program of longitudinal impedance reduction;
- E-cloud mitigation in the SPS.

The main longitudinal limitation for LHC-type beams in the PS are dipolar coupled-bunch instabilities. A dedicated broad-band feedback system using a Finemet cavity as a longitudinal kicker has been installed and commissioned in the PS. Extensive tests with beam have been performed since 2016 to explore the intensity reach with this system. The maximum intensity with nominal longitudinal emittance at PS extraction has been measured to be above 2.0e11 p/b [14]. Due to quadrupolar instabilities and incoherent longitudinal emittance growth, it is not yet clear whether a higher harmonic system will be required eventually to keep the beam longitudinally stable with the desired longitudinal emittance at the design intensity for HL-LHC reported in table 1.

The LIU baseline for the SPS includes an upgrade of the low-level RF and a major upgrade of the 200 MHz RF system [15]. The low-level RF upgrade will allow pulsing the RF amplifiers with the revolution frequency (the LHC beam occupies less than half of the SPS circumference) leading to an increase of the available RF power from the existing power plant up to about 1.05 MW per cavity. The main upgrade consists of the re-arrangement of the four existing cavities and two spare sections into two 4-section cavities and four 3-section cavities, and the construction of two additional power plants providing 1.6 MW each. This will entail a reduction of the beam loading per cavity, an overall increase of the available RF voltage and a reduction of the peak beam coupling impedance at the fundamental frequency. With all this massive upgrade in place, the SPS will be able to provide LHC beams with up to about 2e11 p/b, still limited by coupled bunch longitudinal instabilities on the ramp and at top energy [16]. To achieve 2.3e11 p/b it is necessary to reduce the SPS longitudinal impedance. LIU has foreseen shielding of the vacuum flanges between the focusing quadrupoles and the adjacent straight sections as well as installation of High Order Mode (HOM) couplers to improve the damping of the HOMs of the 200 MHz cavities. Numerical simulations have shown that these two measures will allow matching the HL-LHC beam requirement [17]. Finally, the e-cloud in the SPS is a potential limiting factor for operation with higher intensity. Accelerating the present LHC beam without significant degradation from the e-cloud has required an integrated time of several days of dedicated scrubbing distributed over several years. Scrubbing is preserved from year to year in the SPS regions not exposed to air during the stop, while it is partially lost, but usually quickly recovered, where there has been air exposure. Studies of e-cloud build up in the different SPS chambers have revealed that the Secondary Electron Yield (SEY) thresholds will not change significantly when going to the HL-LHC intensity for most cases [18]. Although instability simulations showed that the beam becomes more sensitive to the e-cloud in the dipoles when increasing the beam intensity, it is believed that scrubbing will work also up to the HL-LHC bunch intensity. The Run 2 experience with beams with 2e11 p/b already injected into the SPS has indeed revealed that scrubbing can be efficiently carried out over few days and results in a clear reduction of the e-cloud induced indicators [19]. Coating with amorphous carbon (a-C) [20] is currently being applied to the chambers of the focusing quadrupoles (QF) and adjacent drift chambers during LS2 in synergy with the impedance reduction campaign, which will also gain an extra margin on the instability threshold. Recent machine development studies (2017-18) with intensities above 1.8e11 p/b have revealed the onset of a horizontal coupled bunch instability in this intensity range. Simulation studies have clearly pinned down the source, which is a combination of resistive wall and narrow band horizontal impedances, whose effect is further enhanced by the destabilizing action of the kicker broadband impedance reduction [21]. PyHEADTAIL simulations can reproduce to a very high degree of accuracy the behaviour of this instability as a function of the horizontal chromaticity and octupole settings, as shown in Fig. 2. As this will need to be operationally stabilized in future operation with chromaticity and/or amplitude detuning, a tradeoff of beam stability with beam lifetime and emittance growth might have to be found when pushing the current toward the LIU values. Another option that is being considered, should the stabilisation be unachievable through operational knobs, is the deployment of a horizontal wide band feedback system, whose proof of principle has been demonstrated at the SPS against TMCI in the vertical plane [22].

Putting together all the points discussed in this section, we can draw the new brightness and intensity curves representing the projected limitations after the implementation of the LIU upgrades or actions, obtaining the limitation diagram in Fig. 3. The HL-LHC required point from Table 1 is also shown in yellow, demonstrating that the LIU upgrades are indeed compliant with the achievement of this final goal.

## HL-LHC CHALLENGES

The HL-LHC layout is based on the nominal LHC ring configuration, in which about 1.2 km of beam line will be changed. The nominal configuration is designed for a realistic, cost-efficient and achromatic implementation of the low $\beta^*$ collision optics, based on the deployment of the Achromatic Telescopic Squeeze (ATS) scheme [23]. The installation of triplet quadrupoles of larger aperture is needed to safely accommodate the beams, which reach large dimensions (peak beta functions >20 km), and the shielding to limit the energy deposition and radiation in the SC coils and cold mass [3]. Single particle stability in HL-LHC is challenged by the large beta functions in the triplets and in the adjacent arcs, which enhance the effect of linear and non-linear errors in those regions leading to potentially low Dynamic Aperture (DA) in absence of correction. Even to allow for basic optics measurements pre-computed corrections based on accurate magnetic measurements will have

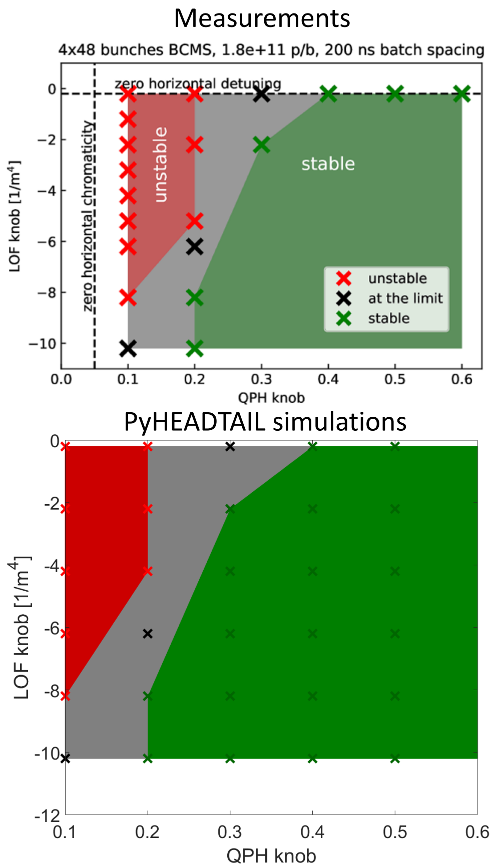


Figure 2: Stability map of the 4 trains of 48 bunches with a current of 1.8e11 p/b and train spacing of 200 ns: Experimental (top) and simulations (bottom). Courtesy of H. Bartosik and C. Zannini

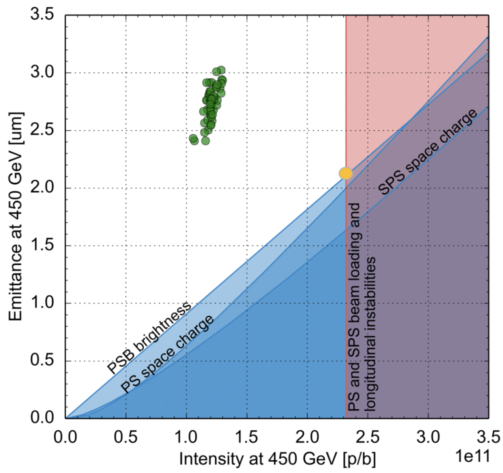


Figure 3: Limitation diagram for the standard LHC beam in the injectors' chain after the LIU upgrades.

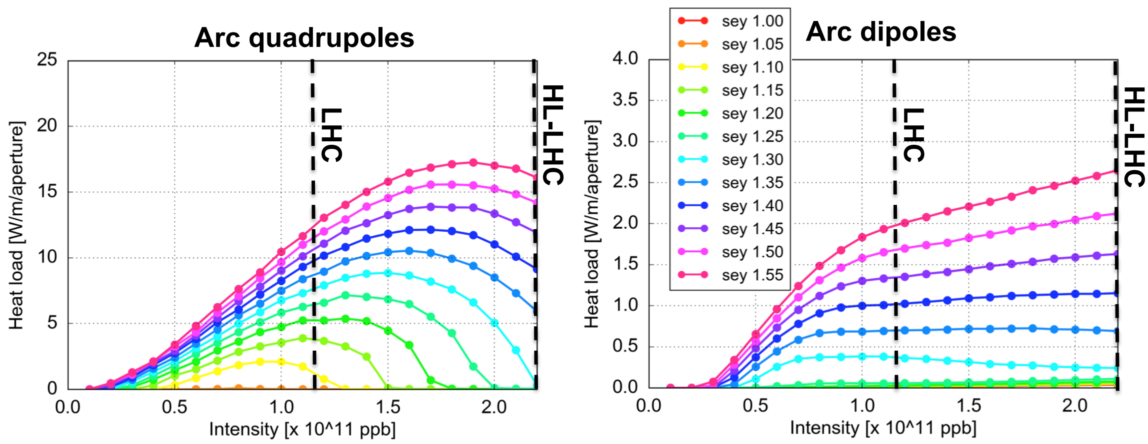


Figure 4: E-cloud generated heat load as a function of bunch intensity in LHC arc dipoles (left) and quadrupoles (right) for different SEYs, as labeled. Courtesy of G. Iadarola and G. Skripka.

to be used. Besides, the $\beta^*$ levelling during many hours of operation at constant luminosity will require the commissioning of a large number of optical configurations. This further challenges the efficiency of the optics measurement and correction tools, needed to fulfil the tight tolerances coming from DA or coherent stability constraints [24].

In terms of effects related to the collective beam dynamics, running HL-LHC with double intensity and brightness will pose notable challenges, such as beam stability, beam induced heat loads in the cold regions and beam-beam [25]. (1) Transverse instabilities have been observed in the LHC with different types of beams and during different machine processes, and have required operation with quite extreme settings, e.g. with Q'=+15, octupole strength close to the maximum, as well as with maximum gain and maximum bandwidth of the transverse feedback (50 turns and 20 MHz, respectively) at high energy. The instabilities observed at injection energy (450 GeV), which are also cured by high chromaticity and octupole strength, are ascribed to e-cloud. Due to some features (such as symmetry between the transverse planes, heat load measurements on single magnets, simulated electron distributions with different magnetic fields), the e-cloud forming in the quadrupoles is likely to be the main culprit. Combined e-cloud build up and instability simulations show that the electron density in quadrupoles decreases for higher bunch currents and therefore these instabilities should become less critical for HL-LHC intensities. The underlying assumption is of course that all beam chambers will scrub for the higher HL-LHC beam intensities at least as much as they have for the present intensity. To gain margin in the octupole strength needed for suppressing instabilities driven at least partly by impedance, impedance reduction will be applied to the main existing contributors (i.e. the collimators) and to new elements in high beta regions (e.g. crab cavities). In particular, all secondary betatron collimators will be replaced with new ones based on a low-impedance design. The present baseline foresees using Mo-Graphite jaws coated with a 5$\mu$m Mo layer. This material exhibits comparable robustness as the present carbon-based secondary collimators, but has an electrical resistivity 5 (uncoated) to 100 times (coated) lower [26]. Through an iterative process between the RF and the impedance teams, the HL-LHC crab cavities have been already designed with attention to minimise the impact of HOMs on beam stability. (2) Within HL-LHC, the SEY in the insertion regions will be actively reduced by surface treatments (a-C coating [20] or laser treatment [27]), with an expected reduction of the heat load due to e-cloud in these regions. However, no intervention is foreseen on the beam screen of the arcs, which cover more than two thirds of the whole machine. When operating with 25 ns beams, the measured heat loads in the arcs have been consistently much larger than those expected from impedance and synchrotron radiation and they exhibited a still unexplained spread between arcs, being very close to the nominal cryogenics limits in the "hottest" arcs [28]. In future operation, we will be faced with two main issues. First, when moving to HL-LHC intensities and 7 TeV, the contribution of impedance and synchrotron radiation will become three-fold, which roughly halves the available margin of the cryogenic system for additional heat loads. Second, the scaling with intensity of the observed additional heat loads is quite uncertain. Making the educated assumption that e-cloud is the most plausible source of these heat loads (since it is compatible with a number of observations), we can however predict the heat load in the new parameter regime, as displayed in Fig. 4. For SEYs in the 1.2-1.4 range, as inferred from the present excess heat load in the various sectors, e-cloud build up simulations foresee a relatively mild change of e-cloud generated heat load when increasing the bunch intensity to HL-LHC values. This scaling needs to be validated experimentally after LS2 (when LIU will make higher intensity beams available from the injectors [29]). When summing up all the heat load contributions from the e-cloud in the different regions and those from impedance and synchrotron radiation, one finds out that, while the heat load in low-load sectors would be below 8 kW/arc and thus compatible with HL-LHC, the heat load in high-load sectors exceeds the maximum value by at least 20%. If this is confirmed, a back-up filling scheme featuring several 125 ns gaps within the bunch trains will be used for keeping the heat load in the high-load sectors within the capacity of the cryogenic plant. This will be at the expense of a 10-30% lower number of bunches in LHC.

(3) The beam-beam interaction introduces additional strong nonlinearities in the particle motion and leads to resonance excitation as well as a large tune spread, potentially resulting in a significant restriction of the DA and thus beam degradation. Operational experience and machine studies have proven that the present LHC has surpassed the head-on beam-beam tune shift limit, which was assumed based on experience from past colliders [30, 31]. However, the HL-LHC represents yet another jump into an unexplored parameter range, furthermore with a baseline configuration of luminosity $\beta^*$ levelling and crossing angle compensation with crab cavities. The beam-beam studies for HL-LHC are performed by tracking the particles over a few million turns under the weak-strong approximation for the beam-beam interaction and for HL-LHC baseline parameters. The DA is calculated and compared with the target value of $6\sigma$ over 1e6 turns. Simulations seem to confirm so far that the target DA is comfortably achieved during the whole levelling process and including the chromaticity and octupole settings necessary for beam stability. This gives room to crossing angle adjustments during the levelling process to reduce the pile-up density and the radiation on the inner triplets [32]. A global exploration of the impact on DA of all the related parameters, including possible compensation of the long-range beam-beam effects with wires or electron lenses, is underway to refine operational scenarios and optimise the projected HL-LHC performance.

## ACKNOWLEDGEMENTS

This paper summarises the enormous and excellent work carried out by the LIU and HL-LHC beam dynamics teams. Special thanks to H. Bartosik, G. Iadarola, R. Tomás and C. Zannini. Then, I would also like to thank S. Albright, R. Alemany, S. Antipov, F. Antoniou, G. Arduini, M. Beck, E. Benedetto, R. Bruce, O. Brüning, X. Buffat, M. Carlà, H. Damerau, G.P. Di Giovanni, R. Di Maria, S. Fartoukh, V. Forte, M. Fraser, B. Goddard, K. Hanke, A. Huschauer, V. Kain, E. Koukovini-Platia, A. Lasheen, K. Li, M. Meddahi, L. Mether, E. Métral, B. Mikulec, Y. Papaphilippou, T. Pieloni, D. Quartullo, S. Redaelli, J. Repond, A. Romano, L. Rossi, B. Salvant, M. Schenk, R. Scrivens, E. Shaposhnikova, G. Skripka, F. Velotti.

## REFERENCES

[1] J. Coupard *et al.*, “LIU Technical Design Report - Volume I: Protons”, CERN, Geneva, Switzerland, Rep. CERN-ACC-2014-0337, Dec. 2014.

[2] J. Coupard *et al.*, “LIU Technical Design Report - Volume II: Ions”, CERN, Geneva, Switzerland, Rep. CERN-ACC-2016-0041, April 2016.

[3] G. Apollinari, I. Béjar Alonso, O. Brüning, P. Fessia, M. Lamont, L. Rossi, and L. Tavian, “High-Luminosity Large Hadron Collider (HL-LHC): Technical Design Report V. 0.1”, CERN, Geneva, Switzerland, CERN Yellow Reports: Monographs, Rep. CERN-2017-007-M, April 2017, `doi:10.23731/CYRM-2017-004`

[4] M. Benedikt *et al.*, “Summary of Session 7: Accelerators and non LHC Experiment Areas Consolidation up to LS3”, in *Proc. Chamonix 2014 Workshop*, Chamonix, France, Sept. 2014, CERN-ATS-2015-002, pp. 31-32.

[5] G. Rumolo *et al.*, “Expected Performance in the Injectors at 25 ns Without and With Linac4”', in *Proc. Review of LHC and Injector Upgrade Plans (RLIUP) Workshop*, Archamps, France, Oct. 2013, CERN-2014-006, pp. 17-24.

[6] S. Albright, E. Shaposhnikova and D. Quartullo, “Longitudinal emittance blow up and production of future LHC beams”, in *Proc. Injector MD days 2017*, Geneva, Switzerland, March 2017, CERN-Proceedings-2017-002.23, pp. 23-26.

[7] E. Koukovini-Platia, M. J. Barnes, H. Bartosik, G. Rumolo, L. Sermeus, and C. Zannini, Phys. Rev. Accel. Beams, vol. 22, p. 124201, December 2019.

[8] G. Arduini *et al.*, “Fast vertical single-bunch instability at injection in the CERN SPS - an update”, in *Proc. PAC07*, Albuquerque, New Mexico, US, June 2007, paper FRPMN065, pp. 4162-4164.

[9] H. Bartosik, “Beam dynamics and optics studies for the LHC injectors upgrade”, CERN, Geneva, Switzerland, Ph.D. thesis CERN-THESIS-2013-257, Nov. 2013.

[10] R. Garoby, *IEEE Transactions on Nuclear Science*, vol. 32, no. 5, pp. 2332 - 2334, Oct. 1985, `doi:10.1109/TNS.1985.4333903`

[11] H. Damerau *et al.*, “LIU: Exploring alternative ideas”, in *Proc. Review of LHC and Injector Upgrade Plans (RLIUP) Workshop*, Archamps, France, Oct. 2013, CERN-2014-006, pp. 127-138.

[12] H. Bartosik and G. Rumolo, “Beams in the injectors”, in *Proc. 5th Evian Workshop on LHC beam operation*, Evian-les-Bains, France, June 2014, CERN-ACC-2014-0319, pp. 93-98.

[13] E. Benedetto *et al.*, “Space charge effects and mitigation in the CERN PS-Booster, in view of the upgrade”, in *Proc. HB2016*, Malmö, Sweden, July 2016, paper THPM9X01, pp. 517-522.

[14] H. Damerau and L. Ventura, “Longitudinal coupled-bunch instability studies in the PS”, in *Proc. Injector MD days 2017*, Geneva, Switzerland, March 2017, CERN-Proceedings-2017-002.59, pp. 59-62.

[15] E.Shaposhnikova, E. Chapala and E. Montesinos, “Upgrade of the 200 MHz RF System in the CERN SPS”, CERN, Geneva, Switzerland, Rep. CERN-ATS-2011-042, Aug. 2011.

[16] M. Meddahi *et al.*, “LHC Injectors Upgrade (LIU) project at CERN”, in *Proc. IPAC15*, Richmond, VA, USA, May 2015, paper THPF093, pp. 3915-3918.

[17] E. Shaposhnikova *et al.*, “Identification and reduction of the SPS impedance”, in *Proc. HB2016*, Malmö, Sweden, July 2016, paper TUAM3X01, pp. 260-265.

[18] G. Iadarola and G. Rumolo, "Electron cloud in the CERN accelerators (PS, SPS, LHC)", in *Proc. ECLOUD'12*, Elba island, Italy, June 2012, CERN-2013-002, pp. 19-26.

[19] G. Rumolo *et al.*, "Electron cloud effects at the CERN accelerators", in *Proc. ECLOUD'18*, Elba island, Italy, June 2018, in course of publication.

[20] C. Yin Vallgren *et al.*, "Amorphous carbon coatings for the mitigation of electron cloud in the CERN Super Proton Synchrotron", vol. 14, p. 071001, July 2011, `doi:10.1103/PhysRevSTAB.14.071001`

[21] C. Zannini *et al.*, "Low-impedance design with example of kickers", elsewhere in these proceedings.

[22] K. Li *et al.*, "Concept and simulations of unconventional damping devices: wideband damper and RFQ", presented at ICFA Mini-Workshop on Impedances and Beam Instabilities in Particle Accelerators, Benevento, Italy, Sept. 2017, unpublished.

[23] S. Fartoukh, "Achromatic telescopic squeezing scheme and application to the LHC and its luminosity upgrade", *Phys. Rev. ST Accel. Beams*, vol. 16, p. 111002, Nov. 2013, `doi:10.1103/PhysRevSTAB.16.111002`.

[24] F. Carlier *et al.*, "Optics Measurement and Correction Challenges for the HL-LHC", CERN, Geneva, Switzerland, Rep. CERN-ACC-2017-0088, Nov. 2017.

[25] G. Arduini *et al.*, *JINST* vol. 11, p. C12081, Dec. 2016, `doi:10.1088/1748-0221/11/12/C12081`.

[26] E. Quaranta *et al.*, "Towards optimum material choices for the HL-LHC collimator upgrade", CERN., Geneva, Switzerland, Rep. CERN-ACC-2016-0062, May 2016.

[27] R. Valizadeh *et al.*, "Low secondary electron yield of laser treated surfaces of copper, aluminum and stainless steel", in *Proc. IPAC 2016*, Busan, Korea, June 2016, paper TUOCB02, pp 1089-1092.

[28] G. Iadarola, G. Rumolo, P Dijkstal, and L. Mether "Analysis of the beam induced heat loads on the LHC arc beam screens during Run 2", CERN, Geneva, Switzerland, Rep. CERN-ACC-Note-2017-0066, Dec. 2017.

[29] G. Rumolo *et al.*, "Update on the HiLumi/LIU parameters and performance ramp up after LS2", presented at HiLumi Collaboration meeting, Madrid, Spain, Nov. 2017, unpublished.

[30] W. Herr *et al.*, "Observations of beam-beam effects in the LHC in 2011", in *Proc. Chamonix Workshop 2012 on LHC Performance*, Chamonix, France, Jan. 2012, CERN-2012-006, pp. 99-104.

[31] T. Pieloni *et al.*, "Colliding high brightness beams in the LHC", in *Proc. HB2012*, Beijing, China, Sept. 2012, paper MOP250, pp. 180-182.

[32] Y. Papaphilippou *et al.*, "Long Range Beam-Beam effects for HL-LHC", presented at LHC Performance Workshop (Chamonix 2018), Chamonix, France, Jan. 2018, unpublished.

# MITIGATION OF COHERENT INSTABILITIES IN LINEAR COLLIDERS AND FCC-HH

D. Schulte*, CERN, Geneva, Switzerland

*Abstract*

Collective instabilities play an important role in projects as diverse as FCC-hh and CLIC and drive some of the choices. In the paper a few examples are shown where the instabilities were mitigated by design choices and the resulting impact on the collider cost and power consumption is highlighted.

## INTRODUCTION

Collective beam instabilities can be mitigated with special technologies which suppres them. Beam-based feedback is a prime example. In some cases they have to be mitigated by design of a facility and can thus be a key design driver. This is the case for CLIC (Compact LInear Collider) [1] and FCC-hh, the hadron collider of FCC (Future Circular Collider) [2] as will be described below.

## CLIC

The CLIC study is preparing a staged electron-positron linear collider design that can be implemented in stages with centre-of-mass energies of 380 GeV, 1.5 TeV and finally 3 TeV. The concept uses 12 GHz normal-conducting accelerating structures in the main linac to accelerate 50 beam pulses per second each about 150 ns long and containing more than 300 bunches. It uses a novel drive-beam concept to produce the power for the main linac.

The first energy stage of CLIC has been systematically optimised for cost for the collision energy of 380 GeV and required luminosity of $1.5 \times 10^{34}\ \mathrm{cm}^{-2}\mathrm{s}^{-1}$ defined by the physics study.

A key ingredient of this optimisation has been the collective effects in the main linac. The particles of the bunches that pass through the accelerating structures extract energy. This beamloading reduces the accelerating field for the subsequent particles in the bunch and can generate an energy spread. The energy spread can in part be compensated by not accelerating the bunch at the moment when the RF field has reached its maximum but rather slightly earlier, typically at an RF phase of 12-15 degress. The RF field at the tail of the bunch is thus larger and can compensate the beamloading. To minimise the spread in acceleration, the bunch length has to be adjusted for the bunch charge; higher bunch charges demand longer bunches. This allows to determine the bunch length as a function of the charge.

Transverse wakefields of the bunch can lead to instabilities if the bunch is not injected perfectly on axis. They have to be suppressed. Whether an instability occurs depends on the focusing strength of the lattice, the RF structure design and the length and charge of the bunch that drives the wakefields. Since stronger focusing helps to mitigate the instability, the strongest practical lattice is chosen, and about 10% of the main linac is filled with quadrupoles. Further increase of this fraction would give minor improvements but start to hurt the effective gradient significantly.

The wakefields produced in each accelerating structure can be calculated based on the structure design. For CLIC a few basic parameters have to be taken into account: The structure length and the iris radius and thicknes for the different cells along the structure. This is achieved by a program developed by K. Sjobaek and A. Grudiev [3]. Since the bunch length is a function of the charge, it is now easy to determine the bunch charge that leads to transverse single-bunch instability. By backing off slightly in order to provide safety margin, this allows to define the maximum bunch charge.

The minimum distance between bunches is given by multi-bunch transverse instabilities. At larger distances the wakefields are weaker with the strong damping in the CLIC structures. The code allows to calculate the long-range wakefield and an analytic estimate can be used to identify the acceptable limit [4].

The number of bunches required to achieve the luminosity goal depends on their charge and the emittances from the damping ring and the beam transport systems as well as the focusing ability at the interaction point. It is a simple function of the charge, since the emittances can also be expressed as a function of the charge.

The number of bunches that is required to reach the luminosity goal is easily estimated. The repetition rate of the collider is fixed at 50 Hz to minimise the impact of magnetic stray fields from the power grid, which operates at 50 Hz[1]. The number of bunches required per beam pulse is thus known. Together with the distance between bunches the length of the RF pulse can be calculated, taking into account the structure design. This allows to determine whether the structure has an acceptable breakdown probability.

This procedure thus defined all relevant beam parameters. Based on the structure and the beam parameters the cost and power consumption of the collider can be estimated. Finally, the cheapest design that reaches the luminosity goal has been used. It has also one of the lowest power consumptions.

## FCC-HH

FCC-hh is designed to provide 100 TeV proton-proton collisions with a luminosity of up to $3 \times 10^{35}\ \mathrm{cm}^{-2}\mathrm{s}^{-1}$. It uses 16 T superconducting $Nb_3Sn$ magnets in its roughly 100 km long collider tunnel to bend the beam on its orbit.

* daniel.schulte@cern.ch

[1] Actually, the repetition rate is locked onto the grid frequency to follow the small deviations from the 50 Hz that occur.

A key parameter in the FCC-hh design is the magnet aperture in the arcs. Larger apertures mean that the magnets need to contain more of the expensive superconductor and thus increases the project cost. At injection, the beamscreen is the main source of impedance and too small aperture can render the beam unstable.

At first glance it might be surprising that impedances play an important role in FCC-hh, since the injection and collision energies of 3.3 and 50 TeV, respectively, are much higher than in LHC. But the larger circumference, lower revolution frequency, and larger betafunctions all increase the sensitivity to impedances.

The impedance efffects depend on the lattice, the bunch charge, spacing and energy as well as on the aperture and the resistivity of the surface. Copper coating is applied to reduce the resitivity at the relevant frequencies. The maximum injection energy is defined by considerations of the LHC as an injector to be 3.3 TeV. Higher energies would slow the ramping of the injector, which is a key ingredient in the integrated luminosity.

To maximise the integrated luminosity, the beam current has to be as high as possible since the beam is burning rapidly in the experiments. The time that one can operate without having to replace the beam with a fresh one is thus limited. It increases with the amount of stored beam; in case of FCC-hh it reaches about 3.2 h. The estimated time to refill the collider and resume luminosity operation is 4 h.

The minium beamscreen aperture of 25 mm has been determined by estimating the instability rise times and allowing for some margin with respect to the speed of mitigation techniques, such as fast feedback. The initial studies of N. Monet and G. Rumolo [5] have been later confirmed with full studies including all the relevant detail of the beamscreen geometry by S. Arsenyev et al. [6]. Adding the space required for cooling and vacuum then allows to determine the minimum aperture for the magnets to be 50 mm.

An important collider parameter of FCC-hh is the bunch spacing. The total beam current is largely limited by the emission of synchrotron radiation and the need to remove it from the cold magnets. The distribution of the current over bunches has some flexibility. A smaller bunch spacing would distribute the luminosity over more collisions and thus reduce the number of background events per collision. This can simplifiy the detector design.

One of the key drivers of the bunch distance is the electron cloud, which can also lead to beam instabilities. In FCC-hh the generation and build-up of the cloud is suppressed by a special beamscreen design that removes most synchrotron radiation photons from the beam chamber. The build-up is suppressed by surfact coating on the beamscreen or by laser treatment, both of which reduce the secondary emission yield—the number of secondary electrons produced by each electron that hits the beamscreen. However, the acceptable secondary emission yield depends on the spacing between the proton bunches. The nominal spacing of 25 ns allows for a yield of up to 1.2 in the quadrupoles, the tightest requirement in any component as shown by studies of L. Mether [6]. For the shorter bunch spacings of 12.5 and 5 ns the limit is reduced to about 1.0 and therefore at the current moment does not provide enough margin to be sure to reach the full performance goal if no additional measures are taken.

Further work to reduce the electron cloud is thus required to enable smaller bunch spacings and potentially ease the design of the detectors.

## CONCLUSION

Collective instabilities play an important role in future coliderdesigns such as CLIC or FCC-hh. They drive important design choices. In CLIC the beam parameters, the cost and power consumption of the project are a direct consequence of wakefield effects in the main linac. The project has been optimised for minimum cost and power consumptions by going to the limit (with required margin) of these effects and by selecting the optimum accelerating structure.

In FCC-hh, collective instabilities are critical in defining the magnet aperture, which impacts the cost of the project. Also the choice of beam time structure is governed by collective effects. They therefore have a direct impact on the physics performance of the collider.

## REFERENCES

[1] CLIC, http://clic.cern

[2] FCC, http://fcc.web.cern.ch

[3] K. Sjobak and Alexej Grudiev, “The CLICopti RF structure parameter estimator”, (2014).

[4] D. Schulte, “Multi-Bunch calculations in the CLIC Main Linac”, (2009).

[5] N. Monet, G. Rumolo, private communication.

[6] Abada, A. et al., “FCC-hh: The Hadron Collider”, Eur.Phys.J.ST 228 (2019) 4, 755-1107.

# MITIGATION OF THE IMPEDANCE-RELATED COLLECTIVE EFFECTS IN FCC-EE*

M. Zobov[1 †], E. Belli[2], R. Kersevan[2], A. Novokhatski[3], S. G. Zadeh[4], and M. Migliorati[5]
[1]INFN-LNF, Frascati, Italy
[2]CERN, Geneva, Switzerland
[3]SLAC, Stanford, California 94309 USA
[4]Rostock University, Rostock, Germany
[5]University of Rome La Sapienza and INFN-Roma1, Rome, Italy

*Abstract*

In order to achieve a high luminosity in the electron-positron Future Circular Collider (FCC-ee), very intense multi-bunch beams with low emittances are accumulated in two separate rings and collide in two interaction regions exploiting the crab waist collision scheme. In order to preserve beam quality and to avoid collider performance degradation a careful study of beam collective effects is required. In this paper we overview impedance related coherent beam effects and instabilities potentially dangerous for FCC-ee and discuss measures and techniques for their mitigation.

## INTRODUCTION

In order to ensure the future worldwide particle physics program, CERN has launched the Future Circular Collider (FCC) study for the design of different circular colliders for the post-LHC era [1–4]. A high luminosity electron–positron collider FCC-ee (former TLEP [5]) is considered as a potential first collider option to cover the beam energy range from 45.6 GeV to 182.5 GeV, thus to allow studying the properties of the Higgs, W and Z bosons and top quark pair production threshold with unprecedented precision. For example, the design luminosity of $2.3\times10^{36}$ $\mathrm{cm^{-2}s^{-1}}$ at the Z resonance (45.6 GeV/beam) is by almost five orders of magnitude higher than the maximum luminosity ever achieved at LEP at the same energy (See Table 2 in [6]). There are several main ingredients that help reaching the high luminosities in FCC-ee: the two separate rings allow colliding many bunches without their parasitic interaction; the longer circumference allows storing higher beam intensities with the same synchrotron radiation loss; the crab waist collision scheme proposed [7, 8] and successfully tested at LNF INFN [9] makes it possible to reduce drastically the beta functions at the interaction points, to collide beams with much lower emittances and to suppress nonlinear resonances induced by the beam-beam interaction [10].

As it can be seen from Table 1 the beam emittances of FCC-ee are very small, comparable to those of the modern synchrotron light sources, while the beam stored currents are close to the best current values achieved in the last generation of particle factories (see Table 2 in [11] for comparison). Therefore, a careful study of collective effects is required in order to preserve the quality of the intense beams, to suppress eventual beam instabilities and to avoid excessive RF power losses leading to a damage of vacuum chamber components and accelerator hardware.

In this paper we present a preliminary study of the collective effects in FCC-ee and discuss eventual measures for their mitigation. A particular focus is given to the vacuum chamber impedance and impedance related instabilities.

Below we will consider only the Z resonance option since it is more vulnerable to the collective effects and instabilities because of the lower beam energy, longer damping times, higher beam intensities and highest number of bunches.

## BEAM COUPLING IMPEDANCE AND ITS MINIMIZATION

As it has been shown in [12], for the 100 km long collider the vacuum chamber size, shape and material conductivity is of crucial importance for beam dynamics and, respectively, for collider design solutions and parameters choice. First of all, it has been decided to use the vacuum chamber with a round cross section in order to avoid the betatron tune variation with beam current in multi-bunch operations due to the qudrupolar resistive wall (RW) wake fields [13, 14]. It has been estimated that for a rectangular vacuum chamber made of copper and having the transverse sizes 70x120 $\mathrm{mm}^2$ the tune shift would be as high as 0.4 for the nominal beam current of 1.4 A. The beam pipe radius of 35 mm has been chosen for FCC-ee as a reasonable compromise between the beam impedance and the power required for magnet power supplies.

Actually the shape of the beam pipe is not totally round but additional antechambers (winglets) are foreseen for pumping purposes and installation of synchrotron radiation (SR) absorbers, similarly to SuperKEKB design [15]. In addition, the antechambers are very helpful in suppression of the electron cloud effects in the positron ring.

In order to reduce the impedance it is desirable to avoid using multiple transitions in the vacuum chamber cross-section. For this reason the FCC-ee twin dipole and quadrupole magnets are designed in such a way to incorporate the beam pipe with the chosen geometry [16]. Fig. 1 shows a CAD model of a 1 m long section with the twin-bore magnets,

* This project has received funding from the European Union's Horizon 2020 Research and Innovation programme under Grant Agreement No 730871.
† mikhail.zobov@lnf.infn.it

| Parameter | Z | W | H | ttbar | ttbar |
|---|---|---|---|---|---|
| Circumference *C* [km] | 97.75 | 97.75 | 97.75 | 97.75 | 97.75 |
| Energy *E* [GeV] | 45.6 | 80 | 120 | 175 | 182.5 |
| Number of bunches/beam | 16640 | 2000 | 328 | 59 | 49 |
| Bunch population *Np* [1.0e11] | 1.7 | 1.5 | 1.8 | 2.2 | 2.3 |
| Beam current *I* [mA] | 1390 | 147 | 29 | 6.4 | 5.4 |
| SR*energy loss per turn [GeV] | 0.036 | 0.34 | 1.72 | 7.8 | 9.21 |
| Bunch length with SR/BS*, σz [mm] | 3.5/12.1 | 3.0/6.0 | 3.15/5.3 | 2.75/3.82 | 1.97/2.54 |
| Bunch energy spread, SR/BS [%] | 0.038/0.132 | 0.066/0.131 | 0.099/0.165 | 0.144/0.196 | 0.150/0.192 |
| Longitudinal damping time [turns] | 1281 | 235 | 70 | 23.1 | 20 |
| Horizontal emittance, εx [nm] | 0.27 | 0.84 | 0.63 | 1.34 | 1.46 |
| Vertical emittance, εy [pm] | 1.0 | 1.7 | 1.3 | 2.7 | 2.9 |
| Luminosity per IP [1.0e34, cm-2s-1] | 230 | 28 | 8.5 | 1.8 | 1.55 |

Table 1: Relevant FCC-ee baseline parameters. * SR: synchrotron radiation, BS: beamstrahlung.

the inserted vacuum chambers and pumping ports for localized pumps [17]. Furthermore, it is being considered using the "comb-type" technology in design of bellows and gate valves [18] with the RF shields fitting the vacuum chamber shape thus providing an electromagnetic continuity. As shown in Fig. 2, the BPM buttons positions are also chosen to fit this vacuum pipe geometry [17].

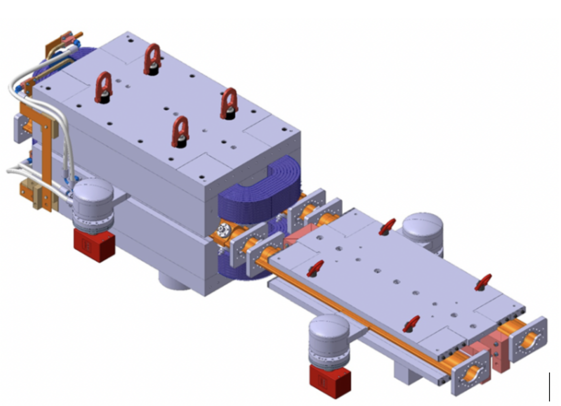

Figure 1: CAD model of the FCC-ee vacuum chamber with installed twin-bore magnets and attached pumping ports.

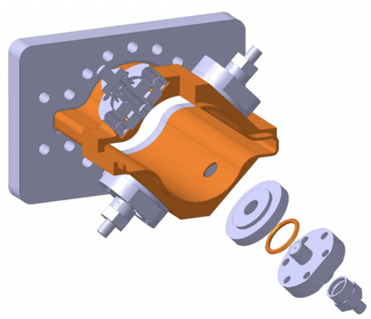

Figure 2: An extended view of one BPM block with button electrodes.

The FCC-ee vacuum chambers have to be coated in order to mitigate the electron cloud effects (beam induced multipacting) in the positron ring and/or to improve the vacuum pumping in both rings. Thin layers of NEG, TiN and AC have been considered for these purposes [19]. It has been demonstrated [12] that under certain assumptions, that are valid for the FCC-ee parameters, the longitudinal and transverse impedances of a two-layer beam pipe are given by the sum of two terms, the first term representing the well-known impedance of a single layer beam pipe and the second one describing an inductive perturbation proportional to the thickness $\Delta$ of the coating:

$$\frac{Z_L(\omega)}{C} \simeq \frac{Z_0\omega}{4\pi cb}\left\{[\mathrm{sign}(\omega)-i]\,\delta_2 - 2i\Delta\left(1-\frac{\sigma_1}{\sigma_2}\right)\right\} \quad (1)$$

$$\frac{Z_T(\omega)}{C} \simeq \frac{Z_0}{2\pi b^3}\left\{[\mathrm{sign}(\omega)-i]\,\delta_2 - 2i\Delta\left(1-\frac{\sigma_1}{\sigma_2}\right)\right\} \quad (2)$$

where $Z_0$ is the vacuum impedance, $c$ the speed of light, $b$ the pipe radius, $\delta_1$, $\sigma_1$ and $\delta_2$, $\sigma_2$ the skin depths and conductivities of the coating and the beam pipe (substrate), respectively.

As it can be seen, for the above assumptions, the real part of the impedance does not depend on the coating thickness and conductivity. The performed numerical studies [12] have confirmed that the resulting RF power losses due to the RW impedance remain almost unchanged for the coating conductivity and thickness varying in a very wide range. In turn, since the perturbation of the imaginary part due to the coating is proportional to its thickness and to the term $(1-\sigma_1/\sigma_2)$, if the coating conductivity is much smaller than the beam pipe material conductivity the impedance depends only on the thickness of the coating layer. On the other hand, if the two conductivities are comparable, this term reduces the coating perturbation. It has been shown that the coating thickness plays a crucial role affecting both single and multibunch beam dynamics [12]. In particular, in order to keep longitudinal microwave instability under control the coating thickness should be as small as 50-100 nm [20]. For this reason, a campaign of dedicated measurements has been launched to to study the properties of NEG thin films with thickness below 250 nm [20,21], such as secondary emission yield and activation performance.

In addition to the RW impedance there are many other impedance sources in the machine. The design of the vacuum chamber components such as RF cavities, kickers, beam position monitors (BPMs), bellows, flanges etc. has not been finalized yet. In order to evaluate their possible impedance contribution, the present strategy consists in adopting the best design solutions of the accelerator components used in the modern synchrotron light sources and the particle factories. These are, for example, comb-like bellows, gate valves and flanges used in SuperKEKB [22], the DAΦNE longitudinal feedback kickers [23] and injection kickers [24], SIRIUS conical beam position monitors [25] etc. The work is ongoing in order to decrease the FCC-ee interaction region impedance and to suppress eventual trapped higher modes (HOM) in the area where the two ring beam pipes merge (Y-chamber) [26], see Fig. 3.

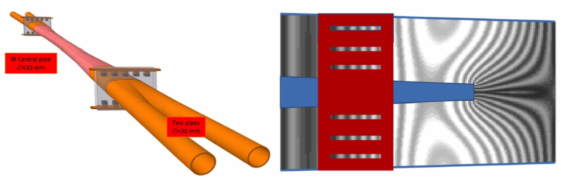

Figure 3: The interaction region Y-chamber with the installed HOM suppressors (see details in [26]).

Special efforts are being dedicated to design the RF cavities with HOM couplers in such a way to keep the HOM parameters under a harmless level [27,28].

For the present impedance model we consider that for running at Z energy the RF system will consist of 56 single cell cavities operating at 400 MHz [29] and arranged in groups of four cavities connected to the beam pipe by 0.5 m long tapers. In order to eliminate the beam halo and to suppress the background, collimators based on PEP-II and SuperKEKB design [30,31] are planned to be installed in the machine, for a total number of 20 (10 for each plane). The impedance contribution of the 10000 absorbers to cope with the SR has been minimized by placing them inside the two rectangular antechambers on both sides of the beam pipe. This model also includes 4000 BPMs [25] and 8000 comb-type bellows with RF shielding [32] to be allocated before and after each BPM. The impedance contribution of the absorbers "hidden" inside the antechambers is almost negligible with respect to the contributions of the other vacuum chamber components.

The coupling impedances and wake fields for these vacuum chamber elements have been evaluated numerically [21]. Figure 4 shows the longitudinal wake potentials of each component for the nominal bunch length of 3.5 mm. Table 2 summarizes the corresponding loss factors. As it can be seen, the resistive walls with 100 nm coating provide the dominating contribution in both the total wake potential

| Component | Number | $k_{loss}$ [V/pC] | $P_{loss}$ [MW] |
|---|---|---|---|
| Resistive walls | 97.75 km | 210 | 7.95 |
| RF cavities | 56 | 18.46 | 0.7 |
| RF double tapers | 14 | 6.12 | 0.23 |
| Collimators | 20 | 38.36 | 1.45 |
| Beam position monitors | 4000 | 31.47 | 1.19 |
| Bellows with RF shielding | 8000 | 49.01 | 1.85 |
| **Total** | | **353.4** | **13.4** |

Table 2: RF power losses due to different vacuum chamber components

and respective power losses that are not negligible compared with the 50 MW power lost by SR. Hopefully, the power losses are expected to be substantially lower due to the bunch lengthening.

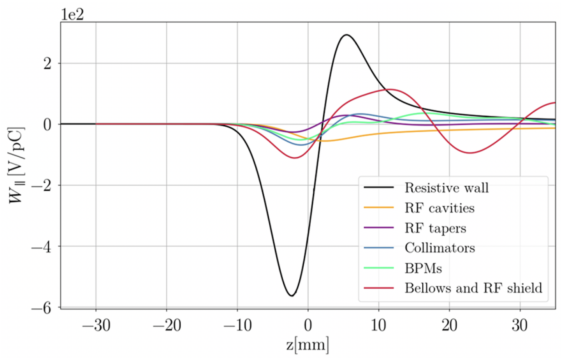


Figure 4: Longitudinal wake potential of different vacuum chamber components calculated for 3.5 mm Gaussian bunch. The resistive wall potential is plotted for 100 nm thin coating.

## IMPEDANCE RELATED EFFECTS AND INSTABILITIES

The electromagnetic beam interaction with a surrounding vacuum chamber, described in terms of wake fields and impedances, affects longitudinal and transverse beam dynamics. It can result in both single and multi-bunch instabilities and overheating of vacuum chamber components. The impedance related collective effects can substantially worsen the overall collider performance.

As it has been shown in [12] the resistive walls give the dominating contribution to the impedance budget of FCC-ee. The resistive wall impedance alone causes a substantial bunch lengthening and bunch shape distortion as shown in Fig. 5, compared to the unperturbed Gaussian bunch (dashed line in the right-hand side of the figure).

The left plot in Fig. 5 shows the rms bunch length as a function of bunch intensity for different thickness of the vacuum chamber coating while the right picture demonstrates the bunch profile distortion for the nominal bunch intensity [12].

In collisions with a large Piwinski angle, as is the case of FCC-ee, the collider geometric luminosity decreases for longer bunches. On the other hand, for longer bunches

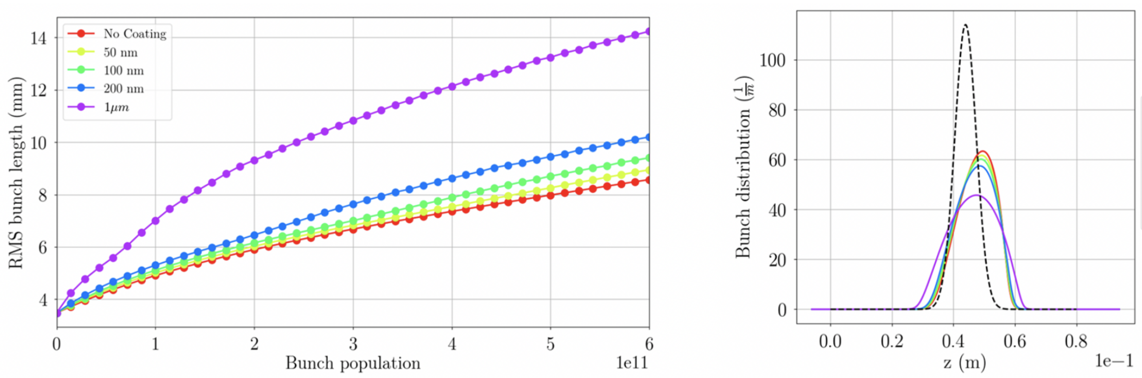


Figure 5: Bunch lengthening (left picture) and bunch shape distortion (right pictures) calculated for different coating thicknesses. The dashed line in the right figure is the unperturbed zero current Gaussian bunch.

the beam lifetime increases and the RF power losses are reduced. However, at certain bunch intensity, microwave instability can take place. Typically the microwave instability does not produce a bunch loss, but the consequent energy spread growth and possible bunch internal oscillations above the instability threshold cannot be counteracted by a feedback system. In addition, the longitudinal wake fields result in the synchrotron tune reduction and a large incoherent synchrotron tune spread. Both these effects influence beam-beam performance shifting the collider working point and affecting the coherent and incoherent beam-beam resonances.

Figure 6 shows the energy spread versus bunch intensity for different values of vacuum chamber coating thickness (left plot) and the synchrotron tune shift and spread calculated for the 100 nm coating thickness (right plot).

As it is seen in Fig. 5 and Fig. 6, in order to avoid the excessive bunch lengthening and, even more important, to stay below the microwave instability threshold the coating thickness should be smaller than 200 nm. This request has resulted in dedicated studies of thin TiZrV films properties for the film thickness below 250 nm [21].

Including the impedance contributions of the other vacuum chamber components does not change the results drastically. The left plots in Fig. 7 show the bunch length in FCC-ee as a function of the bunch population, while the right plots indicate the respective energy spread calculated using the wake potential shown in Fig. 4. The blue curves correspond to the bunch length and energy spread variations for non-colliding bunches. At the nominal intensity the bunch lengthens till about 7 mm, while the microwave instability threshold is by about a factor of 1.5 higher than the nominal bunch population. So there is only a small margin left for eventual impedance increase. In collision, the “beamstrahlung” effect [33] results in an additional energy spread increase leading to the strong bunch elongation and the microwave instability threshold increase beyond the considered bunch intensities (brown curves).

Differently from the longitudinal microwave instability, the transverse mode coupling instability (TMCI) is destructive for intense bunches. The bunches can be lost in few revolution turns. The instability takes place when coherent frequencies of different modes of transverse internal bunch oscillations merge. The TMCI threshold has been evaluated with the analytical Vlasov solver DELPHI [34] by considering the dominating RW impedance and by taking into account the bunch lengthening due to the longitudinal wake fields shown in Fig. 7. It has been found that in the transverse case the TMCI instability threshold is affected to a lesser extent by the coating thickness due to the bunch lengthening effect. For comparison, Fig. 8 shows the real part of the frequency shift of the first coherent oscillation modes as a function of the bunch population for 50 nm (left) and 1 $\mu$m coatings (right), respectively. The dashed line represents the nominal bunch intensity. The TMCI threshold (merging lines) is about a factor 2.5 higher than the nominal intensity.

Analyzing the multi-bunch beam dynamics it has been found that the coupled bunch instability due to the transverse RW long range wake fields is another critical issue for the collider [12]. The growth rate of the fastest coupled bunch mode is estimated to be 435 1/s corresponding to about 7 revolution turns. It is worth noting here that the transverse radiation damping time is 2550 turns, i.e. it is much longer than required for the instability suppression. So a robust feedback system is necessary to mitigate the fast instability. As a possible solution it has been proposed to use a distributed feedback system. A dedicated study is underway to develop such a challenging system [35].

The longitudinal radiation damping alone also cannot suppress the longitudinal coupled bunch instabilities due to the beam interaction with parasitic higher order modes (HOM) trapped in the vacuum chamber components. In order to cope with the instabilities special HOM damping techniques are to be applied to reduce the shunt impedances of the HOM to a harmless level, as discussed in [36]. In addition, also in this case a longitudinal feedback system has to be developed as a further safety knob.

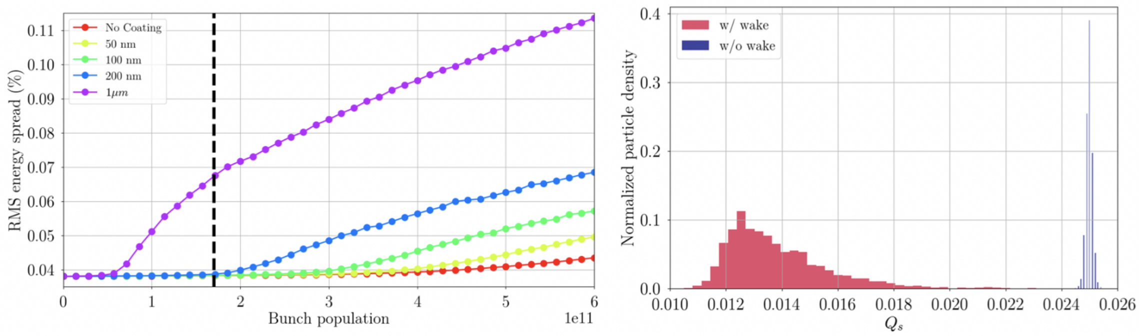


Figure 6: Rms energy spread as a function of the bunch intensity (left picture) and the synchrotron frequency distribution at the nominal bunch current calculated for the coating thickness of 100 nm (right picture).

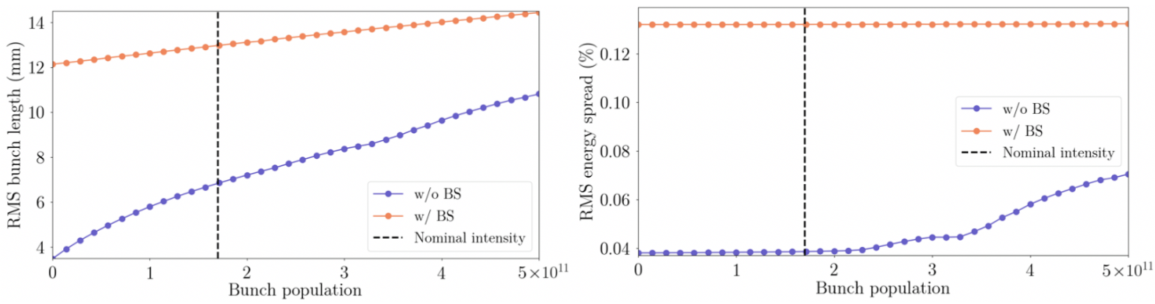


Figure 7: Bunch lengthening (left picture) and the energy spread (right picture) in FCC-ee as a function of the bunch intensity.

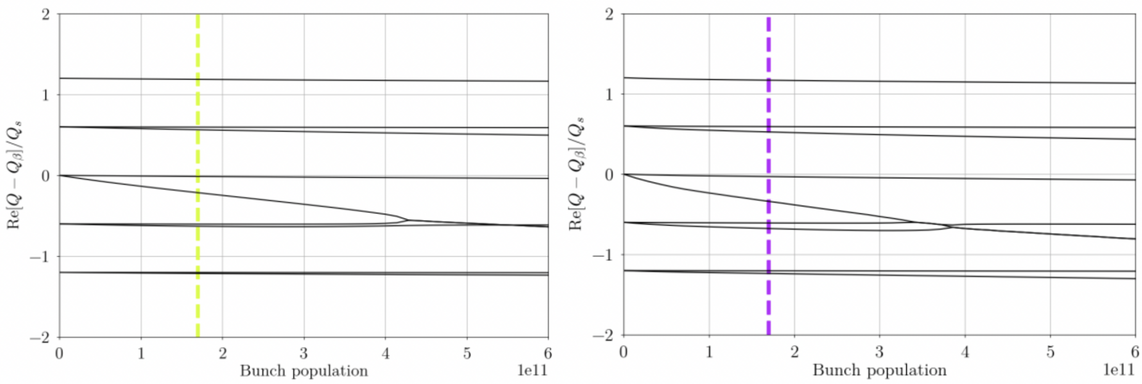


Figure 8: Real part of the frequency shift of the first transverse coherent oscillation modes for 50 nm (left) and 1 $\mu$m (right) coating thickness.

## CONCLUSIONS

FCC-ee beam coupling impedance and related collective effects play an important role for both the parameters choice and design solutions for the 100 km collider. The work is in progress in order to minimize the impedance and to mitigate the related instabilities. The shape of the vacuum chamber pipe was chosen to be similar to that used in SuperKEKB: the round shape should help minimizing the eventual betatron tune shift due to the quadrupolar resistive wall wake fields, while the attached winglets (small antechambers) will be used to install "hidden" absorbers and to connect the pumping ports. In order to avoid using multiple tapers it has been decided to keep the same chamber cross-section all around the ring, in the arcs and straight sections. Moreover, bellows, gate valves, flanges and BPM blocks are being designed in such a way to fit the vacuum pipe shape. The beam dynamics analysis has shown that the pipe coating should be as thin as possible in order to mitigate the impact of the resistive wall impedance. Respectively, a dedicated program has been launched at CERN in order to study the properties of thin TiZeV films. The low impedance vacuum chamber component design will rely on the experience gained during design and commissioning phases of other high intensity particle colliders and modern sources of synchrotron radiation. A particular care now is given to reduce the impedance and to eliminate trapped higher order modes in the FCC-ee interactions region. An optimization of the RF cavity HOM couplers is under way in order to keep the HOM parameters under a harmless level. Since the estimated growth time of the couple bunch instabilities is compared to a few revolutions turns a proposal of using a distributed feedback system has been endorsed and is under study. The work will continue to keep both single and multi-bunch effects and instabilities in FCC-ee under control.

## ACKNOWLEDGEMENTS

This work was partially supported by the European Commission under the HORIZON 2020 Integrating Activity project ARIES, Grant agreement No. 730871, and by INFN National committee V through the ARYA project.

## REFERENCES

[1] FCC Collaboration, "FCC Physics Opportunities: Future Circular Collider Conceptual Design Report Volume 1", Eur.Phys.J. C79 (2019) no.6, 474. DOI:10.1140/epjc/s10052-019-6904-3.

[2] FCC Collaboration, "FCC-ee: The Lepton Collider: Future Circular Collider Conceptual Design Report Volume 2", Eur.Phys.J.ST 228 (2019) no.2, 261-623. DOI:10.1140/epjst/e2019-900045-4

[3] FCC Collaboration, "FCC-hh: The Hadron Collider: Future Circular Collider Conceptual Design Report Volume 3", Eur.Phys.J.ST 228 (2019) no.4, 755-1107. DOI:10.1140/epjst/e2019-900087-0

[4] FCC Collaboration, "HE-LHC: The High-Energy Large Hadron Collider", Eur.Phys.J.ST 228 (2019) no.5, 1109-1382. DOI:10.1140/epjst/e2019-900088-6

[5] M.Bicer at al., "First look at the physics case of TLEP", JHEP 1401 (2014) 164. DOI: 10.1007/JHEP01(2014)164

[6] R. Assmann, M. Lamont, and S. Myers, "A brief history of the LEP collider", Nucl. Phys. B Proc. Suppl., Vol. 109, pp. 17-31, 2002. DOI:10.1016/S0920-5632(02)90005-8

[7] P. Raimondi, "Status on SuperB effort", talk at the 2nd SuperB Workshop, Frascati, Italy, 2006.

[8] P. Raimondi, D. Shatilov, and M. Zobov, "Beam-beam issues for colliding schemes with Large Piwinski angle and crabbed waist", Rep. LNF-07-003-IR, e-Print: physics/0702033, Feb. 2007.

[9] M. Zobov et al., "Test of crab waist collisions at DAΦNE Phi-factory", Phys. Rev. Lett., Vol. 104, p. 114801, Apr. 2010. DOI: 10.1103/PhysRevLett.104.174801

[10] D. Shatilov, E. Levichev, E. Simonov, and M. Zobov, "Application of frequency map analysis to beam-beam effects study in crab waist collision scheme", Phys. Rev. ST Accel. Beams, Vol.14, p. 014001, Jan. 2011. DOI: 10.1103/PhysRevSTAB.14.014001

[11] M. Zobov, "Next generation of electron-positron factories", Phys. Part. Nucl., Vol. 42, pp-799. 782, 2011. DOI: 10.1134/S1063779611050066

[12] M. Migliorati, E. Belli, and M. Zobov, "Impact of the resistive wall impedance on beam dynamics in the Future Circular e+e- collider", Phys. Rev. Accel. Beams, Vol. 21, p. 041001, Apr. 2018. doi: 10.1103/PhysRevAccelBeams.21.041001

[13] A. Chao, S. Heifets, and B. Zotter, "Tune shifts of bunch trains due to resistive vacuum chambers without circular symmetry", Phys. Rev. ST Accel. Beams, Vol. 5, p. 111001, 2002. doi: 10.1103/PhysRevSTAB.5.111001

[14] A. Blednykh et al., "Low-frequency quadrupole impedance of undulators and wigglers", Phys. Rev. Accel. Beams, Vol. 19, p. 104401, Oct. 2016. doi: 10.1103/PhysRevAccelBeams.19.104401

[15] Y. Suetsugu et al., "Design and construction of the SuperKEKB vacuum chamber", J. Vac. Sci. Tech. A, Vol.30, p. 031602, Mar. 2012. doi:10.1116/1.3696683

[16] A. Milanese, "Efficient twin aperture magnets for the future e+e- collider", Phys. Rev. Accel. Beams, Vol. 19, p. 112401, Nov. 2016. doi: 10.1103/PhysRevAccelBeams.19.112401

[17] C. Garion, and R. Kersevan, "Design of the vacuum system of the FCC-ee electron-positron collider", Proc. 10th Int. Particle Accelerator Conf. (IPAC'19), Melbourne, Australia, May 2019, pp. 1319-132. doi: 10.18429/JACoW-IPAC2019-TUPMP035

[18] Y. Suetsugu et al., "Development of bellows and gate valves with a comb-type rf shield for high current accelerators: four-year beam test at KEK B-factory", Rev. Sci. Instrum., Vol. 78, p. 043302, Apr. 2007. doi: 10.1063/1.2723747

[19] E. Belli et al., "Coupling impedance and collective effects for FCC-ee", Proc. 8th Int. Particle Accelerator Conf. (IPAC2017), Copenhagen, Denmark, May 2017, pp. 3734-3737. doi: 10.18429/JACoW-IPAC2017-THPAB020

[20] E. Belli et al., "Single bunch instabilities in FCC-ee", Proc. 9th Int. Particle Accelerator Conf. (IPAC2018), Vancouver, Canada, pp. 3336-3339, doi: 10.18429/JACoW-IPAC2018-THPAK052

[21] E. Belli et al., "Electron cloud buildup and impedance effects on beam dynamics in the Future Circular e+e- Collider and experimental characterization of thin TiZrV vacuum chamber coatings", Phys. Rev. Accel. Beams, Vol. 21, p. 111002, Nov. 2018. doi: 10.1103/PhysRevAccelBeams.21.111002

[22] K. Shibata et al., "Commissioning status of SuperKEKB vacuum system", Proc. 62th ICFA Advanced Beam Dynamics Workshop on High Luminosity e+e- Colliders (eeFACT2018), Hong Kong, China, pp. 226-233. doi: 10.18429/JACoW-eeFACT2018-WEOAB01.

[23] R. Boni et al., "A waveguide overloaded cavity as longitudinal kicker for DA$\phi$NE bunch-by-bunch feedback system", Part. Accel., Vol. 52, pp. 95-113, Dec. 1995.

[24] D. Alesini et al., "Design, test, and operation of new tapered strip-line injection kickers for the e+e- collider DA$\phi$NE", Phys. Rev. Accel. Beams, Vol. 13, p. 111002, 2010. doi10.1103/PhysRevSTAB.13.111002

[25] H.O.C. Duarte, L. Sanfelici, and S.R.Marques, "Design and impedance optimization of the SIRIUS BPM button", Proc. IBIC2013, Oxford, UK, 2013, pp. 365-368.

[26] A. Novokhatski et al., "Unavoidable trapped mode in the interaction region of colliding beams", Phys. Rev. Accel. Beams, Vol. 11, p. 111005, Nov. 2017. doi: 10.1103/PhysRevAccelBeams.20.111005

[27] S.G. Zadeh, “HOM damping design studies for FCC-ee cavities”, presentation at FCC Week 2019, Brussels, Belgium, Jun. 2019. https://indico.cern.ch/event/727555/contributions/3436401/

[28] S. Gorgi Zadeh, T. Flisgen, R.Calaga and U. van Rienen, HOM damping options for the Z-Pole operating scenario of FCC-ee, Journal of Physics: Conference Series, 2019, doi:10.1088/1742-6596/1350/1/012007

[29] A. Butterworth, “Cavity design and beam-cavity interaction challenges”, presentation at FCC Week 2017, Berlin, Germany. https://indico.cern.ch/event/556692/contributions/2484361/

[30] S. DeBarger et al., “The PEP-II movable collimators”, Preprint SLAC-PUB-11752, 2001.

[31] T. Ishibashi, S. Terui, and Y. Suetsugu, “Low impedance movable collimators for SuperKEKB”, Proc. 8th Int. Particle Accelerator Conf., Copenhagen, Denmark, pp. 2929-2932. doi: 10.18429/JACoW-IPAC2017-WEPIK009

[32] Y. Suetsugu, M. Shirai, and K. Shibata, “Possibility of comb-type shield structure for high current accelerators”, Phys. Rev. Accel. Beams, Vol. 6, p. 103201, Dec. 2003. doi: 10.1103/PhysRevSTAB.6.103201

[33] D. Leshenok, S. Nikitin, and M. Zobov, “Model to study interplay between beamstrahlung and coupling impedance in future lepton colliders”, e-Print: 2004.02553, Apr.2020.

[34] https://twiki.cern.ch/twiki/bin/view/ABPComputing/DELPHI

[35] A.Drago, “Feedback systems for FCC-ee”, Proc. 58th ICFA Advanced Beam Dynamics Workshop on High Luminosity Circular e+e- Colliders, 24-27 October 2016, Daresbury, United Kingdom, pp. 136-142. doi: 10.18429/JACoW-eeFACT2016-TUT3AH9

[36] E.Belli et al., “Single beam collective effects in FCC-ee due to beam coupling impedance”, e-Print: 1609.03495, Sep. 2016.

# Mitigation of Coherent Beam Instabilities in CEPC

Na Wang[1†], Yuan Zhang[1, 2], Yudong Liu[1], Saike Tian[1], Kazuhito Ohmi[3], Chuntao Lin[1, 2]
[1]Institute of High Energy Physics, CAS, Beijing, 100049, China
[2] University of Chinese Academy of Sciences, CAS, Beijing, 100049, China
[3]KEK, 1-1 Oho, Tsukuba, 305-0801 Japan

*Abstract*

The collective beam instabilities are potential restrictions in the Circular Electron Positron Collider (CEPC) to achieve high luminosity performance. These instabilities can induce beam quality degradation or beam losses. Different strategies used to mitigate these effects are discussed. The impedances of the dominant contributors are carefully designed and optimized to either reduce the parasitic power dissipation or increase the beam instability threshold. The bunch filling patterns are also optimized to fight the beam ion instability, the electron cloud build up and the transient beam loading effect.

## INTRODUCTION

Potential restrictions from collective beam instabilities include beam current thresholds and beam quality degradations. On the one hand, the beam current thresholds are mainly determined by instability-induced beam losses and heat load in vacuum components due to the parasitic power dissipations. On the other hand, the beam quality degradations include bunch lengthening and beam energy spread increase, synchrotron or betatron tune shift, emittance blow-up, etc.

CEPC is designed to cover beam energies to produce Z and Higgs bosons [1]. Therefore, different operational scenarios need to be considered. The design of the beam parameters for the Z boson shows most critical requirements on the beam instabilities, due to the lowest beam energy, highest beam current, slowest radiation damping, and synchrotron oscillations. In order to estimate the influence of these effects, the impedance model of the CEPC collider is developed. Based on the impedance studies, critical beam instability issues for the Z mode of operation and their mitigations are discussed. The main beam parameters are listed in Table 1.

Table 1: Main beam parameters of CEPC Z

| Parameter | Symbol, unit | Value |
|---|---|---|
| Beam energy | $E$, GeV | 45.5 |
| Circumference | $C$, km | 100 |
| Beam current | $I_0$, mA | 461.0 |
| Bunch number | $n_b$ | 12000 |
| Momentum compaction | $\alpha_p$ | $1.11\times10^{-5}$ |
| Betatron tune | $\nu_x/\nu_y$ | 363.1/365.22 |
| Synchrotron tune | $\nu_s$ | 0.028 |
| Radiation damping | $\tau_x/\tau_y/\tau_z$, ms | 843/843/436 |

† wangn@ihep.ac.cn

## IMPEDANCE MODELING

For the impedance modeling, the dominant impedance contributors are first identified, including both with large impedance and with small impedance but in large numbers. Meanwhile, the impedances of the components are carefully designed and optimized to either reduce the parasitic power dissipation or increase the beam instability threshold.

The resistive wall (RW) impedance is the dominant contribution to the total impedance when the goemetric impedances (GEO) have been kept low by careful design. Nonevaporable getter (NEG) coating is adopted on the copper beam pipe for vacuum pumping and electron cloud mitigation. The influence of the coating thickness on the longitudinal and transverse impedances is studied [2], as shown in Fig. 1 and Fig. 2. The solid and dashed lines correspond to the real and imaginary impedance, respectively. Here, the conductivity of NEG used in the impedance evaluation is 1 MS/m [3].

The results show that both longitudinal and transverse impedances are reduced with thinner NEG coating. In the frequency range of interest (the bunch spectrum extends to ~40 GHz), the NEG coating shows significant influence on the imaginary part of the impedances, which are mainly responsible for bunch lengthening and tune shift, and less impact on the real part, which emphasizes beam energy loss and instability growth rate. In CEPC, coating thickness of 0.2 μm has been chosen to reduce the impedance from resistive wall.

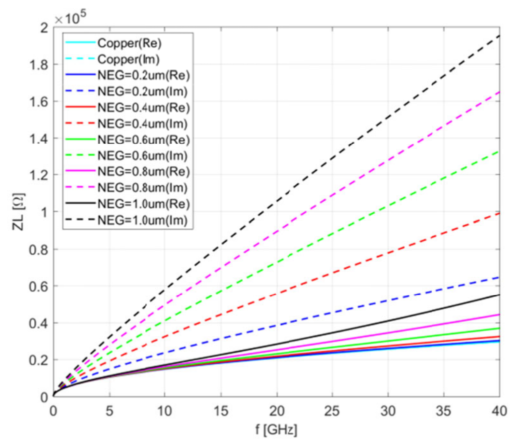


Figure 1: Longitudinal impedance with different thickness of NEG coating (the solid and dashed lines correspond to the real and imaginary impedance, respectively).

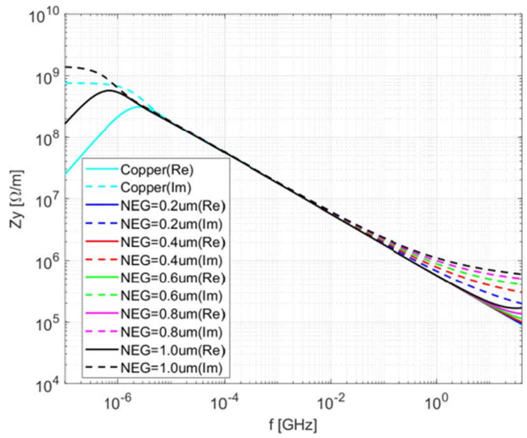


Figure 2: Transverse impedance with different thickness of NEG coating (the solid and dashed lines correspond to the real and imaginary impedance, respectively).

Since only the impedance in the frequency range of the bunch spectrum will affect the beam, the effective broadband impedances are calculated to quantitatively describe the influence of the coating thickness. With rms bunch length of 3 mm, the variations of the longitudinal and transverse effective impedance with different coating thickness are shown in Fig. 3 and Fig.4.

With thickness of NEG coating from 0 to 1 μm, the longitudinal impedance is increased by a factor of ~4 and the transverse kick factor is increased by a factor of ~3. However, the loss factor is only increased by ~20%. Here, we should note that the specific values are quite dependent on the bunch distribution and the radius of the beam pipe.

For the geometrical impedances, RF shielding is adopted for cavity structures, such as flanges, bellows, pumping ports, etc. Taper transitions of less than 1/10 are adopted at aperture discontinuities. Meanwhile, high order mode (HOM) damping is considered for resonant structures, such as the RF cavities, interaction region (IR) and the electro-separators.

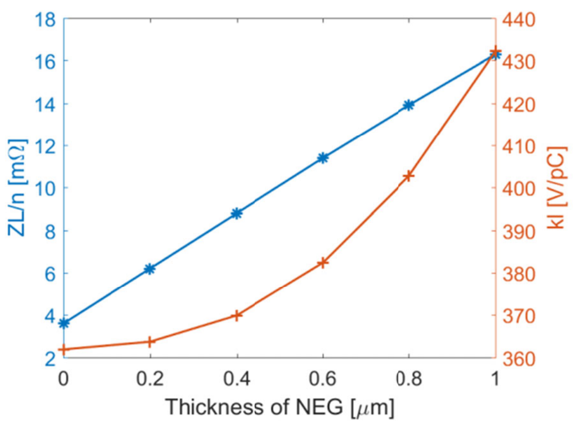


Figure 3: Dependence of the longitudinal effective impedance and loss factor on the thickness of NEG coating.

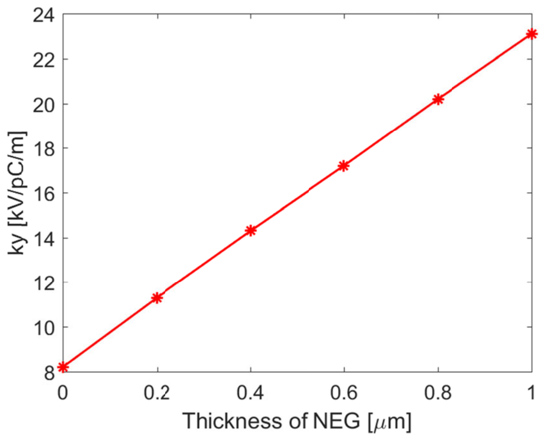


Figure 4: Dependence of the transverse kick factor on the thickness of NEG coating.

Table 2 shows the impedance budget of the main contributors with rms bunch length of 3 mm. With careful designs, the total longitudinal broadband effective impedance is 11.4 mΩ, the total loss factor is 786.8 V/pC, and the total transverse kick factor is 20.2 kV/pC/m. From the budget we can conclude that the longitudinal and transverse broadband impedances are dominated by the resistive wall, flanges and bellows. The loss factor or parasitic power loss of the beam is mainly contributed by the resistive wall and the RF cavities.

Table 2: Impedance budget of the main contributors

| Components | $Z_{\parallel}/n$, mΩ | $k_y$, kV/pC/m |
|---|---|---|
| Resistive wall | 6.2 | 11.3 |
| RF cavities | -1.0 | 0.3 |
| Flanges | 2.8 | 2.8 |
| BPMs | 0.1 | 0.3 |
| Bellows | 2.2 | 2.9 |
| Pumping ports | 0.02 | 0.6 |
| IR | 0.02 | 1.3 |
| Electro-separators | 0.2 | 0.2 |
| Taper transitions | 0.8 | 0.5 |
| Total | 11.4 | 20.2 |

## IMPEDANCE DRIVEN INSTABILITIES

### *Microwave instability*

The microwave instability will rarely induce beam losses, but may reduce the luminosity due to the deformed beam distribution and increase of the beam energy spread. The instability is simulated with the code Elegant [4, 5]. The dependences of bunch length and beam energy spread on the bunch charge are represented by the red curves in Fig. 5 and Fig. 6. The design bunch intensity is just above the instability threshold, and also turbulent distributions in longitudinal phase space are observed above the threshold, as shown in Fig.7.

Possible mitigations for this effect include impedance reduction and beam parameter optimization. Figures 5 and 6 show how the bunch length and beam energy spread evolve with bunch intensity for different impedance models. The purple and green lines show the behavior with only geometrical (GEO) and only resistive wall (RW) impedance, respectively. We can see that resistive wall impedance gives larger contribution to the bunch lengthening, while the geometrical impedance contributes more to the beam energy spread and instability threshold.

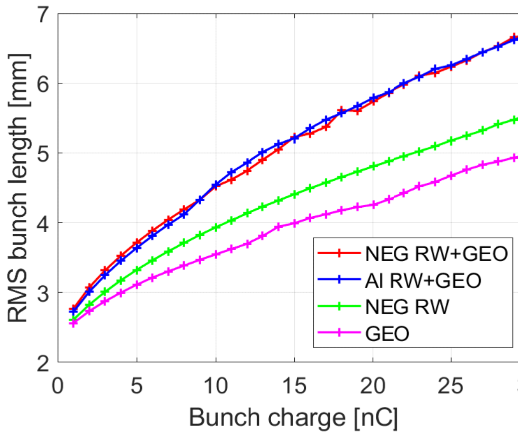


Figure 5: Dependence of bunch length on bunch charge with different impedance models.

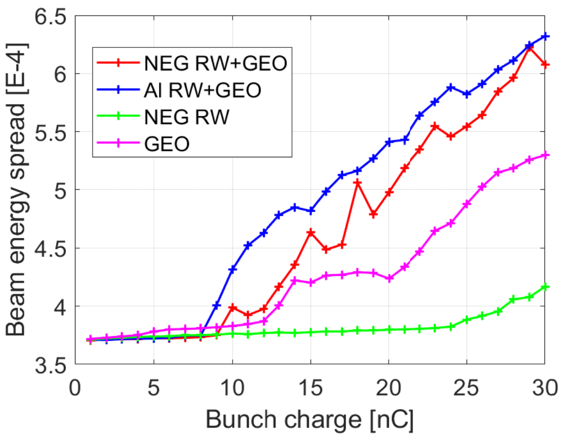


Figure 6: Dependence of beam energy spread on bunch charge with different impedance models.

Moreover, we also considered the case with aluminum (Al) beam pipe, as shown by the blue curves. The bunch lengthening is almost the same as for the NEG-coated beam pipe, but shows higher beam energy spread increase. By combining these results, we can get rough information of how much we can benefit from further impedance optimizations.

For the beam parameter optimization, a simple instruction is given by the Keil-Schnell criterion [6, 7]. We can get linear gain from increasing the momentum compaction, beam energy spread and bunch length. Meanwhile, beamstrahlung can also be beneficial.

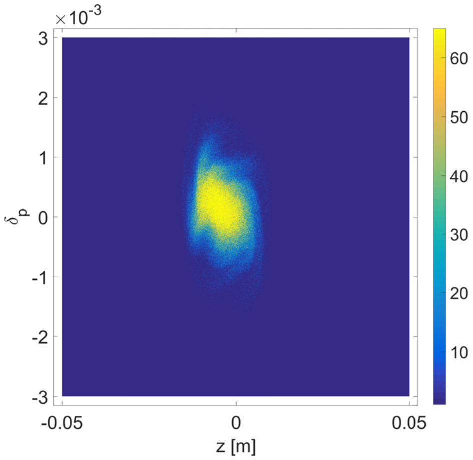


Figure 7: Longitudinal phase space distribution for a bunch charge of 10 nC. The color bar represents the number of macroparticles in each bin.

### *Transverse mode coupling instability*

The threshold for the transverse mode coupling instability (TMCI) is estimated by the eigenmode analysis. The threshold current is comparable with the design value without considering bunch lengthening, as shown in Fig. 8. However, significant bunch lengthening can be induced by the impedance and beamstrahlung at high beam current. Accordingly, the transverse effective impedance will decrease due to its dependence on the bunch distribution. Therefore, larger safety margin is obtained when considering bunch lengthening effects, as shown in Fig. 9.

### *Transverse resistive wall instability*

For the multi-bunch effects, coupled bunch instability can be driven by the resonance at zero frequency of the transverse resistive wall impedance. The most dangerous mode has a growth time of ~4.3 ms, which is about 12 turns. This is much faster than the radiation damping. Therefore, an effective bunch by bunch feedback system will be used to damp the instability. Meanwhile, a non-zero chromaticity can also help to shift the sampled impedance frequencies, and increase the beam current threshold.

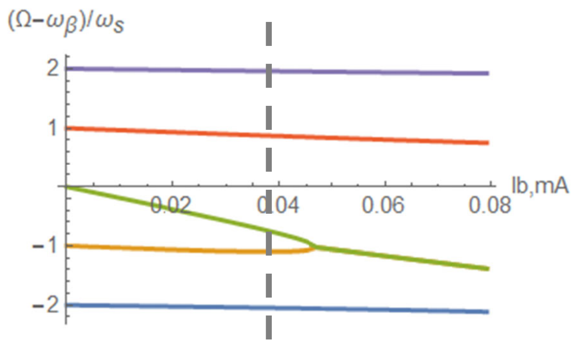


Figure 8: Head-tail mode frequency versus bunch intensity without bunch lengthening (the grey dashed line shows the design beam current).

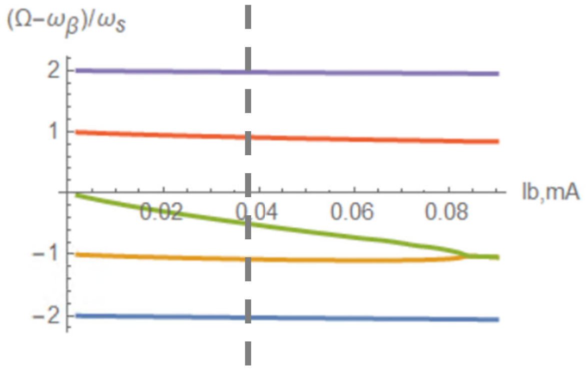


Figure 9: Head-tail mode frequency versus bunch intensity with bunch lengthening from impedance and beamstrahlung (the grey dashed line shows the design beam current).

### *Coupled bunch instabilities from RF HOMs*

Another important contribution to the coupled bunch instability is the high order modes (HOMs) of the accelerating cavities. 120 2-cell superconducting RF cavities (650 MHz) will be used for Z mode. Calculations show that the transverse and longitudinal coupled bunch instability driven by the sum of the RF HOMs is faster than the radiation damping or even feedback damping.

However, considering the whole RF system, HOM frequency spread due to the actual tolerances of the cavity construction can further relax the instability. Figures 10 and 11 show how the total impedance evolves when we consider different HOM frequency spread. Taking into account a HOM frequency spread of larger than 0.5 MHz, the impedance is well below the threshold determined by feedback damping. Meanwhile, strategies to further damp the HOMs are under investigation.

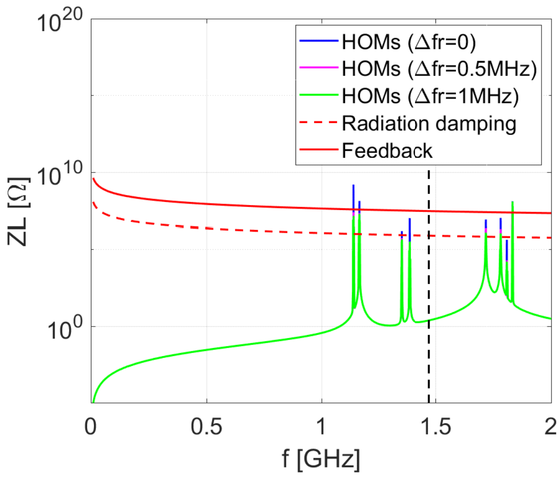


Figure 10: Impedance of the RF cavity monopole HOMs compared with the threshold determined by radiation damping and feedback damping of 5 turns.

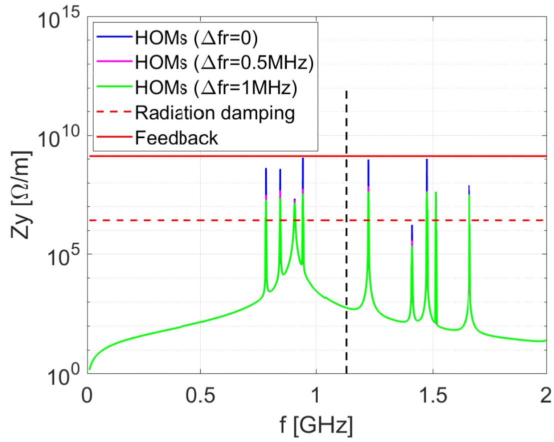


Figure 11: Impedance of the RF cavity dipole HOMs compared with the threshold determined by radiation damping and feedback damping of 5 turns.

## FAST BEAM ION INSTABILITY

In the electron ring, beam ion instability can be severe due to high beam current and small emittance which are required to reach high luminosity. The beam ion interaction can cause emittance blow-up and a positive tune shift along the bunch train. To avoid these effects, low vacuum level is required along with a multi-train filling pattern. The build-up of the ions is calculated, as shown in Fig. 12. With the average ion density, we get the instability growth time of ~2 ms. An efficient transverse feedback is required to damp the instability. More detailed simulation studies are underway.

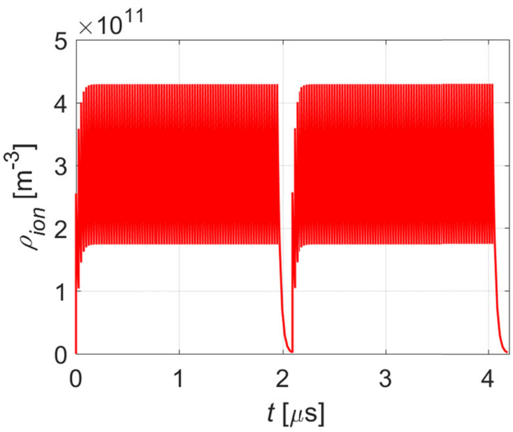


Figure 12: Build-up of the ions along the bunch train.

## ELECTRON CLOUD EFFECTS

Electron cloud can degrade the beam through both single bunch and coupled bunch instabilities, which can induce beam size blow-up or beam losses. To mitigate this effect, multi-train filling pattern with certain bunch spacing is suggested. The electron cloud build-up in both dipole and drift region is simulated with different bunch spacing. The average electron cloud density is around $3.2\times10^{10}$ m$^{-3}$ with secondary electron yield (SEY) of 1.6 and bunch spacing of 25 ns. This is comparable to the threshold determined by the single bunch instability. The build-up of electron cloud will be further suppressed by the NEG coating, for which a lower SEY is expected.

## INTERACTION WITH BEAM-BEAM

In conventional electron positron colliders, only the impedance-lengthened bunch is used in beam-beam simulations, instead of considering the impedance directly. This is not a problem since the longitudinal dynamics is not sensitive to beam-beam interaction. But it is different in high energy colliders since the bunch will also be lengthened during beam-beam interaction by beamstrahlung effect. It is very natural and more self-consistent to consider the longitudinal impedance directly in the beam-beam simulation [8].

By scanning the horizontal tune to see whether the transverse oscillation is stable with beam-beam interaction, it is found that the beam gets more unstable with impedance. One of the examples is demonstrated in Fig. 13. More studies show that reducing $\beta_x$ in the interaction point is efficient to damp this effect. Further optimization of the beam parameters and impedance is required.

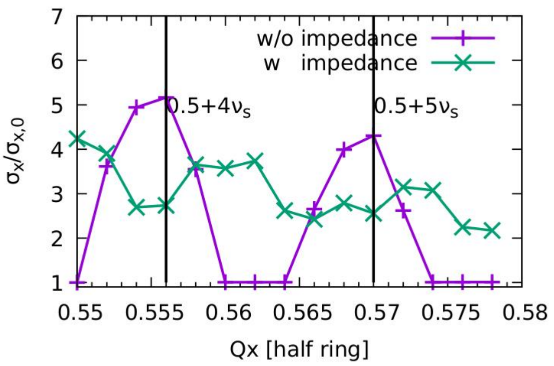


Figure 13: Horizontal beam size blow up in collision obtained by simulation with and without impedance.

## CONCLUSION

The collective beam instabilities are potential restrictions in CEPC to achieve high luminosity performance. Different strategies used to mitigate these effects have been discussed. The single bunch instability is dominated by the microwave instability, which can induce longitudinal phase space distortions and couple with the beam-beam interaction. The beam parameters and impedance need to be further optimized to get larger stable region in tune. The coupled bunch instabilities from the resistive wall and RF HOMs need to be damped by efficient bunch by bunch feedback systems. The two stream instabilities require multi-train filling pattern with certain bunch spacing, along with feedback and vacuum conditioning.

## ACKNOWLEDGEMENT

The authors would like to thank the support from NSFC (11775238, 11775239) and the Youth Innovation Promotion Association, CAS.

## REFERENCES

[1] CEPC Conceptual Design Report: Volume 1 – Accelerator, 2018.

[2] N. Wang and Q. Qin, “Resistive-wall impedance of two-layer tube”, Phys. Rev. ST Accel. and Beams 10, 111003, 2007.

[3] E. Koukovini-Platia, G. Rumolo, and C. Zannini. “Electromagnetic characterization of nonevaporable getter properties between 220-330 and 500-750 GHz for the Compact Linear Collider damping rings”, Phys. Rev. Accel. Beams, 20, 011002, 2017.

[4] M. Borland, “elegant: A Flexible SDDS-Compliant Code for Accelerator Simulation”, Advanced Photon Source LS-287, 2000.

[5] Y. Wang and M. Borland, “Pelegant: A Parallel Accelerator Simulation Code for Electron Generation and Tracking”, Proceedings of the 12th Advanced Accelerator Concepts Workshop, AIP Conf. Proc. 877, 241, 2006.

[6] E. Keil and W. Schnell, CERN Report, TH-RF/69-48, 1969.

[7] D. Boussard, CERN LAB II/RF/Int./75-2, 1975.

[8] Y. Zhang, N. Wang, C. Lin, C. Yu, “Crosstalk of beam-beam effect and longitudinal impedance at CEPC”, in *Proc*. IPAC’19, Melbourne, Australia, MOPGW068, 2019.

# MCBI in an Electron-Ion Collider*

R. Li

Thomas Jefferson National Accelerator Facility, Newport News, VA 23693, USA

*Abstract*

The luminosity performance for an electron-ion collider demands high-current operation for both the electron and ion beams, for a wide range of collision energies. This poses many challenges on the beam stability with regard to collective effects. In this paper, we present preliminary estimations of coherent instabilities for both of the EIC designs, i.e., JLEIC and eRHIC. Mitigation mechanisms or schemes envisioned for suppression of the instabilities are also discussed.

## INTRODUCTION

An electron-ion collider (EIC) is identified by the nuclear physics community as the next exploring machine for answering fundamental questions about QCD structure and dynamics of nuclear matter. To serve this goal, such collider needs to have a wide range of centre-of-mass energy (20-140 GeV), high luminosity ($10^{33}$ ~$10^{34}$ $cm^{-2}$ $sec^{-1}$), a wide range of ion species, and high polarization (~70%) for the electron and light ion beams. In the past two decades, two EIC designs were actively developed, i.e., eRHIC by BNL and JLEIC by Jefferson Lab. Recently after BNL was selected to host EIC, the two labs joined forces in bringing eRHIC to the ultimate EIC.

The luminosity performance of an EIC requires stable beam operation, while the behaviour of beam instability is determined by the luminosity concepts of the collider design. Despite the differences in machine configuration and in detailed parameters, JLEIC and eRHIC share similar luminosity concepts that resemble those used in lepton colliders [1]. For both designs, the high luminosity is achieved by high beam current operation with moderate bunch charge, small transverse bunch emittances, small vertical beta star and a high bunch repetition rate. Here the small beta star is enabled by short bunch length, which is a new regime for hadron beams. The high rep rate is enabled by crab cavities to prevent parasitic collisions. At highest luminosity, a high-energy bunched electron cooling is applied to the hadron beam, making the small transverse emittance and energy spread possible. These features of bunch distribution pattern, i.e., moderate bunch charge, small transverse emittances, and high bunch rep rate, imply that the beams at low energy could be vulnerable to single and coupled bunch instabilities, as well as two-stream instabilities. For a complete design study, the collective effects need to be assessed for a wide range of beam energies and ion species, and also for the entire ion bunch formation process. In this paper, we present preliminary estimations of coherent instabilities for JLEIC, for cases of a few selected collision energies, and discuss possible mitigation schemes. The counterpart studies for eRHIC will also be highlighted.

* This material is based upon work supported by the U.S. Department of Energy, Office of Science, Office of Nuclear Physics under contract DE-AC05-06OR23177.

## MCBI IN JLEIC

The layout of JLEIC is shown in Fig. 1. In this design, the existing CEBAF is used as the full-energy electron beam injector, and the figure-8 shape is chosen for the collider rings to optimize polarization preservation. Table 1 shows the key parameters relevant to the collective effects for the JLEIC [2], and parameters of PEPII are listed for comparison. In the following, we discuss the beam stability at the collision scenarios for the electron beam at energies $E_e$=3, 5, 10 GeV and for the proton beam at $E_p$=100 GeV.

The back-of-envelop assessments are given for impedance-driven instabilities, i.e., single and coupled bunch instabilities, as well as for two-stream instabilities, i.e., the e-cloud effects in the ion ring and the ion effects in the electron ring. This exercise helps us to identify parameter regimes vulnerable to beam instabilities where additional studies and mitigation schemes are called for.

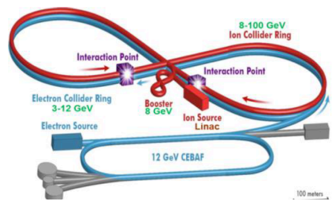


Figure 1: Schematic layout of JLEIC

Table 1: Parameters for JLEIC Instability Estimation

| | **PEP-II** (LER) | **JLEIC** e-Ring | | | **JLEIC** p-Ring |
|---|---|---|---|---|---|
| E [GeV] | 3.1 | 3 | 5 | 10 | 100 |
| $I_{ave}$ [A] | | 2.8 | 2.8 | 0.71 | 0.98 |
| $I_p$ [A] | 113 | 59.0 | 59.0 | 50.6 | 15.6 |
| $\eta$ $(10^{-3})$ | 1.31 | 1.09 | | | 6.22 |
| $\sigma_\delta$ $(10^{-4})$ | 7.7 | 2.78 | 4.64 | 9.28 | 3.0 |
| $\upsilon_s$ $(10^{-2})$ | 3.7 | 0.88 | 1.46 | 2.51 | 5.3 |
| $\langle\beta_\perp\rangle$ [m] | 20 | 13 | | | 18 |

## *Impedance Budget*

The budget of machine broadband impedance requires detailed engineering drawings and careful EM modelling. For initial estimations, we start with the component counts for JLEIC collider rings and use impedance budgets in existing machines, such as PEPII or SUPERKEKB, as references [3, 4, 5]. One reason for using PEPII for reference is that there is consideration for the JLEIC e-ring to adopt the RF cavities, as well as the components for the vacuum and diagnostic systems, from PEPII HER. Another convenient feature is that the bunch length $(\sigma_z \approx 1.2 \text{ cm})$ for JLEIC is comparable to that in PEPII, given that the effective impedances are bunch-length dependent. With the PEPII impedance budget and the JLEIC component counts, and assuming these components are identical with those used in the PEPII HER, we get the estimation for the JLEIC e-ring: the inductance $L \approx 99.2$ nH, the effective longitudinal impedance $|Z_\parallel/n| \approx 0.09\ \Omega$, the loss factor $k_\parallel \approx 7.7$ V/pC, and the effective transverse impedance $|Z_\perp| \approx 60$ k$\Omega$/m. If components in SUPERKEKB are used as reference, the JLEIC e-ring impedance estimation becomes:

$L \approx 28.6$ nH, $|Z_\parallel/n| \approx 0.02\Omega$, $k_\parallel \approx 19$ V/pC, $|Z_\perp| \approx 13$ k$\Omega$/m,

with the note that a shorter bunch length $(\sigma_z \approx 0.5 \text{ cm})$ for beams in SUPERKEKB than that in JLEIC may cause underestimation of the effective impedances.

For the JLEIC ion ring, the ion beam undergoes the bunch formation process including the injection, acceleration, bunch splitting, and finally collision. The bunch length varies through the whole process, and the short ion bunch $(\sigma_z \approx 1.2 \text{ cm})$ at the collision stage is made possible only by employing the envisioned high-energy electron cooling [6]. Since such short bunch length is unprecedented for the ion beams in existing ion rings, it is more appropriate [7] to use the PEPII rings (rather than existing ion rings) for reference when we estimate the impedance budget for the JLEIC ion ring. The ion-ring impedance at the collision scenario is thus estimated as:

$L \approx 97.6$ nH, $|Z_\parallel/n| \approx 0.08\ \Omega$, $k_\parallel \approx 8.6$ V/pC, $|Z_\perp| \approx 80$ k$\Omega$/m.

Note that some special components unique to the JLEIC design, such as the crab cavities and IR chamber, require detailed impedance modelling because references from the existing machines are either inadequate or not available.

## *Longitudinal Microwave Instability (LMWI)*

The LMWI is assessed here by comparison between the theoretical estimation of impedance threshold, as given by the Keil-Schnell criterion,

$$\left|\frac{Z_\parallel(n)}{n}\right|^{\text{th}} \approx \frac{2\pi\beta^2|\eta|E\sigma_\delta^2}{eI_{\text{peak}}},$$

and the expected machine impedance $|Z_\parallel/n|^{\text{ring}}$. For the JLEIC baseline parameters in Table 1, this comparison is shown in Table 2, where “s”, “u”, and “m” denote stable, unstable and marginal respectively. Note that for the JLEIC electron beam, the energy spread gets smaller at lower energies. As a result, at 3 GeV the impedance threshold drops below machine impedance and thus the beam is vulnerable to LMWI. However, for PEPII, with its dipole configuration being different for LER and HER, the beam at 3.1 GeV can have a large energy spread and hence is free from this instability. This situation manifests one major challenge for the e-ring design, i. e., the ring optics should be versatile enough to provide sufficient Landau damping for a wide range of beam energies. This estimation indicates the necessity to apply suppression mechanisms against the microwave instability for the JLEIC e-ring at low energy. Examples of such mechanisms include use of an alternative dipole configuration at low energy, the split-dipole concept in the eRHIC design [8], or damping wigglers. For the ion ring, the machine impedance is expected to be much smaller than the threshold impedance, so the beam is safe from this instability. For the electron ring, detailed simulations are needed to study the bunch lengthening due to potential-well distortion below the LMWI threshold, as well as the turbulent bunch lengthening and increase of energy-spread beyond the instability threshold.

Table 2: Longitudinal Microwave Instability (LMWI)

| | **PEP-II** (LER) | **JLEIC** e-Ring | | | **JLEIC** p-Ring |
|---|---|---|---|---|---|
| E [GeV] | 3.1 | 3 | 5 | 10 | 100 |
| $\lvert Z_\parallel/n\rvert^{\text{ring}}$ [Ω] | ~0.1 | ≤0.1 (expectation) | | | 0.1 |
| $\lvert Z_\parallel/n\rvert^{\text{th}}$ [Ω] | 0.145 | 0.027 | 0.125 | 1.16 | 22.5 |
| LMWI | s | u | m | s | s |

## *Transverse Mode-Coupling Instability (TMCI)*

For TMCI, the approximate theoretical threshold for transverse impedance is

$$|Z_\perp|^{\text{th}} \approx FE\,\nu_s / e\langle\beta_\perp\rangle I_{\text{peak}},$$

with $F$ the bunch form factor ($F \sim 2\pi$ for short bunches). In Table 3, we compare this theoretical threshold, evaluated using parameters in Table 1, with the estimated upper limit of machine transverse impedance $|Z_\perp|^{\text{ring}}$, obtained using impedance budgets of existing machines as references. The comparison shows that the beams are stable with regard to TMCI. Note that there are large uncertainties in both the machine traverse impedance and the simple back-of-envelope formula. Detailed studies of TMCI require an accurate JLEIC impedance model. Such studies include solving the eigenvalue problem of the Vlasov equation [9] or macroparticle tracking that takes into account potential-well distortion in the longitudinal phase space and many other effects [10]. Additionally, special attention needs to be paid to the Christmas-tree-like equilibrium longitudinal charge distribution for the proton bunch under strong electron cooling, which has a very dense core with long tails [11]. Space-charge effects on TMCI will also be assessed, especially for the ion bunches during their formation process [12].

Table 3: Transverse Mode-Coupling Instability (TMCI)

| | **PEP-II** (LER) | **JLEIC** e-Ring | | | **JLEIC** p-Ring |
|---|---|---|---|---|---|
| E [GeV] | 3.1 | 3 | 5 | 10 | 100 |
| $\lvert Z_{\perp}\rvert^{\text{ring}}$ [MΩ/m] | ≤0.1 | ≤0.1 (expectation) | | | ≤0.5 |
| $\lvert Z_{\perp}\rvert^{\text{th}}$ [MΩ/m] | 0.28 | 0.22 | 0.60 | 2.4 | 119 |
| TMCI | s | s | | | s |

## *Coupled-Bunch Instabilities*

In the collider rings, narrowband impedances from RF cavities, crab cavities and various other mode-trapping components can cause longitudinal or transverse coupled bunch instabilities (LCBI or TCBI). The JLEIC electron ring plans to use the PEP-II RF cavities, with the RF HOM parameters listed in Ref. [13]. For the JLEIC ion ring, an RF cavity design was developed with waveguide couplers for efficient HOM damping. The corresponding HOM parameters are listed in Ref. [14]. With these RF HOMs, as well as the resistive wall impedance and broad-band impedance $\left(Z_{\parallel}^{BB}\right)_0 = 2\Omega$ , we estimate the growth rate for the coupled-bunch instabilities (CBI) using ZAP [15] (with Sacherer-Zotter's formulas). For the selected set of collision energies for the electron and proton beams, results are shown in Tables 4 and 5. This calculation assumes an even bunch filling pattern, and Gaussian and parabolic bunch profiles for electron and ion beams respectively. In addition, a non-zero chromaticity of $\xi = 1$ and a finite betatron tune spread of 3e-04 are assumed for the TCBI calculations for both the electron and the proton beams.

In Table 4 and 5, $\tau_{a=1}^{\parallel}$ and $\tau_{a=2}^{\parallel}$ are the growth time for the longitudinal dipole and quadruple modes respectively, and $\tau_{a=0}^{\perp}$ and $\tau_{a=1}^{\perp}$ correspond to the growth time for the transverse rigid and dipole modes. Here $\tau_{\text{damp}}^{\parallel}$ (or $\tau_{\text{damp}}^{\perp}$ ) for the e-ring represents the natural longitudinal (or transverse) damping time due to synchrotron radiation, while $\tau_{\text{damp}}^{\parallel}$ and $\tau_{\text{damp}}^{\perp}$ for the p-ring are the damping times for the proton beam due to the strong electron cooling [16] in the JLEIC design. Note that for the electron ring, the lowest-energy beam ($E_e$ =3 GeV) has the fastest growth time, i.e., $\tau_{a=1}^{\parallel}$ =2.9 ms for LCBI and $\tau_{a=0}^{\perp}$ =1.6 ms for TCBI. With growth rates much faster than the natural damping rates in the low-energy regime, these instabilities are manageable by fast feedback systems (damping time < 1ms) as used in modern electron storage rings. For the proton beam, the resistive-wall induced quadruple mode has a fast LCBI growth time, $\tau_{a=1}^{\parallel}$ =6.2 ms. This is a result of the single-bunch mode spectra for parabolic proton bunch profile. It is well known that electron cooling will change the bunch profile significantly, and its effect on LCBI growth rate remains to be studied. Many topics of CBI and its mitigation schemes need to be addressed by careful studies, such as (1) effects of realistic uneven bunch pattern (with injection/ejection gaps and/or ion clearing gaps), (2) the joint effects of HOMs from both the accelerating/focusing RF cavities and the crab cavities, and (3) the Landau damping for transverse coupled-bunch instability due to tune-shift spread from beam-beam interaction.

Table 4: LCBI in JLEIC

| | e-Ring | | | p-Ring |
|---|---|---|---|---|
| E [GeV] | 3 | 5 | 10 | 100 |
| $\tau_{a=1}^{\parallel}$ [ms] | 2.9 | 4.1 | 72.8 | 30.7 |
| $\tau_{a=2}^{\parallel}$ [ms] | 31 | 43 | 466 | 6.2 |
| $\tau_{\text{damp}}^{\parallel}$ [ms] | 187 | 40.5 | 5.1 | > 30 min |

Table 5: TCBI in JLEIC

| | e-Ring | | | p-Ring |
|---|---|---|---|---|
| E GeV] | 3 | 5 | 10 | 100 |
| $\tau_{a=0}^{\perp}$ [ms] | 1.6 | 2.7 | 64 | 24.4 |
| $\tau_{a=1}^{\perp}$ [ms] | 12.8 | 19.6 | 39.8 | 805 |
| $\tau_{\text{damp}}^{\perp}$ [ms] | 375 | 81 | 10 | > 30 min |

## *Electron Cloud in the Ion Ring*

In an ion ring, the ionization of residual gas and the beam-loss induced surface emission provide the source for the primary electrons, while the electron cloud build-up comes mainly from the secondary electron production [17]. The electron cloud build-up behaviour depends on how the ion beam structure is compared to the reflection time of secondary electrons. For different stages of ion bunch formation in JLEIC, the build-up of electron cloud and its impact on the ion bunch stability can behave very differently. When the bunches are long and the repetition rate is low, as in conventional ion rings, electrons generated ahead of the bunch centre are trapped by the beam potential and are released toward the tail of the bunch, the so called trailing-edge effect. In the collision scenario, the high repetition rate and short bunches of the ion beam make the e-cloud effect similar to those encountered by positron beams in modern lepton colliders. In such case the electron cloud density rises up rapidly and saturates at the neutralization density. For the proton beam at $E_p$ =100 GeV, the neutralization density is

$$\rho_{sat} = \frac{N_b}{\pi b^2 L_{sep}} = 2\times10^{12}\ \mathrm{m}^{-3}\ ,$$

as modelled in Ref. [18] for a similar set of parameters. The threshold for the electron-cloud induced single-bunch transverse mode-coupling instability (TMCI) is estimated using the two-particle model [19],

$$\rho_{th} = \frac{2\gamma Q_s}{\pi r_p C\left\langle \beta_y \right\rangle} = 1.7\times10^{13}\ \mathrm{m}^{-3}.$$

With $\rho_{sat} < \rho_{th}$ , the bunch is stable from the electron-cloud induced strong head-tail instability. The electron cloud may also cause coupled-bunch instability for the JLEIC ion beam, which could be more concerning and requires detailed simulations.

### *Ion Effect in the Electron Ring*

As the electron bunch trains circulate in a storage ring, they scatter with the residual gas molecules and produce ion particles. The ions could be trapped by the e-beam potential well and cause many undesirable effects for the electron beam, such as emittance growth, tune shift, halo formation, and coherent coupled-bunch instabilities. For a symmetric bunch pattern, and for constant rms bunch sizes, the critical mass for the ions to be trapped in either *x*-motion or *y*-motion is given by [20]

$$A_{x,y}^{trap} = \frac{r_p N_b L_{sep}}{2\sigma_{x,y}(\sigma_x + \sigma_y)}.$$

Our estimation shows that for the JLEIC ion ring all ion molecules ( $A \geq 2$ ) will be trapped for even bunch fill.

The ions produced from ionization scattering and then trapped by the beam potential can be cleared by leaving gaps in between the bunch trains [21]. However, even with the ions being cleared after each turn by a clearing gap (or gaps), there is still the fast beam-ion instability (FBII) [22] that could develop within the bunch train during a single-turn circulation. Turn-by-turn, the transverse dipole motion for the electron bunches is propagated within a bunch train and gets amplified, with the dipole amplitude increasing in time and along the bunch train. Under the assumptions that (1) the force between the ion and electron beam is linear to their relative dipole offsets and (2) oscillation frequency is identical for all ions, the growth time $\tau_g$ for FBII is given by

$$y_b(t) \propto \left(t/\tau_g\right)^{-1/4} e^{\sqrt{t/\tau_g}},$$

$$\tau_g^{-1}[s^{-1}] = 5p[Torr]\frac{N_b^{3/2} n_b^2 r_e r_p^{1/2} L_{sep}^{1/2} c}{\gamma\sigma_y^{3/2}(\sigma_x+\sigma_y)^{3/2} A^{1/2}\omega_\beta}.$$

For realistic beams, the horizontal charge distribution could result in the spread of the ion oscillation frequency and therefore the Landau damping of FBII. The dipole amplitude growth in such case is characterized by the e-folding time [23, 24]

$$y_b \propto e^{t/\tau_e},\quad \tau_e^{-1} \approx \tau_g^{-1}\frac{c}{4\sqrt{2\pi}L_{sep}n_b a_{bt} f_i}$$

for $f_i$ the coherent ion oscillation frequency and $a_{bt}$ the ion frequency variation. For a single bunch train in the JLEIC electron ring, $\tau_g$ and $\tau_e$ are shown in Table 6 (for $a_{bt}$ =0.5). Here for $E_e$=10 GeV, the growth time is comparable to its counterpart for the PEPII HER beam. However, for $E_e$=3-5 GeV, the growth time is one or two orders of magnitude shorter and is consequently a serious concern for the electron beam stability. Further reduction of the growth rate is expected if the frequency spread of the ion beam, induced by the beam-size variation due to betatron oscillation, is taken into account. Possible mitigation methods include using (1) chromaticity to Landau damp the FBII, (2) clearing electrode, or (3) multiple bunch trains to reduce the growth amplitude. Comprehensive numerical modelling, for both FBII and the mitigation schemes, need to be performed for JLEIC. Further studies need to combine FBII with the beam-beam induced tune spread, along with the coupled-bunch beam-beam instability in the gear-change collision arrangements [25].

Table 6. Growth time of FBII for JLEIC e-Ring

| $E_e$ [GeV] | 3 | 5 | 10 |
|---|---|---|---|
| $\tau_c$ [$\mu$s] | 0.01 | 0.11 | 13.9 |
| $\tau_e$ [ms] | 0.02 | 0.1 | 3.2 |

## MCBI IN ERHIC

In eRHIC, a polarized electron beam ( 2.5 to 18 GeV) collides with a polarized proton beam (41 to 275 GeV) or beams of other ion species. This EIC design takes full advantages of the existing RHIC, by using one of the RHIC rings as the EIC hadron collider ring and adding two electron rings in the same tunnel: a 400 MeV to 18 GeV rapid cycling synchrotron (RCS) and a full-energy electron collider ring. A schematic layout of eRHIC is shown in Fig. 2.

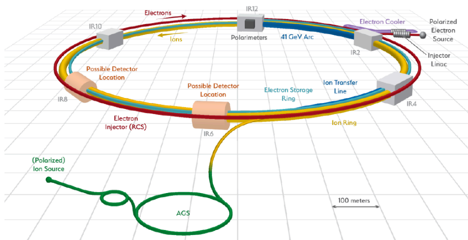


Figure 2: Schematic layout of eRHIC

The coherent instabilities in eRHIC are studied for the electron and hadron beams at several collision energies [26, 27]. The impedance-induced instabilities are modelled by particle tracking using TRANFT [10]. In this code, the beam is represented by 5 bunches (with periodic conditions for even bunch fill) and up to $10^5$ macroparticles per bunch. The particles experience interaction with both short-range and long-range wakefields, along with fields for certain mitigation mechanisms. For the electron beam in the collider ring, weak-strong beam-beam interaction from collision at IR is also included.

### *Collective Effects in the Electron Collider Ring*

For this study, particle tracking is performed for electron beam at 5, 10 and 18 GeV. Here the broadband impedances consist of the geometric, resistive and coherent synchrotron radiation (CSR) impedances. The HOM of the RF cavity (residing near an absorber) and resistive wall impedance are respectively the major contributors for the longitudinal and transverse narrowband impedances. Tracking studies show that at the selected energies, the bunch charge at threshold of microwave instability is two or three times larger than its nominal value, and the increase of bunch length is insignificant. At 10 GeV, the longitudinal coupled-bunch instability can be mitigated by a longitudinal damper with $\mathrm{Im}(Q_s)=0.001$, and the transverse coupled-bunch instability can be Landau damped by beam-beam tune spread with the nominal beam-beam parameter of 0.075~0.1.

The fast ion instability is studied by another code [28]. In this model, 40 ion slices are distributed around the ring to account for the spread of the ion oscillation frequency, due to variation of the transverse bunch size caused by betatron motion. With Landau damping from beam-beam interaction, simulated by Bassetti-Erskine kick once per turn, the threshold for maximum density of CO gas (for nominal gas temperature and pressure) is found to be challenging but achievable.

### *Collective Effects in the Hadron Collider Ring*

Beam dynamics is studied using TRANFT for proton beam at 22.8, 41, and 275 GeV. Because an existing RHIC ring will be used as the EIC hadron collider ring, the short-range wakefield can be constructed from the broadband impedance directly measured from RHIC, while the long-range wakefield can be constructed from the dominant HOMs from the RHIC RF cavity. Additionally, space charge and resistive wall effects are included in the particle tracking. The simulations show that at the microwave instability threshold, the bunch charges at different energies could be an order of magnitude higher than their nominal values, and the bunch lengthening is insignificant. The growth rates for the longitudinal and transverse coupled-bunch instability agree well with simplified analytical results. However, there is an increase of the transverse emittance at 22.8 GeV, probably due to the numerical handling of the space-charge force in the simulation.

Electron cloud is a serious concern for the EIC hadron ring, in terms of high cryogenic loss and beam instability. The plan is to coat the arc chambers with copper. Further reduction of the heat load at high current operation can be achieved by applying an additional layer of coating consisting of amorphous carbon.

## CONCLUSIONS

In this paper, we presented the status of our preliminary study of coherent instabilities and mitigation in the two EIC designs, JLEIC and eRHIC. The discussions show that an EIC takes the collider design to a new parameter regime, where the hadron beam pattern is similar to those in lepton colliders whereas the design of the electron ring needs to ensure electron beam stability for a wide range of energies. These new regimes pose many challenges to the mitigation of coherent beam instabilities. Recently with BNL chosen to host the EIC, the EIC design enters a brand-new phase. Comprehensive studies of the impedance budget, behavior of coherent instabilities, and the possible interplays of different instability mechanisms and their mitigations are currently under way.

### ACKNOWLEDGEMENT

We thank F. Marhauser, R. Rimmer, J. Guo, T. Michalski, K. Deitrick, A. Hutton, and M. Blaskiewicz for helpful discussions.

### REFERENCES

[1] Ya. Derbenev *et al.,* “Achieving High Luminosity in an Electron-Ion Collider”, proceedings of HB2010 Workshop (2010).
[2] Y. Zhang, “JLEIC Baseline Update and New Parameters”, https://www.jlab.org/indico/event/210/ (2017).
[3] “PEP-II an Asymmetric B Factory”, Conceptual Design Report, SLAC-418 (1993).
[4] D. Zhou, SuperKEKB mini optics meeting (2015).
[5] R. Li *et al.,* pg. 90, proceedings of eeFACT2018 (2018).
[6] S. Benson, Cool17 Workshop (2017).
[7] A. Hutton, private communication (2018).
[8] C. Montag, Proc. of IPAC 2017, pg 3035 (2017)
[9] Y.H. Chin, MOSES 2.0, CERN/LEP-TH/88-05 (1988).
[10] M. Blaskiewicz, “The TRANFT User’s Manual version 1.0”, private communication (2017).
[11] A. Sidorin *et al.,* THAP01, Proceedings of COOL 2007 (2007).
[12] A. Burov, Phys. Rev. ST Accel. Beams 12, 044202 (2009); Erratum Phys. Rev. ST Accel. Beams 12, 109901 (2009).
[13] R. Rimmer *et al.,* “PEP-II RF Cavity Revisited”, CBP Tech Note 197, LCC-0032 (1999).
[14] F. Marhauser and R. Rimmer, “Progress on the Design of the JLEIC Ion Ring Cavities”, JLAB-TN-18-041, 2018.
[15] M. Zisman, S. Chattopadhyay, J.J. Bisognano, “ZAP USER’S MANUAL” LBL-21270 (1986)
[16] H. Zhang, “Cooling Simulation Studies”, https://www.jlab.org/indico/event/210/ (2017).

[17] K. Ohmi *et al.*, PRSTAB 5, 114402 (2002).
[18] S. Ahmed *et al.*, "Computational Modeling of Electron Cloud for MEIC", Proc. of IPAC12 (2012).
[19] K. Ohmi, F. Zimmermann, PRL 85, p. 3821 (2000).
[20] Y. Baconnier, G. Brianti, CERN/SPS/80-2 (1980).
[21] M. Q. Baron, NIMA 243, 278 (1986).
[22] T.O. Raubenheimer and F. Zimmermann, Phys. Rev. E, Vol. 52, 5487 (1995).
[23] G. Stupakov, T.Raubenheimer, and F. Zimmermann, PRE, Vol. 52, 5499 (1995).
[24] F. Zimmermann *et al.,* SLAC-PUB-7617 (1997).
[25] V. S. Morozov *et al.,* "Study of Beam Synchronization at JLEIC", arXiv: 1606.09117 (2016).
[26] M. Blaskiewicz, private communication (2019).
[27] Electron Ion Collider of Brookhaven National La boratory, pre-Conceptual Design Report (2019).
[28] M. Blaskiewicz, "Beam-beam damping of the ion instability", Proc. of NaPAC 2019 (2019).

# STATUS OF NEGATIVE MOMENTUM COMPACTION OPERATION AT KARA

P. Schreiber *, T. Boltz, M. Brosi, B. Haerer, A. Mochihashi, A.I. Papash, M. Schuh, A.-S. Müller,
Karlsruhe Institute of Technology, Karlsruhe, Germany

This contribution is based on [1].

*Abstract*

For future synchrotron light sources different operation modes are of interest. Therefore various modes are currently being tested at the Karlsruhe Research Accelerator (KARA) including optics for a negative momentum compaction factor. These optics have been calculated and are under commissioning at KARA. Additionally, studies about expected collective effects in this regime are being performed, including the head-tail and microbunching instabilities. In this contribution we will present the status of operation in the negative momentum compaction regime and discuss expected collective effects that will be studied in this context.

## LATTICE AND OPTICS

The KIT synchrotron light source KARA [2] has a four fold symmetry consisting of two double bend achromat like structures per cell. Each such structure contains five quadrupoles, where corresponding quadrupoles in the different structures are connected to the same power supply, as a so called family. Straight sections between magnetic structures are filled with insertion devices, RF cavities and injection magnets.
The momentum compaction factor $\alpha_c$ can be expressed as

$$\alpha_c = \frac{\frac{\Delta L}{L}}{\frac{\Delta p}{p}} = \frac{1}{L}\oint \frac{D(s)}{\rho(s)}\mathrm{d}s \tag{1}$$

where $L$ is the path length for one revolution for a particle with design momentum $p$, $\Delta L$ and $\Delta p$ are the deviations for particles with different momenta. $D$ describes the dispersion and $\rho$ the local bending radius along the ring. According to this equation, the momentum compaction factor can be influenced by changes to the dispersion in sections where the bending radius is non-zero. For KARA and its lattice, one way to reach smaller values of $\alpha_c$ is to push the dispersion down to negative values by increasing the strength of the center quadrupole in each half-cell, which is acting as a field lens.

At KARA mainly two established operation optics with different momentum compaction factors exist. At maximum energy of 2.5 GeV, the standard operation with a momentum compaction factor of $\alpha_c \approx 9 \cdot 10^{-3}$ is used. The optical functions are displayed in Figure 1. Here, the dispersion is positive over the entire section and therefore in the entire ring.

* patrick.scheiber@kit.edu

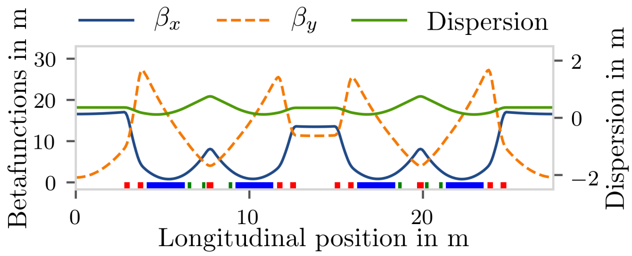


Figure 1: Calculated lattice used for user operation at $\alpha_c = 9 \cdot 10^{-3}$. The bottom depicts the magnets, quadrupoles in red, sextupoles in green and bends in blue.

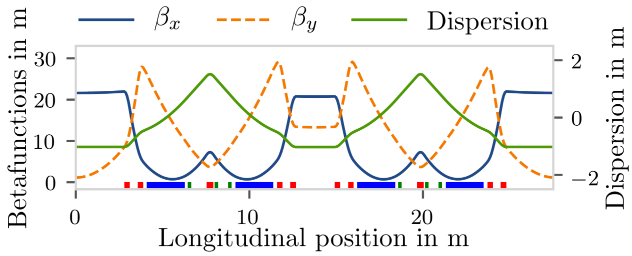


Figure 2: Calculated lattice used for short bunch operation at $\alpha_c = 1 \cdot 10^{-4}$. The dispersion is negative in parts of the bending magnets.

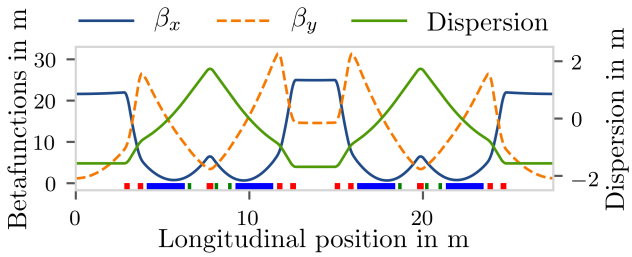


Figure 3: Calculated lattice used for operation with a negative momentum compaction factor of $\alpha_c = -8 \cdot 10^{-3}$. Here the dispersion is largely negative in parts of areas with bending magnets.

At 1.3 GeV a dedicated short bunch mode exists with a momentum compaction factor of $\alpha_c \approx 1 \cdot 10^{-4}$ [3]. Figure 2 shows the optical functions for this operation mode. Note that the dispersion is negative in some areas of the section.

A new mode with various selectable *negative* momentum compaction factors has been implemented recently. Here, as shown exemplary for $\alpha_c = -8 \cdot 10^{-3}$ in Figure 3, the dispersion is largely negative in some parts of the section.

More information about operation optics at KARA can be found in [4].

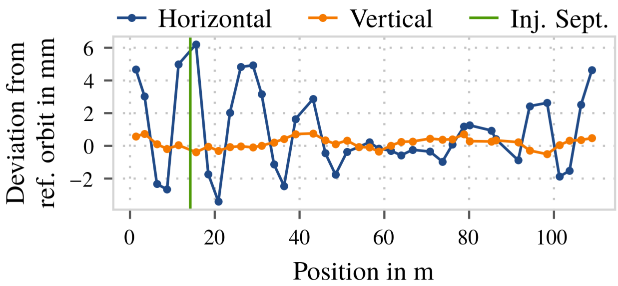


Figure 4: Orbit deviations during injection into an optics with $\alpha_c \approx -8 \cdot 10^{-3}$

## STATUS OF OPERATION

At an energy of 500 MeV, injection into multiple optics with negative values of $\alpha_c$ has been successfully established. However, the maximum beam and bunch current is limited to values lower than for other operation modes. The highest achieved current until the end of 2019 is 17 mA for a filling pattern with 30 bunches and 1 mA for single-bunch operation.

Multiple factors affecting this limit were identified. It seems to be beneficial to have high orbit deviations (shown in Figure 4) during injection. This has been tested by changing the energy of the beam via modifications of the RF-frequency. The resulting optics with a dispersive orbit have larger or smaller deviations and a comparable momentum compaction factor.

Furthermore, lower absolute values of $\alpha_c$ seem to result in higher possible beam currents which could be explained by the fact that lower absolute values come from a less stretched dispersion.

Reducing the sextupole strength while keeping the tunes constant and therefore reducing chromaticities also seemed to be beneficial at some values of $\alpha_c$, which could hint at collective effects.

## WORKING POINT AND CHROMATICITY

For multiple negative values of $\alpha_c$ tunes $\nu$ and chromaticity $\xi$ have been measured. Changing chromaticity with stored beam and also during injection is relatively easy.

Shifting the horizontal chromaticity had almost no influence, even a change of sign did not result in significant changes to injection rate and current limit. The vertical chromaticity has small effects on the current limit, where lower negative values seem to result in higher current limits. Moving the vertical chromaticity to positive values during injection resulted in a beam loss and a sub mA injection limit. However, moving vertical chromaticity to positive values with stored beam without injection did not result in a beam loss.

The transverse working point was moved from $(\nu_x, \nu_y) = (0.767, 0.793)$ via $(\nu_x, \nu_y) = (0.765, 0.821)$ to $(\nu_x, \nu_y) = (0.801, 0.827)$. It was observed that the starting point has the best conditions for injection rate and current limit. The behaviour at the intermediate point was almost the same while the end point was significantly less beneficial for the injection as the injection rate as well as the maximum achievable beam current was lower than for the other two points.

## COLLECTIVE EFFECTS

Various collective effects might change their behaviour for negative momentum compaction which has not been fully studied. One of the most prominent instabilities is the head-tail instability. The growth rate of this instability is given by [5]

$$\tau_{\pm}^{-1} = \mp \frac{N r_0 W_0 c \xi_{\mathrm{v}} \hat{z}}{2\pi\gamma C \eta}, \tag{2}$$

where $N$ is the number of particles, $r_0$ the classical electron radius, $W_0$ is the value of the wake field, $\xi_{\mathrm{v}}$ the vertical chromaticity and $\hat{z}$ describes the amplitude of the synchrotron oscillation. $\eta = \alpha_c - 1/\gamma^2$ is the slip factor and $C$ is the circumference of the ring. It clearly depends on the ratio of the chromaticity $\xi_{\mathrm{v}}$ to the slip factor $\eta$ and therefore on $\alpha_c$. Here the relative sign between the chromaticity and $\alpha_c$ is especially important.

Another instability to consider is the Transverse Mode Coupling Instability (TMCI). Multiple descriptions exist in literature ([5–7]). This instability manifests itself above a certain threshold which can be expressed as (adapted from [7])

$$N_{\mathrm{b,thr}}^{\mathrm{TMC}} \propto \frac{|\eta|}{|Z_y^{\mathrm{BB}}|}\left(1 + \frac{\xi_{\mathrm{v}}\omega_0}{\eta\omega_r}\right), \tag{3}$$

where $Z_y^{\mathrm{BB}}$ is the broadband impedance of the ring, $\omega_0$ is the angular revolution frequency and $\omega_r$ is the resonant angular frequency of the impedance. A higher absolute value of the chromaticity increases the threshold as long as the signs of $\alpha_c$ and $\xi_{\mathrm{v}}$ are the same. This is in accordance to the observed lower limit for a positive vertical chromaticity at negative momentum compaction, which could indicate the occurrence of the TMCI at our experiments.

A third instability possibly occurring is the micro-bunching instability. The equation from [8] predicts a threshold at $I_{\mathrm{thr}} = 0.038$ mA for a positive momentum compaction factor of $\alpha_c = +1.8 \cdot 10^{-3}$. THz emission power has been measured above and below this threshold at the negative equivalent momentum compaction factor of $\alpha_c = -1.8 \cdot 10^{-3}$. These measurements suggest a significantly higher threshold for the negative momentum compaction regime. However more systematic tests are planned. Furthermore, the applicability of Inovesa [9] is under investigation to simulate the micro-bunching instability in the negative momentum compaction regime.

## ACKNOWLEDGEMENT

This project has received funding from the European Union's Horizon 2020 Research and Inovation programme under Grant Agreement No 730871.

P. Schreiber and T. Boltz acknowledge the support by the DFG-funded Doctoral School "Karlsruhe School of Elementary and Astroparticle Physics: Science and Technology"

## REFERENCES

[1] P. Schreiber *et al.*, "Status of operation with negative momentum compaction at KARA," in *Proc.of IPAC2019, Melbourne, Australia, 19-24 May 2019*,M. Boland, H. Tanaka, D. Button, and R. Dowd, Eds.,ser. 10, Melbourne, Australia: JACoW Publishing, Jun. 2019,pp. 878–881, ISBN: 978-3-95450-208-0.DOI: `10.18429/JACoW-IPAC2019-MOPTS017`.

[2] E. Huttel *et al.*, "Operation with a low emittance optics at ANKA," in *Proceedings of the 2005 particle accelerator conference*, 2005, pp. 2467–2469.

[3] M. Klein *et al.*, "Modeling the low-alpha-mode at ANKA with the accelerator toolbox," in *Proceedings of the 24th Particle accelerator Conf. (PAC'11)*, paper WEP005, Apr. 2011, New York, USA. `https://accelconf.web.cern.ch/AccelConf/PAC2011/papers/WEP005.PDF`

[4] A. Papash *et al.*, "New operation regimes at the storage ring KARA at KIT," in *Proc. of IPAC2019, Melbourne, Australia, 19-24 May 2019*, M. Boland,H. Tanaka, D. Button, and R. Dowd, Eds., ser. 10, Melbourne, Australia: JACoW Publishing, Jun. 2019,pp. 1422–1425, ISBN: 978-3-95450-208-0.DOI: `10.18429/JACoW-IPAC2019-TUPGW016`.

[5] A. W. Chao, *Physics of collective beam instabilities in high energy accelerators*, ser. Wiley series in beam physics and accelerator technology. New York: Wiley, 1993,ISBN: 978-0-471-55184-3.

[6] V. Balbekov, "Single bunch transverse instability in a circular accelerator with chromaticity and space charge," *Journal of Instrumentation*, vol. 10, no. 10,P10032–P10032, Oct. 2015. DOI: `10.1088/1748-0221/10/10/P10032`.

[7] W. Herr. (2014). CAS - CERN accelerator school: Advanced accelerator physics course, CERN Document Server, `https://cds.cern.ch/record/1507631`

[8] K. L. F. Bane, Y. Cai, and G. Stupakov, "Threshold studies of the microwave instability in electron storage rings,"*Physical Review Special Topics - Accelerators and Beams*, vol. 13, no. 10, Oct. 7, 2010. DOI: `10.1103/PhysRevSTAB.13.104402`.

[9] P. Schönfeldt *et al.*, *Inovesa/inovesa: Gamma three*, Apr. 29, 2019. DOI: `10.5281/zenodo.2653504`.

# TIME DOMAIN MEASUREMENTS OF THE SUB-THZ RESPONSE OF DIFFERENT COATINGS FOR BEAM PIPE WALLS

A. Passarelli[1]*, A. Andreone[1], Physics Department,
University of Naples "Federico II", 80126 Napoli, Italy
V. G. Vaccaro, M. R. Masullo, INFN Naples Unit, 80126 Napoli, Italy
Y. Papaphilippou, R. Corsini, CERN, 1211 Geneva, Switzerland
[1]also at INFN Naples Unit, 80126 Napoli, Italy

*Abstract*

Modern accelerators and light sources often require special treatment of the vacuum chamber surface in order to avoid undesirable effects and maximize machine performance. Coatings with Non Evaporable Getter compounds and amorphous Carbon have been extensively tested and used with very effective results since they allow to reduce the secondary electron emission from pipe walls and therefore the relevant beam instability. An electromagnetic characterization of such coatings is therefore fundamental to build a reliable impedance model. We present here a method based on time domain measurements of an electromagnetic wave passing through a tailored waveguide, where the material under test is deposited on a planar slab. This configuration allows an easy measure of samples having a homogeneous coating thickness and a reasonable area, with parameters chosen in order to have a good signal-to-noise ratio, avoiding at the same time problems due to peel-off and blistering during deposition. The study on the electromagnetic response is performed in the frequency range from 0.1 to 0.3 THz, corresponding to the first transverse electric (TE) mode propagation inside the designed waveguide.

## INTRODUCTION

One step for the optimization of the machine performance in modern accelerators and light sources is the special treatment of the vacuum chamber surface in order to avoid undesirable effects. In particular, in positron rings the electron cloud mechanism starts when the synchrotron radiation, emitted by the beam, creates a large number of photoelectrons at the wall surface of the beam vacuum chamber. These primary electrons may cause secondary emission or be elastically reflected [1]. If the value of the secondary electron yield (SEY) of the surface material is greater than unity, the number of electrons starts to grow exponentially and may lead to beam instabilities and many other side effects [2, 3]. The reduction of the SEY value in the pipe walls is one of the keypoint in order to avoid these problems. Coating materials, that are exploited for the SEY reduction but also for improvement of the pumping process or other purposes, change the surface impedance of the vacuum chamber. This variation may affect the electromagnetic interaction of the beam with the surrounding vacuum chamber and consequently result in beam instability limiting the machine performance. Therefore, an accurate electromagnetic characterization (EMC) of coating materials is required for building a reliable impedance model and for the characterization of performance limitations in modern particle accelerators and storage rings [4]. Non Evaporable Getter (NEG) coating is a mature and well-established technology currently exploited at CERN for ultra-high vacuum pumping. Coatings of amorphous Carbon (a-C) have been extensively tested [5] and used [6] at the CERN Super Proton Synchrotron (SPS) accelerator and other experiments [7] for SEY reduction with very effective results. There is therefore a demand for a full EMC characterisation of these novel materials.

The present study is in the framework of the Compact Linear Collider (CLIC) damping rings experiment that requires a thorough evaluation of the surface impedance at very high frequencies (i.e. millimeter waves and beyond). Usually, this is done by resorting to standard techniques in the frequency domain, which however show severe limits over 100 GHz in terms of accuracy, complexity and cost. An alternative approach for materials that require a strong wave-matter interaction is THz waveguide spectroscopy [8], where measurements are performed in time domain and information on the sample frequency response is retrieved by Fourier transform. This technique has been used in the past for characterizing thin samples deposited either on dielectric substrates or directly on the waveguide [9, 10].

In the following we first present the THz setup under use and its recent upgrade. Then, we summarize the experimental measurements, already reported in two different papers [11, 12], for the extraction of the electromagnetic properties of high quality NEG samples used to validate the method. Lastly, we describe the setup change and the analytical studies implemented in order to measure the response of a-C coatings overcoming the demanding thickness requirement.

The proposed method overcomes the inconveniences reported in a previous work on the EMC of NEG coatings in the frequency domain [13], like inhomogeneity, blistering and peel-off induced by the high temperature deposition on a standard rectangular waveguide with a complex geometry. We solve this by placing a calibrated waveguide with integrated horn antennas in the optical path of a THz spectrometer and separating the signal guiding system in two parts: a fixed (squared or triangular) waveguide, and a removable slab where the coating is deposited. This choice allows to measure with ease large area coatings deposited on

* andrea.passarelli@unina.it

metallic plates as in the case of accelerators, where averaged quantities are needed.

## Sub-THz SYSTEM UPGRADE

Sub-THz measurements of NEG coatings have been carried out using a Time Domain Spectrometer (TDS) operating in transmission mode. The setup is based on a commercial THz-TDS system (TERA K15, MENLO Systems) customized for the specific coating characterization in the waveguide. The system is driven by a femtosecond fiber laser @1560 nm with an optical power $< 100$ mW and a pulse duration $< 90$ fs. In the standard configuration, the laser output is split into two beams in pump-probe mode. Fiber-coupled photoconductive antenna modules are utilized for both electric field signal emission and detection. A fast opto-mechanical line with a maximum scanning range of approximately 300 ps is used to control the time delay between the pump and the probe beam. Signal detection is performed by a lock-in amplifier that drives the pulse generation at about 90 KHz and integrate the output voltage over an interval of 100 ms. Pulse waveforms are sampled by 2048 data-points in 150 fs intervals of optical delay (step size $\sim 30\ \mu$m). Each scan requires about 10 min of measurement time.

The THz beam system includes a set of TPX (polymethylpentene) lenses, symmetrical with respect to the center line between the transmitter and the receiver, used to collimate the short $(1-2$ ps) linearly polarized pulse on the waveguide. This results in a Gaussian-like beam with a waist of approximately 8 mm in diameter and a quasi-plane wave phase front. The coupling efficiency between the free space signal and the input and output horns is then manually optimized by maximizing the signal transmitted through the waveguide. Under our experimental conditions, we can safely assume that the waveguide works in a single mode regime and mode conversion at the entrance of the horn antennas may be neglected. A sketch of the optical configuration is shown in Fig. 1.

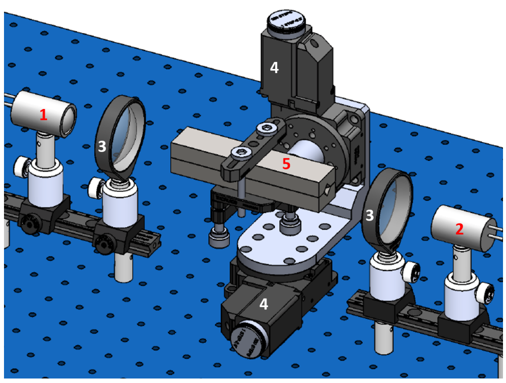


Figure 1: Sketch of the opto-mechanical setup utilized for the measurements: 1) Emitter, 2) Detector, 3) TPX collimating lenses, 4) Micrometric alignment systems, 5) waveguide with embedded horn antennas.

The waveguide is placed on a kinematic mount coupled with a micrometric goniometer in order to achieve an accurate control over the target positioning. The bottom of the waveguide is fixed onto the kinematic mount and the metal slabs can be replaced by removing the upper part of the structure only. The waveguide is firmly tightened with a rigid clamp for minimizing any possible air gap in between the top and the base plate. The area around the waveguide entrance is shielded with a metal sheet with an extrude cut at the center for blocking unwanted free space THz radiation from the emitter to the receiver antennas.

The upgrade of the system, performed last year, improved the spectral range from 3 THz up to 5 THz and the dynamic range from 70 dB up to 90 dB. By changing the optical delay unit, the scanning temporal range increased from 300 to 800 ps with a consequent improvement of the spectral resolution from 3.5 to 1.5 GHz.

A standard Fast Fourier Transform (FFT) algorithm is used to obtain frequency dependent transmission curves from the time domain signals. Figure 2 shows the THz spectrum of the free space signal obtained in air with the upgraded system.

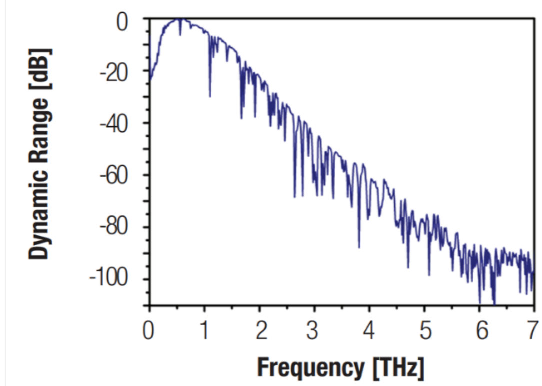


Figure 2: THz frequency domain spectrum of the free space signal for the upgraded system.

## RECENT RESULTS: NEG COATING

All results concerning the characterization of NEG coatings in the sub-THz region have been published in [11]. Here we resume the features of the specifically designed structure (see Fig. 3) that we used. It has a central copper slab 0.050 mm thick, where the material under test is deposited on both sides. This device consists of a cylindrical waveguide having radius 0.9 mm and length 42 mm, connected to two pyramidal horn antennas 39 mm long, with side width from 6 mm to $0.9\sqrt{2}$ mm (external to internal). The antennas are embedded in the device in order to enhance the electromagnetic signal collection and radiation [14]. The external shape of the structure is a parallelepiped having section $16 \times 12 \times 120$ mm$^3$.

Regarding the NEG coating, its growth process was performed at the CERN deposition facilities (under the responsibility of the TE-VSC-SCC section) on both sides of two

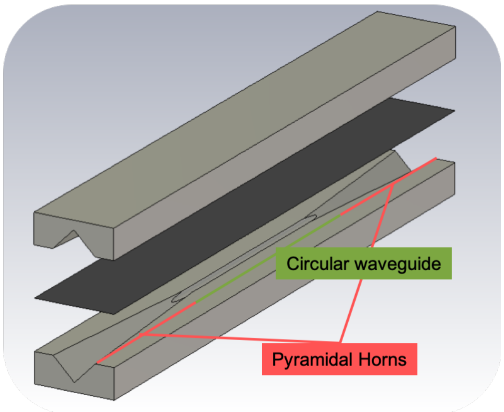


Figure 3: Model of the structure used for the measurements consisting of a circular waveguide and two pyramidal horns. The device is cut into two parts with the coated slab placed in-between.

different copper slabs by using a DC magnetron sputtering technique [5]. Measurements of thickness and composition along the waveguide axis were performed using X-Ray Fluorescence, confirming the good uniformity of the coating.

The d.c. conductivity value of the coated material was obtained from the comparison between the signal amplitude transmitted through the waveguide with the coated slab and the one obtained with an uncoated slab used as a reference. Knowing the coating thickness and resorting to the developed analytical tool, the surface impedance value has been inferred in the frequency range of a single mode transmission. In particular, assuming $TE_{01}$ propagation in both the pyramidal transitions and in the circular waveguide, the overall usable frequency window was from 118 GHz to 283 GHz. For two different samples we found the same conductivity within the error given by the best-fitting procedure. Specific values were: $\sigma_{\text{coat}} = (8.0 \pm 0.4) \times 10^5$ S/m and $\sigma_{\text{coat}} = (8.2 \pm 0.6) \times 10^5$ S/m.

These results well agree with data already obtained with the frequency domain approach published in [13]. From the measured $\sigma_{coat}$ values one can estimate the real part of the surface impedance as a function of frequency, which in turn can be used for modeling the resistive wall component of the beam impedance in modern accelerators.

## FURTHER STEP: a-C COATING

The advantages of the setup employed for the NEG test, mainly (i) the possibility to characterize uniform samples and (ii) the re-usability of the structure for different coating materials, can be profitably exploited for the EMC of amorphous Carbon.

Attempts to make a-C coatings were first performed on copper squared samples $40 \times 40$ mm$^2$ having thickness of 50 $\mu$m. For the configuration shown in Fig. 3, in order to have a reasonable signal attenuation due to the coated slab a minimum a-C thickness $t$ of 5 $\mu$m on both sides of copper is needed. It is important to highlight that the required thickness for EMC is one order of magnitude larger than usual values used for coating of vacuum chambers. Unfortunately, during the high temperature growth the a-C layer induces a residual stress on the copper substrate, producing slab bending (one side deposition) or even coating peel-off and blistering (two side deposition). These problems made impossible to obtain a-C coatings with both planarity and homogeneity suitable for THz characterisation, and led us to design a different test structure. To avoid any possible stress on the coated sample, we changed the measurement configuration depositing a-C on the single side of a bulk copper piece. This overcomes the above mentioned problems, however at the expense of reducing the relative weight of the sample under test in the overall losses of the test structure. Moreover, for the a-C characterization, we carried out an accurate analytical study for different shapes of the guiding device shapes. The first step was to estimate the relative attenuation produced by the coating in a structure having the same upper part as in the waveguide used for the NEG characterization. For the sake of clarity, figure 4 shows the front view of the studied device.

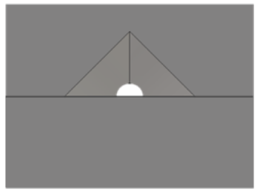

Figure 4: Front view of the structure (horn antenna + waveguide) with half-circular section.

A parametric study was performed for different thicknesses and assuming a coating conductivity $\sigma_{\text{coat}} = 10^4$ S/m. The amorphous carbon conductivity is chosen by considering the worst case scenario, using values obtained by d.c. measurements on the same material [15]. Formulas used for the evaluation are reported in [11]. Corresponding values for the relative attenuation (difference between losses with and without the coating on top of the copper bulk piece) are plotted in Fig. 5 as a function of frequency for three different a-C thicknesses. Maximum thickness was chosen to be 3 $\mu$m because of the technological constraints given by the deposition process. Results show that in all cases the evaluated relative attenuation is lower than 1 dB, too low for a reliable detection by using the available measurement system.

Therefore, we modified the waveguide geometry with the aim to increase, for the same thickness, the relative weight of the test material coating on the overall attenuation. The new structure presents the half-square section rotated by 45°, that is a triangular section (see Figure 6) with side 1.1 mm and length 62 mm, that maximizes the losses of the planar coating with respect to the copper walls. This configuration has also the advantage to minimise the sharp transition from the two pyramidal horn antennas and the central sector, further reducing spurious contributions to losses and improving the signal transmitted through the structure.

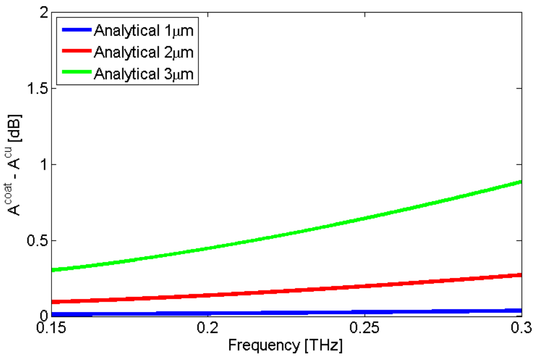


Figure 5: Test structure with half-circular waveguide: analytical evaluation of the relative attenuation on the slab vs frequency for the $TE_{01}$ propagating mode, assuming different coating thicknesses and $\sigma_{\mathrm{coat}} = 10^4$ S/m.

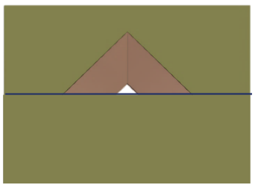

Figure 6: Front view of the structure (horn antenna + waveguide) with triangular section.

Figure 7 shows an exploded view of the new configuration. The relative attenuation is analytically evaluated [11] and results are shown in Fig. 8 as a function of frequency, for the same thicknesses and conductivity values considered before.

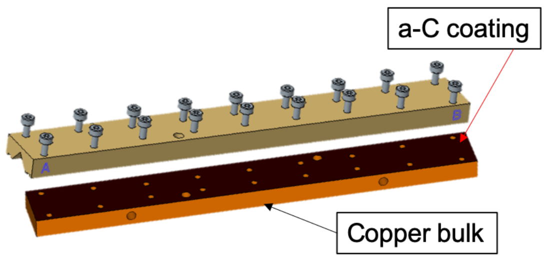


Figure 7: Exploded view of the newly designed configuration. The test structure is cut into two pieces: the upper part is a triangular waveguide with two half pyramidal horns, the lower part is a copper bulk slab on which the a-C coating is deposited.

For this modified structure, the expected relative attenuation for a 3 $\mu$m thick a-C coating having $\sigma_{\mathrm{coat}} = 10^4$ S/m is higher than 1 dB, ideally large enough to be detected using the measurement system available in our laboratory.

Nevertheless, because of the many unknown variables that may largely affect the quality of the deposited layer, we performed a parametric study of the relative attenuation as a function of frequency keeping the coating thickness constant (3 $\mu$m) and assuming different values of the conductivity. This is shown in Fig. 9 in different curves, where $\sigma_{\mathrm{coat}}$ is varied from $10^4$ S/m to $5 \times 10^5$ S/m. Since we are testing a bilayered system (a-C coating and bulk copper), as far as conductivity decreases the material skin depth $\delta$ increases, and the EM field penetrates more and more in the bulk copper. From the plot, one can see that the relative attenuation increases with $\sigma_{\mathrm{coat}}$, reaches its maximum for a value $\sigma_{\mathrm{coat}} = 10^5$ S/m, where the skin depth is comparable with the coating thickness, then starts again to decrease because the field penetrates only in the coating layer. The frequency evolution changes also varying the value of $\sigma_{\mathrm{coat}}$, since it depends on the ratio $t/\delta$. This behavior needs to be realistically taken into account during measurements.

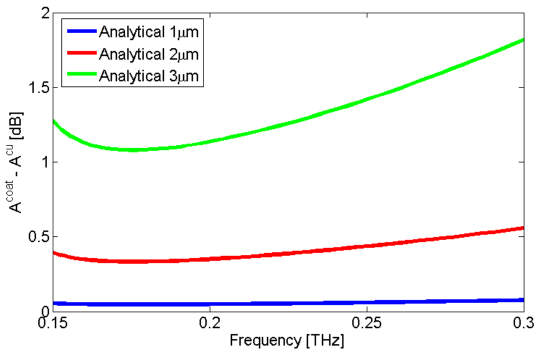


Figure 8: Test structure with triangular waveguide: analytical evaluation of the relative attenuation on the slab vs frequency for the $TE_{01}$ propagating mode, assuming different coating thicknesses and $\sigma_{\mathrm{coat}} = 10^4$ S/m.

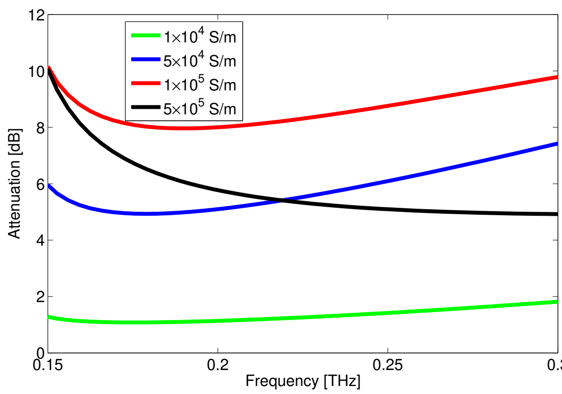


Figure 9: Test structure with triangular waveguide: analytical evaluation of the relative attenuation on the slab vs frequency for the $TE_{01}$ propagating mode, assuming different conductivity values and coating thickness $t = 3$ $\mu$m.

Following this preliminary study, samples of 3 $\mu$m amorphous carbon coating on bulk copper have been prepared (i.e. after the MCBI2019 workshop in Zermatt) using DC magnetron sputtering at CERN deposition facilities (see Fig. 10). EM characterisation measurements on the first a-C sample are planned in a very near future.

Figure 10: 3 $\mu$m a-C coating deposited on a copper slab.

## CONCLUSION

We developed a reliable, handy and affordable technique for the time domain evaluation of the electromagnetic properties of coatings for beam pipe walls. The method is based on the measurements of the signal transmitted through a tailored waveguide operating in single mode propagation in the sub-THz region. In comparison to previous techniques, the main advantages of this novel approach are:

- an inherently simplified approach for handling different coating materials;
- the possibility to test samples having a uniform deposition on copper or other wall constituents;
- the ability to extend the EM characterisation to larger area coatings and at higher frequencies.

Measurements performed on different NEG samples well agree with previous data obtained with a frequency domain approach and confirm the high potential of the proposed method.

For the test of a-C coatings, the setup was upgraded and the guiding system structure implemented, in order to overcome the demanding thickness requirement in amorphous carbon deposition. EMC on first samples will start very soon.

## ACKNOWLEDGEMENTS

This research is carried out in the framework of the INFN MICA project. The partial support of the CLIC project is also gratefully acknowledged. We thank M. Taborelli and W. Vollenberg for their excellent work in the coating fabrication process.

## REFERENCES

[1] M. A. Furman, “Electron cloud effects in accelerators,” in *Proceedings, 5th Workshop on Electron-Cloud Effects (ECLOUD’12): La Biodola, Isola d’Elba, Italy, June 5-9, 2012*, 2013. `https://inspirehep.net/record/1257435/files/arXiv:1310.1706.pdf`

[2] G. Rumolo, F. Ruggiero, and F. Zimmermann, “Simulation of the electron-cloud build up and its consequences on heat load, beam stability, and diagnostics,” *Phys. Rev. ST Accel. Beams*, vol. 4, p. 012 801, 1 Jan. 2001. `https://link.aps.org/doi/10.1103/PhysRevSTAB.4.012801`

[3] R. Cimino, L. A. Gonzalez, R. Larciprete, A. Di Gaspare, G. Iadarola, and G. Rumolo, “Detailed investigation of the low energy secondary electron yield of technical Cu and its relevance for the LHC,” *Phys. Rev. ST Accel. Beams*, vol. 18, p. 051 002, 5 May 2015. `https://link.aps.org/doi/10.1103/PhysRevSTAB.18.051002`

[4] M. Migliorati, E. Belli, and M. Zobov, “Impact of the resistive wall impedance on beam dynamics in the Future Circular $e+e^-$ Collider,” *Phys. Rev. Accel. Beams*, vol. 21, p. 041 001, 4 Apr. 2018. `https://link.aps.org/doi/10.1103/PhysRevAccelBeams.21.041001`

[5] C. Yin Vallgren *et al.*, “Amorphous carbon coatings for the mitigation of electron cloud in the CERN Super Proton Synchrotron,” *Phys. Rev. ST Accel. Beams*, vol. 14, p. 071 001, 7 Jul. 2011. `https://link.aps.org/doi/10.1103/PhysRevSTAB.14.071001`

[6] M. Taborelli, P. Chiggiato, P. Costa Pinto, and P. Cruikshank, “Nine years of carbon coating development for the SPS upgrade: achievements and heritage.,” CERN, Tech. Rep., Dec. 2015. `https://cds.cern.ch/record/2126930`

[7] M. Palmer *et al.*, “Electron cloud at low emittance in CesrTA,” *Conf. Proc.*, vol. C100523, TUYMH02, 2010.

[8] M. Theuer and J. S. Melinger, “High resolution waveguide terahertz time-domain spectroscopy,” *Journal of Infrared, Millimeter, and Terahertz Waves*, vol. 32, no. 11, pp. 1267–1284, Nov. 2011. `https://doi.org/10.1007/s10762-011-9816-3`

[9] M. Razanoelina *et al.*, “Parallel-plate waveguide terahertz time domain spectroscopy for ultrathin conductive films,” *Journal of Infrared, Millimeter, and Terahertz Waves*, vol. 36, no. 12, pp. 1182–1194, Dec. 2015. `https://doi.org/10.1007/s10762-015-0194-0`

[10] A. Khachatrian, J. S. Melinger, and S. B. Qadri, “Waveguide terahertz time-domain spectroscopy of ammonium nitrate polycrystalline films,” *Journal of Applied Physics*, vol. 111, no. 9, p. 093 103, 2012.

[11] A. Passarelli *et al.*, “Novel measurement technique for the electromagnetic characterization of coating materials in the sub-THz frequency range,” *Phys. Rev. Accel. Beams*, vol. 21, p. 103 101, 10 Oct. 2018. `https://link.aps.org/doi/10.1103/PhysRevAccelBeams.21.103101`

[12] A. Passarelli, C. Koral, M. R. Masullo, W. Vollenberg, L. L. Amador, and A. Andreone, “Sub-THz waveguide spectroscopy of coating materials for particle accelerators,” *Condensed Matter*, vol. 5, no. 1, 2020, ISSN: 2410-3896. `https://www.mdpi.com/2410-3896/5/1/9`

[13] E. Koukovini-Platia, G. Rumolo, and C. Zannini, “Electromagnetic characterization of nonevaporable getter properties between 220–330 and 500–750 GHz for the Compact Linear Collider damping rings,” *Phys. Rev. Accel. Beams*, vol. 20, p. 011 002, 1 Jan. 2017. `https://link.aps.org/doi/10.1103/PhysRevAccelBeams.20.011002`

[14] J. F. Johansson and N. D. Whyborn, “The diagonal horn as a sub-millimeter wave antenna,” *IEEE Transactions on Microwave Theory and Techniques*, vol. 40, no. 5, pp. 795–800, May 1992, ISSN: 0018-9480.

[15] D. Dasgupta, F. Demichelis, and A. Tagliaferro, “Electrical conductivity of amorphous carbon and amorphous hydrogenated carbon,” *Philosophical Magazine B*, vol. 63, no. 6, pp. 1255–1266, 1991. `https://doi.org/10.1080/13642819108205558`

# WAKE FIELDS EVALUATION FOR BEAM COLLIMATORS AND THE 60 PC ELECTRON BEAM AT THE COMPACT ERL AT KEK*

O. A. Tanaka†, N. Nakamura, T. Obina, Y. Tanimoto, T. Miyajima, M. Shimada, High Energy Accelerator Research Organization, KEK, Tsukuba, Japan
N. P. Norvell, SLAC National Accelerator Laboratory, Menlo Park, USA

*Abstract*

In high-intensity particle accelerators, unwanted transverse and longitudinal wakefields arise when the high-charge particle beam passes through the narrow chambers or locations with small transverse apertures, such as collimator jaws. The transverse wake field may affect the beam emittance and the longitudinal wake field can cause the energy loss and the energy spread. In the present study we investigated the collimator's impact to the beam performance. In this paper, we have shown numerical, analytical and measurement results on the collimator's wakefields that will be important for the next step operation. Thus, considering future cERL upgrade to the IR-FEL, a possibility of consequent degradation of the FEL performance should be taken into account. The correspondent power loss was obtained as 13.7 W (81.25 MHz, 5 mA, 2 ps).

## INTRODUCTION

The Compact ERL (cERL) at KEK [1] has five collimators (one in the injector section, one in the merger section and three in the recirculation loop, see Fig. 1) to remove the beam halo and to localize the beam loss. An operation at 10 mA average beam current and 1.3 GHz repetition rate is planned in the near future. The collimator's wakefields are expected to play an important role in CW operation, when the bunch charge will be increased up to 80 pC. The current beam parameters of the cERL are summarized in the Table 1.

All cERL collimators consist of four cylindrical rods of 7 mm radius made from copper. They could be independently inserted from the top, bottom, left and right sides of the beam chamber. Collimators COL1 – 3 were designed for the straight sections, therefore they have a round chamber 50~mm radius made from stainless still. Its schematic is given at Fig. 2.a. Note that the beam energy at collimators COL 1 – 2 is 2.9 MeV, while the energy at the rest of them is 17.6 MeV. Collimators COL4 – 5 are dedicated to the arc section, thus their chambers have elliptical shape with 70x40~mm diameter. Materials used are the same. The detailed scheme can be found at Fig. 2.b.

In the present study, first, we have estimated the transverse kicks imposed by the collimator's rods. This calculation is needed to account for the beam blow up (emittance growth) associated with collimator's wake. Then, the longitudinal wakes are calculated to obtain the expected energy losses of the beam passing through the collimator and its energy spread. Finally, those results are compared with the beam measurements in cERL. The present study is neccessary towards the IR-FEL upgrade of cERL [2 – 3].

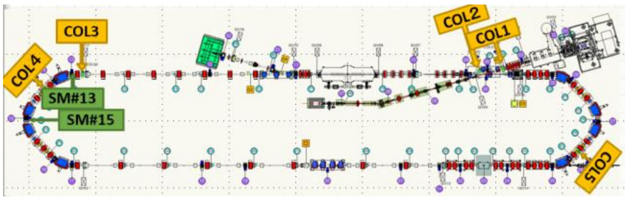


Figure 1: Layout of the cERL and its collimators.

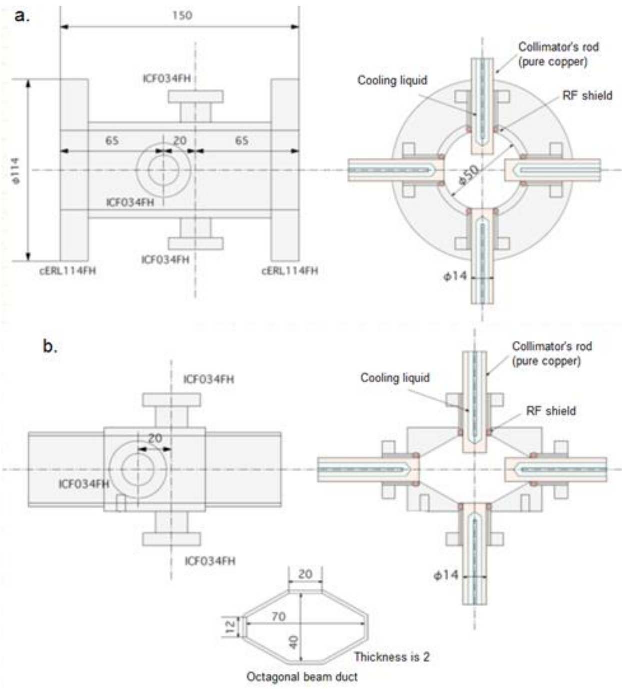


Figure 2: Schematic of the collimators with chambers made of stainless steel and rods made of copper: a. Collimators COL 1 – 3 for the straight sections; b. Collimators COL 4 – 5 for the arc sections.

Table 1: cERL electron beam parameters

| Parameter | Design | In operation |
|---|---|---|
| Beam energy [MeV]: | | |
| Injector | 2.9 | 2.9 |
| Recirculation loop | 18 | 17.6 |
| Bunch charge [pC] | 60 | 60 |
| Repetition rate [GHz] | 1.3 | 1.3 |
| Bunch length (rms) [ps] | 2 | Under tuning |
| Energy spread [%] | 0.088 | Under tuning |
| Normalized emittance (rms) in injector $\gamma\epsilon_x$, $\gamma\epsilon_y$ [μm·rad] | 1, 1 | Under tuning |

† olga@post.kek.jp.

## TRANSVERSE WAKES AND EMITTANCE GROWTH

Let us consider transverse wakefields created by the vertical rods of the collimator. The simplified scheme of the collimator is demonstrated at Fig. 3. Here the vacuum duct's half aperture is b = 25 mm. The collimator's half gap is a = [0; 25] mm. There is no tapers, so that the taper angle is $\alpha = \pi/2$. The rod's length is $L = 14$ mm. The value $y_0$ denotes the beam offset. The longitudinal beam distribution $\lambda(s)$ considered to be Gaussian.

For the geometry given at Fig. 3 in the beam near-axis approximation, when the dipole kick is applied to the centroid of the bunch, one can write down the dipolar mode of the *geometric component* of the transverse wake kick factor as follows [4]:

$$k_g = \frac{Z_0 c}{4\pi}\left(\frac{1}{a^2} - \frac{1}{b^2}\right) \quad for \quad \sqrt{\frac{\alpha a}{\sigma_z}} > 0.37. \tag{1}$$

Here we consider the collimator to be in purely diffractive regime [5]. In Eq. (1) the value $Z_0 = 120\pi$ is the impedance of the free space, $c = 2.9979 \times 10^8$ m/s is the speed of light, and $\sigma_z = 0.6$ mm is the rms bunch length.

Then, the *resistive component* of the collimator wake kick factor was evaluated with [6]:

$$k_r = \frac{\pi}{8a^2}\Gamma\left(\frac{1}{4}\right)\sqrt{\frac{2}{\sigma_z \sigma Z_0}}\left(\frac{L}{a} + \frac{1}{\alpha}\right). \tag{2}$$

Note that Eq. (2) refers to the so-called "long collimator" regime [7] that is exactly our case. Thus, the condition $0.63\left(2a^2 / Z_0\sigma\right)^{1/3} \ll \sigma_z \ll 2a^2 Z_0 \sigma$ is satisfied. The value $\Gamma(1/4) = 3.6265$ , while $\sigma = 5.96 \times 10^7$ S/m is the electrical conductivity of copper.

The CST Particle Studio [8] was used for the wakefields simulations The 3D models of the collimators are shown in Fig4. Since the differences coming from the various chamber geometries was found to be negligible, we focused for simplicity on the circular one. Six million hexahedral meshes were set for the simulation. The half gap a was scanned from 0.1 mm up to 1.5 mm. The dipolar impact was calculated by setting the integration path to $y = 0$. The quadrupolar impact is calculated by setting the integration path to $y_0 = 0.05$ and 0.2 mm. A direct integration method was used.

The summary of simulation results together with analytical calculations is demonstrated at Fig. 5. The analytical curve for the geometrical component (blue line) is several orders bigger than those for the resistive-wall component (magenta line). Therefore, the total kick graph (red line) almost coincides with those for the geometrical component (blue line). The results of the corresponding CST simulations for the beam offsets $y_0 = 0.05$ mm (triangle) and $y_0 = 0.2$ mm (circles) are also shown in Fig 5 and are in very good agreement with the analytical calculations. The resistive-wall component is small due to relatively short length of the collimator (14 mm). The geometrical component is slightly bigger due to the absence of tapers in the collimator's design.

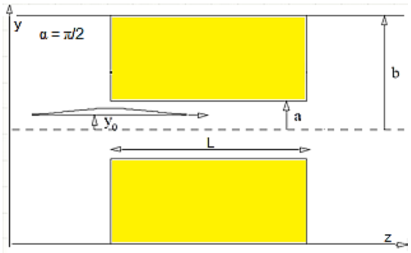


Figure 3: Simplified scheme of the collimator.

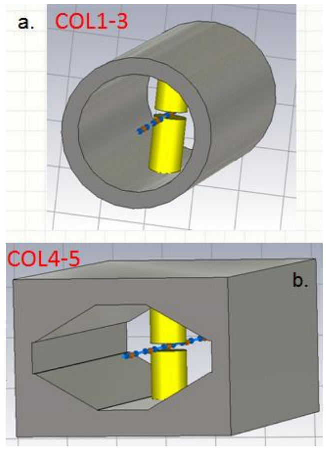


Figure 4: CST 3D models of the collimators with chambers made of stainless steel and rods made of copper: a. Collimators COL 1 – 3 for the straight sections; b. Collimators COL 4 – 5 for the arc sections.

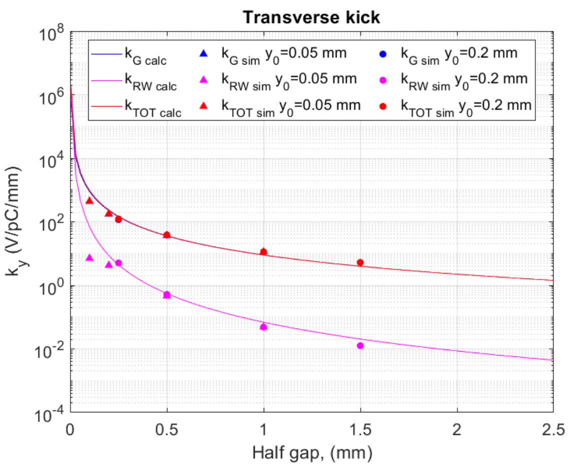


Figure 5: Transverse wake kick factors of the collimators found from analytical calculations and CST simulations for the geometrical and resistive wall component and different beam offsets.

The emittance blow-up for the 60 pC electron bunch at cERL was estimated. To account for this effect, the following analytical expression was treated [9]:

$$\frac{\Delta\varepsilon_y}{\varepsilon_{y0}} = \sqrt{1 + \frac{\beta_y \sigma_\omega^2}{\varepsilon_{y0}}} - 1, \tag{3}$$

where the value $\Delta\varepsilon_y$ is the *transverse emittance growth* with respect to the initial emittance $\varepsilon_{y0}$. The rms of the centroid kicks caused by the longitudinally varying field $\sigma_\omega$ could be found as follows [10]:

$$\sigma_\omega = \frac{Q}{E/e} k_\perp^{rms} y_0. \quad (4)$$

The value $E$ is the beam energy at the location of collimator (see Table 1). The value $Q = 60$ pC is the bunch charge. The value $y_0$ is the beam centroid offset (see Fig. 3), and lastly, the value $k_\perp^{rms}$ is the rms kick factor, estimated for the bunch head-tail difference in the kick. For Gaussian bunch $k_\perp^{rms} = k_\perp/\sqrt{3}$.

The resulted emittance blow-up found from Eq (3) are summarized in Table 2. The values of the initial emittances and beta functions at all locations are design values outputted from the tracking codes (General Particle Tracer [11] for the injector, and Strategic Accelerator Design for the recirculation loop [12]). The value of the transverse kick $k_\perp$ is taken with respect to the collimator half gap a = 1.5 mm, and the beam centroid offsets $y_0 = 0.05$ mm and 0.2 mm. The emittance growth was found to be of the order of one percent or less.

Table 2: Expected values of the emittance blow-up for the collimator half gap 1.5 mm

| **Collimator** | **$\varepsilon_{y0}$ [µm×rad]** | **$\beta_y$ [m]** | **$\Delta\varepsilon_y/\varepsilon_{y0}$ [%]** |
|---|---|---|---|
| COL1 E=4 MeV | 1.15 | 27.47 | 1.05 |
| COL2 E=4 MeV | 1.25 | 19.23 | 0.84 |
| COL3 E=17.6 MeV | 0.954 | 34.76 | 3.82 |
| COL4 E=17.6 MeV | 0.954 | 6.99 | 1.61 |
| COL5 E=17.6 MeV | 0.954 | 6.99 | 1.61 |

## LONGITUDINAL WAKES AND ENERGY SPREAD

Now let us consider the longitudinal wake fields excited by the particles passing through the collimators. The values of the wake-loss factor were evaluated numerically through CST simulation for half-gap values in the range of 0.1 to 1.5 mm. The dependence of the energy spread on the collimator's half gap for the designed (2 ps) and current (4.5 ps) bunch length is demonstrated at Fig. 6.

For the analytical description, the following equation was used [13]:

$$k_\parallel = \frac{Z_0 c}{2\pi^{3/2}\sigma_z} \ln\left(\frac{b}{a}\right), \quad (5)$$

where the value $Z_0$=120π is the impedance of the free space, c is the speed of light, $\sigma_z$ is the bunch length, b = 25 mm is the vacuum duct's half aperture, and a is the collimator's half gap.

The energy loss of the bunch at one collimator for the 60 pC per bunch burst mode with bunch length 2 ps, and collimator half gap a=1.5mm:

$$\Delta E = k_\parallel Q^2 = 46.86V/pC \times (60pC)^2 = 168.7nJ. \quad (4)$$

The voltage received by the electrons is ΔV=$k_\parallel$×Q=2812 V. The energy of one electron is reduced by eΔV=2812 eV. If E=17.6 MeV, and since E=17.6 MeV, the relative energy change is eΔV/E=0.016%. For Gaussian bunch the energy spread due to one collimator is σE=0.4×$k_\parallel$×Q=1124V. With respect to the beam energy the wake-induced energy spread reads σE/E=0.0063%. Unfortunately estimated values are beyond the limits of the resolution of our monitors, and we could not detect them.

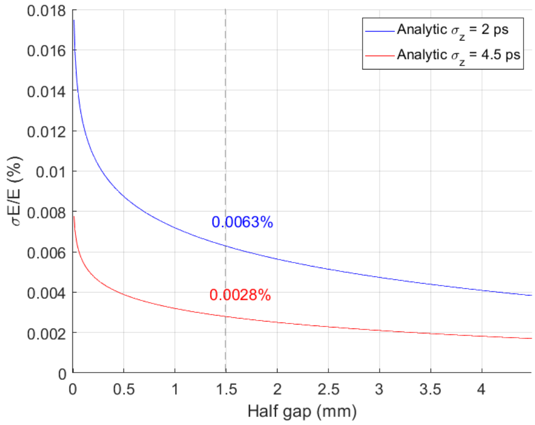


Figure 6: Wake-induced energy spread for different values of the collimator half gap and bunch lengths 2 ps (blue line) and 4.5 ps (red line).

## BEAM-BASED MEASUREMENTS

For the measurement of the energy spread caused by the collimator's longitudinal wake, we used collimator COL3 located in the end of the north straight section, screen monitor SM#13 located between collimator COL3 and the entrance of the are section, and screen monitor SM#15 located just in the middle of the arc (see Fig. 1). The screen monitor SM#13 needed to monitor the beam spot, which was successively cut by collimator's rods. The measurement itself was done by the screen monitor SM#15. To do so, first, we have restored the history of the quadrupole magnets to have the best beam spot at the collimator COL3 location. Then we have degaussed all quadrupoles of the first arc between screen monitors SM#13 and SM#15 to maximize the dispersion. We have measured the dispersion to be 2.41 m. The default energy spread was σE/$E_{default}$=$\sigma_x$/η=0.117%. It is the ratio of the rms beam size to the dispersion. However, in the following we care only on the changes of the energy spread and not on its absolute value.

The next step was to insert the collimator COL3. We used two horizontal rods, because the beam spot at the collimator location is known for its vertical beam halo. Therefore, we have avoided an influence of the halo on our energy spread measurement. We have performed the measurement for the half gap values 2 mm, 1.5 mm, 2 mm, 2.5 mm, 4 mm, COL out accordingly. Related rms beam sizes and beam profile peak positions were recorded at the screen monitor SM#15. The raw data of the beam profile was fitted by Gaussian fitting routine and weight analysis. An example on how the measured data were processed are shown in Fig. 7. Here the upper image is a SM#15 beam spot, the blue curve at the bottom plot is the raw data, the red line is its Gaussian fit, and the magenta mark denotes the peak position with respect to the data weight.

Weight analysis [14] gives the following expression for the profile peak position:

$$x_c = \frac{1}{N}\sum_{i=1}^{659} x_i N_i, \qquad N = \sum_{i=1}^{659} N_i. \tag{6}$$

Here $N$ is the number of data points, and $x_i$ is the value of the i^th data point. The rms beam size is given by:

$$\sigma_x = \sqrt{\frac{1}{N}\sum_{i=1}^{659} N_i\left(x_i - x_c\right)^2}. \tag{7}$$

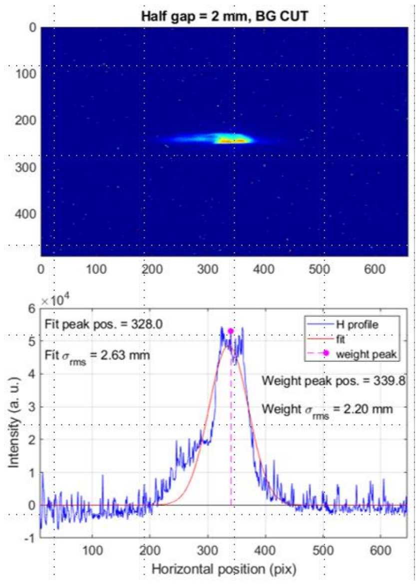


Figure 7: Energy spread measurement data at the screen monitor SM#15: the beam spot (top), the raw data and its fit (bottom).

Results of the processing of all six measurements are demonstrated at Fig. 8. The rms beam size is not changed significantly within the error bar except in the case of the 1.5 mm half gap. It was predicted by simulation and calculation. The beam size drop at the half gap 1.5 mm indicates that the beam core was damaged by the collimator’s rod.

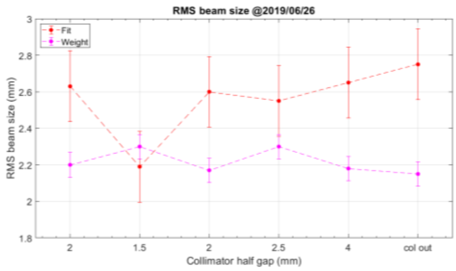


Figure 8: Horizontal beam size at the screen monitor SM#15 with respect to the horizontal collimation: fitting result (red), weight analysis result (magenta).

## CONCLUSION AND OUTLOOK

The effect of the collimator's transverse and longitudinal wakes on the 60 pC electron beam performance was studied. It should be taken into account for an intense short bunch, when a considerable beam collimation is required. We have estimated the expected emittance growth due to collimator’s wake field under the current operational conditions at cERL to be a few percent or less. The additional energy spread due to collimator’s wake at cERL is found to be 0.0028 % at 17.5 MeV, which is negligibly small.

Experimentally we have found, that for the current beam parameters even with the collimator's half gap at 2mm, the emittance and energy spread are not considerably affected. Thus the beam collimation at cERL was approved.

Considering the future cERL upgrade to the IR-FEL, the possibility of a consequent degradation of the FEL performance should be taken into account. The estimated power loss of 13.7 W was obtained for 81.25 MHz, 5 mA, 2 ps.

## ACKNOWLEDGEMENTS

This research is carried out with the support of NEDO project “Development of next generation laser technology with high brightness and high efficiency”.

## REFERENCES

[1] R. Kato, *et.al*., “Current status of KEK Compact ERL”, in in *Proceedings of the 16th Annual Meeting of Particle Accelerator Society of Japan,* Kyoto, Japan, (in press).

[2] R. Kato *et al*., “Development of high repetition middle infrared free electron laser using cERL”, in *Proceedings of the 16th Annual Meeting of Particle Accelerator Society of Japan,* Kyoto, Japan, (in press).

[3] O. Tanaka *et al*., “High bunch charge operation of cERL for infrared free electron laser test”, in *Proceedings of the 16th Annual Meeting of Particle Accelerator Society of Japan,* Kyoto, Japan, (in press).

[4] G.V. Stupakov, “High-Frequency Impedance of Small-Angle Collimators”, in Proc. of 2001 Particle Accelerator Conf. (PAC01), Chicago, USA, June. 2001, pp. 1859-1861.

[5] M. Dohlus, I. Zagorodnov, O. Zagorodnova, “Impedances of Collimators in European XFEL”, TESLA-FEL Report 2010-04, July 2010.

[6] P. Tenenbaum, “Collimator Wakefield Calculations for ILC-TRC Report”, LCCNOTE-0101, 2002.

[7] I. Zagorodnov and K.L.F. Bane, “Wakefield calculations for 3D collimators’, in *Proc. of 10th European Particle Accelerator Conference (EPAC 2006)*, Edinburgh, UK, June. 2006, pp. 2859 – 2861.

[8] CST-Computer Simulation Technology, CST PARTICLE STUDIO, `http://www.cst.com/Content/Products/PS/Overview. aspx`.

[9] M. Dohlus, T. Limberg, “Impact of Optics on CSR-Related Emittance Growth in Bunch Compressor Chicanes”, in *Proc. of 21st Particle Accelerator Conference (PAC05),* Knoxville, USA, May. 2005.

[10] S. Di Mitri, PhysRevSTAB 13,052801 (2010).

[11] GPT - A simulation tool for the design of accelerators and beam lines, `http://www.pulsar.nl/gp`.

[12] Strategic accelerator design, `http://acc-physics.kek.jp/SAD`.

[13] S. Heifets and S. Kheifets, “Coupling impedance in modern accelerators”, *Rev. Mod. Phys*. vol. 63, p. 631, Jul. 1991. `doi:10.1103/RevModPhys.63.631`

[14] P. R. Bevington and D. K. Robinson, *Data Reduction and Error Analysis for the Physical Sciences*, McGraw-Hill, 1992.

# CLIC-DR ELECTRON CLOUD BUILD UP SIMULATIONS

F. Yaman*, İzmir Institute of Technology, İzmir, Turkey
G. Iadarola, D. Schulte, CERN, Geneva, Switzerland

*Abstract*

This study investigates impact of beam pipe material and external magnetic field on electron cloud build up mechanism. The machine parameters are in the scope of CLIC damping rings. Two different filling schemes for 0.5 and 1 ns bunch spacings are considered. VSim Plasma Discharges and Plasma Acceleration package is employed to perform 2D electrostatic particle in cell simulations such that the space charge effect and Furman-Pivi secondary emission yield model are included in the computations. It is illustrated that the build up time varies due to bunch spacing while the external magnetic field influences the number of electrons generated by initial seeds. The evolution of generated secondary electrons due to bunch passes and the corresponding energy levels are presented in details.

## INTRODUCTION

CLIC damping rings reduce the emittance of particle beams to achieve design considerations of the $e^-$ and $e^+$ main linacs. Smaller emittance for a sufficiently short damping time can be obtained via long wiggler magnet sections. Accordingly, quantification of magnetic field on the electron build-up is of interest. Initial studies for CLIC-DR simulations with ECLOUD 2.4 and PyECLOUD are presented in [1,2], respectively. Both studies predict electron cloud formations for certain secondary emission yields and scenarios, i.e. including residual gas and photoemission mechanisms. Within this framework, the present study employs alternatively VSim package [3] and Furman-Pivi secondary emission yield model [4] for the CLIC damping ring simulations by modifying machine/beam parameters slightly compared to the former works. Here a similar simulation set-up presented in [5] is used for two dimensional case. However, not only stainless steel but also copper as a beam pipe material is investigated. Additionally the external magnetic field variations are examined in this study.

## MACHINE & SIMULATION PARAMETERS

The circumference of the damping ring is 427.5 m such that an elliptical beam pipe with the horizontal and vertical radii 40 and 6 mm, respectively is considered. The energy of the beam is 2.86 GeV given for the bunch population $4.1 \times 10^9$ positrons per bunch. The beam is elliptical with the transverse horizontal and vertical emittances $\epsilon_x = 500$ and $\epsilon_y = 5$ nm. Two filling patterns for 2 batches per beam i.e. 312 bunches per batch with 0.5 ns bunch spacing and 156 bunches per batch with 1 ns bunch space are studied. The Gaussian shaped bunches with the length of 1.8 mm in the longitudinal direction are used. Initial electron density is chosen as $5 \times 10^{12}$ $m^{-3}$, based on the results in [6]. Furthermore it is assumed that initial electrons having Gaussian distribution on the transversal plane are confined at a circular cross section of radius $\approx 4$ mm in the beam pipe at time zero. Afterwards the Poisson's equation is computed at each time step $\approx 3.23 \times 10^{-12}$ sec. via the SuperLU direct solver on a uniform two dimensional cartesian grid. More than 4.4 M of time steps are calculated in a parallel manner via a desktop-type workstation using 4 cores to simulate a single revolution period. The accuracy and the convergence of the solution are evaluated by considering the number of macro particles and grid cells. Throughout the paper, Furman-Pivi model is employed for copper, with max(SEY) = 2.1 at a primary energy of $E_{max}$ = 271.0 eV and for stainless steel with max(SEY) = 2.05 at of $E_{max}$ = 292.0 eV, see [4].

* fatihyaman@iyte.edu.tr

## NUMERICAL RESULTS

Firstly, quantifications of electron densities for 0.5 ns and 1 ns bunch spacings for copper and stainless steel beam pipes are illustrated in Fig. 1. As it is expected the shorter bunch spacing increases the number of generated electrons. Additionally, one can conclude that the impact of steel beam pipe on electron generations is more significant compared to shorter bunch spacing, i.e. electron density for 1 ns steel is larger than 0.5 ns copper. Furthermore, for the case 1 ns copper the lowest density and the longest build-up time is obtained.

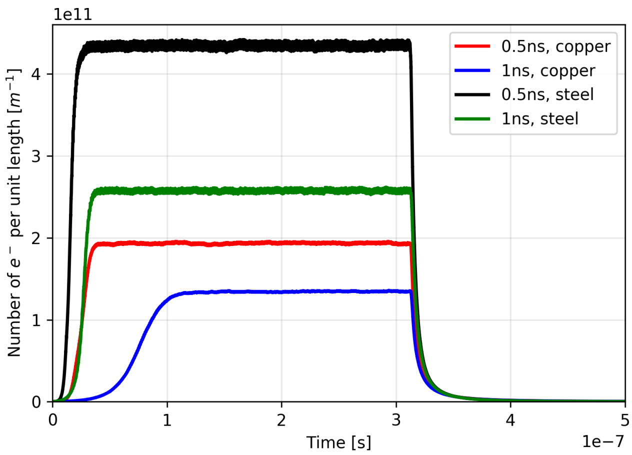


Figure 1: Ecloud build up for two types of bunch spacings and beam pipe materials.

Next, the dependence of electron cloud build up for externally applied magnetic field in the transverse direction is examined. The beam pipe material is chosen as copper and bunch spacing is 0.5 ns. The maximum value of the magnetic field in Fig. 2 is limited by considering a possible choice of the wiggler field, see [7]. Here the effect of magnetic field on the reduction of the secondarily generated electrons is confirmed. This nonlinear effect slightly shortens the dissipation time of the existing electrons in the chamber.

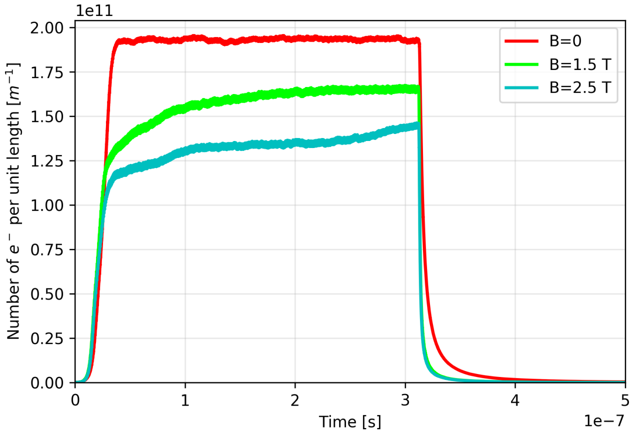


Figure 2: Effect of magnetic field on the Ecloud build up for 0.5 ns bunches, copper beam pipe.

Additionally, the external magnetic squeezes the electrons in a regular form at the center of the beam pipe and decreases the interaction of the electrons with the pipe surface, see Fig.3. A similar distribution as in Fig.3b is presented in [2] for the simulations of CLIC-DR wiggler magnets with PyECLOUD.

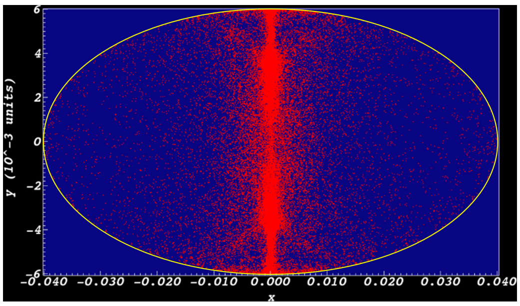


(a) B = 0

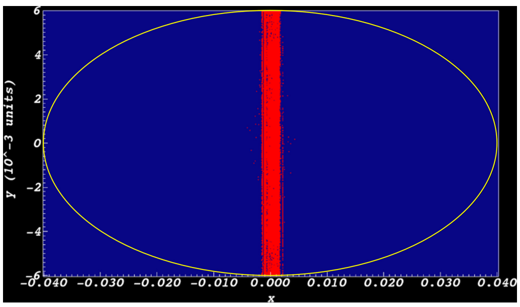


(b) B = 2.5 T

Figure 3: Electron distribution w.r.t external magnetic field for 0.5 ns copper pipe @21.376 ns.

The impact of the magnetic field for different bunch spacings and materials can be seen by comparing Fig. 1 and Fig. 4. In all cases the number of electrons is reduced and the decrease rate depends non-linearly on the material type. Furthermore, rapid electron generations in the build-up regime is observed. Particularly for the stainless steel beam pipe material the magnitude of the oscillations is increased.

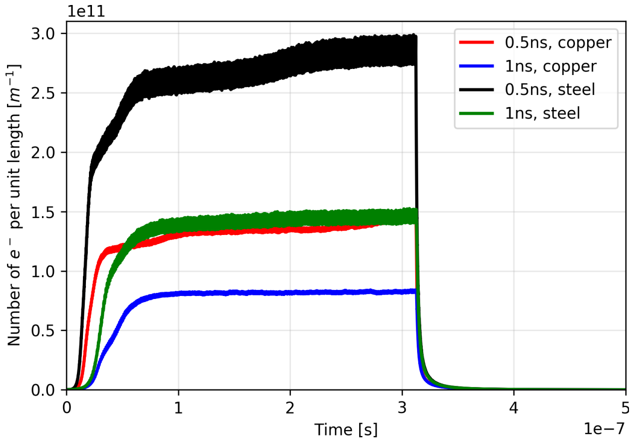


Figure 4: Ecloud build up for two types of bunch spacings and beam pipe materials with 2.5 T magnetic field.

The energy of the electrons for the copper beam pipe for 0.5 and 1 ns bunch spacings is illustrated in Fig. 5. Certain ranges from build-up, saturation and dissipation regions are zoomed as well. The increase in the energy is consistent with the bunch spacing which indicates the energy gains due to bunch passes. The maximum energy 3.95 $\mu$J is observed in 30 ns for the 0.5 ns bunches while 2.1 $\mu$J is reached after 50 ns using 1 ns bunch spacing. Afterwards, electrons oscillate in the saturation region and gain energy up to $\approx$ 1.62 $\mu$J during 275 ns and $\approx$ 1 $\mu$J during 255 ns for the 0.5 and 1 ns, respectively. Finally, electron cloud formation dissipates exponentially in 20 ns after the bunch passes, for both bunch spacing scenarios. The time needed to vanish electrons from the computational domain does not change significantly with respect to pipe material. Furthermore, similar energy plots but for the different values are obtained using stainless steel pipe. For instance, electrons reach 7.1 and 3.6 $\mu$J maximums in 20 and 40 ns for 0.5 and 1 ns bunches, respectively. The saturation is also longer for the 0.5 ns case compared to 1 ns bunch spacing, i.e. 285 and 265 ns. The behaviours of the energy patterns agree well with the number of generated electrons for the investigated scenarios. The number of electrons reaches largest values consistently with the computed maximum energy gains for shorter bunch spacing using steel pipe, see Fig. 1 and Fig. 4. In particular, similar number of electrons for the 0.5 ns copper and 1 ns steel is obtained in saturation, see Fig. 4, from the similar number of energy gains, i.e. 3.4 $\mu$J . Furthermore it is noted that the behaviours of the CLIC-DR simulation results for copper and steel pipes agree with those presented in [8] by considering the FNAL recycler machine for the parameters, pipe radii: (22, 47) mm, energy: 8 GeV, proton bunch population: $5.25 \times 10^{10}$, bunch length: 60 cm, beam radius: 3 mm and bunch spacing: 18.94 ns.

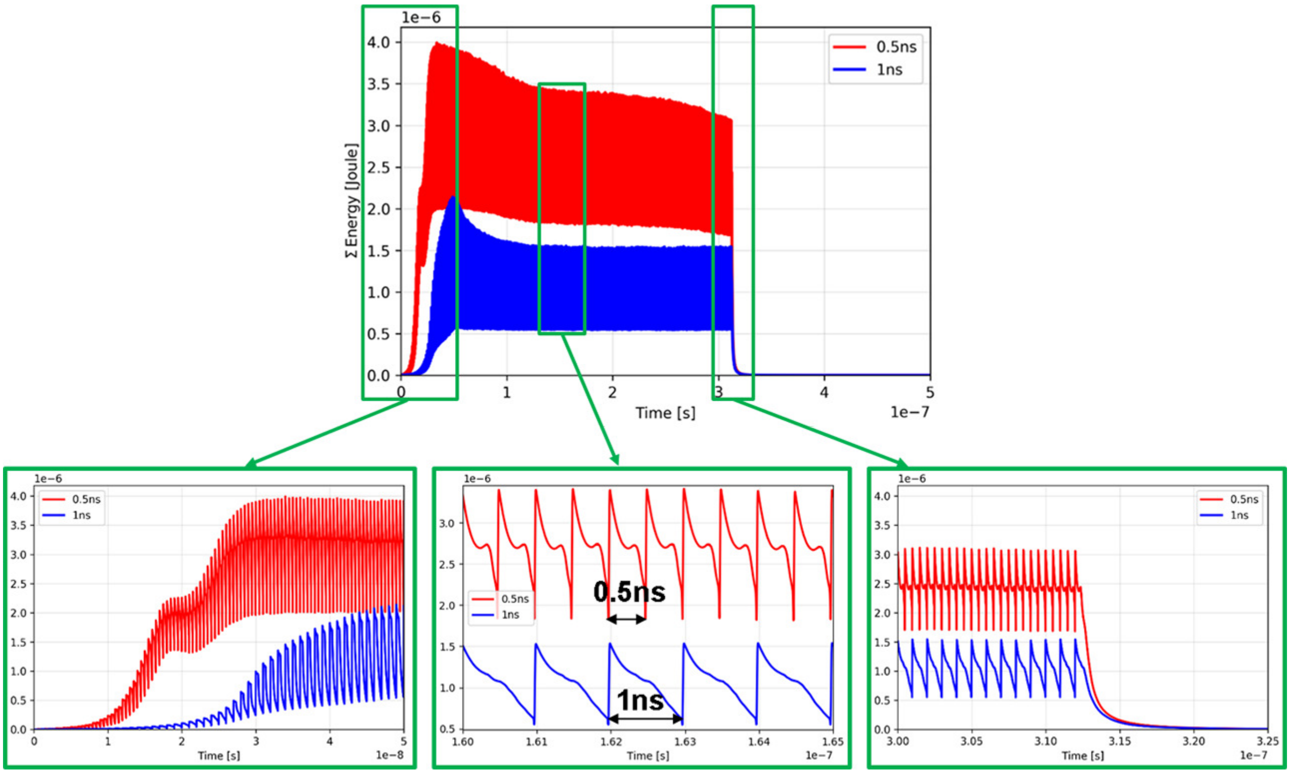


Figure 5: Energy of the electrons for two types of bunch spacings with copper beam pipe.

## CONCLUSION

In this study, effects of external magnetic field and copper/stainless steel pipe materials on the number of electrons and corresponding energies are quantified via VSim for the CLIC-DR machine for positron beam parameters. The computational domain is loaded with initial electrons as seeds of the secondaries generated according to Furman-Pivi secondary emission yield model. The collisions of the positron beam with the residual gases and photoemission mechanisms are omitted in simulations in order to focus on magnetic field and pipe material effects. It is confirmed that applying external dipole magnetic field and increasing bunch spacing reduces the electron cloud density. Furthermore, stainless steel has a significantly higher capability to emit electrons as compared to copper. External magnetic field aligns electrons at the center of the beam pipe in a narrow region as a stripe and reduces the interaction area of the pipe surface for the electrons. Moreover, magnetic field decreases number of secondaries in different ratios for steel and copper pipes.

## ACKNOWLEDGEMENTS

We would like to thank S.A. Veitzer and J. Smith for their help on VSim.

## REFERENCES

[1] D. Schulte, R. Wanzenberg and F. Zimmermann, "Electron-Cloud Effects in the TESLA and CLIC Positron Damping Rings", Proc. ECLOUD04, Napa, 2004, CERN-2005-001 (2005)

[2] G. Iadarola, G. Rumolo and H. Bartosik, "Electron Cloud Build up Studies for the CLIC Positron Damping Ring", presented in TWIICE2014 (2014), `https://indico.cern.ch/event/277919/`

[3] VSim, Powered by Vorpal; Empowered by Tech-X Corp.

[4] M.A. Furman and M.T.F. Pivi, "Probabilistic Model for the Simulation of Secondary Electron Emission", PRST-AB, 5, 124404, (2002)

[5] S. A. Veitzer and P. H. Stoltz, "Electron Cloud Buildup and Dissipation Models For PIP-II", IPAC2015, Richmond, VA, USA, MOPMA037, (2015)

[6] G. Rumolo, W. Bruns and Y. Papaphilippou, "Electron Cloud Build up and Instability in the CLIC Damping Rings", Proc. EPAC08, Genoa, Italy, MOPP050, (2008)

[7] E. K. Platia, "High Frequency Effects of Impedances and Coatings in the CLIC Damping Rings", PhD Thesis EPFL, CERN-THESIS-2015-152, (2015).

[8] F. Yaman, "A Numerical Investigation for the Electron Cloud Build-up Mechanism" Proc. HEZARFEN, İzmir, Turkey, (2019).

# CONSEQUENCES OF LONGITUDINAL COUPLED-BUNCH INSTABILITY MITIGATION ON POWER REQUIREMENTS DURING THE HL-LHC FILLING

I. Karpov*, P. Baudrenghien, L. E. Medina Medrano, H. Timko, CERN, Geneva, Switzerland

*Abstract*

During the filling of the Large Hadron Collider (LHC), it is desirable to keep the RF cavity voltage constant both in amplitude and phase to minimize the emittance blow-up and injection losses. To have a constant voltage and to minimize power consumption, a special beam-loading compensation scheme called half-detuning is used in the LHC, for which the cavity fundamental resonant frequency needs to be detuned from the RF frequency by an appropriate value. This, however, can result in fast coupled-bunch instabilities caused by the asymmetry of the fundamental cavity impedance. To mitigate them, a fast direct RF feedback and a one-turn delay feedback are presently used in the LHC. The semi-analytical model that describes the dynamics of the Low-Level RF system in the LHC shows that, depending on the mitigation scenario, the required transient RF power during injection could significantly exceed the steady-state value. This means that for High-Luminosity LHC (HL-LHC) beam intensities, one can potentially reach the limit of available RF power. In this paper, the model is described, and benchmarks with LHC measurements are presented. We also shortly revisit the damping requirements for the longitudinal coupled-bunch instability at injection energy, to find a compromise between longitudinal stability and RF power requirements for the HL-LHC beam.

## INTRODUCTION

During the filling of the Large Hadron Collider (LHC), it is desirable to reduce RF power requirements and to minimize the emittance blow-up and injection losses. This can be achieved if half-detuning beam loading compensation scheme is used [1], which keeps the RF cavity voltage constant both in amplitude and phase. Detuning causes asymmetry of the fundamental cavity impedance, which can drive longitudinal coupled-bunch instabilities. In the LHC, they are mitigated by a direct RF feedback [2] and a one-turn delay feedback (OTFB) [3] which reduce the impedance seen by the beam and defined as the closed-loop impedance

$$Z_{\rm cl}(\omega) = \frac{Z(\omega)}{1 + e^{-i\tau_{\rm delay}\omega} G(\omega) Z(\omega)}. \tag{1}$$

Here, $Z$ is the RF cavity impedance, $\tau_{\rm delay}$ is the loop delay, and $G$ is the frequency dependent gain. The feedback can reduce the impedance at frequencies where the absolute value of the denominator is significantly larger than 1.

In steady-state operation, feedbacks do not require significant additional power to suppress longitudinal coupled-bunch instabilities. Operational experience, however, suggests that power transients between beam- and no-beam segments need to be included in the analysis [4]. In the present work, we evaluate RF power transients during the injection process. If there is a large power overshoot, one can potentially reach the limit of the available RF power in the klystrons (about 300 kW [5]) for High-Luminosity LHC (HL-LHC) requiring higher-intensity beams.

## BEAM-GENERATOR-CAVITY INTERACTION MODEL

To evaluate power transients during the injection process in the LHC, the present work extends the description of beam-generator-cavity interaction [6] taking into account the details of the Low-Level RF (LLRF) system in the LHC [5] (see Fig. 1). The LHC employs superconducting cavities which are connected to generators (klystrons) via circulators, so that the whole reflected current ($I_r$) is absorbed in a load. The RF voltage $V$ is defined by the RF component of the beam current $I_{b,\rm RF}$ and the generator current $I_g$ fed into the cavity via a main coupler [6]:

$$I_g(t) = \frac{V(t)}{2(R/Q)}\left(\frac{1}{Q_L} - 2i\frac{\Delta\omega}{\omega_{\rm RF}}\right) + \frac{dV(t)/dt}{\omega_{\rm RF}(R/Q)} + \frac{I_{b,\rm RF}(t)}{2}. \tag{2}$$

Here $(R/Q) = 45\,\Omega$, $\Delta\omega = \omega_r - \omega_{\rm RF}$ is the cavity detuning, $f_r = \omega_r/2\pi$ is the cavity resonant frequency, $\omega_{\rm RF} = 2\pi f_{\rm RF} = 2\pi h f_0$, $f_{\rm RF} = 400.79$ MHz is the RF frequency, $f_0 = 1/T_0$ is the revolution frequency, $T_0$ is the revolution period, and $h = 35640$ is the harmonic number. The loaded quality factor $Q_L = (1/Q_{\rm ext} + 1/Q_0)^{-1}$ is calculated from the cavity quality factor $Q_0$ and the coupler quality factor $Q_{\rm ext} = Z_c/(R/Q)$ defined by $Z_c$, the line impedance transformed to the gap by the main coupler. For a superconducting cavity with $Q_0 \gg Q_{\rm ext}$, $Q_L \approx Q_{\rm ext}$. Note that in Eq. (2) $V$, $I_{b,\rm RF}$ and $I_g$ are the complex phasors and the corresponding phases are chosen such that in the absence of the beam the cavity voltage is real.

Equation (2) allows to treat the case when $I_{b,\rm RF}$ is modulated due to the gaps in the ring filling. In reality, the RF power chain (klystron, circulator, etc.) has limited bandwidth and cannot track the fast bunch-by-bunch variations of the beam current. In addition, the synchronous clock is used for processing in the LHC with a sampling time corresponding to the bunch spacing of $t_{\rm bb} = 10\ t_{\rm RF}$, where $t_{\rm RF} = 1/f_{\rm RF}$ is the RF period. In what follows, time is discretized with a the sampling frequency $f_{\rm bb} = 1/t_{\rm bb}$. We use a function $u$, which describes the filling scheme. It is defined on $h/10$ sampling points per turn, $u = 1$ in the filled buckets, and

* ivan.karpov@cern.ch

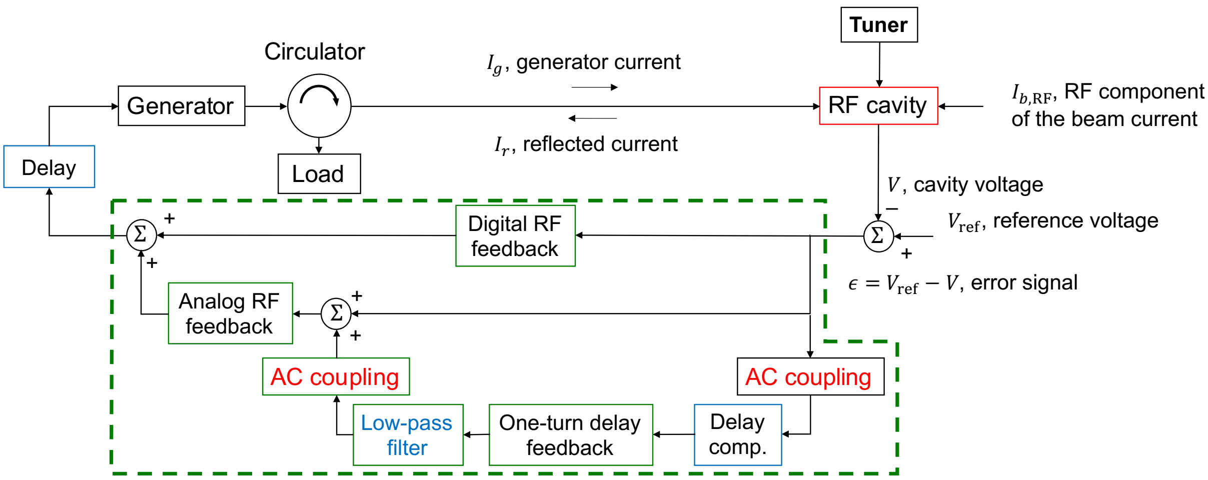


Figure 1: Beam-generator-cavity interaction model. The elements inside the dashed contour are the part of the low-level RF system.

$u = 0$ in the gaps. Thus, the RF component of the beam current in Eq. (2) is

$$I_{b,\mathrm{RF}}(t) = i\frac{eN_pF_b}{t_{\mathrm{bb}}}u(t)e^{i\phi_b(t)} = i\hat{I}_{b,\mathrm{RF}}e^{-i\phi_s+i\phi_b(t)}u(t), \tag{3}$$

where $\hat{I}_{b,\mathrm{RF}} = |F_b|eN_p/t_{\mathrm{bb}}$, $N_p$ is the number of particles per bunch, $\phi_s$ is the average bunch position, and $\phi_b$ is the bunch-by-bunch phase modulation. The complex form factor [7]

$$F_b = 2\frac{\mathcal{F}\left[\lambda(t)\right]_{\omega=\omega_{\mathrm{RF}}}}{\mathcal{F}\left[\lambda(t)\right]_{\omega=0}} = |F_b|e^{-i\phi_s} \tag{4}$$

is obtained from the bunch profile $\lambda$ as the ratio of the Fourier transform of $\lambda$ at the RF frequency to $\lambda$ at DC. It depends on the particle distribution function [8]. For symmetric Gaussian bunches with rms bunch length $\sigma$, the magnitude of the form factor can be approximated as $|F_b| \approx 2\exp\left[-(\omega_{\mathrm{RF}}\sigma)^2/2\right]$ and $\phi_s$ is the same as the synchronous phase.

The generator current in Eq. (2) depends on detailed implementation of the LLRF loops which are described in the following subsections. For each element, the transfer function $H$ is defined as

$$H(s) = \frac{Y(s)}{X(s)}$$

in Laplace notation, with the complex variable $s$, the input signal being $X$, and the output signal being $Y$. Note that $s = i(\omega - \omega_{\mathrm{RF}})$ is related to the angular frequency $\omega$, so that the LLRF response is centered at $\omega_{\mathrm{RF}}$. In the past, a part of the model was developed using MATLAB and Simulink software packages [9]. At present, two similar implementations (stand-alone and in the BLonD particle tracker suite [10]) are available in Python. The corresponding transfer functions are replaced by their discrete time-domain forms in the codes and solved together with Eq. (2) using the Euler method. The LLRF loops act on the error signal $\epsilon$ (difference between the actual value $V$ and the reference value $V_{\mathrm{ref}}$ of the cavity voltage) to control the RF voltage in the cavity.

Finally, to evaluate the time evolution of the RF power, the following equation is used [6]

$$P(t) = \frac{1}{2}(R/Q)Q_{\mathrm{ext}}|I_g(t)|^2 \approx \frac{1}{2}(R/Q)Q_L|I_g(t)|^2. \tag{5}$$

### *Direct RF feedback*

The LHC direct RF feedback consists of two branches: the analog and the digital paths. They can be described by a transfer function as the sum of high-pass and low-pass filters in Laplace notation

$$H_{a,d}(s) = G_a\frac{\tau_a s}{1+\tau_a s} + G_d\frac{1}{1+\tau_d s}, \tag{6}$$

where $G_a$ is the gain of the high-pass filter, $\tau_a$ is the high-pass filter time constant, $G_d$ is the gain for the low-pass filter, and $\tau_d$ is the time constant of the low-pass filter. While in the presence of the analog RF feedback, the closed-loop impedance is smaller than the cavity impedance, the digital RF feedback ensures precise control of the static cavity voltage amplitude and phase due to a higher gain ($G_d > G_a$) in the low-frequency range, $|f - f_r| < f_0$. In the LHC, the following values are used in operation: $\tau_a = 170\,\mu\mathrm{s}$, $\tau_d = 400\,\mu\mathrm{s}$, $G_d = 10\ G_a$, and $G_a = G_a^m = 6.79\times10^{-6}\ 1/\Omega$ is chosen to obtain a flat closed-loop response $H_{\mathrm{cl}}$ for loop delay of $\tau_{\mathrm{delay}} = 650\,\mathrm{ns}$,

$$G_a^m = \frac{1}{2(R/Q)\omega_{\mathrm{RF}}\tau_{\mathrm{delay}}},$$

where the closed-loop transfer function is defined as

$$H_{\mathrm{cl}}(s) = \frac{2e^{-\tau_{\mathrm{delay}}s}H_{a,d}(s)Z(s)}{1+2e^{-\tau_{\mathrm{delay}}s}H_{a,d}(s)Z(s)}. \tag{7}$$

The factor of 2 in Eq. (7) is coming from the fact that the transfer function from $I_g$ to $V$ based on Eq. (2) is twice the RF cavity impedance $Z(s)$, which is approximated as

$$Z(s) = \frac{(R/Q)Q_L}{1+2Q_L(s-i\Delta\omega)/\omega_{\mathrm{RF}}}.$$

### *One-turn delay feedback*

An additional means to reduce the closed-loop impedance is to use OTFB. In the LHC, the input and output signals of the OTFB branch are AC-coupled, so there is no influence on the average voltage in the cavity. The transfer function of the AC-coupling is

$$H_{\mathrm{AC}}(s) = \frac{\tau_{\mathrm{AC}} s}{1 + \tau_{\mathrm{AC}} s}, \tag{8}$$

with the time constant $\tau_{\mathrm{AC}} = 110\,\mu\mathrm{s}$. The OTFB response is modeled as a comb filter [2]

$$H_{\mathrm{OTFB}}(s) = G_{\mathrm{OTFB}} \frac{(1 - a_{\mathrm{OTFB}}) e^{-(T_0 - \tau_{\mathrm{delay\ comp}})s}}{1 - a_{\mathrm{OTFB}} e^{-T_0 s}}, \tag{9}$$

where $G_{\mathrm{OTFB}} = 10$ is the OTFB gain, $a_{\mathrm{OTFB}} = 15/16$ is the constant defining the bandwidth of the resonances, and $\tau_{\mathrm{delay\ comp}}$ is an adjustable delay that compensates for the delay of the closed-loop response defined in Eq. (7). In the LHC, $\tau_{\mathrm{delay\ comp}} \approx 1.2\,\mu\mathrm{s}$ is used, while it will be shown below that this delay affects the evolution of RF power transients during the injection process.

Finally, a symmetric, finite-impulse response (FIR) filter is used to control (and limit) the OTFB bandwidth. The transfer function of this low-pass filter (LPF) is

$$H_{\mathrm{LPF}}(s) = e^{(N_{\mathrm{tap}}-1)t_{\mathrm{bb}}s/2} \sum_{k=0}^{N_{\mathrm{tap}}-1} b_k e^{-k t_{\mathrm{bb}} s}, \tag{10}$$

where $N_{\mathrm{tap}}$ is the number of taps of the FIR filter ($N_{\mathrm{tap}} = 63$ in the LHC), and the filter coefficients $b_k$ are listed in the Appendix.

Apart from stabilising the beam, the feedback loops provide also transient beam-loading compensation. The particular compensation scheme that is used during the injection process in the LHC is described in the following section.

## HALF-DETUNING SCHEME

To keep the cavity voltage amplitude and phase constant ($V(t) = V_{\mathrm{cav}} = \text{constant}$), the feedback loops will try to compensate the beam-induced voltage. For a non-uniform filling of the ring, the steady-state RF power in this scheme is at its minimum and is the same in beam and no-beam segments if the following frequency detuning and loaded quality factor are used [1]

$$\Delta\omega_{1/2} = -\omega_{\mathrm{RF}} \frac{\hat{I}_{b,\mathrm{RF}}(R/Q)}{4V_{\mathrm{cav}}}, \quad Q_{L,1/2} = \frac{2V_{\mathrm{cav}}}{(R/Q)\hat{I}_{b,\mathrm{RF}}}. \tag{11}$$

The corresponding steady-state power is

$$P_{\mathrm{th}} = \frac{V_{\mathrm{cav}} \hat{I}_{b,\mathrm{RF}}}{8}. \tag{12}$$

During Run I and Run II operation, the RF power at injection was typically around 100 kW and the main coupler was not adjusted to minimise the RF power, but rather to be at a constant working point corresponding to $Q_L = 20000$ during injection. The cavity was detuned automatically after beam injection using the algorithm described below.

### *Tuning algorithm*

To optimize the RF power requirements in steady-state operation, a cavity detuning algorithm was proposed and implemented in the LHC [11]. The cavity detuning changes between consecutive turns $n$ and $n + 1$ as

$$\left(\frac{\Delta f}{f_0}\right)_{n+1} = \left(\frac{\Delta f}{f_0}\right)_n - \frac{\mu}{2} \frac{\mathrm{Im}\left[V I_g\right]_{\min} + \mathrm{Im}\left[V I_g\right]_{\max}}{|V_{\mathrm{cav}}|^2}, \tag{13}$$

where $\mu$ sets the rate of convergence with a time constant of the detuning process in the order of a second. The quantities in the square brackets are down-sampled using a Cascaded-integrator–comb (CIC) filter with the following transfer function

$$H_{\mathrm{CIC}}(s) = \frac{1}{64} \left(\frac{1 - e^{-8 t_{\mathrm{bb}} s}}{1 - e^{-t_{\mathrm{bb}} s}}\right)^2, \tag{14}$$

and then $\mathrm{Im}\left[V I_g\right]_{\min}$ and $\mathrm{Im}\left[V I_g\right]_{\max}$ are obtained within one turn. In our model, the tuner model was implemented together with the direct RF feedback and OTFB, and it was benchmarked with measurements in the steady-state case, which is described in the following subsection.

### *Comparison with measurements in steady-state*

The half-detuning scheme was employed during the whole LHC cycle until 2014. The modulations of the generator forward power, the generator current phase, the cavity voltage amplitude, and the cavity voltage phase measured at 6.5 TeV with a full machine are shown in Fig. 2 (measured data from Ref. [12]). The modulation pattern is defined by gaps in the filling scheme: 225 ns due to the Super Proton Synchrotron (SPS) injection kicker rise time, 900 ns due to the LHC injection kicker rise time, and finally 6.85 µs due to the LHC abort gap. There were 2244 bunches (36 bunches in the Proton Synchrotron (PS) batches, either one, three or four PS batches per SPS batch) circulating in the machine with the average bunch intensity of $N_p = 1.2 \times 10^{11}$ protons per bunch (p/b) and a bunch length of about 1 ns ($|F_b| = 1.64$). We used the implemented LLRF and tuner models to evaluate the modulations for the same parameters (red dashed lines in Fig. 2).

The tuning algorithm in the model results in $\Delta\omega = 0.935 \times \Delta\omega_{1/2}$, which is close to the theoretically predicted value of -4.6 kHz. In the steady-state situation, the model takes also into account that the bunch-by-bunch phase modulation follows the cavity phase modulation, so that the stable phase for all bunches is 180°. In general, we see that calculations reproduce well the measured modulations for $\tau_{\mathrm{delay\ comp}} = 1175$ ns, while the measured value of the delay is not available in Ref [12]. Another uncertainty is the exact value of the cavity detuning in measurements. Note also that the corresponding steady-state power is $P_{\mathrm{th}} \approx 200$ kW [see Eq. (12)] in this case, while the peak power reaches more than 280 kW both in calculations and in measurements. This means, that Eq. (12) does not include the power transients caused by the transitions between beam and no-beam seg-

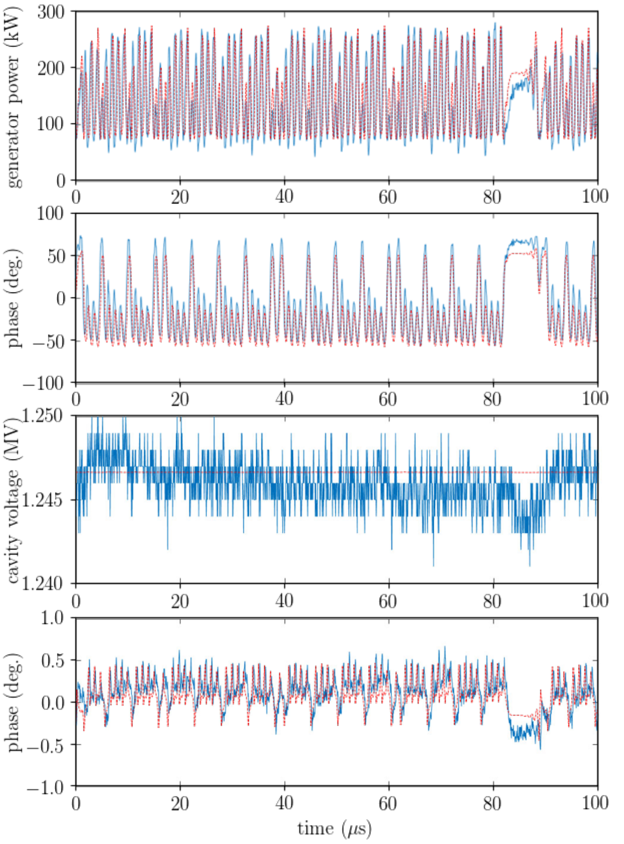


Figure 2: Comparison of generator forward power, generator current phase, cavity voltage amplitude, and cavity voltage phase (from top to bottom) from measurements (solid blue lines) and calculations using the developed model (red dashed lines). The plots are obtained by the overlap of the calculations with the data from Ref [12]. The modulations in the signals along the ring are due to beam-current modulations between batches. The beam and LLRF parameters are 2244 bunches, $N_p = 1.2 \times 10^{11}$ p/b, $\tau_{4\sigma} = 4\sigma = 1$ ns, $V_{\text{cav}} = 1.25$ MV, $Q_L = 60000$, $\Delta\omega = 0.935\Delta\omega_{1/2}$, $G_a = G_a^m$, $G_d = 10\ G_a$, and $G_{\text{OTFB}} = 10$, and $\tau_{\text{delay comp}} = 1175$ ns.

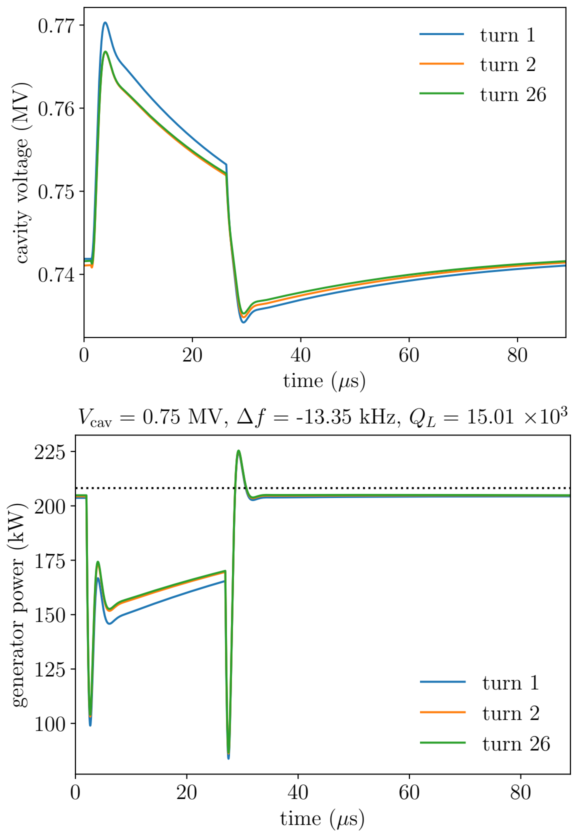


Figure 3: Cavity voltage amplitude (top) and RF power requirements (bottom) for selected turns after injection with the direct RF feedback on and the OTFB off. A beam without gaps is considered, with the first bunch at 1.3 μs and the last bunch at 26.3 μs. Parameters: $\hat{I}_{b,\text{RF}} = 2.22$ A, $G_a = G_a^m$, $G_d = 10\ G_a$, and $G_{\text{OTFB}} = 0$. The dashed line is the expected RF power in the steady-state [see Eq. (12)].

ments. In the next section we use the implemented model to evaluate the power transients during the injection process.

## POWER EVOLUTION DURING INJECTION

The bunches extracted from the SPS 200 MHz main RF system are mismatched to the 400 MHz RF bucket of the LHC RF system, which results in their filamentation. In general, one has to model the dynamics of the interaction of the beam with the LLRF system in order to accurately evaluate transient effects. The present work focuses only on timescales which are shorter than the synchrotron period. This allows to assume that the beam parameters do not change during the calculation. In the cases presented below, a single batch of 1000 Gaussian bunches with $\tau_{4\sigma} = 4\sigma = 1.2$ ns ($|F_b| = 1.5$) and $N_p = 2.3 \times 10^{11}$ p/b (HL-LHC baseline) is injected into the LHC for $V_{\text{cav}} = 0.75$ MV (6 MV of total RF voltage per beam) and different configurations of feedback loops. We also assume that the cavities are pre-detuned to the optimal frequency with beam loading and the quality factor is adjusted according to Eq. (11). In the following, the system of equations is initially solved for several tens of turns without beam to obtains steady-state conditions before injection and then the beam is taken into account in the calculations.

### *Case of direct RF feedback only*

Considering the case when $G_a = G_a^m$ and the OTFB is switched off ($G_{\text{OTFB}} = 0$), the modulations of the cavity voltage amplitude and of the RF power during the few first turns after injection are shown in Fig. 3. There is a small difference between traces due to a short time constant of its analog part defined by the physical loop delay $\tau_{\text{delay}} = 650$ ns. A small difference between the first and the second turns comes from the action of the digital part of the direct RF feedback which has a time constant of several turns. The modulation of the cavity voltage amplitude in this case is of

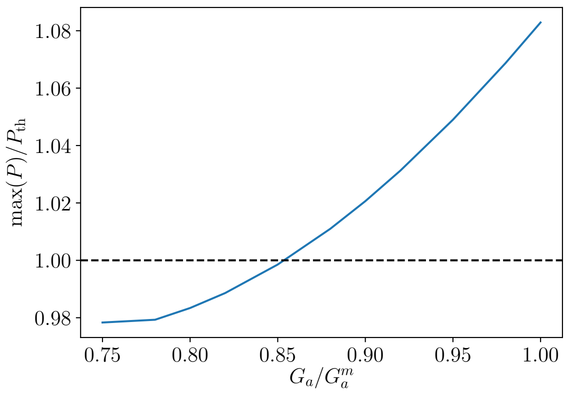


Figure 4: Normalized maximum needed RF power as a function of the direct RF feedback gain.

the order of 2-3 %. There is an overshoot in power in the no-beam segment behind the batch, which depends on the feedback gain (see Fig. 4). For $G_a < 0.85G_a^m$, the power does not exceed the theoretical value [see Eq. (12)], but this might affect the longitudinal multi-bunch stability, since the closed-loop impedance will increase.

### *Case of direct RF feedback and OTFB*

Similar calculations for the case with OTFB ($G_{\mathrm{OTFB}} = 10$) are shown in Fig. 5. The first turn after injection is the same as for the case without OTFB because of the one turn delay. The beam loading compensation from the OTFB takes several turns to develop due to its narrow bandwidth, resulting in a much smaller modulation of the cavity voltage after 26 turns. However, this comes at the expense of larger power transient at the batch head and after its tail, in comparison to the previous case. The power evolution depends on the adjustment of the delay in the OTFB branch: there is an overshoot either during transients or in the steady-state (see Fig. 6). The optimum delay is about 1100 ns, which corresponds to about 20 % excess in power, in short peaks of a few µs.

Considering the case of $G_a = 0.85\ G_a^m$ and $\tau_{\mathrm{delay\ comp}} =$ 1100 ns, the peak power as a function of OTFB gain is shown in Fig. 7. For example, for $G_{\mathrm{OTFB}} \approx 5$ the power overshoot approximately corresponds to the one without OTFB and $G_a = G_a^m$. However, the use of the direct RF feedback alone will be less favorable for the beam stability as the compensation of the beam-induced voltage is reduced.

According to Ref. [13], for $V_{\mathrm{cav}} = 0.75$ MV (6 MV of total RF voltage) and $\tau_{4\sigma} = 1$ ns at injection energy, there is a stability margin of almost a factor of 3 for the case of the direct RF feedback alone and a factor of 40 with additional impedance reduction by OTFB. Still, further optimization requires benchmarking the model with injection transients observed during measurements performed in 2018 [14]. Moreover, particle tracking simulations including beam losses are required to optimize the system for future intensities.

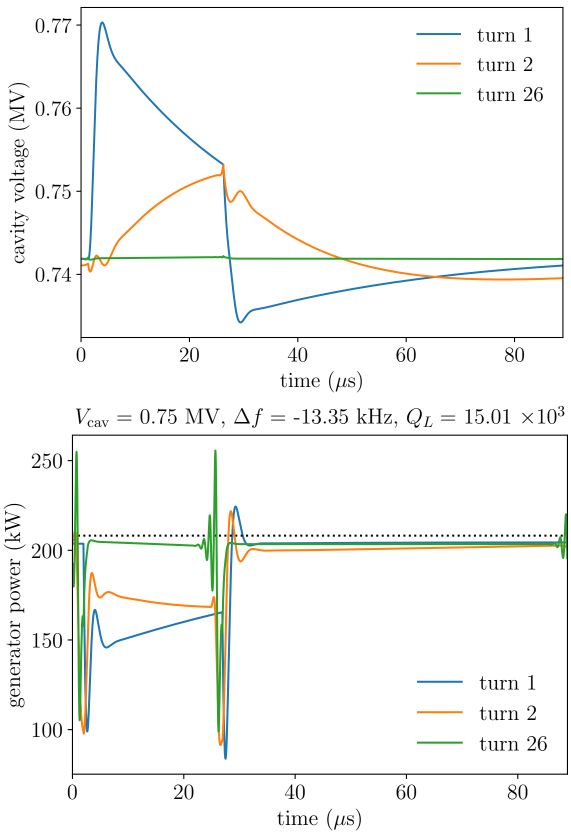


Figure 5: Cavity voltage amplitude (top) and RF power requirements (bottom) for selected turns after injection for HL-LHC parameters with both the direct RF feedback and OTFB on. The first bunch is at 1.3 µs and the last at 26.3 µs. Parameters: $\hat{I}_{b,\mathrm{RF}} = 2.22$ A, $G_a = G_a^m$, $G_d = 10\ G_a$, and $G_{\mathrm{OTFB}} = 10$, and $\tau_{\mathrm{delay\ comp}} = 1200$ ns. The dashed line is the expected RF power in the steady-state [see Eq. (12)].

## SUMMARY

The LHC LLRF model was implemented using Python. It was benchmarked against measurements in steady-state condition and the comparison with power transients measured during injection is ongoing. Both the direct RF feedback and OTFB cause a power overshoot during the injection process in calculations and measurements. While power transients can be reduced by adjusting the feedback gains and the delay in the OTFB branch, there are potential consequences on beam stability. A more detailed analysis of coupled-bunch instability and possibly full beam dynamics simulations are still required to draw conclusions about the RF power requirement during the injection of HL-LHC beams.

## ACKNOWLEDGEMENTS

We would like to thank Rama Calaga, Heiko Damerau, Wolfgang Höfle, John Molendijk, and Elena Shaposhnikova for useful comments and discussions.

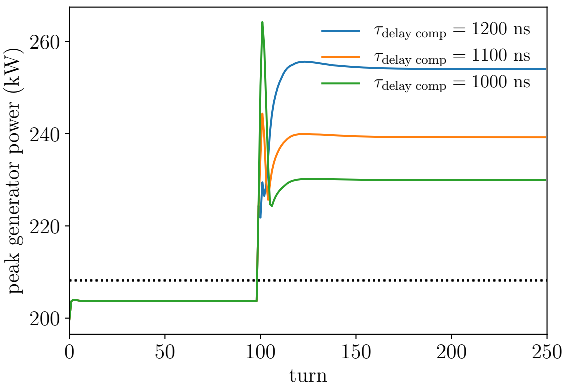


Figure 6: Evolution of the peak RF power for different delay compensations at injection. The first bunch is at 1.3 µs and the last at 26.3 µs. Parameters: $\hat{I}_{b,\text{RF}} = 2.22$ A, $G_a = G_a^m$, $G_d = 10\ G_a$, and $G_{\text{OTFB}} = 10$. Equations are solved without beam for the first 100 turns. The dashed line is the expected RF power in the steady-state [see Eq. (12)].

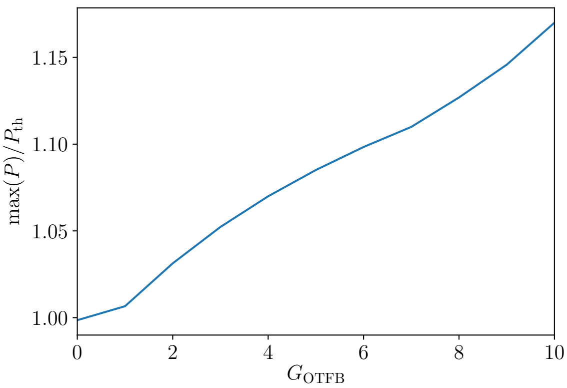


Figure 7: Normalized maximum needed RF power as a function of the OTFB gain for $G_a = 0.85\ G_a^m$ and $\tau_{\text{delay comp}} =$ 1100 ns.

## APPENDIX

The following coefficients of the FIR LPF [see Eq. (10)] are used in the LHC, $b_k$ = [-0.038636, -0.00687283, -0.00719296, -0.00733319, -0.00726159, -0.00694037, -0.00634775, -0.00548098, -0.00432789, -0.00288188, -0.0011339, 0.00090253, 0.00321323, 0.00577238, 0.00856464, 0.0115605, 0.0147307, 0.0180265, 0.0214057, 0.0248156, 0.0282116, 0.0315334, 0.0347311, 0.0377502, 0.0405575, 0.0431076, 0.0453585, 0.047243, 0.0487253, 0.049782, 0.0504816, 0.0507121, 0.0504816, 0.049782, 0.0487253, 0.047243, 0.0453585, 0.0431076, 0.0405575, 0.0377502, 0.0347311, 0.0315334, 0.0282116, 0.0248156, 0.0214057, 0.0180265, 0.0147307, 0.0115605, 0.00856464, 0.00577238, 0.00321323, 0.00090253, -0.0011339, -0.00288188, -0.00432789, -0.00548098, -0.00634775, -0.00694037, -0.00726159, -0.00733319, -0.00719296, -0.00687283, -0.038636].

## REFERENCES


[1] D. Boussard, "RF power requirements for a high intensity proton collider; parts 1 (chapters I, II, III) and 2 (chapters IV, V, VI)", CERN, Geneva, Switzerland, Rep. CERN-SL-91-16-RFS, May 1991.

[2] D. Boussard, "Control of cavities with high beam loading", IEEE Trans. Nucl. Sci., vol. 32, no. 5, pp. 1852–1856, 1985, `doi:10.1109/TNS.1985.4333745`.

[3] D. Boussard, G. Lambert, "Reduction of the apparent impedance of wide band accelerating cavities by RF feedback", IEEE Trans. Nucl. Sci., vol. 30, no. 4, pp. 2239-2241, 1983, `doi:10.1109/TNS.1983.4332774`.

[4] H. Timko, E. Shaposhnikova, K. Turaj, "Estimated LHC RF system performance reach at injection during Run III and beyond", CERN, Geneva, Switzerland, Rep. CERN-ACC-NOTE-2019-0005, Sep. 2018.

[5] O. Brüning *et al.*, "LHC design report vol.1: The LHC main ring", CERN, Geneva, Switzerland, Rep. CERN-2004-003, Jun. 2004.

[6] J. Tückmantel, "Cavity-beam-transmitter interaction formula collection with derivation", CERN, Geneva, Switzerland, Rep. CERN-ATS-Note-2011-002 TECH, Jan. 2011.

[7] P. F. Tavares, A. Andersson, A. Hansson, and J. Breunlin, "Equilibrium bunch density distribution with passive harmonic cavities in a storage ring", *Phys. Rev. ST Accel. Beams*, vol. 17, no. 6, p. 064401, Jun. 2014, `doi:10.1103/PhysRevSTAB.17.064401`.

[8] I. Karpov and P. Baudrenghien, "Transient beam loading and RF power evaluation for future circular colliders", *Phys. Rev. Accel. Beams*, vol. 22, no. 8, p. 081002, Aug. 2019, `doi:10.1103/PhysRevAccelBeams.22.081002`.

[9] J. Holma, "The model and simulations of the LHC 400 MHz cavity controller", CERN, Geneva, Switzerland, Rep. CERN-AB-2007-012, Feb. 2007.

[10] CERN beam longitudinal dynamics code BLonD, `http://blond.web.cern.ch`.

[11] P. Baudrenghien, "The tuning algorithm of the LHC 400 MHz superconducting cavities", CERN, Geneva, Switzerland, Rep. CERN-AB-2007-011, Feb. 2007.

[12] T. Mastoridis, P. Baudrenghien, and J. Molendijk, "Cavity voltage phase modulation to reduce the high-luminosity Large Hadron Collider RF power requirements", *Phys. Rev. Accel. Beams*, vol. 20, no. 10, p. 101003, Oct. 2017, `doi:10.1103/PhysRevAccelBeams.20.101003`.

[13] P. Baudrenghien and T. Mastoridis, "Fundamental cavity impedance and longitudinal coupled-bunch instabilities at the High Luminosity Large Hadron Collider", *Phys. Rev. Accel. Beams*, vol. 20, no. 1, p. 011004, Jan. 2017, `doi:10.1103/PhysRevAccelBeams.20.011004`.

[14] L. E. Medina Medrano *et al.*, "LHC MD 3165: RF power limitations at flat bottom", CERN, Geneva, Switzerland, Rep. CERN-ACC-NOTE-2019-0030, Jul. 2019.

# SYNCHRONOUS PHASE SHIFT MEASUREMENTS FOR EVALUATION OF THE LONGITUDINAL IMPEDANCE MODEL AT THE CERN SPS

M. Schwarz*, A. Farricker, I. Karpov, A. Lasheen
CERN, Geneva, Switzerland

*Abstract*

The High Luminosity LHC (HL-LHC) requires 2.3×10$^{11}$ protons per bunch (ppb) at LHC injection. For the SPS, the injector to the LHC, this goal requires a doubling of the injected intensity to 2.6×10$^{11}$ ppb. Longitudinal instabilities were observed in the SPS for intensities below the required 2.6×10$^{11}$ ppb. Identifying, and ultimately mitigating, the impedance sources driving the instabilities requires an accurate impedance model. Here, we report on measurements of the synchronous phase shift with intensity and corresponding energy loss at the SPS injection. Using the loss factor to compute the energy loss from the measured bunch spectrum and the SPS impedance model leads to significant disagreements with measurements. This issue is investigated for the simplified case of a single resonator. However, simulating matched bunches using the SPS impedance model yields better agreement with measurements.

## INTRODUCTION

The longitudinal impedance model of the SPS [1] is shown in Fig. 1 (blue curve). The dominant contribution at 200 MHz arises from the Travelling Wave Cavities (TWC) together with their Higher-Order Modes (HOM) at 630 MHz and 915 MHz. The peak at 800 MHz is due to the fourth-harmonic TWCs used as Landau cavities. Contributions above 1.2 GHz are caused mainly by the vacuum flanges and HOMs of the 800 MHz TWC. An extensive upgrade program is currently under implementation to reduce the machine impedance. It includes rearranging the sections of the main TWCs, damping of the 630 MHz HOM, and shielding of the vacuum flanges. The result (orange curve in Fig. 1) is a 20% reduction of the impedance at 200 MHz, 66% at 630 MHz, as well as a significant reduction in the impedance around 1.4 GHz.

One method to verify this complex impedance model, to identify missing impedance sources, or to see in future the result of upgrades, is to measure the synchronous phase shift of a bunch with intensity and to compare it to the model predictions [2–5]. Since any impedance source $Z$ leads to an energy loss $U$, the bunch adjusts its phase $\phi$ w.r.t. to the RF to recuperate this energy loss

$$\frac{U}{eV_{\mathrm{RF}}} = \sin\phi \simeq \phi\,(N,\sigma)\ , \tag{1}$$

where $e$ denotes the elementary charge and $V_{\mathrm{RF}}$ the RF amplitude. Since $\phi$ is small, we linearize the sin-function here and in the following. We have emphasized that the bunch

* now at KIT, markus.schwarz@kit.edu

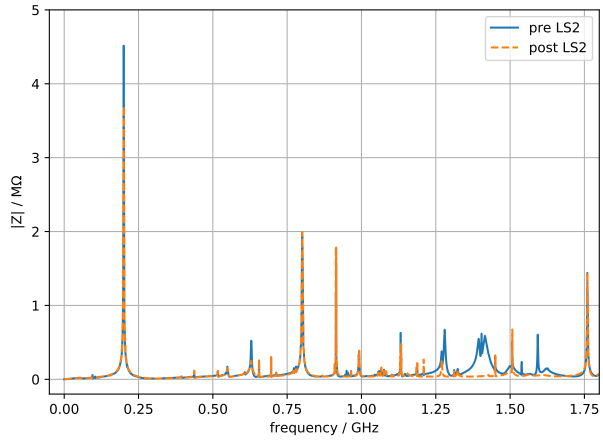


Figure 1: The longitudinal SPS impedance models before (blue) and after (orange) the impedance reduction campaign conducted during Long Shutdown 2 (LS2).

phase depends on the number of particles per bunch (ppb) $N$ and the bunch shape, represented by the bunch length $\sigma$. By measuring the bunch phase $\phi$, one can, thus, measure the lost energy $U$ and compare to the impedance model prediction.

There are two possible methods to find out how the energy lost due to an impedance changes the bunch position. In the following, we normalize the energy loss by the number of particles, and denote it by an overbar, e.g. $\bar{U} = U/N$. The first is the (normalized) average energy loss $\bar{U}_\kappa$ and is given by [6]

$$\bar{U}_\kappa = e^2 N \kappa\,, \tag{2}$$

with the loss factor $\kappa$ defined as

$$\kappa = 2\int_0^\infty \mathrm{Re}Z(f)\,|\Lambda(f)|^2\,\mathrm{d}f\,. \tag{3}$$

Here, $\Lambda(f)$ denotes the Fourier transform of the longitudinal line density $\lambda(\tau)$, normalized as $\int_{-\infty}^{\infty}\lambda(\tau)\mathrm{d}\tau = 1$. By using the wake function instead of the impedance $Z$, the energy loss $\bar{U}_\kappa$ can be rewritten in terms of the average induced voltage. Hence, it is related to the center-of-mass, or *mean* position of the bunch $\tau_{\mathrm{mean}} = \int_{-\infty}^{\infty}\tau\,\lambda(\tau)\mathrm{d}\tau$ as

$$\bar{U}_{\mathrm{mean}} = eV_{\mathrm{RF}}\,\omega_{\mathrm{RF}}\tau_{\mathrm{mean}}\,. \tag{4}$$

The second method is to compute the phase shift $\delta\phi_{\mathrm{s}} = \phi_s - \phi_{s0}$ of the synchronous particle, i.e. the particle synchronous with the RF wave, due to potential well distortion. In first order perturbation theory, it is given as [7]

$$\delta\phi_{\mathrm{s}} = \frac{2e\,N}{V_{\mathrm{RF}}\cos\phi_{s0}}\int_0^\infty \mathrm{Re}\left[Z(f)\Lambda_0(f)\right]\,\mathrm{d}f\,. \tag{5}$$

The index '0' refers to the unperturbed, zero-intensity quantities, e.g. the unperturbed synchronous phase $\phi_{s0}$. If the line density $\lambda(\tau)$ is symmetric, the spectrum $\Lambda(f)$ is real as well. This synchronous phase shift $\delta\phi_s$ indicates an energy loss of

$$\bar{U}_{\phi_s} = eV_{\mathrm{RF}}\,\delta\phi_s/N\,. \tag{6}$$

The position of the synchronous particle $\tau_s = \phi_s/\omega_{\mathrm{RF}}$ is not directly accessible to measurements. However, the synchronous particle, by definition, sits at the minimum of the potential well formed by the RF- and induced voltage. For a stable, i.e. time-independent, bunch, the minimum of the potential well coincides with the maximum or peak of the bunch profile. Hence, we can obtain the position of the synchronous particle by measuring the *peak* position $\tau_{\mathrm{peak}}$ of the stable bunch profile. For a given profile, we obtain $\tau_{\mathrm{peak}}$ by fitting a parabola to a window of ±0.5 ns around the profile maximum. The corresponding energy loss is then

$$\bar{U}_{\mathrm{peak}} = eV_{\mathrm{RF}}\,\omega_{\mathrm{RF}}\tau_{\mathrm{peak}}\,. \tag{7}$$

While we have access to the unperturbed spectrum $\Lambda_0$ in simulation, it is not measurable in practice, where we can only measure the bunch profile perturbed by the potential well distortion. We, thus, use the (measurable) perturbed spectrum $\Lambda(f)$ in Eq. (5) to obtain an approximate value for $\Delta\phi_s$ and the resulting energy loss $\bar{U}_{\phi_s,\mathrm{approx}}$.

Notice that both $\bar{U}_\kappa$ and $\bar{U}_{\phi_s}$ depend only on the real part of the impedance. Since both losses depend on the overlap of the impedance with the bunch spectrum, shorter bunches tend to have a higher energy loss, but in general the energy loss is non-monotonic. First, the bunch spectrum is non-monotonic since the proton bunches do not have a Gaussian shape. Second, the machine impedance is highly non-monotonic, see Fig. 1.

## NARROW-BAND RESONATOR MODEL

To illustrate the above discussion, we first did a particle tracking simulation of a single bunch with the longitudinal tracking code BLonD [8]. Instead of the complex SPS impedance model, we only take a single resonator into account. The shunt impedance of 4.5 MΩ and quality factor $Q = 140$ give a rough estimate for the impedance of the 200 MHz TWC [3], while we vary the resonant frequency $f_r$. We fix the bunch intensity at $1 \times 10^{11}$ ppb, which is slightly below the present nominal LHC intensity. The initial bunch distribution including four million macro-particles is generated from a binomial profile

$$\lambda_0(\tau) = A\left[1-\left(\frac{2(\tau-\tau_{\max})}{\tau_L}\right)^2\right]^{\mu+1/2}, \tag{8}$$

and is matched to the RF bucket with intensity effects. We used $\mu = 2.4$ and the bunch length $4\sigma_{FWHM} \simeq 0.78\tau_L = 2.5$ ns. To take into account that the matching is not perfect, we let the bunch filament a little by tracking for 15 synchrotron periods (1000 turns) before 'measuring' the bunch profiles during another 15 synchrotron periods. We compute the average bunch profile, and do the same data analysis as with the measured profiles.

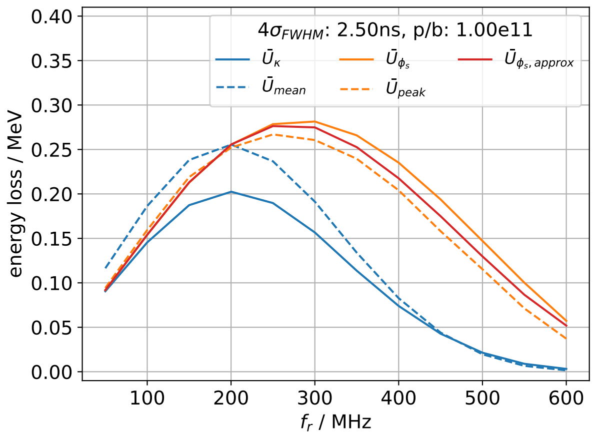


Figure 2: Simulated energy loss using a single resonator. Energy losses obtained from a bunch position are plotted as dashed lines, while those derived from the impedance model are plotted as solid lines.

Figure 2 shows the resulting simulated and calculated energy losses for different resonant frequencies. All losses decrease for higher resonant frequencies, as the overlap between bunch spectrum and impedance decreases. Since we have access to the unperturbed bunch spectrum $\Lambda_0$ in simulations, we can use equations (5) and (6) directly to compute the energy loss $\bar{U}_{\phi_s}$ causing the synchronous phase shift (orange curve). From the 'measured' peak position $\tau_{\mathrm{peak}}$, we obtain the corresponding energy loss $\bar{U}_{\mathrm{peak}}$ using Eq. (7) (orange dashed curve). The two curves are in agreement also with the approximate result (red curve), calculated from the 'measured' perturbed bunch spectrum $\Lambda$.

The blue curve shows the model prediction for the average energy loss of the bunch according to Eq. (2). This is compared to the energy loss obtained from the 'measured' mean bunch position $\tau_{\mathrm{mean}}$ using Eq. (4) (blue dashed curve). We observe good agreement for resonant frequencies above 400 MHz, but significant deviations when the resonant frequency $f_r$ is close to the RF frequency of ~200 MHz. At this frequency, the 'measured' $\bar{U}_{\mathrm{mean}}$ agrees with the energy loss from the synchronous phase shift.

For $f_r = f_{\mathrm{RF}}$, the results can be analyzed and explained by treating the narrow-band impedance as a $\delta$-function centered at $f_{\mathrm{RF}}$. In this case, the induced voltage just leads to an amplitude and phase shift of the RF voltage, rather than an asymmetric potential well distortion. Therefore, the total voltage seen by the beam is still symmetric around the synchronous particle. The matched, perturbed, bunch profile $\lambda$ equals the unperturbed profile $\lambda_0$, but shifted by an amount given by Eq. (5). Since the profile $\lambda$ is symmetric, the peak $\tau_{\mathrm{peak}}$ and mean $\tau_{\mathrm{mean}}$ positions coincide, which explains why $\bar{U}_{\mathrm{peak}}$ equals $\bar{U}_{\mathrm{mean}}$. Moreover, $\bar{U}_\kappa = \Lambda_0(f_{\mathrm{RF}})\bar{U}_{\phi_s}$ in this case. Using the analytic expression for the spectrum with the bunch parameters given above yields $\Lambda_0(f_{\mathrm{RF}}) \simeq 0.8$, which is in quantitative agreement with Fig. 2. For other resonance frequencies, the potential well becomes asymmetric, which leads to an asymmetric bunch profile. Now, the synchronous particle is no longer at the bunch center, and $\bar{U}_{\mathrm{peak}}$ disagrees with $\bar{U}_{\mathrm{mean}}$.

## MEASUREMENTS

Measuring the phase between the bunch and the RF wave is difficult in practice. Instead, we employed a reference and a witness bunch [2]. The reference bunch had a fixed small intensity. The witness bunch followed at a sufficiently large distance so as not to be affected by the wake field of the reference bunch (1.5 µs in our case). We then recorded the bunch profiles, starting 500 ms after injection to give the bunches time to filament and reach a stable state. To measure the bunch intensity, we calibrated the integrated profile against the intensity of the DC Beam Current Transformer, see [9] for details. The relative phase between the bunches is determined from their bunch positions as

$$\Delta\phi = \omega_{\mathrm{RF}} \left[ (t_w - t_r) \,\%\, T_{\mathrm{RF}} \right] \,, \tag{9}$$

where % is the modulo operation and $t_{r,w}$ denote the position of the *r*eference and *w*itness bunch, respectively. We then scanned the bunch intensity and length, while keeping the shape of reference and witness bunch the same. In practice, we considered two bunch shapes the same, if their bunch lengths do not differ by more than 5%. For a fixed bunch length, the absolute phase distance scales linearly with intensity, i.e.

$$\phi(N, \sigma = const) \simeq N \Delta\phi(\sigma)/\Delta N \,. \tag{10}$$

Finally, the normalized energy loss $\bar{U}(\sigma)$ is given by

$$\bar{U}(\sigma) \simeq eV_{\mathrm{RF}} \, \Delta\phi(\sigma)/\Delta N \,. \tag{11}$$

We used three methods to compute the bunch position from the measured bunch profile. As discussed above, two of them are the mean $\tau_{\mathrm{mean}}$ and peak $\tau_{\mathrm{peak}}$ positions. By fitting the profile to the line density in Eq. (8) we obtained the position of the maximum of the fitted profile $\tau_{\mathrm{fit}}$.

Figure 3 shows the measured phase difference obtained by using $\tau_{\mathrm{fit}}$ in Eq. (9). It shows the expected qualitative behavior, i.e. an increasing phase shift for either increasing intensity at fixed bunch length, or decreasing bunch length at fixed intensity. To obtain the slope $\Delta\phi(\sigma)/\Delta N$, we binned the data according to bunch length (using a window of ±0.2 ns) and performed a linear fit. An example is shown in Fig. 4, together with the linear fit. The error in the fitted slope then directly transfers into the error of the energy loss $\bar{U}$. The corresponding value for the bunch length is the mean bunch length of all data points within that window, and their RMS gives the bunch length error. Notice that we do not consider an error in neither the bunch intensity, nor the RF voltage $V_{\mathrm{RF}}$.

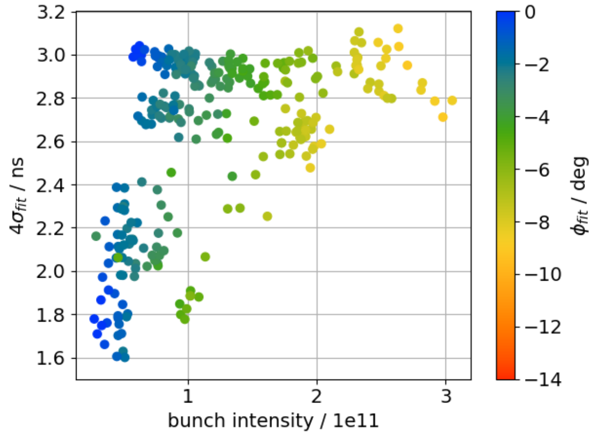


Figure 3: Measured phase shift for different bunch lengths and intensities. The bunch position and length $4\sigma_{\mathrm{fit}}$ were obtained by fitting a binomial to the measured profile.

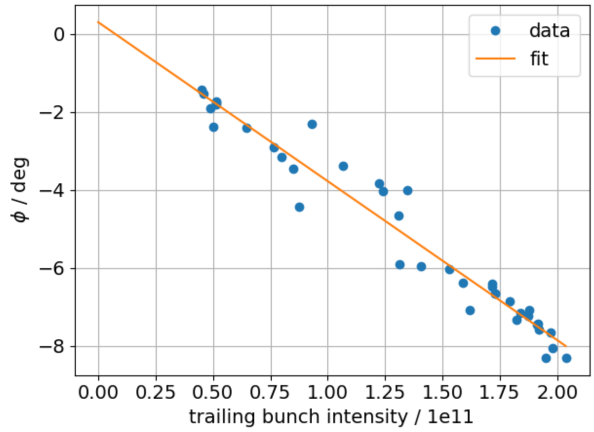


Figure 4: Data points of Fig. 3 in the interval $4\sigma_{\mathrm{fit}} = 2.44\,\mathrm{ns} \pm 0.2\,\mathrm{ns}$ together with the linear fit.

## RESULTS

First, we use the peak position $\tau_{\mathrm{peak}}$ in Eq. (9), and proceed as described in the previous section. The results for $\bar{U}_{\mathrm{peak}}$ are shown as the orange points in Fig. 5[1]. An energy loss in the order of $10\,\mathrm{keV}/10^{10}$ ppb was reported in [3], roughly agreeing with our $\bar{U}_{\mathrm{peak}}$. From the discussion of the narrow-band resonator model, $\bar{U}_{\phi_s,\mathrm{approx}}$ is the most relevant quantity to compare to and is shown as the red data points. We compute $\bar{U}_{\phi_s,\mathrm{approx}}$ for the measured bunch spectra $\Lambda$ and the full longitudinal SPS impedance model in Fig. 1.

Surprisingly, we see a large discrepancy between the two. At face value, this would mean that the model significantly overestimates an impedance source. Since $\bar{U}_{\phi_s,\mathrm{approx}}$ exceeds $\bar{U}_{\mathrm{peak}}$ for all bunch lengths, it would suggest an overestimation in the low-frequency regime of the model. However, this impedance model was used many times in BLonD sim-

[1] Here, and in the following figures, the data points are joined to guide the eye.

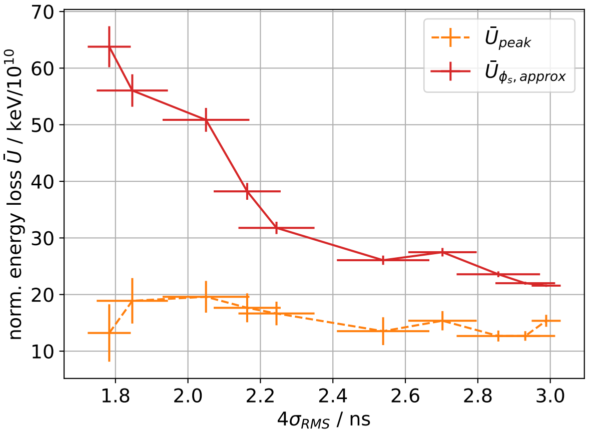


Figure 5: Comparison between the measured $\bar{U}_{\text{peak}}$ (orange, dashed) and the impedance model prediction $\bar{U}_{\phi_s,\text{approx}}$ (red, solid).

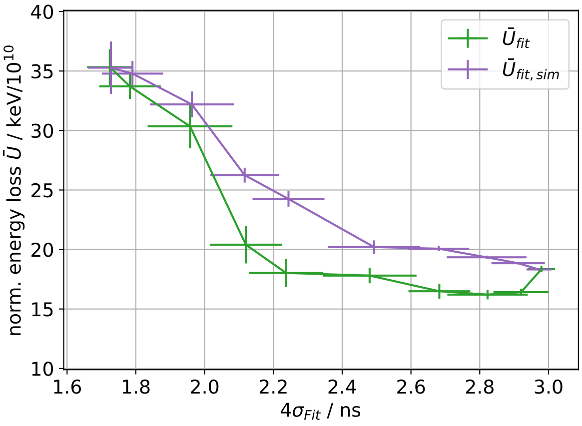


Figure 7: Energy loss obtained by fitting the measured profiles $\bar{U}_{\text{fit}}$ (green) and the energy loss $\bar{U}_{\text{fit,sim}}$ obtained by simulating bunches created from these fit parameters (purple).

ulations that successfully reproduced measured intensity effects in the SPS. This makes a large error in the impedance model unlikely, but, so far, we have not been able to find an error in the computation of $\bar{U}_{\phi_s,\text{approx}}$.

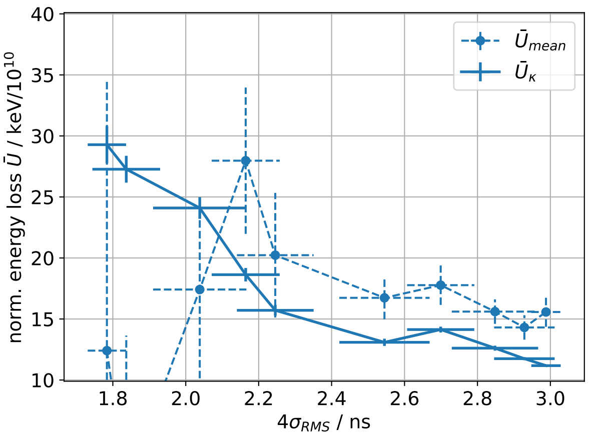


Figure 6: Comparison between the measured $\bar{U}_{\text{mean}}$ (blue, dashed) and the impedance model prediction $\bar{U}_{\kappa}$ (blue, solid).

As a second method, we compare $\bar{U}_{\text{mean}}$ obtained from $\tau_{\text{mean}}$ and compare to average energy loss $\bar{U}_{\kappa}$, see Fig. 6. For bunch lengths longer than 2.2 ns, the measured energy loss is above the impedance model prediction, but both have the same shape. Reminding the fact that the SPS impedance is dominated by the fundamental cavities, we are in a similar situation as discussed for the narrow-band resonator model. The simulation of the 'measured' energy loss was systematically above the model prediction. This is reaffirmed by the fact that longer bunches mainly sample the impedance of the 200 MHz TWCs and are less affected by the higher-frequency impedances. For smaller bunch length, the deviation increases, but the error bars increase significantly as well.

Finally, we fit the binomial line density in Eq. (8) to the measured profiles for the reference and witness bunch, thus obtaining $\tau_{\text{fit}}$. The resulting $\bar{U}_{\text{fit}}$ is shown in Fig. 7 as the green data. To compare with the impedance model, we create matched distributions from these fit parameters and track them in BLonD, including the intensity effects due to the full SPS impedance model. The reference and witness bunches are tracked independently, thus ignoring any interaction between them. We also do not include the phase loop in simulations, which was active during the measurements. This is justified by the fact that the phase loop (before the upgrade during LS2) can only act on the reference bunch, and that we only consider the stable situation 500 ms after injection. As in the simulations for the narrow-band model, we track an initial 1000 turns to reach a stable situation, and then save the bunch profiles averaged over another 1000 turns. We again do a binomial fit to find $\tau_{\text{fit,sim}}$, and display the corresponding energy loss $\bar{U}_{\text{fit,sim}}$ as the purple data points in Fig. 7. Again, the simulated energy loss is above the measured one, but both agree for long and short bunches.

## CONCLUSION

The narrow-band resonator model suggests to compare $\bar{U}_{\text{mean}}$ with $\bar{U}_{\kappa}$ and $\bar{U}_{\text{peak}}$ with $\bar{U}_{\phi_s,\text{approx}}$. However, these comparisons work less well for measured energy losses and their counterparts from the SPS impedance model (see Figs. 5 and 6). There are still a couple of error sources which were not considered. First, the data points used for the linear fits did not include errors on the bunch intensity, and the error in the RF voltage is not considered. Likely more important is the error on the bunch positions, as often the difference between $\tau_{\text{mean}}$ and $\tau_{\text{peak}}$ is only a few pico-seconds, compared to the bunch length of a few nano-seconds. Moreover, we found that the parabolic fit to find $\tau_{\text{peak}}$ fits the data very well, but the error on $\tau_{\text{peak}}$ depends on the absolute displacement of the bunch. This can give errors on the peak position well above 10 ns for a bunch that is only 2 ns long! The reason for this dependence is yet to be understood. At least, using 'brute force' simulations, based on the fit parameters of the measured bunch profiles, yield a reasonable agreement.

Other methods exist to compare a machine impedance model to a real one. For example, the quadrupole frequency shift with intensity was used to gain information on the reactive part of the SPS impedance model [10]. Another method is to inject long bunches with a small energy spread without an RF voltage. Before debunching, different impedance sources can drive instabilities that leave a 'finger print' on the bunch profile [11, 12]. In this case, one can also use the drift of the bunch center due to the energy loss as a measure of the mean energy loss $\bar{U}_\kappa$.

To validate the impedance model after LS2, injections of long bunches and measurements of both the synchronous phase and quadrupole frequency shifts are planned. The former method is sensitive to the impedance reduction at 1.4 GHz (due to the shielding of vacuum flanges), while measurements of the synchronous phase and quadrupole frequency shifts probe the low-frequency part of the machine impedance. The latter measurement can also readily extended and used as a measurement of the synchronous phase. It will be aided by the availability of automatic over-night parameter scans, yielding more data points with identical machine parameters. This would also help with quantifying the systematic errors arising from the imprecise knowledge of the beam intensity and RF voltage.

## ACKNOWLEDGMENTS

We acknowledge fruitful discussions with our colleagues S. Albright, T. Bohl, G. Papotti, and E. Shaposhnikova, as well as the LIU SPS Beam Dynamics working group and the BLonD Development Team. The help of the PS and SPS operators during measurements is appreciated.

## REFERENCES

[1] J. E. Campelo *et al.*, "An Extended SPS Longitudinal Impedance Model," in *Proc. IPAC'15*, Richmond, Virginia, USA, May 2015, pp. 360–362. doi:10.18429/JACoW-IPAC2015-MOPJE035

[2] N. S. Sereno, Y.-C. Chae, K. C. Harkay, A. H. Lumpkin, S. V. Milton, and B. X. Yang, "A Potpourri of Impedance Measurements at the Advanced Photon Source Storage Ring," in *Proc PAC'97*, Vancouver, Canada, May 1997, pp. 1700–1702. http://accelconf.web.cern.ch/accelconf/pac97/papers/pdf/7V026.PDF

[3] E. Shaposhnikova, T. Bohl, A. Hofmann, T. P. R. Linnecar, and J. Tückmantel, "Energy Loss of a Single Bunch in the CERN SPS," in *Proc. EPAC 2004*, Lucerne, Switzerland, 2004, pp. 1909–1911. https://accelconf.web.cern.ch/e04/PAPERS/WEPLT036.PDF

[4] J. F. Esteban Müller *et al.*, "Measruements of the LHC Longitudinal Resistive Impedance with Beam," in *Proc HB'12*, Beijing, China, May 2012, pp. 183–186. http://accelconf.web.cern.ch/AccelConf/HB2012/papers/mop252.pdf

[5] P. Schönfeldt *et al.*, "Study of the Influence of the CSR Impedance on the Synchronous Phase Shift at KARA," in *Proc IPAC'18*, Vancouver, Canada, May 2018, pp. 2223–2226. DOI: doi:10.18429/JACoW-IPAC2018-WEPAL028.

[6] B. W. Zotter and S. Kheifets, *Impedances and Wakes in High Energy Particle Accelerators*. WORLD SCIENTIFIC, 1998. DOI: 10.1142/3068.

[7] K. Y. Ng, *Physics of Intensity Dependent Beam Instabilities*. WORLD SCIENTIFIC, 2005. DOI: 10.1142/5835.

[8] *CERN Beam Longitudinal Dynamics code BLonD*. https://blond.web.cern.ch/

[9] M. Schwarz, H. Bartosik, A. Lasheen, J. Repond, E. Shaposhnikova, and H. Timko, "Studies of Capture and Flat-Bottom Losses in the SPS," in *Proc. HB'18*, Daejeon, Korea, Jun. 2018, pp. 180–185. doi:10.18429/JACoW-HB2018-TUP2WA03

[10] A. Lasheen and E. Shaposhnikova, "Evaluation of the CERN Super Proton Synchrotron longitudinal impedance from measurements of the quadrupole frequency shift," *Phys. Rev. Accel. Beams*, vol. 20, p. 064 401, 6 Jun. 2017. DOI: 10.1103/PhysRevAccelBeams.20.064401.

[11] T. Bohl, T. P. R. Linnecar, and E. Shaposhnikova, "Measuring the resonance structure of accelerator impedance with single bunches," *Phys. Rev. Lett.*, vol. 78, pp. 3109–3112, 16 Apr. 1997. DOI: 10.1103/PhysRevLett.78.3109.

[12] A. Lasheen, T. Argyropoulos, T. Bohl, J. F. Esteban Müller, H. Timko, and E. Shaposhnikova, "Beam measurement of the high frequency impedance sources with long bunches in the CERN Super Proton Synchrotron," *Phys. Rev. Accel. Beams*, vol. 21, p. 034 401, 3 Mar. 2018. DOI: 10.1103/PhysRevAccelBeams.21.034401.

# IDENTIFICATION OF IMPEDANCE SOURCES RESPONSIBLE FOR LONGITUDINAL BEAM INSTABILITIES IN THE CERN PS

A. Lasheen*, H. Damerau, G. Favia, P. Kozlowski, B. Popovic,
CERN, Geneva, Switzerland

*Abstract*

Longitudinal instabilities in the CERN PS are an important limitation to obtain the expected beam intensity and longitudinal emittance at the PS extraction in the framework of the LHC Injector Upgrade (LIU) project. The observed coupled-bunch instabilities lead to dipolar and quadrupolar oscillations, as well as to an uncontrolled longitudinal emittance blow-up for proton beams. A microwave instability observed with ion beams develops quickly at transition crossing. To identify the potential impedance sources of these instabilities, two strategies were adopted. Firstly, beam measurements were performed for different impedance configurations, i.e. by partially detuning the main RF cavities. Secondly, a thorough survey of the machine elements together with the RF studies allowed to refine the PS impedance model in order to find potentially missing contributions. Measurements were compared with particle simulations using the updated impedance model of the PS. Although the source of the dipolar coupled-bunch instability was already identified in the past, this study led to an identification of the impedance sources driving other types of longitudinal instabilities.

## INTRODUCTION

An important objective of the High Luminosity-LHC (HL-LHC) project at CERN is to double the beam (and bunch) intensity [1]. This target intensity is challenging for the injectors, which are being upgraded in the framework of the LHC Injector Upgrade (LIU) project [2]. The Proton Synchrotron (PS) is the second synchrotron in the injector chain and it accelerates the proton beam up to $p = 26$ GeV/c before extraction to the Super Proton Synchrotron (SPS). The present nominal intensity of LHC-type beams extracted from the PS is $N_p = 1.3 \times 10^{11}$ protons per bunch (p/b), and the LIU target is $N_p = 2.6 \times 10^{11}$ p/b with the same longitudinal emittance. Main limitations in the PS to reach these parameters are longitudinal beam instabilities.

Before the LIU upgrades, the dipolar coupled-bunch instability was the most critical instability in the PS, with a threshold close to the nominal LHC-beam intensity. Using analytical studies and particles simulations [3], its impedance source was identified to be the fundamental impedance of the main RF system (10 MHz ferrite-loaded cavities). In the framework of the LIU project, a dipolar coupled-bunch feedback was developed and successfully implemented as mitigation measure, allowing to raise the beam intensity up to $N_p = 2.3{\times}10^{11}$ p/b. Although close to the target intensity, the goal was not yet reached due to other intensity effects.

The quadrupolar coupled-bunch instability, which is not damped by the dipolar coupled-bunch feedback, limits the beam from reaching the parameters required for the LIU project. This instability was mitigated before, even without understanding the driving impedance source, by using one of the 40 MHz cavity as a Landau RF system [4]. This provided the stability margin allowing to achieve beam parameters beyond the LIU target. Although the required longitudinal beam parameters were reached in the PS, the impedance source driving the quadrupolar coupled-bunch instability was yet to be identified. In this paper, we start from an overview of the present PS impedance model including the latest identified sources. Next, we describe the limitations other than coupled-bunch instabilities for which the driving impedance sources were already identified. Finally, the main focus of this paper is to describe the methods used to identify the impedance source responsible for the quadrupolar coupled-bunch instability.

## PS BEAM-COUPLING IMPEDANCE MODEL

The present PS impedance model, shown in Fig. 1, was developed over the course of several years. The model is based on electromagnetic simulations, as well as beam measurements of the impedance [5] and includes [6]

- RF systems (with frequencies 2.8-10, 20, 40, 80, 200 MHz, and a broadband Finemet system);
- kicker magnets (injection/extraction, 6 elements);
- vacuum equipment (pumping manifolds, bellows, sector valves);
- longitudinal space charge and beam pipe resistive wall impedance;
- single elements, such as internal beam dumps, beam pick-ups.

Although not all different versions of the equipment are included (e.g. all possible variations of the pumping manifolds), the most relevant elements are present in the model. The principal impedance sources driving the instabilities are therefore expected to be in the list of elements.

The impedance sources have different effects depending on their wavelength-to-bunch length ratio given by the parameter $f_r \tau$ where $f_r$ is the resonant frequency of the impedance and $\tau$ the bunch length. The contributions at low frequencies, $f_r \tau \sim 1$ ($\lesssim$ 40 MHz in Fig. 1), are expected to drive dipole and quadrupole coupled-bunch instabilities, while high frequency sources, $f_r \tau \gg 1$ ($\gg$ 40 MHz), are

* alexandre.lasheen@cern.ch

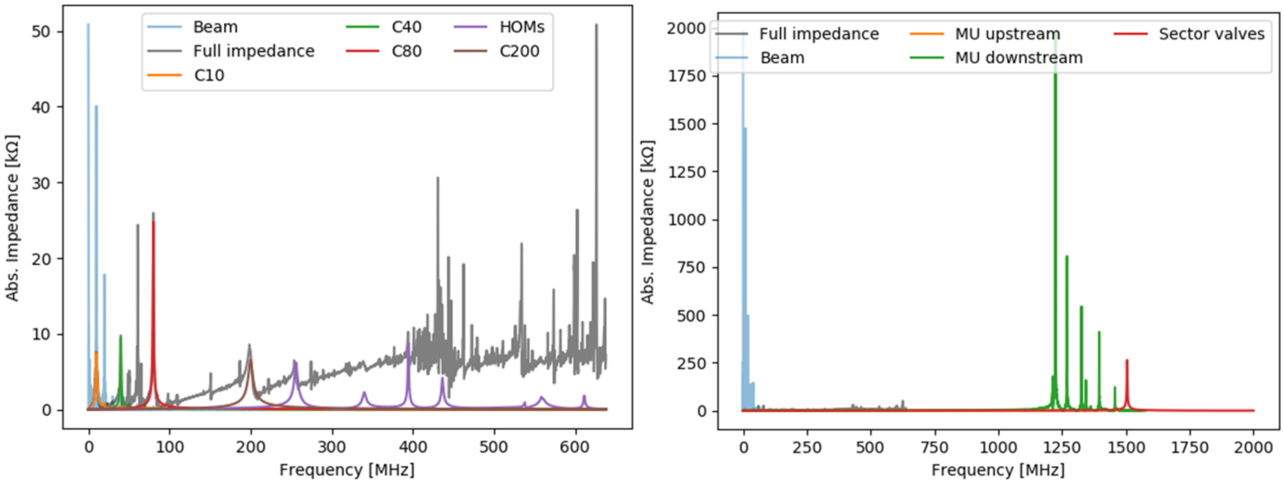


Figure 1: Absolute value of impedance versus frequency for the present PS impedance model. The cavity impedances are labeled with a 'C' followed by their resonant frequency. The equipment around the main magnet units (MU) consists of bellows upstream and pumping manifolds downstream. These also house pick-ups of the trajectory measurement system. The kicker magnets are not labeled but contribute to the broadband impedance. The beam spectrum is displayed in blue (in arbitrary units) to illustrate which contributions are considered to be low frequency, $f_r\tau \sim 1$, and high frequency, $f_r\tau \gg 1$.

expected to drive microwave instability leading to uncontrolled emittance blow-up. The broadband impedances can also lead to loss of Landau damping.

## IDENTIFIED LIMITATIONS

One of the limiting intensity effects in the PS was an uncontrolled emittance blow-up arising during the acceleration ramp and the beam splittings at top energy. The source of the instability was rapidly identified as the high frequency RF system (80 MHz cavities). Three of these cavities are installed in the ring, but only two are required for proton operation (non-adiabatic bunch shortening before extraction to the SPS). When not in use, the cavity impedance is shielded from the beam by closing the gap with a pneumatic short-circuit. The contribution to the uncontrolled emittance blow-up of these cavities was brought to light by comparing the longitudinal beam quality with the 80 MHz cavity gaps opened and closed. Another applied technique consisted in measuring the beam spectrum during the slow debunching with RF off [7]. An example of measured beam profile and spectrum is shown in Fig. 2. The uncontrolled emittance blow-up was removed using a multi-harmonic RF feedback to reduce the impedance of the high frequency cavities, as demonstrated in [8], allowing to reach the LIU beam intensity at the nominal longitudinal emittance.

Another potential source of uncontrolled emittance blow-up is the microwave instability cause by the very high frequency impedance sources. Presently it has no critical impact on proton beam operation. However, for the ion beam, the microwave instability occurs right after transition crossing, as illustrated in Fig. 3. The frequency analysis of the bunch profile allowed to have an indication of the frequency of the driving impedance source [9]. However, short bunches are not ideal for these measurements and

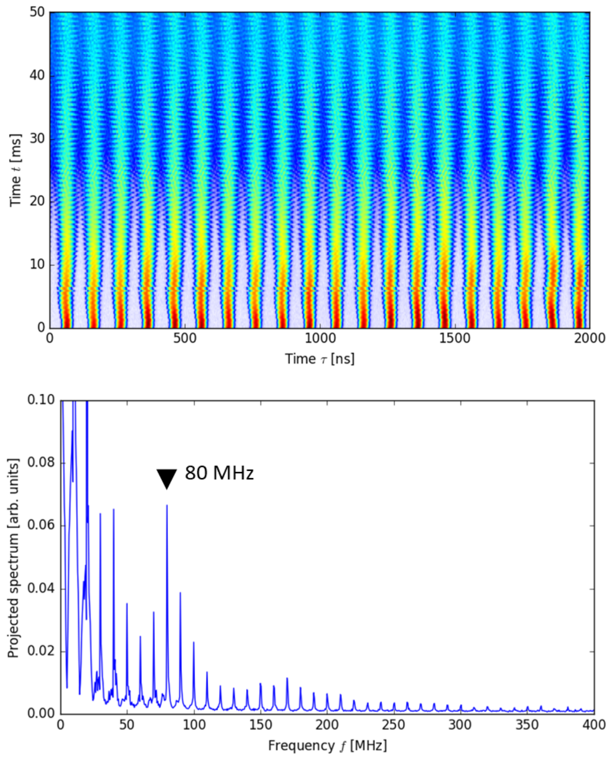


Figure 2: Measurement of beam modulation by the 80 MHz cavities impedance during adiabatic reduction of the RF voltage. The profiles (top) are shown with the corresponding projected spectrum (bottom, maximum spectral amplitude).

only provide poorly resolved information about the resonant frequency of the impedance, in the frequency range above 1 GHz. Empty pumping manifolds are the suspected main impedance source at high frequency and were already considered in 1975 [10], when damping resistors were installed. Although not critical for proton beam operation, these sources of impedance need to be carefully monitored as they might be responsible for the generation of tails in the longitudinal distribution. This could lead to losses during PS-SPS transfer [11], as well as to high frequency structures on the extracted bunch profile.

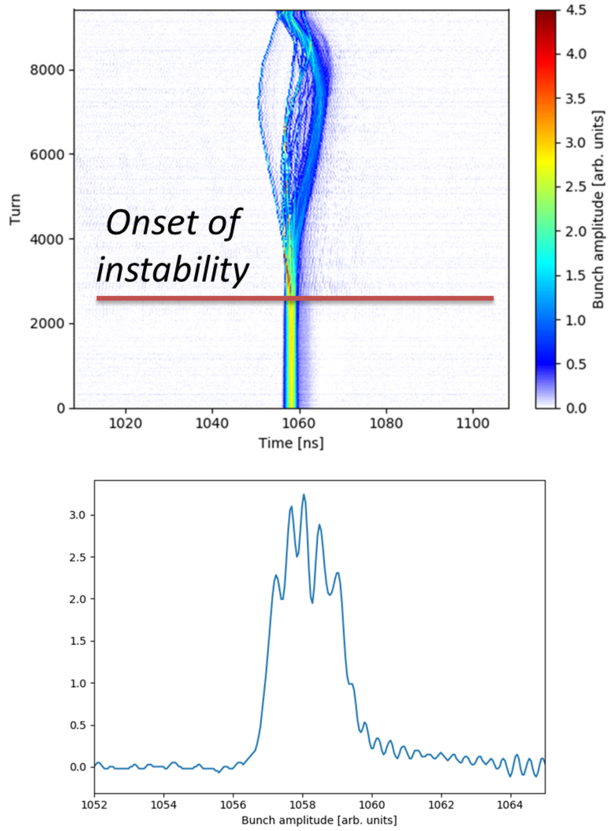


Figure 3: Microwave instability at transition crossing with ion beam ($^{208}Pb^{54+}$). The evolution of the bunch profile (top) is shown together with the one right after the onset of the instability (bottom), where the profile is modulated by beam induced voltage due to high frequency impedance sources (> 1 GHz).

## MEASUREMENTS AND ANALYSIS OF THE QUADRUPOLAR COUPLED-BUNCH INSTABILITY

The beam in the PS is accelerated using ferrite-loaded cavities, tuneable from 2.8 MHz to 10 MHz. During the acceleration ramp, the cavities are tuned at $h = 21$ (about 10 MHz) and follow the RF voltage program shown in Fig. 4. For the nominal beam, $n_b = 18$ bunches are accelerated. On the arrival to the flat top, the RF voltage is adiabatically reduced to $V_{\mathrm{RF}} = 20$ kV and the bunches are split four times before being compressed and extracted to the SPS. The RF voltage during the ramp is distributed over 10 cavities, each of them being composed of 2 gaps. One extra cavity is installed in the ring as a spare. The cavities are distributed in 3 groups (A,B,C) sharing the same bias tuning current and 4 voltage program groups (1,2,3,4, different shades of purple in Fig. 4). Each RF gap of the cavities is equipped with a relay to short-circuit the gap and to minimize the beam-coupling impedance, when not in use, independently for each voltage program group. Unused cavities can also be 'parked' by tuning them to a low, non-integer harmonic number (e.g. $h = 6.5$). This slightly reduces the impedance with closed gap relays, independently for each tuning group.

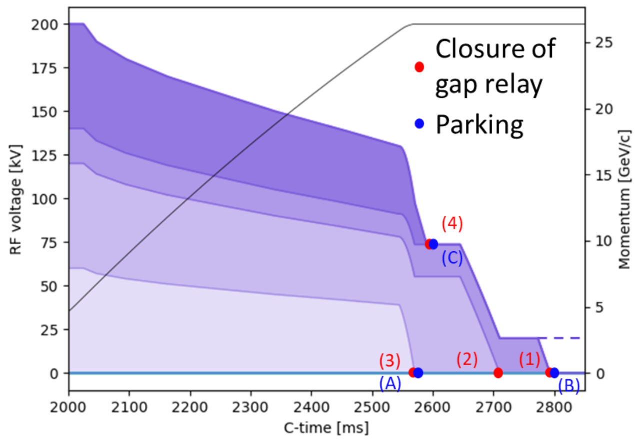


Figure 4: Momentum (black) and RF voltage (purple) programs as a function of time during the acceleration ramp, starting at transition crossing. During coupled-bunch instability studies, the beam splitting process at the flat-top is disabled and the RF voltage is kept at $V_{\mathrm{RF}} = 20$ kV till the end of the cycle (dashed line).

The coupled-bunch instabilities (dipolar and quadrupolar), usually occuring at top energy, can also be observed during the ramp for high intensities or smaller longitudinal emittances. An example of such instability is shown in Fig. 5. In this particular example, a full ring with $n_b = 21$ bunches in $h = 21$ was accelerated for easier mode analysis. Each bunch oscillates with an amplitude $A_b$, at the frequency $m\omega_s$ (where $f_s = \omega_s/(2\pi)$ is the synchrotron frequency) and a phase $\phi_b$. The coupling between the bunches can be analyzed using the expression

$$A_\mu \sin\left(m\omega_s t + \phi_\mu\right) = \frac{1}{n_b}\sum_{b=0}^{n_b-1} A_b \sin\left(m\omega_s t + \phi_b - \frac{2\pi b\mu}{n_b}\right), \qquad (1)$$

where $b$ is the bunch index, $\mu$ is the mode number, $A_\mu$ is the mode amplitude and $\phi_\mu$ the mode phase. The Eq. (1) corresponds to the spectral analysis of the bunch oscillations based on a discrete Fourier transform, assuming that all bunches oscillate with the same synchrotron frequency. In practice, the bunch position oscillations are analyzed to get the dipolar mode spectrum $m = 1$ and bunch length oscillations for quadrupolar mode spectrum $m = 2$.

Results from measurements performed with $n_b = 18$ bunches at the LIU intensity of $N_p = 2.6 \times 10^{11}$ p/b

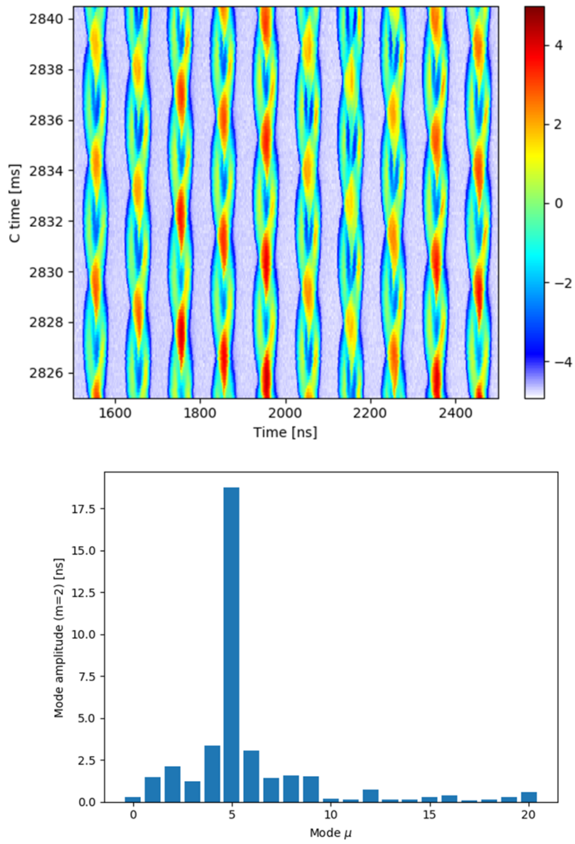


Figure 5: Example of measured bunch profiles undergoing quadrupolar coupled-bunch oscillations (top, color scale in arbitrary units) with the corresponding mode spectrum of the bunch length oscillations using Eq. (1). The dominant mode is $\mu_{n_b=21} = 5$ (i.e. every 5th bunch oscillates in phase).

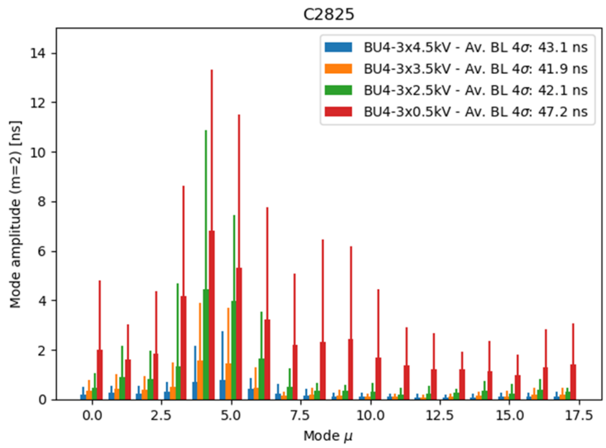


Figure 6: Mode spectrum of quadrupolar oscillations for various longitudinal emittances. The emittance is set by the controlled emittance blow-up (BU) during the ramp. The error bars correspond to the maximum amplitude spread measured over 10 cycles. The average bunch length is given at extraction, and it is larger for the smallest blow-up setting (red) due to the beam instability.

at extraction are shown in Fig. 6. In this set of measurements, the longitudinal emittance was scanned by varying the amplitude of the controlled emittance blow-up (phase modulation of a very high harmonic RF system at 200 MHz, 6 cavities). The nominal blow-up setting 3x4.5 kV yields a longitudinal emittance at extraction of $\varepsilon_l = 0.35$ eVs. Reducing the blow-up setting down to 3x0.5 kV decreases the longitudinal emittance by about 20%. The amplitude of the oscillations stays reasonably small for the nominal longitudinal emittance, but rapidly increases when reducing the emittance by a few percents.

Systematic measurements of coupled-bunch instabilities during the Run 2 (2013-2018) were conducted and lead to reproducible results. One of the remarkable results is that the dominant oscillation modes $\mu$ always remained identical with $n_b = 18$: $\mu_{n_b=18} = [1, 2]$ during the acceleration ramp and $\mu_{n_b=18} = [4, 5]$ at top energy, both for dipolar $m = 1$ and quadrupolar $m = 2$ instabilities. This information is essential to identify the impedance source driving the instability.

## IDENTIFICATION AND EXPERIMENTAL CONFIRMATION OF THE IMPEDANCE SOURCE

First estimates of the characteristics of the impedance responsible for quadrupolar coupled-bunch instabilities were done analytically.

### *Unstable Synchrotron Frequency Side-bands*

To drive the instability in the case of a ring filled with equidistant bunches, an impedance source must cover a synchrotron frequency side-band of the beam spectrum given by

$$f_{n,\mu} = (nh + \mu)\, f_0 + m f_s, \tag{2}$$

where $n \in \mathbb{N}$ is the revolution mode number. In the case of the PS, where bunches are partially filling the ring, the expression can be approximated by

$$f_{n,\mu} = \left( nh + \left\lfloor \mu \frac{h}{n_b} \right\rceil \right) f_0 + m f_s, \tag{3}$$

where $\lfloor \cdot \rceil$ denotes the rounding to the nearest integer value, and $\mu$ is obtained from the mode analysis in Eq. (1) on the actual number of bunches $n_b$. For example, the mode $\mu_{n_b=21} = 5$ obtained with $n_b = 21$ bunches (Fig. 5) corresponds to the mode $\mu_{n_b=18} = 4$ obtained with $n_b = 18$ bunches (Fig. 6) and they both are excited by an impedance source at a fixed frequency.

The first condition defines possible frequencies of the impedance source responsible for the instabilities. For low values of $\mu = [1, 2]$, the driving impedance source is expected to be not further than approximately 1 MHz above the main RF harmonics (the revolution period is $f_0 \approx 477$ kHz at top energy in the PS). This is the case for the RF systems, in particular the 10 MHz RF cavities with a bandwidth large enough to cover modes $\mu_{n_b=18} = [1, 2]$ and it was shown to be the source of dipolar coupled-bunch instability [3]. For the larger values of $\mu_{n_b=18} = [4, 5]$, the impedance is expected to be around 2.5 MHz above the main RF frequency on its harmonic, which is beyond the bandwidth of the RF cavities. Two assumptions can be made: Another source of impedance should hence be suspected, or the resonant frequency of the same impedance source is changing and drives both instabilities during the ramp and at flat-top energy.

### *Threshold in Shunt Impedance vs. Frequency*

A limitation of the criterion used above is that, due to the sampling with the bunch frequency, the impedance source is expected to be at a resonant frequency of $f_{n,\mu}$, but for any $n$. To further restrict the possible frequency range and the amplitude of the impedance, another criterion can be obtained from the shunt impedance threshold for coupled-bunch instabilities given by [12]

$$R_s < \frac{|\eta|\, E}{e I_0 \beta^2} \left(\frac{\Delta E}{E}\right)^2 \frac{\Delta\omega_s}{\omega_s} \frac{F}{f_0 \tau} G\left(f_r \tau\right), \tag{4}$$

where $\eta = \gamma_{\mathrm{tr}}^{-2} - \gamma^{-2}$ is the slippage factor, $E$ the beam energy, $e$ the elementary charge, $I_0$ the average beam current, $\beta$ the relativistic velocity factor, $\Delta E/E$ the energy spread, $\Delta\omega_s/\omega_s$ the synchrotron frequency spread, $F \sim 0.3$ a form factor defined by the particle distribution and $G$ is a form factor defined as

$$G\left(x\right) = x \min\left\{J_m^{-2}\left(\pi x\right)\right\}. \tag{5}$$

where $J_m$ is the Bessel function of the first kind and min denotes the minimum value over all modes $m$.

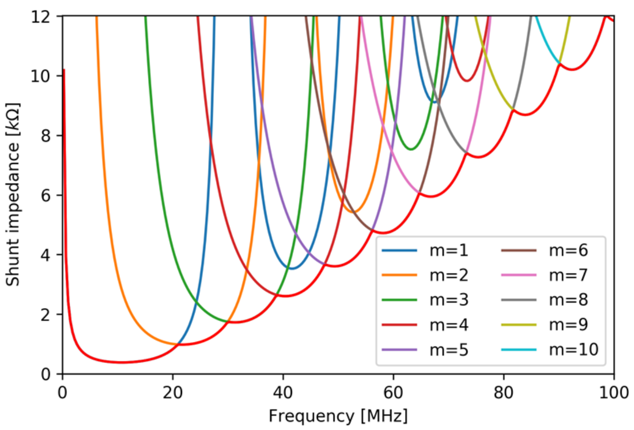


Figure 7: Shunt impedance threshold for coupled-bunch instabilities according to Eq. (4) up to mode $m = 10$. The red line corresponds to the minimum of all modes $m$ considered.

Applying Eq. (4) to beam parameters on the PS flat top provides the curves shown in Fig. 7. The instability threshold depends on the wavelength-to-bunch length ratio $f_r\tau$. For the dipolar mode $m = 1$, the required shunt impedance is minimum in the region around 10 MHz (compatible with the observation that the main RF system is responsible for dipolar instabilities), while for the quadrupolar mode $m = 2$ the required shunt impedance is minimum in the region around 20 MHz. Combining both criteria, the most likely impedance source for quadrupolar instabilities has a resonant frequency of about 22.5 MHz and a minimum shunt impedance, $R_s$ of about 1 kΩ.

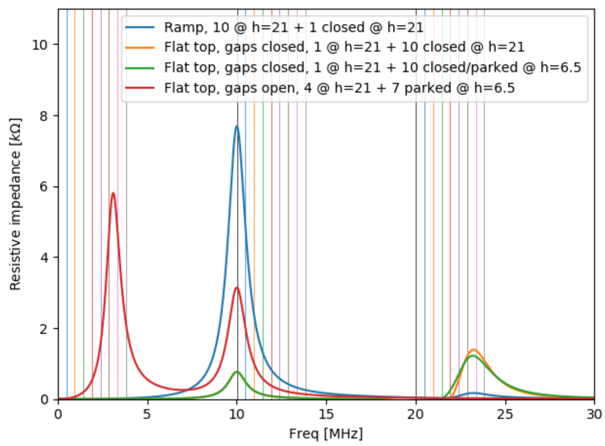


Figure 8: Impedance of the 10 MHz cavities (11 in total) for different configurations. The frequency of the unstable modes according to Eq. (3) with $n_b = 21$ bunches are displayed as vertical lines.

Using the present PS impedance model, the closest impedance source with the expected characteristics are therefore the 10 MHz cavities when the gap relay is closed. The gap relay is not perfect and this contribution, which was assumed negligible in the past, should be included in the model. Indeed, the shunt impedance of the cavity with closed gap is $R_s \approx 70\ \Omega$ per gap at a resonant frequency of $f_r \approx 23.1$ MHz [13]. During the ramp, the voltage program of all the cavities except one is reduced to zero, immediately followed by the closure of the gap relays and parking to $h = 6.5$ (see Fig. 4). Although small, the residual impedance of all cavities is summed up and amounts to an impedance of $R_s \approx 1.4$ kΩ, as shown in Fig. 8 (blue line during the ramp, orange line at flat top). Note that changing the tuning current of the cavity with the gap relay closed has no major influence on its impedance (green line in Fig. 8). A final point is that the impedance of the 10 MHz cavities changes along the ramp, which explains the observation that the mode $\mu$ changes from the acceleration ramp to the flat-top. Overall, the impedance of the 10 MHz cavities, including their residual impedance when the gap relays are closed, fulfills all the conditions to explain the behavior of both dipolar and quadrupolar coupled-bunch instabilities.

### *Experimental Verification*

Additional measurements were therefore conducted to validate this hypothesis experimentally. The test consisted of measuring the quadrupolar coupled-bunch instabilities

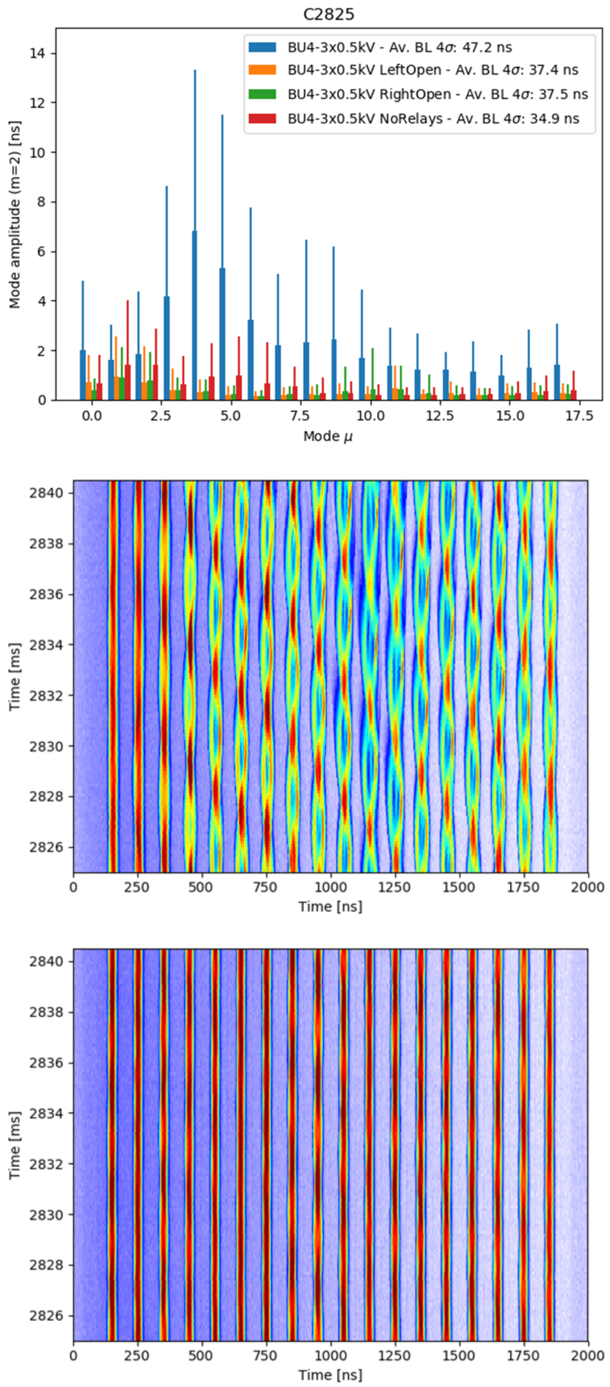


Figure 9: Quadrupolar mode spectrum with $n_b$ = 18 bunches for different 10 MHz cavities impedance configurations (top). The bottom plots show the measured beam profiles with the gap relays closed (middle) and opened with the cavities parked to $h$ = 6.5 (bottom).

with different configurations of the 10 MHz cavities. Note that the longitudinal emittance was set to the lowest possible value (with the BU setting at 3x0.5 kV) in order to provoke the instability. Furthermore, note that the dipolar coupled-bunch feedback was kept enabled. To confirm the fact that the impedance at 23 MHz is responsible for the quadrupolar instabilities, the gap relays of cavities were blocked opened. Unused cavities belonging to the same harmonic group were parked at $h = 6.5$ with their impedance at the fundamental resonance affecting the beam. In this case, all impedance contributions are far from the parameter region driving quadrupolar instabilities, as shown in red in Fig. 8. Even though the overall impedance is much larger with the gap relays opened, it is expected that in this frequency range the impedance should drive dipolar instabilities, which are damped by the coupled-bunch feedback.

The results are summarized in Fig. 9. The amplitude of quadrupolar oscillations is drastically reduced by moving the impedance far away from the critical region around 20 MHz, confirming all hypotheses above. Note that the average bunch length at extraction is smaller for the case with the gap relays open, which is an indication that the beam is simply not stabilized by any other source of emittance blow-up occurring before the quadrupolar instability could rise. The residual impedance of the cavities with closed gap relays can therefore be assumed responsible for the quadrupolar coupled-bunch instabilities of modes $\mu_{n_b=18} = [4, 5]$. An immediate question is whether it is possible to profit from this observation in operation. Unfortunately, detuning the impedance to very low frequency triggers other effects, like degradation of the RF manipulations due to transient beam loading. An example of bunch-by-bunch variation with and without the gap relays is shown in Fig. 10, where the first bunch is too large to be extracted to the SPS without losses. Possible improvements of the gap relay circuit or other measures to reduce the impedance of the spurious resonance at 23 MHz are therefore being considered.

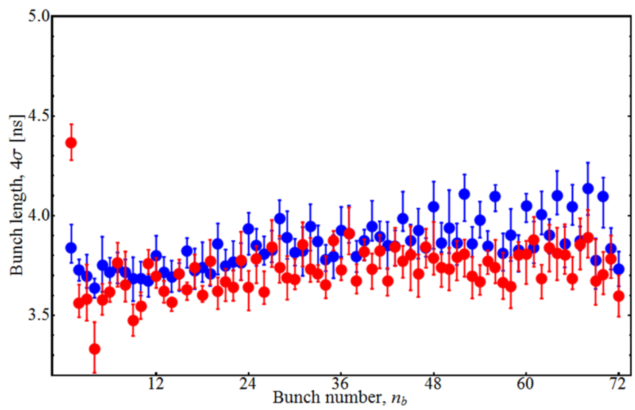


Figure 10: The bunch length at PS extraction with opened and closed gap relays. The case with the gap relays opened was obtained with the cavities parked at $h$ = 6.5. The source of degradation of the longitudinal emittance of the first bunch only remains to be identified.

## CONCLUSIONS

The development of the PS longitudinal impedance model makes progress by combining efforts of modeling the devices in the machine, but also by performing beam-based measurements of the impedance. The main impedance sources responsible for longitudinal instabilities are mostly identified or have clear suspects:

- The 80 MHz cavities are responsible for uncontrolled blow-up during splitting.
- High frequency impedance sources (e.g. pumping manifolds, sector valves) are suspected to drive the microwave instability at transition crossing for ions.
- The 10 MHz cavities with closed gap relay have a resonance at about 23 MHz responsible for the quadrupolar coupled-bunch instability at flat top.

Further work will consist in improving the analytical estimations in order to evaluate the evolution of the instability threshold along the ramp, including the variations on bunch length. Moreover, the criterion used in [12] provides pessimistic values and the criterion presented in [14] should provide more accurate results. Progress in particle simulations is also ongoing and will require an accurate modeling of feedbacks to reproduce all measured instabilities.

## ACKNOWLEDGMENTS

We would like to thank the PS operators for their support during MD sessions, colleagues from the RF-IS section for their help with measurements of cavities impedance, as well as all contributors to the PS impedance model.

## REFERENCES

[1] G. Apollinari, I. Béjar Alonso, O. Brüning, P. Fessia, M. Lamont, L. Rossi, and L. Tavian, "High-Luminosity Large Hadron Collider (HL-LHC): Technical Design Report V. 0.1," Tech. Rep. CERN-2017-007-M, Geneva, 2017.

[2] H. Damerau, A. Funken, R. Garoby, S. Gilardoni, B. Goddard, K. Hanke, A. Lombardi, D. Manglunki, M. Meddahi, B. Mikulec, G. Rumolo, E. Shaposhnikova, M. Vretenar, and J. Coupard, "LHC Injectors Upgrade, Technical Design Report, Vol. I: Protons," Tech. Rep. CERN-ACC-2014-0337, CERN, Geneva, Switzerland, 2014.

[3] H. Damerau, S. Hancock, C. Rossi, E. N. Shaposhnikova, J. Tuckmantel, J. L. Vallet, and M. Mehler, "Longitudinal Coupled Bunch Instabilities in the CERN PS," in *Particle accelerator. Proceedings, 22nd Conference, PAC'07, Albuquerque, USA, June 25-29, 2007*, vol. C070625, p. 4180, 2007.

[4] H. Damerau, A. Lasheen, and M. Migliorati, "Observation and Damping of Longitudinal Coupled-bunch Oscillations in the CERN PS," *CERN Yellow Rep. Conf. Proc.*, vol. 1, pp. 33–37. 5 p, 2018.

[5] M. Migliorati, S. Persichelli, H. Damerau, S. Gilardoni, S. Hancock, and L. Palumbo, "Beam-wall interaction in the cern proton synchrotron for the lhc upgrade," *Phys. Rev. ST Accel. Beams*, vol. 16, p. 031001, 2013.

[6] "PS Longitudinal Impedance Database." https://gitlab.cern.ch/longitudinal-impedance/PS/.

[7] A. Lasheen, H. Damerau, and G. Favia, "Uncontrolled longitudinal emittance blow-up during rf manipulations in the CERN PS," *Journal of Physics: Conference Series*, vol. 1067, p. 062018, 2018.

[8] H. Damerau, F. Bertin, G. Favia, and A. Lasheen, "Active methods of suppressing longitudinal multi-bunch instabilities," in *these proceedings*.

[9] T. Bohl, T. P. R. Linnecar, and E. Shaposhnikova, "Measuring the resonance structure of accelerator impedance with single bunches," *Phys. Rev. Lett.*, vol. 78, pp. 3109–3112, 1997.

[10] D. Boussard, "Observation of microwave longitudinal instabilities in the CPS," Tech. Rep. CERN-LabII-RF-INT-75-2. LabII-RF-INT-75-2, CERN, Geneva, Switzerland, 1975.

[11] A. Lasheen, H. Damerau, J. Repond, M. Schwarz, and E. Shaposhnikova, "Improvement of the Longitudinal Beam Transfer from PS to SPS at CERN," in *Proc. 9th International Particle Accelerator Conference (IPAC'18), Vancouver, BC, Canada, April 29-May 4, 2018*, no. 9 in International Particle Accelerator Conference, (Geneva, Switzerland), pp. 3060–3063, JACoW Publishing, 2018. https://doi.org/10.18429/JACoW-IPAC2018-THPAF042.

[12] E. Shaposhnikova, "Longitudinal beam parameters during acceleration in the LHC," Tech. Rep. LHC-PROJECT-NOTE-242, CERN, Geneva, Switzerland, 2000.

[13] G. Favia, "Study of the beam-cavity interaction in the CERN PS 10 MHz cavities and investigation of hardware solutions to reduce beam loading," no. CERN-THESIS-2017-166, 2017.

[14] I. Karpov and E. Shaposhnikova, "Longitudinal Coupled-Bunch Instability Evaluation for FCC-hh," in *Proc. 10th International Particle Accelerator Conference (IPAC'19), Melbourne, Australia, 19-24 May 2019*, no. 10 in International Particle Accelerator Conference, (Geneva, Switzerland), pp. 297–300, JACoW Publishing, Jun. 2019. https://doi.org/10.18429/JACoW-IPAC2019-MOPGW083.

# VLASOV SOLVERS AND SIMULATION CODE ANALYSIS FOR MODE COUPLING INSTABILITIES IN BOTH LONGITUDINAL AND TRANSVERSE PLANES

E. Métral†, CERN, Geneva, Switzerland and M. Migliorati, University La Sapienza, Rome, Italy

*Abstract*

Two Vlasov solvers for the longitudinal and transverse planes are used to study the frequency shift of coherent oscillation modes and possible mode coupling instability for the two cases of a proton bunch interacting with either a constant inductive or a broad-band resonator impedance. In parallel to this approach, a new method to study the coherent frequency shift from the results of simulation codes is presented. Comparisons between the two methods are discussed, as well as simple analytical formulae (valid in the "long-bunch" regime), which clearly reveal how to mitigate these instabilities.

## INTRODUCTION

Starting from the Vlasov equation and using a decomposition on the low-intensity eigenvectors, as proposed by Laclare and Garnier [1,2], the effect of a transverse damper in the transverse plane was added and a new Vlasov solver code was developed, called GALACTIC (for GArnier-LAclare Coherent Transverse Instabilities Code), which helped to shed light on the destabilising effect of resistive transverse dampers such as in the CERN LHC [3,4]. A similar approach can be used in the longitudinal plane, leading to GALACLIC (for GArnier-LAclare Coherent Longitudinal Instabilities Code), which helped to understand the details of the mode coupling behind some longitudinal microwave instabilities [5,6].

The purpose of this paper is to compare the results from the Vlasov solvers and the ones from macroparticle tracking simulation codes. In the first section devoted to the longitudinal plane, the results from GALACLIC are compared to the ones obtained from the macroparticle tracking simulation code SBSC [7] (as well as BLonD [8] and MuSIC [9]) for the two cases of Constant Inductive (CI) and Broad-Band Resonator (BBR) impedances above transition, assuming a "Parabolic Line Density" (PLD) longitudinal distribution [1]. In the second section devoted to the transverse plane, GALACTIC is compared to the macroparticle tracking simulation code PyHEADTAIL [10] for the case of a BBR impedance, assuming a "Water-Bag" (WB) longitudinal distribution [1]. In the third section, simple analytical formulae are provided, which clearly reveal the different mitigation methods.

## LONGITUDINAL

In the case of a PLD longitudinal distribution, the effect of the Potential-Well Distortion (PWD) is given by (with $Q_s$ and $Q_{s0}$ the intensity-dependent and low-intensity synchrotron tunes and $Q$ the coherent synchrotron tune)

$$\frac{Q}{Q_{s0}} = \frac{Q}{Q_s} \times F_{PWD} \quad \text{with} \quad F_{PWD} = \frac{Q_s}{Q_{s0}} = \frac{1}{\sqrt{1-\frac{3}{4}x}} \tag{1}$$

where $x$ is a normalised parameter proportional to the bunch intensity given by

$$x = \frac{\mathrm{Im}\left[\frac{Z_l(p)}{p}\right]_{p=0} 4\, I_b}{\pi^2\, B^3\, \hat{V}_T\, h \cos\phi_s}\,. \tag{2}$$

Here, the simplified case of a constant shape of the longitudinal distribution was assumed and $Z_l(p)/p$ is the longitudinal impedance (at the bunch spectrum line $p$), $I_b = N_b\, e\, f_0$ the bunch current (with $e$ the elementary charge, $N_b$ the number of charges and $f_0$ the revolution frequency), $B = f_0\, \tau_b$ the bunching factor with $\tau_b$ the full (4 $\sigma$) bunch length, $\hat{V}_T$ the total (effective) peak voltage, $h$ the harmonic number and $\phi_s$ the RF phase of the synchronous particle ($\cos\phi_s > 0$ below transition and $\cos\phi_s < 0$ above). It is important to note that $B$, $\hat{V}_T$ and $\phi_s$ depend on the bunch intensity due to the PWD. The cases of CI and BBR impedances, above transition and taking into account PWD, are depicted on Figs. 1 and 2 respectively, considering the same numerical values as the ones used for the SBSC simulations discussed below.

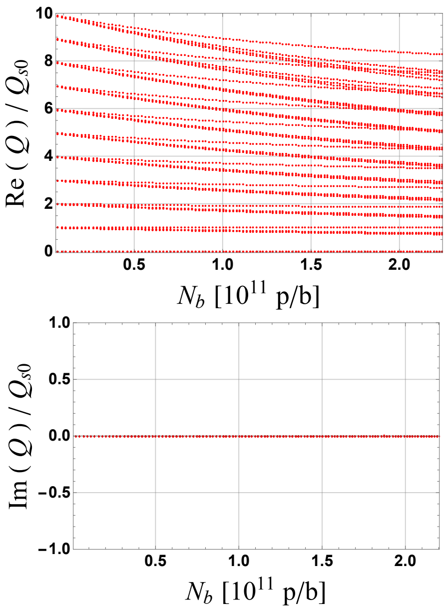


Figure 1: Normalised (to the low-intensity synchrotron tune) mode-frequency shifts from GALACLIC in the case of a CI impedance, above transition, taking into account the PWD and for a PLD longitudinal distribution, with the parameters mentioned below: (upper) real part and (lower) imaginary part.

† Elias.Metral@cern.ch

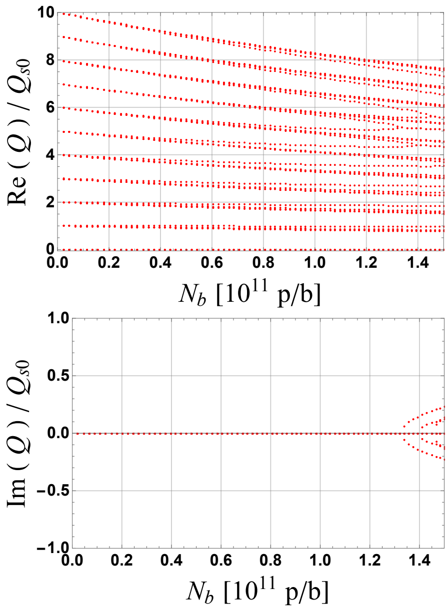


Figure 2: Normalised (to the low-intensity synchrotron tune) mode-frequency shifts from GALACLIC in the case of a BBR impedance (with a quality factor of 1 and a resonance frequency $f_r$ such that $f_r\,\tau_b = 2.7$), above transition, taking into account the PWD and for a PLD longitudinal distribution, with the parameters mentioned below: (upper) real part and (lower) imaginary part.

The SBSC code is a macroparticle tracking code (Single-Bunch Simulation Code) for the longitudinal plane. The beam and machine parameters used for the benchmarks of this paper are the following (close to the CERN SPS case): the relativistic mass factor is $\gamma$ = 27.73, the relativistic mass factor at transition is $\gamma_{tr}$ = 22.77, the machine circumference is $C$ = 6911 m, the peak RF voltage is $\hat{V}_{RF}$ = 6 MV, the harmonic number is $h$ = 462 (instead of 4620 used in the CERN SPS, to be in a linear RF system and not mix other possible effects from the nonlinearities of the longitudinal phase space), the full bunch length (4 $\sigma$) is $\tau_b$ = 2.7 ns and the low-intensity synchrotron tune is $Q_{s0} = 3.26 \times 10^{-3}$. As concerns the impedance, a BBR model is considered, with a quality factor of 1, a resonance frequency $f_r$ such that $f_r\,\tau_b = 2.7$ ($f_r$ = 1 GHz) and $\mathrm{Im}\,[\,Z_l(p)\,/p\,] = 8.67\,\Omega$ at low frequency. The case of a CI impedance corresponds to the case where the resonance frequency $f_r$ tends to infinity.

The initial stationary distribution, taking into account collective effects for protons, has been obtained with BLonD and a good agreement has been reached between SBSC and BLonD (and MuSIC), as can be seen from Fig. 3 revealing clearly the intensity threshold of the longitudinal "microwave instability" at ~ $1.2 \times 10^{11}$ p/b for the case of the BBR impedance. In the case of CI impedance, no instability is observed as predicted from GALACLIC (see Fig. 1): a real part of the impedance is needed for mode coupling to take place. A similar result is also obtained for the transverse plane. It is worth noting also from Fig. 3 that a perfect agreement has been obtained between GALACLIC and the macroparticle simulation codes for the bunch lengthening due to the PWD (see red point).

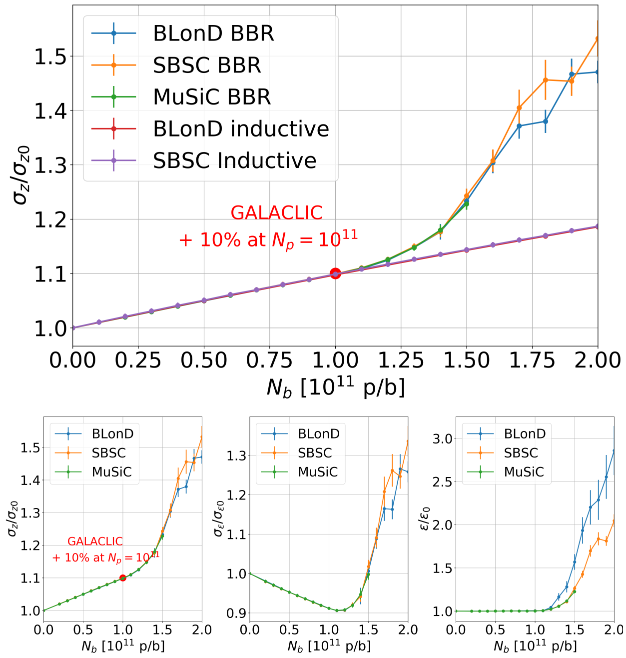


Figure 3: Simulation results from BLonD, SBSC and MuSIC codes with the parameters mentioned above: (upper) evolution of the normalised rms bunch length vs. bunch intensity for the cases of BBR and CI impedances; (lower) evolution of the normalised rms bunch length, energy spread and longitudinal emittance vs. bunch intensity for the case of the BBR impedance.

To analyse this instability in more detail, a new mode analysis was implemented for the post-processing of the results obtained through macroparticle tracking simulations, by computing

$$M_{n,l} = \left( \int_{-\infty}^{+\infty} z^n \lambda(z;t) dz \right)^{1/n} \simeq \left( \int_{-\infty}^{+\infty} z^n \lambda_0(z) dz \right)^{1/n} \left(1 + K_n e^{j\Omega_n t}\right) \quad (3)$$

with $\lambda(z;t)$ the total longitudinal distribution, $\lambda_0(z)$ the stationary distribution, $\Omega_n$ the coherent (angular) frequency of the $n^{th}$ mode and $K_n$ a time constant parameter depending on machine parameters, the mode pattern and its amplitude. The important feature of Eq. (3) is that its dependence on time is only related to the coherent (complex) frequency. Indeed $M_{n,l}$ oscillates at frequency $\mathrm{Re}[\Omega_n]$ with a time amplitude dependence proportional to $\mathrm{Im}[\Omega_n]$. Therefore, by evaluating Eq. (3) turn after turn, and by doing its FFT (Fast Fourier Transform), we obtain the (complex) frequency of the $n^{th}$ mode. If we sum the spectra of the first lowest modes, we obtain the result of Fig. 4 for both cases of a CI impedance and the BBR model. In the bottom figure, we have also represented the intensity threshold deduced from Fig. 3. Some mode coupling could be guessed but this is not easy to say from Fig. 4 alone.

Superimposing the plots from GALACLIC and SBSC, as shown in Fig. 5, a good agreement is obtained for both cases of a CI impedance and the BBR model, even if for the latter some slight shift is observed for the higher-order modes. This would need to be investigated in more detail in the future but it should be reminded that the simplest model of PWD was used here, which assumes that the shape of the longitudinal distribution does not change and that only the bunch length changes with the bunch intensity. The model could be refined in the future to take into account the variation of the bunch profile with intensity. However, the agreement seems already sufficiently good to state that the longitudinal "microwave instability" observed in Fig. 3 is a Longitudinal Mode Coupling Instability (LMCI) of high-order modes (6 and 7).

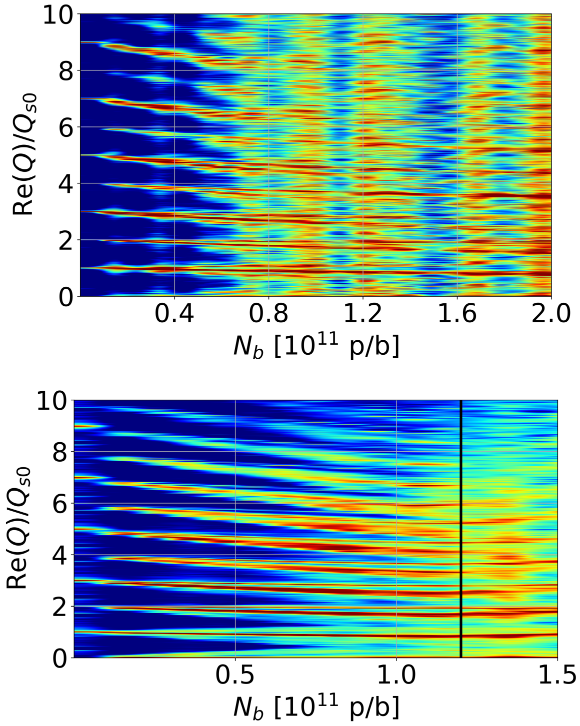


Figure 4: Real part of the normalised mode-frequency shifts from the SBSC tracking code, using the new mode analysis described in Eq. (3), for the case of CI (upper) and BBR (lower) impedance.

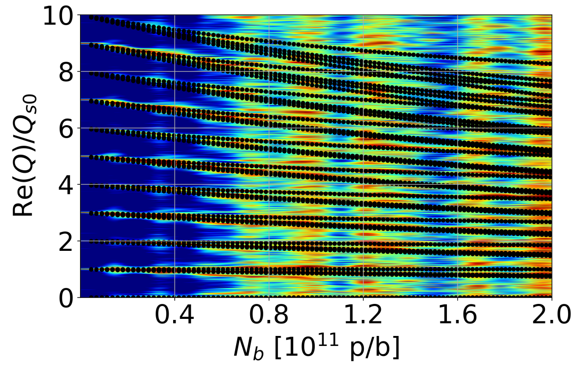


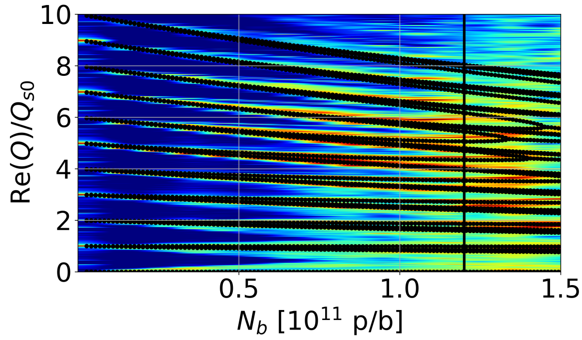


Figure 5: Real part of the normalised mode-frequency shifts: comparison between GALACLIC (black lines) and SBSC for the cases of CI (upper) and BBR (lower) impedances.

## TRANSVERSE

A similar detailed comparison in the transverse plane, between GALACTIC and the PyHEADTAIL macroparticle tracking code [10], revealed an excellent agreement as can be observed in Figs. 6 and 7 for the case of a BBR impedance and assuming a WB longitudinal distribution. As already mentioned above, there is no instability in the case of a CI impedance as a real part of the impedance is needed for mode coupling to take place.

As done for the longitudinal plane, a new mode analysis was implemented for the post-processing of the results obtained through macroparticle tracking simulations, by computing

$$M_{n,\perp} = \left( \int_{-\infty}^{+\infty} dy \int_{-\infty}^{+\infty} z^n \rho(z, y; t)\, y\, dz \right)^{1/n} \simeq A\left(1 + K_n' e^{j\Omega_n t}\right) \tag{4}$$

Here $A$ is a constant depending on the stationary distribution, and $K_n'$ a time constant parameter depending on some machine parameters, the mode pattern and amplitude. As for Eq. (3), $M_{n,\perp}$ oscillates at the coherent (angular) frequency $\mathrm{Re}[\Omega_n]$ with a time amplitude dependence proportional to $\mathrm{Im}[\Omega_n]$. The FFT of $M_{n,\perp}$ highlights the (complex) frequency of the $n^{th}$ mode, and by summing the lowest first modes, we obtain the results of Fig. 6.

Finally, the growth rates shown in Fig. 7 have been obtained from PyHEADTAIL by considering the betatron oscillations of the bunch center of mass turn after turn, and by using an exponential fit for its maximum amplitude.

## SIMPLE FORMULAE AND POSSIBLE MITIGATIONS

In the "long-bunch" regime (where $2\, f_r\, \tau_b \gg 1$), simple analytical formulae can be obtained in both longitudinal and transverse planes, which correspond to the coasting-beam formulae with peak values [1], and with no dependence anymore on the synchrotron tune.

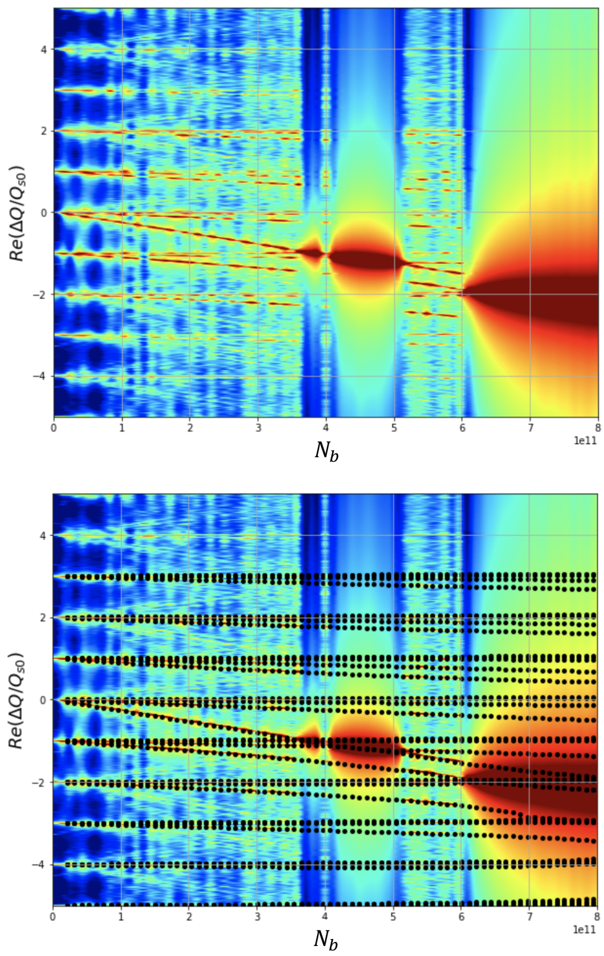


Figure 6: Real part of the normalised mode-frequency shifts: comparison between PyHEADTAIL (top) and GALACTIC (black dots, bottom) for the case of a BBR impedance (with a resonance frequency $f_r$ such that $f_r\,\tau_b = 2.7$) and assuming a WB longitudinal distribution.

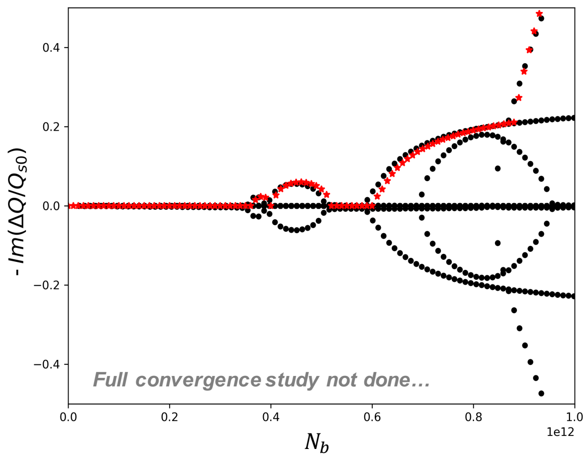


Figure 7: Imaginary part of the normalised mode-frequency shifts: comparison between PyHEADTAIL (red dots) and GALACTIC (black dots) for the case of a BBR impedance (with a resonance frequency $f_r$ such that $f_r\,\tau_b = 2.7$) and assuming a WB longitudinal distribution.

In the longitudinal plane, the stability criterion corresponds to the Keil-Schnell-Boussard criterion (i.e. the Keil-Schnell criterion for coasting beams applied with peak values for bunched beams as proposed by Boussard) whose scaling is given by [1]

$$N_{b,th}^{l} \propto |\eta|\,\varepsilon_l\,\frac{\Delta p}{p_0} \Big/ \left|\frac{Z_l(p)}{p}\right| \tag{5}$$

where $\eta$ is the slip factor (measuring the distance to transition), $\varepsilon_l$ the longitudinal emittance and $\Delta p/p_0$ the longitudinal momentum spread. Therefore, to increase the longitudinal intensity threshold one needs to reduce the impedance and/or increase the slip factor (i.e. move further away from transition) and/or increase the longitudinal emittance and/or increase the momentum spread. Note that as it is the product between the longitudinal emittance and the momentum spread which matters (and as protons are considered in this paper), it is more effective to increase the momentum spread than increasing the bunch length. Indeed, increasing for instance the RF voltage, and assuming that the longitudinal emittance is preserved (as protons are considered), the momentum spread increases and therefore the longitudinal intensity threshold as well.

In the transverse (e.g. vertical $y$) plane, a similar criterion can be obtained, whose scaling is given by [11]

$$N_{b,th}^{y} \propto |\eta|\,\varepsilon_l\,Q_y\,f_r \,/\, |Z_y| \tag{6}$$

where $Q_y$ is the vertical tune. Therefore, to increase the transverse (vertical) intensity threshold one needs to reduce the impedance and/or increase the slip factor (i.e. move further away from transition) and/or increase the longitudinal emittance and/or increase the vertical tune. Equation (6) was successfully used in the past to significantly increase the intensity threshold at the CERN SPS, even if the role of space charge still needs to be fully understood [12].

## CONCLUSION

A good agreement has been reached between the GALACLIC Vlasov solver and the SBSC longitudinal macroparticle tracking code (as well as BLonD and MuSIC) for the two cases of CI and BBR impedances above transition, taking into account the simplest model of PWD (where the shift of the synchronous phase is neglected). For the BBR impedance model, the longitudinal "microwave instability" observed in Fig. 3 has been explained by a LMCI (see Fig. 5 lower), whose intensity threshold is very close to the Keil-Schnell-Boussard criterion. The scaling of the latter is shown in Eq. (5), which reveals how to increase the longitudinal intensity threshold.

An excellent agreement has also been reached in the transverse plane between the GALACTIC Vlasov solver and the PyHEADTAIL macroparticle tracking code for the case of a BBR impedance model, as can be observed from Figs. 6 and 7. In this case, the scaling of the intensity threshold is shown in Eq. (6), which also reveals how to increase the transverse intensity threshold.

## REFERENCES


[1] J.L. Laclare, "Bunched beam coherent instabilities", in *Proc. CAS - CERN Accelerator School: Accelerator Physics*, Oxford, UK, 16 - 27 September 1985, pp. 264-326 (CERN-1987-003-V-1).

[2] J.P. Garnier, "Instabilités cohérentes dans les accélérateurs circulaires", Ph.D. thesis, Grenoble, France, 1987.

[3] E. Métral *et al.*, "Destabilising effect of the LHC transverse damper", in *Proc. 9th Int. Particle Accelerator Conf. (IPAC'18)*, Vancouver, BC, Canada, Apr.-May 2018, pp. 3076-3079. doi:10.18429/JACoW-IPAC2018-THPAF048

[4] E. Métral, "Destabilising effect of resistive transverse dampers", these proceedings.

[5] E. Métral, "GALACTIC and GALACLIC: two Vlasov solvers for the transverse and longitudinal planes", in *Proc. 10th Int. Particle Accelerator Conf. IPAC2019*, Melbourne, Australia, 19-24 May 2019, pp. 312-315. doi:10.18429/JACoW-IPAC2019-MOPGW087

[6] E. Métral and M. Migliorati, "Longitudinal Mode-Coupling Instability: GALACLIC Vlasov solver vs. macroparticle tracking simulations", in *Proc. 10th Int. Particle Accelerator Conf. IPAC2019*, Melbourne, Australia, 19-24 May 2019, pp. 320-323. doi:10.18429/JACoW-IPAC2019-MOPGW089

[7] M. Migliorati *et al.*, "Beam-wall interaction in the CERN Proton Synchrotron for the LHC upgrade", *Phys. Rev. ST Accel. Beams*, vol. 16, p. 031001, March 2013. doi: 10.1103/PhysRevSTAB.16.031001

[8] CERN BLonD code, https://blond.web.cern.ch

[9] M. Migliorati, L. Palumbo, "Multibunch and multiparticle simulation code with an alternative approach to wakefield effects", *Phys. Rev. ST Accel. Beams*, vol. 18, p. 031001, March 2015. doi:10.1103/PhysRevSTAB.18.031001

[10] K. Li, "Headtail code," 2015. https://indico.cern.ch/event/378615/, [Online; accessed 16.05.2019].

[11] E. Métral, "Stability criteria for high-intensity single-bunch beams in synchrotrons", in *Proc. 8th European Particle Accelerator Conf. EPAC 2002*, Paris, France, 3-7 June 2002, pp. 1532-1534.

[12] E. Métral *et al.,* "Space charge and transverse instabilities at the CERN SPS and LHC", in *Proc. 13th Int. Computational Accelerator Physics Conf. ICAP2018,* Key West, FL, USA, 20-24 October 2018, pp. 80-86. doi:10.18429/JACoW-ICAP2018-SUPAG01

# SYSTEMATIC STUDIES OF THE MICROBUNCHING AND WEAK INSTABILITY AT SHORT BUNCH LENGTHS

M. Brosi*, E. Blomley, T. Boltz, E. Bründermann, M. Caselle, J. Gethmann, B. Kehrer, A. Papash, L. Rota†, P. Schönfeldt‡, P. Schreiber, M. Schuh, M. Schwarz, J. L. Steinmann§, M. Weber and A.-S. Müller, Karlsruhe Institute of Technology, Karlsruhe, Germany
P. Kuske, Helmholtz Zentrum Berlin, Berlin, Germany

*Abstract*

At KARA, the Karlsruhe Research Accelerator of the Karlsruhe Institute of Technology synchrotron, the so-called short-bunch operation mode allows the reduction of the bunch length down to a few picoseconds. The microbunching instability resulting from the high degree of longitudinal compression leads to fluctuations in the emitted terahertz radiation. For highly compressed bunches at KARA, the instability occurs not only in one but in two different bunch-current ranges that are separated by a stable region. The additional region of instability is referred to as short-bunch-length bursting or weak instability. We will presents measurements of the threshold currents and fluctuation frequencies in both regimes. Good agreement is found between the measurement and numerical solutions of the Vlasov-Fokker-Planck equation. This contribution is based on the PRAB paper Phys. Rev. Accel. Beams 22, 020701 [1].

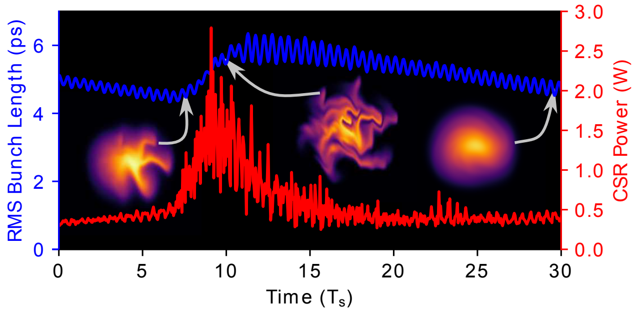


Figure 1: Simulation showing a burst in emitted CSR power (red) as well as the corresponding bunch length (blue) as a function of time (given in synchrotron oscillation periods $T_s$). For three time steps, the charge distribution in the longitudinal phase space is displayed, showing the corresponding structures. The simulation was performed with the Vlasov-Fokker-Planck solver Inovesa [7, 8].

## MOTIVATION

In the short-bunch operation mode of KARA the bunch length is reduced down to a few picoseconds. Due to this, coherent synchrotron radiation (CSR) in the sub-THz frequency range is emitted by the electron bunches. This coherent synchrotron radiation can act back on the electrons of the bunch as additional potential. This leads to a position dependent energy gain. As the electrons have slightly different paths around the ring depending on the magnet optics, this change in the energy distribution results in substructures in the longitudinal charge density. Under certain conditions the micro-bunching instability occurs as these substructures lead to the emission of CSR at higher frequencies causing a self-amplification. The wake potential growing stronger causes intense bursts of CSR emission in the THz frequency range. Such a burst is shown in Fig. 1. The name giving micro-structures on the charge distribution in the longitudinal phase space are displayed for three points in time during the burst in emitted CSR.

As shown in simulations (e.g. [2]) and by measurements at several electron storage rings (e.g. [3–6]), the micro-bunching instability occurs above a certain threshold current, which depends on different parameters, like the momentum compaction factor or the bunch length.

The instability can be diagnosed and observed by detecting the changes in the CSR power emitted by each bunch over its revolutions. This is achieved at KARA with fast THz detectors and the readout system KAPTURE, as described in the next section (see also [4]). Multiple aspects (e.g. the threshold current) of the instability have already been studied and described in detail in e.g. [1, 3, 4, 9–13].

One aspect studied in detail is the behavior of the micro-bunching instability at low bunch currents and small rms bunch length of approximately two picoseconds and less. Under these conditions an additional region of instability occurs below the previously mentioned threshold current, which is referred to as short-bunch-length bursting. In the following, an overview is given of the results concerning this second region of instability. First, a short description of the simple scaling law predicting the threshold currents based on simulations is given. Then the measurement setup and technique are introduced. At the end the experimental observations are described and compared to dedicated simulations.

## PREDICTION OF THRESHOLD CURRENT

In [2] Bane, Cai and Stupakov introduced a simple, linear scaling law which describes the threshold current of the micro-bunching instability in dependence of the parameters of the electron beam. The scaling law was derived from simulations conducted with a Vlasov-Fokker-Planck solver.

* miriam.brosi@kit.edu
† now at SLAC, Stanford, USA
‡ now at DLR-VE, Oldenburg, Germany
§ on leave at Argonne National Laboratory, Lemont, IL, USA

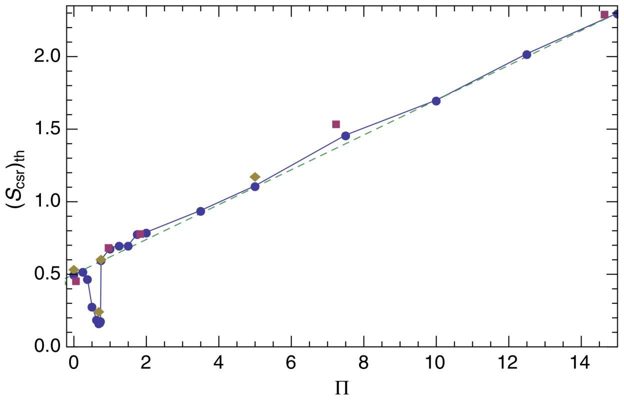


Figure 2: Simulated instability thresholds on which the simple linear scaling law was based, by [2]. "*For the CSR wake, threshold value of $S_{csr}$ vs shielding parameter, $\Pi = \rho^{1/2}\sigma_{z0}/h^{3/2}$. Symbols give results of the VFP solver (blue circles), the LV code (red squares), and the VFP solver with twice stronger radiation damping (olive diamonds).*" ( [2], figure 3).

The CSR impedance was considered in form of the parallel plates model, which simplifies the situation to a single electron bunch moving in vacuum on a circular trajectory between two perfectly conducting, infinitely large, parallel plates with the distance $h$ equal to half of the height of the vacuum chamber.

The threshold current of the instability was given as [2]:

$$(S_{\mathrm{CSR}})_{\mathrm{th}} = 0.5 + 0.12\,\Pi \tag{1}$$

Two dimensionless parameters $\Pi$ and $S_{\mathrm{CSR}}$ were introduced as the shielding parameter $\Pi = \frac{\sigma_{\mathrm{z},0}\rho^{1/2}}{h^{3/2}}$ and the CSR strength $S_{\mathrm{CSR}} = \frac{I_{\mathrm{n}}\rho^{1/3}}{\sigma_{\mathrm{z},0}^{4/3}}$, with the normalized current $I_{\mathrm{n}} = \frac{\sigma_{\mathrm{z},0}I_{\mathrm{b}}}{\alpha_{\mathrm{c}}\gamma\sigma_{\delta}^{2}I_{\mathrm{A}}}$. $\alpha_c$ is the momentum compaction factor, $\sigma_{\mathrm{z},0}$ the natural bunch length, $\rho$ the bending radius, $h$ half of the gap between the parallel plates, $I_{\mathrm{b}}$ the bunch current, $\sigma_{\delta,0}$ the natural energy spread, $\gamma$ the Lorentz factor and $I_{\mathrm{A}}$ the Alfvén current[1].

Equation 1 was established by a linear fit to simulated threshold currents at different parameters (see Fig. 2). Low values of the shielding parameter $\Pi$ correspond to short bunch length for fixed values of the vacuum chamber height $2h$ and the bending radius $\rho$. The "dip" visible in the simulated threshold currents around $\Pi \approx 0.7$ is caused by the short-bunch-length bursting. This additional region of instability was not considered in the linear scaling law (which is displayed as dashed line). The simulations further indicate that the extend to which this additional instability occurs not only depends on the value of the shielding parameter $\Pi$ but also on the ratio of the longitudinal damping time to the period of the synchrotron frequency, given in from of the parameter $\beta = 1/(2\pi f_s \tau_d)$ [2]. This is also supported by the measurements discussed in [1, 13]. The instability is therefore often referred to as "weak instability".

[1] Alfvén current $I_{\mathrm{A}} = 4\pi\varepsilon_0 m_{\mathrm{e}}c^3/e = 17\,045$ A.

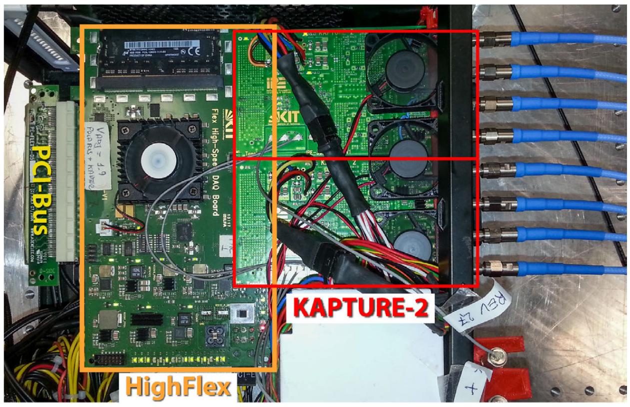


Figure 3: Photo of the KAPTURE-2 system consisting of two KAPTURE boards, the high-flex board with the FPGA and the PCI Bus connecting KAPTURE with the control PC [15]. Courtesy of Matthias Martin.

Further simulations were conducted at the exact parameters of the measurements (including same values of $\Pi$ and $\beta$) to allow a detailed comparison [1].

## MEASUREMENT SETUP AND METHOD

Fast THz detectors can be used to detect the changes in the emitted CSR power and gain insight into the dynamics under the influence of the micro-bunching instability. Room-temperature, zero-biased Schottky barrier diode detectors are commercially available with response times fast enough to resolve each bunch in a multi-bunch filling (RF frequency at KARA is 500 MHz). For the measurements presented in this contribution a quasi-optical, broad-band Schottky barrier diode detector from ACST GmbH [14], with a sensitivity range from 50 GHz to 2 THz and an analog bandwidth of 4 GHz (Pulse FWHM ≈130 ps), limited by an internal amplifier, was used.

As data acquisition system the in-house developed KAPTURE system was used. KAPTURE [16, 17] allows the simultaneous monitoring of all 184 possible bunches in KARA. KAPTURE consists of four sampling channels with a 12-bit ADC each. The idea behind KAPTURE was to selectively sample only the short detector pulses with four points and not the long "dark" time inbetween to save memory space and accomplish continuous sampling. The continuous turn-by-turn readout of the detector pulse for each bunch with 500 MHz results nevertheless in a data rate of 32 Gb/s. The newest version, KAPTURE-2 [18], provides eight sampling channels with up to 1 GHz sampling rate (Fig. 3).

A fast measurement method to gain information about the bunch-current dependent behavior of the instability could be established due to KAPTURE bunch-by-bunch capabilities [4]. The snapshot measurement method reduces the measurement time necessary for revealing the current dependence from hours to one second. As described in detail in [4, 13], the observed fluctuations in the emitted CSR power of each of the stored bunches in a multi-bunch filling pattern

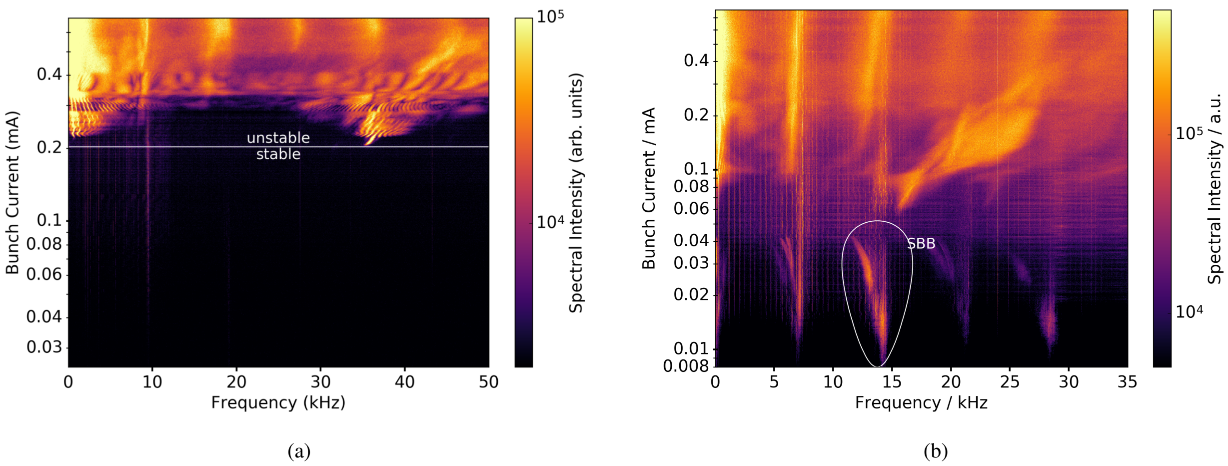


Figure 4: Spectrograms of the fluctuations of the THz intensity as a function of the decaying bunch current, showing the micro-bunching instability. It was obtained in a single-bunch measurement lasting several hours while the bunch current decreased. In (a) no short-bunch-length bursting occurs, as the bunch was not compressed strongly enough. The natural bunch length was $\sigma_{z,0} = 3.8$ ps. (b) In this measurement the natural bunch length was reduced to $\sigma_{z,0} = 2.4$ ps and the additional region of instability due to SBB is visible [1].

is used instead of just the information from a single bunch. The two spectrograms displayed in Fig. 4 are the result of a slow measurement of a single bunch while Fig. 5a show the result of a snapshot measurement focused on the bunch current region of interest.

A common way to visualize the dynamics of the instability is to display the fluctuation spectrum of the emitted CSR power, measured as a function of revolutions. These frequencies are directly connected to the frequencies of the dynamic processes changing the charge distribution in the longitudinal phase space. The current-dependency of these fluctuation frequencies is displayed in form of a spectrogram as shown in Fig. 4. The threshold current and other features of interest can be easily extracted in this representation.

## OBSERVED SHORT-BUNCH-LENGTH BURSTING

As stated above, the second region of instability occurs only for highly longitudinally compressed bunches and is therefore referred to as short-bunch-length bursting (SBB). The measurements of the emitted CSR power are displayed as spectrograms to show the current-dependence of the fluctuation frequencies and to provide information about the dynamics of the instability. In Fig. 4a such a spectrogram is displayed for settings resulting in a natural bunch length of $\sigma_{z,0} = 3.8$ ps. The spectrogram shows the presence of fluctuations with different frequencies depending on the bunch current. Below the threshold current of about 0.2 mA no fluctuations due to the instability are present anymore. Figure 4b shows a measurement at settings where the SBB occurred ($\sigma_{z,0} = 2.4$ ps). Below the threshold current an additional region with fluctuations is visible. The fluctuation frequencies are also dependent on the bunch current and are located directly below twice and four times the synchrotron frequency.

## RESULTS

Figure 5 shows a comparison of a snapshot measurement of the lower bunch current region showing the occurrence of the short-bunch-length bursting and the result of a simulation run for the same beam parameters. Both spectrograms show the additional region of instability due to the SBB below the main threshold current. While the bunch current values of the main threshold and the upper bound of the SBB coincide quite well, the current values of the lower bound differ slightly. The fluctuation frequencies in the emitted CSR power during the SBB are located directly below twice and four times the synchrotron frequency, which in the shown measurement is around $f_s = 6.55$ kHz. Also, the change observed in the fluctuation frequencies with decreasing bunch current is the same for the measurement and the simulation. The frequencies approach the 2nd (4th) harmonic of synchrotron frequency with decreasing current.

A scan over different values of $\Pi$ (corresponding to different natural bunch lengths) was performed. The measured thresholds obtained during this scan will in the following be compared with Vlasov-Fokker-Planck solver simulations conducted individually for the beam parameters of each measurement. From each measurement and the corresponding simulation the main threshold current and, if present, the upper as well as lower bound of the short-bunch-length bursting was extracted. The values are displayed in Fig. 6 as a function of the shielding parameter $\Pi$. The simple linear scaling law for the main threshold current is shown as a grey, straight line.

Qualitatively, the simulated and measured thresholds show the same behavior. They both show the “dip” at approxi-

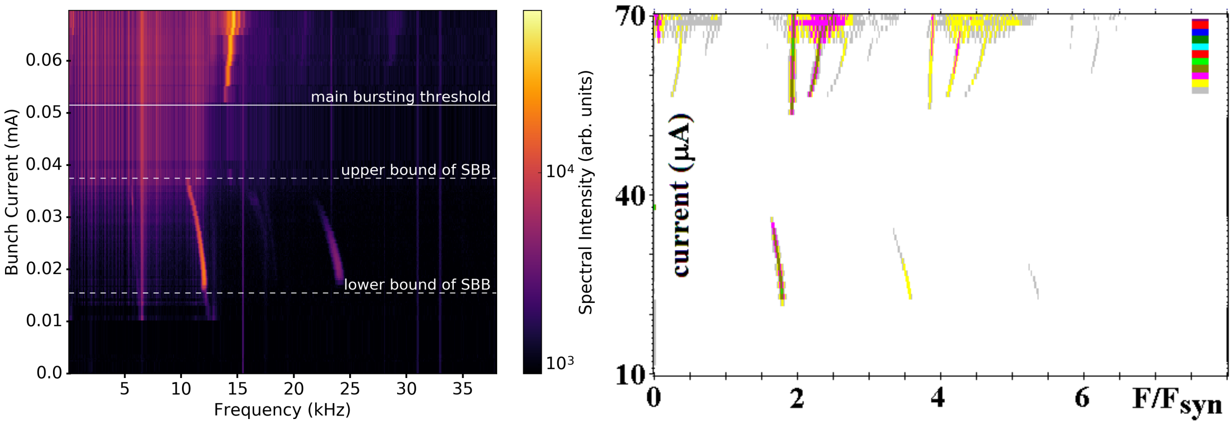


(a)

(b)

Figure 5: Comparison of (a) a snapshot spectrogram of the fluctuations frequencies in the emitted CSR power as a function of bunch current. Below the end of the micro-bunching instability (main bursting threshold) around 0.052 mA, a second region of instability occurs between 0.038 mA and 0.016 mA. (b) Simulated spectrogram showing the end of the micro-bunching instability (main bursting threshold) around 0.054 mA as well as the short-bunch-length bursting between 0.036 mA and 0.022 mA. The frequencies of the SBB are in both spectrograms directly below two and four times the synchrotron frequency ($f_s = 6.55$ kHz). (Adapted from [1]).

mately $\Pi = 0.7$ which was not considered in the simple scaling law. Quantitatively, small differences are visible. The threshold in the results of the VFP solver are in general slightly higher than in the measurements. Also the range in $\Pi$ where the SBB occurs is slightly smaller in the simulation results. This means, the measurements indicate the presence of instability also at parameters (current and $\Pi$) where the simulations predict only stable behavior. This is not easily explained by detector effects. One possible explanation for the small deviation could be slight fluctuations in the machine settings (e.g. noise on quadrupole power supplies). The measured thresholds would correspond more to the floor (the lowest observed threshold) while simulated would give an average value for the threshold.

Another possible explanation for the differences are the simplifications done in the simulations. The CSR impedance was approximated using the parallel plates model. This rather simple model does not consider any resistive wall or geometric impedances. In [19], for example, it was shown that an additional geometric impedance for an aperture slightly reduces the threshold current of the micro-bunching instability. Also the additional impedance of edge radiation leads to a slightly lower threshold current. This was not considered in the simulations. Last but not least, a stronger CSR-interaction than expected from the simple circular orbit simulated could be caused by an interaction extending into the straights behind the dipole magnets.

## SUMMARY

For certain conditions a second region of instability can be observed below the threshold current of the longitudinal micro-bunching instability. This instability occurs at KARA in the short-bunch operation mode for $\alpha_c \leq 2.64 \times 10^{-4}$ and a high RF voltage resulting in a natural bunch length of $\sigma_{z,0} \leq 0.723\,\mathrm{mm} \mathrel{\hat{=}} 2.43\,\mathrm{ps}$ and is therefore referred to as short-bunch-length bursting (SBB). Due to its dependence on the damping time it is also called weak instability. The measurements agree qualitatively with the simulation by [2] and the corresponding simple scaling law (Eq. 1). In comparison with the detailed simulations for each measurement point small differences could be revealed. Considering small additional impedances e.g. contributions by apertures and/or CSR-interaction extending further into the straight sections, could reduce the observed differences.

## ACKNOWLEDGEMENTS

This work has been supported by the German Federal Ministry of Education and Research (Grant No. 05K16VKA). MB, PS, and JLS acknowledge the support by the Helmholtz International Research School for Teratronics.

## REFERENCES

[1] M. Brosi *et al.*, "Systematic studies of the microbunching instability at very low bunch charges", *Phys. Rev. Accel. Beams* 22 (2019), Feb, 020701. `http://dx.doi.org/10.1103/PhysRevAccelBeams.22.020701`.

[2] K. L. F. Bane, Y. Cai, and G. Stupakov, "Threshold studies of the microwave instability in electron storage rings", *Phys. Rev. ST Accel. Beams*, vol. 13, p. 104402, Oct. 2010. `doi:10.1103/PhysRevSTAB.13.104402`

[3] A.-S. Müller *et al.*, "Far Infrared Coherent Synchrotron Edge Radiation at ANKA", in *Proc. 21st Particle Accelerator Conf. (PAC'05)*, Knoxville, TN, USA, May 2005, paper RPAE038.

[4] M. Brosi *et al.*, "Fast mapping of terahertz bursting thresholds and characteristics at synchrotron light sources", *Phys. Rev.*

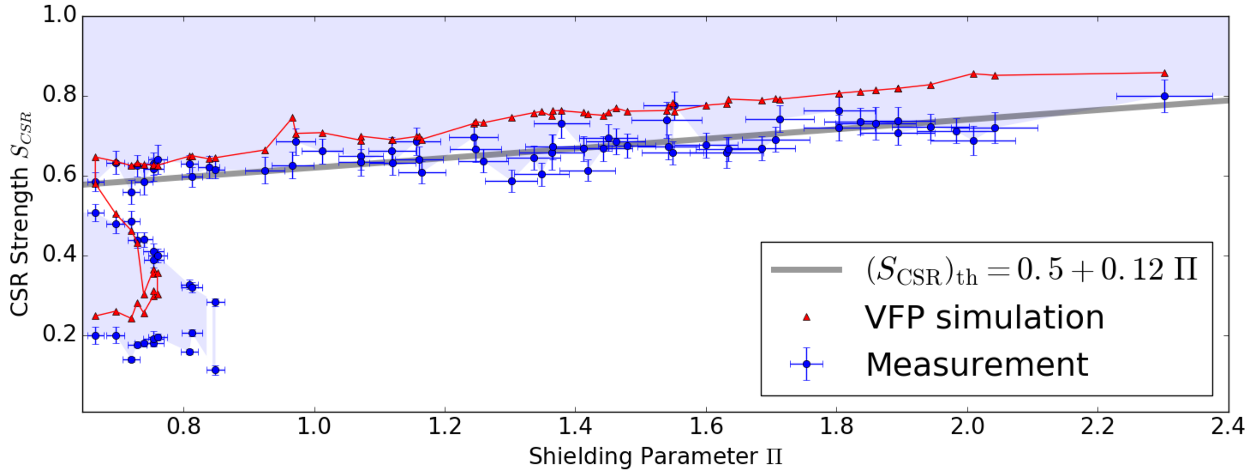


Figure 6: Threshold currents for different beam parameters gained from snapshot measurements and VFP solver simulations are displayed using the dimensionless parameters $S_{\mathrm{CSR}}$ and $\Pi$. The measured area of instability is indicated with a light blue shade and confined by the measured thresholds (blue discs) with the error bars displaying the standard deviation error of each measurement. The red triangles show the results of the VFP solver calculations at the corresponding beam parameters (red line to guide the eye). The linear scaling law for the main bursting threshold given by Eq. 1 is indicated by the gray line [1].


*Accel. Beams*, vol. 19, p. 110701, Nov. 2016. `doi:10.1103/PhysRevAccelBeams.19.110701`

[5] M. Ries *et al.*,"Thz bursting thresholds measured at the metrology light source," in Proceedings of 2012 International Particle Accelerator Conference (2012) p. 3030.

[6] W. Shields *et al.*,"Microbunch instability observations from a thz detector at diamond light source," Journal of Physics: Conference Series 357, 012037 (2012).

[7] P. Schönfeldt *et al.*, "Parallelized Vlasov-Fokker-Planck solver for desktop personal computers", *Phys. Rev. Accel. Beams*, vol. 20, p. 030704, Mar. 2017. `doi:10.1103/PhysRevAccelBeams.20.030704`

[8] P. Schönfeldt *et al.*, Inovesa/Inovesa: Gamma Two. (2018), Jul. `http://dx.doi.org/10.5281/zenodo.1321580`.

[9] M. Brosi *et al.*, "Studies of the Micro-Bunching Instability in Multi-Bunch Operation at the ANKA Storage Ring", in *Proc. 8th Int. Particle Accelerator Conf. (IPAC'17)*, Copenhagen, Denmark, May 2017, pp. 3645–3648. `doi:10.18429/JACoW-IPAC2017-THOBA1`

[10] M. Brosi *et al.*, "Studies of the Micro-Bunching Instability in the Presence of a Damping Wiggler", in *Proc. 9th Int. Particle Accelerator Conf. (IPAC'18)*, Vancouver, Canada, Apr.-May 2018, pp. 3273–3276. `doi:10.18429/JACoW-IPAC2018-THPAK029`

[11] M. Brosi *et al.*, "Synchronous Measurements of Electron Bunches Under the Influence of the Microbunching Instability", in *Proc. 10th Int. Particle Accelerator Conf. (IPAC'19)*, Melbourne, Australia, May 2019, pp. 3119–3122. `doi:10.18429/JACoW-IPAC2019-WEPTS015`

[12] J. L. Steinmann *et al.*, "Continuous bunch-by-bunch spectroscopic investigation of the microbunching instability", *Phys. Rev. Accel. Beams*, vol. 21, p. 110705, Nov. 2018. `doi:10.1103/PhysRevAccelBeams.21.110705`

[13] M. Brosi, "In-Depth Analysis of the Micro-Bunching Characteristics in Single and Multi-Bunch Operation at KARA", Ph.D. thesis, Karlsruhe Institute of Technology, 2020, defended, to be published.

[14] ACST GmbH, `http://www.acst.de/`

[15] M. Martin, "Rekonstruktion der Form von THz-Pulsen aus kurzen Elektronenpaketen mit hohen Wiederholraten an KARA", Master thesis, Karlsruhe Institute of Technology, 2019

[16] M. Caselle *et al.*, "An ultra-fast data acquisition system for coherent synchrotron radiation with terahertz detectors", *J. Instrum.*, vol. 9, p. C01024, Jan. 2014. `doi:10.1088/1748-0221/9/01/C01024`

[17] M. Caselle *et al.*, "Commissioning of an Ultra-fast Data Acquisition System for Coherent Synchrotron Radiation Detection", in *Proc. 5th Int. Particle Accelerator Conf. (IPAC'14)*, Dresden, Germany, Jun. 2014, pp. 3497–3499. `doi:10.18429/JACoW-IPAC2014-THPME113`

[18] M. Caselle *et al.*, "KAPTURE-2. A picosecond sampling system for individual THz pulses with high repetition rate", *J. Instrum.*, vol. 12, p. C01040, Jan. 2017. `doi:10.1088/1748-0221/12/01/c01040`.

[19] P. Schönfeldt, "Simulation and measurement of the dynamics of ultra-short electron bunch profiles for the generation of coherent THz radiation", Ph.D. thesis, Karlsruhe Institute of Technology, 2018, `http://dx.doi.org/10.5445/IR/1000084466`

# WAKEFIELD OF TWO COUNTER-ROTATING BEAMS

L. Teofili[12], M. Migliorati*[12], Sapienza University of Rome, Rome, Italy
I. Lamas, CERN, Geneva, Switzerland
[1]also at CERN, Geneva, Switzerland, [2]also at INFN, Rome, Italy

*Abstract*

This paper deals with the problem of defining the wakefunction for two counter-moving charges, i.e. two charges moving in opposite direction. In this case, the distance between the charges cannot be considered constant. From the counter-moving wakefunction the counter-moving wakepotential is derived. An example of this kind of wakepotential for a lossless pill-box cavity is obtained analitically and compared with numerical simulations.

## INTRODUCTION

During their motion in an accelerator, the beam particles interact electromagnetically with the accelerator vacuum chamber generating the so-called wakefields. These wakefields dissipate heat on the vacuum chamber materials (RF-heating) and act back on the beam particles triggering instabilities. In the case of a single beam traversing the vacuum chamber all the particles move in the same direction and this could be defined as co-moving wakefield [1] or simply wakefield (refer to Fig. 1a).

The physical model for quantifying the effects of the co-moving wakefield has been object of studies since many years, and the works of Chao [2], Ng [3], Bane et al. [4] are well known examples of the current understanding on the topic.

However, in particle colliders there is an extra complication due to the presence of two counter-rotating particle beams. Usually, the two beams pass in two separate vacuum chambers. However, in the collision regions and, sometimes, also in other components, they transit in the same vacuum chamber. In this case, the particles of one beam move in opposite direction with respect to the particles of the other beam and one talks about counter-moving wakefield [1], (refer to Fig. 1b).

In particular, in the Large Hadron Collider (LHC) [5] at the laboratories of the European Council for Nuclear Research (CERN) two counter-rotating beams circulate. They transit in the same vacuum chamber in the collision chambers, at the four interaction points, and in few other components as the LHC injection absorber also known with the acronyms TDI [6] (Target dump injection) which is the device currently installed and TDIS [7] (Target dump injection segmented) which is the upgrade of the TDI to be installed in 2020.

The TDI had major issues due to unexpected severe RF-heating [8] still not fully understood. A possible explanation could be linked to the RF-heating resulting from the interaction of the two counter-rotating beams. In order to avoid these issues with the TDIS, CERN allocated resources to investigate the counter-rotating beam effects.

Few studies have investigated the interaction between two counter-moving beams via their wakefield[1]: Pellegrini [10] and Wang [1] studied longitudinal and transverse two-beam instabilities linked to resonant modes for the Large Electron Positron storage ring (LEP) [11]. Zimmerman [12] discussed the resistive wall wakefield problem for two counter-moving beams. Zannini et al. [13, 14] and Grudiev [15] focused on the RF-heating induced in a vacuum chamber traversed by the counter-moving beams.

This paper proposes a formal physical model to describe the counter-moving wakefield effects starting from the wakefield hypotheses. It defines a counter-moving wakefunction for two point charges, a source charge S and a test charge T. The counter-moving and co-moving cases are represented in Fig. 1. In this figure, most of the quantities needed for understanding the paper are presented.

The paper introduces also the counter-moving wakepotential. Furthermore, it benchmarks the model against simulations results for a lossless cylindrical resonant cavity. Future works will test the model to re-obtain the results of Wang, [1], Zimmerman [12], Zannini et al. [13, 14] and Grudiev [15].

## THE PHYSICAL MODEL

The approximations on which the definition of wakefield is based are two [3]:

1. **Rigid Beam Approximation.** The trajectories of S and T are given, they are straight and parallel with each other. Furthermore, the speed modulus of T and S is equal and constant $v_{q_S} = \beta_{q_S} c = v_{q_T} = \beta_{q_T} c = v$ while the two particles traverse the vacuum chamber.

2. **Kick Approximation.** The effects of the electromagnetic force, continuously acting on S and T all along the vacuum chamber, are represented as a lumped kick acting after the particles passage.

Often in the literature the first hypothesis is reformulated as follows: the trajectories of S and T are given, they are straight and parallel with each other and the longitudinal relative position of T with respect to S (represented as $s_{ST}$ in Fig. 1) during the particle transit in the vacuum chamber is constant, i.e. time-independent.

The authors want to stress that this is not the rigid beam approximation but only one of its consequences. The time

* mauro.migliorati@uniroma1.it

[1] This is not to be confused with the Beam-Beam interaction [9] that does not consider the beams environment.

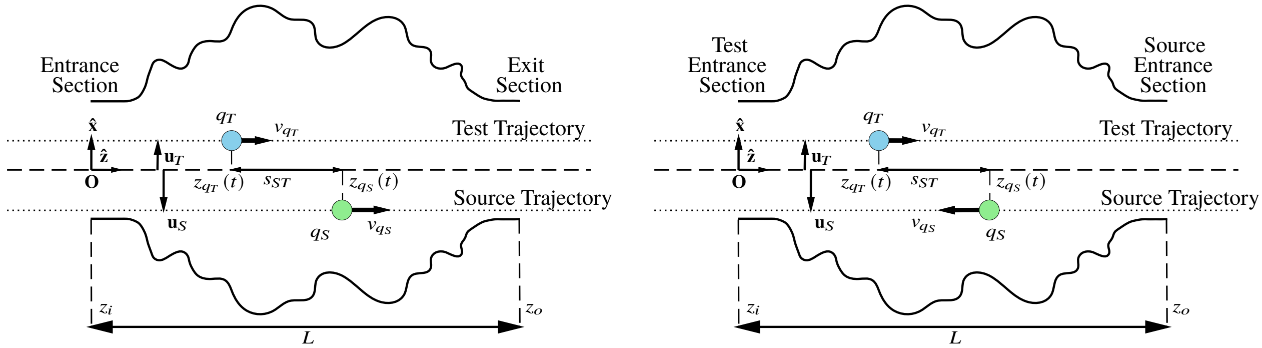


(a) Co-moving case, S and T move in the same direction.

(b) Counter-moving case, S and T move in opposite direction.

Figure 1: Source ($q_S$) and Test ($q_T$) charge transiting inside a vacuum chamber. The cartoon underlines the instantaneous $z$ positions of the two charges $z_{q_S}(t)$ and $z_{q_T}(t)$, their speeds $v_{q_S}$ and $v_{q_T}$, their longitudinal distance $s_{ST}(t)$ and the transverse position of their trajectories with respect to the main reference frame $\mathbf{u}_T$ and $\mathbf{u}_S$. The fixed reference system $\mathbf{O}$, with origin in the entrance section of the test particle and the $\hat{\mathbf{z}}$ axis aligned with the test particle velocity vector. The length of the vacuum chamber $L$ is also indicated.

independence of the relative position of T with respect to S can be derived from the rigid beam approximation adding the extra hypothesis that T and S move in the same direction (co-moving case). The rigid beam approximation, as stated in this paper, remains valid also if the relative positions between the particles is changing inside the vacuum chamber. This is the case for the counter-moving wakefield scenario where the particle distance $s_{ST}$ changes while T and S are traversing the vacuum chamber, i.e. $s_{ST}$ is time dependent (refer to Fig. 1b).

The physical formal model that describes quantitatively the effects of the wakefield is well known and tested for the co-moving case. The interested reader can refer for instance to the work of Chao [2] for more detail. However, this model relies on the time independence of the longitudinal test source distance $s_{ST}$.

If one considers the counter-moving case the longitudinal test source distance $s_{ST}$ is not constant any more and the formal model used for the co-moving case is not applicable as it is. However, it can be adapted as it is explained in the following.

Primarily, one notes that there is a time delay between the entrance in the vacuum chamber of the source charge S and of the test charge T. This time entrance delay is defined as:

$$\Delta t_{ST} = t_{Ti} - t_{Si}, \tag{1}$$

where $t_{Ti}$ is the entrance time of the test particle into the vacuum chamber and $t_{Si}$ is the entrance time of the source particle into the vacuum chamber. For the sake of clarity, the test particle enters into the vacuum chamber when crosses the Test Entrance Section, while the source particle enters into the vacuum chamber when crosses the Source Entrance Section, (see Fig. 2).

One defines also the space entrance delay as the distance that T has to cover to enter into the vacuum chamber at the

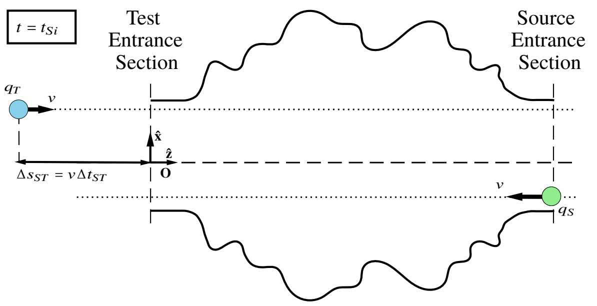


Figure 2: Counter-moving Wakefield scenario. The cartoon represents the position of S and T at the time at which the source is entering into the vacuum chamber, $t_{Si}$. The space entrance delay $\Delta s_{ST}$ is also represented, it is the distance that T has to cover to enter into the vacuum chamber at the time at which S is entering.

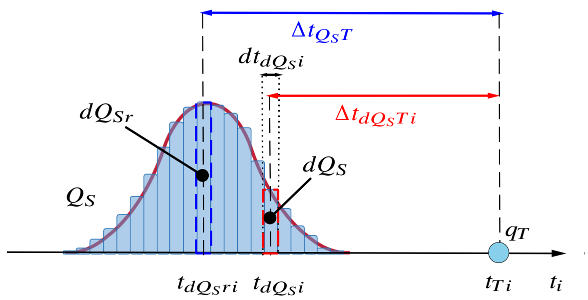

Figure 3: Representation of the charge distribution $Q_S$ and of the test charge $q_T$ as a function of their entrance time into the vacuum chamber $t_i$. In the picture $t_{dQ_{Si}}$ is the entrance time of $dQ_S$, the generic infinitesimal charge composing the distribution $Q_S$, $t_{dQ_{Sri}}$ is the entrance time of $dQ_{Sr}$, the reference infinitesimal charge of the distribution $Q_S$. The entrance time delay of the test charge $q_T$ with respect with this two charges, $\Delta t_{ST}$ and $\Delta t_{Q_ST}$ is also shown.

time at which S is entering into the vacuum chamber :

$$\Delta s_{ST} = \Delta t_{ST} v, \tag{2}$$

where $v$ is the particles speed. The authors want to stress that, in the co-moving case the space entrance delay is coincident with the longitudinal distance between T and S and the concepts of time entrance delay, space entrance delay and longitudinal particle distance are equivalent. This is not the case in the counter-moving scenario.

Subsequently, one has to recall the physical meaning of the wakefunction: the wakefunction represents the integrated effect (change of energy in the longitudinal direction and change of transverse momentum in the transverse plane) that the electromagnetic field excited by the transit of the source charge S in the vacuum chamber has on the test charge T that enters the vacuum chamber with a time delay $\Delta t_{ST}$ with respect to S.

Thus, the counter-rotating wakefunction is defined as:

$$\begin{aligned}\mathbf{w}(\mathbf{u}_T, \mathbf{u}_S, \Delta t_{ST}) = {} & \frac{1}{q_S q_T} \\ & \times \int_{t_{Ti}}^{t_{To}} \mathbf{F}(\mathbf{u}_T, \mathbf{u}_S, \Delta t_{ST}, t) v dt,\end{aligned} \tag{3}$$

where, $\mathbf{F}$ is the instantaneous Lorentz force acting on T and $t_{To}$ is the exit time of the test particle from the vacuum chamber. The counter-rotating wakefunction $\mathbf{w}$ defined by Eq. 3 is a vector of three components, the component along the $\hat{\mathbf{z}}$ axis is called longitudinal and the other two transverse. Further, the definition of wakefunction given by Eq. 3 is general and can be used for both the co-moving and counter-moving cases.

From the counter-moving wakefunction one can pass to the counter-moving wakepotential considering the source as a charge distribution $Q_S(t) = q_S \lambda_S(t)$ composed by slices of charge $dQ_S$. Each slice of charge can be thought as a point charge that enters into the vacuum chamber at a time $t_{dQ_S i}$ and has a different entrance delay with respect to the test charge. The charge of each slice can be expressed as $dQ_S(t_{dQ_S i}) = q_S \lambda_S(t_{dQ_S i}) dt_{dQ_S i}$. It is also useful to define $\Delta t_{Q_S T}$, the time entrance delays between the source distribution $Q_S$ and the test charge T, as the entrance delay between the test charge and a reference slice in the distribution (as for instance the slice with the highest charge). The space entrance delay between the source distribution $Q_S$ and the test charge T, $\Delta s_{Q_S T}$, follows from the time entrance delay as: $\Delta s_{Q_S T} = v \Delta t_{Q_S T}$.

A visualization of these quantities is given in Fig. 3. The figure represents the sliced charge distribution $Q_S$ and the test charge $q_T$ as a function of their entrance time into the vacuum chamber $t_i$.

Finally, the counter-moving wakepotential is defined as the convolution between the wakefunction $\mathbf{w}$ and the normalized charged distribution $\lambda_S$:

$$\begin{aligned}\mathbf{W}(\mathbf{u}_S, \mathbf{u}_T, t_{Ti}) = {} & \int_{-\infty}^{\infty} \lambda_S(t_{dQ_S i}) \\ & \times \mathbf{w}(\mathbf{u}_T, \mathbf{u}_S, t_{Ti} - t_{dQ_S i}) dt_{dQ_S i}.\end{aligned} \tag{4}$$

The longitudinal component of Eq. 4 can be used to obtain an expression of the energy gained or lost by the test particle, however, this topic will be discussed in future works.

## EXAMPLE: PILL-BOX CAVITY

This section gives an example of counter-moving longitudinal wakepotential for the case of a lossless pill-box cavity. The wakefunction is obtained semi-analytically integrating the expression of the longitudinal electric field generated by a short burst disk of electrons emitted by one side of the cavity that travels towards the other side at a speed $v_S$, refer to Fig. 4. The wakefunction is subsequently convolved with a Gaussian bunch distribution to obtain the wakepotential. This wakepotential is benchmarked against the results of the PIC solver [16] of the CST studio suite commercial software.

The analytic expression of transient longitudinal electric field generated by a disk of electrons moving from one side of a pill-box cavity of radius $a$ and length $L$, and that travels towards the other side at a speed $v_S = \beta_S c$, was found by Faust [17] as:

$$\begin{aligned}E'_z(r'_{q_T}, z'_{q_T}, t) = & -\frac{eN}{\epsilon_0}\left\{\frac{\beta_S}{L}\left[ctU(ct) - \left(ct - \frac{L}{\beta_S}\right)U\left(ct - \frac{L}{\beta_S}\right)\right] - U\left(ct - \frac{z'_{q_T}}{\beta_S}\right) - \dots\right. \\ & - \frac{2a\beta_S}{L}\sum_{m=1}^{m=\infty}\frac{J_0(r'_{q_T}\rho_m/a)}{J_1(\rho_m)\rho_m^2}\left[\sin\left(\rho_m\frac{ct}{a}\right) - \sin\left(\rho_m\frac{ct - L/\beta_S}{a}\right)U\left(ct - \frac{L}{\beta_S}\right)\right] - \dots \\ & - \frac{4a\beta_S}{L}\sum_{m=1}^{m=\infty}\sum_{n=1}^{n=\infty}\frac{J_0(r'_{q_T}\rho_m/a)}{J_1(\rho_m)}\rho_m \cdot \frac{\sin(\gamma_1 ct/a) - (-1)^n\sin(\gamma_1\frac{ct-L}{\beta_S a})U\left(ct - \frac{L}{\beta_S}\right)}{\gamma_1\gamma_2^2}\cos\left(\frac{n\pi z'_{q_T}}{L}\right) + \dots \\ & \left. + \frac{2}{\pi}\sum_{n=1}^{n=\infty}\frac{I_0(r'_{q_T}n\pi\gamma_S/L)}{nI_0(an\pi\gamma_S/L)}\left[\sin\left(n\pi\beta_S\frac{ct}{L}\right) - (-1)^n\sin\left(n\pi\beta_S\frac{ct - L/\beta_S}{L}\right)U\left(ct - \frac{L}{\beta_S}\right)\right]\cos\left(\frac{n\pi z'_{q_T}}{L}\right)\right\},\end{aligned} \tag{5}$$

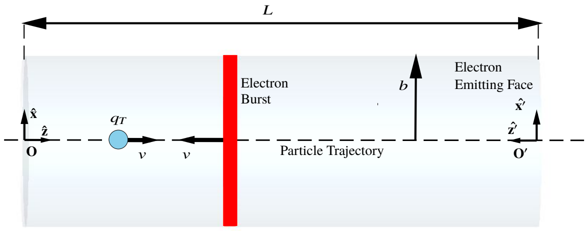


Figure 4: Pill-Box cavity excited by an electron burst emitted from one of the circular faces, counter-moving case scenario. Note that in this case the reference frame in which the wakefunction is needed, **O**, and the reference frame in which Eq. 5 gives the electric field, **O′**, are not coincident.

where, $N$ is the number of electrons per square meter, $J_0(x)$ is the Bessel function of order zero, $\rho_m$ are the roots of the Bessel function $J_0$, $I_0(x)$ is the modified Bessel function of order zero, $U(t)$ is the unit function, $\gamma_S = 1-\beta_S^2$, $\gamma_1^2 = \rho_m^2 + (n\pi a/L)^2$ and $\gamma_2^2 = \rho_m^2 + (n\pi a)^2(1-\beta_S^2)/L^2$. Furthermore, $r_{q_T}(t)'$ and $z_{q_T}(t)'$ are the generic radial and longitudinal position of a test particle T in a reference frame **O′** with origin in the electron emission face and $\hat{\mathbf{z}}'$ oriented in the direction of motion of the electrons. The electric field $E_z'$ given by Eq. 5 is also expressed in the **O′** reference frame. Finally, $t$ is the generic time. Considering the expression of the electric field in the device as a function of time, it is possible to compute the counter-moving wakefunction.

The geometry of the problem is drawn in Fig. 4. In the counter-rotating wakefield case the reference frame in which the wakefunction is defined, **O**, is not the same as that in which the longitudinal electric field of the electron disk is given by Eq. 5, **O′**. Indeed **O** has its origin in the test entrance section and its $\hat{\mathbf{z}}$ axis points in the direction of motion of T while **O′** has its origin in the source entrance section and its $\hat{\mathbf{z}}'$ axis points in the direction of motion of the electron burst, that is opposite to the one in which T is moving in the counter-rotating case, refer to Fig. 4. The quantities in **O′** are linked to the quantities in the **O** by the following equations:

$$\begin{aligned} r'_{q_T} &= r_{q_T} \\ z'_{q_T} &= L - z_{q_T} \\ E'_z &= -E_z. \end{aligned} \tag{6}$$

Considering Eq.s 6, the first two equations can be intuitively derived looking at Fig. 4, where both reference frame **O** and **O′** are represented. The third relation is true because the $z$ axes of the two frames point in opposite directions. Thus, if $E_z$ is positive in one of the frames, **O** for example, i.e. $E_z$ is directed as the $z$, it is naturally negative in the other, **O′**, i.e. $E_z$ is directed against $\hat{\mathbf{z}}$.

If $t = 0$ is chosen as the time at which the electron disk leaves the emitting face, the relation $z_{q_T}(t) = vt - \Delta s_{ST}$ holds as equation of motion of T. Substituting this relation into Eq.s 6 one has:

$$\begin{aligned} r'_{q_T} &= r_{q_T} \\ z'_{q_T} &= L - vt + \Delta s_{ST} = L - vt + v\Delta t_{ST} \\ E'_z &= -E_z, \end{aligned} \tag{7}$$

where, $v = v_S = v_T$ and Eq. 2 were used.

The counter-moving wakefunction is defined in a reference frame with the longitudinal axis towards the direction of motion of T, the **O** frame in this case. Thus, using Eq.s 7 into the expression of the longitudinal electric field, Eq. 5, the electric field can be rewritten in the wanted frame (**O**) as a function of time and entrance delay.

Once the electric field is know in the **O** frame, the longitudinal counter-moving wakefunction can be computed using Eq. 3. Note that only the electric field play a role in the Lorentz force along the direction of motion.

To obtain the counter-moving wakefunction one has to recall that, since $t = 0$ has been chosen as the time at which the source electron burst is emitted from the cavity surface, $\Delta t_{ST}$ represents also the time at which T enters into the pillbox cavity, thus: $t_{Ti} = \Delta t_{ST}$ and $t_{To} = t_{Ti} + \frac{L}{v}$. The last one of the previous relations is true because of the rigid beam approximation.

This process was repeated to compute also the longitudinal co-moving wakefunction. To do so, Eq. 3 was used and the longitudinal electric field acting on the test charge was computed using Eq. 5, considering the following relations instead of the Eq.s 6 and 7: $r'_{q_T} = r_{q_T}$, $z'_{q_T} = z_{q_T} = vt - v\Delta t_{ST}$, $E_z = E'_z$. These relations hold because in the co-moving case the reference systems **O** and **O′** are coincident, i.e. they have the same origin (the electron emission face that is also the entrance section of T) and their corresponding axis are oriented in the same way.

The co and counter-moving wakefunctions were numerically evaluated for the case in which both the electrons and the test particle are ultra-relativistic, i.e. $\beta_S = 1$ and $v = c$. As a function of the entrance delays, they are reported in Fig. 5 and their Fourier Transforms, the co and counter-moving impedance, in absolute values, are reported in Fig. 6.

Unfortunately, the real and imaginary part of the co-moving and counter-moving impedance were affected by high noise, thus, in this paper, a comparison of the real and imaginary part of the co-moving and counter-moving impedance is not reported. This comparison is left for future work.

To obtain the wakepotential, the wakefunction was numerically convolved with a beam distribution $\lambda_S$. The considered beam distribution was Gaussian.

To benchmark the validity of the calculations, numerical simulations were performed. Using the Particle in Cell (PIC) solver of CST, the excitation of a loss free pillbox (length $L =$ 0.6 m and radius $a = 0.1$ m) by a burst of electrons emitted by one of the circular face was simulated. The cavity material was set to be perfect electric conductor (PEC), so that the cavity was loss free. The electrons were emitted uniformly from the face with a Gaussian longitudinal distribution ($\sigma_b =$

0.07 m). One bunch of electrons with a total charge of 1 nC ($6.24 \cdot 10^9$ electrons) was emitted. The kinetic energy of the electrons was set to an ultra-relativistic value ($\gamma = 5 \cdot 10^{10}$) to avoid space charge effects. The total simulation time was set to 20 ns, electric field monitors were set to register and store the value of the longitudinal electric field every 1.5 mm along the whole cavity axis, that is every $5 \cdot 10^{-3}$ ns. The position of the test particle T is known at every time $t$ as a function of the entrance delay ($z_{q_T}(t) = vt - \Delta s_{ST} = vt - v\Delta t_{ST}$), i.e. fixing an entrance delay $\Delta s_{ST}$ or $\Delta t_{ST}$, one knows the T longitudinal position $z_{q_T}$ at the time $t$. If $z_{q_T}$ at the time $t$ is known, one can obtain the value of the longitudinal electric field acting on T at the time $t$ from the fields monitors. If this operation is repeated for every $t$ one obtains the longitudinal electric field experienced by T traversing the cavity as a function of time (or equivalently as a function of its longitudinal position). Integrating this longitudinal electric field one has the wakepotential value for the set entrance delay, and repeating the integration for different entrance delays gives the whole wakepotential.

The counter-rotating wakepotentials as a function of the entrance delay between $Q_S$ and T ($\Delta s_{Q_ST}$ and $\Delta t_{Q_ST}$) obtained from the formal model and the CST PIC solver are reported and compared in Fig. 7. The agreement between the two methods is excellent.

## DISCUSSION

In Fig. 5 the co-moving and counter-moving wakefield and wakepotential for a pill-box cavity excited by a burst of electrons were presented and compared.

Further, in Fig. 6, the co-moving and counter-moving longitudinal impedance are reported.

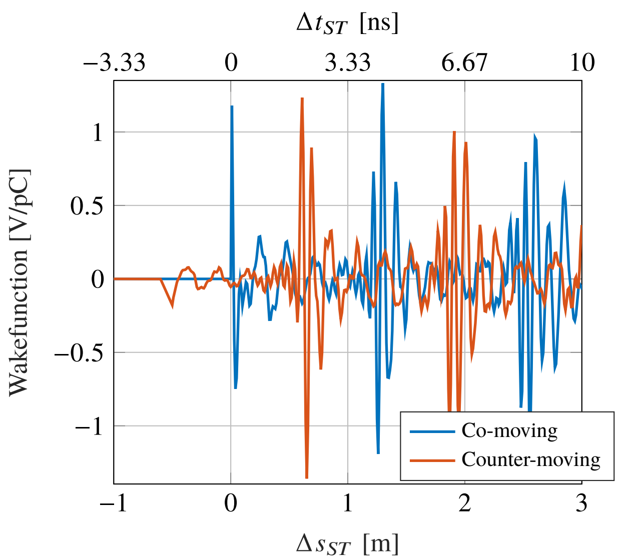


Figure 5: Comparison between the co-moving and the counter-moving wakefunction of a pill box cavity excited by a burst of electrons emitted by one of the faces. The wakefunctions have been obtained with the Faust theory.

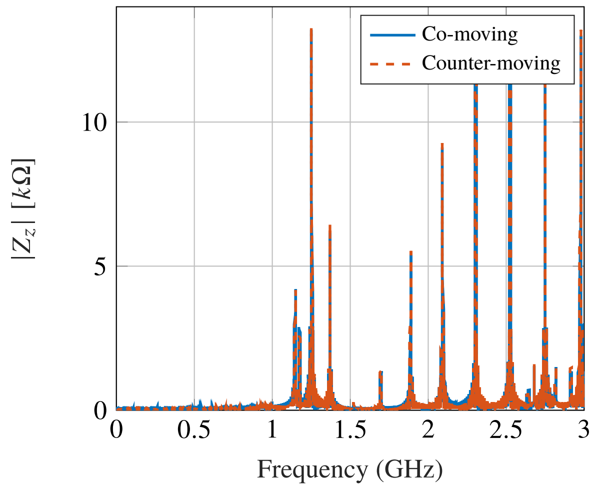


Figure 6: Comparison between the co-moving and the counter-moving impedance of a pill box cavity excited by a burst of electrons emitted by one of the faces.

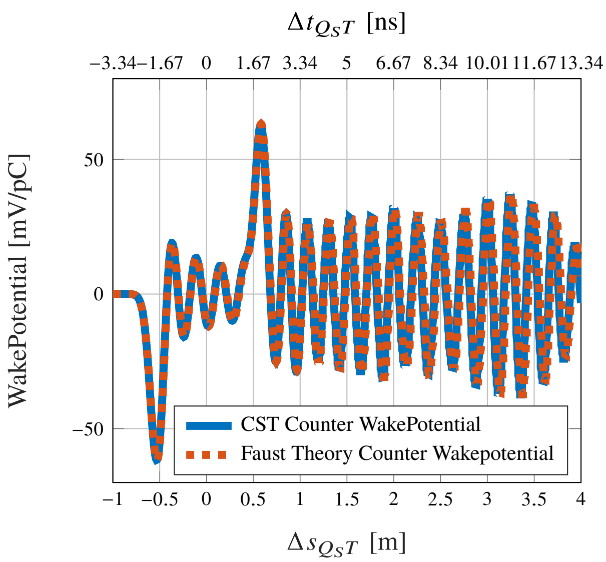


Figure 7: Comparison between the counter-moving wakepotentials of a burst of ultra-relativistic electrons (1 nC or $6.24 \cdot 10^9$ electrons and $\beta_S \to 1$ or $\gamma_S = 5 \cdot 10^{10}$) traversing a pill box cavity (length $L = 0.6$ m and radius $a = 0.1$ m) computed by the proposed model (Using the Faust Theory [17]) and the CST PIC solver [16]. The electrons are emitted uniformly from one of the circular faces of the cavity. Their longitudinal distribution is a Gaussian bunch ($\sigma_b = 0.07$ m). The cavity material is perfect electric conductor (PEC), loss free. Test particle speed is $v = c$.

Let us label as transient the interval of time for which the source particle is inside the cavity, ($\Delta s_{ST} < 0.6$ m for the discussed example), and as long range interval the period of time after the transient, i.e. $\Delta s_{ST} > 0.6$ m.

With reference to Fig. 5, co-moving and counter-rotating wakefunction are different in the transient region, around null entrance delay between T and S, while for further entrance delay they seem to be similar but translated. This indicates that the effects of the transient wakefield generated by S is experienced in a very different way if T moves in the same (co-moving wake) or in opposite (counter-moving) direction with respect to S. However, it appears that the effects of the long range wakefield generated by S are quite similar in both the co-moving and the counter-moving case. This makes sense since the long range interval is dominated by the resonant electromagnetic modes trapped in the pill-box, and the geometry of the mode fields and the mode resonant frequency is invariant with respect to the direction of the test particle. This last observation is backed up by the fact that, co-moving and counter-moving longitudinal impedance modulus compare very well, refer to Fig. 6, i.e. the resonant modes have similar effects on the test charge T independently from its propagation direction.

Finally, Fig. 7 compares the counter-moving wakepotential obtained using the proposed physical model (with the Faust equations) and the CST PIC solver simulations. There is an excellent agreement between the results of the proposed model and the results of the simulations. This can be thought both as a first benchmark for the proposed model, and for the CST software.

## CONCLUSION

This paper has introduced a physical model to define and quantify the wakefunction of two particle moving in opposite directions. The paper has first reviewed the two approximations on which the co-moving wakefunction definition is based, and it has been observed that they can be used also in the counter-moving case. Furthermore, the paper has introduced the concept of space and time entrance delay. Using them, a coherent physical model to describe the wakefield effects in the counter-moving case has been developed. It was also shown that such a model is suitable both for computing the co-moving wakefield and the counter moving one. An example of application of this model has been proposed: the co-moving and counter-moving wakefield of a lossless pill box cavity has been computed. The results of the method (the wakepotential) were benchmarked against numerical simulations results with excellent agreement.

Despite the results showed in the paper are preliminary, they are really encouraging because they show that the model can correctly estimate the wakefield effects in simple systems as a pill-box cavity. Future work will develop further this model, benchmarking it against other literature results and expanding it to obtain a quantification of the RF-heating induced by two counter rotating beams circulating in the same vacuum chamber. The authors strongly believe that the application of this model could be crucial in the design of the future high intensity accelerators interaction chambers and in the design of all the components traversed by two beams.

## ACKNOWLEDGEMENT

This work was partly supported by the European commission under HORIZON 2020 integrating activity project ARIES, grant agreement no 730871.

## REFERENCES

[1] J. Wang, "Transverse Two-Beam Instability," CERN, Tech. Rep., 1987. https://cds.cern.ch/record/183705

[2] A. W. Chao, *Physics of Collective Beam Instabilities in High Energy Accelerators*. Wiley-VCH, 1993.

[3] K. Ng, "Physiscs of Intensity Dependent Beam Instabilities," in *U.S. Particle Accelerator School (USPAS 2002) Long Beach, California, January 14-25*, 2002. http://lss.fnal.gov/cgi-bin/find_paper.pl?fn-0713

[4] K. L. F. Bane, P. B. Wilson, and T. Weiland, "Wake fields and wake field acceleration," in *AIP Conference Proceedings*, Stanford Linear Accelerator Center, vol. 127, AIP, 1985, pp. 875–928. DOI: 10.1063/1.35182. http://aip.scitation.org/doi/abs/10.1063/1.35182

[5] O. S. Bruning *et al.*, *LHC Design Report*, ser. CERN Yellow Reports: Monographs. Geneva: CERN, 2004. DOI: 10.5170/CERN-2004-003-V-1. http://cds.cern.ch/record/782076

[6] D. Carbajo Perez *et al.*, "OPERATIONAL FEEDBACK AND ANALYSIS OF CURRENT AND FUTURE DESIGNS OF THE INJECTION PROTECTION ABSORBERS IN THE LARGE HADRON COLLIDER AT CERN," *Proceedings, 8th International Particle Accelerator Conference (IPAC 2017): Copenhagen, Denmark, May 14-19*, 2017. DOI: 10.18429/JACoW-IPAC2017-WEPVA108.

[7] L. Teofili, M. Migliorati, D. Carbajo, I. Lamas, and A. Perillo, "Design of the Target Dump Injection Segmented (TDIS) in the Framework of the High Luminosity Large Hadron Collider (HL-LHC) Project," in *61st ICFA Advanced Beam Dynamics Workshop on High-Intensity and High-Brightness Hadron Beams*, Daejeon, Korea, 2018, pp. 122–126, ISBN: 9783954502028. DOI: 10.18429/JACoW-HB2018-TUP2WE04.

[8] B. Salvant *et al.*, "BEAM INDUCED RF HEATING IN LHC IN 2015," Tech. Rep., 2016.

[9] W. Herr and T. Pieloni, "Beam-Beam Effects," *CERN Yellow Reports*, no. 1, pp. 431–459, Jan. 2016. http://arxiv.org/abs/1601.05235%0Ahttp://dx.doi.org/10.5170/CERN-2014-009.431%20http://arxiv.org/abs/1601.05235%20http://dx.doi.org/10.5170/CERN-2014-009.431

[10] C. Pellegrini, "Longitudinal Coupled Bunch Instability for Two Counterrotating Beams," CERN, Tech. Rep., 1986. http://cds.cern.ch/record/170396

[11] S. Myers, *The LEP Collider, from design to approval and commissioning*, ser. John Adams' Lecture. Geneva: CERN, 1991, Delivered at CERN, 26 Nov 1990. DOI: 10.5170/CERN-1991-008. http://cds.cern.ch/record/226776

[12] F. Zimmermann, "Two-Beam Resistive-Wall Wake Field," in *Proceedings of PAC07*, Albuquerque, New Mexico, USA, 2007, pp. 4237–4239, ISBN: 1424409179.
[13] C. Zannini, G. Rumolo, G. Rumolo CERN, and G. Iadarola, "Power loss calculation in separated and common beam chambers of the LHC," CERN, Geneva, Switzerland, Tech. Rep., 2014. https://cds.cern.ch/record/1742192/files/CERN-ACC-2014-0122.pdf
[14] G. Rumolo and C. Zannini, "Beam induced power loss with two beams," CERN, Tech. Rep., 2018. https://indico.cern.ch/event/809558/contributions/3372399/attachments/1820527/2977428/Beam_induced_power_loss_with_two_beam_review.pdf
[15] A. Grudiev, "LHC Project Note 413 Simulation and reduction of longitudinal and transverse impedances of a collimation device with two beams in one vacuum chamber," CERN, Tech. Rep., 2008.
[16] CST Solvers, *CST Solvers Website*. https://www.3ds.com/products-services/simulia/products/cst-studio-suite/solvers/
[17] W. R. Faust, "Transient behavior of a cavity," *Journal of Applied Physics*, vol. 43, no. 10, pp. 3983–3987, 1972, ISSN: 00218979. DOI: 10.1063/1.1660860.

# Physics modelling and numerical simulation of beam-ion interaction in HEPS

Chao Li,[1,*] Saike Tian,[1] Na Wang,[1] Haisheng Xu,[1] and Qing Qin[1]

[1] *Key Laboratory of Particle Acceleration Physics and Technology, Institute of High Energy Physics, Chinese Academy of Sciences, 19(B) Yuquan Road, Beijing 100049, China*

The beam-ion interaction is one of the potential limitations of beam performance in ultra-low emittance electron rings. The High Energy Photon Source (HEPS), under construction in Beijing, is one example for which the beam-ion effect has to be carefully evaluated. In this paper, we will introduce the beam-ion interaction models applied in HEPS. Based on these models, a new numerical simulation code is developed. Currently, the code includes modules such as ionization, beam-ion interaction, synchrotron radiation damping, quantum excitation, bunch-by-bunch feedback etc. Settings such as weak-strong, strong-strong and arbitrary number of interaction points can be launched in the code. It will be shown that the beam instability excited by the beam-ion interaction can be effectively suppressed by the bunch-by-bunch feedback system.

PACS numbers: 41.75.-i, 29.27.Bd, 29.20.Ej
Keywords: Beam-Ion Effects, Bunch-By-Bunch Feedback System

## I. INTRODUCTION

The beam-ion interaction, a two-stream effect coupled by the nonlinear Coulomb force, may pose an operation risk in high intensity, low emittance electron rings. This effect has been observed in many existing machines such as ALS [1, 2], PLS [3], SSRF [4] CESR-TA [5], SOLEIL [6], etc. The accumulated ions, derived from ionization between electron particles and residual gas molecules, interact with the electron beam particles resonantly, causing coherent and incoherent electron beam deformation such as beam centroid oscillation, beam rms emittance growth, rms beam sizes increase, energy spread blow up, and even a possible beam loss.

In the previous studies, the beam-ion effect [7–9] is divided into two circumstances known as the ion trapping effect and the fast ion effect. In the ion trapping study, ions are usually assumed to be constant as an "equilibrium" state, which means the transient electron beam induced ionization is not taken into account. In the fast ion effect study, on the other hand, the ions are considered to be cleaned turn by turn. The ions generated in the first turn do not disturb the beam performance in the second turn, which means the memory of the ionization is erased turn by turn. Thus, the beam-ion trapping studies can be considered as an effect in a long term sense and the fast ion effect in a transient sense. In both cases, the ions generated by the leading bunches oscillate transversely and resonantly disturb the motions of the subsequent bunches – a coupled bunch instability.

Generally, the methodologies to mitigate the beam-ion effect are: (1) adjust the beam filling pattern by including empty buckets long enough in the bunch train; (2) get rid of ions with certain accelerator elements; (3) cure the beam-ion instability by introducing a feedback system before it grows [10]. The first approach can extensively reduce the number of accumulated ions. With sufficiently large empty gaps, the trapped ions would drift to large amplitudes, where they may get lost on the pipe or form a diffuse ion halo. However, this approach is a partial solution since the disturbed bunch can not erase the memory of its prior interaction with the ions. The beam deformation by the beam-ion interaction will accumulate and the influence could appear eventually. The second and the third approaches both require extra hardware, which brings in new sources of lattice impedance. However, the bunch-by-bunch feedback system is a versatile [11] technique, since it can be also adopted to suppress the beam instabilities due to impedances.

In the code developed by our group, the ion-trapping and fast ion effects are not distinguished but treated consistently. The code is bascially based on the "quasi-strong-strong" model, in which electron particles and ions are both represented by multiple macroparticles. Modules of ionization, beam-ion interaction, synchrotron radiation damping, quantum excitation and bunch-by-bunch feedback are also established. The HEPS [12] lattice is adopted as an example, to show the beam-ion interaction in simulation. This paper is organized as follows. In section II, the physical process and models of beam-ion interaction will be discussed briefly. The logic flow and basic numerical simulation approaches used will be given. In section III, the beam-ion instability and its mitigation with a bunch-by-bunch feedback system in HEPS will be given. A brief discussion and conclusion are given in Section IV.

* lichao@ihep.ac.cn

## II. PHYSICS MODEL AND NUMERICAL APPROACHES USED IN SIMULATION.

### A. Basic model of beam-ion interaction

Denote $P$ and $T$ as the residual gas pressure and temperature, the molecular density $n$ can be obtained,

$$PN_A = nRT, \tag{1}$$

where $R$ and $N_A$ are the ideal gas constant and the Avogadro number. Denoting $\sum$ as the ionization collision cross-section and $N_b$ as the number of electron particles passing by, the number of ions generated due to beam-residual gas collision per unit length is

$$\lambda = \sum nN_b. \tag{2}$$

For simplicity, we assume the beam-ion interaction is localized at the lumped interaction locations and only affects the beam transversely. In addition, ions generated do not move longitudinally. When the beam bunches pass through the interaction points one by one, new ions will be randomly generated within the sizes of the electron bunches passing by. The beam filling pattern decides the interval time of the generation of the new ions. The accumulated ions, generated due to the former passed bunches, interact with the passing beam bunch and thereafter freely drift in transverse until the next beam bunch comes. Meanwhile, some ions might get lost on the pipe. Due to the ion generation and loss mechanisms, a dynamical quasi-equilibrium ion distribution can be foreseen finally.

Figure 1 shows the logic flow of the simulations. $S_i$ represents the lumped interaction point. When one electron bunch passes by, the transverse momentum and position of the accumulated ions are updated according to the time interval from itself to next coming bunch. As to the bunched electron particles, after the momentum kicks induced by the accumulated ions, taking into account the effect of synchrotron radiation and quantum excitation, they are transferred to the next interaction point $S_{i+1}$ by applying a linear transport matrix $M(S_{i+1}|S_i)$.

### B. Coulomb interaction

In general, the motion equations of the $i$th accumulated ion $\vec{X}_i$ and the $k$th electron particle in the $j$th bunch $\vec{x}_{k;j}$ can be expressed as

$$\frac{d^2\vec{X}_i}{dt^2} + K_i(s)\vec{X}_i + \sum_{k=0}^{N_j} \vec{F}_C(\vec{X}_i - \vec{x}_{k;j}) = 0$$
$$\frac{d^2\vec{x}_{k;j}}{ds^2} + K_e(s)\vec{x}_{k;j} + \sum_{i=0}^{N_i} \vec{F}_C(\vec{x}_{k;j} - \vec{X}_i) = 0, \tag{3}$$

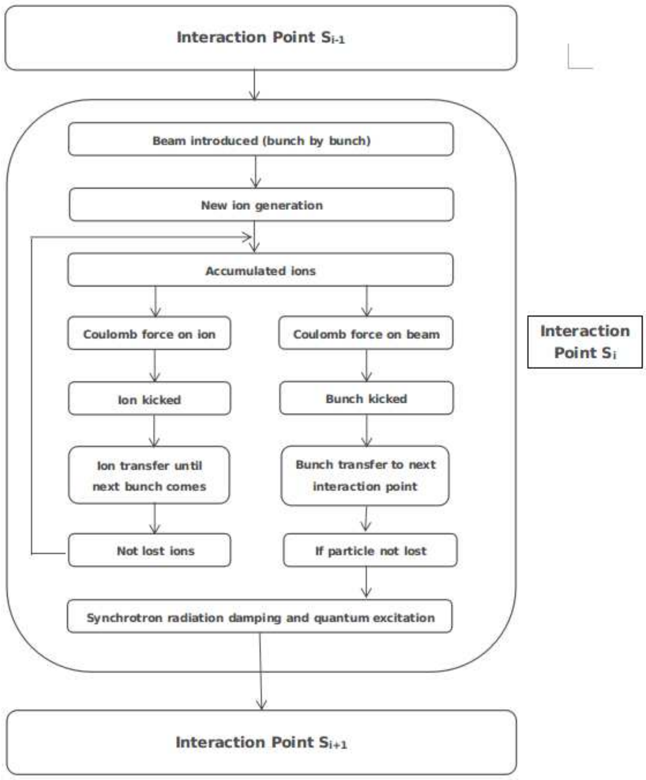


FIG. 1. Logic flow of the beam-ion interaction in simulation at the interaction points $S_i$. The ion generation, beam-ion interaction, beam and ion loss assertion, effect of synchrotron radiation and quantum excitation and beam transportation are sequentially calculated.

where $\vec{F}_C$ is the Coulomb force between the ions and electron particles, $K_i(s)$ and $K_e(s)$ represent the lattice focusing strength on ion and electron particle. In our model, since the bunched beam is assumed to follow the Gaussian distribution, the field generated by a beam bunch at spatial location $(x, y)$, with respect to the bunch centre, is obtained with the 2D Bassetti-Erskine formula [13] ,

$$E_{C,y} + iE_{C,x} = \frac{n_b}{2\epsilon_0\sqrt{2\pi(\sigma_x^2 - \sigma_y^2)}}\{w(\frac{x+iy}{\sqrt{2(\sigma_x^2-\sigma_y^2)}}) - \exp(-\frac{x^2}{2\sigma_x^2} - \frac{y^2}{2\sigma_y^2}) + w(\frac{x\frac{\sigma_y}{\sigma_x} + iy\frac{\sigma_x}{\sigma_y}}{\sqrt{2(\sigma_x^2-\sigma_y^2)}})\}\delta(s_i), \tag{4}$$

where $n_b$ is the line density of the electron beam, $w(z)$ is the complex error function, $i$ is the complex unit, $\sigma_x$ and $\sigma_y$ are the rms bunch size in x and y direction respectively. Substituting Eq. 4 into Eq. 3, the explicit momentum kick on ions is

$$\Delta p_{i,y} + i\Delta p_{i,x} = \frac{2n_b r_e m_e c}{\gamma_e}(E_{C,y} + iE_{C,x}), \tag{5}$$

where $r_e$ is the classical electron radius, $m_e$ is the electron mass, $\gamma_e$ is the relativistic factor of electron beam. The accumulated ion momentum change induced by the electron bunch passed by can be obtained by integrating Eq. 5 along the length of adjacent electron bunches.

As to the space charge potential well generated by the ions, since the ion distribution is usually not a Gaussian type, the Bassetti-Erskine formula is not suitable any more. A self-consistent particle-in-cell (PIC) [14] solver or ion density profile fitting [15] is needed to ensure a better resolution. In our model, a compromise approach is applied–the "quasi-strong-strong" model. The ion distribution is truncated at 10 rms bunch sizes. The rms and centroid information of the truncated ion distribution are substituted in the Bassetti-Erskine formula to get the Coulomb potential produced by the ions. Although this approach is not strictly correct, it still shows the main features of the bunched beam and can explore this complex coupled dynamics in a reasonable computing time.

### C. Beam transportation

We employ the accelerator coordinate $\boldsymbol{x} = (x, p_x, y, p_y, z, p_z)$ to describe the motion of particles. Here $x$, $y$, $z$ are horizontal, vertical and longitudinal coordinates respectively, while $p_x$, $p_y$, $p_z$ are the corresponding momenta normalized by the total momentum of a reference particle. Following Hirata's BBC code [16], in general the transportation consists of the following steps.

#### 1. *From accelerator coordinates to normalized coordinates*

The transformation from accelerator variable $\boldsymbol{x}$ to normalized variable $\boldsymbol{X}$ can be written as

$$\boldsymbol{X} = \boldsymbol{BRHx}, \tag{6}$$

here $\boldsymbol{H}$ is the dispersion matrix characterized by the transverse dispersion functions $D_x$, $D_{px}$, $D_y$, $D_{py}$; $\boldsymbol{R}$ is the Teng matrix representing the coupling between the horizontal and vertical planes; $\boldsymbol{B}$ represents the Twiss matrix. More details can also be found in Ref. [17].

In our study, the dynamic is limited to the transverse plane, furthermore, the beam-ion interaction is assumed to take place in the dispersion and coupling free region so that the $\boldsymbol{H}$ and $\boldsymbol{R}$ are further degenerated to the unit matrix.

#### 2. *Synchrotron radiation and quantum excitation*

With the Synchrotron radiation and quantum excitation effects, the transportation in the normalized coordinates is

$$\begin{pmatrix} \boldsymbol{X_1} \\ \boldsymbol{X_2} \end{pmatrix} = \lambda_x \begin{pmatrix} \boldsymbol{X_1} \\ \boldsymbol{X_2} \end{pmatrix} + \sqrt{\epsilon_x(1-\lambda_x^2)} \begin{pmatrix} \boldsymbol{\hat{r}_1} \\ \boldsymbol{\hat{r}_2} \end{pmatrix}, \tag{7}$$

$$\begin{pmatrix} \boldsymbol{X_3} \\ \boldsymbol{X_4} \end{pmatrix} = \lambda_y \begin{pmatrix} \boldsymbol{X_3} \\ \boldsymbol{X_4} \end{pmatrix} + \sqrt{\epsilon_y(1-\lambda_y^2)} \begin{pmatrix} \boldsymbol{\hat{r}_3} \\ \boldsymbol{\hat{r}_4} \end{pmatrix}. \tag{8}$$

Here $\hat{r}$'s are independent Gaussian random variables with unit variance, $\lambda_i = \exp(-1/T_i)$ with $T_i$ the damping time in units of the number of turns.

#### 3. *From normalized coordinates to accelerator coordinates*

The coordinates transformation from normalized variable $\boldsymbol{X}$ to accelerator variable $\boldsymbol{x}$,

$$\boldsymbol{x} = \boldsymbol{H}^{-1}\boldsymbol{R}^{-1}\boldsymbol{B}^{-1}\boldsymbol{X}. \tag{9}$$

#### 4. *Beam transportation from interaction point $S_i$ to $S_{i+1}$*

The beam transportation is modelled by a linear map

$$\boldsymbol{x(S_{i+1})} = M(S_{i+1}|S_i)\boldsymbol{x(S_i)}. \tag{10}$$

### D. Bunch-by-bunch feedback system

In time domain, Eq. 11 is the general form of a FIR filter

$$\Theta_n = \sum_{k=0}^{N} a_k x_{n-k}, \tag{11}$$

where $a_k$ represents the filter coefficient, $x_{n-k}$ and $\Theta_n$ are the input and output of the filter, corresponding to beam position data at the $(n-k)$th turn and kick strength on the beam at the $n$th turn. The number of the input data $N+1$ is defined as taps. Following the approaches shown in Ref. [18], the time domain least square fitting (TDLSF) method is used to get the filter coefficients $a_k$.

In the code, the beam momentum change by the bunch-by-bunch feedback at the $n$th turn is modelled as

$$\Theta_{x,n} = K_x \sum_{k=0}^{N} a_{k,x} x_{n-k},$$
$$\Theta_{y,n} = K_y \sum_{k=0}^{N} a_{k,y} y_{n-k}, \tag{12}$$

here $x_{n-k}$ and $y_{n-k}$ are the beam centroids of the $k$th previous turn at the pickup. The beam motion transfer function in one turn including feedback is

$$\left[\begin{pmatrix} x_{n+1} \\ x'_{n+1} \\ y_{n+1} \\ y'_{n+1} \end{pmatrix}\right] = M_0 \left[\begin{pmatrix} x_n \\ x'_n \\ y_n \\ y'_n \end{pmatrix} + \begin{pmatrix} 0 \\ \Theta_{x,n} \\ 0 \\ \Theta_{y,n} \end{pmatrix}\right], \tag{13}$$

where $M_0$ is the one turn matrix at the kicker.

TABLE I. HEPS Lattice Parameters

| Parameters | Values |
|---|---|
| Energy | 6 GeV |
| Circumference | 1360.4 m |
| Nominal emittance | 34.2 pm |
| Working points | 114.14/106.23 |
| Number of super-periods | 24 |
| Average betatron function | 4.5/8.1 m |
| Number of RF buckets | 756 |
| Beam current | 200 mA |
| SR damping time (x/y) | 2386/4536 turns |
| rms beam size (x/y) | 12.4/5.26 $\mu$m |
| Ion species | CO |
| Gas pressure | 1 nTorr |
| Gas temperature | 300 K |

## III. SIMULATION STUDY OF BEAM-ION INTERACTION IN HEPS.

HEPS is a 1.3 km ultra-low emittance electron storage photon source being built in Beijing, China. The main parameters of the HEPS lattice are listed in Tab. I. Carbon monoxide (CO) with a temperature 300 K and pressure 1 nTorr is assumed as the main leaked gas. In the following study, the total electron beam current 10 mA is adopted to evaluate the beam-ion effect. To save computing time, one beam-ion interaction point is set per turn. However, the setting of multi-interaction points is necessarily to investigate due to the variation of the betatron and dispersion functions. The beam filling pattern is one continuous bunch train following 76 empty bunch gaps. The synchrotron radiation damping and quantum excitation [17] are both taken into account.

As to the bunch-by-bunch feedback system, constrained by the maximum kicker power 1 KW, a 9-taps FIR filter is designed to launch the signal processing. The FIR filter coefficients, frequency response of phase and gain of the 9-taps filters is shown in Fig. 2. For clarity, the pickup and kicker are assumed to be located at the same place with zero dispersion, which means the phase responses at target tunes are -90 degrees.

In the weak-strong simulation, a comparison at the 5000th turn with and without feedback is explicitly shown in Fig. 3. When the bunch-by-bunch feedback is turned on, the maximum bunch action $\sqrt{J_y}$ is well maintained around 0.1 rms beam size, Fig. 3a; the bunch oscillations due to beam-ion interaction are well eliminated, Fig. 3b; the power spectrum of bunch oscillations is roughly one order of magnitude smaller Fig. 3c. The position of the unstable bunch modes does not shift since the intrinsic beam-ion interaction is not violated.

As to the strong-strong simulations, Fig. 4 shows the emittance evolution as the function of tracking turns when the bunch-by-bunch feed back is turned on and off. As suspected, the beam emittance in $y$ direction is well suppressed. More simulations and discussion in detail can be found in Ref. [19].

## IV. CONCLUSIONS

In this paper, we have discussed the beam-ion instability and its mitigation by the bunch-by-bunch feedback system. To study the beam-ion interaction consistently, a simulation code is developed including modules such as ionization, beam-ion interaction, synchrotron radiation damping, quantum excitation and bunch-by-bunch feedback. As an example, the lattice parameters of the HEPS project are adopted to show the influence of the beam-ion instability and its mitigation.

## ACKNOWLEDGMENTS

This work is supported by the Key Research Program of Frontier Sciences CAS (QYZDJ-SSW-SLH001) and NSFC (11775239, 11805217). Special thanks to professor Takeshi Nakamura in Synchrotron Radiation Research Institute in Japan for his helpful discussion on FIR filters.

[1] F. Zimmermann, A. Chao, S. Heifets, M. Minty, J. Seeman, G. Stupakov, J. Byrd, J. Thomson, and T. Raubenheimer, *Experiments on the fast beam-ion instability at the ALS*, Tech. Rep. (Stanford Univ., Stanford Linear Accelerator Center, CA (US);, 1997).
[2] J. Byrd and A. Chao, Phys. Rev. Lett. **79**, 79 (1997).
[3] M. Kwon, J. Y. Huang, T.-Y. Lee, I. S. Ko, Y. H. Chin, H. Fukuma, M. Isawa, K. Ohmi, and M. Tobiyama, Phys. Rev. E **57**, 6016 (1998).
[4] B. Jiang, G. Xia, L. Han, G. Liu, Z. Dai, and Z. Zhao, Nuclear Instruments and Methods in Physics Research Section A: Accelerators, Spectrometers, Detectors, and Associated Equipment **614**, 331 (2010).
[5] A. Chatterjee, K. Blaser, M. Ehrlichman, D. Rubin, and J. Shanks, in *Proceedings, 5th International Particle Accelerator Conference (IPAC 2014): Dresden, Germany, June 15-20, 2014* (2014) p. TUPRI036.
[6] R. Nagaoka, M. P. Level, L. Cassinari, M. E. Couprie, M. Labat, C. Mariette, A. Rodriguez, and R. Sreedharan, in *2007 IEEE Particle Accelerator Conference (PAC)* (2007) pp. 2019–2021.
[7] T. Raubenheimer and F. Zimmermann, Physical Review E **52**, 5487 (1995).
[8] G. Stupakov, T. Raubenheimer, and F. Zimmermann, Physical Review E **52**, 5499 (1995).
[9] K. Ohmi, Phys. Rev. E **55**, 7550 (1997).

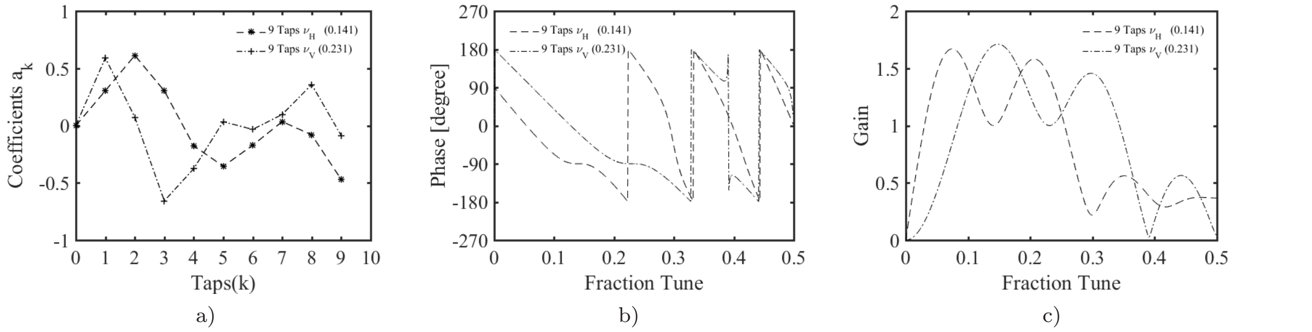


FIG. 2. FIR filter coefficients (a), frequency response of phase (b) and gain (c) of the 9-taps filters used in a bunch-by-bunch feedback system. The horizontal and vertical target tunes are 0.141 and 0.231.

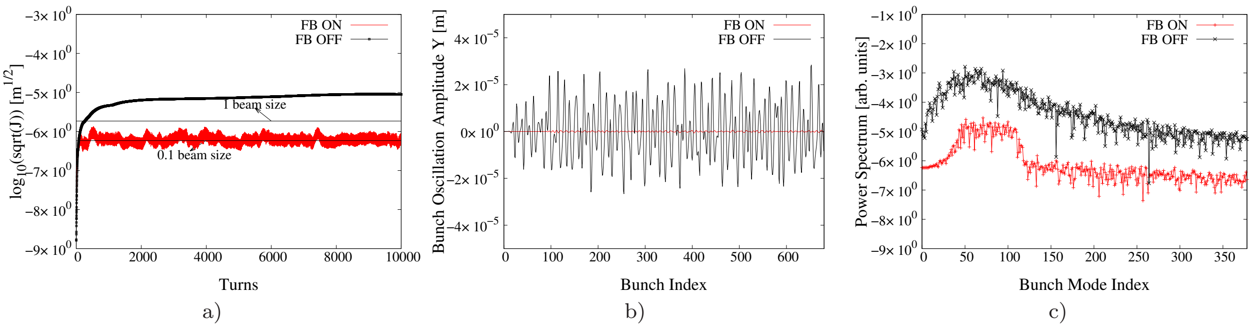


FIG. 3. The red and black curve show the maximum beam actions (a), the beam bunches oscillations (b) and the related coupled bunch modes power spectrum (c) in vertical plane with and without bunch-by-bunch feedback at the 5000th turns. The results are obtained from the “weak-strong” model taking the synchrotron radiation damping into account.

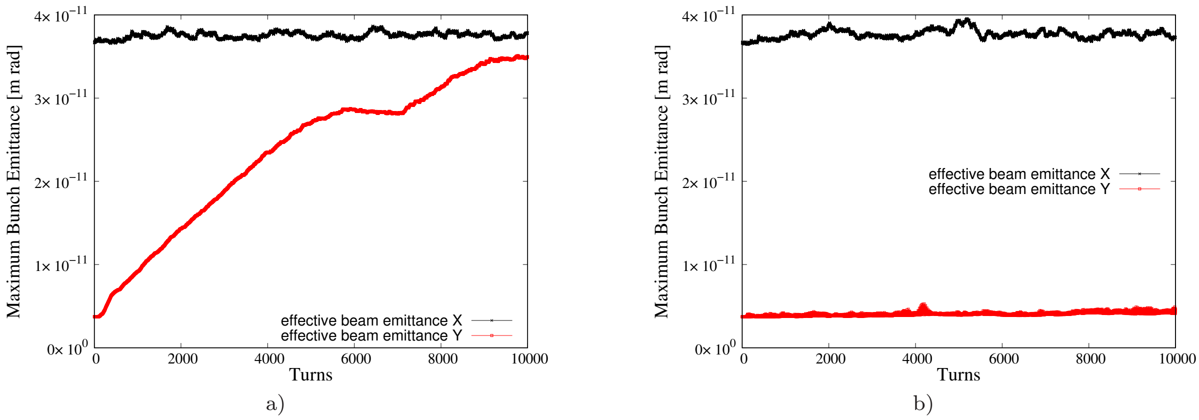


FIG. 4. The maximum bunch emittance references to the ideal orbit as function of passing turns without (a) and with (b) bunch-by-bunch feedback; The synchrotron radiation damping is taken into account. The beam current is 10 mA and the simulation results are given by “quasi-strong-strong” model.


[10] L. Wang, Y. Cai, T. Raubenheimer, and H. Fukuma, Physical Review Special Topics-Accelerators and Beams **14**, 084401 (2011).

[11] M. Lonza and H. Schmickler, “Multi-bunch feedback systems,” (2016), arXiv:1601.05258 [physics.acc-ph].

[12] Y. Jiao, G. Xu, X.-H. Cui, Z. Duan, Y.-Y. Guo, P. He, D.-H. Ji, J.-Y. Li, X.-Y. Li, C. Meng, Y.-M. Peng, S.-K. Tian, J.-Q. Wang, N. Wang, Y.-Y. Wei, H.-S. Xu, F. Yan, C.-H. Yu, Y.-L. Zhao, and Q. Qin, Journal of Synchrotron Radiation **25**, 1611 (2018).

[13] Bassetti, M and Erskine, George A, *Closed expression for the electrical field of a two-dimensional Gaussian charge*, Tech. Rep. CERN-ISR-TH-80-06. ISR-TH-80-06 (CERN, Geneva, 1980).

[14] C. Li, Z.-L. Zhang, X. Qi, X.-B. Xu, Y. He, and L. Yang, Chinese Physics C **38**, 037005 (2014).

[15] https://ops.aps.anl.gov/manuals/elegant_latest/elegant.pdf.
[16] K. Hirata, CERN SL Note 97-57 AP (1997).
[17] Y. Zhang, K. Ohmi, and L. Chen, Phys. Rev. ST Accel. Beams **8**, 074402 (2005).
[18] T. Nakamura, "single-loop muli-dimensional digital feedback by fir filters," http://acc-web.spring8.or.jp/~nakamura/reports/Feedback_with_FIR_Filter_draft1.pdf.
[19] C. Li, S. Tian, N. Wang, and H. Xu, Phys. Rev. Accel. Beams **23**, 074401 (2020).

# IMPLEMENTATION OF RF MODULATION IN BOOSTER FOR MITIGATION OF THE COLLECTIVE EFFECTS IN THE TRANSIENT PROCESS AFTER THE SWAP-OUT INJECTION *

Haisheng Xu†, Zhe Duan‡, Na Wang§, Gang Xu¶
Key Laboratory of Particle Acceleration Physics and Technology,
Institute of High Energy Physics, Chinese Academy of Sciences, Beijing, China

*Abstract*

On-axis swap-out injection is a promising injection scheme for the diffraction-limited storage rings with small dynamic apertures. However, some previous studies have shown that the initial mismatch in the longitudinal phase space may lead to transverse collective instability before approaching the equilibrium state, especially in the high bunch charge situation. We present our study of mitigating the collective effects in the transient process after injecting beam into storage rings by implementing RF modulation technique in booster. Both bunch lengthening and the increase of energy spread could be observed in the extracted bunch from booster. The reduction of particle loss in the transient process after the swap-out injection is demonstrated via simulations.

## INTRODUCTION

The development of the next generation synchrotron light sources, which are based on the diffraction-limited storage rings (DLSRs), has been the frontier of the synchrotron light source community for years. Generally speaking, stronger focusing is needed to reach the ultra-low emittance, with the drawback that the natural chromaticities are usually large negative values. To correct the chromaticities to an acceptable level, one has to implement very strong sextupole magnets, which eventually, limit the dynamic aperture (DA). The limited DA of the DLSRs provides great challenges to the injection. It therefore triggers a plenty of research in developing injection schemes for the DLSRs, in which, the on-axis swap-out injection scheme [1, 2] is one of the promising injection schemes.

High Energy Photon Source (HEPS) [3], which is a 6 GeV DLSR-based synchrotron light source, is currently under civil construction in Beijing, China. The on-axis swap-out injection scheme has been chosen as the baseline injection scheme of the 6-GeV storage ring of HEPS. There are two operation modes, named the "High-Brightness Mode" (680 bunches, 200 mA) and the "High-Bunch-Charge Mode" (63 bunches, 200 mA), proposed for the HEPS storage ring. The injection of a 14.4 nC bunch, corresponding to the "High-Bunch-Charge Mode", is very challenging for both the injector and the storage ring. Recent study [4] indicated that the injection transient instability, which was essentially a 'head-tail' type, transverse single-bunch instability, might seriously limit the achievable single-bunch charge in the HEPS storage ring. Many possibilities to cure the injection transient instability have been also proposed and discussed in [4]. Simulations showed that the higher transmission efficiency can be expected if the length of the injected bunch can be longer. This fact inspired us to try lengthening the bunch in booster before extraction, in order to cure the injection transient instability in the storage ring. In this paper, we would like to present our studies on the implementation of RF modulation in the HEPS booster, which is one possible way to lengthen the bunch in the booster.

The rest of the paper will be arranged as follows: firstly, the basic theories of the RF modulation will be reviewed. Afterwards, the results of the tracking simulations will be presented. Conclusions and discussions will be presented at the end.

## THEORY OF RF MODULATION

Generally speaking, any arbitrary signal added up to the ideal RF signal becomes the so-called RF modulation, e.g., the white noise on top of RF signal. However, this kind of broad-band modulation was usually called "RF noise" instead of "RF modulation". In the following text, when we mentioned 'RF modulation', we actually limited ourselves to the situations where a single frequency sinusoidal RF modulation was considered.

In this section, we mainly followed the analyses of the effects of a single-frequency sinusoidal RF voltage modulation and RF phase modulation in [5] to understand the effectiveness of both above mentioned modulation methods. No synchrotron radiation effect was taken into account in the analyses of this section.

The Eq.(3.111) and Eq.(3.112) in [5] represent the equations of synchrotron motion in the normalized phase space $(\phi, \mathcal{P})$ with RF voltage modulation, where $\mathcal{P}$ is the normalized momentum deviation defined by $\mathcal{P} = -h|\eta|\delta/\nu_s$. We hereby rewrote the above mentioned two equations in the $(\phi, \delta)$ phase space, shown as Eq.(1) and Eq.(2), and carried

* Work supported by National Natural Science Foundation of China (No. 11805217, No. 11775239, and No. 11605212), NKPSTRD (2016YFA0402001), and Key Research Program of Frontier Sciences CAS (QYZDJ-SSW-SLH001)
† xuhs@ihep.ac.cn
‡ duanz@ihep.ac.cn
§ wangn@ihep.ac.cn
¶ xug@ihep.ac.cn

out the analyses from these equations.

$$\phi_{n+1} = \phi_n + 2\pi h\eta\delta_n \quad (1)$$

$$\delta_{n+1} = \delta_n + V_{RF}\left[1 + \delta V_m \sin\left(\nu_m\theta_{n+1} + \chi\right)\right] \cdot \frac{e}{\beta^2 E_0} \cdot \left(\sin\phi_{n+1} - \sin\phi_s\right) \quad (2)$$

where $h$ represents the harmonic number; $\eta$ is the the phase slip factor; $E_0$ represents the total energy of the reference particles; $V_{RF}$ stands for the peak RF voltage; $\phi_s$ is the synchronous phase; $\delta V_m = \Delta V / V_{RF}$ is the fractional RF voltage modulation amplitude; $\nu_m = \omega_m/\omega_0$ is the modulation tune, where $\omega_m$ stands for the angular frequency of the modulation; $\theta = \omega_0 t$ is the orbital angle; $\chi$ is the phase of the modulation signal.

By plugging the optical parameters of a candidate lattice of the HEPS booster in Eq.(1) and Eq.(2) and solving the mapping equations, we could obtain the particles' distribution in the longitudinal phase space $(\phi, \delta)$. A preliminary result, in $(z, \delta)$ phase space with the definition of $z = C\left(\phi - \phi_s\right)/2\pi h$, is shown in Figure 1. Here the modulation amplitude $\delta V_m$ was set as 15%, while the modulation tune $\nu_m$ was set as $2\nu_s$. Figure 1(a) shows the particles' equilibrium distribution in the $(z, \delta)$ phase space without turning on the RF voltage modulation. Using the distribution as the initial state, and tuning on the RF voltage modulation with the above mentioned settings, we got the particles' distribution in the 20,000th turn, as shown in Figure 1(b). The structure indicating the second-order parametric resonance driven by the voltage modulation can be clearly seen in Figure 1(b).

Following the corresponding equations in [5], we've obtained the synchrotron mapping equations with RF phase modulation as Eq.(3) and Eq.(4):

$$\phi_{n+1} = \phi_n + 2\pi h\eta\delta_n + \left[\delta P_m \sin\left(\nu_m\theta_{n+1} + \chi\right) - \delta P_m \sin\left(\nu_m\theta_n + \chi\right)\right] \quad (3)$$

$$\delta_{n+1} = \delta_n + \frac{eV_{RF}}{\beta^2 E_0}\left(\sin\phi_{n+1} - \sin\phi_s\right) \quad (4)$$

where $\delta P_m$ represents the RF phase modulation amplitude, $\nu_m$ is the phase modulation tune.

Using the similar approach as mentioned above for the study of RF voltage modulation, we set up the RF phase modulation amplitude and modulation tune as $\delta P_m = 0.1$ rad and $\nu_m = 2\nu_s$, respectively. The equilibrium particles' distribution without RF phase modulation is given in Figure 2(a). The particles' distribution in the 20,000th turn after turning on the phase modulation is given in Figure 2(b). Similarly, the effectiveness of the phase modulation was demonstrated as the parametric resonance structure shown in Figure 2(b).

## TRACKING SIMULATIONS

In the previous section, we demonstrated the effectiveness of both the RF voltage modulation and the RF phase modulation on bunch lengthening using the existing theories. However, we got information [6] that the RF phase modulation is generally less challenging than the voltage modulation in the high-power operation of the cavities. We therefore would like to continue the study of RF phase modulation only as suggested.

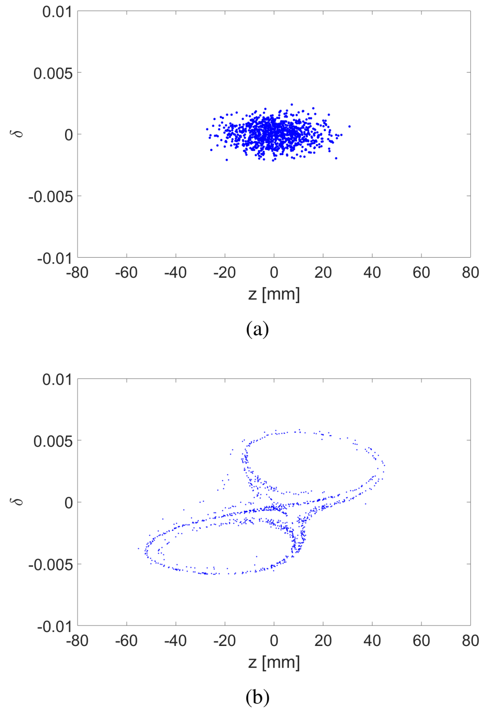


Figure 1: Particles' distributions in the longitudinal phase space $(z, \delta)$. (a): equilibrium distribution without voltage modulation; (b): particles' distribution in the 20,000th turn after turning on the voltage modulation with the amplitude $\delta V_m = 15\%$ and the modulation tune $\nu_m = 2\nu_s$.

However, the main purpose of implementing the RF modulation technique in booster is to suppress the injection transient instability in the storage ring. Therefore, the demonstration of the effectiveness of RF modulation is only the first step. The second step is to double check whether the injection efficiency can benefit from the modulated bunch. We hereby first generated the turn-by-turn bunch distribution by multi-particle tracking (the multi-particle tracking code `elegant` [7] was used), and then used these distributions as initial bunches for the storage ring to study the injection efficiency. Element-by-element tracking, with the consideration of both the transverse and longitudinal broad-band impedance, was carried out to check the injection efficiency.

We first carried out the multi-particle tracking in booster with RF phase modulation. The modulation amplitude and the modulation tune are set as $\delta P_m = 10°$ and $\nu_m = 2\nu_s$, respectively. The turn-by-turn data of both the bunch length and energy spread are shown in Figure 3.

Figure 3 indicates that both the bunch length and energy spread oscillate violently turn-by-turn. However, it's very difficult to make sure always extracting the bunch at a certain bunch length. We selected the data in 100 continuous turns as examples, and carried out element-by-element tracking in

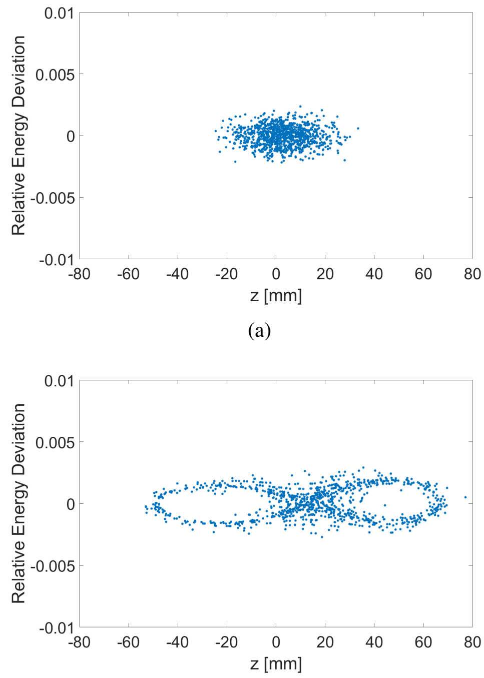


(a)

(b)

Figure 2: Particles' distributions in the longitudinal phase space $(z, \delta)$. (a): equilibrium distribution without phase modulation; (b): particles' distribution in the 20,000th turn after turning on the phase modulation with the amplitude $\delta P_m = 0.1$ rad and the modulation tune $\nu_m = 2\nu_s$.

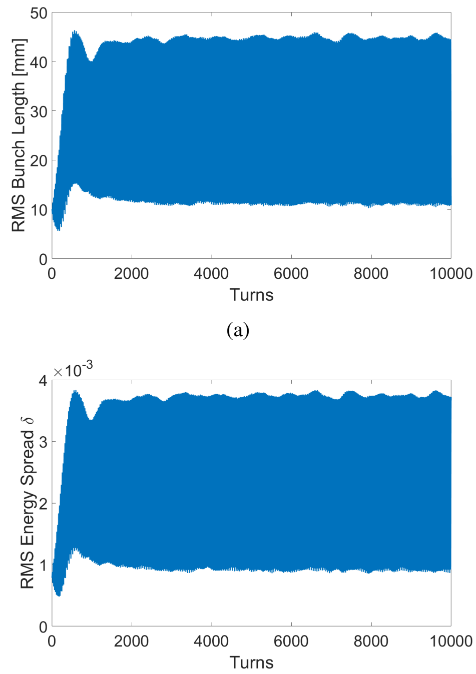


(a)

(b)

Figure 3: Turn-by-turn data after turning on RF phase modulation at the 0th turn. (a): RMS bunch length vs. turns; (b): RMS energy spread vs. turns.

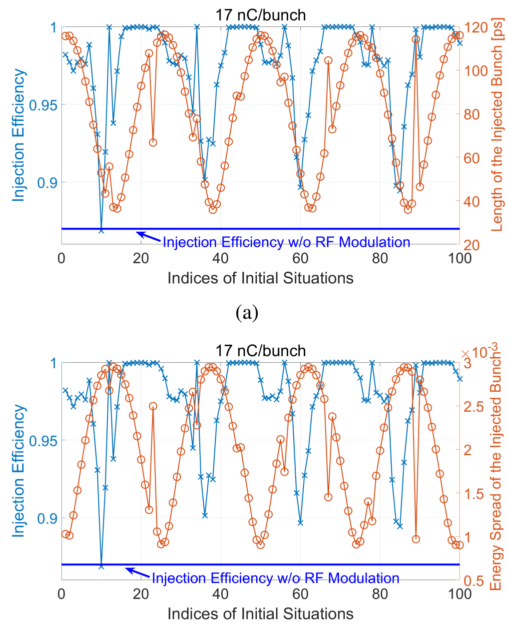


(a)

(b)

Figure 4: Turn-by-turn data after turning on RF phase modulation at the 0th turn. (a): RMS bunch length vs. turns; (b): RMS energy spread vs. turns.

the storage ring for each case. The injection efficiency, RMS bunch length, and RMS energy spread of the 100 cases are given in Figure 4.

Comparing to the injection efficiency without RF modulation, one can see clearly that most of the cases with RF modulation correspond to higher injection efficiency. The cumulative distribution function shown in Figure 5 shows that the possibility of getting injection efficiency higher than 95% is above 80%, which is significantly higher than the injection efficiency without RF modulation (about 87%).

## CONCLUSIONS AND DISCUSSIONS

For improving the injection efficiency in HEPS storage ring, we proposed to implement RF modulation technique in the booster before extracting bunches.

The effectiveness of both RF voltage modulation and RF phase modulation on bunch lengthening was demonstrated using the existing theories. We then continued the studies of RF phase modulation and the influence on injection efficiency by carrying out multi-particle tracking. Tracking results confirmed the effectiveness of RF phase modulation on increasing the injection efficiency.

However, in the preliminary studies, we didn't pay much attention in the optimization of the settings. There are still many parameters, such as the modulation tune and the modulation amplitude, needed further optimizations. Furthermore, many technical tests, proposed by us together with our RF experts, are needed to double check the possibility of implementing RF phase modulation in HEPS Booster.

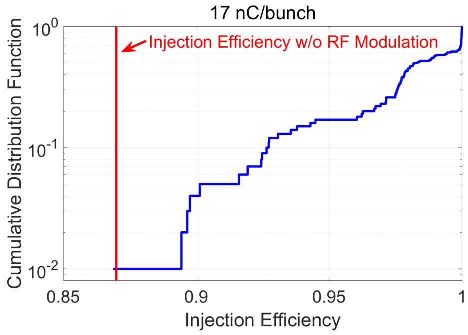


Figure 5: Cumulative distribution function

## ACKNOWLEDGMENT

The authors would like to thank the colleagues in Accelerator Physics Group of IHEP for the fruitful discussions.

The simulations were mainly carried out on the cluster operated by the IHEP computing center. The authors would like to thank the staff in the IHEP computing center for their kind support.

## REFERENCES

[1] R. Abela, W. Joho, P. Marchand, S. V. Milton, and L. Z. Rivkin. Design Considerations for a Swiss Light Source (SLS). In *Proceedings, Third European Particle Accelerator Conference (EPAC 92): Berlin, Germany, March 24-28, 1992*, pages 486–488, 1992.

[2] L. Emery and M. Borland. Possible Long-Term Improvements to the Advanced Photon Source. In *Proceedings, the 2003 Particle Accelerator Conference (PAC 2003): Portland, Oregon, U.S.A, May 12-16, 2003*, page TOPA014, 2003.

[3] Yi Jiao, Gang Xu, Xiao-Hao Cui, Zhe Duan, Yuan-Yuan Guo, Ping He, Da-Heng Ji, Jing-Yi Li, Xiao-Yu Li, Cai Meng, Yue-Mei Peng, Sai-Ke Tian, Jiu-Qing Wang, Na Wang, Yuan-Yuan Wei, Hai-Sheng Xu, Fang Yan, Cheng-Hui Yu, Ya-Liang Zhao, and Qing Qin. The HEPS project. *Journal of Synchrotron Radiation*, 25(6):1611–1618, Nov 2018.

[4] Z. Duan, N. Wang, and H.S. Xu. Simulations of the Injection Transient Instabilities for the High Energy Photon Source. In *Proc. 10th International Particle Accelerator Conference (IPAC'19), Melbourne, Australia, 19-24 May 2019*, number 10 in International Particle Accelerator Conference, pages 1524–1527, Geneva, Switzerland, Jun. 2019. JACoW Publishing. https://doi.org/10.18429/JACoW-IPAC2019-TUPGW053.

[5] S Y Lee. *Accelerator Physics*. WORLD SCIENTIFIC, 3rd edition, 2011.

[6] Private Communication with Mr. Q. Y. Wang and Dr. P. Zhang.

[7] M. Borland. elegant: A flexible sdds-compliant code for accelerator simulation. *Advanced Photon Source LS-287*, September 2000.

# MEASUREMENTS AND DAMPING OF THE ISIS HEAD-TAIL INSTABILITY

R. E. Williamson*, B. Jones, A. Pertica, D. W. Posthuma de Boer, C. M. Warsop,
ISIS, Rutherford Appleton Laboratory, STFC, UK
J. P. O. Komppula, CERN, Geneva, Switzerland

*Abstract*

ISIS is the pulsed spallation neutron and muon source at the Rutherford Appleton Laboratory in the UK. Operation centres on a rapid cycling proton synchrotron (RCS) which accelerates $3\times10^{13}$ protons per pulse from 70 MeV to 800 MeV at 50 Hz, delivering a mean beam power of 0.2 MW.

Research and development at ISIS are focused on key aspects of high intensity operation with a view to increasing beam intensity on target, understanding loss mechanisms and identifying viable upgrade routes. At present, the main limitation on beam intensity at ISIS is beam loss associated with the head-tail instability.

This paper presents new measurements of the head-tail instability in both RCS and storage ring modes whilst highlighting the differences between these and theoretical predictions. Macro-particle simulations of the instability are shown in comparison with experimental data. Finally, preliminary tests of an active transverse feedback system to damp the instability are also presented.

## INTRODUCTION

The head-tail instability is a primary concern for high intensity operation in many hadron synchrotrons including ISIS and its proposed upgrades [1]. The instability imposes an intensity limit on operations through associated beam loss and consequent undesired machine activation.

### *The ISIS Synchrotron*

ISIS operation centres on a 10 superperiod rapid cycling synchrotron (RCS) with a 163 m circumference. It accelerates $3\times10^{13}$ protons per pulse from 70 – 800 MeV on the 10 ms rising edge of a sinusoidal main magnet field (below transition throughout). The repetition rate of 50 Hz results in an average beam power on target of 0.2 MW.

Injection into the synchrotron is via charge exchange of a 70 MeV, 25 mA $H^-$ beam over ~150 turns with painting over both transverse acceptances, collimated at ~300 $\pi$ mm mrad. The un-chopped, injected beam is non-adiabatically bunched and accelerated by the ring dual harmonic RF system ($h$ = 2, 4) ramping in frequency from 1.3 – 3.1 MHz ($h$ = 2). This results in two long bunches equally spaced around the ring. Nominal betatron tunes are $(Q_x, Q_y) = (4.31, 3.83)$ with peak incoherent tune shifts exceeding ~ -0.5. Beam intensity is currently limited by beam loss and associated activation with the main driving mechanisms being foil losses, longitudinal trapping, transverse space charge and the head-tail instability [2].

### *Head-Tail Observations at ISIS*

Measurements of head-tail on the ISIS synchrotron have consistently shown that the two proton bunches exhibit vertical head-tail motion 1 – 2.5 ms through the 10 ms acceleration cycle [3, 4]. ISIS operates at the natural machine chromaticities ($\xi_x = \xi_y = -1.4$, normalised), without sextupole correction. The instability is currently suppressed by ramping the vertical tune down, away from the integer ($Q_y = 4$), and making the longitudinal charge distribution asymmetric during the time of the instability using the dual harmonic RF system. Both longitudinal and vertical injection painting also have a strong influence on the sensitivity to the instability. However, with increasing beam currents these mitigation strategies become less effective. Lowering the tune further tends to induce beam loss associated with the half integer resonance [5, 6] and injection painting and longitudinal distribution asymmetry have already been optimised fully.

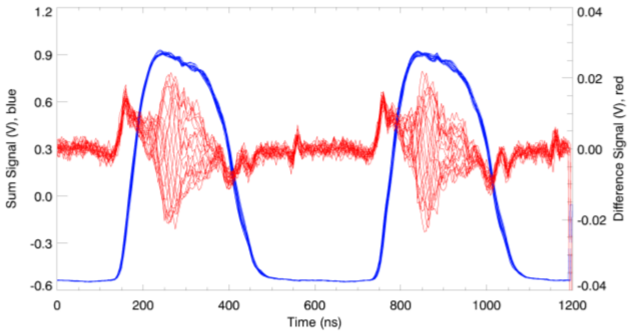


Figure 1: Example sum (blue) and difference (red) vertical position monitor signals over several turns around 2 ms through the acceleration cycle during normal operations.

A typical example of observed head-tail motion during normal, high intensity operations is shown in Fig. 1. The longitudinal bunch asymmetry is clear in the Beam Position Monitor (BPM) sum signal and intra-bunch, head-tail motion is indicated by the difference signal.

In order to remove some of the complexities of high intensity dynamics, further measurements of the instability were made at lower intensity and with single harmonic RF to test against Sacherer theory [7]. These demonstrate a clear $m$ = 1 mode structure (one node along the bunch) as shown in the BPM difference signal in Fig. 2; while theory predicts a higher growth rate for the $m$ = 2 mode (2 nodes along the bunch). Studies are ongoing to determine the cause of this discrepancy.

* rob.williamson@stfc.ac.uk

## SIMULATION MODEL

A stand-alone macro-particle simulations code has been written to study head-tail behaviour on ISIS [4]. The code includes a benchmarked longitudinal dynamics code with smooth focusing transverse dynamics and transverse wakefield kicks to simulate the interaction between the beam and its environment.

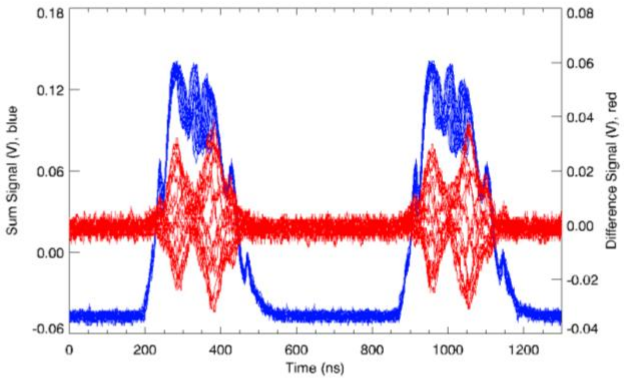


Figure 2: Example sum (blue) and difference (red) vertical position monitor signals over several turns for lower intensity, single harmonic RF operation.

In order to calculate the wake due to a resistive wall or resonator impedance the beam is sliced longitudinally and the wake calculated at each slice due to upstream slices. This may include wakes from previous bunches, preceding turns or from slices within the same bunch.

### *Benchmark*

Following on from previous comparisons with coasting beam theory [4], the code has been evaluated against Sacherer theory for single, low intensity bunched beams in the presence of a narrowband resonator wake. The head-tail instability was characterised by its mode number and its growth rate as a function of beam intensity, tune and chromaticity.

For this benchmark study, one ultra-relativistic bunch was simulated with single harmonic RF, a Hofmann-Pedersen longitudinal distribution [8] of length 100 ns and a matched transverse waterbag distribution of 100% emittance 300 $\pi$ mm mrad. The narrowband resonator had a resonant frequency of 312 kHz, a transverse shunt impedance of 10 MΩ/m and a quality factor of 15.

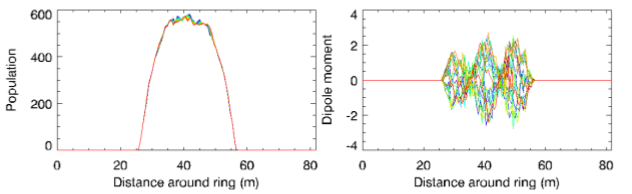


Figure 3: Example simulation output with sum (left) and difference (right) vertical position monitor signals over several turns.

To simulate a BPM the average transverse displacement ($\Delta y_i$) and the macro-particle population ($I_i$) was calculated for each longitudinal slice ($i$) and each simulated turn of the machine. The BPM difference signal was then computed as the product of these factors ($\Delta y_i I_i$ = the dipole moment of the beam), example shown in Fig. 3. The growth rate was deduced from an exponential fit to the largest betatron sideband as a function of time, calculated from Fourier transforms of the simulated difference signal segmented in time.

Figure 4, left, shows the growth rate as a function of betatron frequency. The dependence of growth rate on chromaticity is shown in Fig. 4, right. All key aspects of physics behaviour are correct with the growth rate peaking at the resonant frequency and decreasing as the chromatic frequency shifts away from the low resonant frequency of the impedance (a chromatic frequency of 312 kHz occurs at a chromaticity of 0.0017). The head-tail mode number also changes with chromaticity as predicted.

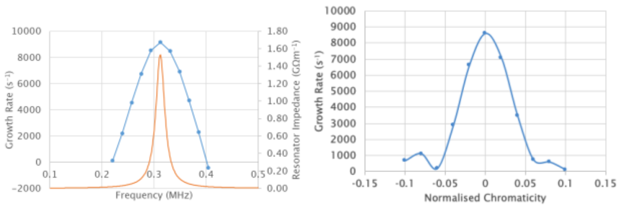


Figure 4: Growth rate (blue) and resonator impedance (red) versus frequency (left) and growth rate versus normalised chromaticity (right).

### *Comparison with Measurement*

Initial comparisons between theory, simulation and observation have been made for lower intensity, single harmonic RF beams at ISIS. Simulations assumed a thick resistive wall impedance with the beam pipe conductivity artificially modified to match the measured impedance at the dominant, lowest betatron sideband. Recent beam-based measurements of the effective impedance at ISIS [4] indicate a low frequency (85 kHz) narrowband type impedance together with resistive wall.

Figure 5 shows the measured (left) and simulated (right) vertical beam position monitor difference signal over several turns. Simulations agree with established theory showing a $m = 2$ mode structure. However, as with previous studies, this does not match experimental observations which exhibit a persistent $m = 1$ mode structure.

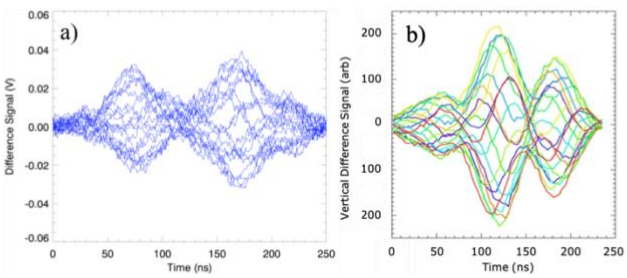


Figure 5: Comparison of BPM difference signals for a) experiment with b) simulation for low intensity, single harmonic RF, RCS beams at approximately 2 ms through acceleration.

## THE ISIS DAMPING SYSTEM

Head-tail motion may be counteracted with the use of a transverse feedback system [9]. This method has been implemented at ISIS by using one of the existing BPMs as a pickup and the vertical betatron exciter [10] as a kicker, allowing for a reduced development time for a working prototype. The kicker and BPM are separated by a betatron phase advance of 266° for a vertical tune $Q_y$ = 3.80 [11]. The processing electronics and power amplifiers are located 150 m away in an area free of ionizing radiation.

ISIS BPMs are cylindrical split electrode type with their performance characterised by the ratio of electrode voltage to beam current [12]. The cut-off frequency of the BPM has been lowered to 11 kHz by terminating the capacitive electrodes into 100 kΩ resistors. Finite element simulations of a simplified version of this monitor were performed with both CST Particle and Microwave Studios to verify the expected performance [13].

The ISIS vertical betatron exciter or “Q-Kicker” is a balanced transmission line kicker with window frame ferrites surrounding electrodes above and below the beam. Seven lumped capacitors connect each electrode to the body and a high power resistor terminates each electrode at the upstream aperture. A photograph of the kicker prior to installation is shown in Fig. 6, the ceramic chamber maintains the vacuum whilst the plates and ferrite are in air.

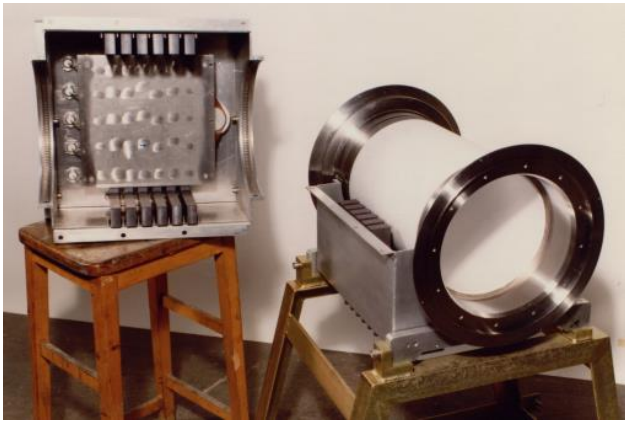

Figure 6: “Q-kicker” with the top half on the left, revealing the ferrites, plates, ceramic vacuum vessel and a terminating resistor.

### *LLRF and Digital Signal Processing*

The feedback system electronics block diagram is shown in Fig. 7. The low-level RF (LLRF) analogue electronics prepare the BPM signals for processing, providing amplification and gating. The Field Programmable Gate Array (FPGA) block consists of a National Instruments NI-5781, 100 MS/s transceiver Flex-Rio front end module [14], backed by a PXIe-7962R Flex-Rio FPGA card.

Each BPM electrode signal is amplified separately at the pick-up, and fed to the LLRF block 150 m away where the differential signal is obtained through a 180° hybrid combiner. This signal is then amplified and fed into the FPGA block which samples the signal, applies the required filtering, delays and software gain, as well as converting the processed signal back to the analogue domain.

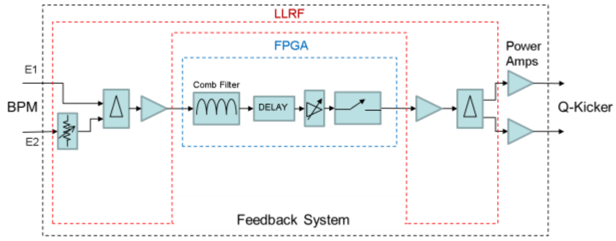


Figure 7: Feedback system electronics block diagram.

The driving clock of the digital processing stage is obtained by multiplying the fundamental RF harmonic by 30. This creates a fixed length filter and digital delays proportional to the ramping revolution frequency. The output gating control and the filter coefficients switching are driven by fixed frequency clocks. A variable digital delay is applied to the processed signal in order to compensate for the fixed delay of the cables and electronics. This delay decreases as the revolution frequency increases, synchronising the correction signal with the beam arrival at the kicker.

### *Digital filter*

A digital Finite Impulse Response (FIR) filter is used for closed orbit offset suppression and betatron phase advance correction. Without proper filtering, constant closed orbit offsets cause DC dipole kicks and can saturate the power amplifiers. The phase advance between the pickup and the kicker, together with a 3 turn signal processing delay, cause a variable betatron phase shift with the changing tune during acceleration (partly to mitigate head-tail). This phase shift is also compensated with the filter.

A 3-tap FIR filter was implemented to cover the range of betatron tunes whilst the head-tail instability is present. The filter calculation is shown in Eq. (1) where the required kick, $y$, at turn, $n$, is the weighted sum of the beam slice position measurements $x$, from three previous turns. The weights ($b_0$, $b_1$ and $b_2$) are the calculated filter coefficients.

$$y[n] = b_0x[n] + b_1x[n-1] + b_2x[n-2]. \qquad (1)$$

To include the full tune range the filter coefficients are matched at several points during the ramp to the set tune and its associated betatron phase, turn delay and phase advance [15-17]. Initial tests of the dynamic filters provided more efficient damping along the instability region. Figure 8 shows the vertical tune variation during the instability and the filter coefficients for the indicated tune values.

### *Power Amplifiers*

As the kicker is a 10 Ω system, each electrode is connected to a custom design Eltac RA994 power amplifier [18] by five URM-67 50 Ω cables terminated in parallel at the kicker end. This amplifier provides five 20 W outputs from a single input.

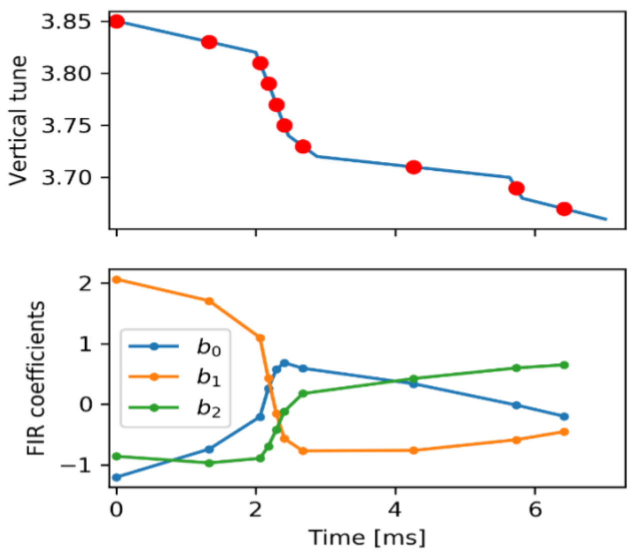


Figure 8: ISIS vertical tune (top) versus time with corresponding optimised 3-tap FIR filter coefficients (bottom).

## EXPERIMENTAL RESULTS

The damping system has been successfully tested during normal ISIS, high intensity operation, at the full repetition rate of 50 Hz. Figure 9 illustrates the effect of the damping system on the vertical head-tail motion around 2 ms through acceleration. The purple and red traces show the BPM sum signals with and without damping showing a negligible effect on the longitudinal charge distribution as expected. The BPM difference signals with (green) and without (blue) damping demonstrate the efficacy of the damping system on the vertical head-tail motion.

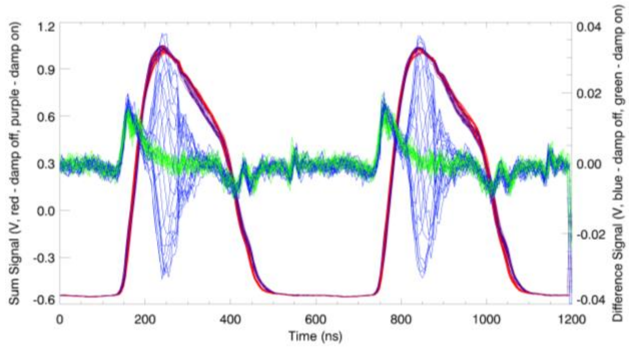


Figure 9: BPM sum and difference signals with (purple, green respectively) and without (red, blue respectively) damping, over 20 turns around 2 ms through acceleration.

The sum of all the beam loss monitors around the ISIS synchrotron is shown in Fig. 10 with and without damping (green and grey respectively). This further validates the usefulness of the ISIS damping system: reducing beam loss and hence machine activation. Figure 10 represents a > 50% reduction in loss above 120 MeV. The residual loss observable at 2 ms is likely due to the rapidly varying tune and RF modifications put in place to mitigate head-tail without the damping system.

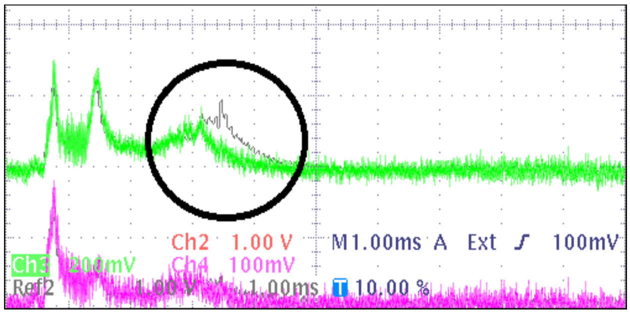


Figure 10: Sum of all beam loss monitors versus time with (green) and without (grey) damping; beam loss outside collimator region (pink).

In order to operate safely without supervision, it is planned to install a system to protect the terminating resistors on the kicker against long term over-voltage conditions. These could occur if the amplifiers or feedback system fail and start oscillating at maximum amplitude. Further commissioning tests are planned with a slower tune variation and without the imposed longitudinal bunch profile asymmetry.

## SUMMARY AND FUTURE WORK

### *Simulation Model*

Research and development into the mechanism and mitigation of the head-tail instability at ISIS has been identified as a high priority. Ongoing work to build an instability simulation model verified against theory has been presented. The macro-particle tracking code has been qualitatively benchmarked for a narrowband resonator as a function of beam intensity, tune and chromaticity.

Further work is planned to benchmark the code with resistive wall wakes and compare the results with similar codes such as PyHEADTAIL [19] and TRANFT [20]. Once verified with Sacherer theory, simulations will be compared against a comprehensive set of head-tail measurements made at ISIS as a function of intensity, tune and longitudinal structure. Development of the simulation model will aid in diagnosis of the driving impedance behind head-tail at ISIS, help provide mitigation strategies and support improvements of the damping system.

### *ISIS Damping System*

A damping system has been developed for the vertical plane in the ISIS synchrotron using an existing BPM and a ferrite loaded kicker. The challenges of a fast ramping accelerator with dynamic tune variation have been addressed with a 3-tap FIR filter with updating coefficients through the acceleration cycle. Effective damping of the head-tail motion present during normal ISIS operations has been achieved during tests at the full repetition rate of 50 Hz. This has resulted in a beam loss reduction of > 50% for beam energies above 120 MeV.

The damping system currently uses set tunes, which are input manually, rather than measured values. Calculated values should provide better filter coefficients and as such damp instabilities more efficiently. It is planned to automate the calculation of filter coefficients from measured tunes to improve the system's flexibility during machine setup and operation.

A protection system for the kicker's terminating resistors is proposed to enable more robust, 50 Hz unsupervised operation of the damping system.

## REFERENCES


[1] W. Herr, "Overview — Intensity Limitations in Particle Accelerators", *CERN Yellow Reports: School Proceedings, Vol. 3/2017, CERN-2017-006-SP*, Geneva, Switzerland, 2–11 November 2015.

[2] D. J. Adams *et al*., "Operational Experience and Future Plans at ISIS", in *Proc. HB'16*, Malmö, Sweden, Jul. 2016, pp. 333-337. doi:10.18429/JACoW-HB2016-TUPM3Y01

[3] G.H. Rees, "Interpretation of the higher mode, head tail motion observed on ISIS", *Particle Accelerators*, May 1992, Vol. 39, pp. 159 – 167.

[4] R.E. Williamson, B. Jones, C.M. Warsop, "Development of Physics Models of the ISIS Head-Tail Instability", in *Proc. HB'16*, Malmö, Sweden, Jul. 2016, pp. 155 – 159. doi:10.18429/JACoW-HB2016-MOPR031

[5] C.M. Warsop, D.J. Adams, B. Jones, and B.G. Pine, "Simple models for beam loss near the half integer resonance with space charge", in *Proc. HB'16*, Malmö, Sweden, Jul. 2016, pp. 150-154. doi:10.18429/JACoW-HB2016-MOPR030

[6] C.M. Warsop et al., "High intensity loss mechanisms on the ISIS rapid cycling synchrotron", in *Proc. HB'14*, East Lansing, MI, USA, Nov. 2014, pp. 203 – 207.

[7] F. Sacherer, "Transverse bunched beam instabilities", in Proc. First Course of the International School of Particle Accelerators of the 'Ettore Majorana' Centre for Scientific Culture, Rep. CERN 77-13, Jul. 1977, pp. 198 – 218.

[8] A. Hofmann, F. Pedersen, "Bunches with Local Elliptic Energy Distributions", *IEEE Trans. Nucl. Sci., 26-3*, p.3526 (1979).

[9] V. Danilov and E. Perevedentsev, "Transverse feedback systems for the strong head-tail effect", *CERN SL/92-58 (AP)*, Geneva, Dec. 1992.

[10] A. Pertica and D. W. Posthuma de Boer, "Experimental Damping System with a Ferrite Loaded Kicker for the ISIS Proton Synchrotron", *Proc. IBIC 2017*, Grand Rapids, MI, USA, Aug. 2017, pp. 287 - 291.

[11] Z. Xie, "Transverse Beam Stability and Determination of Gain and Delay for Mixed-signal Transverse Feedback Dampers in Particle Accelerators", *Ph.D thesis*, University of Wisconsin-Madison, 2015.

[12] P. Forck, D. Liakin, and P. Kowina, "Beam Position Monitors", 2009, CERN Document Server, https://cds.cern.ch/record/1213277.

[13] B. G. Pine, "Position monitoring on the ISIS synchrotron", *Proc. 4th CARE-HHH-ABI Workshop*, Lüneburg, Germany, Nov./Dec. 2006, pp. 28 - 32.

[14] "NI-5781 Transceiver Adapter for FlexRIO", http://www.ni.com/en-gb/support/model.ni-5781.html.

[15] J. Komppula, X. Buffat, G. Kotzian, K. S. B. Li, D. Valuch. Zur Elektrodynamik bewegter Körper. (German) [MD4036: New ADT signal processing for large tune acceptance]. CERNACC-NOTE-2019-0008, http://cds.cern.ch/record/2668389.

[16] G. Kotzian, "Possibilities for transverse feedback phase adjustment by means of digital filters", in *Proc. IPAC'17*, Copenhagen, Denmark, May 2017, TUPIK095.

[17] M. Lonza, H. Schmickler, "Multi-bunch Feedback Systems", in *Proc. CAS - CERN Accelerator School: Advanced Accelerator Physics Course*, Trondheim, Norway, August 2013, pp. 503-546.

[18] "Eltac Ltd", http://www.eltac.co.uk.

[19] K. S. B. Li *et al*., "Code Development for Collective Effects", in *Proc. 57th ICFA Advanced Beam Dynamics Workshop on High-Intensity and High-Brightness Hadron Beams (HB'16)*, Malmö, Sweden, Jul. 2016, pp. 362-367. doi:10.18429/JACoW-HB2016-WEAM3X01

[20] M. Blaskiewicz, "The TRANFT User's Manual", Brookhaven Technical Report, BNL-77074-2006-IR, 2006. doi:10.2172/896444

# STUDY OF COLLECTIVE EFFECTS IN THE CERN FCC-EE TOP-UP BOOSTER

D. Quartullo*, INFN-Rome1, Rome, Italy
M. Migliorati, Sapienza University and INFN-Rome1, Rome, Italy
M. Zobov, LNF-INFN, Frascati, Italy

*Abstract*

The CERN FCC-ee top-up booster synchrotron will accelerate electrons and positrons from an injection energy of 20 GeV up to an extraction energy between 45.6 GeV and 182.5 GeV depending on the operation mode. These accelerated beams will be used for the initial filling of the high-luminosity FCC-ee collider and for keeping constant the beam current over time using continuous top-up injection. Due to the high-intensities of the circulating beams, collective effects may represent a limitation in the top-up booster. In this work we present a first evaluation of the impedance model and the effects on beam dynamics. Methods to mitigate possible instabilities will be also discussed.

## INTRODUCTION

The CERN $e^+e^-$ Future Circular Collider (FCC-ee) is a high-luminosity and high-precision electron-positron circular collider envisioned in a 100 km tunnel in the CERN-Geneva area [1]. The FCC-ee will allow detailed studies of the heaviest known particles (Z, W, H bosons and the top quark) offering also great sensitivity to new particle physics.

The FCC-ee target luminosities of $10^{34} - 10^{36}$ $cm^{-2}$ $s^{-1}$ will lead to short beam lifetimes, due to beamstrahlung, radiative Bhabha scattering and Touschek effect [1]. In order to sustain these short beam lifetimes, a full-energy booster will provide continuous top-up injection, in addition to initially filling the FCC-ee.

The booster will be built in the same tunnel used for the collider and the circumference lengths of the two machines will be the same, almost 100 km. The booster will accelerate batches of electrons and positrons from an injection energy of 20 GeV up to an extraction energy of 45.6 GeV, 80 GeV, 120 GeV, 182.5 GeV for Z, W, H and top quark production, respectively [1]. This design injection energy, which corresponds to a magnetic field $B = 6$ mT, could change in the future, depending on the quality and reproducibility of the magnetic field in the dipole magnets.

In order not to affect the collider luminosity and to diminish the background generated by lost particles, the booster is expected to provide, at extraction, an equilibrium transverse emittance similar to the one in the collider. Since the FCC-ee lattice will be optimized for two optics, one with 60° phase advance for the Z and W experiments, the other with 90° phase advance for the H and top quark productions, the optics in the booster will change depending on the phase advance in the collider.

The synchrotron radiation (SR) transverse damping time at booster injection-energy will be longer than 10 s, leading to incompatibility with the booster cycle [2]. In addition, the horizontal normalized equilibrium emittance of 12 pm rad will cause emittance blow-up along the cycle due to intra-beam scattering. In order to solve these issues, 16 wigglers should be installed in the booster, leading to a damping time of 0.1 s and an emittance of 240 pm rad and 180 pm rad for the 60° and 90° optics respectively.

The high nominal intensity of $N_b = 3.4\times10^{10}$ particles per bunch (ppb) could lead to collective effects able to severely limit the booster operation. In particular, the resistive wall effect, due to the foreseen beam-pipe in stainless steel with radius $r_c = 25$ mm, could cause strong instabilities in both longitudinal and transverse planes.

The importance of collective effects in the booster at injection energy was already reported in Ref. [3], where it was shown that, without wigglers, an intensity threshold of $0.1 \times 10^{10}$ ppb, significantly lower than the nominal intensity, was defined by the microwave instability (MI) caused by the resistive wall impedance. In the transverse plane, the intensity threshold due to transverse mode-coupling instability (TMCI) was only $0.6 \times 10^{10}$ ppb. Moreover, analytical estimations of the resistive wall transverse coupled-bunch instability (TCBI) found a rise time of just few revolution turns which requires new feedback schemes [4].

This work aims at finding possible cures to the impedance-induced instabilities in the booster, focusing on the beam dynamics at injection energy and assuming an optics with 60° phase advance and no wigglers installed in the machine.

The next section highlights the machine and beam parameters considered in the present study. Then, careful estimations of the resistive-wall impedance are given, together with a possible way to lower it. The work continues studying the MI in the longitudinal plane through macroparticle simulations, providing a possible cure to increase the intensity threshold. Subsequently, choosing a proper combination of parameters which allows having stable beams at the nominal intensity, the study shifts to the transverse plane, where a semi-analytical Vlasov solver is used to find the TMCI intensity threshold. Finally, estimations of the TCBI rise-time are provided using analytical formulae.

## MACHINE AND BEAM PARAMETERS CONSIDERED IN THE STUDY

Table 1 shows the machine and beam parameters used in the study of collective effects in the booster.

* Danilo.Quartullo@roma1.infn.it

Table 1: Main machine and beam parameters relevant for the booster studies. Most of these quantities can be found in Ref. [1].

| **Parameter** | **Value** |
|---|---|
| Machine circumference ($C_r$) | 97.756 km |
| Beam energy at injection ($E_0$) | 20 GeV |
| Beam rev. frequency at injection ($f_0$) | 3.06 kHz |
| Nominal bunch intensity ($N_b^{nom}$) | $3.4 \times 10^{10}$ ppb |
| Number of bunches per beam ($M_b$) | 16640 |
| SR 1 $\sigma$ rel. energy spread ($\sigma_{dE0,r}$) | $0.166 \times 10^{-3}$ |
| SR energy loss per turn ($U_0$) | 1.33 MeV |
| SR longitudinal damping time ($\tau_z$) | 15013 turns |
| SR 1 $\sigma$ long. bunch length ($\sigma_{z0}$) | 1.26 mm |
| RF frequency ($f_{rf}$) | 400 MHz |
| Harmonic number ($h$) | 130432 |
| RF voltage ($V_{rf}$) | 60 MV |
| Arc phase advance ($\phi_a$) | 60° |
| Momentum compaction factor ($\alpha_c$) | $1.48 \times 10^{-5}$ |
| Synchrotron tune ($Q_s$) | 0.0304 |
| Betatron tunes ($Q_{x,y}^{nom}$) | 269.139 |

As shown below, the study of the booster beam dynamics at injection energy is the most critical as concerns intensity effects in both the longitudinal and transverse planes.

The considered $\phi_a = 60°$ directly determines $\alpha_c$ and influences $Q_s$ and $\sigma_{z0}$. As reported later, the MI intensity threshold is proportional to $\alpha_c$ and $\sigma_{z0}$ while the TMCI intensity threshold is proportional to $Q_s$. A phase advance of 90° would lead to lower values for $\alpha_c$, $Q_s$, $\sigma_{z0}$ and therefore to more critical scenarios.

The main three SR parameters $\sigma_{z0}$, $U_0$ and $\tau_z$ can be directly computed assuming an average dipole-magnet bending radius $\rho_b = 10.6$ km in the absence of wigglers.

The booster main RF system consists of 400 MHz superconducting cavities [1]. In the present work, a voltage $V_{rf} = 60$ MV at injection energy is assumed. This value is significantly higher than $U_0$ so that the bunch sees the linear part of the RF voltage at each revolution turn. In addition, the chosen $V_{rf}$ is expected to be substantially lower than the total available voltage, so that $V_{rf}$ can be increased during acceleration according to the cycle needs.

The number of bunches simultaneously accelerated in the booster will depend on the collider experiment. Table 1 indicates the largest planned $M_b$, which relates to the Z-boson experiment [1].

Concerning the transverse plane, the horizontal and vertical tunes are assumed to be equal to the horizontal tune foreseen in the FCC-ee for the Z-boson experiment [1].

## ESTIMATION OF THE RESISTIVE WALL IMPEDANCE

The resistive wall impedance is the dominant component of the booster impedance model and it is the only impedance contribution considered in this paper.

The baseline for costs minimization is to have a circular beam-pipe in stainless steel (resistivity $\rho_r = 7 \times 10^{-7}\Omega$m) with radius $r_c = 25$ mm. However, the corresponding resistive wall impedance would lead to a peak induced voltage even higher than the peak RF voltage for a bunch with the nominal intensity, see Fig. 1.

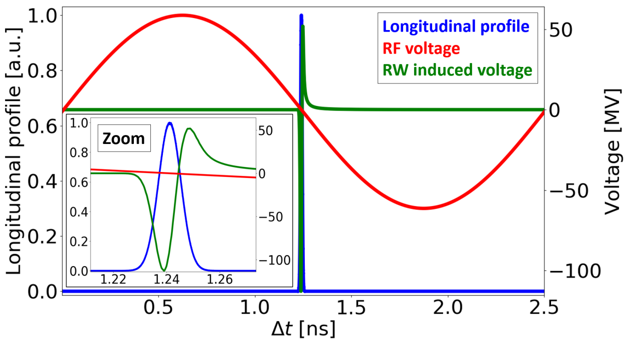


Figure 1: Longitudinal profile (blue), RF voltage (red) and resistive wall induced voltage (green) as a function of time in the FCC-ee booster considering the parameters in Table 1 and a stainless steel beam pipe with radius $r_c = 25$ mm.

In order to reduce this impedance, the possibility of applying a copper coating to the beam-pipe was investigated. Specifically, the CERN IW2D code [5] was used to evaluate the longitudinal and transverse resistive wall impedances of a two-layer vacuum chamber, being the external layer in stainless steel and the internal layer in copper ($\rho_r = 1.7 \times 10^{-8}\Omega$m) with variable thickness $\delta_l$, see Fig. 2.

For single-layer beam-pipes, the dependences of the longitudinal and transverse-dipolar resistive wall impedances on the frequency are [6]

$$|Z_{\parallel}(f)| \propto \frac{1}{r_c}\sqrt{\rho_r f}, \quad |Z_{x,y}(f)| \propto \frac{1}{r_c^3}\sqrt{\frac{\rho_r}{f}} \qquad (1)$$

in a certain asymptotic range of frequencies. These dependencies are highlighted in Fig. 2, where all the axes are in logarithmic scale.

The plots in Fig. 2 also show that, for a given $\delta_l$, both longitudinal and transverse impedances converge to the single-layer stainless-steel and copper impedances respectively for low and high frequencies. In particular, for a given $\delta_l$, the two frequencies where the longitudinal and transverse impedances converge to the corresponding single-layer copper impedances are essentially the same and will be denoted by $f_{\delta_l}$ below.

In the next section, the MI thresholds will be evaluated for the different impedances shown in Fig. 2 (top). As reported in Ref. [7], MI can occur when the wavelength of the wakefield is much shorter than the bunch length, i.e. $f_c\tau \gg 1$, where $f_c$ is the frequency of the impedance which drives MI and $\tau$ is the full bunch length. Therefore, it is expected that the impedance related to a given $\delta_l$ and the impedance of the single-layer copper beam-pipe will lead to the same MI intensity threshold if these two impedances coincide for frequencies larger than $1/\tau$, i.e. when $f_{\delta_l} < 1/\tau$.

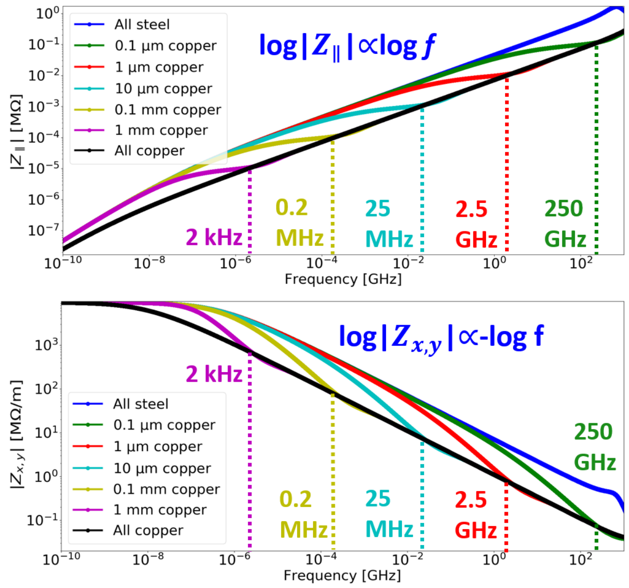


Figure 2: Longitudinal (top) and transverse dipolar (bottom) resistive wall impedance as a function of frequency in the FCC-ee booster assuming a beam-pipe in stainless steel with radius $r_c$ = 25 mm and different values for the thickness of the internal copper layer. The five vertical dashed lines mark the frequencies $f_{\delta_l}$ above which the corresponding impedances converge to the single-layer copper impedance. The dependences of the single-layer impedances on the frequency are also reported in both plots. All the impedance curves have been obtained with the IW2D code.

Finally, it should be noted that, being the booster a fast-cycling machine, eddy currents in presence of a copper layer could be an issue during acceleration and their effects should be separately investigated.

## CURES FOR INCREASING THE MICROWAVE-INSTABILITY INTENSITY THRESHOLD

Single-bunch macroparticle longitudinal beam dynamics simulations were performed with the CERN BLonD code [8] in order to evaluate the MI intensity threshold ($N_{b,\mathrm{th}}^{\mathrm{MI}}$) taking into account the parameters of Table 1 and the resistive-wall impedance shown in Fig. 2 (top) with a variable $\delta_l$.

Simulation tracking lasted $10^6$ revolution turns, which is more than 6 times the SR longitudinal damping time, in such a way to reach a SR equilibrium at the end of simulations. It should be noted that $10^6$ turns corresponds to 32.6 s, which is comparable to the flat-bottom duration of 51.1 s in the booster for the Z-boson experiment [1].

The resistive-wall induced voltage was computed in frequency domain, multiplying the bunch spectrum by the impedance and performing an inverse Fourier transform. Due to the short bunches and to have an acceptable resolution in the longitudinal profile binning (at least 50 slices for 4-$\sigma$ bunch length), the maximum frequency considered in computations was 500 GHz. This obliged to use a large number of macroparticles per bunch (more than $10^7$) in order to counteract the numerical noise obtained when multiplying impedance and bunch spectrum, which are increasing and decreasing functions of frequency, respectively (Fig. 3).

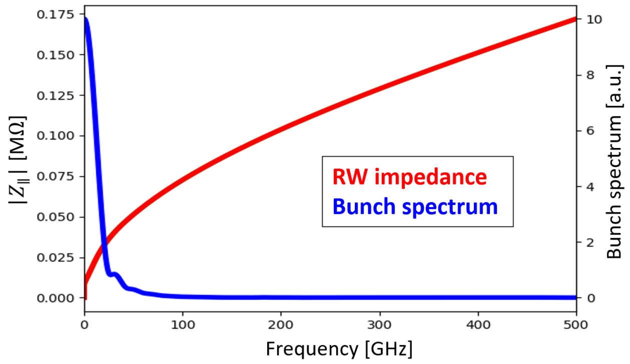


Figure 3: Resistive wall impedance and bunch spectrum used to compute the induced voltage in BLonD simulations. Case of $\delta_l = 1\,\mu$m, $\sigma_z$ = 4 mm at SR equilibrium.

Figure 4 shows the simulation results, specifically the equilibrium $\sigma_{dE,\mathrm{r}}$ and $\sigma_z$ (averaged over the last 10000 revolution turns) as a function of $N_b$ and varying $\delta_l$.

When observed in simulation, MI led to a $\sigma_{dE,\mathrm{r}}$ increase relative to $\sigma_{dE0,\mathrm{r}}$. More specifically, up to a certain intensity threshold $N_{\mathrm{b,th}}^{\mathrm{MI}}$, $\sigma_{dE,\mathrm{r}} \approx \sigma_{dE0,\mathrm{r}}$, while $\sigma_{dE,\mathrm{r}}$ becomes an increasing function of $N_b$ when $N_b > N_{\mathrm{b,th}}^{\mathrm{MI}}$. In Fig. 4 (top), to unambiguously determine $N_{\mathrm{b,th}}^{\mathrm{MI}}$, the MI intensity threshold is chosen so that, when $N_b = N_{\mathrm{b,th}}^{\mathrm{MI}}$, then $\sigma_{dE,\mathrm{r}} = 1.1\sigma_{dE0,\mathrm{r}}$.

Figure 4 (top) shows that, even with a beam-pipe entirely made of copper, the threshold $N_{\mathrm{b,th}}^{\mathrm{MI}}$ is only $1.5 \times 10^{10}$ ppb, significantly lower than the nominal bunch intensity. This value for $N_{\mathrm{b,th}}^{\mathrm{MI}}$ can be also obtained with good approximation when $\delta_l = 1\,\mu$m.

Concerning the equilibrium bunch length, Fig. 4 (bottom) shows that $\sigma_z$ is an increasing function of $N_b$ and the bunch lengthening relative to $\sigma_{z0}$ is higher when the resistive-wall impedance is larger (smaller $\delta_l$). This bunch lengthening occurs even when $N_b < N_{\mathrm{b,th}}^{\mathrm{MI}}$ and no clear changes in curve behaviour are visible in correspondence of $N_b = N_{\mathrm{b,th}}^{\mathrm{MI}}$.

With a vacuum-chamber entirely in copper, the equilibrium full bunch-length is $\tau \approx 4\sigma_z = 36$ ps when $N_b = 1.5 \times 10^{10}$ ppb (Fig. 4, bottom). Therefore, following the reasoning of the previous section, a copper coating should lead to the highest possible MI intensity-threshold ($1.5 \times 10^{10}$ ppb) when $f_{\delta_l} < 1/\tau \approx 30$ GHz. This is in good agreement with the $f_{\delta_l}$ values reported in Fig. 2 (top), since $f_{\delta_l}$ is larger than 30 GHz when $\delta_l = 0.1\,\mu$m and lower than 30 GHz when $\delta_l = 1\,\mu$m.

Since the reduction of the longitudinal resistive-wall impedance by adding a copper layer to the beam-pipe did not avoid MI for the nominal bunch intensity, a second cure for instability has been studied.

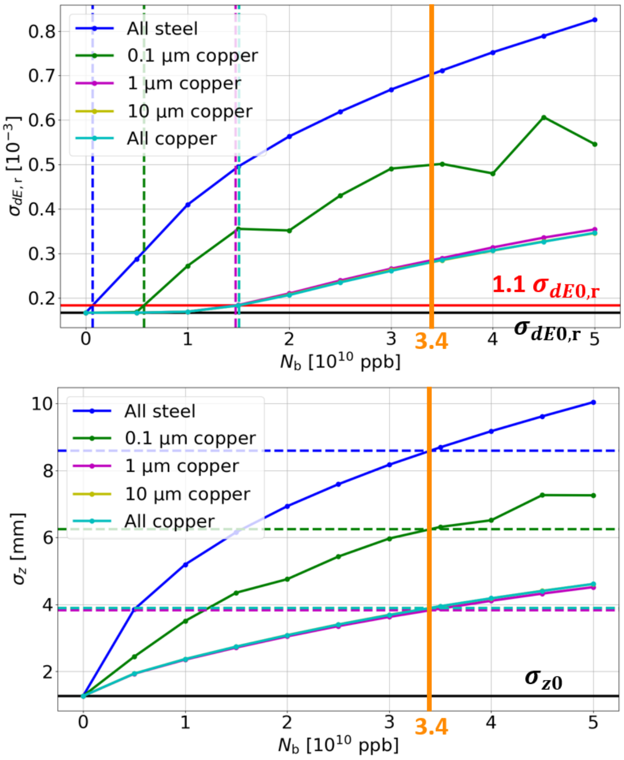


Figure 4: Equilibrium rms relative energy spread (top) and bunch length (bottom) as a function of bunch intensity obtained with BLonD simulations. The used parameters are reported in Table 1 and the resistive wall impedance shown in Fig. 2 (top) has been included in simulations varying $\delta_l$. Top: the horizontal lines mark $\sigma_{dE0,r}$ and its increase by 10%. The dashed vertical lines mark $N_{b,th}^{MI}$ for the corresponding curves. Bottom: the black line marks $\sigma_{z0}$, while the dashed horizontal lines indicate the values of $\sigma_z$ when $N_b = 3.4 \times 10^{10}$ ppb and $\delta_l$ varies. In both images the yellow and cyan curves are overlapped.

For the Boussard criterion [9], $N_{b,th}^{MI}$ scales as

$$N_{b,th}^{MI} \propto \frac{\alpha_c E_0 \sigma_{dE0,r}^2 \sigma_{z0}}{|Z_\parallel|/n}, \tag{2}$$

where $n = f/f_0$. As expected, this expression shows that the MI intensity threshold increases when the longitudinal resistive wall impedance is reduced. Equation (2) clarifies also the observation done above concerning the major strength of MI at booster injection-energy with the 90° phase-advance optics (lower $\alpha_c$). Moreover, Eq. (2) shows that $N_{b,th}^{MI}$ depends quadratically on $\sigma_{dE0,r}$ and linearly on $\sigma_{z0}$.

One way to increase $\sigma_{dE0,r}$ consists in installing wigglers in the booster with a consequent increase in $U_0$. Indeed, the two scaling relations [10]

$$\tau_z = \frac{1}{U_0(1 + C_1 U_0)}, \quad \sigma_{dE0,r} \propto \sqrt{\frac{U_0}{1 + C_2 U_0}}, \tag{3}$$

where $C_1$ and $C_2$ are positive quantities not depending on $U_0$, show that a larger $U_0$ leads to lower $\tau_z$ and higher $\sigma_{dE0,r}$.

Therefore, the BLonD simulations were repeated varying $U_0$ and considering $\delta_l = 1\,\mu$m, which is a compromise between an increase in $N_{b,th}^{MI}$ (Fig. 4, top) and a decrease in production costs and potential eddy-current issues related to the copper-layer thickness.

Figure 5 (top) shows the new intensity thresholds. As foreseen by Eqs. (2) and (3), the plot shows that $N_{b,th}^{MI}$ increases with $U_0$. In particular, values of $U_0$ not larger than 3 MeV lead to MI for the nominal bunch intensity.

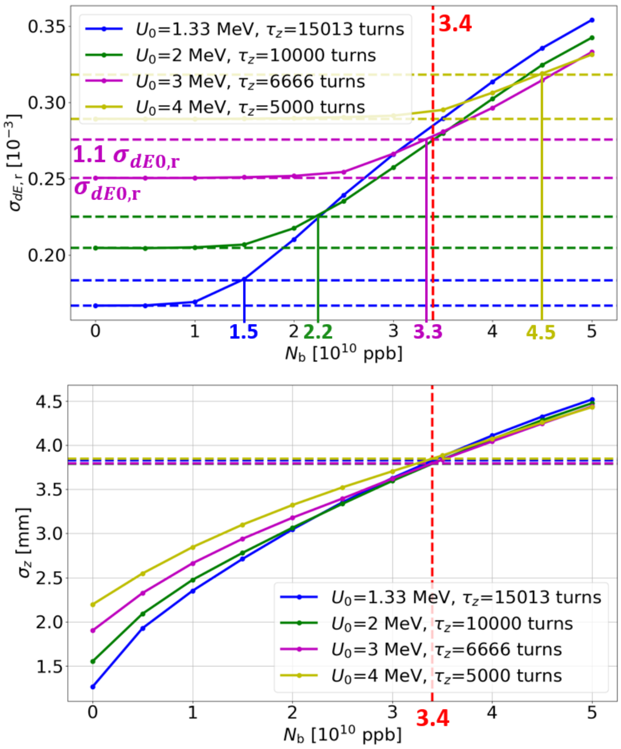


Figure 5: Equilibrium rms relative energy spread (top) and bunch length (bottom) as a function of bunch intensity obtained with BLonD simulations. The used parameters are reported in Table 1, except for the SR quantities which vary following Eq. (3). The resistive wall impedance with $\delta_l = 1\,\mu$m (Fig. 2, top) has been included in simulations. Top: for each curve, the corresponding horizontal lines mark $\sigma_{dE0,r}$ and its increase by 10%, while the vertical line marks $N_{b,th}^{MI}$. Bottom: the horizontal lines indicate the values of $\sigma_z$ when $N_b = 3.4 \times 10^{10}$ ppb and $U_0$ varies.

Regarding the bunch lengths, Fig. 5 (bottom) shows that $\sigma_{z0}$ increases as a function of $U_0$, helping in increasing $N_{b,th}^{MI}$ as Eq. (2) suggests. The plot also indicates that the increase of $\sigma_z$ with $U_0$ is less and less significant as $N_b$ approaches the nominal bunch intensity.

This second additional cure for MI, i.e. installing wigglers in the booster to increase $U_0$, is in full agreement with the current machine design-plan. Indeed, as already mentioned above, considerations concerning the transverse plane would lead to the installation of 16 wigglers able to provide $U_0$ = 126 MeV [1,2]. Simulations with such a value for $U_0$ require a much larger $V_{rf}$, moreover there would be likely no need to add a copper layer to the beam pipe due to the larger $\sigma_{dE0,\mathrm{r}}$ in Eq. (2). Further studies are needed to cover this scenario.

## TRANSVERSE MODE-COUPLING INSTABILITY INTENSITY THRESHOLD

The previous section showed that a bunch with nominal intensity does not suffer MI when $U_0 = 4\,\mathrm{MeV}$ and $\delta_\mathrm{l} = 1\,\mu\mathrm{m}$. Taking into account these two conditions, beam dynamics studies in the transverse plane were needed to verify that the bunch is not unstable due to TMCI.

The intensity threshold for TMCI scales as [11]

$$N_{\mathrm{b,th}}^{\mathrm{TMCI}} \propto \frac{Q_{x,y} Q_s E_0 \sigma_z}{\mathrm{Im}(Z_{x,y})}, \tag{4}$$

where $\mathrm{Im}(Z_{x,y})$ is the imaginary part of the transverse resistive-wall impedance.

The quantity $\mathrm{Im}(Z_{x,y})$ was decreased adding a copper-layer to the beam pipe in order to cope with MI. Equation (4) shows a linear dependence of $N_{\mathrm{b,th}}^{\mathrm{TMCI}}$ on the equilibrium $\sigma_z$ which, for a certain $U_0$, increases with $N_\mathrm{b}$ (see bottom plots in Figs. 4 and 5). This bunch-lengthening in the longitudinal plane helps increasing $N_{\mathrm{b,th}}^{\mathrm{TMCI}}$. Note also that, at least for bunch intensities close to or above the nominal value, increasing $U_0$ would not lengthen the bunch (Fig. 5, bottom) and therefore would not help to counteract TMCI.

The CERN DELPHI code [12], which is a semi-analytical Vlasov solver for impedance-driven modes, was used to evaluate $N_{\mathrm{b,th}}^{\mathrm{TMCI}}$ without taking into account the radiation damping. The values for $\sigma_z$ needed in DELPHI have been taken from the BLonD simulation results described above (yellow curve in the bottom plot of Fig. 5).

Figure 6 shows the real and imaginary parts of the complex tune shift of the first coherent oscillation modes obtained with DELPHI.

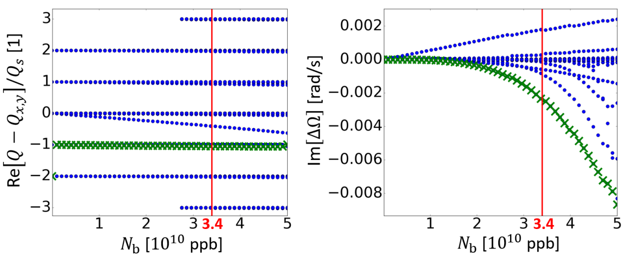


Figure 6: Real (left) and imaginary (right) parts of the tune shift of the first coherent oscillation modes as a function of the bunch intensity obtained with DELPHI. In both plots the green cross associated to a given $N_\mathrm{b}$ marks the unstable mode with largest growth rate. The parameters needed in simulation are taken from Table 1, except for the equilibrium $\sigma_z$ which depends on $N_\mathrm{b}$ according to the yellow curve in Fig. 5 (bottom, $U_0 = 4$ MeV). The value $\delta_\mathrm{l} = 1\mu$m is assumed for the dipolar resistive-wall impedance.

No mode coupling occurs up to $N_\mathrm{b} = 5 \times 10^{10}$ ppb (Fig. 6, left). In addition, the rise times of the unstable modes (Fig. 6, right) are longer than 125 s, and these values are large compared to the SR transverse damping-time (3.26 s) and the flat-bottom durations in the booster, which vary from 1.6 s to 51.1 s according to the collider experiment [1].

Therefore, $N_{\mathrm{b,th}}^{\mathrm{TMCI}} > 5 \times 10^{10}$ ppb and, in particular, no TMCI is observed for the nominal bunch intensity. Figure 7 shows 20 consecutive transverse-amplitude (Head-Tail) signals obtained with DELPHI when $N_\mathrm{b} = N_\mathrm{b}^{\mathrm{nom}}$. Notice that the mode -1 largely prevails while the mode 0 only creates an asymmetry between the amplitudes of the two signal halves.

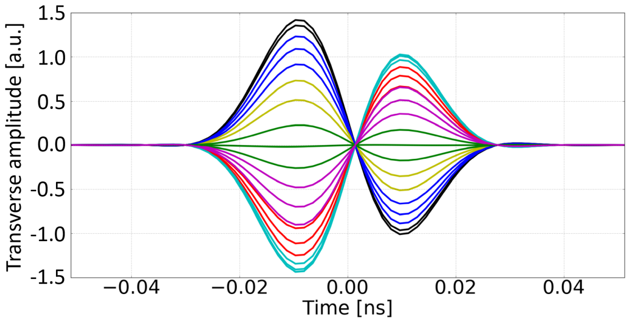


Figure 7: Twenty consecutive Head-Tail signals as a function of the longitudinal coordinate (0 ns corresponds to the bunch centre). These signals were obtained with DELPHI and refer to the simulation results shown in Fig. 6 when $N_\mathrm{b} = N_\mathrm{b}^{\mathrm{nom}}$.

## RESISTIVE-WALL TRANSVERSE COUPLED-BUNCH INSTABILITY

The longitudinal resistive-wall wakefield decays along a distance much shorter than the bucket length in the booster. On the contrary, the transverse resistive-wall wakefield is long-range and can lead to TCBI.

In the following, analytical estimations of the TCBI growth-rate are provided. The needed parameters are taken from Table 1 and a layer thickness of $1\,\mu\mathrm{m}$ is assumed as concerns the resistive-wall impedance.

Assuming $M_\mathrm{b}$ equally-spaced bunches in the ring, the motion of the entire beam can be considered as the sum of $M_\mathrm{b}$ coherent coupled-bunch modes. The transverse growth-rate $\alpha_\mu$ for the $\mu$-th coupled-bunch mode, where $\mu$ is an integer between 0 and $M_\mathrm{b} - 1$, can be easily computed taking into account only the most prominent radial mode in the azimuthal $m = 0$ and assuming Gaussian bunches. The expression for $\alpha_\mu$ is [13]

$$\alpha_\mu = -\frac{ceM_\mathrm{b}N_\mathrm{b}f_0}{4\pi E_0 Q_{x,y}} \sum_{q=-\infty}^{\infty} \mathrm{Re}\left[Z_{x,y}\left(f_{\mu,q}\right)\right], \tag{5}$$

where $E_0$ is in $e$V units and $f_{\mu,q} = f_0(qM_\mathrm{b} + \mu + Q_{x,y})$.

Considering the value of $Q_{x,y}^{\mathrm{nom}}$ and the shape of the transverse resistive-wall impedance near plus or minus $f_0$, it can be seen that the most unstable mode $\bar{\mu}$ satisfies the condition $(qM_\mathrm{b} + \bar{\mu} + Q_{x,y}^{\mathrm{nom}}) \in [-1, 0]$ for a certain $q$ (Fig. 8). This condition is satisfied for $\bar{\mu} = 16370$ and $q = -1$. Note also that for the most unstable and stable modes, equal to

16370 and 16371 respectively, the most significant term in the summation of Eq. (5) comes when $q = -1$.

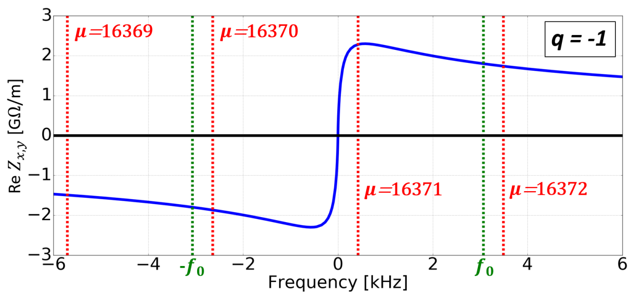


Figure 8: Resistive-wall transverse dipolar impedance (blue) as a function of frequency assuming $\delta_1 = 1\,\mu$m. The two green lines mark plus or minus $f_0$. The four red lines mark $f_{\mu,q}$, where $q = -1$, $Q_{x,y} = Q^{\rm nom}_{x,y}$ and $\mu$ varies as shown.

Figure 9 (left) shows $\alpha_\mu$ as a function of $\mu$ and confirms that $\bar{\mu}$ leads to the largest growth-rate $\alpha_{\bar{\mu}} = 2320$ 1/s.

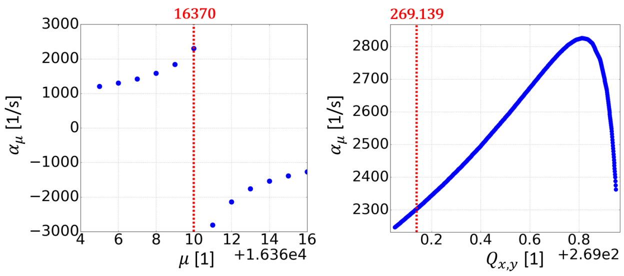


Figure 9: Left: TCBI growth rate, as a function of the coupled-bunch mode, obtained with Eq. (5) assuming $\delta_1 = 1\,\mu$m. The most unstable mode is marked by a red line. Right: TCBI growth rate as a function of $Q_{x,y}$ with $\lfloor Q_{x,y} \rfloor$=269 and $\mu = 16370$. The value $Q^{\rm nom}_{x,y}$ is marked by a red line. All the other needed parameters are taken from Table 1.

Figure 9 (right) shows $\alpha_\mu$ as a function of $Q_{x,y}$ when $\mu = 16370$ and the integer part of the tune is $\lfloor Q_{x,y} \rfloor$=269. Note that $\mu = 16370$ is the most unstable mode for all these values of $Q_{x,y}$. The plot indicates that the maximum growth rate of 2830 is achieved when $Q_{x,y} = 269.812$.

The value $\alpha_{\bar{\mu}} = 2320$ calculated for the nominal tune corresponds to a TCBI rise-time of 0.435 ms or 1.33 revolution turns. If $Q_{x,y} = 269.812$, then the rise-time is 1.08 turns. These rise-times are shorter than the SR transverse damping-time by several orders of magnitude. Therefore SR cannot help suppressing TCBI.

Transverse bunch-by-bunch feedback systems are usually used in other lepton factories to counteract TCBI [14]. However, these systems cannot act on the short time of one revolution turn. Therefore new feedbacks are required and some schemes have already been proposed [4].

## CONCLUSION

The present contribution showed that the first-designed parameters for the FCC-ee booster cannot provide stable beams to the main ring. This is due to the resistive-wall impedance which leads to microwave instability for nominal-intensity beams even if a copper layer is added to the stainless-steel beam pipe for impedance reduction. Therefore, a second mitigation technique was also taken into account, i.e. the increase of the power lost by the beam for synchrotron radiation. This second mitigation is in agreement with the current baseline plans, which foresee the installation of several wigglers in the booster. Using a proper combination of parameters, microwave and transverse-mode-coupling instabilities were not observed for nominal-intensity beams. However, analytical estimations indicated that the transverse-coupled-bunch-instability rise-time is only about one revolution turn making necessary the design of a new feedback system.

## ACKNOWLEDGEMENTS

Special thanks go to E. Belli, R. Kersevan, K. Oide and F. Zimmermann for their precious support. This work was partly supported by the European Commission under HORIZON 2020 Integrating Activity project ARIES, Grant agreement nº 730871, and by INFN National committee through the ARYA project.

## REFERENCES


[1] A. Abada *et al.*, “FCC-ee: The Lepton Collider,” *Eur. Phys. J. ST*, vol. 228, no. 2, pp. 261–623, 2019.

[2] B. Härer, B. Holzer, Y. Papaphilippou, and T. Tydecks, “Status of the FCC-ee Top-Up Booster Synchrotron,” no. CERN-ACC-2018-111, p. MOPMF059. 3 p, 2018.

[3] M. Migliorati *et al.*, “Collective Effects in the Booster Synchrotron,” FCC Week 2019, Brussels, Belgium, 2019.

[4] A. Drago, “Feedback Systems for FCC-ee,” in *Proceedings, 58th ICFA Advanced Beam Dynamics Workshop on High Luminosity Circular $e^+e^-$ Colliders: United Kingdom*, 2017.

[5] “CERN IW2D Code.” `https://twiki.cern.ch/twiki/bin/view/ABPComputing/ImpedanceWake2D`.

[6] O. Henry and O. Napoly, “The Resistive Pipe Wake Potentials for Short Bunches,” *Part. Accel.*, vol. 35, pp. 235–248, 1991.

[7] E. Shaposhnikova, “Signatures of Microwave Instability,” Tech. Rep. CERN-SL-99-008-HRF, Feb 1999.

[8] “CERN BLonD Code.” `https://blond.web.cern.ch`.

[9] D. Boussard, “Observation of Microwave Longitudinal Instabilities in the CPS,” Tech. Rep. CERN-LabII-RF-INT-75-2, CERN, Geneva, Apr 1975.

[10] R. H. Helm, M. J. Lee, P. L. Morton, and M. Sands, “Evaluation of Synchrotron Radiation Integrals,” *IEEE Transactions on Nuclear Science*, vol. 20, pp. 900–901, June 1973.

[11] F. J. Sacherer, “Transverse Bunched Beam Instabilities - Theory,” *Conf. Proc.*, vol. C740502, pp. 347–351, 1975.

[12] “CERN DELPHI Code.” `https://twiki.cern.ch/twiki/bin/view/ABPComputing/DELPHI`.

[13] K. Y. Ng, *Physics of Intensity Dependent Beam Instabilities*. World Scientific, 2005.

[14] A. Drago *et al.*, “High Current Multibunch Operation at DAΦNE,” in *Proceedings of the 2001 Particle Accelerator Conference*, vol. 5, pp. 3543–3545, 2001.

# LANDAU DAMPING WITH ELECTRON LENSES

V. Gubaidulin*, O. Boine-Frankenheim[1], TU Darmstadt, 64289 Darmstadt, Germany
V. Kornilov, GSI Helmholtzzentrum, 64289, Darmstadt, Germany
E. Metral, CERN, CH-1211 Geneva, Switzerland
[1]also at GSI Helmholtzzentrum, 64289 Darmstadt, Germany

*Abstract*

Electron lenses provide an incoherent betatron tune spread for Landau damping of transverse coherent beam instabilities. We investigated the effect of the transverse electron beam size and shape for Landau damping with an electron lens. Another point of interests is Landau damping provided by a pulsed electron lens with homogeneous transverse beam profile. This type of electron lens is developed for space-charge compensation in SIS18.

## INTRODUCTION

Impedance driven transverse beam instabilities in hadron synchrotrons are damped by either an active feedback system or passive mitigation via Landau damping [1] due to dedicated Landau octupole magnets.

For high energy and high-intensity synchrotrons a number of proposals of alternative sources of Landau damping have been proposed [2, 3]. In this contribution, we are comparing stability boundaries from dispersion relations for an electron lens proposed in [2] with our simulation results. In addition, we will analyse Landau damping from a pulsed electron lens [4].

We compare the stability boundaries obtained from the dispersion relations with the ones obtained from particle tracking simulations using an effective impedance.

Table 1: LHC and FCC-hh parameters

| | LHC | FCC |
|---|---|---|
| Circumference, C [km] | 27 | 100 |
| Beam energy, E [GeV] | 7 | 50 |
| Average beta function, $\beta_{\text{avg}}$ [m] | 72 | 140 |
| Betatron tune, $Q_x$ | 59.31 | 111.31 |
| Betatron tune, $Q_y$ | 63.32 | 109.32 |
| Synchrotron tune, $Q_s$ | $2.2 \cdot 10^{-3}$ | $1.2 \cdot 10^{-3}$ |
| Number of octupoles, $N_{\text{oct}}$ | 168 | $\approx 4200$ |

### *Landau damping due to octupole magnets*

From the dispersion relations, it is possible to obtain an estimation of the stability area due to Landau damping for the given tune spread. For octupole magnets the incoherent betatron tune spread is linear with amplitude:

$$\Delta Q_x = a_{xx} J_x/\epsilon_x + a_{yx} J_y/\epsilon_x,$$
$$a_{xx} \propto N_{oct} I_{\text{oct}} \epsilon_{\text{n}}/\gamma^2$$

where $I_{\text{oct}}$ is octupole current, $\epsilon_{\text{n}}$ – normalized emittance, $\gamma$ – relativistic gamma, $N_{\text{oct}}$ – number of octupoles.

Assuming that FCC-hh would use LHC-like octupoles one can obtain for the parameters given in table 1 that FCC-hh would need $\approx 25$ times the number of octupoles currently used in the LHC operation to obtain the same order of incoherent betatron tune spread. (See Fig. 1.)

For this betatron tune spread we estimate the stability of the beam in the FCC-hh due to Landau damping from the dispersion relation. (See Fig. 2.) For the case of the rigid mode and two-dimensional betatron tune spread dependent on the transverse amplitudes the dispersion relation has been derived by F. Ruggiero and J.S. Berg [5]:

$$1 = -\Delta Q_{\text{coh}} \int_0^\infty dJ_x \int_0^\infty dJ_y \frac{J_x \dfrac{\partial \psi(J_x, J_y)}{\partial J_x}}{Q - Q_x(J_x, J_y)}, \tag{1}$$

where $J_x$, $J_y$ – transverse action variable, $\psi(J_x, J_y)$ – particle distribution function.

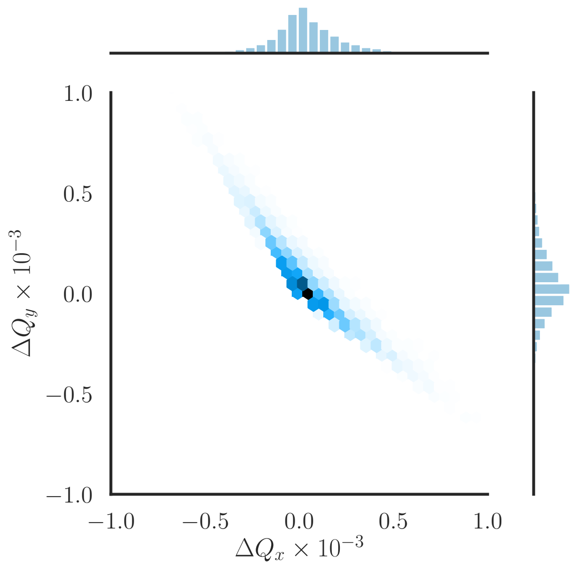


Figure 1: Tune spread for LHC-like octupoles with $Q_s = 1.2 \cdot 10^{-3}$, $\xi_{x,y} = 0$ and rms tune spread $\delta Q_{\text{rms}} \approx 2.1 \cdot 10^{-4}$.

### *Landau damping due to an electron lens*

Electron lenses have been proposed as a potential Landau damping source [2]. An electron lens creates a non-linear dependence of the incoherent betatron tunes on the transverse amplitudes:

* gubaidulin@temf.tu-darmstadt.de

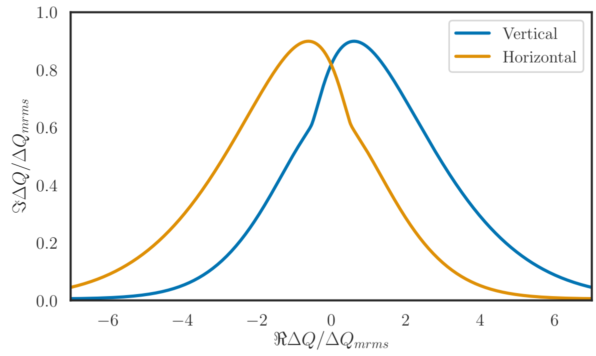


Figure 2: Stability diagram for LHC-like octupoles in vertical and horizontal plane.

$$\Delta Q_x \propto \delta Q_{\max} \iint \left( \frac{\int_0^r j_e(r')r'dr'}{r^2} \right) \left( \frac{\sin^2 \phi_x}{(2\pi)^2} \right) d\phi_x \, d\phi_y, \tag{2}$$

where $\delta Q_{\max}$ – maximal tune shift, $r^2 = 2J_x \sin^2 \phi_x + 2J_y \sin^2 \phi_y$, $j_e(r)$ – transverse current density distribution of an electron beam, $\phi_x$, $\phi_y$ – betatron phases.

In this contribution, we will focus on the case of Gaussian current distribution of $j_e(r)$. Tune shift from the electron lens is at it largest for particles with $J_x, J_y = (0,0)$ and it's decreasing with larger amplitude resulting in a diamond shape for the electron and proton beams of equal size. For this case maximal tune shift will be expressed as (See Fig. 3):

$$\delta Q_{\max} = \frac{I_e}{I_A} \frac{m_e}{m_p} \frac{\sigma_x^2}{\sigma_e^2} \frac{L_e}{4\pi\epsilon_n} \frac{1 \pm \beta_e}{\beta_e}, \tag{3}$$

where $I_e$ is electron beam current, $I_A = \frac{m_e c^3}{e}$ 17kA – Alfven current, $m_e$, $m_p$ – masses of electron and proton, $\sigma_e$, $\sigma_x$ – electron and proton beam rms sizes, $\beta_e$ – relativistic beta of the electron beam. (It is assumed here that $\beta_p \approx 1$ for the proton beam.) [2]

Let us fix the maximum tune shift $\delta Q_{\max}$ and vary the electron beam size $\sigma_e$. To give an intuition of how the tune distribution will be changing let us look at two asymptotic cases. First, let $\sigma_e \ll \sigma_p$. In this situation, most particles will experience a weak Coulomb force and their tunes will be close to the unperturbed tune. Second, if $\sigma_e \gg \sigma_p$, every particle of the proton beam is lying on the center of the electron beam, thus these particles will be experiencing the linear part of the force corresponding to $\delta Q_{\max}$. With these examples it is clear that changing the electron beam size leads to a redistribution of particles between $(0,0)$ and $(\delta Q_{\max}, \delta Q_{\max})$. We can study how this affects the stability area using the dispersion relation from Eq. 1. This leads us to plot from Fig. 4, from which we can conclude that decreasing the rms size of the electron beam $\sigma_e$ changes the stability area significantly towards a enlargement of the stable area for positive real coherent tune shifts. Increasing $\sigma_e$ leads only to marginal benefits and $\sigma_e = 0.9\sigma_x$ is the optimal size ratio from the analytical estimation.

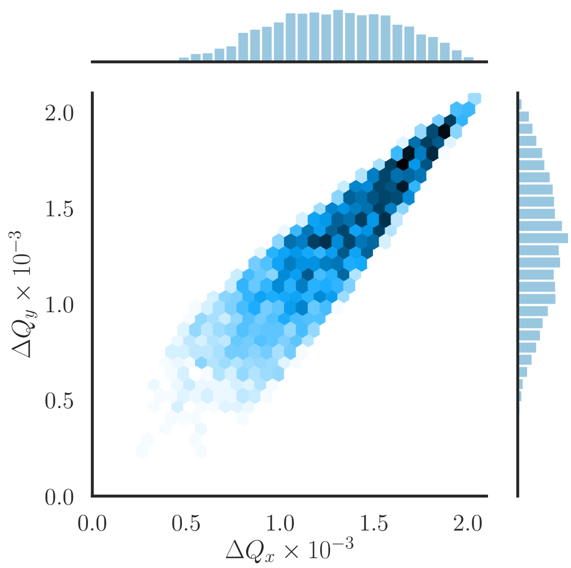


Figure 3: Tune spread from an electron lens with $\sigma_e = \sigma_x$, $\Delta Q^{\max}_{x,y} = 2 \cdot 10^{-3}$ with $Q_s = 1.2 \cdot 10^{-3}$, $\xi_{x,y} = 0$ and rms tune spread $\delta Q_{\text{rms}} \approx 3.5 \cdot 10^{-4}$.

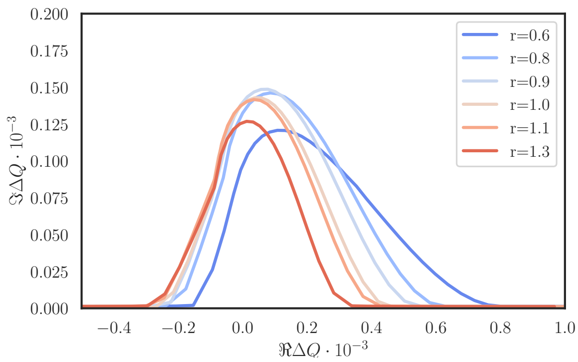


Figure 4: Stability diagram with electron lens beam sizes $\sigma_e$ from, $r = 0.6 - 1.3$ of proton beam sizes $\sigma_x$.

## *Pulsed electron lens*

For space-charge compensation, a pulsed electron lens has been proposed for SIS18 at GSI [4]. This type of an electron lens also creates incoherent betatron tune spread (Fig. 5), that depends on the longitudinal action $J_z$. This is similar to Radio Frequency Quadrupole proposed as a source of Landau damping for FCC-hh [3]. For tune spread depending on the longitudinal amplitude we are using the J.S.Berg and F.Ruggiero dispersion relation [5]:

$$1 = \int_0^\infty \Delta Q_{\text{coh}} \frac{\psi(J_z)|J_z|^m}{Q_x - Q(J_z) - mQ_s} dJ_z, \tag{4}$$

where $J_z$ – longitudinal action variable, $m$ – mode number (in this contribution we are always assuming $m = 0$).

In the next section, we are going to establish a method to reconstruct stability diagrams from particle tracking simulation and compare the results from simulation to the solution of the dispersion relations. Stability diagrams in this study are normalised by rms tune spread to compare all three sources as if they had the same rms tune spread.

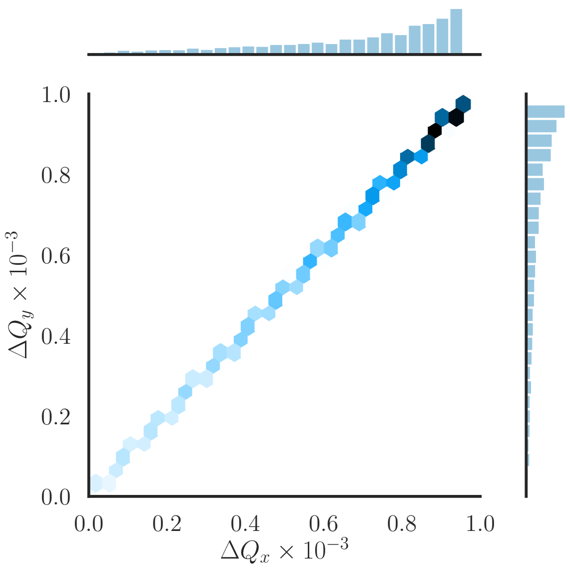


Figure 5: Tune spread from an pulsed electron lens with $\sigma_e = 4\sigma_x$, $\Delta Q^{\max}_{x,y} = 10^{-3}$ with $Q_s = 1.2 \cdot 10^{-3}$, $\xi_{x,y} = 0$, $\delta Q_{\mathrm{rms}} \approx 2.4 \cdot 10^{-4}$. Transverse distribution is assumed to be homogeneous.

## STABILITY DIAGRAM RECONSTRUCTION

It is necessary to confirm with particle tracking simulations that the actual stability area would correspond to the one obtained from an analytical estimation of dispersion relations. Typically, this is done with Beam Transfer Functions(BTFs) both in experiments and in simulations. We will instead employ an effective impedance model to excite a rigid head-tail mode with a given $\Re\Delta Q$, $\Im\Delta Q$ similar to what has been done in [6]. Using this model allows us to follow the particle offset evolution and intrabunch motion during the simulation for all selected coherent tune shifts ($\Re\Delta Q, \Im\Delta Q$) and determine individually for each pair the stability of the beam due to Landau damping. This method corresponds to the use of a transverse damper as an impedance source to excite an instability experimentally.

The effective impedance [7]

$$\Delta Q = -\frac{i\beta c^2}{2Q\omega_0^2 E_0}\frac{eI_0}{C}Z^{\perp}$$

, where $C$ is the machine circumference, I is the beam current; is implemented as a kick in the tracking code

$$\Delta x' = 4\pi\Im\Delta Q_{\mathrm{coh}}\bar{x}' + 4\pi\Re\Delta Q_{\mathrm{coh}}\frac{\bar{x}}{\hat{\beta}_x} \tag{5}$$

$\bar{x}'$ and $\bar{x}$ are the offset and its derivative averaged over all particles in the bunch and taken at the position of the kick. Within the above implementation the kick we only excite rigid ($k = 0$) bunch modes, which allows a direct comparison to the dispersion relations given by Eq. 1 and Eq. 4.

### *Reconstructed stability diagrams for octupoles and electron lens*

The PyHEADTAIL particle tracking code with $\approx 30000$ macroparticles is used to track the development or damping of the instability driven by the effective impedance for FCC-hh parameters. In order to determine if for given parameters the beam is stable or not, we used two simple criteria. First, if the maximal beam offset observed during simulation is greater than a given threshold ($5\mu m$), the point is considered to be unstable. Second, if the beam offset evolution is exponential, it is also considered to be unstable even if the amplitude did not reach the threshold during the run.

In Fig. 6 we can observe the reconstructed stability diagram for LHC-like octupoles with rms tune spread $\Delta Q_{\mathrm{rms}} \approx 2.1 \cdot 10^{-4}$ showed in Fig. 1. From the simulations, we are only showing coherent tune shifts for which the beam is stable. The agreement between the theoretical stability boundary and one obtained in particle simulation is achieved.

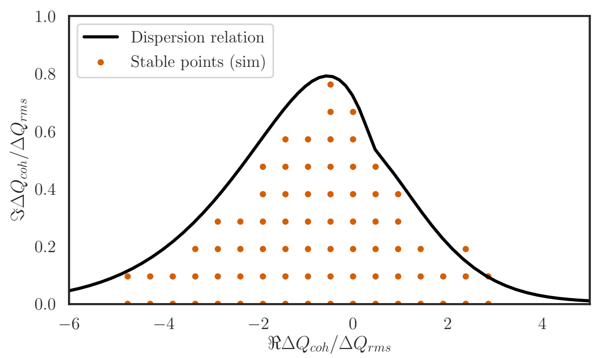


Figure 6: Stability diagram reconstruction for LHC-like octupoles using FCC parameters for the vertical plane($\xi_{x,y} = 0$, $Q_s = 1.2 \cdot 10^{-3}$), $\Delta Q_{\mathrm{rms}} = 2.1 \cdot 10^{-4}$. Solid line is the theoretical stability boundary and each point is obtained from particle tracking simulation.

In Fig. 7 we present the result of reconstructing stability boundary for an electron lens with $\delta Q_{\max} = 0.002$ and $\delta Q_{\mathrm{rms}} \approx 3.5 \cdot 10^{-4}$ and matched size $\sigma_e = \sigma_x$. This demonstrates that electron lens is a source of betatron tune spread that leads to Landau damping. The stability area normalised by the rms tune spread for electron lens is smaller than for octupole magnets but electron lens can achieve larger rms tune spread by scaling $\Delta Q_{\max}$ up to 0.01 [2].

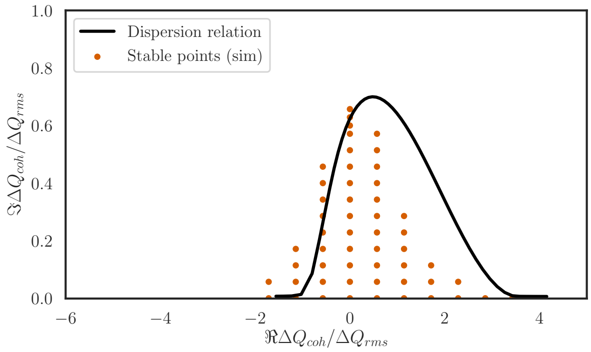


Figure 7: Stability diagram reconstruction for electron lens matched to the proton beam size($\xi_{x,y} = 0$, $Q_s = 1.2 \cdot 10^{-3}$). Solid line is the theoretical stability boundary and each point is obtained from particle tracking simulation.

Let us compare results from solving dispersion relation from Eq. 4 to the results of the simulation with a pulsed lens with homogeneous transverse profile. Electron beam sizes was chosen to be $\sigma_e = 4\sigma_x$ in order to ensure that tune spread during the simulation runs comes from the longitudinal amplitude only. In Fig. 8 we can see that similarly to an RFQ [8, 9] stability boundary is asymmetric with respect to $\Re\Delta Q_{coh} = 0$ line but contrary to the RFQ case pulsed electron lens provides the same stability diagram in both $x$ and $y$ planes. It is possible to overcome this asymmetry by trying a different transverse beam profile for the pulsed lens or combining it with octupoles. We have achieved a qualitative agreement between our simulation with the pulsed electron lens and existing dispersion relation theory.

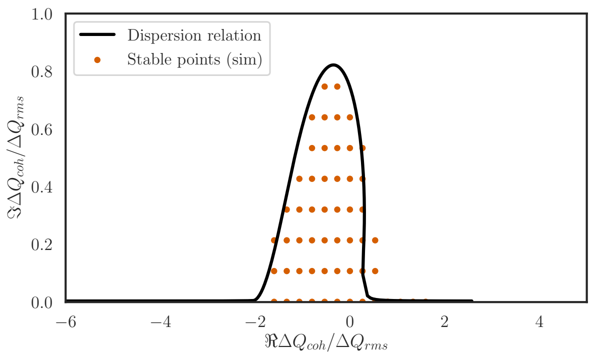


Figure 8: Stability diagram reconstruction for pulsed electron with $\sigma_e = 4\sigma_x$, $\Delta Q^{\max}_{x,y} = 10^{-3}$ with $Q_s = 1.2 \cdot 10^{-3}$, $\xi_{x,y} = 0$, $\delta Q_{\mathrm{rms}} \approx 2.4 \cdot 10^{-4}$. Transverse distribution is assumed to be homogeneous. Solid line is the theoretical stability boundary and each point is obtained from particle tracking simulation.

## CONCLUSION

For an effective instability model stability diagrams were reconstructed from particle tracking simulation. We only account for rigid bunch oscillations and zero chromaticity. Additionally, the tracking studies account for the dynamic change in beam size and betatron tune spread over the course of the simulation, which can affect Landau damping[10]. In both [6, 10] it has been shown that the agreement between particle tracking and dispersion relations, as expected, is not perfect and the latter overestimates the stability boundary in comparison to the former, which agrees with our results.

For a standard electron lens, we showed that relative transverse size of the electron beam $\sigma_e$ can serve as an additional knob to adjust stability boundary due to Landau damping. According to the dispersion relation, the relative beam size slightly smaller than 1.0 ($\sigma_e/\sigma_x \in (0.8, 1.0)$) provides a marginal benefit over the matched beams.

Our simulations show that both DC and pulsed electron lenses serve as a source of betatron tune spread that leads to the stabilisation of the beam due to Landau damping. It has been demonstrated that electron lens with an incoherent betatron tune spread of the same order as octupoles provides similar stability area in the complex tune shift space. Importantly, betatron rms tune spread from electron lens even with the modest maximal tune shift of $\Delta Q_{\max} = 0.002$ is already two times larger than the tune spread from $\approx 4200$ LHC-like octupoles.

## OUTLOOK

Further research into the discrepancy between DC electron lens simulation and dispersion relation results is necessary.

Firstly, for SIS18/SIS100 at GSI the incoherent space charge tune spread is significant. We plan to use the same method to study the stability boundary in the presence of space charge. Additionally, this method could be used to estimate the stability boundary for a combination of octupoles and RFQ or pulsed electron lens.

Secondly, the study of higher-order modes is especially necessary for the pulsed electron lens and the RFQ because dispersion relation in Eq.4 has a $|J_z|^m$ dependence on head-tail mode number $m$ that implies a significant difference between stability diagrams for different modes.

## REFERENCES

[1] Lev Landau. “On Oscillations of electron plasma.” In: *J. Phys. USSR* 10.25 (1946).

[2] V. Shiltsev et al. “Landau Damping of Beam Instabilities by Electron Lenses.” In: *Physical Review Letters* 119.13 (Sept. 2017), p. 134802.

[3] A. Grudiev. “Radio frequency quadrupole for Landau damping in accelerators.” In: *Physical Review Special Topics - Accelerators and Beams* 17.1 (Jan. 2014), p. 011001.

[4] O. Boine-Frankenheim and W.D. Stem. “Space charge compensation with pulsed electron lenses for intense ion beams in synchrotrons.” In: *Nuclear Instruments and Methods in Physics Research Section A: Accelerators, Spectrometers, Detectors and Associated Equipment* 896 (July 2018), pp. 122–128.

[5] J. Scott Berg and Francesco Ruggiero. “Stability diagrams for Landau damping.” In: *Proceedings of the 1997 Particle Accelerator Conference (Cat. No.97CH36167)*. Vol. 2. IEEE, 1998, pp. 1712–1714.

[6] V. Kornilov, O. Boine-Frankenheim, and I. Hofmann. “Stability of transverse dipole modes in coasting ion beams with nonlinear space charge, octupoles, and chromaticity.” In: *Physical Review Special Topics - Accelerators and Beams* 11.1 (2008), p. 014201.

[7] K. Y. Ng. *Physics of Intensity Dependent Beam Instabilities*. WORLD SCIENTIFIC, Dec. 2005.

[8] M. Schenk et al. “Analysis of transverse beam stabilization with radio frequency quadrupoles.” In: *Physical Review Accelerators and Beams* 20.10 (Oct. 2017), p. 104402.

[9] M. Schenk et al. “Experimental stabilization of transverse collective instabilities in the LHC with second order chromaticity.” In: *Physical Review Accelerators and Beams* 21.8 (Aug. 2018), p. 084401.

[10] V. Kornilov and O. Boine-Frankenheim. “Landau damping due to octupoles of non-rigid head–tail modes.” In: *Nuclear Instruments and Methods in Physics Research, Section A: Accelerators, Spectrometers, Detectors and Associated Equipment* 951 (2020), p. 163042.

# TAILORED METAMATERIAL-BASED ABSORBERS FOR HIGH ORDER MODE DAMPING

M. R. Masullo*, V. G. Vaccaro, INFN Naples Unit, [80128] Napoli, Italy
N. Chikhi, A. Passarelli[1], A. Andreone[1], Physics Department,
University of Naples "Federico II", [80128] Napoli, Italy
[1]also at INFN Naples Unit, [80128] Napoli, Italy

*Abstract*

In modern particle accelerators, satisfying the desired beam properties (high currents, high luminosities, etc) increasingly implies limiting the total beam coupling impedance, which depends on the machine and the parameters of the circulating beams. A number of different reduction techniques have been proposed during the years depending on the specific applications, ranging from higher order modes (HOM) damping to solutions entailing high electrical-conductivity coatings of the pipe. This paper investigates the use of metamaterial-based absorbers for sensibly reducing or nearly cancelling the HOM contribution to the impedance. We design and fabricate sub-wavelength two-dimensional metallic resonant structures based on the split ring resonator (SRR) geometry that can be employed as mode dampers in accelerating structures. Experimental results inside a pillbox cavity well agree with full wave electromagnetic simulations. In this work we present the first results on a SRR geometry tailored for LHC collimators. We showed how metamaterials can be a valid alternative for impedance mitigation in experimental devices commonly operating along a particle beam line.

## INTRODUCTION

The last generation accelerators require high quality beams with larger beam currents and luminosity values than what is currently achievable. To fulfill these requirements, beam instabilities must be avoided and/or limited optimizing machine parameters and studying the particle dynamics [1]. An important parameter for the study of the forces acting on beam is the beam-coupling impedance. It is defined as the integral over the normalized Fourier transform of the electro-magnetic (EM) force along the particle trajectory [2].

Following this definition, the impedance value depends on the surrounding chamber and on the beam velocity only [3]. The complexity of the vacuum vessel, with different cross-section variations due to the presence of several components and the diversity of constituent materials, gives different adding contributions to the total machine impedance [3]. In most cases, the discontinuities in the geometry behave like resonant (parasitic) cavities, where higher order modes (HOMs), excited by the travelling beam, may remain trapped increasing the total machine impedance and leading to excessive power losses. The use of HOM suppressors is crucial to mitigate the coupling impedance growing, to preserve the beam dynamics and reduce the relevant heat load. Each of these modes is described by a specific quality factor Q, a resonance frequency $f_{\mathrm{res}}$ and a shunt impedance $R_{\mathrm{sh}}$ [4]. Techniques oriented at the reduction of $R_{\mathrm{sh}}$ and/or Q are commonly referred to as mode damping strategies. In real cavities, HOM-removal mechanisms can be realized using external waveguides [5], unconventional resonant dielectric [6] or hybrid (metallo-dielectric) [7, 8] structures. In parasitic cavities, conventional approaches more often entail the use of dispersive or resistive materials acting as microwave absorbers when placed in specific points of the structure itself. Our work explores the possible use of metamaterials as an alternative and efficient mode damping strategy to be exploited for the improvement of the beam quality in future accelerators. Metamaterials are artificial materials acquiring their properties from geometry rather than composition, using inclusions or small inhomogeneities as "meta-atoms" to produce an effective macroscopic behaviour. They are generally comprised of sub-wavelength metallic elements in periodic patterns and are proving to be capable to achieve control over reflection, absorption, and propagation of EM waves by geometry only and in a wide frequency range by combing devices of different geometries [9]. Moreover, since they usually possess inherently resonant features, metamaterials have been widely used in the past for the development of filters with a large out-of-band signal rejection [10]. In this context, metamaterials can be designed and tailored in order to specifically address the features of single accelerator components. Very recently, metamaterial structures have been also proposed for the development of high-power, high-gradient wakefield accelerators [11].

The present work aims to investigate the use of periodic arrays based on simple split-ring resonators (SRR) [12], which stand out for simplicity amongst other designs, as possible beam coupling impedance reducer devices. The insertion in particle accelerators of SRR-based metamaterials has already been theoretically studied, showing their impact on resistive-wall impedance both longitudinally and transversely [13]. Their impact on the electromagnetic response of a well known resonant structure, a pill-box cavity, has been numerically investigated and experimentally measured [14]. Starting from the results of our previous analysis, in the present work we explore SRR configurations to be located inside LHC collimators as ad-hoc resonant mode dampers.

* masullo@na.infn.it

## SPLIT RING RESONATORS IN PILLBOX CAVITY

SRRs are commonly used as unit cells of a periodic array formed by one or more concentric structures, each one interrupted by a gap (see Fig. 1(a)). When exposed to an external electromagnetic field, they have an inherently resonant response, which strongly depends on their dimensions. Due to the gap presence, dimensions of the SRRs are much lower than those of structures without gap and resonating at the same frequency [9]. The assembling of two or more rings in a row or in an array induces a coupling between adjacent "meta-atoms," which depends on their relative distance and orientation (see Fig. 1(b)). This coupling influences the intrinsic resonances by varying the Q-factor and/or the frequency values. The collective behavior is, therefore, a function of their dimensions and geometrical arrangement [15, 16].

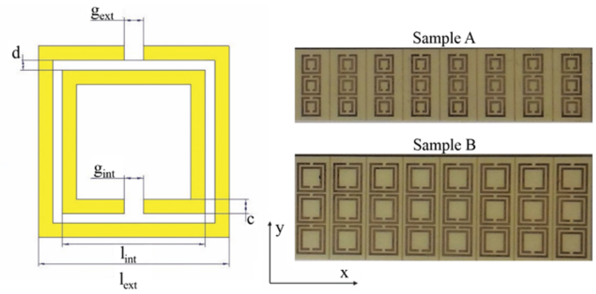


Figure 1: (a) Sketch of the metamaterial unit cell, consisting of a double square SRR ("meta-atom"). (b) SRR-based two-dimensional metamaterials realized on Alumina.

As a case study, we used an aluminum cylindrical pillbox cavity (see Fig. 2), which is well known from an analytical point of view. Due to the cylindrical symmetry of the pillbox, the mode contribution to the coupling impedance is given by the electric-field component along the cavity axis [17]. Therefore, in the following, we will focus on transverse magnetic (TM) modes only.

The analysis reported in this paragraph summarizes the work done in [14] and is useful as an introduction to what is described in the following paragraph.

In order to study the SRR impact on the pill-box EM response, we loaded the cavity with a metamaterial based on unit cells consisting of a thin (<5 $\mu$m) metallic layer having a squared double SRR strip geometry on polycrystalline Al2O3 (Alumina), with thickness 0.5. Structures based on them can then be easily realized in the microwave region using a standard PCB technology or any other lithography process.

Two-dimensional periodic SRR arrays have been fabricated having outer dimensions $l_{ext}$ very similar, 5 mm and 8 mm for samples A and B respectively, see Fig. 1(b). The SRR dimensions and geometrical arrangements have been chosen so that the metamaterial intrinsic operational frequency and the SRR array stop-band lay in the 1-5GHz band where the first TM modes of the pill-box cavity are clearly visible. This choice maximizes the SRR effect on the working resonances of the accelerating structure [18]. Complete parameters of the two investigated metamaterials are reported in [14].

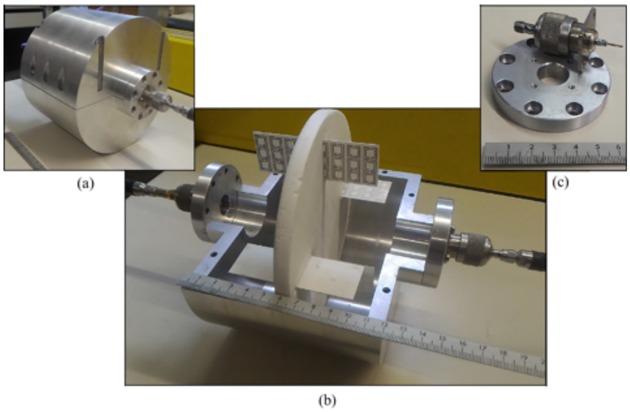


Figure 2: (a) The cylindrical pillbox cavity. (b) Open view of the SRR loaded cavity, where the input and output ports are shown. (c) Detail of the measurement antennas.

The commercial code CST Microwave Studio™ has been used to study the EM behavior of both the pillbox cavity and the SRR-based structures. Specifically: (i) Eigenmode solver for the evaluation of the pillbox resonant modes and field distributions, (ii) Frequency and Time domain solvers for the analysis of the scattering parameters of single and coupled SRRs first, and then cavity without and with metamaterial absorbers. The EM behaviour of single and coupled SRRs arranged in a planar array has been studied evaluating their reflection response to a plane wave incident along the y-direction with the magnetic field perpendicular to the ring plane and the electric field polarized along the direction parallel to the gap-bearing sides. This configuration has been chosen in order to have an EM field distribution similar to the one excited in the pill-box cavity used for the measurements (TM mode, see below).

Table 1: Single SRR resonance frequency $f_{res}$, stop-band (SB) array (3×8) and amplitude $A_s$ from simulated $S_{21}$ parameters.

| **Sample** | **A** | **B** |
|---|---|---|
| **$f_{res}$ SRR (GHz)** | 4.40 | 2.10 |
| **SB SRR (GHz)** | 4.18-4.39 | 2.01-2.28 |
| **$A_s$ SRR (dB)** | −18.6 | −21.4 |
| **$A_s$ array (dB)** | −26.0 | −35.0 |

The resonance frequency of single SRR, the stop-band (SB) for the arrays and the corresponding amplitude minima $A_s$ are calculated by means of full-wave analysis, looking at the scattering transmission parameter ($S_{21}$). Values are reported in Table 1. When compared to the corresponding single SRR, the main effect of the collective behaviour in each array is the appearance of a clear stop band, with multiple resonances starting at lower frequencies, and an increase in the power absorption testified by the larger $A_s$ values.

The cylindrical pillbox cavity used for the experimental analysis and loaded with the SRR arrays is shown in Fig. 2, with details of the input and output beam pipes and the antennas. It works in the range 1-5 GHz and the first five TM modes are the $TM_{010}$, $TM_{011}$, $TM_{012}$, $TM_{020}$, $TM_{021}$, which resonate at 1.54 GHz, 2.16 GHz, 3.38 GHz, 3.56 GHz and 3.89 GHz respectively [14]. Four identical arrays of SRRs are placed on a rigid support (made of Rohacell®), spaced by $\pi/2$ in azimuthal angle, with the SRR plane perpendicularly oriented with respect to the magnetic field and facing the lateral cavity wall at a distance of 10 mm. In the following text, the term "empty cavity" stands for the pillbox with the rigid support only.

The effect of metamaterial insertion on the EM response of the pillbox cavity has been measured looking at the scattering transmission and reflection parameters, $S_{21}$ and $S_{11}$ respectively. A 2-port Vector Network Analyser (VNA) Rohde & Schwarz ZNB 20 has been used in the frequency range between 1 and 5 GHz.

In Fig. 3, the measured $S_{21}$ parameter of the empty cavity is compared with the case loaded with the sample A, whose damping effect is clearly visible on the $TM_{021}$ resonance peak. The measured behaviour of the SRR-array in the cavity is in agreement with its foreseen transmission spectrum as shown in the same figure by the simulated $S_{21}$ curve in red. A clear lack in the transmission response of the stand-alone metamaterial is visible in correspondence of its working band [19].

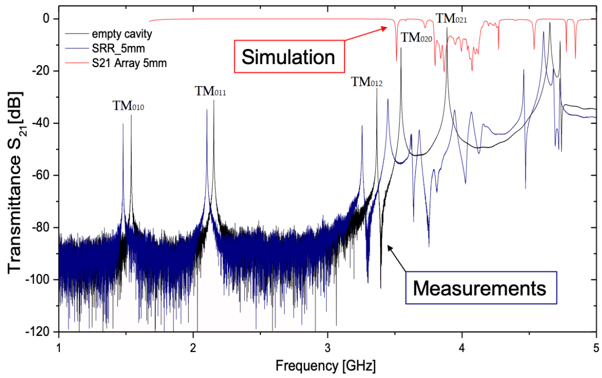


Figure 3: Measured $S_{21}$ transmission parameter of the empty pillbox cavity (black curve) and of the loaded with sample A (blue curve). The red curve shows the simulated $S_{21}$ response of the stand-alone SRR array.

For both SRR array samples in Fig. 4, a rigid shift towards lower values is clearly observed for all the resonance frequencies of the TM cavity modes. The effect is larger than the one given by the mere insertion of the dielectric substrates. Experimental data shows a change in frequency that goes from 2% to 8% in percentage. A "disruption" effect is visible in the spectrum (and highlighted in the squared box), where the intrinsic frequency bandwidth of the SRR

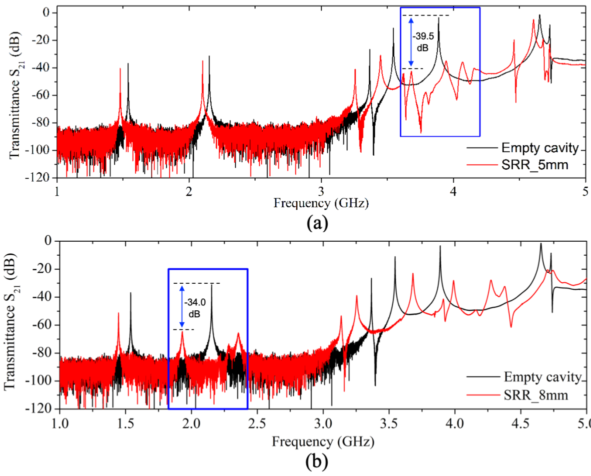


Figure 4: $S_{21}$ transmission parameter of the empty pillbox cavity (black curve), compared with the cavity loaded with the SRR-based metamaterial, (a) sample A (red curve), (b) sample B (red curve).

array overlaps a resonance of the empty cavity. Indeed, for both samples, the corresponding cavity resonance is damped and red-shifted as expected from electromagnetic simulations. In the cavity loaded with sample B (see Fig. 4(b)), the $TM_{011}$ mode decreases in amplitude ($-34$ dB), resonating now at 1.93 GHz. At the empty cavity design frequency (@2.15 GHz), the transmitted signal lies in the noise level, with an overall amplitude reduction of $-53$ dB. The same behaviour occurs for the $TM_{021}$ mode inserting sample A in the pillbox ($-39.5$ dB amplitude reduction and red shift to 3.68 GHz). Correspondingly, the signal level for the intrinsic mode drops to $-47.5$ dB @3.9 GHz, as shown in Fig. 4(a). Moreover, it is evident that sample B has a minor effect on the $TM_{021}$ mode too, since at that frequency the intrinsic SRR second order harmonic comes into play.

A comparative analysis of the empty and loaded cavity EM field mode distributions for some resonant modes is reported in [14]. This analysis demonstrated that far from their intrinsic frequency stop-band, SRRs have no influence on mode damping and the field mode patterns remain the same as its amplitude. However, approaching the SRR resonance region their influence is clearly visible. It is worthwhile to observe that the loss mechanism produced by the SRR array critically depends on the mode distribution [20] and consequently on metamaterial relative position inside the pillbox cavity.

Finally, we estimated the variation of the $R_{sh}$ values for the empty and loaded (with both samples A and B) pillbox cavity in correspondence of the $TM_{010}$, $TM_{011}$, and $TM_{021}$ modes by using the simulated $R_{sh}/Q$ ratios and resorting to the measured quality factors Q [14]. As expected, the insertion of the SRR array sample A (B) drastically reduces the shunt impedance, and the coupling impedance, for the mode $TM_{021}$ ($TM_{011}$) by a factor $10^2$ ($2 \times 10^1$). On the contrary, for the first $TM_{010}$ mode the shunt impedance is almost unchanged.

## TAILORED SPLIT RING RESONATORS IN LHC COLLIMATOR

Analysis done on a resonant cavity loaded with SRR arrays confirmed the possibility to damp specific cavity modes with metamaterials, so reducing the shunt impedance. Our studies showed how this loss mechanism critically depends on the resonator mode distribution. Next step has been the study of a possible use of this methodology in a real accelerator element: LHC collimators which are among the main contributors to the accelerator impedance. In this case the impedance exhibits many resonant peaks in a wide frequency range, between a few hundred MHz and 3 GHz [21]. Parasitic HOMs are created in the collimator tank, trapped between the sliding contacts as shown in Fig. 5. This is the slot region where ferrite blocks are normally located to damp HOMs. We studied mode distributions in this region performing CST simulations of a simplified collimator structure. For most modes the E-field is orthogonal to the slot, as in the example shown in Fig. 5(a) at 0.542 GHz. The H-field is parallel to the slot plane along the two orthogonal directions depending on the selected mode, see Fig. 5(b) at 0.542 GHz and Fig. 5(c) at 0.889 GHz.

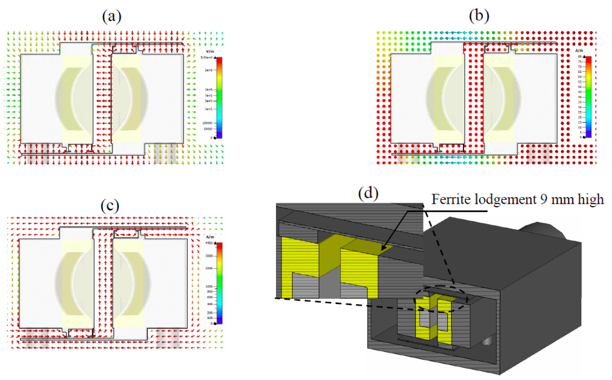


Figure 5: LHC collimator: simulation of (a) electric field at 0.542 GHz and of (b) and (c) magnetic field, at 0.542 GHz and 0.889 GHz respectively, distribution of different modes inside the structure. (d) Sketch of the section view highlighting the ferrite housing.

For the choice of right metamaterial, we have to keep in mind some constraints: the collimator geometry, the mode field distribution, the required operating frequency and the SRR working condition (H-field orthogonal to the ring area and E-field parallel to the ring gap). To fit all these requirements and guarantee a strong absorption response with a quite large bandwidth, we studied several SRR array samples working on ring geometry, their coupling and dielectric substrate.

Changing the substrate from Alumina to SL390 (a Kyocera type of ceramics with $\epsilon = 40$) and using a "Twin" configuration with no spacing between SRR, we obtained a larger bandwidth with a stronger response at lower frequencies without enlarging the ring dimension. The presence of a collimator trapped mode at around 0.2 GHz required to further extend the SRR electrical path. To this scope we analysed the behaviour of an inclined slab which allowed to further increase the rectangle small side length (see Fig. 6(a)). The simulated transmittance response of an SRR Twin sample is shown in Fig. 6(b). The metamaterial structure consists of two parallel arrays with long side length equal to 40 mm and 50 mm respectively, the same short side (20 mm) and inclined at an angle of 25°. A multi-band response, suitable for damping, is clearly visible in the range 0.2 – 0.35 GHz and at 0.42 – 0.53 GHz. Further studies of larger arrays with different lengths and coupling are under study in order to design an optimized metamaterial structure inside a real collimator.

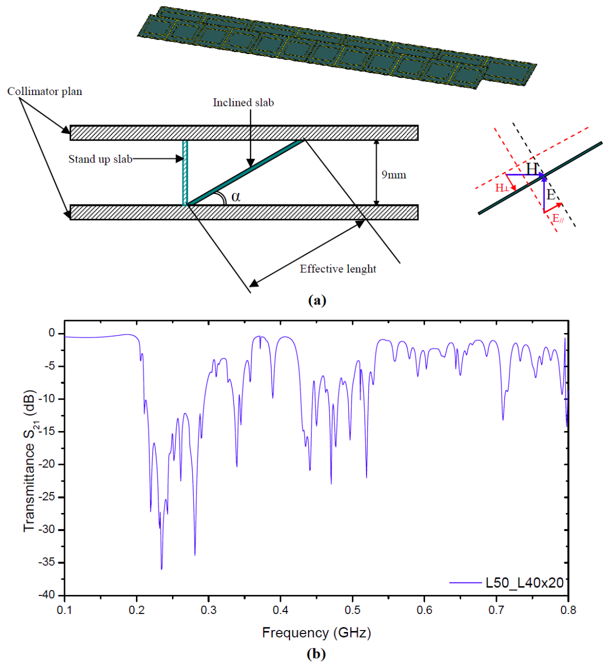


Figure 6: (a) A sketch of the "inclined" Twin configuration chosen for the SRR slab; (b) simulated transmittance at an angle of 25° with $L_{S1}$ = 50 mm, $L_{S2}$ = 40 mm, and W = 20 mm.

## CONCLUSION

The present work investigated the introduction of novel mode damping strategies based on metamaterials for the reduction of the coupling impedance between particles and vacuum pipe environment. Simulations and measurements performed on SRR-based structures inside a simple pillbox cavity show their potential use as single mode dampers in a wide frequency range.

We proved that the reduction of $R_{sh}$ and/or Q in resonant modes might be done through the insertion of tailored metamaterials acting as absorbers in specific positions inside the resonant cavities or, in general, in other critical components of an accelerating machine.

In this paper we proposed the use of a new configuration of SRR arrays (Twin structure) which can be easily adapted to different accelerator device geometries and mode distributions, as in the case of an LHC TCT collimator. A multi-band absorption response can be obtained using different size ring arrays. Furthermore, they can be easily positioned in the collimator using a smaller space with respect to ferrite.

Further studies, on the heat load and thermal response, also using different dielectric materials, of the Twin configuration inside real collimators are required to confirm our proposal.

## ACKNOWLEDGEMENTS

This research is carried out in the framework of a collaboration between INFN Naples (MICA project) and CERN, Geneva.

## REFERENCES

[1] A. W. Chao, *Physics of collective beam instabilities in high-energy accelerators*. 1993, ISBN: 9780471551843. http://www.slac.stanford.edu/~achao/wileybook.html

[2] L. Palumbo, V. Vaccaro, and M. Zobov, "Wake fields and impedance," no. physics/0309023. LNF-94-041-P, 331–390. 70 p, Sep. 1994. DOI: 10.5170/CERN-1995-006.331. https://cds.cern.ch/record/276437

[3] N. Mounet, "The LHC transverse coupled-bunch instability," p. 226, 2012. DOI: 10.5075/epfl-thesis-5305. http://infoscience.epfl.ch/record/174672

[4] D. M. Pozar, *Microwave engineering*. John Wiley & Sons, 2009.

[5] H. Padamsee, *RF superconductivity: Science, technology, and applications*, Jul. 2009.

[6] E. Di Gennaro *et al.*, "Mode confinement in photonic quasicrystal point-defect cavities for particle accelerators," *Applied Physics Letters*, vol. 93, no. 16, p. 164 102, 2008. DOI: 10.1063/1.2999581. https://doi.org/10.1063/1.2999581. https://doi.org/10.1063/1.2999581

[7] M. R. Masullo *et al.*, "Study of hybrid photonic band gap resonators for particle accelerators," *Microwave and Optical Technology Letters*, vol. 48, no. 12, pp. 2486–2491, 2006. DOI: 10.1002/mop.22016. https://onlinelibrary.wiley.com/doi/pdf/10.1002/mop.22016. https://onlinelibrary.wiley.com/doi/abs/10.1002/mop.22016

[8] E. D. Gennaro *et al.*, "Hybrid photonic-bandgap accelerating cavities," *New Journal of Physics*, vol. 11, no. 11, p. 113 022, Nov. 2009. DOI: 10.1088/1367-2630/11/11/113022. https://doi.org/10.1088%2F1367-2630%2F11%2F11%2F113022

[9] N. Engheta and R. W. Ziolkowski, *Metamaterials: physics and engineering explorations*. John Wiley & Sons, 2006.

[10] J. Garcia-Garcia *et al.*, "Microwave filters with improved stopband based on sub-wavelength resonators," *IEEE Transactions on Microwave Theory and Techniques*, vol. 53, no. 6, pp. 1997–2006, Jun. 2005, ISSN: 1557-9670. DOI: 10.1109/TMTT.2005.848828.

[11] X. Lu *et al.*, "Generation of high-power, reversed-cherenkov wakefield radiation in a metamaterial structure," *Phys. Rev. Lett.*, vol. 122, p. 014 801, 1 Jan. 2019. DOI: 10.1103/PhysRevLett.122.014801. https://link.aps.org/doi/10.1103/PhysRevLett.122.014801

[12] J. B. Pendry, A. J. Holden, D. J. Robbins, and W. J. Stewart, "Magnetism from conductors and enhanced nonlinear phenomena," *IEEE Transactions on Microwave Theory and Techniques*, vol. 47, no. 11, pp. 2075–2084, Nov. 1999, ISSN: 1557-9670. DOI: 10.1109/22.798002.

[13] A. Danisi, C. Zannini, A. Masi, R. Losito, and B. Salvant, "Theoretical analysis of metamaterial insertions for resistive-wall beam-coupling impedance reduction," no. CERN-ACC-2014-0191, 4 p, Jun. 2014. https://cds.cern.ch/record/1749084

[14] M. R. Masullo *et al.*, "Metamaterial-based absorbers for the reduction of accelerator beam-coupling impedance," *IEEE Transactions on Microwave Theory and Techniques*, vol. 68, no. 4, pp. 1340–1346, Apr. 2020, ISSN: 1557-9670. DOI: 10.1109/TMTT.2019.2957463.

[15] R. Marques, F. Martin, and M. Sorolla, *Metamaterials with Negative Parameters: Theory, Design, and Microwave Applications*, ser. Wiley Series in Microwave and Optical Engineering. Wiley, 2011, ISBN: 9781118211564. https://books.google.it/books?id=LItxc5Oenr4C

[16] P. Gay-Balmaz and O. J. F. Martin, "Electromagnetic resonances in individual and coupled split-ring resonators," *Journal of Applied Physics*, vol. 92, no. 5, pp. 2929–2936, 2002. DOI: 10.1063/1.1497452. https://doi.org/10.1063/1.1497452. https://doi.org/10.1063/1.1497452

[17] S. A. Heifets and S. A. Kheifets, "Coupling impedance in modern accelerators," *Rev. Mod. Phys.*, vol. 63, pp. 631–673, 3 Jul. 1991. DOI: 10.1103/RevModPhys.63.631. https://link.aps.org/doi/10.1103/RevModPhys.63.631

[18] A. Danisi, M. Grech, A. Masi, R. Losito, and N. Sammut, "FEM simulations of metamaterial impact on the longitudinal beam-coupling impedance of a rectangular beam pipe," in *2015 9th International Congress on Advanced Electromagnetic Materials in Microwaves and Optics (METAMATERIALS)*, Sep. 2015, pp. 49–51. DOI: 10.1109/MetaMaterials.2015.7342504.

[19] R. A. Shelby, D. R. Smith, S. C. Nemat-Nasser, and S. Schultz, "Microwave transmission through a two-dimensional, isotropic, left-handed metamaterial," *Applied Physics Letters*, vol. 78, no. 4, pp. 489–491, 2001. DOI: 10.1063/1.1343489. https://doi.org/10.1063/1.1343489. https://doi.org/10.1063/1.1343489

[20] P. Hulsmann, H. W. Glock, H. Klein, and M. Kurz, "Determination of field Strength and quality factor of heavily HOM damped accelerator cavities," 1992. http://cds.cern.ch/record/920645

[21] O. Frasciello, "Wake fields and impedance calculations of LHC collimators real structures," PhD thesis, U. Rome La Sapienza (main), 2015.

# TMCI, WHY IS THE HORIZONTAL PLANE SO DIFFERENT FROM THE VERTICAL ONE ?

T. Günzel*, ALBA-CELLS, Cerdanyola del Vallés, Spain

*Abstract*

Based on the recent work of R. Lindberg on transverse collective instabilities [1] it was observed that if the ratio of quadrupolar to dipolar impedance $\rho$ is equal to $-1$ there is no TMC-instability. This relationship is actually fulfilled by resistive wall (RW)-impedance on the horizontal plane in case of a flat vacuum chamber. HEADTAIL [2]-simulations were carried out to check if this observation can be confirmed. Additionally the effect of radial modes on the TMC-instability was studied.

## INTRODUCTION

The motion of particles in a single bunch can be described by the Vlasov equation as it was found by [3]. The linearisation of the Vlasov equation was solved by several authors [4–7]. In particular under the effect of dipolar impedance the transverse motion of particles of a bunch was described by [13] by decomposition into azimuthal and radial modes. In the meantime it was found that quadrupolar impedance is significant in many synchrotrons and has a sensible effect on the transverse motion [8–10]. Shortly after the discovery of its importance its effect was just superimposed on the dipolar mode detuning. However, R. Lindberg showed [1] that its effect has to be fully included into the dynamics of the bunch motion. Therefore the main purpose of this work is to demonstrate the difference between the Lindberg's description and the more naive descriptions in the past [11]. Whereas on the vertical plane the naive superposition of the dipolar and quadrupolar detuning corresponds quite well to Lindberg's result this is no longer true for the horizontal plane: a naive superposition of the mode detuning caused by dipolar and quadrupolar impedance indeed leads to a zero slope of mode 0 as expected, but mode 0 would still couple with mode -1, but in Lindberg's description the coupling is not compulsory. In order to support this observation HEADTAIL simulations were applied.

## SUMMARY OF LINDBERG'S MODE EVOLUTION THEORY

In [1] the Vlasov equation is linearized with the Planck-Fokker terms included but truncated to a matrix equation. In the following it is assumed that the TMCI is strong enough for the disregard of the Planck-Fokker terms. This leads to the following equation:

$$\Delta\omega^m a_p^m + \sum_{n,q} (D+Q)_{p,q}^{m,n} a_q^n = 0$$

with $\Delta\omega^m = \Delta\Omega + m\omega_s$ (with $\omega_s$ as synchrotron ang. frequency), with dipolar and quadrupolar matrix elements (with $C_{p,q}^{m,n} = \sqrt{(p+|m|)!(q+|n|)!}$, $\epsilon_m = (-1)^{m(1-\delta_{|m|}^m)}$, $\Lambda = \frac{I}{4\pi(E/e)}$ as intensity parameter, and $\sigma_\tau$ as bunch length):

$$D_{p,q}^{m,n} = \frac{\Lambda i^{m-n+1}\epsilon_m\epsilon_n}{\sqrt{p!q!}C_{p,q}^{m,n}} \int_{-\infty}^{\infty} Z_D^\beta(\omega) e^{-(\omega\sigma_\tau)^2} \left[\frac{\omega\sigma_\tau}{\sqrt{2}}\right]^{2p+|m|} \left[\frac{\omega\sigma_\tau}{\sqrt{2}}\right]^{2q+|n|} d\omega \tag{1}$$

with $Z_D^\beta(\omega)$ as $\beta$-weighted dipolar impedance and

$$Q_{p,q}^{m,n} = \frac{\Lambda i^{m-n+1}\sqrt{p!q!}}{C_{p,q}^{m,n}} \int_{-\infty}^{\infty} Z_Q^\beta(\omega) e^{\frac{-(\omega\sigma_\tau)^2}{2}} I_{p,q}^{m,n}(\omega) d\omega$$

with $Z_Q^\beta(\omega)$ as $\beta$-weighted quadrupolar impedance and the following abreviation:

$$I_{p,q}^{m,n}(\omega) = \int_0^\infty dr e^{-r} r^{\frac{-(|n|+|m|)}{2}} J_{m-n}(\omega\sigma_\tau\sqrt{2r}) L_p^{|m|}(r) L_q^{|n|}(r)$$

with $L_p^n(x)$ as general Laguerre-polynomials.[1] This formalism can be applied to any type of transverse impedance. In the first part we will focus on RW-impedance as it fulfills the requirement $\rho = -1$ in case of horizontal RW-impedance of a horizontally flat parallel-plate beam pipe geometry which is at least approximately very common in many synchrotrons. The parameters used in the simulations can be looked up in table 1.

Table 1: simulation parameters used

| parameter | value | unit |
|---|---|---|
| $E/e$ | 3 | GV |
| $\omega_s$ | 59.39 | kHz |
| $\sigma_\tau$ | 0.0154 | ns |
| $\kappa_\perp^{RW}$ | 4-11 | $\frac{kV}{pC}$ |
| $f^{bbr}$ | 1.5, 3, 5 | GHz |
| $Q^{bbr}$ | 2.3 | |
| $\beta_\perp \cdot R_\perp^{bbr}$ | 52.9, 100, 41.1, 17.3 | MΩ |

### *RW-impedance*

In order to study the evolution of the headtail-modes, the linearized and truncated Vlasov-equation is solved for a 2-mode system of two modes m=-1 and m=0 with radial mode number $r = 0$ (Higher radial modes are only discussed in the conclusions.). This was already done in the past by MOSES [13] for a pure dipolar impedance. In order to include the quadrupolar impedance the detuning slope related to it was added to the dipolar mode detuning computed

* tguenzel@cells.es

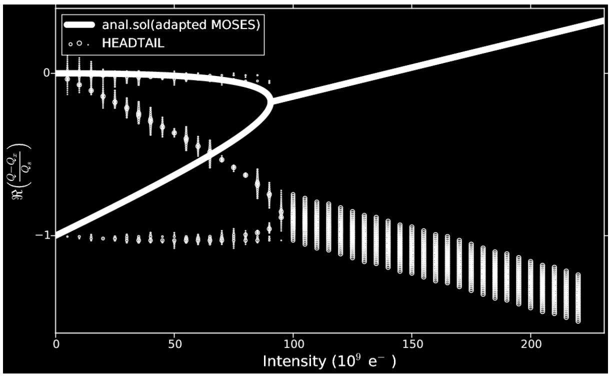


Figure 1: Imposing quadrupolar tune shift on the horizontal mode detuning from dipolar RW-impedance: For $\rho = -1$ mode 0 detuning is $\Delta\Omega \approx 0$, whereas the TMCI threshold is maintained.

by MOSES (this procedure is called adapted MOSES). All modes were correspondingly shifted, but the onset of the TMC-instability did not change (Fig. 1). So in case of horizontal impedance generated in a flat parallel-plate like beam pipe geometry the dipolar detuning of mode $m = 0$ was compensated by the quadrupolar detuning resulting in zero detuning of the mode. It seemed that mode m=0 still hit an instability if it met the mode m=-1, now with a strong positive slope. This was supported by measurements at the ESRF [11]. It had also the advantage that the measured threshold current allowed an estimation of the effective horizontal impedance even in the case of the zero slope. The mode evolution can be found from Vlasov's equation by the solution of the secular equation here demonstrated for the 2-mode system:

$$\begin{vmatrix} \Delta\Omega + \overbrace{A_H + A_Q}^{=0} & \alpha A \\ -\alpha A & \Delta\Omega + \omega_s + \frac{\tilde{\beta}}{2} A_H + A_Q \end{vmatrix} = 0 \qquad (2)$$

where $A \equiv A_H = -A_Q = \frac{I}{2(E/e)} \beta_\perp \kappa_\perp$ and $\alpha = \frac{\Gamma(3/4)}{\Gamma(1/4)\sqrt{2}}$ the coupling parameter and $\tilde{\beta} = 1/4$. $\kappa_\perp$ is the horizontal dipolar respectively quadrupolar RW-impedance's kick factor of the beam pipe. To account for the quadrupolar detuning, the term $A_Q$ was introduced which is the same as the dipolar detuning $A_H$ apart from the sign. Including $A_Q$ does not change the threshold which can be found by solving the secular equation and searching for the detuning $\Delta\Omega$ where it becomes complex. But this description was obviously not complete as HEADTAIL-simulations cannot reproduce this behaviour (Fig. 1). If, however, for the consideration of the quadrupolar impedance Lindberg's formalism is used the secular equation for the 2-mode system looks differently:

$$\begin{vmatrix} \Delta\Omega + \overbrace{A(1+\rho)}^{=0} & \alpha A(1-\rho) \\ -\alpha\, \overbrace{A(1+\rho)}^{=0} & \Delta\Omega + \omega_s + A\frac{1+7\rho}{8} \end{vmatrix} = 0 \qquad (3)$$

As one of the off-diagonal terms cancels out the coupling disappears. Both modes still approach and meet, but do not couple, they just pass through each other (Fig. 2). This is qualitatively an important change. A couple of questions pop up: Will there be no TMCI-threshold anymore on the horizontal plane ? How will it be possible to estimate the effective horizontal impedance from single-bunch detuning? Some answers can be found in the next section.

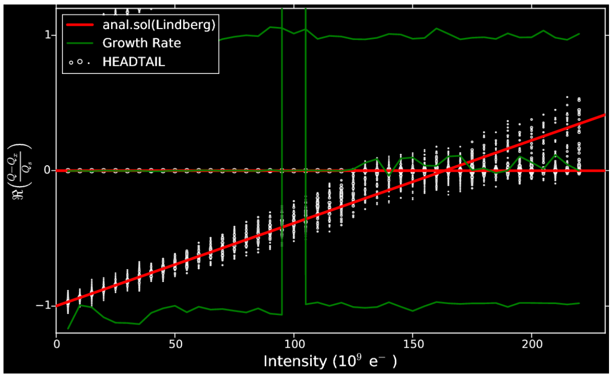


Figure 2: Applying Lindberg's full theory on horizontal RW-impedance leads to very good agreement with HEADTAIL. The growth rate (green) is not excited at the meeting point of the modes.

## *BBR-impedance*

In case of Broad Band Resonator (BBR) impedance (with $(R_\perp, Q, \omega_r)$ and $Q' = \sqrt{Q^2 - 0.25}$) the quadrupolar impedance is also of importance when the cross section changing beam pipes generating it are not circular. It will be shown that the modes principally behave the same as they do in case of horizontal RW-impedance if the rule $\rho = -1$ is imposed. So initially the spectral distribution of dipolar and quadrupolar impedance are assumed to be the same in order to demonstrate that qualitatively there is no difference to RW-impedance (Fig. 3). The secular equation for this case turns out to be very similar:

$$\begin{vmatrix} \Delta\Omega + \overbrace{B(1+\rho)}^{=0} & \alpha B(1-\rho) \\ -\alpha\, \overbrace{B(1+\rho)}^{=0} & \Delta\Omega + \omega_s + \rho B + B\frac{\tilde{\beta}}{2}(1-\rho) \end{vmatrix} = 0 \qquad (4)$$

where $\alpha = \frac{Re[sw(s)]}{\sqrt{2} Im[w(s)]}$, $\tilde{\beta} = \frac{Im[s^2 w(s)]}{Im[w(s)]} + \frac{\omega_r \sigma_\tau Q'}{Im[w(s)] Q \sqrt{\pi}}$ with $s = \frac{\omega_r \sigma_\tau}{Q}\left(\frac{i}{2} - Q'\right)$ and $w(s) = \frac{i}{\pi}\int_{-\infty}^{\infty} dt \frac{e^{-t^2}}{s+t}$. Finally $B = \frac{I}{2(E/e)} \beta_\perp \kappa_\perp$.

[1] Actually we stick to the mode expansion of [12].

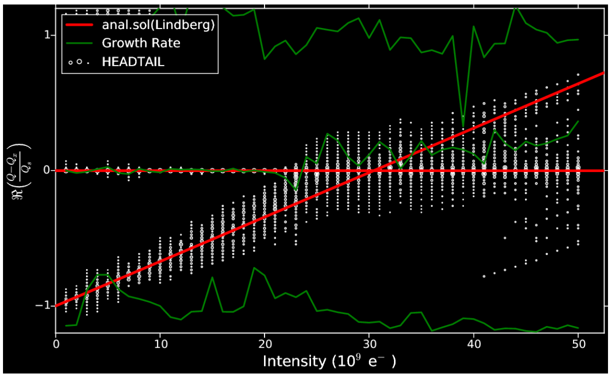


Figure 3: Modes under the effect on the common dipolar and quadrupolar BBR-impedance essentially show the same behaviour as in the RW-impedance case [14].

Before we discuss more involved cases for completeness the vertical mode detuning will be touched upon. As for vertical impedance $\rho \sim 0.5$, we are far away from the intriguing case $\rho = -1$. So in Lindberg's theory the 2 azimuthal modes m=-1 and m=0 couple (Fig. 4) as they do in adapted MOSES including the naively superimposed quadrupolar impedance. However, the threshold current can be different. But the difference between adapted MOSES (with naive superimposed quadrupolar detuning) and Lindberg's theory is rather small and above all does not go necessarily in the desired direction. So at this level of study Lindberg's theory does not give an explanation for the notorious failure of matching the measured vertical impedance in single bunch with the computed one found in electron synchrotrons [15]. The picture becomes a bit more complicated for higher frequency and with the consideration of radial modes, but this is out of scope of this work.

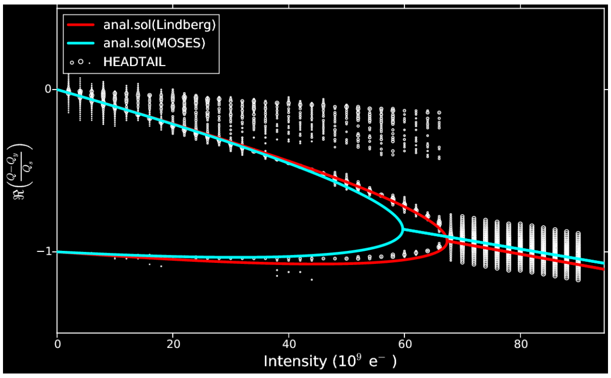


Figure 4: A low-frequency BBR-impedance HEADTAIL simulation agrees well with 2-mode case of Lindberg's theory (red), even better than with the adapted MOSES(cyan). For higher frequency the radial modes have to be considered which change the picture slightly.

Finally we assume that the spectral distribution of the dipolar impedance is different from the quadrupolar one since it is much more realistic but with still agreeing the kick factors. This is actually easy to achieve as BBR-impedance is described by 3 parameters to play with. So instead of requiring $\rho = \frac{Z_Q(\omega)}{Z_D(\omega)} = -1$ we only require

$$\rho = \frac{Z_Q^{eff}(\omega)}{Z_D^{eff}(\omega)} = -1 \tag{5}$$

We keep on studying the horizontal plane. In this case (at least) 2 BBR-models (here indexed with $H$ for horizontal and $Q$ for quadrupolar) are needed, one for the dipolar part and another one for the quadrupolar part. Including both in the formalism the secular equation for the eigenvalues amounts to ($B :\equiv B_H = -B_Q$):

$$\begin{vmatrix} \Delta\Omega + \overbrace{B_H + B_Q}^{=0} & B(\alpha_H + \alpha_Q) \\ B(-\alpha_H + \alpha_Q) & \Delta\Omega + \omega_s + B_Q + B_H\frac{\tilde{\beta}_H}{2} + B_Q\frac{\tilde{\beta}_Q}{2} \end{vmatrix} = 0 \tag{6}$$

It yields essentially two different cases, one where $\alpha_Q - \alpha_H < 0$ and the other one where $\alpha_Q - \alpha_H > 0$. In the first case $\alpha_Q < \alpha_H$, there is coupling (Fig. 5), whereas in

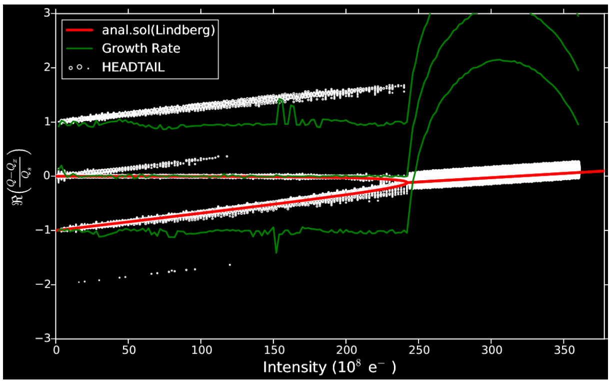


Figure 5: If the same effective dipolar and quadrupolar BBR-impedance of opposite sign but with different resonance frequencies are assumed modes can still couple as in this example ($\alpha_H > \alpha_Q$) confirmed by HEADTAIL modes (white) and their growth rate (green).

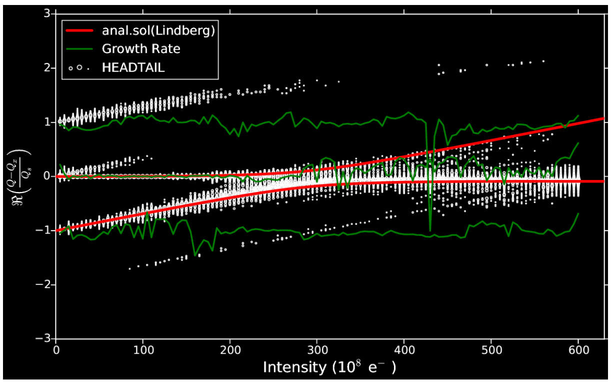


Figure 6: Essentially the same case as in the precedent figure, but different coupling coefficients of dipolar and quadrupolar BBR-impedance. Mode coupling no longer occurs as confirmed by the low growth rate (green).

the second case $\alpha_H < \alpha_Q$ (Fig. 6), there is no coupling anymore. One of most important consequences is that it is indeed possible that mode 0 and -1 meet without coupling. This seems also to be possible in more complex impedance models.

## CONCLUSIONS

Now impedance budgeting on the horizontal plane is rather different from the vertical plane. It cannot be relied upon the horizontal threshold anymore for the measurement of the effective impedance. There might be even no horizontal threshold at all.

Even the threshold on the vertical plane changes with respect to the results of MOSES. However, the change is much smaller than on the horizontal plane.

In this report only examples with low BB-resonance frequency are studied. At higher frequency there might be deviations between Lindberg's mode theory and HEADTAIL.

In the future the 2-mode example will be extended to larger number of modes including also radial modes. It was already observed that higher radial modes of m=-1 do not couple with m=0 in the pure case $\rho = -1$.

## ACKNOWLEDGEMENTS

I would like to thank Pol Pastells for his work on HEADTAIL-simulations, in particular for the acceleration of the execution of the computations. The author is grateful for the support of CERN (especially to Eirini Kouvkini-Platia and Michael Schenk) for the supply of a couple of analysis tools of HEADTAIL-simulations results, in particular for the mode detuning display.

## REFERENCES

[1] Ryan Lindberg, Fokker-Planck analysis of transverse collective instabilities in electron storage rings, PRAB 19,124402

[2] G. Rumolo, F. Zimmermann, Practical User Guide for HEADTAIL, CERN-SL-Note-2002-036 AP

[3] F. Sacherer, Methods for computing bunched beam instabilities, CERN/SI-BR/72-5

[4] A. Chao and Y. Yao, Transverse Instability excited by RF-deflecting Modes for PEP, PEP-note 321 (1979)

[5] G.Besnier, D.Brandt, B.Zotter, The Transverse Mode-Coupling Instability in Large Storage Rings, Part. Acc. 1985, Vol.17, p.51

[6] JL. Laclare, Bunched Beam Instabilities, CAS CERN-87-03, Vol.1, April 1987

[7] A. Burov, Nested Headtail Vlasov-solver PRST Accelerators and Beams, 17, 021007, 2014

[8] K. Yokoya, Resistive Impedance of Beam Pipes of General Cross section, Part. Acc. 41 1993, 221

[9] R. Nagaoka, Impact of resistive wall wakefields generated by low-gap chambers on the beam at the ESRF, PAC 2001, Chicago, p.3531-3533

[10] A. Chao, S. Heifets, B. Zotter, Tune shifts due to resistive vacuum chambers without circular symmetry, PRST AB Vol.5 111002 (2002)

[11] T.F. Günzel, The Transverse Coupling Impedance of the storage ring at the European Synchrotron Facility, PRST, Accelerators and Beams 9, 114402 (2006)

[12] T. Suzuki, Fokker-Planck Theory of Transverse Mode-Coupling Instability, Part. Acc. Vol.20 (1986), p.79

[13] Yong Ho Chin, User's guide for New Moses, CERN/LEP-TH/88-05

[14] Pol Pastells, Transverse Intra-bunch effects, ALBA internal report, April 2019

[15] Victor Smaluk, Impedance computations and beam-based measurements: A problem of discrepancy, NIM A 888 (2018) p.22-30

**Acknowledgements**

The workshop chairpersons are very thankful to:

• The members of the International Advisory Committee, who enthusiastically responded to the request for input in terms of subjects and speakers. It is thanks to their suggestions that the scientific program of the workshop turned out to be so rich and interesting;
• All the colleagues who accepted to serve as chairpersons of the different sessions. Their successful effort in running impeccably their sessions was highly appreciated;
• All the speakers and poster presenters for the high quality of their material;
• All the students who have shown their commitment in the poster competition session;
• Alessia Valenza and Hervé Martinet for the excellent logistics support;
• The CERN library team for their great assistance in setting up these proceedings.

**International Advisory Committee**

Riccardo Bartolini (DIAMOND, UK): Riccardo.Bartolini@physics.ox.ac.uk
Mike Blaskiewicz (BNL, USA): blaskiewicz@bnl.gov
John Byrd (ANL, USA): jbyrd@anl.gov
† Yong Ho Chin (KEK, Japan): yongho.chin@kek.jp
Micha Dehler (PSI, Switzerland): Micha.Dehler@psi.ch
Stefano De Santis (LBNL, USA): SDeSantis@lbl.gov
Alessandro Drago (LNF, Italy): alessandro.drago@lnf.infn.it
Giuliano Franchetti (GSI, Germany): G.Franchetti@gsi.de
Ubaldo Iriso (ALBA-CELLS, Spain): uiriso@cells.es
Maria Rosaria Masullo (INFN Naples, Italy): Masullo@na.infn.it
Elias Métral (CERN, Switzerland): Elias.Metral@cern.ch
Mauro Migliorati (Sapienza University of Rome, Italy): mauro.migliorati@uniroma1.it
Andrea Mostacci (Sapienza University of Rome, Italy): andrea.mostacci@uniroma1.it
Sergei Nagaitsev(FNAL, USA): nsergei@fnal.gov
Katsunobu Oide (KEK, Japan): oide@kek.jp
Stefania Petracca (University of Sannio, Italy): Petracca@sa.infn.it
Tatiana Pieloni (EPFL, Switzerland): Tatiana.Pieloni@epfl.ch
Ji Qiang (LBNL, USA): jqiang@lbl.gov
Qing Qin (IHEP, China): qinq@ihep.ac.cn
Lenny Rivkin (EPFL, Switzerland): leonid.rivkin@psi.ch
Giovanni Rumolo (CERN, Switzerland): Giovanni.Rumolo@cern.ch
Dmitry Shwartz (BINP, Russia): D.B.Shwartz@inp.nsk.su
Vittorio Vaccaro (University of Naples, Italy): vittorio.vaccaro@na.infn.it
Ursula Van Rienen (Rostock University, Germany): ursula.van-rienen@uni-rostock.de
Simon White (ESRF, France): simon.white@esrf.fr
Fatih Yaman (IYTE, Turkey): fatihyaman@iyte.edu.tr
Frank Zimmermann (CERN, Switzerland): Frank.Zimmermann@cern.ch
Mikhail Zobov (LNF, Italy): Mikhail.Zobov@lnf.infn.it

# A random collection of photographs from the Workshop


rkhotel Beau-Site
BEAU-SITE
BRASSERIE



CERN
TOBLERONE

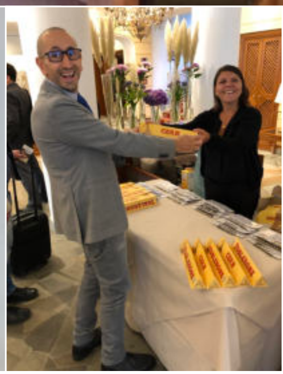
CERN



Matterhorn
GRAND TOUR
of Switzerland
STANFORD
UNIVERSITY


HAUS DARIOLI




24
Gletschergarten
Hängebrücke
Hängebrücke 10 min
Gletschergarten 25 min